EIGHTH INTERNATIONAL CONFERENCE

on

X-RAY OPTICS AND MICROANALYSIS

and

TWELFTH ANNUAL CONFERENCE

of the

MICROBEAM ANALYSIS SOCIETY

August 18-24, 1977

BOSTON SHERATON
BOSTON, MASSACHUSETTS

Additional copies of these and previous
Proceedings may be obtained from:

K. F. J. Heinrich
Analytical Chemistry Division
National Bureau of Standards
Washington, D.C. 20234

EIGHTH INTERNATIONAL CONFERENCE

on

X-RAY OPTICS AND MICROANALYSIS

and

TWELFTH ANNUAL CONFERENCE

of the

MICROBEAM ANALYSIS SOCIETY

August 18-24, 1977

BOSTON SHERATON
BOSTON, MASSACHUSETTS

PREFACE

It has been a great pleasure to play a part in organizing the Twelfth Annual Conference of the Society, which has the honor of hosting the VIII International Conference on X-Ray Optics and Microanalysis. We also have the benefit of holding our fourth joint meeting with EMSA.

It is obvious from the number of excellent papers that have been submitted this year that it will be one of our most successful meetings. However, we must give credit to Don Beaman and the session chairmen for bringing together the outstanding program, and to Paul Lublin for his guidance, assistance, and support in taking care of the necessary details for a successful meeting.

We want to thank the exhibitors for their contributions and, in particular, the National Science Foundation for their partial support of the invited speakers.

The preparation of these Proceedings is a formidable task and we are particularly indebted to Lynna Beaman, Elizabeth McCarthy, and Louise Valkenburg for their assistance with organization and typing.

Bob Ogilvie

Dave Wittry

MICROBEAM ANALYSIS SOCIETY

HONORARY MEMBERS

L. L. Marton
Museum of History and Technology
Room 5025
Smithsonian Institution
Washington, D. C. 20560

Raymond Castaing
University of Paris
Faculte des Sciences
Orsay, France

I. B. Borovskii
142432 Chernogolovka Moscow Reg.
Institute of Solid State Physics
Academy of Sciences
Moscow, U.S.S.R.

Peter Duncumb
Tube Investments Research Laboratories
Hinxton Hall
Nor. Saffron Walden
Essex, England

L. S. Birks
Naval Research Laboratory
Washington, D. C. 20390

VIII INTERNATIONAL CONFERENCE ON X-RAY OPTICS AND MICROANALYSIS

Advisory Committee

I. B. Borovskii	Academy of Sciences	U.S.S.R.
R. Castaing	Université de Paris-Sud	France
V.E. Cosslett	University of Cambridge	England
G. Möllenstedt	Universität Tübingen	Germany
R. E. Ogilvie	Massachusetts Institute of Technology	U.S.A.
G. Shinoda	Osaka University	Japan
D. B. Wittry	University of Southern California	U.S.A.

Organizing Committee

R. E. Ogilvie	Massachusetts Institute of Technology	General Co-Chairman
D.B. Wittry	University of Southern California	General Co-Chairman
D. R. Beaman	The Dow Chemical Company	Program Chairman

Session Co-Chairmen

Introductory	R. E. Ogilvie	D. B. Wittry
Scanning Electron Microscopy	O.C. Wells K.C.A. Smith	R. Shimizu
Instrumentation & Electron Optics	A. Broers	I. B. Borovskii
Quantitative Analysis	K. F. J. Heinrich	R. Castaing
Automation	W. T. Kane	T. Shiraiwa
X-Ray Optics	R. E. Ogilvie	G. Shinoda
Surface Analysis	D. R. Beaman	J. D. Brown
Ion-Induced X-Ray Spectroscopy	W. Reuter	W. Hink
Energy Dispersive Spectroscopy	E. Lifshin	L. Meny
Analytical Transmission Electron Microscopy	D. F. Kyser	P. Duncumb
Solid State Electronics	D. B. Wittry	T. Ichinokawa
Secondary Ion Mass Spectrometry & IMA	C. A. Evans, Jr.	G. Slodzian
Electron and X-Ray Microfabrication	T. E. Everhart	
Materials Applications	J. I. Goldstein	J. Philibert
Biological Applications, Part I	C. Lechene	T. A. Hall
Biological Applications, Part II	A. P. Somlyo	P. Galle
Mineralogy	A. E. Bence	S. J. B. Reed
Electron Energy Loss Spectrometry	D. C. Joy	V. E. Cosslett

Arrangements

R. E. Ogilvie	Massachusetts Institute of Technology
P. Lublin	General Telephone & Electronics

Technical Exhibits and Displays

D. F. Kyser	IBM at San Jose
O. C. Wells	IBM Watson Research Center

Awards

O. C. Wells	IBM Watson Research Center

Publications

D. R. Beaman	The Dow Chemical Company

INVITED SPEAKERS

J. L. Abraham, M. D., University of California at San Diego, U.S.A.

N. S. Andrushenko, Leningrad University, U.S.S.R.

L. J. Balk, Fachbereich Elektrotechnik - Gesamthochschule Duisburg, Germany

I. B. Borovskii, Physics Academy of Sciences, U.S.S.R.

A. N. Broers, IBM Watson Research Center, U.S.A.

R. Castaing, Université de Paris-Sud, France

J. R. Coleman, University of Rochester, U.S.A.

C. Colliex, Université de Paris-Sud, France

V. E. Cosslett, University of Cambridge, England

L. Costrell, National Bureau of Standards, U.S.A.

P. B. DeNee, Appalachian Laboratory for Occupational Safety and Health, U.S.A.

A. Dörge, Universität Müchen, Germany

P. Duncumb, Tube Investments Research Laboratories, England

C. A. Evans, Jr., University of Illinois, U.S.A.

W. Fuchs, University of the Saarland, Germany

P. Galle, Faculté de Médecine de Créteil, France

R. H. Geiss, IBM at San Jose, U.S.A.

A. Gopinath, University College of North Wales, England

T. A. Hall, Cambridge University, England

W. T. Hatfield, General Electric, U.S.A.

B. L. Henke, University of Hawaii, U.S.A.

J. Henoc, C.N.E.T., France

W. Hink, Universität Würzburg, Germany

S. H. Igamberdiyev, Academy of Sciences, U.S.S.R.

M. Isaacson, University of Chicago, U.S.A.

D. E. Johnson, University of Washington, U.S.A.

D. C. Joy, Bell Telephone Laboratories, U.S.A.

H. L. Leamy, Bell Telephone Laboratories, U.S.A.

FRAME C: A Compact Procedure for Quantitative Energy-Dispersive Electron Probe X-ray Analysis

R. L. Myklebust, C. E. Fiori and K. F. J. Heinrich
Analytical Chemistry Division
National Bureau of Standards
Washington, D. C. 20234

Abstract

The correction procedure FRAME C has been developed for quantitative electron probe microanalysis with a lithium-drifted silicon detector. This program is a modification of our FRAME program [1]; it was designed to compute the mass fractions of the elements present in a specimen based on a minimum amount of input.
The x-ray intensities utilized by the program are the summed contents of small blocks of adjacent channels (regions of interest) of a multi-channel analyzer, rather than entire spectra. This restriction renders possible the on-line execution of the program with small (24 K) computers. The program requires a region of interest for each analyzed element, and two regions of interest free from peaks for the background subtraction. Also needed are the atomic number and x-ray line for each element and the operating voltage. FRAME C has been made to operate both in a computer-oriented multi-channel analyzer and in a time-shared computer. The time-share version is in BASIC and is approximately 850 statements long.
The procedure consists of a background correction calculated from the two background regions of interest [2], a simple method of resolving overlapping peaks [3], and the matrix corrections previously described [1]. FRAME C is a collection of 21 subroutines organized to perform three different operations (see figure 1). For a typical analysis, in the first of these operations the information needed from spectra of standards is computed and stored in a file. Either pure elements or compounds of known compositions may be used. In the second operation we compute the mass fractions of elements in the specimen points from their spectra and from the previously stored information on the standards. Another part of FRAME C is a routine for computing the thicknesses of the beryllium window and the silicon dead layer in the detector from a carbon spectrum. This part is used occasionally because the thicknesses of the beryllium window and silicon dead layer are needed for the determination of detector efficiency, particularly at x-ray energies from one to three kilovolts. The thickness determination is based upon the expression for the intensity of the continuum previously described [2]:

$$I_E = \frac{1}{E} [K_1(E_o-E) + K_2(E_o-E)^2] \, P_E \, f_E \qquad (1)$$

where f_E is the specimen absorption factor for the continuum at energy E, K_1 and K_2 are the two coefficients determined from two background regions of interest, E_0 is the operating voltage, and P_E is the detector efficiency:

$$P_E = \exp[-\mu_{Si}t_{Si}-\mu_{Be}t_{Be}-\mu_{Au}t_{Au}] * [1-\exp(-\mu_{Si}t_{det})]. \qquad (2)$$

In this expression the μ_i is the mass absorption coefficient of i, and the t_i is its thickness in g/cm^2 (t_{Si} = Si dead layer, t_{Be}= beryllium window, t_{Au} = gold layer, and t_{det} = thickness of silicon detector). The detector thickness is taken from the detector specifications and the gold layer is assumed to be 3.86×10^{-5} g/cm^2. Four regions of interest of the continuum are selected for the computation. Estimated values for t_{Be} and t_{Si} are entered and two regions are used to compute K_1 and K_2 in equation (1). The second two regions (one must be below the silicon absorption edge and the other just above the edge) are then used to compute t_{Be} and t_{Si}, and this procedure is iterated until their values converge.

The analysis routines for computing the x-ray intensities from standards and compositions of unknowns are parallel options of the program. Except for the order in which subroutines are called, these two operations are essentially the same (figure 1). The matrix and background corrections are performed as previously described [1,2]. The peak overlap computation presented by us has been incorporated in the program and includes 17 x-ray lines ($K\alpha$, $K\beta_1$, $L\alpha_1$, $L\alpha_2$, $L\beta_1$, $L\beta_2$, $L\beta_3$, $L\beta_4$, $L\gamma_1$, $L\gamma_3$, $L\eta$, $L\ell$, $M\alpha$, $M\beta$, $M\gamma$, $M\zeta_1$, $M_{II}-N_{IV}$) plus their escape peaks [3]. One line of each element is used for the analytical procedure. All additional lines are interferences which must be subtracted if they fall within the region of interest of an analytical line. For this purpose we assume that the detector efficiency and absorption factor of the interfering line are the same as for the selected line with which it overlaps. All overlaps may then be directly calculated and subtracted if the weights of lines are known. Overlap coefficients that predict the contribution of one peak to the integrated region of another peak with which it interferes are computed once early in the program.
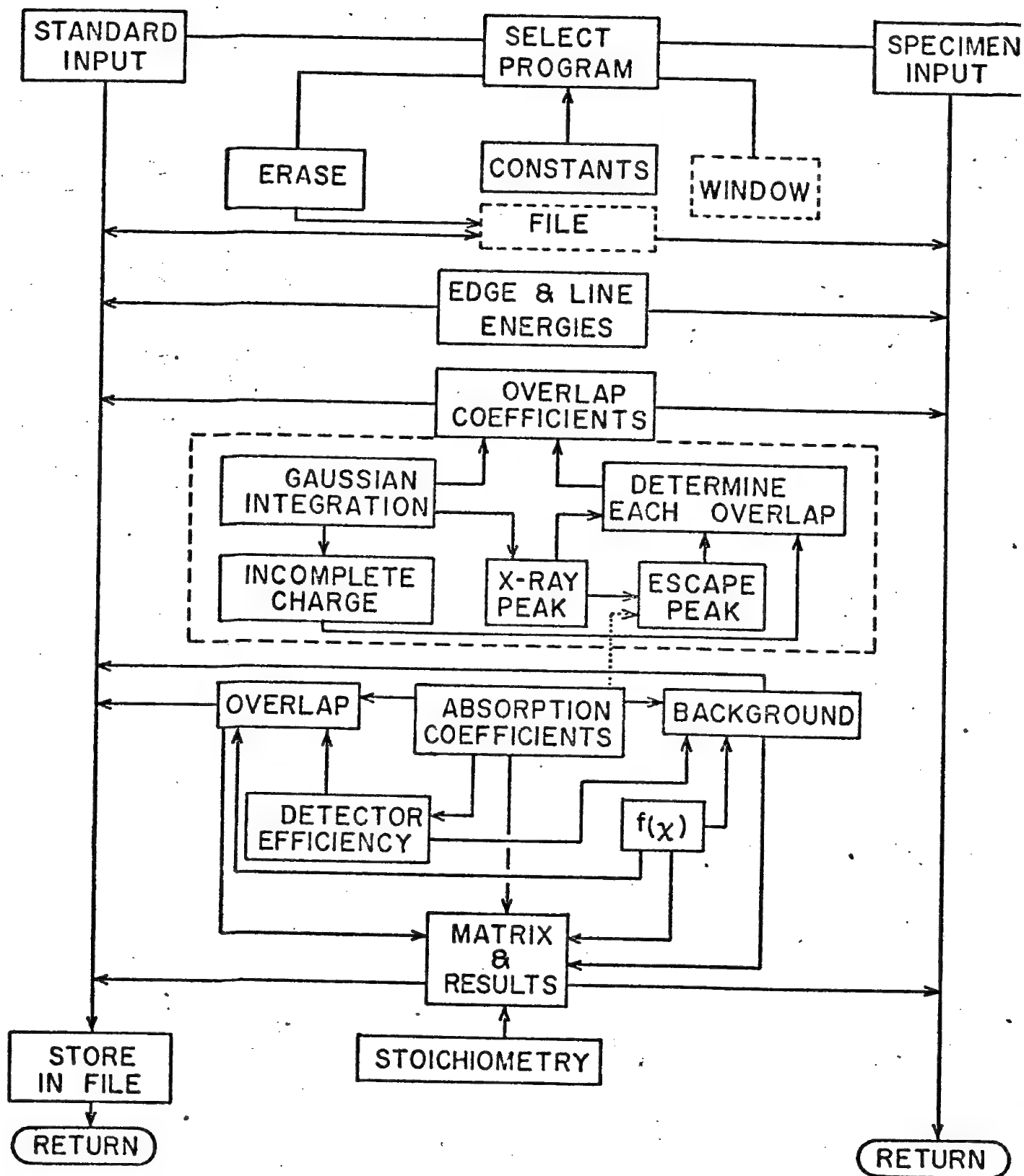
Overlap coefficients are obtained by formal integration of the peak shape function of an interfering line over the region of interest of the analytical line with which it interferes. Since the overlap coefficients are independent of the peak intensities, they need be computed only once for each set-up of regions of interest and stored in the file with the standards information. They must be recomputed if the size or position of the regions of interest of the elements involved is changed. For a particular element, the regions of interest must be the same for the standard and the specimens; however, another element may have a different number of channels in its region of interest or may even be assymetrically placed on the peak so as to minimize interferences. The treatment of interferences between lines originating from shells other than the analytical line is presently being studied. Practical examples will be demonstrated.

References

[1] Yakowitz, H., Myklebust, R. L., and Heinrich, K. F. J.,
     FRAME: An On-Line Correction Procedure for Quantitative
     Electron Probe Microanalysis, NBS Technical Note 796,
     National Bureau of Standards, Washington, D. C. (1973).

[2] Fiori, C. E., Myklebust, R. L., and Heinrich, K. F. J.,
     and Yakowitz, H., Anal. Chem. 48, 1, 172-176 (1976).

[3] Fiori, C. E., Myklebust, R. L., and Heinrich, K. F. J.,
     Proc. 11th Annual Conf. of Microbeam Analysis Society,
     Miami Beach, Florida, August 9-13, 1976, paper 12 (1976).

Figure Caption

Figure 1. Block diagram of FRAME C. Each block represents
one of the program subroutines. The subroutine ERASE clears
the FILE. The WINDOW routine also calls subroutines: EDGE &
LINE ENERGIES, ABSORPTION COEFFICIENTS, DETECTOR EFFICIENCY,
$f_{(x)}$, and BACKGROUND.

```
┌──────────┐            ┌──────────┐            ┌──────────┐
│ STANDARD │───────────→│  SELECT  │←───────────│ SPECIMEN │
│  INPUT   │            │ PROGRAM  │            │  INPUT   │
└──────────┘            └──────────┘            └──────────┘

        ┌──────────┐    ┌──────────┐    ┌ ─ ─ ─ ─ ┐
        │  ERASE   │    │CONSTANTS │     WINDOW
        └──────────┘    └──────────┘    └ ─ ─ ─ ─ ┘
                       ┌ ─ ─ ─ ─ ─ ┐
                          FILE
                       └ ─ ─ ─ ─ ─ ┘

            ┌──────────────┐
            │ EDGE & LINE  │
            │   ENERGIES   │
            └──────────────┘

            ┌──────────────┐
            │   OVERLAP    │
            │ COEFFICIENTS │
            └──────────────┘

    ┌ ─ ─ ─ ─ ─ ─ ─ ─ ─ ─ ─ ─ ─ ─ ─ ─ ─ ─ ─ ─ ─ ─ ┐
      ┌──────────────┐              ┌──────────────┐
    │ │   GAUSSIAN   │              │  DETERMINE   │ │
      │ INTEGRATION  │              │ EACH OVERLAP │
    │ └──────────────┘              └──────────────┘ │
      ┌──────────────┐   ┌───────┐  ┌──────────┐
    │ │  INCOMPLETE  │   │ X-RAY │  │  ESCAPE  │     │
      │    CHARGE    │   │ PEAK  │  │   PEAK   │
    │ └──────────────┘   └───────┘  └──────────┘     │
    └ ─ ─ ─ ─ ─ ─ ─ ─ ─ ─ ─ ─ ─ ─ ─ ─ ─ ─ ─ ─ ─ ─ ┘

   ┌─────────┐   ┌──────────────┐   ┌────────────┐
   │ OVERLAP │←──│  ABSORPTION  │   │ BACKGROUND │
   └─────────┘   │ COEFFICIENTS │   └────────────┘
                 └──────────────┘
       ┌──────────────┐          ┌──────┐
       │   DETECTOR   │          │ f(χ) │
       │  EFFICIENCY  │          └──────┘
       └──────────────┘

               ┌──────────┐
               │  MATRIX  │
               │    &     │
               │ RESULTS  │
               └──────────┘

 ┌──────────┐           ┌──────────────┐
 │  STORE   │           │ STOICHIOMETRY│
 │ IN FILE  │           └──────────────┘
 └──────────┘
      │
  ( RETURN )                              ( RETURN )
```

MAS COMMITTEES - 1977

Awards Committee	L. S. Birks
Presidential Awards	O. C. Wells
Membership	J. I. Goldstein
Sustaining Membership	D. R. Beaman (Chairman) J. Tabock D. F. Kyser
Legal	P. Lublin
Standards	A. A. Chodos
Employment Services	W. G. Fricke
Nominations Committee	G. Cleaver (Chairman) P. Lublin J. Bomback J. Gilfrich P. DeNee
MicroNews	P. DeNee (Editor) V. E. Shull A. S. Miller
Future Meeting Sites	P. Lublin
Section Liaison:	
Speaker's Tour	J. I. Goldstein
Local Sections	J. D. Brown
Publications	K. F. J. Heinrich
Certificates and Scrolls	D. F. Kyser
1978 Meeting: General Co-Chairmen:	W. C. Bigelow J. L. Bomback
Program Chairman	D. F. Kyser

MICROBEAM ANALYSIS SOCIETY

1977 National Officers

President

Joseph I. Goldstein
Dept. of Metallurgy & Materials Science
Whitaker Lab #5
Lehigh University
Bethlehem, PA 18015
(215)691-7000, X627

President-Elect

Jim D. Brown
University of Western Ontario
London, Canada
(519)679-3317

Past President

Eric Lifshin
Research & Development Center
General Electric Company
Schenectady, N.Y. 12301
(518)385-8220

Treasurer

Art Chodos
Division of Geological & Planetary Sciences
California Institute of Technology
Pasadena, CA 91125
(213)795-6811, X2126

Secretary

Bob Myklebust
Analytical Chemistry Division
National Bureau of Standards
Washington, D. C. 20234
(301)921-2875

Members-at-Large

3 Years

Mary C. Finn
Lincoln Laboratory
244 Wood Street
Lexington, MA 02173
(617)259-8465

2 Years

Gordon Cleaver
General Electric Company
Vallecitos Nuclear Center
Pleasanton, CA 94566
(415)862-2211

1 Year

Oliver Wells
IBM
Thomas J. Watson Research Center
P.O. Box 218
Yorktown Heights, N.Y. 10598
(914)945-2321

MICROBEAM ANALYSIS SOCIETY

SUSTAINING MEMBERS

The following organizations are Sustaining Members of the Microbeam Analysis Society. This means that they support the principles and goals of the Society and provide vital financial assistance for the Society's programs. A listing of these companies, their complete addresses, and their product lines can be found at the back of these Proceedings.

AMR CORPORATION
Bedford, Massachusetts

APPLIED RESEARCH LABORATORIES
Sunland, California

BABCOCK & WILCOX COMPANY
ALLIANCE RESEARCH CENTER
Alliance, Ohio

CAMECA INSTRUMENTS, INC.
Stamford, Connecticut

EDAX INTERNATIONAL, INC.
Prairie View, Illinois

ETEC CORPORATION
Hayward, California

INTERNATIONAL SCIENTIFIC INSTRUMENTS, INC.
Mountain View, California

JEOL U.S.A. INC.
Medford, Massachusetts

KEVEX CORPORATION
Burlingame, California

WALTER C. McCRONE ASSOCIATES, INC.
Chicago, Illinois

MICROSPEC CORPORATION
Sunnyvale, California

3M COMPANY
St. Paul, Minnesota

**UNITED SCIENTIFIC CORPORATION
ANALYTICAL INSTRUMENT DIVISION**
Mountain View, California

ORTEC INCORPORATED
Oak Ridge, Tennessee

THE PERKIN-ELMER CORPORATION
Mountain View, California

PHILIPS ELECTRONIC INSTRUMENTS INC.
Mahwah, New Jersey

PHYSICAL ELECTRONICS INDUSTRIES, INC.
Eden Prairie, Minnesota

PRINCETON GAMMA-TECH, INC.
Princeton, New Jersey

QBI INTERNATIONAL
San Francisco, California

CHARLES M. TAYLOR CO.
Stanford, California

TRACOR NORTHERN
Middleton, Wisconsin

**VARIAN ASSOCIATES
VACUUM DIVISION**
Palo Alto, California

ANNUAL AWARDS MADE BY THE MICROBEAM ANALYSIS SOCIETY

MACRES AWARD

This award of $300 was established in 1973 to honor the memory of Dr. Victor Macres, one of the pioneers of electron probe analysis, a dedicated teacher, and a competitive instrument manufacturer. The award is given for the best instrumentation paper presented at the annual meeting. In 1976 the award was made to R. F. EGERTON, C. J. ROSSOUW, and M. J. WHELAN.

JEOL AWARD

The Japan Electron Optics Laboratory Corporation sponsors this award of $300, but it is administered by the Microbeam Analysis Society. The award is given for an outstanding student paper presented at the annual MAS meeting. In 1976 the JEOL Award was given to G. R. MERRIAM.

CORNING AWARD

In 1975 the Corning Glass Works established an award of $300 for the most outstanding contributed paper presented at the annual MAS meeting. The award is administered by the Microbeam Analysis Society. The 1976 award was made to P. STATHAM.

THE MAS STUDENT SUPPORT PROGRAM

The encouragement of student participation at the annual meeting is an important objective of the Microbeam Analysis Society. The registration fee is reduced for student attendees, of course, but the Student Support Program is specifically pointed towards soliciting the presentation of research papers by students at the annual meeting. In addition to being good training for the students, such presentations often bring refreshing new views of theoretical, as well as experimental, aspects of microbeam analysis.

The guidelines for the support program are simple:
1. The paper must be co-authored by a bona fide student and his or her professor.
2. It must be of a quality to be accepted by the Program Committee.
3. It must be presented at the meeting by the student.
4. The professor is asked to attest to the kind and amount of contribution made by the student to each facet of the work presented.

Travel support for the student is furnished by MAS to ensure that his or her attendance will not be an undue financial burden to either the student or the university. The amount of travel support will generally cover round trip economy fare plus partial coverage of food and lodging.

In addition to the student travel support, the Microbeam Analysis Society administers the annual JEOL Award for an outstanding student presentation (see accompanying description of the MAS awards).

MEETING ANNOUNCEMENT

THIRTEENTH ANNUAL CONFERENCE OF THE MICROBEAM ANALYSIS SOCIETY

hosted by

Midwest Probe Users Group

June 19 - 23, 1978

Campus Inn
615 East Huron Street
Ann Arbor, Michigan 48108

(adjacent to the University of Michigan campus)

Co-Chairmen: Professor W. C. Bigelow
                  University of Michigan
                  Department of Materials and Metallurgical Engineering
                  Room 4213 East Engineering Building
                  Ann Arbor, Michigan 48109

                  Dr. J. L. Bomback
                  Ford Motor Company
                  Scientific Research Laboratory
                  Room 1022
                  Dearborn, Michigan 48121

Program Chairman: Dr. D. F. Kyser
                  IBM Research Laboratory
                  5600 Cottle Road
                  San Jose, California 95193

PROGRAM SUMMARY

Thursday, August 18

Introductory Session	9:30AM - 2:00PM	Commonwealth Room
Scanning Electron Microscopy	2:15AM - 6:45PM	Commonwealth Room
Instrumentation & Electron Optics	7:45PM - 10:45PM	Commonwealth Room

Friday, August 19

Quantitative Analysis	8:00AM - 3:30PM	Commonwealth Room
Automation	3:30PM - 6:15PM	Commonwealth Room
X-Ray Optics	2:10PM - 6:10PM	Hampton Room
MAS Affiliated Local Sections Luncheon	12:30PM	
ICXOM-MAS Reception	6:30PM - 8:30PM	Swimming Pool

Saturday, August 20

Surface Analysis	8:30AM - 4:50PM	Commonwealth Room
Ion-Induced X-Ray Spectroscopy	10:40AM - 4:50PM	Hampton Room
MAS Business Meeting	5:00PM	Gardner Room

Sunday, August 20

ICXOM-MAS Clambake		Wentworth by the Sea

Monday, August 22

Energy Dispersive Spectroscopy	8:00AM - 12:35PM	Commonwealth Room
Analytical Transmission Electron Microscopy	1:20PM - 5:55PM	Commonwealth Room
50th Anniversary of Electron Diffraction	9:00AM - 4:45PM	Independence Room
Solid State Electronics	7:00PM - 10:40PM	Commonwealth Room

Tuesday, August 23

Secondary Ion Mass Spectrometry & IMA	8:30AM - 4:30PM	Commonwealth Room
Materials Applications	10:00AM - 5:00PM	Fairfax Room
Electron and X-Ray Microfabrication	1:30PM - 4:30PM	Hynes B Room
Tutorial: ATEM	4:30PM - 6:00PM	Hynes B Room
MAS Sustaining Members Luncheon	12:00 noon	Exeter Room
ICXOM-MAS Banquet	6:30PM	Constitution Room

Wednesday, August 24

Biological Applications	8:00AM - 5:30PM	Fairfax Room
Mineralogy	8:10AM - 12:00 Noon	Hynes A Room
Electron Energy Loss Spectrometry	8:30AM - 4:45PM	Commonwealth Room
Late Breaking Events	2:00PM	Hynes A Room
MAS-EMSA Awards Luncheon	12:00 Noon	Grand Ballroom

Thursday and Friday, August 25 and 26

National Institute of Health Biological Workshop
EMSA Session continue

PROGRAM

EIGHTH INTERNATIONAL CONFERENCE

ON

X-RAY OPTICS AND MICROANALYSIS

AND

TWELFTH ANNUAL CONFERENCE

OF THE

MICROBEAM ANALYSIS SOCIETY

INTRODUCTION TO THE

EIGHTH INTERNATIONAL CONFERENCE ON X-RAY OPTICS AND MICROANALYSIS

Thursday, August 18 9:30 a.m. - 2:00 p.m.

Commonwealth Room

Co-Chairmen

R. E. Ogilvie, Massachusetts Institute of Technology

D. B. Wittry, University of Southern California

1	9:30AM	**INVITED:** "Electron Energy Loss Spectrometry" V. E. Cosslett University of Cambridge, England
2	10:00	**INVITED:** "Analysis of Solid Surfaces by Thermal Ionization of Sputtered Particles" R. Castaing and G. Blaise Université de Paris-Sud, France
3	10:30	**INVITED:** "A Summary of Microanalysis in Japan" and "Some Topics of Mechanically Worked Layer Research in Japan" G. Shinoda Osaka University, Japan
*	11:00	**INVITED:** "Some Questions Concerning X-Ray Optics" I. B. Borovskii Academy of Sciences, U.S.S.R.
4	11:30	**INVITED:** "Combined Electron Microscopy and Microprobe Analysis" P. Duncumb Tube Investments Research Laboratories, England
	12:00	Lunch
5	1:30PM	**INVITED:** "Monte Carlo Calculations in Electron Probe Microanalysis and Scanning Electron Microscopy" R. Shimizu Osaka University, Japan
	2:00	End of Session

* Abstract not received in time to be reviewed and published in the Proceedings.

SCANNING ELECTRON MICROSCOPY

Thursday August 18 2:15 p.m. - 6:45 p.m.

Commonwealth Room

Co-Chairmen

O. C. Wells, IBM Watson Research Center

K. C. A. Smith, Cambridge University, England

R. Shimizu, Osaka University, Japan

Part I. Computational Aspects of SEM - Chairman, O. C. Wells

6	2:15PM	**INVITED:** "Some Aspects of Computer Aided Scanning Electron Microscopy" K. C. A. Smith Cambridge University, England
7	2:45	"A New Technique for Quantitative Metallography Employing a Scanning Electron Microscope and a Solid State X-Ray Detector" R. E. Ogilvie and M. F. McKittrick Massachusetts Institute of Technology
8	3:00	"Fourier Analysis of the Imaging Properties of the Scanning Electron Microscope" H. E. Purdum West Virginia University
9	3:15	"Signal Analysis and Instrument Characterization for Scanning Electron Microscope" G. V. Lukianoff IBM at Hopewell Junction
	3:30	Discussion

Part II. Image Formation in the SEM - Chairman, K. C. A. Smith

10	3:45	**INVITED:** "Imaging of Heavy Metal Stained Biological Tissue With Backscattered Electrons, Secondary Electrons and Transmitted Electrons" P. B. DeNee Appalachian Laboratory for Occupational Safety and Health and West Virginia University
11	4:15	**INVITED:** "Multiple Imaging and Microanalytical Modes for Biological Specimens--Electron and Ion Beam Studies" J. L. Abraham, M.D. University of California at San Diego
12	4:45	"Factors Affecting the Spatial Resolution of Auger Electron Spectroscopy" E. K. Brandis IBM at Hopewell Junction
13	5:00	"Scanning Electron Microscopy: Secondary Electron Image Contrast and Electron Spectroscopy of Surface Layers" C. LeGressus*, F. Pellerin*, and H. Okuzumi** *CEA - Centre D"Etudes Nucleaires de Saclay, France, ** JEOL Ltd., Europe

	5:15	Discussion

Part III. Further Aspects of Image Formation in the SEM – Chairman, R. Shimizu

| 14 | 5:30PM | "Surface Distribution of Backscattered Electrons in the SEM and EPMA"
K. Murata, M. Kotera, and K. Nagami
University of Osaka Prefecture, Japan |

| 15 | 5:45 | "Experimental Techniques for High Resolution SEM"
R. Anderson
IBM at Hopewell Junction |

| 16 | 6:00 | "Comparison Pairs of Surface Topography Images Obtained by Varying the Electron Detector Conditions"
S. H. Moll and K. R. Benoit
AMR Corporation |

| 17 | 6:15 | "Directionally-Sensitive Electron Detector for Scanning Electron Microscope (SEM)"
O. C. Wells
IBM Watson Research Center |

| | 6:30 | Discussion of Session |

| | 6:45 | End of Session |

| | 7:45 | Evening Session: Instrumentation and Electron Optics |

INSTRUMENTATION AND ELECTRON OPTICS

Thursday August 18 7:45 p.m. – 10:45 p.m.

Commonwealth Room

Co-Chairmen

A. Broers, IBM Watson Research Center
I. B. Borovskii, Physics Academy of Sciences, U.S.S.R.

18	7:45PM	**INVITED:** "Some Thoughts on Electron Energy Loss Spectroscopy (ELS) Within the Electron Microscope: Where Does It Stand and Where Is It Going" M. Isaacson The University of Chicago
19	8:20	**INVITED:** "Calculation of the Combined Effects of Diffraction, Spherical Aberration, Chromatic Aberration and Finite Source Size in the SEM" E. Munro IBM Watson Research Center
20	8:55	"An Attempt to Investigate the Quality of Plane Surfaces by Use of an Electron-Mirror-Interference-Microscope" H. Lichte and G. Möllenstedt Universität Tübingen, Germany
21	9:15	"On a Method to Increase the S/N in Microanalysis" C. A. Ribeiro Universidade Estadual de Campinas, Brazil
22	9:35	"New Four-Crystal Spectrometer for a Scanning Electron Microprobe" B. Kenessey Applied Research Laboratories
23	9:55	"An Improved Aperture System and Alignment Procedure for ARL EMX-SM Electron Microprobes" L. F. Allard and W. C. Bigelow The University of Michigan
24	10:15	"A Video Signal Level Indicator and Control Circuit for SEM Image Photography" H. K. Gille Applied Research Laboratories
	10:30	Discussion of Session
	10:45	End of Session

QUANTITATIVE ANALYSIS

Friday August 19 8:00 a.m. – 3:30 p.m.

Commonwealth Room

Co-Chairman

K. F. J. Heinrich, National Bureau of Standards

R. Castaing, Université de Paris, France

25	8:00AM	**INVITED:** "Quantitative Microanalysis" S. J. B. Reed University of Cambridge, England
26	8:35	**INVITED:** "Applications of Statistics to Electron Probe Microanalysis" M. Ancey, F. Bastenaire, and R. Tixier Institut de Recherches de la Sidérurgie Francaise, France
27	9:10	"A Monte Carlo Procedure Employing Single and Multiple Scattering" D. E. Newbury, R. L. Myklebust, and K. F. J. Heinrich National Bureau of Standards
28	9:30	"Monte Carlo Simulation of Plasma and Characteristic Energy Losses in Thin Films" G. L. Sheldon and R. E. Ogilvie Massachusetts Institute of Technology
29	9:50	"Distribution Des Electrons D'un Faisceau Dans Une Cible Homogene" C. Landron, M. Andreani, and P. Azou Ecole Centrale Des Arts Et Manufactures - Grande Voie des Vignes, France
30	10:10	"Distribution Energetique Des Electrons Retrodiffuses" C. Landron, M. Andreani, and P. Azou Ecole Centrale Des Arts Et Manufactures - Grande Voie des Vignes, France
31	10:30	"Direct Measurements of the Voltage-Dependence of Inner-Shell Ionization Cross-Sections" D. F. Kyser and R. H. Geiss IBM at San Jose
32	10:50	"Continuum-Radiation in Quantitative Electron Microprobe Analysis" J. Böcker and Th. Hehenkamp Universität Göttingen, Germany
33	11:10	"Geometrical Considerations for ZAF Corrections in the SEM" S. H. Moll*, N. Baumgarten*, and W. Donnelly** *AMR Corporation, **Microspec Corporation
34	11:30	"Use of the Electron Backscatter Factor to Normalize X-Ray Microanalysis" J. C. Russ EDAX Laboratories
35	11:50	"Some Examples of Quantitative Analysis of Very Light Elements (Z<9)" J. Ruste Ecole des Mines of Paris, France
36	12:10PM	"Electron Probe Investigation Methodic of Structural Defects in Semiconductor Materials" Sh. Kh. Igamberdiyev Uzbek Academy of Sciences, U.S.S.R.

QUANTITATIVE ANALYSIS

	12:30PM	Lunch - Luncheon for representatives of MAS affiliated local sections
37	1:30	"Review of the Empirical Methods Used in Electron Microanalysis" R. E. Ogilvie Massachusetts Institute of Technology
38	1:45	"Non-Linearities of Electron Microprobe Matrix Corrections in the System $MgO-Al_2O_3-SiO_2$" A. E. Bence and W. Holzwarth State University of New York at Stony Brook
39	2:00	"Preparation of Microprobe Standards Using the Laserglaze^{TM} Process" J. M. Walsh*, K. P. Gumz*, and E. M. Breinan** *Pratt and Whitney Aircraft, **United Technologies Research Center
40	2:15	"On-Line Magic IV: Direct Computer Reduction of Data Acquired for up to 42 Elements" L. A. Ray, L. K. Griffith, W. J. Hamilton, and J. R. Hinthorne Applied Research Laboratories
41	2:30	"Quantitative Individual Particle Analysis: A Comparison and Evaluation of Microprobe Techniques" J. T. Armstrong and P. R. Buseck Arizona State University
42	2:45	"Development of a Characteristic Fluorescence Correction for Thin Films and Particles" J. T. Armstrong and P. R. Buseck Arizona State University
43	3:00	"Electron-Probe Analysis of Micron-Size Inclusions" G. Springer Falconbridge Metallurgical Laboratories, Canada
*	3:15	INVITED: "Rapid Method of Quantitative Analysis and a New Method of Measuring Chemical Shifts" N. S. Andrushenko Leningrad University, U.S.S.R.
44.		"A Low Cost Method for Analyzing Electron Microprobe Data" P. B. Fraundorf McDonnell Center for Space Sciences, Washington University
	3:30	End of Session

*Abstract not received in time to be reviewed and published in the Proceedings.

AUTOMATION

Friday August 19 3:30 p.m. – 6:15 p.m.

Commonwealth Room

Co-Chairmen

W. T. Kane, Corning Glass Works

T. Shiraiwa, Sumitomo Metal Industries, Ltd., Japan

45	3:30PM	**INVITED:** "Future Trends in Microprobe Automation" W. T. Hatfield General Electric
46	4:00	**INVITED:** "Automation of the Electron Microprobe" J. Henoc* and M. Tong** *C.N.E.T., **Cameca, France
47	4:30	**INVITED:** "CAMAC Instrumentation and Interface System for Computer Automated Measurement and Control" L. Costrell National Bureau of Standards
48	5:00	"A computerized Cameca Ion Probe System" J. R. Roth and G. H. Morrison Cornell University
49	5:15	"Automated Electron Microprobe: Performance and Use Techniques" W. R. DeBoskey and G. Glade IBM at Research Triangle Park
50	5:30	"Combined EDS and WDS Analysis with an Automated Electron Microprobe" J. J. Friel*, J. I. Goldstein*, J. J. McCarthy**, and N. F. Wodke** *Lehigh University, **Tracor Northern, Inc.
51	5:45	"A Modular Microprobe Automation System" J. J. McCarthy and F. H. Schamber Tracor Northern, Inc.
52	6:00	"Automated Electron Microprobe Analysis: A System for the ARL-SEMQ Based on Mass Storage and Speed Capabilities of the Flexible Magnetic Disk" W. J. Hamilton, J. R. Hinthorne, L. A. Ray, and T. A. Whatley Applied Research Laboratories
	6:15	End of Session
	6:30	ICXOM-MAS Reception - Swimming Pool

X-RAY OPTICS

Friday August 19 2:10 p.m. – 6:10 p.m.

Hampton Room

Co-Chairman

R. E. Ogilvie, Massachusetts Institute of Technology

G. Shinoda, Osaka University, Japan

53	2:10PM	**INVITED:** "Some Recent Work in Low Energy X-Ray Physics" B. L. Henke University of Hawaii
54	2:50	"X-Ray Optics of a Micro-Diffraction Goniometer" H. Maruyama*, T. Iwai*, and V. E. Buhrke** *Rigaku Corporation, Japan, **Buhrke Corporation
55	3:10	"Development of an X-Ray Stress Analyzer for Field Service and its Applications" K. Ogiso Rigaku Corporation, Japan
56	3:30	"Composite X-Ray Pinholes for Time-Resolved Microphotography of Laser Compressed Targets" D. T. Attwood University of California
57	3:50	"Tomography of Laser Fusion Plasmas" N. M. Ceglio University of California
58	4:10	"X-Ray Microradiography of Laser Fusion Targets" R. H. Day, R. P. Kruger, R. L. Whitman, and T. L. Elsberry Los Alamos Scientific Laboratory
59	4:30	"Thin Zoneplates for Soft X-Rays" J. Kirz Stanford University and State University of New York at Stony Brook
60	4:50	"X-ray Microscopy of Biological Specimens with Zone Plates and Synchrotron Radiation" G. Schmahl, D. Rudolph, and B. Niemann Universitäts-Sternwarte, Germany
61	5:10	"X-Ray Mapping with the Electron Microprobe and the Wavelength Dispersive Spectrometer" T. Hsu Etec Corporation
62	5:30	**INVITED:** "X-Ray Optics of Diffraction Techniques Employing the Energy Dispersive Spectrometer" R. E. Ogilvie Massachusetts Institute of Technology
	6:10	End of Session
	6:30	ICXOM-MAS Reception - Swimming Pool

Saturday August 20 8:30 a.m. - 4:50 p.m.

Commonwealth Room

Co-Chairmen

D. R. Beaman, The Dow Chemical Company

J. D. Brown, University of Western Ontario, Canada

63	8:30AM	**INVITED:** "Concerted ESCA-ISS-SIMS Investigations in Surface Analysis" G. D. Mateescu Case Western Reserve University
64	9:10	**INVITED:** "The Scanning Auger Microprobe: A Review" N. C. MacDonald and C. T. Hovland Physical Electronics Industries, Inc.
65	9:50	"Scanning Electron Spectroscopy for Chemical Analysis" C. T. Hovland Physical Electronics Industries, Inc.
66	10:10	"New Instrumental Capabilities in Auger Electron Microscopy" W. R. Bottoms and J. A. Schoeffel Varian Associates
67	10:30	"The Determination of Auger Electron Cross Sections and Attenuation Lengths Using Proton-Excited X-Rays" P. B. Needham, Jr., and T. J. Driscoll Bureau of Mines
68	10:50	"Techniques to Study Orientation Dependent Surface Chemistry" J. L. Bomback, W. C. Johnson, and P. Wynblatt Ford Motor Company Research Staff
69	11:10	"Auger Elemental Mapping with Real Time Correction for Sample Topography" N. J. Taylor, T. A. Pendolfi, and W. R. Bottoms Varian Associates
70	11:30	"Differentiation of Surface and Subsurface Auger Sources by Linearization of the Secondary-Electron Cascade" E. N. Sickafus Ford Motor Company Research Staff
71	11:50	"Materials Applications of Spatially Resolved Electron Stimulated Desorption" A. Joshi and L. E. Davis Physical Electronics Industries, Inc.
	12:10PM	Lunch
72	1:10	"High Resolution Scanning Auger Microscopy of Fracture Surfaces" R. G. Rowe, C. L. Briant, and F. Bacon General Electric Corporate Research and Development
73	1:30PM	"Quantitative Auger Analysis of Gold-Copper-Oxygen and Gold-Nickel-Oxygen Surfaces Using Relative Sensitivity Factors" P. M. Hall and J. M. Morabito Bell Telephone Laboratories Incorporated

SURFACE ANALYSIS

74	1:50	"Experiments in Quantitative Auger Electron Spectroscopy" H. E. Klassen and D. R. Beaman The Dow Chemical Company
75	2:10	"SAM/SIMS Investigation of Pt Films on Yttria-Stabilized Zirconia" K. E. Lawson and R. M. Rusnak Bendix Research Laboratories
76	2:30	"The Routine Application of the SIMS/SEM/EDXA Combination to Practical Surface Problems" E. J. Fasiska and P. B. Janocko Materials Consultants and Laboratories, Inc.
77	2:50	"Extension of SEM Capabilities with SIMS" D. A. Nauman Western Electric
78	3:10	"Combined SIMS/SEM for Three Dimensional Surface Analysis" G. R.Sparrow 3M Analytical Systems
79	3:30	"Monocrystalline Surface Analysis Using Ion-Focussing Effect" E. S. Mashkova, V. A. Molchanov, and A. D. Pavlova Moscow State University, U.S.S.R.
80	3:50	"Measurements of H^+ and He^+ Yields for H_2^+ and He^+ Elastically Scattered from Ag and Pd" P. J. Adelmann, H. F. Helbig, and A. W. Czanderna Clarkson College of Technology
81	4:10	"The First 50 Å: Practical Applications of Surface Analysis by ISS" G. R. Sparrow 3M Analytical Systems
82	4:30	"Ion Scattering Profiles of Polypropylene Coatings on $CuO_{0.67}^{18}$ Films Before and After Oxidative Degradation of the Polymer" A. C. Miller, A. W. Czanderna, H. H. G. Jellinek, and H. Kachi Clarkson College of Technology
	4:50	End of Session
	5:00	MAS Business Meeting - Gardner Room
		August 21, Sunday, ICXOM-MAS Clambake - Wentworth by the Sea

ION-INDUCED X-RAY SPECTROSCOPY

Saturday August 20 10:40 a.m. – 4:50 p.m.

Hampton Room

Co-Chairmen

W. Reuter, IBM Watson Research Center

W. Hink, Universität Würzburg, Germany

83	10:40AM	**INVITED:** "Carbon Fluorescence Yield with Proton and Electron Bombardment" K. Brunner, W. Hink, B. Krause, and T. Scharnagl Universität Würzburg, Germany
84	11:30	"The Doppler-Tuned Spectrometer: A New Tool for High-Resolution X-Ray Spectroscopy" J. R. Mowat North Carolina State University
85	11:50	"Excitation of Carbon K X-Rays by 1 to 40 MEV Carbon, Nitrogen and Oxygen Ions" F. W. Martin University of Maryland
	12:10PM	Lunch
86	1:30	"Proton Induced Inner Shell Ionisation Cross-Sections in the 1 - 3 MeV Region of Interest in Microanalysis" Md. R. Khan, A. G. Hopkins, and D. Crumpton University of Aston in Birmingham, England
87	1:50	"Measurement of The Relative Intensities of the L X-rays from High Z Elements Induced by 1 - 3 MeV Proton" Md. R. Khan, M. Karimi, A. S. Lodhi, and P. Sioshansi Atomic Energy Organization, Iran
88	2:10	"Doubly Differential K- and L-Ionization Cross Sections of Ne for Electron Impact" W. Hink, B. Krause, and W. Storch Universität Würzburg, Germany
89	2:30	"Analysis of Thin Films on GaAs by He+-Induced X-rays and Backscattering" R. L. Kauffman, L. C. Feldman, R. P. H. Chang, and P. J. Silverman Bell Telephone Laboratories, Incorporated
90	2:50	"Detection Sensitivities in Proton and Electron Induced X-ray Spectroscopy" W. Reuter and A. Lurio IBM Watson Research Center
91	3:10	"Applications of Proton-Excited X-Ray Analysis to the Study of Metallic Corrosion" B. D. Sartwell and P. B. Needham, Jr. Bureau of Mines, U. S. Dept. of the Interior
92	3:30	Quantitative Applications of Proton-Induced X-Ray Emission Analysis in the Fields of Medicine and Biology" J. T. Dabek, N. A. Dyson, and A. E. Simpson University of Birmingham, England

93	3:50	"Trace Element Analysis of Biological Material Using **PIXE**" E. K. Biegert and V. Valkovic Rice University
94	4:10	"Quantitative Analysis of Trace Elements in Blood and Urine Samples of Diabetic Patients" P. Sioshansi, A. S. Lodhi, Md. R. Khan, H. Payrovan, S. Ghafourian, and M. Tavakoly Atomic Energy Organization, Iran
	4:30	Discussion of Session
	4:50	End of Session
	5:00	MAS Business Meeting - Gardner Room

August 21, Sunday, ICXOM-MAS Clambake - Wentworth by the Sea

ENERGY DISPERSIVE SPECTROSCOPY

Joint ICXOM-MAS-EMSA Session

Monday August 22 8:00 a.m. – 12:35 p.m.

Commonwealth Room

Co-Chairpersons

E. Lifshin, General Electric Corporation

L. Meny, Centre D'Etudes Nucléaires de Saclay, France

95	8:00AM	INVITED: "Reliability in Data-Analysis Procedures for X-Ray Spectra" P. Statham University of California
96	8:35	"FRAME C: A Compact Procedure for Quantitative Energy-Dispersive Electron Probe X-Ray Analysis" R. L. Myklebust, C. E. Fiori, and K. F. J. Heinrich National Bureau of Standards
97	8:55	"Getting Accurate Intensity Values from Energy Dispersive X-Ray Spectra Using Fixed Energy Windows" J. C. Russ EDAX Laboratories
98	9:15	"Least-Squares Fit with Digital Filter: The Method and Its Application to EDS Spectra" F. H. Schamber, N. F. Wodke, and J. J. McCarthy Tracor Northern, Inc.
99	9:35	A Real Time Floppy Disk Operating System" S. Shulman EDAX International, Inc.
100	9:55	"A Technique for Rapid Semiquantitative Energy Dispersive Microanalysis" N. C. Barbi, M. Foster, and D. P. Skinner Princeton Gamma-Tech, Inc.
101	10:15	"A Dedicated, Low Cost Data Processor for Semi-Quantitative X-Ray Microanalysis" D. A. Gedcke, E. Elad, and P. E. Henry Ortec, Incorporated
102	10:35	"Automatic Fitting of Calculated Background in Energy Dispersive X-Ray Spectra" J. C. Russ EDAX Laboratories
103	10:55	"Resolution Enhancement of X-Ray Spectra" P. J. Statham University of California
104	11:15	"New Measurements of the Voltage Dependence of Absolute X-Ray Yields Using Energy Dispersive Spectrometry" E. Lifshin, M. F. Ciccarelli, and R. B. Bolon General Electric Corporate Research and Development

ENERGY DISPERSIVE SPECTROSCOPY

105   11:35AM   "Measuring Detector Entrance Windows"
                  J. C. Russ
                  EDAX Laboratories

106   11:55   "SEM of High Sulfur Coal"
                  R. T. Greer
                  Iowa State University

107   12:15PM   "An Energy Dispersive Spectrometer for Elements from 6 to 92"
                  A. Sandborg and R. Lichtinger
                  EDAX Laboratories

       12:35   Lunch

ANALYTICAL TRANSMISSION ELECTRON MICROSCOPY

Joint EMSA-ICXOM-MAS Session

Monday   August 22   1:20 p.m. – 5:55 p.m.

Commonwealth Room

Co-Chairmen

D. F. Kyser, IBM at San Jose

P. Duncumb, Tube Investments Research Laboratories, England

108	1:20PM	**INVITED:** "Quantitative Analytical Electron Microscopy" G. W. Lorimer University of Manchester, England
109	2:00	**INVITED:** "Micro Analytic Methods in STEM: Diffraction, EDS and Dark Field Imaging" R. H. Geiss IBM at San Jose
110	2:40	"Spatial Resolution of X-Ray Microanalysis in STEM" D. F. Kyser and R. H. Geiss IBM at San Jose
111	3:00	"Ultimate Spatial Resolution of the X-Ray Microanalysis of Thin Foils Using an Energy Dispersive Spectrometer" R. König Battelle-Institut e.V., Germany
112	3:20	"Contamination and Absorption Effects in X-Ray Microchemical Analysis of Thin Metal Films" N. J. Zaluzec and H. L. Fraser University of Illinois
113	3:40	"A Study of Spurious X-Ray Production in a Philips EM 300 TEM/STEM" D. B. Williams and J. I. Goldstein Lehigh University
114	4:00	"Influence of X-Ray Induced Fluorescence on Energy Dispersive X-Ray Analysis of Thin Foils" E. A. Kenik and J. Bentley Oak Ridge National Laboratory
115	4:20	"Graphite Support Grids for X-ray Analysis in the Electron Microscope" R. H. Packwood, E. E. Laufer, W. N. Roberts Centre for Mineral and Energy Technology, Canada
116	4:40	"Application of the Monte Carlo Simulation to Quantitative Electron Microprobe Analysis of Refractory Thin Films" S. Cvikevich and C. Pihl IBM East Fishkill Facility
117	5:00	"X-Ray Microanalysis in the STEM" P. Bovey, I. Wardell, and P. M. Williams VG Microscopes Ltd., England

ANALYTICAL TRANSMISSION ELECTRON MICROSCOPY

118   5:20   "Microchemical Analysis in Sensitized Austenitic Stainless Steel"
P. Rao and E. Lifshin
General Electric Corporate Research and Development

5:40   Discussion of Session

5:55   End of Session

7:00   Evening Session: Solid State Electronics

SOLID STATE ELECTRONICS

Monday August 22 7:00 p.m. - 10:40 p.m.

Commonwealth Room

Co-Chairmen

D. B. Wittry, University of Southern California

T. Ichinokawa, Waseda University, Japan

119	7:00PM	**INVITED:** "Microcharacterization of Semiconductors by Cathodoluminescence (CL) and Electron Beam Induced Current (EBIC) Techniques" L. J. Balk and E. Kubalek Fachbereich Elektrotechnik - Gesamthochschule Duisburg, Germany
120	7:35	**INVITED:** "Single Crystal Characterization by SEM" H. J. Leamy, L. C. Kimerling, and S. D. Ferris Bell Telephone Laboratories, Incorporated
121	8:10	**INVITED:** "Sampling SEM for Semiconductor Device Studies" A. Gopinath and K. G. Gopinathan University College of North Wales, England
122	8:45	"Electron Microprobe Analysis of Chemical Compounds by X-Ray and Cathodoluminescence Spectroscopy" E. Wolfgang Siemens Research Laboratories, Germany
123	9:05	"Difficulties of Interpreting Cathodoluminescence Spectra" M. J. Mitchell and J. N. Ramsey IBM East Fishkill Facility
124	9:25	"Measurement of Diffusion Lengths of Excess Carriers in Semiconductors by the Voltage Dependence of Electron Beam Induced Currents at Schottky Barriers" C. J. Wu and D. B. Wittry University of Southern California
125	9:45	"Secondary Electron Energy Spectra Under Bombardment of Electrons and Ions on Si" T. Ichinokawa, T. Kawamura, and T. Takagi Waseda University, Japan
126	10:05	"X-Ray Imaging and Analysis of Defect Structure Induced by Sputtered Metal Film Deposits" H. Suga and S. Weissmann Rutgers University
	10:25	Discussion of Session
	10:40	End of Session

SECONDARY ION MASS SPECTROMETRY AND ION MICROPROBE ANALYSIS

Tuesday August 23 8:30 a.m. - 4:30 p.m.

Commonwealth Room

Co-Chairmen

C. A. Evans, Jr., University of Illinois

G. Slodzian, Université de Paris-Sud, France

127	8:30AM	**INVITED:** "A 'Transfer Optics' for microanalysis by Secondary Ion Emission" G. Slodzian and A. Figueras Université de Paris-Sud, France
128	9:10	**INVITED:** "Secondary Ion Mass Spectrometry: A Review of Recent Advances" C. A. Evans, Jr. University of Illinois
129	9:50	"Critical Problems in Quantitative Secondary Ion Mass Spectroscopy" D. B. Wittry University of Southern California
130	10:10	"Use of a Cesium Primary Ion Source on an Ion Microprobe Mass Spectrometer" R. K. Lewis*, P. Williams**, C. A. Evans, Jr.**, and P. R. Hanley*** *California Institute of Technology, **University of Illinois, ***General Ionex Corp.
131	10:30	"DIDA: A Multipurpose Scanning Ion Microprobe" K. Wittmaack Gesellschaft für Strahlen-und Umweltforschung mbH, Germany
132	10:50	"A Computer-Based Recording System for High Mass-Resoluiton Ion-Probe Analysis" J. V. P. Long, D. M. Astill, J. N. Coles, and S. J. B. Reed N.E.R.C. Ion Probe Unit, University of Cambridge, England
133	11:10	"A New Secondary Ion Emission Microanalyzer" J. M. Rouberol, M. Lepareur, B. Autier, and J. M. Gourgout Cameca, France
134	11:30	"Rapid Data Acquisition Using an Automated SIMS Quadrupole Mass Analyzer for Solids: Application to High Resolution Depth Profiling" R. L. Conrad, T. A. Whatley, and R. D. Fralick Applied Research Laboratories
	11:50	Lunch - MAS Sustaining Members Luncheon - Exeter Room
135	1:30PM	"Improved SIMS Depth Profiles by Control of Sample Surface Potential" T. A. Whatley, R. L. Conrad, and R. D. Fralick Applied Research Laboratories
136	1:50	"Irradiation Effects in SIMS Analysis, Their Consequences on Depth Resolution" Y. Limoge, R. Seguin, and J. L. Seran Commissariat A. L'Energie Atomique, Centre D'Etudes Nucleaires de Saclay, France

SECONDARY ION MASS SPECTROMETRY AND ION MICROPROBE ANALYSIS

137   2:10PM   "Empirical Standards for Quantitative Analysis of Biological Tissues
by Secondary Ion Mass Spectrometry"
M. B. Bellhorn* and D. M. File**
*Albert Einstein College of Medicine, **Naval Weapons Support Center

138   2:30   "Quantitative Ion Microprobe Mass Analysis Using Negative Secondary Ions"
J. D. Brown* and J. M. Short**
*The University of Western Ontario, Canada, **Xerox Corporation

139   2:50   "Matrix Species Ratio Method for Quantitative Ion Probe Analysis"
J. D. Ganjei, D. P. Leta, J. R. Roth, and G. H. Morrison
Cornell University

140   3:10   "Quantitative Analysis of Glasses by Secondary Ion Mass Spectrometry"
D. E. Newbury
National Bureau of Standards

141   3:30   "Contribution to the Study of Ion Emission in the Ni-Cu, Ni-Fe, Al-Cu
and Al-Fe Alloys: Influence of the Chemical Affinity of Components for
Oxygen"
Y. Limoge, F. Maurice, and J. L. Seran
CEA - Centre D'Etudes Nucleaires de Saclay, France

142   3:50   "IMMA Surface Analysis of Alloy Steel Using N_2^+ Primary Ion"
T. Shiraiwa, N. Fujino, J. Murayama, and N. Usuki
Sumitomo Metal Industries, Ltd., Japan

143   4:10   "Secondary Ion Microanalysis of Some Phosphate and Carbonate of
Calcium Biomineralisations"
R. Lefevre
Université de Paris, France

        4:30   End of Session

        4:30   EMSA Tutorial on Analytical Transmission Electron Microscopy by
G. W. Lorimer - Hynes B Room

        6:30   ICXOM-MAS Banquet - Constitution Room

MATERIALS APPLICATIONS

Tuesday August 23 10:00 a.m. - 5:00 p.m.

Fairfax Room

Co-Chairmen

J. I. Goldstein, Lehigh University

J. Philibert, Université de Paris-Sud, France

144	10:00AM	INVITED: "Applications de la Microanalse en Science des Materiaux" J. Philibert Université de Paris-Sud, France
145	10:40	"Magnetic Domain Observation in Fe-3% Si Steel" W. G. Morris*, P. Rao*, and J. W. Shilling** *General Electric, **Allegheny-Ludlum Research Center
146	11:00	"Microsegregation in Al-Zn-Mg Alloys" A. Wirsing and G. Judd Rensselaer Polytechnic Institute
147	11:20	"Diffusion Processes and Weldability of Hot Pressed RENE' 41 Superalloys" S. Tosto and M. Sattin Fiat, Italy
148	11:40	"Electron Probe Testing for Homogeniety of Standards" K. F. J. Heinrich, R. B. Marinenko, and F. C. Ruegg National Bureau of Standards
	12:00	Lunch - MAS Sustaining Members Luncheon - Exeter Room
149	2:00PM	"Microprobe Analysis of PuO_2-UO_2 Nuclear Fuel" W. I. Clark, D. E. Rasmussen, R. L. Carlson, and D. M. Highley Hanford Engineering Development Laboratory
150	2:20	"Electron Probe Microanalysis in Inhomogeneous Thin Films" J. D. Brown*, J. M. Short**, and R. W. LaForce** *The University of Western Ontario, Canada, **Xerox Corporation
151	2:40	"X-Ray Microanalysis of Boron-Rich Layers Grown During B-Predeposition in Silicon" A. Armigliato*, G. G. Bentini*, A. Desalvo*, R. Rinaldi**, R. Rosa*, and G. Ruffini* *Laboratorio LAMEL-C.N.R., **Instituto di Mineralogia dell'Universita, Italy
152	3:00	"The Determination of the Optimum Conditions for Quantitative X-Ray Microanalysis of Carbon in Austenitic Stainless Steels" F. Coppola*, F. Maurice**, and J. Ruste*** *Nuclear Energy National Committee, Italy, **Nuclear Research Center of Saclay, ***Ecole des Mines of Paris, France
153	3:20	"Study of the Carburization of an Austenitic Stainless Steel (the local Concentration of C Being Less than 2 wt. %) Through Optical and Scanning Electron Microscopy, Microhardness, and Quantitative X-Ray Microanalysis of Carbon" M. Champigny*, L. Meny*, and J. Ruste** *Nuclear Research Center of Saclay, **Ecole des Mines of Paris, France

MATERIALS APPLICATIONS

154   3:40PM   "The Study of Chemical Effect on the $FeK\alpha_{1,2}$ Emission Lines with
an Electron Microprobe for Some Iron Compounds Applied in Metallurgy"
St. Jasieńska, D. Tomkowicz, and J. Janowski
Academy of Mining and Metallurgy, Poland

155   4:00   "Accurate Quantitative Analysis of Oxy-Nitrides Using Sialon as
a Standard"
A. J. Mardinly and W. C. Bigelow
The University of Michigan

156   4:20   "The Role of the Electron Microprobe in Workmen's Compensation
and Personal Injury Litigation"
J. T. Armstrong*, E. F. Holdsworth**, and P. R. Buseck*
*Arizona State University, **SEM/TEC Laboratories

157   4:40   "Effects of Elastic Lattice Bending on X-Ray Transmission Patterns
of Silicon Crystals"
Z. H. Kalman, H. Suga, and S. Weissmann
Rutgers University

       5:00   End of Session

       4:30   EMSA Tutorial on Analytical Transmission Electron Microscopy by
G. W. Lorimer - Hynes B Room

       6:30   ICXOM-MAS Banquet - Constitution Room

ELECTRON AND X-RAY MICROFABRICATION

Joint EMSA-ICXOM-MAS Session

Tuesday August 23 1:30 p.m. - 4:30 p.m.

Hynes B Room

Chairman

T. E. Everhart, University of California at Berkeley

158	1:30PM	INVITED: "Electron Beam Microfabrication Systems" A. N. Broers IBM Watson Research Center
159	2:30	INVITED: "Microfabrication for Integrated Electronics" E. D. Wolf Hughes Research Laboratories
160	3:30	INVITED: "X-Ray Replication of Submicrometer Linewidth Patterns" H. I. Smith and D. C. Flanders Massachusetts Institute of Technology
	4:30	End of Session
	4:30	EMSA Tutorial on Analytical Transmission Electron Microscopy by G. W. Lorimer, University of Manchester
	6:30	ICXOM-MAS Banquet - Constitution Room

BIOLOGICAL APPLICATIONS, Part I

Wednesday August 24 8:00 a.m. – 12:05 p.m.

Fairfax Room

Co-Chairmen

C. Lechene, Harvard Medical School

T. A. Hall, Cambridge University, England

161	8:00AM	**INVITED:** "Electron Probe Analysis of Ultra Small Volumes in Physiology" C. Lechene, R. R. Warner, and T. H. Strunk Harvard Medical School
162	8:35	**INVITED:** "Some Aspects of the Microanalysis of Frozen-Hydrated Tissue Sections" B. L. Gupta, T. A. Hall, and R. B. Moreton Cambridge University, England
163	9:10	**INVITED:** "Electronprobe Microanalysis of Frozen Hydrated Bulk Specimens: Basic Experiments" W. Fuchs University of the Saarland, Germany
164	9:45	**INVITED:** "Electron Probe Analysis of Muscle" A. P. Somlyo, A. V. Somlyo, and H. Shuman University of Pennsylvania
165	10:20	**INVITED:** The Effects of Cytochalasin B on Calcium Transport by the Chorioallantoic Membrane of the Chick Embryo" J. R. Coleman and A. R. Terepka University of Rochester
166	10:55	**INVITED:** "Determination of Cellular Electrolyte Concentrations in Freeze-Dried Biological Soft Tissues Using Electron Microprobe Analysis" A. Dörge, R. Rick, K. Gehring, R. Bauer, and K. Thurau Universität München, Germany
167	11:30	**INVITED:** "Microanalysis in Biology: A Review of Some Specific Problems" P. Galle and J. P. Berry Faculté de Médecine de Créteil, France
	12:05PM	Lunch
	12:00	MAS-EMSA Awards Luncheon - Grand Ballroom

BIOLOGICAL APPLICATIONS, Part II

Wednesday August 24 2:00 p.m. - 5:30 p.m.

Fairfax Room

Co-Chairmen

A. P. Somlyo, University of Pennsylvania

P. Galle, Faculté de Médecine de Créteil, France

168	2:00PM	"Chromium Concentration by Proximal Renal Tubular Cells: An Ultrastructural, Microanalytical and Cytochemical Study" J. P. Berry*, J. Hourdry**, P. Galle*, and G. Lagrue*** *Faculté de Médecine de Créteil, **Université de Paris-Sud, ***Néphropathies Hôpital Henri Mondor, France
169	2:20	"Analytical Electron Microscopy of Calcium Sites in a Giant Smooth Muscle Cell: Preliminary Results" G. Nicaise and M. L. Hernandez-Nicaise Université Claude-Bernard, France
170	2:40	"Maturation of Membrane Transport Function in Dog Red Blood Cells: An Electron Probe Study" R. G. Kirk*, P. Lee**, and D. C. Tosteson* *The University of Chicago, **West Virginia University
171	3:00	"X-Ray Microanalysis of Active Transepithelial Na Transport in Amphibian Skins: Evidence for a Syncitial Na Transport Compartment" R. Rick, A. Dörge, K. Gehring, R. Bauer, A. Macknight, A. Leaf, and K. Thurau Universität München, Germany
172	3:20	"Specimen Damage Considerations in Choosing the Probe for the Microanalysis of Thin Biological Materials" J. Kirz*, D. Sayre**, and J. Dilger* *State University of New York at Stony Brook, **IBM Watson Research Center
	3:40	Break
173	3:50	"Electron Probe Analysis of Fluorine Uptake in Mineralized Tissues" J. W. Edie University of Iowa
174	4:10	"X-Ray Microanalysis of Calcium Phosphate Solids Prepared Anhydrously as Calibration Standards for Mineralized Tissues" W. J. Landis Harvard Medical School
175	4:30	"Use of Electron-Beam Lithography in the Fabrication of Multichannel Depth Probes for Studies of Neural Activity" P. Pochay, L. F. Allard, L. T. Rutledge, and K. D. Wise The University of Michigan
176	4:50	"A Scanning Electron Microscopy Study of the Attachment of a Thromboresistive Surface Coating to a Membrane Blood Oxygenator" H. S. Borovetz, R. K. Matta, K. J. Goitein, T. K. Hung, M. H. Weissman, and R. L. Hardesty University of Pittsburgh
	5:10	Discussion of Session
	5:30	End of Session

MINERALOGY

Wednesday August 24 8:10 a.m. – 12:00 noon

Hynes A Room

Co-Chairmen

A. E. Bence, State University of New York at Stony Brook

S. J. B. Reed, University of Cambridge, England

---

177 **8:10AM** "Electron Microanalysis of Organic Sulfur in Coal"
R. Raymond, Jr., T. G. Gregory, and R. Gooley
Los Alamos Scientific Laboratory

178 **8:30** "Technique for the 'Before and After' Study of Clay Minerals Using
the Scanning Electron Microscope and Energy Dispersive X-Ray Analysis"
R. L. Thomas, C. W. Crowe, and B. E. Simpson
The Dow Chemical Company

179 **8:50** "The Use of Phase Transformations and Exsolution in Calcic Plagioclase
Felspar as Indicators of Geologic History"
T. L. Grove
Harvard University

180 **9:10** "Ion Microprobe Analysis of Plagioclase Feldspars $(Ca_xNa_{1-x}Al_{1+x}Si_{3-x}O_8)$
for Major and Minor Elements"
I. M. Steele, I. D. Hutcheon, T. N. Solberg, R. N. Clayton, and J. V. Smith
The University of Chicago

181 **9:30** "The Use of Energy Dispersive Analysis for the Study of Phase Aggregates"
A. A. Chodos, A. L. Albee, and J. E. Quick
California Institute of Technology

182 **9:50** "Rock Compositions by Defocussed Beam Analysis"
J. F. Bower, J. A. Wood, S. M. Richardson, H. Y. McSween, Jr., and G. Ryder
Smithsonian Astrophysical Observatory

183 **10:10** "Minor and Trace Element Analysis in the Automated Mode: Selection of
Optimum Sampling Conditions"
S. Brande and A. E. Bence
State University of New York at Stony Brook

184 **10:30** "Quantitative Analysis of Trace Element Concentrations of Ni and Cr in
Basaltic Glasses"
C. H. Nielsen
University of Rhode Island

185 **10:50** "A Rapid-Analysis Program for Use in Microprobe Studies of Plagioclase
and Olivine"
H. D. Huntington, S. A. Morse, and W. A. Ranson
University of Massachusetts

186 **11:10** "The Use of an Automated Microprobe in Geosciences Applications"
G. Remond*, R. Giraud*, C. Conty**, and M. Tong**
*Bureau for Research in Geology and Mining, **Cameca, France

MINERALOGY

187   11:30AM   "Multi-user Microprobe Operating System"
G. Yagunoff
University of Massachusetts

11:50   Discussion of Session

12:00   End of Session

12:00   Lunch, MAS-EMSA Awards Luncheon - Grand Ballroom

ELECTRON ENERGY LOSS SPECTROMETRY

Joint EMSA ICXOM–MAS Session

Wednesday August 24 8:30 a.m. – 4:45 p.m.

Commonwealth Room

Co-Chairmen

D. C. Joy, Bell Laboratories

V. E. Cosslett, University of Cambridge, England

188	8:30AM	**INVITED:** "Trends in Electron Energy Loss Spectroscopy" C. Colliex and P. Trebbia Université de Paris-Sud, France
189	9:15	"On the Design of Magnetic Spectrometers for Electron Energy Loss Spectroscopy" J. R. Fields The Johns Hopkins University
190	9:30	"Computer Control of a Hitachi HU 11A - Wien Spectrometer Electron Spectroscopy-Microscopy System" P. E. Batson* and J. Silcox** *University of Cambridge, England, **Cornell University
191	9:45	"Data Acquisition and Handling Unit for a Quantitative Use of Electron Energy Loss Spectroscopy" P. Trebbia, P. Ballongue, and C. Colliex Université de Paris-Sud, France
	10:00	Break
192	10:15	"Data Analysis in Electron Energy Loss Spectroscopy" J. C. H. Spence Arizona State University
193	10:30	**INVITED:** "The Uses of Electron Energy Loss Spectrometry in Biology" D. E. Johnson University of Washington
194	11:00	**INVITED:** "Considerations on the Use of Electron and Photon Beams for Determining Micro-Chemical Environment" M. Isaacson and M. Utlaut The University of Chicago
195	11:45	"Subcellular Localization of Fluorinated Serotonin in Human Platelets by Electron Energy-Loss Spectroscopy" J. L. Costa*, D. C. Joy**, D. M. Maher**, K. L. Kirk***, and S. W. Hui**** *National Institute of Mental Health, **Bell Laboratories, ***NTAMDD, ****Roswell Park Memorial Institute
	12:00	Lunch, MAS-EMSA Awards Luncheon - Grand Ballroom

ELECTRON ENERGY LOSS SPECTROMETRY

196   2:00PM   **INVITED:** "The Use of Electron Energy Loss Spectrometry for the Study of Materials"
J. Silcox
Cornell University

197   2:45   "Quantitative Metallurgical Applications of Plasmon Energy Loss Microanalysis"
D. B. Williams
Lehigh University

198   3:00   "The Effect of Energy Loss on Lattice Fringe Images of Dysprosium Oxide"
A. J. Craven and C. Colliex
University of Cambridge, England

3:15   Break

199   3:30   **INVITED:** "Practical Materials Microanalysis by Electron Spectrometry"
D. C. Joy and D. M. Maher
Bell Laboratories

200   4:15   "The Application of Electron Energy Loss Spectroscopy in Glass-Ceramic Microstructural Analysis"
R. M. Anderson and A. Kumar
IBM at Hopewell Junction

201   4:30   "Cross-Sections for K-Shell Excitation by Fast Electrons"
R. F. Egerton* and D. C. Joy**
University of Alberta, Canada, **Bell Labortories

4:45   End of Session

LATE BREAKING EVENTS

Joint MAS-ICXOM-EMSA Session

Wednesday August 24 2:00 p.m. - ?

Hampton Room

202   2:00PM   "An Efficient Lensing Element for X-Rays"
N. M. Ceglio* and H. I. Smith**
*Univeristy of California, **Massachusetts Institute of Technology

203   2:20   "Electron and Ion Microprobe Analysis of Clayified Roots in Thin Sections of Soil"
A. P. von Rosensteil*, J. D. Brown**, D. J. Gras*, E. B. A. Bisdom**, S. Henstra*, and A. Jongerius**
*Metal Research Institute TNO, The Netherlands, **University of Western Ontario, Canada

204   2:40   "Quantitative Carbon Analysis in Steels with the Ion Microprobe"
A. P. von Rosensteil*, J. D. Brown**, and D. J. Gras*
*Metaalinstituut TNO, The Netherlands, **University of Western Ontario, Canada

PROCEEDINGS

EIGHTH INTERNATIONAL CONFERENCE

ON

X-RAY OPTICS AND MICROANALYSIS

AND

TWELFTH   ANNUAL   CONFERENCE

OF   THE

MICROBEAM   ANALYSIS SOCIETY

Electron Energy Loss Spectrometry

V.E. Cosslett

Cavendish Laboratory, University of Cambridge, Cambridge, England.

The spectrometry of electron energy losses promises to be a valuable supplementary technique to conventional microprobe analysis, especially for the estimation of light elements. Most of the work done so far has been in transmission through thin specimens; surface observation is complicated by larger background effects. In transmission, the method is simple to apply in a normal electron microscope by fitting an energy analyser (magnetic or electrostatic) below the camera chamber. In a STEM such a system is even easier to attach, if it is not already part of the equipment as supplied.

The spectrum of energy loss from a pure element has three regimes, each of which may display fine structure: low loss (0-10eV) due to atomic excitations (corresponding to u-v absorption spectra), intermediate loss (10-30eV) due to collective (plasmon) excitations, and high loss (30eV) due to intra-band and inter-band transitions. Of the latter, those involving inner shells are most important for microanalysis, since they are characteristic of the particular element, corresponding to the K-, L, M, etc. X-ray spectra.

The plasmon losses can also be used for elementary microanalysis, but are less specific and have sharp peaks only for a few elements such as aluminium. In addition they are contained within a narrow total range of energies (about 20eV) over the whole of the periodic system, and the changes produced on alloying are small, so that high resolution is needed in the electron spectrometer. Nevertheless a number of applications in metallurgy have been usefully carried out. For a recent review, see Williams and Edington (1976); also Ditchfield and Cullis (1976).

The inner shell (X-ray level) losses are more suitable for purposes of microanalysis. Although much less frequent than plasmon losses by two or three orders of magnitude, they are spread over a great range of energies and especially in the K-series have sharp edges well separated from each other. An electron spectrometer is thus required to have a wide working range but not very high energy resolution. It is inconvenient, however, to record losses much above 1keV (AℓK = 1.5keV), beyond which the L-series is utilised or the M-series for elements above the middle of the periodic table, although the peaks become more frequent and less sharp. In any event elements of high Z can be analysed by microprobe X-ray emission.

The energy loss method finds application mostly for light elements, from which the X-rays are both weak in intensity and of long wavelength, and so are difficult to detect. The cross-section for K-excitation in (for instance)

carbon is in fact relatively great but the fluorescent yield is low, most of the excitations producing Auger electrons not characteristic X-rays. On the other hand practically all the electrons that suffer K-loss are contained within the transmitted beam, if the specimen is sufficiently thin ($\approx$ mean free path for elastic scattering) in relation to the energy of the incident beam. It is simply a matter of fitting an energy analyser, with appropriate limiting aperture, at some point behind the specimen. In a conventional electron microscope it is best put after the camera, with an aperture in the viewing screen to select the area to be analysed, although systems have been devised for fitting an analyser into the projector system (see Metherell, 1971). In STEM the analyser is built into the detection system immediately behind the specimen.

This method of microanalysis was originally proposed by Hillier and Baker (1944) but their experiments were indecisive owing to technical limitations in the electron microscope, and especially the high rate of contamination. It was revived in my laboratory nearly 25 years later (Wittry 1969), by which time improvements in vacuum technology and electron detection enabled us to show that elementary microanalysis of the light elements was practicable with high sensitivity. Since then it has been taken up and improved in many laboratories, not only for metallurgical applications but also in biology (Isaacson and Johnson, 1975). A comprehensive survey of the present state of the subject has recently appeared (Colliex et al, 1976).

The basis of the technique and its practical limitations have been discussed and experimentally explored by several authors (Colliex and Jouffrey, 1972; Hills, 1973; Egerton and Whelan 1974; Egerton, 1975; Isaacson and Johnson, 1975; Leapman, 1976; Leapman and Cosslett, 1976a). In principle it ought to be possible to detect isolated aggregates of less than 100 atoms or about 10^{-22}g. of a single element. In practice the signal is confused by the noise due to background electrons and in the detection system; also, in a realistic situation, by the effect of the matrix and the support film, if any. The magnitude of the signal itself and the signal/noise ratio will depend on the current density of the illuminating beam and on the efficiency of the detection system, in which optimum conditions are set by the angular spread of the transmitted beam, determined in turn by the nature of the specimen, its thickness and the operating voltage.

With a tungsten thermionic filament in a conventional electron microscope the detection limit at present is between 10^{-17}g. and 10^{-18}g. for carbon (at 60kV), depending on the matrix. This limit can be improved by at least an order of magnitude by introducing digital recording and deconvolution of the signal by computer processing. An appreciable further gain is to be

expected from using a field emission gun or from operating at much higher voltages, 500-100kV (Darlington and Sparrow, 1976; Perez, 1976).

A STEM system with field emission gun can give a still better detection limit, owing to its greater brightness. Isaacson and Johnson (1975) report a mass detectability of carbon of less than 10^{-18}g. (at 25kV) and estimate that this could be improved by two to three orders of magnitude by instrumental optimisation. The minimum mass fraction that could be detected varied according to the element and its matrix from 10% to 0.8%, which in their opinion should be lowered by an order of magnitude in an improved apparatus. They were able to detect the iron in ferritin supported on a 30Å thick carbon substrate; assuming that only a single ferritin molecule was covered by the electron probe of 100Å diameter, this would correspond to the detection of 5×10^{-19}g. iron.

Electron spectrometry of inner shell excitations has already exceeded the limits of conventional microprobe analysis by X-ray detection, and is capable of further improvement, especially for quantitation of the light elements. Other capabilities of the technique will be discussed in the full presentation; discrimination between different organic macromolecules from the fine structure on the low energy side of the characteristic X-ray peak (Isaacson and Johnson 1975), and investigation of the atomic environment of an excited element from the fine structure on its high energy side, corresponding to the X-ray absorption fine structure, EXAFS (Leapman and Cosslett, 1976b).

References

Colliex, C. and Jouffrey, B. (1972). Phil. Mag. 25, 471.

Colliex, C., Cosslett, V.E., Leapman, R.D. and Trebbia, P. (1976). Ultramicroscopy 1, 301.

Darlington, E.H. and Sparrow, T.G. (1975). J. Phys. E: Sci. Instrum. 8, 596.

Ditchfield, R.W. and Cullis, A.G. (1976). Micron, 7, 133.

Egerton, R.F. (1975). Phil. Mag. 31, 199.

Egerton, R.F. and Whelan, M.J. (1974). J. elect. Spectrosc. 3, 232.

Hillier, J. and Baker, R.F. (1944). J. Appl. Phys. 15, 663.

Hills, R.P.T. (1973). Ph.D. Thesis, Cambridge University.

Isaacson, M. and Johnson, D. (1975). Ultramicroscopy, 1, 33.

Leapman, R.D. (1976). Ph.D. Thesis, Cambridge University.

Leapman, R.D. and Cosslett, V.E. (1976a). Phil. Mag. 33, 1.

Leapman, R.D. and Cosslett, V.E. (1976b). J. Phys. D: Appl. Phys. 9, L29.

Metherell, A.J.F. (1971). Adv. Opt. Electron Microsc. 4, 263.

Perez, J.P. (1976). D. Sc. Thesis, Toulouse University.

Williams, D.B. and Edington, J.W. (1976). J. Microsc. 108, 113.

Wittry, D.B. (1969). J. Phys. D: 2, 1757.

Wittry, D.B., Ferrier, R.P. and Cosslett, V.E. (1969). J. Phys. D: 2, 1767.

Analysis of solid surfaces by thermal ionization of sputtered particles

R. Castaing and G. Blaise

Université de Paris–Sud, Orsay, France

Several techniques are presently available for measuring the distribution in depth of the various component elements near the free surface of a solid sample. Some of them provide three-dimensional localization by combining ion milling with local analysis of the etched surface; in the best conditions, the overall depth resolution of the analysis is controlled by the mixing up of the surface layers which occurs during the ion milling process; a similar depth resolving power will be obtained for example by using Auger electrons or secondary ions for analyzing the material that the ion milling process has brought to the free surface.

Now, both techniques are limited, concerning the accuracy and absoluteness of quantitative elemental analysis, by specific features. In Auger analysis, the measurements are performed on a surface whose composition has been eventually modified by the ion milling process; furthermore, quantitative measurements, if we leave apart the difficulties due to surface topography, are hindered by the fact that the thickness of the emitting layer is not well defined and depends on the Auger line and on the sample composition. In secondary ion analysis, matrix effects make necessary, except in the simple case of isotope analysis, a previous calibration from standard samples of similar composition and structure; furthermore the presence of polyatomic clusters in the spectrum of the emitted ions may cause serious troubles if the mass resolving power is too low for distinguishing between the various ions of the same unit mass number. We have investigated the possibilities of a modified procedure, where the material sputtered from the sample surface is collected as a whole and subsequently dissociated and ionized in a separate device for mass analysis.

When an homogeneous sample is bombarded with ions of moderate energy, say a few keV, a steady state is reached, after the sputtering of a few atomic layers, where the surface composition has adjusted in such a way that the atomic contents of the various component elements are identical in the sputtered material and in the underlying target. That is still true for a sample whose composition is varying with depth, as long as that variation is not extremely steep. The problem is to analyze quantitatively that sputtered material, independently of any parameter such as the proportion of ions that it contains or the aggregation of the sputtered atoms in polyatomic clusters. The procedure that we have investigated consists in collecting a well-defined fraction of the sputtered material in a hot chamber (Joule heated furnace made of a refractory material such as carbon, tantalum, tungsten, rhenium ..). The sputtered particles, after entering the chamber, are progressively brought to thermal equilibrium by their successive adsorptions and desorptions on the walls, until they leave the furnace by a small exit aperture. For furnace temperatures of the order of 3,000 K, the proportion of polyatomic clusters among the outcoming particles is generally quite low; on the other hand the surface concentration of the adsorbed phase on the furnace walls is very low in typical conditions, so that the proportion of ions among the outcoming atoms is controlled essentially by the properties of the free atoms and by the temperature and the work function of the clean walls; as a consequence all the matrix effects due to the sample structure are eliminated, so that a measurement of the outcoming ions with a mass spectrometer makes possible to deduce for each element the total flux from the ionic flux and to get in an absolute way the composition of the sputtered material, which is identical, in quasi-steady conditions, to the local composition of the original sample.

Those points were checked by measurements on various alloys. The thermal spectra were found to be practically devoid of polyatomic ions, except in the case of molecular ions with extremely high binding energy, such as UO^+. On the other hand, the calibration

curves show that linear relations hold between the concentrations and the thermionic emissions over the whole range of compositions, so that there is a reasonable hope to get in this way an absolute technique for in-depth analysis of solid samples, at least for elements whose ionization energy is low enough (say less than 9 eV) for ensuring a reasonable yield of the thermal production of positive ions. Many of the other elements show positive electron affinity, so that a slight modification of the experimental arrangement will probably make possible to measure them as negative ions.

The essential problem will arise from the very high degree of purity which is required for the material of the furnace walls. At the present time, it may be concluded that the detectability limit, as well as the possibility for that technique of accomodating the low primary beam intensity of an ion probe, are depending essentially on the possibility of getting materials devoid of those impurities which cannot be eliminated by heating in high vacuum.

Some Topics of Mechanically Worked Layer Research in Japan

Gunji SHINODA, Osaka Univ.

Since present author's classical work on the determination
of thickness of deformed layer of mechanically worked   surface
(1), in which 20 μm was obtained for sand paper finished surface
and residual stress distributions were determined, many works
have been published and the distributions of residual stress
have become clear. Recently, the relation between this field
and the surface science became intimate, especially in the
field of abrasion, lubrication and surface characterization
for cutting action.

During cutting cleaning and contamination processes are repeat-
ed simultaneously and at the same time microcrack formation
would occur. Abrasion phenomena should be partly related to
the mechanical working, however, we can expect that somewhat
different phenomena would be expected during frictional motion,
because the duration of mechanical action is exceedingly long.
Therefore, these phenomena are closely related to the problem
of surface characterization.

During working by cutting tools, fresh surface without any
contamination would appear and immediately afterwards contamina-
tion by cutting oils and/or ambient gases follows. It is wellknown
that tensile and fracture behaviors of carbon steel depend on
the ambient atmosphere. Usually, the frequency of serration of
stress-strain curve decreases in a high vacuum. From this we
can expect that if we cut the surface in a high vacuum rough
surface would be obtained. Such effect of atmosphere would be
attributed to the concentration of oxygen. Therefore, if we
use oxygen jet instead of ordinary air jet or cutting oil, we
can expect much improvement in cutting behaviors. Furuichi et al
(2) observed remarkable decrease of cutting force and obtained
very fine surface in oxygen atmosphere. As the cutting is a
kind of successive formation of microfracture surface, the effect
of oxygen should be similar to that observed in tensile fracture.

It is wellknown that in an abraded surface in addition to the
amorphous-like structure some phase transformed structure is
observed. However, the temperature rise in the abraded surface
is not so high and usually much lower than the phase trnsition
temperature of the material. Therefore, such effects should be
attributed to influences of mechanical action on the thermo-
dynamical potential of the system. During abrasion test using
boron carbide ion-plated shaft and amorphous carbon bearing,
present author(3) observed an enhancement of graphitization
process which would occur very much higher temperature for
ordinary heat treatment without such mechanical action. After
abrasion experiment the atomic distance of hexagonal base changed
from 3.386 Å to 3.360 Å converging to that of graphite.

Nakajima et al (4) investigated hard surface layer of abraded tin bronze bearing using Auger electron spectroscopy. They found appearance of ϵ phase, Cu_3Sn, from initially a phase structure. As the ϵ phase is the most stable intermetallic compound in the copper-tin system, appearance of such compound at the final state would be quite natural.

Such tendencies are also found in another system, such as copper-zinc. Nearly twenty years ago present author and Amano (5) presented a new equilibrium diagram in which β phase decomposes to a and γ phases by eutectoid transformation. However, such transformation is very much suppressed and never observed for usual heat tratment unless repeated cold working, quenching and prolonged tempering of more than half a year are done. As the γ phase is very stable it would be expected that after abrasion test appearance of γ phase on the surface layer is experienced in an alloy initially a or β structure. This was confirmed by Nakajima et al (6).

Similar surface structure change would be expected, if we scratch the surface by a sharp needle. Takahashi et al (7) observed the same tendency in β brass. Also they (8) have investigated surface character of the scratched trough of 18-8 stainless steel by Auger electron spectroscopy. All the alloying elements showed remarkable increase of Auger peak and among them that of chromium was predominant.

(1)   G.Shinoda,   Engineering 34 (1946) 8, in Japanese.
(2)   R.Furuichi, K.Tamamura and K.Uegami,   Lubrication 18 (1973)
                                         839, in Japanese.
(3)   Research carried out at the Oval Instrument Co.
(4)   K.Nakajima, A.Isogai and Y.Taga, Proc. 6th Internl. Congr.
         1974, Japan J. Appl. Phys. Suppl. 2pt1,1974,p.309.
(5)   G.Shinoda and Y.Amano, Trans. JIM, 1(1960) No.1.
(6)   Private Communication.
(7)   N.Takahashi, K.Okada and M.Hatta,C.R.Acad. Sc.Paris t 280
                                         (1975) Serie B-73.
(8)   N.Takahashi, K.Okada and Y.Nagasawa, Paper presented to
         the General Assembly of Applied Physics Society,Japan,
         Oct. 1976, Sendai.

Combined Electron Microscopy and Microprobe Analysis

P. Duncumb

Tube Investments Research Laboratories
Hinxton Hall, Saffron Walden,
Essex, England

The development of the electron probe microanalyser in the late 1950's and early 60's provided scientists with a working tool for the elemental analysis of regions in the sample surface down to 1 micrometre in diameter. The early success which this achieved, notably in the metallurgical and mineralogical fields, quickly led to the recognition that any further improvement in resolution would open up for study the whole field of precipitation reactions on which the properties of many materials depend. This could be achieved by the use of thin specimens in the electron microscope, where the greatly reduced scattering of the incident electron beam should allow a considerable improvement in analytical resolving power. In addition, the capability for electron diffraction from selected areas would present the user with information on the crystal structure of the sample to supplement that on morphology and elemental composition. It was a prerequisite of any design philosophy that these three types of information should be readily available without moving the sample, so that an interactive and adaptive style of investigation could be pursued by the operator without undue time delays.

To achieve a workable instrument there are two main objectives to be achieved:- (a) the provision of a fine enough electron probe of adequate intensity and (b) the development of a high efficiency X-ray spectrometer system to fit in the limited space available. The variety of instruments available has derived largely from the different ways in which these problems have been solved.

In the first EMMA built at Tube Investments in 1961-62, the electron gun and lens design relied heavily on techniques developed for the X-ray point-projection microscope and the scanning microprobe analyser, both of which needed a high intensity probe for satisfactory X-ray imaging. The X-ray spectrometer consisted initially of a gas proportional counter, offering an excellent detection efficiency but poor energy resolution. This was subsequently

replaced with twin linear focusing spectrometers of high enough efficiency to permit the analysis of particles down to below 300nm in size. The instrument and its applications were described at the "zeroth" meeting of what is now the Microbeam Analysis Society in 1964.

Since the early work three streams of development have taken place. The concept described above was developed further, in conjunction with AEI Scientific Apparatus Ltd, to provide a commercial instrument EMMA-4 based on the AEI EM802 electron microscope, and this has given rise to numerous applications in metallurgy and biology. Secondly, the emergence of the silicon detector has allowed a reversion to energy dispersive spectrometry in place of the more costly, less efficient (but much higher resolution) crystal spectrometers. This in turn has enabled EMMA facilities to be provided more easily on conventional types of electron microscope with the use of pre-field focusing or a combined condenser/objective lens system. Commonly, a modern 'workhorse' instrument of this type will offer an analytical resolution better than 30nm. Thirdly, the high brightness of the field emission gun embodied in a scanning transmission electron microscope (STEM) with energy dispersive spectrometer, may extend this limit to below 10nm.

Where next? The quantitative basis for analysis has been well established and applications will clearly be extended. STEM is not yet widely used but could become so. Minicomputers and microprocessors have been increasingly applied to thick-specimen microprobe analysers and will be extended to EMMA instruments; there is a particular opportunity in the interpretation of electron diffraction patterns. Crystal spectrometers are far from obsolete, and need to be properly integrated with the energy dispersive system, both from the point of view of operation and subsequent data processing; indeed this is true also of the thick-specimen microprobe analyser. Overall, there is a growing emphasis on the ease with which the operator can interact with the equipment, allowing him to concentrate more fully on the problem itself, and this is a mark of healthy maturity in the development of any instrument.

Monte Carlo Calculations in Electron Probe Microanalysis
and Scanning Electron Microscopy

Ryuichi Shimizu

Department of Applied Physics, Osaka University,
Suita-shi, Osaka 565, Japan

Monte Carlo Calculations have become a powerful technique for the study of the characteristics and distributions of various signals generated in the electron-specimen interaction. This evaluation is based on the simulations of the events occurring in a large number of simulated electron trajectories in the specimen.

Thus, the accuracy in the evaluation depends on how many trajectories are calculated besides how precisely the calculation simulates the real complicated electron trajectories in the specimen.

The Monte Carlo Calculations may be divided into two classes. Those aimed at the evaluation of signals generated in a large number of scattering process in each trajectory, e.g., signal distribution and backscattering in bulk specimen, and those dealt with particular problems in which each electron trajectory consists of rather small number of the scattering events, e.g., characteristics of the transmitted electrons in thin film specimens etc.

The first class makes it effective to decrease the number of scattering events in the simulated trajectories by using the average values of the physical quantities, energy loss, angular distribution of the scattered electrons etc. Hence this enables us to save both the computing time and use of uniform random number generated in a computation.

In practice this leads to the use of the continuous slowing down approximation for the energy loss and/or the angular distribution of the scattered electrons derived from the multiple scattering theory for elastic scattering process.

The Monte Carlo study of type II magnetic domain contrast in scanning electron microscopic observation is one of the best use of the first class. In this study the difference between the numbers of backscattered electrons in two magnetic domains of opposite magnetizations causes the contrast and this requires the calculations of numerous number of trajectories for precise evaluation of the magnetic contrast[1].

The second class, however, makes such averaging of the physical quantities less effective as clearly seen in the argument of the energy distribution of the transmitted electrons. Thus, this leads to either introduction of any specific consideration for statistical nature in energy loss, closed up by the limited number of the scattering events, or the direct simulation of each single energy loss event of different type excitations instead of those based on the conventional continuous Bethe deceleration law.

Another improvement in Monte Carlo calculations is the use of differential scattering cross-section derived by partial wave expansion method instead of the conventional Rutherford scattering formula.

This enables us not only to obtain more accurate description of the elastic scattering, especially, for heavy elements, but also to extend the calculations to the lower energy region. This extension offers useful knowledge of the contribution of the secondary electrons as well as backscattered electrons to the generation of signals of low excitation energies, which is particularly important in quantitative surface analysis in Auger electron spectroscopy[2].

In this paper the various approaches to Monte Carlo Calculations are reviewed and some recent applications to the electron probe microanalysis and scanning electron microscopy including scanning Auger electron microscopy are presented.

In addition, as an approach of quite new type, it is briefly introduced the Monte Carlo simulation of multiple inelastic scattering of rather high energy electrons in crystal[3]. This intended to solve the particular problem of the contribution of inelastically scattered electrons to the image formation in electron microscopy suggesting that Monte Carlo calculation technique is useful for understanding of electron scattering processes even in crystals as well as those in amorphous specimens.

References

Major part of the works introduced here is covered very well by the publication;

"Use of Monte Carlo Calculations in Electron Probe Microanalysis and Scanning Electron Microscopy," Eds. K. F. J. Heinrich, D. E. Newbury and H. Yakowitz, NBS Special Publication 460, 1976.

(1) D. J. Fathers and J. P. Jakubovics, "Magnetic domain wall contrast in the scanning electron microscope, "Phys. Stat. Sol. (a) 36, K 13 (1976)

(2) R. Shimizu, M. Aratama, S. Ichimura, Y. Yamazaki and T. Ikuta, "Application of Monte Carlo calculation to Fundamentals of Scanning Auger Electron Microscopy" (in Japanese) - Proc. 24th Annual Meeting of Japan Society of Applied Physics, (Kawasaki, March 26 - 29, 1977) 29-F-5.

(3) Y. Kamiya and R. Shimizu, "Monte Carlo Simulation of Multiple Inelastic Scattering in Crystals,": Japan. J. Appl. Phys. 15, 2067 (1976)

Some Aspects of Computer Aided Scanning Electron Microscopy.

K. C. A. Smith

University Engineering Department, Trumpington Street,
Cambridge CB2 1PZ, England.

The digital computer has been applied extensively in X-ray micro-analysis for the purposes of on-line control and data reduction but its use in scanning electron microscopy has been limited to a rather small number of applications, generally of a specialist nature. However, a number of recently published papers indicate that interest in the use of the digital computer for microscopy is becoming more widespread (1, 2, 3, 4).

The main value of the digital computer for microscopy, as for microanalysis, lies in the extraction of quantitative information. Two examples will serve to indicate future lines of development from the point of view of the general microscopist. The first concerns the extraction of quantitative three-dimensional information from the SEM image. One method of employing the on-line computer for this purpose has been described by Lebiedzik and White [5]. In this, a calibrated multi-detector array is used to form a composite video signal. With the aid of the computer the microtopography of the specimen can be deduced from this composite signal.

An alternative method, more akin to conventional stereogrammetry, is illustrated in Fig. 1. In this method a stereo pair is formed in the usual fashion by tilting the specimen or the beam, and each image is stored in the computer. Complementary pairs of points are then indexed in the two images by means of a spot cursor (arrow in Fig. 1(a)). From the resulting data (Fig. 1(b)) the microtopography of the specimen can be determined.

The second example concerns methods for focusing and correcting astigmatism in the SEM. One possible approach based on gradient processing is now under investigation. For focusing, the computer is used to calculate the total modulus of the gradient vector over the image field. A running average of several frame scans is formed to reduce noise. Fig. 2(a) shows how the modulus of the gradient changes as the objective lens current is varied. The in-focus condition is indicated by a well-defined peak, and this can be located automatically by the computer. A somewhat similar method of computer focusing has been described by Burge et al [6] for use with STEM.

Detection and correction of astigmatism is accomplished by computing the direction of the gradient vector at every point in the image field. This information is presented in the form of a polar histogram [7] (Fig. 2(b)). An ellipse may be fitted to the histogram as shown, and the dimensions and orientation of this ellipse give an indication of the degree of 'directionality' in the image. Changes in direction of the astigmatic line foci above and below focus are, therefore,

reflected in small changes in the ellipse, and it has been found possible to achieve a certain measure of correction using this information. The speed and accuracy of such methods are, of course, limited fundamentally by noise and it may not be possible to devise a completely automatic system. However, the results obtained so far indicate that computer aided focusing, at least, is feasible.

The above examples illustrate that radical changes in the mode of operation of the SEM, and in the way images are observed, may be brought about by the on-line computer.

References.

1.   M. Oron and D. Gilbert, "Combined SEM-Minicomputer System for Digital Image Processing", Scanning Electron Microscopy / 1976 (Part I), (O.Johari ed.) IIT Res. Inst., Chicago, 1976, 121-127.

2.   G. Grant, J. S. Hall, A. F. Reid and M. Zuiderwyk, "Multicompositional Particle Characterization using the SEM-Microprobe", Scanning Electron Microscopy / 1976 (Part III), (O.Johari ed.) IIT Res. Inst., Chicago, 1976, 401-408.

3.   D. R. Dinger and E. W. White, "Analysis of Polished Sections as a Method for the Quantitative 3-D Characterization of Particulate Materials; ibid., 409-415.

4.   S. Ekelund and T. Werlefors, "A System for the Quantitative Characterization of Microstructures by Combined Image Analysis and X-Ray Discrimination in the SEM", ibid., 417-423.

5.   J. Lebiedzik and E. W. White, "Multiple Detector Method for Quantitative Determination of Microtopography in the SEM", Scanning Electron Microscopy/ 1975, (Part I), (O.Johari ed.), IIT Res. Inst., Chicago 1976, 181-187..

6.   R. E. Burge, M. T. Browne, J. C. Dainty, M. Derome and S. Lackovic, "High Resolution with STEM", 6th European Congress on Electron Microscopy, (D. G. Brandon ed.), Jerusalem 1976, 442-444.

7.   B. M. Unitt, "A Digital Computer Method for Revealing Directional Information in Images", J. Phys. E.: Scientific Instruments, 8, 423, (1975).

(a)

(b)

Fig. 1. On-line evaluation of stereo images.

Modulus of gradient

Lens current

(a)

(b)
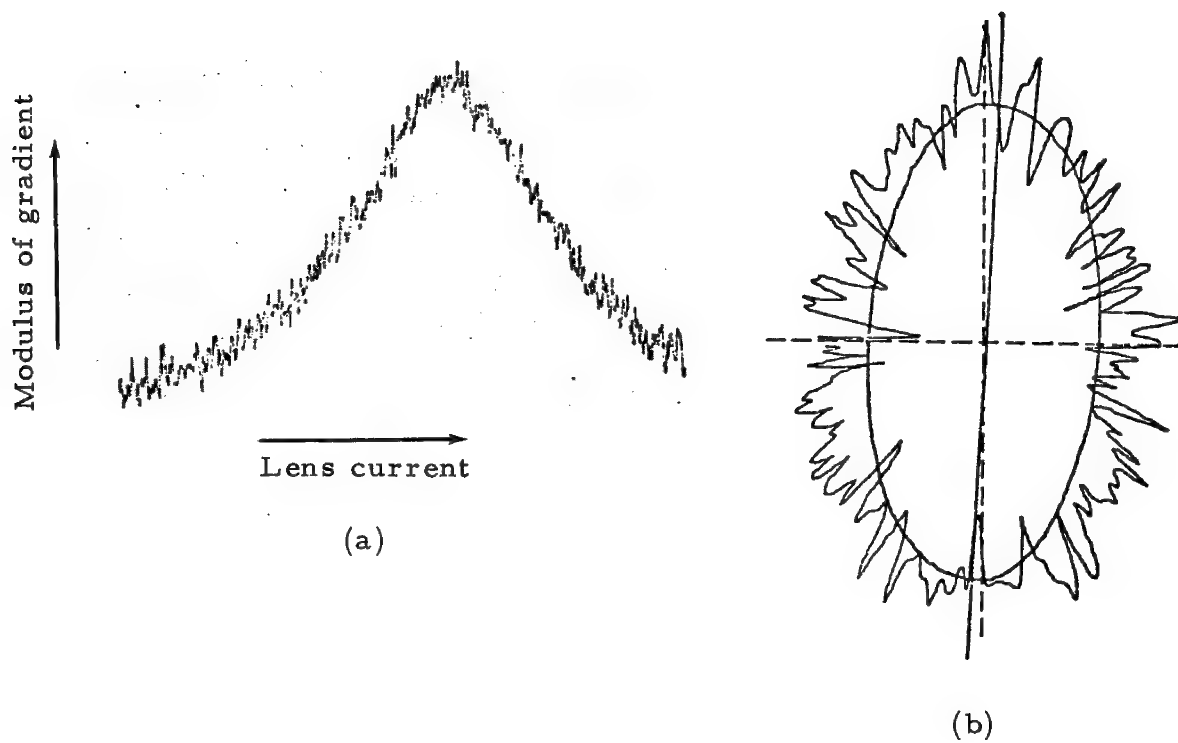
Fig. 2. Computer aided focusing and astigmatism correction by means of 'gradient' information.

A NEW TECHNIQUE FOR QUANTITATIVE METALLOGRAPHY

EMPLOYING A SCANNING ELECTRON MICROSCOPE

AND A SOLID STATE X-RAY DETECTOR

by

Robert E. Ogilvie and Michael F. McKittrick
Department of Materials Science and Engineering
Massachusetts Institute of Technology
Cambridge, Massachusetts 02139

Introduction

It has long been realized among metallurgists and geologists that a fast, reliable method for the quantitative determination of the volume fractions of the various constituents of multiphase alloys or mineral systems would be of great benefit in studies of phase equilibrium and transformations in the solid state. It is well known that the physical properties of multiphase alloys are dependent on the relative percentages of the phases present. For example, high temperature alloys are usually strengthened with a fine dispersion of hard, second-phase particles. The presence of too much of the second phase results in a brittle behavior of the alloy. However, the presence of less than the optimal amount reduces the desired properties. The geologist must determine the relative amounts of useful minerals in an ore in order to determine if the ore can be mined and processed economically.

Methods of volume-fraction analysis using a two-dimensional plane of polish have been available for over 100 years. However, most of these methods are limited by the resolution of light optics and in some cases by the degree of tedium which the person performing the analysis can endure.

The purpose of this paper is to describe a technique of volume-fraction analysis employing the scanning electron microscope and the solid state X-ray detector or an Aüger analyzer. However, this method is applicable only to systems with phases that differ in chemical composition.

The determination of the volume fraction of a particular phase within a three-dimensional matrix was first developed by A. Delesse (1), a French petrographer, in 1848. At this time, Delesse proved mathematically that from a plane of polish through an aggregate, the area fraction occupied by each phase is equal to its volume fraction. Then in 1898 Rosinal (2) developed the fundamentals of lineal analysis. Rosinal showed that from a test line on the plane of polish the volume fraction of a particular phase is equal to the lineal fraction occupied by that phase. It was not until 1930 that Thompson (3) introduced the powerful method of point counting. In this latter case it was shown by Thompson that the volume fraction of a particular phase was equal to the fraction of intersections of a test grid that fell on the phase of interest.

These three methods form the basis for volume-fraction analysis as used in quantitative microscopy. We will not go into the many techniques employed by the metallographer to obtain this information but refer the reader to the excellent text, "Quantitative Microscopy," edited by Dehoff and Rhines (4).

Procedure

To employ the scanning electron microscope for volume-fraction analysis it is necessary to measure a signal that is characteristic of the phases present from each picture element. There are several characteristic signals that can be used with this technique. They include characteristic X-rays, Aüger electrons, cathodoluminescence, backscattered and secondary electrons. The first two, characteristic X-rays and Aüger electrons, are more applicable to problems confronting the materials scientist.

The solid state X-ray detector and a multichannel analyzer are well suited for our problem. First we will consider a plane of polish that contains the phases α, β, γ, ... i. When the incident electron beam is placed

on the i phase, there will be a count rate r_j^i (counts/sec) for each element
A, B, C, ... j in that phase. Therefore, we will first measure the count rate
for the major elements from each phase. Then if a raster is scanned over an
area of interest for a total time interval, T, counts will accumulate for
each element at a count rate r_i^j while the beam is on the i phase. The total
counts C_j for the j element are then related to the counting rates from each
phase and the time (t^i) spent on each phase as shown in the following equations:

$$C_A = r_A^\alpha \, t^\alpha + r_A^\beta \, t^\beta + \ldots r_A \, t$$

$$C_B = r_B^\alpha \, t^\alpha + r_B^\beta \, t^\beta + \ldots r_B \, t$$

or generally

$$C_j = \sum_i r_j^i \, t^i$$

(1)

Since the volume fraction of the i phase V_v^i is equal to t^i/T the equations
can be simplified to the following:

$$C_j = \sum_i r_j^i \, V_v^i \, T$$

(2)

Both sides of these equations can be divided by T to give the final form
of the equations:

$$I_A = r_A^\alpha \, V_v^\alpha + r_A^\beta \, V_v^\beta + \ldots r_A^i \, V_v^i$$

$$I_V = r_B^\alpha \, V_v^\alpha + r_V^\beta \, V_v^\beta + \ldots r_B^i \, V_v^i$$

or generally

$$I_j = \sum_i r_j^i \, V_v^i$$

(3)

where I_j is the intensity given in counts per unit time (T) for element i
from the scanned area and V_v^i is the volume fraction of the i phase.

We see that if we measure for example three characteristic signals for
three phases that are present we get the following solutions:

$$V_v^\alpha = \frac{\begin{array}{ccc} I_A & r_A^\beta & r_A^\gamma \\ I_B & r_B^\beta & r_B^\gamma \\ I_C & r_C^\beta & r_C^\gamma \end{array}}{\begin{array}{ccc} r_A^\alpha & r_A^\beta & r_A^\gamma \\ r_B^\alpha & r_B^\beta & r_B^\gamma \\ r_C^\alpha & r_C^\beta & r_C^\gamma \end{array}}$$

$$V_v^\beta = \frac{\begin{array}{ccc} r_A^\alpha & I_A & r_A^\gamma \\ r_B^\alpha & I_B & r_B^\gamma \\ r_C^\alpha & I_C & r_C^\gamma \end{array}}{D}$$

$$V_v^\gamma = \frac{\begin{array}{ccc} r_A^\alpha & r_A^\beta & I_A \\ r_B^\alpha & r_B^\beta & I_B \\ r_C^\alpha & r_C^\beta & I_C \end{array}}{D}$$

Results

The results of two leaded brass specimens and two tungsten carbide-cobalt (WC-Co) cutting alloys are given in Table I.

Table I

Results from Leaded Brass and WC Cutting Tool

Specimen	Volume Frac. V_v		Std. Dev. σ_v	Std. Dev. of Mean $\sigma_{\bar{v}}$
Leaded Brass (20 meas.)	Pb	1.81	0.27	0.60
	Brass	98.29	1.15	0.25
	Total	100.10		
Leaded Brass (10 meas.)	Pb	1.61	0.39	0.13
	Brass	99.78	3.94	1.31
	Total	101.39		
WC-Co (10 meas.)	WC	53.87	1.08	0.38
	Co	46.33	0.95	0.30
	Total	100.20		
WC-Co (6 meas.)	WC	60.33	0.80	0.32
	Co	39.45	0.93	0.38
	Total	99.78		

Conclusions

The volume fractions obtained with the solid state detector are very repeatable. They have also shown good agreement with point counting techniques. We have also shown that for low accelerating voltages the influence of the depth of signal and grain boundary orientation is of little importance.

It should be clear that this technique could be made a very simple operation with the aid of a mini-computer.

References

1. A. Delesse, Procédé méchanique pour déterminer la composition des roches, Ann. Mines (IV) 13, 379 (1848)

2. A. Rosiwal, On Geometric Rock Analysis. A Simple Surface Measurement to Determine the Quantitative Content of the Mineral Constituents of a Stony Aggregate, Verhandl. K.K. Geol. Reich. Wien 5-6, 143 (1898).

3. E. Thompson, Quantitative Microscopic Analysis, J. Geol. 27, 276 (1930).

4. R. DeHoff and F. Rhines, Quantitative Microscopy, McGraw-Hill Book Co. (1968).

Fourier Analysis of the Imaging Properties
of the Scanning Electron Microscope

Howard E. Purdum

West Virginia University Department of Physics

The quality of the image displayed by the SEM is usually described by the traditional terms that originated from studies on conventional optical systems. However, terms such as sharpness are essentially qualitative in nature while more quantitative parameters are often limited in their range of application and in some cases are misleading, notably the Rayleigh resolution criterion.

A major deficiency in traditional parameters is that they can be used in system analysis only by input variation - output description of one value of the correlate. Hence, it is desirable to describe the quality of an image in quantitative terms that apply to a broad range of image variables in such a manner as to reveal the operation of the components of the system. These conditions have been met for other optical systems using Fourier techniques; this paper discusses the Fourier analysis of the SEM.

To apply Fourier techniques to an imaging system, certain conditions must be satisfied. It may be experimentally observed that the SEM satisfies the conditions of being isotropic (rotationally symmetric) and isoplanatic (maintaining the same shape over the whole image field) at least within the central regions of the display screen. Since the SEM contains a condenser, the question of partially coherent illumination must be considered. Although Fourier techniques can account for partial coherence, great simplifications are possible if the system may be considered as incoherently illuminated. This paper is restricted to image formation with secondary electrons; since secondary electrons are emitted with random phase the system may be considered as satisfying the condition of incoherent illumination, as experimentally confirmed by the absence of observable diffraction patterns. An experimental condition of correspondence between testing conditions and typical operating conditions is desirable from a practical viewpoint because Fourier analysis describes the imaging behavior of the system for specific object properties under specific operating conditions.

The specific object properties of interest are employed in choosing a test object. A commonly employed test object is a line spread distribution, however, a line spread is not practical at high magnifications. Therefore an image of an edge object may be obtained, noting that the derivative of an edge yields the desired line spread. Crystalline cleavage planes are suitable edge distributions; $K Mg F_3$ crystals are used in this study. An evaporated coating of carbon and gold-palladium on the crystal not only reduces charging but also limits emission of electrons from the vertical face of the crystal because the range of secondary electrons in the higher Z metal is shorter than the range in the lower Z crystal. Insufficiently

coated crystals and enhanced edge emission both result in bright edges in the image yielding an asymmetric, widened line distribution upon differentiation. Since asymmetry and widening could also be caused by the components of the SEM, charging and edge emission should be suppressed as much as possible so that the line spread data relates to the behavior of the system rather than to peculiarities of the test object.

Upon obtaining acceptable line spread data, the appropriate symmetry and asymmetry transfer functions may be calculated for the specific summation interval and noise limit. The resulting Modulation Transfer Function (MTF) and Phase Transfer Function (PTF) describe the response of the system in terms of spatial frequency. The close relationship at specific frequencies between the Fourier analysis and the traditional analysis is noted, particularly the evaluation of resolution. One important aspect of the MTF of the total system is that it is the product of the MTF of each component of the system. Thus Fourier techniques provide the desired quantitative information and component analytic capability for the SEM.

SIGNAL ANALYSIS AND INSTRUMENT CHARACTERIZATION FOR SCANNING ELECTRON MICROSCOPE

G. V. Lukianoff

IBM System Products Division—East Fishkill
Hopewell Junction, New York 12533

The scanning electron microscope (SEM), being an image-forming instrument, requires an analysis approach compatible with signal-processing methods. Fourier analysis offers such an approach. It is adaptable to signal analysis and to characterization of the SEM system by a mutually compatible formalism. The compatibility arises from performance of the analysis on a common basis, which is a Fourier frequency scale.[1] The frequency scale is a common ground for the representation of signals by their frequency spectra and for the description of equipment performance.[2,3]

The common-ground approach is especially useful in SEM systems, in which the signal passes through different domains and physical forms. An SEM signal originates from a spatial distribution in the form of an electron cloud, is sequentially transformed into an electric current, into a light flux, and back into the electric current, and, finally, is displayed as a spatial pattern. It passes from its original spatial domain, to the temporal, and back to the spatial. In its progress through the system, the signal changes forms and domains, remaining a carrier of the same information. Thus, a common ground for an analysis should be compatible with the representation of the information content. The frequency spectrum selected above is such a common ground. It is based on the data content of the signal and offers an analysis technique of the entire signal chain, which starts with the object, proceeds through the electronics, and ends at the display.

The equipment interacts with the signal along the entire video chain. The interaction, in general, perturbs the spectral content of the signal and/or its amplitude values. Since it has a common frequency scale, the Fourier domain affords the possibility of visualizing and quantitatively determining the interaction by the plotting of both, the signal composition and the equipment, on the same graph.

One advantage of the Fourier analysis approach is its applicability to characterization of the performance of an entire system as well as of any part of it. The characterization descriptors, called Modulation Transfer Functions (MTFs), specify the capability for handling the frequency spectrum of the signals. The MTFs are operators on the frequency spectrum and are suitably characterized by the frequency bandpasses and by the degree of amplitude changes. The sum of both factors is a measure of the signal degradation produced.

Figure 1 illustrates the use of graphical representation in evaluating the effects of equipment on signal-frequency content.

REFERENCES

[1] R. V. Pole, private communication (IBM Research Report RC 750), T. J. Watson Research Center, Yorktown Heights, New York.

[2] A. Papoulis, Fourier Integral (McGraw-Hill, New York, 1962), Chaps. 2 and 5.

[3] S. Goldman, Frequency Analysis, Modulation and Noise (McGraw-Hill, New York, 1948), Chaps. 1 and 4.
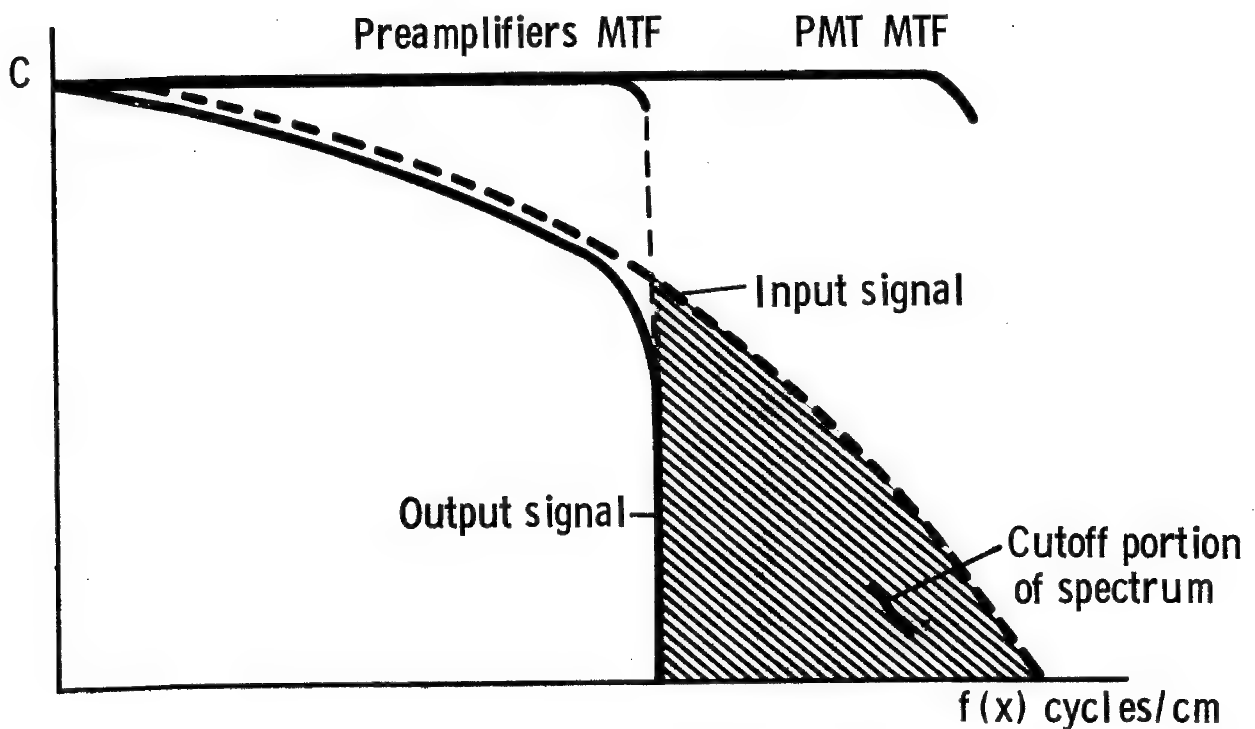
Fig. 1. Use of a common frequency scale for signal evaluation. Note the truncation of the input signal's frequency spectrum by the narrow bandpass of the preamplifier.

IMAGING OF HEAVY METAL STAINED BIOLOGICAL TISSUE WITH BACKSCATTERED ELECTRONS, SECONDARY ELECTRONS AND TRANSMITTED ELECTRONS

Phillip B. DeNee, Ph.D.

Appalachian Laboratory for Occupational Safety and Health
National Institute for Occupational Safety and Health

and

Department of Anatomy, West Virginia University

Morgantown, West Virginia 26505

The ability to selectively stain and differentiate intra and extra cellular components of tissue with heavy metals has been widely exploited in the biological sciences. For many years these heavy metal staining (HMS) techniques have been used in both light microscopy and transmission electron microscopy. Recently HMS tissue has been studied in the Scanning Electron Microscope (SEM) using three different modes; Backscattered Electron Imaging (BSI), Secondary Electron Imaging (SEI) and Transmitted Electron Imaging (TSEM).[1] In this presentation the three types of images will be compared and contrasted and the variety of information available in each mode illustrated. In addition, the mechanisms for each type of image formation will be discussed. Also, the effect of combining modes will be shown.

Backscattered Electron Imaging of HMS tissue reveals the internal structure of the cells. It involves a modified Z contrast which I shall call tZ contrast. This contrast increases with both increasing atomic number Z and thickness t of the "stained areas". This type of contrast applies not only to HMS tissue but also to particles (e.g., respirable dust) whose average atomic number is greater than the surrounding matrix (e.g., lung tissue or dust sampling filters).[2] There is an additional effect (although very small) in BSI contrast when the specimen is tilted from normal (0°) incidence to 45°. This applies to both embedded and non-embedded tissue.

Secondary Electron Imaging of non-embedded HMS tissue differs considerably from SEI of embedded HMS tissue. For non-embedded tissue, i.e., which has either had the embedding material removed (e.g., sections cut from a paraffin embedded tissue, then de-paraffinized with Xylene) or tissue which had never been embedded, the SEI shows surface topography and occassionally some internal HMS structures. The amount of internal structure which can be seen in this tissue increases as the tilt angle is decreased from 45° to 0°. The internal structure for the

embedded tissue is visible in the SEI and is nearly identical
to that seen in the BSI. For embedded tissue, there is virtu-
ally no surface topography evident in the SEI.

The transmitted electron image also reveals the HMS tissue.
If one compares the TSEM image and BSI, it is apparent that
certain details e.g., fine extracellular fibrils[1], can be seen
with TSEM but are not visible in a BSI.

Unstained embedded tissue gives little contrast in BSI, SEI
or TSEM, while unstained, non-embedded tissue has very good
contrast only in the SEI. This is the usual secondary electron
image showing surface topography. In addition, foreign bodies,
e.g., respirable dust particles and naturally occurring higher
Z material, e.g., bone or calcified tissue, can be seen in
either embedded or un-embedded tissue by BSI or TSEM.

Recent advances in instrumentation which have led to
improvements in BSI will be discussed. They include the use
of a LaB6 gun, the use of larger BSE detectors and the use of
improved signal handling.

References:

1. P. B. DeNee, R. G. Frederickson and R. S. Pope, "Heavy Metal
Staining of Paraffin, Epoxy and Glycol Methacrylate Embedded
Biological Tissue for Scanning Electron Microscope Histology",
IITRI/SEM/1977, 83-92.

2. P. B. DeNee, "The Detection of Microfibers in Airborn Dust
Samples in Biological Tissue Using Backscattered Electron
Imaging in the Scanning Electron Microscope", Presented at the
Conference on Electron Microscopy of Microfibers, Penn State
University, University Park, PA., Aug. 23-25, 1976, Sponsored
by U. S. Food and Drug Administration. Abstracts to be published.

MULTIPLE IMAGING AND MICROANALYTICAL MODES FOR BIOLOGICAL SPECIMENS-

Electron and Ion Beam Studies

Jerrold L. Abraham, M.D.
Department of Pathology
University of California, San Diego
La Jolla, California   92093

Many individuals incorrectly consider scanning electron microscopy (SEM) synonomous with secondary electron (SE) imaging. It is the intent of this paper to illustrate the value of using several signals in the SEM and also other instrumentation in a logical sequence to yield the most morphological as well as analytical information from biological specimens. The need to both image and analyze portions of biological specimens presents the analyst with a range of test samples more varied than those usually prepared to demonstrate aspects of electron-specimen interaction.

In searching for new methods to assist diagnostic pathology the ion microprobe mass analyzer[1] (IMMA) was used to analyze tissue samples from known and suspected cases of beryllium disease in humans[2,3]. It was found that routinely prepared paraffin sections supported on carbon discs, as used for SEM and x-ray microanalysis[4], were satisfactory for the IMMA analysis for light elements such as beryllium. Even with such a small sample of tissue the IMMA has been shown to be capable of semiquantitative analysis for beryllium in tissue, yielding results directly related to the bulk concentration determined by standard spectrochemical techniques[3].

The use of multiple imaging and analytical techniques is essential in this type of case. No single technique allows the collection of all the needed information. Each technique is best used as it supplements and complements the others. This problem presents an opportunity to illustrate this approach. By light microscopy the tissue showed characteristic granulomas, and no microorganisms could be found using histochemical techniques. The reaction in the tissue is not specific for beryllium disease: it could also represent sarcoidosis or other granulomatous disease of unknown etiology. The tiny sample of tissue (2x2x1 mm) was insufficient for wet chemical analysis. Furthermore, the destructive bulk chemical analytical methods do not allow correlation between the analyzed material and the focal reaction in the tissue. SEM analysis of sections of this tissue facilitate localization of the particulates and their correlation with the tissue reaction. Owing to slight differences in backscattered electron yield the nuclear detail can be roughly imaged in such a section mounted on carbon[4]. The

localization of inorganic particulates and their size and shape can be determined directly in the SEM. Many of these particulates can be analyzed using the convenient energy dispersive x-ray analysis (EDXA) for elements sodium through uranium. However, x-ray analytical techniques are not sensitive for the very light elements. The IMMA allows rapid scanning of the tissue section with controllable rates of specimen destruction. The high yield from pure beryllium (up to 4×10^7 counts per/sec) allows ion mapping at rapid scan rates. Once an area containing beryllium is located careful distribution maps for beryllium and other elements of interest can be made (Figure 1). A helpful technique to preserve the material for subsequent morphological analysis is the rastering of the ion beam in a line scan pattern immediately beneath the mapped raster between mapping for different ions. In addition to reducing the destruction of the mapped area, this simple technique etches through the tissue underneath the area, in a sense underlining it to make finding it in the SEM quite simple.

A major limitation of the IMMA is the optical visualization of the specimen. Limits of instrument design at present permit only a 250 X reflected light imaging system. This is inadequate for resolving much tissue detail. One can ascertain whether or not the area analyzed is tissue or substrate, but not much more. Thus subsequent examination of the IMMA mapped areas is essential at present. The preparation of the samples does not facilitate good light optical imaging (unstained sections on opaque carbon). The morphology and stereometry of the region of interaction of the IMMA beam with the specimen can be best studied with the SEM[2]. The SEM is able to document the localization of the mapped areas and to document the particles within them, and to supplement the IMMA analysis with EDXA or WDXA studies. In this case the nature of the beryllium containing particle had to be further documented using wavelength dispersive x-ray analysis (WDXA). The SEM documented the location, size and shape of the particle, as well as the absence of other elements by EDXA and the presence of oxygen by WDXA (Figure 2).

Such tissue samples also provide a test of the theoretical considerations of electron backscattering and contrast for low atomic number materials. Some calculated backscattered electron (BSE) coefficients (7) and expected contrast between pairs of materials are given in Table 1.

Table 1: Calculated Atomic Number Contrast in Backscattered Electron Signal*

Paired Materials Compared	Be $(\eta=8.65\times10^{-2})$	C $(\eta=1.15\times10^{-1})$	BeO $(\eta=1.22\times10^{-1})$	SiO_2 $(\eta=1.76\times10^{-1})$
C $(\eta=1.15\times10^{-1})$	0.25	0	0.058	0.35
Carboxymethylcellulose (CMC) $(C_9H_{16}O_5)\eta$ $(\eta=1.20\times10^{-1})$	0.28	0.040	0.016	0.32
Beryl $(Be_3Al_2Si_6O_{18})$ $(\eta=1.68\times10^{-1})$	0.49	0.32	0.27	0.045

* η calculated for pure elements = $-0.0254 + 0.016\ Z - 0.000186\ Z^2 + 8.31\times10^{-7}Z^3$
(assumes flat sample) (Reference 6)

η compound = $\sum_i C_i\ n_i$ (C = weight fraction)   (Reference 7)

Contrast = $\dfrac{\eta_{max} - \eta_{min}}{\eta_{max}}$ (Reference 8)

The BSE coefficient has its greatest rate of change with atomic number at the low atomic number end of the scale, thus greater contrast will be apparent for a given difference of atomic number between light materials than between heavier ones. This is apparent in Figure 3 showing contrast between between carbon, CMC and beryllium metal and between carbon and beryllium oxide in Figure 2.

The limits of detection of inorganic material in tissues using BSE extend to very light materials such as beryllium oxide. Even organic materials such as carboxymethylcellulose (CMC) had a backscattered electron yield sufficiently greater than the carbon to produce visible contrast in the image. The contrast observed between carbon and CMC
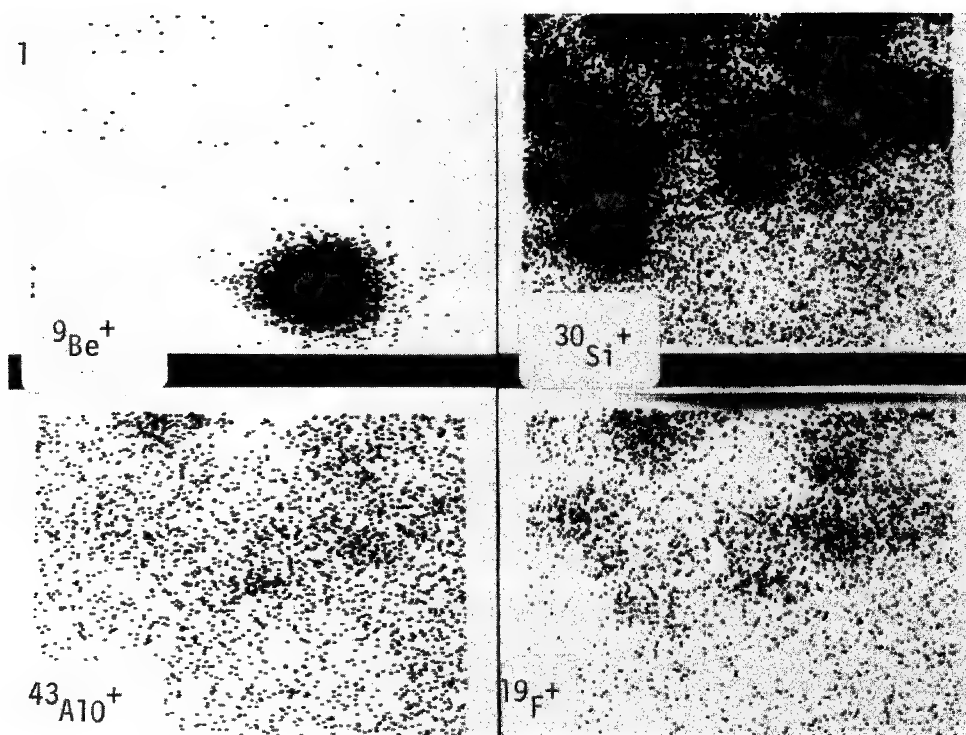
Figure 1, IMMA ion distribution maps of the same area for beryllium, silicon, aluminum and fluorine. Note that no silicon, aluminum or fluorine was associated with the beryllium-containing material, also that the high count rates for silicon and aluminum necessitated the use of minor isotopes or compounds of these elements for successful distribution mapping. IMMA conditions 20KV O_2^+ ions, specimen current approximately 40 nanoamps, beam diameter approximately 30 micrometers. Raster width 150 μm plus beam diameter.
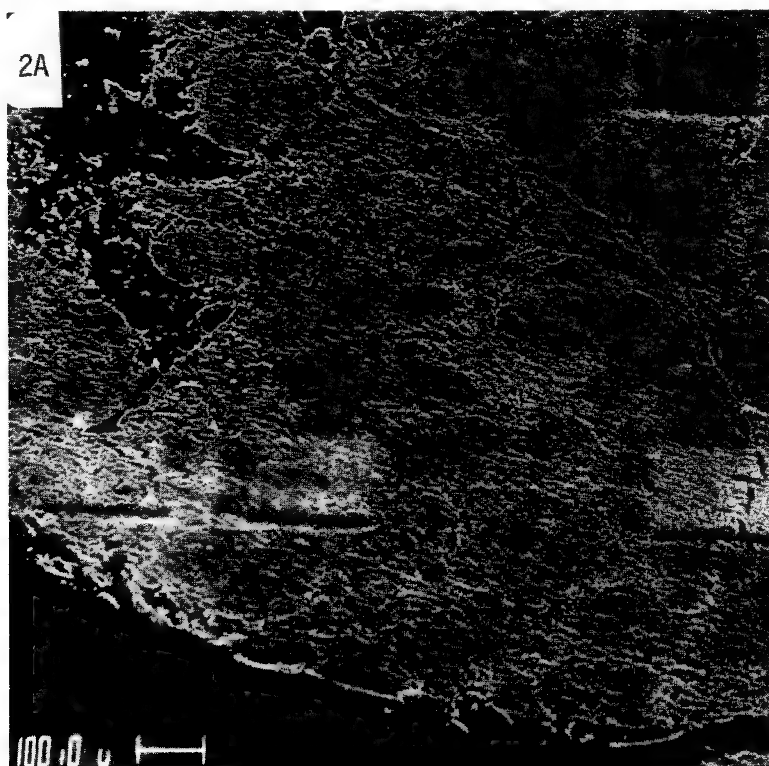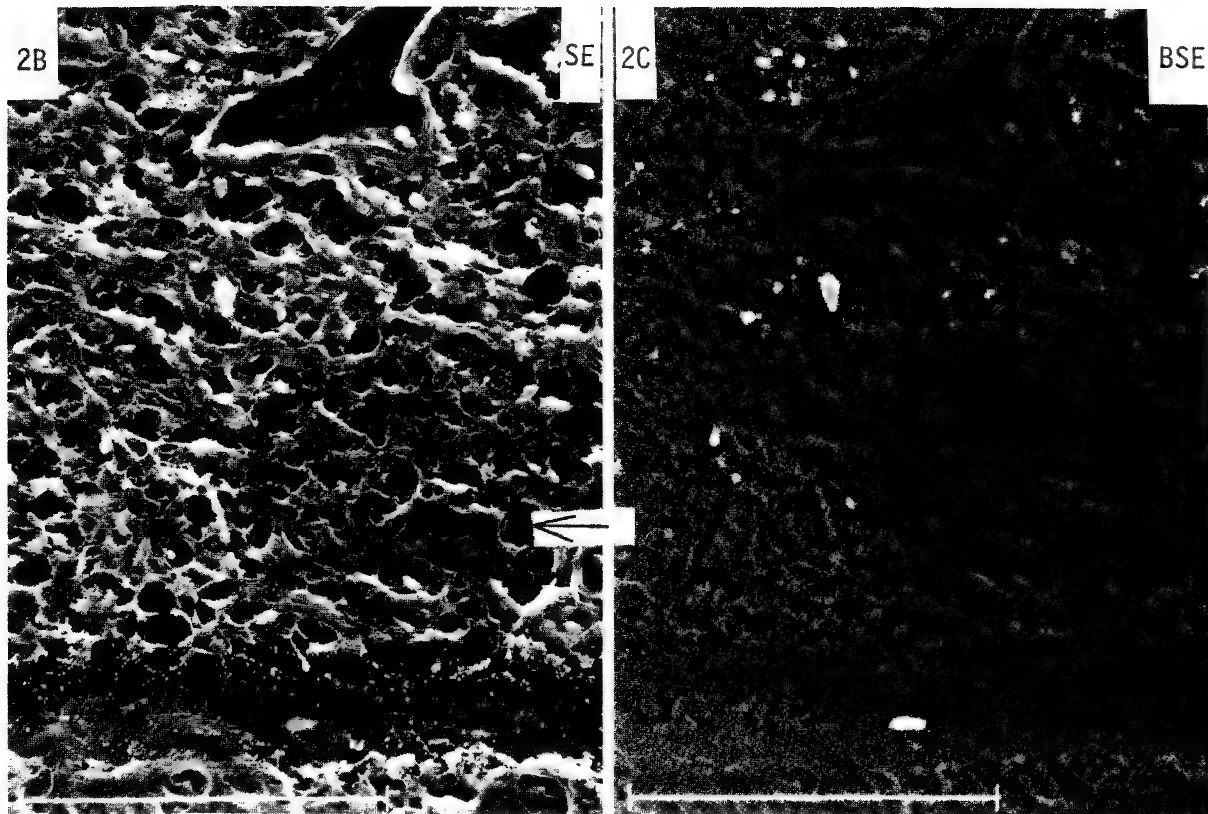
Figure 2, A: SEM view of same section after IMMA analysis, with deeply etched lines beneath mapped rasters. Marker = 100 μm. B and C: Area corresponding to IMMA maps of Figure 1. Note preservation of tissue in mapped area and presence of smooth area (arrow) corresponding to epithelioid granuloma; in the backscattered electron image (C) the presence of several bright dust particles in the tissue. D and E: Higher magnification shows the presence of a single hexagonal structure within the epithelioid granuloma corresponding to the location of beryllium in the IMMA distribution maps. Note higher backscattered electron yield from this particle than from surrounding tissue. (No detectable BSE compositional contrast was observed at 45°tilt). F: The wavelength dispersive distribution map of the same area for oxygen shows the presence of oxygen in the same particle. SEM conditions 0°tilt, 20KV, specimen current 1.0 nanoamps using ETEC SEM with solid state BSE detector.5 Wavelength dispersive map done using 5KV beam and approximately 10 nanoamp beam current with Applied Research Labs SEM Q. Specimen uncoated for IMMA analysis and carbon coated for subsequent SEM analysis. Marker in D and E = 1.0 μm.
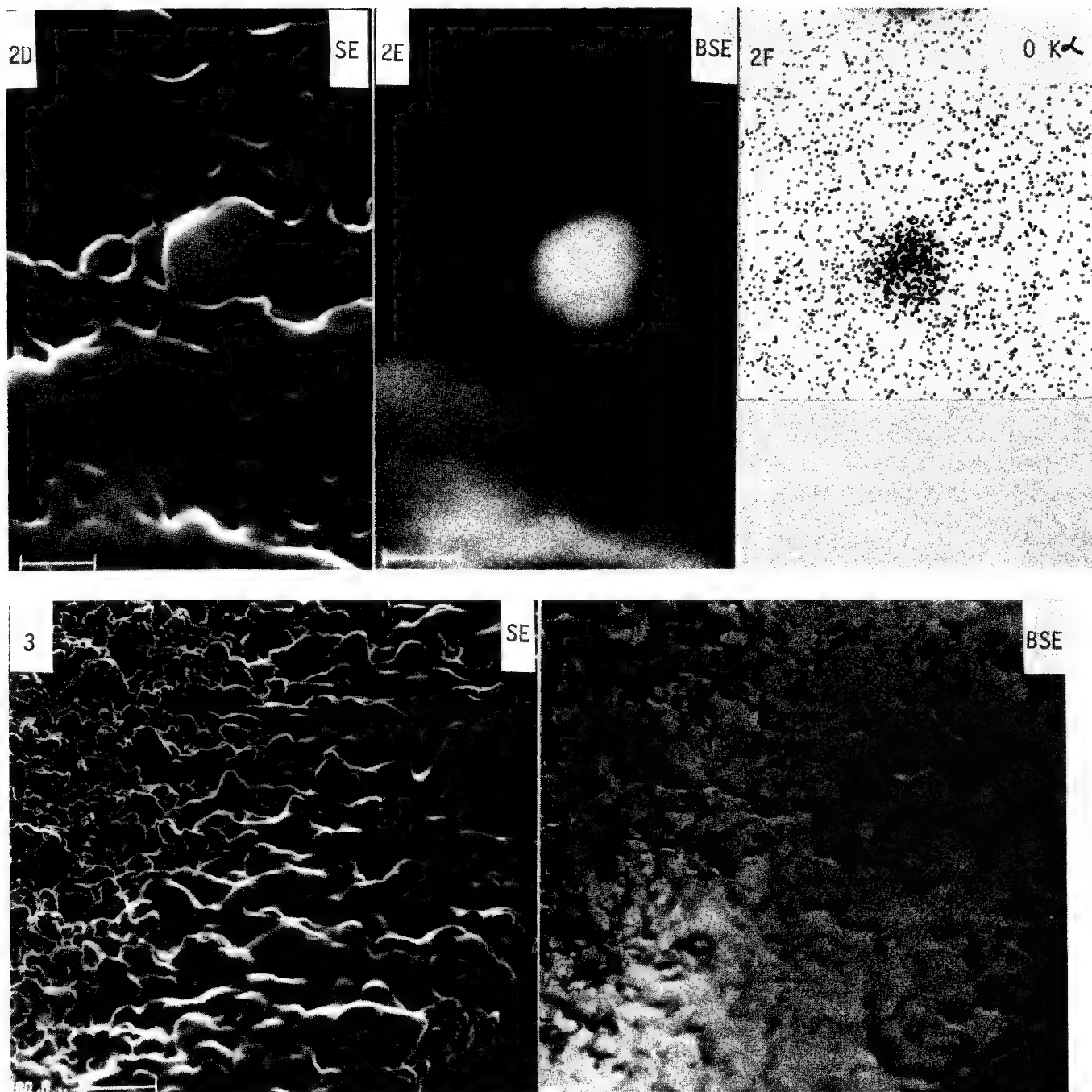
Figure 3, A suspension of beryllium metal flakes in aqueous carboxy-
methylcellulose (CMC) solution was placed on a carbon disc and dried
at 80°C. The central portion was analyzed with the IMMA until a
constant beryllium count rate was obtained. The backscattered elec-
tron image shows the edge of the carbon disc on the right, the CMC
towards the center the exposed pure beryllium to the left. The
intensity of the BSE signal produces detectable contrast between
the beryllium and the carbon discs and barely detectable contrast
between the carbon and the CMC. Note there is also some beryllium at
the edge of the sample drop. Examined at 20KV, specimen current 0.5
nanoamps, 45°tilt. Marker = 100 μm.

(calculated 0.040) is near the limits of detectability under the conditions tested. The contrast revealed between nuclear chromatin material and the surrounding cellular tissue and carbon substrates is detectable and represents the same range of contrast as seen between CMC and carbon. However, exact calculations of the expected back-scattered electron coefficient for the nuclear chromatin (containing a mixture of nucleic acids, sugars, proteins and salts) are not feasible.

References:
1. C.A. Anderson and J.R. Hinthorne. Ion microprobe mass analyzer. Science 175, 853-857, 1972.
2. J.L. Abraham, R. Rossi, N. Marquez and R.M. Wagner. Ion microprobe mass analysis of beryllium in situ in human lung. In "Scanning Electron Microscopy/1976" (Johari, O. and I. Corvin, eds.) I, p. 501-506, I.I.T. Research Institute, Chicago, 1976.
3. J.L. Abraham and T.A. Whatley. Ion microprobe analysis of beryllium containing particulates in situ in human lungs. Fed. Proc. 36, 1090, 1977.
4. J.L. Abraham. Scanning electron microscopy as an aid in diagnosis-An overview. In "Scanning Electron Microscopy/1977" (Johari, O. and I. Corvin, eds.), II, p. 119-128, I.I.T. Research Institute, Chicago, 1977.
5. J.L. Abraham and P.B. DeNee. Biomedical applications of back-scattered electron imaging--One year's experience with SEM histochemistry. In "Scanning Electron Microscopy/1974" (Johari, O. and I. Corvin, eds.), p. 251-258, I.I.T. Research Institute, Chicago, 1974.
6. W. Reuter. The ionization function and its application to the electron probe analysis of thin films. in "X-ray Optics and Microanalysis" (G. Shinoda, K. Kohra and T. Ichinokawa, eds), University of Tokyo Press, p. 121-130, 1972.
7. K.F.J. Heinrich. Electron probe microanalysis by specimen current measurement. in "X-ray Optics and Microanalysis" (R. Castaing, P. Deschamps and J. Philibert, eds) Hermann, Paris, p. 159-165, 1966.
8. D.E. Newbury. Fundamentals of Scanning Electron Microscopy for Physicists: Contrast Mechanisms. In "Scanning Electron Microscopy/1977" (Johari, O. and I. Corvin, eds.), I, p. 553-568, I.I.T. Research Institute, Chicago, 1977.

FACTORS AFFECTING THE SPATIAL RESOLUTION OF AUGER ELECTRON SPECTROSCOPY

E. K. Brandis
IBM Systems Products Division
East Fishkill
Hopewell Junction, N.Y. 12533

In a SEM the spatial resolution is a function of the beam diameter, the sample and the type of information displayed. In the emissive mode the spatial resolution is limited by the escape depth of the secondary electrons which is approximately 50 Å. Everhart discussed the recordings of noise-free secondary electron images and found that 10^4 electrons are necessary for each picture point. To record an electron image consisting of 500 x 500 = 250,000 picture points in 5 minutes, a current of 10^{-12}A is required.

Auger Electrons ranging in energy from 10 - 2000 eV have a mean escape depth of approximately 20 Å. In principle, therefore, it appears possible to perform Auger micro analysis with the same spatial resolution. However, only one in 10^5 reflected electrons is an Auger electron. For an equivalent signal to noise ratio (S/N) a higher current and or longer recording times are necessary.

In the emissive mode of the SEM where one is interested in surface topography only those secondary electrons produced within the area on which the primary electron beam is incident carry information on high spatial resolution surface topography. Therefore for high spatial resolution secondary electron images the signal generated by the secondary electrons generated by backscattered electrons is suppressed. This signal suppression is possible because all secondary electrons have the same mean energy of 10 eV and do not carry any additional information.

Auger electrons are generated both within the small area on which the electron beam is incident and within the larger area from which the high energy reflected electrons leave the surface. In this sense the production of secondary electrons and Auger electrons is very similar.

However, when the surface composition changes abruptly at an interface the energy of the Auger electrons produced by the incident electron beam is not the same as the energy of the Auger electrons generated by the high energy reflected electrons. Although the actual interface is abrupt the Auger signal does not change as abruptly despite the fact that the incident beam diameter is sufficiently small to delineate the interface in the emissive mode. A suppression of the signal due to Auger electrons generated by high energy reflected electrons is not possible because from the Auger peak measurement alone it is not clear if the gradual change in the Auger peak intensity is due to a gradual change in composition or due to the affect of backscattered electrons.

For this reason the spatial resolution of Auger electron spectroscopy is limited to an area from which reflected electrons escape. An improvement in spatial resolution can be expected if lower beam energies are employed such that the resulting backscattered electrons leaving the surface are of insufficient energy to excite Auger electrons.

REFERENCES
1.   T. E. Everhart, Dissertation, Cambridge Univ. (1958).

SCANNING ELECTRON MICROSCOPY : SEI CONTRAST AND

ELECTRON SPECTROSCOPY OF SURFACE LAYERS

————————

C. LE GRESSUS [*] - F. PELLERIN [*] - H. OKUZUMI [**] -

Service de Chimie Physique - CEN Saclay - [**] JEOL EUROPE.

Ultra High Vacuum (U.H.V) Scanning electron Microscopes (SEM) are now associating with the Auger electron Spectroscopy (AES)[1]. The secondary electron image (SEI) contrast is sensitive to the surface composition and allows for example the observation of organic monomolecular layer on metallic substrate [2] or helps the choise of sample reactive zones for a further AES measurments. However with the standard SEM working conditions (Ip = 10^{-12}A., spatial resolution better than 50Å, frame definition 1024 lines · 1024 points, scan speed : 1 to 100 s) the current density reaches 10^{20} electrons cm^{-2} . s^{-1} and the dose in the elementar spot varies from 10^{14} to 10^{16} electrons cm^{-2}. Such a primary current is too low for AES as the Auger Yield is in the range of 10^{-4} - 10^{-5} Ip [3] but these doses are high enough to produce an electron stimulated desorption (ESD)[4], a beam cracking or a polymerisation of organic species [5] an oxyde reduction [7] ... The electron beam damage often [6] produces a dark scanned area as the true secondary emission (TSE) is modified. Moreover we observed that the TSE is due to different peaks located around 6,8,13, 17,20 eV... which also vary under the primary beam as the sample current and SEI contrast. These TSE peak intensities are far higher than the Auger peak of the target and their understanding could increase the SEM facilities in surface Science.

Some preliminary results reported are obtained with a U.H.V. JEOL-JAMP 3 [8] equiped with a LaB_6 gun , which brightness is modulated [9] in order to obtain the En(E) energy electron distribution through a cylindrical mirror analyser (CMA, energy resolution $\Delta E = 0,003$ E) and a

lockin amplifier detection. The typical experimental conditions are :

- 1. primary current Ip measured in a Faraday cup : 2. 10^{-9}A.
- 2. accelerating voltage Ep : 0.3 keV $\ll$ Ep $\ll$ 30 keV
- 3. frequency of beam brightness modulation : from 3 to 50 KHz
- 4. signal to noise ratio measured at the elastic peak Ep = 500eV, 3KHz, of a gold foil : 2.10^3

The samples are either a thin film (100Å) of gold evaporated on a collodion film or a pure gold foil (99,999 %) before and after ion etching (Ar, 2 keV, 10^{-5}A. Cm^{-2}). Measurements are acheived after stabilisation of the sample current under the electron beam bombardment. The results are :

(i). The TSE intensity of a contamined sample is from 10 to 100 times higher than the TSE intensity of a pure sample. For a pure sample the main features of the En (E) distribution are the elastic peak, the energy loss peaks and Auger peaks.

(ii). The intensity of the 6 eV peak measured on the thin film varies as $Ep^{-2/3}$.

(iii). For the uncleaned foil of gold the intensities of the 6 eV, 20 eV, the elastic peak at Ep and the loss peak at Ep-20 eV vary similarly.

The usual interpretation of subsidiary peaks STE resulting to plasmon[10] decay or interband transitions does not allow to explain all experimental data[12]. We suggest that these emissions also could be produced from excited states of adsorbed molecules (CO, $C_n H_m$...) or of adatoms-matrix boundaries. The excited states could be induced by plasmon decay or direct energy losses of the impinging primary electron, then their deexitation could produce secondary electrons or ions.

The SEI images of the foil of gold show a crystallographic contrast for Ep values higher than a few keV. This contrast is due to backsattering contribution under channeling effect when the penetration deepth of the primary beam is higher than the contamined layer thickness The same backscattering contribution is used to separate surface details and deeper features as inclusions in a matrix for example [13]. All these informations make SEM a powerful tool.

BIBLIOGRAPHY

(1) A.N. Broers, E.K. Brandis, in Scan. elect. Micros. IITRI, 1969, 15, NC. MC Donald, ITTRI, 1971, 89.

(2) M. Vandevyver, C. Le Gressus, (1972) 6th Int. Conf. on X Ray optics, Tokyo, 467, A. Barraud and Al. (1974) 8th Int. Cong. on electron microscopy, Camberra, vol. I, 682.

(3) H.E. Bishop, J.C. Rivière, j. appl. phys. 40, (1969) 1740

(4) T.E. Madey, J.T. Yates In., Journal of vacuum sci. and technolo. 8 (1971) 525

(5) M. Isaacson, J. Chem. Phys., 56 (1972) 1813.

(6) C. Le Gressus, D. Massignon, R. Sopizet, ISSC3, York, 1977, C. Le Gressus, D. Massignon, B. Blanchard, 3° Col. Int. Phys. et Chim. Surf. Sol. (1977) Grenoble – France –

(7) J.S. Johannesen, Faraday Discussion, Chem. Soc., 60 (1975) 313.

(8) A. Mogami and Al., Proc. 8th Int. Cong. on electron Microscopy, Canberra I(1974), 60.

(9) C. Le Gressus, D. Massignon, R. Sopizet, Comptes Rendus Acad. Sci., 280B (1975) 439.

(IO) R.A. Ferrel, Phys. Rev. 107, (1957) 450.

(11) A.J. Dekker, Solid State Phys. 6 (1958) 25

(12) D. Massignon, C. Le Gressus, R. Sopizet, J.P. Duraud, Compte rendus 281B (1975) 579.

(13) H. Seiler, in Scanning electron Microscopy – 1976, ITTRI, 9.

Surface Distribution of Backscattered Electrons in the SEM and EPMA

K.Murata, M.Kotera and K.Nagami

Department of Electronics
University of Osaka Prefecture
Sakai, Osaka, Japan

It is useful to know the emission area of backscattered electrons in scanning electron microscopy(SEM), electron probe microanalysis(EPMA) and scanning auger electron microscopy(SAM). Also this is essential to study of a proximity effect in pattern fabrication in electron lithography. One of the authors has already reported[1] some results on the spatial distribution of backscattered electrons calculated by Monte Carlo simulation. To check a reliability of the calculated results, we performed some experiment.

A Si wafer was spin-coated with the positive electron resist poly-methyl-methacrylate(PMMA, molecular weights of 700,000-750,000). The resist layer thickness is around 1000 Å. The film is so thin that we can discriminate the energy dissipation by primary electrons from the one by backscattered electrons from the substrate. The sample was baked at 170°C for 20 min. After exposure by a stationary electron beam at various doses, the sample was developed in 95% ethanol for 150 sec. The area with PMMA removed was observed with a bright contrast in the SEM because of higher secondary electron emission from the substrate. An unremoved area where the polymer cross-linked appeared in the central part at excess doses. One example of measurements of a dot radius is shown in Fig.1 as a function of dose. In this case an electron probe size is less than 2000 Å.

The Monte Carlo technique was used to calculate the spatial distribution of energy dissipation in the polymer thin film. A calculation procedure is the same as previously published[2]. If we assume a critical absorbed energy density which gives an energy density required to be dissolved with the developer, we can produce a dot radius versus dose curve. Similarly a critical energy density is assumed also for a cross-linking event. These results are also shown in Fig.1. A rather good agreement is obtained between experiment and theory. The assumed critical absorbed energy densities ε_{cs} and ε_{cl} are 5.7×10^{21} eV/cm^3 and 3.7×10^{23} eV/cm^3, respectively. Note here that use of a different value of ε_c only translates the theoretical curve along the abscissa, but does not change a shape of the curve. The value of ε_{cs} is relatively smaller than that by Shimizu et al[3]. At present a reason for this difference is not understood.

Fig.2 shows the radial distribution of backscattered electrons which give rise to energy dissipation in the polymer in the wide region around a beam incident point. The quantitative agreement in energy dissipation between experiment and theory guarantees a relatively high reliability of the above calculated radial distribution. The present result will be discussed in comparison with a previous work[4,5,6,7).

1.   K. Murata, J. Appl. Phys. 45, 4110(1974).

2.   D.F. Kyser and K. Murata, IBM J. Res. Develop. 18, 352 (1974).

3.   R. Shimizu, T. Ikuta, T.E. Everhart and W.J. DeVore, J. Appl. Phys. 46, 1581(1975).

4.   R.F.W. Pease, J. Sci. Instrum. 42, 158(1965).

5.   R.D. Heidenreich and L.F. Thompson, Appl.Phys. Lett. 22, 279(1973).
     R.D. Heidenreich, L.F. Thompson, E.D. Feit and C.M. Melliar-Smith, J. Appl. Phys. 44,4039(1973).

6.   R.J. Hawryluk, H.I. Smith, A. Soares and A.M. Hawryluk, J. Appl. Phys. 46, 2528(1975).

7.   T. Yamamoto, phys. stat. sol. (a)38, 361(1976).
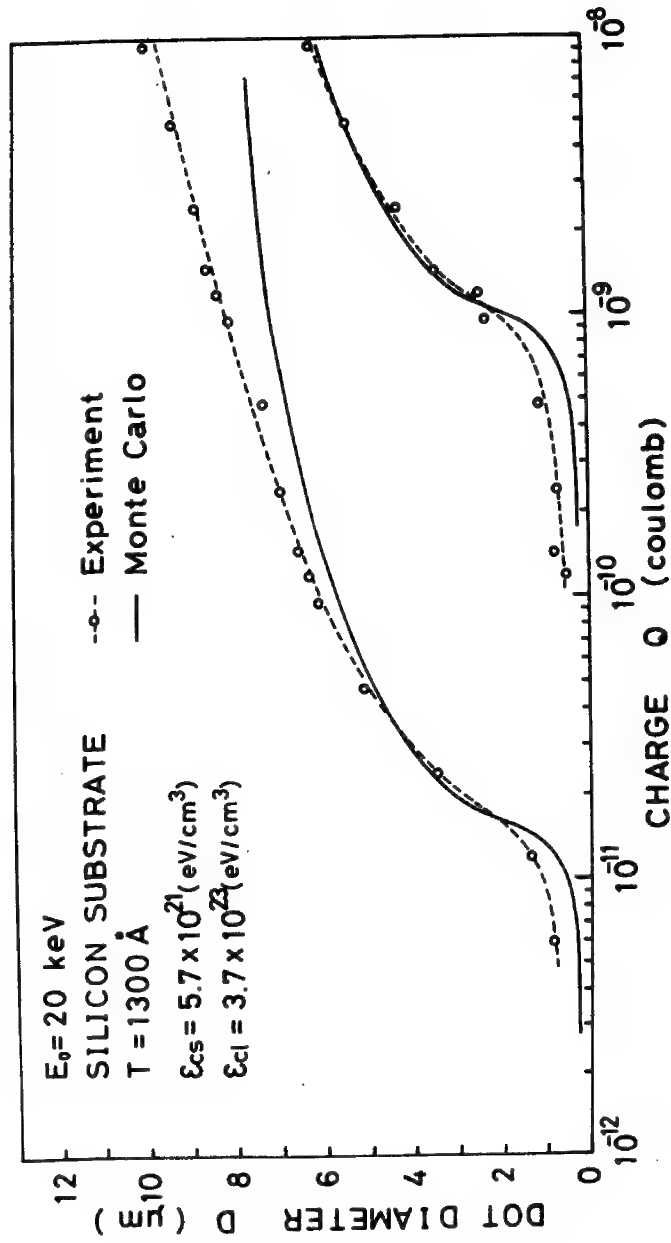
Fig.1 Dot diameter as a function of the total incident electric charge. Right: cross-linking.
Left: degrading.
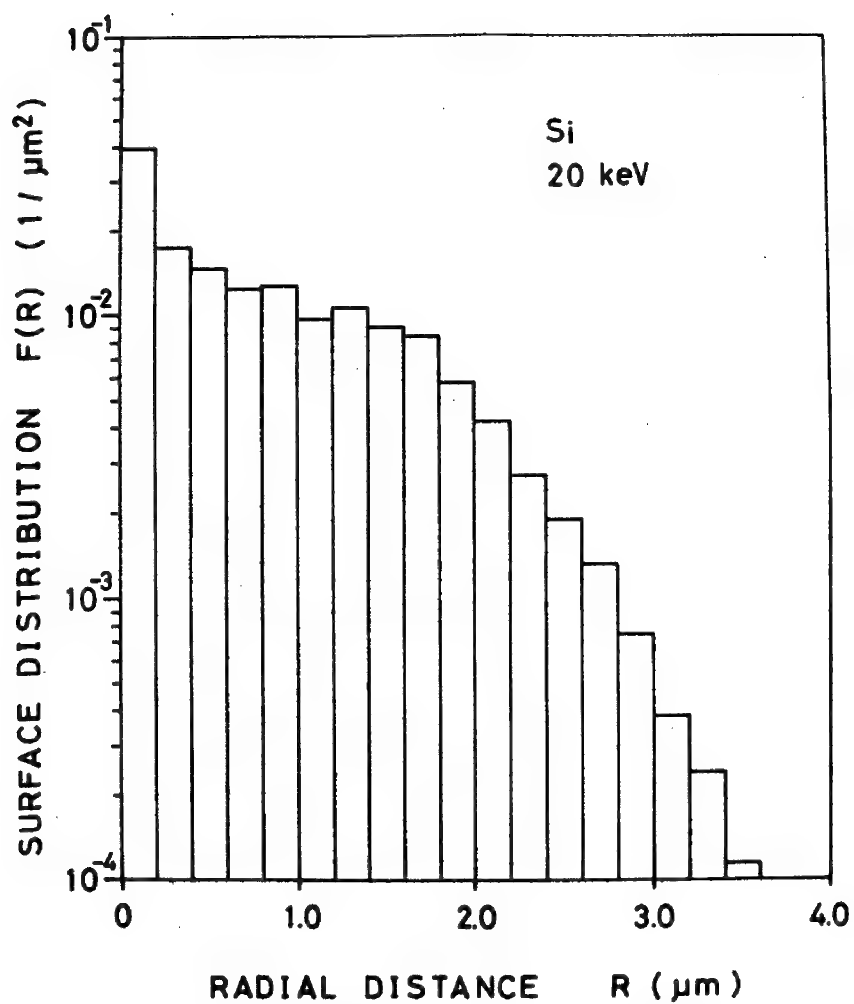
Fig.2 The radial distribution of backscattered
electrons for Si, 20 keV. 4000 incident
electron trajectories are calculated.

EXPERIMENTAL TECHNIQUES FOR HIGH RESOLUTION SEM

Ron Anderson, IBM, Dept 875, Bldg 300-400
Hopewell Junction, NY 12533

Very recently it has become possible to make SEM micrographs with resolutions on the order of 20A or better with commercial instruments. This opens up the magnification range above 50,000X for high quality work. The instruments required for this type of analysis must meet rigid specifications. Ultimately, it is the brightness, electron energy spread, and the aberration of the final probe forming lens that determine an electron beam instrument's ability to obtain high resolution scanning images. In our laboratory, we use a JEOL 100C transmission electron microscope equipped with a thermally assisted field emission gun, to provide an electron source with a brightness of 5×10^8 A/cm·str and an electron energy spread of 0.5 eV at 80 kV, and a strongly excited objective lens, with a C_S about 1/40 that of a conventional SEM, to perform scanning image analysis. In scanning mode, secondary electrons are directed in the reverse direction to the incident electron probe by means of the pre-field of the objective lens, whereas in the standard scanning electron microscope, the specimen is placed beneath the objective lens and the secondary electrons are directed at an angle of 90° with respect to the incident electron probe.

Possession of an instrument capable of high resolution SEM analysis does not guarantee high quality results. Careful focusing and astigmation is, of course, required. In addition, the operator must insure that the electron optical alignment of the instrument is perfect; this means daily checks and touching up. Further, given a perfectly aligned, focussed instrument, it is still possible (probable?) that one is taking high magnification pictures of artifacts. Very careful cleaning of the specimen is mandatory. Pulling a collodion extraction replica and ion-milling the specimen surface are two useful methods for cleaning specimens. The greatest source of artifacts, at magnifications over 50,000X, is the photography of structure associated with the thin film conductor deposited on the sample surface for charge neutralization purposes. In this regard, gold films are the worst offenders. Even extremely thin films of gold nucleate relativly large, irregularly shaped, islands that are readily observed at magnifications over 50,000X. Sputtered Pt-Pd and carbon thin films produce superior, nearly amorphous, thin films. One coating method we find satisfactory is to sputter 50-150A of Pt-Pd in quick flashes, alternating two seconds of sputtering with two seconds of rest, to produce a thin film containing very little structure visible at less than 100,000X. The best evaporated metal

films seen in our lab to date were produced by evaporation from a tungsten needle source. These films allow artifact-free magifications up to 150,000X.

The next most serious source of quality loss in high magnification SEM analysis is contamination of the sample. Contamination arises from two sources: in-situ contamination, mainly from rotary and diffusion pump oil infiltration; and ex-situ contamination, brought into the system already on the specimen. Cold traps and modern column design minimize the in-situ contamination in most instruments. Ex-situ contamination becomes serious when mobile surface ions rapidly diffuse to the beam site, building up large contamination mounds or the familiar black raster marks. Some control can be obtained by heating the entire specimen, in its mount, to 125-200°C immediately before insertion into the column; if your specimens can tolerate such treatment. Also, scanning the specimen at low magnification with a raster centered on the specimen area of interest, before high magnification examination, will tend to fix mobile surface ions in place.

It is clear that for SEM work at magnifications over 50,000X, utilizing the new class of SEM/TEM instruments now commercially available, there are requirements for very careful specimen preparation and operational procedures.

COMPARISON PAIRS OF SURFACE TOPOGRAPHY IMAGES OBTAINED BY VARYING THE ELECTRON DETECTOR CONDITIONS

S. H. MOLL and K. R. BENOIT

AMR CORP., BEDFORD, MASS.

In recent years a number of specialized backscattered electron detectors suitable for various SEM applications have been developed. Among these are the low-loss detector[1] for surface imaging at high resolution, solid state detectors in various configurations[2,3], for examining heavy metal staining in biological specimens, as well as for high resolution imaging of surface features on coated, low atomic number specimens, and highly efficient scintillation type detectors for both high resolution imaging and for the examination of uncoated specimens[4].

The Thornley-Everhart (T-E) scintillation-photomultiplier detector[5] appears in some geometrical configuration in essentially all SEM's in use today, where it is primarily utilized for the collection of secondary electrons. As a result of the configuration, size and location of these detectors in the SEM specimen chamber, only a small fraction of the spatial distribution of backscattered electrons are collected. However, when configured with a voltage biased collector screen (or operated with or without high voltage at the scintillator) to reject secondary electrons, the detector may be used to form backscattered electron images. Due to their relatively low solid angle of collection and orientation in the specimen chamber with respect to the specimen, detectors of this configuration are highly directional for BSE. As a result, images obtained in this mode exhibit a great deal of "shadowing" if the specimen contains a coarse surface topography.

Although this characteristic of the typical T-E detector is well known, it is the simple purpose of this paper to review the advantageous use of the directional shadowing observed in backscattered electron SEM images in order to illustrate how such features may aid in the better

understanding of the sample surface topography.

Figure 1 is a typical secondary electron image obtained with the T-E detector on a ductile fractured Cr, Mn, Fe alloy metal specimen. Figure 2 is a backscattered electron image obtained with the T-E detector of the same area. The elimination of the bright edges and the distinct shadows produced in the backscattered electron image clearly aid in understanding the three-dimensional aspects of the surface features which are not so readily interpreted in the secondary electron image. What may be described as a mixed SE and BSE image may be obtained utilizing a bias voltage on the collector screen which is intermediate between that used for the SE or BSE image. It is roughly estimated that in this case (Figure 3), the total signal is comprised of approximately equal amounts of SE and BSE contribution. The mixed image is less harsh than the BSE image and some information is contributed from formerly highly shadowed areas.

A second example involving a sheared medium carbon steel bolt is shown in Figures 4 and 5, comparing the SE and BSE images, respectively. The topography of the specimen is more clearly revealed in the BSE image.
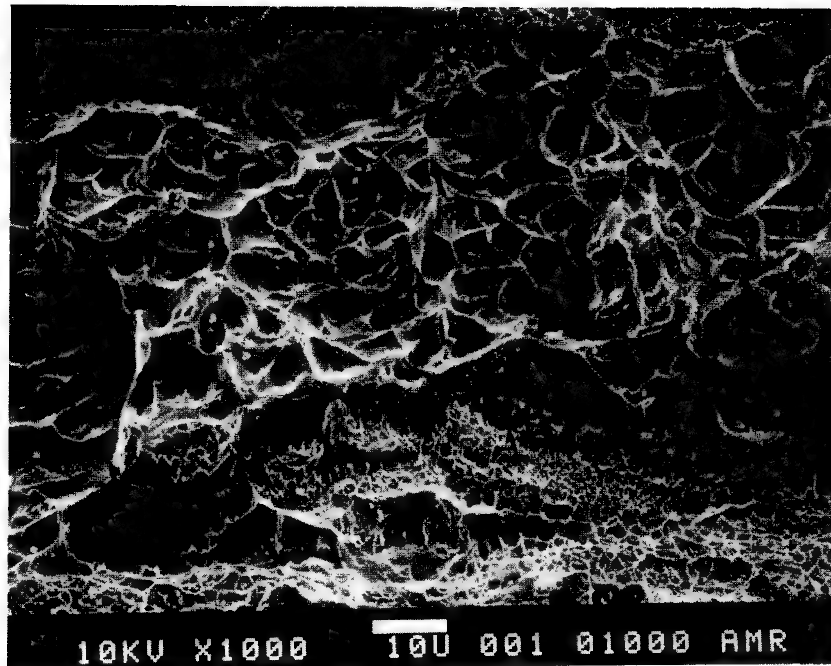
Figure 1 - Fractured Cr-Mn-Fe Alloy, 30° Tilt
SE Image, Collector +300V
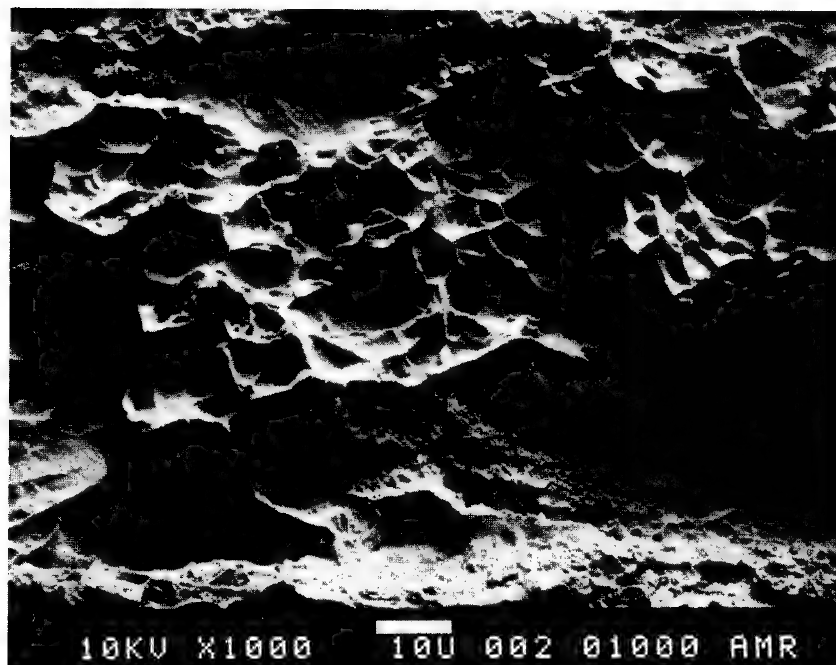
Figure 2 - Fractured Cr-Mn-Fe Alloy, 30° Tilt
BSE Image, Collector -100V
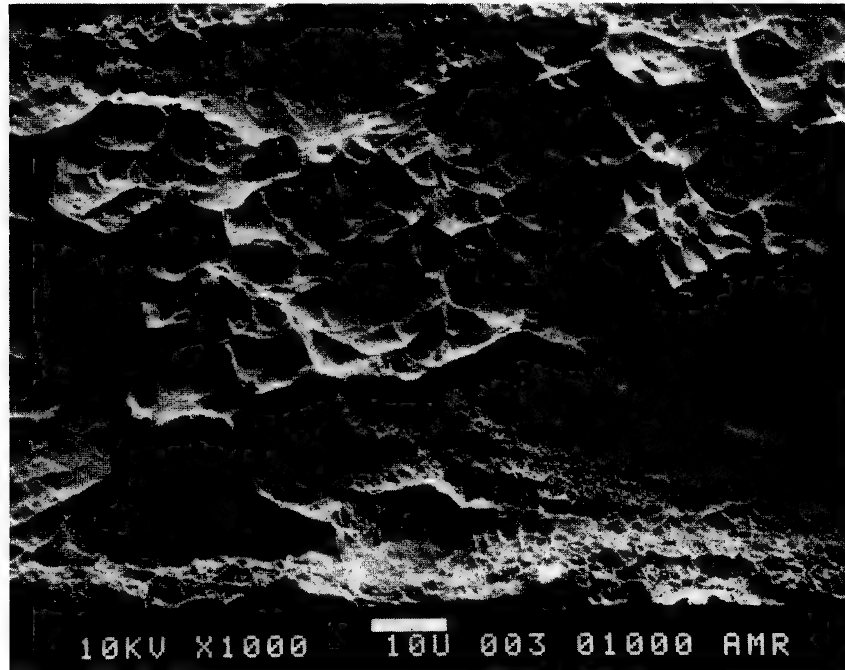
Figure 3 - Fractured Cr-Mn-Fe Alloy, 30° Tilt, "Mixed" Image, Collector OV
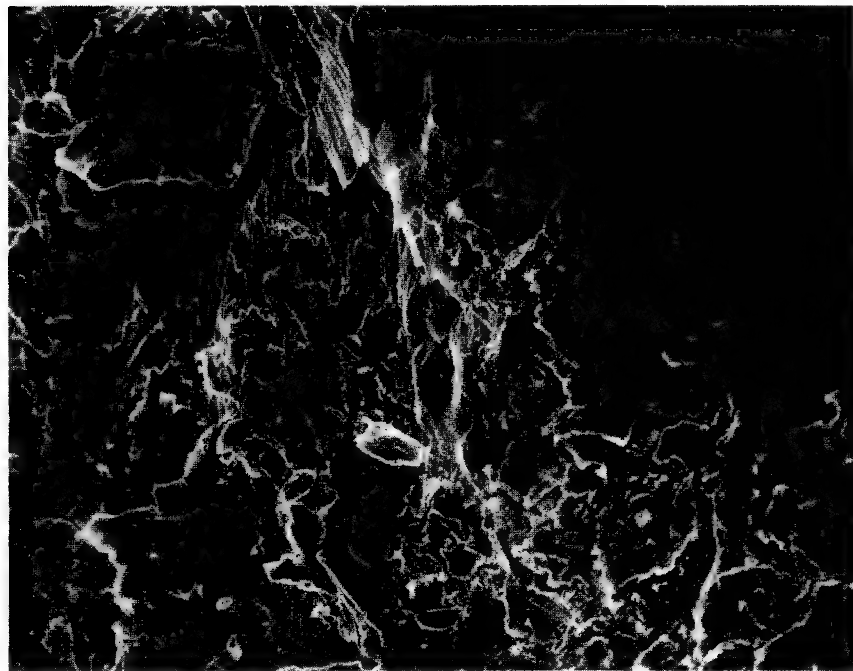
Figure 4, Sheared Medium Carbon Steel Bolt, 1000X, 64° Tilt, 20KV, SE Image
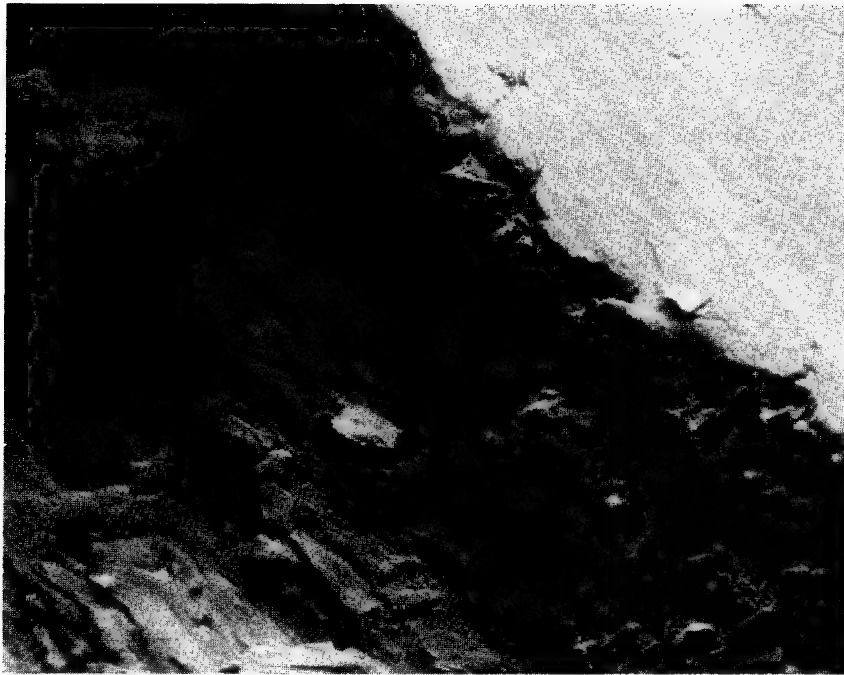
Figure 5 - Sheared Medium Carbon Steel Bolt,
1000X, 64° Tilt, 20KV, BSE Image

(1)   Wells, O.C., "Low-Loss Image for Surface Scanning Electron Micro-
      scope"; App. Phys. Vet., 19, 1971, 232-235.

(2)   Abraham, J.L., and DeNee, P.B., "Biomedical Applications of Back-
      Scattered Electron Images", SEM/IITRI/1974, 251-258.

(3)   Lin, P.S.D., and Becker, R.P., "Detection of Back-Scattered Electrons
      with High Resolution", SEM/IITRI/1975, 61-70.

(4)   Robinson, V.N.E., "Back-Scattered Electron Imaging", SEM/IITRI/1975,
      61-60.

(5)   Everhart, T.E., "Reflections on Scanning Electron Microscopy", SEM/
      IITRI/1968, 1-12.

DIRECTIONALLY-SENSITIVE ELECTRON DETECTOR
FOR SCANNING ELECTRON MICROSCOPE (SEM)

Oliver C. Wells

IBM Thomas J. Watson Research Center
P.O. Box 218, Yorktown Heights, NY 10598

In the usual form of the low-loss electron detector[1-4], electrons from the specimen in the SEM are either accepted or rejected by a retarding-field energy filter and, since this has the effect of reducing them to a low energy in the plane of the filter grid, they can then be collected from the entire area of that grid by a scintillator which is held at a positive potential of several kilovolts relative to the filter grid[5-7]. Normally, if a scintillator is used to collect the backscattered electrons, then the collection solid angle is established by the physical size of the scintillator and by its distance from the specimen, whereas with this arrangement the low-loss electrons can be collected from the entire area of the filter grid. This collector system is generally positioned with a low takeoff angle relative to the specimen surface so that, with an oblique angle of electron incidence, the forward lobe of the backscattered electron angular distribution pattern enters the collector (Fig. 1). This collector system has the advantage that it is equally effective for collecting either the secondary electrons or the low-loss electrons, depending on the potentials which are applied to the grids and to the scintillator.

Some preliminary results have now been obtained in the secondary electron mode from a modified version of this detector in which the compartment which contains the scintillator behind the filter grid has been divided into two halves by a vertical partition[8]. Each of these sub-compartments contains a scintillator which is coupled to a photomultiplier, so as to give a pair of output signals. These outputs can be either added, subtracted or displayed individually, in the same manner as with Kimoto and Hashimoto's solid-state backscattered electron detector system[9]. (The control box selects the signals from either the anode or the final dynode of each photomultiplier.)

A pair of secondary electron images is shown in Fig. 2. The sample was a silicon wafer coated with a pattern in photoresist, which had been cleaved to give a sharp edge. The photoresist had been exposed and developed to give a number of slots down to the underlying silicon. This was not metallised. Normally, when such a sample is examined by the secondary electron method, the details close to the edge are obscured by a bright fringe having a width which is related to the total electron penetration depth. This can be explained by supposing that the secondary electrons which give rise to the useful details in the image are released from the upper surface of the specimen, while the secondaries which give rise to the bright fringe are released beyond the edge. The secondary electron images which were obtained by taking each photomultiplier output individually were found to be different in the respect that the penetration fringe was much more noticeable in one of them. This was explained by supposing that the secondary electrons which were released beyond the edge were prevented (by the edge) from reaching the input area of the collector which was above the flat part of the specimen.

References

1. O. C. Wells, "Low-loss image for surface scanning electron microscope", Appl. Phys. Lett. **19**, 232-235 (1971).

2. O. C. Wells, pp. 106-107 in "Scanning Electron Microscopy", by O. C. Wells, A. Boyde, E. Lifshin and A. Rezanowich, McGraw Hill, New York (1974).

3. A. Christou, "Correlation of low-loss electron images with Auger images of semiconductor substrate surfaces", IITRI/SEM/77/I, 159-166.

4. M. Pitaval et al., "Advances in crystalline contrast from defects", IITRI/SEM/77/I, 439-444.

5. The phosphor/photomultiplier system for detecting secondary electrons in the SEM was described by V. K. Zworykin, J. Hillier and R. L. Snyder, "A scanning electron microscope", ASTM Bulletin, No. 117, 15-23 (Aug. 1942).

6. The scintillator/photomultiplier system for detecting backscattered electrons in the SEM was described by K. C. A. Smith, pp. 123-125 and Fig. 6.5 in "The scanning electron microscope and its fields of application", Ph.D. Diss., Cambridge Univ., (1956).

7. The scintillator/photomultiplier system in its modern form was described by T. E. Everhart and R. F. M. Thornley, "Wide-band detector for micro-microampere low-energy electron currents", J. Sci. Instrum. **37**, 246-248 (1960).

8. O. C. Wells, "Proposed scheme for a directional low-loss detector", MAS, Proc. 11th. Annual Conference, 35A-35B (1976). (Was also printed in EMSA Proc.)

9. S. Kimoto and H. Hashimoto, "Stereoscopic observation in scanning microscopy using multiple detectors", pp. 480-489 in "The Electron Microprobe", Proc. Symp. held in Washington, D.C., Oct. 1964, T. D. McKinley et al., Eds., Wiley, New York (1966).
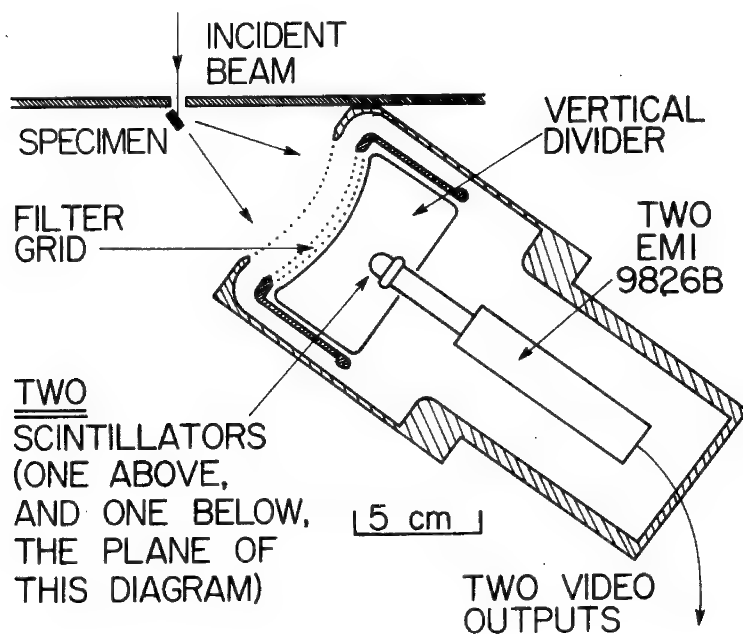
Fig. 1 Directionally-sensitive energy-filtering electron detector system.
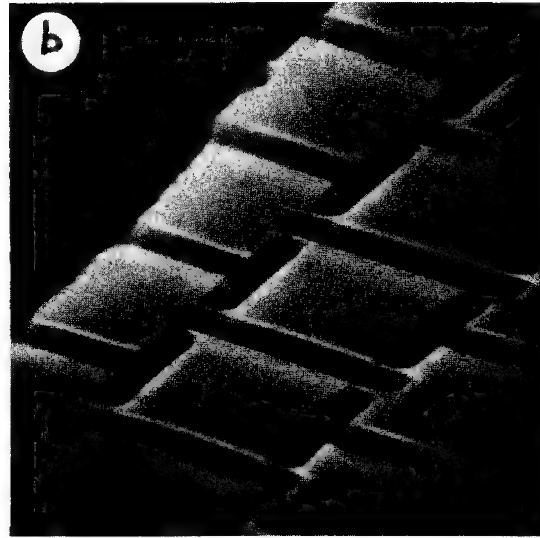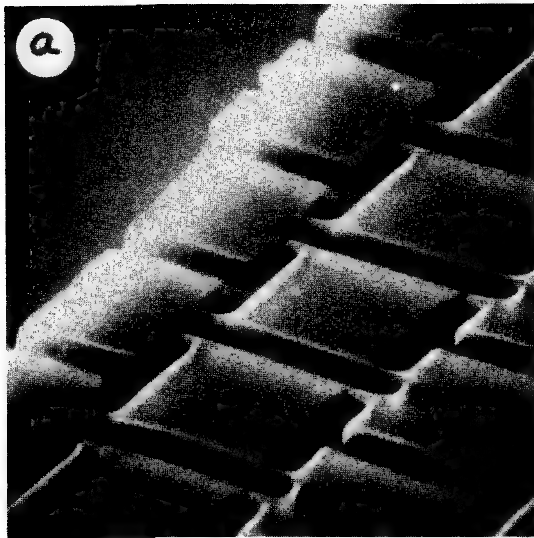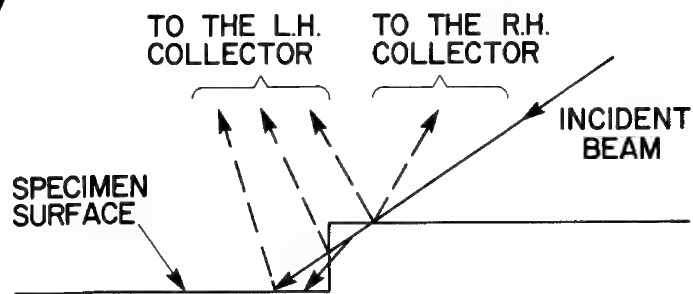
Fig. 2(a) and (b): Secondary electron images of resist-coated silicon wafer obtained by displaying the two photomultiplier outputs individually. Note the disappearance of the penetration fringe in Fig. 2(b). Beam energy = 20 keV. (c) Explanatory diagram.

SOME THOUGHTS ON ELECTRON ENERGY LOSS SPECTROSCOPY (ELS) WITHIN THE ELECTRON MICROSCOPE: WHERE DOES IT STAND AND WHERE IS IT GOING?*

Michael Isaacson[†]

Department of Physics and the Enrico Fermi Institute, The University of Chicago, Chicago, Illinois 60637

In many problems in the biological and materials sciences, electron micro-scopy provides useful information concerning the structural (spatial) proper-ties of thin specimens. However, there are important areas of research where this information could be greatly enhanced if one could couple it with the chemical characterization of the specimen on a similar scale. The need for this micro-characterization has seen in the last decade the growth of a trend which may be called analytical electron microscopy [1].

In this paper we will consider only that aspect of analytical electron micro-scopy having to do with exploitation of the fact that when fast electrons pass through matter, the amount and distribution of energy they lose is dependent upon the characteristics of the material through which they have passed. In particular, we will only concern ourselves with the utilization of the energy spectrum of these transmitted electrons. The concentration will center on: 1) what information is available using the transmitted energy loss electrons?, 2) how is information extracted (instrumentally)?, 3) what are the fundamental and experimental problems involved in this extraction?, 4) where does the present state of the art lie?, and 5) where is it heading (in this author's opinion)?

Although the technique of trying to obtain elemental information by analyzing the energy lost by electrons transmitted through thin specimens was first proposed (and attempted) by Hillier and Baker more than three decades ago [2], the technique lay virtually dormant for two decades and has only recently gained a large interest in the past decade due to the work of various re-search groups throughout the world [e.g., 3-9]. The technique is of interest for two reasons. First, transmitted energy loss electrons tend to be concen-trated around the direction of the incident electron beam so that a small detector aperture can collect a large fraction of them (unlike the detection of x-rays or Auger electrons which to a first approximation are emitted isotropically). Second, for every excitation or ionization of an atom in the specimen, there is an electron which has lost energy in producing it (i.e.,no fluorescent yield is involved). Thus, electron energy loss spectroscopy (ELS) has the promise of being an extremely efficient method of detecting both elemental and chemical composition of small micro-areas within the electron microscope.

There are, however, problems which will ultimately limit the sensitivity and applicability of this technique. Some are instrumental problems (and these may be correctable). Others are more fundamental and we may have to live with them.

Before we continue, let us consider the appearance of a typical electron energy loss spectrum. This is shown in figure 1 for a specimen consisting of a 20 Å thick carbon film evaporated onto a 200 Å-thick aluminum film after exposure to air (atmospheric pressure). The main features here are: 1) the valence shell excitation lines below 50 eV energy loss (the surface plasmon loss near 7 eV, the volume aluminum plasmon loss near 15 eV, and the broad

loss near 25 eV corresponding to the broad volumn loss in both carbon and the Al_2O_3 layer), 2) the fact that the intensity falls off with energy loss as an inverse power law (in general), and 3) the peaks modulating this intensity which occur for aluminum L shell excitation and ionization (starting near 75 eV), carbon K shell ionization (near 285 eV) and oxygen K shell ionization (near 535 eV) in the oxide layer. (The spectrum is not shown extending to the aluminum K excitation line near 1500 eV.)

The general nature of these K shell excitation elemental peaks is shown schematically in figure 2 where we see that there is sometimes fine structure near the edge (the abrupt increase in signal) as well as coarser structure away from the edge. Examples of these different types of structure are shown in figures 3 and 4. The coarse structure (see figure 3) is similar to the x-ray absorption extended fine structure (EXAFS) observed in photo-absorption experiments [10] and the fine structure near the edge is due to excitation of inner shell electrons to higher bound states. Both types of structure give information about the chemical surrounding of the constituent atoms. Whether or not one observes the particular structures depends upon the energy resolution of the analyzing spectrometer.

The types of spectrometers which have been fitted onto electron microscopes are too numerous to individually refer to in this extended abstract. They consist of attaching magnetic or electrostatic prisms or Wien filters beneath the column of a conventional electron microscope (CTEM) to inserting cylindrically symmetric electrostatic or magnetic prism systems within the CTEM column to combinations of electrostatic mirror-magnetic prism or magnetic mirror-magnetic prism devices installed beneath the objective lens of the CTEM. For scanning transmission electron microscopes (STEM's), the devices have been simpler and mainly electrostatic or magnetic prisms attached beneath the specimen.

There are different opinions as to which design is more appropriate for performing ELS within an electron microscope or whether one should slow down the electrons before the analysis or not. Without elaborating, each system has its own advantages and disadvantages, a particular design generally being determined by different requirements (and probably the disposition of the experimenter!). In addition, the requirement of the energy resolution of which a spectrometer should be capable depends upon the problem one wants to solve. That is, resolutions of 10-20 eV are perfectly adequate for elemental analysis in which elemental peaks are separated by more than that. But for determining chemical states, the fine structure can be separated by less than 1 eV (see figure 4).

Generally, for elemental analysis one wants a spectrometer with a reasonable acceptance angle since a large angle collects more electrons (see figure 5). On the other hand, the product of resolving power times acceptance solid angle is of the order unity for a spectrometer in which aberrations have not been corrected [11], so that one sacrifices efficiency for resolution. This may not be so disastrous since a pre-spectrometer lens can demagnify the scattering angles somewhat to increase the effective angular acceptance of the spectrometer (although there are limits to the increase one can achieve which are due to lens aberrations [12]). Moreover, some experiments seem to indicate that for K shell excitations, there is an optimum aperture size for highest signal to noise ratio [13, 14]. This seems to be due to the fact that the angular distribution of the electrons comprising the background beneath the peak (see figure 2) is broader than those comprising the peak for the few cases experimentally investigated. Since one could not collect all the electrons in a peak without being overwhelmed by background, this could be a fundamental limit on detectability. However, the few measurements that have been made [13, 14] indicate an optimum aperture size of about 10-15 mrads for light elements using 60-80 keV electrons and this corresponds to

collection of almost one-third to one-half of all the K shell excitations (see figure 5).

At present, concentrations of only about 1-10% are generally detectable using ELS even though one expects much less. This may be due primarily to the primitive state of ELS data collection and analysis and the scarcity of measurements. In fact, ELS techniques today are much like x-ray techniques were a decade ago with regard to instrumentation, analysis, and data collection.

One big instrumental limit to ELS at present is that data collection is generally obtained by sweeping a spectrum across a slit, looking at only one slice of the spectrum at a time. This is done primarily to eliminate the non-linear effects of photographic recording and for the ease of data processing. However, in doing so, the collection efficiency is greatly decreased by the fraction of counting time per channel divided by the total counting time. Parallel data collection (as one obtains with a photographic plate) allows one to record all electrons passing through the spectrometer. At present there are no useful parallel recording systems (except film), and I suspect that the introduction of single electron sensitive, electronic parallel recording devices will revolutionize ELS in the same way that the development of x-ray analysis increased a quantum jump after the introduction of energy dispersive detectors.

Looking ahead, we need to know accurate electron scattering cross sections and angular distributions, the exact nature of the background beneath the peaks in ELS, and, in some cases, the structure in the excitation peaks. Then, we can begin to design optimal electron-optical systems for performing energy loss spectroscopy on micro-areas. ELS is in a primitive state, and it suffers some limitations as a quantitative technique at present. But coupled with microscopy at the 10 Å level, it has the potential of becoming a powerful technique and I anticipate new and promising results to come forth in this conference and in the future.

1. M. Isaacson and J. Silcox, Ultramicroscopy, 2, in press (1977).
2. J. Hillier and R.F. Baker, J. Appl. Phys., 15, 663 (1944).
3. D.B. Wittry, R.F. Ferrier and V.E. Cosslett, Brit. J. Appl. Phys., 2, 1867 (1969).
4. C. Colliex and B. Jouffrey, Phil. Mag., 25, 471 (1972).
5. M. Isaacson and D. Johnson, Ultramicroscopy, 1, 33 (1975).
6. R.F. Egerton and M.J. Whelan, Proc. 8th Int. Cong. on Electron Microscopy, I, Canberra, 384 (1974).
7. G.H. Curtis and J. Silcox, Rev. Sci. Inst., 42, 630 (1971).
8. Y. Kokubo, H. Koike and T. Someya, Proc. 8th Int. Cong. on Electron Microscopy, I, Canberra, 374 (1974).
9. A.J.F. Metherell, Adv. in Optical and Electron Microscopy, 4, 263 (1971).
10. S. Doniach, K. Hodgson, P. Eisenberger and B. Kincaid, Proc. Nat. Acad. Sci. (USA), 72, 111 (1975).
11. M. Isaacson and A.V. Crewe, Ann. Rev. Biophys. and Bioeng., 4, 165 (1975).
12. A.V. Crewe, Optik, in press (1977).
13. R.D. Leapman, PhD Dissertation, University of Cambridge.
14. R.F. Egerton, Phil. Mag., 31, 199 (1975).
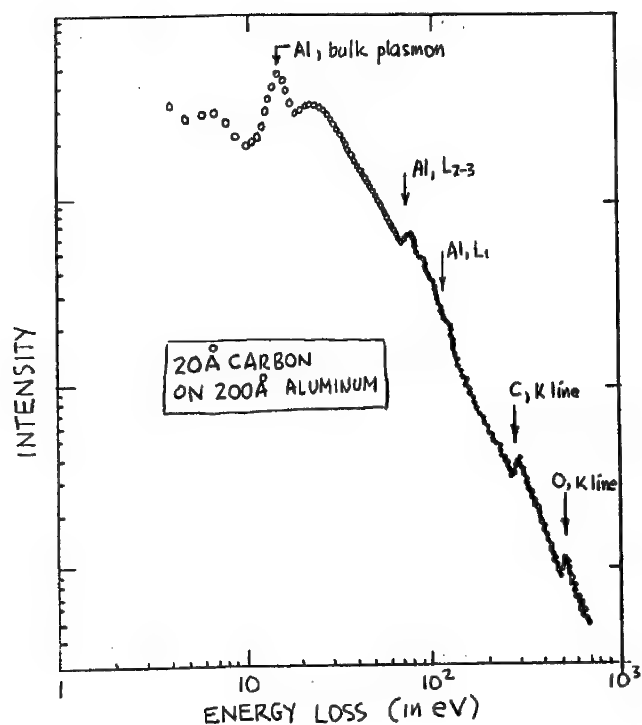
Fig. 1. Transmitted energy loss electron spectrum of 25 KeV electrons passing through a specimen consisting of a 20 Å thick carbon film deposited on a 200 Å thick evaporated aluminum foil. The effective spectrometer acceptance aperture was 12.5 mrad, the slit width about 6 eV, and the spectrum obtained in approximately 300 sec.
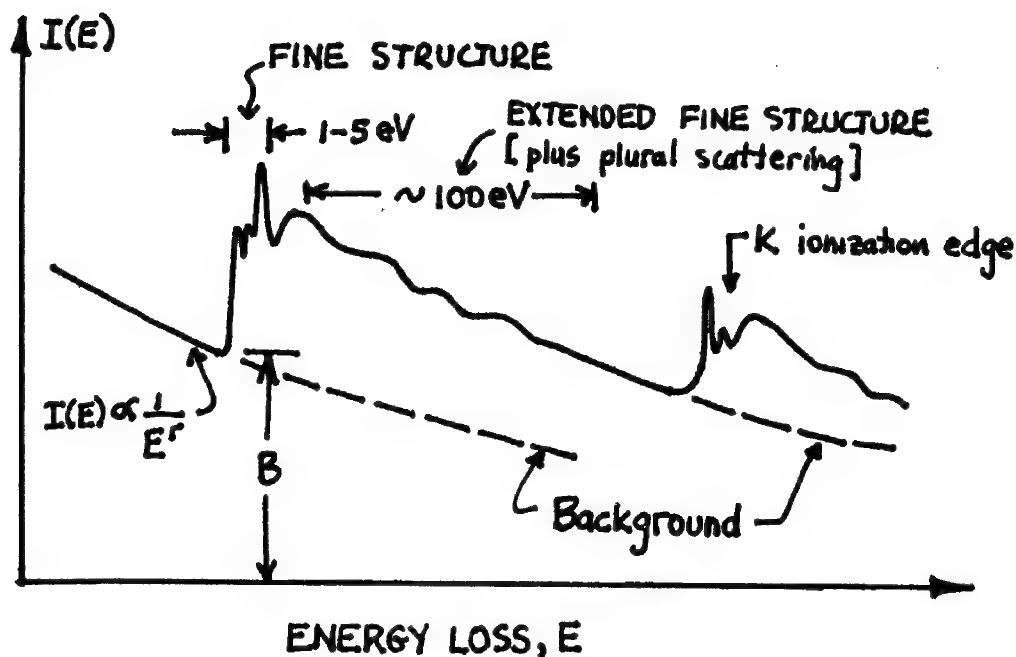
Fig. 2. A schematic diagram of an ELS spectrum in the region of inner shell excitation. The background beneath the ionization edge falls off as E^{-r} where r is between 3 and 5. The fine structure at the edge consists of peaks separated in some cases by less than 0.8 eV.

EXAFS [with electrons]

CARBON

● GRAPHITIZED
□ "AMORPHOUS"

RELATIVE INTENSITY

ENERGY LOSS (in eV)
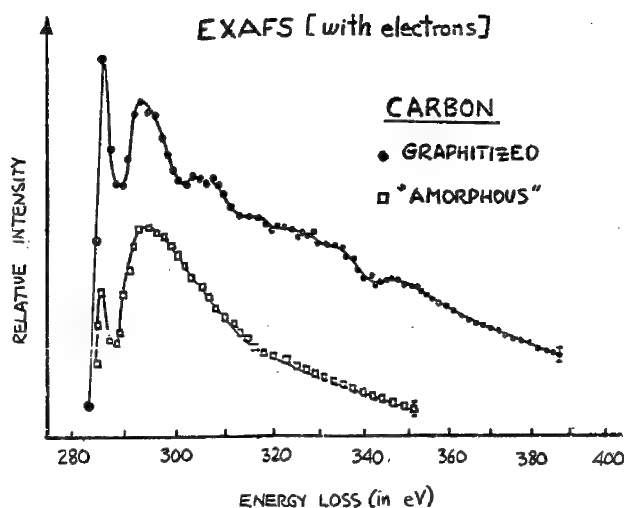
Fig. 3. An ELS spectrum in the region of carbon K shell excitation for two different forms of carbon. The spectrum is plotted on a log-log graph to illustrate the E^{-r} dependence of intensity away from the edge. The specimens were each about 20-30Å thick and the spectra have been displaced vertically for clarity.

RELATIVE INTENSITY

280 285 290 295

280 285 290 295

280 285 290 295
ENERGY LOSS (in eV)

RELATIVE INTENSITY

280 285 290 295

280 285 290 295

280 285 290 295
ENERGY LOSS (in eV)
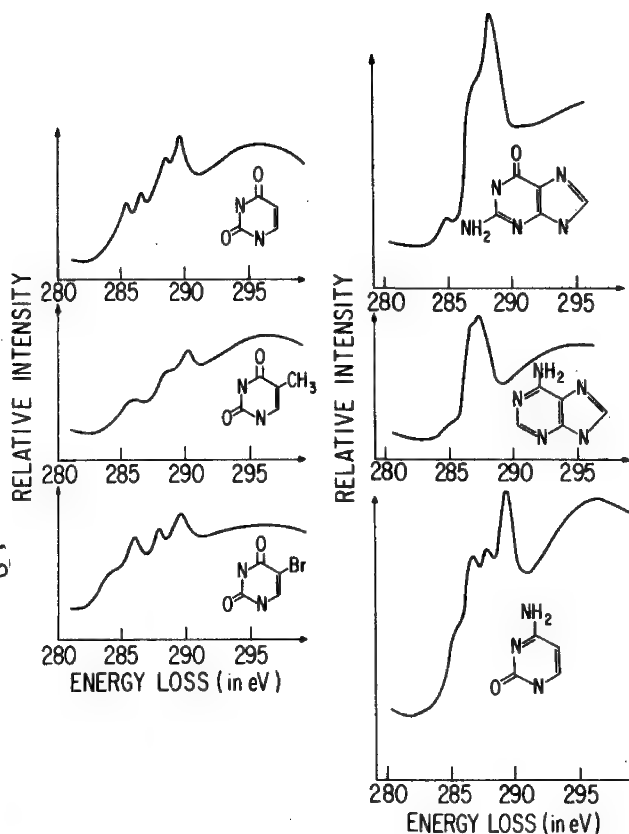
Fig. 4. ELS spectra in the region of carbon K shell excitation showing the fine structure near the edge of six types of common nucleic acid bases (after ref. 5, 11). Note that an energy resolution of at least .75 eV is necessary to distinguish these peaks and that with a resolution of 10 eV we would just observe a classical K shell ionization edge.

SCATTERING APERTURE, a (rads)

75%
50%
40%
30%
20%
10%

10^{-1}

10^{-2}

10^{-3}

10^{-4}

10^{-5}

10^4 10^3 10^2 10
ENERGY LOSS (eV)
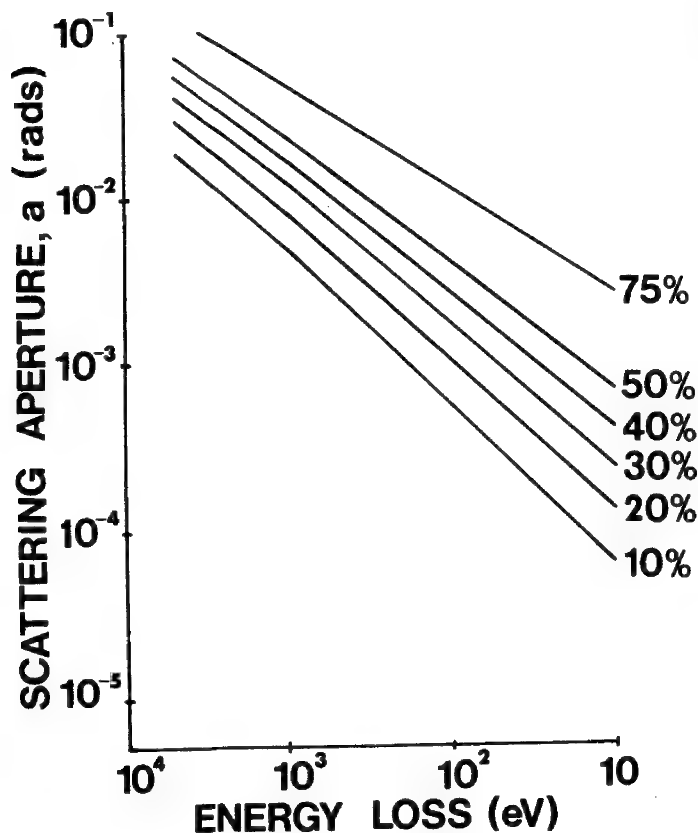
Fig. 5. Graph of the collection efficiency of a spectrometer for 10 keV incident electrons (on the specimen) and an effective acceptance angle a. Each line corresponds to the aperture necessary to collect a certain percentage of electrons which have lost a given amount of energy. (That is, a 10^{-3} rad aperture will allow one to collect 30% of those electrons which have lost 100 eV.) We assume the collected fraction for an energy loss E is given by $\ln(1+a^2/\theta_E^2)/\ln(2/\theta_E)$ for $a < \sqrt{2}\theta_E$, with $\theta_E = E/pv$, p being the momentum of the incident electron of velocity v.

CALCULATION OF THE COMBINED EFFECTS OF DIFFRACTION, SPHERICAL ABERRATION, CHROMATIC ABERRATION AND FINITE SOURCE SIZE IN THE SEM

E. Munro

IBM T. J. Watson Research Center
Yorktown Heights, New York 10598

In a high-resolution scanning transmission electron microscope[1] or a high-resolution surface scanning microscope[2], the beam profile at the specimen plane is determined by the combined effects of diffraction, spherical aberration, chromatic aberration, and the demagnified image of the electron source. The diffraction, spherical and chromatic aberration effects are themselves functions of the aperture angle and the amount of defocusing. It is important to be able to calculate accurately how the beam profile depends on all of these parameters, since this information is required in order to establish the optimum operating conditions for the microscope. This paper summarizes the theory required for performing such a calculation. Computed results, based on this theory, are also presented to illustrate the influence of the various parameters on the beam profile.

The usual method of estimating the combined effects of diffraction, spherical aberration, chromatic aberration and finite source size is to calculate the spot size due to each effect separately and then add them in quadrature[3]. This technique gives only a qualitative estimate of the overall spot size, and gives no information at all about the current density distribution in the probe. In order to obtain quantitative information about the size and shape of the probe, it is necessary to perform accurate numerical computations based on a wave optical theory[4]. (The wave optical treatment is required in order to properly take account of diffraction effects.) Such calculations were first done for the transmission electron microscope by Glaser[5], for the special case where the resolution is assumed to be limited solely by spherical aberration and diffraction.

The current density distribution in the specimen plane can conveniently be calculated in three stages:

(1) The calculation is first done for a point source of electrons with fixed initial energy. In this case, the intensity distribution is determined solely by the effects of spherical aberration and diffraction, and will be called the "monochromatic point spread function".

(2) The calculation is then extended to a point source of electrons with an initial energy distribution. The resulting intensity distribution, which takes account of chromatic aberration effects, will be called the "polychromatic point spread function".

(3) Finally, the calculation is extended to the general case of an extended source, by convolving the polychromatic point spread function with the intensity distribution of the demagnified source. The resulting distribution will be called "the overall intensity distribution for an extended source".

The formulae required for each part of the calculation are summarized below.

THE MONOCHROMATIC POINT SPREAD FUNCTION

Let a point source of electrons with a fixed initial energy be focused by an objective lens, as shown in Fig. 1. Let the specimen plane be located at a small distance h from the Gaussian

image plane. (The Gaussian image plane is the geometrical image plane for paraxial trajectories.) The distance h defines the amount of defocusing; a positive value of h means that the specimen plane is located on the lens side of the Gaussian image plane. Let α_1 be the aperture angle, let C_s be the spherical aberration coefficient of the lens, let λ be the wavelength of the electron beam, let I be the total beam current passing through the aperture, and let $J_{mono}(r)$ be the current density in the specimen plane at a radial distance r from the optical axis. Then the value of $J_{mono}(r)$ is given by the following expressions:

$$\psi(r) = \frac{2\pi}{\lambda}\sqrt{\frac{I}{\pi\alpha_1^2}} \int_0^{\alpha_1} \exp\left[i\ \frac{2\pi}{\lambda}\left(\frac{1}{4}C_s\alpha^4 - \frac{1}{2}h\alpha^2\right)\right] J_0\left(\frac{2\pi}{\lambda}r\alpha\right)\alpha\ d\alpha$$

$$J_{mono}(r) = \left|\psi(r)\right|^2$$

$$\left.\begin{array}{c}\\\\\\\\\end{array}\right\}\ (1)$$

In (1), J_0 denotes the Bessel function of the first kind of order zero, and $i = \sqrt{-1}$. $J_{mono}(r)$ is the monochromatic point spread function. For the special case where $C_s = 0$ and $h = 0$, the formula reduces to the expression for the Airy disc. For the general case where C_s and h are non-zero, the integral has to be evaluated numerically.

THE POLYCHROMATIC POINT SPREAD FUNCTION

In order to account for the effect of the initial energy distribution, (1) must be modified because the defocus distance h will be different for different initial energies. Let h_1 denote the distance from the specimen plane to the Gaussian image plane for zero initial energy (see Fig. 2), let C_c be the chromatic aberration coefficient of the lens, let V_0 be the initial energy of an electron, and let V_1 be its energy at the specimen plane. Then, as shown in Fig. 2, h is related to V_0 as follows:

$$h = h_1 + C_c\frac{V_0}{V_1}$$

Let $N_E(V_0)$ be the energy distribution of the emitted electrons, defined such that the probability of an electron being emitted with an initial energy between V_0 and $(V_0 + dV_0)$ is $N_E(V_0)dV_0$. Let $J_{poly}(r)$ be the current density distribution in the specimen plane at radial distance r from the axis. Then the value of $J_{poly}(r)$ is given by the following expressions:

$$\psi(r,V_0) = \frac{2\pi}{\lambda}\sqrt{\frac{I}{\pi\alpha_1^2}} \int_0^{\alpha_1} \exp\left\{i\ \frac{2\pi}{\lambda}\left[\frac{1}{4}C_s\alpha^4 - \frac{1}{2}\left(h_1 + C_c\frac{V_0}{V_1}\right)\alpha^2\right]\right\} J_0\left(\frac{2\pi}{\lambda}r\alpha\right)\alpha\ d\alpha$$

$$J_{mono}(r,V_0) = \left|\psi(r,V_0)\right|^2$$

$$J_{poly}(r) = \int_0^\infty J_{mono}(r,V_0)\ N_E(V_0)\ dV_0$$

$$\left.\begin{array}{c}\\\\\\\\\\\\\\\end{array}\right\}\ (2)$$
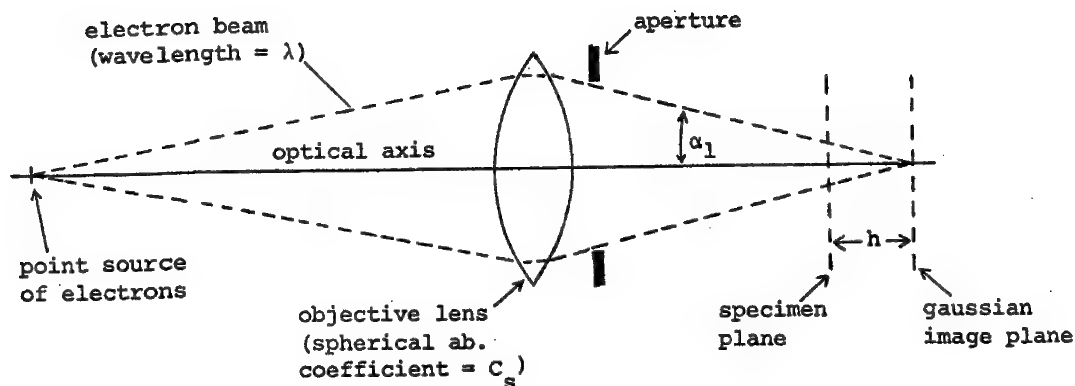
Parameters used in calculating the monochromatic point spread function
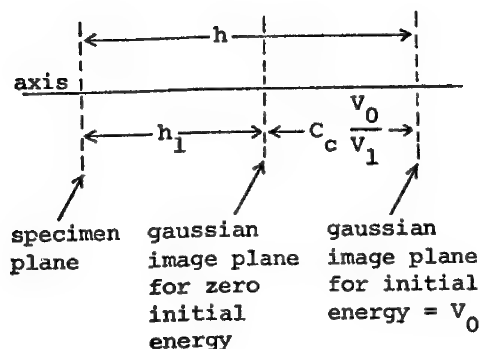
Fig. 2 Parameters used in calculating the polychromatic point spread function
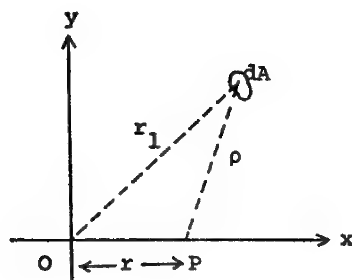
Fig. 3 Cross-section of specimen plane showing parameters used in calculating the overall intensity distribution for an extended source

THE OVERALL INTENSITY DISTRIBUTION FOR AN EXTENDED SOURCE

Assuming that the source is spatially incoherent, the effect of the finite source size can be taken into account by convolving the intensity distribution of the demagnified source with the polychromatic point spread function. Let $\beta(r)$ denote the brightness (current/unit area/unit solid angle) of the demagnified image of the source in the specimen plane, at a radial distance r from the optical axis. Let dA be an element of area in the specimen plane at distance r_1 from the axis (see Fig. 3), and let ρ be the distance from dA to the point P where the intensity distribution is to be calculated. Let $J_{poly}^{(1)}(r)$, as defined in (2), be the polychromatic point spread function calculated for $I/\pi\alpha_1^2 = 1$ amp/sterradian. Then the overall current density distribution is given by the following convolution integral:

$$J_{overall}(r) = \iint \beta(r_1) \, J_{poly}^{(1)}(\rho) \, dA \tag{3}$$

This integral is evaluated over the entire area of the specimen plane. In general, this two-dimensional integration must be done numerically. However, the brightness distribution $\beta(r)$ can often be adequately approximated by a Gaussian distribution of the form:

$$\beta(r) = \beta_0 \exp\left(-\frac{r^2}{r_0^2}\right).$$

In this case, (3) can be rewritten as follows:

$$J_{overall}(r) = \beta_0 \exp\left(-\frac{r^2}{r_0^2}\right) \int_o^\infty J_{poly}^{(1)}(\rho) \exp\left(-\frac{\rho^2}{r_0^2}\right) I_0\left(\frac{2r\rho}{r_0^2}\right) 2\pi\rho \ d\rho \qquad (4)$$

In (4), I_0 denotes the modified Bessel function of the first kind of order zero. $J_{overall}(r)$ is the overall intensity distribution for an extended source.

ILLUSTRATIVE RESULTS

Fig. 4 shows computed values of the monochromatic point spread function, obtained by evaluating the integral in (1) numerically using Simpson's rule. For convenience, the curves have been plotted in dimensionless form. The normalized current density $J(r)/J(0)$ has been plotted as a function of the normalized radial distance $r/(\lambda^{0.75}C_s^{0.25})$. It appears from inspection of these curves that the optimum operating conditions lie somewhere in the vicinity of $\alpha_1 = 1.5(\lambda/C_s)^{0.25}$ and $h = \sqrt{\lambda C_s}$. The optimum value of α_1 appears to be significantly larger than the value predicted by the usual method of adding the individual aberrations in quadrature.

Additional computed results will be included in the more detailed paper, to illustrate how the shape of the polychromatic point spread function (2) depends upon the chromatic aberration coefficient C_c, and also how the overall intensity distribution for an extended source (4) depends upon the effective radius r_0 of the demagnified source. These results will illustrate how the spot size deteriorates as C_c and r_0 are increased.

REFERENCES

1. A. V. Crewe and J. Wall, J. Molec. Biol., _48_, 375-393 (1970).
2. O. C. Wells, A. N. Broers and C. G. Bremer, Appl. Phys. Lett., _23_, 353-355 (1973).
3. C. W. Oatley, R. F. W. Pease and W. C. Nixon, Adv. in Electronics and Electron Physics, _21_, 181-247 (1965).
4. M. Born and E. Wolf, "Principles of Optics", 5th Ed., Pergamon Press, Oxford, 1975, pp. 459-490.
5. W. Glaser, Zeitschrift für Physik, _121_, 647-666 (1943).
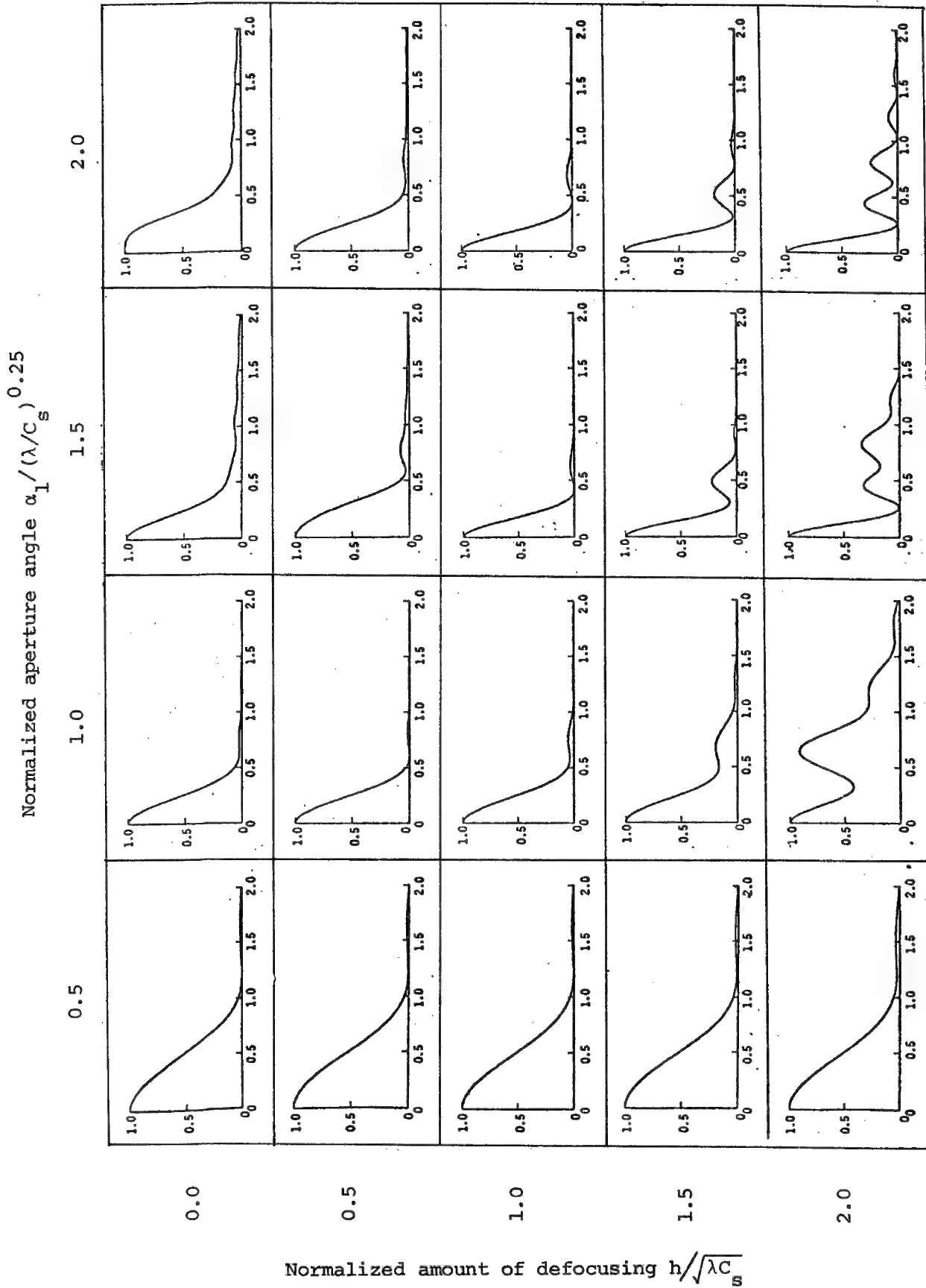
Fig. 4 Computed curves for the monochromatic point spread function. On each plot, the vertical axis is normalized current density $J(r)/J(0)$, and the horizontal axis is normalized radial distance $r/(\lambda^{0.75}C_s^{0.25})$

AN ATTEMPT TO INVESTIGATE THE QUALITY OF PLANE SURFACES BY USE OF AN ELECTRON-MIRROR-INTERFERENCE-MICROSCOPE

H.Lichte   and   G.Möllenstedt

Institut für Angewandte Physik, Universität Tübingen
Tübingen, Germany

In space science the total reflection of X-rays (1) is used for imaging in X-ray telescopes. The efficiency of a Giacconi objectiv for instance essentially depends on the flatness of the reflecting surfaces.

A first criterion for the flatness of a surface can be obtained by use of an interference microscope for visible light. Due to the large wavelengths ($\lambda \approx 5000$ Å) this method cannot be successfully applied to examinate the microstructures that are of importance for the reflection of X-rays.

In this paper an attempt ist made to solve this problem by use of an electron-mirror-interference-microscope, since the wavelengths of electrons are smaller in magnitude by a factor of about 10^5 ($\lambda_{el} \approx 0.08$ Å). Fig.1 shows the principle operation of this microscope (2).
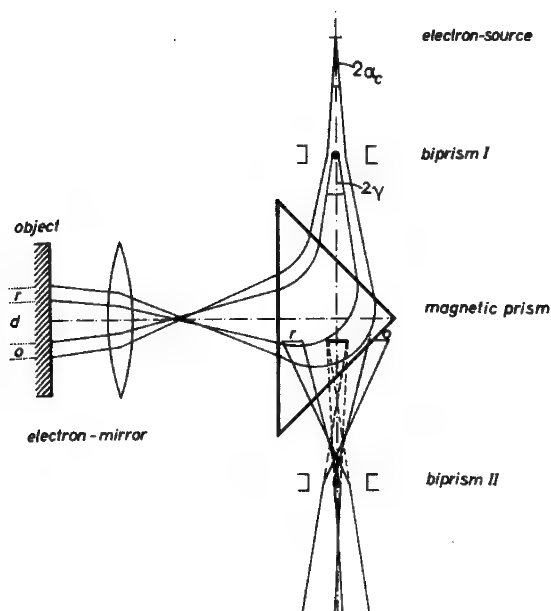
Fig.1 Principle operation of an electron-mirror-interference-microscope

The electron optical biprism I is coherently illuminated by monoenergetic electrons ($\Delta U/U = 4 \cdot 10^{-5}$) emitted by a source of 2000 Å diameter. By application of a negative voltage of about 5 Volt to the filament of the biprism a splitting of the electron beam into two coherent partial beams is obtained. A magnetic prism of Castaing type (3) causes a 90° deflection of both beams to the left hand side. An electron mirror which has a slightly negative potential $-U_{bias}$ with respect to the acceleration voltage of the electrons reflects both partial beams, the latter beeing seperated about 5µm in the vicinity of the mirror surface, when the microscope works under usual conditions. The electrons reflected by the mirror are again deflected in the magnetic prism so that finally the beam axis is the same as it was originally. The second biprism II, a positive voltage of 5 Volt beeing applied to its filament, causes a coherent superposition of both partial beams so that two-beam-interferences are produced.

If the reflecting surface of the electron mirror is not completely plane, the phases of both partial waves are changed in a different manner and this effect is as stronger as closer the electrons approach to the surface of the mirror (4). As the voltage U_{bias} decreases, the unevenness of the surface can be observed by an increasing phase shift in the interferogram. This effect will be first demonstrated at artificially produced square steps at the surface (fig.2) their height beeing about 25 Å and the spatial period of the squares beeing about 12 µm.
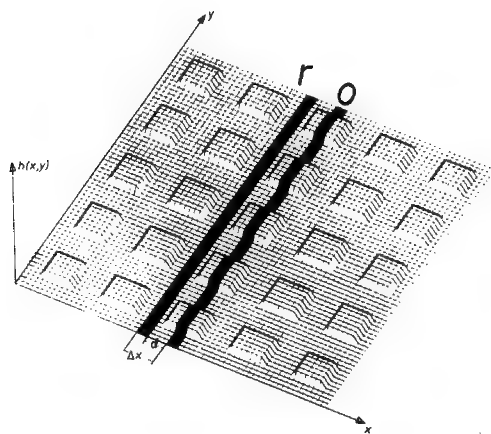
Fig.2 An artificially produced specimen for demonstrating the phase shift in an electron mirror; the two partial waves reflected in the area r and o are brought to interference by biprism II.

Fig.3 shows the dependance of the phase shift on the minimum
distance $z_u = U_{bias}/E$ between the electrons and the mirror.

$z_u = 6\mu m$ $4\mu m$ $3\mu m$

$\Delta\varphi/_{2\pi} = 0.5$ 1.5 23

12 µm

1 µm
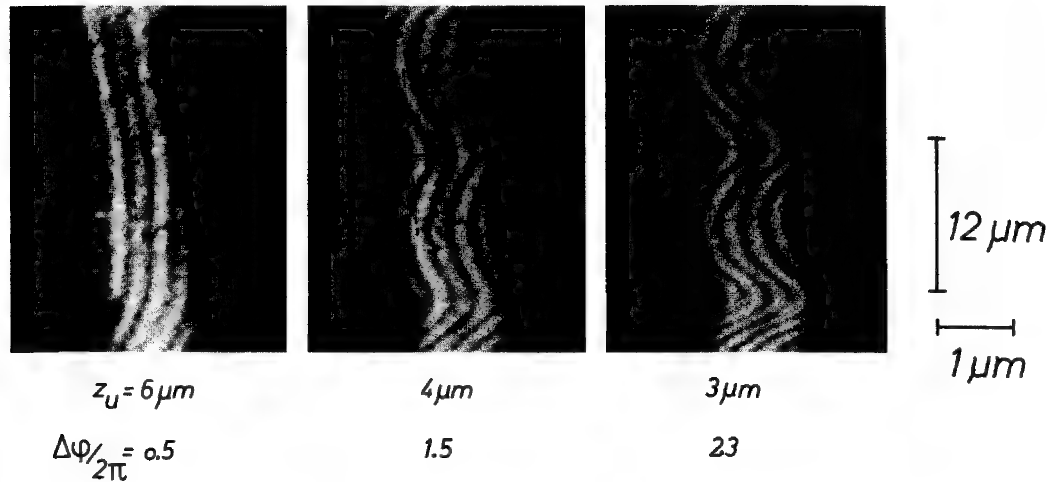
Fig.3 Phase shift caused by the specimen of fig.2
for different values of the reversal distance z_u

Fig.4a shows a photograph of an interferogram obtained with a
specimen, the surface of which has been grinded planely by use
of modern methods (Carl Zeiss), polished (flatness $\lambda/100$) and
covered with gold in a vaporblast process. As the reversal points
of the electron paths approach the surface as close as 1.5 µm,
one obtains distinctly observable phase shifts.

a   b

5 µm

1 µm
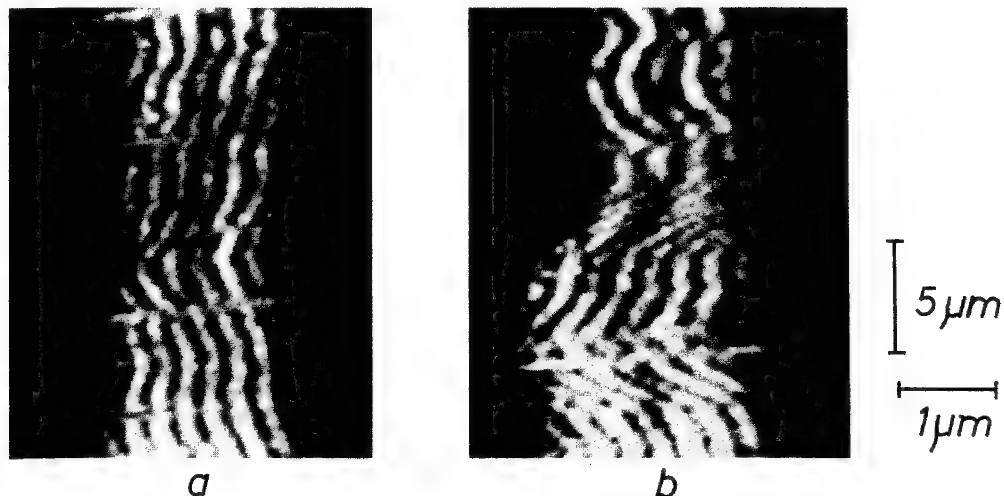
Fig.4 Interferograms of specimens with different flatness
a: $\lambda/100$; b: $\lambda/20$.

In comparing this interferogram with one obtained from a surface with a flatness $\lambda/2o$ one distinctly notices the stronger influence on the phase, the reversal distance z_u beeing equal (fig.4b).

Our investigations are now concerned in the quantitative interpretation of the phase shift. The two photographs in fig.4 already clearly demonstrate that the electron-mirror-interference-microscope is a suitable instrument to investigate the quality of surfaces; in a special experiment we produced a phase shift of 2π by a height difference of 1 Å.

References:
(1)   Wolter,H.   Ann.Phys. 1o,94,286 (1952)
(2)   Lichte,H., G.Möllenstedt and H.Wahl   Z.Phys. 249,456 (1972)
(3)   Castaing,R.   X-ray optics and microanalysis p.48
                     Hermann,Paris (1965)
(4)   Hermans A.J. and J.A.Petterson   J.Engineering Math.
                                        4, 141 (197o)

ON A METHOD TO INCREASE THE S/N RATIO IN MICROANALYSIS

C. A. Ribeiro
Universidade Estadual de Campinas

We present here a method to increase the signal to noise ratio in microanalysis, based on the phase-synchronous detection technique.

For this we make, electronically, the electron probe to jump alternatelly between two adjacent positions: one on the sample and the other on a special sample which can be the matrix of the material of the sample and which does not contain the element under analysis.

With this setup, we can measure alternately the intensity of the X-ray signal of the sample plus background and noise, and the back - ground and noise separately, which is supposed to be almost equal to that of the sample.

The results can be obtained easily in analog or digital form.

For the analog form we use an adapted lock-in configuration,which is represented in the figure below.
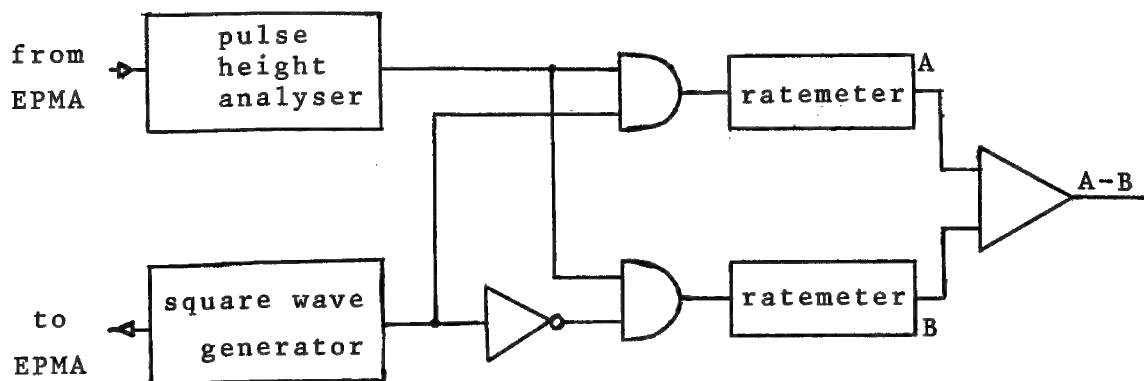
The square wave generator controls the position of the electron probe and also the two gates synchronously. Which allows the pulses that comes from the two samples to be sent to one or the other separate ratemeter (which acts as integrators for each of the samples). A differential amplifier receives the signal from both ratemeters, and performs the difference between them, which is then the final result,

For the digital form, we simply use two gated counters which are controlled by the square wave generator. The countings can then be treated, for example, by an on line computer.

If we vary linearly the amplitude of the square wave signal to the microanalyser, we can obtain a kind of line scan, still having the detection method.

The technique presented here, should be mainly useful where small concentration are being examined; because in this case the back‌ground has almost the same magnitude as the signal, and this also simplifies the application of the hypothesis that the background and noise measured, is not very different from that present on the sample.

We think that something should also be said about the sample preparation.

- For our special case, of semiconductor lasers, we are inte‌rest in the concentrations of impurities on different sides of the junction. In this case we have the sample and the ma‌trix, one adjacent to the other, and by cleavage we obtain both in the same plane.

- For homogeneons samples, a matrix can be prepared and put adjacent to the sample. Both surfaces can then be polished giving a plane in the two sides. If this polishing is not feasible, the two parts can be positioned the best way, and a correction factor for the countings, can be easily found, to compensate the difference in height of the parts.

- For inclusions (heterogeneous samples), we have a similar configuration as that of laser diodes, if one considers the two adjacent ones as sample and matrix.

We are applying this method to semiconductor lasers, to mea‌sure the doping of the different layers of the junction. Difficulties encountered and results will be discussed.

NEW FOUR-CRYSTAL SPECTROMETER
FOR A SCANNING ELECTRON MICROPROBE

B. Kenessey

Applied Research Laboratories
Sunland, California 91040

ABSTRACT

Multi-crystal wavelength dispersive spectrometers have been in use for a good
number of years, however, typically with some compromises in wavelength coverage
or in the capability of crystal selection. Ideal characteristics of a multi-
crystal spectrometer should include large Bragg angle range, independently
adjustable crystals, interchangeability of spectrometer positions and full
compatibility with the light optical system that is coaxial with the electron
beam.

The spectrometer we have developed has a 52.5° take-off angle, 127mm radius
focal circle and a 14.4° to 71.8° Bragg angle range. In other words, with a
given crystal in position, the wavelength coverage obtainable is the same as
with the previous dual crystal scanning spectrometer. As shown in Figures 1 and
2, the four crystals are mounted on a cylinder segment with individual peaking
adjustments and rotated into analyzing position about a common axis. The basic
determining factor in establishing this configuration was the geometry of the
final electron beam forming lens and the viewing optics objective cone assembly.
The new four-crystal arrangement makes it possible to select crystals even with
the spectrometer set at the minimum Bragg angle without interference at the
viewing system objective assembly. Consequently the crystals may be interchanged
at any spectrometer position. A small stepper motor that is located at the
selector assembly receives a set of pulses to move the desired crystal into
analyzing position. Electrical contacts are also provided at the selector assembly
to read out the position at all times. A logic circuit is employed to determine
the number of pulses required to select a given crystal based on a command from
the operator or computer. When the new crystal has moved into position the motor
is de-energized and a very precise mechanical detent takes over for final
positioning. The mounting of each crystal provides tilt and translation adjust-
ments. For efficient x-ray detection over the entire wavelength range, a special
dual detector is utilized consisting of a flow proportional counter and a sealed
proportional counter in tandem.

With the clearly established trend towards increasing emphasis on automation, the
four-crystal spectrometer under computer control can contribute significantly
to the flexibility of scanning spectrometers and to the speed of elemental
determinations. Furthermore, in the analysis of small particles or rough surfaces,
all x-ray data may be collected along the same x-ray emergence path for all
wavelengths from 1.0 to 95.0Å to simplify interpretation of the data when the
absorption corrections are important.

FIGURE 1

STEPPER MOTOR

VIEWING SYSTEM
OBJECTIVE

FINAL LENS

CRYSTAL SUPPORT

CRYSTAL

SAMPLE SURFACE
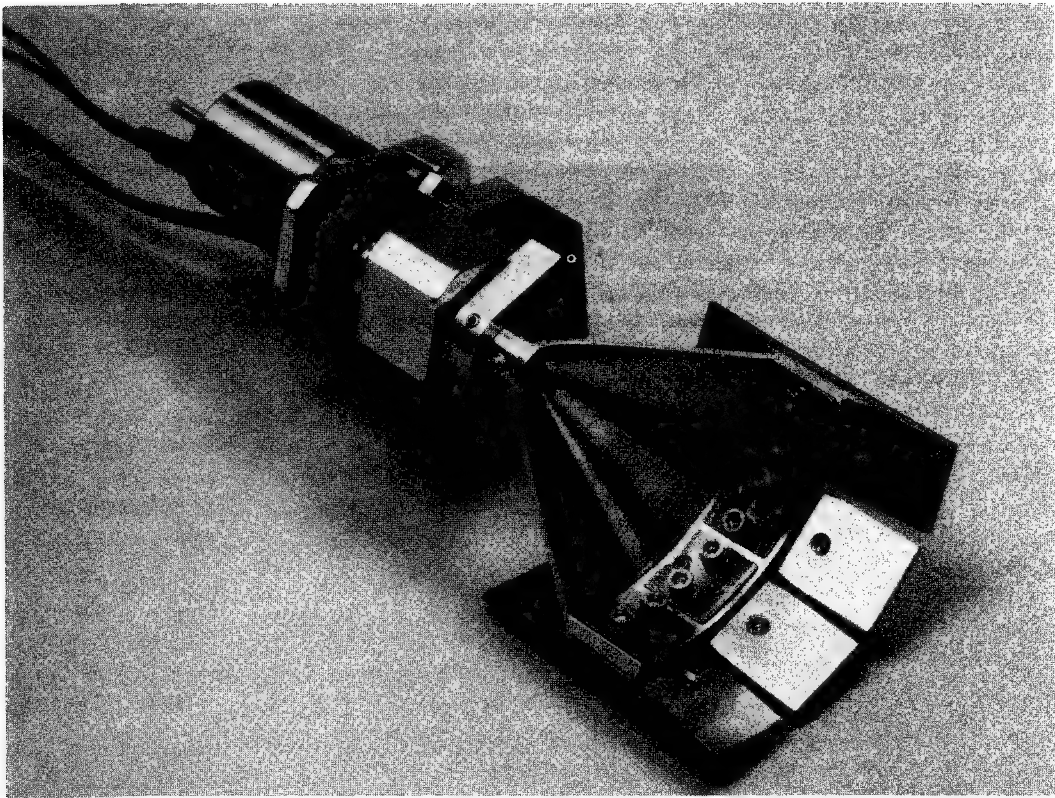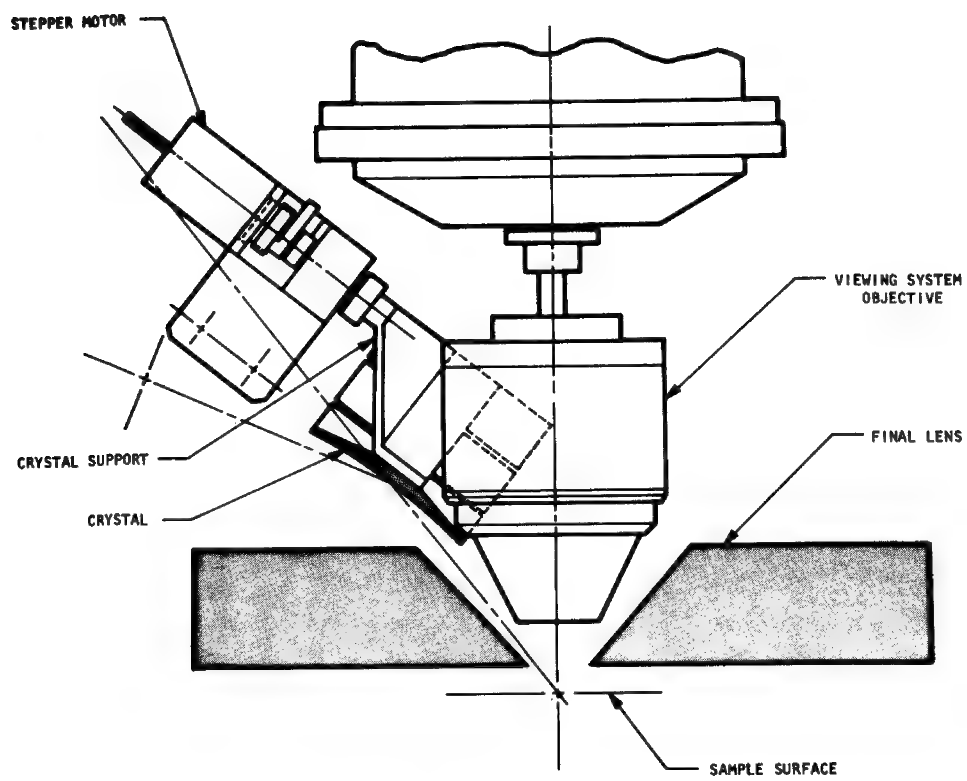
FIGURE 2

AN IMPROVED APERTURE SYSTEM AND
ALIGNMENT PROCEDURE FOR ARL EMX-SM ELECTRON MICROPROBES

L. F. Allard and W. C. Bigelow
Department of Materials and Metallurgical Egnieering
The University of Michigan
Ann Arbor, MI 48109

Accurate alignment of the electron optical system of an electron microprobe is highly desirable to ensure stable operation for accurate analytical work and to provide best resolution for secondary electron imaging. The electron optical systems of most microprobes consist of two or three lenses which are analogous to the double condenser lens system of most transmission electron microscopes. In electron microprobe analysis, the first of these lenses (L1) is used to control the magnitude of the electron beam current incident on the sample. In secondary electron imaging, L1 serves also to control the minimum beam diameter attainable on the specimen. In both cases, the second lens (L2) is used to control the actual diameter of the beam of the specimen by focusing or defocusing the image of the focused beam or "crossover spot" produced by L1. Both lenses normally have apertures which limit the semiaperture angle of the electron beam to keep aberrations within acceptable limits.

For accurate alignment of such a lens system, the following conditions must be achieved. The beam from the electron gun must be parallel to the axis of L1 and pass through the center of L1. The beam transmitted by L1 must be parallel to the axis of L2 and pass through the center of L2. The apertures of both lenses must be accurately centered around their axes. In a well-aligned system, the focused beam spot produced by L1 moves up and down along the optical axis of L2 as the current in L1 is changed, so that the beam reaching L2 is symmetrical about its axis and aperture.

In a poorly aligned system, the focused spot produced by L1 usually does not coincide with the axis of L2 except over a limited range of current for L1. Outside this range the illumination is asymmetrical with respect to L2 and its aperture (A2). This can cause several problems. Usually the basic problem arises from misalignment of the electron gun, or the aperture of L1 (A1), with respect to L1. This can cause asymmetrical contamination of A1 and increase astigmatism. Asymmetric illumination of A2 will also cause asymmetric contamination of this aperture and provide additional astigmatism. The misaligned beam usually causes some loss of resultion for scanning imaging. With a poorly aligned instrument it is usually necessary to make major alignment adjustments when the accelerating voltage is changed.

In the ARL EMX-SM's there is a system of apertures for monitoring beam current during analysis. It is particularly advantageous to use this monitored beam current in conjunction with a current digitizer to control counting time during quantitative analysis to compensate for minor instabilities in lens or beam currents. If the beam is not symmetrical with respect to the monitor aperture, serious departures from linearity can result. It was these latter two problems which prompted us to make an extensive study of the alignment characteristics of our instrument. The result of this study has been the development of an aperture system and alignment procedure which have eliminated the above problems.

APERTURE SYSTEM: Although it may not be the case in all ARL EMX-SM's, it appears that in our instrument the original aperture holder did not position the aperture of L1 accurately around the lens axis, preventing the beam leaving L1 from being aligned parallel to the axis of L2. To overcome this problem, we have designed a centerable aperture system for L1. This has a tube which extends down into the top of L1 and carries the aperture disc, as shown in Fig. 1. The tube is suspended from a sliding ring which can be moved by drive screws that are actuated by control rods which extend out through the spectrometer tank near the viewing window. This device is relatively simple to construct and install. Detailed drawings can be obtained by writing the authors.

In this system we use a molybdenum aperture disc 0.25" in diameter, 0.001" thick, with a 400 or 600 μm hole. The aperture holder is designed so that it touches the aperture disc only around the very edge, giving rather poor conduction of heat from the aperture to the holder. Under these circumstances the thin aperture is heated enough by the electron beam to virtually eliminate aperture contamination.

We use a similar arrangement to greatly reduce contamination of the aperture of L2. In this case, a 0.310" diameter molybdenum aperture disc, .001" thick, with a 200 μm hole, rests on a fine wire ring in the bottom of the upper part of the cavity in the 45° mirror block and is held loosely in place with a spring retaining ring, as shown in Fig. 2. Again, because of the poor thermal conductivity, the electron beam heats the thin aperture enough so that it can be used for several months without development of appreciable astigmatism. A 0.01" thick platinum aperture with a larger hole placed in the usual aperture position serves to absorb x-rays from the thin molybdenum aperture, preventing beam tailing effects. All three aperture discs are standard sizes available from E. F. Fullam, Inc.

BEAM ALIGNMENT PROCEDURE: The alignment procedure we have adopted is relatively simple and straight-forward. Although we developed it for use with a centerable aperture in L1, it should work well with instruments having standard aperture systems, except that it may not be possible to eliminate beam sweep in Step 4 (indicating that the mechanical and optical axes of L1 are not coincident). If this procedure is used with a standard aperture system, we would suggest adjusting the aperture holder tube of L1 so that it extends 3-4 cm up into the lens. This will place the aperture A1 well above the central plane of L1, in which case Step 3 will be most likely to bring the beam parallel to the lens axis, minimizing complications from beam sweep due to beam inclination in Step 4.

STEP 1. Mechanical Centering. Use a broken-in filament which is not likely to warp during subsequent steps. Accurately center the filament in the grid cap (use a 5X magnifier - small displacements of the filament cause large deviations of the beam from the axis of the gun). Accurately center the anode plate with respect to the interior of the gun housing. If a centerable aperture is used in L1, carefully center the extension tube with respect to the retaining ring. Using the gun translate screws, translate the gun so that it is concentric within the gun mounting ring.

STEP 2. Center Gun Over L1. Set the current in L1 to about 50 mA. Set the beam current selector switch to the "ALIGN" position. Adjust the gun
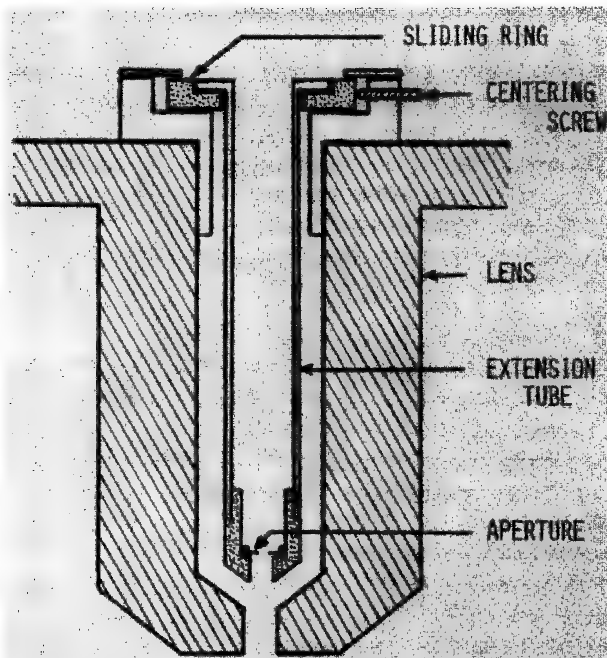
FIG. 1. CENTERABLE APERTURE ASSEMBLY FOR FIRST LENS.
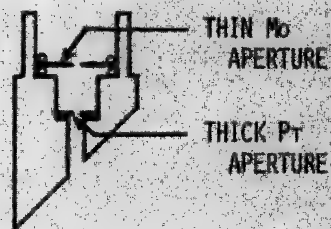
FIG. 2. APERTURES FOR LENS 2.

translate screws to obtain maximum alignment beam current. Small adjustments in the filament centering may also be helpful. Do not move the anode plate.

STEP 3. Center L1 over L2. (a) Switch the picoammeter to read sample current. Reduce the current in L1 in small increments, each time adjusting the L1 translate screws to obtain the highest sample current, until a maximum sample current is reached when the lens current is about 20 mA. Do not move the anode plate.

It is helpful and advisable to follow the progress of this step by observing the beam image on a fluorescent sample with L2's current set at the highest value attainable with the coarse lens current control (i.e., 3-4 amps). Under these conditions, you should initially see the aperture A2 of the second lens illuminated by the beam from L1. As the current in L1 is decreased, the focused spot produced by L1 moves down the beam column. At a L1 current of about 20 mA this focused spot should reach the position of A2. The translation of L1 should bring this focused spot through A2, giving the maximum in sample current nearly equal to the beam current of Step 2. Since the diameter of the focused beam is smaller than the aperture hole, it will probably not be possible to see the outline of the aperture when the focused beam is centered in the aperture.

We have found that it may be necessary to displace L1 considerably from its "mechanically centered" position to accomplish this step. This apparently results from chance inaccuracies in assembly of the instrument, the presence of stray magnetic and electric fields, etc., and is not unexpected.

(b) While observing the process on the fluorescent specimen, center the focused beam accurately inside A2 by adjusting the L1 translate screws, then carefully adjust the filament centering and gun translation to give maximum specimen current. Do not move the anode plate. Tighten the L1 translate screws securely to prevent subsequent unwanted movement of this lens.

STEP 4. Center the Aperture in L1. If L1 is equipped with a centerable aperture, it should now be centered around the lens axis. Observe the focused beam spot of L1 and note the position of its center. Now turn L1's current a bit off the focus value. Note the center of the beam image in this slightly defocused condition. Adjust the centerable aperture to bring the center of the defocused beam to coincide with the position of the center of the focused spot.

This is the same procedure as is routinely used to center the aperture of L2, except now you are using L2 to view the focused spot of L1, the aperture A2 may restrict the field of view slightly, and the focused spot from L1 will appear larger and less sharply defined than the spot of L2 you are used to looking at. When A1 is properly centered, the beam image will expand concentrically about the focused spot as the current in L1 is varied through the focus value. If A1 is not centered on the axis of L1, the center of the defocused beam will not coincide with the center of the focused beam and the beam will appear to "sweep" or "swing" as the L1's current is varied through the focus value.

If L1 is not equipped with a centerable aperture and there is negligible beam sweep at this stage, then a centerable aperture system is not needed. If

there is appreciable sweep or swing of the beam at this point, and if A1 has been inserted 3-4 cm up into L1 as suggested above, then a centerable aperture would probably be helpful in achieving refined alignment.

STEP 5.   Center A2.   Turn the current of L1 to about 50 mA.   Adjust the current of L2 to obtain a focused spot on the fluorescent specimen.   Center A2 in the usual manner (i.e., note the position of the focused spot carefully. Defocus L2 slightly and adjust the aperture centering controls to bring the center of the defocused spot coincident with the position of the focused spot. Repeat until the beam does not sweep as L2's current is varried through focus.)

Refine Alignment by repeating Steps 3b, 4 and 5.   Do not move the anode plate.

ROUTINE OPERATION: Once the instrument has been carefully aligned by this procedure we have not found it necessary to adjust the centering of either L1 or the anode plate during routine operation.

Filament saturation can be set more accurately using the beam ALIGN current, with the current in L1 set above 50 mA, than with the emission current.   This optimizes beam stability and filament life.

Trimming of alignment to compensate for filament warpage and other instrumental drift can usually be accomplished satisfactorily by setting the current in L1 to about 50 mA and adjusting the filament centering and gun translate to obtain maximum specimen current.

After making large changes in operating voltage, or otherwise as desired, a more critical trimming of alignment can be achieved by setting the current in L1 to about 20 mA, setting the current in L2 to about 3.5 amps, and adjusting the gun translate screws to center the beam accurately in A2 (while viewing the process on a fluorescent sample, as was done in Step 3). Also adjust the filament centering to obtain maximum sample current.

After installing a new filament, difficulties may be encountered in re-establishing alignment.   Sometimes no measurable beam or sample current will be obtained when a new filament is first turned on.   Such difficulties are almost always caused by movement of the gun while the filament is being changed or by miscentering of the filament in the grid cap.   When this happens, stabilize the filament by allowing it to operate at saturation current level for about 15 minutes, then open the gun and accurately recenter the filament in the grid cap (use a magnifying lens).   Set the current in L1 to about 50 mA, watch the ALIGN current reading, and adjust the filament centering to maximize the reading as filament current is increased to saturation.   Then maximize the MONITOR current using the filament translate screws.   A beam image should now appear, but will probably focus somewhat off the center of the A2 image when viewed as described in Step 3.   Make slight adjustments of the gun translate to center the focused beam spot in A2, as described in Step 3, then trim the filament translate to maximize sample current for final alignment.

A VIDEO SIGNAL LEVEL INDICATOR AND CONTROL CIRCUIT FOR SEM IMAGE PHOTOGRAPHY

H. K. Gille

Applied Research Laboratories
Sunland, California

With an SEM it is necessary for the instrument operator to correctly adjust the video signal peak amplitude or contrast and DC offset or brightness before attempting an exposure. A number of techniques have been instrumented that allow the operator to see the effect of these adjustments before taking a photograph. These include video level panel meters, waveform monitors and automatic gain control circuitry. They require that the operator preview the video signal and adjust the amplitude and offset controls to a predetermined level which should result in a proper exposure. Often the calibration is valid for only a single photo recording frame time. Since recording rates are much slower than viewing rates it may take several frames before the video signal is properly adjusted.

To eliminate these difficulties, a combination video signal level indicator and control circuit are proposed. The level indicator would sample the entire frame at viewing rates and detect areas of possible over or under exposure. It would provide feedback to the operator allowing rapid adjustment of brightness and contrast. Then it is only necessary to attenuate the video signal if a slower than normal recording frame or line rate is selected.

A simplified diagram of the video level indicator is shown in Figure 1. The video signal is split into alternating and direct current components. The AC component containing contrast information is fed to the positive and negative peak detectors. Positive and negative contrast peaks gate current sources which are compensated for the selected viewing rate. The current sources charge the over and under contrast integrators whenever the contrast exceeds preset levels. If the integrator output exceeds a preset level at the end of a frame, the appropriate indicator will light. If the contrast level is correct, both lights remain off.

The brightness indicator operates in a similar manner except that the integration time constant is longer. The video signal DC level is converted to a rate compensated current which charges the brightness integrator. At the end of a frame, if the brightness level is correct, neither light will be on.

Once the video signal is adjusted to a predetermined amplitude and offset, it is only necessary to select a photo recording rate. This programs a video signal attenuator so that photographs taken at different rates show the same image contrast and brightness.

Fig. 1 VIDEO LEVEL INDICATOR DIAGRAM
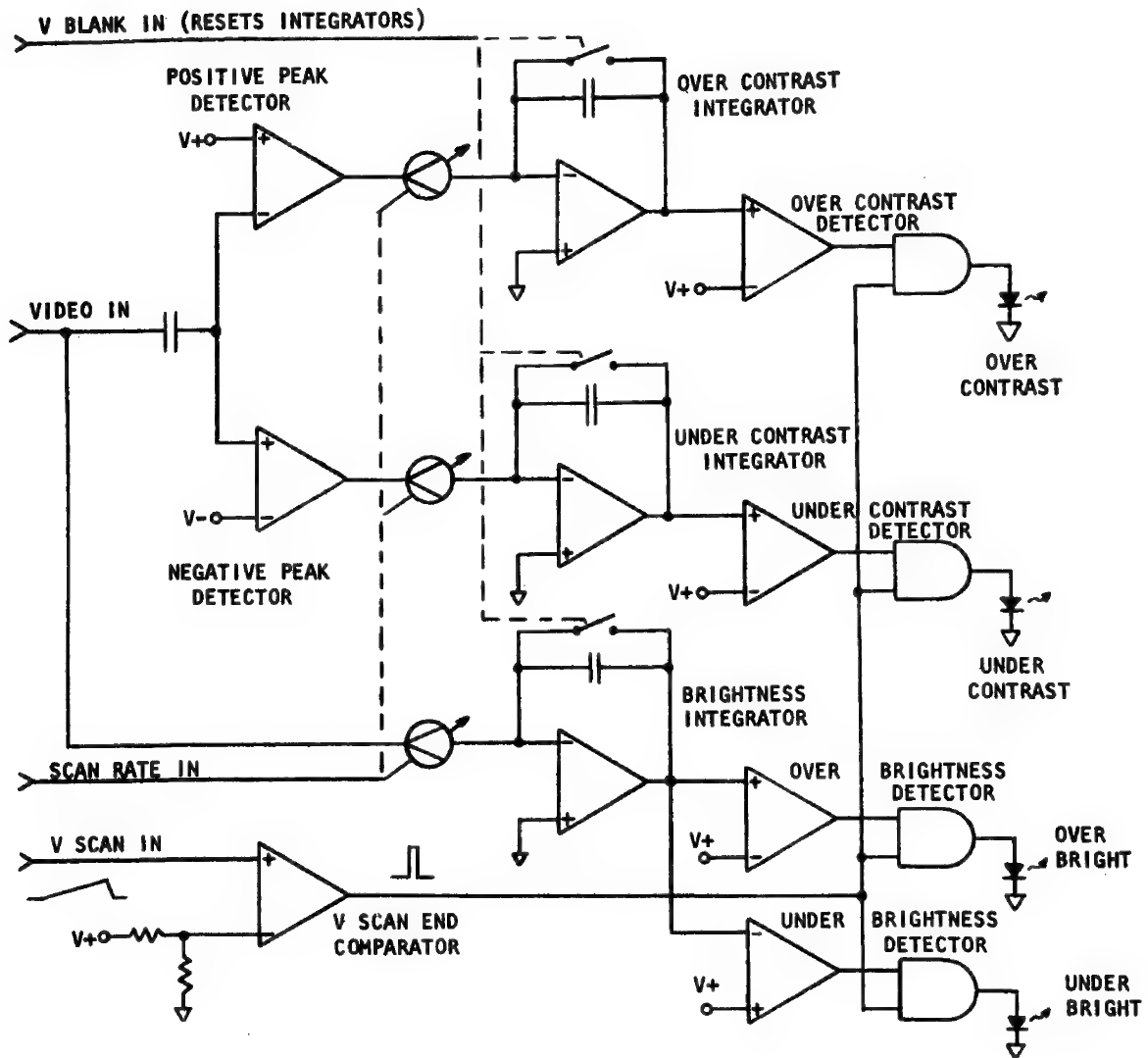
QUANTITATIVE MICROANALYSIS

S.J.B.Reed

Dept. of Mineralogy & Petrology, Downing Place, Cambridge CB2 3EW, England.

Introduction

The experimental aspect of quantitative microanalysis consists of measuring relative intensities of characteristic X-ray lines in specimen and standards, and will not be discussed further here. Empirical procedures for relating intensities to concentrations (e.g. alpha coefficients) are often quite satisfactory, but are limited in application. It is intended to deal here with the approach to the problem via X-ray physics. A brief outline of the present state of ZAF corrections will be given, pointing out recent advances and where further improvements appear possible.

Stopping power

The stopping power correction (part of the atomic no. correction) takes account of the dependence of the mass penetration of the incident electron beam on atomic no. In spite of its known limitations, Bethe's law is still used for calculating stopping power corrections. This approach assumes the 'continuous slowing-down approximation' whereby the discrete character of the energy loss processes is neglected. The main area of debate has been in connection with the mean atomic excitation energy J, and there is still some uncertainty as to which values to use.

Backscattering

The other half of the atomic no. correction, which allows for the loss of X-ray production due to electron backscattering, is in a reasonably satisfactory state, and little new work has been done in this area. There is still some uncertainty as to how to calculate the average correction factor for a compound specimen, and for non-normal electron incidence.

Absorption

In order to calculate the absorption of X-rays emerging from the sample we need to know their depth distribution. Various methods have been used to determine the depth distribution $\phi(\rho z)$ experimentally, and such data have served as the basis for expressions for the absorption factor $f(\chi)$.
The most commonly used formula is that proposed by Philibert, in its simplified form, which is fairly adequate for $f(\chi) > 0.5$. Its shortcomings are well known and a number of alternatives have been proposed. Two approaches to this question can be distinguished: firstly to use the simplest possible formulation that will be adequate for relatively low-absorption situations, and secondly to set up more elaborate expressions based on $\phi(\rho z)$ functions which are more realistic, and which should be more reliable under high-absorption conditions, but are rather complicated.

Mass attenuation coefficients

Measured m.a.c. values are available only for certain absorbing elements and wavelengths. In order to derive a comprehensive set of values it is therefore necessary to use an interpolation formula such as: $\mu = c\lambda^n$.
The well known Heinrich tables were compiled in this way, using values of c and n fitted to the experimental data then available (1964).

Since then there has been a trickle of new experimental data which should in principle have led to improved accuracy of m.a.c. data for absorption corrections. There have also been advances in theory which may enable the accuracy of interpolation to be improved. The more recent tabulation by Veigele (in Handbook of Spectroscopy, vol.1, ed. J.W.Robinson, CRC Press, Cleveland, 1974) agrees quite closely with Heinrich for wavelengths below 5 Å, but there are major discrepancies elsewhere, which it is important to resolve.

Monte-Carlo calculations

Computer simulation of electron scattering and X-ray production by the Monte-Carlo method has been an area of considerable activity in the last decade. Two basic approaches are used: either multiple scattering theory is used to derive the distribution of electron deflection angles after travelling a finite distance, or alternatively single elastic scattering acts are treated individually. The latter procedure is more rigorous in principle but more expensive in computer time. Generally Bethe's law is used to calculate energy loss, but it is possible to set up a more realistic model in which different kinds of inelastic process are treated separately, thus avoiding the continuous slowing-down approximation. As a rule Monte-Carlo calculations are not used directly for correction calculations because of the amount of computing time required, but the method has proved useful for testing other correction procedures, and for estimating corrections in conditions not covered by the usual methods.

Characteristic fluorescence

The theory of fluorescence is well understood and in principle the correction can be calculated rigorously, though normally a simplified form is used in order to reduce the amount of calculation. As regards K-K fluorescence the situation is satisfactory both with respect to the model and the input data (e.g. fluorescence yields), but there is room for improvement in K-L and L-K fluorescence corrections.

Continuum fluorescence

The theoretical basis for calculating fluorescence excited by the continuous X-ray spectrum is the same as for characteristic fluorescence except that integration over the relevant range of continuum energies is necessary. The correction is small (nearly always < 5%) but ideally should be included in the ZAF procedure. The full correction formula is somewhat forbidding, but simplified versions are available.

Additional topics relevant to energy-dispersive analysis

The use of E.D. spectrometers for quantitative analysis has stimulated interest in certain aspects of X-ray physics which may usefully be discussed alongside those pertaining to ZAF corrections. These include: the continuum, its shape, dependence on atomic no., and depth distribution for absorption calculations; relative intensities of different lines for overlap corrections (e.g. K_β/K_α); dependence of characteristic radiation intensity on atomic no., in relation to 'no-standards' analysis.

APPLICATIONS OF STATISTICS TO ELECTRON PROBE MICROANALYSIS

M. ANCEY, F. BASTENAIRE, R. TIXIER

Institut de Recherches de la Sidérurgie Française
185, rue Président Roosevelt - 78100 SAINT GERMAIN EN LAYE - France

I - INTRODUCTION.

It is well known that X-ray counts are random variables, a fact which results in limitations in the precision of micro-probe measurements.

The object of the present paper is to show that this very general situation should not be regarded as a curse on the analyst. If the fundamental properties of these random variables are indeed duly taken into account, it is possible to conduct the measurements more efficiently and to obtain better results more economically.

Various aspects of this statistical approach will be presented here, some of which are straightforward applications of well-known statistical science, the others resulting from recent research work which permitted the rigorous treatment of some of the precision problems that X-ray analysis brings up.

II - INSTRUMENT CONTROL.

X-ray counts obtained in a fixed time mode can be proved to follow Poisson distributions. This property can be used to test the homogeneity of n counts x_i (i = 1, 2, ..., n) with the statistic

$$X^2 = \sum_{i=1}^{n} \frac{(x_i - m)^2}{m} \quad , \quad m = \frac{1}{n} \sum_{i=1}^{n} x_i \quad (n \geq 2)$$

which is asymptotically distributed as a chi-square variable with n - 1 degrees of freedom.

The value of X^2 is calculated and compared to the critical chi-square value for the chosen significance level (e.g. 5 per cent) which can be found in the appropriate table. If X^2 is less than this critical value there is no reason to suspect the counts of not being Poissonian and this can be regarded as a proof that the measurements are good. This same test can also be used to test the homogeneity of

a sample.

In the case where X^2 is greater than the critical value, various tests can be used to detect possible rogue values in the set of measurements.

III - ROGUE VALUE DETECTION.

Having examined the few tests available in the statistical literature for this kind of measurements, we have found the following two tests well suited :

Dixon test : the count values taken in ascending order being re-named x_1, x_2, ..., x_n, the hypothesis that x_n is an outlier is tested using the ratio :

$$r_1^n = \frac{x_n - x_{n-1}}{x_n - x_1}, \qquad (n \geq 3)$$

Grubbs test : m denoting the mean of the count values and m' their mean when x_n is left out, the statistic used in this test is :

$$\frac{s_n^2}{s^2} = \frac{\sum_{i=1}^{n-1} (x_i - m')^2}{\sum_{i=1}^{n} (x_i - m)^2}, \qquad (n \geq 3)$$

For both tests the computed value is compared to the critical values listed in appropriate tables.

If there are only few rogue values in the sample, they are generally rejected. The tests for outliers, however, are not responsive to excess scatter as such. In this case the operator is warned that he should make new measurements.

In the following sections, each set of counts referring to supposedly constant conditions is assumed to have been checked for its homogeneity and Poissonian character. There remains to specify the precision on the apparent concentration which, as a combination of random variables, is also a random variable.

IV - APPARENT CONCENTRATION CONFIDENCE INTERVAL.

The estimated apparent concentration is an homographic function of Poisson variables. Though it is always implicitly assumed in the literature that this function is Gaussian, this is not generally true.

Using the following notations for the intensities, count durations and counts :

	Intensity	Count duration	Count
Specimen peak	I_E	t_E	n_1
Spec. background	B_E	$\alpha_E t_E$	n_2
Standard peak	I_t	t_t	n_3
Stand. background	B_t	$\alpha_t t_t$	n_4

and C for the concentration we have given a proof that :

$$\chi^2 = \frac{[(n_1 - n_2 / \alpha_E) - C \cdot (t_E / t_t)(n_3 - n_4 / \alpha_t)]^2}{n_1 + n_2 / \alpha^2_E + C^2 (t_E / t_t)^2 \cdot (n_3 + n_4 / \alpha_t^2)}$$

is asymptotically distributed as a chi-square with one degree of freedom. A confidence interval for the apparent concentration C is defined by those values of C such that χ^2 is smaller than the critical values chosen in the table. Replacing χ^2 by the critical value corresponding to the chosen significance level (for instance $\chi^2 = 10.83$ for $\alpha = 99.9$ %) one gets a second degree equation for C whose two roots are always real in the conditions of X-ray measurements. They are the limits of the confidence interval at the α confidence level. Practically, the calculation reduces to the resolution of a second degree equation and can be made with a pocket scientific calculator.

V - TIME OPTIMIZATION.

We have derived from this χ^2 statistic that the optimal allocation of operating time to the various counts resulting in maximal precision in a given time is given by :

$$t_E = K \frac{\sqrt{I_E}}{I_E - B_E} \, , \quad t_t = K \frac{\sqrt{I_t}}{I_t - B_t}, \quad \alpha_E \, t_E = K \sqrt{B_E}, \quad \alpha_t \, t_t = K \sqrt{B_t}$$

where $K = T / [(I_t - B_t)^{-1} (I_t^{\frac{1}{2}} + B_t^{\frac{1}{2}}) + (I_E - B_E)^{-1} (I_E^{\frac{1}{2}} + B_E^{\frac{1}{2}})]$

then the mathematical expectancies of the precision is :

$$E \left[\left(\frac{\Delta C}{C}\right)^2 \right] = \frac{4 \, \chi^2}{K^2/T}$$

(the above formula being applicable only for an optimized division of time).

T is the total time, $T = t_E + \alpha_E \, t_E + t_t + \alpha_t \, t_t$.

Practically, the various intensities can be, as usual, obtained at the start of the experiment and the time allocation calculated for the required precision.

For non dispersive detectors $\alpha_E = \alpha_t = 1$ and peak and background are measured simultaneously, $T = t_E + t_t$. One gets then for the optimum division of time :

$$t_E = K \, (I_E + B_E)^{\frac{1}{2}}/(I_E - B_E), \quad t_t = K \, (I_t + B_t)^{\frac{1}{2}} / (I_t - B_t)$$

$$K = T / [(I_t + B_t)^{\frac{1}{2}} / (I_t - B_t) + (I_E + B_E)^{\frac{1}{2}} / (I_E - B_E)].$$

The mathematical expectancies of the precision is then given by the same formula as above.

This strategy results in considerable savings in total time and the increase in efficiency is quite substantial.

VI - <u>DETECTION THRESHOLD</u>.

Giving consideration to the probability for the value $C = 0$ to belong to the above-mentioned confidence interval, it is possible to define the conditions under which this probability is equal to some value β which can be chosen arbitrarily.

One gets for the apparent concentration under proper measuring conditions ($\alpha_E = 1$) :

$$C_{min} = \frac{\lambda}{2 \, t_E} \left(\frac{1 + \sqrt{1 + 8 \, B_E \cdot t_E / \lambda}}{I_t - B_t} \right) \cdot C_t$$

C_t being the standard concentration (the formula applies equally to dispersive and non dispersive spectrometers).

λ is the non-centrality parameter of a non-central χ^2. The value of this parameter λ is defined by the condition that the non central χ^2 exceeds the α significance level of the central χ^2 with probability $1 - \beta$ (α and β are thus the risks of error of the first and second kind respectively). Taking $\alpha = 0.05$ and $\beta = 0.10$ for instance, one finds from the appropriate table $\lambda = 10.507$.

B_E is the background, usually for traces detection it is measured on a similar specimen which does not contain the element of interest.

VII - CONCENTRATION COMPARISONS.

When the concentrations existing at different locations of the same specimen are to be compared, the most expedient and, from the statistical point of view, soundest procedure is to introduce the corresponding peak counts directly into the X^2 statistic of section II. If only two series of counts are compared, Student's t test can also be applied to the mean values of the counts. It is also possible to use the technics of analysis of variance to compare several mean counts values.

For the general case where the concentrations to be compared have been measured in various conditions (for instance this happens in thin variable thickness specimen analysis), this probleme is more difficult and possible solutions will be presented.

VIII - OTHER STATISTICAL PROBLEMS.

Further problems occur in X-ray analysis such as comparisons of degrees of heterogeneity between specimens, sampling strategy and so on. These will be briefly discussed.

IX - CONCLUSIONS.

We think that a correct statistical approach is already important from an economic and rationality view point, for manual instruments.

For automated instrument it is a must and in facts it is clear that such systems should be used with an entirely new strategy, taking account of the statistical planning of experiments and evaluation of the results.

* *

*

A Monte Carlo Procedure Employing Single
and Multiple Scattering

D. E. Newbury, R. L. Myklebust, and K. F. J. Heinrich
Analytical Chemistry Division
National Bureau of Standards
Washington, D. C. 20234

Abstract

Monte Carlo electron trajectory calculations fall into
two general types [1]: (1) those which employ a "single-
scattering" model for elastic scattering in which each discrete
scattering event with scattering angles as small as approximately
1° are considered [2,3] and (2) those which model the elastic
scattering using a "multiple-scattering" approach, in which 10
to 20 single-scattering events are replaced by an individual
"multiple-scattering step" which produces a displacement which
is equivalent, on average, to the net displacement of all the
individual steps which comprise it [4,5,6].
The single-scattering Monte Carlo calculation is expected
to be the more accurate of the two techniques, since the
resolution of detail in a trajectory is about 20 times greater
due to the smaller mean free path. This accuracy is bought
at the price of the necessity for several hundred to several
thousand scattering calculations per trajectory, and typically
one thousand or more trajectories are needed to adequately
describe a given interaction situation. The multiple-scattering
calculation, while giving a coarser description of the individual
trajectories, can provide a quite reasonable description of the
general interaction volume with 60 scattering calculations per
trajectory. The interaction volume in copper with a 30 keV beam
energy is mapped by both techniques in figures 1 and 2. The
individual trajectories plotted by the multiple-scattering model
(figure 2) are ragged compared to the smooth trajectories of the
single-scattering calculation (figure 1). The overall description
of the interaction volume is similar by both techniques. Extensive
testing of the multiple-scattering model Monte Carlo calculation
has demonstrated that it is capable of determining parameters
which correspond closely to experimentally determined values [5].
The tests included calculating the properties of the backscattered
electrons (backscattering coefficient, η, vs atomic number Z;
η vs tilt, θ; and the energy distribution of backscattered
electrons) and the properties of x-rays generated in the sample
($\phi(z)$, $f(\chi)$, and emission as a function of particle size) [5].
The multiple-scattering Monte Carlo calculation provides greater
calculational efficiency than the single-scattering Monte Carlo
and is applicable in most cases where the specimen size represents

Copper
$E_o = 30 \, keV$
$\theta = 0°$
Single Scattering

0·5 µm
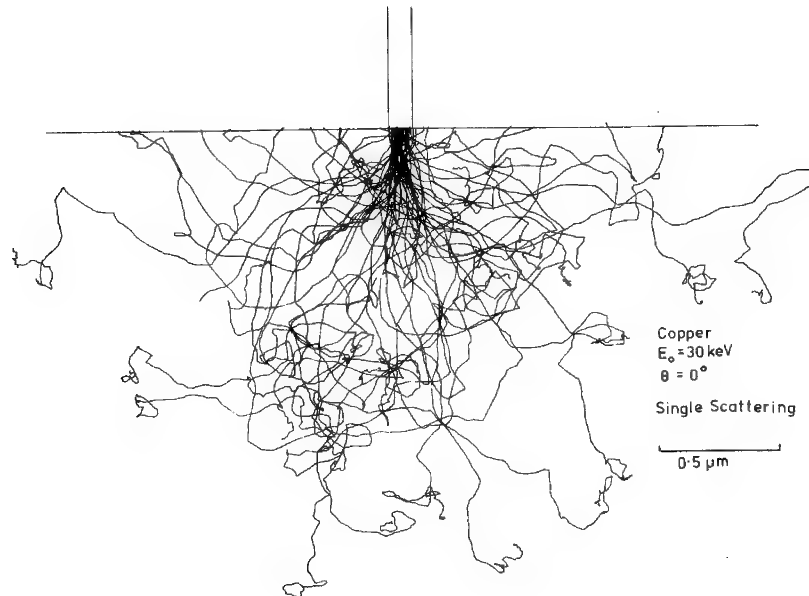
1. Monte Carlo trajectory plot for copper, 30 keV electrons, single-scattering model, 50 trajectories.

Copper
$E_o = 30 \, keV$
$\theta = 0°$
Multiple Scattering

0·5 µm
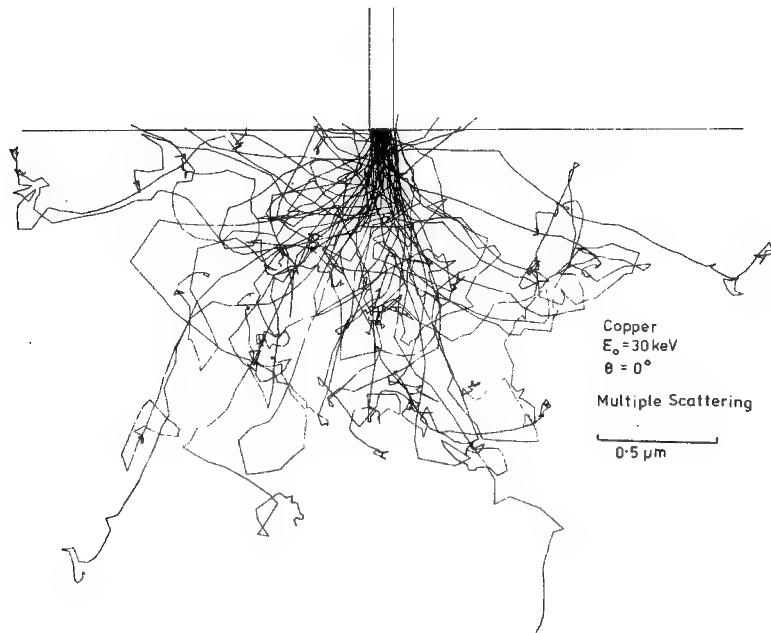
2. Monte Carlo trajectory plot for copper, 30 keV electrons, multiple-scattering model, 50 trajectories.

a significant portion of the interaction volume. The multiple-scattering Monte Carlo calculation becomes inapplicable in those cases where the specimen dimensions are of the same order of magnitude as the multiple-scattering mean free path, e.g., 50 nm. Examples of such specimens include thin films and extremely fine particles.

To overcome these limitations of the multiple-scattering model, we have devised a hybrid Monte Carlo calculation which incorporates aspects of both single- and multiple-scattering. It is clear that the need for accuracy in modeling the electron trajectories is greatest in the near-surface region where the primary beam enters the specimen. The hybrid model adopts the single-scattering model widely used in Monte Carlo calculations [3] where the cross-section is given by

$$\sigma_E = 5.2 \times 10^{-21} \frac{(Z_i)\ (Z_i+1)}{E^2}\ \frac{\pi}{(1+\alpha)}\quad cm^2 \qquad (1)$$

where Z is the atomic number, E is the energy in keV, and $\alpha = 3.4 \times 10^{-3} Z^{2/3}/E$. The step length between collisions, S, is calculated from the mean free path, Λ, with a statistical distribution as follows [7]:

$$S = -\Lambda\ \log_e R \qquad (2)$$

where R is a random number $0 < R < 1$. The Bethe energy loss law was used to model inelastic scattering. The complete single-scattering model has been used to calculate the electron behavior over the initial five percent of the energy loss. This energy loss is equivalent to a path length along the trajectory of approximately 200 nm in gold. The calculation is then switched to a multiple-scattering model for the remainder of the energy loss. The multiple-scattering model is based on that of Curgenven and Duncumb [4] and has been modified to make use of a variable step length and a scattering angle distribution which allows all angles 0-180° [5].

A partial trajectory plot is given in figure 3 which shows the transition from single-scattering to multiple-scattering with the accompanying increase in the step length.

As a test of the hybrid model, a calculation was carried out for the energy distribution of backscattered electrons from gold with a 30 keV incident beam. The energy distributions for the hybrid model (single scattering to 95 percent E_o, multiple scattering for the balance) and for a pure multiple scattering model are shown in figures 4(a) and (b). The hybrid model shows a more distinct energy peak and eliminates the anomalous scattering in the first step observed with multiple scattering models [8]. The energy distribution determined experimentally by Bishop [9] for gold at 30 keV beam energy is plotted in figure 5(a). The experimental curve for gold shows a much

sharper peak than that calculated with the hybrid model.
However, the comparison is not justified because the Monte
Carlo calculation gives the distribution of energy of all
electrons which backscattered, regardless of direction, while
the experiment gives the energy distribution at a take-off
angle of 45°. Bishop [9] has shown that the shape of the energy
distribution varies considerably with take-off angle, figure 5(b).
The proper comparison for the Monte Carlo distribution would be
an experimental measurement over the complete solid angle of
emission. A Monte Carlo calculation could be made for the
energy distribution into a given solid angle, but due to the
large number of electrons required, the cost would be prohibitive.

Additional testing of the x-ray production parameters as
well as other electron scattering parameters is being carried
out. The hybrid Monte Carlo calculation is expected to produce
superior results compared to the multiple-scattering Monte Carlo
in the analysis of fine particles and thin films.
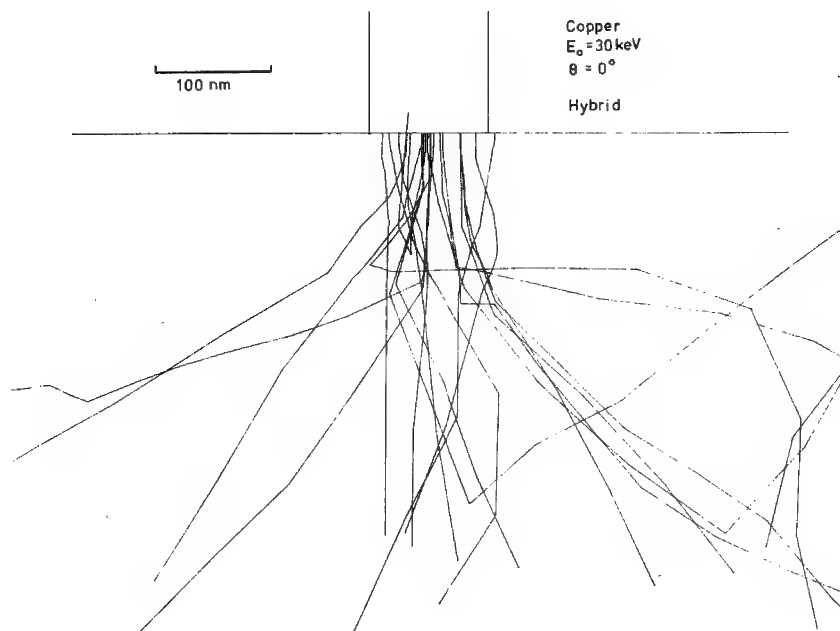
3. Initial portion of trajectories, hybrid Monte Carlo calcu-
lation; copper, 30 keV electrons.
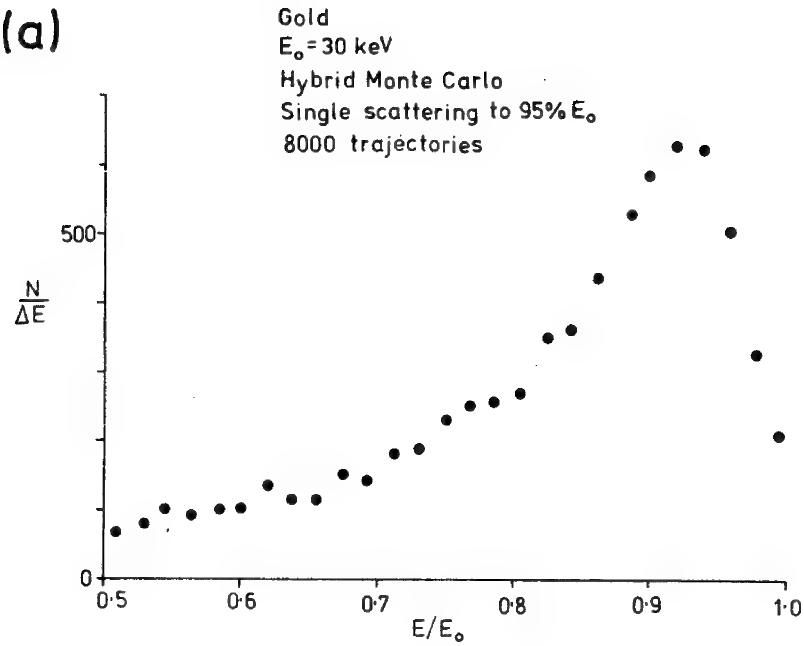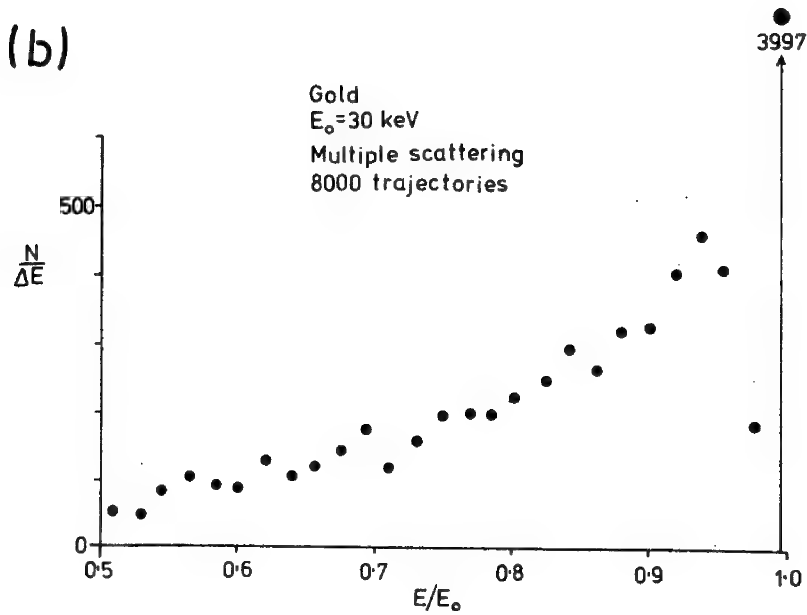
4. Energy distribution of 30 keV incident electrons backscattered from gold calculated with (a) hybrid Monte Carlo model and (b) multiple-scattering Monte Carlo model.
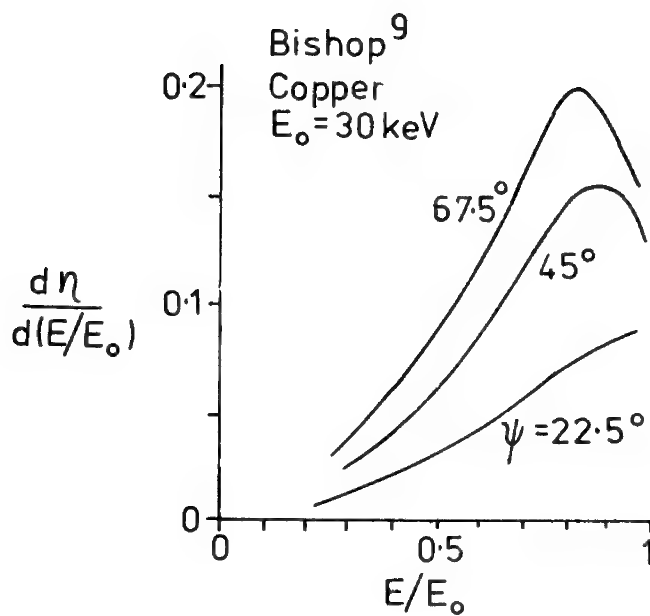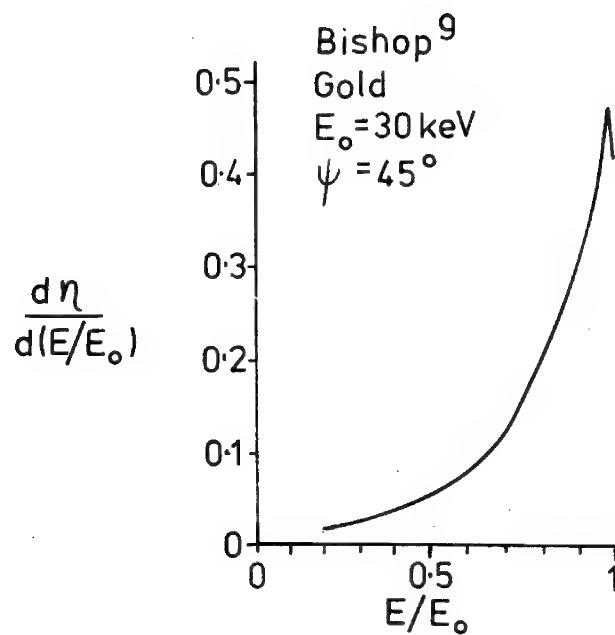
5. (a) Energy distribution of 30 keV incident electrons back-
    scattered from gold determined experimentally by Bishop [9]
    with normal beam incidence and detector take-off angle of
    45°. (b) Energy distributions from copper as a function
    of take-off angle.

References

1. Shimizu, R., Ikuta, T., and Murata, K., J. Appl. Phys. 43, 4233 (1972).

2. Murata, K., Matsukawa, T., and Shimizu, R., Jap. J. Appl. Phys. 10, 678 (1971).

3. Kyser, D. F. and Murata, K., IBM J. of Res. and Dev. 18, 352 (1974).

4. Curgenven, L. and Duncumb, P., Research Report No. 303, Tube Investments, Saffron Walden, Essex, England (1971).

5. Myklebust, R. L., Newbury, D. E., and Yakowitz, H. in Use of Monte Carlo Calculations in Electron Probe Microanalysis and Scanning Electron Microscopy, NBS Spec. Publ. 460, Heinrich, K. F. J., Newbury, D. E., and Yakowitz, H., eds., Washington, D. C., 105 (1976).

6. Love, G., Cox, M. G. C., and Scott, V. D., J. Phys. D: Appl. Phys. 10, 7 (1977).

7. Reimer, L. and Krefting, E. R., NBS Spec. Publ. 460, Heinrich, K. F. J., Newbury, D. E., and Yakowitz, H., eds., Washington, D. C., 45 (1976).

8. Bishop, H. E., ibid., 5 (1976).

9. Bishop, H. E. in X-ray Optics and Microanalysis, Castaing, R., Deschamps, P., and Philibert J., eds., Hermann, Paris, 153 (1966).

MONTE CARLO SIMULATION OF PLASMA AND
CHARACTERISTIC ENERGY LOSSES IN THIN FILMS

by

Garret L. Sheldon and Robert E. Ogilvie
Department of Materials Science and Engineering
Massachusetts Institute of Technology
Cambridge, Massachusetts 02139

Introduction

A thorough understanding of the electron-specimen interaction is a fundamental requirement in the fields of transmission electron microscopy, microprobe analysis, electron diffraction, and high energy electron physics. The individual interaction processes have been studied theoretically and experimentally for many years; yet no model or theory has been presented which adequately explains completely the experimental data. All models have suffered from real and practical limitations, such that full advantage cannot be taken of the experimental and theoretical information.

Experimental (empirical) models suffer from statistical and systematic errors in measurements. The inability to obtain adequate resolution in the examination of any of these processes is a serious limitation to the empirical models. In any case, discrimination between effects of different interaction phenomena is difficult since only integral and indirect measurements can be made.

Theoretical models relying on analytical mathematical expressions of the model have always required simplifying assumptions in order to obtain a solution. Thus geometric, and other boundary conditions, large-angle scattering or the statistical nature of energy losses, among others, have been ignored or simplified. In addition, those parameters which relate semiempirical models to experiment suffer from the above-mentioned experimental limitations.

Early computer simulation models were limited by slow CPU speeds which required simplification of the model in order to obtain a solution. Later computer simulations do not suffer this limitation, yet are still inadequate, since the understanding of the basic physical process has not been completely incorporated. Discrepancies between theory and experiment, multiplied by the number of degrees of freedom inherent in the system, have made these computer solutions qualitatively correct and useful but quantitatively inaccurate for detailed study.

This paper is an _attempt_ to formulate an electron penetration and interaction model that is consistent with existing empirical models and is not only qualitatively useful but also quantitatively correct. Therefore, we will try to accurately describe the real electron-solid system. With this system description, in terms of its elements, the basis for our Monte Carlo simulation will be provided. The goal has been to transform this into a computerized model of electron interactions in thin films.

The authors would like to point out that considerable insight, detail, and guidance was obtained from the outstanding papers of Berger (1963), Green (1965), Swanson (1966), Ritchie (1969), Shimizu (1971, 1972, 1975), Bolon (1973), Newbury (1973), and in particular the excellent paper by Marton (1962).

The Monte Carlo Program

A Monte Carlo simulation program has been developed in which all interactions are included separately. Specifically, each transformational process is separately stated.

Path Lengths. The electron straggling phenomenon has generally been treated by examining the statistical variation of energy loss in traveling some distance in the solid (Landau, 1944). The straggling phenomenon is easier to treat in the model by allowing a statistical variation in the mean-free-path between events assuming a known energy loss (Belyaev, 1973). To determine the randomly varying MFP we use the following procedure.

Assume that the collision probability of the particle for some small ΔS is constant and is independent of other events. Then the path length can be drawn from a geometric distribution, where the probability of occurrence in step one is given by:

$$P_1 = \Delta S/MFP \tag{1}$$

and the probability of occurrence in step n is given by:

$$P_n = (1 - \Delta S/MFP)^{n-1}(\Delta S/MFP) \tag{2}$$

A reasonable ΔS would be the average distance to the nearest neighbors in the solid.

To relate a randomly chosen number (r) to the path length we use the following procedure. Let x equal the number of steps. ΔS is represented by r. The probability that the event occurs after x steps is given by:

$$P_x = (1 - \Delta S/MFP)^x = (1 - r) \tag{3}$$

Thus the path length (PL):

$$PL = \Delta S \log (1 - r)/\log (1 - \Delta S/MFP) \qquad (4)$$

Interaction Choice. We would like to know the simultaneous angular energy differential cross sections for each interaction process. To use these in the Monte Carlo model we must convert them to occurrence probabilities. Let $P_n(E_0, K, \Theta)$ be the probability that even n will occur at incident energy E_0, with an energy loss K, and a scattering angle Θ. The probability that event n occurred can be described by:

$$P_n(E_0) = \sigma_n/\sigma_{TOT} \qquad (5)$$

where $\sigma_{TOT} = \Sigma \sigma_n$.

The probability (P) that n occurred with a particular value K (between K and K + dK) and Θ (between Θ and Θ + dΘ) can be given by:

$$P_n (E_0, K, \Theta) = [(d^2\sigma_n/dKd\Theta)/\sigma_n] dKd\Theta \qquad (6)$$

This σ_n series of conditional probabilities forms the basis for our atomic element interaction design. Thus we can:

1. Calculate the MFP by calculating the total interaction cross section.
2. Use the MFP to find the position of the next interaction.
3. Decide which event n occurred using equation (5).
4. Finally decide the value of (K, Θ) using equation (6).

Module Description. The function of the modules used by the SIMULE program are described below.

BEAM. Generates the primary electrons. The present version generates a perpendicular incident beam, with an energy fluctuation of $\pm$ 0.5 eV.

BREMSS. Generates the electron energy loss and scattering angle of a Bremsstrahlung interaction. Calculates the cross section for Bremsstrahlung interactions.

COORD. Calculates the cartesian coordinates of the electron at the end of the present path.

ELASC. Generates the elastic scattering angle. This module can use either scattering formulas or tabular values. It can calculate a small momentum transfer. Calculate the cross section for elastic scattering.

IONIZE. Generates energy loss and scattering angle for interactions with inner shell electrons. Calculates the total cross section for all ionizations.

PATH. Generates a path length based on the total cross section.

PLASMA. Generates the energy loss and scattering angle for a plasma interaction. Calculates the cross section for plasma losses.

<u>SECOND</u>. Generates the energy loss and scattering angle for a single-electron interaction not included in the IONIZE module. Calculates the cross section for single-electron interactions.

<u>STATS</u>. This module produces the output from the system. It directly accumulates some statistics. However, it also creates a history file of all trajectories that may be used later.

<u>SURFCE</u>. This module can be used to generate a surface plasma on entering the system. The present version does not use this facility.

<u>PROBTB</u>. Generates a scattering probability table for PLASMA and may be used by IONIZE and SECOND. The approximation used for the probability of entry n occurring in step i is:

$$P(i) = \Delta\Theta/(\Theta_E^2 + \bar{\Theta}_i^2)/\sum_{i=0}^{i_{max}} [\Delta\Theta/(\Theta_E^2 + \bar{\Theta}_i^x)] \tag{7}$$

when $\Delta\Theta$ is the table step size (rad)

  x is the loss function factor

  $\bar{\Theta}_i = (i + 0.5) \Delta\Theta$

  i_{max} = maximum table entries

<u>RANDOM</u>. The random number generator.

<u>Results</u>

Figures 1, 2, 3, and 4 present results of the program SIMULE for 200 A and 400 A aluminum thin film specimens at 20 keV. These results are in qualitative agreement with the experimental results of Swanson (1966) and Marton (1962).

A comparison of the zero loss peaks in Figure 1 compared to Figure 2 shows an increased intensity of multiple loss peaks in the 400 Å case, in agreement with the assumption of a Poisson distribution of loss peaks. The geometric path length assumption generates the correct peak distribution.

A comparison of Figures 2 and 3 shows the angular dependence of the loss intensity. The first and second loss peaks increase relative to the zero loss peak as the angle of scattering increases. The same trend is seen in going from Figure 3 to 4. This change in relative peak intensity with larger analyzer acceptance angle is one of the characteristics noted by Marton (1962).

<u>Conclusions</u>

A detailed Monte Carlo simulation of the electron-solid interactions has been developed which incorporates specific element transformational processes. The results are qualitatively correct and with proper adjustment of middle parameters should become quantitatively correct.

References

Berger, M. J., <u>Methods in Computational Physics</u>, I, N.Y. Academic Press (1963).

Bolon, R. B. and Lifshin, E., Use of Monte Carlo Techniques, G. E. Research Rep. 73CRD082 (1973).

Green, M., Ph.D. Thesis, Cambridge University, England (1962).

Landau, L., J. Phys. USSR, <u>8</u> 201 (1944).

Marton, L., Simpson, J., <u>et al</u>,, Phys. Rev., <u>126</u>, 182 (1962).

Newbury, D. E., Yakowitz, H., and Myklebust, R., Appl. Phy. Lett., <u>23</u>, 488 (1973).

Ritchie, R., Garber, F., <u>et al</u>., Adv. in Rad. Biology, <u>31</u>, 1 (1969).

Shimizu, R., Ikuta, T., and Murata, K., J. Appl. Phy., <u>43</u>, 4233 (1971).

Shimizu, R., Nishigori, N., and Murata, K., <u>Proc. of Sixth Int. Conf. on X-Ray Optics and Microanalysis</u>, Univ. of Osaka, Tokyo Press, 131 (1972).

Shimizu, R., Kataoka, Y., and Matsukawa, T., J. Phys. D., <u>8</u>, 820 (1975).

Swanson, N. and Powell, C., Phys. Rev., <u>145</u>, 195 (1966).
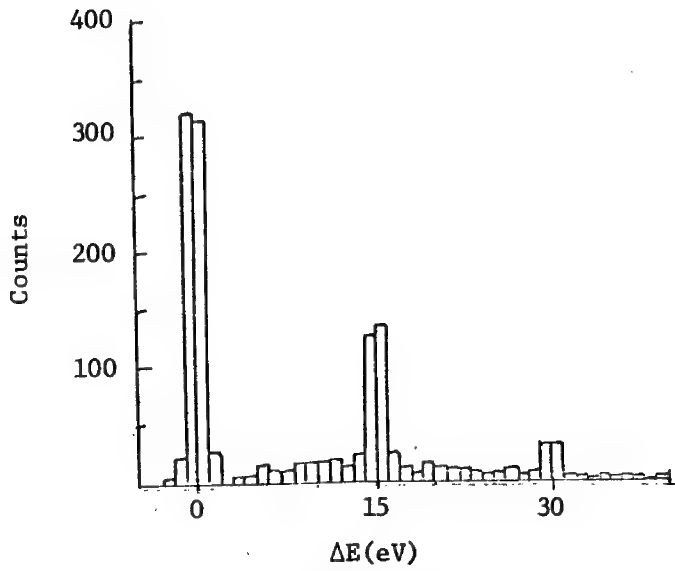
Figure 1.   SIMULE Results
200 Å (A1) 0-1 mrad (20 keV)
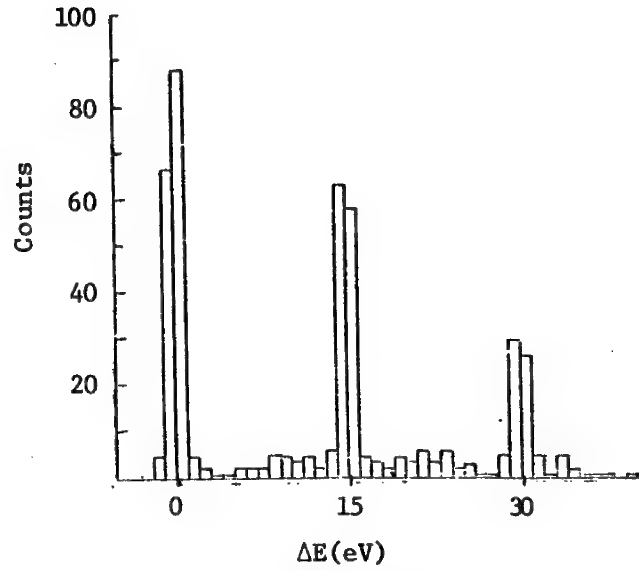
Figure 2.   SIMULE Results
400 Å (A1) 0-1 mrad (20 keV)
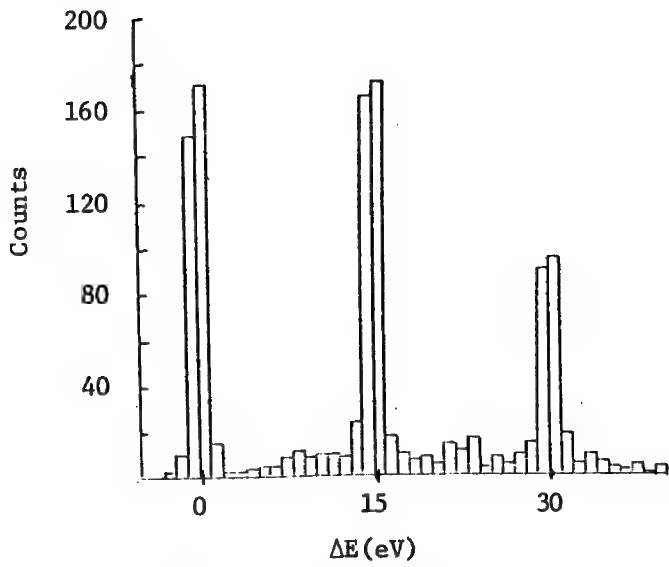
Figure 3.   SIMULE Results
400 Å (A1) 0-5 mrad (20 keV)
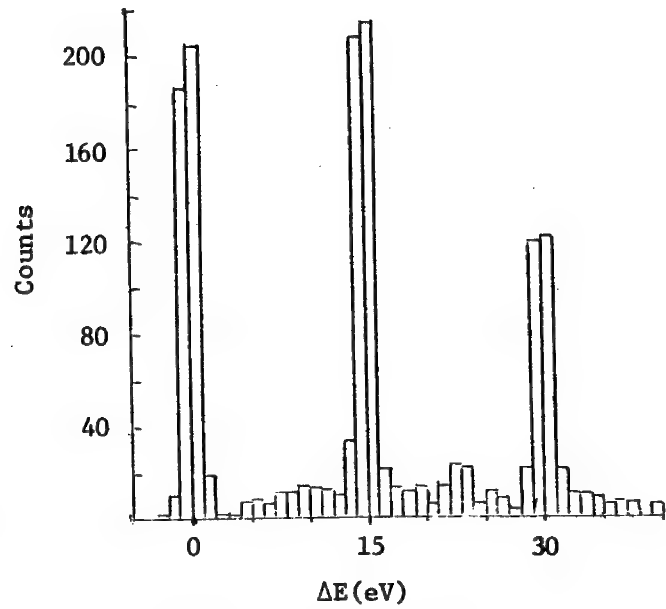
Figure 4.   SIMULE Results
400 Å (A1) 0-10 mrad (20 keV)

DISTRIBUTION DES ELECTRONS D'UN FAISCEAU DANS UNE CIBLE HOMOGENE

C. LANDRON, M. ANDREANI, P. AZOU

Laboratoire des Faisceaux Electroniques - Institut de Physique

ECOLE CENTRALE DES ARTS ET MANUFACTURES - Grande Voie des Vignes
92290 CHATENAY-MALABRY - FRANCE

-=-=-=-=-=-=-=-=-=-=-=-=-=-=-=-

Nous nous proposons de déterminer une solution analytique au problème de la propagation d'un faisceau d'électrons monocinétique dans une cible homogène et isotrope et ceci pour les raisons suivantes :

- Une expression analytique de la distribution des électrons dans une cible permet de résoudre les problèmes de micro-analyse à l'aide d'un simple calculateur.

- Une solution analytique permet d'aborder de façon continue le problème de la propagation d'un faisceau d'électrons dans une cible et non de façon discrète comme dans la méthode de MONTE-CARLO ou la résolution numérique de l'équation de transport de BOLTMANN (1).

- Une solution analytique permet de mieux dégager l'influence des différents paramètres qui interviennent lors de la diffusion des électrons dans la cible.

Dans ce modèle, nous supposons connus les différents types d'interaction intervenant entre les électrons du faisceau incident et les constituants de la cible, leurs effets se traduisent (2) :

- D'une part par l'expression de la section efficace de diffusion simple :

$$\sigma(\theta) = \frac{Z^2 e^4}{16 E^2} \frac{1}{\left(\sin^2 \frac{\theta}{2} + \alpha\right)^2}$$

- D'autre part par l'expression de la loi de perte d'énergie moyenne par unité de parcours :

$$\frac{dE}{d\rho s} = -\frac{2\pi N e^4 Z}{E A} \log 1{,}166 \frac{E}{I}$$

29B Désignons par $\varphi_n(x)$ la densité de probabilité de parcours élémentaire, en projection sur la direction initiale des électrons, à la suite du n ième choc et soit $\Phi_n(q)$ sa fonction caractéristique. Désignons par $f_n(x)$ la distribution des électrons dans la cible à la suite du n ième choc et soit $F_n(q)$ sa fonction caractéristique (3) :

$$F_n(q) = \prod_{i=1}^{m} \Phi_n(q)$$

En comparant le développement de la fonction Fn (q) avec celui de la fonction caractéristique de la distribution gamma, on constate que la distribution des électrons dans la cible, à la suite d'un nombre de chocs suffisamment élevé tend vers la fonction suivante

$$f(x) = 0 \qquad\qquad x > s$$

$$f(x) = \frac{1}{\Gamma(\nu)} \; \exp{-\frac{s-x}{b}} \; \frac{(s-x)^{\nu-1}}{b^\nu} \qquad , \quad x < s$$

s, parcours des électrons d'énergie résiduelle E dans la cible b et ν étant reliés aux paramètres caractéristiques de la distribution par la relation

$$b = \frac{\langle x^2 \rangle - \langle x \rangle^2}{s - \langle x \rangle}$$

$$\nu = \frac{(s - \langle x \rangle)^2}{\langle x^2 \rangle - \langle x \rangle^2}$$

Ces paramètres caractéristiques sont calculés en multipliant l'équation de transport de BOLTZMANN, par chacune des variables spatiales et par son carré et en intégrant sur tout l'espace :

$$\frac{\partial f}{\partial s} + \cos\theta \, \frac{\partial f}{\partial x} = N \int [f(\cos\theta') - f(\cos\theta)] \, \sigma(\eta) \, d\omega$$

Ces équations permettent de calculer de façon simple les valeurs de $< x >$ et de $< x^2 >$ en fonction de l'énergie résiduelle des électrons et des caractéristiques de la cible.

Le problème de la détermination des distributions $f_{si.}(x)$ des électrons dans des cibles semi-infinies est traité en remarquant que l'équation de transport de BOLTZMANN est linéaire par rapport à x ; on recherche alors une solution particulière de cette équation de transport comme une combinaison linéaire de solutions particulières de cette équation qui satisfont aux conditions aux limites :

$$f_{si}(x) = \frac{(s-x)^{\nu-1} \exp{-\frac{s-x}{b}} - (s+x)^{\nu-1} \exp{-\frac{s+x}{b}}}{b^\nu \; \Gamma(\nu)}$$
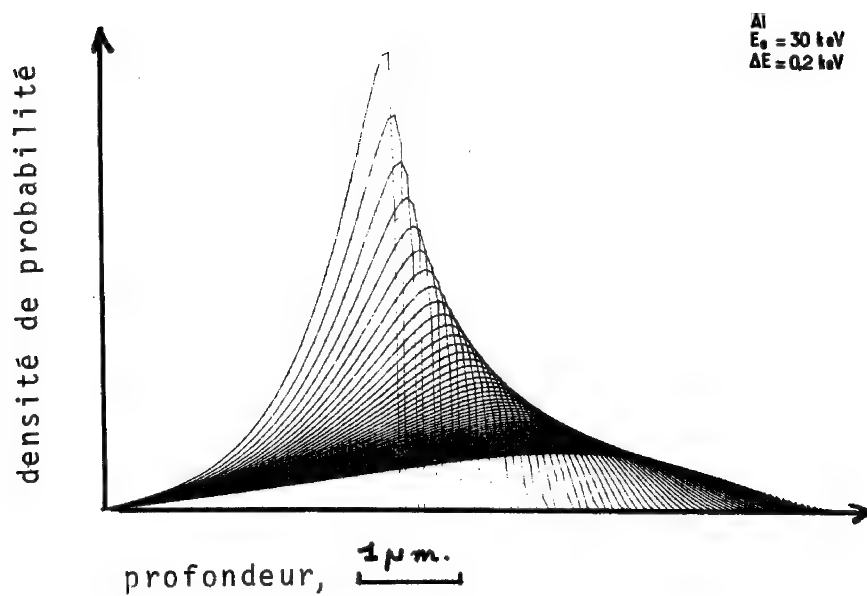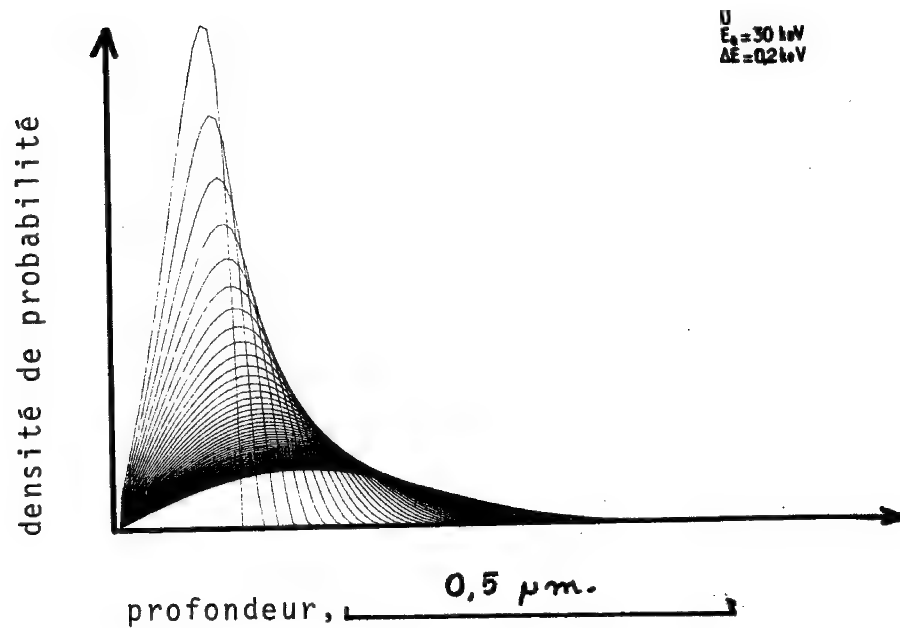
densités de probabilité de présence des électrons d'un faisceau
pour des étapes successives de la propagation .

A partir de cette expression, il est possible de calculer :

- le coefficient de retrodiffusion

$$\eta_r = \lim_{\varepsilon \to 0} 2 b \, f(o)$$

- la profondeur moyenne atteinte par les électrons en milieu semi-infini

$$\langle x \rangle_{si} = \frac{\langle x \rangle}{1 - 2 b \, f(o)}$$

- le deuxième moment de la distribution des électrons dans une cible semi-infinie

$$\langle x^2 \rangle_{si} = \frac{\langle x^2 \rangle - b^3 f(o)}{1 - 2 b \, f(o)}$$

Les valeurs numériques des distributions des électrons dans la cible et des paramètres caractéristiques de ces distributions montrent qu'il y a un bon accord entre les résultats obtenus à l'aide de notre modèle et ceux qui sont obtenus par la méthode de MONTE-CARLO (4).

———————

(1) BROWN D.B. - Journal Appl. Phys. 1969. 40 - 1627

(2) MAURICE F. - Journal de Microscopie Vol. 15. 3. 1972, P 285.

(3) LOEVE M. Journal Math. Pure et Appl. 24 - 1945 - P 32.

(4) BISHOP M.E. Brit. J. Appl. Phys. 1- 1968 - P 673.

DISTRIBUTION ENERGETIQUE DES ELECTRONS RETRODIFFUSES

C. LANDRON, M. ANDREANI, P. AZOU

Laboratoire des Faisceaux Electroniques - Institut de Physique

ECOLE CENTRALE DES ARTS ET MANUFACTURES - Grande Voie des Vignes

92290 CHATENAY-MALABRY - FRANCE

=-=-=-=-=-=-=-=-=-=-=-=-=-=-=-=-=-=

La répartition énergétique des électrons retrodiffusés est mesurée pour différentes cibles homogènes et isotropes. Le spectromètre qui a été mis au point pour réaliser ces mesures devait jouir des propriétés suivantes :

- bonne résolution,
- adaptabilité à un microscope électronique,
- possibilité d'intégration de la résolution électronique,
- autofocalisation.

Un spectromètre, basé sur le principe de l'action simultanée et dans le même espace d'un champ électrique normal à une induction magnétique, chacun d'eux étant lui-même normal à la direction initiale de propagation des électrons a été réalisé. La conception de cet appareil a été guidée par ses performances ainsi que par ses dimensions. Il a été situé à la place du mouvement objet d'un microscope à balayage, ce qui permet d'avoir un faisceau électronique très stable et une détection adaptée aux énergies utilisées.

Dans ce type d'appareil les électrons suivent des trajectoires représentées par les courbes suivantes (1):

Trajectoires des électrons dans un plan axial contenant la direction du champ électrique.
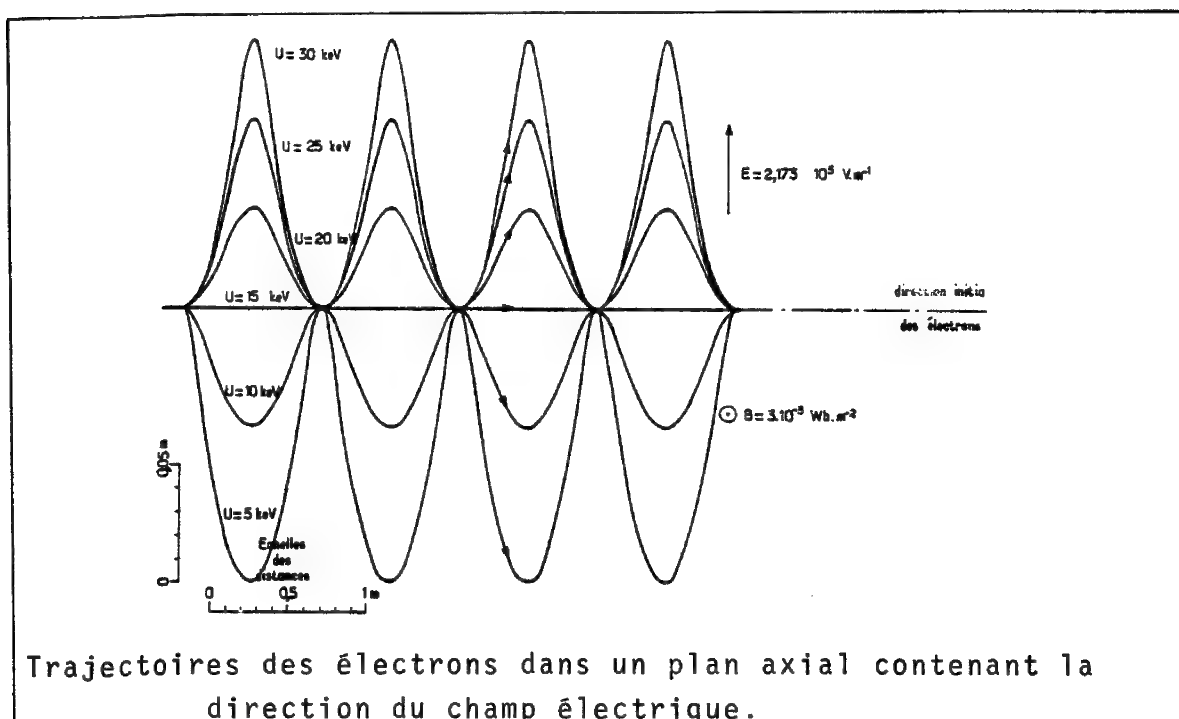
La résolution de cet analyseur est calculée, les caracté-
ristiques de cet appareil ont été choisies pour rendre ce paramètre
optimal, il est montré que pour ces conditions optimales de fonction-
nement, cet appareil est aussi autofocalisant.

Trajectoire des électrons dans un plan axial du spectromètre
contenant la direction du champ électrique en fonction de
l'angle d'incidence.
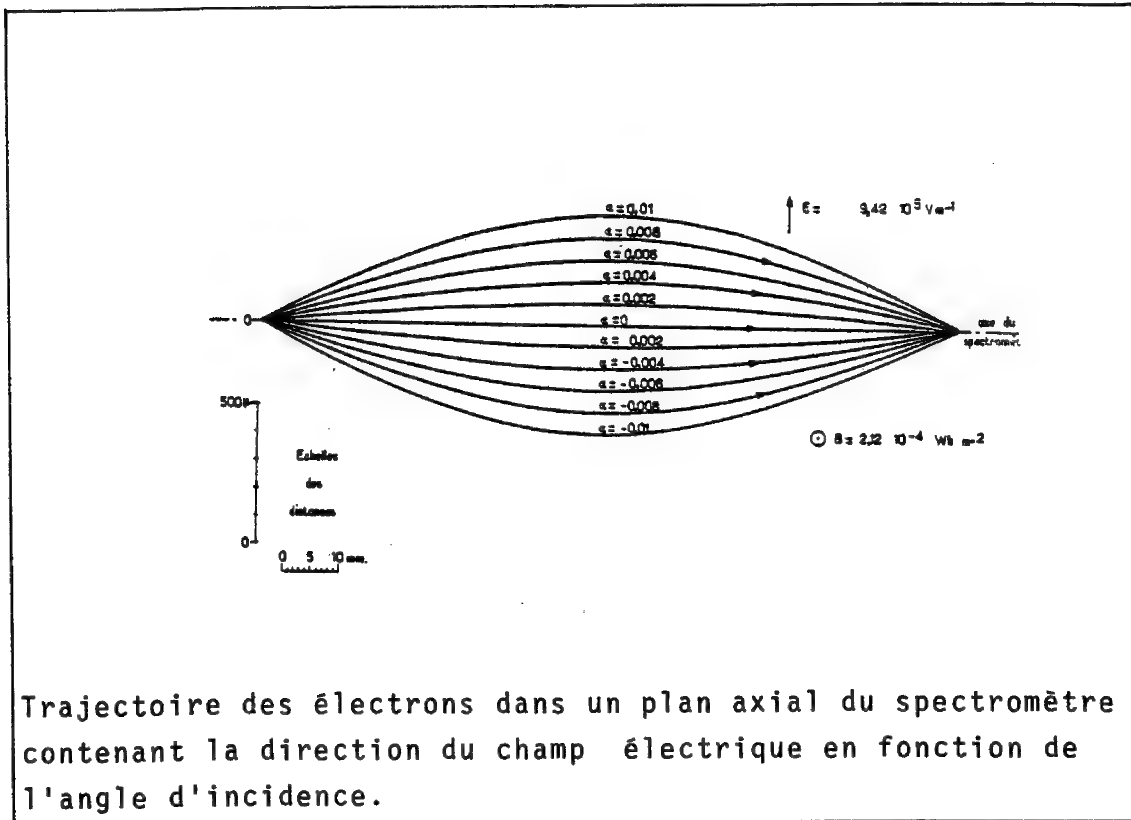
L'étude expérimentale de la distribution des électrons
retrodiffusés comprend quatre étapes.

- Production d'un faisceau d'électrons, monocinétique
  et parallèle,
- choix et préparation de la cible,
- Analyse des électrons en énergie,
- Détection et comptage des électrons.

Pour obtenir un faisceau électronique stable et suffisamment
fin, un microscope électronique à balayage a été utilisé en sonde
fixe. Ce faisceau tombe normalement à la surface plane d'une cible.
Celles-ci sont obtenues par métallisation sous vide sur la surface
plane d'un échantillon du même métal.

Pour atteindre la résolution optimale du spectromètre, un
contrôle de l'uniformité du champ électrique et de l'induction
magnétique a été effectué . La perpendicularité de ces deux
champs a été vérifiée par une double reflexion d'un faisceau
Laser sur les plaques du condensateur et les pièces polaires de
l'électro-aimant .
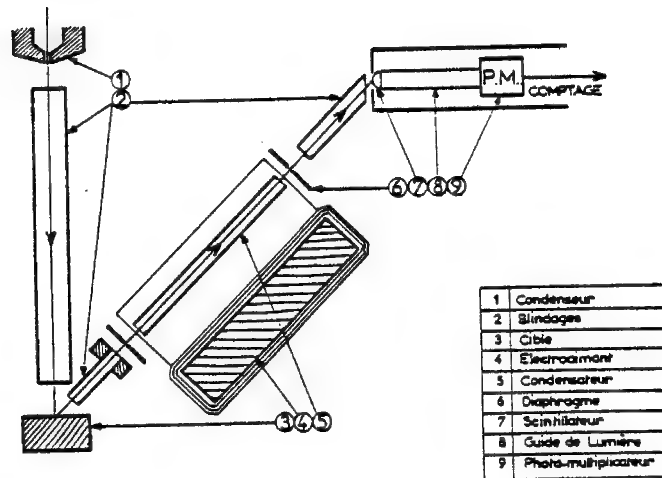
Schéma du montage permettant l'analyse en énergie des électrons rétrodiffusés.

Le spectromètre a été étalonné ce qui permet de fixer les valeurs de la tension appliquées aux bornes du condensateur et de l'intensité parcourue par la bobine de l'électro-aimant pour atteindre les conditions optimales de fonctionnement de cet appareil.
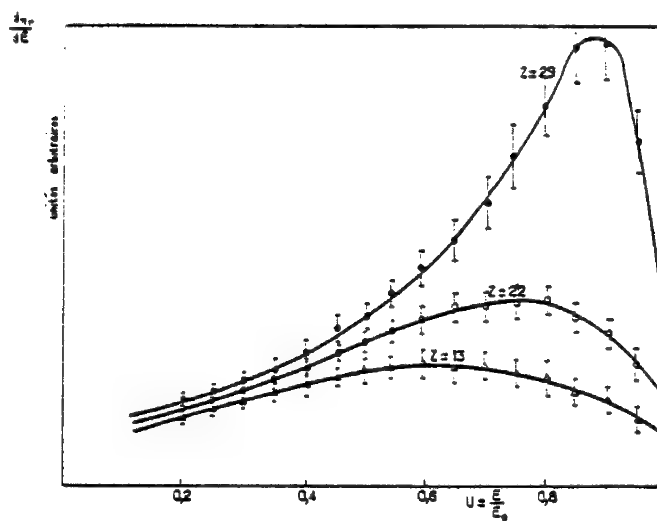
Distribution énergétique des électrons rétrodiffusés pour quelques cibles.

Les distributions énergétiques des électrons rétrodiffusés confirment les expériences effectuées avec des appareils d'un autre type que l'analyseur à champs croisés (2). L'examen des courbes obtenues montre l'intérêt du filtrage en énergie des images électroniques obtenues par un microscope à balayage, dans le but d'améliorer la résolution et le contraste des images.

---

1) LANDAU et LICHITZ - Théorie des champs - Editions MIR

2) BISHOP H.E. - Thèse Université de CAMBRIDGE.

DIRECT MEASUREMENTS OF THE VOLTAGE-DEPENDENCE OF INNER-SHELL IONIZATION CROSS-SECTIONS

D. F. Kyser and R. H. Geiss

IBM Research Laboratory
San Jose, California 95193

The voltage-dependence of the cross-section Q(E) for ionization of inner-shell electrons by electron impact is an important factor in quantitative analysis. In conventional electron probe microanalysis, the absolute value of Q(E) is not necessary for quantitative analysis since it cancels itself out when the k-value is formed experimentally using bulk standards. However, the voltage-dependence still enters into the determination of the "atomic number" correction [1]. If standardless quantitative analysis of thick samples is attempted, then the absolute value of Q and its voltage-dependence must be known when K, L, or M lines from different elements are mixed together in the measurements.

In high-voltage analytical electron microscopy (AEM) of thin foils, X-ray production is approximately described by mono-energetic electron impact [2]. If foil standards are utilized in AEM, the analysis is much simpler because then even the "atomic number" correction becomes very small at high voltages. However, the more practical method of AEM, due to the difficulties encountered in fabrication and characterization of foil standards, is to simply measure the relative intensity of K, L, or M lines from different elements in the same sample. Because of the wide range of over-voltages, the voltage-dependence of Q(E) for each element is then a critical factor in quantitative AEM [3].

In this paper we report some "direct" measurements of the voltage-dependence of inner-shell cross-sections for ionization. Thin foil metallic samples were prepared by "sputter-gun" deposition in vacuum onto a very thin carbon foil substrate which in turn was supported by a 200 mesh TEM Cu grid. The relative intensity of a characteristic X-ray line from the foil was measured in a commercial electron probe microanalyzer [4] equipped with crystal spectrometers. The sample was mounted from one edge only in cantilever style, and the electron beam was allowed to pass through the hollow column of the sample holder and stage, eventually being stopped by the bottom vacuum wall of the sample chamber. With such a configuration, no electrons could be backscattered from surfaces nearby

the sample. The electron beam current was set to the same value at each voltage with a Faraday cup, and the crystal spectrometer was not detuned from its peak position. The line/background ratio from the foil was always greater than 100/1, and counting times of 100 seconds were used for all measurements. The beam was slightly defocussed and set within a particular grid square for each measurement of intensity. The background intensity observed when the beam was purposely set in an open grid hole was negligible as long as the condenser lens excitation was weak. With strong excitation, foil and grid material radiation was observed, perhaps due to beam tailing [5]. The beam current was typically $0.1 \mu A$, and the count rate was sufficiently high to achieve reasonable precision. The beam current was held constant by a floating aperture signal to a feedback-controlled condenser lens supply [6]. The high-voltage electron gun power supply (0 - 50kV) was equipped with a modification which enables the filament voltage to be regulated instead of the grid voltage, and the voltage was calibrated to within 0.05%. All of these experimental conditions were necessary to achieve accurate and reproducible data.

Some results of these measurements are given in Tables 1 and 2. The observed intensities have been normalized at their respective maximum in order to allow rapid comparison with a variety of theoretical expressions for the voltage-dependence of Q(E) which have been proposed in the literature. Comparison will also be made with the "indirect" measurements and calculations of Q(E) which were presented previously [7]. Additional work with a STEM-EDS instrument is in progress to enable measurements of Q(E) for harder X-rays.

References

[1] S. Reed, Electron Microprobe Analysis (Cambridge Univ. Press, 1975), Ch. 12.

[2] J. Philibert and R. Tixier, Physical Aspects of Electron Microscopy and Microbeam Analysis (Wiley, 1975), p. 333.

[3] J. Goldstein, J. Costley, G. Lorimer, and S. Reed, SEM/1977 (IIT Res. Institute, 1977), p. 315.

[4] Applied Research Laboratories, model EMX-SM.

[5] R. Bolon and M. McConnell, SEM/1976 (IIT Res. Institute, 1976), p. 163.

[6] D. Kyser and D. Horne, Rev. Sci. Inst. 43, 1334 (1972).

[7] D. Kyser, Proc. 11th MAS Conference (Miami Beach, 1976), paper no. 28.

Table 1. Normalized Intensity Observed Versus Electron Beam Voltage for SiKα from 100 Å Si Foil

E_o(kV)	U_o	*I/I(max)
3	1.633	.720
4	2.177	.911
5	2.722	.988
6	3.266	1.000
7.5	4.083	.973
10	5.444	.927
12.5	6.805	.853
15	8.165	.784
20	10.887	.680
25	13.609	.605
30	16.331	.534
35	19.053	.484
40	21.775	.458

* σ = ± 0.010

E_c(SiKα) = 1.837kV

Table 2. Normalized Intensity Observed Versus Electron Beam Voltage for ZrLα from 25 Å Zr Foil

E_o(kV)	U_o	*I/I(max)
3	1.351	.598
4	1.802	.906
5	2.252	.983
6	2.703	1.000
7	3.153	.999
8	3.604	.962
9	4.054	.932
10	4.505	.876
12.5	5.631	.831
15	6.757	.761
20	9.009	.665
25	11.261	.588
30	13.514	.540
35	15.766	.501
40	18.018	.445
45	20.270	.422

* σ = ± 0.015

E_c(ZrLα) = 2.220kV

J.Böcker and Th. Hehenkamp
Institut für Metallphysik der Universität Göttingen

Continuum-radiation in Quantitative Electron Microprobe Analysis

The background for characteristic lines in quantitative microprobe analysis can be determined without shifting the spectrometers employing a relationship between X-ray continuum intensity and atomic number Z. A formula for calculation of the background $I(Z)$ was worked out [1] on the basis of measurements $I(Z)/I(Zn)$ on pure metals and alloys using an ARL-probe with an emergence angle of 52.5°:

$$I(Z) = I_{Zn}(A_0 + A_1 Z^n) \cdot (F_A(Zn)/F_A(Z) \tag{1}$$

with

$A_0 = -0.75$

$A_1 = 0.226 + 0.043 \lambda(\text{Å})$

$n = 0.5800 + 0.0364 \lambda(\text{Å})$

F_A is the absorption correction of Philibert with a modification in Heinrich's sigma formula (E_c is replaced by E_ν).
The uncertainty of formula (1) is about 1% in the range of investigation. The measurements were made at the wavelengths 1.66 Å, 2.1 Å, 2.29 Å and 2.75 Å with acceleration voltages up to 50 kV and constant beam current. The background of a binary alloy can be calculated combining equ.(1) with equ.(2)

$$Z_{All} = (c_1 Z_1^{0.25} + c_2 Z_2^{0.25})^4 \tag{2}$$

where c_1, c_2 are weight concentrations. Controlling measurements with a JEOL[2] and a CAMECA-probe demonstrate the immediate applicability of the results to microprobes having different emergence angles down to at least 18°.
For the continuum fluorescence correction the g e n e r a t e d continuum intensity as a function of Z needs to be known. Different absorption corrections [2] may equally straighten X-ray continuum intensities reduced through absorption in the specimen and may equally yield consistent values for emergence angles of 52.5°, 30° and 18°. But in general one obtains different functions of Z. Therefore it is a problem to decide from experimental measurements which kind of absorption correction has to be applied in order to calculate generated intensities in a unique sense.
On the other hand it is doubtful to calculate the generated continuum intensity as a function of Z without knowing the correct mean excitation energy J as function of Z in the Bethe expression for stopping power.
Therefore we propose a new absorption correction considering the energy dependence of the cross-section Q in Philibert's method. It can be shown that experimental data corrected in this kind can be fitted best to computer calculations by variation of $J(Z)$. With this correction one obtains energy independence of J and fairly good agreement with measurements of J by Rauth and Thomas.[3]

References
1 J. Böcker and Th. Hehenkamp, Mikrochim. Acta (Wien), Suppl. 7 (1977)
2 T.S. Rao-Sahib and D.B. Wittry, J.Appl.Phys.(45),11, 5060 (1974)
3 V.E. Cosslett, in: R. Castaing et al., eds., Optique des Rayons X et Microanalyse, Hermann, Paris 1966, p.89

GEOMETRICAL CONSIDERATIONS FOR
ZAF CORRECTIONS IN THE SEM

S. H. Moll and N. Baumgarten - AMR Corp.

W. Donnelly - Microspec Corp.

In the early days of electron microprobe analysis, specimen/ stage/spectrometer geometry for quantitative x-ray chemical analysis was quite simple. The specimen was usually flat and smooth and the construction of the specimen stage was such that the incident electron beam was perpendicular to the specimen surface (the horizontal plane). The x-ray spectrometer, either of the wavelength dispersive or energy dispersive type, examined the x-rays along a path which was at a simple angle to the specimen surface, usually psi, the x-ray takeoff angle or x-ray emergence angle.

Specimen/x-ray spectrometer geometry in the SEM is by no means as simple. Commonly, the specimen is tilted such that the incident electron beam is no longer perpendicular to the specimen surface even if it is flat and smooth. In addition, the x-ray spectrometer, or detector, is generally rotated through some azimuth angle from the tilt direction of the specimen. In essence, the specimen is not tilted directly "toward" the energy dispersive x-ray detector or the analyzing crystal plane of the wavelength dispersive x-ray spectrometer. Finally, the geometry may be complicated by the fact that the specimen surface may not be flat and smooth, but rather rough or faceted, such that the surface tilts and x-ray emergence paths are dictated locally by the specimen surface itself as well as by the specimen stage manipulations.

The ZAF correction factors (1) which now appear amenable to theoretical treatment and practical approximation have been applied and solved by the use of computer programs such as "FRAME" or "MAGIC" which allow the analyst to simply supply the necessary intensity data,

appropriate geometry, and acceleration potential. The result, in terms of the concentration of each of the elements present, is then given by the computer program. The accuracy of these analyses is in many cases better than 10% (relative to the amount present) and often within 2%, thus approaching the statistical precision of the intensity data collection itself. Unfortunately, it now seems that the computer programs, or calculation techniques, have not kept pace with the complex geometries currently utilized in practical SEM configurations.

The correction factors for absorption (A) and fluorescence (F) will be found to be related to the sample orientation by the "takeoff angle", which is the angle between the emergent x-ray beam being collected and the sample surface. The correction factor for the atomic number or backscatter effect (Z) will be related to geometry by the sample surface tilt angle. More directly, the geometry affects the total x-ray path length in the specimen. It should be pointed out that the x-ray path length in the specimen must be determined in the plane described by the incident electron beam and the line taken by the emerging x-rays which are collected by the x-ray spectrometer system. Previous attempts to describe the takeoff angle in complicated geometrical situations may be incorrect for computer application purposes if this angle is not determined in the appropriate plane (2,3,4).

The geometrical condition commonly encountered in the SEM is shown in Fig. 1. In this case, the incident beam is not perpendicular to the tilted sample and the x-ray detector system examines the emerging x-rays along a path which is rotated through an azimuth angle with respect to the tilt direction. If the takeoff angle is determined in the vertical plane described by the incident electron beam and the pertinent emergent x-ray beam path, the absorption path length is given by....

$$D3 = L \cos B \csc (E + B) \tag{3}$$

$$\text{where; } \tan B = \tan M \cos A \tag{4}$$

L, an effective penetration depth, is generally set to unity. A is the azimuth angle, measured in the horizontal plane, of the detector orientation with respect to the stage tilt direction and M is the stage tilt angle. Angle B, the rotated tilt angle, is the angle between the tilted sample surface and the horizontal, <u>measured</u> <u>in the vertical plane</u> determined by the electron beam and the pertinent emergent x-ray path.

The absorption path length may be expressed solely in terms of the angles M, A and E:

$$D3 = \frac{L \cot M}{(\cos A \cos E + \sin E \cot M)} \tag{5}$$

Some programs, such as MAGIC (6), simplify the problem of complex geometries by use of an "effective takeoff angle". Although not properly correcting for the geometrical effect in the backscatter correction (Z), if the total absorption path length is known, then this value is allowed to equal the cosecant of a fictitious angle (T_{eff}) which would yield the same path length as the situation when the sample is not tilted and the electron incidence is perpendicular. In this case....

$$T_{eff} = \csc^{-1} D \tag{6}$$

or in general:

$$T_{eff} = \csc^{-1} (\cos B \csc (E + B)) \tag{7}$$

For older ZAF correction programs, such as early versions of FRAME (5), MAGIC (6), and rewritten versions of FRAME by Russ, the Z or backscatter factor is not corrected for the non-perpendicular incidence. The latest FRAME (7) does correct Z with the electron beam incidence angle (theta in FRAME nomenclature) which is the complement of the stage tilt angle M (8). In the Russ programs for EDAX, the stage tilt is defined as S. The FRAME and Russ programs then go on to use the takeoff angle (psi or T) to determine the x-ray absorption path length

for the A and F factors. In the case of SEM geometry, the Z factor would have to be corrected by the stage tilt but the A and F factors would have to be corrected using the stage tilt (M), elevation angle (E), and azimuth (A). The programs ask for M or (90°-M) and T, and the path length is computed from

$$D = \cos M \csc (E + M) \tag{8}$$

$$\text{or: } D = \cos M \csc T \tag{9}$$

If the operator supplies the stage tilt M or (90°-M) for the electron incidence angle, and (E + B) for T, the Z factor is corrected properly for non-perpendicular incidence, but the absorption path length is determined incorrectly. The program uses cosM or sin (90°-M) instead of functions of B. If the operator supplies B for M and (E + B) for T, then the absorption path length is computed correctly but the Z factor is corrected by the wrong angle (B instead of M). A reconstruction of these programs will be required such that ultimately the operator can input the stage tilt (M), the azimuth angle (A), and the elevation angle (E) for proper analysis of the geometrical terms. Fortunately, when using standards, if the standard is tilted in the same way as the unknown, then the geometrical correction factors for the Z effect appear as simple ratios and cancel out. Therefore, it does not matter <u>for the Z correction</u> what angle is used as long as the angle is the same for standards and unknowns (9).

Summary

The determination of x-ray takeoff angles for SEM geometry where a combination of sample tilt, elevation of the detector above the sample, and a detector azimuth angle combine to complicate the analysis, has been described. Unfortunately, computer programs which have been developed to correct for the ZAF effects do not account for x-ray path geometry in the general SEM situation. These programs should be rewritten such that the Z term is corrected for

sample tilt, but the A and F terms are corrected for sample tilt and detector orientation. At the present time, the user's probable best choice is to input the angle B or $(90^{o}-B)$ when the program asks for the surface or stage tilt angle or incidence angle, and then input the angle $(E + B)$ when the program asks for T (takeoff angle).
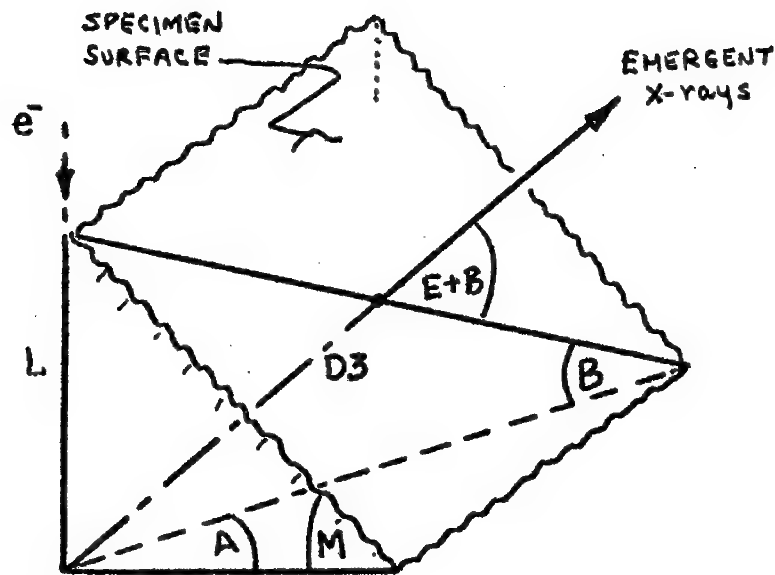
FIG. 1 ABSORPTION PATH LENGTH/NON-PERPENDICULAR BEAM INCIDENCE
X-RAY PATH ROTATED THROUGH AZIMUTH ANGLE WITH RESPECT
TO TILT DIRECTION

(1) Heinrich, K.F.J., "Quantitative Electron Probe Microanalysis", NBS Special Publication 298, October 1968.

(2) Shimizu, Murata, et.al.; "Practicality of Monte Carlo Technique to Quantitative Microanalysis in Inclined Target", Proc. 7th Nat'l. Conf. on Electron Probe Analysis, 1972, Paper 6a.

(3) Russ, J. C., "Microanalysis of Thin Sections, Coatings and Rough Surfaces", IITRI Proc. Scanning Electron Microscopy Symposium, 1973, p. 114-120.

(4) Beaman, D.R., "X-ray Analysis with Energy Dispersive Spectrometers"; Tutorial Session, 8th Nat'l. Conf. on Electron Probe Analysis, 1973, p. 73-85.

(5) Myklebust, R. L., Yakowitz, H., Heinrich, K.F.S., "Performance Evaluation of Frame", Proc. 8th Nat'l. Conf. on Electron Probe Analysis, 1973, paper 26.

(6) Colby, J.W., "Magic IV - A New Improved Version of Magic", Proc. 6th Nat'l. Conf. on Electron Probe Analysis, 1971, Paper 17.

(7) Fiori, C.E., Mykelbust, R.L., Henrich, K.F.S., Yakowitz, H., "Frame B, etc.", Proc. 10th Nat'l. Conf. on Electron Probe Analysis, 1975, Paper 20.

(8) Russ, J.C., "A Simple Correction for Backscattering from Inclined Specimens", Proc. 10th Nat'l. Conf. on Electron Probe Analysis, 1975, Paper 7.

(9) Myklebust, R.L., Private Communication.

USE OF THE ELECTRON BACKSCATTER FACTOR TO NORMALIZE X-RAY MICROANALYSIS

John C. Russ
EDAX Laboratories
Prairie View, IL   60069

Introduction

X-ray analysis is a relative technique; that is, it gives concentrations of an element in one sample relative to another sample, or one element relative to another in a given sample. It is only by referring the measured data to a standard specimen that absolute results are obtained. There are several ways to do this, both direct and indirect. For example, the use of pure element standards for the elements analyzed is a direct method, and the use of calculations to estimate pure element intensity from a standard of complex composition, or of another element is an indirect one. Also, for a given instrument and set of operating conditions the standardization may be preserved over time by using beam current or some measure of beam current such as x-ray yield from a chosen point on the specimen stage.

The method presented here is another indirect method. Its usefulness is primarily in situations where some tradeoff in absolute accuracy can be given to gain speed (by omitting the analysis of standards), and in particular when the sample being analyzed contains an un-analyzeable element such as carbon or oxygen. The intensity ratios for the analyzed elements in the spectrum can be converted to approximate concentration ratios (actually to relative K values) with an expression of the form[1]

$$C_1 : C_2 : C_3 : \ldots = \frac{I_1}{P_1} : \frac{I_2}{P_2} : \frac{I_3}{P_3} : \ldots$$

in which P is the relative pure element intensity and can be taken from graphs, or calculated from

$$P \propto R\,(U-1)^{5/3}\, \omega\ F\,T\,/\,A$$

where R   =   the effective current
U   =   the overvoltage E_o/E_c
ω   =   the fluorescence yield
F   =   the absorption correction
T   =   the spectrometer efficiency
A   =   the atomic weight.

This expression, combined with conventional Z A F correction equations, can be used to compute absolute concentrations provided that we can write one more equation:

$$\Sigma\ C_i = X$$

For a metal alloy, "X" is likely to be $99^{+}\%$, but for minerals, oxides, carbides, etc. there is no way to know "X" since a majority of the SEM's and probes are not equipped to analyze the light elements. This is particularly true for energy-dispersive systems, which is unfortunate since the ease of calculating P is greatly increased by the invariant spectrometer efficiency T of the energy dispersive spectrometer.

Back-scatter factor

In principle, the backscatter factor η (the fraction of the beam current that leaves the sample surface) can provide the other equation. It is commonly written[2]

$$\Sigma \ C_i \eta_i = \eta_{matrix}$$

although a more rigorous expression is[3]

$$\Sigma \ C_i/(1-\eta_i) = 1/(1-\eta_{matrix})$$

For the range of elements to which we have applied this, the difference between these expressions is less than the error of measurement. It could become significant, however, if this method was used to solve cases of peak overlaps such as that of the lead -M, sulfur-K lines.

Measuring the true value of η is quite difficult in most SEM's. The "backscattered electron detector" is placed to collect a small fraction of the electrons, and is usually in a position where the signal is strongly dependent on surface orientation. The use of an annular detector (of interest for electron channeling patterns as well) improves things considerably, but even so, because of the proximity of the polepiece and other hardware it is unlikely that good absolute values can be obtained. We have found the signal to be quite uniform and independent of modest (up to 35° tilt) surface inclinations.

Another method is to measure the specimen current flowing to ground. This would be the difference between the beam current and backscatter current if it were not for secondary electron emission. We found it was impossible to correlate the specimen current values we measured with η when the secondary electron collection voltage of +250 volts was turned on[4]. Turning it to -250 volts eliminated the random variations and gave us reproducible curves which could be correlated with η although there was not absolute agreement. In general, the values measured with the backscatter detector appeared to be better (more accurately measurable, more reproducible) than specimen current.

Figures 1 and 2 summarize the apparent η values obtained from these two approaches. Measurements were made on a number of pure elements, using surface inclinations of 0° (beam perpendicular to the surface), 20°, and 35°. All data presented were measured at 12kV. The variation does not follow the expected relationship

$$\eta \ \alpha \ \exp (1-\cos \ S)$$

but we found the curves could be combined if the data were normalized. As shown in Figure 3 we chose the copper point since it was the heaviest element and also readily measured on the corner of our specimen holder. This makes it possible to

get the apparent η value for any condition by using copper as a reference. The overall reproducibility of these measurements, at varying tilt and beam current, is generally within 2%.

Since the values obtained still are not in agreement with best published values[5], a correlation table was used to convert our measured apparent value to the actual value. Table 1 shows the values used. For the purposes of this study, the table values were used directly.

TABLE 1

Element	η Table	"Apparent" η Spec. current	b.s.e. det.
C	.066	.087± .033	.072± .001
O	.093	.124*	.099*
F	.107	.142*	.113*
Na	.136	.181*	.142*
Mg	.150	.200 ±.003	.156 ±.001
Al	.164	.216 ±.001	.167 ±.002
Si	.176	.228 ±.002	.177 ±.003
S	.201	.247 ±.004	.203 ±.001
Ca	.243	.270*	.244*
Ti	.263	.281 ±.002	.264 ±.001
Fe	.300	.308 ±.002	.301 ±.002
Cu	.325	.325**	.325**

* interpolated
** normalized to Cu

Interpolation of values for unmeasured elements was made using the relationship[6]

$$\eta = a \log Z + b$$

Example of Application

For binary compounds, as has been long realized[7,8], the backscatter coefficient can be used directly to get composition. We measured apparent η values and converted them to absolute η values for three compounds: SiO_2, Fe_2O_3, and Fe_3C.

$$\eta = \quad 0.134 \quad 0.242 \quad 0.286$$

Then the equation,

$$C_1 \eta_1 + (1-C_1) \cdot \eta_2 = \eta_{mtx}$$

can be solved to give concentrations as shown below

	SiO_2		Fe_2O_3		Fe_3C
Si	49.4	Fe	71.9	Fe	94.0
O	50.6	O	28.1	C	6.0

These results were encouraging, so we proceeded to more complex samples as listed in Table 2:

TABLE 2

Concentration of samples used for test

Element Sample	C	O	F	Na	Mg	Al	Si	Ca	Fe	Theoretical η
SiO2		53.3					46.7			.132
Fe2O3		30.1							69.9	.238
Fe3C	6.7								93.3	.284
Cryolite			54.3	32.9		12.9				.124
Spinel		45.0			17.1	37.9				.130
Tremolite		49.3			18.7		21.6	10.3		.137
Cenorthite		39.0				21.9	22.8	16.3		.152
Wollastonite		41.3					24.2	24.5		.165

These compounds can be reduced to psuedo-binaries by calculating the relative concentration of the analyzed heavy elements. As an example, for the tremolite the measured intensities, calculated relative pure element intensities, and calculated relative K values are shown in Table 3. These were used with the measured (and converted) η value of 0.138 to get the total of these three elements =0.4911, which gave K ratios to run in the FRAME Z.A.F. program[9]. The calculation was renormalized after each of the three iterations with the stored η values to get the oxygen.

The equation used is simply

$$C_{oxy}\, \eta_{oxy} \;+\; (1-C_{oxy}) \cdot \eta_{eff} \;=\; \eta_{mtx}$$

$$\eta_{eff} \;=\; \Sigma\, C_j\, \eta_j \quad \text{for the analyzed elements.}$$

The result is in excellent agreement with actual values from stoichiometry.

TABLE 3

Element	I	P	K_{rel}	K_{norm}	C_{calc} iter 1	2	3	C_{actual}
Ca	67395	1.282	0.5443	0.1132	.1241	.1040	.1033	10.3
Si	153392	1.5339	1.0000	0.2079	.2608	.2226	.2172	21.6
Mg	60601	.7412	0.8176	0.1700	.2185	.1866	.1820	18.7
					.3966	.4868	.4975	49.3

The results for the other minerals are listed in Table 4. The overall accuracy is good, especially considering the 5% error anticipated in the η values. The results are not as good as can be obtained for these samples by specifying the oxide stoichiometry, but that is just another way to supply the missing $\Sigma\, C_j$ = "x" equation drawing on the operator's judgment, and will not work if the wrong stoichiometry is input.

TABLE 4

Element sample	O	Calculated concentration results						Measured η
		F	Na	Mg	Al	Si	Ca	
cryolite		51.0	36.6		12.4			.125
spinel	41.5			18.0	40.4			.132
amorthite	36.9				22.7	23.6	16.9	.154
wollastonite	38.8					25.2	36.0	.169

The mean (rms) error of these values is about 5% relative, which we consider useful for some applications, considering the involvement of unanalyzed light elements and the fact that no standards were analyzed.

It is worth noting that this same principle can be applied in another way if at least one analytical standard is used. In that case, the heavy elements can be calculated exactly and the η value used to determine whether the unanalyzed portion of the sample is, for example, carbon, oxygen, or both.

Applying the method to any SEM equipped with a suitable backscatter detector or a specimen current meter requires some initial calibration, in return for which the user has one more possible approach to analysis when it is needed.

Figure 1

Backscatter fraction determined from specimen current
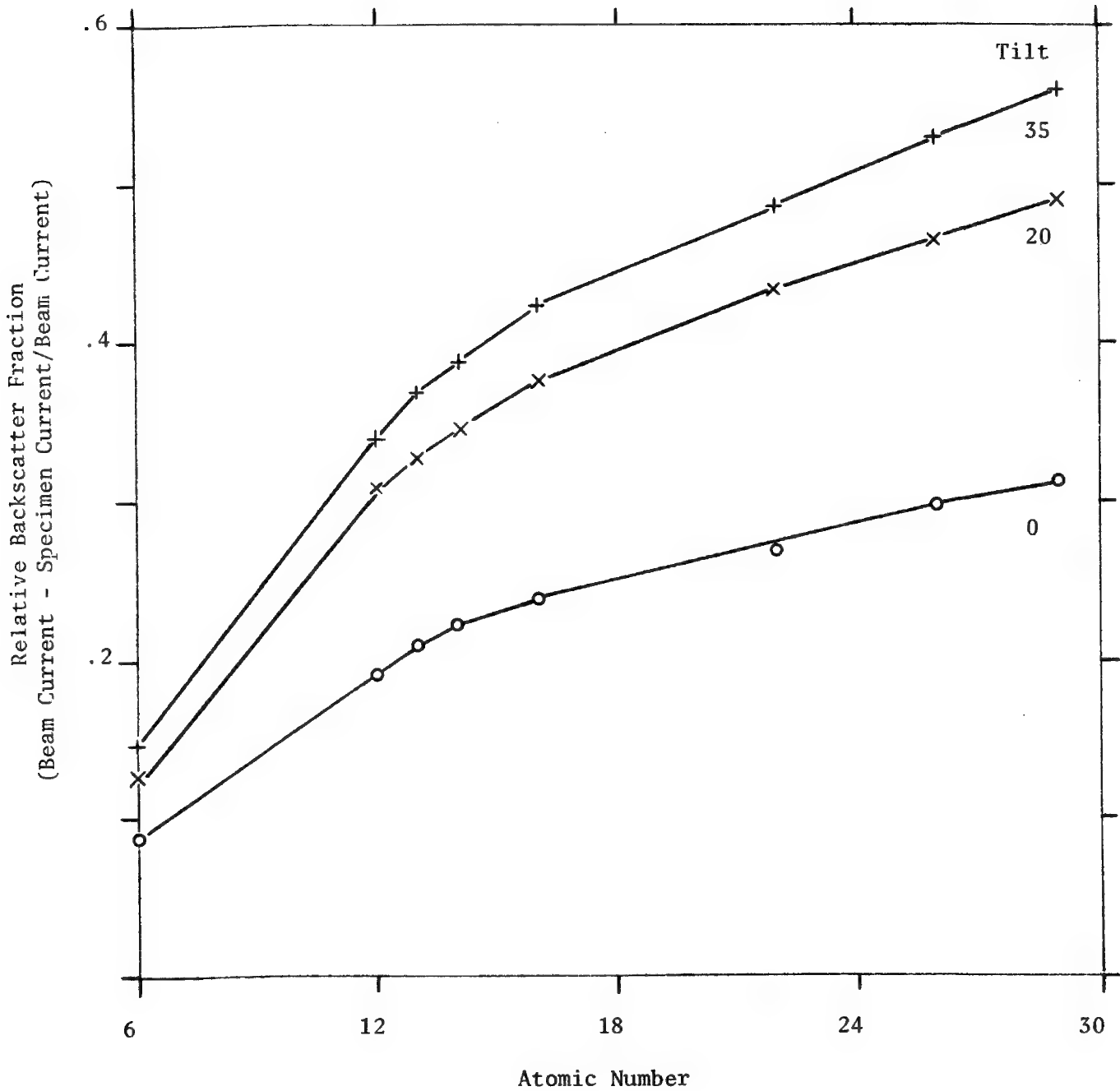
Figure 2

Backscatter fraction determined from detector voltage
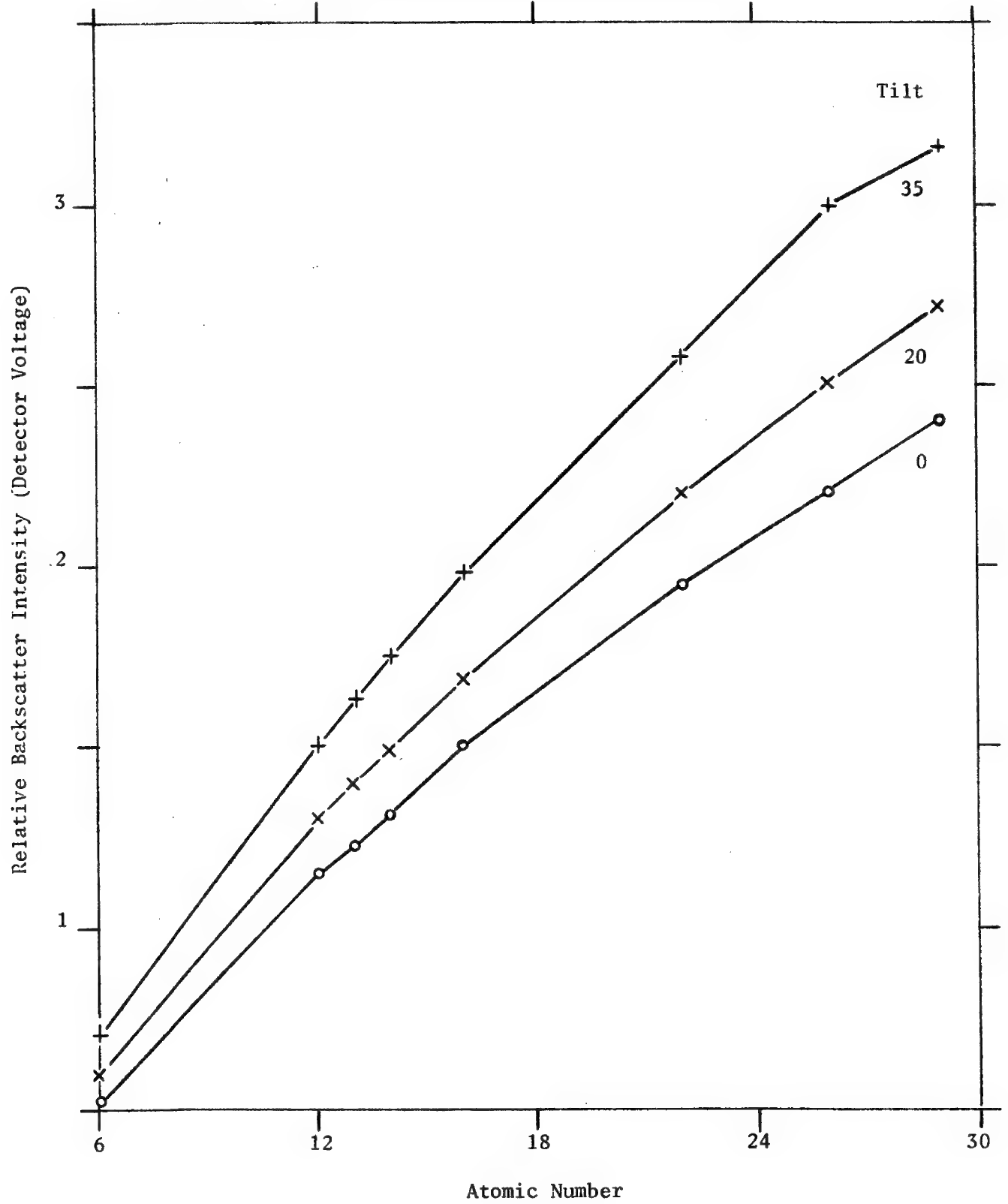
Figure 3
Normalized backscatter curves (nominal values)
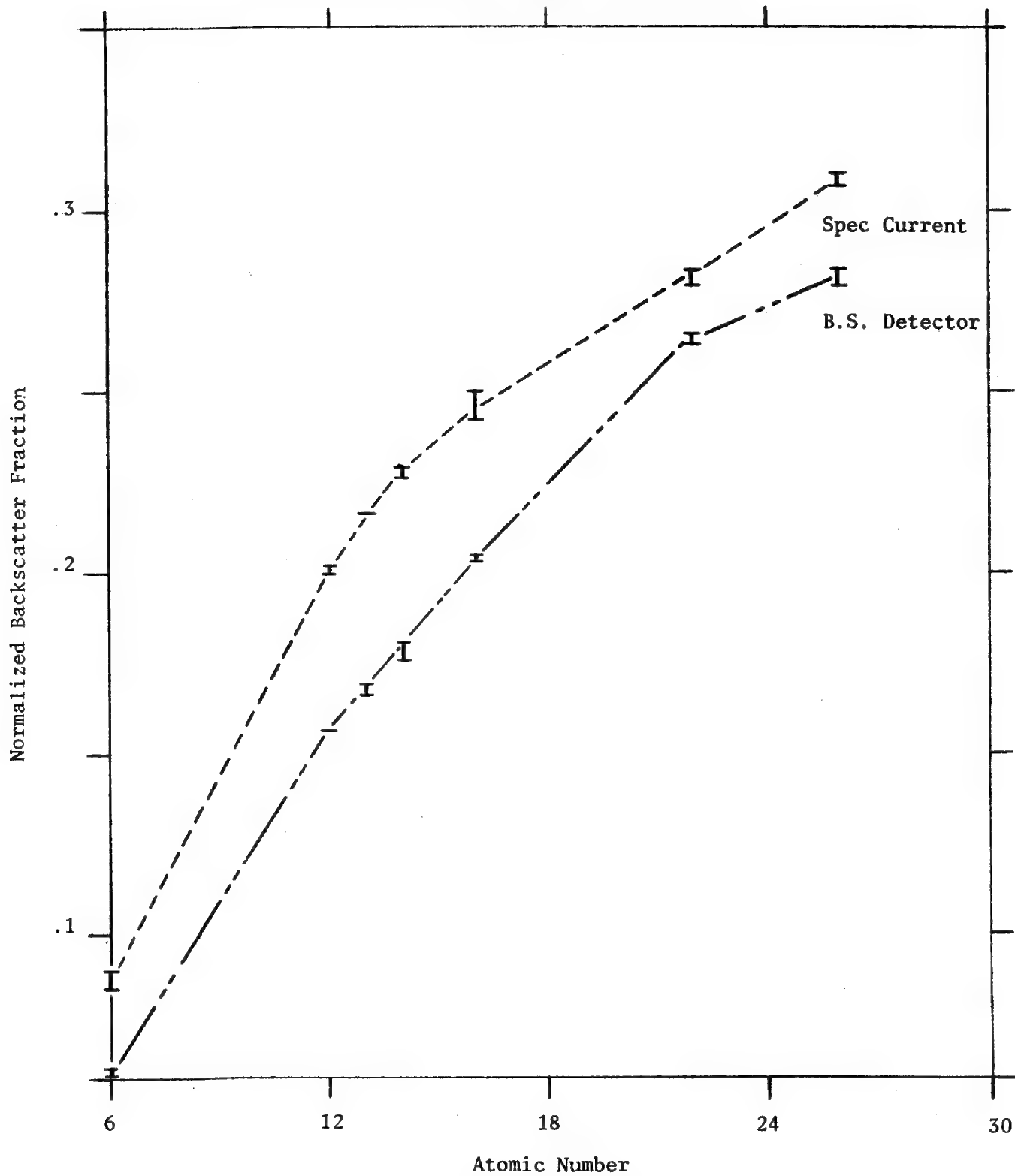
References

1) J. Russ, Quantitative Microanalysis with Minimum Pure Element Standards, in 9th Annual Proc. Electron Probe Analysis Society, Ottawa, Canada, 1974, p.22A-C.

2) R. Castaing, Electron Probe Microanalysis in Advances in Electronics and Electron Physics, Vol. 13, p.317-386, Academic Press, New York, 1960.

3) D. Wittry, An Electron Probe for Local Analysis by Means of X-ray, Ph.D. Thesis, Calif. Inst. of Tech. (1957).

4) H. E. Bishop, in Optique des Rayons X et Microanalyse (R. Castaing ed), Herrmann, Paris, 1966, p.153.

5) S.J.B. Reed, Electron Microprobe Analysis, p.220-227, Cambridge Univ. Press, 1975.

6) S. G. Tomlin, Proc. Phys. Soc., Vol. 82, 1963, p.465.

7) D. M. Poole, P. M. Thomas, in X-Ray Optics and X-Ray Microanalysis (H. Pattee ed), p.411, Academic Press, New York 1963.

8) R. E. Ogilvie, Quantitative Electron Microprobe Analysis, in X-Ray and Electron Methods of Analysis, p.55-75, Plenum Press, New York, 1968.

9) M. Yakowitz et al, FRAME, an On-Line Correction Procedure for Quantitative Electron Probe Microanalysis, National Bureau of Standards Technical Note 796, 1973.

SOME EXAMPLES OF QUANTITATIVE ANALYSIS OF VERY LIGHT ELEMENTS (Z < 9)

by J. RUSTE

Materials Research Center of the
"Ecole des Mines" of Paris

EVRY-FRANCE

The basic principles of a previously reported ZAF correction method for the quantitative analysis of very light elements [1] [2] are discussed. In particular, for the absorption correction, the complete function $f(\chi)$ of Philibert is used, with Reuter's superficial ionisation $\varphi(o)$ [3]. The absorption coefficients are the Henke's ones [4] (Table I) but with some modifications for several elements [2] (Table I).

	μ/ρ CK g/cm^2	μ/ρ (Henke)
22 Ti	8093	8094
23V	9089	8840
24Cr	10152	10590
25Mn	11290	11470
26Fe	12500	13300
27Co	13790	14730
28Ni	15157	17270
41Nb	24203	33990*
42Mo	15500	32410*
72Hf	18500	18030
73Ta	20000	18390
74W	21500	18750

* Values extrapolated near absorption edges

Table I - Some differences between our absorption coefficients and Henke's ones for carbone K.

New developments of this model are described. In particular, for atomic number corrections a new formula for mean ionisation energy is used [2].

$$J = 9.29 Z \left(1 + 1.287 Z^{-2/3} \right)$$

For Z $>$ 13, this expression is close to Berger-Seltzer's and very near experimental values for Z $<$ 13.

For the f(χ) function, a sigma parameter, with an atomic number variation has been obtained. This model can be considered as a link between the classical Heinrich's model and our own model for low atomic number (5) :

$$\sigma = \frac{\sigma_o \; 10^5}{E_o^m - E_j^m}$$

$$\begin{cases} \sigma_o = 4.5 + 8.95 \; \exp\left(-Z^{2.5}/500\right) \\ m = 1.65 + 1.08 \; \exp\left(-Z^2/100\right) \end{cases}$$

For h, an expression which depends on energy is used

$$h = 4.6 \cdot 10^{-6} \; \sigma_L \; E_o^{1.5} \; \sum_j C_j A_j / Z_j^2$$

where $\qquad \sigma_L = \sigma_o \, 10^5 / E_o^m$

Two examples of the application of this method are given. In each case, a Cameca micropobe "Camebax", with a take off angle of 40° was used, the high tension was 10kV and the probe current intensity about 100nA.

The study of a great number of boron-carbide specimens, with a large range of composition, has allowed the precise determination of the phase limits of the boron-carbon diagram; microanalysis have been completed with several other analysis methods(6).

The second example is the study of diffusion couples $Al_2O_3-N_4Si_3$ and more specifically, the compositions of the different phases of the $N_4Si_3-SiO_2$ diagram. The precise compositions of several crystalline phases have been determined, and several unknown amorphous phases have been detected (7).

In these two examples, the precise information could not have been obtained without the techniques for quantitative analysis of very light elements.

REFERENCES

1. J. RUSTE, M. GANTOIS, J. of Phys. D, 8, 872, 1975.
2. J. RUSTE, Thesis (Nancy) 1976.
3. W. REUTER, Proceedings fo the VIth International Conference on Xray optics and microanalysis - Osaka 1971. University of Tokyo Press, 121, 1972.
4. B.L. HENKE, E.S. EBISU, Advances in Xray analysis 17, 150, 1974.
5. J. RUSTE, C. ZELLER, Comptes Rendus à l'Academie des Sciences de Paris - presented the 25th of April 1977 - to be published (June 1977).
6. M. BOUCHACOURT, F. THEVENOT, J. RUSTE, 3 papers submitted to publication at the Journal of Less Common Metal.
7. J.P. TORRE, J. RUSTE, A. MOCELLIN, Submitted to publication at the American Ceramic Society.

ELECTRON PROBE INVESTIGATION METHODIC OF STRUCTURAL DEFECTS IN SEMICONDUCTOR MATERIALS

Sh. Kh. Igamberdiyev

Institute of Electronics, Uzbek Academy of Sciences,
Tashkent, USSR

An inderect method of structure defects discovery is suggested by the author. These defects are linear dislocation and gradients of doping elements concentration in monocrystal semiconductor materials such as Si, GaAs, GaP, and heterostructures on their base, decorated by such impurities as B, P, S, Sb, Te by using electron probe microanalysis.

It is known that nonuniform impurity distribution and doping (trace) elements concentration (C) rising is known to take place in dislocations. In the earlier work (1) Te was suggested to accumulate on the dislocations and to enter a solid solution irregulary. In contradiction to work (2), where microinsertion parts were investigated, in present work dislocation regions decorated by doping elements with the atomic concentration of 10^{15}-10^{20} at. cm.$^{-3}$ are investigated. The presence of B, P, S, Sb, Te was determined in these samples. Their concentrations correspond to sensitivity limit of electron probe microanalysis.

To exclude different secondary phenomena connected with impurities and defects influence the investigations were carried out both on absolutely dislocation-free high-resistance silicon with residual impurity concentration of 10^{12} at. cm.$^{-3}$, and as well as epitaxial silicon films 10 μ thick, ρ -1-2·10^3 ohm. cm. grown on dislocation-free silicon substrates (111). The B concentration of films surface is 2,0·10^{20} at. cm.$^{-3}$ and that of antimony and phosporus in epitaxials silicon films is 2·10^{16} at. cm.$^{-3}$. The Te concentration in GaAs sample is 3·10^{17} at. cm.$^{-3}$ and that of S in GaP (111) sample is 6·10^{16}-3·10^{17} at. cm.$^{-3}$. When obtaining GaAs$_{1-x}$P$_x$ and Ga$_{1-x}$AsAl$_x$ heterostructures on GaAs substrates by orientation (111) and (100), GaAs added to melt is doped by Te and GaP is doped by S with the above mentioned atom concentrations.

Technique of Experiment

To analyse small concentration of impurities (traces of

elements) the areas near dislocations were scanned in spectral region of the element to be determined. It is known that characteristic X-ray radiation is superimposed by solid spectrum radiation caused by electrons retardation in a sample (background radiation) that determines essentially the background level at spectral curves. The spectrum region for the given element was treated with the help of Furier-analysis according to PEAK programme, made on FORTRAN for Computers BESM-6 and ES and noises superimposed on the element spectral line were distinguished (weak signal at $C \rightarrow O$). Noises are divided into two types, i.e. noise caused by statistic fluctuations that exists when the number of definite quanta is small and noises of electron circuit.

Spectral curve, obtained at microanalysis MS-46 "Cameca" was decomposed in Furier series, that served as a filter, allowing to eliminate "the upper part of the spectrum". At Furier series expansion only those harmonics which contain not more periods than M in initial function task interval are represented in the spectrum and the ratio is selected between basic frequency and background interference frequency.

The method realization consists of some subprograms. The FORIT subprogram calculates the indicated number of (M) coefficients in Furier series approximating the initial tabulated function given on the section $[0,2\pi]$ in $2N+1$ points with $2\pi/(2N+1)$ step determined at the discrete set of points. The FORIF subprogram calculates the coefficients of Furier series, approximating the initial function, the value of which is calculated by means of subprogram-function on the section $[0,2\pi]$ in $2N+1$ points with the same step. According to the values of Furier series expansion coefficients the intensity of characteristic and continuous spectrum is defined and a smoothed curve is plotted, using the PEAK program for this purpose. (FORIT and FORIF programs are borrowed from the scientific subprograms of IBM firm 1976, (3)).

The examples of the application of Furier series expansion, as a filter are illustrated in Fig.1-3, where the initial function (experimental curve) is shown in the upper figure and the calculated one (lower curve) obtained at Furier series expansion. M is a number of harmonics taking part in the expansion.

Using "filtration method" and comparing the value of absolute intensity of "filtered" spectrum according to 3σ criterion, it is possible to reveal the main peak, correspondent to the presence of characteristic X-ray radiation of impurity element. Such method of experimental data analysis enabled to increase the sensitivity limit by one order or more without the large statistics accumulation of time measuring. Usually 3σ criterion of reading sorting of $N_p > N_b + 3\sqrt{N_b}$ impulses quantity, where N_p - X-ray intensity from the sample in line maximum, N_b - background intensity, is applied in the process of measurements (4).

The existence and the distribution of trace elements (Fig. 1-3,c,d) are determined both from the concentration curves, obtained by electron probe scanning along the sample profile in the region of linear dislocations applying the "filtration method". Doping (trace) elements concentration increase corresponds to the parts with structural defects of the dislocation type and stacking faults.

Impurities segregations on the dislocations change the field of atoms displacement around the dislocations in a certain way, as a result, the character of electronic microscope contrast from the dislocation is to be changed. The existence of dislocation decorated by impurity elements as well as structural defects are confirmed by electronmicrographs of the samples (Fig.4).

References

1. Azimov S.A., Bustanov Kh.Kh., Igamberdiyev Sh.Kh., Mirzabaev M. and Tursunov M.N. (1976), "Investigation of components $GaAs_{1-x}P_x$ epitaxial layers by electron probe microanalysis", Izvestiya (News) Publishing House Uzb. Acad. of Sci., series of phys.-math.sci., no.2, 55-58.

2. Ditsman S.A., Kupriyanova T.A. and Seleznova M.A. (1975), "Studying the composition of inclusions into single crystals of germanium and silicon", Izvestiya (News) Publishing House USSR Acad. of Sci., Inorganic materials, vol.11, no.3, 537-538.

3. IBM (360) SYSTEM/360, Scientific Subroutine Package (360-CM-03X), version 11, Programmer's Manual.

4. Electron Probe Microanalysis, (1974). The translation from English is ed., by I.B.Borowski, Mir (Peace) Publi.House,M.,41p.
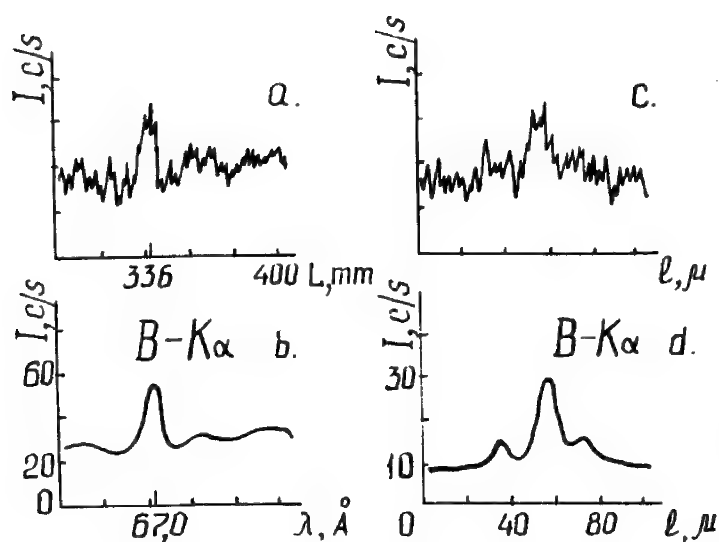
Fig.1. Detection of trace element B.
a) this chart shows a B-Kα peak profile of doping epitaxial silicon films containing 0,14% boron. The abscissa denoted the analyzing crystal ODPb position and the ordinate the X-ray intensity. The X-ray intensites, measured by continuous scan of the spectrometer, were plotted.

b) this chart shows a B-Kα peak profile after Furier-analysis application, M=25. The X-ray intensites, were plotted after smoothing. c) this chart shows a boron distribution in epitaxial monocrystal silicon films. d) this chart gives the same curve after Furier-analysis application, M=20. Peak on the curve correspond to the regions with structural defects.
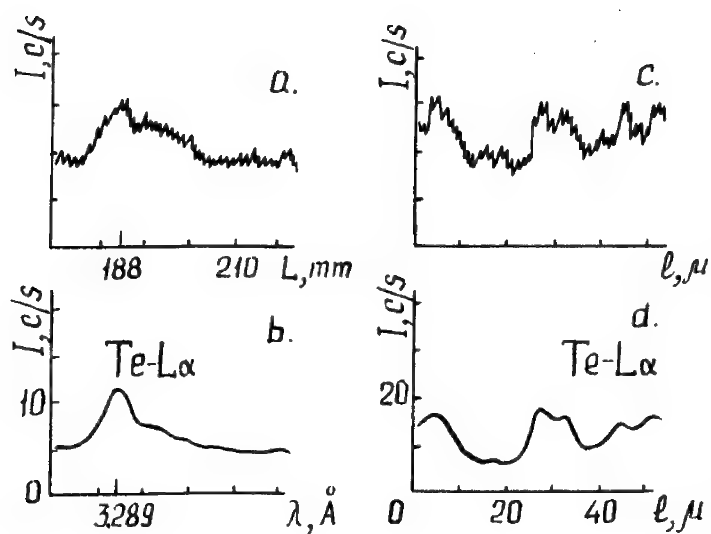
Fig.2. Detection of trace element Te.
a) this chart shows a Te-Lα peak profile of monocrystal GaAs sample containing 0,003% Te. The abscissa denoted the analyzing crystal PET position and the ordinate the X-ray intensity.

b) this chart shows a Te-Lα peak profile after Furier-analysis application, M=10.

c) this chart shows a Te distribution in monocrystal GaAs.
d) this chart gives the same curve after Furier-analysis appli-

cation, M=30. Peak on the curve correspond to the regions with structural defects.
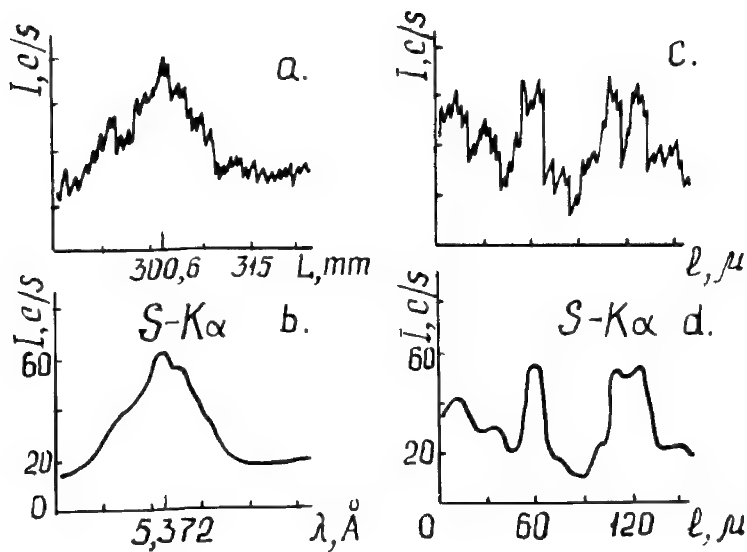
Fig.3. Detection of trace element S.
a) this chart shows a S-Kα peak profile of monocrystal GaP sample containing 0,001% S. The abscissa denoted the analyzing crystal PET position and the ordinate the X-ray intensity.
b) this chart shows a S-Kα peak profile after Furier-analysis application, M=20. c) this chart shows a S distribution in monocrystal GaP. d) this chart gives the same curve after Furier-analysis application, M=50. Peaks on the curve correspond to the regions with structural defects.
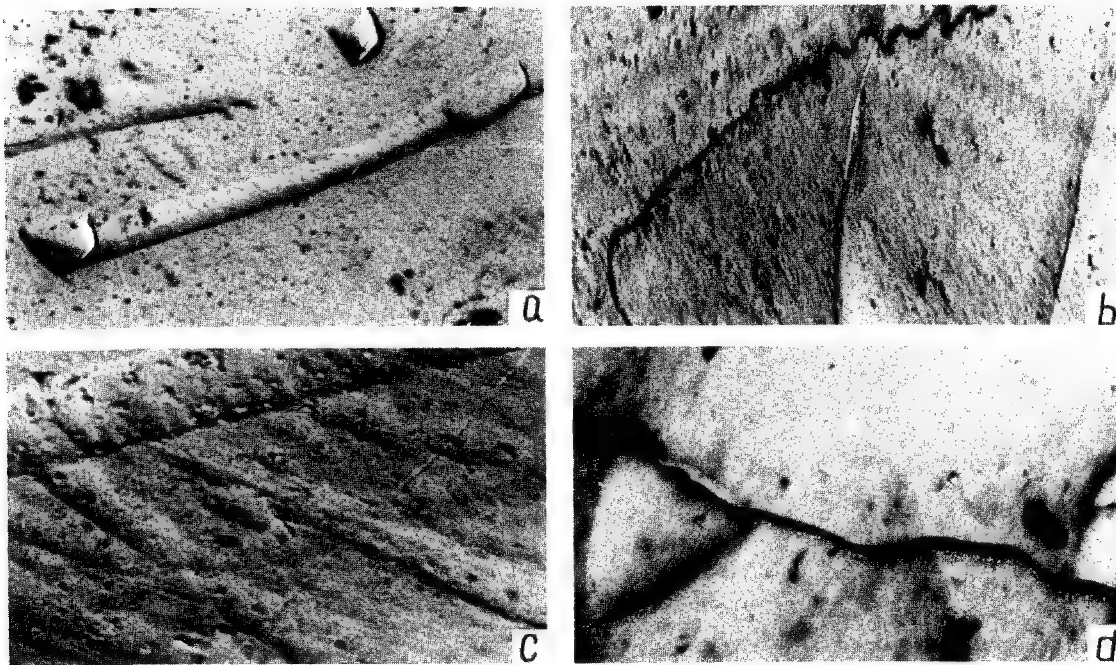
Fig.4. Electronmicrographs of dislocations and stacking faults in epitaxials silicon layers by boron doping.
a),b),c) - film surface,
d) - metallurgical boundary.

REVIEW OF THE EMPIRICAL METHODS

USED IN ELECTRON MICROANALYSIS

by

Robert E. Ogilvie
Department of Materials Science and Engineering
Massachusetts Institute of Technology
Cambridge, Massachusetts 02139

Introduction

In making a quantitative analysis of an unknown specimen with the electron microanalyzer, one measures the intensity of a particular characteristic X-ray line emitted from the unknown sample and compares this intensity with that emitted from a reference standard under the same conditions. The reference standard can be a pure element, known alloy, or a complex compound. The intensities, of course, must be corrected for background and dead-time. The normalized intensities, that is, the intensity of the unknown divided by the intensity of the standard, must be corrected for the effects of the matrix on the observed X-ray intensities. This requires calculating the appropriate factors for the absorption, fluorescence, and atomic number effects employing well established equations. In our laboratory we use the MAGIC IV program by Colby [1] for reducing the data. However, there are many such programs that give equally good results, and there are many cases where MAGIC IV or any of the other programs do not give satisfactory results, in particular, cases where $f(x) < 0.7$ and many of the mineral systems. Therefore, many approaches have been developed employing empirical equations to determine the analysis of the specimen.

Empirical Equations

The basis of several of the empirical equations comes from the second approximation of Castaing [2]; namely,

$$K_A' = \frac{\alpha_A C_A}{\sum_i \alpha_i C_i} \tag{1}$$

where K' is the ratio of the <u>generated</u> X-rays from the unknown and the pure standard and α_i is an empirical coefficient to take into account atomic number effects.

Ziebold and Ogilvie (3) put Equation 1 into another form. For the binary case we have:

$$\frac{1-K_A}{K_A} = a_{AB} \frac{1-C_A}{C_A} \tag{2}$$

where K_A is defined as the <u>measured</u> relative X-ray intensity and $a_{AB} = \alpha_B/\alpha_A$. It should be pointed out that Equation 2 cannot be justified on theoretical grounds. However, many binary systems were observed to give a linear plot when C/K was plotted against C. Such a plot follows from Equation 2, that is:

$$(C/K)_A = a_{AB} + (1-a_{AB})C_A \tag{3}$$

It was suggested by Ziebold and Ogilvie (3) that Equation 2 could be extended to multicomponent systems by using the following:

$$\frac{1-K_A}{K_A} = \bar{a}_{AB..i} \frac{1-C_A}{C_A} \tag{4}$$

where

$$\bar{a}_{AB..i} = \frac{a_{AB}C_B + a_{AC}C_C + \ldots a_{Ai}C_i}{C_B + C_C + \ldots C_i} \tag{5}$$

It was initially intended to determine the binary coefficients a_{Ai} from well established standards. However, an analytical equation was evaluated to calculate the coefficients. Also using reverse MAGIC IV we can determine K's from which the coefficient can be determined. This latter point seems foolish and indeed it is. If you have MAGIC IV available, then use it to reduce your data.

It was first suggested by Ogilvie and Pinella (4) that for the case of mineral systems it was not necessary to employ pure elemental standards but to use compounds that make up the end-members of the system of interest.

This was employed in the ternary, $MgO-FeO-SiO_2$. It was also shown that the a_{Ai} coefficients for a pseudo-binary can be calculated from the binaries that make up a ternary system. For example, for the ternary A-B-C which has a pseudo-binary $AB-BC_2$ it can be shown that

$$\frac{1-K_A^{ABC}}{K_A^{ABC}} = a_{AB-BC_2} \frac{1-C_A^{ABC}}{C_A^{ABC}} \qquad (6)$$

and from a mass balance

$$a_{AB-BC_2} = \frac{a_{AC}C_C^{BC2} + a_{AB}C_B^{BC2}}{C_A^{AB} + a_{AB}C_B^{AB}} \qquad (7)$$

It should be pointed out that A, B, and C need not be pure elements but they can be compounds.

Lachance and Trail (5) put Equation 3 in the following form:

$$C_A = K_A(1 + \alpha_{AB}C_B) \qquad (8)$$

where $\alpha_{AB} = a_{AB} - 1$. This form will give the same results as Equation 3. It was then suggested by Claisse and Quintin (6) that a second order term be added to Equation 8 to take care of strong fluorescence effects:

$$C_A = K_A(1 + \alpha_{AB}C_B + \alpha_{ABB}C_B^2) \qquad (9)$$

The solution for C_A from Equation 4 or equally well for Equation 6 we have

$$C_A = \frac{\bar{a}_{Ai}K_A}{K_A(\bar{a}_{Ai}-1) + 1} \qquad (10)$$

and

$$\bar{a}_{Ai} = \frac{a_{AB}C_B + a_{AC}C_C + \ldots a_{Ai}C_i}{C_B + C_C + \ldots C_i} \qquad (11)$$

Bence and Albee (7) combined Equations 10 and 11, which gives the following:

$$C_A = (\frac{C_A + a_{AB}C_B + a_{AC}C_C + \ldots a_{Ai}C_i}{C_A + C_B + C_C + \ldots C_i}) \, K_A \qquad (12)$$

The term in the brackets is referred to as the $\beta_A^{AB\ldots i}$ correction factor.

Laquitton, Rousseau, and Claisse (8) have evaluated the following equations for several ternary systems:

$$C_A = K_A(1 + \alpha_{AB}C_B + \alpha_{AC}C_C) \qquad (13)$$

$$C_A = K_A(1 + \alpha_{AB}C_B + \alpha_{ABB}C_B^2 + \alpha_{AC}C_C + \alpha_{ACC}C_C^2) \qquad (14)$$

$$C_A = K_A(1 + \alpha_{AB}C_B + \alpha_{ABB}C_B^2 + \alpha_{AC}C_C + \alpha_{ACC}C_C^2 + \alpha_{ABC}C_B C_C) \quad (15)$$

There are several other empirical equations. However, they are very similar to those presented. Therefore, they will not be presented here.

Evaluation of the Empirical Equations

Several five-component systems were evaluated with the equation described above. The factors considered were the number of coefficients needed to evaluate the problem and the ease of programing on a H.P. 67 calculator and the number of iterations necessary to converge to the correct value.

It was found that Equations 10 and 11 gave identical results with Equation 12, which of course they should. They also converged in four iterations (no change in the fourth significant figure). The form of Equation 12 is easier to program than the other equations. Equations of the form of 13, 14, and 15 did not converge to acceptable values in six iterations. The reason, of course, is that Equations 11 and 12 have a normalizing factor in their denominator, the terms that control the values of C_i.

The above equations for the five-component systems were programed on a H.P. 67. This program for Equations 10, 11, and 12 is available on request.

Conclusions

From the evaluation of the data it can be shown that Equation 12 gives the desired results with the minimum expense of time. However, it is suggested that one should employ Equation 7 for evaluating the more complex mineral

systems. It is also suggested that well established standards be evaluated to obtain the desired coefficients rather than calculating them from ZAF procedures.

References

1. Colby, J., Advances in X-ray Analysis 11, 287-305 (1968).

2. Castaing, R., "Application of Electron Probes to Local Chemical and Crystallographic Analysis," Ph.D. Thesis, University of Paris, 1951.

3. Ziebold, T. O., and Ogilvie, R. E., Anal. Chemistry 36, 322-327 (1964).

4. Ogilvie, R. E. and Pinella, A., Proceedings of the First National Conf. on Electron Probe Microanalysis, p. 33 (1966).

5. Lachance, G. R. and Trail, R. J., Canadian Spectroscopy 11, 43-48 (1966).

6. Claisse, F. and Quintin, M., Canadian Spectroscopy 12, 129 (1967).

7. Bence, A. E. and Albee, J., Geol. 76, 382-403 (1968).

8. Laquillon, D., Rousseau, R., and Claisse, F., Anal. Chemistry 47 2174 (1975).

Non-Linearities of Electron Microprobe Matrix Corrections in the System

$MgO-Al_2O_3-SiO_2$
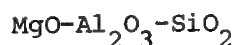
A. E. Bence and W. Holzwarth

Department of Earth and Space Sciences

State University of New York

Stony Brook, New York   11794

The application of alpha coefficients to quantitative electron probe analysis assumes a linear relationship between the concentration of each element and the magnitude of the matrix correction for each radiation intensity in the system. Ziebold and Ogilvie (1964) have shown by empirical methods that for simple binary systems where fluorescence is not severe, the linear relationship between relative concentration (c_{AB}^A) and relative intensity (K_{AB}^A) for an element A in the binary system AB is: $c_{AB}^A/K_{AB}^A = \alpha_{AB}^A + (1 - \alpha_{AB}^A)c_{AB}^A$. The empirical correction α_{AB}^A is equal to c_{AB}^A/K_{AB}^A when c_{AB}^A approaches zero. It is a readily determinable parameter in a binary system where numerous standards of intermediate composition are available. Alternatively, it may be calculated from programs that treat absorption, fluorescence, and atomic number effects separately. The alpha coefficient is, in effect, the sum of the matrix effects.

Ziebold and Ogilvie (1964) suggested that extrapolation to poly-component systems could be achieved by using the compositionally weighted binary alpha coefficients. For these multicomponent systems, linear simultaneous equations are generated. These can be solved by matrix inversion or iteration.

The technique was applied to silicate analysis by Lachance and Trail (1966) and Bence and Albee (1968). In the latter case, alpha coefficients, as functions of oxide concentrations, were developed in part by empirical techniques and in part through calculation. Subsequently, Albee and Ray (1970) calculated alpha coefficient matrices from MAGIC IV for a variety of operating conditions suitable for applications to instruments having different take-off angles.

The approximation has worked well for many mineralogical systems and it has been employed in numerous mineralogical laboratories around the world. However, with the refinements in instrumentation, including the

introduction of computer-controlled data collection and on-line reduction, and the increased need for precise crystal-chemical data that have occurred over the past few years some disturbing biases have been noted for some mineralogical systems. Serious biases are noted for minerals in the system $MgO-Al_2O_3-SiO_2$ where high totals and significant deviations from stoichiometry are commonplace. These deviations are frequently observed in olivines (Mg_2SiO_4), spinels ($MgAl_2O_4$), and pyropic garnet ($Mg_3Al_2Si_3O_{12}$). In the case of forsteritic olivine, high totals are accompanied by deficiencies of Si in the tetrahedral site and excesses of Mg in the octahedral site. These biases are consistent with the overcorrection of MgK_α radiation for SiO_2 matrix effects.

The Bence-Albee alpha coefficients for the $MgO-SiO_2$ system were determined by the replicate analysis of synthetic MgO and SiO_2 crystals and glasses of Mg_2SiO_4 and $MgSiO_3$ compositions. A least-squares calculation was used to determine the respective alpha coefficients. Systematic biases now apparent suggest that the relationships between concentration and correction factor, especially that for MgK_α radiation, are not linear.

To document these non-linearities as well as non-linearities in the system $MgO-Al_2O_3$, synthetic single crystals of Mg_2SiO_4, $MgSiO_3$, $MgAl_2O_4$, and non-stoichiometric spinel ($Mg_{0.69}Al_{2.31}O_4$) were obtained and analyzed on an ARL electron probe operating at 15 kv over a period of several months. Pure single crystals of the end-member oxides were used as standards. Results of this study are shown in Figs. 1(a) and 1 (b).

In the four cases considered, the variations of C/K with C are not linear but can be expressed in terms of second order polynomials (Table 1).

Matrix coefficients have also been calculated for the system $MgO-Al_2O_3-SiO_2$ from MAGIC IV. These coefficients are contoured in Figs. 2(a), (b), (c) and are plotted on the $MgO-SiO_2$ and $MgO-Al_2O_3$ binaries (Fig. 1 (a) and 1 (b)). Significant deviations are observed between the calculated values and those obtained by empirical methods. These differences, as well as the deviations of the fitted curves from the least-squares fits, are consistent with the biases noted when the calculated or least squares fits are used in data reduction.

In recognition of possible non-linearities, Albee and Ray (1970) suggest that alpha coefficients determined from midpoint extrapolations of

binary curves, more closely approximate the corrections in most mineralogical systems. The results of this study suggest that for some systems, this approach may not be sufficient and some form of curve fitting is necessary.

To this end, programs have been developed which determine alpha coefficients from the polynomial expression that best fits the empirical data. Equations obtained for the empirical data in the $MgO-SiO_2$ and $MgO-Al_2O_3$ systems are given in Table 1. In an analysis the measured parameter K is used as a first approximation of concentration to determine the projected position on the curve of each binary system. An alpha parameter, determined by extrapolation through this point, is used in data reduction. Iterative procedures are used to refine the alpha coefficients.

Table 1

$MgO-SiO_2$

$$C/K^{Mg} = 1 - 0.0182\chi + 0.1778\chi^2$$

$$C/K^{Si} = 1 + 0.3672\chi - 0.0926\chi^2$$

$MgO-Al_2O_3$

$$C/K^{Mg} = 1 + 0.0152\chi + 0.0174\chi^2$$

$$C/K^{Al} = 1 + 0.4639\chi + 0.3435\chi^2$$

References

Albee, A. L. and L. Ray, Correction factors for electron probe micro-analysis of silicates, oxides, carbonates, phosphates, and sulfates, Anal. Chem., 42, 1408-1414, 1970.

Bence, A. E. and A. L. Albee, Empirical correction factors for the electron microanalysis of silicates and oxides, J. Geol., 76, 382-403, 1968.

Traill, R. J. and G. R. LaChance, A practical solution to the matrix problem in x-ray analysis. II. Application to a multi-component alloy system, Canadian Spectr., 11, 63-71, 1966.

Ziebold, T. O. and R. E. Ogilvie, An empirical method for electron micro-analysis, Anal. Chem., 36, 322-327, 1964.
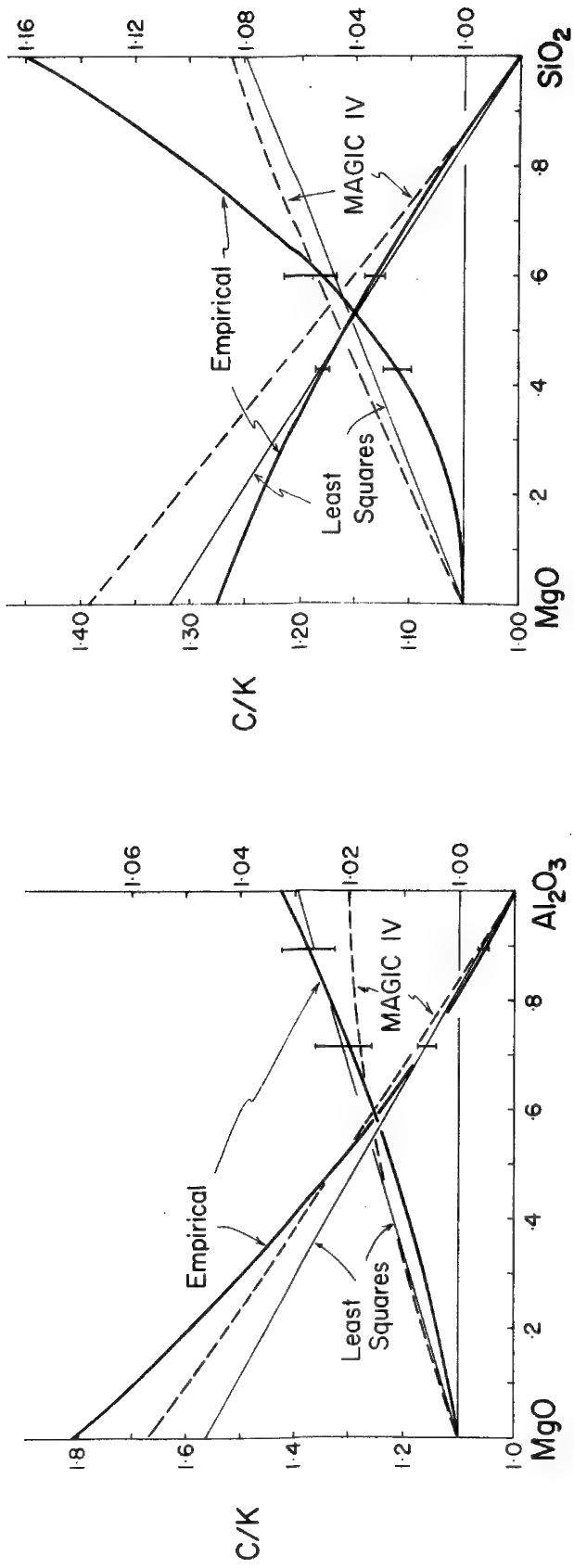
Fig. 1a

Fig. 1b
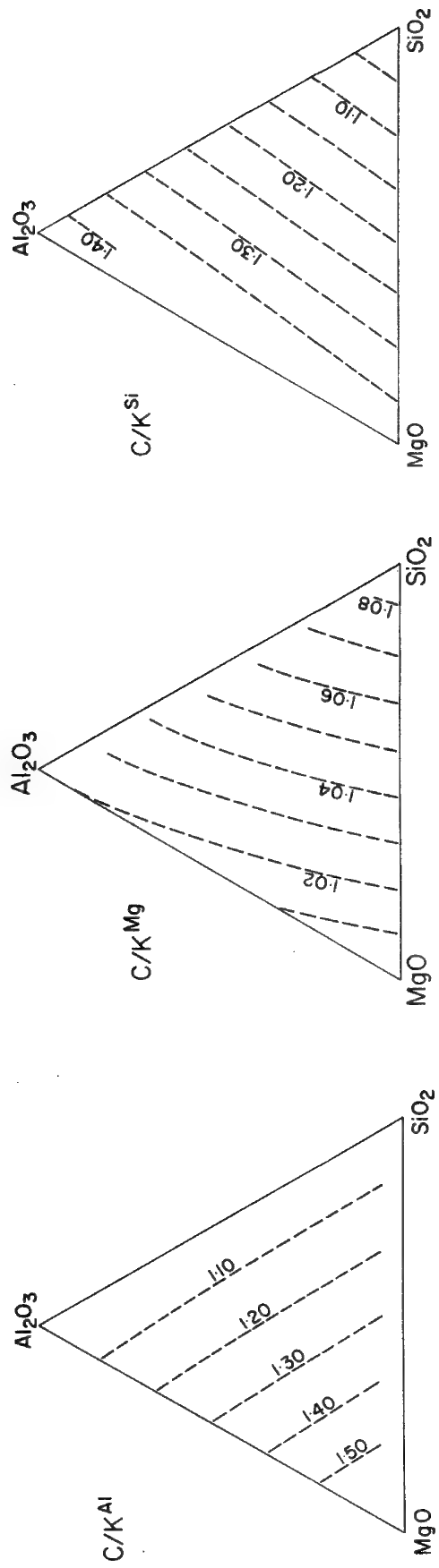
Fig. 2a

Fig. 2b

Fig. 2c

PREPARATION OF MICROPROBE STANDARDS USING THE LASERGLAZE[TM] PROCESS

by

J. M. Walsh,[*] K. P. Gumz[*] and E. M. Breinan[+]

* Pratt and Whitney Aircraft, Middletown, Connecticut
+ United Technologies Research Center, E. Hartford, Connecticut

Over the past 25 years, significant progress has been made in quantitative electron microprobe analysis using pure element standards and theoretical ZAF correction schemes. While these methods are in fact at an advanced stage at the present time, there are still occasions where it is desirable to relate measurements directly to a chemically characterized standard similar to the unknown. This is especially true in certain industrial applications where material is being controlled on the basis of a microprobe analysis. Standards are also important in the testing of correction models. The problem of preparing standards homogeneous enough for microprobe analysis is a long standing one. Goldstein et. al.[1] made an interesting contribution in this area in 1966 with a modified Duwez splat cooling method. This paper describes the preparation of microprobe standards using a new rapid solidification laser technique.

The LASERGLAZE[TM] process, developed within United Technologies Corporation is a new method for formation of rapidly chilled layers on the surface of bulk substrates. The basis of the technique is the use of the high power density of the laser to melt thin zones at high melting efficiencies, i.e., to limit almost all of the energy input to the molten zone so as not to heat up the substrate material. Once surface melting is accomplished, and the laser moves on to another location, rapid self-quenching of the surface layer occurs. Cooling rates up to approximately 10^8 °C/sec are possible in layers of 2.5×10^{-3} mm thickness in nickel base alloys when incident power densities in the 10^6 watt/sq. cm range are employed. Figure 1 defines the relationship of the LASERGLAZE[TM] process to other laser materials processing operations in the speed/power-density spectrum. The development of the process and its effects on microstructure, as well as its future potential uses are outlined in references 2-4.

The alloys studied in the current investigation were a series of nickel-base alloys containing Co, Cr, Al and Y. These alloys exhibit an extremely coarse, heterogeneous structure in the as cast condition. A continuous, convectively cooled CO_2 laser was used to LASERGLAZE[TM] these alloys. Specimens were traversed beneath the focussed laser beam at speeds ranging from 12.7 to 101.6 cm/sec. to form shallow melt zones which experienced subsequent rapid chilling. Specimens were shielded from atmosphere while liquid by passing the laser beam through the center of a 7.5 cm diameter "gas lens" flowing pure helium.

A light micrograph of a specimen subjected to a single laser pass is shown in Fig. 2 and clearly shows the coarse structure of the as cast material surrounding the fine structure of the laser-glazed area. The degree of homogeneity in the laser pass was measured with the electron microprobe by accumulating x-ray quanta for each element of interest at random points and determining the experimental standard deviation, S_c, and the standard counting error, σ_c. A similar series of measurements was made on the as cast material. X-Ray intensity data for Cu and Al in the single laser pass shown in Fig. 2 are given in Table I. The single laser pass provides a very large improvement in homogeneity over the as cast condition. Specimens were also "step-homogenized" by employing a deeper, longer-dwell time, slower cooling rate pass to partially homogenize the starting casting, followed by a faster, shorter dwell-time, higher cooling rate pass using the slower, partially homogenized pass as the substrate.

In summary, the LASERGLAZE^{TM} process has produced useful standards in a complex alloy system.

References:

1. J. I. Goldstein, F. J. Majeske and H. Yakowitz, in "Advances in X-Ray Analysis", Vol. 10, Plenum Press, New York (1971), pp. 431-446.

2. E. M. Breinan, B. H. Kear, L. E. Greenwald and C. M. Banas, "Laserglazing- A New Process for Production and Control of Rapidly-Chilled Metallurgical Microstructures", Society of Manufacturing Engineers Technical Paper MR76-867, 1976.

3. E. M. Breinan, B. H. Kear, C. M. Banas and L. E. Greenwald, "Surface Treatment of Superalloys by Laser Skin Melting," in "Superalloys: Metallurgy and Manufacture", Proceedings of 3rd International Superalloy Symposium, Seven Springs, PA., Claitor's, Baton Rouge, 1976, pp. 435-450.

4. E. M. Breinan, B. H. Kear and C. M. Banas, Physics Today, Nov. 1976, pp. 44-50.
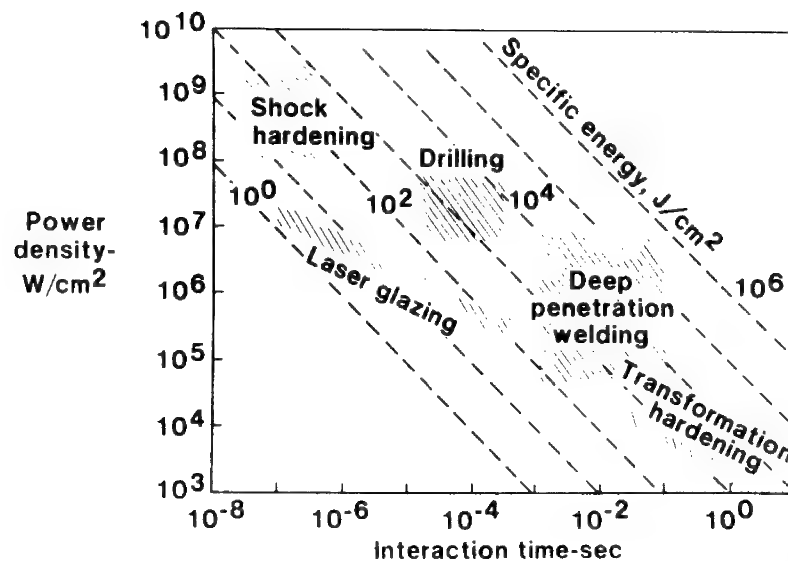
Fig. 1 - Operational Regimes for Various Laser Materials Processing Techniques.

100 μm
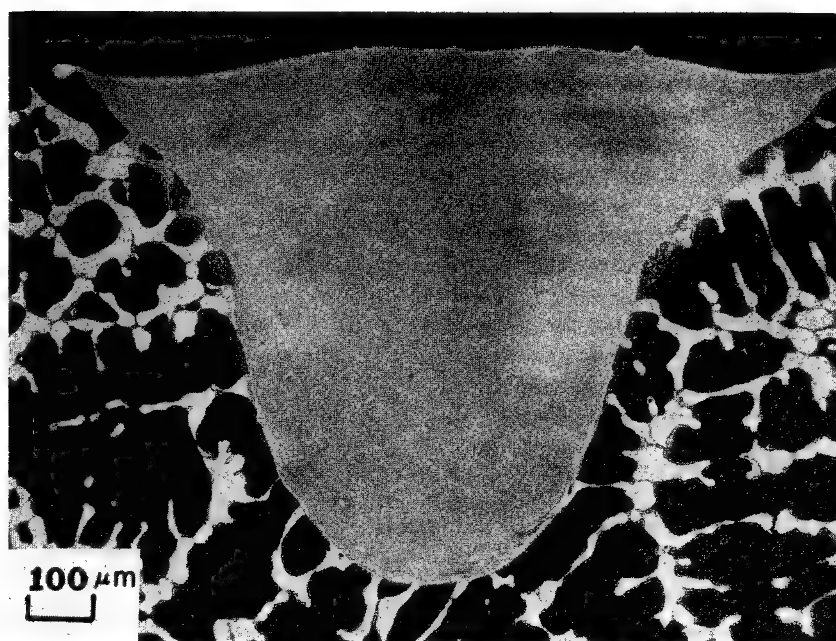
Fig. 2 - Light Micrograph of Single Laser Pass.

TABLE I

Location	Element	Number of Points, n	Average Total Counts Accumulated, $\bar{N}$	S_c *	σ_c **	S_c/σ_c
Laser Pass	Al	25	78,700	1,543	281	5.5
As Cast	Al	21	93,072	26,507	305	87
Laser Pass	Cr	25	144,979	2,789	381	7.3
As Cast	Cr	21	122,914	43,715	351	125

$$* \quad S_c = \left[\sum_{i=1}^{n} (N_i - \bar{N}_i)^2 / n-1 \right]^{1/2} , \qquad ** \quad \sigma_c = \sqrt{\bar{N}}$$

"ON-LINE" MAGIC IV: DIRECT COMPUTER REDUCTION
OF DATA ACQUIRED FOR UP TO 42 ELEMENTS

L. A. Ray, L. K. Griffith

W. J. Hamilton and J. R. Hinthorne

Applied Research Laboratories
9545 Wentworth Street
Sunland, California 91040

INTRODUCTION

Currently available versions of the computer program MAGIC IV (Colby, 1968; and pers. comm) for reduction of data from electron microprobe analysis generally require transfer of the data from the analytical instrument to the computer via relatively slow procedures such as punch cards, paper tape, and for some small computers, keyboard entry. The input and output routines of MAGIC IV have been modified by the present authors to allow immediate and rapid data reduction without the necessity of operator inter-action. Matrix operations within the program have been simplified to allow x-ray intensity data from an analysis of up to <u>42 elements</u> to be corrected within a small minicomputer. Further, analysis of oxides has been greatly facilitated by modifications allowing input of data and output of results in terms of oxide concentrations and formula proportions. The correction scheme used for the data reduction has not been modified: Raw intensity data is corrected for deadtime losses, background, absorption (Heinrich, Duncumb-Shields, Philibert), characteristic fluorescence (Reed), backscatter losses (Duncumb), and ionization-penetration losses (Philibert-Tixier), but uses the Berger-Seltzer equation for the mean ionization potential.

In order to ascertain that the modifications to MAGIC IV had not altered the data correction, identical data was input to both the "on-line" program and the unmodified "off-line" program. In all test cases, the results of the two data reductions were identical.

OPERATING ENVIRONMENT

The MAGIC IV program was reconfigured to operate as an integral part
of a new automation system for electron microprobe data collection
and analysis using the ARL-SEMQ, a PDP-11 computer and a "floppy disk".
This system allows rapid and efficient analyses by transferring the
raw microprobe x-ray intensity data to a magnetic disk data file which
is immediately accessed by MAGIC IV. Results are printed on the
operator's console or a line printer and stored in a disk file for
future retrieval, and the system then returns to the data acquisition
mode. The use of high speed bulk storage of data and program material
on magnetic disk creates the efficient communication link between
data collection and analysis programs. Furthermore, the ability to
"swap" program and data in and out of central (core) memory allows
considerably larger programming tasks to be accomplished in available
core. This "on-line" MAGIC IV will perform data reduction on up
to a 42 element electron microprobe analysis within a core memory
space of 16K words. For speed and efficiency the program and
modifications are written in FORTRAN IV and compiled under Digital
Equipment Corporation RT-11 system. The computational procedures
of MAGIC IV have not been modified and since these represent the
greatest fraction of the data reduction time, the execution times
for the "on-line" version are similar to those for the earlier
"off-line" MAGIC IV available to minicomputer users. A typical
analysis of 9 elements running through three iterations requires on
the order of two minutes in a PDP 11/05. This is, of course, reduced
by a faster central processor such as the PDP 11/34 and can be
reduced still further by addition of fast floating point processor
hardware. In addition, "on-line" MAGIC IV computation time is con-
siderably reduced by the storage of the concentration-independent
correction factors for unknowns and total correction factors for
pure and multielement standards in a disk file during the first "pass"
through. A "flag" is set so that additional data reduction using
the same analytical parameters avoids recomputation of the correction
factors.

INPUT DATA

The input of data to "on-line" MAGIC IV is provided by disk data files

created by data acquisition programs written in BLISS (ARL's Basic
Language Integrated Software System). All parameters necessary
for the data reduction such as the elements and x-ray lines analyzed,
compositions of compound standards used, and the raw intensity data
collected are transferred to the data files. A FORTRAN user
subroutine-library added to MAGIC IV accesses the BLISS data files.
"On-line" MAGIC IV allows the use of up to 15 multielement standards
with as many as 19 elements per standard. The concentration data
for these compound standards may be entered as elemental weight
fractions, elemental weight percent, stoichiometric formula, or
oxide weight fraction. This provides a convenient mechanism for
the use of "on-line" MAGIC IV for the analysis of oxide specimens;
for the same reasons, MAGIC IV has been modified to provide an output
for both routine elemental analyses and oxide analyses.

OUTPUT FORMAT

The printout of the results includes extensive information beyond the
compositional data. This information is intended to provide the
analyst with criteria for judging the quality of his analysis and
ease of future interpretation. The printout line for each element
includes the element, x-ray line, weight %, the standard deviation,
the k-ratio, the raw peak and background counts and counting times
for both unknown and standard, the total correction factor applied
to the unknown and to the standard, and the name of the standard used.
In addition, the atomic percent is computed and printed for elemental
output and the formula proportion (based on 24 oxygens in the formula)
is output for oxides.

CREATION OF ALPHA FACTOR FILES

The Bence and Albee (1968) data correction scheme is generally imple-
mented with the alpha factors tabulated by Albee and Ray (1970).
These factors were obtained by running a version of MAGIC "backwards"
at specific accelerating voltages. Because the new SEMQ automation
system includes a "Bence-Albee" data reduction option, one of us
(L.A.R.) has written a second FORTRAN program, based on MAGIC IV,

to calculate alpha factors for any set of elements at any accelerating potential and take-off angle and to store the factors in permanent disk files in the proper format for use by other segments of the automation system. Oxide-normalized or metals normalized tables may be generated. Factors for an array as large as 80 elements may be calculated in a PDP-11 with 16K of core memory.

SUMMARY

MAGIC IV has been modified so that data reduction of electron microprobe results occurs "on-line" in an automated data collection and reduction system. The modifications have included such features as the ability to provide data reduction of up to 42 elements in a 16K word minicomputer, input and output formatting convenient to a variety of analytical problems, and a version to calculate alpha factor tables.

REFERENCES

Albee, A. L. and Ray, L. A. (1970) Anal. Chem., 42, 1408-1414.
Bence, A. E. and Albee, A. L. (1968) J. Geol., 76, 382-403.
Colby, J. W. (1968) Advan. X-ray Anal., 11, 287-305.

QUANTITATIVE INDIVIDUAL PARTICLE ANALYSIS:
A COMPARISON AND EVALUATION OF MICROPROBE TECHNIQUES

John T. Armstrong and Peter R. Buseck
Departments of Chemistry and Geology
Arizona State University, Tempe, Arizona 85281

A variety of semiempirical techniques have been proposed for quantitative or semiquantitative analyses of individual unpolished microparticles. These procedures include: (a) applying no correction procedures (except normalizing the results to 100%) or treating the particles as if they were thick polished materials in the correction procedures [1]; (b) analyzing a suite of particle standards and setting up a calibration curve for element pairs of I_A/I_B vs. C_A/C_B [2,3,4] or comparing intensities in unknown particles to those in "equivalent particles" [5]; and (c) analyzing the particles at very high accelerating potentials, assuming that there is no absorption, and treating the particles as thin films [6,7,8].

The development of theoretical equations which predict the amount of X-ray production, absorption, and secondary fluorescence in particles of given size and shape [9,10,11] makes it possible to evaluate these procedures, determine under which sample and analytical conditions they are most applicable, and predict the magnitude of error which can be expected when employing these methods.

No particle corrections approach

Treating a particle as if it were a thick polished specimen (by either applying no corrections or conventional corrections) results in (a) overestimation of the amount of absorption and (b) underestimation of the number of energetic electrons scattering out of the sample. As a result, this

approach results in consistent errors in analyses -- the calculated concentrations for elements with low energy X-ray lines will be too high and the calculated concentrations for elements with high energy X-ray lines will be too low.

Table 1 shows the analysis of a particle of olivine obtained with and without particle corrections. Not applying particle corrections results in considerable overestimation of the Mg concentration and underestimation of the Fe concentration. Table 2 shows an extreme example of this type of error.

A "no corrections" approach should only be attempted if particle simulations indicate that the $R_{A/B}$ [9] values of interest are close to 1 (i.e., that the relative intensities of element pairs in the particle are approximately equal to those in a thick polished specimen of the same composition). The greater the deviation of simulated $R_{A/B}$ values from 1 (when both sample and standard in the simulation have the same composition), the greater is the predicted error in a "no corrections" analysis.

Calibration curve method

Using particles as standards and developing calibration curves of relative intensity vs. relative concentration for element pairs eliminates some of the problems inherent in a "no corrections" approach. However, there are several major sources of error in the calibration curve approach as well. It is accurate only if the relative intensities of element pairs do not vary significantly with particle size and shape, and vary with composition in a predictable manner (e.g., a linear or hyperbolic relation between I_A/I_B vs. C_A/C_B).

Figures 1 and 2 show the ranges of I_A/I_B that are predicted for various compositions. Simulations were performed, using the corrections of Armstrong

and Buseck [9], for particles from 0.5 to 30μm in diameter for a variety of particle shapes. As can be seen in Figure 1, under certain conditions, the error inherent in a calibration curve can be quite severe. For a relative I_{Fe}/I_{Si} of 1.5 in the fayalite-forsterite system (at E_0 = 15keV and ψ = 18°), the C_{Fe}/C_{Si}, relative to 50% fayalite, can vary approximately between 1.25 and 2 (i.e., from 63% fayalite to 100% fayalite). On the other hand, if the two elements being compared have similar atomic numbers and emitted characteristic X-ray energies, accurate results can be obtained, as in I_{Mn}/I_{Zn} in the willemite-tephroite system (Figure 2).

Calibration curves are more accurate if particles in only a limited size range are examined. In this case the limiting factor in the accuracy of the analysis is the range of $R_{A/B}$ with shape which, under optimum analytical conditions, can be less than 5% relative.

In order to determine whether a calibration curve approach is feasible, particle simulations should be performed to determine the variations in $R_{A/B}$. If values of $R_{A/B}$ for each of the element pairs of interest are fairly constant over the range of particle compositions, shapes, and sizes that will be encountered, then calibration curves can be profitably used.

High voltage analysis

A modification of the calibration curve method has been proposed [6, 7,8] for the analysis of small particles (<2μm diameter) at very high electron beam accelerating potentials (40 to 80keV).

If the particles are very small, the X-ray path lengths, regardless of particle shape, should be small and thus the amount of X-ray absorption that occurs is minimal. When the energy of the electron beam is extremely high and the particles are very small, little retardation of the electrons

occurs and the whole particle is excited by electrons having roughly their original accelerating potential (i.e., atomic number effects are minimized).

If the absorption and atomic number effects are minimal, then the relative intensities of an element pair would be insensitive to particle shape or size and a calibration curve could be accurately used. The range of compositions and sizes over which such an approximation is accurate must be tested. (It should be noted that the amount of X-ray production which occurs in a very small particle, when bombarded by a very high energy electron beam, is minimal. This factor greatly limits the detection limits and thus the utility of this procedure.)

Figures 3 and 4 present the results of simulations performed for particle diameters from 0.1 to 2µm and various particle shapes, at an accelerating potential of 80keV and a take-off angle of 52.5°. Since particle thickness is a critical factor in determining whether the bombarding electrons are significantly slowed or not, simulations are given for particle thicknesses ranging from 0.5 to 2 times the particle diameter.

As can be seen from the results in Figures 3 and 4, at least for the fayalite-forsterite system at 80keV and 52.5°, a calibration curve is not useful for particles in the size range of 0.1 to 2µm. For example, under the conditions listed in Figure 3, a relative intensity ratio of 1.75 for $I_{Fe/Si}$ is only indicative of a relative concentration ratio of 1 to 2 -- a 100% range. Better results are obtained for $I_{Mg/Si}$, a case where both elements are similar in their atomic number and their absorption by the matrix. As can also be seen in Figures 3 and 4, if the particle size range considered is limited to 0.1 to 0.5µm, the accuracy of a calibration curve approach should improve dramatically -- resulting in uncertainties in

relative concentration of generally 15% or less for the cases simulated.

Summary

There are severe limitations to all existing empirical methods. However, under certain well-specified conditions, it is possible to obtain relatively accurate results using empirical techniques. Proper use of these techniques requires limiting the sizes, shapes, and compositions to be analyzed. Simulation calculations utilizing theoretical particle corrections are valuable in determining what these limitations are.

Some of the empirical methods have the advantages of relative simplicity, and ease of use, and avoid the initial necessity of performing lengthy theoretical calculations. In general, however, use of theoretical correction procedures provide a more versatile and reliable method for the quantitative analysis of individual microparticles.

References

1. F. W. Wright, P. W. Hodge and C. C. Langway, J. Geophys. Res., 68, 5575-5587 (1963).

2. E. W. White, Am. Mineral. 49, 196-197 (1964).

3. E. W. White, P. J. Denny and S. M. Irving in "The Electron Microprobe", T. D. McKinley, K. F. J. Heinrich and D. B. Wittry, Ed., John Wiley and Sons, Inc., New York, New York, 1966, pp 791-804.

4. R.J.R.S.B. Bhalla, E. W. White and R. Roy, J. Luminesc., 6, 116-124 (1973).

5. H. J. Hoffman, J. H. Weihrauch and H. Fechtig in "Vth International Congress on X-Ray Optics and Microanalysis", G. Mollenstedt and K. H. Gaukler, Ed., Springer-Verlag, Berlin, 1969 pp 166-169.

6. M. Bayard, in "Microprobe Analysis," C. A. Andersen, Ed., Wiley-Interscience, New York, New York, 1973, pp 323-348.

7. J. C. Russ, EDAX Editor, 5 (3), 3-6 (1975).

8. A. Hendricks, EDAX Editor, 5 (3), 7-12 (1975).

9. J. T. Armstrong and P. Buseck, Anal. Chem. 47, 2178-2192 (1975).

10. J. T. Armstrong and P. R. Buseck, Proceedings, 10th Annual Conference of the Microbeam Analysis Society, Las Vegas, Nev., August 1975, No. 9.

11. J. T. Armstrong, Ph.D. Dissertation, Arizona State University, Tempe, Arizona (1977).

TABLE 1

ANALYSIS OF AN OLIVINE PARTICLE

(Normalized composition in element weight %.)

	Actual composition	Uncorrected for particle geometry	% error	Corrected by particle model
Mg	26.50	29.64	11.8	26.49
Fe	13.30	9.48	-28.7	13.36
Mn	.23	.16	-30.4	.23
Si	18.07	17.97	- .6	18.04
O	41.90	42.75	2.0	41.88

Particle diameter = 8 μm; E_o = 15 keV; ψ = 18°; oxygen calculated by stoichiometry; particle geometric effects corrected by the method of Armstrong and Buseck [9].

TABLE 2

ANALYSIS OF ACMITE PARTICLE EXPECTED WHEN
CORRECTIONS FOR PARTICLE GEOMETRY NOT APPLIED

(Normalized composition in element weight %.)

	Actual composition	Uncorrected for particle geometry (calc.)	% error
Na	9.95	32.86	230
Fe	26.87	5.01	- 81
Si	24.32	23.02	- 5
O	38.87	39.11	0.6

Simulated analysis obtained by: (1) calculating (by the method of Armstrong and Buseck [9]) ratios of intensities of elements in a 5 μm square pyramidal particle of acmite to those in a thick polished standard of the same composition as the particle, (2) multiplying the intensity ratios by the concentrations of the elements in the standard, and (3) normalizing the results to 100%. Simulation performed for E_o = 30 keV and ψ = 18°. Oxygen calculated by stoichiometry.

$(Fe,Mg)_2SiO_4$
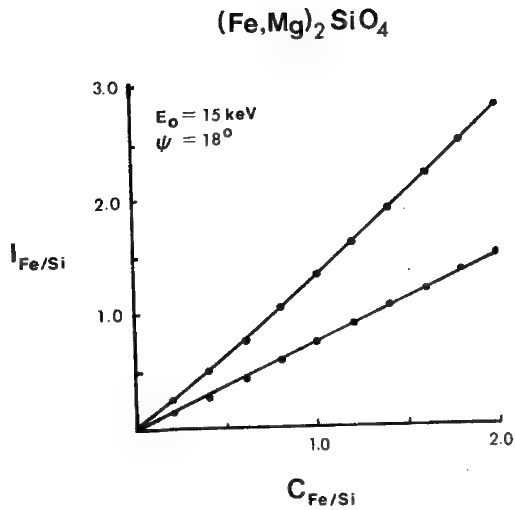
FIGURE 1. Simulated range of calibration curves of relative intensity vs. concentration for the element pair Fe/Si in the system fayalite-forsterite.

$(Zn,Mn)_2SiO_4$
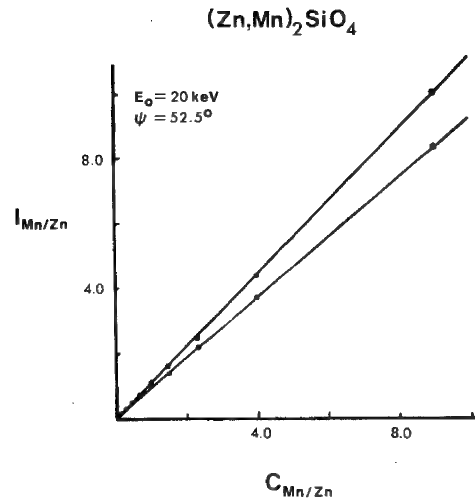
FIGURE 2. Simulated range of calibration curves of relative intensity vs. concentration for the element pair Mn/Zn in the system willemite-tephroite.

All I and C values are divided by the corresponding values for a 5 μm diameter particle of 50% fayalite ($FeMgSiO_4$) in Figure 1 and for a 5 μm particle of 50% willemite ($ZnMnSiO_4$) in Figure 2. The two curves in each figure enclose the range of values calculated for .5 to 30 μm particles of various geometries.

$(Fe,Mg)_2SiO_4$
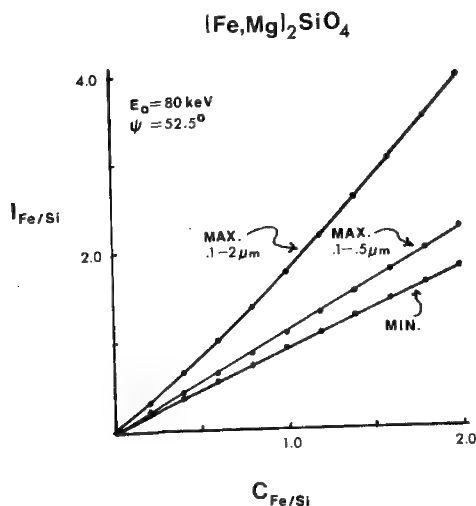
FIGURE 3. Simulated range of calibration curves for the element pair Fe/Si in the system fayalite-forsterite.

$(Fe,Mg)_2SiO_4$
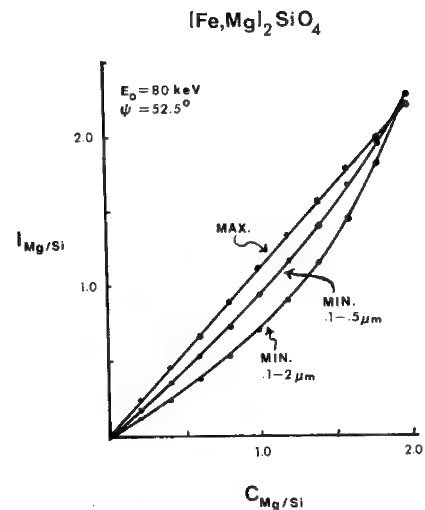
FIGURE 4. Simulated range of calibration curves for the element pair Mg/Si in the system fayalite-forsterite.

All I and C values are divided by the corresponding values for a .5 μm diameter particle of 50% fayalite. The outermost curves enclose the range of values calculated for .1 to 2 μm particles of various geometries and with thicknesses varying from half to twice the diameter. The "MIN" and "MAX .1-.5 μm" curves in Figure 3 and the "MAX" and "MIN .1-.5 μm" curves in Figure 4 enclose the range calculated for .1 to .5 μm particles.

DEVELOPMENT OF A CHARACTERISTIC FLUORESCENCE CORRECTION FOR THIN FILMS AND PARTICLES

John T. Armstrong and Peter R. Buseck
Departments of Chemistry and Geology
Arizona State University, Tempe, Arizona 85281

Procedures for the quantitative analysis of particulate and thin film materials generally ignore correction for characteristic fluorescence effects [1,2]. In many instances the magnitude of the fluorescence correction for such specimens is too low to warrant its calculation. However, for certain particle and thin film compositions, characteristic fluorescence can account for 15% or more of observed X-ray intensities and thus should not be ignored. In this paper, both comprehensive and simplified corrections will be proposed for the cases of fluorescence produced: (a) within a homogeneous thin film, (b) in a thin film by X-ray emission from a substrate, and (c) in a spherical particle.

Figure 1 illustrates the generation of secondary X-ray fluorescence by primary, electron-produced X-rays. Using a derivation similar to that described by Criss and Birks [3] for a conventional thick polished specimen, a general equation for the amount of fluorescence of the k line of element A by the j lines of elements B in a sample of undefined shape can be expressed as:

$$I_{f,Ak} = D' \int_{z=0}^{T} \frac{1}{a_0} \int_{y=\alpha_1(z)}^{\alpha_2(z)} \int_{x=\beta_1(y,z)}^{\beta_2(y,z)} \int_{\xi=0}^{2\pi} \int_{\theta=0}^{\pi} \int_{s=\gamma_1(z,y,x,\xi,\theta)}^{\gamma_2(z,y,x,\xi,\theta)}$$

$$[\phi_{Bj}(z,y,x) \tan \theta \; e^{-\mu_B^j \sec \theta \; s} \; e^{-\mu_A^k \; g(z,y,x,\xi,\theta,s)}]$$

$$ds \; d\theta \; d\xi \; dx \; dy \; dz \tag{1}$$

where D' is an operator defined by:

$$D'Q = C_A \frac{r_A^k - 1}{r_A^k} \omega_A^k p_A^k \frac{\Delta\Omega}{(4\pi)^2} \sum_B \sum_j I_{Bj}'' \mu_{B,A}^j Q \tag{2}$$

(In the above equations, dimensions x, y, z, and s are in terms of mass distance [i.e., distance multiplied by density]; α, β, and γ are functions expressing the sample boundaries; T is the sample thickness; and the other symbols are given in Figure 1 or follow the nomenclature of Armstrong and Buseck [1] and Heinrich [4].)

Equation 1 can be solved exactly for a thick polished specimen if $\phi(z)$ is expressed as a simple exponential function [3,5]. Evaluation of this expression for a thin film or a particle of a given geometry is considerably more complicated and requires numerical integration.

For the case of a homogeneous thin film of mass thickness T, with no fluorescence contribution from the substrate, Equation 1 can be simplified to:

$$I_{f,Ak} = D' \int_{z=0}^{T} \phi_{Bj}(z) \, e^{-\chi z} \frac{1}{\chi} [\log (\mu + \chi) - \log (|\mu - \chi|)] \, dz$$

$$- D' \int_{z=0}^{T} \int_{t=-1}^{1} \phi_{Bj}(z) \frac{1}{\mu + \chi t} e^{-\chi T} e^{-(\mu/t)(T - z)} \, dt \, dz \tag{3}$$

where $\mu = \mu_{Bj}$, $\chi = \mu_{Ak} \csc \psi$, and $t = \cos \theta$.

For the case of a substrate of thickness $T_2 - T_1$ inducing characteristic fluorescence in a thin film of thickness T_1, Equation 1 can be simplified to:

$$I_{f,Ak,substrate} = D' \int_{z=T_1}^{T_1+T_2} \int_{t=-1}^{0} \phi_{Bj,substrate}(z-T_1) \frac{1}{\mu_1 + \chi_1 t}$$

$$e^{-(\mu_2 - \mu_1) z/t} [e^{-(\mu_1 - \mu_2) T_1/t} e^{-\chi_1 T_1} - e^{\mu_2 T_1/t}] \, dt \, dz \tag{4}$$

where $\mu_1 = \mu_{Bj,thin\ film}$, $\mu_2 = \mu_{Bj,substrate}$, and $\chi_1 = \mu_{Ak,thin\ film} \csc \psi$.

Equations 3 and 4 are discontinuous about $t = 0$ and, if $\chi > \mu$, about $t = -\mu/\chi$. However, the integrations are symmetrical and of opposite signs about these points. Using a thin film $\phi(z)$ expression, such as that of Reuter [2], and numerically integrating with respect to t and z, Equations 3 and 4 can be readily evaluated.

In the case of a particle, Equation 1 cannot be simplified to the extent that it could for a thick polished specimen or a thin film. We have derived an expression for the fluorescence correction for a spherical particle. The expression involves numerical integration of a hexaintegral. This equation has been evaluated for spherical particles of varying diameters, for a variety of matrix compositions requiring large fluorescence corrections, at accelerating potentials of 15 and 20 keV and spectrometer take-off angles of 18°, 40°, and 52.5°.

Examining the results of these simulations, we have found that the amount of characteristic fluorescence in a spherical particle can be reasonably well approximated as a simple function of the amount of characteristic fluorescence produced from a thick polished specimen having the same composition. Least squares fits of our simulation results indicate that the following approximate relation can be employed:

$$\frac{I_{f,ptc}}{I_{f,tps}} = A + Bx + Cx^2 \tag{5}$$

where

$$x = 1 - e^{-\mu_{Bj}\rho r} \tag{6}$$

$$A = 0.0260 \tag{7}$$

$$B = 1.1409 + 0.2012\, y \tag{8}$$

$$C = -0.2471 - 0.2741\, y + 0.01315\, y^2 \tag{9}$$

and

$$y = \chi_{Ak}/\mu_{Bj} \tag{10}$$

(r is the particle radius and ρ is the particle density).

Table 1 presents the results of simulations of the amount of Fe Kα characteristic fluorescence in spherical particles of $FeNi_3$, using the full and the simplified fluorescence equations. As can be seen, the results obtained using the two equations are quite similar.

The equations described in this paper can be employed to determine those matrix compositions for which the fluorescence corrections will be significant. They can be used in thin film and particle correction programs to obtain superior results for specimens producing considerable fluorescence.

REFERENCES

1. J. T. Armstrong and P. R. Buseck, Anal. Chem., 47, 2178-2192 (1975).

2. W. Reuter in "Proceedings of the Sixth International Conference on X-Ray Optics and Microanalysis", G. Shinoda, K. Kohra, and T. Ichinokawa, Ed., Univ. of Tokyo Press, Tokyo, 1972, pp 121-130.

3. J. W. Criss and L. S. Birks in "The Electron Microprobe", T. D. McKinley, K. F. J. Heinrich, and D. B. Wittry, Ed., John Wiley and Sons, Inc., New York, N.Y., 1966, pp 217-236.

4. K. F. J. Heinrich, Nat. Bur. Stand. (U.S.), Tech. Note, 521 (1970).

5. S. J. B. Reed, Brit. J. Appl. Phys. 16, 913-926 (1965).
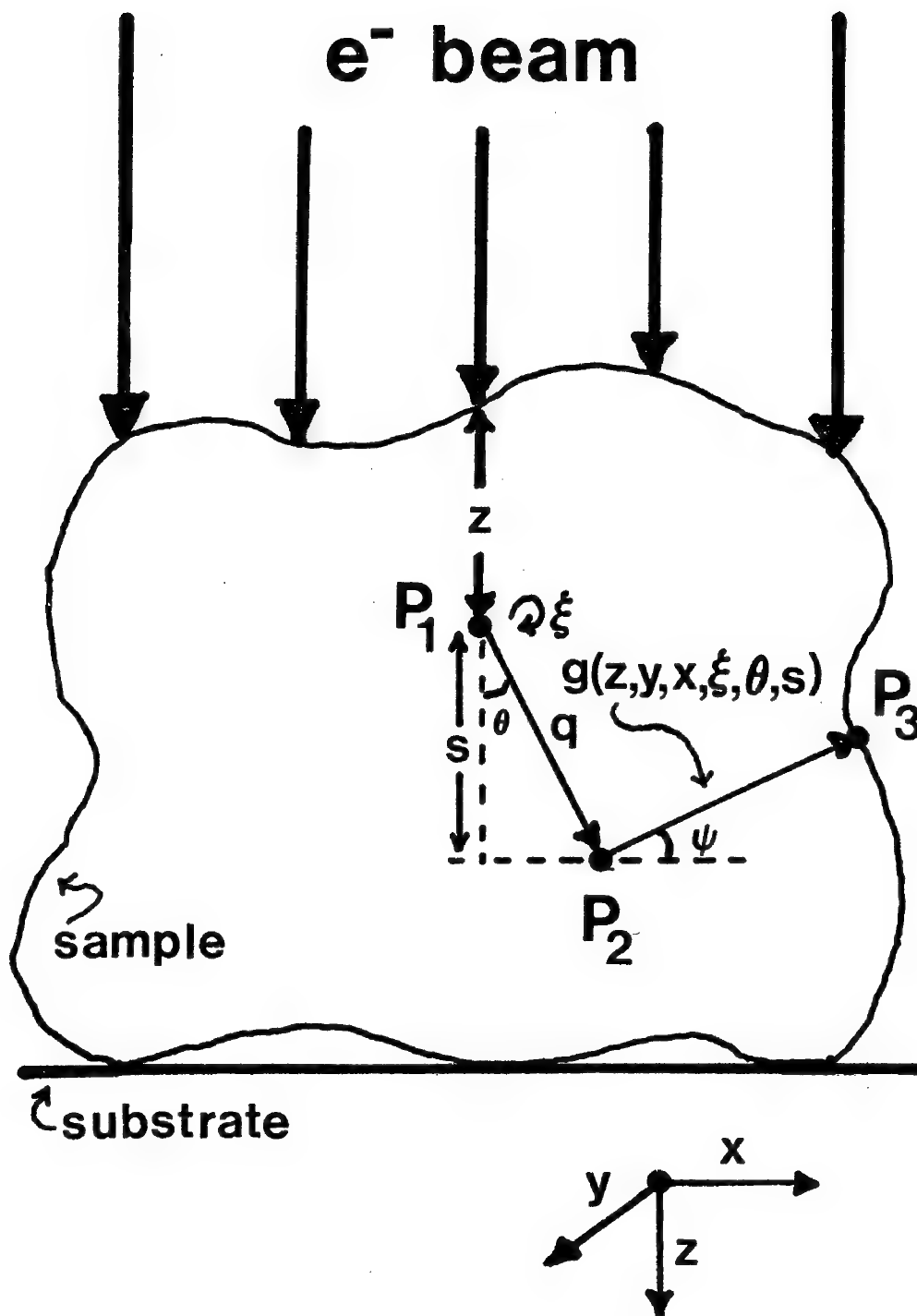
FIGURE 1. Schematic of characteristic fluorescence in an irregular sample. P_1 represents the point of production of a characteristic X-ray of the j-line of the fluorescing element B. P_2 represents the point of absorption of the Bj X-ray and corresponding emission of a k-line X-ray of the fluoresced element A. In order for the Ak X-ray to be detected, it must travel pathlength g (at a take-off angle ψ) and exit the sample at P_3. The Ak X-ray pathlength, $g(z,y,x,\xi,\theta,s)$, must be calculated for all Bj X-ray pathlengths, q (= s sec θ), for all points P_1 in the sample.

TABLE 1

COMPARISON OF FULL SPHERICAL PARTICLE FLUORESCENCE CORRECTION WITH
SIMPLIFIED NUMERICAL FIT

Fluorescence of Fe Kα by Ni Kα in FeNi$_3$ at E$_O$ = 15 keV.

$\psi = 18^O$

D(μm)	FULL	SIMPLE	DIFF.
	% FLUORESCENCE		
100	12.94	11.30	-1.64
10	7.87	7.44	- .43
5	5.09	4.82	- .27
1	1.49	1.45	- .04

$\psi = 40^O$

D(μm)	FULL	SIMPLE	DIFF.
	% FLUORESCENCE		
100	13.47	14.37	.89
10	7.79	8.34	.55
5	5.07	5.28	.21
1	1.49	1.59	.11

$\psi = 52.5^O$

D(μm)	FULL	SIMPLE	DIFF.
	% FLUORESCENCE		
100	13.79	14.03	.24
10	7.77	7.94	.17
5	5.05	5.01	- .04
1	1.49	1.51	.02

% FLUORESCENCE = $(I_{f,Fe~K\alpha} / I_{p,Fe~K\alpha})$ x 100%

ELECTRON-PROBE ANALYSIS OF MICRON-SIZE INCLUSIONS

by
G. Springer

Falconbridge Metallurgical Laboratories
Thornhill, Ontario
Canada

INTRODUCTION

Although electron-probe analysis is a most powerful microanalytical technique, its spatial resolution is limited. The reason for this is that electrons diffuse a short distance away from the point of impact. In addition, there is fluorescence radiation produced in a fairly large volume either by primary-produced characteristic spectral lines or by bremsstrahlung.

Qualitative assessment of small particles is not normally affected by the spread of X-ray production because secondary intensities are much smaller than primary intensities, but quantitative results are less readily achieved. In the following, a method of estimating the magnitude of the secondary intensity is suggested so that more accurate quantitative results can be obtained for micron-size inclusions.

INCLUSION SIZE

How large an inclusion must be to contain all of the electron-excited production can be calculated from well-known electron-deceleration functions such as those given by Thompson-Whiddington, Webster or Bethe. Typically, the electrons penetrate 1-2 μm before they lose so much energy as to prevent them from generating characteristic X-radiation. Since the diameter of the electron beam can be made as small as 0.1 μm in most electron-probe analyzers, the volume of primary excitation is therefore approximately a half-sphere of 2-4 μm diameter.

The spatial distribution of secondary excitation has been considered by Green (1964). This author found that, in general, the volume of secondary excitation is one to two orders of magnitude greater than the volume of primary excitation. In view of this, one can expect that the matrix will be excited to a considerable extent by secondary fluorescence, but all the primary excitation occurs within the inclusion, if the inclusion size is not greater than about 5 μm. Exact size and shape of the inclusion are of minor importance because the volumes of direct and indirect production are of greatly different proportions.

One can evaluate the effect of matrix interference if one can assume that all primary production is contained in the inclusion and all secondary production occurs in the matrix. This makes it possible to perform quantitative analyses of inclusions in the important size range of several microns.

METHOD OF CALCULATION

The magnitude of secondary production can be evaluated using the correction formulae for characteristic and continuum fluorescence. The formula by Reed (1965) gives the ratio, γ, of characteristic fluorescence intensity to the measured intensity of directly-produced characteristic radiation. The ratio, ϕ, of continuum fluorescence intensity to the measured intensity of directly-produced radiation can be calculated using a formula proposed by Springer (1971, 1973). In applying these formulae, account must be taken that the sample is not homogeneous but consists of the inclusion in which primary production occurs and the matrix in which these primary X-rays produce fluorescence radiation.

As can easily be realized, the primary part differs from the intensity obtainable from a solid sample by the factor $1/(1+\gamma_A^i+\phi_A^i)$ where γ and ϕ are calculated for the inclusion, considering a particular element A. On the other hand, if γ and ϕ are calculated for the matrix, the fluorescence part of the total intensity can be derived. However, as this causes the intensity to be referred to primary intensity from the matrix, γ and ϕ must be multiplied by the ratio of the primary intensities from inclusion and matrix. In addition, a factor c_B^i/c_B^m must be applied to γ if the concentrations of the exciting element B are not equal in inclusion and matrix, and a factor $\overline{Z}_i/\overline{Z}_m$ must be applied to ϕ to take account of differences in the average atomic numbers $\overline{Z}$ of inclusion and matrix. The concentration of an element A in the inclusion, as measured by an electron-probe analyzer, is therefore

$$c_A^{app} = \frac{c_A^i}{1+\gamma_A^i+\phi_A^i} + c_A^m \cdot \frac{\gamma_A^m \cdot c_B^i/c_B^m + \phi_A^m \cdot \overline{Z}_i/\overline{Z}_m}{1+\gamma_A^i+\phi_A^i} \cdot \frac{(R/S)_A^m \cdot f(\chi)_A^m}{(R/S)_A^i \cdot f(\chi)_A^i}$$

This formula may be used to calculate c_A^i from c_A^{app}. The terms R/S and $f(\chi)$ are the correction factors for atomic number and absorption to be calculated for the measured element A in inclusion (subscript i) and matrix (subscript m).

EXAMPLES

A special case is met if element A is present only in the inclusion, and element B, occurring only in the matrix, is excited by a characteristic line of A. This special case is related to many practical applications. For instance, it pertains to the question whether an element predominant in the matrix, also occurs in the inclusion or whether its apparent presence is simply due to matrix interference. Furthermore, if the concentration c_A of an inclusion element is found to be less than an expected concentration, an assessment can be made whether or not the inclusion is large enough to contain all secondary production.

(EXAMPLES, cont'd.)

Several examples are given in Table I. The table shows true, stoichiometric compositions for several kinds of inclusions and the concentrations which would be measured if the conditions of the special case were met. The matrix is assumed to be free of any elements occurring in the inclusion.

TABLE I: Inclusion Analysis (Calculated Examples)

Inclusion (A)	Matrix (B)	c_A^{true}	c_A^{app}	c_B^{true}	c_B^{app}
Al_2O_3	Fe	52.9	52.8	0	1.2
MnS	Fe	63.2	61.5	0	2.6
NiS	Fe_3O_4	64.7	62.0	0	6.8
TiC	Fe	80.0	78.7	0	2.7
Au	$CuFeS_2$	100.0	92.5	0	6.4
Ta_2C	Fe	97.8	91.1	0	14.0

(Au–Lα, Ta–Lα, else Kα)

As may be seen, matrix effects can reach considerable proportions. They tend to become the more important the higher the average atomic number of the inclusion.

The advantage of using a correction formula in inclusion analysis is clearly demonstrated.

REFERENCES

1. GREEN, M. (1964): The Angular Distribution of Characteristic X-Radiation and its Origin within a Solid Target. Proc. Phys. Soc., 83, 445.

2. REED, S.J.B. (1965): Characteristic Fluorescence Corrections in Electron-Probe Microanalysis. Brit. J. Appl. Phys. 16, 913–926.

3. SPRINGER, G. (1971): Fluorescence by Continuous Radiation in Multi-Element Targets. Proc. Sixth Internat. Conf. X-Ray Optics and Microanalysis. (G. Shinoda et al., Editors). Univ. Tokyo Press, 1972.

4. SPRINGER, G. (1972): Review of the Method for Continuum Fluorescence Correction. Proc. Meeting at Inst. Techn. Physik. Kernforschung Jülich, W. Germany (E. Preuss, Editor).

A LOW COST METHOD FOR
ANALYSING ELECTRON MICROPROBE DATA

Philip B. Fraundorf
McDonnell Center for the Space Sciences
Washington University
St. Louis, Missouri 63130

The increasing availability of personal programmable calculators is opening the door to extremely low cost ways to implement some analytical techniques which have heretofore required a small computer or a large calculator (1). The application described here uses interelement effect data, stored on magnetic cards, to create a problem-library as large as one might wish for analysing five-element (or oxide) chemical systems under specified analysis conditions. Thus, within the five-element limit imposed by the size of the processing unit, on-line convenience, as well as low cost, is possible. This should be useful both to the lab that is looking for low cost quantitative capability (for whose analysis conditions interelement effect data can be obtained), and to the lab that has access to a computer, but can use an on-line backup system.

The algorithm used is the well-known multi-element routine based on the empirical Ziebold and Ogilvie linear approximation for binary systems:

$$c_i/k_i = \alpha_{ij} + (1 - \alpha_{ij}) c_i.$$

Here, c_i is the mass fraction of element (or oxide) i in the binary mixture, k_i is the ratio between the peak height on the unknown and the peak height on the pure element (or oxide) under the same analysis conditions, and α_{ij} is the interelement effect coefficient denoting the effect of element (or oxide) j on the intensity of the line of element (or oxide) i in a binary mixture of i and j. Discussions of its applicability in electron probe microanalysis (EPMA) to systems of elements and, after Bence and Albee, to complicated systems of oxides, are well known in the literature (e.g. 2,3,4,5). The range of application, and the potential accuracy, will therefore not be discussed here.

The alpha-coefficients for a particular set of five elements (or oxides) must be specified for the desired operating voltage and analysis geometry. For the usual case of a thick polished specimen, operating voltage (E_0), surface tilt with respect to the electron beam (T), and detector takeoff angle (Ψ) are the usual variables specified. The coefficients can be obtained empirically, in which case a good number of binary standards are usually necessary; or they can be calculated for the desired analysis conditions from one of the variety of computer programs designed for modeling peak intensities as a function of concentrations. In this latter case, access to a computer and the necessary software is a requisite. The other alternative is to find lists of coefficients appropriate to the geometry of interest, as for example are found for some oxides and analysis conditions in (4). Sufficient demand for such lists should result in calculated lists being made available to specification, at least in the case of polished thick specimen geometries.

Given listings of the alpha-coefficients for the analysis conditions of interest, the twenty inter-element coefficients appropriate to a given set of five elements (or oxides) are then formatted and recorded on a data card for inclusion into the problem library. The details of the data formatting, program listing, and instructions developed for use of this scheme on the HP-67 or HP-97 programmable calculators are included in the Appendix. Routine data analysis then requires only loading of the program, loading of the appropriate data card, loading of the measured k-values, and approximately one minute of the k to C calculation. C to k conversion and a difference option are included in the program, as well as a couple of support routines: sum of concentrations, concentration normalization, and a short routine for converting peak intensities to k-values.

References

(1) Benenati, Robert F., Chemical Engineering, (Feb 28 1977) 201.
(2) Ziebold, T. O., and Ogilvie, R. E., Anal. Chem., 36, (1964) 322.
(3) Bence, A. E., and Albee, A. L., J. Geol., 76, (1968) 382.
(4) Albee, A. L., and Ray, L., Anal. Chem., 42, (1972) 1408.
(5) Laguitton, D., Rousseau, R., and Claisse, F., Anal. Chem., 47, (1975) 2178.

Appendix

A). Data Formatting.

In defining a system of five elements (or oxides), begin first by numbering the system members from 0 to 4, usually in order of increasing energy of the x-ray line being considered. Keep in mind that the "0th" element (or oxide) is the one that can be done by "difference". For example, the system of oxides: MgO, Al_2O_3, SiO_2, Cr_2O_3, and FeO might be numbered, from left to right, 0 through 4. In this way, the magnesium oxide concentration can optionally be calculated by the difference method.

Then, the inter-element coefficients are stored in paired form (one on each side of the decimal point) in the ten secondary memory registers of the calculator, as shown in the example of Figure 1. This data is then recorded onto a magnetic card, which may be labeled as shown in Figure 2. The primary registers stored on this data card are available to store other information about the system being analysed. This could be useful for other support routines, such as a program to convert between oxide and elemental concentrations (or k-values).

i/j	0	1	2	3	4
0	1.00	1.06	1.15	1.82	2.24
1	1.92	1.00	1.05	1.48	1.76
2	1.58	1.67	1.00	1.25	1.43
3	1.12	1.10	1.12	1.00	0.90
4	1.13	1.12	1.13	1.13	1.00

Example: α_{ij} values published in (4) for $E_0 = 20$ kev, $T = 0^\circ$, and $\psi = 52.5^\circ$ with the system of oxides mentioned in the text.

Memory Register	α-value pairs	Data Stored
S0	$\alpha_{01} \cdot \alpha_{10}$	01060.01920
S1	$\alpha_{02} \cdot \alpha_{20}$	01150.01580
S2	$\alpha_{03} \cdot \alpha_{30}$	01820.01120
S3	$\alpha_{04} \cdot \alpha_{40}$	02240.01130
S4	$\alpha_{12} \cdot \alpha_{21}$	01050.01670
S5	$\alpha_{13} \cdot \alpha_{31}$	01480.01100
S6	$\alpha_{14} \cdot \alpha_{41}$	01760.01120
S7	$\alpha_{23} \cdot \alpha_{32}$	01250.01120
S8	$\alpha_{24} \cdot \alpha_{42}$	01430.01130
S9	$\alpha_{34} \cdot \alpha_{43}$	00900.01130

Figure 1.

B). User Instructions.

1. Load Program (both sides of card).
2. Load interelement-effect coefficients, properly formatted,
   into secondary registers either manually or with a data card.
   This defines the set of elements or oxides, and geometry to
   to be analysed.
3. Initialize for problem: clear primary registers by pushing
   the keys: [f] [CLREG].
4. Difference option: Choose to calculate the "Oth" element
   (or oxide) concentration in all conversions by setting it
   equal to the difference between one and the sum of the other
   four concentrations. This might be done, for example, in the
   case of an unanalysed peak. Repeated pushing of the
   keys: [f] [D] will flip the flag for the difference option
   ON (1 will appear in the display) and then OFF (0 in display).

k to C conversion

5. Optional at any time: Calculate an unknown peak ratio, k_x, given
   peak height on the unknown, P_x, peak height on the standard, P_s,
   and k-value for the standard, k_s, by keying the following:
   P_x [ENT↑] P_s [ENT↑] k_s [f] [A]. Output of k_x results.
6. Load k-values (peak ratios for elements: unknown/pure element;
   for oxides: unknown/pure oxide) by storing k_0 through k_4 in
   memory registers A through E respectively. For example, input
   k_3 and then press [STO] [D] .
7. Optional at any time: Review k-values by pushing [A] : k_i, i = 0,4.
8. Calculate concentrations from k-values (three iterations) by
   pushing [C] . Concentrations are automatically output: C_i, i = 0,4.
   The k-values are used as the initial concentration guess, and
   the equation used is:

$$c_m^i = k_m(\frac{1}{\sum_\ell c_\ell^{i-1}}) \sum_{n=0}^{4} \alpha_{mn} c_n^{i-1}, \ m = 0,4; \ \text{and} \ \alpha_{mm} \equiv 1.$$

9. If further iteration is desired, a single iteration using existing
   C-values as initial guesses is accomplished by pushing [f] [C].
   This terminates with a display of C_0 only.
10. Optional at any time: Review C-values by pushing [D] : C_i, i = 0,4.
11. Optional at any time: Find Sum of C-values by pushing [E] .

C to k conversion

12. Load C-values (mass fractions) by storing C_0 through C_4 in memory registers 0 through 4 respectively. For example, input C_1 and then press $\boxed{\text{STO} \ 1}$.

13. Optional at any time: Normalize the concentrations so that they add up to one: $\boxed{f \ E}$.

14. Calculate k-values from concentrations by pushing $\boxed{B}$. The k-values are automatically output: k_i, $i = 0,4$. This is a direct calculation which uses the equation:

$$k_m = C_m \left\{ \left(\frac{1}{\sum_\lambda C_\lambda} \right) \sum_{n=0}^{4} \alpha_{mn} C_n \right\}^{-1} \ , \ m = 0,4.$$

15. For new k or C values, go to Step 3.

16. For new chemical system or analysis conditions, go to Step 2.

Running times: k to C (3 iterations) around 1 minute;
C to k (direct) around 20 seconds.

Sample Data Card
$E_0 = 20$ kev, Tilt $= 0°$, Take-off Angle $= 52.5°$.

| MgO | Al₂O₃ | SiO2 | Cr₂O₃ | FeO |

Influence Coefficient EPMA Program Card: 5 elements.

| $P_x \uparrow P_s \uparrow k_s \rightarrow k_x$ | | REITERATE $\rightarrow$ | Difference Option? | Normalize C. |
| $\rightarrow k_i$ | C to k | k to C | $\rightarrow C_i$ | Sum C |

Figure 2

001–032		033–064		065–096		097–128		129–160		161–192		193–224	
Step	Code	Step	Code	Step	Code	Step	Code	Step	Code	Step	Code	Step	Code
*LBLC	312513	9	09	STO&7	336107	RCL4	3404	GSB3	312203	RCLO	3400	1	01
RCLE	3415	STOI	3533	RCLO	3400	GSB2	312202	RTN	3522	RCL5	3405	RCL4	3404
STO4	3304	RCL3	3403	GSB1	312201	STO&8	336108	*LBL1	312501	/	81	–	51
RCLD	3414	STO8	3308	STO&6	336106	GSBE	312215	RCLi	3424	STOA	3311	RCL3	3403
STO3	3303	GSB1	312201	RCL1	3401	STO/5	338105	DSZ	3133	RCL1	3401	–	51
RCLC	3413	STO9	3309	GSB2	312202	STO/6	338106	FRAC	3283	RCL6	3406	RCL2	3402
STO2	3302	RCL2	3402	STO&5	336105	STO/7	338107	EEX	43	/	81	–	51
RCLB	3412	STO7	3307	RCL2	3402	STO/8	338108	2	02	STOB	3312	RCL1	3401
STO1	3301	GSB1	312201	GSB2	312202	STO/9	338109	x	71	RCL2	3402	–	51
RCLA	3411	STO&9	336109	STO&5	336105	F?2	357102	x	71	RCL7	3407	STO0	3300
STO0	3300	RCL2	3402	RCL3	3403	GTO6	2206	RTN	3522	/	81	RTN	3522
GSBc	322213	GSB1	312201	GSB2	312202	RCL9	3409	*LBL2	312502	STOC	3313	*LBLe	322515
GSBO	312200	STO&8	336108	STO&6	336106	RCLE	3415	ISZ	3134	RCL3	3403	GSBE	312215
GSBO	312200	RCL1	3401	RCL4	3404	x	71	RCLi	3424	RCL8	3408	STO/4	338104
*LBLD	312514	STO6	3306	STO&9	336109	STO4	3304	INT	3183	/	81	STO/3	338103
RCLO	3400	GSB1	312201	GSB2	312202	RCL8	3408	EEX	43	STOD	3314	STO/2	338102
RCL1	3401	STO&9	336109	STO&5	336105	RCLD	3414	3	03	RCL4	3404	STO/1	338101
RCL2	3402	RCL1	3401	RCL2	3402	x	71	/	81	RCL9	3409	STO/0	338100
RCL3	3403	GSB1	312201	GSB2	312202	STO3	3303	x	71	/	81	GTOD	2214
SPACE	3584	STO&8	336108	STO&6	336106	RCL7	3407	RTN	3522	STOE	3315	*LBLa	322511
STK	3284	RCL1	3401	RCL3	3403	RCLC	3413	*LBLE	312515	*LBLA	312511	/	81
RCL4	3404	GSB1	312201	GSB2	312202	x	71	RCLO	3400	RCLA	3411	/	81
PRTX	3184	STO&7	336107	STO&6	336106	STO2	3302	RCL1	3401	RCLB	3412	RTN	3522
SPACE	3584	RCLO	3400	RCL4	3404	RCL6	3406	&	61	RCLC	3413	*LBLd	322514
RTN	3522	STO5	3305	GSB2	312202	RCLB	3412	RCL2	3402	RCLD	3414	1	01
*LBLB	312512	GSB1	312201	STO&7	336107	x	71	&	61	SPACE	3584	F?1	357101
SF2	355102	STO&9	336109			STO1	3301	RCL3	3403	STK	3284	0	00
*LBLc	322513	RCLO	3400			RCL5	3405	&	61	RCLE	3415	CF1	356101
F?1	357101	GSB1	312201			RCLA	3411	RCL4	3404	PRTX	3184	Xne0?	3161
GSB3	312203	STO&8	336108			x	71	&	61	SPACE	3584	SF1	355101
*LBLO	312500	RCLO	3400			STO0	3300	RTN	3522	RTN	3522	RTN	3522
1	01	GSB1	312201			F?1	357101	*LBL6	312506	*LBL3	312503		

Set Status: All Flags clear, Degree mode, Fix 3.

Figure 3: Program Listing

FUTURE TRENDS IN MICROPROBE AUTOMATION

W. T. Hatfield
General Electric Corporate Research and Development

An extensive bibliography of microprobe automation can be found in last year's Proceedings[1]. This paper will be concerned specifically with microcomputers, which are already making an impact on this field[2]. Their effect, in fact, can be expected to increase as a result of drastic reductions in the cost of 8-bit microcomputer systems and the introduction of the 16-bit microprocessor.

In addition to serial and parallel input-output chips, standard interfaces for floppy discs, cassette tapes and video terminals along with digital to analog and analog to digital converter boards are now available for the more popular microcomputer systems. LSI chips have recently become available which can be used as timer/scalars, stepper motor controllers, and for general functions such as beam blanking, crystal flipping and status indicators. Furthermore, very powerful BASIC interpreters and FORTRAN compilers are now available along with disc based operating systems which make rapid program development possible. These components can be easily incorporated into a microcomputer system resulting in reduction of both size and cost of automation systems.

It will be the intent of this paper to discuss the ramification of these new developments with regard to microprobe and SEM automation.

REFERENCES

1. "Microprobe Automation, Past, Present and Future," W. T. Hatfield, Proc. Eleventh Annual Conference of the Microbeam Analysis Society, Miami Beach, Florida (1976)

2. "A Programmable EPMA Controller Using A Micro-Processor," M. Fujisawa and K. Hirata, Proc. Eleventh Annual Conference of the Microbeam Society, Miami Beach, Florida (1976)

AUTOMATION OF THE ELECTRON MICROPROBE

J. HENOC

C.N.E.T., 92220 Bagneux (France)

M. TONG

CAMECA, 92400 Courbevoie (France)

A procedure has been developed to perform automatic analysis within the CAMEBAX instrument provided with a PDP 11 mini computer.

The raw data from the microprobe are reduced by runing a FORTRAN program written to fulfill the storage requirements of the mini-computer. The OVERLAY structure allowed by the DISK OPERATING SYSTEM has been carefully defined to avoid multiple swappings which are time-consuming. The mass fraction of the elements present in the specimen are computed by a full classical ZAF approach (1-5). Only the correction for continuous fluorescence has been omitted because its contribution to the total radiation intensity is generally negligible. No significant difference was observed from the results given by COR2 for a great amount of routine analysis.

The program may be executed "ON LINE" or "OFF LINE" at user's request. When the microprobe is "OFF LINE" input data are directed from the keyboard of the terminal to the computer according to a conversational mode. These input data are reduced to a strict minimum (accelerating voltage, element and analyzed line symbols and compound standards if used) ; the management of suitable answers does not need trained people. If the microprobe is "ON LINE" the computer takes care of the instrument by means of a package which deals with the commands needed either for qualitative analysis or for data collection in view of a further execution of the ZAF process.

TECHNICAL OVERVIEW

HARDWARE

The hardware is based on a 16 to 28 K words of 16 bits minicomputer with a floppy or cartridge disk and a console terminal. The microprobe modules are linked to the minicomputer by means of an interface connected to the bus.

SOFTWARE

RT 11 *   supports standard FØRTRAN IV ; a minicomputer fitted with a 16 K memory can accomodate up to 15 elements in the specimen on an "OFF LINE" mode.

The best way to show the general trend of the program catalog is to give a rough description of the whole procedure.

1 - STARTING THE PROCEDURE

When the system is powered on for a new problem to be solved, the program INIT is run to define the configuration and the experimental conditions at the user's wishes. These conditions are stored on a file and may be restored into the computer memory for an "OLD" problem by reading out the contain of this file.

2 - GOING INTO THE PROCEDURE

Depending upon the job to be executed the user can select a program from the catalog listed below :

STATUS   gives the list of DATA contained in the file created during execution of INIT

CDMBX   is especially designed to perform controls of the Camebax modules (axis positioning, scaler initialization, Scaler readout, backlash correction, etc...) by means of some basic functions. It can be used also

* DIGITAL registered trade mark.

to execute more sophisticated routines such as peak
search, counting procedure, DATA Store, DATA Restore,
etc...

QUALI   is a program for qualitative analysis by WDS-Scanning
OUTPUT are : element symbols, characteristic wavelength
peak minus background intensities on peak position

CØRREX   is an "ON LINE" ZAF correction which uses I/Ø perma-
nent files

CORX   is an "OFF LINE" ZAF correction which uses also I/Ø
permanent files

QUANTI   is a shortcut for quantitative analysis of specimen
belonging to the same family as those already studied
in a former problem by runing CØRREX. The OUTPUT
files of CØRREX are then used as INPUT Files for
QUANTI

PHYSIC   Prints experimental conditions of analysis and perma-
nent physical quantities encountered in the ZAF
Calculation. This full list is skipped in a regular
run of CØRREX.

3 - LEAVING THE PROCEDURE

Before switching off the user runs BYE to maintain the sys-
tem in the proper initial conditions.

At first sight this list of routines may appear a little
bit redundant but it is the only way to avoid endless chattering with
the computer running a multipurpose program .

The set of procedures summarized herein has a great
flexibility and high efficiency.

REFERENCES

(1) – D.R. Beaman, A critical examination of computer programs used
in quantitative electron microprobe analysis,
Anal. Chem. 42, 13, 1540-1568 (1970)

(2) – J. Colby, MAGIC IV, A new improved version of MAGIC,
Proc. of the VIth Nat. Conference of E.P.A.S.A., Pittsburgh (1971)

(3) – J. Hénoc, K.F.J. Heinrich and R.L. Myklebust, A rigorous correction
procedure for quantitative electron probe microanalysis (COR2),
NBS TN-759, National Bureau of Standards, US Department of Commerce (1973)

(4) – H. Yakowitz, R.L. Myklebust and K.F.J. Heinrich, An on-line correc-
tion procedure for quantitative electron probe microanalysis, NBS
TN-796, National Bureau of Standards, US Departement of Commerce (1973)

(5) – S.J.B. Reed, Electron Microprobe analysis, Cambridge University
Press (1975)

CAMAC* INSTRUMENTATION AND INTERFACE SYSTEM FOR COMPUTER AUTOMATED MEASUREMENT AND CONTROL

Louis Costrell
National Bureau of Standards
Washington, D.C. 20234

The CAMAC* instrumentation system for computer automated measurement and control is gaining wide international acceptance for industrial and laboratory applications. The system features a fully specified dataway together with modular functional units that are completely compatible with each other and that are available from diverse sources. The system is non-proprietary and can be freely used without license or restriction of any kind.

CAMAC has a high degree of computer independence, providing system flexibility and resulting in reduction of special hardware and of software effort. The multisourcing advantage and the ability to considerably reduce stores inventories are attractive in many applications. Since updating and restructuring of systems can be readily accomplished with minimum engineering effort and with low hardware and software costs, system obselescence is radically reduced.

The CAMAC system is defined in standards documents of the Institute of Electrical and Electronics Engineers (IEEE) and the International Electrotechnical Commission (IEC) based on reports of the NIM Committee (National Instrumentation Methods Committee) of the U.S. Energy Research and Development Administration and the ESONE Committee of European Laboratories, as listed in Table II**

The basic CAMAC Standard (IEEE Std 583-1975) specifies CAMAC modules and crates together with a data highway (Dataway) and "rules of the road" for the Dataway and Dataway signals. Also defined are:

(a) A serial highway interface system for interconnecting CAMAC crate assemblies and for communicationg between crates and computers or other external controllers, using bit serial or byte serial data transmission (IEEE Std 595-1976).

(b) A parallel highway interface system, also for use with crate assemblies but using bit parallel transmission of data (IEEE Std 596-1976).

(c) Recommended block-transfer alogorithms to increase system compatibility by encouraging the use of a limited number of such algorithms (IEEE Std 683-1976).

ERDA reports have been published on CAMAC analog signals in a 50Ω system (TID-26614) and on CAMAC software (TID-26615 and TID-26619). An ERDA report on multiple crate controllers for distributed control in CAMAC system is to be issued as TID-26617. The use of CAMAC in various industrial, laboratory, medical and aerospace applications is described in the literature.

---

*Computer Automated Measurement and Control
**Though the IEEE Standards and ERDA reports are referred to in this paper, the corresponding IEC, EUR and ESONE documents listed in Table II are equally applicable.

There is an increasing awareness of the importance of software economy in installations involving computers. The standardization and transportability of software becomes feasible with CAMAC systems because of the standardized Dataway operations and the high degree of computer independence. Developments in CAMAC software have been described in the literature including a set of standardized subroutines and an intermediate language (IML) for CAMAC applications. A standard on IML has been issued and a standard on Real-Time BASIC for CAMAC is to be issued soon.

Software implications in industrial control applications of CAMAC, based largely on compatibility with Fortran, have been studied. Program transportability using CAMAC was demonstrated at the 1973 Purdue Workship on Industrial Computer Systems and reported on at the 1974 Annual Meeting of the Instrument Society of America.

A significant number of users in the industrial and medical areas and in a variety of laboratories in America, in Europe and in other parts of the world have independently arrived at the conclusion that CAMAC is cost effective. Table I lists the numerous advantages of CAMAC that have been important factors in the decisions to implement CAMAC systems and that are directly or indirectly translatable into cost savings. CAMAC is truly a user-developed system which permits the configuration of installations that can be easily upgraded with time and which can be made practically independent of the control computer except for small sections of hardware and software. Updating of installations, such as industrial control systems, has traditionally been very difficult. Since these difficulties are not present in CAMAC systems with standardized multisource functional units, economical modernizing of systems utilizing CAMAC instrumentation will become a fact of life.

TABLE I - ADVANTAGES OF CAMAC

1. FLEXIBILITY - INTERCHANGEABILITY
2. OPTIMIZATION OF SYSTEMS
3. EASE OF RESTRUCTURING
4. DEFERRED OBSOLESCENSE, UPDATING CAPABILITY
5. HIGH DEGREE OF COMPUTER INDEPENDENCE
6. REDUCTION OF INTERFACES
7. READY INTERCHANGE BETWEEN INSTALLATIONS
8. REDUCTION OF INVENTORIES
9. INCREASED UTILIZATION
10. EASE OF SERVICEABILITY
11. REDUCTION OF DOWN TIME
12. ON-THE-SHELF BLANK MODULES
13. REDUCTION OF DESIGN EFFORT
14. AVAILABILITY OF NUMEROUS COMPATIBLE INSTRUMENTS FROM MANY COMMERCIAL SUPPLIERS
15. SOFTWARE ECONOMIES

TABLE II - CAMAC SPECIFICATIONS AND REPORTS

Title	IEEE Std No.	IEC No.	ERDA No.	EURATOM (EUR) No. or ESONE No.
Modular Instrumentation and Digital Interface System (CAMAC)	583-1975*	516	**	EUR 4100e
Serial Highway Interface System (CAMAC)	595-1976	††	**	EUR 6100e
Parallel Highway Interface System (CAMAC)	596-1976*	552	**	EUR 4600e
Block Transfers in CAMAC Systems	683-1976	††	**	EUR 4100 suppl
CAMAC Instrumentation and Interface Standards†	SH06437† (Library of Congress No. 76-39660)	-	-	-
Amplitude Analoge Signals within a 50Ω System	-	-	TID-26614	EUR 5100e
The Definition of IML - A Language for use in CAMAC Systems	-	-	TID-26615	ESONE/IML/01
Distributed Control in CAMAC Multiple Crate Controllers	-	-	TID-26617††	††
CAMAC Tutorial Articles	-	-	TID-26618	-
Real-Time BASIC for CAMAC	-	-	TID-26619††	ESONE/RTB/02††

*Includes supplementary information

**Superseded by corresponding IEEE Standard listed.

AVAILABILITY OF DOCUMENTS

IEEE — IEEE Service Center, 445 Hoes Lane, Piscataway, New Jersey 08854, U.S.A.

IEC — International Electrotechnical Commission, 1, rue de Varembe, CH-1211 Geneva 20, Switzerland

ERDA (TID Reports) — National Bureau of Standards, Washington, D.C. 20234, U.S.A., Attn: L. Costrell

EURATOM — Office of Offical Publications of the European Communities, P. O. Box 1003, Luxembourg

ESONE — Commission of the European Communities, CGR-BCMN, B-2440 GEEL, Belgium, Attn: ESONE Secretariat, H. Meyer

A Computerized CAMECA Ion Probe System

James R. Roth and G. H. Morrison

Department of Chemistry
Cornell University
Ithaca, N. Y. 14853

Most solid materials are complex assemblages of chemically differenti-
ated microstructures. It is obvious that a thorough understanding of such
a material comes only from a knowledge of its component parts and their
interrelationships.

Ion sputtering mass spectrometry is capable of performing both surface
and interior microanalysis of solid materials for all elements from H to U
at sensitivities in the parts-per-million range and below depending on the
element and the matrix. Since ion sputtering is used to remove material
from the surface of the sample and generate data, microcompositional infor-
mation can be obtained on a three-dimensional basis. Thus, in addition to
lateral images of the surface, concentration profiles can be established
over depths varying from less than 1000 Å to several microns.

The CAMECA ion microprobe is capable of several modes of analysis.
The mass scan mode is usually the first mode used in analyzing a new sample.
Normal analog magnet mass scans provide identification of species present
as well as an indication of relative amounts of each. Computerized mass
scans produce upwards of 65,000 data points covering the mass range of H
to U.

Quantitative single element measurements are rapidly made for elemen-
tal concentration calculations. The data requirements are minimum once a
detailed knowledge of the sample is known.

Depth profile measurements are widely used to provide concentration
depth profiles of several elements over several microns in depth. Up to
30 preselected masses using line scan techniques can produce several
hundred thousand data points for a single depth profiles to a few microns.

Computer analyses of the lateral surface images produced by the CAMECA
ion microscope provide quantitative information about lateral distribution
of an element. Since this is an off-line computer system it has been
covered in a separate study.

The system hardware on the PDP 11/20 computer consists of two separate
components. The data acquisition hardware provides computer acquisition of
ion microprobe information for its various modes of operation. Computer-
instrument hardware provides for ion probe instrument control for selected
modes of operation.

The acquisition hardware functions around a sophisticated computer
programable clock that provides time resolution from one microsecond to
several days and controls the data acquisition pulse counters as well as
the digital-to-analog converter connected to the magnet control system.

Variable times are allowed for magnet shifts and data acquisition with no loss of time resolution or data collection dead time. Figure 1 is a block schematic of the clock and data acquisition system.

The computer control system for the ion microprobe is limited to two functions. The main function is the control of the magnet for mass scans and multielement depth profiles. A 16-bit optically isolated digital-to-analog converter either loaded on command from the computer or by the clock interrupt pulse from the acquisition system provides for magnet control.

An optically isolated computer controlled offset voltage is available for the sample high voltage for analysis of insulating samples. There are various other signals from the ion microprobe to the computer as indicators of instrument conditions.

The software system is broken into several parts which in general are all part of a main interpretative control program. This program allows for mass scans, depth profiles for up to 30 individual masses, and soft and hard copies of the data.

Figure 1. TIMING AND PULSE COUNT DATA ACQUISITION SYSTEM
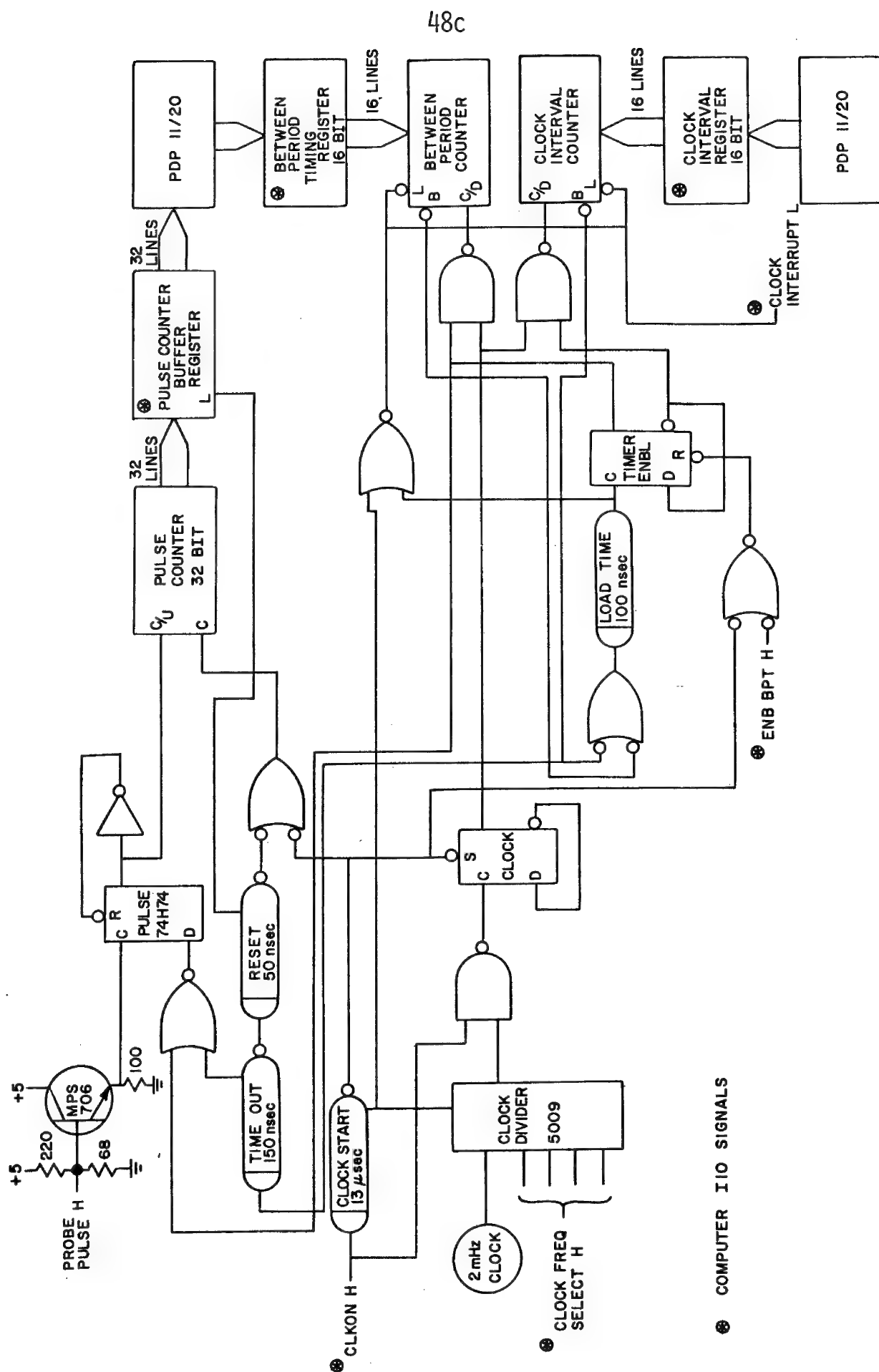
AUTOMATED ELECTRON MICROPROBE: PERFORMANCE AND USE TECHNIQUES

W. R. DeBoskey and G. H. Glade

IBM

This paper will describe and discuss the operational techniques developed through use, and the resultant performance of a commercial automatic electron microprobe. This system is a combined instrument capable of 100 Å secondary electron resolution with both WDX and EDX spectrometers. At microprobe current levels of 100 ua at 20 KeV the resolution is 2000-4000 Å with better than one percent per hour stability using a tungsten wire filament. The automation controls beam positioning, data gathering, and data reduction envolving interactive WDX qualitative, EDX qualitative/ quantitative and WDX quantitative programs.

The WDX quantitative program may utilize the X-Ray reduction routines of Bence-Albee (oxide or metal), Magic IV, or Frame B. Comparative results will be presented. Elements defined for analysis are standardized per the instrument set parameters. Slight instrument non-stability during initial standardization usually requires re-standardization via separate specific command. Since each analysis determination is very rapid due to the interactive programming, the data reduction result becoming available within seconds of the last data entry, the technique of check analyzing, each pure element standard was introduced to ascertain and improve the quality of element standardization.

Typical statistical data ($\bar{X}$, S & R) taken for the standardization of the NBS 479 Chromium Iron-Nickel microprobe standard are: Chromium, 1495.45 c/s, 11.31, 35.21; Iron, 1283.46 c/s, 5.67, 16.04; and Nickel 812.23 c/s, 5.11, 13.90 at beam conditions of 15KeV and 30 ma. Subsequent check analysis of the pure elements gave: Chromium, 1498.66 c/s, 8.25, 19.22; Iron, 1284.74 c/s, 6.34, 18.69; and Nickel, 816.33 c/s, 8.36, 20.86 yielding 100.29%, 0.56, 1.35; 100.06%, 0.55, 1.42; and 100.45%, 1.08, 3.06 corrected data analysis for the three elements.

The accessed accuracy and precision of the unknown analysis as defined by the NBS microprobe standard is one percent or less with a sigma of one half of one percent or less, based on a limited number statistic. Such a limited statistic three element set-up and quantitiative analysis is conveniently completed in one day. Accuracy is defined as the difference between the statistical data mean and the NBS chemical pedigree value.

COMBINED EDS AND WDS ANALYSIS
WITH AN AUTOMATED ELECTRON MICROPROBE

J. J. Friel,[*] J. I. Goldstein,[*] J. J. McCarthy[**] and N. F. Wodke[**]

*Department of Metallurgy & Materials Science, Lehigh University
**Tracor Northern, Inc., Middleton, Wisconsin

INTRODUCTION

The advantages and disadvantages of using an energy dispersive detector rather than the traditional wavelength dispersive spectrometer for quantitative X-ray microanalysis have been discussed at some length in the literature.[1][2] The advent of combined EPMA-WDS-EDS and SEM-WDS-EDS instruments makes it possible to compare the performance of EDS and WDS under more closely controlled experimental conditions. It is also possible to investigate conditions under which this type of combined instrument may be used most effectively.

The introduction of sophisticated automation packages for the wavelength spectrometer complicates the picture further by providing a speed of analysis for WDS comparable to that achieved by EDS.[3] The elemental sensitivities that can be achieved by EDS and WDS analysis may also be subject to modification by the addition of an automation system. This paper presents the results of several studies carried out on an automated combined EPMA-WDS-EDS instrument.

INSTRUMENTATION

The data were acquired with the ARL-EMX microprobe at Lehigh University. The microprobe has three WDS spectrometers which have been reworked for automation. A Princeton Gamma-Tech EDS detector has been mounted on the microprobe with the same X-ray take-off angle (52.5°) as the WDS spectrometers. Automation of data acquisition and reduction from both types of detectors is under the control of a mini-computer-based automation system supplied by Tracor Northern. A unique feature of this system is the ability to simultaneously acquire data from the WDS and EDS detectors and to reduce the combined data on-line. The EDS data reduction is a fully quantitative procedure based on the multiple least square (with digital filter) routine supplied with the automation system.[4] This technique has been shown to yield quantitative results even in the presence of difficult background or overlap problems.

COMPARISON OF EDS AND WDS

An attempt was made to evaluate each of these detection systems by performing EDS, WDS, and combined analyses on one material. The sample chosen was a well-analyzed chromite standard. All analyses were made under identical conditions; namely, 15 kv accelerating voltage and 0.05 μa specimen current. A dead time of ~ 25% was measured on the solid state detector and was due to the presence of a graphite collimator between the sample and the solid state detector. This collimator arrangement permits combined EDS-WDS analyses with the same beam current.

The sample was analyzed for: Fe, Cr, Al, Mg, Ti, Mn, and Ni. Three of these were present in concentrations of < 1% (Ti, Mn, Ni), which provided a test of the minimum detectability for each system. The light elements, Mg and Al provided a test for the fitting routine in the low energy region of the spectrum.

The results of these analyses are given in Table I, and the EDS spectrum is shown in Fig. 1. It is apparent that both techniques give similar results for major elements. Even the relatively light elements, Mg and Al, are adequately analyzed with EDS. The minimum detectability, however, is better for WDS, but the analytical sensitivity is similar.

The detectability limits were calculated from the Ziebold equation as follows:[5]

$$C_{DL} \geq 3.29a/(n \tau P \cdot P/B)^{\frac{1}{2}}$$

where "a" (Ziebold-Ogilvie factor) is assumed equal to 1; n = 1 (number of repetitions); τ (counting time) = 100 secs. for EDS and 30 secs. for WDS; P and P/B are peak intensity and peak to background ratio obtained from a pure element standard. The analytical sensitivity was calculated from the following relationship:[5]

$$C \geq \frac{2.33C \cdot 2\sigma_c}{(\bar{N} - \bar{N}_B)}$$

where C = measured concentration in weight fraction; $\sigma_c = \sqrt{\bar{N}}$ (the theoretical standard deviation); $\bar{N}$ = the average total number of counts; $\bar{N}_B$ = the average background counts. Since the actual standard deviation is usually about two times larger than σ_c, that value was used for the sensitivity calculations. The sensitivities for trace elements present in concentrations approaching the detectability limit was set equal to the minimum detectability limit. A counting time of 100 secs. for EDS produced about the same number of counts under the characteristic peak for each element as a counting time of 30 secs. for WDS. This accounts for the similar sensitivities. The total count rate of the solid state detector was 5000 counts/sec. This result can be compared with 1000-5000 counts/sec. for the peak of each of the major elements with WDS.

The combined analysis was only slightly faster than the others, but if more elements were analyzed the speed advantage would become more apparent. Combining the systems does, however, offer the flexibility of analyzing trace elements or very light elements with crystal spectrometers and all others simultaneously with the solid state detector. This usually allows the crystals and possibly even the spectrometers to remain fixed thus improving reproducibility. In these analyses no attempt was made to optimize operating conditions for any particular element or for trace elements. Conditions were chosen such as might be used to analyze a broad range of elements at the same time with the combined detection systems.

Another test of the combined analysis technique comes from a multielement analysis of a lunar, rare earth element-bearing, calcium phosphate mineral (whitlockite).[6] In all, 23 elements were analyzed. All of the rare earth elements were taken with WDS because of peak overlaps and low concentrations. The L peaks in these elements are often within 25 ev of each other, which approaches the limit of resolution of even the crystal spectrometers. Fluorine (Z=9) was also analyzed by WDS because of its long wavelength. Eight other elements (Ca, P, Fe, Na, Si, Mg, Y, Cl) were analyzed simultaneously with EDS, and the results are shown in Table II.

The time required to acquire this data was 12 min., and 25 min. were required for the minicomputer to perform an on-line ZAF matrix correction. In this case the combined system permitted the analyses to be taken without changing analyzing crystals, which would otherwise have been required. Even though the total time was 37 min., the automation system performed the multielement analysis efficiently and reproducibly.

BENEFITS OF COMBINATION EDS-WDS INSTRUMENTS

On the basis of the results given above, it is possible to conclude that WDS and EDS may be viewed as complementary analysis techniques. On an automated instrument these benefits

include the ability to assign difficult measurements (light elements, low concentrations, serious overlaps) to the WDS while simultaneously analyzing remaining elements with the EDS. The result is a significant increase in analysis efficiency with little or no compromise in accuracy.

REFERENCES
1. D. R. Beaman and J. A. Isasi, Electron Beam Microanalysis, ASTM Special Publication 506, ASTM, Philadelphia, Pa.
2. E. Lifshin, M. F. Ciccorelli and R. B. Bolon, Practical Scanning Electron Microscopy, J. I. Goldstein and H. Yakowitz eds., Plenum Press, 1975, Chap. 6.
3. J. D. Geller, Minimum Detection Limits in An Automated Microprobe, Proc. 11th Ann. Cont. Microbeam Analysis Society, Miami Beach, Fla., 1976, pp. 73A-73G.
4. F. H. Schamber, A Modification of the Linear Least Squares Fitting Method which Provides Continuum Suppression, in X-ray Fluorescence Analysis of Environmental Samples, T. G. Dzubay, ed., Ann Arbor Science, 1977, p. 241.
5. J. I. Goldstein and J. W. Colby, Practical Scanning Electron Microscopy, J. I. Goldstein and H. Yakowitz, eds., Plenum Press, 1975, Chap. 12.
6. J. J. Friel and J. I. Goldstein, The Relationship between Lunar Metal Particles and Phosphate Minerals, Lunar Science VIII, 1977, pp. 325-327.
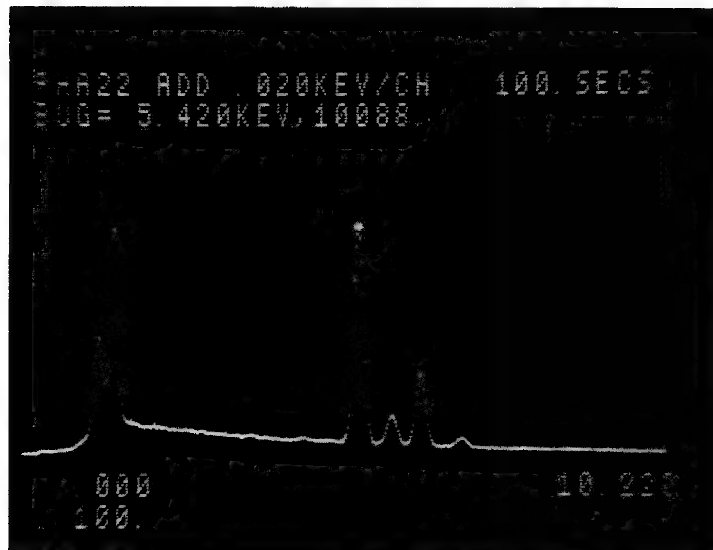
Figure 1: EDS spectrum of chromite standard between 0 and 10 kev.

TABLE I

WDS/EDS COMPARISON

TYPE OF ANALYSIS	XTAL	WDS CONC.(WT%)	ΔC	C_{DL}	EDS CONC.(WT%)	ΔC	C_{DL}	WDS/EDS CONC.(WT%)	ΔC	WET CHEM
FeO	LiF	21.84	.57	0.05	21.60	0.52	0.23	22.85 E	0.52	22.09
TiO_2	LiF	0.41	.06	0.02	0.45	0.15	0.15	0.39 E	0.15	.46
MnO	LiF	0.38	.06	0.01	0		0.31	0.39 W	0.06	.21
Al_2O_3	RAP	20.52	.50	0.07	20.18	0.32	0.07	20.80 E	0.32	19.40
MgO	RAP	13.25	.36	0.03	13.83	0.38	0.06	13.36 W	0.36	12.21
Cr_2O_3	LiF	44.43	.53	0.03	44.28	0.74	0.19	43.94 E	0.74	44.55
NiO	LiF	0.05	.07	0.05	0		0.28	0.01 W	0.05	.14
V_2O_3		n.a.*			n.a.			n.a.		.25
CoO		n.a			n.a.			n.a.		.04
TOTAL		100.89			100.34			101.73		99.35
COUNTING TIME/EL.		30 sec.			100 sec.			30/100		
DATA ACQUISITION TIME		3.5 min.			1.7 min.			1.7 min.		
DATA REDUCTION TIME		.5 min.			2.0 min.			1.9 min.		
TOTAL TIME		4.0 min.			3.7 min.			3.6 min.		

*n.a. = not analyzed
E = EDS
W = WDS

TABLE II

MULTI-ELEMENT ANALYSIS OF
LUNAR WHITLOCKITE MINERAL

Elements Taken WDS		Elements Taken EDS	
Element	Conc. (wt%)	Element	Conc. (wt%)
La_2O_3	0.82	CaO	42.12
Ce_2O_3	1.99	P_2O_5	45.50
Pr_2O_3	0.35	FeO	1.67
Nd_2O_3	1.17	MgO	3.10
Sm_2O_3	0.35	Na_2O	0.72
EuO	n.d.	SiO_2	n.d.
Gd_2O_3	0.23	Cl	0.10
Tb_2O_3	0.11	Y_2O_3	2.17
Dy_2O_3	0.11		
Ho_2O_3	0.22	TOTAL	100.92
Er_2O_3	0.002		
Tn_2O_3	0.11		
Yb_2O_3	0.05		
Lu_2O_3	0.03		
F	n.d.		

OPERATING CONDITIONS: WDS COUNTING TIME = 30 sec./el.

EDS COUNTING TIME = 60 sec./el.

SPECIMEN CURRENT = 0.05 μa

E_o = 15 Kv

DATA ACQUISITION TIME = 12 min.

DATA REDUCTION TIME = 25 min.

TOTAL TIME = 37 min.

A Modular Microprobe Automation System

J. J. McCarthy and F. H. Schamber

TRACOR NORTHERN, INC.

Middleton, Wisconsin

INTRODUCTION

In the past several years the use of Si(Li) detectors and minicomputers for X-ray analysis has grown rapidly. Despite the advances in silicon detector technology and improvements in EDS data reduction techniques, the superior resolution and light element coverage of the WDS spectrometer require its use for some analysis problems. Some major disadvantages of the WDS spectrometer compared to an EDS detector are the following:

1) A WDS spectrometer can analyze only a single element at a time.

2) WDS spectrometers are complex mechanical devices that require careful positioning.

3) High precision WDS spectrometers are relatively expensive.

A carefully designed automation system can offset these disadvantages by permitting high speed spectrometer operation with minimal operator intervention. Data acquisition time can be reduced substantially by operating several spectrometers simultaneously. Human errors are reduced and instrument throughput increased by eliminating manual positioning operations. Finally, automated crystal changing coupled with high speed positioning can reduce the number of WDS spectrometers required in an instrument and thus lead to substantial cost savings.

This paper will describe the components of a minicomputer-based automation system (denoted as MECCA, an acronym for Modular Electron Column Control and Automation) that provides digital control and data reduction for both WDS and EDS spectrometers. Difficulties that arise in automating WDS spectrometers and solutions to such problems will also be discussed.

HARDWARE

An overall view of the hardware is presented in Figure 1. The three basic components are the Central Processor (DEC PDP-11), a Data Acquisition Control Terminal (NS-880), and an Automation Interface (TN-1310). The control terminal includes various input and output interfaces, a CRT data and character display, ADC interface, and cassette mass storage system.

The interface hardware consists of various special purpose modules such as scalers,

LED readouts, dual DACs (Digital to Analog Converters), axis positioners, parallel I/O registers, and timers. Each module consists of one or more printed circuit boards that are plugged into slots in a single system chassis about the size of a NIM instrument bin. Modules in the chassis may communicate with each other along an internal data bus, or with the system computer via the CPU bus. Up to twenty-one modules can be put into a single chassis. The modular format allows the system to be easily expanded by adding additional modules as required. The interface may be reconfigured at any time by pulling a module out of the chassis, with no effect on the remaining modules. Additional modules provide manual control functions for backup or semi-automated operation.

SOFTWARE

The system software is composed of a mixture of assembly language library routines and a high-level interpretive language (FLEXTRAN). The assembly language routines are used to perform a variety of device control operations where rapid execution speed is essential. The overall control and data reduction programs are written in the interpretive language which allows convenient program modifications for the addition of new functions or modification of existing ones.

At the time it is initialized the control routine has the ability to "poll" each of the modules present in the chassis and determine its type. This permits the system software to automatically configure itself for the type and number of modules present.

Many of the system modules (timer, scalers, stepping motor controllers) are driven by interrupt-level routines which permit operation of these modules to occur simultaneously with each other and with background computations. The multi-tasking structure of the control software also permits multi-step operations to be performed simultaneously. For example, one spectrometer can be performing a peak search while another is performing a crystal change.

APPLICATION TO MICROPROBE AND SEM AUTOMATION

The system has been used to automate a variety of WDS spectrometers, including modern types designed for stepping motor operation, and older models that have been reworked for automation. Mechanical registration is maintained with a combination of hardware and software techniques, including automatic backlash takeup, provisions for sensing limit and proximity switches, and ramping speed transitions for high stepping speeds. Other effects (shifts of the peak position with crystal change, electronic noise in one counting channel due to motion of a spectrometer) are addressed by purely software measures.

Very good reproducibility and high precision can be obtained with a modern automated spectrometer. Performance data for two such spectrometers are presented in Table I. The numbers in parenthesis are the RMS deviations after repeated positionings. Two different algorithms were used to calculate the peak

location after scanning; a centroid calculation (Part A) and a Quartic Fit (Part B). Both techniques produce peak locations that are reproducible to within the spectrometer specifications.

An important aspect in achieving rapid and reliable operation is the interface to the human operator. An extensive applications program has been written for this system which responds to a set of english language commands issued by the operator. One group of commands performs single-step operations such as moving a stage axis (POSITION TO 1000) or a spectrometer (SPECTRO TO 1.540), counting (COUNT) or defining system variables and constants (DEFINE, SET). These commands are useful in initialization procedures and during set up stages of an analysis. A group of more complex commands each perform an entire measurement and data reduction process, such as peak searching followed by peak and background intensity measurement and k-ratio calculation (MEASURE). Finally, another set of commands call specific matrix correction subprograms (ZAF, BA). For routine repetitive analysis, these commands may be grouped into "schedules" that can be executed by a single command or stored for later recall and use. A typical schedule, with example output, is shown in Figure 2. In either mode of operation different operations may be in progress upon several devices simultaneously.
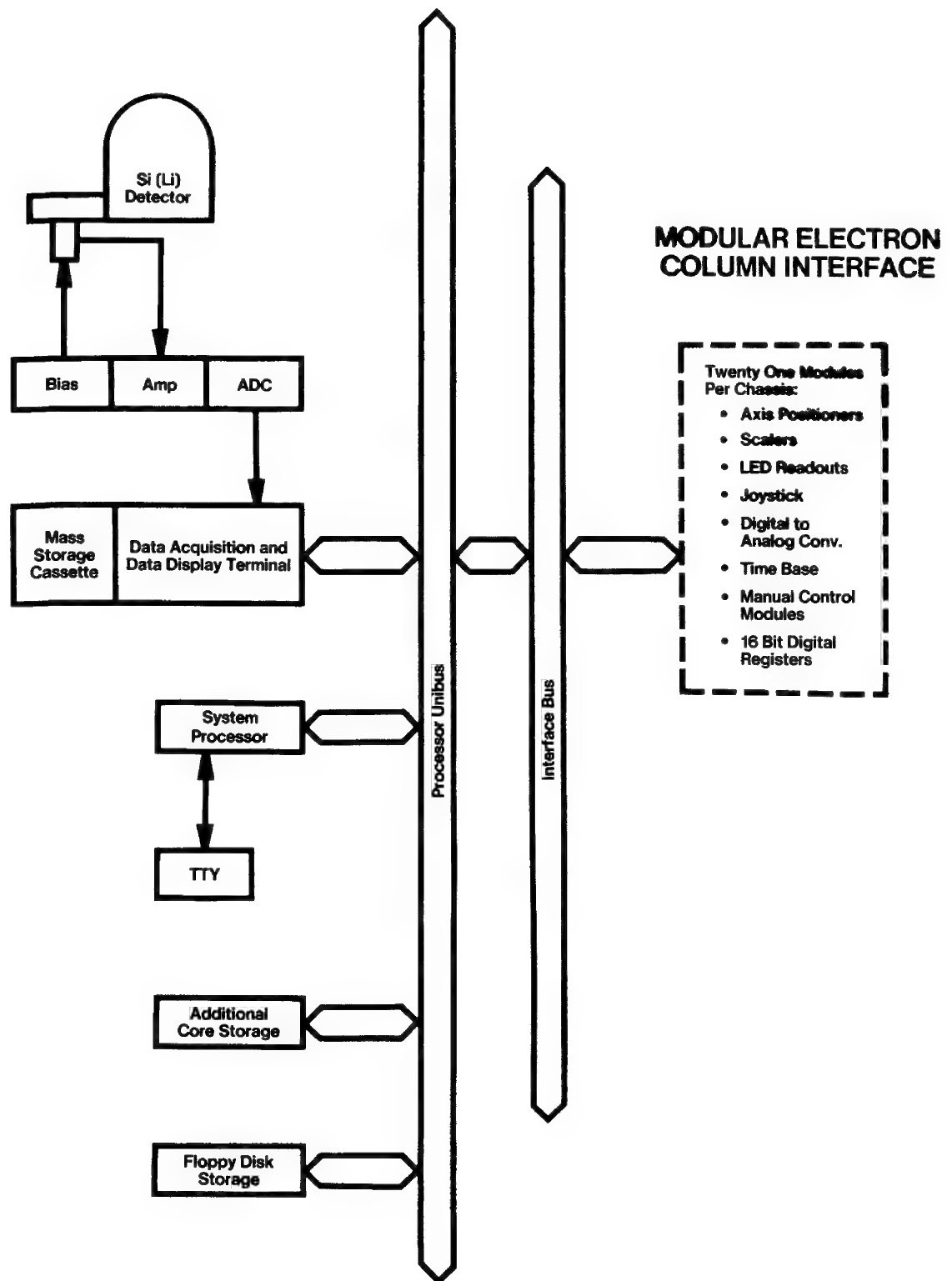
FIGURE 1. Mecca System Block Diagram

TABLE I. PERFORMANCE DATA FOR AUTOMATED SPECTROMETERS

A. MICROSPEC SPECTROMETER

X-ray Characteristic Line	Crystal Type	Expected Position	Average Experimental Position	Peak to Background	
				Measured	Mfgrs. Specs
ALK	RAP	1.2856	1.2857 (.0007)	2015:1	1300:1
CK	STE	1.787	1.784 (.003)	108:1	90:1
TIK	PET	1.2665	1.2660 (.0002)	470:1	450:1
CUK	LIF	1.5418	1.5414 (.0001)	270:1	250:1[a]

B. CAMECA SPECTROMETER: (ALK$_\alpha$, TAP CRYSTAL)

Spectrometer	Average Experimental Position	Intensity
Inclined	32381 (.8)	199747$\pm$0.33%
Vertical	32556 (.8)	237005$\pm$0.23%
Inclined[b]	32387 (4.4)	195096$\pm$0.61%
Vertical[b]	32561 (.6)	235530$\pm$0.32%

a. This data taken without collimator slits in position.

b. This data taken with intervening crystal change.

```
.LIST SCHED GC
>GC
>*P !"GOLD-COPPER">WT 0
>PKCNT CUK 20,AUM 20
>ZAF 20 2 CUK AUM
>GET SCHED GC
>END
```

SCHEDULE OUTPUT

```
    GOLD-COPPER
    BG CNTS= 2573.47

    CUK PK POS=1.5444 K RATIO= 8.14529E-01
    ASPEC LIF 2.60002E+05 CTS 1.30001E+04/SEC 1.30001E+04/BEAM
    BG CNTS= 617.73

    AUM PK POS=2.2145 K RATIO= 1.36345E-01
    BSPEC ADP 1.53902+04 CTS 7.69513E+02/SEC 7.69513E+02/BEAM

    ZAF CALCULATION
    NO. OF EL= 2
    EXCIT. ENERGY= 20 KV
    CSC=   1.2605

    ITER 2
         K     [Z]     [A]     [F]    [ZAF]   CONC
    CU  0.814  0.958  1.009  1.000  0.967  0.788
    AU  0.136  1.221  1.242  0.999  1.516  0.206
    TOTAL=  0.995
```

FIGURE 2: EXAMPLE ANALYSIS SCHEDULE

AUTOMATED ELECTRON MICROPROBE ANALYSIS: A SYSTEM FOR THE ARL-SEMQ BASED ON MASS STORAGE AND SPEED CAPABILITIES OF THE FLEXIBLE MAGNETIC DISK

W. J. Hamilton, J. R. Hinthorne, L. A. Ray, and T. A. Whatley

Applied Research Laboratories
9545 Wentworth Street
Sunland, California 91040

INTRODUCTION

An automated data collection and reduction system for quantitative electron microprobe analysis has been designed to utilize the bulk storage capacity, relatively high speed, and random access capability of the magnetic "floppy" disk. These capabilities provide distinct advantages over systems operating from paper tape or tape cassette. Among the advantages realized are: (1) the ability to program more complicated tasks, since program segments may be loaded rapidly from the disk as needed; (2) the elimination of time consuming chores such as determining spectrometer positions from wavelength data and correction coefficients for data reduction from published tables and keyboard entry of these parameters, by storing all such data on disk files and accessing as needed during program execution; (3) the storage of intermediate results, such as data acquired on standards, which allows repeated collection and reduction of data from unknowns without repeated entry of the data or re-standardizing; (4) the ability to avoid repeated entry of data and operating parameters by permitting the user to create permanently resident disk files of data for his standards and commonly used analytical parameters which may be called up from the disk for repeated future use; (5) the ability to communicate between programs written, compiled and/or assembled in various programming languages through common access to disk files, e.g., MAGIC IV, a data reduction FORTRAN program, uses disk data files created by BLISS (Basic Language Integrated Software System) programs; (6) the ability to commit more core memory to conversational operator-computer communication as a result of the automatic loading of modular program segments allows a far higher level of operator control and interaction; and (7) the low computer hardware cost compared with "hard disk" systems.

BLISS is an exceptionally user-oriented version of BASIC emphasizing simplified programming of instrument control, typical data reduction calculations, mass storage access for programs and data, and program editing and testing.

FUNCTIONAL MODULES

Program modules have been created to operate as a system from the setting up of user standards and operating parameters through standardization, analysis, data reduction and printout. The programs link together in proper sequence automatically and will cycle repeatedly through data collection and reduction with automatic stage positioning or operator selection of individual analysis points. The operating parameters and other data are accessed as needed from the files. The program modules include: (1) a program to construct files containing data on compositions, stage positions, etc. of standards; (2) a program to construct files of user-defined analytical parameters such as elements and x-ray lines to be analyzed, spectrometer assignments, accelerating voltage, data reduction scheme and other operating functions allowing repeated use of a particular analytical procedure; (3) a program module to define beam conditions and operating conditions particular to a given analytical run; (4) programs to perform data acquisition for standardization and for unknowns analysis; (5) programs to provide "on-line" data correction by a variety of accepted methods, print-out results and return to data acquisition programs. Additional data acquisition and reduction programs written in BLISS, FORTRAN or assembly language may be easily added to the system by individual users.

DATA FILES

Data are maintained on the disk in permanent, semi-permanent and transient data files. The permanent files include the x-ray data file and the alpha factor master tables; semi-permanent files include those containing the user-specified data on standards and instrumental operating parameters, and indexes to these files. Transient files are maintained to pass data between program modules including FORTRAN and BLISS programs.

The x-ray data file contains wavelengths of x-ray lines, absorption
edges, atomic weights, oxide formulas and similar data for 92 elements.
It is arranged in order of atomic number so as to allow easy random
access to the data. The data is called up by the programs and used
for such tasks as automatically computing and setting spectrometer
positions on wavelength-scanning spectrometers, thus eliminating these
time consuming procedures for the operator.

In a similar fashion master alpha factor tables (Albee & Ray, 1970)
have been provided so that data reduction by the method of Bence and
Albee (1968) may be performed on a given set of elements analyzed by
specifying only the accelerating voltage. Transfer of the specific
alpha factors from the master table to a transient file for an analytical
run is rapidly and efficiently accomplished under automatic program control.

DATA ACQUISITION

A combination of dual crystal scanning monochromators and optimized,
fixed wavelength monochromators are generally employed for the data
acquisition with the automated SEMQ. Using previously specified and
stored sets of parameters, peak seeking, peak counting and background
counting are accomplished automatically (and simultaneously on multiple
spectrometers, whenever possible). The minimum integration time is
specified by the operator when an analytical run is started; all fixed
channels, and scanning channels which have completed their assignments,
continually accumulate peak data (for improved statistics) while the
scanners complete their assignments. At the completion of an analysis
the data are organized and stored on disk in the proper format for the
operator-specified data reduction method.

DATA CORRECTION

Data correction is accomplished "on-line" through transfer of operating
parameters and raw x-ray intensity data in disk files to the data
reduction programs. Written in FORTRAN, "on-line" MAGIC IV provides
rapid quantitative results for analyses of up to 42 elements. Using an
assembly language routine, the Bence-Albee data reduction method pro-
vides very rapid and reliable corrections for mineralogical samples.

Additionally, a simple k-ratio output routine is included.

Printout of results and data is extensive allowing ease of interpretation and judgement of quality of data collected; e.g., the total peak and background counts and counting times for standards and unknowns are always included in addition to the calculated concentrations, k-ratios and names of the standards used for each element. Atom percent or formula proportions (for oxides) are automatically reported. In addition, the storage of results on user specified disk files allows future retrieval of the information for evaluation, digital plotting or other uses.

SUMMARY

A modular set of computer programs for integrated "on-line" data collection and quantitative data reduction has been constructed utilizing the best features of magnetic disk storage devices: random access, program linkage, high speed and data storage.

References

Albee, A. L. and Ray, L. A. (1970) Anal. Chem., 42, 1408-1414.

Bence, A. E. and Albee, A. L. (1968) J. Geol., 76, 382-403.

SOME RECENT WORK IN LOW ENERGY X-RAY PHYSICS. B. L. Henke

Department of Physics and Astronomy, University of Hawaii, Honolulu, Hawaii 96822.

1. <u>X-Ray Sources</u>--High intensity, monochromatic excitation sources are essential for quantitative studies of the emission processes for photoelectrons, Auger and secondary electrons and for fluorescent x-rays. Such sources are also needed for the calibration of the detectors and analyzers employed for these studies and for subsequent applications. In the low-energy x-ray region (10-100 A/100-1000 eV) the direct radiation from an x-ray tube anode, with the appropriate filter and anode voltage, may be sufficiently monochromatic because the line radiation often dominates the associated continuum radiation. The line-continuum profiles have been measured and will be presented here for several useful K, L, and M characteristic line sources in order to illustrate the effect of filters and anode voltage. The absolute brightness of these sources (in photon/sec-stearadian) will also be presented.

2. <u>Electron Spectroscopy</u>--The electron spectroscopy of x-ray produced photoemissions has recently become an important tool in surface analysis. Photoelectron and Auger electron spectroscopy most effectively probe core electron states and the secondary electron spectroscopy probes the valence electron band states of the surface material. The basic processes that determine the photoemission spectra are the excitation, transport and the escape processes. In order that electron spectroscopy can be fully realized as a quantitative tool, considerably more must be known of the physics of these processes. This is particularly the case for secondary electron emission which is the most complex and for which there is no complete theory at this time.

Theoretical model results will be presented here along with examples of recently measured secondary electron energy distributions of metals and dielectrics. The secondary emission spectra rise sharply from zero electron kinetic energy to a peak value of about one eV and with a FWHM usually in the two to five eV region. These are being measured with a resolution of .04 eV using a hemispherical electrostatic analyzer. A uniform preacceleration field is employed which permits the application of a simple and accurate correction for a change in electron optical brightness associated with preacceleration (acceptance energy of the spectrograph is set at 15 volts).

It is hoped that measurements as these will also be helpful in gaining a more complete understanding of the secondary electron contrast dependence upon the surface state in scanning electron microscopy, and in the choice of x-ray photocathode materials particularly as used for pulsed x-ray measurements for temporal resolutions in the picosecond region.

3. <u>X-Ray Spectroscopy</u>--The low energy x-ray spectroscopy has been demonstrated to be a very useful tool for light element analysis, valence band and molecular orbital analysis, and for high temperature plasma diagnostics. The light elements emit only in the long wavelength x-ray region. Spectra from all elements involving transitions from the valence or molecular orbital levels to the nearby, relatively sharp core levels are in the one-to-several hundred eV region and do sensitively portray important outer electronic state structure. Plasma in the ten-million degree range (astrophysical and CTR, for example) emit most strongly in the low energy x-ray region. To accomplish this type of x-ray spectroscopy, the simpler and higher efficiency crystal spectroscopy is sometimes more appropriate than the grating spectroscopy even though the latter is inherently capable of higher resolution.

Presented here will be some examples of atomic and molecular, fluorescent spectroscopy of gaseous and solid samples using the multilayer analyzer (Langmuir-Blodgett type). The measured reflection coefficients and resolution for the lead myristate crystal will be presented in detail. And a simple method for unfolding the spectrographic lines and for decomposing overlapping spectra in order to gain spectral resolutions in the 0.5 eV range will be described.

X-RAY OPTICS OF A "MICRO-DIFFRACTION" GONIOMETER

BY: H. Maruyama, T. Iwai, Rigaku Corp.,
12-9-3, Matsubara, Akishima, Tokyo
and V. E. Buhrke, Buhrke Corporation
2180 Sand Hill Road, Suite 160,
Menlo Park, California

Conventional X-Ray powder diffractometers are frequently used as indispensable tools for non-destructive analysis of the state of materials, but they are not suitable for obtaining diffraction patterns from a very small amount of and/or a very small area of samples. In order to overcome those difficulties, the authors have developed a "Micro-diffractometer" using the principle of X-Ray optics as shown in Fig. 1.[1]) With this diffractometer the following results have been obtained.

I) Diffraction patterns from samples as small as a few micrograms can be detected.

II) Even in the case where diffraction patterns show extreme spottiness in photo-graphic films, nearly ordinary diffraction recording can be obtained so that the identification of the samples is easy.

Aiming to increase the performance of this diffractometer, several improvements have been made this time.

In diffractometry, the intensity of the background shows not a constant but a broad maximum near at 40 degrees in 2θ angle, because of the effective width of a ring-shaped receiving slit has 2θ-dependence. This trend is enhanced when fluorescence x-rays yielded from a sample is too strong in such a way that makes it impossible to record almost all of diffraction peaks without any scale out. In order to avoid this inconvenience, we have developed a dual proportional counter and introduced the technique of balanced filter into the goniometer optics. The former is constructed so that two anode wires are arranged in turn along a center line of a doughnut-shaped counter as shown in Fig. 2. The two anodes are electrically independent of each other, and so the two counting signals are

independently taken out from each of the two sensitive regions of counter. Xenon

gas is filled at 1 atmosphere in the counter. The counting efficiency is 80%

for CuKγ radiations. In this way, moreover, when each of the balanced filters

is arranged over each of the windows of the counter so as to absorb the diffracted

intensity with different wavelength characteristics, we can obtain peaks diffracted

only by the characteristic X-Rays using the subsequent electronic circuit which is

constructed by two preamplifiers and ratemeters, and a differential amplifier.

For demonstration the diffraction pattern from Al_2O_3 powder is shown in Fig. 3 (a),

(b) and (c). Fig. 3(a) and (b) shows the chart recordings of diffraction filtered

by Ni and Co filters respectively. It is clearly shown that Fig. 3(c) gives a

nearly constant background intensity by the technique and diffraction peaks obtained

mostly within the width of the chart.

When grain size of a sample is larger compared with a cross section of incident

beam, the diffraction becomes frequently spotty so that the identification becomes

a difficult even by the present diffractometry. In order to overcome such difficulties,

we have introduced a mechanism into the specimen holder so that the specimen is

rotated or oscillated around an axis, for-instance, a horizontal axis not including

the direction of the incident beam. With this function we can get several peaks

so as to be able to identify the sample.

Moreover, we have tried a change of the driving mechanism of counter. This

is done by using numerical control for the straight movement of the counter. It

makes it easy to control the goniometer by a programmer. Of course, the movement

of counter is held so as to be linear for 2θ angle. In this paper the details

will be discussed.

1) H. Maruyama, T. Nomura and M. Yoshimatsu;
   S239, Tenth International Congress of Crystallography Collected Abstracts.

Fig.1 Schematic diagram of X-ray optical arrangement

Fig.2 Counting system block diagram
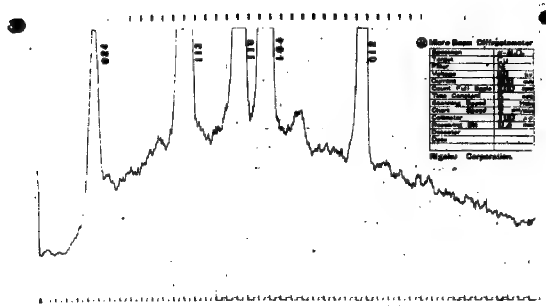
a) Ni-filter used
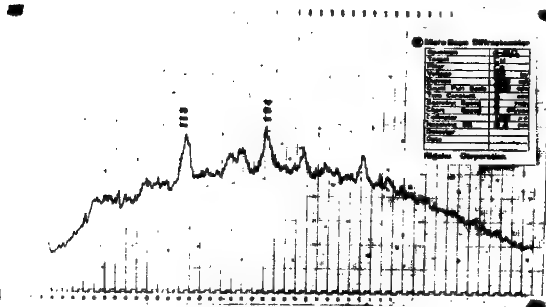
b) Co-filter used
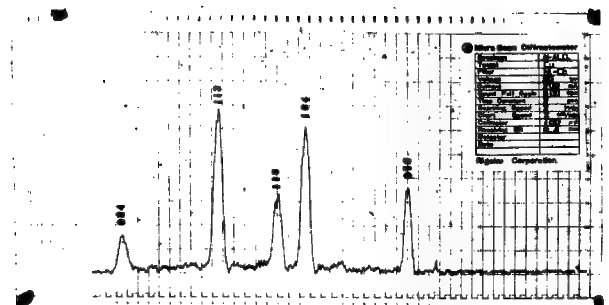
c) Ni-Co balanced filter used

Fig.3 Diffraction charts from Al_2O_3 powder

Development of an X-ray Stress Analyzer
for Field Service and its Applications

KATSUHIKO OGISO
Department of X-ray Diffraction
Rigaku Corporation
3-9-12,Matsubara, Akishima,Tokyo,Japan.

A portable, counter-method X-ray stress analyzer consisting
of four components according to function has been developed for
field use. This paper reports its construction, performance and
actual measurement examples.

On-site X-ray stress measuring operation has been so far coducted
by using Back reflection cameras because of their compactness.
However, in the case of measuring coarse grained materials such as
welded structures and castings, the resulting Debye rings are spotty,
making the reliability of the measurement very low. This is due to
the use of a collimator for their optics, which causes insufficiency
of the number of crystal grains that contribute to diffraction in
an X-ray irradiated areas.

The newly developed analyzer employs a soller slit for its improved
optics, broadening the X-ray irradiated area to 2x2 mm^2 to 4 x 16
mm^2. Further, coupled with the new introduction of the X-ray
incident angle oscillation method(ψ oscillation method), the analyzer
now makes it possible to measure Austenite grain size Nos. 3 to 4
with high accuracy as compared with the grain size Nos. 8 to 9 as
a measurable limit by the photographic method.

For ease of transportation, the analyzer is designed to be
separable according to function, with each component of a lightweight
and compact size.   Fig. 1 shows the overall view of the analyzer.
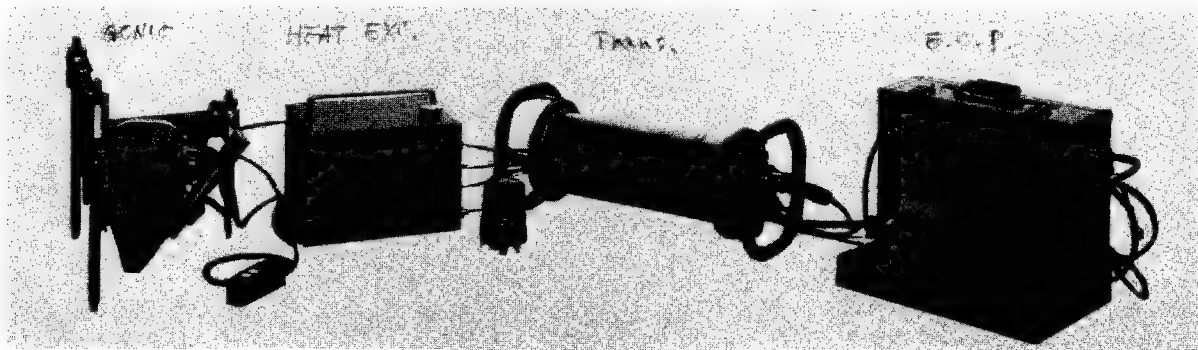
Fig.1 Overall view of the analyzer

The average weight of each of the four components is approximately
16 Kg, totalling less than 80 Kg (176 pounds). this is roughly
one - seventh of the weight of X-ray stress analyzer of the equivalent
performance on the market. The drastic reduction in size and weight
has realized measurements in such a location as shown in Fig. 2 where
it is extremely difficult to
gring and set the conventional
analyzer. This new analyzer is
being used for residual stress
measurements of welded portions
of the piping for atomic furnaces,
the stress relief effect of stress
corrosion cracking in chemical
plants, and others, and is providing
valuable informations.
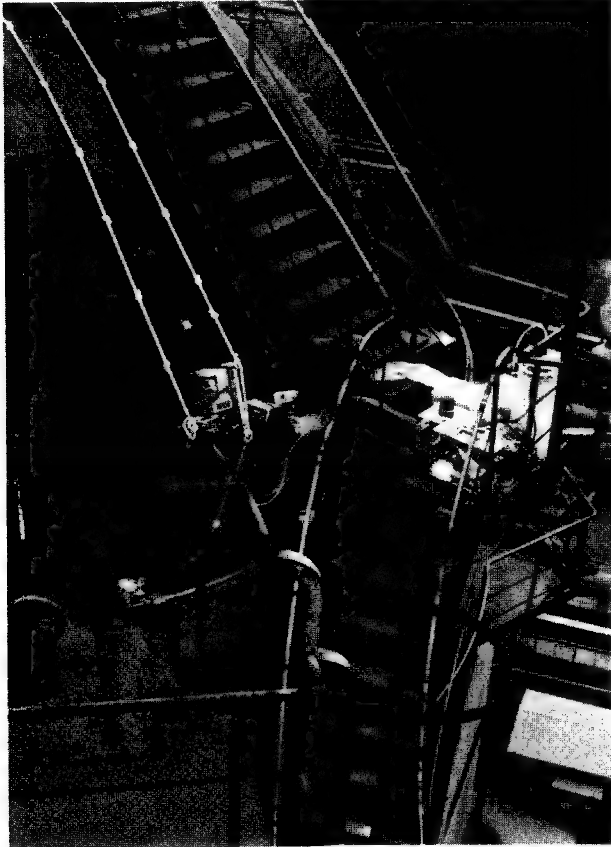
Fig.2 Inspection of high
pressure vessel at 70 Mates
from the ground.

COMPOSITE X-RAY PINHOLES FOR TIME-RESOLVED
MICROPHOTOGRAPHY OF LASER COMPRESSED TARGETS*

D. T. Attwood

Lawrence Livermore Laboratory
University of California
Livermore, California 94550

Experiments designed to study laser driven implosion of glass micro-shells are underway in several laboratories around the world. The ultimate goal of these experiments is to drive the encapsulated deuterium-tritium fuel to a sufficiently high density and temperature that the resultant thermonuclear reaction produces a net energy gain.[1] In preliminary experiments it has been shown that modest compressions are achieved[2,3] and that the resulting neutrons are of a thermonuclear origin.[4] It is important that these early experiments be understood in sufficient detail that future experiments can be accurately designed. Because of the high densities and temperatures involved, x-ray emission from the compressed target provides a primary source of data regarding dynamics of the implosion process. A typical implosion experiment involves an approximately 100 micron initial diameter target which implodes to a fraction of its initial size on a time scale of roughly 100 picoseconds. The x-ray data must therefore be resolved spatially to microns and temporally to several picoseconds in order to provide direct data describing the heating and implosion processes. However, diagnostics available to date have not had the capability of simultaneously providing the required space-time resolutions. Time-integrated x-ray imaging studies provide spatially resolved photographs showing target compression[2,3]. Spatially integrated streak camera studies provide temporally resolved x-ray spectral signals interpretable in terms of implosion tiems.[5] In this paper we report the first temporally resolved x-ray images of laser compressed targets with sufficient resolutions to continuously follow the implosion process. The resultant space-time characteristics provide

directly observable implosion velocities, and as such provide direct, detailed data of the type required for meaningful comparison with numerical simulations.

The key to these measurements is that of successfully mating micron sized pinholes to fast x-ray detectors such as Livermore's 15 psec x-ray streak camera. The basic scheme is shown below in Fig. 1.
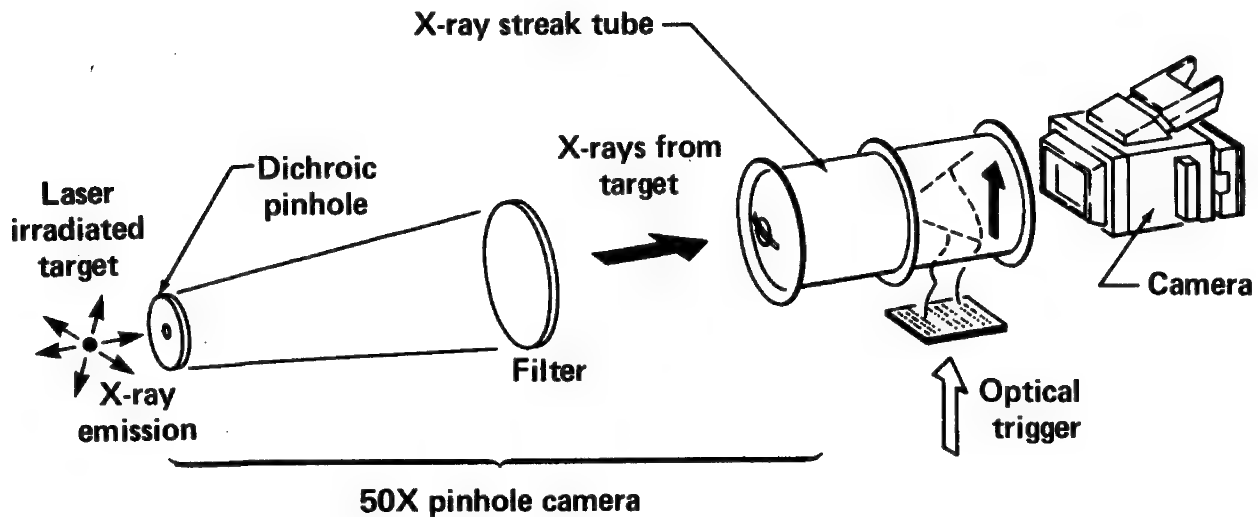
Fig. 1. Fifty times magnification x-ray imaging of target self-emission is shown. Note that the image must be centered on the slit photocathode of the x-ray streak camera. A vertical target displacement of one radius renders the image tangent to the slit and therefore unrecordable.

With a 50X magnification the streak camera spatial resolution of about 100 microns is transformed to 2 microns in the target plane. Pinhole diameter is then the determining factor in overall spatial resolution. Assuming that the laser irradiated target yields sufficient x-radiation to achieve these space-time measurements,[6] the next critical problem is alignment of the pinhole relative to the target and the detector photocathode. The absence of sufficiently intense and convenient x-ray alignment sources generally requires pinhole alignment with visible sources. The difficulty which arises is one of diffraction. Pinhole cameras are generally designed to be near diffraction limited for x-ray wavelengths of several Angstroms and thus exhibit intolerable diffraction for visible alignment schemes where the wavelength is a factor of 1000 longer. The solution to this apparent conflict is to construct "composite pinholes", that is pinholes whose apparent size is correct for both x-rays and visible light. In this paper

we describe composite or "dichoric pinholes" which are appropriately small for micron resolution x-ray imaging, but which present a sufficiently large visible aperture to allow simple and accurate optical alignment. Composite pinholes such as this can be formed using x-ray absorbing glass as the pinhole material and concentrically overlaying a larger diameter hole in a metal foil.[7] Such a pinhole is shown in Fig. 2. In this particular case, x-rays are transmitted
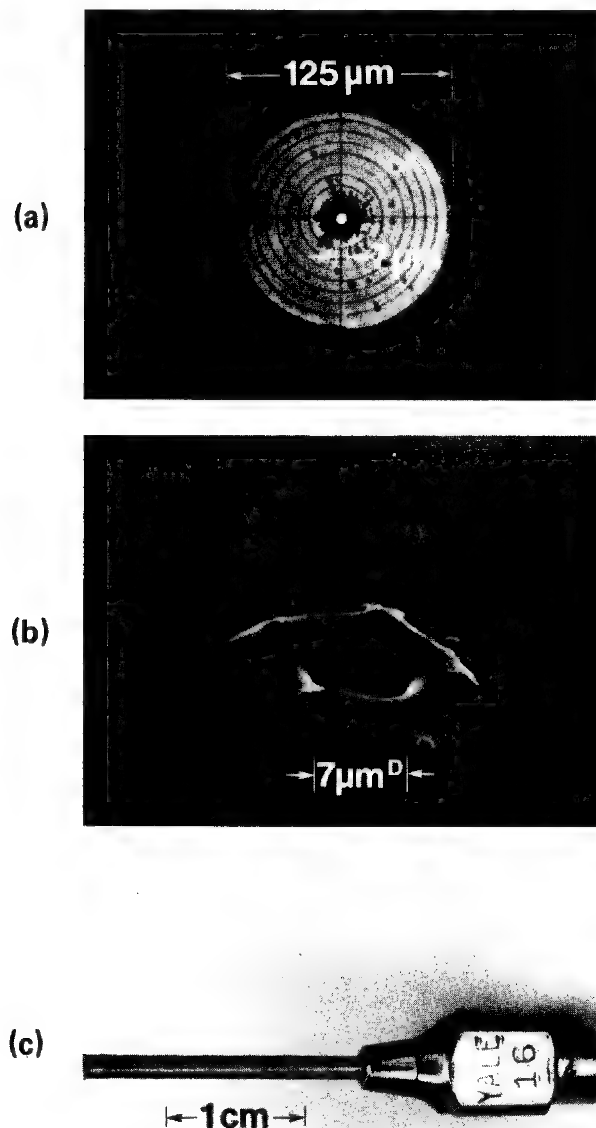
Fig. 2. Composite x-ray pinhole. Part (a) shows a 125 µm diameter hole mechanically drilled in a gold foil, and a 7 µm diameter laser drilled hole in the overlaid glass. Part (b) shows a closeup of the laser drilled hole as seen by a scanning electron microscope. Part (c) shows the pinhole mounted on the tip of a hypodermic syringe.

only by the 7 μm hole laser drilled in the glass. The visible alignment light
is passed by the glass and "sees" only the larger 125 μm diameter aperture.
The circular lines of the superposed reticle are shown to demonstrate concen-
tricity of the x-ray and visible apertures. It is evident that within two or
three microns, the x-ray pinhole can be aligned as accurately as the larger
visible aperture. With proper use of Airy rings, the visible aperture can be
aligned to several micron accuracy. Appropriate alignment schemes will be dis-
cussed at the conference.

Sample streak records of imploding laser fusion targets, obtained with
a 6 μm^D tantalum glass pinhole and the 15 psec x-ray streak camera, are shown
in Figs. 3 and 4. Fig. 3 shows the approximately symmetric space-time implo-
sion and subsequent target disassembly of a 69 μm diameter glass microshell
target irradiated simultaneously from two sides with a total laser power of
approximately 0.4 TW. Fig. 4 shows the implosion of a second target in this
series of experiments. In this last case, the target was irradiated from only
one side. As seen in Fig. 4 this resulted in a one sided implosion which con-
verged to peak emission near the target center, followed by a two-sided but
asymmetric target disassembly. In Figs. 3 and 4 we present a reproduction of
the original streak record as well as contour plots of monotonically increasing
film density. The dashed lines in Figs. 3b and 4b follow peak x-ray emission
of the imploding target. Since this is a space-time diagram, the slope of these
lines represents a velocity and, therefore, the dashed lines provide a direct
experimental measure of target implosion velocity. Note that variations from a
straight line imply acceleration of the inwardly propagating x-ray emission
front. Typical implosion velocities, as indicated in the figures, are on the
order of 3 X 10^7 cm/sec. Acceleration values derived from Fig. 3 are in the
range of 3 to 4 X 10^{17} cm/sec^2. The approximate spatial and temporal resolutions
achieved in these measurements, 6 μm and 15 psec, are indicated by the dark
rectangles. Further analysis of these results and their impact on our understand-
ing of the physical processes involved, is presented in reference 8.

(a)

(b)
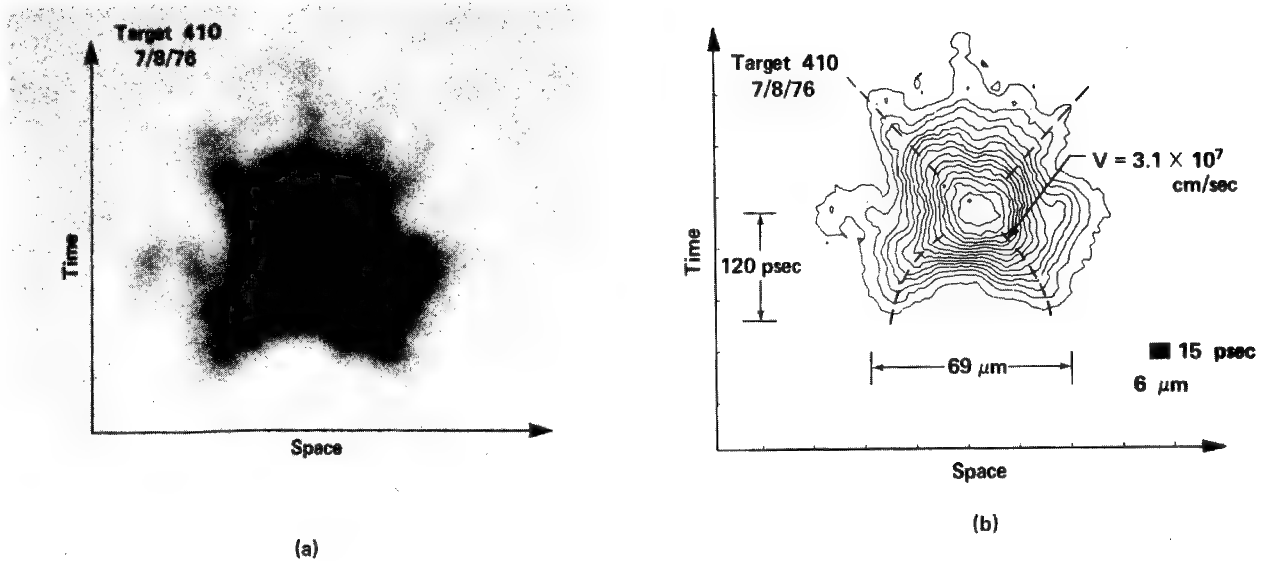
Fig. 3. (a) Reproduction of the spatially resolved x-ray streak record of a symmetrically imploding target irradiated from two sides. Target diameter was 69 μm, wall thickness was 0.44 μm, and deuterium-tritium (DT) fill was 1.7 mg/cc. Total laser power to target was 0.43 TW in a 64 psec FWHM, 1.06 μm pulse.

(b) Monotonically increasing isodensity contours of the original streak record. Density contour interval is 0.20. Dashed lines follow ridge of peak x-ray emission. The slope of these lines on the space-time diagram indicate final implosion velocities on the order of $3x10^7$ cm/sec, and accelerations of $3-4x10^{17}$ cm/sec^2.

(a)

(b)
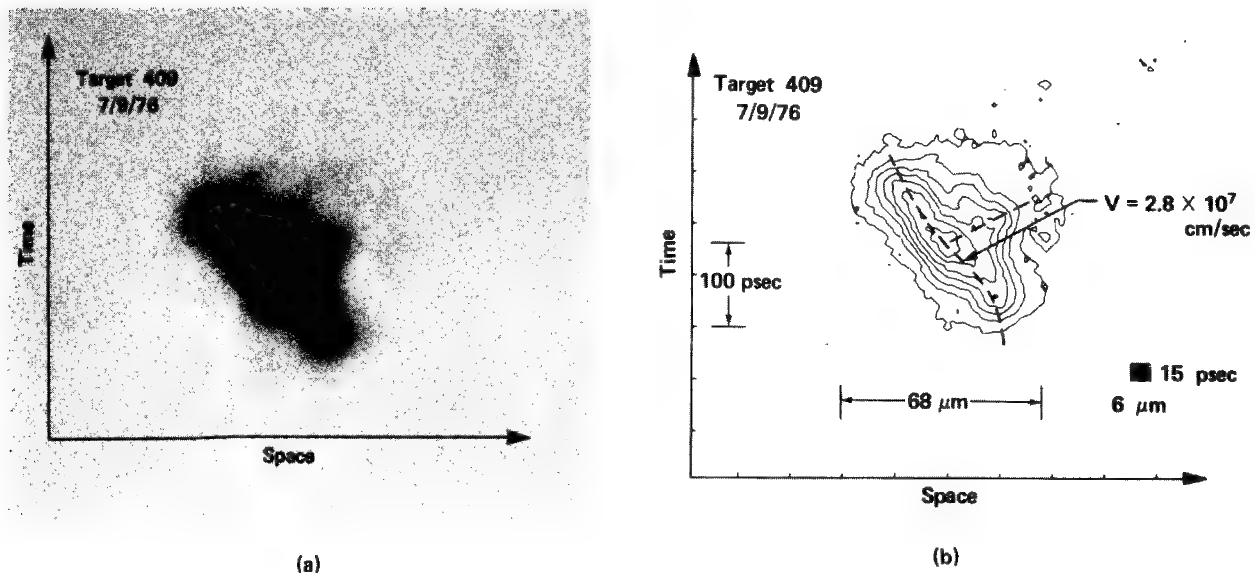
Fig. 4. Data is similar to that in Fig. 3, except that single sided irradiation has resulted in a one sided implosion with hydrodynamic convergence near the target center. Peak emission is seen to coast (conservation of momentum) to the far side. Target assembly is observed to be two sided, albeit, asymmetric. Initial target diameter was 68 μm, wall thickness was 0.57 μm, and DT fill was 1.8 mg/cc. With target irradiation blocked on one side, power delivered was approximately 0.22 TW in a 70 psec pulse.

REFERENCES

1. J, Nuckolls, L. Wood, A. Thiessen and G. Zimmerman, Nature 239, 139 (1972).

2. P. M. Campbell, G. Charatis, and G. R. Monty, Phys. Rev. Lett., 34, 74 (1975).

3. F. Seward, J. Dent, M. Boyle, L. Koppel, T. Harper, P. Storeing and A. Toor, Rev. Sci. Instrum., 47, 464 (1976).

4. V. W. Slivinsky, H. G. Ahlstrom, K. G. Tirsell, J. Larsen, S. Glaros, G. Zimmerman, and H. Shay, Phys. Rev. Lett., 35, 1083 (1975).

5. D. T. Attwood, L. W. Coleman, J. T. Larsen, and E. K. Storm, Phys. Rev. Lett., 37, 499 (1976); references to similar instruments cited therein.

6. D. T. Attwood, XII Int'l. Congress on High Speed Photography, paper DA-2, Toronto (1976). Lawrence Livermore Report UCRL-77743.

7. D. T. Attwood, B. W. Weinstein, and R. F. Wuerker, Applied Optics 16, May 1977.

8. D. T. Attwood, L. W. Coleman, M. J. Boyle, J. T. Larsen, D. W. Phillion, and K. R. Manes, Phys. Rev. Lett. 38, 282 (1977).

TOMOGRAPHY OF LASER FUSION PLASMAS*

N. M. Ceglio

Lawrence Livermore Laboratory
University of California
Livermore, California 94550

Introduction

Experimental programs exist in a number of laboratories throughout the world to test the feasibility of using powerful laser systems to drive the implosion of hydrogen isotope fuel to thermonuclear burn conditions. In a typical experiment multiple laser beams are focused onto a glass microshell (typically 50 μm - 200 μm diameter) filled with an equimolar D-T gas mixture. X-ray and particle emissions from the target provide important information about the hydrodynamic implosion of the glass shell and the associated compression and heating of the D-T fuel. Standard diagnostics for imaging such emissions are the grazing incidence reflection (GIR) x-ray microscope[1] and the pinhole camera. Recently, a particular coded imaging technique, Zone Plate Coded Imaging (ZPCI), has been successfully used for x-ray and particle microscopy of laser fusion plasmas. ZPCI is highly attractive for investigating laser produced plasmas because it possesses a tomographic capability not shared by either the GIR or pinhole imaging techniques. This abstract provides a brief discussion of the tomographic potential of ZPCI. In addition, the first tomographic x-ray images (tomographic resolution $\sim$ 74 μm) of a laser produced plasma are presented.

ZPCI was first proposed by Mertz[2] for stellar x-ray imaging. It has also enjoyed considerable attention in the field of nuclear medicine.[3] ZPCI is a two-step imaging technique. In the first step the radiation distribution to be imaged casts a shadowgraph through a Fresnel zone plate (coded aperture) onto a photographic emulsion or other detector array. The shadowgraph is a coded image of the source emission distribution. Image reconstruction (decoding) is achieved via procedures similar to those used in holography. The shadowgraph transparency is illuminated with a coherent light source. The Fresnel diffraction pattern of the transmitted light produces a three dimensional reconstruction of the original source distribution. The image is inverted, reversed front to back, and magnified by the ratio of the (coded) image to object distances.

The tomographic capability of ZPCI may be understood very simply. Consider a three dimensional source distribution represented by three, non-coplanar points. Each source point will cast a zone plate shadow onto the shadowgraph plane. The size and position of each shadow in the shadowgraph uniquely characterizes the position of its associated source point. Points close to the coded aperture project large shadows, distant points project small shadows, off-axis points project off-axis shadows, and so on. Upon reconstruction each zone plate

shadow focuses the incident radiation to a diffraction limited point - the image of its associated source point. The information contained in the three dimensional image distribution is retrieved by viewing the image in "sections", that is, in separate reconstruction planes. Ideally there is a one to one correspondence between each reconstruction plane and each source plane.[4] In this way a three dimensional source distribution may be synthesized plane by plane.

Tomographic Resolution Limit

A tomographic resolution criterion for the ZPCI technique has been derived from reconstruction calculations for an on-axis point source pair of equal intensity separated by a longitudinal (i.e., normal to the zone plate) distance, Δ. Such a criterion, based on point pair resolutions, can at best serve only as a crude figure of merit for determining the tomographic discrimination capability of ZPCI for a particular three dimensional source distribution. The precise three dimensional intensity distribution within the source will significantly affect the tomographic discrimination capability of the technique.

Fig. 1 displays results of the reconstruction calculations for a point source pair. The (on axis) intensity distribution in the reconstructed image is plotted versus normalized axial distance for four representative values of the tomographic parameter, α.

$$\alpha = 2\pi N \frac{\Delta}{S_1} \left(\frac{S_2}{S_1 + S_2} \right) \qquad (1)$$

where

   N equals the total number of zones in the coded aperture
   Δ is the axial separation of the point source pair

(a)
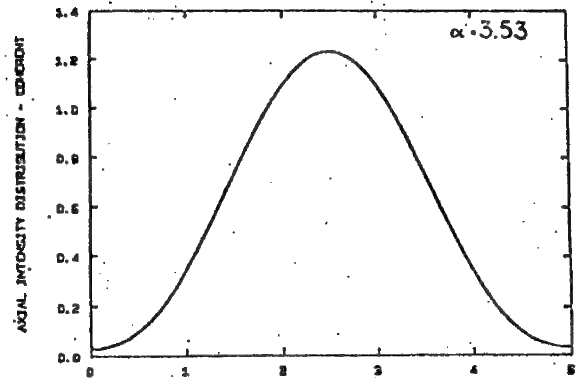
(b)
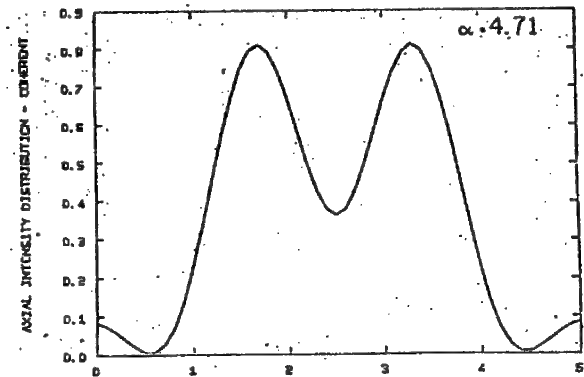
(c)
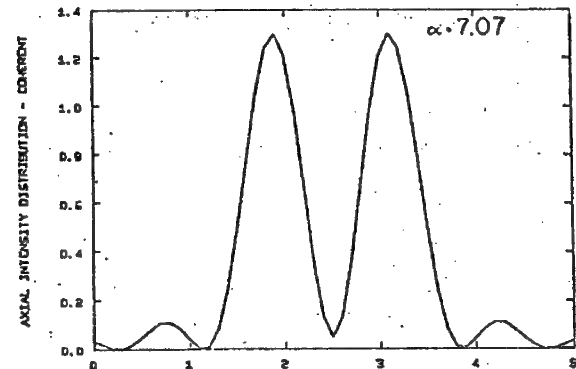
(d)
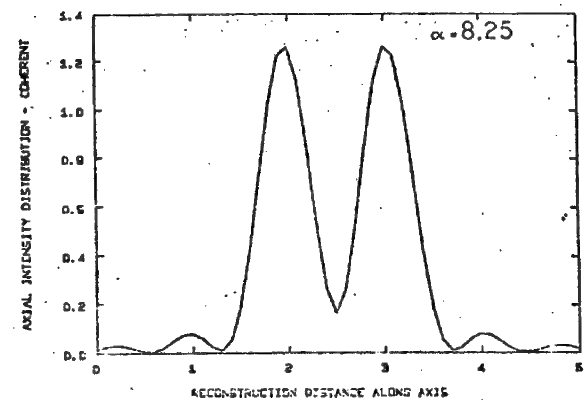
Figure 2: RECONSTRUCTION CALCULATIONS

S_1, S_2 are the source to zone plate and zone plate to shadowgraph distances respectively. ($\Delta \ll S_1$)

Distance along the horizontal axis is normalized to the nominal point-pair image separation distance. The nominal reconstruction positions for the point images in Fig. 1 are at values 2 and 3 along the horizontal axis. Fig. 1(d) shows that at $\alpha = 8.25$ the two points are well resolved and the peaks of the double hump intensity distribution occur at the nominal reconstruction positions. At $\alpha = 3.53$ (Fig. 1(a)) the two points are not resolved. Within the range of $4.71 < \alpha < 7.07$ a double hump intensity distribution occurs in the image reconstruction, but interference from sidelobe contributions causes the peak-to-peak separation to exceed the nominal separation for the reconstructed points. For the purpose of this discussion $\alpha = 4.71$ (Fig. 1(b)) shall be chosen to define a ·condition of suitable tomographic resolution.[5] This provides an intensity ratio greater than two between peak and saddle, allowing the clear identification of the existence of two spatially separated contributions to the reconstructed image. This yields an expression for the ZPCI tomographic resolution limit[6]

$$\Delta \simeq \frac{.75}{N} \frac{S_1}{S_2} (S_1 + S_2) \tag{2}$$

Experimental Results

The experiment reported here was conducted using the Cyclops laser-target irradiation facility at Lawrence Livermore Laboratory. The target was a deuterium-tritium filled glass microshell, 90 μm in diameter. The target was irradiated simultaneously from two anti-parallel directions by an intense neodymium laser pulse. X-ray emission from the irradiated target was imaged using ZPCI.

The zone plate camera used in this experiment had a coded aperture of 100 zones. The width of the narrowest zone was 5.3 μm. The zone plate material was gold, 1.4 μm thick. The camera had an 8 μm planar resolution and a 74 μm tomographic resolution (Eq. (2)). It viewed the laser produced plasma in a spectral window 2Å - 6Å. The imaging geometry was characterized by the parameters $S_1 \simeq .93$ cm, $S_2/S_1 \simeq 16.1$.

ZPCI results are shown in Figs. 2 and 3. Fig. 2 shows the coded image for a low power laser shot (5 joules in 53 psec) in which no target compression occurred. Fig. 3 displays tomographic data reconstructed from the coded image in Fig. 2. Shown are isodensity contour maps for reconstructed images viewed in three separate reconstruction planes. Fig. 3(a) is representative of the source plane at the geometrical
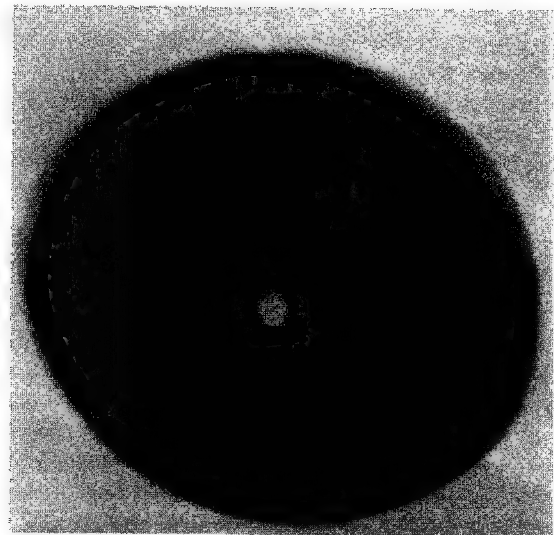
|←——————————36 mm——————————→|

Figure 2: CODED IMAGE

center of the plasma shell; Fig.3(b) is an image of the source plane a distance 37 μm behind (viewed from the zone plate camera) the central plane; and Fig. 3(c) is an image of the source plane a distance 74 μm behind the central plane.[4] A careful analysis of the images in Fig. 3 supports the contention that true tomographic information is .represented. Most convincing is the migration of the region of peak density in the contour pattern on the left. In Fig. 3(a) the peak density region is approximately 23 μm above the equatorial plane of the plasma shell (perhaps the laser beam hit high on target). It migrates down toward the equatorial plane as we view rear sections of the plasma shell until in Fig. 3(c) it is only 4 μm above the equatorial plane. This migration is to be expected from the spheroidal curvature of the source distribution.

Investigations into the tomographic capability of ZPCI are continuing at Lawrence Livermore Laboratory. A new zone plate camera having a nominal tomographic resolution of ~ 33 μm (N = 240 zones) has been built, and will soon be used to image the x-ray emission from laser irradiated targets. Work is underway on the fabrication of a zone plate camera having a nominal tomographic resolution of ~ 10-15 μm (N = 1000 zones). The use of a number of such cameras, viewing the laser produced plasma from independent directions may provide a full three dimensional characterization of the x-ray emission from the target.

References

1. F. Seward, J. Dent, M. Boyle, L. Koppel, T. Harper, P. Stoering and A. Toor, Rev. Sci. Instr. 47, April 1976.
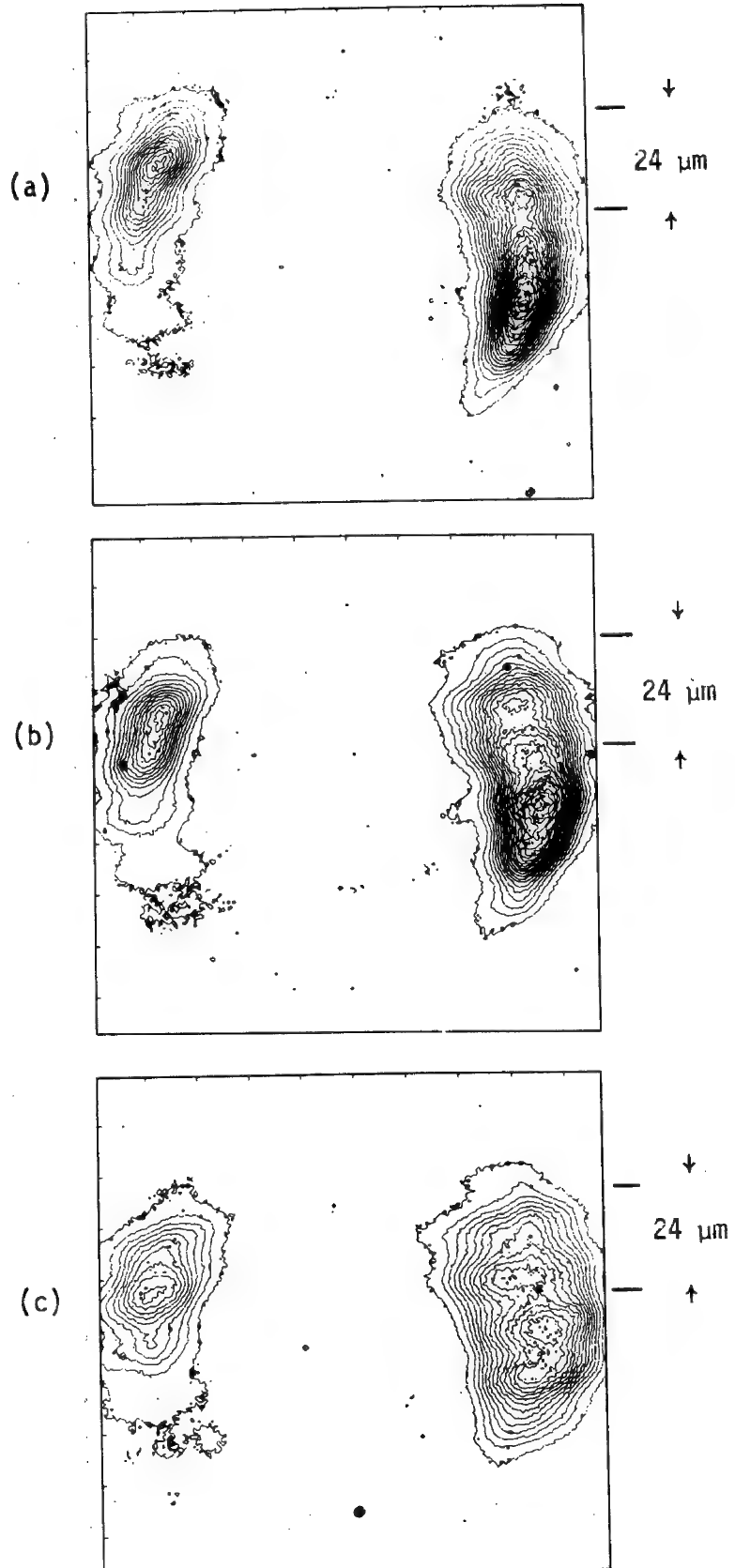
Figure 3: TOMOGRAPHIC DATA

2. L. Mertz and N. O. Young, Proc. Int. Conf. on Opt. Instr., London (1961) p. 305.

3. H. H. Barrett, J. Nucl. Med. 13, 382 (1972).

4. In practical terms the image viewed in a given reconstruction plane is representative of the radiation contribution from a slice of the source distribution equal in thickness to the tomographic resolution of the technique.

5. An application with different tomographic discrimination requirements may dictate a different choice for a suitable α value. However, it is clear from Fig. 1 that an appropriate choice for α must lie within the range $3.53 < \alpha \leq 8.25$.

6. An earlier published treatment (ref. 6) of the tomographic capability of ZPCI gives a smaller value for the tomographic resolution limit, Δ. However, that treatment overlooked coherence effects in image reconstruction, and is therefore incorrect.

7. H. H. Barrett and F. A. Horrigan, Applied Optics 12, 2686 (1973).

X-RAY MICRORADIOGRAPHY OF LASER FUSION TARGETS*

R. H. Day, R. P. Kruger, R. L. Whitman, T. L. Elsberry

Los Alamos Scientific Laboratory
Los Alamos, N.M.

Theoretical calculations of laser driven implosions indicate that highly uniform, symmetric targets will be required for successful laser fusion. To date, optical techniques have proven adequate for the common transparent microspheres.[1] For optically opaque targets, however, contact x-ray microradiography has been suggested as an appropriate technique.[2] In this paper we will show how various parameters of the radiographic system affect sensitivity to asymmetries in the microspheres and compare experimental radiographs to a theoretical model.

THE RADIOGRAPHIC SYSTEM

The radiographic system has three major components: 1) the x-ray source, 2) the microsphere-film imaging system, and 3) the radiograph readout system. Each of these must be optimized if the greatest sensitivity is to be achieved.

Two x-ray sources have been used at Los Alamos to radiograph laser fusion pellets. One is a low voltage bremsstrahlung source for use from 2 to 10 kV. The second is a typical "Henke tube" source[3] which generates a beam of nearly monoenergetic x rays selectable in energy from 200 eV to 1.5 keV.

The images are formed as contact microradiographs on Kodak HRP plate. The H-D curve of the HRP plate has been measured over the x-ray energy region of interest. The geometry of the sources are designed to give 1 micron resolution for the monoenergetic source and 0.1 micron for the bremsstrahlung source. These two sources yield maximum contrast in different regions of the image, and thus the resolution was matched to the resolution required for each region.

The image readout system used in this work is a Photometric Data Systems 1050 scanning densitometer. A 2x2 micron region of the image is sampled in 1 micron steps in both the x and y coordinates over a 128x128 micron grid. The flatness of background is better than 1% over the images. The single point noise of the film-densitometer system was empirically fit to a power law:

$$\sigma_{rms} \text{ (noise)} = 0.062 \times D^{0.6}.$$

The results reported here are all for radiography of glass microshells which could be optically characterized for comparison. They have diameters of order 100 microns and wall thicknesses of order 1 micron. However, by changing the x-ray source energy, the results can be extrapolated to similar systems with different absorption coefficients.

EXPERIMENTAL RESULTS AND SYSTEM SENSITIVITIES

In the radiographic technique, one can measure differences in areal density as differences in optical density in the image. Different thicknesses of material, however, require different energy x rays to achieve maximum
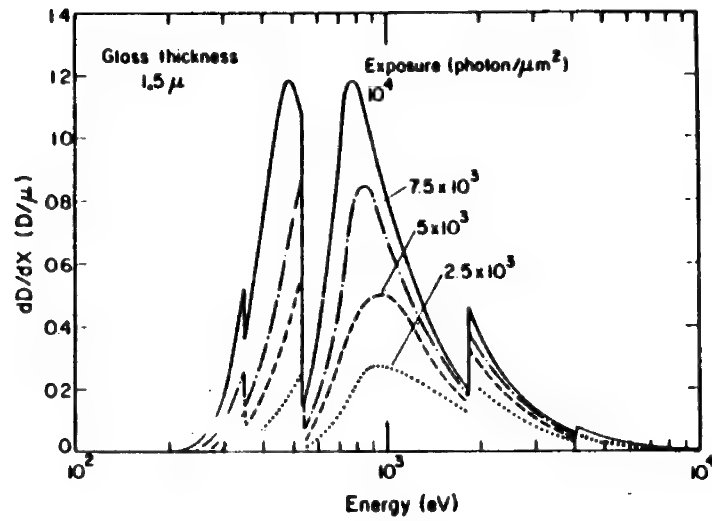
Fig. 1.   Contrast per micron of glass versus energy for thin glass.
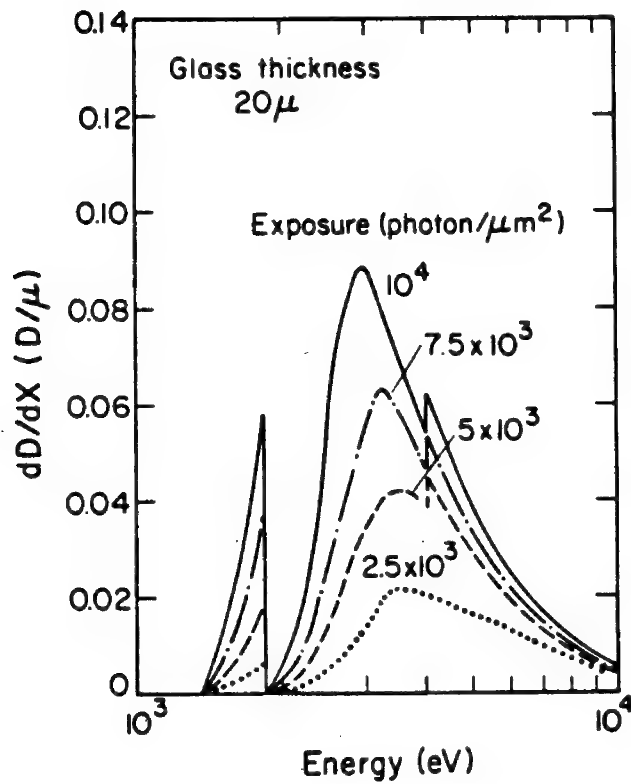
Fig. 2.   Contrast per micron of glass versus energy for thick glass.

contrast. Two such cases are shown in Figs. 1 and 2 where contrast per micron of glass, dD/dx, is plotted versus x-ray energy. Near the center of the image the glass thickness is typically a few microns for which the optimum x-ray energy is about 1 keV and the radiation should be nearly monochromatic. Near the edges of the images, the glass is tens of microns thick for which 3 to 4 keV radiation is optimum and the limits on mono-chromaticity are less severe. Even though the value of dD/dx is much larger for low energy radiation, larger differences in glass thickness are expected near the rims yielding similar contrast for the two cases.

We have observed three different classes of defects in these micro-spheres. The first can be modeled as a nonconcentricity of the spherical surfaces defining the inner and outer walls of the microshell. The second is modeled as a nonsphericity of one or both of these walls. The third class of defect is associated with small scale nonuniformities in the wall com-position or thickness.

A cross section of the image of a typical microsphere is shown in Fig. 3. Also shown on the figure are the results of a simulation code which models the actual source-radiograph-readout system. These results are for a monoenergetic exposure at 930 eV. For defects of the first class, several cases of inner versus outer shell displacement, XD, are shown. The data agree very well with the prediction using parameters derived from optical characterization.
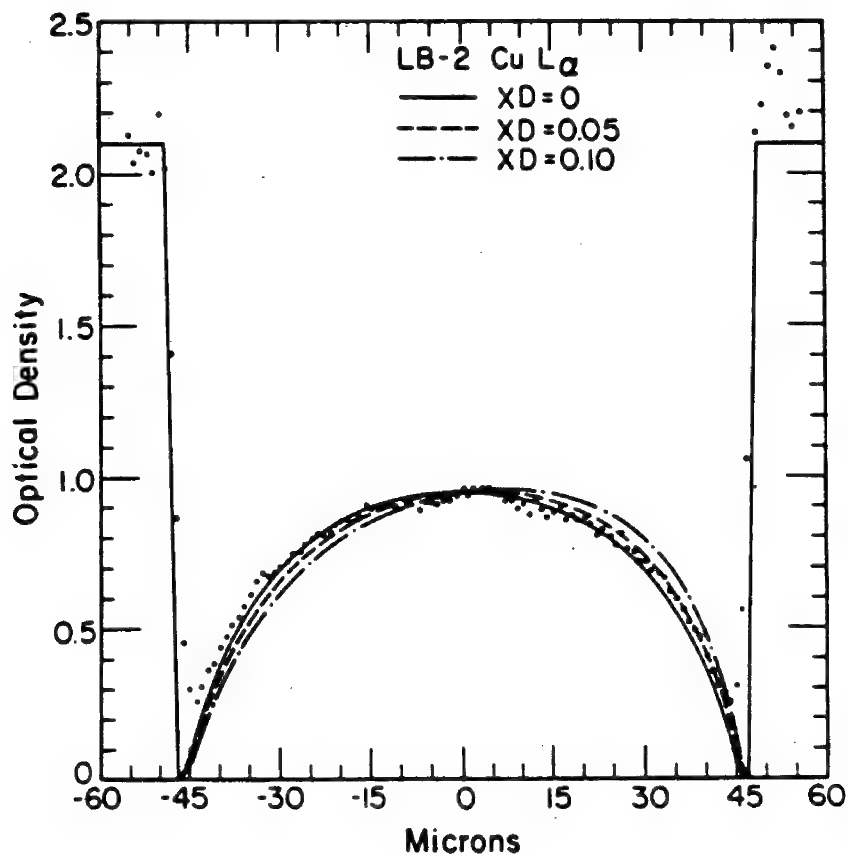
Fig. 3. Radiograph cross section of a 96 micron diameter sphere with a 0.68 micron thick wall taken with 930 eV radiation. The solid curves are computer simulations vor various values of inner and outer shell nonconcentricity, XD, in microns.

Fig. 4. Radiograph cross section of a 96 micron diameter
sphere with a 0.68 micron thick wall taken with 4 kV
bremsstrahlung radiation. The solid curves are computer
simulations for various values of inner and outer shell
nonconcentricity, XD, in microns.

The wall thickness value agrees to ±500 Å (which is the uncertainty in the
optical determination). The uncertainty from radiography is ±250 Å. A
similar comparison on the same microsphere radiographed with bremsstrahlung
radiation is shown in Fig. 4 where the spectrum was assumed to have a mean
energy of 3.3 keV. The agreement is less impressive since the actual
spectrum is polychromatic. Also, the contrast for a given asymmetry is signi-
ficantly less than for the 930 eV case over most of the image.

If we use this model to predict the sensitivity of radiography to
inner versus outer sphere offset, we get the results shown in Fig. 5 for
930 eV radiation. We have plotted signal to noise ratio versus sphere offset.
The signal is defined as the sum of the absolute value of the density dif-
ferences of opposing points across the sphere center. Noise is the 3σ noise
of readout system summed in quadratures with worst case density difference
due to uncertainty in the location of the image's geometric center. It should
be possible to determine the geometric center to ±0.25 microns which would
result in an uncertainty of ±250 Å in the concentricity of the inner and
outer shells. The limit of accuracy of the optical system is about ±500 Å.
A similar calculation for the same ball radiographed with 3.3 keV radiation
yields half the 930 eV sensitivity.
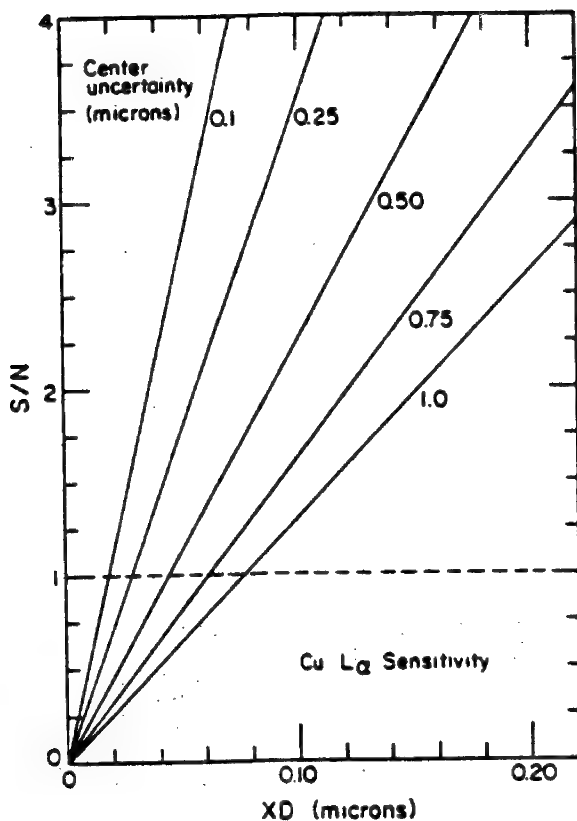
Fig. 5. Signal to noise ratio ·(see text) versus shell wall non-concentricity for various values of uncertainty in the image geometric center.

If one or both walls of the microshell are nonspherical, however, we can use the difference in wall thickness as viewed through the sphere center in different orientations to predict contrast as per Fig. 1. If the central 310 square microns of the image are used to define a mean optical density, a 3σ sensitivity of ± 350 Å in wall thickness is achieved for 930 eV radiation with an exposure of 3000 photons/μm^2.

The same calculation for small scale nonuniformities viewed near the center of the image yields a sensitivity, S, in Å of glass: $S = 5.1 \times 10^3/\sqrt{A}$, where A is the area of the asymmetry in square microns. Such small scale defects are common in the surface of some microspheres.

CONCLUSIONS

Under optimal conditions, x-ray microradiography is a very sensitive technique to determine the characteristics of microspheres. This technique exceeds the capabilities of present optical techniques for most types of defects. The inherent slowness of the image analysis can be accelerated by simultaneously radiographing large numbers of microspheres, then scanning the images visually and with increasingly sophisticated levels of computer analysis to weed out various levels of asymmmetry. We are presently investigating a microscope-Vidicon scanning system which will decrease the image sampling time significantly while improving the resolution. With such systems it will be possible to scan large numbers of laser fusion targets with high sensitivity to defects. This capability will be required for practical laser fusion systems.

REFERENCES

1. B. W. Weinstein, LLL Report No. UCRL - 76968 (1975).

2. T. M. Henderson, D. E. Cielaszyk, R. J. Simms, KMS Fusion Report No. KMSF U543 (1976).

3. R. H. Day and E. J. T. Burns, Adv. X-Ray Anal., 19, 597 (1975).

THIN ZONEPLATES FOR SOFT X-RAYS

Janos Kirz

W. W. Hansen Laboratories of Physics
Stanford University, Stanford, CA., 94305, and

Department of Physics
State University of New York, Stony Brook, N.Y., 11794[*]

The work of Niemann, Rudolph and Schmahl[1] demonstrates that Fresnel zone plates can be used both as dispersive and as image forming elements in the ultrasoft x-ray region (46Å) with submicron resolution. It is also possible, at least in principle, to build phase zone plates for this wavelength region with better signal/noise characteristics.[2]

High resolution zone plates for shorter wavelengths would have to be thick relative to the ring spacing for best efficiency as the x-rays become more penetrating, and as the dispersion parameter $\delta = Re\ (1-n)$ diminishes. Fabrication of such zoneplates appears to pose difficult problems. We shall consider therefore the use of zoneplates which are thin relative to the optimum, but which can be more easily fabricated. These plates, by definition will throw a smaller fraction of the incident x-ray flux into the first order image. They may be useful nevertheless for producing small, intense, monochromatic x-ray spots for scanning microscopy, spectroscopy, etc., where an aperture stop near the focal spot can be used to remove the undesired orders.

As an example we consider zoneplates made of gold. We parametrize the index of refraction for the range $8Å < \lambda < 45Å$, in the form $n = 1-\delta-ik$ with $\delta = 4 \times 10^{-5}\ \lambda^{1.5}$, and $k = 6 \times 10^{-6}\ \lambda^2$ based on the data tables of Hagemann, Gudat and Kunz[3]. The efficiency η obtained as a function of wavelength for a 1000A thick zoneplate is shown in Fig. 1. Also shown in the figure is the transmission coefficient, T, for a 1000Å thick gold foil, and the efficiency for a zone plate thick enough to make the alternate zones fully opaque. (Dashed line).

Clearly, even at wavelengths where the zoneplate is essentially transparent to the x-rays, the efficiency remains large enough to be useful in many applications. In this region the zoneplate acts essentially as a phase object.

---

[*] permanent address.

1. B. Niemann, D. Rudolph, and G. Schmahl, Appl. Opt. 15, 160 (1976).
2. J. Kirz, J. Opt. Soc. Am. 64, 301 (1974).
3. H.-J. Hagemann, W. Gudat, and C. Kunz, Optical Constants from the Far Infrared to the X-ray Region: Mg, Al, Cu, Ag, Au, Bi, C, and Al_2O_3, DESY report SR-74/7 (1974).
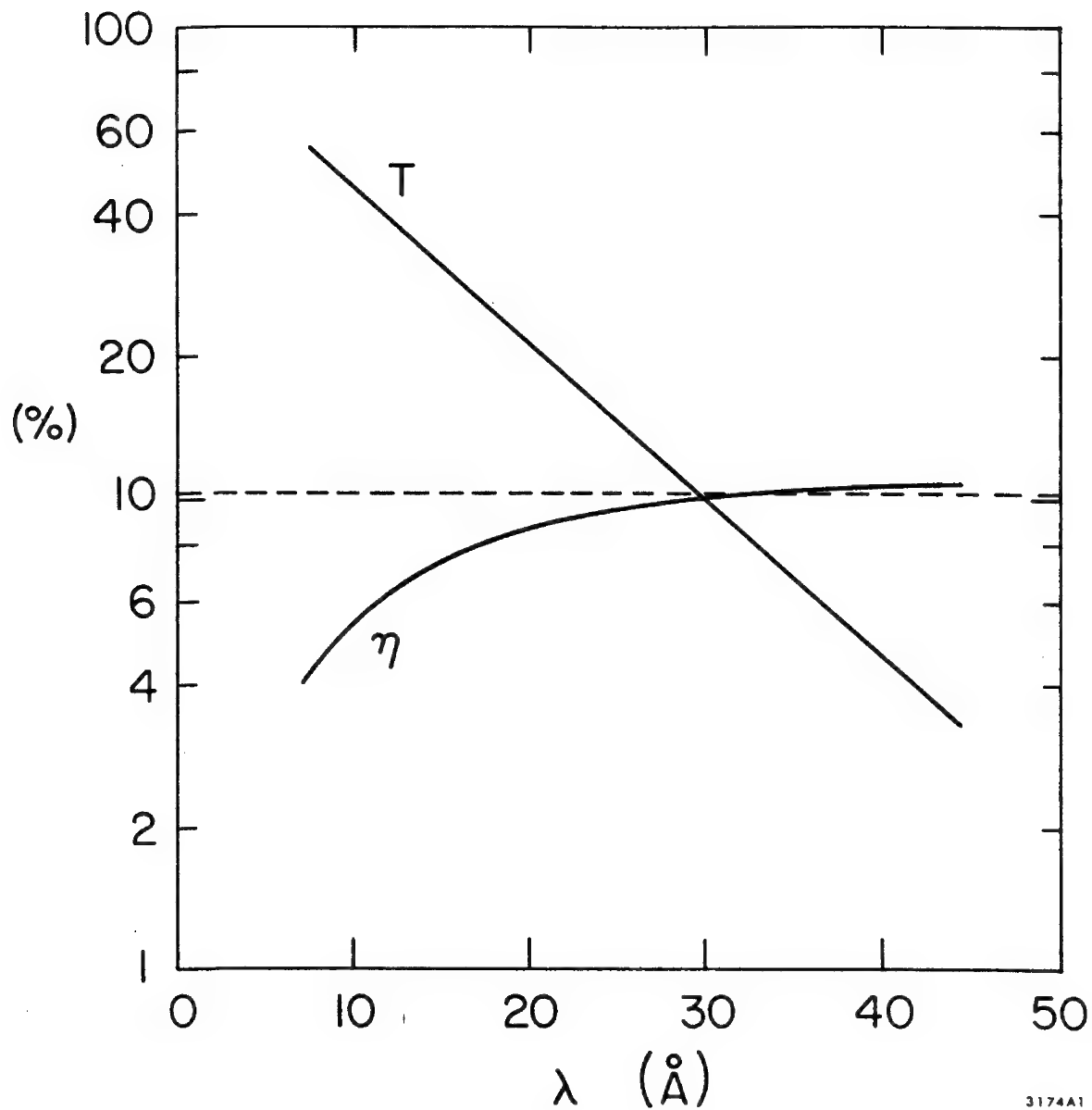
Fig. 1. The efficiency, η, with which a 1000Å thick zoneplate made of gold collects incident x-rays into its first order focus. For a zoneplate thick enough to make alternate zones fully absorbing, η=1/π² (dashed line). The transmission through a 1000Å thick gold foil is indicated by the curve T.

X-Ray Microscopy of Biological Specimens with Zone Plates and Synchrotron Radiation

G.Schmahl, D.Rudolph and B.Niemann
Universitäts-Sternwarte Göttingen, Germany

Suitable for x-ray microscopy is the wavelength region between about 0.5 nm and 10 nm. The image formation in this region is dominated by photoelectric absorption which depends critically on the used wavelength, the density and the chemical composition of the microscopic object. A great advantage of x-ray microscopy is that biological objects can be examined directly in a living state in an aqueous environement.

We have built a microscope for soft x-radiation using holographically made zone plates as imaging optical elements. Zone plates are a special case of diffraction optics, namely circular gratings with radial increasing line density. The zone plates with large zone numbers are realized by superpositioning of two coherent spherical waves. The interference pattern is produced by using the radiation of Ar^+ or Kr^+ lasers. By subsequent preparation the interference pattern is converted into a zone plate consisting of opaque gold rings on a thin organic layer transparent to soft x-rays.

The microscopic experiments are done using the synchrotron radiation of the Deutsches Elektronen Synchrotron (DESY), Hamburg.Figure 1 shows the experimental arrangement. The polychromatic, slightly divergent radiation is dispersed by a holographic laminar grating used in grazing incidence. A condensor zone plate generates a reduced monochromatic image of the synchrotron source in the object plane. A magnified image of the object is generated by a micro zone plate in the image plane.

The use of synchrotron radiation for x-ray microscopy is advantageous becaus of the high intensity and the possibility to change the wavelength continuously.

Image Plane

Micro Zoneplate

Condensor
Zoneplate

Microscopic Object

Synchrotron
Radiation

Grating
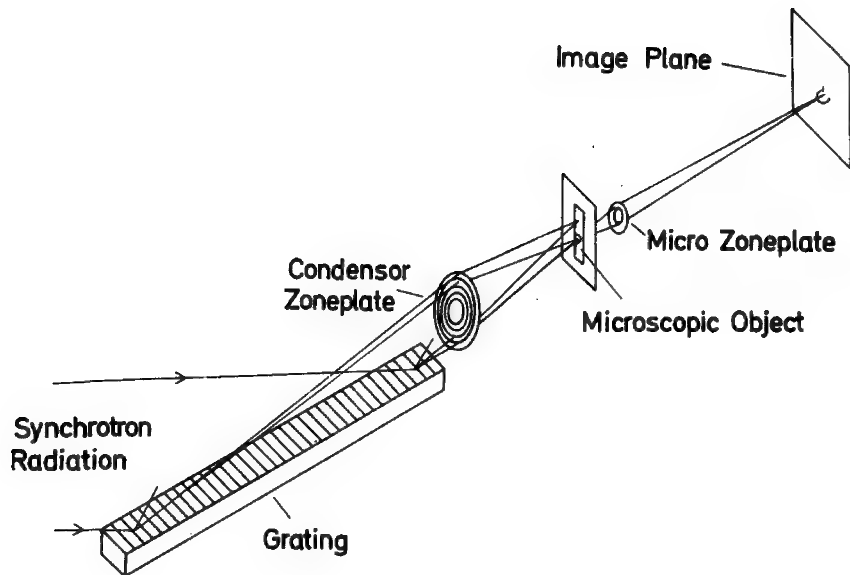
Fig.1   The experimental arrangement

A zone plate can be characterized by the following parameters:
r_1 = radius of the innermost zone, r_n = radius of the n-th
zone, n = number of zones. The focal length of a zone plate
used in the spectral order m is approximately given by
$f_m = r_1^2/\lambda \cdot m$. The width of the outermost zone is given by
$dr_n = \lambda \cdot f_m \cdot m/2r_n$. The smallest distance of two object points
which can be resolved in a microscope is given by

$$\delta = 1{,}22 \; \lambda \cdot f_m/2r_n = 1{,}22 \; dr_n/m \; .$$

Up to now micro zone plates with e.g. following properties
have been built: r_1 = 18,6 μm, r_n = 900 μm, n = 2340,
$f_{4,5 \; nm, m=3}$ = 25,7 mm, dr_n = 0,19 μm. The theoretical reso-
lution with such a zone plate in the third order is 0,077 μm.

Typical values of a condensor zone plate are r_1 = 43.8 μm,
r_n = 3500 μm, n = 6400, $f_{4,5nm, \; m=1}$ = 436 mm.

Because of the severe chromatic aberration of zone plates
one has to use rather monochromatic light. The second error

of practical importance is sperical aberration. This error occurs with zone plates built with visible light and used with x-radiation. This error can by avoided by using aspheric wavefronts during the construction of zone plates.

Up to now a resolution of up to 0,2 μm has been reached, mainly limited by the chromatic error. It is possible to increase the resolution by about a factor of ten.
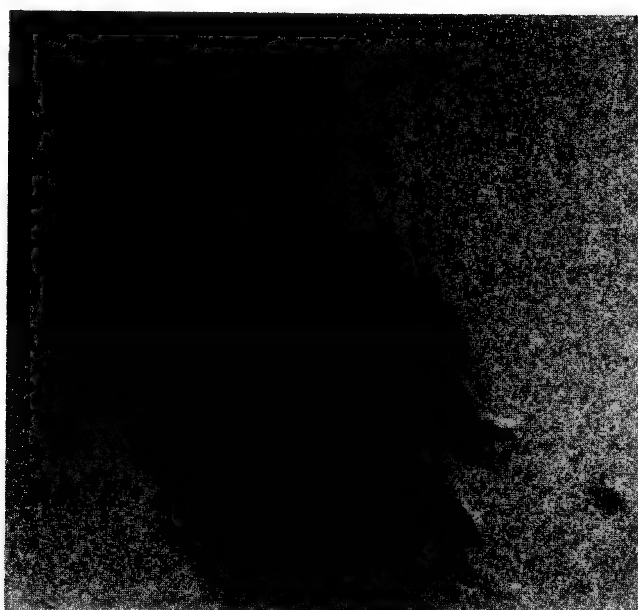
Fig.2 3T3-mouse cell, λ = 4.6 nm, x-ray magnification 15 x, total magnification 1270 x

Microscopic images have been made of several anorganic and organic specimen, e.g. of cotton fibres, algae, He-La cells and mouse cells. Fig.2 shows as an example a mouse cell, imaged with 4,6 nm.

Further results, possible improvements and limitations are discussed.

X-RAY MAPPING WITH
THE ELECTRON MICROPROBE
AND THE WAVELENGTH DISPERSIVE SPECTROMETER

Tung Hsu
Etec Corporation
3392 Investment Blvd.
Hayward, Cal. 94545

I. INTRODUCTION

The capability of mapping the elemental distribution and concentration of a solid specimen is one of the major advantages of the x-ray analysis with the elctron microprobe.[1] When comparing the energy dispersive spectrometer(EDS) and the wavelength dispersive spectrometer(WDS) it is generally considered a disadvantage that the WDS is sensitive to the x-ray source's position and size and therefore non-uniform x-ray dot densities can be plotted from a large specimen area with uniform concentrations.[2,3] This "defocusing effect" is caused by the x-ray emitting point not located exactly at the focal point of the curved analysing crystal.

This paper analyses the geometry of the Probe-WDS system and makes some suggestions on conquering the inconvenience of the defocusing effect.

II. THE Z-AXIS EFFECT ON THE WAVELENGTH MEASUREMENT

The x-ray emmitting point, i.e. the point where the electron beam strikes the specimen, can be moved arround by two mechanisms:
1. It can be moved along the electron beam by adjusting the specimen stage. This is generally referred to as the "specimen height" or the "z-axis position" since the electrons generally come down vertically.
2. It can be moved along the specimen surface by deflecting the electron beam with the scan coil.

The two mechanisms make no difference in their end result of moving the x-ray emmitting point to and from the focal point of the spectrometer. We will discuss them separately only for the convenience of comparing with the experimental results.

For a spectrometer employing Johanson or Johan's arrangement for focusing, the wavelengths are usually measured by converting the source to crystal distance(S-C distance) h into the LiF-equivalent Å following the equation

$$\lambda = \frac{d}{R} h,$$ (1)

which is derived from the Bragg's Equation

$$\lambda = 2d \sin\theta, \tag{2}$$

where d is the crystal lattice spacing of the LiF(200) crystal, R is the radius of the Rowland circle, and θ is the incidence angle of the x-rays.

We assume that when the x-ray source is at S_0, some x-rays of wavelength λ_0 is diffracted off the crystal at the position C_0. (Fig. 1) When the x-ray source moves in the plane of the Rowland circle to a new position S, the crystal would have to be scanned to position C in order to secure the Bragg angle θ_0. The error $\Delta\lambda$ which is the difference between h_0 and h, can be derived from Eqs. 1 and 2 as

$$\Delta\lambda = -\frac{d(4d^2-\lambda_0^2)^{1/2}}{\lambda_0 R}\Delta k \tag{3}$$

where $\Delta k = \overline{S_0 S}$ and the direction of the vector $\overrightarrow{\Delta k}$ will be called the K-axis. If the Z-axis makes an angle ψ with respect to the K-axis, then Eq.3 can be written as

$$\Delta\lambda = -\frac{d(4d^2-\lambda_0^2)^{1/2}}{\lambda_0 R}\Delta z \cos\psi \tag{4}$$

A curve of $\Delta\lambda$ vs. λ_0 with $\Delta z = 0.1$mm is plotted according to the geometry ($\psi=53°$) of ETEC's WDS. (The solid line in Fig.2) This curve is independent of the crystals used if all the wavelengths are measured in LiF-equivalent Å.

Experiments were run by shifting the specimen along the Z-axis in steps and measuring the peak positions of x-ray lines at each step. Results are also plotted in Fig. 2.
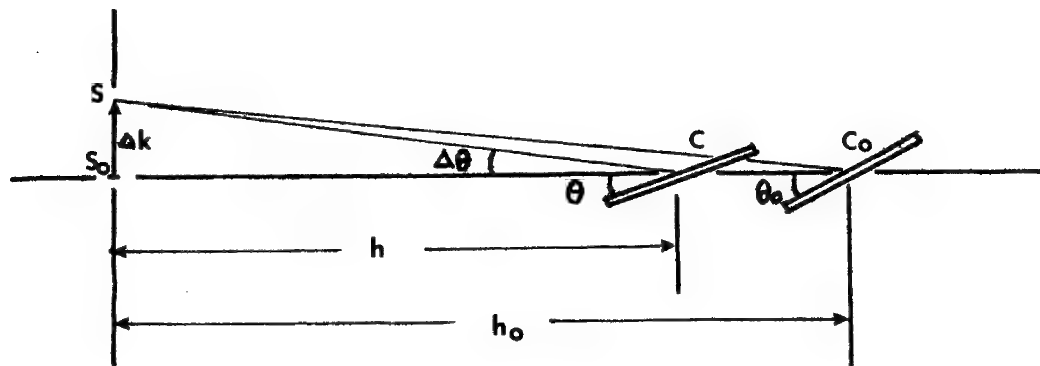
Fig.1. When the x-ray source is off by Δk, the crystal has to be scanned to C for diffraction.
$$\theta + \Delta\theta = \theta_0$$
The crystals are shown as flat instead of curved for simplicity.

III. MAPPING OF LARGE SPECIMEN AREA

The displacement from the specimen center to an x-ray emiting point on the surface of a specimen can be resolved into a component parallel to the K-axis and another perpendicular to the K-axis. Similar to the Δz, it is the component that is parallel to the K-axis that effects the mapping. Therefore, to a stationary crystal,(which it is when the x-ray mapping is underway) the maximum area can be mapped, or the maximum Δk can be tolerated, without significant loss of x-ray intensity is dependent on the S-C distance.

When a large area is to be mapped, the intensity error can be reduced by selecting an x-ray line that is on the high wave-length end of the crystal's scan range, i.e. large S-C distance. This is accomplished by selecting a line with greater wave-length, a higher order line, or a crystal of smaller 2d spacing. Figs. 3 and 4 illustrate the difference between plotting aluminum with RAP and PET crystals.

Even larger specimen areas can be covered by following the "dynamic mapping" procedure:
1. Turn on a fast electron beam raster over the area to be mapped.
2. Scan the crystal to record a peak of the chosen x-ray line and record the wavelength readings at both ends of the peak, λ_1 and λ_2.(Fig. 6)
3. Run the crystal to λ_2. Begin the wavelength scan at very slow speed.
4. At the same time, begin to integrate the x-ray dots with the camera or other device, with the elctron beam scanning at a proper rate.
5. Stop the integration when the crystal reaches λ_1.
The reason for this procedure is that when the crystal is at any position between λ_1 and λ_2, for example λ_k, some area on the specimen with a Δk that fits Eq. 3 (by taking $\Delta\lambda = \lambda_k - \lambda_0$) gets mapped. The result of the dynamic mapping is shown in Fig. 5.

Although the area that can be mapped with the dynamic mapping technique is not comparable to the capability of the EDS, it does have some advantages:
1. It can map very light elements which are not detectable by the EDS.
2. The wavelength resolution of the WDS suffers when the specimen area increases. But the WDS is still much better than the EDS in resolving the neighboring peaks and elements, even if the specimen area is a few mm in dimension.
3. The WDS has better peak to background ratio, therefore its mapping shows better contrast.

Figures 7, 8, and 9 show some mappings of NaF salt in conducting mounting compound containing copper. Figure 7 is a dynamic mapping of FKα which is below the limit of the EDS. Figure 8 is a dynamic mapping of NaKα and Fig. 9 is an EDS mapping of NaKα. The higher backgroud in Fig. 9 is obvious. It is partially due to the CuLα peak which is not completely resolved from the NaKα peak.

References:

1.Birks, L.S. and Grilfrich, J.V. Anal. Chem., 46,360R(1974)
2.Beaman, D.R. and Isasi, J.A. "Elentron Beam Microanalysis," ASTM, Special Technical Publication 506 (1972)
3.Walker, H., File, D., and Lewis, R., Microbeam Analysis Society, Proceeding of Tenth Annual Coference, Las Vegas, Nevada, Aug. 1975.
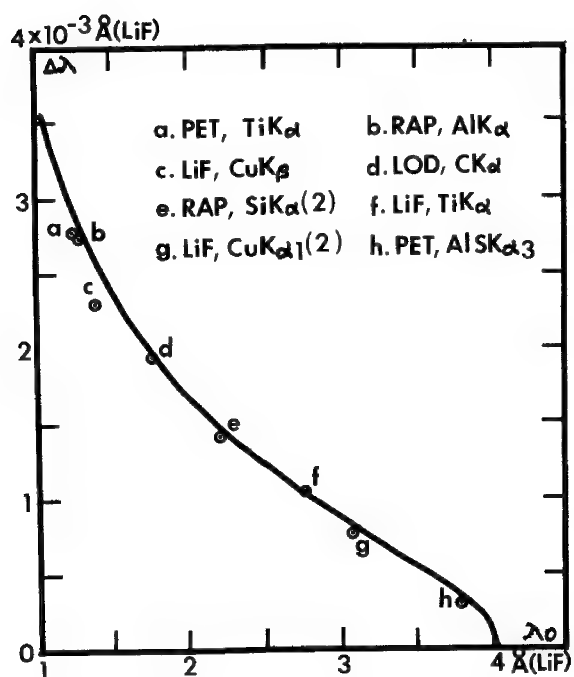
Fig. 2. The calculated and experimental results of the Z-axis effect on the wavelength measurements.
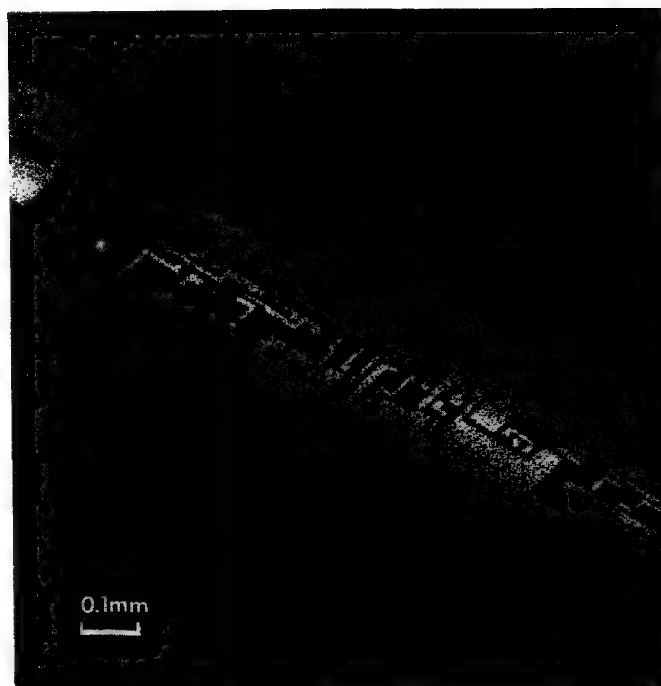
Fig. 3. The AlKα of this IC is mapped with RAP crystal (λ = 1.2856A-LiF).
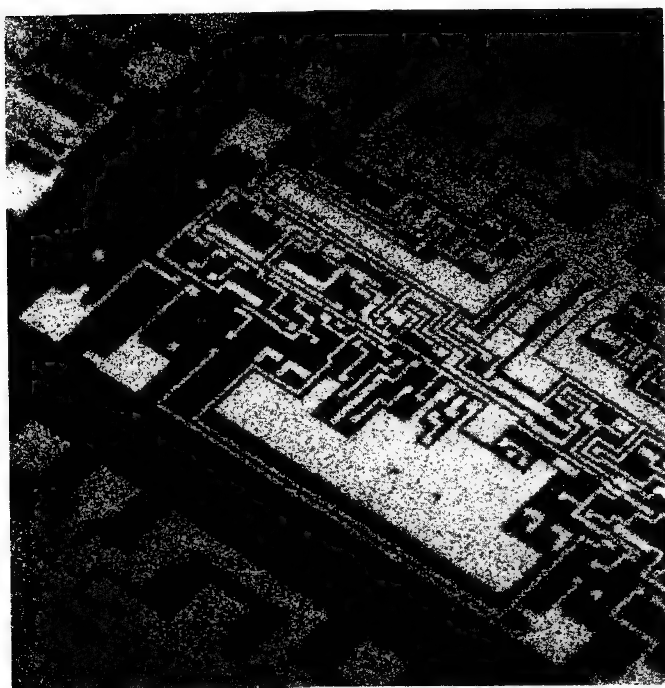
Fig. 4. The AlKα mapping with PET crystal (λ=3.8415A-LiF).
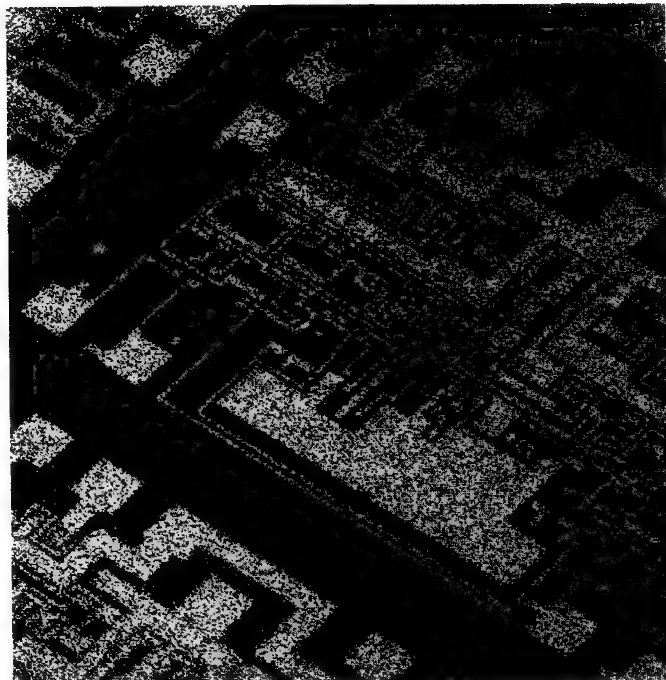
Fig. 5. The dynamic mapping of AlKα with PET cystal.
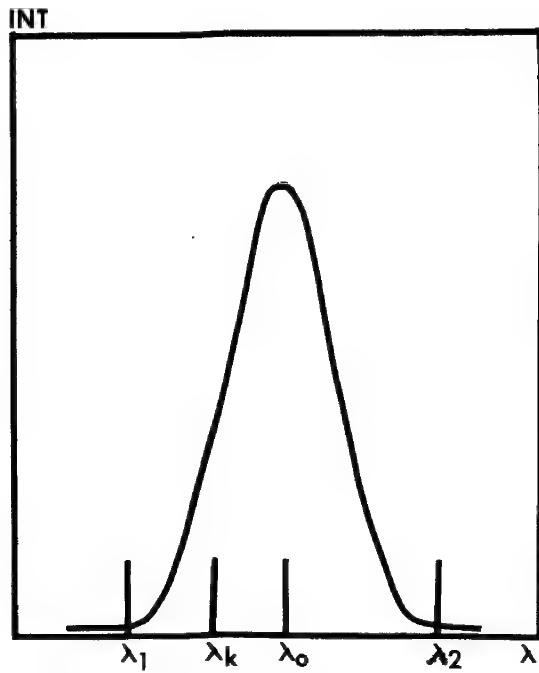
Fig. 6. The x-ray peak recorded for the dynamic mapping.
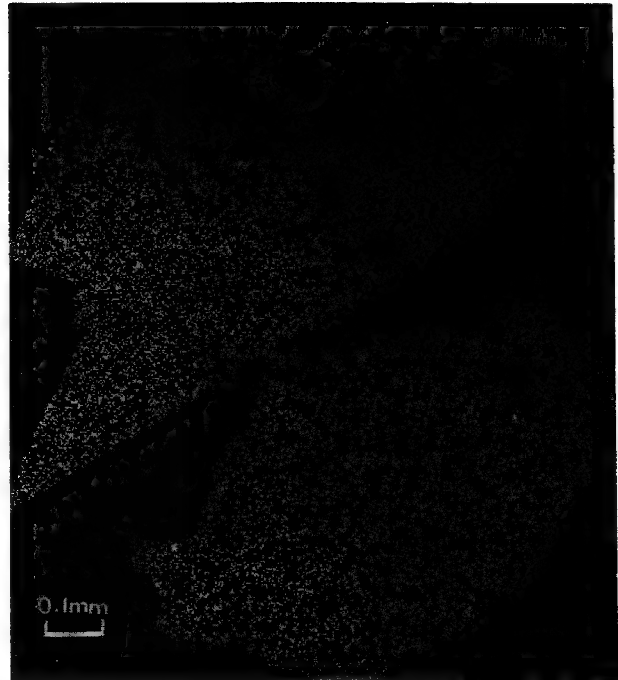
Fig. 7. The dynamic mapping of FKα, using RAP crystal.
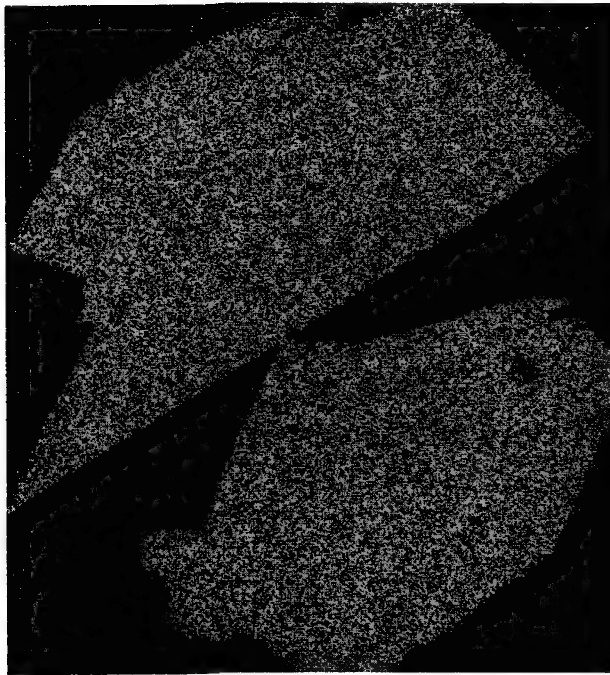
Fig. 8. The dynamic mapping of NaKα ,using RAP crystal.
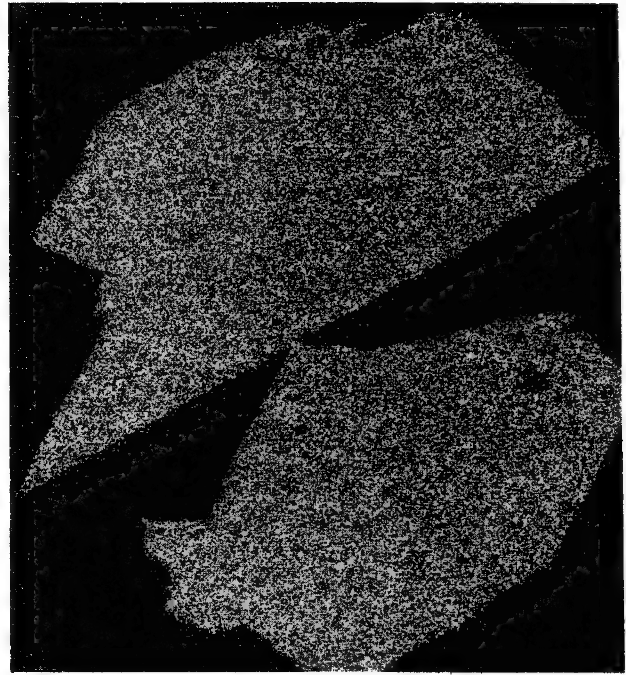
Fig. 9. EDS mapping of NaKα.

X-RAY OPTICS OF DIFFRACTION TECHNIQUES
EMPLOYING THE ENERGY DISPERSIVE SPECTROMETER

by
Robert E. Ogilvie
Department of Materials Science and Engineering
Massachusetts Institute of Technology
Cambridge, Massachusetts 02139

Introduction

It was first shown by Giessen and Gordon (1968) that the Energy Dispersive Spectrometer was well suited for obtaining diffraction patterns in an extremely short period of time. They demonstrated that it was possible to produce a diffraction pattern in which the various diffraction maxima are distinguished by the different energies of the diffracted X-rays. This is in contrast to the normal diffraction techniques where X-rays of the same energy diffract at different Bragg angles from the various d spacings.

The basic principle of the technique is to maintain the angle between the incident and diffracted beam a fixed value between 20° and 40° in 2θ. Each particular value of the d spacings which has a non-zero structure factor (F) will select an appropriate wavelength, therefore a particular energy, from the continuous spectrum emitted by the X-ray tube. This is somewhat similar to the diffraction from a single crystal in a Laue photograph. Here the 2θ values are fixed; therefore, the various atomic spacings (d) select the appropriate wavelength that will satisfy Bragg's Law.

The success of the Giessen-Gordon technique stems from the high resolution of the solid-state X-ray detector and the stability of its associated electronics.

Basic Principles

It is necessary to use an X-ray tube which will produce a high-intensity polychromatic X-ray beam. However, we do not want to use a source which will have characteristic lines with energies in the range of the diffracted energies. A line source tungsten tube would be the best selection. However, several of the L_β's and L_γ's can cause problems. A molybdenum tube is not satisfactory because of the interference of the k lines. It turns out because of the absorption in the target at the low take-off angle used in X-ray tubes (3°-6°) that a chromium tube is the best selection. It also does not have any interfering characteristic lines.

Each set of interplanar spacings (d) in the powder sample will select the proper wavelength from the continuous spectrum in order to diffract through the fixed 2θ value. This is illustrated in Figure 1.

Since we are employing an EDS system, it is better to consider the energy of the diffracted rays:

$$E = hc/\lambda \tag{1}$$

and from Bragg's Law

$$\lambda = 2d \sin \theta \tag{2}$$

we obtain

$$E = hc/2d \sin \theta$$
$$E(eV) = 6199/d(\overset{o}{A}) \sin \theta \tag{3}$$

therefore

$$1/d = E \sin \theta/6199 \tag{4}$$

However, since we employ a multichannel analyzer with the solid-state detector we determine the peak position by the channel number. Since $1/d$ vs E usually does not go through zero we will use the following expression for E:

$$E = (dV/dN)N + E_0 \tag{5}$$

where (dV/dN) is the eV/channel, N the channel number, and E_0 the intercept on the ordinate. Substitution of Equation (5) into (4) gives:

$$1/d = AN + B \tag{6}$$

where A is $(dV/dN)(\sin \theta/6199)$ and B is equal to $E_0 \sin \theta/6199$.

The intensities of the diffracted beams are not similar to those obtained by conventional powder diffraction techniques. The measured integrated intensity is determined by two factors:

$$P^{\alpha'}_{hkl} = P^{\alpha}_{hkl} \cdot R(E) \tag{7}$$

where $R(E)$ is the detector efficiency, which is illustrated in Figure 2. P^{α}_{hkl} is given by the following:

$$P^{\alpha}_{hkl} = [P(E)/16\pi R)(e^4/m^2c^4)(\lambda^3/2\mu)|F|^2 L.P. \ e^{-2M}]V_{\alpha}/v^2 \tag{8}$$

where $P(E)$ is the emitted power of energy E, μ the linear absorption coefficient, F the structure factor, R the radius of the diffractometer, p the multiplicity of hkl, L.P. the Lorentz-Polarization factor, e^{-2M} the temperature factor, V_{α} the volume fraction of the α-phase, and v the volume of the unit cell.

Applications

Lattice Parameter Measurement

Giessen and Gordon (1968) reported lattice parameter measurement with an uncertainty of 0.18%. Fukamachi et al. (1973) reported an accuracy of 0.01%.

The author has been able to obtain an accuracy of better than 0.005%. This has been achieved by using a silicon standard to determine A and B in Equation (6). The peak positions of the silicon pattern were determined by fitting a parabola to the peaks by the method of least squares. Therefore, N can be determined to $\pm$ 0.05. Figure 3 illustrates a typical pattern from the silicon standard.

Willson (1973) has treated the errors in the peak positions. However, the author employs a conventional G.E. diffractometer with a line source with the conventional solar slits to reduce cross divergence, and probably the most important factor is to use a curved specimen holder which has been described by Ogilvie (1963). The specimen holder has a radius given by the following equation:

$$R_{spec} = R/2 \sin \theta \qquad (9)$$

Using the curved specimen reduces the ΔE in the diffraction peaks and reduces the displacement of the peak.

The main problem is the shift in peak position with count rate. If this is controlled, lattice parameter measurements can be made with an accuracy of 0.005%. This then lends itself very well to the measurement of residual stresses. This latter technique has considerable advantage over the conventional X-ray method, in that areas can be examined that cannot be done by other methods.

<div align="center">Retained Austenite</div>

The determination of the volume fraction of a particular phase in a multi-phase alloy can be determined from Equation 8. If we take the example of retained austenite in steel we can write Equation (8) for P^{α}_{hkl} and P^{γ}_{hkl}. If we assume that the steel has the following phases:

$$V_{\alpha} + V_{\gamma} = 1 - V_c$$

where V_c is the volume fraction of carbides. Since carbides do not give suitable diffraction patterns, V_c is determined by point counting with a light microscope. Therefore, from the equations for P^{α}_{hkl} and P^{γ}_{hkl} and Equation (10) we can obtain the following:

$$V_{\gamma} = (1 - V_c)/(P^{\alpha}_{hkl}/P^{\gamma}_{hkl})K + 1 \qquad (11)$$

where K is a constant that could be evaluated if we could evaluate P(E) in Equation (8). However, we have evaluated K from specimens of V_{γ}. It is a simple procedure to integrate the peaks P^{α}_{hkl} and P^{γ}_{hkl}, measu background on both sides of the peaks with the multichannel analyzer. Again this procedure

has allowed us to measure the retained austenite in areas that would be difficult by the conventional methods.

Figure 4 illustrates the diffraction pattern from a specimen of 52100 which has 30% retained austenite. A similar pattern has been presented by Lauriat and Perio (1972).

Micro Diffraction

A new technique has been developed to obtain diffraction patterns from small specimens, and it has been used to determine retained austenite on the edges of razor blades. This technique uses a circular aperture located on the window of the solid state detector; thus, the complete cone of the diffracted X-rays enters the detector. The experimental setup is shown in Figure 5.

Conclusion

The diffraction pattern by the Giessen-Gordon technique can be obtained from specimens that are not suitable for conventional methods. The lattice parameter can be determined with an accuracy that is approaching that by standard procedures. However, the data can be obtained in a much shorter time and can be reduced with a computer coupled with the multichannel analyzer in seconds. With these advantages we should see a wider use of this technique.

The author would like to thank Ortec for the use of the high resolution detector, his students in 3.081 for taking the data on the lattice parameters and the retained austenite measurements.

References

Giessen, B. and Gordon, G., Science 159, 973 (1968).

Fukamachi, T., Hosoya, S., and Terasaki, O., J. Appl. Cryst. 6, 117 (1973).

Laurita, J. and Perio, P., J. Appl. Cryst. 5, 177 (1972).

Ogilvie, R. E., Rev. Sci. Inst. 34, 1344 (1963).

Wilson, A. J. C., J. Appl. Cryst. 6, 230 (1973).
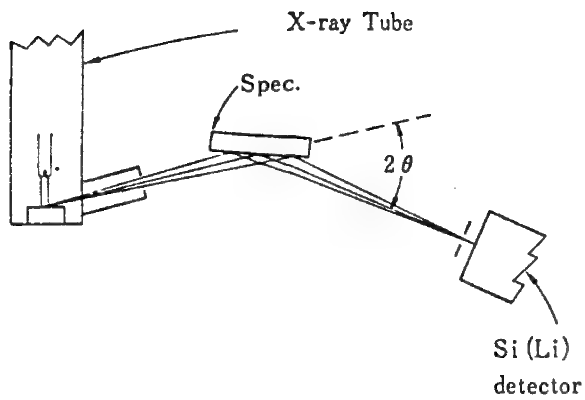
Figure 1. Schematic of the X-ray optics for the Giessen-Gordon technique.
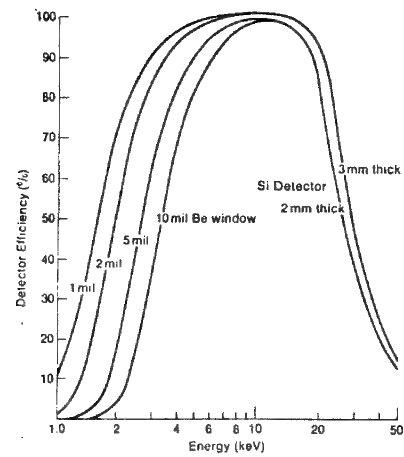
Figure 2. Efficiency of the solid state detector.

(111)   (220)(311) (222)(400)(331)
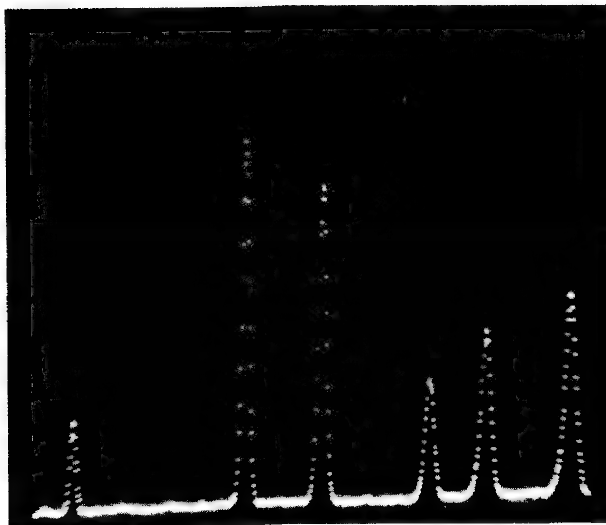
Figure 3. Diffraction pattern of the Si standard.

(110)α (200)γ   (200)α (220)γ (211)α
(111)γ
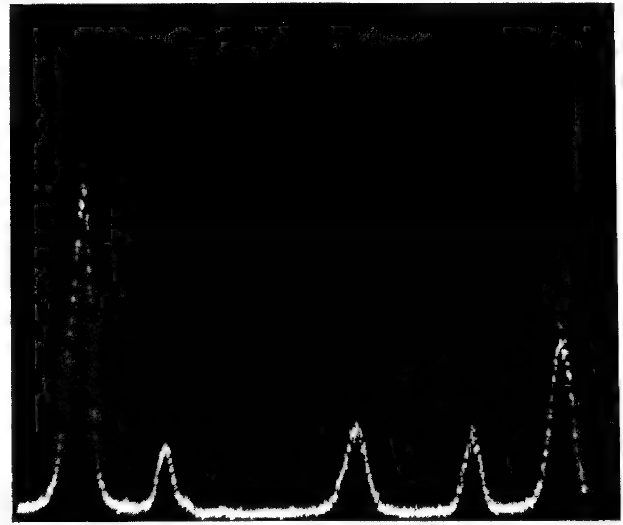
Figure 4. Diffraction pattern of a steel (30% austenite).
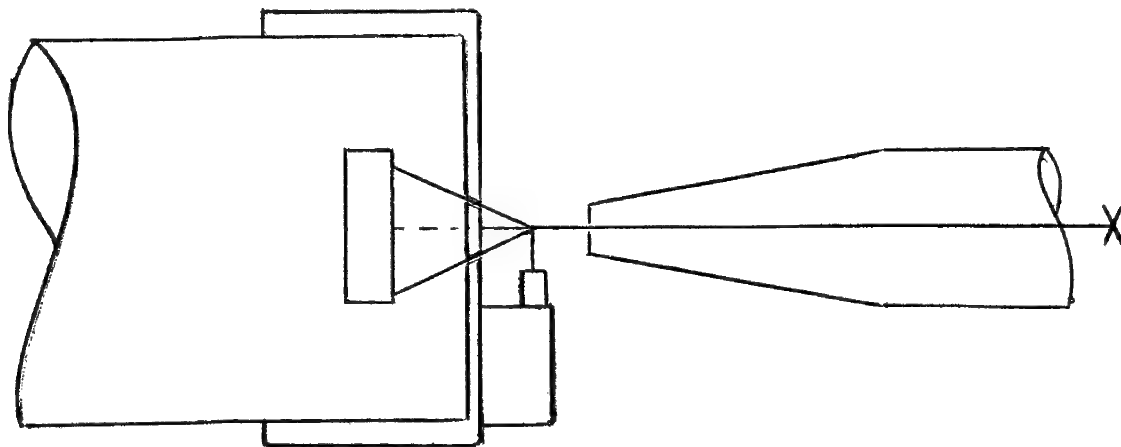
Figure 5. Schematic of the micro diffraction technique.

CONCERTED ESCA-ISS-SIMS INVESTIGATIONS IN SURFACE ANALYSIS

Gheorghe D. Mateescu
Dept. of Chemistry
Case Western Reserve Univ.
Cleveland, Ohio 44106

There are several important characteristics which render ESCA (Electron Spectroscopy for Chemical Analysis) a particularly powerful method to be applied in surface chemistry: (1) the relation between the core electron binding energy (F_b) and the gross atomic charge distribution, (2) the detectability of ground and/or final state multiplicities, (3) the time-scale of the photo-ionization process, (4) the almost overlap-free distribution of characteristic E_b's, (5) the possibility of probing surface and subsurface layers of solid specimens. Each of these characteristics will be discussed by means of practical examples.

In connection with the potentiality of ESCA in surface studies we will describe a recent association of this method with Ion Scattering Spectroscopy (ISS) and Secondary Ion Mass Spectrometry (SIMS) which yields structural information on organometallic compounds.

The basic principles and instrumentation will be presented in order to make it possible to follow the discussion for participants who are not familiar with ESCA, ISS, and SIMS.

THE SCANNING AUGER MICROPROBE: A REVIEW

N. C. MacDonald and C.T. Hovland
Physical Electronics Ind., Inc.
6509 Flying Cloud Drive
Eden Prairie, Minnesota 55343

The first Scanning Auger Microprobe (SAM) was introduced during the 1973 meeting of the Electron Probe Analysis Society of America. This first SAM instrument had a minimum probe diameter of five micrometers, which in 1973, was a considerable improvement over previous commercially available Auger Spectroscopy equipment with a minimum probe diameter of 25 micrometers. During the past three years the probe diameter of the SAM has been reduced to less than 0.2 micrometers in diameter and automated and multiple surface analytical techniques analysis features have been added.

The primary function of the SAM instrument is to determine the elemental composition of the first few atomic layers of a solid. The surface composition is of importance for the understanding of surface phenomena in semiconductor processing, corrosion resistance of materials, grain boundary segregation in materials, the adhesive properties of materials, the chemical reactivity of spatially inhomogenous surfaces, and other surface related phenomena. In general, SAM analyses of practical materials have shown vast differences between the elemental composition of the surface and the "bulk composition" of a solid determined by an electron microprobe which measures the elemental composition of a layer approximately 1μm in depth.

The use of the SAM instrument with in-situ ion beam etching of the specimen allows the in-depth elemental analysis of materials with an in-depth resolution approaching 10-20Å and a lateral spatial resolution of less than 0.2 micrometer diameter. With SAM and ion beam etching, the elemental composition of a solid can be analyzed with a volume resolution of less than $10^{-16}cm^3$. For example, in-depth elemental analysis, or thin film analysis, is routinely used to analyze thin films on microelectronic circuits to identify interfacial chemistry that can affect the electrical properties of microelectronic circuits, the mechanical strength of wire bonds, or the adherence properties of thin films. Other applications include the thin film analysis of optical or metal coatings.

Recent trends in scanning Auger microbeam analysis include smaller probe diameters, programmable control of the electron beam, and automated, quantitative elemental surface analysis and thin film analysis. In special cases, the Auger peak

shape or Auger peak shift has been used to determine chemical information for some elements in submicrometer diameter areas.

There is also a trend to combine SAM analysis with other surface analysis techniques. Multiple-technique instruments have revealed a significant degree of synergism when two or more surface techniques are combined. This synergism extends beyond the resolution of routine data interpretation problems such as peak overlaps or sensitivity variations and permits a more complete analysis to be performed. Correlation of different kinds of data obtained from the same surface using different techniques often substantiates or denies conclusions suggested by information obtained with only one technique. Multiple techniques such as Electron Spectroscopy for Chemical Analysis (ESCA), Secondary Ion Mass Spectrometry (SIMS), Ultraviolet Photoelectron Spectroscopy (UPS) and Low Energy Electron Diffraction yield additional chemical, molecular, and structural information for a more complete in-situ characterization of solid surfaces.

For submicrometer probe diameters, the chemical spatial resolution (not spot size) is usually limited by the lateral distribution of backscattered electrons. The resultant lateral distribution of Auger Electrons depends not only on the probe size but also the energy of the Auger transition, the primary probe energy, the angle of incidence of the electron probe and the composition and surface topography of the specimen. For submicrometer diameter probes, improvement in the lateral chemical spatial resolution is observed for decreasing beam voltage,for normal beam incidence and for higher energy Auger transitions.

Simple theoretical models are now used for quantification of the Auger signals. As the models are improved and verified experimentally, SAM analysis should approach the precision and accuracy associated with electron probe analysis for selected, smooth specimens. Characterization of surface topography appears to be one of the main error factors for quantitative SAM analysis.

During the past four years SAM instruments have been placed in many industrial, government, and educational laboratories throughout the world. The SAM is routinely used to complement results obtained with other standard analytical instruments such as the electron microprobe, scanning electron microscope, and X-Ray diffraction instruments. Future trends in Scanning Auger microanalysis include a marriage of other surface analytical techniques with the SAM for automated in-situ analysis of a solid surface.

SCANNING ELECTRON SPECTROSCOPY FOR CHEMICAL ANALYSIS

C. T. HOVLAND
PHYSICAL ELECTRONICS INDUSTRIES, INC.
6509 Flying Cloud Drive
Eden Prairie, Minn. 55343

Spatially resolved and scanning ESCA (Electron Spectroscopy for Chemical Analysis) capabilities have been recently realized experimentally. A theoretically proposed experiment by J. Cazaux[1] has lead to demonstration of scanning, small area ESCA on certain specially prepared specimens[2].

X-rays created by a scannable, high resolution electron beam in a thin aluminum foil pass through the thin foil and create photoelectrons from the foil side opposite the incident electron beam (Fig. 1). The photoelectrons are then energy analyzed with a double pass cylindrical mirror analyzer (CMA)[3] (Fig. 2). A thin specimen may be placed opposite the incident electron beam resulting in a spatially resolved photoelectron source from the specimen surface. The aluminum foil thickness is important due to heat dissipation from the electron beam, filtering of the continuous radiation created by the electron beam, an exponential decrease of intensity of the x-rays with increasing foil thickness, and the penetration of electrons into the thin foil. The specimen thickness and mass absorption coefficient for Al K_α x-rays in the specimen are also important.

Experiments were conducted with three foil thicknesses, 2 μm, 4 μm, and 6 μm, to determine which foil thickness gave
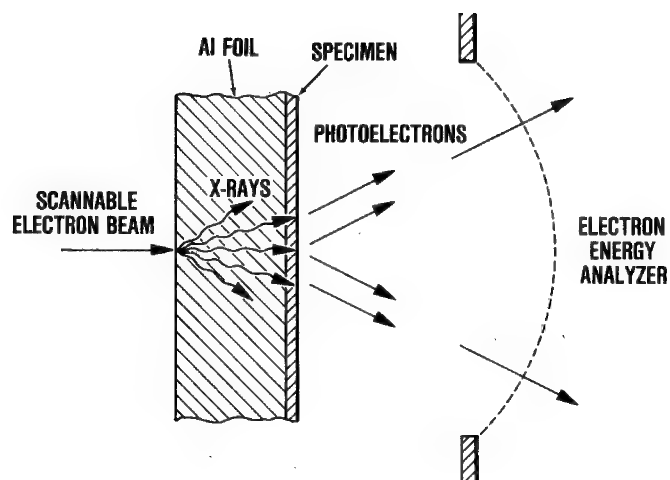
Fig. 1 Scanning ESCA Technique for Photoelectron Production.
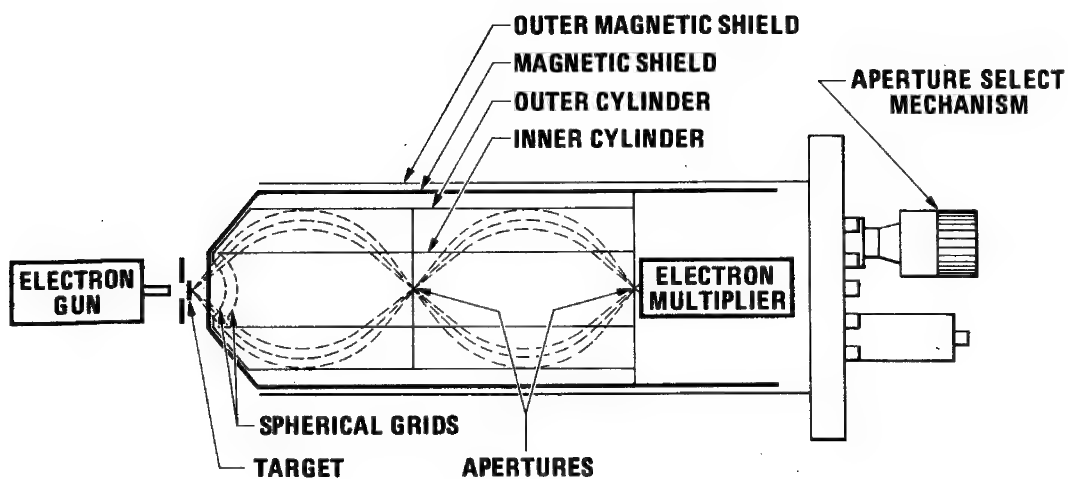
Fig. 2. Configuration to Produce and Analyze Photoelectrons From a Spatially Resolved Area.
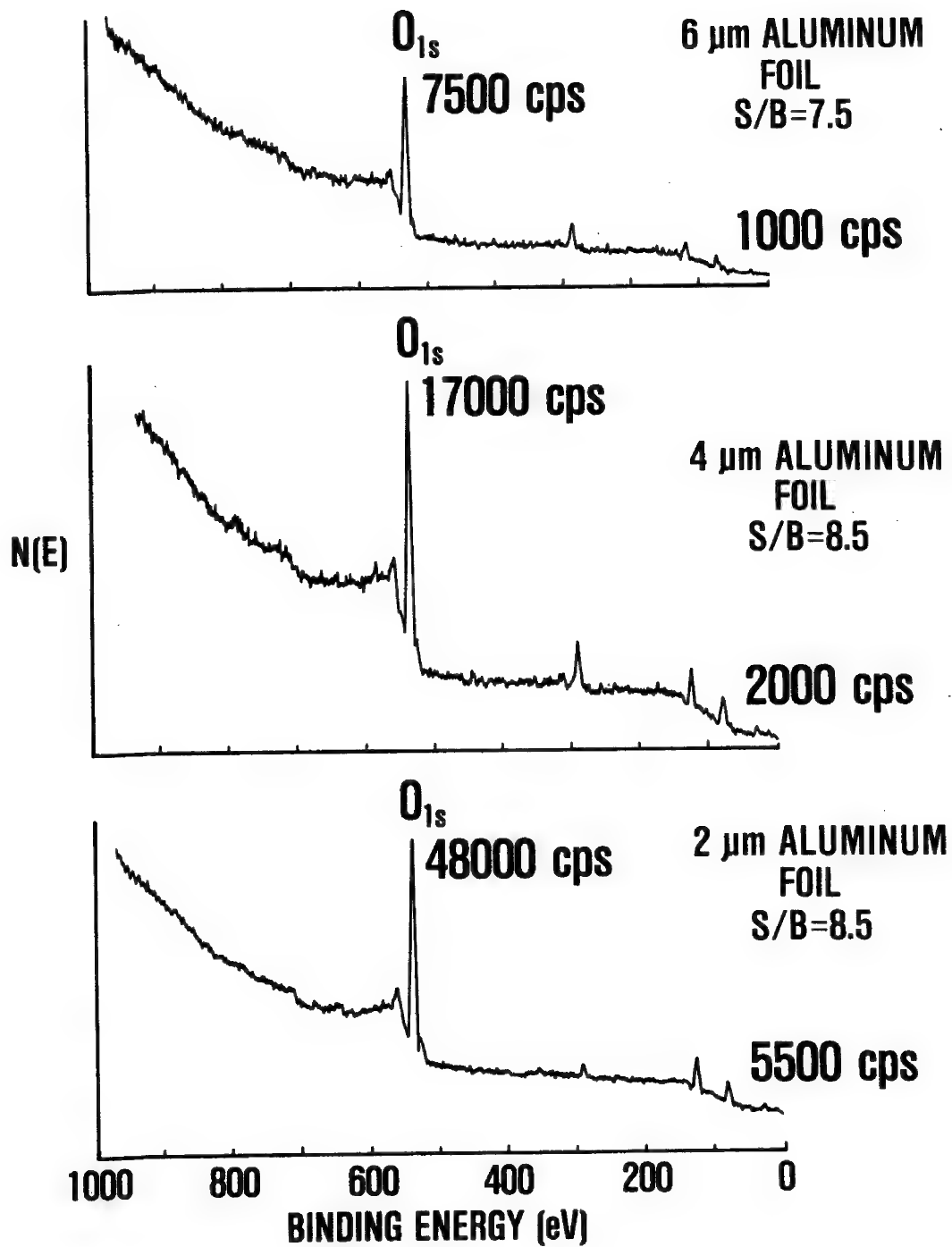
Fig. 3. Signal Intensity and Signal to Background Measurements for Three Foil Thicknesses.

optimum signal intensity and signal background ratio (Fig. 3). The measurements were conducted at 10 keV primary electron energy, 37 µA primary current, and without specimens mounted on the foil. Signal to background values were measured as the ratio of the oxygen photoelectron peak intensity to the background intensity at 0 eV binding energy. The results show that the 2 µm aluminum foil yields the highest intensity signal with a signal to background ratio similar to the thicker foils.

The combined thickness of the aluminum foil and specimen determines the photoelectron source area from the specimen surface. A greater combined thickness results in an increase in the photoelectron source area. Therefore minimizing the specimen thickness is necessary. Previously reported experiments[2] have demonstrated approximately 20 µm resolution with a 6 µm aluminum foil (Fig. 4) as measured by utilizing an intensity modulated line deflection and assuming a Gaussian photoelectron source area distribution. More recent experiments have shown that approximately 12 µm photoelectron source area resolution is possible with 2 µm aluminum foil.

REFERENCES

1. J. Cazaux, Rev. Phys. Appl. 10, pp 263-280 (1975).

2. C. T. Hovland, Appl. Phys. Lett. 6, Vol. 30, pp. 274-275 (1977).

3. P. W. Palmberg, J. Electron Spectroscopy Relat. Phenom. 5, pp. 691-703 (1974).
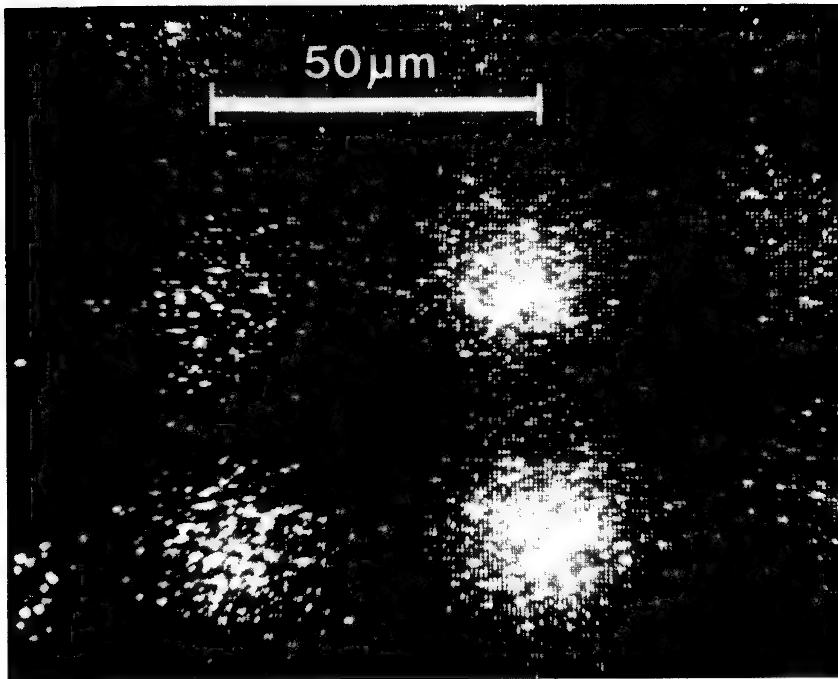
Fig. 4a. Scanning ESCA Image for Oxygen Photoelectron Line
on 6 μm Aluminum Foil Masked by a 50 μm Center to
Center Nickel Grid.
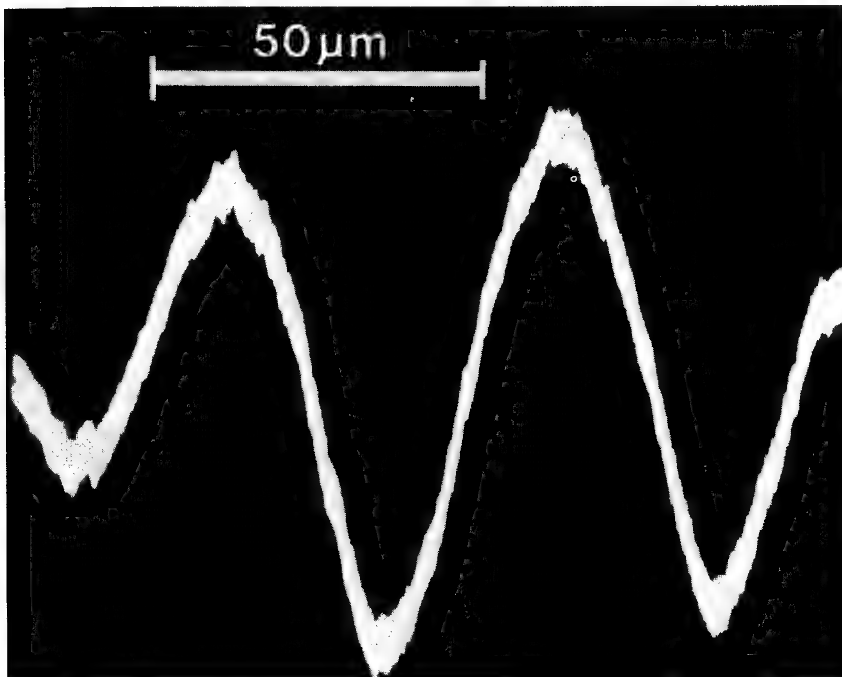
Fig. 4b. Intensity Modulated Line Deflection in Area of
4a. Demonstrating Approximately 20 μm Spatial Resolu-
tion.

NEW INSTRUMENTAL CAPABILITIES IN AUGER ELECTRON MICROSCOPY

W.R. Bottoms and J.A. Schoeffel
Varian Associates
Palo Alto, California 94303

INTRODUCTION

Auger Electron Spectroscopy is entering a new era. Significant improvements in electron optics now provide spatial resolution for integral gun Auger analysis in the sub-micron range. Both high current and sub-micron spot size are available from a single, three lens electron optics package. A double pass cylindrical mirror analyzer (CMA) designed for use with this sub-micron gun provides an increased field of view and a variable exit aperture allows the operator to make the trade-off between high sensitivity and high energy resolution for chemical shift information. A new approach to the electronics required for data acquisition and reduction provides for direct measurement of $E \cdot N(E)$ spectra. These spectra are acquired in a true signal averaging mode so that the elemental sensitivity may be extended by increased counting times. Subsequent to (in some cases concurrent with) the acquisition of data, a series of operations may be carried out on the data stored in digitial memory to allow smoothing, differential, integration, etc. These data may also be acquired and stored in various presentations to provide elemental surface maps in various formats and depth profiles at multiple points on a sample with a single ion beam etch.

ELECTRON OPTICS

The electrostatic electron gun employed in this system is illustrated in Fig. 1. It is integral to the CMA and can produce, through the demagnification of its three condenser lenses, a beam diameter of less than $0.2 \mu m$. Through judicious choices of apertures and their positioning, close to the theoretical maximum beam currents consistent with energy, lens design and source brightness are obtained over a range of beam diameters up to 10 μm. At 5 keV the maximum beam current obtainable from the prealigned LaB_6 cathode is in excess of $20 \mu A$, while that at $0.5 \mu m$ is greater than 10nA. Under conditions consistent with this performance and under sputtering conditions, cathode life is in excess of 500 hours. This electron gun also provides beam energy

of up to 10 keV. The voltages of the lenses, the alignment plates situated between the lenses, the stigmator, and the deflection plates which poisition the beam on the sample, all track the beam voltage. This assures that the electron trajectories will be constant through the gun and onto the samples, thereby maintaining focus when beam energy is changed. Typical images are illustrated in Fig. 2.

The gun is contained in a two-stage CMA (Fig. 1) which provides adequate length for the necessary electrodes and, on account of its dispersion/imaging properties[1] enables Auger maps to be made of almost twice the linear dimensions of those from a single-stage analyzer of the same diamter (for the same edge reduction in signal and for the same analyzer resolution). Line scans scross the center of field for the three aperture settings of the spectrometer are illustrated in Fig 3. These were made on the elastic peak which is intrinsically narrow. Flatter characteristics are obtained even on the relatively narrow Ni, LMM or Cu, LMM peaks, where a 10% increase in field width at the 0.6% setting is obtained. Much greater improvement is found on the P, MVV, the Si, LVV or the C peaks due to their increased intrinsic width ($\Delta E/E$), thereby providing an even larger usable field of view.

DATA ACQUISITION

The data acquisition system of the Varian Automated Auger Microprobe is totally digitized. It acquires direct $E \cdot N(E)$ data through measurement of the current flowing through the exit aperture of the CMA. There is no modulation of the voltage on the CMA or of the electron beam. The digital character of the data stream provides insensitivity to thermal drifts, phase shifts, and other problems inherently associated with phase-lock amplification techniques. The data stream is transformed to digital format immediately adjacent to the CMA (Fig. 4). The output of the CMA is converted to a digital signal through the use of a voltage to frequency converter. The frequency is decoded by a counter and input as a digital number to the system memory. This technique provides fast, accurate analog to digital conversion with an exceptionally high dynamic range. The resolution of the voltage to frequency converter-counter combination is one part in 65535. This

high dynamic range in the data acquisition assures that both very large and very small Auger peaks are obtained in the spectrum without the loss of either extreme because of a miscalculation of required gain settings. The typical problem encountered in analog systems of the necessity to change gain settings during the acquisition of an Auger spectrum is eliminated. This new system allows a choice of the scale factor in both the X and Y axes to be made after data is acquired. It is, therefore, not possible to encounter a situation where the operator overruns the field in either dimension.

DATA STORAGE AND REDUCTION

The system design provides for permanent, portable storage of data in the format desired by the operator. All data storage, which is accomplished via an IBM format dual floppy disk drive, contains with it a header in which every parameter pertinent to the conditions of the data acquisition is recorded. This facility allows direct comparison, for instance, of data taken on similar samples many months apart with the assurance that all conditions of data acquisition remain identical. The data storage is also performed with high dynamic range, allowing the operator to reduce that data by various post-acquisition data reduction schemes. The digital removal of high frequency noise, deconvolution of background, differential analysis between spectra, and other data reduction sequences important to materials characterization are possible.

REFERENCES
1. V.V. Zashkvara, M.I. Korsunskii and O.S. Kosmachev:
    Sov. Phys. Tech. 11 (1966) 96.
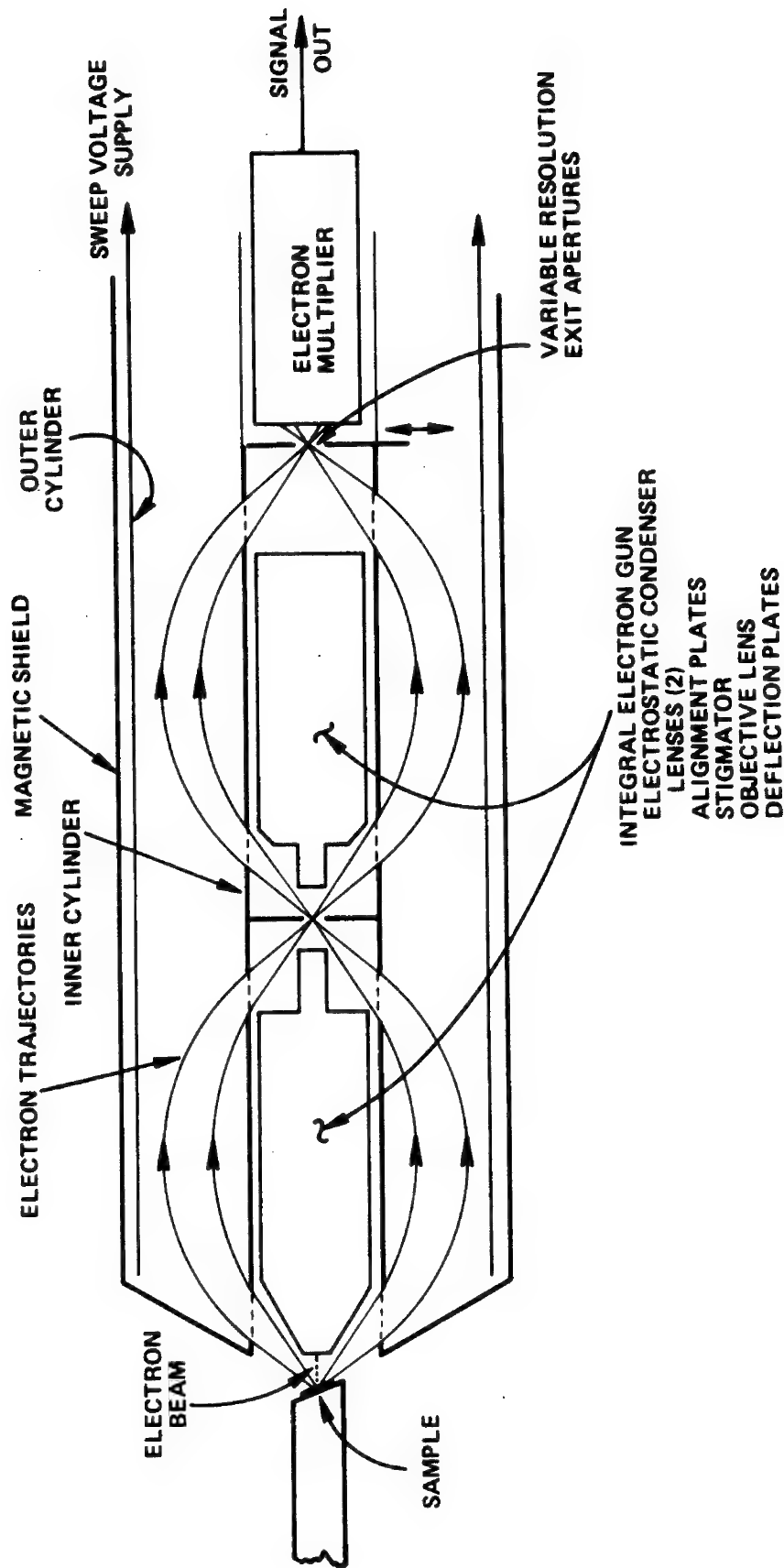
CROSS SECTION OF THE
TWO-STAGE CYLINDRICAL MIRROR ANALYZER

FIG. 1
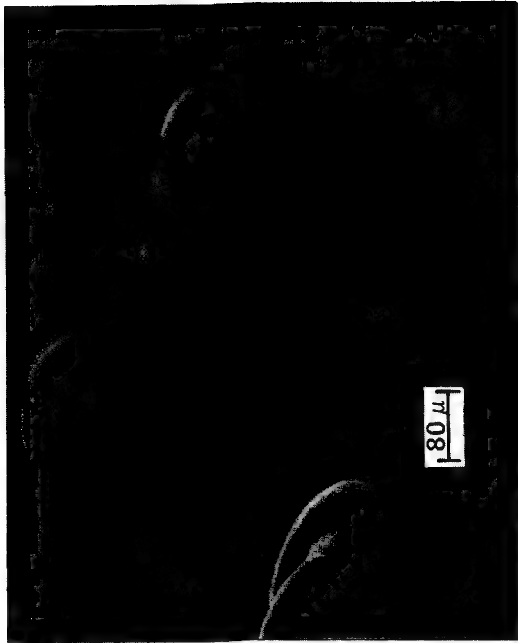
SLOW SCAN IMAGES
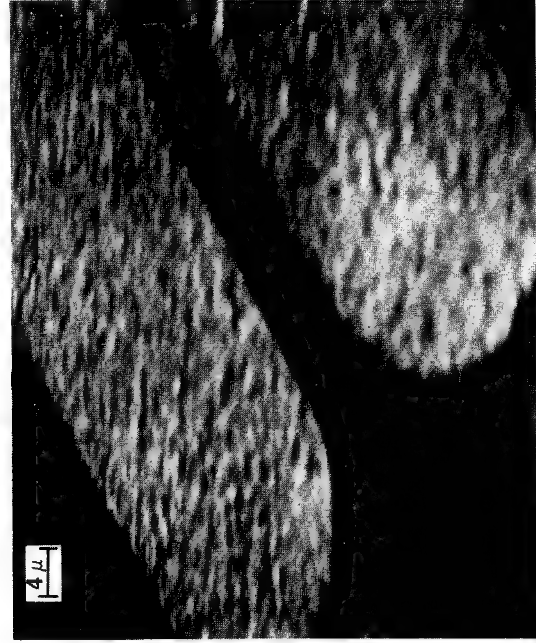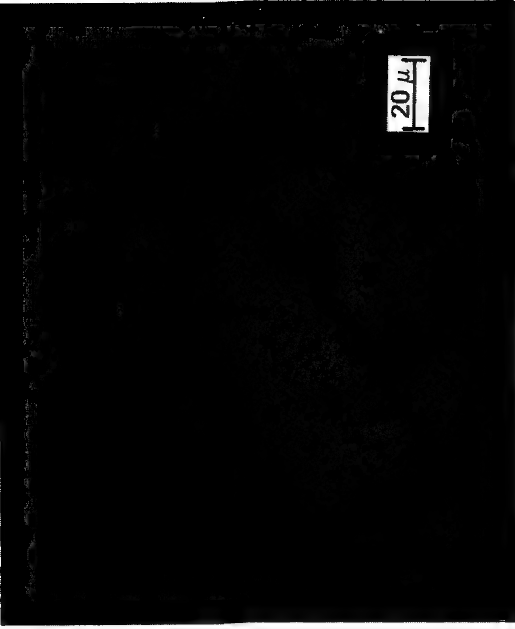
TV MONITOR IMAGES
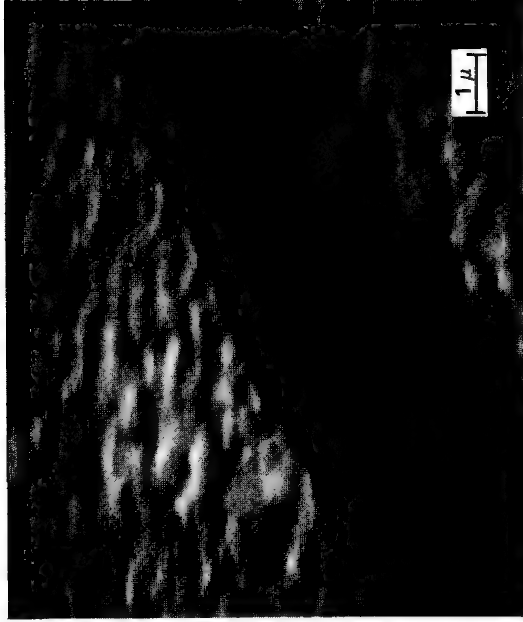
SECONDARY ELECTRON IMAGES
MICROWAVE FIELD EFFECT TRANSISTOR
FIG. 2

1.2% RESOLUTION APERTURE

0.375

0.600

X-SWEEP mm

0.5

0.3%

0.6%

1.0
0.9

0.5

ANALYZER RESPONSE

FIG. 3

CONTROL
CONSOLE

DUAL
CRT DISPLAY

FLOPPY
DISKS

X-AXIS

Y-AXIS

Z (INTENSITY)

SYSTEM
CONTROLLER

SYSTEM
MEMORY

SCAN ENERGY
(X-Y) COORDIN-
ATES AND
OTHER
PARAMETERS

PRE-
PROCESSOR

DIGITIZER
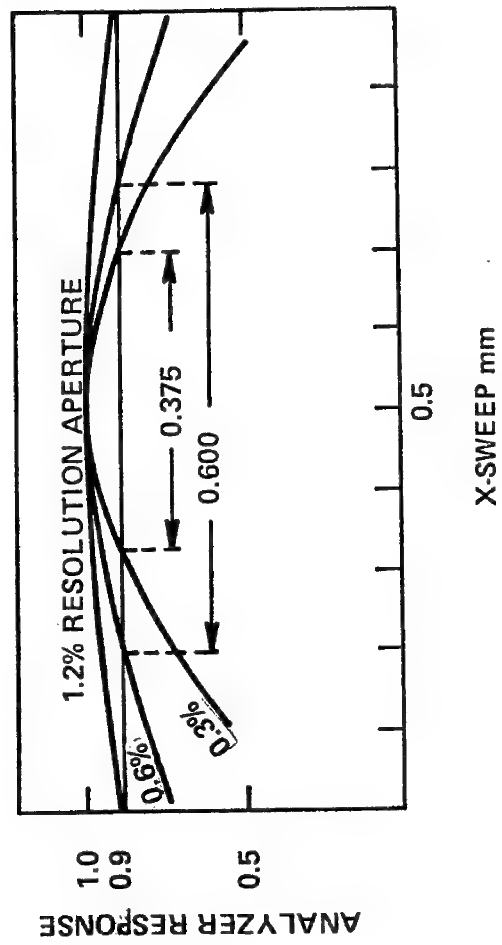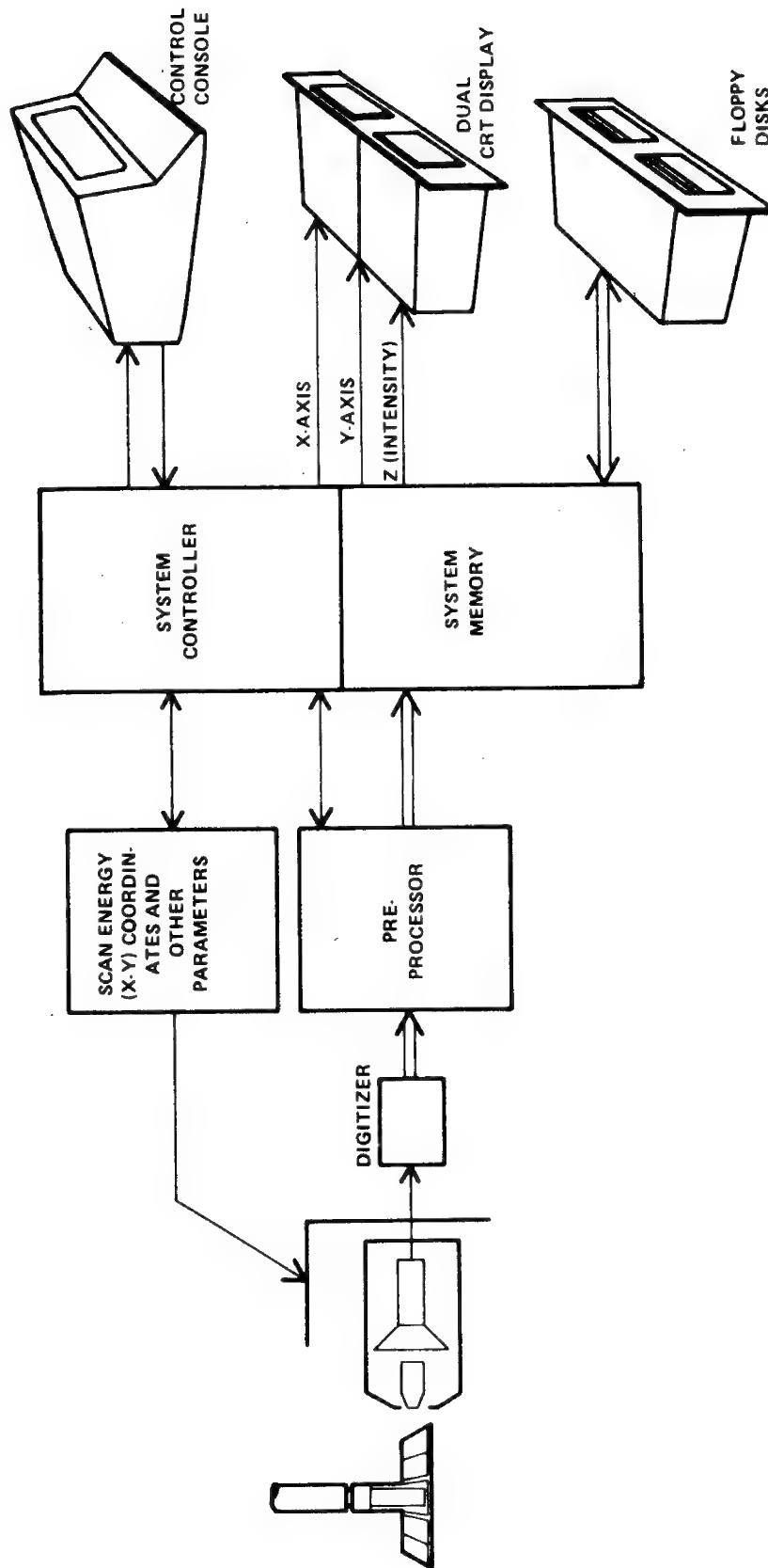
COMMAND AND DATA FLOW PATHS

AUTOMATED AUGER MICROPROBE

FIG. 4

THE DETERMINATION OF AUGER ELECTRON CROSS SECTIONS AND ATTENUATION
LENGTHS USING PROTON-EXCITED X-RAYS

P. B. Needham, Jr., and T. J. Driscoll

College Park Metallurgy Research Center, Bureau of Mines,
U.S. Department of the Interior, College Park, Maryland 20740

Proton-excited X-ray emission (PEX) offers a unique approach to obtaining
information related to Auger electron phenomena that can be very important to
full development of the Auger electron spectroscopy (AES) technique. AES
plays an important role in the analysis of solid surfaces and, with ion
sputtering, thin films. Although calibration techniques have been reported
that produce semiquantitative AES results, there are, however, two major
Auger electron phenomena for which specific knowledge is necessary in order
to develop the full potential of AES as a quantitative spectroscopy. These
are (1) the Auger electron production cross sections due to electron beam
impact and (2) the inelastic attenuation lengths for these electrons through
bulk solids.

Auger electron production cross sections have been determined for oxygen,
carbon, sulfur, aluminum, and iron by obtaining values of monolayer-level
coverages of these elements using PEX, while at the same time obtaining the
Auger electron yields due to electron beam impact. The coverages, N_x, in
atoms/cm^2, were determined from[1] $N_x = L_x/\sigma_x$ where L_x is the experimentally
measured X-ray yield and σ_x is the appropriate experimentally determined
thick target X-ray production cross section for proton impact. The Auger
electron yield, Y, was obtained from the second derivative Auger spectra
using Taylor's equation

$$Y = i_A/i_o = \left[\frac{11.8}{Z_o T}\right] \left[\frac{\sigma^2}{k^2}\right] \Gamma_A \tag{1}$$

where i_A is the detected Auger current, i_o is the incident electron beam
current, T is the transmission coefficient for the four-grid retarding-field
analyzer (RFA), 2σ is the width of the Auger peak (assumed to be Gaussian),
2k is the peak-to-peak amplitude of the modulation voltage, and Γ_A is the
normalized experimental Auger amplitude in $\mu V/\mu A$. The Auger electron yields,
Y, the monolayer surface coverages, N_x, and the electron ionization cross
sections, $\sigma_A(U)$, are related with Bishop's and Riviere's equation[3]

$$Y = N_x(\Omega/4\pi)r \csc \Psi \, \sigma_A(U) \tag{2}$$

where r is the backscattering coefficient, Ψ is the electron beam angle of
incidence, $\sigma_A(U)$ is the Auger electron production cross section, $U = E_o/E_k$,
E_o is the incident electron beam energy, and E_k is the critical absorption
energy of the inner shell to be ionized. Finally, the Auger electron pro-
duction cross sections, which are essentially equal to the ionization cross
sections for the cases considered here, were obtained from Eq. 2 and the
experimentally-determined values of N_x and Y as

$$\sigma_A(U) = (4\pi/\Omega) \, (r \csc \Psi)^{-1} \, (Y/N_x) \tag{3}$$

The use of PEX to determine Auger electron production cross sections is
limited in accuracy primarily by the uncertainties associated with values of

the proton-excited X-ray production cross sections. While these uncertainties are about ±25% for the elements of interest here, the cross sections obtained here are still substantially more accurate than those obtained by other methods. We will also describe how the more general use of these derived values of σ_A with a linearization of the Bethe equation[4] for ionization cross sections can result in values of the Bethe coefficients, b_{nl} and c_{nl}[4].

Inelastic attenuation lengths are generally determined through the monitoring of a specific substrate Auger transition while layers of another material are evaporated onto the substrate surface. The morphological characterization of these thin layers (of thickness comparable to the attenuation length) is necessary but extremely difficult. There is also the question as to whether these thin layers correctly simulate the practical situation encountered in AES.

The use of energetic protons to excite Auger electron transitions and the subsequent use of PEX-determined ionization cross sections provides a method for the determination of electron attenuation lengths in semi-infinite solids. The basis of the method is the generation of a calculable source of electrons in a semi-infinite solid by proton bombardment.[5] The inelastic attenuation lengths for carbon KVV (270 eV) electrons in semi-infinite thick films (>10^3 Å) of carbon evaporated onto an aluminum substrate have been determined using a simple electrontransport model described elsewhere.[6] The 270 eV Auger electrons were produced by impact of 160-keV protons. First and second derivative Auger spectra were used to derive the Auger electron yield, Y_p (Auger electrons/incident proton). The electron attenuation length, λ, was then calculated from the equation[6]

$$\lambda = Y_p/NGT\sigma_i \tag{4}$$

where G is a geometrical factor, N is the number density for bulk carbon, T is the transmission coefficient for the RFA, and σ_i is the proton ionization cross section for carbon. The electron attenuation length was found to be 5(±2.1) Å. The uncertainty in this value is due to systematic errors in the proton-excited X-ray production cross sections and in values of the associated fluorescent yields. While the total uncertainty in the value obtained here is quite large, it is amenable to substantial reduction in future experiments.

1. P. B. Needham, Jr., and B. D. Sartwell, Advances in X-ray Analysis, Vol. 14, 184, (1971).
2. N. J. Taylor, Rev. Sci. Instr. 40, 792 (1969).
3. H. E. Bishop and J. C. Riviere, J. Appl. Phys. 40, 1740 (1969).
4. H. Bethe, Ann. Phys. 5, 325 (1930).
5. R. G. Musket and W. Bauer, Thin Solid Films 19, 69 (1973).
6. P. B. Needham, Jr., T. J. Driscoll, C. J. Powell, and R. J. Stein, Appl. Lett. 30 No. 7, 357 (1977).

TECHNIQUES TO STUDY ORIENTATION DEPENDENT SURFACE CHEMISTRY

J. L. Bomback, W. C. Johnson and P. Wynblatt
Engineering and Research Staff - Research
Ford Motor Company

Surface segregation theory predicts that the degree of solute surface enrichment in certain dilute alloys depends on the surface crystallographic orientation. This compositional anisotropy is due to anisotropy of surface properties such as surface energy. Thus far, little if any experimental evidence has been obtained in this area, presumably because of the tedious procedure required to prepare different crystallographic faces of a given alloy single crystal. We have approached this problem by determining the surface compositions and orientations of many grains in a dilute polycrystalline Ni-Au alloy foil.

Two micro-analytical techniques were employed: the scanning Auger microprobe (SAM) gave the surface concentrations of the various grains while their orientations were obtained using selected area channelling patterns (SACP) taken in the scanning electron microscope (SEM). A grain size on the order of 100 microns was achieved by strain annealing the foil at $\simeq 1000°C$ and $\varepsilon = 0.02$ for 20 hours. This treatment gave several hundred randomly oriented grains and twins on a centimeter square sample which were large enough to accommodate the resolution limitations of the two instruments ($\simeq 3$ μm for the SAM and $\simeq 7$ μm for SACP).

The procedure was greatly simplified due to the grain-to-grain contrast obtained in the microscopy mode of both instruments. Sample current micrographs taken in the SAM exhibited strong intergrain contrast assumed to be due to channelling. These micrographs served as grain maps when the foil was transferred to the SEM where grains and twins were also easily delineated in the channelling microscopy mode.

A computer program was written to aid in the orientation determination. The program accepted linear measurements from the channelling patterns, calculated the Miller indices of the surface, and plotted the surface poles on a standard stereographic projection.

Some 20 grains having a wide range of surface orientations were analyzed for surface composition and orientation after equilibration in the SAM at several temperatures ranging from 650 to 900°C. A strong anisotropy of gold surface enrichment was observed; for example the gold surface concentration at 700°C varied by as much as an order of magnitude over the range of surface orientations investigated. A plot of the variation of surface composition within the standard stereographic triangle shows trends that are comparable with the known anisotropy of surface energy in fcc metals. It is concluded that surface orientation does indeed play an important role in the degree of surface enrichment in dilute Ni-Au alloys and that the synergism of these two experimental techniques provides a powerful tool for the study of surface segregation anisotropy.

AUGER ELEMENTAL MAPPING WITH REAL TIME CORRECTION FOR SAMPLE TOPOGRAPHY

N.J. Taylor, T.A. Pandolfi and W.R. Bottoms
Varian Associates
Palo Alto, California 94303

It has long been established that the most important contribution to imaging of solid surfaces with secondary electrons is sufrace topography. This is due primarily to the variation in collection efficiency for secondary electrons from surfaces, tilted at various angles to the collector. In many cases portions of a surface may be shielded entirely from the collector by other material. In the scanning electron microscope (SEM) this property gives rise to topographic images. The electric field used to collect the secondary emission signal causes emitted electrons to travel in curved trajectories and a few reach the detector even from areas shielded from line of sight.

Until recently Auger elemental mapping was carried out primarily on large, flat surfaces with beam diameters of several microns. Under those conditions surface topography could be ignored in the interpretation of data. The recent improvements in beam spot size provided by integral gun geometry Auger electron spectrometers are now allowing elemental mapping of sub-micron geometries. With the advent of sub-micron resolution, the effects of surface topography become significant (in many cases dominant) and must be taken into account when interpreting data. Conventional Auger mapping systems can be used to provide some first order deconvolution of topographic effects. This is accomplished by obtaining a secondary image and an elemental map of the same area and subsequently, using the secondary image to visually normalize the map data. In this case, dark areas in the secondary emission image must be considered area of which no meaningful Auger data has been taken. This technique has two problems. The first is that the secondary image is typically taken with a detector having a different geometric relationship to the sample than that of the Auger analyzer and, therefore, different topographic shadowing. The second problem is that the secondary image represents an integral of all

electron energies rather than a narrow, fixed energy window. This results in an image which is dominated by the inelastic peak and, therefore, much more sensitive to small variations in surface charging.

We have developed and implemented a simple technique through which both of these difficulties may be overcome. We must provide for the acquisition of an Auger elemental map over the area of interest, the acquisition of a second map over the same area using a voltage window close to the Auger peak to measure the background signal, and a subtraction of these two maps. This procedure provides a true measure of the relative strength of Auger emission from various portions of the area under study. It corrects for small changes in charge on the sample as well as for the larger artifacts in the data caused by changes in the collection efficiency due to surface topography.

The technique which we have implemented is simpler but equivalent. It involves the acquisition of data from two voltage windows for each pixel in a map. One is for the Auger peak of the element being mapped and another of an adjacent operator-chosen background voltage. The background signal and the Auger peak signals are digitized and subtracted for each pixel. The resulting number is plotted on a graphics terminal and stored on an IBM compatible floppy disk. These data are stored in 32 bit format so that a high dynamic range is provided. This allows the use of digital signal processing to display a much larger range of concentration variation than can be shown in grey scale images. Fig. 1 illustrates a map taken of a Au bonding pad using this procedure. For convenience it is displayed in "Isogram" format using 10 contours of constant concentration. The variation in Au signal amplitude corresponds to changes in surface carbon concentrations.

Fig. 2 illustrates a map taken over the same area under identical conditions but without the background subtraction. To ensure accurate comparison, this was accomplished using the same procedure except that the background energy chosen, 2500eV, was greater than the primary beam energy, 2000eV. In each case we have made one pass through the data with a digital smoothing algorithm. It is apparent that there are

significant differences. Regions A and B in particular correlate directly with the secondary image and therefore represent its convolution with the Auger map.

This simple yet powerful technique makes possible meaningful elemental mapping for samples where surface topography previously made such analysis impractical.
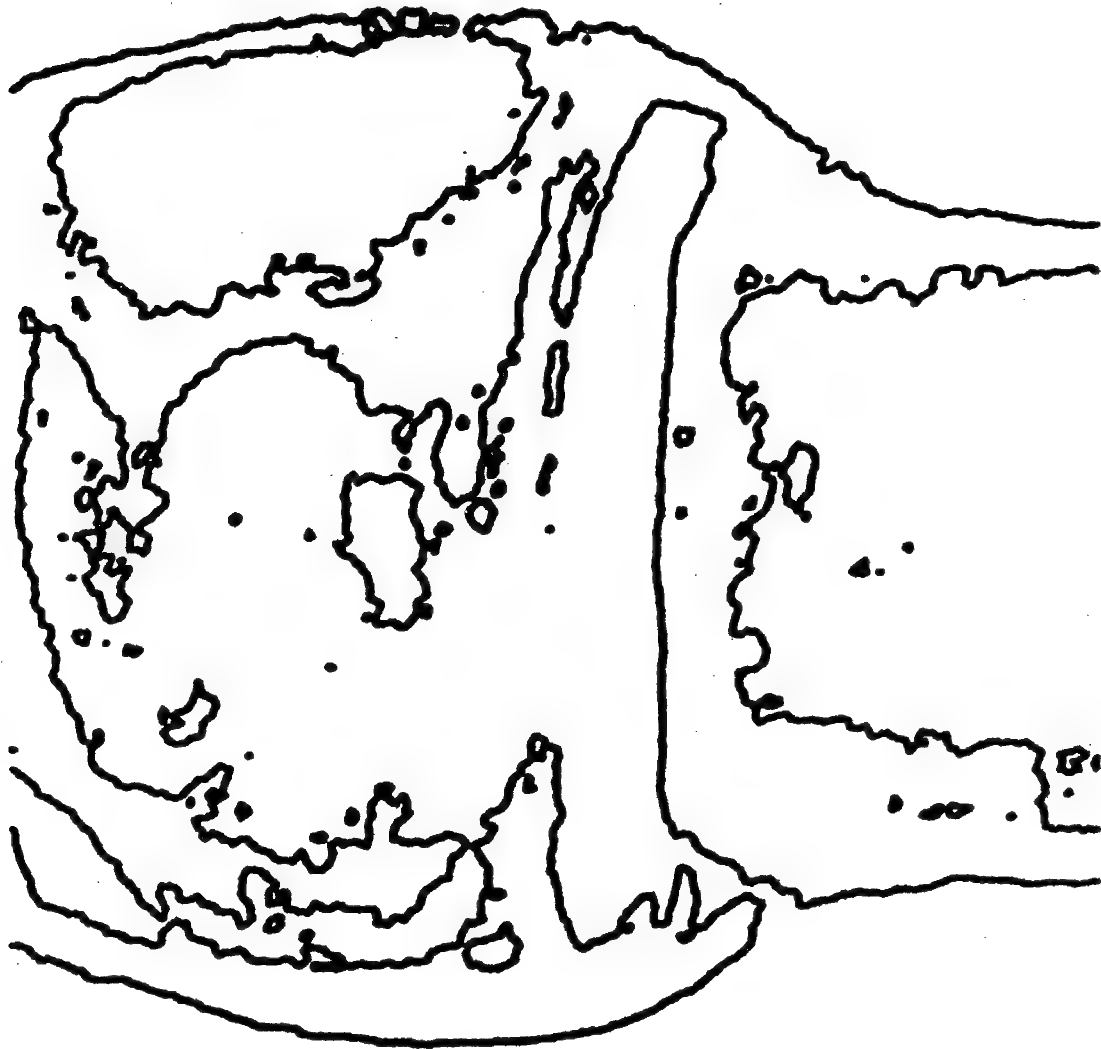
FIGURE 1
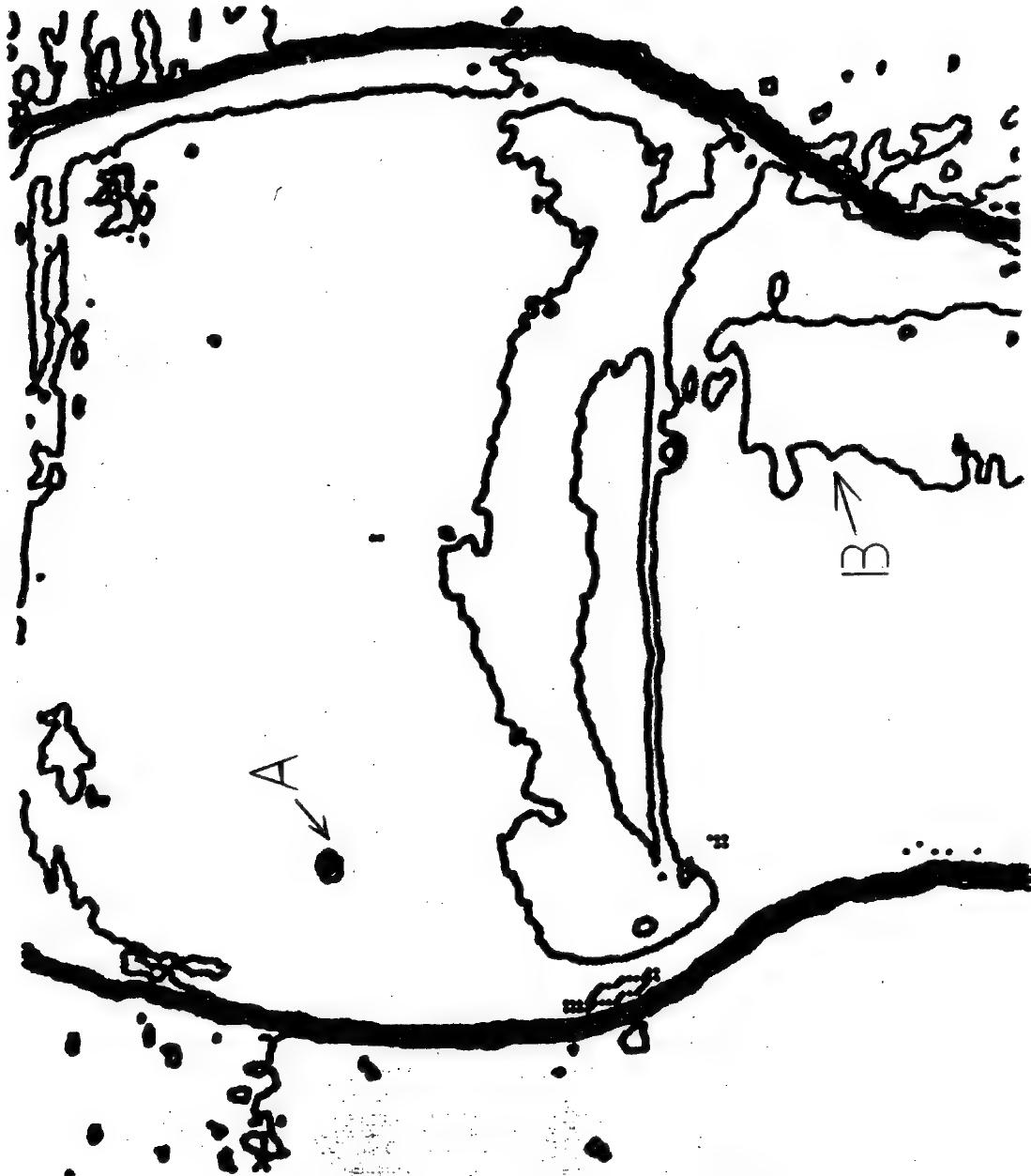
FIGURE 2

Differentiation of Surface and Subsurface Auger Sources
by Linearization of the Secondary-Electron Cascade

E. N. Sickafus
Research Staff, Ford Motor Company, Dearborn Michigan   48121

Abstract

Auger electron spectroscopy of surfaces is directed generally toward analysis of derivative-mode spectra. In this method surface constituents and their concentrations are inferred from the energy derivative of the Auger emission current and its accompanying background currents. The function being differentiated may be affected by the type of analyzer used. For example, a retarding potential analyzer can provide the derivative of the energy dependent emission current $j(E)$ while a dispersive-type analyzer provides $E \cdot j(E)$ for differentiation. In either case, the derivative spectra do not provide insight into the synthesis of the emission current according to the types of sources that produce the observed current $j(E)$. We describe here a new method for analyzing the secondary emission current. The method is based on a log $j(E)$ vs log E display mode and a hypothetical model for characterizing surface, subsurface, and composite sources of Auger emission.

The log $j(E)$ vs log E display mode has the property of emphasizing the functional form of the cascade. The result of displaying a secondary electron emission spectrum in this mode is that the cascade components have a linear characteristic.[1] Consequently, the presence of sources such as Auger emission appear as additional emission superimposed on the linearized cascade.

The log j(E) vs log (E) spectra shown here for a copper single crystal were obtained with a retarding potential analyzer. This is a four-grid system made from a commercial low-energy electron diffraction system having an acceptance aperture of ∿ 96°. The function j(E) (commonly referred to as N(E) in Auger spectroscopy literature) is obtained by standard potential-modulation and synchronous-detection techniques. The logarithmic operations were performed on the analog signals that otherwise would have been directed to an xy-recorder for j(E) vs E displays. Commercially available integrated circuit, 6 decade logarithmic amplifiers were used for this purpose.

The nature of the log j(E) vs log E spectrum is shown for a Cu(110) surface. It is noted that the cascade is divided into linear segments that are demarcated near energies characteristic of electronic core states of the specimen. In most cases, a characteristic emission line appears at the high energy end of a linear segment. The synthesis of the observed spectral features can be explained on the basis of the following model. Although the model is hypothetical it is based on numerous observations of linearized cascades in several materials.

The linearized cascade that appears in a log j(E) vs log E display can be described as a function of the form $j(E) = AE^{-m}$. A solution of the Boltzmann diffusion equation predicts the same functional form for a homogeneous source.[2] Thus we take the linear portions of the display, on the high energy side of an Auger emission threshold, as eivdence of a thermalized internal distribution function N(E) which results from all sources lying at higher energies. We have now to characterize the emission line shape following the threshold toward lower energy: We first divide the specimen into

thin parallel-sided slabs of thickness $\ell_i(E)$, where $\ell_i(E)$ represents the inelastic mean free path of an electron having an energy E. The first slab at the surface represents a homogeneous surface source. From this source electrons can escape the surface elastically and be detected as a characteristic line. Emission from this slab that is directed into the solid can reappear at the surface only after suffering inelastic collisions. Thus this emission is in effect also thermalized and adds to the cascade strength. It therefore results in a step following the emission threshold. There remains that small amount of emission from the first slab and most of the forward emission from deeper slabs that escapes the surface inelastically but with too few collisions to become thermalized. It produces a new (linear) function that appears with a cascade slope having a larger magnitude than the prethreshold cascade.

This model is used to differentiate emission from surface and subsurface sources.[3] A surface source is characterized by a strong (elastic) characteristic line plus a parallel cascade step. A subsurface source has no characteristic spectral line but will have a new cascade slope and may have a parallel step. A composite source has all features.

References

1. E. N. Sickafus, Rev. Sci. Instrum., 42, 933 (1971).

2. P. A. Wolff, Phys. Rev., 95, 56 (1954).

3. E. N. Sickafus, (to appear in Phys. Rev. B, 1977).

MATERIALS APPLICATIONS OF SPATIALLY RESOLVED
ELECTRON STIMULATED DESORPTION

A. Joshi and L. E. Davis
PHYSICAL ELECTRONICS INDUSTRIES, INC.
6509 Flying Cloud Drive
Eden Prairie, Minn. 55343

The technique of electron stimulated desorption (ESD)[1-6] combined with ion mass analysis was used to study ionic species desorbed from selected metal and oxide surfaces. The finely focused scanning electron beam enhanced the capability of the technique in probing the surface, thereby providing information on spatial distribution of surface species. The capability of the technique is discussed with selected examples that demonstrate (i) availability of chemical information from desorbed ion mass analysis, (ii) capability to study chemical distribution on specimen surfaces, and (iii) complimentary nature of ESD with other surface analytical techniques, in particular scanning Auger electron spectroscopy. The present experiments are also suggestive of many practical applications for the technique in metallurgy, catalysis, microelectronics and organic materials and bring out some of its limitations.

The apparatus used in the study consisted of a PHI Model 545 Scanning Auger Microprobe (SAM) system[7] with a Secondary Ion Mass Spectroscopy (SIMS) attachment[8] (PHI Model 2500). Fig. 1 shows the geometrical arrangement of the components housed in the UHV test chamber capable of base pressures in 10^{-10} Torr (1.3 x 10^{-8} pa) range. With the specimen situated in position it was possible to simultaneously obtain the SAM and SIMS or SAM and Scanning electron stimulated desorption (SESD) information from any selected area of the surface. The integral electron gun situated in the SAM analyzer provided a finely focused ($\sim$3 μm in the low limit) electron beam needed for obtaining the SAM as well as SESD information. The primary electron beam voltages in the 2-5 keV range and beam currents in the 1-5 μA range were used in the present studies. The mass
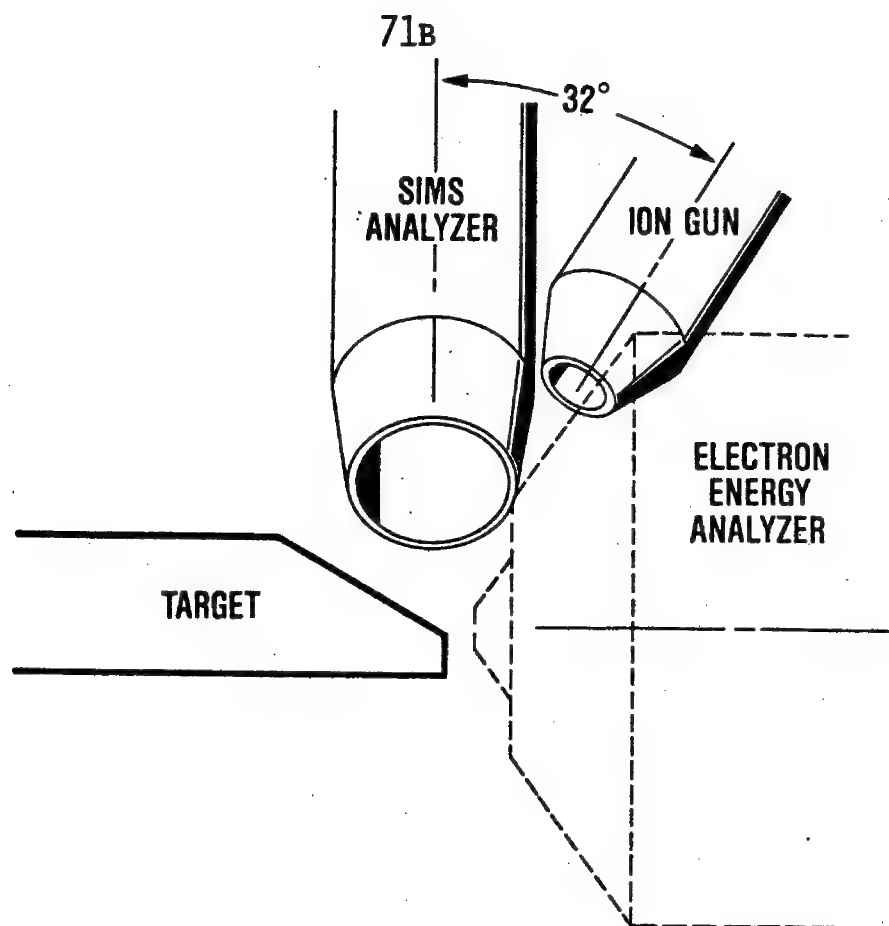
FIG. 1. Configuration of the SAM analyzer with integral electron gun, SIMS analyzer, ion gun and sample target in the vacuum chamber.
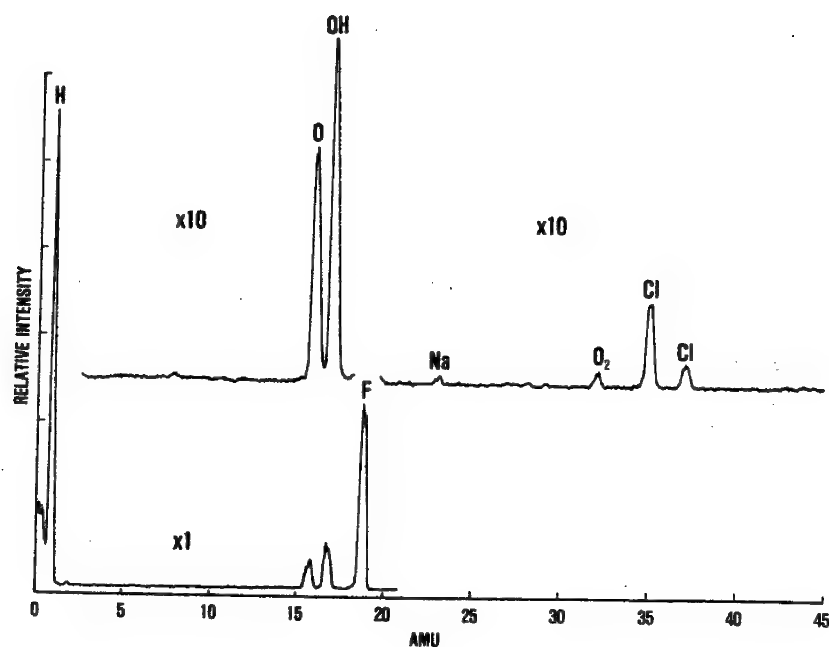
FIG. 2. ESD positive ion mass spectrum from the platinum catalyst on Alumina substrate.

analyzer was operated in the high sensitivity mode, the enhancement in sensitivity resulting from bias applied to the grids in front of the energy prefilter. The ESD selected ion images were obtained by intensity modulating the oscilloscope with the peak of a specific mass as the electron beam scanned the surface. This procedure is similar to that used in obtaining Auger images[7].

While electron beam desorption is a nuisance and sometimes limits the usefulness of many electron beam techniques, the mass analysis of desorbed ions provides some of the missing information. Fig.2 shows the ESD positive ion mass spectrum obtained from a large area of Pt catalyst distributed on an alumina substrate. Large amounts of H, O, OH, F, and Cl are noticed in addition to traces of Na. The Auger spectrum obtained from this surface has shown Al_2O_3 and traces of Pt, but no detectable F or Cl. Obviously, the electron beam desorbed the halides to leave them below their AES detectability limits at the surface. The OH and H species in the ESD spectrum suggest desorption of adsorbed water.

Detection of species such as H, OH, CO, CO_2 and F can be very useful in identifying surface oxidation and corrosion products

FIG. 3
ESD positive ion mass
spectrum of finger print
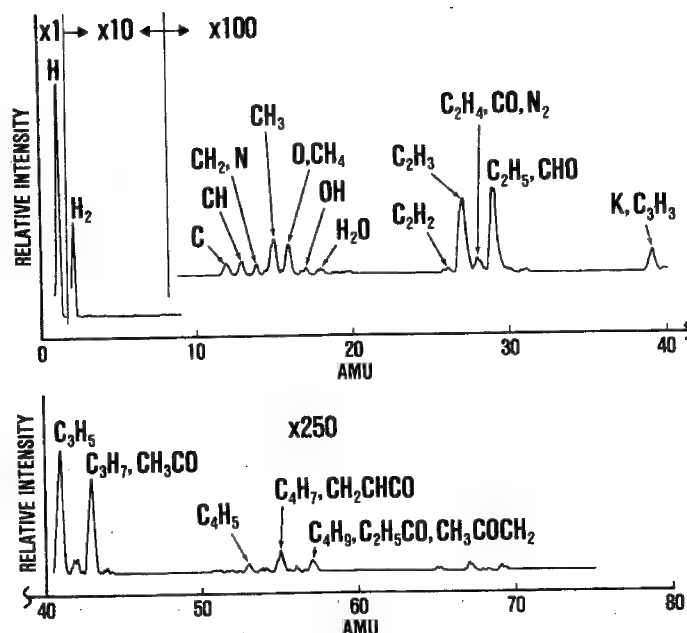
on metal surfaces and in understanding reasons for failure of
microelectronic devices.

Chemical information obtained by ESD can be particularly
valuable for study of organic materials, coatings or contamin-
ants. Since the desorbed ion fragments represent, as in SIMS,
ligands of the surface compound, useful information can be derived
from the ESD spectra. Fig. 3 shows an ESD spectrum obtained from
the surface of a cleaned Ni foil on which a finger print was
imprinted. Several probable components, besides the very pro-
minent H^+ peak, are marked on the spectrum and suggest high
probability for methyl (CH_3-) and ethyl (C_2H_5-) ions and fragments

FIG. 4.
Finger print on nickel
foil, Absorbed current
micrograph (top), H^+ ESD
image (bottom).
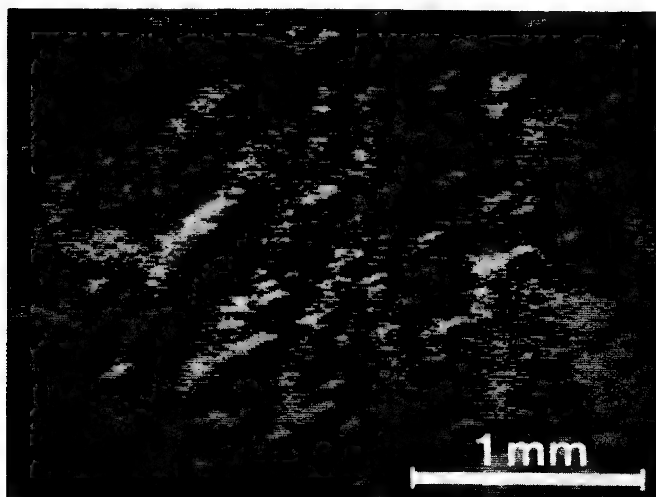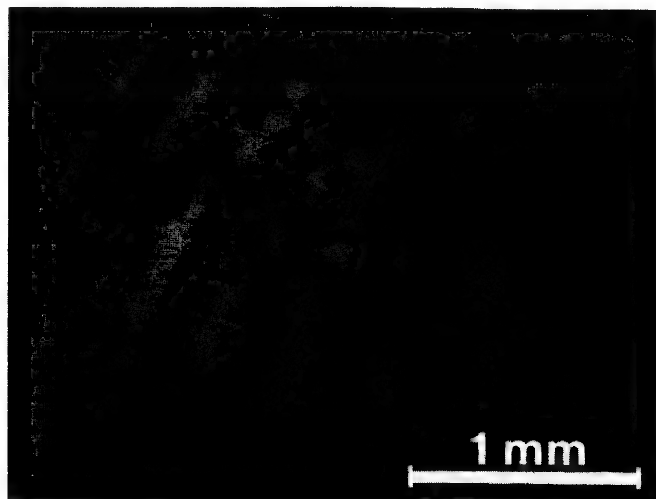
of acetone ($CH_3CO\ CH_3$). Several heavy hydrocarbons with masses up to 69 were also detected. The spatial distribution of the desorbed H^+ ions is shown in Fig. 4(b) and corresponds to the absorbed current micrograph shown in Fig. 4(a). It is apparent from this example that imaging of large areas as well as imaging selected masses is also possible. The wealth of information obtainable from localized areas is likely to create many applications for the technique in the study of metal and organic material surfaces as well as biological materials.

High desorption cross-sections and efficient detection of desorbed ions by the mass analyzer provide high sensitivities for surface analysis by the ESD technique. In case of H^+ ions, the high detection sensitivity of mass analyzer easily offsets its low desorption cross-section[1] (10^{-22} to 10^{-23} cm^2). As a result ESD can be highly complimentary to other analytical techniques since many of them, including surface analysis techniques such as AES, ESCA and ISS, are not capable of detecting hydrogen. Hydrogen plays a very important role on mechanical as well as stress corrosion properties of metals and alloys. It is believed that its interaction with metalloid elements is at least partly responsible for property deterioration and needs further understanding. A simple experiment has been designed to study metalloid element - hydrogen interaction in a low alloy steel. The selected 3340 steel (nominal composition in weight percent : 3.5 Ni, 1.5 Cr, 0.4 C) containing 620 ppm Sb was temper embrittled following the schedule: quench from 1140°K, temper at 920°K for 1 hour, water quench and embrittle at 750°K for 24 hours. This treatment results in grain boundary embrittlement under impact at low temperatures and is known to contain Sb segregated at selective grain boundaries[9]. The steel was then electroyltically charged with hydrogen and it is believed that Sb acting as a hydrogen recombination poison selectively adsorbs hydrogen and accelerates its diffusion along grain boundaries by keeping it in atomic state. The specimen was then inserted in the vacuum test chamber containing

the SAM- SESD apparatus, cooled to approximately 150°K and fractured by impact with the system pressure in the high 10^{-10} Torr ($\sim 10^{-7}$ Pa). The selected areas of the fracture surface were immediately imaged for hydrogen by SESD and then for Sb and Fe by SAM. Typical information obtained from these experiments is shown in Fig. 5. The fracture surface, shown in the absorbed current image Fig. 5(a), has mixed (brittle intergranular and ductile transgranular) modes of fracture. The Sb concentration at certain grain boundaries is as high as 10 atomic percent while in others Sb was undetectable (<0.5%) by AES. Most prominent in the data is the very high concentration of H in the ductile areas compared to the intergrannular portions. This is expected since dislocation motion and associated plasticity would enhance hydrogen migration and its build up in localized regions.

The differences in hydrogen concentration among boundaries enriched with Sb are, however, not significantly different from those not enriched with Sb. These preliminary experiments show that H^+ desorption is actually lower from Sb enriched areas than from other grain boundaries. Factors determining this behavior in the two types of areas (Sb enriched and Sb undetected) include (i) hydrogen coverage (ii) coverage dependent variation of H^+ desorption cross-section [10] and (iii) surface chemistry dependent variation of H^+ desorption cross-section. Detailed analysis of these factors and more ESD studies in this direction and at free surfaces would be extremely valuable in fully understanding the hydrogen bonding at surfaces. Further understanding of the role played by hydrogen recombination poisons such as P, S, As, Sn, etc., in hydrogen assisted intergranular embrittlement and stress corrosion cracking properties would also be invaluable. Likewise, the role of some of these elements as catalytic poisons in hydrogenation catalysis can also be better understood by ESD kinetic experiments on selected surfaces.
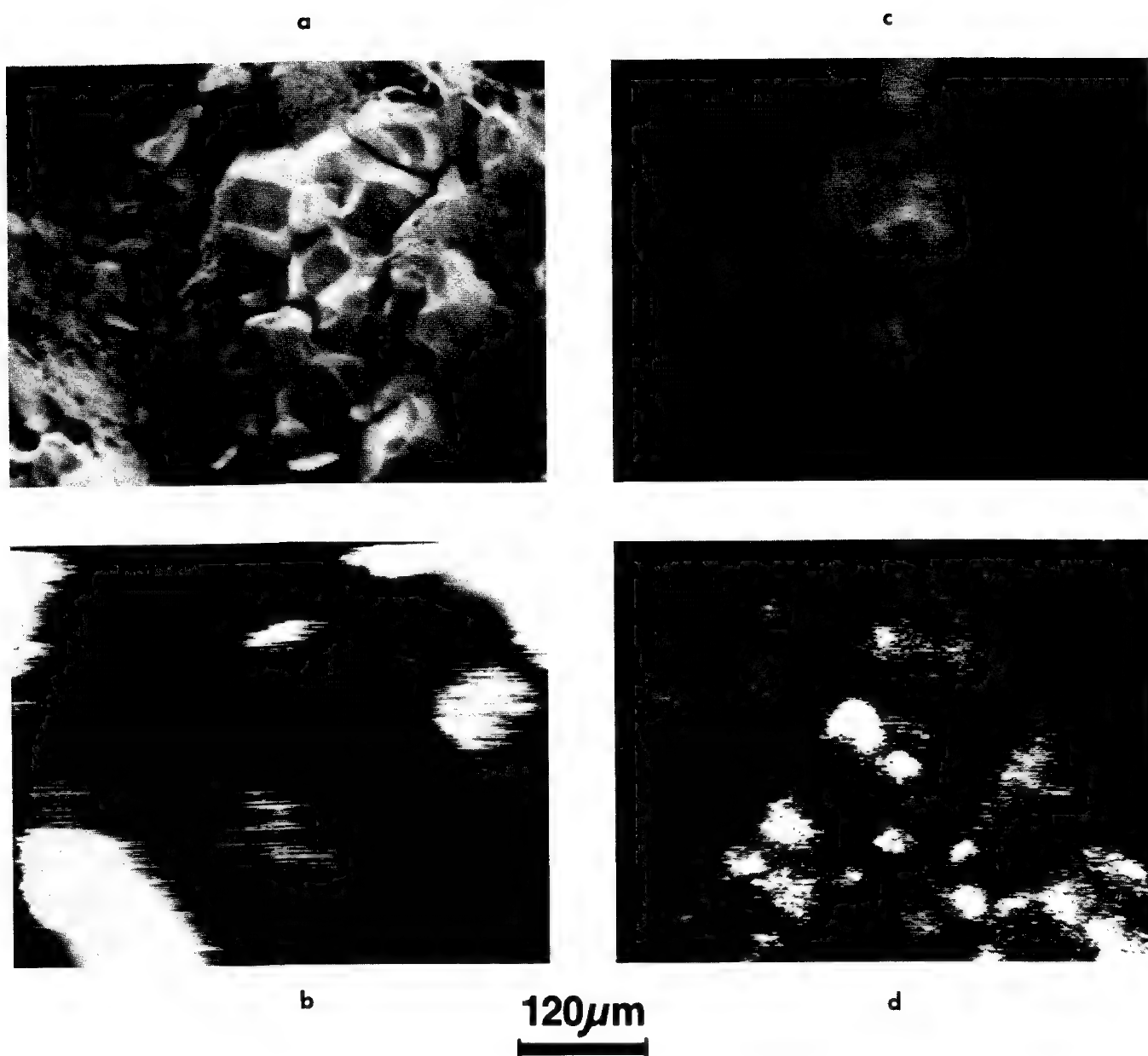
FIG. 5. SESD and SAM study of a 3340 Steel: (a) Absorbed
current image, (b) Hydrogen ESD image (c) Fe Auger
image and (d) Sb Auger image.

While these initial experiments are greatly encouraging, several limitations of the technique are notable. Some of these arise due to the inherent destructive nature of the technique, particularly the electron beam artifacts that include changes in binding states[1] of adsorbates as well as possible accelerated migration of elements to or away from surfaces, where the ion and neutral desorption occurs. Other complications for its application as an analytical tool arise as a result of possibly large changes in desorption cross-section with crystal orientation, surface coverage, chemistry, topography and the presence of active gases in the vacuum system. The ratio of ions to neutral desorption cross-sections is also an unknown variable for most real material surfaces and, as in the case of SIMS, needs extensive investigation.

REFERENCES

1) T. E. Madey and J. T. Yates, Jr., J. Vac. Sci. and Technol. **8**, 525 (1971).

2) T. E. Madey and J. T. Yates, Jr., Proceedings of 4th NEVAC Conference, Eindhoven, The Netherlands, June, 1976.

3) G. D. Rork and R. E. Consoliver, Surface Sci. **10**, 291 (1968)

4) D. Lichtman, R. B. McQuistan and T. R. Kirst, Surface Sci. **5**, 120 (1966).

5) J. C. Potosky and D. B. Wittry, Microbeam Analysis Society Proceedings, 10th Annual Conference, Aug. 11-15, 1975, Las Vegas.

6) H. F. Dylla and J. G. King, Bull. of the Amer. Phys. Soc., Ser. 2, **21**, 241 (1976).

7) A. Joshi, L. E. Davis and P. W. Palmberg, in Methods of Surface Analysis, Edited by A. W. Czanderna (Elsevier, New York, 1975), P. 159.

8) R. L. Gerlach and L. E. Davis, J. Vac. Sci. and Technol., **14**, 339 (1977).

9) A. Joshi, Scripta Met., **9**, 251 (1975).

10) T. E. Madey, Surf. Sci., **36**, 281 (1973).

High Resolution Scanning Auger Microscopy
of Fracture Surfaces
R. G. Rowe, C. L. Briant, and F. Bacon
General Electric Corporate Research and Development
Schenectady, New York

High resolution scanning Auger microscopy has been applied to the study of grain boundary segregation in several steel alloys. Individual grain boundaries have been analyzed and their Auger spectra compared with spectra from both cleavage facets and from other grain boundary surfaces. This has been possible due to a scanning secondary electron imaging capability with a spatial resolution of less than 0.25 micron. This resolution has permitted the discrimination between grain boundary, cleavage, and ductile fracture regions of the fracture surface produced by in situ fracture.

Auger analyses of intergranular fracture surfaces of iron-3% silicon alloys, sensitized stainless steels and temper embrittled low alloy steels have been performed and will be presented to illustrate some of the unique capabilities and practical limitations of the technique. In-situ intergranular fracture of these alloys, is accomplished by cooling below the ductile-brittle transition temperature of the material prior to fracture. Gaseous hydrogen embrittlement has also been used and will be discussed as a technique to expose grain boundary surfaces.

The Auger spectra and secondary electron imaging of grain boundary surfaces have shown the segregation of both solute elements and precipitate particles at grain boundaries. Auger spectra from individual precipitate particles as small as one micron in diameter have been obtained and distinguished from the spectra of the surrounding grain boundary surface.

Figure 1 shows an SEM micrograph and Auger spectra of a high purity iron-3% silicon alloy grain boundary surface. This specimen was equilibrated at 1100°C in 1 atm. nitrogen gas which resulted in the development of precipitate particles large enough for individual Auger analysis. Chemical analysis of the original ingot indicated 93 ppm sulfur and 23 ppm carbon as impurities. The nitrogen content of the alloy was estimated to be 25 ppm after heat treatment. The fracture surface of this alloy showed silicon-bearing second phase particles approximately one micron in diameter strongly interacting with the grain boundary. The high magnification micrograph in Figure 1 shows a region of the grain boundary

surface where a particle was torn from the boundary surface during fracture. Auger spectra from this particle-matrix interface and from the grain boundary surface (spectra 1 and 2 respectively) show a concentration of sulfur on the particle interface which is not observed on the grain boundary surface. Carbon and oxygen peaks observed in the Auger spectra of both regions are also observed on cleavage facets and have built up with time indicating slow contamination of the fracture surface.

Analyses of the precipitate particles by both Auger and energy dispersive x-ray analyses indicated no sulfur in the particles remaining on the grain boundary. This suggests sulfur segregation to the particle-matrix interface either as sulfides or solute sulfur. The micrograph in Figure 1, obtained in a separate scanning electron microscope after Auger analyses of the surface, shows fine detail which suggests either the presence of smaller precipitates around the large particle or faceting of the particle itself. Transmission electron microscopy of the area surrounding the large silicon-bearing precipitate particles will be required to resolve whether finer sulfides are in fact nucleating around the larger particles. The complementary techniques of SEM, TEM and energy dispersive x-ray analysis all provide information about fracture surfaces not attainable by Auger analysis alone. Characterization by several techniques is in fact vital if the correct interpretation of fracture surface Auger analyses are to be obtained.

With the combination of techniques utilized here and the capability to spatially resolve Auger emission from this region on the grain boundary surface, we have been able to determine that in this case it was sulfur concentration at the particle interfaces and not at grain boundary surfaces that was observed. In any system in which precipitate particles are observed at grain boundaries, the separation of precipitate and grain boundary segregation effects will require a spatial resolution for Auger analysis at least on the order of the precipitate particle size. Current scanning Auger microscopy systems are unable to resolve detail much finer than one micron so that for systems with smaller particle sizes than this, particle and grain boundary segregation effects cannot be separated. To resolve smaller particle sizes, longer measurement times or lower signal to noise requirements must be accepted.

The grain boundary chemistry of sensitized stainless steel has also been examined. In order to produce intergranular fracture in these alloys, a gaseous hydrogen fracture technique has been developed and the capability to introduce and remove hydrogen from the scanning Auger microscopy has been established.

Prior to employing in-situ hydrogen induced fracture, technique development has been performed external to the system. Figure 2 shows the secondary electron scanning image of a stainless steel fracture surface broken in hydrogen and transferred to the scanning Auger system. The accompanying electron energy spectrum was obtained from the individual grain boundary surface denoted by a white point in Figure 2 after sputtering the surface with argon ions for 10 minutes.

Grain boundary, cleavage and ductile tearing regions of the fracture surface have been easily distinguished in the microscope permitting the capability of comparing grain boundary and cleavage surface Auger spectra. If the spectra from cleavage areas represent bulk composition levels, the relative concentrations of alloying elements at grain boundaries may be obtained. Sputtering into the matrix from a grain boundary surface may, in the absence of shadowing effects, permit at least a qualitative assessment of concentration profiles into the matrix. In sensitized stainless steels, one is then capable of examining the extent and magnitude of chromium depletion at grain boundaries and near carbide precipitate particles. By comparing the depth profiles of both grain boundary and cleavage areas on the fracture surfaces, some account of sputtering induced artifacts may be taken.

The segregation of trace elements to internal surfaces such as grain boundaries and particle-matrix interfaces require in-situ fracture in hydrogen gas to expose these surfaces without contamination. Results of in-situ hydrogen gas fracture will be reported.

The analysis of fracture surfaces by high spatial resolution scanning Auger spectroscopy represents a significant step in the analysis of the chemistry of grain boundaries and other internal surfaces. The examination of these surfaces requires an intimate blend of fracture technique development and surface analysis techniques. Characterization of the nature of the surfaces exposed in the fracture process and whether they represent grain boundary, cleavage, ductile deformation regions or precipitate particle surfaces is also a vital part of the analyses. It will be shown that when these elements are brought together through the use of complementary analysis techniques, there is considerable potential for understanding segregation effects in metals.
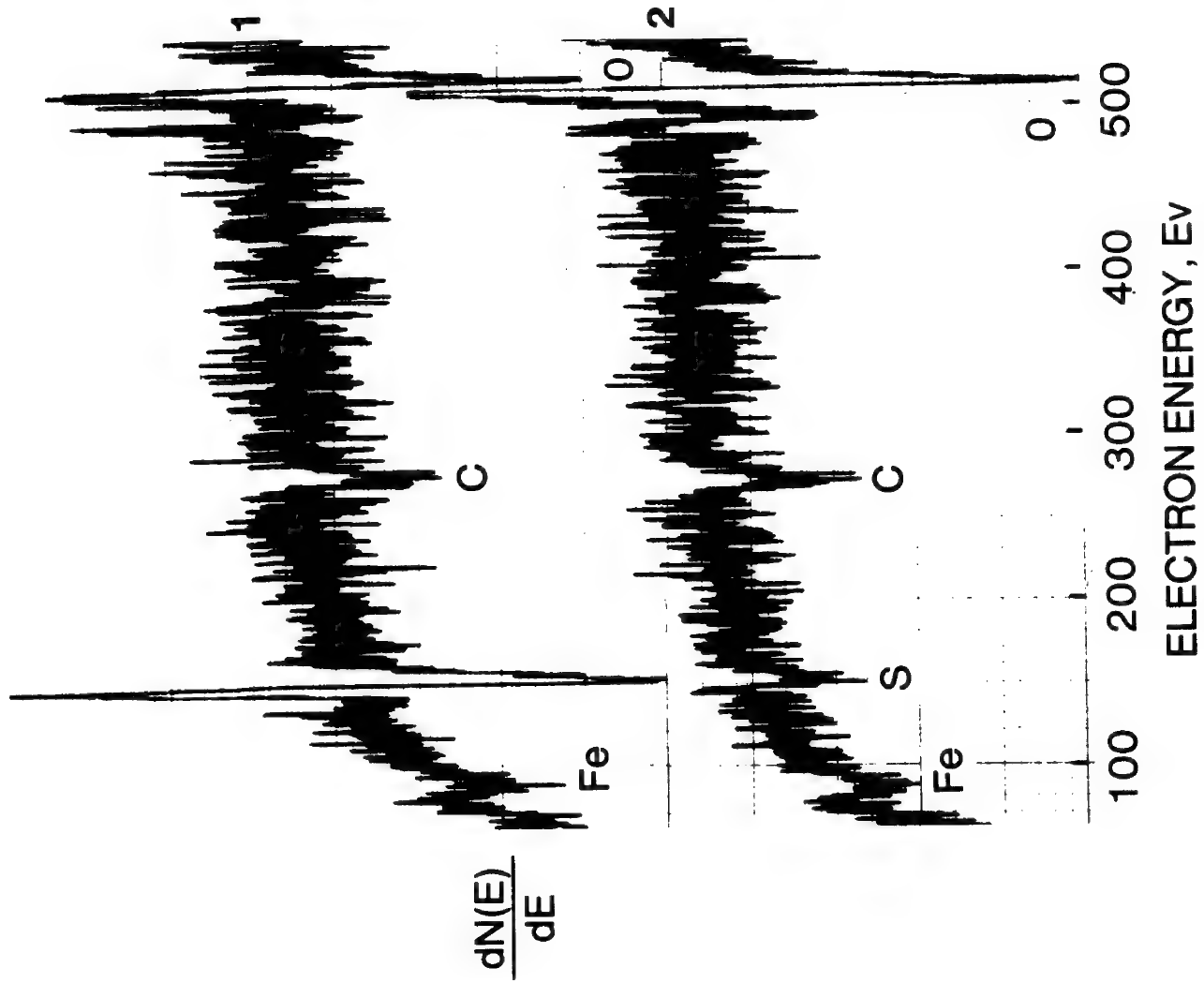
Figure 1. Auger analysis of the interface between the matrix of a high purity silicon-iron alloy and a second phase particle at a grain boundary. Points 1 and 2 correspond the particle-matrix interface and the grain boundary surface respectively.
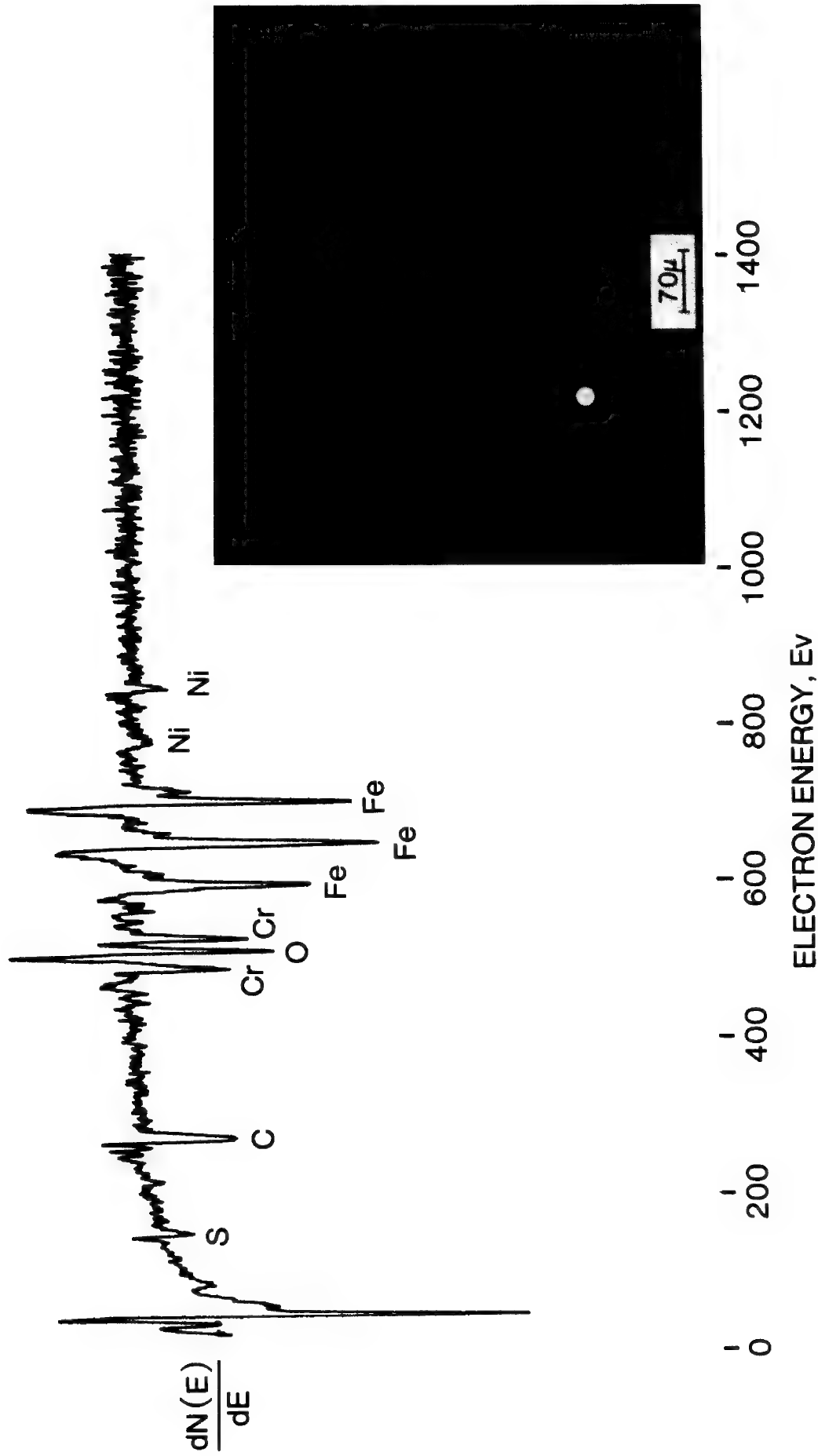
Figure 2. Auger spectrum and corresponding micrograph for sensitized 304 stainless steel.

QUANTITATIVE AUGER ANALYSIS OF GOLD-COPPER-OXYGEN AND GOLD-NICKEL-OXYGEN SURFACES USING RELATIVE SENSITIVITY FACTORS *

by

P. M. Hall and J. M. Morabito
Bell Telephone Laboratories, Incorporated
Allentown, Pennsylvania   18103

ABSTRACT

Quantitative Auger analysis is becoming routine for unoxidized binary alloys. Many specimens of technological importance, however, contain large amounts of oxygen, which can complicate quantitative analysis by changing a) peak shapes (e.g. line widths, δ), b) energy position of the peaks, c) Auger currents, and d) the sputtering correction factor (R). This paper describes quantitative Auger analysis of the Gold-Copper-Oxygen and Gold-Nickel-Oxygen systems, based on relative sensitivity factors before (P_{rel}) and after (P_{rel}^{S}) sputtering. The relative sensitivity factors, P_{rel}^{S} were found to be independent of the gold and oxygen concentrations for both systems. In the Gold-Copper-Oxygen system this is attributed to the sharpness of the 920 eV (LMM) copper transition compared to the energy resolution (0.6%) of the CMA analyzer used. For the Gold-Nickel-Oxygen system it is ascribed to a fortuitous cancellation of two effects 1) increased line width, δ, hence a decreased 848 eV (LMM) peak

height upon oxidation, and 2) increased Auger emission of the 848 eV peak due to oxidation. The sputtering correction factors were found to be $R(O,Cu) = 1.0$ for the composition of Cu_2O and $R(O,Ni) = 0.75$ for the composition NiO. A single crystal standard of Cu_2O was used to confirm the 2:1 ratio of Cu to O in the ternary samples. The variation in R with Au concentration is negligible. The variation in R with oxygen concentration, hence the variation in P^S_{rel} (since $P^S_{rel} = P_{rel}R$), has not been studied. The major limitation on the quantitative Auger analysis of these ternary systems has been found to be uncertainties in the sputtering correction factor R.

* Full manuscript submitted to Surface Science.

EXPERIMENTS IN QUANTITATIVE AUGER ELECTRON SPECTROSCOPY

H. E. Klassen and D. R. Beaman

The Dow Chemical Company

Auger electron spectroscopy provides a unique means for obtaining the surface and three-dimensional composition of solids. Commercial instrumentation is sophisticated and provides reproducible data, but there are difficulties involved with quantitation. This report describes some results of measurements on known alloys, discusses electron beam induced effects, and illustrates the use of Auger spectral details in the analysis of manganese oxides.

QUANTITATIVE ANALYSIS OF KNOWN MATERIALS

The compositions of several homogeneous standards previously characterized by electron probe analysis[1] were determined from Auger spectra using elemental sensitivity factors[2] and the expression[3]

$$C_a = I_a S_a^{-1} / \sum_i I_i S_i^{-1} \qquad (1)$$

where C is the atomic concentration, I is the measured Auger electron peak to peak height, and S is the elemental sensitivity factor. In the Cu-Zn and Ti-Nb alloys, concentrations were also measured using pure element standards and the relationship

$$C_a = I_a / I_a^o \Big/ \sum_i I_i / I_i^o \qquad (2)$$

where the superscript o denotes the pure material. The ratio I_a^o/I_b^o can be compared with the ratio of published[2] sensitivity factors S_a/S_b. More detailed corrections were not attempted in view of the variation in published backscatter values and electron escape depths. All samples and standards were metallographically polished, ultrasonically cleaned, and examined in a Physical Electronics scanning Auger microanalyzer. The analyses were usually performed using a 5kV electron beam scanned over an area of about 160 x 270 μm, while argon ion sputtering was carried out at 3kV (4.5 nm/min. sputter rate on Ta_2O_5).

The results are presented in Table I. The measured equilibrium composition was computed using Eqs. 1 or 2 and Auger spectra which did not change with additional sputtering. Sputtering to depths of 5 to 50 nm was required to attain equilibrium. These equilibrium concentrations were corrected for differences in elemental sputtering yields using the expression from Shimizu, et. al[4],

$$\left.\frac{C_a}{C_b}\right|_{\substack{\text{before sputtering}\\\text{yield corrected}}} = \frac{Y_a}{Y_b} \left.\frac{C_a}{C_b}\right|_{\substack{\text{after sputtering}\\\text{at equilibrium}}} \tag{3}$$

where Y is the sputtering yield for argon.[5,6] This correction is questionable because of the sparse amount of yield data available (none at 3kV) and the variation in reported yields. In addition, Eq. 3 neglects the fact that elemental yields may be a function of concentration. In comparing the equilibrium or sputtered compositions with the true chemical compositions, the relative errors ranged from 1 to 45% and averaged about 20%. Correcting for yield differences with 500 to 600 eV yield data does not reduce these errors, but use of the 5kV yield data changes the range to 1 to 35% and reduces the average error to about 10%.

The yield corrected concentration in the case of Cu-Zn was not calculated because the yield for Zn was unknown. However, it was possible to measure the surface concentration because the concentration did not change during initial sputtering at 0.6 nm/min. There appeared to be an incubation period which persisted for about 5 nm prior to changing to the equilibrium concentration. This measured concentration of 75Cu-25Zn (column 4 in Table I) was independent of electron beam voltage and current, and was close to the bulk composition. The sputtered equilibrium concentration was unaffected by large variations in the ion beam current density, implying that the difference between the surface and equilibrium values was not due to thermal effects. The Cu-Zn system was examined using pure element standards and I^o_{Cu}/I^o_{Zn} was 1.19 ± 0.04 in good agreement with published S values[2] because $S_{Cu}/S_{Zn} = 1.21$.

No incubation period was observed in the Ti-Nb alloy, but it was possible to measure the surface concentration before appreciable conversion to the equilibrium value occurred. The equilibrium concentration was markedly different than the bulk concentration and the available yield data cannot account for this large

difference. The analyses were obtained using pure standards and all data were collected during sputtering to avoid oxidation. The I_{Nb}^O/I_{Ti}^O value of 0.44 was considerably lower than the published[2] S_{Nb}/S_{Ti} value of 0.62. The slower the sputtering rate, the more closely the I_{Nb}^O/I_{Ti}^O values approached the 0.62 value because I_{Ti}^O decreased as the oxygen and carbon levels increased. This indicates the need for using experimentally-determined sensitivity factors when analyzing highly reactive surfaces. The results for Cr-Co-Mo, ZrC, and Mn oxides were calculated from elemental sensitivity factors.

ELECTRON BEAM INDUCED EFFECTS

Chemical Alteration

Thomas[7] has thoroughly discussed the problem of SiO_2 dissociation or reduction to Si^O under electron and ion beam bombardment. We have measured the ratio, R, of the 92eV Si^O peak height to the 76eV SiO_2 peak height (R = I(92eV)/I(76eV)) in Vycor glass in an attempt to determine how the dissociation problem might be circumvented. When the scanned area was greater than 30μm x 50μm, the maximum attainable value of R was 0.40 (at 5kV) and could easily be kept below 0.1 using currents that provided adequate sensitivity. With a 20μm beam R was only below 0.1 when using low current. With an ion beam current density of about 140μa/cm^2 and low electron beam current, no Si^O was detected (R = 0) possibly because simultaneous reduction and recombination occur under these conditions. There is synergism when electron and ion bombardment occur simultaneously, because where electron bombardment alone yielded R = 0.35 and ion sputtering alone gave R = 0, simultaneous ion and electron bombardment gave R = 0.55. Recombination occurs slowly when the electron beam current is reduced.

Sample Charging

Sample charging, particularly in polymeric materials, can seriously hinder Auger analysis. Charging from electron beam bombardment is alleviated in many materials by: 1) increasing the secondary electron emission (low acceleration potential and grazing electron beam incidence); 2) reducing the accumulated charge by lowering the current density (increased electron beam diameter, low beam current, electron beam scanning); and 3) increasing the conductivity (lower sample temperature, thin samples in intimate contact with conductive substrates, locating

samples under metal masks with small (<1mm) openings. These steps are often insufficient in the case of polymers.

For the case of polyethylene under an Al mask (600μm opening), the maximum acceleration potential, E_o, that could be used without charging was 1.4keV, (inadequate Auger emission) and simultaneous sputtering and depth profiling was impossible at any E_o. By coating the sample with 15 nm of Au it was possible to obtain Auger spectra and depth profiles at 5kV with relatively high currents in small areas. The bulk of the Au film was removed in 15 nm, but low (<1%) levels of embedded Au persisted. The polyethylene was still conductive after removal of 200 nm, where the Au was below the detection limit.

In the case where a coating cannot be tolerated, conductive strips (not islands) can be vacuum evaporated onto the polymer surface using a transmission electron microscope grid without cross grids as a mask. The sample is analyzed with a scanning beam which spans the 60μm separation between conductive strips.

SPECTRAL CHARACTERISTICS OF Mn OXIDES

In attempting to distinguish between the various oxides of manganese, quantitative Auger analysis was surprisingly useful as indicated in columns 2 and 3 of Table II. In addition, there were several spectral features involving the 542eV and 589eV Mn transitions and the 510eV oxygen transition that were useful in identifying the oxides. These are shown in the schematic drawing below Table II and evaluated in that table. It is easy to distinguish between the three groups: Mn^o, MnO_2 - Mn_2O_3, and Mn_3O_4 - MnO.

REFERENCES

1) D. R. Beaman and L. F. Solosky, Anal. Chem., Vol. 44, 1972, p. 1598.

2) L. E. Davis, N. C. MacDonald, P. W. Palmberg, G. E. Riach, and R. E. Weber, Handbook of Auger Electron Spectroscopy, Physical Electronics Ind., Inc., MN, 1976.

3) P. W. Palmberg, Anal. Chem., Vol. 45, 1973, p. 549A.

4) H. Shimizu, M. Ono, and K. Nakayama, Surface Science, Vol. 36, 1973, p. 817.

5) G. K. Wehner in Methods of Surface Analysis, A. W. Czanderna, ed., Elsevier Scientific Publishing Co., Amsterdam, 1975, p. 5.

6) L. I. Maissel in Handbook of Thin Film Technology, L. I. Maissel and R. Glang, Eds., McGraw Hill, New York, 1970, P. 4-40.

7) S. Thomas, JAP, Vol. 45, 1974, p. 161.

TABLE I

QUANTITATIVE AES ANALYSIS OF MATERIALS OF KNOWN COMPOSITION

| | | | | | Yield Corrected (Eq. 3) | |
| | | | | Measured | | |
Alloy	Element	True Chemical	Measured Surface*	Equilibrium (Eq. 1 or 2)	Using 500 or 600 eV Yields	Using 5kV Yields
				Concentration in Weight Percent		
NBS brass C1102	Cu	72.9	75.3 ± 1.3	85 (2)		
	Zn	27.1	24.7 ± 1.3	15		
Ti-Nb MEPUG	Ti	35.0	33	20 (2)	19	27
	Nb	65.0	67	80	81	73
	Ti	35.0	39	25.8 ± 0.3 (1)	24	34
	Nb	65.0	61	74.2 ± 0.3	76	66
Cr-Co-Mo MEPUG	Cr	9.9		9 (1)	9	9
	Co	80.6		82	84	85
	Mo	9.4		10	7	6
ZrC MEPUG	Zr	88.5		76 (1)	92	
MnO_2	Mn	63.2		65 (1)		
	O	36.8		35		

(1) = Calculated using elemental sensitivity factors.

(2) = Calculated using pure element standards.

± = One standard deviation in 4 or 5 determinations.

MEPUG = Supplied by the Midwestern Electron Probe Users Group.

* = Composition measured before sputtering-induced changes occur.

TABLE II: AUGER SPECTRAL FEATURES ASSOCIATED WITH MANGANESE
OXIDE

Materials	Weight Percent		ΔE at 542ev[2]	ΔE at 510ev[3]	E/F at 589ev[4]	Minor Peaks 537, 552, 647 ev[5]
	True[1]	AES				
Mn°			3.6		0.34	well defined
MnO_2 – Mn O	63 37	65 35	4.7	3.6	0.52	$\sim$1/2 intensity of Mn°
Mn_2O_3– Mn O	70 30	68 32	4.8	3.7	0.58	$\sim$1/2 intensity of Mn°
MnO – Mn O	77 23	74 26	7.3	7.4	0.59	slight shoulders
Mn_3O_4– Mn O	72 28	75 25	6.5	6.1	0.60	slight shoulders

1) from stoichiometry; 2) C=ΔE for the 542ev Mn peak at half the
peak to peak intensity; 3) A=ΔE for the 510ev oxygen peak at an
arbitrary value of 25% of the peak to peak intensity; 4) E/F= the
ratio of peak to peak intensities above and below the baseline for
the 589 ev Mn peak; baseline determine from total spectrum; 5)
peak B at 537 ev and peak D at 552ev
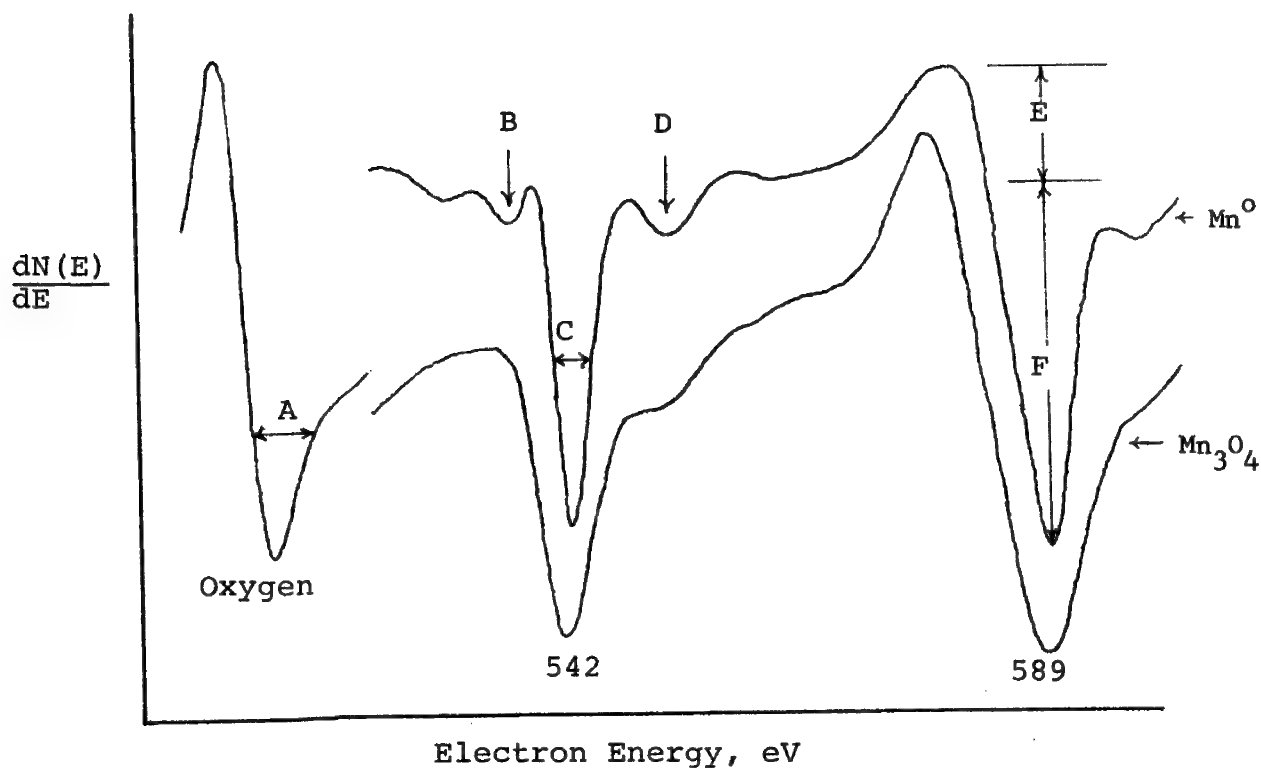
SAM/SIMS Investigation of Pt Films on Yttria - Stabilized Zirconia

K. E. Lawson and R. M. Rusnak

Materials and Chemistry Department
Bendix Research Laboratories
Southfield, Michigan 48076

The utilization of a platinum coating on oxide electrolyte for sensing oxygen concentration has prompted a number of investigations into the nature and kinetics of the metal-oxide interface reactions[1-3]. The oxygen sensor systems have a variety of applications ranging from the determination of oxygen in furnace atmospheres[4] to on-vehicle detection of engine exhaust gas composition[5]. Our concern is related to the latter application wherein the sensor is located in an engine exhaust manifold and used to indicate the air/fuel ratio of the intake mixture. Typically, the sensor consists of a phase-stabilized zirconia electrolyte thimble, the inner and outer surfaces of which are coated with porous platinum. The outer Pt electrode is exposed to the exhaust stream while the inner one is exposed to air. The emf output of the sensor varies with the operating temperature and the partial pressure of oxygen. The chemical composition of species in the electrolyte and near the metal-oxide interface strongly influence electrical properties as well as mechanical and thermal shock resistance of the devices. Previous investigators have shown that sensors have a propensity for debonding of the Pt electrodes from the zirconia as a result of side reactions, forming Pt-Zr solid solutions or intermetallics in reducing atmospheres. There is also experimental evidence from ESCA studies for the presence of platinum oxide formation in films sputtered from Pt onto alumina in oxidizing environments. The present work was undertaken to identify chemical species and extent of reaction, in the vicinity of the Pt-oxide interface as a function of temperature in an oxidizing atmosphere.

A combined scanning Auger microscopy/secondary ion mass spectroscopy (SAM/SIMS) technique was used to study the chemical compositions in the interface region. X-ray diffraction was also used to determine phases present. Specimens were prepared by vacuum evaporation of Pt onto zirconia surfaces which had been polished to a 3 μm finish. Unfired samples and samples fired in air at various temperatures in excess of 400°C for 1/2 to 2 hours were analyzed. Depth profiles were obtained using a primary electron beam of 2.7 μA at 3KeV and a modulation voltage of 6V peak-to-peak. The ion gun used in the profiling provided a 5KV/25 mA argon ion beam. The platinum 64-eV, zirconium 147eV, and oxygen 510eV Auger electron peaks were monitored.

The composition profile from the platinum surface shows that the oxygen signal begins to rise with significant strength prior to the rise of the zirconium signal and before the complete diminution of the Pt signal, suggesting the formation of platinum oxides. The extent of the oxide reaction zone increases with increasing heat treatment temperatures. Analysis with the positive SIMS spectra in the atomic mass unit range of PtO and PtO_2 species also indicates the presence of these oxides with the relative concentrations depending on the heat treatment temperature. These findings were also confirmed by x-ray analysis. The results indicate that SIMS can be an effective tool in identifying phases in addition to determining chemical variations.

REFERENCES:

1. A. S. Darling, G. L. Selman, and R. Rushforth, Platinum Metals Rev. 14, 124 (1970).

2. S. K. Rhee, J. Am Ceram. Soc. 58 [11-12], 540 (1975).

3. P. J. Meschter and W. L. Warrell, Met. Trans. A, 8A, 503 (1977).

4. D. D. Mog, Corning Glass Works, Public Relations Department Press Information, Mar. 11, 1977.

5. G. T. Engh and S. Wallman, SAE #770295;
    E. Hamann, H. Manger, and L. Steinke, SAE #770401.
    See also Auto. Engr. 85 (2), 45 (1977).

THE ROUTINE APPLICATION OF THE SIMS/SEM/EDXA
COMBINATION TO PRACTICAL SURFACE PROBLEMS

Edward J. Fasiska and Philip B. Janocko

Materials Consultants and Laboratories, Inc.

The development of scanning electron microscopy (SEM), which was introduced almost a decade ago, made a tremendous impact on the materials science field. Implementation of this tool made it possible to examine materials, in their natural state, at high magnifications with almost dramatic three-dimensional detail. It was soon discovered that the addition of an energy dispersive x-ray analysis (EDXA) system to the microscope greatly enhanced the effectiveness of the instrument for solving materials problems. The resulting micro-chemical analysis combined with the capability of a high magnification three-dimensional examination of surfaces created a powerful analytical system. However, as is the case with any analytical tool, SEM/EDXA has its limitations, not the least of which is its inability to detect light elements. Further, chemical data taken with this instrument represents an average analysis taken within the material from the surface to a depth, typically, of about one micrometer.

The addition of secondary ion mass spectroscopy (SIMS) instrument to the SEM/EDXA systems was almost a natural combination since it added a true surface analysis capability, light element sensitivity and the ability to analyze chemical complexes as well. SIMS, like any other analytical tool will not solve every surface problem, but it has been very successful in the problems we have encountered and the analysis is rapid and in many instances almost routine. In short, the SIMS technique is a logical addition effectively complimenting the SEM/EDXA system.

As opposed to EDXA elemental sensitivities, which vary, more or less, continuously, and are of the same order of magnitude, throughout the periodic table, SIMS elemental sensitivities vary cyclically with the periods of the periodic table over four orders of magnitude. Because of this, interpretations of SIMS spectra are not obvious and in fact, unless done carefully may be misleading. However, we have eliminated this problem by routinely using a system which weights the peak heights of the principal isotopes of the elements by the reciprocal of imperically calculated ion yield values. This enables quantitative estimates of the detected elements and greatly facilitates the interpretation of the SIMS spectra.

Some typical examples of the materials problems solved with SEM/EDXA/SIMS combination are given:

- <u>Micro-defects in Tin Plating On Copper Tubing</u> - SEM/EDXA examination of the samples indicated only tin and copper at the defect areas with occasional trace levels of silicon, iron and sulfur. However, when the defect areas were analyzed in the SIMS mode, tin, copper, oxygen and a highly aromatic organic contaminant were detected at high levels. The presence of the organic contaminant was found to be a result of a poor cleaning procedure which was used to remove a lubricant necessary for the forming of the copper tubing.

- ## Dust Formation During a Brazing Operation in the Interior of Gas Cylinder Bottles

The analytical techniques used in this case were SEM/EDXA/SIMS and X-ray diffraction (XRD). As is often the case, the data collected by any of the techniques alone was not sufficient to identify the problem. The combination of information gathered from all of the analyses, however, led to the conclusion that the detrimental dust was iron metal formed by the reduction of iron oxides by carbon monoxide at the interior surface of the cylinder. Further, as a result of this information, a baking process was developed which formed a thin continuous, epitaxially bonded to the matrix, iron oxide film. This thin oxide layer was much more resistant to reduction, probably because of surface area considerations. The SIMS technique played an important role in detecting the problem and monitoring the final iron oxide film thickness.

- ## Possible Material Transfer From Shot to Shot-Peened Parts

SEM/EDXA analyses of the shot, a shot-blasted sample and a control sample inconclusively indicated a possible transfer of aluminum and silicon from the shot to the shot-blasted sample. The SIMS analysis mode indicated, very dramatically, a transfer of the aluminum and silicon and in addition that trace levels of sodium were also being transferred. Estimated transferred sodium levels were in the 0.1 weight percent range. The sodium was confined to a depth of about $100\overset{\circ}{A}$ of the surface. In this case, the volume levels of the transferred elements were extremely low since they were concentrated at the surface. Because of this, the SIMS technique was invaluable in detecting the material transfer.

- ## Motor Winding Failures in Large (50 H. P.) Electric Motors

Motor winding insulation breakdown causing excessive current flow, subsequent localized heating, and ultimate failures was examined by SEM/EDXA/SIMS and XRD. The failures were traced to a corrosive sulfuric acid environment. Localized high sulfur levels were first detected, on the winding wire insulation, by SEM/EDXA. The sulfur was found to be associated as $SO_4^=$ ions by SIMS. XRD analysis of some of the material indicated the presence of a low level of sulfate salts. This is a classical example of how the SIMS technique was used to both corroborate results and to facilitate XRD interpretation of data.

These examples clearly illustrate the manner in which the SIMS technique compliments a SEM/EDXA system. The technique adds a whole new dimension of analysis which is currently opening up many new doors in materials problem solving.

Extension of SEM Capabilities with SIMS

D. A. Nauman
Western Electric
Indianapolis, Indiana

During the past few years Western Electric Indianapolis Works has experienced numerous production problems thought to be caused chiefly by surface contamination. Some cases of surface contamination are turned into interface contamination by subsequent processes before a problem is detected.

Investigation of these problems was done on a MAC 400S microprobe with 3 WDX spectrometers and an ETEC autoscan. Detection of very thin layers of low atomic no. material by X-ray is difficult and their detection is nearly impossible when covered by layers of high atomic no. material.

Problems of intermittent opens in gold electrical contacts during initial contact when there is only very, very low contact pressure have caused great concern and expense and had been studied extensively for 1½ to 2 years with X-ray in-house and Auger at our Columbus and Murray Hill BTL locations.

From those results and also what we failed to find it was concluded that a method of surface analysis and depth profiling was necessary at our own location. Auger and SIMS development had been closely followed for several years and seemed to be the answer, but which.

Available Auger systems would require a new vacuum pumping system taking much more space than was conveniently available to us. To do X-ray analysis, element maping and surface analysis by Auger would require shifting the sample from one instrument to another. Auger system prices appeared to be considerably in excess of $100K but a SIMS could be installed on our SEM for about ½ that price.

With our space restrictions and the price advantage of SIMS, when mounted on our SEM, efforts were centered on that objective. A couple of installations of SIMS on an SEM were found and were carefully investigated. Those operating SIMS and Auger systems at other Bell System locations were contacted and their opinions sought concerning advantages and restrictions on the system I was proposing to assemble. Vacuum requirements, background contamination and low Z sensitivities, were discussed extensively and Auger and SIMS seemed to provide comparable information. Comments were favorable to both systems with the one general qualification - "a clean vacuum must be maintained." My SEM was running in the mid to lower 10^{-5} Torr range but was capable of doing better.

Leak checking disclosed leaks around the door seal and all the rotary seals around the sample manipulation controls. Cleaning, relubricating and tightening these o-ring seals produced an immediate improvement to the mid 10^{-6} torr range with a slower improvement of another half decade in 6-8 days, probably due to clean up of the surfaces. Now, after several months it pumps to the low to mid 10^{-7} Torr range within 15 to 30 minutes if the LN_2 cold trap is filled. This vacuum level has not been difficult to maintain and seems to be roughly two decades better than many other SEMs. However, it is felt that all SEMs are easily capable of this through maintenance of the vacuum seals. The mass spectrometer of the SIMs functions as a leak detector in the RGA mode, making vacuum maintenance relatively simple.

A further consideration for putting a SIMs on our SEM was that a sample is almost always investigated by secondary imaging and BSE. After this investigation it is convenient to be able to perform a surface analysis without moving the sample to another instrument. A series of alternate X-ray and surface investigations can be performed on the sample in this manner.

This alternating procedure can be exemplified with an investigation
of an intermittently recurring problem from our thin film production.
Our thin film circuits are a laminate of high purity (99.97%) titanium
wire evaporated onto tantalum with paladium and gold over that.
Problems of severe undercut during etching and/or blistering were
found to be associated with the titanium layer. Previous X-ray analyses
of the titanium layer after separation showed only oxidization and
analysis of the wire by X-ray and various other means failed to disclose
any impurities. With SIMS and EDX in the SEM, however, another story
unfolded. A very thoroughly cleaned sample of titanium wire produced
small X-ray peaks at the potassium and chlorine wavelengths but nothing
more. A SIMS spectra showed heavy sodium and potassium peaks and
very quickly gave additional peaks for aluminum, magnesium, and silicon.
With continued sputtering the sodium and potassium peaks reduced somewhat
before becoming constant for an additional two hours. The sample was
removed from the SEM to examine the sputtered area with a visible light
microscope and numerous particles were detected using polarized light.
Analysis of these particles by EDX in the SEM showed them to contain
all of the above elements except chlorine and sodium. These contaminants
had been invisible to X-ray until the overlying titanium was sputtered
away.

A second problem involving anodizing tantalum for our thin film circuits
illustrates further capabilities of SIMS. Properly anodized tantalum
has a pink color but a sample was submitted which was green when held
at certain angles to the light. Visual examination at 1000X disclosed
a surface contamination of very fine particles. EDX in the SEM showed
nothing, however, BSE by atomic no. contrast indicated the particles
to be low atomic no.

This indicated organic contamination and residual photo resist was
suspect. A SIMS analysis gave a profusion of peaks for organics
showing mass peaks for saturated hydrocarbons through the butyl series

and aromatics including probable nitrogen substituted rings. A mass
spectra was generated for photoresist but lacked the aromatic portion
produced by the sample. At this writing the problem remains unresolved
but it exemplifies the wealth of information about organic contamination
which is believed to be obtainable only by SIMS. Additional investi-
gation will be made to determine if the anodizing process can alter
photoresist to produce the spectra obtained and to check other sources
of contamination such as bleedout from a new PVC anodizing tank (plasticizer,
unreacted plastic components, etc.).

Although our SIMS has been in operation for only a couple of months
we are obtaining information never before possible. The wealth of
information is often more than can be effectively interpreted but
it is expected that experience will solve most of that. Our single
biggest problem thus far has been marksmanship, positioning the sample
to hit the desired spot with the first shot from the ion gun.
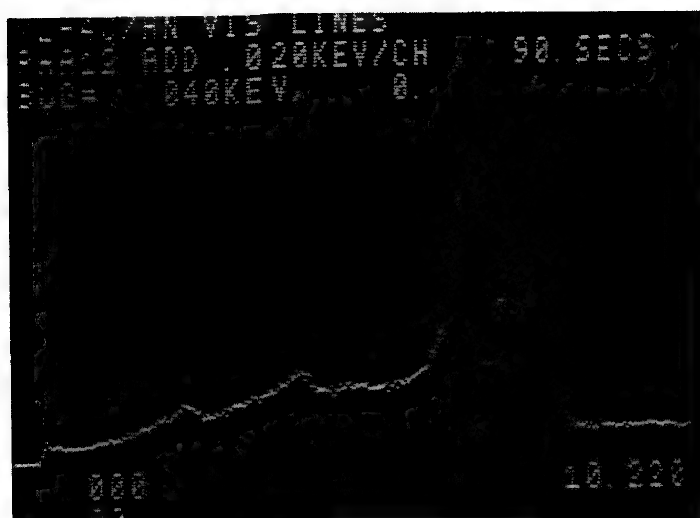
X-RAY SPECTRA OF HIGH PURITY
TITANIUM WIRE AFTER THOROUGH
CLEANING AS PREPARED FOR
VACUUM DEPOSITION.
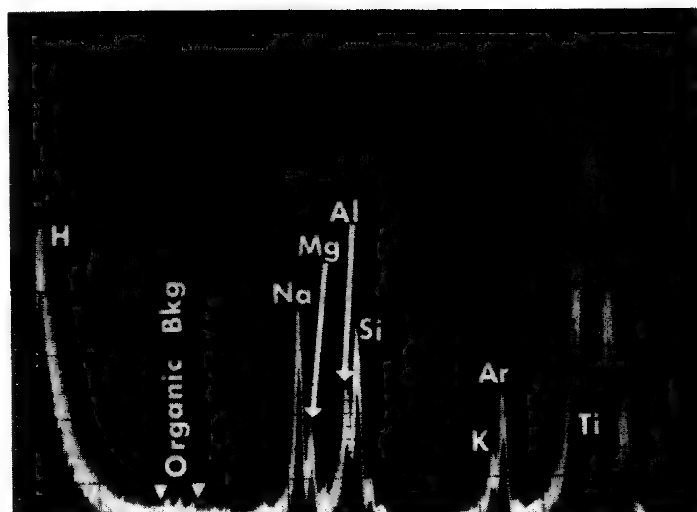
AMU SPECTRA OBTAINED ON SAME
TITAMIUM WIRE WITH THE SIMS
ON AN SEM.
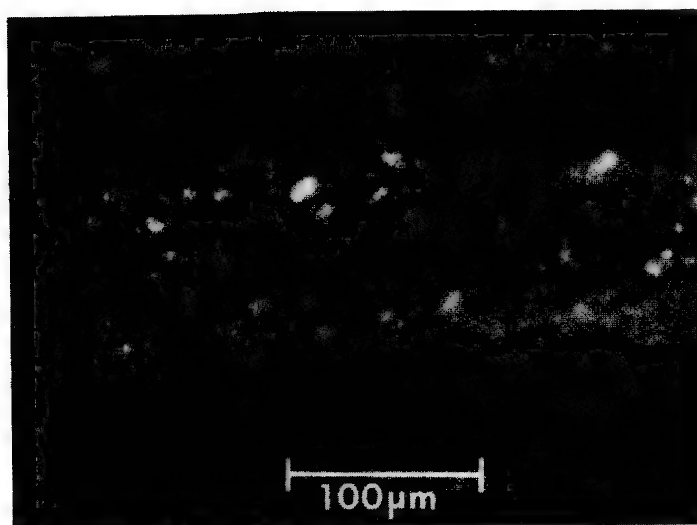
VISUAL EXAMINATION OF THE AREA
SPUTTERED FOR 3 HOURS DURING THE
SIMS INVESTIGATION. PARTICLES
ARE MADE VISIBLE USING POLARIZED
LIGHT WITH CROSSED POLARS. AN
ESTIMATED 9 - 10μm OF TITANUM
WAS REMOVED.
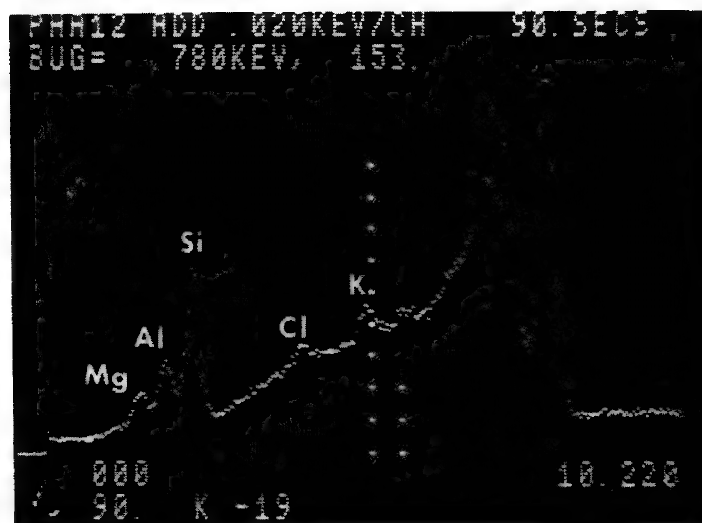
X-RAY SPECTRA OF THE SPUTTERED
AREA SHOWING CLEARLY IDENTI-
FIABLE PEAKS FOR MAGNESIUM,
ALUMINUM, AND SILICON WHICH
WERE QUESTIONABLE BEFORE REMOVAL
OF THE OVERLYING TITANIUM.

COMBINED SIMS/SEM FOR THREE DIMENSIONAL SURFACE ANALYSIS

Gene R. Sparrow, 3M Analytical Systems, 3M Center, St. Paul,
  Minnesota 55101

The concept of a "surface" is not well defined but basically depends
on the particular requirement of analysis. Classically the physical
microtopography including high spatial resolution in the x, y di-
rections of a specimen is the first parameter used to describe a
"surface". Excellent physical characterization of a specimen rou-
tinely accomplished using the SEM provides definition of surface
relief such as inclusions, films, texture, microdefects, etc.
Limited chemical identification can be accomplished in the SEM using
X-ray techniques. However, X-ray techniques exhibit some major
shortcomings which are eliminated by incorporating SIMS (Secondary
Ion Mass Spectroscopy) into the SEM.

The new capabilities added by combining SIMS with existing SEM
systems and its convenient installation to commerical SEM's such
as JEOL, Cambridge, and ETEC have made it a rapidly accepted an-
alytical technique for surface characterization studies. All
three scientific techniques; SEM, X-ray, and SIMS complement one
another when combined into one unit. SIMS analysis is improved by
the high spatial resolution of SEM which aids locating and ob-
serving the specific sample area of interest. Analysis time re-
quired by SIMS is substantially reduced by X-ray analysis of the
same specimen area thus minimizing lengthy concentration depth
profiles which would otherwise be necessary.

X-ray analysis by SEM detects signals originating from several
hundred $\overset{\circ}{A}$ within the specimen, thus thin films of 1 to 50 mono-
layers are almost entirely transparent to such analysis. Fre-
quently the chemistry of this top layer of 5 to 200 $\overset{\circ}{A}$ is criti-
cally important to the success or failure of a device, especially
in problems related to grain boundary fractures, adhesion, lubri-
cation, catalysis, and reactivity. SIMS using a beam of low
energy 50 to 5000 eV inert ions provides a depth resolution of
less than 5 $\overset{\circ}{A}$ enabling elemental characterization of a specimen
surface from its top monolayer into the bulk. Depth information
is obtained by observing SIMS elemental signals as the outermost
layers of the specimen are successively removed by ion sputtering.

Low Z elements such as H, Li, Be, B, C, N, O, F, Na, Mg, and Al can
be totally undetected by normal SEM X-ray analysis. SIMS is highly
sensitive to these low Z metals especially elements of Periodic
Group I, II, and III and extends routine analysis to include the
entire periodic chart.

Unfortunately, SIMS has historically been associated with expensive
ion microprobe studies. These studies generally utilized very in-
tense, high energy ion beams with sputtering rates precluding anal-
sis of the top 100 to 200 $\overset{\circ}{A}$. The use of low density, low energy
inert ion beams as discussed below provides the high depth resolution
needed to analyze the top few monolayers of a sample.

Most samples including polymers, ceramics, glass, etc., can be analyzed by SIMS without resorting to C, Al, or Au coatings. In microelectronics, SEM can often locate physical microdefects causing device failure. However, one common device failure not readily identified by SEM/X-ray is that related to unreliable bonding to Al bonding pads in IC's. Typical cases include devices on which all Al bonding pads were essentially identical to X-ray and SEM, yet SIMS analysis clearly indicated defective bonding pads resulted from a 50 to 100 Å thick surface contamination. Similar applications illustrate how surface contaminations of less than 100 Å drastically reduce adhesive bonding performance of polymers and metals to other substrates.

MONOCRYSTALLINE SURFACE ANALYSIS USING ION-FOCUSSING EFFECT

E.S.Mashkova, V.A.Molchanov, A.D.Pavlova

Institute of Nuclear Physics, Moscow State University,

117234 Moscow, USSR

A focussing of a scattered particle flux is known /1/ to take place,under certain condition, in the case of ion scattering by single crystals. The effect consist in that the scattered particles flux is compressed in space much stronger than at similar conditions in the case of both random scatterer (amorphous or polycrystalline) and random orientation of the monocrystalline target relative to primary ion beam. Ion focussing effect leads, in particular,to characteristic dependences of the scattered ion intensity on the target rotation azimuthal angle. Namely, drastically nonmonotonic angular dependences of the number of particles scattered at fixed direction are observed. Sharp and complex maxima exhibit when the scattering plane becomes parallel to crystallographic axes lying in the target surface.It whould be noted that such behaviour occurs when total ion reflection yield does not maximum /2/. The aim of the present work is to examine the sensitivity of the method to primary ion type, ion energy and the scattering geometry.

The experimental techniques were conventional /3/. Noble gas ions (Ne^+, Ar^+, Kr^+) with energies of 5-30 keV impinged on the (110) face of a copper crystal. The sliding angle α varied from $0°$ to $40°$, the polar scattering angle β varied from $0°$ to $55°$. The scattered particles were detected by

the fast particle detector described elsewere /3/. On the
one hand the detector choice was conditioned by the fact
that during noble gas scattering the particles leave the
target surface mostly as neutral ones. One the other hand,
it is known /4/ that the anisotropy of the angular dependen-
ces. Of total (ion plas neutrals) scattered flux is more
pronounced than in the case of only ion registration. The
azimuthal angle of tar-
get rotation   was
varied over a wide range
($\pm 110°$ relative any
choosen direction on
the target surface).
About 200 angular
dependences were
measured and analy-
sed. General character
of the observed depen-
dences is sharply nonmono-
tonic. When at the same ti-
me both sliding and out-
let angles are small, only
main crystallographic di-
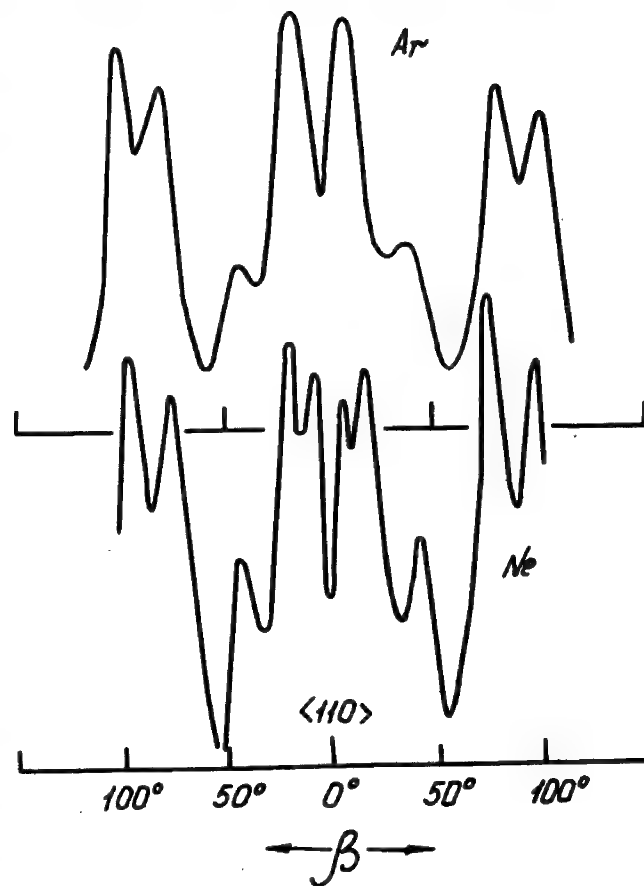
Fig.1.

rections (for example $\langle 100 \rangle$ and $\langle 110 \rangle$) are exhibited.
At azimuthal angles of target rotation β , corresponding
of these directions the sharp narrow maxima are observed.

The increase sliding or (and) outlet angle leads to ri-
se a sensitivity in two aspects. Firstly, main maxima become
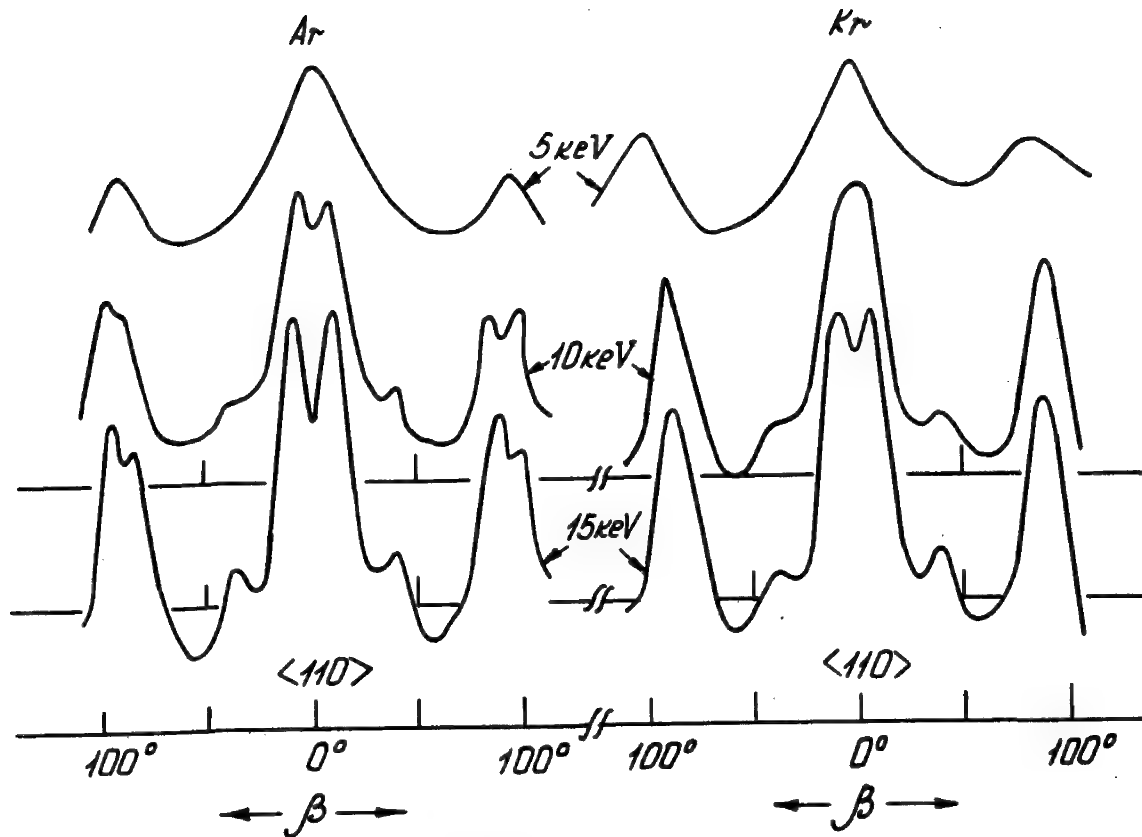
Fig.2.

wider and splits.The acuteness of a splitting dip in some

cases guarantees better accuracy of main axes detection. It

has been found that a depth and acuteness of the splitting

dips increases as the atomic number of primary ion decreases,

see Fig.1,where comparative data for neon and argon ions with

30 keV energy presented (α = 20°, θ = 40°). Secondly,

anisotropic character observed curves between the main maxi-

ma exhibit more distinctly giving possibility more detail

analysis of studies surfaces.The primary ion energy decrease

leads to broadening of the maxima and to anistoropy smoothing,

see Fig.2, where comparative data presented for 5-15 keV

argon and crypton ions at α = 20°, θ = 37°.

References
1. E.S.Mashkova,V.A.Molchanov,Rad.Effects,13, 183, 1972.
2. M.W.Thompson,Contemp.Phys., 9, 375 (1968).
3. E.C.Mashkova,V.A.Molchanov,Rad.Effects, 16, 143(1972).
4. E.S.Mashkova,V.A.Molchanov, Rad.Effects, 23,215 (1974).

MEASUREMENTS OF H^+ AND He^+ YIELDS FOR H_2^+ AND He^+ ELASTICALLY

SCATTERED FROM Ag AND Pd.   P. J. Adelmann, H. F. Helbig and A. W. Czanderna, Department of Physics, Clarkson College of Technology, Potsdam, New York, 13676, U.S.A.

A recent outgrowth of ion scattering spectrometry (ISS) is the technique of recording the energy dependence of the yield of noble gas ions elastically scattered from solid surfaces. This ion scattering double spectroscopy (ISDS) technique was pioneered by Erickson and Smith (1); four classes of yield curves have been identified by Rusch and Erickson (2) for a large number of noble ion-surface systems. Based on Smith's original ISS work (3) attention in this field has been confined to noble gas projectiles because of the obscuring effects of the large inelastic ion yield characteristic of reactive projectile ions. The present work, however, presents a technique whereby hydrogen ion projectiles can produce satisfactory ISDS spectra. By using a mixed ion beam ($H_2^+ + He^+$), the position in energy of elastically scattered protons may be inferred from the corresponding position of the well defined elastic helium peak.

The yields of protons and helium ions have been measured for 90° elastic scattering of monoenergetic (300 to 2700 eV) He^+ and mixed beams of [$H_2^+ + He^+$] (gas mixture 10 H_2 to 1 He) from polycrystalline surfaces of Ag and Pd. The proton yield from Ag was found to be about an order of magnitude smaller than that for Pd over the entire energy range, while the He^+ yields are approximately the same for both metals. Furthermore, the proton yield vs energy curves for Ag and Pd (both of which fall into the category which Rusch and Erickson have called class I) peak at 637 eV and 510 eV, respectively. The differences in yields and in the ISDS peak positions, which cannot be attributed to cross-section effects, will be discussed in terms of the neutralization mechanisms which are thought to be effective.

Although the peaks used to identify Ag and Pd are difficult to separate by obtaining the energy loss spectrum with the usual ISS equipment, the difference in proton yields provides a simple method for identifying Ag and Pd using the same equipment. Because of the chemically active nature of the H_2^+-surface interaction, the possibility exists that other nearly identical masses can be distinguished using ISS in a similar manner. Furthermore, the possibility of using ISS, with its unique monolayer detection capability, for studying the catalytically interesting silver-palladium solid solution system will be discussed.

(1).   R.L. Erickson and D.P. Smith, Phys. Rev. Lett. 34, 297 (1975).
(2).   T.W. Rusch and R.L. Erickson, J. Vac. Sci. Technol. 13, 374 (1976).
(3).   D.P. Smith, Surf. Sci. 25, 171 (1971).

THE FIRST 50 Å: PRACTICAL APPLICATIONS OF SURFACE ANALYSIS BY ISS

Gene R. Sparrow, 3M Analytical Systems, 3M Center, St. Paul, Minnesota 55101

Present day Materials Research is greatly facilitated by modern Surface Analytical tools. Problems relating to nearly every field of research, development, and production have been encountered. Many have been success-fully solved. However, in numerous cases, detailed analysis of the first 50 Å of a surface can provide substantially more information and frequently new information not previously accessible.

The unique monolayer depth resolution of Ion Scattering Spectroscopy, ISS, makes it especially amenable to extending surface analysis capabilities to obtain detailed elemental concentration depth profiles from the first monolayer to the bulk material. Such monolayer surface detection sensitivity is not limited to a few certain elements as it is in AUGER and ESCA techniques, but is applicable to all elements as well as isotopes of low Z elements such as B, C, N, O, etc. ISS, often used simultaneously with SIMS, utilizes a beam of positive inert ions such as $^3He^+$, $^4He^+$ or $^{20}He^+$ to probe the surface. The energy of ions scattered from the top monolayer of the surface is dependent upon the mass of the particular elements present. The rate of removal of atoms from the surface due to sputtering is precisely controlled throughout the range of less than 0.01 Å per min. to over 300 Å per min. Sensitivities of greater than 10,000 counts per sec. per nanoampere beam current enable spectral acquisition rates of less than 1 sec. through a data acquisition device with automatic transfer to magnetic storage.

Application of ISS to studying segregation of Sb at grain boundaries in steel has been reported previously. Detailed depth profiles of the first 10 Å of such a fracture clearly indicated nearly a single monolayer of Sb existed on the fracture surface.

Investigations of cleaned surfaces prior to adhesion have been useful for improving techniques necessary in development of more reliable bonding. Recontamination of Al surfaces by common organic materials after cleaning procedures was found to cause significant reduction in bond strength. ISS measurements clearly indicated monolayer organic contaminations and offered strong correlation of the contaminants to paper and cloth materials utilized throughout cleaning procedures.

ISS has been used for detailed studies of polymer and glass surfaces. Its low energy input to these surfaces was found to result in little damage to the specimen. These samples were analyzed routinely using charge neutralization hence they were not coated with C or Au. Detailed analysis of the first 30 Å provided results that correlated well with treatments and physical testing of adhesive strength to Al. The application of ISS to biological materials such as hair, hemoglobin, animal tissue, etc., will also be discussed. The high sensitivity of ISS to high Z elements such as Ba, Sn, W, Pb, etc., enabled monitoring trace levels of Pb in these types of samples, as well as in most metals. Surface concentrations of less than 100 ppm are readily detected. The accompanying figures illustrate a few typical ISS spectra obtained from these studies.

ISS DEPTH PROFILE
Soda Lime Glass

He^{+3} Probe Ion
1500 ev

O

Na

10Å

O

100Å

Na Si

200Å

O

Si

Na

Si

Ca

Ca

Ca

C

S

N O

Al

Na

K

Leave-in
rinse

with Shampoo

ISS of Treated Hair

Top Monolayer

~30 Å

^{3}He 3keV

Sputtered Ion

C N O Na

Ca Fe

A

Sputtered Ion

C

O

Ca

N F Al Si

Cl

Fe

Mg

Na

A

C

O

Si

Fe

B

C

N

F

Si

K

Fe

B

C O

C

C

C

N

O

Na

Fe

C

C

O

D

C

O

N

Na Cl Fe

D
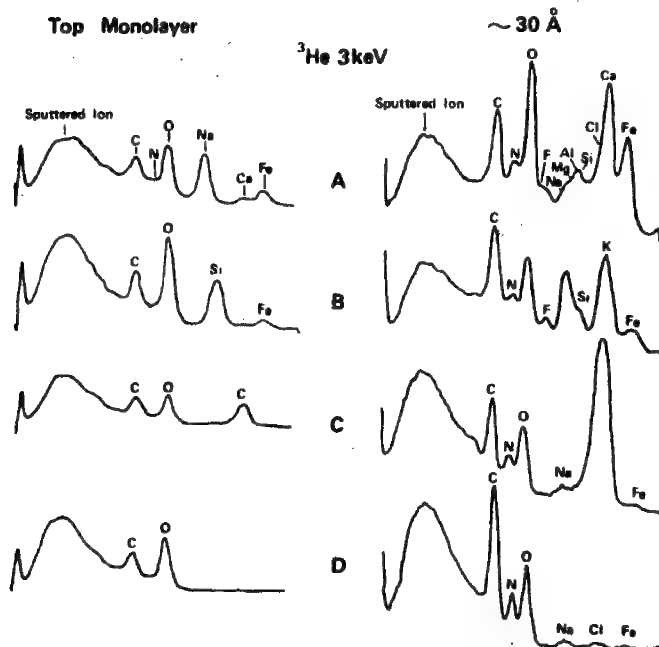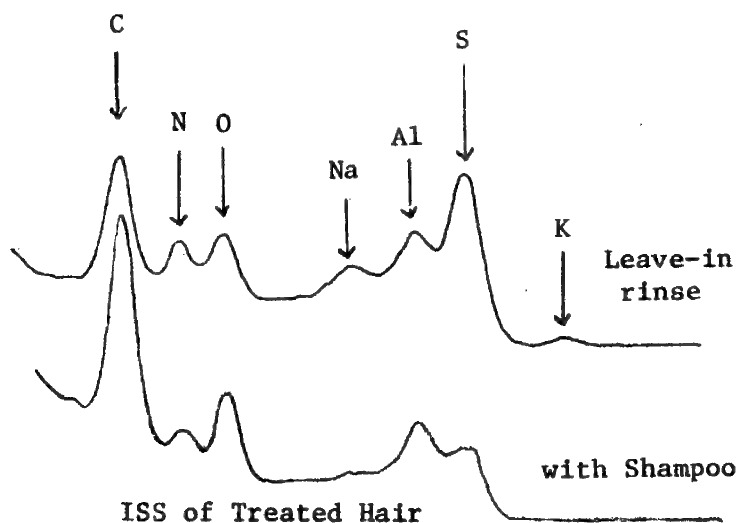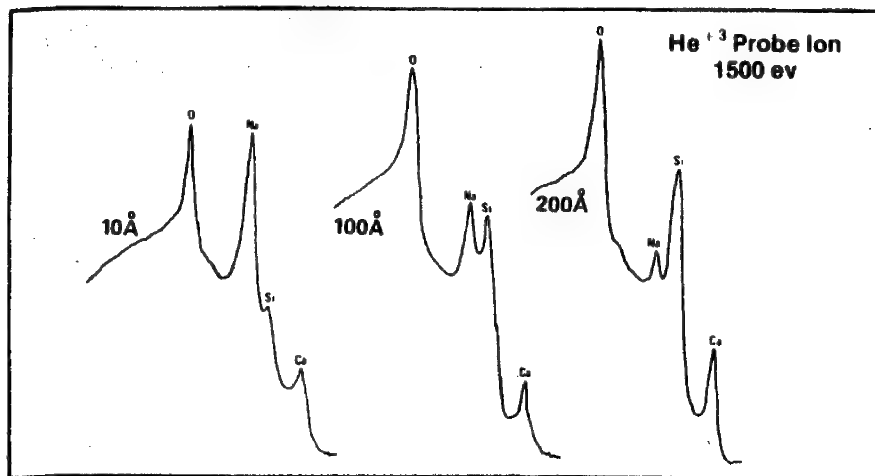
ISS of Treated Polyimide

ION SCATTERING PROFILES OF POLYPROPYLENE COATINGS ON $\underline{CuO^{18}_{0.67}}$ $\underline{FILMS}$
<u>BEFORE AND AFTER OXIDATIVE DEGRADATION OF THE POLYMER.</u> A. C. Miller, A. W.
Czanderna, H. H. G. Jellinek, and H. Kachi, Department of Physics and
Chemistry, Institute of Colloid and Surface Science, Clarkson College of
Technology, Potsdam, New York, 13676, U.S.A.

Polymers are known to oxidatively degrade in the presence of copper
and its salts. In this work, the basic question was to determine the role
of the polymer-copper oxide interface in the catalyzed oxidative degradation
of polypropylene. Subsidiary questions including determining the use of Ion
Scattering Spectrometry (ISS) with the oxygen-18 isotope and if potential for
ISS quantitative analysis of the isotope exists.

Copper films were deposited on glass substrates and oxidized
partially or completely to $CuO_{0.67}$ in oxygen-16 or oxygen-18. The 44 nm thick
oxide films were overlaid with 40 to 110 nm of polypropylene (pp) by a dip
coating process. The $pp|CuO_{0.67}|$glass samples were heated in oxygen-16 at
temperatures of 90, 100, 110 and 120° in the presence and absence of getters
for the product gases. ISS depth profiles were obtained using 1500 eV He^3 at
1 mm FWHM and ca.200 nA in a 3M-ISS, 90° scattering angle instrument. Profiles
were obtained for deposited copper films, partially and completely oxidized
films (both labeled and unlabeled) and for undegraded and oxidatively degraded
polymer/oxide sandwiches.

The profiles of partially oxidized copper films provided Cu/O peak
height ratios through the copper oxide/copper interface region. Analysis of
the copper oxides formed in oxygen-16 and oxygen-18 showed the expected separa-
tion of the maxima of 0.03 E/E_0 in the energy loss spectrum. The gaussian
shaped peak permitted quantitative identification of as little as 5% of
oxygen-18 in the presence of oxygen-16 in the film. The oxygen peak is suf-
ficiently narrow to permit adding the peak height intensities of the signal
from oxygen-16 and oxygen-18 to obtain the total oxygen concentration. For all
16-18 combinations, the sum of the peak intensities is the same as for the
intensity of oxygen-16 in $CuO_{0.67}$.

With non-degraded polypropylene overlayers, surprisingly high Cu/O
ratios were obtained, suggesting reduction of the copper oxide results during
profiling. A possible mechanism involves dissociation of the polymer and sub-
sequent reaction of hydrogen with the copper oxide. The Cu/O ratio depended
on the polymer overlayer thickness but could be reproduced for any given set
of polymer/copper oxide samples. Accordingly, one coated sample was divided
into four pieces. These were profiled as follows: with the coating dissolved
without degradation, as coated without degradation, after degradation in the
presence of getters and after degradation in the absence of getters for the
product gases.

In the presence of getters, the copper oxide film is reduced by the
polypropylene but is not reoxidized, leaving the copper oxide film nearly all
reduced to copper. The O^{16}/O^{18} ratio in the unreduced oxide remained unchanged
from the original ratio. The degraded polypropylene was more difficult to
sputter and the profile showed copper was present throughout the polymer thick-
ness.

In the absence of getters, the copper oxide film is reduced but reoxidized by the oxygen ambient used during the oxidative degradation. The O^{16}/O^{18} ratio in the oxide after degradation exhibits a marked increase in oxygen-16. Extensive oxidation of the polypropylene is evident from the O^{16} signal in the polymer and, again, copper ions are found distributed throughout the polypropylene.

In conclusion, polypropylene partially reduces copper oxide films during oxidative degradation at 90-120°C. Partial reoxidation of the reduced copper occurs if the degradation is carried out in the absence of getters for the product gases. Oxygen-16 and Oxygen-18 peaks are sufficiently separated in the ISS energy loss spectrum to permit identification of oxygen 18 between the limits of 5 and 95%.

Carbon fluorescence yield with proton and electron bombardment

K. Brunner, W. Hink, B. Krause and T. Scharnagl

Physikalisches Institut der Universität Würzburg, Würzburg, Germany

Introduction: Experimental data on the K-shell fluorescence yield ω_K - roughly defined as the probability that a K-shell vacancy is filled by a radiative transition - for elements of low atomic numbers such as Be, B etc. are very rare. For carbon different measurements exist, but the results spread within a factor of 3 with quoted uncertainties of less than $\approx 20\%$ (for a survey see Bambynek, 1973[1]). This situation is even more complicated as early measurements with proton-induced K-shell vacancies seemed highly indicative of an energy-dependent fluorescence yield due to multiple ionization processes (see discussion of Langenberg and van Eck, 1973[2]).

As carbon has developed to some kind of standard - relative X-ray and Auger measurements are referred to the absolute ionization cross section of carbon - the removal of possible discrepancies in its fluorescence yield occurs as highly important. The results to be discussed in this paper are based on recently published work and on measurements of our group; they remove most of these discrepancies for electron and proton impact.

Experimental method: The basic experimental technique used here consists in measuring with a flow proportional counter (2 μm thick Makrofol window) the produced X-rays in solid graphite and gaseous methane under electron and proton bombardment, thus delivering the carbon X-ray emission cross section σ_X of graphite and methane. Furthermore, the emitted Auger electrons of carbon in gaseous methane are detected with a cylindrical mirror analyzer followed by a channel electron multiplier, delivering the Auger emission cross section σ_A which effectively is identical with the K-ionization cross section σ_I of carbon in methane.

By taking the ratio of σ_X to σ_A, one immediately obtains the fluorescence yield $\omega_K = \sigma_X/\sigma_I \simeq \sigma_X/\sigma_A$. Comparing σ_X for graphite and for carbon in methane, ω_K for graphite is inferred.

Results for electron impact (Fig. 1): The X-ray emission cross sect-
ions for thin solid non-backed graphite films ($\rho \cdot d \geq 5 \; \mu g/cm^2$) meas-
ured by our group (Erlwein, 1974[3]) in the energy range of 5 - 40 keV
electron impact energy - making use of an experimental method for
correcting data as to electron scattering within the target - differ only
by a constant factor over the whole range (5 - 17 keV) of comparison
with the X-ray emission cross sections of carbon in methane as given
by Tawara et al., 1973[4]. As the deviation of this factor from 1 is less
than the experimental error of the X-ray data ($\approx 15\,\%$), this suggests
the conclusion that within experimental error ω_K is the same for sol-
id graphite and carbon in gaseous methane.

Our measured Auger emission cross sections for carbon in gaseous
methane (Hink and Krause, 1976[5]) reveal in the range of 0.35 - 14 keV
electron impact energy the same impact energy dependence as the X-
ray emission cross sections. This allows deducing of an energy inde-
pendent fluorescence yield

$$\omega_K = (2.4 \pm 0.3) \cdot 10^{-3}.$$

(The fitting curves for the two sets of data are related within 3 % by
ω_K as scaling factor.)

Results for proton impact (Fig. 2): Methodically in the same way we
relate our measured X-ray emission cross sections for massive gra-
phite (Brunner and Hink, 1973[6]) and for carbon in gaseous methane
(Scharnagl, 1974[7]) in the range of 10 - 60 keV proton impact energy
together with the data of Langenberg and van Eck, 1976[8] in the high
impact energy range (0.1 - 1.1 MeV) to the Auger electron cross sec-
tions of Stolterfoht and Schneider, 1975[9]. As the high energy Auger
data smoothly run into our low energy X-ray data, it is concluded - as
already was shown in 8) for impact energies ≥ 100 keV - that the K-
fluorescence yield of carbon in methane independently of impact ener-
gy amounts to

$$\omega_K = (2.4 \pm 0.4) \cdot 10^{-3}.$$

The X-ray emission cross sections for carbon in methane and solid
graphite agree within experimental error ($\approx 15\,\%$). Thus as for elec-
trons the same value for ω_K is to be assigned to solid graphite and to
carbon in gaseous methane.

Discussion: Within experimental error, electron and proton impact measurements lead to the same energy-independent value of the K-shell fluorescence yield of carbon which agrees well with the recently calculated values by Walters and Bhalla, 1971[10] ($\omega_K = 2.36 \cdot 10^{-3}$) and by McGuire, 1970[11] ($\omega_K = 2.6 \cdot 10^{-3}$). As ω_K should be determined from X-ray and Auger electron cross section data for the same well defined initial state of the specified atomic or molecular species – a condition which certainly is not fulfilled in the above described measurements – this apparently simple result for ω_K has to be refined with respect to the influence of multiple ionization processes and highly excited Rydberg states. This influence and major errors of the measuring procedures will be discussed.

References:

1) Bambynek, W., Proc. Int. Conf. Inn. Shell Ion. Phenomena, Atlanta 1972, p. 80

2) Langenberg, A. and van Eck, J., Phys. Rev. Lett. 31 (1973) 71

3) Erlwein, M., Diploma-Thesis, University of Würzburg, 1974

4) Tawara, H., Harrison, K.G. and de Heer, F.J., Physica 63 (1973) 351

5) Hink, W. and Krause, B., Abstr. of II. Int. Conf. Inn. Shell Ion. Phenomena, Freiburg 1976, p. 232

6) Brunner, K. and Hink, W., Z. Phys. 262 (1973) 181

7) Scharnagl, T., Diploma-Thesis, University of Würzburg, 1974

8) Langenberg, A. and van Eck, J., J. Phys. B: Atom. Mol. Phys. 9 (1976) 2421

9) Stolterfoht, N. and Schneider, D., Phys. Rev. A 11 (1975) 721

10) Walters, D.L. and Bhalla, C.P., Phys. Rev. A 3 (1971) 1919

11) McGuire, E.J., Phys. Rev. A 2 (1970), 273

12) Rudge, M.R.H. and Schwartz, S.B., Proc. Phys. Soc. 88 (1966) 563

13) Basbas, G., Brandt, W. and Laubert, R., Phys. Rev. 77 (1973) 983
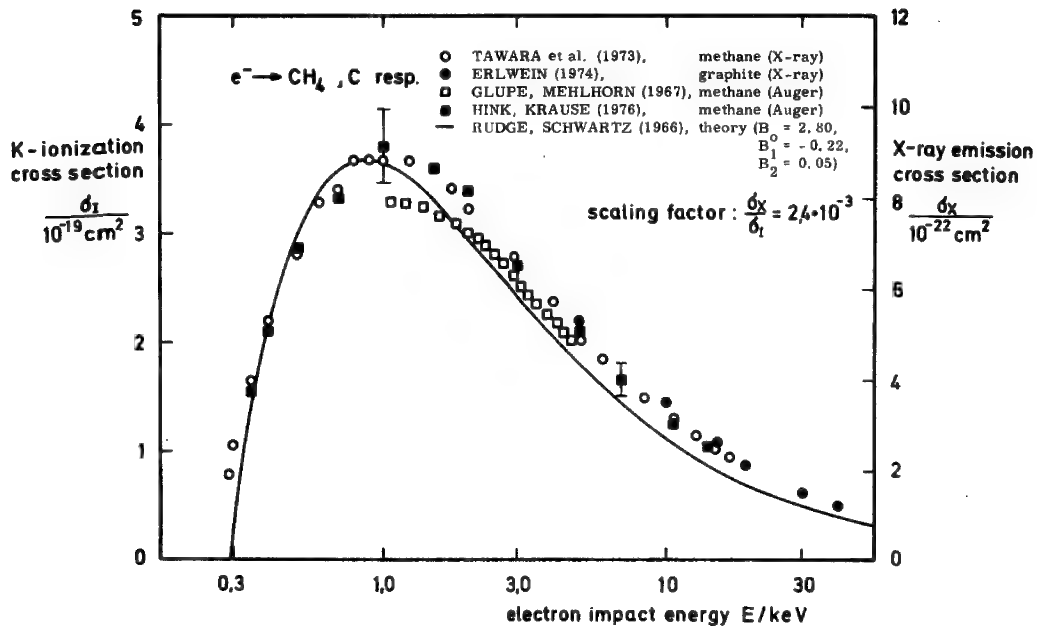
Fig. 1: Experimental electron impact cross section data. The curve represents σ_I as calculated according to Rudge and Schwartz[12].
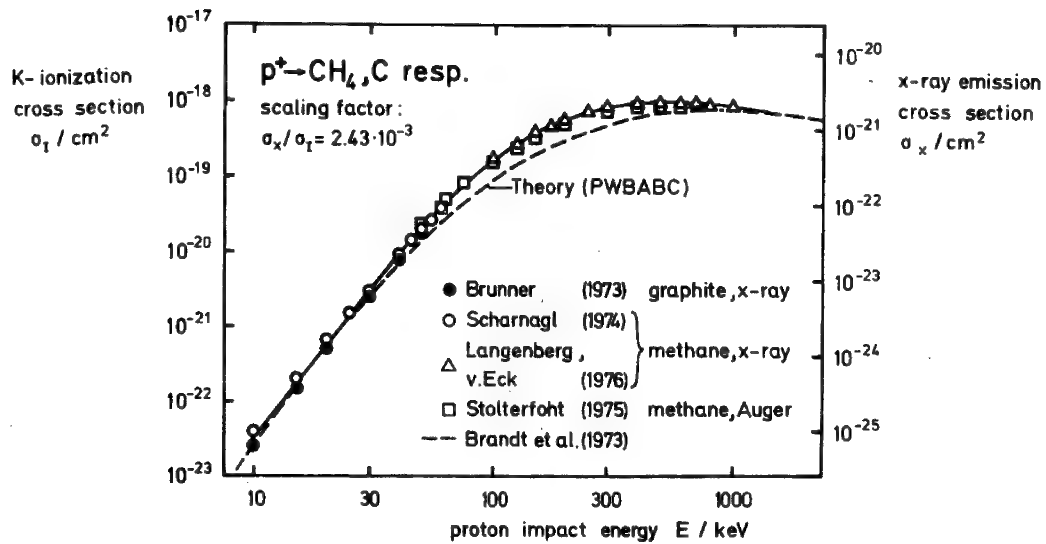
Fig. 2: Experimental proton impact cross section data. The broken curve represents σ_I in PWBABC calculation by Basbas, Brandt and Laubert[13].

THE DOPPLER-TUNED SPECTROMETER: A NEW TOOL FOR HIGH-RESOLUTION X-RAY SPECTROSCOPY

J. RICHARD MOWAT
North Carolina State University
Raleigh, North Carolina

A. DESCRIPTION OF THE SPECTROMETER

The devices conventionally used to measure x-ray energies are inadequate when the x-ray source is very weak, e.g., on ion beam, and when high resolution is needed, e.g., to energetically resolve $2p \rightarrow 1s$ transitions from three- and two-electron ions. The gas-filled proportional counter [or the solid-state Si(Li) detector] offers the needed sensitivity but has inadequate energy resolution, whereas the crystal spectrometer offers the needed resolution but has inadequate sensitivity. The recently developed Doppler-tuned spectrometer[1] (DTS), on the other hand, is ideally suited for high-resolution x-ray energy analysis when *the source is weak but fast moving.*

1. Components

The DTS consists of three elements: a proportional counter, a collimator, and an absorber (see Fig. 1)
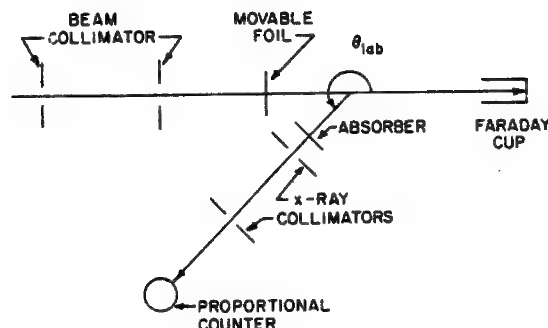
FIG. 1. Schematic diagram of apparatus.

(a) A proportional counter, which can be positioned at a variable viewing angle with respect to the ion beam direction, serves as a *wide-band* x-ray detector. The copper counter used in this experiment is operated at 1000 V with 200 Torr of P-10 gas and is sealed by a 440-$\mu g/cm^2$ aluminum window. The counter's relatively high resolution (20% full width at half-maximum at 6.4 keV) permits effective use of upper- and lower-level pulse-height discrimination to reduce background. The dark count is less than 1 sec^{-1}.

(b) An x-ray collimator defines the angle θ_{lab} between the beam direction and the direction of the detected photon. It consists of two $\frac{1}{16}$ in.-wide slits spaced 6 in. apart that limit the x-ray divergence to 1.2^o and define a beam segment of length 0.104 in. at $\theta_{lab} = 90^o$.

(c) An absorber, so chosen that a characteristic edge lies near the energy of the emitted photon, is placed in the path of the detected x-rays. With an 810 $\mu g/cm^2$ aluminum absorber the total thickness traversed (absorber plus counter window) is 1250 $\mu g/cm^2$. The transmission[2] is estimated to be 65% near the low-energy side of the K absorption edge (E_{abs} = 1559.9 eV).[3] The corresponding transmission near the high-energy side is 0.3%. This large, abrupt transmission discontinuity accompanies the onset of the photoelectric effect and is used for x-ray energy discrimination as described in the following paragraph.

2. *Operation*

The DTS exploits the Doppler shift of photons emitted by swiftly moving ions to disperse the x-rays according to their emission angle. When the absorber is properly chosen, there will be a well-defined polar angle at which the Doppler-shifted photon energy exactly coincides with the absorption edge. (Our spectrometer covers the range $210^{\circ} \le \theta_{lab} \le 330^{\circ}$.) At some forward angles the blue-shifted photon's energy will lie above the absorption edge, and the absorber will be essentially opaque. As the angle of observation is decreased (see Fig. 1), the lab energy of the detected photon decreases. At a certain critical angle θ the lab energy will precisely coincide with the filter's absorption edge E_{abs}, and beyond that angle the absorber will be essentially transparent. The photon's energy (E) in the *ionic* rest frame is given by

$$E = \gamma[1 - (v/c)\cos\theta]E_{abs},$$

where v is the beam velocity, c is the speed of light, and $\gamma = [1 - (v/c)^2]^{-1/2}$.

3. *Resolution*

The DTS obtains its high resolution from the natural abruptness of the absorber's transmission discontinuity.[4] For K edges the absorber typically changes from opaque to transparent within less than 1 eV. The resolution of this device is usually limited by the finite beam and x-ray divergences. Differentiation of the Doppler-shift formula above gives

$$\Delta E/E_{abs} = \gamma(v/c)(\sin\theta)\Delta\theta_{lab},$$

so that a spread $\Delta\theta_{lab}$ in observation angle contributes an uncertainty ΔE to the deduced rest-frame energy E. Based on the maximum beam and x-ray divergences described above the maximum fractional uncertainty $\Delta E/E_{abs}$ for a 1564-eV photon emitted by a 50-MeV Al ion is 0.18%.

4. Calibration

An angular distribution taken with the spectrometer viewing a point 2.3 cm downstream from an exciter foil is shown in Figure 2. The 50 MeV aluminum ion beam was accelerated by the Brookhaven National Laboratory MP tandem Van de Graaf. X-ray counts were accumulated at each angle for a fixed amount of integrated beam current. The angular increment was 0.32°. This integral spectrum contains three distinct features that are interpreted as 2p → 1s transitions in two- and three-electron ions. If the step at 249° results from the onset of absorption for the 1598.4-eV $(2^1P_1 \to 1^1S_0)$ photon,[5] then the step at 255.1° corresponds exactly to the 1588-eV $(2^3P_{2,1} \to 1^1S_0)$ photon.[5] This internal consistency suggests using these He-like lines as energy calibrations. Then the step at 269.3° in this particular spectrum corresponds to the absorption of a 1564.2-eV photon.

B. SOME EXPERIMENTAL RESULTS AND DISCUSSION

Nine spectra were taken at beam energies of 25, 50, and 75 MeV. The 1564-eV feature was weaker at 50 MeV than at 25 MeV and was not detectable at 75 MeV. A total of seven measurements were made of the position of the 1564-eV step and nine calibration measurements were made of the 1588- and 1598-eV steps. The average of all measurements is

$$E(^4P^o_{5/2} \rightarrow {}^2S^e_{1/2}) = 1563.65 \pm 0.90 \text{ eV},$$

where the quoted error is due to uncertainties in the calibration and spans the scatter of all seven measurements. The full width of the step (Fig. 2) is about 1.5^o, which corresponds to an energy spread of 2.6 eV (0.17%), which agrees with the estimate made above (0.18%) and indicates that the energy resolution is limited by instrumental geometry.
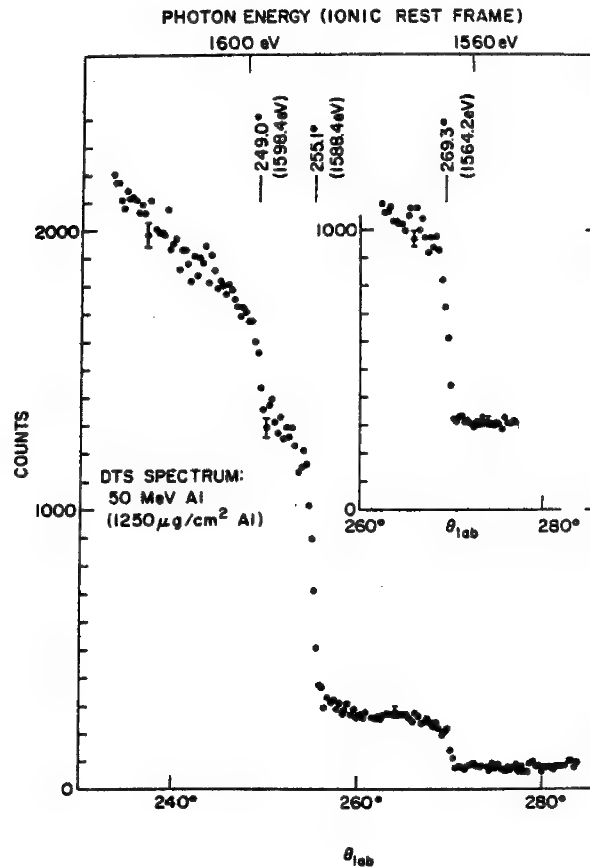
FIG. 2. DTS spectrum taken through a 1250-μg/cm^2 Al absorber 1.2 nsec after foil excitation of a 50-MeV Al beam. (Error bars indicate counting statistics.) The origin of the upward slope below 250° is not completely known. Part is due to cosecant brightening (see Ref. 1), and the remainder may occur as follows: When the viewing angle is decreased from 249° to 235°, the length of upstream beam segment viewed increases from 0.056 to 0.064 in. This will cause a fast exponential rise in detected x rays from cascade-fed prompt decays. (At this foil position the foil is out of view.)

The energy loss of 50-MeV Al ions during passage through a 20-μg/cm^2 C foil is estimated to be 0.3 MeV. Neglect of this energy loss leads to an error of less than 0.025 eV in the determination of E.

The $^4P^0_{5/2}$ excitation energy in Al^{+10} has been computed by Cheng, Lin, and Johnson from Dirac-Hartree-Fock wave functions. Their value is 1563 eV. Ford[7] has obtained the value 1563.7 eV after applying relativistic corrections[8] to nonrelativistic eigenvalues computed by the 1/Z expansion method.[9]

C. SUMMARY

We have observed two metastable components in x-ray spectra emitted by a foil-excited aluminum beam. One of these has a measured transition energy (1563.65 ± 0.90 eV) that agrees with theoretical calculations of the transition energy of the (1s2s2p) $^4P^0_{5/2} \rightarrow$ (1s^{2}2s)$^2S_{1/2}$ decay in the Li-like ion Al^{+12}.

D. ACKNOWLEDGEMENTS

who assisted in data analysis, and the operations staff of the BNL tandem accelerator, whose conscientious efforts produced the high-quality beams needed for this experiment.

[1] R.W. Schmieder and R. Marrus, Nucl. Instrum. Methods 110, 459 (1973); R.W. Schmieder, Rev. Sci. Instrum. 45, 687 (1974).

[2] Wm. J. Veigele, Atomic Data Tables 5, 51 (1973).

[3] J.A. Bearden and A.F. Burr, Rev. Mod. Phys. 39, 125 (1967).

[4] H. Neddermeyer, Phys. Rev. B, 13, 2411 (1976).

[5] H. Flemberg, Ark. Mat. Astron. Fys. A 28, (No. 18), 1 (1942).

[6] K.-T. Cheng, C.-P. Lin, and W.R. Johnson, Phys. Lett. 48A, 437 (1974), and private communication.

[7] A.L. Ford (private communication).

[8] C. Laughlin, J. Phys. B 8, 842 (1975); H.T. Doyle, Adv. At. Mol. Phys. 5, 337 (1969).

[9] J.S. Onello, L. Ford, and A. Dalgarno, Phys. Rev. A 10, 9 (1974); J.S. Onello and L. Ford, *ibid.* 11, 749 (1975).

EXCITATION OF CARBON K X RAYS BY 1 TO 40 MEV CARBON, NITROGEN, AND OXYGEN IONS

F. W. Martin

Department of Physics and Astronomy
University of Maryland
College Park, Maryland 20742

Measurements of the carbon K X-ray emission spectra of evaporated carbon films have been made using a double-focusing spectrometer having a lead stearate pseudocrystal. The spectra indicate a lack of multiple ionization of the carbon atom in this conducting solid target.[1] Absolute cross sections σ_x for X-ray emission are obtained by calibrating the spectrometer transmission.[2] Reduced cross sections (defined as σ_x/Z_1^2, where Z_1 is the atomic number of the projectile) are shown in the Figure, together with data for methane gas, for ions at lower energies, and for protons.[3] Since the production of delta-ray electrons is proportional to Z_1^2 at high velocities, the reduced cross section gives a measure of the X-ray signal to the secondary bremsstrahlung which may be expected for a given ion. At a given velocity it is apparent that ions are superior to protons, particularly in the case of gas targets where the fluorescence yield of the target is increased because of multiple vacancy effects. At high velocities the signal-to-damage ratio may be estimated using the electronic stopping power, which in the Bethe theory is also proportional to Z_1^2 at a given velocity. It is thus apparent that ion produce more X-ray signal per unit damage to organic molecules than protons or electrons of the same velocity. Using experimental stopping powers, which are smaller than those given by the Bethe theory (because the effective charge of the ion becomes smaller than Z_1 as the moving ion picks up electrons), it may be computed that the molecular dose required for X-ray emission from solid adenine excited by 16 MeV oxygen ions is about 2.0 MeV, comparable to the 1.8 MeV required for X-ray emission stimulated by the 25 KeV electrons typically used in microscopes. If quenching of the multiple carbon vacancies can be prevented, the dose may approach 200 KeV. However, even though the signal-to-background of the X-ray process is much superior to that involved in inelastic electron scattering, it does not appear that X-ray production by C, N, and O ions can compete with inelastic scattering of 25 KeV electrons from carbon in adenine, which only requires a molecular dose of 2.5 KeV per event.

1. F. W. Martin, W. Freeman, and J. Sauls, submitted to J. Phys. B
2. F. W. Martin, W. Freeman, and J. Sauls, submitted to Physical Review
3. F. W. Martin, in "Workshop on Short Wavelength Microscopy" (Annals of the New York Academy of Sciences, in press)
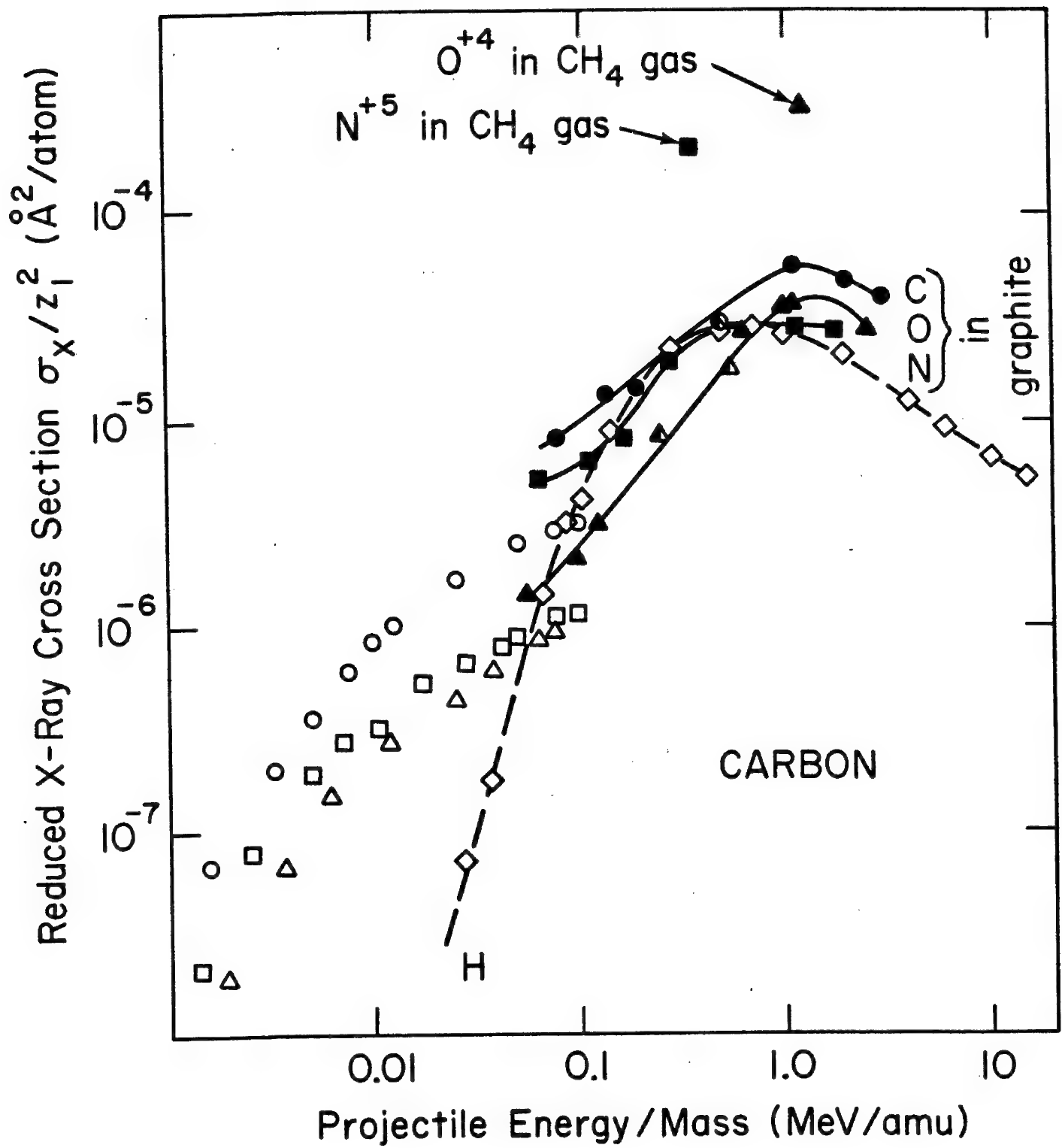
O^{+4} in CH_4 gas

N^{+5} in CH_4 gas

Reduced X-Ray Cross Section σ_X / z_i^2 ($\mathring{A}^2$/atom)

$\left.\begin{array}{c} C \\ N \\ O \end{array}\right\}$ in graphite

CARBON

H

Projectile Energy/Mass (MeV/amu)

Proton Induced Inner Shell Ionisation Cross-Sections in the 1 - 3 MeV
Region of Interest in Microanalysis.

Md. Rashiduzzaman Khan,[*] A.G. Hopkins and D. Crumpton.
Department of Physics, University of Aston in
Birmingham B4 7ET, England.

Extended Abstract

Quantitative multielemental microanalysis based on the proton
induced X-ray emission technique requires a comprehensive knowledge
of ionisation cross-section data for all elements likely to be
encountered in an analysis. Ideally the variation of the ionisation
cross-section with proton energy should also be known so that the
choice of the incident proton energy is not restricted. In the
case of thick or semi-thick samples, where the proton energy changes
markedly within the sample, a knowledge of the excitation function is
also required to enable correct evaluation of the reaction-yields.

Measurements have been made of the K X-ray production of
several elements between Z = 20 and 50, bombarded with protons from
the 3MV Dynamitron accelerator of the Joint Birmingham Radiation Centre.
Thick target X-ray yields were measured in steps of 200 keV in the
energy range 1 to 3 MeV, a range which is particularly important for
analytical purposes.

Measurements were made on spectroscopically pure elements
positioned at 45° to the incident proton beam. Data accumulation
times of 100 seconds were used with beam currents of the order of
30 nanoamps. An energy dispersive Si(Li) detector spectrometer
system was employed for the X-ray detection and the resultant spectra
analysed by an on line computer, enabling rapid calculation of the
total X-ray yields.

The uncertainty associated with the experimental measurements
was estimated to be less than 2% due to counting statistics and
beam current measurements, and less than 4% for the total uncertainty
on the absolute yield for the majority of elements.

From these measurements the K shell ionisation cross-sections, σ_I,
have been calculated after the manner described by Merzbacher:

$$\sigma_I = \frac{\sigma_p}{\omega_K} = \frac{N^{-1}}{\omega_K} \left[\frac{dE}{dx} \frac{dY}{dE} + \mu Y \right]$$

[*] Present address: Nuclear Research Centre, Atomic Energy
Organisation of Iran, Tehran.

where:

σ_p = X-ray production cross-section

ω_K = fluorescence yield

N = number of atoms per unit volume

μ = self absorption coefficient

$\dfrac{dE}{dx}$ = stopping power

Y = photon yield per proton

The slopes of the yield curves, $\dfrac{dY}{dE}$, were obtained by differentiation of polynomials fitted to the experimental data.

To enable an extension of the data to intermediate elements not covered by the present measurements, empirical equations are proposed for the calculation of the thick target X-ray yields and the K-shell ionisation cross-sections. The coefficients of these equations have been evaluated by means of regression analysis of the experimental data at several energies in the region of interest. The equations have the following formats:-

(1) $\quad \log Y(E) = \left[a_0(E) + a_1(E) Z \right]$

(2) $\quad \log \sigma_I(E) = \left[b_0(E) + b_1(E) \log Z + b_2(E) (\log Z)^2 \right.$

$$\left. + \ldots\ldots\ldots\ldots\ldots \right]$$

For convenience polynomials have been fitted to the energy dependent coefficients of the cross-section equations and a single equation was obtained which incorporates both the energy and atomic number dependence. A similar procedure was adopted in the case of the yield equations.

In addition, the K shell ionisation cross-sections have been reduced to the format of the Binary Encounter Approximation universal function and a suitable polynomial fitted to the reduced data.

Measurement of the Relative Intensities of the L X-rays from High

Z Elements Induced by 1-3 MeV Proton.

Md. Rashiduzzaman Khan, M. Karimi, A. S. Lodhi

and P. Sioshansi.

Van de Graaff Laboratory, Nuclear Research Center,

Atomic Energy Organization of Iran, P.O. Box 3327,

Tehran, Iran.

In proton induced x-ray emission analysis it is often found that the K_α or K_β line of one element is mixed with either the K lines of the neighbouring elements or some of the L lines of the higher Z elements. If any of these lines remains seperated a knowledge of K_β / K_α , L_β / L_α or L_γ / L_α ratios may be used to find the intensities of unresolved or semiresolved lines. The K_β / K_α ratio for an element is invariant with energy and mode of the ionizing radiation and are well known. On the other hand L_β / L_α and L_γ / L_α ratios are dependent both on the energy and the character of the ionizing radiation. The amount of data on the L intensity ratios are limited. Authors in some of the recent articles have reported data on the subshell ionization cross-sections σ_1 , σ_2 and σ_3

which are not readily usable for practical analysis. Moreover the L ratios are useful for the evaluation of the prediction of different theories.

Proton beams of energies 1-3 MeV in steps 100 keV, obtained from the Tehran Nuclear Research Center Van de Graaff accelerator, were used to bombard thin targets of Sm, Hg, Pb, Bi, Th and U. Targets in elemental or in nitrate form prepared on 7.5 μ thin Kapton foil were placed at an angle of 45° with the beam direction. Si(Li) detector with a resolution of 180 eV was mounted at an angle 90° to the beam direction for the collection of the x-rays. The data were analyzed by multichannel analyzer and an online PDP-11 computer. The excitation functions for the intensity ratios L_ℓ / L_α , L_β / L_α and L_γ / L_α have been obtained after due corrections for the absorptions and detector efficiency.

The experimental ratios L_ℓ / L_α , L_β / L_α and L_γ / L_α have been compared with the prediction of the binary encounter approximation (BEA) and constrained wave binary encounter approximation (CBEA). The theoretical calculations for the plane wave Born approximation (PWBA) are in progress and will be incorporated. Tables of Garcia et.al[1] , Hansen[2] and Choi et.al[3] were used respectively for the calculation of the BEA, CBEA and PWBA predictions of subshell ionization cross-sections σ_1, σ_2 and σ_3. These subshell ionization cross-sections were used along with the published values of the Coster-Kronig transitions, subshell fluorescent yields and radiative widths to find the L_ℓ , L_α , L_β and L_γ production cross-sections from the known relations.

Theoretically the ratio L_ℓ / L_α are expected to be constant and

should be equal to $\Gamma_{3\ell}$ / $\Gamma_{3\alpha}$ because L_ℓ and L_α are the transitions to the same subshell L_3. In the present measurement the L_ℓ / L_α ratios were found to be constant within experimental error and the mean values are 0.042±0.002, 0.053±0.003, 0.054±0.003, 0.056±0.003, 0.062±0.003 and 0.065±0.003 for the elements Sm, Hg, Pb, Bi, Th and U respectively. These values agree with the theoretical values to within 5%. The ratios, however, show a slight increase towards lower proton energies, but the variation is no more than 6%.

The CBEA and BEA predictions for L_β / L_α and L_γ / L_α ratios in this energy range, agree within 15% and 25% respectively for the elements studied. The measured data on both L_β / L_α and L_γ / L_α are found to be increasing functions of energy. At higher energies the experimental data are in general higher than the theoretical predictions whereas at lower energies the present data are either lower than the prediction of the theories or agree with them.

The present data on Bi and Pb agree with those reported by Madison et.al[4]. Good agreement is also found between the present L_γ /L_α data on Sm and those reported by Abrath et.al[5].

References

1. J. D. Garcia, R. J. Fortner and T. M. Kavanagh, Rev. Mod. Phys. 45, No.2, 111 (1973).

2. J. S. Hansen, Phys. Rev. A8, No.2, 822 (1973).

3. B. H. Choi, E. Merzbacher and G. S. Khandelwal, Atomic Data, 5, 291 (1973).

4. D. H. Madison, A. B. Baskin, C. E. Busch and S. M. Shafroth, Phys. Rev. A9, 675 (1974).

5. F. Abrath and T. J. Gray, Phys. Rev. A10, 1157 (1974).

Doubly differential K- and L-ionization cross sections of Ne for electron impact

W. Hink, B. Krause and W. Storch

Physikalisches Institut der Universität Würzburg, Würzburg, Germany

Introduction: Data of σ_I – the total cross section for the production of a vacancy in a particular inner shell – are used to predict the yield of X-rays in EPMA or of Auger electrons in AES and to evaluate inner shell energy-loss spectra of electrons. Unfortunately, these basic data for the mentioned methods of elemental analysis are rather rare (Powell, 1976[1]). Even worse, the agreement between measured and in different approximations calculated cross sections is still not satisfying. It is the accepted view that by measuring multiply differential cross sections a discrimination between competing theoretical approaches should be possible, thus allowing prediction of cross section data reliable over a wide range of elements.

To obtain multiply differential cross sections, it is usually necessary to use coincidence techniques, giving rise to very low true coincidence rates. Moreover, in the case of K-shell ionization processes, the true coincidence signal is to be extracted from a high background, resulting from outer shell processes which are more probable by orders of magnitude.

Experimental: In our experiments, monoenergetic electrons in the keV-region are scattered in a target chamber by Ne-atoms (10^{-3} torr). Outgoing electrons (scattered or emitted) within a small solid angle $\Delta\Omega$ at 90° and 270°, respectively, with respect to the primary electron beam are energy-analyzed in cylindrical mirror analyzers ($\Delta E/E = 0.05$). In each channel, the electrons are detected by a channel electron multiplier, followed by a preamplifier and a constant fraction discriminator. To select K-ionization processes, the outgoing electrons in $\Delta\Omega$ with energy in ΔE are measured in coincidence with K-LL

Auger electrons, passing the second channel. To this, the output pulses of both the discriminators are fed to a time-to-amplitude converter. From the resulting time spectra (coincidence resolution time $\approx$ 5 ns, true coincidence rate $\approx$ 10 counts/hour, typically; see Fig. 1), the doubly differential cross sections (DDCS; differential in energy and solid angle) are extracted.

As the probability for a K-ionization process is small compared with an L-ionization process, the L-shell ionization DDCSs for Ne are obtained in good approximation simply by measuring the electrons, outgoing at fixed solid angle and fixed energy interval.

Results: The preliminary result of our measured K-ionization DDCSs $d^2\sigma/d\Omega dE$ of Ne at 3 keV electron impact energy is shown in Fig. 2 as function of outgoing electron energy. For a first comparison with theoretical data, the DDCSs for scattered and for emitted atomic electrons as calculated in Born approximation by Burhop, 1940[2], are also given. In this approximation of distinguishable particles, the measured DDCSs may be compared with the sum of both the DDCSs, except in the region of the same electron energy. A pronounced deviation occurs mainly at the high energy limit (given by energy conservation) of outgoing electrons. This behaviour - an increase of the experimental DDCSs near the high energy limit - seems plausible as will be seen in the presented L-ionization DDCSs of Ne. These show a steep monotonic decrease with increasing electron energy, and near the high energy limit the same increase occurs.

References:

1) Powell, C. J. P., Rev. Mod. Phys. 48 (1976) 33

2) Burhop, E. H. S., Proc. Cambr. Phil. Soc. 36 (1940) 43
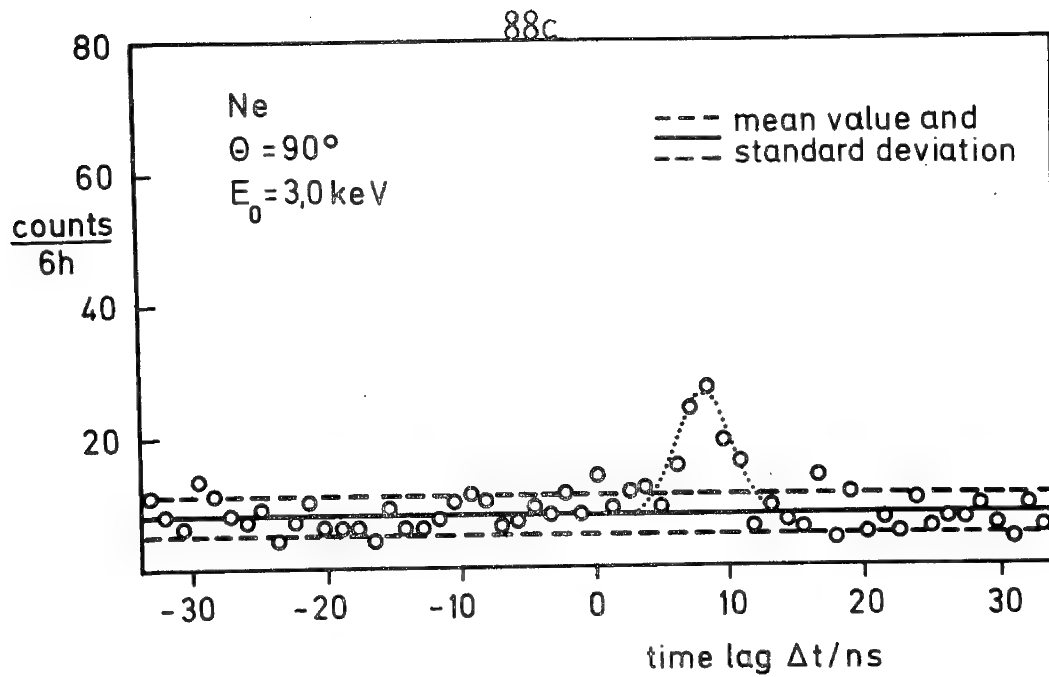
Fig. 1: Time spectrum (channel width 1.2 ns). The peak results from coincidences between an outgoing electron with 2090 eV at $\Theta = 90°$ with respect to the primary electron beam and an emitted K-LL Auger electron as indicator for a K-shell ionization process for Ne. E_O: electron impact energy.
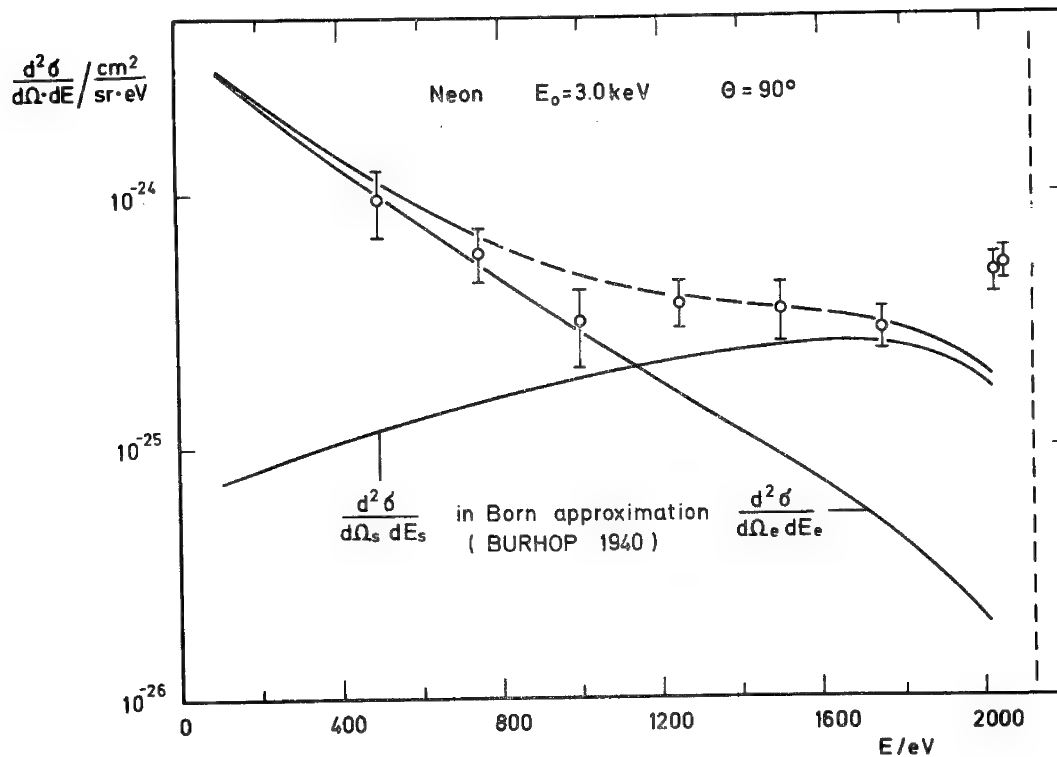
Fig. 2: K-ionization DDCS for Ne, differential in solid angle and energy E of outgoing electrons. E_O: electron impact energy; Θ: direction of outgoing electron with respect to the primary beam. ϕ : measurements with error bars; curves: calculated according to 2) and sum curve.

<u>Analysis of Thin Films on GaAs by He+-Induced</u>
<u>X-Rays and Backscattering</u>. R. L. KAUFFMAN*, L. C.
FELDMAN, R. P. H. CHANG and P. J. SILVERMAN, <u>Bell Labs</u>.
We have used a combination of ion beam techniques,
including ion induced X-rays, to characterize thin films
grown on GaAs. The systems studied include metal over-
layers (∿3000 Å) and oxide films grown by a number of
differenct techniques. A complete understanding of
these structures requires a quantitative measure of the
stoichiometry as a function of the depth of the film.
Such a measure has been difficult to achieve unambigu-
ously, since all techniques brought to bear on the
problem (i.e. Auger, neutron activation etc.) have
important limitations.

Initial studies with Rutherford scattering provide a
good deal of quantitative information. For example in
the case of the oxides, one can determine the oxide
thickness and the O:Ga+As ratio as a function of depth,
unambiguously. Unfortunately, the Ga:As ratio is not
revealed due to the inherent ambiguity between mass and
depth in the backscattering technique. Ion induced
X-rays provide the Ga:As ratio in the film, although
integrated over much of the film thickness. Since the
trajectory of the He+ ions and the X-ray production
cross section are well understood one can confidently
confine the interactions to the film thickness of
interest. By calibrating the energy dependence of the
X-ray production cross section and using the known
stopping power for He+, a depth profile can be deter-
mined in principal. In practice, the complete extrac-
tion of the profile is exceedingly difficult, although
the depth information can be useful for qualitative
thickness variations.

As an example Fig. 1 shows the variation with depth of
the Ga Kα and As Kβ yield in a Pt-GaAs film which has
been heated at 500°C for two hours. Rutherford back-
scattering clearly shows that a chemical reaction has
occurred between the Pt overlayer and the GaAs sub-
strate. The vertical scale of Fig. 1 is normalized to

---

*Postdoctoral research fellow.

the yield from a pure GaAs sample; the horizontal scale
is obtained by varying the angle θ, the angle between
the beam and the sample surface. Thus the horizontal
scale is simply sin θ or t/t_{crit} where $t_{crit} \simeq 8000$ Å
for 1 MeV He$^+$. For small sin θ, or grazing incidence,
the X-ray yield is almost entirely that of Ga; as nor-
mal incidence is approached the As yield increases with
a corresponding decrease in Ga. Further considerations
show that the reacted system is composed primarily of a
Pt-Ga layer of $\sim$1500 Å at the surface, a Pt-As layer
below and finally the GaAs substrate.

We shall discuss the use of these techniques and the
general use of ion beam techniques for thin film
analysis. We shall also show how those techniques can
provide important calibration points for use with the
Auger technique which is capable of superior depth
resolution.
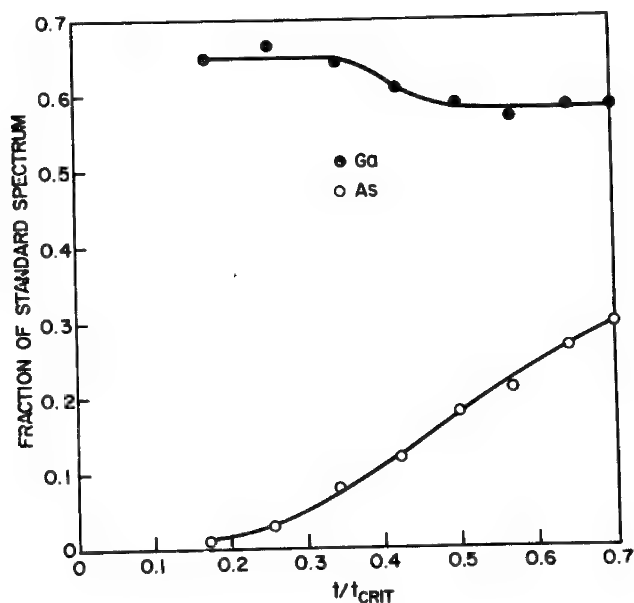
Fig. 1. Yield of Ga and As K X-rays as a function
of angle for the reacted Pt-GaAs system.

Detection Sensitivities in Proton and Electron Induced X-ray Spectroscopy

Wilhad Reuter and Allen Lurio

IBM Thomas J. Watson Research Center

P.O. Box 218, Yorktown Heights, N. Y., 10598

Both electron and proton induced x-rays can be used for analytical purposes. We have compared their relative sensitivities for detecting various constituents in a well characterized NBS low alloy steel standard. Both energy dispersive and wavelength dispersive spectroscopy were used in detection, and optimum beam energies were used in excitation. We find that for an equal accumulated charge the detection sensitivity by proton induced x-rays was a factor of two to three times greater than by electron induced x-rays for all elements. The increase of x-ray production by using proton energies above the level available to us (3 MeV) is rarely warranted in view of a corresponding increase of x-ray absorption losses in the target.

APPLICATIONS OF PROTON-EXCITED X-RAY ANALYSIS TO THE STUDY OF METALLIC CORROSION

B. D. Sartwell and P. B. Needham, Jr.

College Park Metallurgy Research Center, Bureau of Mines, U.S. Department of the Interior, College Park, Maryland 20740

During the past eight years, the Bureau of Mines has been engaged in a program to study various aspects of the corrosion of iron and iron-based alloys. The goal of this program is to develop iron-based alloys with increased resistance to aqueous and gaseous corrosion in order to conserve domestic mineral resources, to reduce the annual loss (estimated at 20 billion dollars) to the economy, and to reduce the dependency of the United States on foreign sources for domestically-unavailable alloying metals such as chromium and nickel.

Metallic corrosion can be defined as the interaction of a metal surface with its environment. Whereas the phenomena related to corrosion have been studied for over one hundred years, many of the mechanisms responsible for corrosion processes are, at present, not well understood. In many cases the initiation of a corrosion process involves the adsorption of one atomic layer of a foreign species on the metal surface, with subsequent chemical combination and then growth of a thin film. The kinetics of these initial processes can be influenced by ionic diffusion or by the electronic structure of the film. For alloys, differing chemical free energies of formation can result in the depletion of a particular element or elements at the film/metal interface. This can also result in the formation of a protective oxide film by the element with the lowest free energy of formation. The final phases of corrosion can involve the formation of thick corrosion products with corresponding changes in the substrate alloy composition that extend several thousands of angstroms. Therefore, a general study of the corrosion process must involve: (a) surface analyses that include only the first few atomic layers and are sensitive to small fractions of an atomic layer, (b) thin film analyses that include regions extending from the surface of the substrate to films up to 500 Å in thickness, and (c) substrate bulk analyses that extend to regions deeper than a few hundred angstroms from the surface.

The use of PEX for surface, thin film, and bulk analyses each requires special considerations of the appropriate equations that include X-ray production cross sections and X-ray yield parameters. These are briefly described along with a method of obtaining particular X-ray production cross sections and X-ray yields for elements for which direct experimental data is not available.

The PEX technique has been routinely used as an integral part of Bureau research related to a wide variety of materials research problems. These include: oxidation of Fe and Fe-Cr alloys, analyses of corrosion films formed in aqueous electrochemical studies, determining the optimum parameters for obtaining erosion-resistant TiB_2 coatings by molten salt electrodeposition, structural failures in powerplant turbines, development of ion implantation as an alloying technique, analyses of corrosion products from components used in geothermal brines, development of platinum-group metal alloys using electroplating from molten cyanide baths, studies of corrosion film formation in high-temperature, hydrometallurgical processes, and interaction of SO_2 with polycrystalline iron surfaces. From this group, specific examples that relate to each of the three stages of corrosion processes will be discussed in detail.

For surface analyses, the combination of PEX with Auger electron spectroscopy (AES) has provided a very powerful tool. The nature of each technique is such that the strengths or advantages of one technique covers the weaknesses or disadvantages of the other. Results to be presented demonstrate the use of PEX and PEX/AES in studies related to the adsorption of oxygen onto polycrystalline iron surfaces, the subsequent initial formation of 3-dimentional oxide films at 100°, 200°, and 300° C, and the segregation of bulk impurities onto the surface of polycrystalline iron following heat treatment.

For thin film analyses, results will be presented for PEX measurements of the oxidation kinetics of Fe and Fe-Cr alloys at temperatures ranging from 100° to 300° C providing information related to the electronic structure of, and ionic diffusion through, the oxide films. In addition, PEX has been combined with low-energy argon-ion sputtering (IS) to give quantitative thin film composition profiles. The use of PEX/IS to obtain concentration depth profiles of alloying elements in ion-implanted "surface alloys" and to study diffusion phenomena of alloys subjected to heat treatment will be described.

For bulk analyses, the use of PEX to study the corrosion products on and the redistribution of alloying elements in superalloy turbine components that had suffered a catastrophic failure due to corrosion fatigue will be described. In addition, results will be presented for the use of PEX in study of the corrosion of a series of alloys exposed to a hydrometallurgical process environment consisting of $40\%HCl-60\%H_2O$ in the vapor phase at temperatures up to 800° C.

Quantitative applications of proton-induced x-ray emission analysis in the fields of medicine and biology

J.T. Dabek, N.A. Dyson and A.E. Simpson

(Departments of Physics and Experimental Pathology, University of Birmingham, Birmingham, U.K.)

Introduction

We are employing the technique of proton-induced x-ray emission analysis, using the 3 MV 'Dynamitron' accelerator in the Birmingham Radiation Centre, to study certain minor elements, notably copper and zinc, in material of human origin, including blood and liver tissue.

Copper, zinc and iron are important trace or minor elements typically present in adult man in total quantities of 100 mg, 2.5 g and 4 g respectively (ICRP-23, 1975). Following absorption they are transported to the liver by the portal circulation. In the portal blood most of the absorbed copper is loosely bound to albumin but it is complexed in the liver cell and secreted as ceruloplasmin into the systemic circulation. Zinc is mainly bound to red cells and iron is complexed with transferrin, its transport protein, as it leaves the intestinal cell. The liver stores all three elements, and typically, in the healthy adult, has 12 mg Cu, 85 mg Zn and 750 mg Fe (ICRP-23, 1975).

In Wilson's disease an increased avidity of body tissues for copper, though associated with a decreased plasma copper, often due to a low ceruloplasmin level, leads to a high liver copper, sometimes reaching 1 g (Sherlock, 1968). However, liver copper may be raised in other forms of cirrhosis such as primary biliary cirrhosis (Hunt et al. 1963) and occasionally in alcoholic cirrhosis (Sheldon and Ramage, 1931). Plasma zinc levels may be depressed in alcoholic cirrhosis, possibly due to a raised urinary zinc excretion (Sullivan, 1964), though plasma copper and ceruloplasmin may be raised, or normal. In addition, in all these types of cirrhosis there may be an iron-deficiency anaemia with a low liver iron.

Therefore, because the method reported in this work simultaneously measures copper, zinc and iron in tissue samples it should prove useful in investigating cirrhosis. The method and some clinical results in normals and cirrhotic patients are reported.

Method and target preparation

Protons of 2.5 MeV energy are used to bombard the samples of liver and blood (prepared as described below), and the emission spectra of characteristic radiation are analysed. The samples are mounted in the vacuum system, in a target chamber which, in our earlier measurements, was of a simple "T-piece" design, but which has more recently been replaced with a chamber in which 8 targets can be mounted, and stepped remotely without disturbing the vacuum system. The x-rays leave the target chamber through a 0.001" Melinex window, and a Si(Li) detector is used for obtaining the spectra. The detector is on-line to a HPDS1-5406B nuclear data-processing system, and the counts in selected peaks (together with standard deviations) are obtained by appropriate programming. Beam currents are normally restricted to the region of 20 nA (at 2.5 MeV) to

avoid carbonising the specimen due to localised heating of the specimen in the region of the beam spot, which is approximately 2 mm in diameter. Each sample requires about 45 minutes of running time to accumulate sufficient data.

The limits of detection have been investigated (for lead and for zinc) by using blood samples to which known small amounts of these elements have been added. By statistical analysis of the results we have established that the limit of sensitivity (for thick targets) improves rapidly as the proton energy is increased reaching a limit in the region of 2-3 MeV, at which the detection limit (referred to whole blood) is 0.3 ppm and 0.1 ppm respectively for lead and zinc. (The samples were prepared by evaporating a few drops of the 'doped' blood to dryness as described below, and the sensitivity limits when referred to this solidified material are 2.0 and 0.7 ppm respectively.) At higher proton energies the increase in background from Bremsstrahlung is expected to prevent further substantial improvement in the sensitivity for the elements studied.

The limits quoted above may be taken as representative of heavy and medium-Z elements respectively, the latter including the copper, zinc, and iron investigated in the present study. These limits may be compared with the limits of 50-100 ppm obtained by electron microanalysis.

In earlier measurements (including all the "normal" specimens), the specimens of liver tissue were sectioned when still wet (but frozen) and mounted on to Al foil, being retained in place by a covering foil with a single central aperture to permit unimpeded passage for both bombarding protons and fluorescent x-rays. The mounted specimens were then dried in a vacuum desiccator before being bombarded in the high vacuum of the beam tube and target chamber. The corresponding standards were made using specimens of whole blood to which known quantities of the requisite trace elements had been added. These doped blood specimens were then evaporated on to Al foil over a warm hotplate, before fitting a retaining Al cover as with the liver specimens.

Later measurements (including all the cirrhotic liver specimens) used a different technique; the tissue specimens were first freeze dried, and then sectioned (when completely dry), before mounting on to an Al "stub" with a small trace of adhesive. The corresponding dried blood standards were made (after Boro and Cipolla, 1975) by freeze drying doped blood specimens, and pressing the resultant powder into a self-supporting pellet 8 mm in diameter by 0.5 mm thick. In order to overcome target charging and discharging effects, these targets were then coated with a sputtered layer of Au ($\sim$500 Å thick).

The data on blood quoted in the table was obtained from targets prepared by the above methods (without the addition of any extraneous material other than anticoagulant), and the concentrations were obtained by reference to the above standards.

Calibration of the concentrations of elements in liver was carried out by comparison with these same standards. Correction has to be applied to the data for the different proportions of water present in liver and blood (71% and 85% respectively), but the corrections for self-absorption, and also the stopping-power correction (dependent upon atomic number) may readily be shown to be negligibly small if our method of calibration is employed. Furthermore, because our target chamber allows for suppression

of secondary electrons by means of an electrode at a negative potential
surrounding the target, any errors due to variation of the coefficient of
secondary electron emission are avoided. It should also be noted that the
fraction of protons backscattered is very small compared with the fraction
of electrons backscattered in electron bombardment techniques. Therefore
any corrections which would be necessitated due to this effect can be
neglected in the present work.

Results and Discussion

We have measured concentrations of the trace metals Fe, Cu and Zn in
both normal and diseased human livers. The "normal" liver specimens were
taken post mortem from patients with no history of liver disease, and with
visually normal livers at autopsy. The results from these specimens are
shown in the table together with those from three cirrhotic livers: one
case (F.W.) of primary biliary cirrhosis, and two cases (J.R. and W.H.) of
alcoholic cirrhosis. Typical x-ray emission spectra are shown in Figs.
1-3.
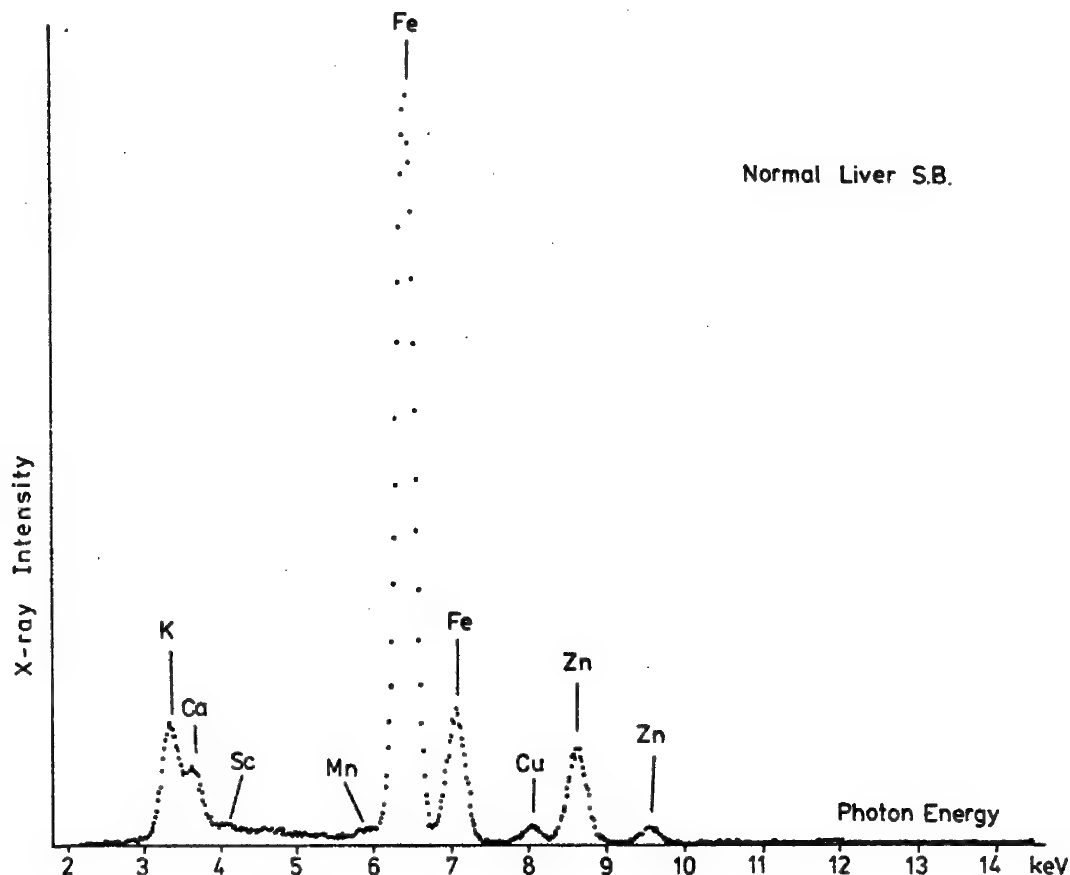
Fig. 1. Proton-induced x-ray emission spectrum of normal liver tissue.

The measurements on the normal specimens show a wide range in the
concentrations of these trace metals, though this is in agreement with the
observations of other authors (Hunt et al., 1963; Robison et al., 1973).
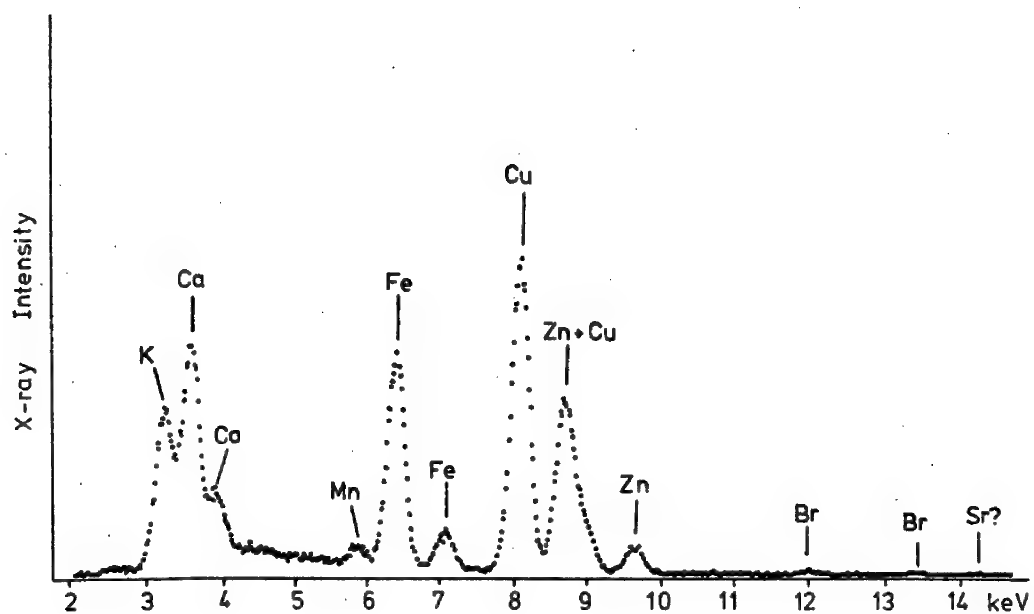
Fig. 2. X-ray spectrum of cirrhotic liver (Primary biliary cirrhosis).
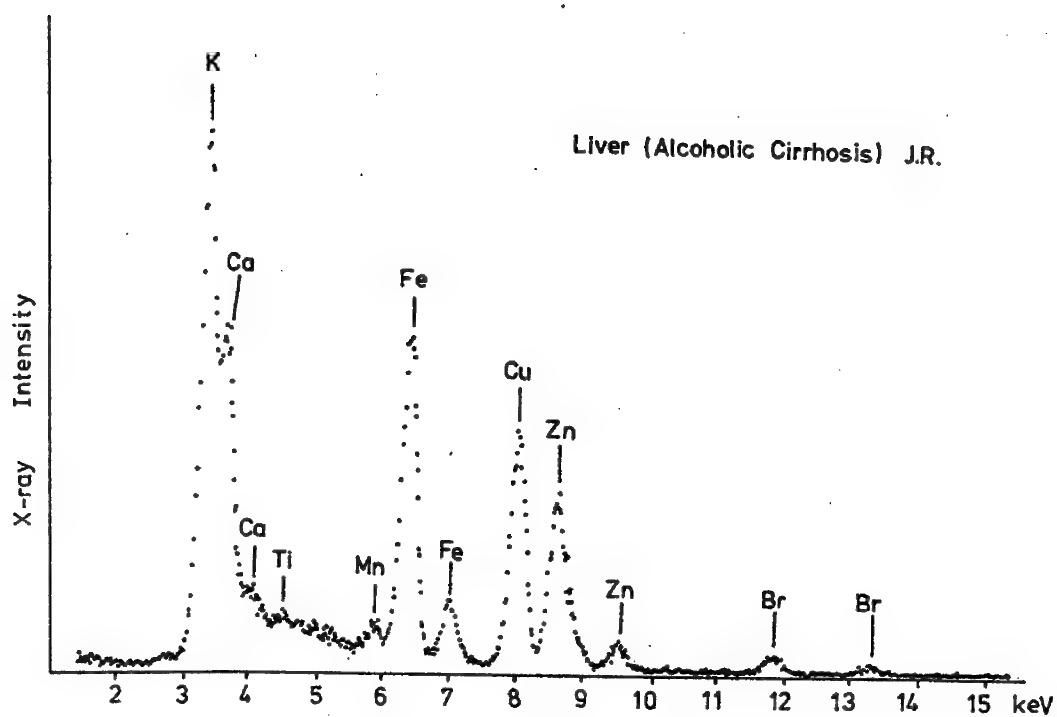
Fig. 3. X-ray spectrum of cirrhotic liver (Alcoholic cirrhosis).

Elemental concentrations in blood and liver for normals and cirrhotic patients

LIVER

		Diagnosis	Cu	Zn	Fe	Comments
1	AW	Normal	2.5	36.0	32.2	—
2	PJ	"	9.5	83.1	333	—
3	SB	"	9.5	92.0	429	—
4	—	"	2.5	20.1	524	—
5	IH	"	19.9	42.3	232	—
Mean		"	8.1	54.5	380	The mean for iron excludes AW
6	WH	Alcoholic Cirrhosis	19	26	491	Micronodular
7	"	"	11	16	266	"
8	"	"	18	23	345	"
9	"	"	19	23	373	
Mean	"	"	16.8	22	369	"
10	JR	Alcoholic Cirrhosis	21	23	37	{Macronodular; anaemic
11	"	"	57	32	49	"
12	"	"	53	29	48	"
13	"	"	44	42	65	"
14	"	"	108	39	53	"
15	"	"	78	41	45	"
Mean	"	"	60	34	50	"
16	FW	Primary Biliary Cirrhosis	484	217	—	{Macronodular; mean of 5 determinations

BLOOD

	Diagnosis	Cu	Zn	Fe	Comments
1	Normal	0.8	2.7	227	—
2	"	2.1	7.9	391	—
Mean	"	1.45	5.3	309	—
3	Primary Biliary Cirrhosis	1.9	1.0	347	—
4	"	1.5	1.6	387	—
Mean	"	1.7	1.3	367	Zinc is low
5	Wilson's Disease	1.7	6.5	599	—
6	"	0.6	1.6	453	—
Mean	"	1.15	4.05	526	—

The liver of the patient with primary biliary cirrhosis has strikingly high copper levels and it is interesting that the zinc level is also increased. The mean copper in the liver from the macronodular alcoholic cirrhotic patient is significantly higher than normal confirming the findings of Sheldon and pointing to a possible rôle for copper in the cirrhotic process in these patients that needs further assessment. Even in the patient with micronodular cirrhosis the mean copper level is raised. The low liver zinc in these patients is also noteworthy and these results are in agreement with those of Sullivan.

We have observed a low level of liver iron in JR, this patient being a case of alcoholic cirrhosis, in which the iron-deficient anaemia often associated with advanced alcoholism was in fact found. The very low liver iron seen in AW shows depleted iron stores though she was not clinically anaemic. This result appears to us to be anomalous.

As well as measurements on liver specimens, we have also carried out analyses of blood samples, and the results of these measurements are included in the table. Although the specimens from the cirrhotic patients all show slightly low zinc, all three elements fall generally within the normal range, although the significance of the somewhat low zinc levels requires further elucidation. In the case of the patient with Wilson's disease (another condition associated with abnormally high liver copper), the blood copper levels are also low. This is in agreement with previous reports.

Conclusions

Our measurements of raised copper levels in primary biliary cirrhosis confirm the findings of Hunt et al. Our findings in cases of alcoholic cirrhosis extend those of Sheldon. Our measurements on blood samples highlight the blood zinc deficiency in primary biliary cirrhosis; and we also note the marked liver iron deficiency in macronodular alcoholic cirrhosis in association with clinical anaemia. The technique of proton--induced x-ray emission analysis is clearly of value in investigations of this type, especially when only small quantities of material are available.

References

Boro R.T., and Cipolla S.J., 1975, Nucl. Inst. and Meth., 131, 343.
Hunt A.H., Parr R.M., Taylor D.M., and Trott N.G., 1963, Brit. Med. J.,
    II, 1498.
ICRP, 1975, ICRP-23. "Report of the Task Group on Reference Man"
    (Pergamon).
Robison W.L., Auspaugh, L.R., Martin W.H., and Lowe O.A., 1973, Lawrence
    Livermore Laboratory Report, UCRL-51013.
Sheldon J.H., and Ramage H., 1931, Biochem. J., 25, 1608.
Sherlock S., 1968, "Diseases of the Liver and Biliary System" (Blackwell).
Sullivan J.F., 1964, J. Lab. Clin. Med., 64 (6), 1008.

TRACE ELEMENT ANALYSIS OF BIOLOGICAL MATERIAL USING PIXE*

Ed. K. Biegert & Vlado Valković
Rice University, Houston, Texas

A number of elements have been recognized as essential trace elements for living matter, including F, Si, V, Cr, Mn, Fe, Co, Ni, Cu, Zn, Se, Mo, Sn, and I (for warm-blooded animals). Proton-induced X-ray emission spectroscopy allows simultaneous determination of all essential trace elements in targets prepared from biological material. We have studied different biological materials including blood, tissue, hair, cells, plants, marine and aquatic organisms, microorganisms, etc. We will report on

    (a)   Trace element distributions in human and animal hair and factors inducing distributions along the hair

    (b)   Trace element distributions in tree rings

    (c)   Trace elements in microorganisms and the possibility of influencing concentration factors by magnetic fields

    (d)   Accumulation of heavy metals and toxicity in marine organisms.

TRACE ELEMENTS IN LIVING MATTER

One of the most important characteristics of living cells is their ability to take up elements from a solution against the concentration gradient. This is most obvious for marine microorganisms which obtain their nutrients directly from the sea water. The concentration factor is then defined as the ratio of element concentration in the organism and the element concentration in sea water. The organisms concentrate all elements present in their environment. However, all of these elements are not essential for life. Criteria which an element must satisfy to be essential for life are well established.[1] The relation of the uptake of essential elements to yield or growth may be considered as a definition of essentiality. There is a rather narrow range of adequacy of element concentration in the organisms. Smaller concentrations result in different abnormalities induced by deficiencies which are accompanied by pertinent specific biochemical changes. Higher concentrations result in toxicity. In plants it is possible to have, under severe deficiency conditions, a decrease in concentration of an element which results in a small increase in growth. This phenomenon is knows as the Steenbjerg effect.

The bulk of living matter consists of eleven elements which have very low atomic weights (H, C, N, O, Na, Mg, P, S, Cl, K, and Ca). These elements have been known to be essential for life for a long time because their presence is easy to detect. The problem of essential trace elements is much more difficult. So far, the elements F, Si, V, Cr, Mn, Fe, Co, Ni, Cu, Zn, Se, Mo, Sn, and I have been recognized as the essential trace elements for warm-blooded animals. The great majority of the essential trace elements serve as key components of the enzyme system or of proteins with vital functions. If the metal atom is removed, the protein usually loses its capacity to function as an enzyme. Of fourteen elements recognized until now as essential trace elements for warm-blooded animals, only fluorine and silicon are below 20 in atomic number. It

is interesting to point out that none of the 30 elements beyond iodine have ever been shown to be of any physiological significance. The distribution of essential trace elements within the periodic table of elements might have some significance with respect to the development of prebiotic time.

TRACE ELEMENTS IN HAIR

Human hair analysis appears to offer a unique approach to the investigation of human trace element nutrition. Human head hair is a recording filament which can reflect metabolic changes of many elements over a long period of time. The idea of hair analysis is very inviting because hair is easily sampled, shipped, and analyzed.

Examining blood and urine provides immense insight into human diseases. One would like to add to these examinations a routine analysis of hair. A definition of "normal" hair for different population groups is different for various geographical areas because of the strong environmental influence. X-ray emission spectroscopy was found to be a very convenient method in the determination of these normal values. These are indications that some diseases produce characteristic trace element concentrations ratios which may be used as a diagnostic tool.

Because of its growth, hair reflects previous elemental concentrations in blood and body, as well as previous effects of the environment. This suggests the importance of measurements of trace element concentrations along the hair. It has been shown[2] that the elements whose concentrations increase monotonically along the hair can be identified as pollutants in the area. For widespread pollutants (such as lead) even the medium value of a group of subjects can be used as a measure of the exposure.

The effects of ionizing radiation on hair have been studied to some extent. In man, scalp hair is the most sensitive hair to irradiation. First, only temporary depilation occurs; with exposure to a higher dose, permanent depilation results. Pigment anomalies have been observed in hair growth after temporary depilation: the hair is usually darker. In an effort to evaluate radiation effects, trace element analysis of mouse hair has been performed.[3] Hair from mice irradiated with 600 rad (γ-rays) and hair from a control group have been analyzed. Figure 1 indicates some of the changes observed.
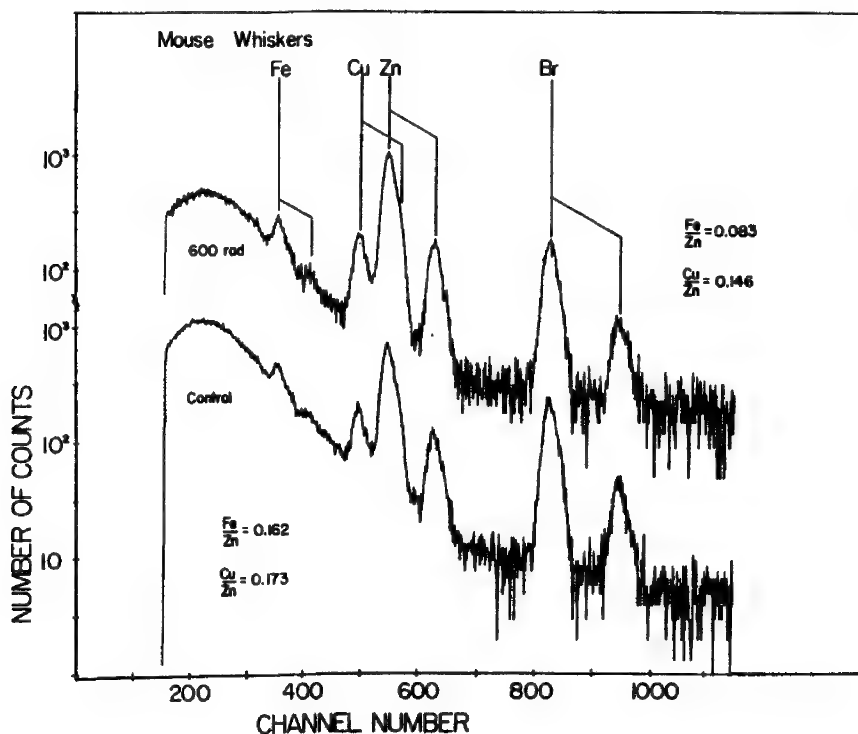
Fig.1: X-ray spectra from mouse whiskers.
Top: mouse irradiated with 600 rad (Cu/Zn=0.146; Fe/Zn=0.083).

Bottom: control (Cu/Zn=0.173; Fe/Zn=0.162).

TRACE ELEMENTS IN TREE RINGS

Data on the uptake of the elements from soils by higher plants are very scarce although it is known that certain species have the ability to accumulate uniquely high concentrations of a particular element.

Tree-rings have been studied for some time. It seems that the trees store a record of atmospheric temperature in their rings. This is of interest to the historical meteorology since in some areas the tree-ring records extend back for up to eight millenia. The science of dendroclimatology is based on the observation that the narrow rings represent a cold (or dry) year. Since the water conduction remains limited to the outmost annual ring, tree rings offer also the possibility to study the historical trends in the movements of the elements. Elemental concentrations in tree rings should reflect the availability of the elements in question. One possible source of the additional element loading is the atmospheric discharge.

In the recent measurements[4] samples from an approximately 500 year old tree were analyzed for trace elements using PIXE. Peaks associated with K, Ca, Ti, Mn, Fe, Cu, Zn, As, Pb, Br, Rb, and Sr could be identified in all spectra. Figure 2 shows the variations in the Rb/Br and K/Br concentration ratios. The top of the figure shows the variations in the K/Rb concentration ratios across the tree rings from the center of the tree outwards. Within the error bars, the ratio K/Rb is 1000 across the tree. This fact should be explained by keeping in mind that Rb is a member of the series NH_4-K-Rb-Cs, and that the members of this series are more similar in their chemical and physical properties than are the members of any other group, with the exception of the halogens. The radius of the Rb ion is 1.48 A (only about 10% larger than the potassium ion radius); as a result, the Rb ion can be accommodated into the same structures as the K ion.
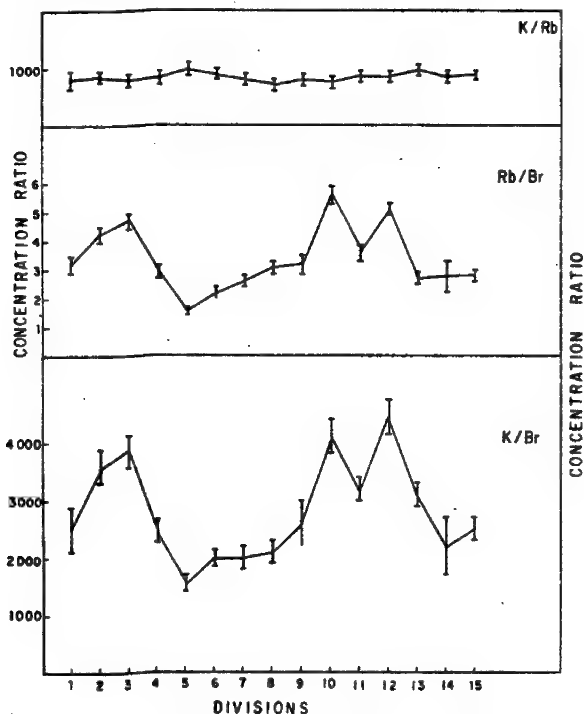
Fig.2: Variations in the K/Br and Rb/Br concentration ratios. K/Rb concentration ratios across the tree rings show no variations.

The Pb/Zn concentration ratio shows two peaks corresponding to the divisions 5 and 8 (one division covers approximately 30 years). A recent increase in the Pb/Zn ratio (divisions 14 and 15) is probably due to the atmosphere particulate loading resulting from the industrial activities and automobile traffic. If the two peaks in the Pb/Zn concentration ratio distribution are due to the Pb increase, data would suggest past particulate loading of the atmosphere due to the natural events (volcano activities and similar). The alternate approach to Pb/Zn distribution data is to assume that the observed peak structure is due to Zn depletion. In this case Zn depletion is strongly correlated with the peak in K/Ca distribution.

TRACE ELEMENTS IN MICROORGANISMS

Concentration factors for some elements in microorganisms are known.[5] Microorganisms require small quantities of Mn, Fe, Zn, Co, Cu, and Mo for their growth. Some diseases caused by microorganisms result in modified trace element levels. Microorganisms must compete with host metal-binding agents for these essential elements. It is well established that in the distant past massive faunal extinctions have occurred. There is mounting evidence that a correlation exists between major faunal extinctions and geomagnetic polarity reversals. The validity of this correlation in recent geological time seems to have been well established by studies of fossil species of single-celled marine microorganisms.[6]

Several mechanisms linking changes in the geomagnetic field with effects on living organisms have been propsed. Most of them are based on the assumption that during polarity reversals the dipole component of the geomagnetic field probably weakens or disappears for periods of a few thousands of years, allowing a much greater flux of both solar protons and galactic cosmic rays to bombard the surface of the earth. The effect of increased exposure is, however, now believed to be probably insignificant. Other mechanisms include climate change (which also may result from intense solar proton bombardment during polarity reversals), and the effects of a large reduction in the content of ozone in the atmosphere, which would increase exposure to ultraviolet radiation. Direct magnetic field effects on growth were proposed by Hays[6] and Crain.[7] A direct cause-and-effect link between magnetic field reversals and species extinctions could explain how marine organisms easily could have been affected. There is also the possibility that extinctions discussed here may have resulted from the simultaneous effect of several factors.

In order to try to explain the geomagnetic effects on living organisms, the concentration factor dependence on magnetic field intensity has been recently proposed.[8] Magnetic field dependence of concentration factors can bring living organisms into the range of deficiency or toxicity without changing trace element availability in the environment. Experiments aiming to establish functional relationships between concentration factors and the magnetic field intensity for some elements and some living organisms were reported.[9] The measurements involved the growth of single cell organisms in defined media and controlled external magnetic field intensity. Trace element analysis of harvest is performed by proton-induced X-ray emission spectroscopy.

The organism used is a respiratory deficient mutant of M. bacilliformis which in addition has lost the ability to grow as mycelium. Instead, it exists as spherical cells which reproduce only by budding at the expense of alcoholic fermentation.[10] A defined growth medium was used. It contains two vitamins, nine amino acids, glucose as an energy source, K salts, and the salts of five trace elements: Mg, Zn, Fe, Mn, and Cu.

Growth took place at room temperature in round-bottom flasks containing 14 ml of medium. Each flask was inoculated so as to have 10^3 cells/ml. Six flasks were placed in solenoids whose magnetic fields were extremely uniform over the active region of growth and six flasks were used as a control group. Growth (increase in cell number) was monitored daily by measurements of the turbidity of the cell suspensions. After ten days, when the cell number was maximum, the cells were harvested by filtration.

Figure 3 shows a typical X-ray spectrum from a mold sample (Mucor). The
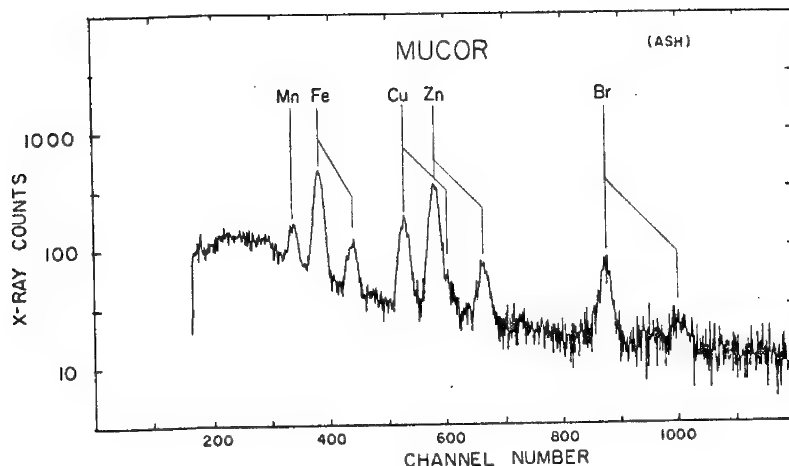
Fig.3: X-ray spectrum obtained from the
bombardment of a mold sample on a
scotch tape backing with a 3 MeV
proton beam.

microorganisms were harvested
by filtration through filter
paper which was then exposed
to the beam of 3 MeV protons
at 150 nA for 500 seconds. The
observed spectra indicate that
the following elemental concen-
tration ratios can be measured
for both the mold and the growth
medium; Mn/Zn, Fe/Zn, Ni/Zn,
and Cu/Zn. The results obtained
so far are inconclusive about
the existence of possible mag-
netic field dependence of the
concentration factor.

TRACE ELEMENTS IN AQUATIC ORGANISMS

The introduction of abnormal quantities of heavy metals into the environment
as industrial waste can have adverse effects on organisms exposed to such pollu-
tion. Organisms record a cumulative exposure to toxins as they are exposed to
temporal conditions in the environment. The difficulty in establishing causal
relationships between toxins released intermittantly or in "slug" doses and fish-
kills may be resolved partially by tissue analyses revealing some critical, lethal
dose. To date, no definitive work has documented such a lethal dose.

Biological data were generated on toxicity to three organisms; Rainbow
trout (Salmo gairdneri), Fathead minnows (Pimephales promelas), and Brown shrimp
(Penaeus).[11] These organisms were exposed to various aquaeous concentrations of
Pb, Hg, Cu, Zn, and a bimetallic Zn:Cu misture in a ratio of 6:1. Each of these
five metal groups were used in aquaeous concentrations of 10, 1, 0.1, and 0.01 ppm.
Each metal concentration combination was examined at two temperature ranges; one
range near the species optimum and the other producing temperature stress.

In general it was found that the lower the concentration of heavy metals
in the water, the longer the survival time of the organism. Results from the
shrimp showed no significant correlation between the exposure concentration and
time of death for any metal. Shrimp were tolerant to almost all metals except
the highest concentrations of Hg, Cu, and Zn, and then survival time was an
order of magnitude greater.

The survival time data also indicate relative toxicity of the metals and
relative susceptibility of the three test species to the toxins. Hg and Cu are
most toxic to all species at the higher two concentrations. The Cu:Zn mixture
is next, followed by Zn and Pb. Trout and fatheads are significantly more sen-
sitive to all toxins than shrimp, and shifting temperatures from the species
optimum reduces the mean survival time. The change in mortality with temperature
is not reflected in the amount of metal accumulated except in isolated cases.

No consistent threshold exists above which any of the metals is definitely
toxic. In some cases the amount of metal accumulated in a living organism

exceeded that found in a dead organism. This essentially contradicts the hypothesis that a given amount of metal found in the tissues of an organism could be directly correlated with toxicity. Of course, there is some maximum amount tolerable to an organism in a long term test, but, from our experience, such a threshold in a short term study is too high and too variable to be of much practical use. There is also a region of overlap in which the amount of accumulated metal does not determine either survival or death of the organism.
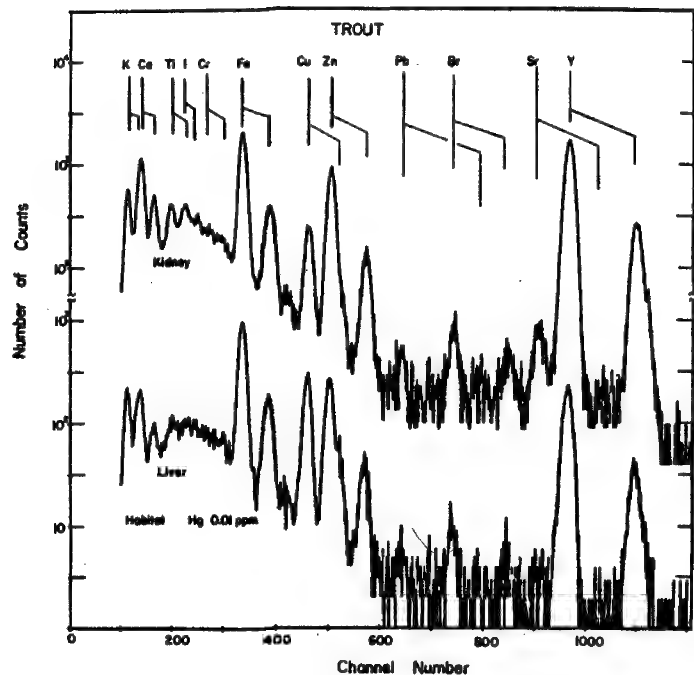
Fig.4: X-ray spectra of trout organs from an aquaeous concentration of Hg 0.01 ppm. No Hg lines are present.

Apparently there is an effective lethal threshold in the range of the LC-50 (concentration in the water lethal to 50% of the organisms) which, except for shrimp, occurred between 1.0 and 0.1 ppm. However, this reaction threshold is not reflected in toxin accumulations. For example, mortality in trout fell from 90% to 10% between 1.0 and 0.1 ppm lead: tissue accumulation however, actually increased from 3.3 to 9.9 ppm lead.

Although the amount of metal accumulated in tissue cannot be correlated with a lethal or non-lethal response, it can be correlated with the amount of metal to which the organism was exposed for at least some of the metals. This does have some consequence for organisms consumed and passed along a food chain, especially those for which man is frequently the consumer.

REFERENCES

[1]Chadwick, J. Phil.Mag. 24 (1912) 594.
[2]Valkovič, V. D. Rendic, G. C. Phillips, Env.Sci.& Tech. 9 (1975) 1150.
[3]Biegert, Ed.K., V. Valkovič, V. Otte, E. Andrade, to be published.
[4]Andrade, E., Ed. K. Biegert, D. Rendic, V. Valkovič, to be published.
[5]Bowen, H. J. M., Trace Elements in Biochemistry, Academic Press (1966).
[6]Hays, J. D. Bull.Geol.Soc.Am. 82 (1971) 2433.
[7]Crain, I. K. Bull.Geol.Soc.Am. 82 (1971) 2603.
[8]Valkovič, V. Origins of Life (1977), to be published.
[9]Biegert, Ed. K., M. Craig, V. Valkovič, R. Storck, Proc.4th Conf. on Appl. of Small Accelerators, Denton, Texas, 1976.
[10]Storck, R., R. C. Morrill, Biochem.Genetics 5 (1971) 467.
[11]Biegert, Ed. K., C. A. Wingate, J. K. Jones, M. E. Alexander, R. S. Thurston, T. Zabel, V. Valkovič, D. C. Marks, to be published.

Quantitative Analysis of Trace Elements in Blood and Urine Samples of Diabetic Patients

P. Sioshansi, A. S. Lodhi, Md. Rashiduzzaman Khan

and H. Payrovan

Van de Graaff Laboratory

S. Ghafourian and M. Tavakoly

Nuclear Medicine Section

Tehran Nuclear Research Center, Atomic Energy Organization of Iran,

P. O. Box 3327, Tehran, Iran.

Some 50 samples of both blood and urine taken from diabetic patients have been analyzed for trace elemental contents by using Proton Induced X-ray Emission (PIXE) analysis. Thin uniform targets doped with 100 ppm of yttrium were prepared on a 7.5 micron thick kapton backing. Each of these targets was bombarded with 1.2 and 2.54 MeV proton beams from Van de Graaff Accelerator of Tehran Nuclear Research Center. The resulting X-ray spectra were analyzed for the quantitative determination of trace elements present in the samples.

The results of this analysis are being tabulated and will be presented. The trace element contents in blood and urine from diabetic and normal person are compared. Attempt is made to determine whether abnormal levels of trace elements is an important factor in diabetes.

RELIABILITY IN DATA-ANALYSIS PROCEDURES FOR X-RAY SPECTRA

Peter Statham

Dept. Electrical Engineering and Computer Sciences,
University of California, Berkeley, Ca 94720, U.S.A.
ooo000ooo

Even with the vast improvements in solid-state x-ray energy spectrometers over the past decade(1) we are still left in a situation where the resolution, peak-to-background ratio and counting statistics are considerably worse than for a crystal spectrometer for energies below 10 keV. Therefore, in many situations we have to blindly trust the results of computer analysis of the recorded spectrum because some peaks of interest are simply not visible. In recent years several investigators have reported on accurate systems for microprobe analysis and full quantitative software can be purchased with most energy-dispersive systems so it might appear that data analysis is a closed book as regards further improvements. However, it is not unusual for discepancies in results to exceed quoted error estimates and peaks may be either missed altogether or 'detected' when they are not present in the spectrum. Such defficiencies amount to unreliability because the results cannot be trusted to fall within the prescribed limits of experimental error. This paper considers what factors can lead to unexpected errors in various stages of spectrum treatment.

ESCAPE PEAK SUBTRACTION

Escape peaks can be removed by a channel-by-channel subtraction routine starting at the high-energy end of the spectrum:

$$N(I-IS) = N(I-IS) - k.N(I) \tag{1}$$

where IS corresponds to 1.74 keV and channel I contains $N(I)$ counts. The factor k has been determined by Reed and Ware(2) but requires modification if the incident x-rays make an angle θ with the normal to the detector surface, which is greater than 0°(3). Thus, when I corresponds to E keV,

$$k = 0.02/(1+(mE+b)E^2) \tag{2}$$

where
$$m= 0.01517\cos\theta - 0.000803$$
$$b= 0.0455\cos\theta - 0.01238$$

If the geometry effect is ignored, residual peaks corresponding to 0.2% concentration could be left after escape peak subtraction(3).

PILE-UP EFFECTS

The pile-up inspector circuit should always be adjusted by the user for optimum performance but even then is generally rather ineffective for low-energy x-ray pulses(4) . As a consequence, counting losses from a peak, the pile-up continuum and sum-peak areas can be considerably greater than would correspond to the quoted resolving time of the rejector circuit. Although first order corrections are feasible(4) it is still advisable to keep count rates as low as is convenient and to be wary of artefacts when peaks are present in the energy range below 2keV.

MODELLING PEAKS WITH MATHEMATICAL FUNCTIONS

Although a single peak is nominally Gaussian in shape it can be distorted. Improvements in electronic circuit design have gone far to reduce the effects of baseline fluctuations but peaks are still subject to 'low-energy tailing' caused by incomplete charge collection in the detector. Aperturing the detector down to its central active region does help to reduce the effect but it is still common to observe a tail of variable length and up to 5% of the peak height below peaks in the region 1.84 to about 5 keV (X-rays in this energy region are absorbed strongly in silicon so the energy-to-charge conversion takes place close to the surface where charge is more easily lost through trapping and recombination of electron-hole pairs). It is often assumed that the centroid, x_o , and f.w.h.m of a peak at energy E can be predicted with the simple linear formulae

$$x_o = (\text{zero const.}) + (\text{gain const.})\text{x } E$$

$$\text{fwhm}_E^2 = \text{fwhm}_{noise}^2 + (\text{constant})\text{x } E \qquad (3)$$

However, the combined effects of incomplete charge collection in the detector and non-linearities in pulse-processor and ADC result in overall non-linearities which could lead to departures of up to 5 eV from these simple equations.

The accuracy of the peak model is vital for the success of peak unfolding routines. Adding more terms to the mathematical model can account for peak tailing distortion(6) and the spectrometer can be calibrated for non-linearities (5,7) but perhaps the simplest solution is to avoid mathematical modelling altogether and just store the peak profile channel-by-channel on disk or magnetic tape for later use. When a series of peaks(e.g. L line series) or the corresponding stored standard profile is used to represent a single element, the relative peak heights should really be corrected for differential absorption of x-rays in the specimen. Omitting this correction may result in spurious trace concentrations appearing in analyses whenever an absorption edge of another major element falls between two lines of the series.

BACKGROUND SUBTRACTION

Peak detection is the most basic application of background subtraction and one of the best ways to accomplish this is to convolve the spectrum with a 'top-hat' type of function (fig.1). This leaves positive lobes whenever peaks occur(✔) although some small peaks are lost in the negative lobes of their neighbours (✗) . This method of peak detection is used in the iterative peak stripping approach to background subtraction(8) but greater accuracy can be obtained using the method suggested by Schamber(9) and used in the 'ML' program. In ML , stored experimental spectra are used to provide standard peak profiles. Both specimen and standard spectra are filtered with a 'top-hat' function as in fig.1 and the distorted standard peak profiles are fitted to the distorted specimen spectra by the least squares method, thus eliminating the influence of the slowly-varying background. This technique is the closest yet to a 'panacea' for all problems since selection of peak-free points and explicit knowledge of the background shape are not required. Spectra from non-flat specimens (e.g. small particles) can therefore be analysed for peak areas and so also can gamma-ray and XRF spectra.

In the low-energy region (less than 3keV) curvature of the background is severe so peak areas may be underestimated. Absorption edge steps also introduce errors, although use of experimental standard spectra tends to cancel out such effects. Finally, the prefiltering of spectra tends to sharpen the central peak and makes the peak deconvolution process slightly more sensitive to shift and resolution changes(see below). These disadvantages can be minimised by suitable choice of weighting function; as a result of a number of numerical calculations I would suggest that M=3 , N=4 , for a 20eV/ch spectrum where peaks have fwhm's around 150 eV , is an optimum choice when the simple 'top-hat' is used as the filter.

In the special case where polished flat samples are being analysed, the background shape can be predicted and fitted to peak-free positions in the spectrum. 'Explicit' techniques of this type were discussed in last year's proceedings(10) where the results of preliminary theoretical calculations were also presented. Further work has suggested a slightly different formula for the background where Kramers' "constant" varies as $(c+E^a)$ instead of E^a as originally proposed. However, since I have not had the opportunity to make more experimental measurements, I hesitate to put additional complexity in the formula and just present the following for the background at energy E keV:

$$B(E)_{sp} \; \alpha \; \frac{(E_o - E)}{E^{1+a}} \cdot (b_1 + b_2 E) \cdot \left[Rf \cdot f(\chi)_{char} \right] \cdot (\text{detector efficiency}) \quad (4)$$

where $Rf = (1 + C.(3\times10^{-6} + C.4.5\times10^{-13}))/(1 + C.(3.34\times10^{-6} + C.5.59\times10^{-13}))$

and $C = \chi \times (E_o^{1.65} - E^{1.65})$

Values of the constant 'a' can be interpolated in the following table to give a reasonable approximation to the predicted intensity over the energy range 1 to E_o keV:

Atomic number Z	Incident electron energy, E_θ, keV			
	10	15	20	25
6	0.350	0.370	0.387	0.411
13	0.245	0.251	0.256	0.262
22	0.193	0.173	0.181	0.184
29	0.164	0.148	0.138	0.143
56	0.1191	0.1047	0.0965	0.0991
79	0.0944	0.0860	0.0796	0.0728

The few results of anisotropy calculations have been fitted to give

$$b_1 = 0.94 + 0.00216 \, Z - 0.0000172 \, Z^2$$
$$b_2 = -0.0082 + 0.000237 \, Z - 0.00000197 \, Z^2$$

for normal incidence, 40° take-off-angle geometry and

$$b_1 = 0.89 + 0.00361 \, Z - 0.0000295 \, Z^2$$
$$b_2 = -0.023 + 0.000795 \, Z - 0.00000674 \, Z^2$$

for 45° incidence and 45° take-off-angle.

In order to eliminate the detector efficiency term and minimise errors in the theoretical prediction, an experimentally recorded background curve, $B(E)_{st}$ can be used to predict the shape of the spectrum viz

$$B(E)_{sp} \quad \alpha \quad B(E)_{st} \cdot {}_E{}^{(a_{st}-a_{sp})} \cdot \frac{(b_1+b_2E)_{sp}}{(b_1+b_2E)_{st}} \cdot \frac{Rf_{sp}}{Rf_{st}} \cdot \frac{f(\chi)_{sp}}{f(\chi)_{st}} \qquad (5)$$

The resulting shape is then smoothed (to account for detector broadening), scaled and subtracted from the spectrum. The number of points used for scaling determines the statistical error and since low-energy tailing on peaks, sum peaks and pile-up continuum can remove much of the spectrum from consideration, the detection limits may be well above the attainable minimum. However, the worst aspect of this type of approach is the possibility of small systematic errors in the predicted shape of the background. Although the strength of the method lies in the explicit correction for curvature and absorption edges in the spectrum, tests, as outlined below, should still be used to check if this is successful in the practical environment.

PEAK DECONVOLUTION

If the background is only subtracted at peak positions, 'overlap factors' can be used to correct the integral of counts over each peak window for low-energy tailing and overlap of neighbouring $K\alpha$ and $K\beta$ peaks (2,11). An extension of the idea is to use a mathematical function for each peak to calculate the overlap factors for various integration windows(6) but this is almost equivalent to doing a least-squares fit. Whether overlap factors, least-squares fitting or the 'ML' approach are used, it is important to realise that significant errors can result from very slight errors in position or width of the peak models(8). In practice, calibration errors, drift in the elctronics and count-rate effects can produce such discrepancies and shifts as large as 5eV are virtually undetectable to the naked eye. The problem is worst when we are trying to determine whether an element is present when there is a large interfering peak.

RELIABILITY TESTS

In order to feel confident using a particular program, it is advisable to try a number of 'worst-case' examples that could be met in practice so that realistic error estimates can be obtained. A test where a spectrum is simulated by superposition of standard peak profiles does not prove anything if the same profiles are used as fitting functions. Therefore a suitable test must be on a real spectrum where standard peak profiles have been obtained independently. Detection limits for EDS are typically quoted to be around 0.1% concentration by weight for a spectrum of about 500 K counts but this usually only applies to isolated peaks. The following type of test can be used to find the detection limit in the presence of overlaps and absorption edge steps. For example, try taking several spectra of pure iron and telling the computer that Fe,Co and Ni are present; the results should of course be 100% Fe, 0% Co , 0% Ni ! Similarly, take a spectrum with a well-defined Barium L peak multiplet and tell the program that both Ba and Ti are present to see how much spurious Ti (positive or negative) is picked up. The region below 3keV poses new problems due to curvature. To test reliability in this region, take a spectrum which does not contain

Na,Mg,Al or Si and see what values (again,positive or negative) are
obtained for these elements. Finally, test to see how much spurious
Al results from analysis of a spectrum containing large Mg and Si peaks.

SUMMARY

Whether quantitative or qualitative analysis is being performed.
standards for use in determining peak profiles are virtually
indispensable for accurate work and calibration of zero and gain
should be carried out frequently because slight errors in peak position
and width are the major causes of inaccuracy in resolving peak overlaps.
A series of simple tests can be used to determine realistic detection
limits for practical analysis and with this measure of the overall
accuracy of the system, the credibility of the results can be
established.

REFERENCES

1. R.WOLDSETH, Proc.11th Ann.Conf.MAS,Miami
2. S.J.B.REED&N.G.WARE, X-Ray Spectrom. 2, 69-74, 1973
3. P.J.STATHAM, J.Phys.E-Sci.Instr. 9, 1023, 1976
4. P.J.STATHAM, X-Ray Spectrom.(In press,1977)
5. P.J.STATHAM, Ph.D Thesis,University of Cambridge,England,1975
6. C.E.FIORI,R.L.MYKLEBUST&K.F.J.HEINRICH, Proc.11th Ann.Conf.MAS,
            Miami Beach,1976 ,12A-12C
7. M.F.CICCARELLI,R.B.BOLON&E.LIFSHIN, Proc.10th Ann.Conf.MAS,Las Vegas
            1975, 23A
8. P.J.STATHAM, X-Ray Spectrom. 5, 16, 1976
9. F.H.SCHAMBER, Proc.Symposium on "X-ray fluorescence of environmental
            samples",held Jan.1976 at Chapel Hill,North Carolina,
            pub.Ann Arbor Science Publications, T.Dzubay(editor).
10.P.J.STATHAM, Proc.11th Ann.Conf.MAS, Miami Beach,1976,10A-10I
11.D.G.W.SMITH, Proc.10th Ann.Conf.MAS, Las Vegas,1975, 21A-21D

ooooOOOOoooo

FIG. 1 95F

Background subtraction (peak searching) by convolution with a symmetric zero-area function. The result of convolution has been arbitrarily scaled to match the vertical scale of the original spectrum for comparison purposes.

COUNTS

Si

Spectrum of kaersutite recorded for 10 live seconds at 3 kPPS output rate. Horizontal scale is channels where 1 channel $\cong$ 10 eV and obvious peaks are noted. (Noise fwhm= 100eV , Mn Kα fwhm= 160 eV)

CaKα

Al

Mg

K   CaKβ TiKα FeKα

Na   TiKβ FeKβ

10 keV
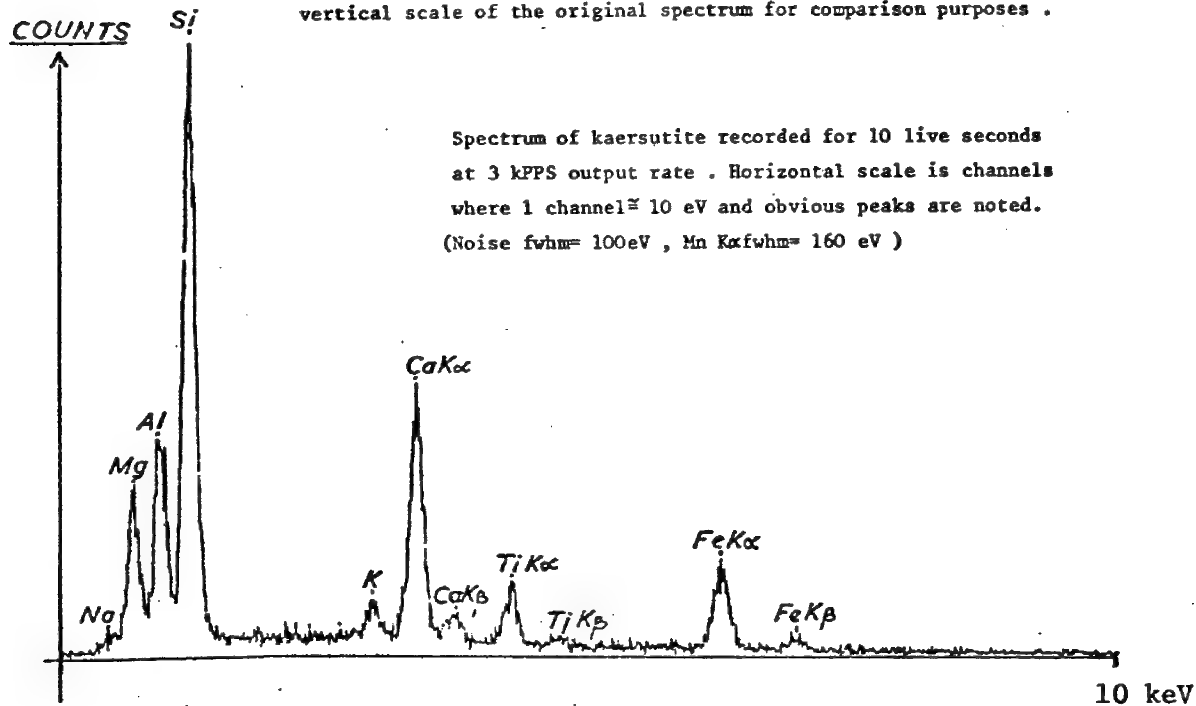
The result of convolution with a 'top-hat' function; If N(I) is the original count in channel I then

$$\widetilde{N(I)}= \sum_{-M}^{M} N(I) / (2M+1) - \left[\sum_{M+1}^{M+N} N(I) + \sum_{-(M+1)}^{-(M+N)} N(I) \right] / 2N$$

←2M+1→
←N→   ←N→
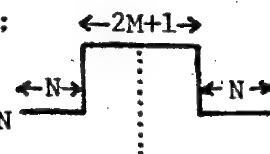
Note that negative lobes appear in the wings of each peak and that the Na Kα peak is consequently not detected. Background subtraction and smoothing is quite effective and some new peaks marked ? are exposed, some of which are probably the result of pile-up.

O

10 keV

FRAME C: A Compact Procedure for Quantitative
Energy-Dispersive Electron Probe X-ray Analysis

R. L. Myklebust, C. E. Fiori and K. F. J. Heinrich
Analytical Chemistry Division
National Bureau of Standards
Washington, D. C. 20234

Abstract

The correction procedure FRAME C has been developed for
quantitative electron probe microanalysis with a lithium-drifted
silicon detector. This program is a modification of our FRAME
program [1]; it was designed to compute the mass fractions of
the elements present in a specimen based on a minimum amount
of input.
The x-ray intensities utilized by the program are the
summed contents of small blocks of adjacent channels (regions
of interest) of a multi-channel analyzer, rather than entire
spectra. This restriction renders possible the on-line
execution of the program with small (24 K) computers. The
program requires a region of interest for each analyzed element,
and two regions of interest free from peaks for the background
subtraction. Also needed are the atomic number and x-ray line
for each element and the operating voltage. FRAME C has been
made to operate both in a computer-oriented multi-channel
analyzer and in a time-shared computer. The time-share version
is in BASIC and is approximately 850 statements long.
The procedure consists of a background correction calculated
from the two background regions of interest [2], a simple method
of resolving overlapping peaks [3], and the matrix corrections
previously described [1]. FRAME C is a collection of 21 sub-
routines organized to perform three different operations (see
figure 1). For a typical analysis, in the first of these
operations the information needed from spectra of standards is
computed and stored in a file. Either pure elements or compounds
of known compositions may be used. In the second operation we
compute the mass fractions of elements in the specimen points
from their spectra and from the previously stored information
on the standards. Another part of FRAME C is a routine for
computing the thicknesses of the beryllium window and the silicon
dead layer in the detector from a carbon spectrum. This part is
used occasionally because the thicknesses of the beryllium window
and silicon dead layer are needed for the determination of
detector efficiency, particularly at x-ray energies from one
to three kilovolts. The thickness determination is based upon
the expression for the intensity of the continuum previously
described [2]:

$$I_E = \frac{1}{E} [K_1(E_o-E) + K_2(E_o-E)^2] \, P_E \, f_E \qquad (1)$$

where f_E is the specimen absorption factor for the continuum at energy E, K_1 and K_2 are the two coefficients determined from two background regions of interest, E_o is the operating voltage, and P_E is the detector efficiency:

$$P_E = \exp[-\mu_{Si}t_{Si} - \mu_{Be}t_{Be} - \mu_{Au}t_{Au}] * [1 - \exp(-\mu_{Si}t_{det})]. \quad (2)$$

In this expression the μ_i is the mass absorption coefficient of i, and the t_i is its thickness in g/cm^2 (t_{Si} = Si dead layer, t_{Be} = beryllium window, t_{Au} = gold layer, and t_{det} = thickness of silicon detector). The detector thickness is taken from the detector specifications and the gold layer is assumed to be 3.86×10^{-5} g/cm^2. Four regions of interest of the continuum are selected for the computation. Estimated values for t_{Be} and t_{Si} are entered and two regions are used to compute K_1 and K_2 in equation (1). The second two regions (one must be below the silicon absorption edge and the other just above the edge) are then used to compute t_{Be} and t_{Si}, and this procedure is iterated until their values converge.

The analysis routines for computing the x-ray intensities from standards and compositions of unknowns are parallel options of the program. Except for the order in which subroutines are called, these two operations are essentially the same (figure 1). The matrix and background corrections are performed as previously described [1,2]. The peak overlap computation presented by us has been incorporated in the program and includes 17 x-ray lines (Kα, Kβ_1, Lα_1, Lα_2, Lβ_1, Lβ_2, Lβ_3, Lβ_4, Lγ_1, Lγ_3, Lη, Lℓ, Mα, Mβ, Mγ, Mζ_1, M$_{II}$-N$_{IV}$) plus their escape peaks [3]. One line of each element is used for the analytical procedure. All additional lines are interferences which must be subtracted if they fall within the region of interest of an analytical line. For this purpose we assume that the detector efficiency and absorption factor of the interfering line are the same as for the selected line with which it overlaps. All overlaps may then be directly calculated and subtracted if the weights of lines are known. Overlap coefficients that predict the contribution of one peak to the integrated region of another peak with which it interferes are computed once early in the program.

Overlap coefficients are obtained by formal integration of the peak shape function of an interfering line over the region of interest of the analytical line with which it interferes. Since the overlap coefficients are independent of the peak intensities, they need be computed only once for each set-up of regions of interest and stored in the file with the standards information. They must be recomputed if the size or position of the regions of interest of the elements involved is changed. For a particular element, the regions of interest must be the same for the standard and the specimens; however, another element may have a different number of channels in its region of interest or may even be assymetrically placed on the peak so as to minimize interferences. The treatment of interferences between lines originating from shells other than the analytical line is presently being studied. Practical examples will be demonstrated.

References

[1] Yakowitz, H., Myklebust, R. L., and Heinrich, K. F. J.,
     FRAME: An On-Line Correction Procedure for Quantitative
     Electron Probe Microanalysis, NBS Technical Note 796,
     National Bureau of Standards, Washington, D. C. (1973).

[2] Fiori, C. E., Myklebust, R. L., and Heinrich, K. F. J.,
     and Yakowitz, H., Anal. Chem. 48, 1, 172-176 (1976).

[3] Fiori, C. E., Myklebust, R. L., and Heinrich, K. F. J.,
     Proc. 11th Annual Conf. of Microbeam Analysis Society,
     Miami Beach, Florida, August 9-13, 1976, paper 12 (1976).

Figure 1. Block diagram of FRAME C. Each block represents one of the program subroutines. The subroutine ERASE clears the FILE. The WINDOW routine also calls subroutines: EDGE & LINE ENERGIES, ABSORPTION COEFFICIENTS, DETECTOR EFFICIENCY, $f_{(\chi)}$, and BACKGROUND.

Getting Accurate Intensity Values
from Energy Dispersive X-Ray Spectra
Using Fixed Energy Windows

by John C. Russ
EDAX Laboratories

Most integration of peaks in energy dispersive x-ray spectra is carried out using fixed energy "windows" or "regions of interest" set in terms of channels in the multi-channel analyzer (whether of the hardware or software based type). This gives rise to two sources of error that can be very significant but can each be corrected with modest calculation effort.

The error due to miscalibration of peak shift arises because the fixed energy window does not shift with the peak. It is compounded if the peak does not initially lie at the exact center of the energy window (which it rarely does). In theory, the use of standards will compensate for this since the same "off center" window will be used for the peak in the standard as in the unknown. In practice, shifts of a few eV are common even in well-maintained systems, due to changes in grounds, count rate, temperature, etc. If the user does not take care to calibrate his system the misalignment can be much greater, and it is not easy to adjust peak positions by eye to less than 5 eV. The plots that follow show the change in integrated "window" intensity with miscalibration or peak shift for several cases. The important variables are:

1. Window width: The figures show widths of approximately 1.2, 1.6, and 2 FWHM, rounded to the nearest integral number of channels. A wider window is clearly less sensitive to small shifts, but can increase problems of overlap from neighboring peaks as well as degrading statistical precision because of the greater fraction of background counts.

2. eV per channel of the analyses: The greatest effect of this parameter is in limiting the window width setting to an approximation of the exact multiple of FWHM desired.

3. Peak width: Since this varies with energy and spectrometer resolution, we have made plots for peaks of aluminum (1.487 keV), cobalt (6.924 keV), and strontium (14.140 keV), for an assumed spectrometer resolution of 160 eV.

4. Peak-to-background ratios: Small peaks appear to change less with shift but actually this is due to the counts from bakcground, which degrades the statistical precision of the results.
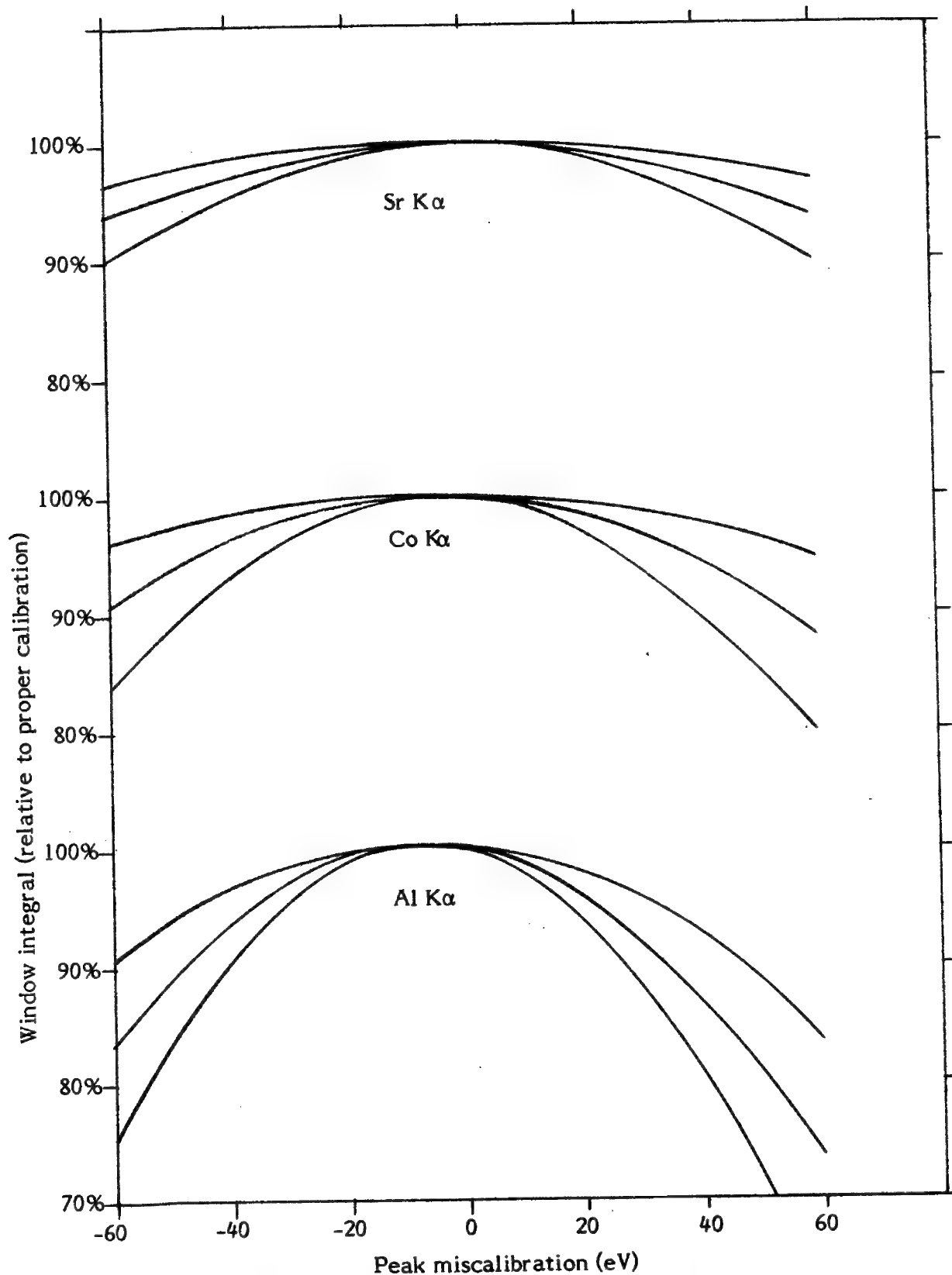
FIGURE 2 - Change in window integral with peak shift. 20eV/channel, 100:1 P/B ratio, varying window width (from top to bottom 1.2, 1.6, 2 FWHM) for Al, Co, Sr Kα peaks.
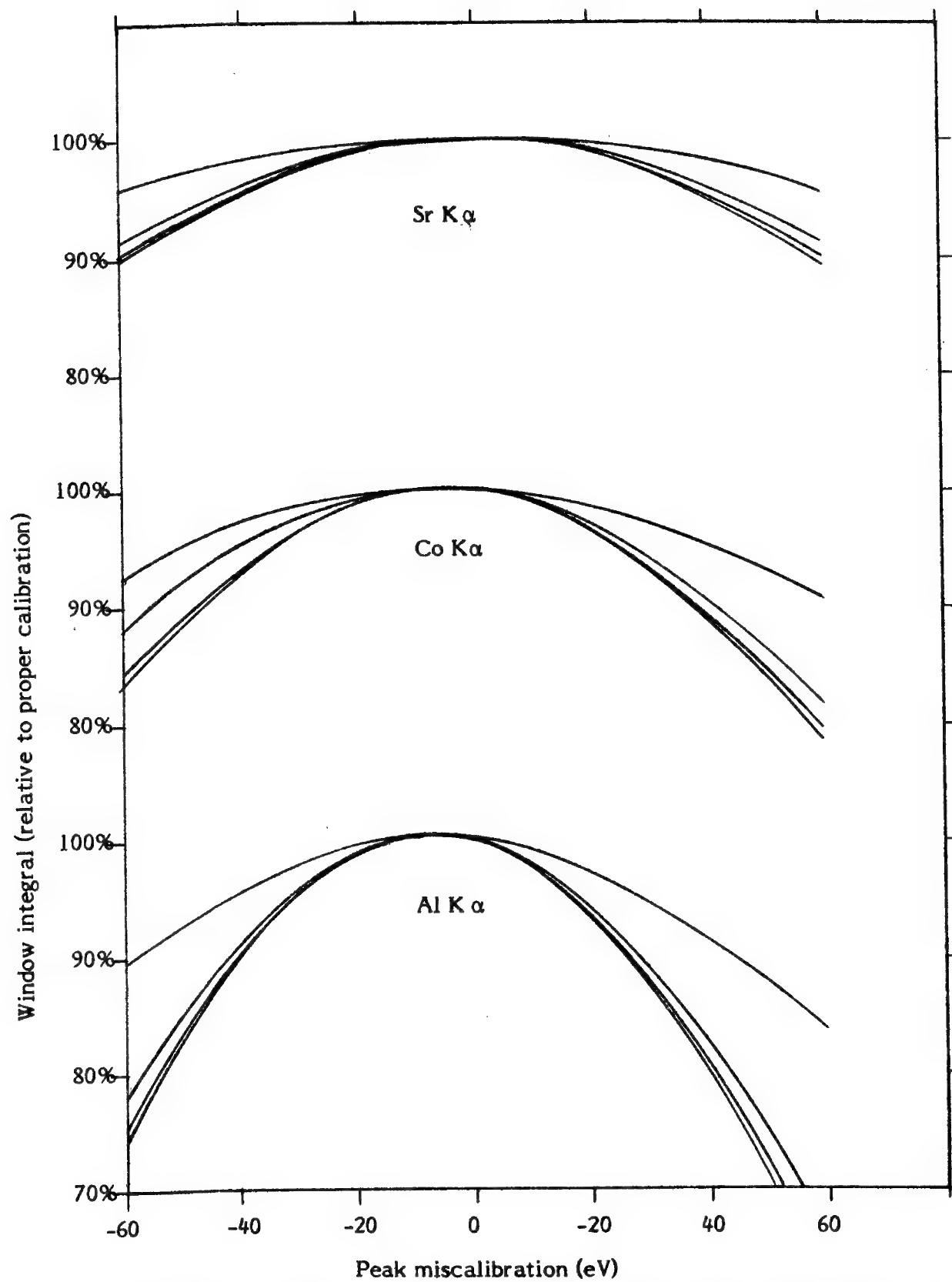
FIGURE 1 - Change in window integral with peak shift. 20eV/channel, 1.2 FWHM window, varying P/B ratios (from top to bottom 1:1, 10:1, 100:1, 1000:1) for Al, Co, Sr Kα peaks.

From these figures we see that there is a significant effect of peak shift, especially for those large peaks that should give good analytical precision and hence be useful for obtaining good accuracy. The asymmetric effects of shift on peaks not centered exactly on the channel positions is also evident.

To control the effects of miscalibration it is first of all important to know the actual peak centroid position. This can be used either to readjust gain and zero, or mathematically correct the intensity values obtained by fixed window integration using the method to be shown below. Finding actual peak centroids requires a fitting method such as the one developed by Nocholds[1], in which a second-degree polynomial is fit to the logarithm of the channel (intensity) heights. The centroid of the resulting parabola is a very sensitive and reproducible method for getting the peak centroid, except at very high energies (20 keV) where K , K separation becomes too great.

The error due to the changes of peak width with energy is unimportant if a standard is used for every element. However, since energy-dispersive systems lend themselves to extrapolation or interpolation of elemental intensities from other, nearby elements[2,3], it is useful to set a window width consistent for all peaks. Peak widths increase with energy as:

$$FWHM = R^2 + 2.735(E - 5.894)$$

where R is the resolution for manganese, E is the centroid energy of the peak, and the 2.735 value includes the Fano factor and so may vary slightly from one system to another. This means that the fraction of the peak contained in a window set to the nearest integral number of channels will vary with energy as shown in the figure below.

References

1. C. Nockolds "Computer-Assisted Analyzer Calibration", EDAX EDITor, Vol. 6 No. 3 (1976), p. 57-58

2. F. Blum, M. Brandt, "Evaluation and Use of an SEM Combined with an Energy Dispersive X-Ray Analyzer for Quantitative Analysis", XRay Spectrometry, Vol 2 (1973), p. 121-124

3. J. Russ, "Quantitative Microanalysis with Minimum Pure Element Standards", Proc. 9th Annual Conf., Microbeam Analyses Society, Ottawa, (1974), p. 22a-c
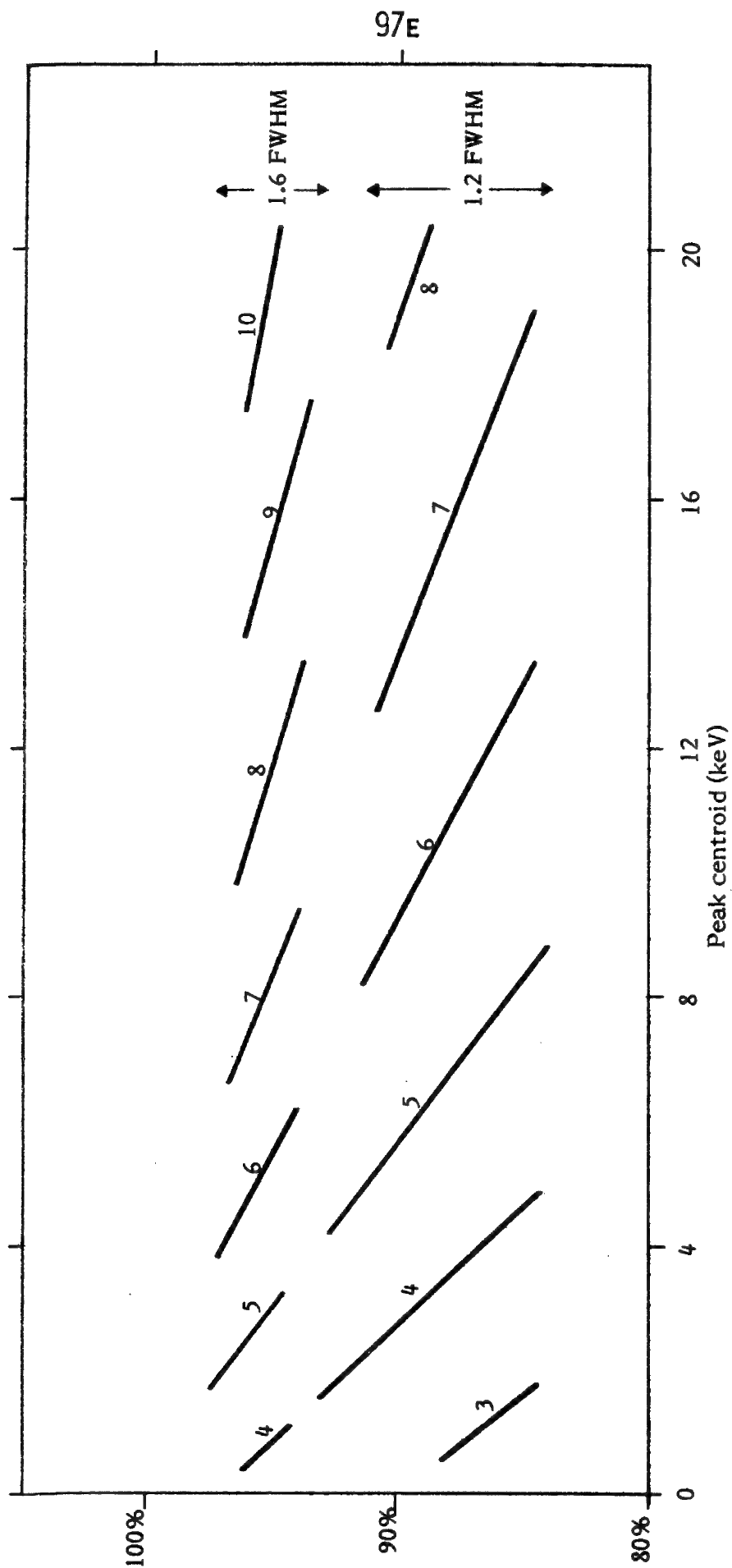
FIGURE 3 – Fraction of peak area in window set to nearest integral number of channels (1.2 and 1.6, FWHM) as a function of energy.

To correct for this variation, it seems best to convert all integrated intensities from fixed energy windows to total peak areas, using the error function (the area under a Gaussian curve). This same calculation can also take into account any assymetrical positioning of the window on the peak, and by using the centroid determined by least squares fitting, can correct for peak shift. The error function can be calculated using the short program listed below, in BASIC. The use of 30 terms of the polynomial expansion (line 9560) is not really needed, since beyond about six terms there is little further change, but the calculation is so fast that we have kept them all.

```
9000    REM    CONVERT WINDOW INTEN TO PEAK INTEN
9010    PRINT "ENTER WINDOW LIMITS IN KEV (REMEMBER, LIMIT LIES"
9015    PRINT "HALFWAY BETWEEN ACTUAL CHANNEL ENERGIES!)"
9020    PRINT "LOWER EDGE=";
9030    INPUT W1
9040    PRINT " UPPER EDGE=";
9050    INPUT W2
9060    PRINT
9070    PRINT "ENTER PEAK CENTROID ENERGY=";
9080    INPUT E
9090    PRINT " AND SPECTR. RES'N @ MN KA=";
9100    INPUT E0
9110    PRINT
9120    LET F0= SQR (E0*E0+2735*(E-5.894))/1000
9130    LET X=(E-W1)/F0
9140    GOSUB 9500
9150    LET W=X
9160    LET X=(W2-E)/F0
9170    GOSUB 9500
9180    LET W=W+X
9190    PRINT "MULTIPLY WINDOW INTENSITY BY";1/W
9200    STOP
9500    REM  ERROR FUNCTION CALC.
9510    LET X=2.35482*X
9520    LET T=1
9530    LET Y=1
9540    LET P=1
9550    LET F=1
9560    FOR N=1 TO 30
9570      LET F=-F*N
9580      LET P=P*X*X
9590      LET Y=Y*2
9600      LET T=T+P/F/Y/(2*N+1)
9610    NEXT N
9620    LET X=T*X*.398943
9630    RETURN
9640    END
```

This routine can be easily added to any quantitative routine using intensity values obtained by integration over a fixed number of channels.

Least-Squares Fit with Digital Filter:

The Method and Its Application to EDS Spectra

F. H. Schamber
N. F. Wodke
J. J. McCarthy
Tracor Northern, Inc.
Middleton, WI 53562

The successful application of solid-state silicon detectors to routine quantitative X-ray analysis requires suitable procedures for the determination of elemental peak intensities. The two most significant problems in quantitative EDS analysis are those of 1) separation of peak overlaps, and 2) elimination of underlying continuum (background).

In 1973, a computer method for extracting X-ray peaks from EDS spectra was developed and reported at this conference[1]. This method was implemented in a computer program known as "ML" (Multiple Least-squares fitting); since that time, the ML program has been successfully applied to a wide range of quantitative EDS problems and the utility of the method has also been expanded by the development of a more comprehensive program known as "SUPER-ML."

In recent years, other techniques for quantitative EDS analysis have also been reported which differ from the ML technique in several respects, but most significantly in the treatment of continuum. Because of such differences, there has been increased interest in a more complete discussion of the fitting algorithms used by the ML programs. The oral presentation of this paper will provide a full mathematical description of the unfolding procedures employed in the ML and SUPER-ML programs and the main points are summarized in the following paragraphs.

In describing the spectral analysis method employed by the two ML programs, there are three points of particular interest:

(1) Use of multicomponent least-squares fitting to resolve peak overlaps.

(2) Elimination of peak modeling and parameterization requirements by permitting measured single-element spectra (reference spectra) to be used as fitting functions.

(3) The use of a digital filter operator as a means of suppressing the continuum prior to fitting.

Of these features, it is the last which is the most important to the success of the method and represents the primary innovation incorporated in the ML programs.

If one presumes that a multielement spectrum is the simple sum, in appropriate proportions, of a series of individual single-element spectra, then its analysis reduces to the determination of the proportionality constants which provide the best match of the summed reference spectra to the unknown spectrum to be analyzed. Linear least-squares fitting is a mathematical procedure which results in the best fit possible and also is capable of predicting the statistical uncertainties in each of the fitted coefficients. One of the attractive features of the linear least-squares procedure is that, by utilizing actual measured spectra as fitting functions, the need for mathematical modeling of peak shapes can be eliminated and the number of fitting parameters can be minimized. Since a measured spectrum with good statistics provides the most accurately detailed description of peak shape and positions possible, the use of measured spectra as fitting functions results in an analysis method which is not only simple to implement and use, but is also nearly optimum in terms of accuracy and precision. It does, however, require careful attention to the stability of the detector electronics.

The greatest obstacle to the application of the linear least-squares fitting method to X-ray spectra arises due to the presence of the underlying continuum which is present in all spectra. This continuum, though generally quite smooth, is nonetheless sufficiently complex that simple approximations such as straight line or low-order polynomial approximation cannot describe it accurately enough for quantitative analysis. In recent years, a number of workers have reported progress in modeling bremsstrahlung continuum using a basic Cramer's-law expression with corrections for absorption in the sample and detector window[2]. This method requires detailed knowledge of detector response and matrix absorption which is a particular concern for low energy analysis where absorption in the detector window and sample are typically large effects. Also, the method is currently applicable only to thick-sample bremsstrahlung and is not suited for thin-film analysis nor for those cases where there are significant non-bremsstrahlung contributions to the continuum.

The ML method takes a different approach to this problem in that it makes no explicit assumptions about the method of production or the functional form of the continuum. Rather, it is based upon the observation that continuum is predominantly a "smooth" curve which varies relatively slowly in comparison to the X-ray peaks. That is to say, in an EDS spectrum, the peak intensity information is distinguishable from the continuum by characteristic "frequency." This suggests that continuum components can be selectively eliminated from a spectrum by the application of an appropriate frequency band-pass filter. It is relatively simple to construct a "digital filter" operator which suppresses continuum and yet retains essential peak information. However, such a filter also modifies peak shapes and inter-peak interference is increased somewhat by the correlating effect of the filter. Thus frequency filtering alone is not an accurate method for analysis of complex spectra, but in conjunction with least-squares fitting these properties are not a problem. In the ML programs, the procedure is to apply the same digital filter operator to the unknown spectrum and each of the references and then to

perform an ordinary least-squares fit (with appropriate modification of the statistical weighting) using the filtered spectra[3]. Thus, by applying an appropriate digital filter to the unknown and reference spectra before fitting, one suppresses the continuum effectively, and the resulting fit is a best-fit of peak structure only.

An obvious concern with this procedure is whether, by assuming a smooth continuum, the method exhibits sensitivity to bremsstrahlung discontinuities at absorption edges. In practice, this has not been observed to be a problem. The reasons for this are probably related to the following facts: 1) Absorption edges are actually quite small relative to peak amplitudes. 2) When measured spectra are used as fitting functions, the absorption edges are also present in these spectra and thus are partially compensated in the fit. 3) Absorption edges are reduced to local disturbances by the digital filter and do not couple effectively to adjacent peaks.

REFERENCES

1. F. H. Schamber, "A New Technique for Deconvolution of Complex X-ray Energy Spectra," Proceedings of the Eighth National Conference on Electron Probe Analysis, New Orleans, Paper 85 (1973).
2. C. E. Fiori, R. L. Myklebust, K. F. J. Heinrich and H. Yakowitz, "Prediction of Continuum Intensity in Energy-Dispersive X-ray Microanalysis," Anal. Chem. 48 (1): 172 (1976).
3. F. H. Schamber, "A Modification of the Linear Least-Squares Fitting Method which Provides Continuum Suppression," in X-ray Fluorescence Analysis of Environmental Samples, T. G. Dzubay, Ed., (Ann Arbor, Michigan: Ann Arbor Science Publishers, Inc., 1977), pp. 241-257.

A Real Time Floppy Disk Operating System

S. Shulman
EDAX International, Inc.

Increasingly, Energy Dispersive X-ray Systems incorporate computers, with software of ever-increasing complexity. The software is partly for calculations, as our mathematical models describing the physics of X-ray analysis become more exact, and partly for control and/or communication with other parts of the analytical system (the microscope, other spectrometers or a large remote computer). Also, it is possible to program decisions that allow complex and ever-changing analytical sequences to be carried out with minimum operator attention.

These trends have, of course, required increases in computer size and power, and in the available mass storage. Early systems with a small part of this capability relied on cassette tapes. These have now been superseded by flexible (floppy) disks which offer random access to programs and data.

If floppy disks are used only as faster versions of cassette storage devices, the opportunity is lost to achieve the major step forward in computer power and capability. Instead of a simple disk operating system which treats the floppy disk as a peripheral storage device, we have incorporated in EDAX floppy disk-based systems an EDAX Disk Management System (EDMS).

EDMS Managment is real time oriented since it can schedule and allocate program control to many different subprogram tasks to provide simultaneous use of system resources, maximizing throughout and insuring efficiency and economy of total program operation.

EDMS will operate in a NOVA computer with as little as 16K core memory, but can support additional core storage (up to 32K words) plus a variety of peripherals including communications adapters. It can be used interactively from a keyboard as well as in BATCH mode.

The EDMS executive constitutes the main framework of the operating system, and it must be resident in main memory before any continous and coordinated processing can occur. Functions performed by the resident portion of EDMS include interrupt processing, overlay and buffer management, system call processing and device interrupt servicing. Other modules of the system are brought into main memory from disk storage as they are required to perform specific functions such as full or partial system and device initializations, file maintenance operations such as opening, closing, renaming or deleting files.

Any program running under EDMS can suspend its own execution and either invoke another distinct program or call for a new section of itself. The current program is overwritten in both cases.

The program chain facility permits programs to be run which require more core storage than is ever available at one time. To use chaining, a program must be written in serially executable segments, each of which calls the next segment.

The program swap facility, by contrast, permits distinct programs to call one another in much the same manner as subroutines are called. The primary difference is the size of the routine and the manner of argument passing. Whereas subroutines are always smaller than the total amount of resident core, program swaps are as large as total user program space (or as large as multiples of user address space if chaining is performed). The program whose core images are overwritten during a program swap operation is stored temporarily on disk. Information saved enables the program to be restarted upon return from the swap.

When user address space is not sufficient to contain all the programs which are necessary for a system's operation, some form of program read-in scheme must be employed whereby programs, upon demand, are brought in from disk storage. The EDMS system can reserve portions of user address space for this function, and for programs of a limited size. This allows the EDMS user to segment his/her program into one or more parts which fit into the fixed-size core areas at execution time. These program segments are called user overlays and are stored on disk in core image format to facilitate rapid loading when their execution is desired.

User overlays differ from program swaps in that user overlays overwrite only a fixed area within a root program which remains active and core resident during the load time. Moreover, user overlays are more flexible than program swaps, since the user is permitted to be executing program segments in one or more currently resident overlays while a non-resident overlay is being loaded by the system. EDMS itself uses overlays to enhance its own operations; these overlays are called system overlays to distinguish them from user overlays.

An important function of any real time operating system is the efficient handling of input-output operations. Optimum usage of machine devices and central processor time in the accomplishment of tasks is the real reason for designing and implementing a multi-tasking system. Since I/O devices are slow compared to the internal speed of the computer, they must be programmed to overlap their operations with computations, when possible, in order to:

Increase usable CPU time by allowing one task to operate while I/O is in progress

Greatly increase efficiency of I/O operations

Provide more throughput of data by removing bottlenecks caused by slow peripherals (like Teletypes and plotters).

The responsibility of EDMS I/O control is to react during normal program execution to the structuring of I/O requests, making assignments for requests to machine devices when they are idle, and queuing requests for devices which are busy. Through the queuing facility, EDMS makes it possible to achieve maximum and continous overlap of program tasks without direct intervention by the programs themselves.

When spooling is provided, and the output device is busy, the output is temporarily stored on disk, and is later returned to core when the device is idle. The significance of spooling is that queuing of output information can now be accomplished easier without putting excessive loads on user core partitions. This also frees the user from having to optimize his message requests, thus permitting more effective use of the device.

EDMS can be used for both the development and the implementation of user programs. EDMS includes all the file capabilities normally available only on large machine disk operating systems, allowing the user to edit, assemble, execute, debug, compile, create and delete files.

Utilities currently supported by EDMS include the following:

Extended Assembler producing relocatable or absolute binary output from symbolic source programs.

Text editor to edit and create source programs

Relocatable Loader for linking relocatable binary files into an output core image (save) file.

Extended FORTRAN IV with real time and file control extensions. A Compile-Load-and-Go capability also exists to facilitate the running of FORTRAN IV programs.

Extended ALGOL compiler which provides many features in addition to those of ALGOL 60.

Several forms of single and multi-user extended BASIC which permit the BASIC interpreter to run under EDMS.

A Library File Editor enabling the user to separate, edit and to maintain relocatable binary program libraries with ease.

While it is likely that no single system or user will use all of the features of the EDMS system, its flexibility allows the system to grow in complexity to match whatever requirements may be needed by future analytical tasks.

A TECHNIQUE FOR RAPID SEMIQUANTITATIVE ENERGY DISPERSIVE MICROANALYSIS

N. C. Barbi, M. Foster, D. P. Skinner

Princeton Gamma-Tech, Inc.
P.O. Box 641
Princeton, New Jersey

The efficiency of an energy dispersive spectrometer at a given energy should remain reasonably constant over long periods of time[1]. The implication is that if one pure element intensity were measured, all other pure element intensities could be calculated. Therefore, the number of standard measurements required at the time of analysis would be minimized. Methods to exploit this characteristic of EDS systems have ranged from purely theoretical[2] to purely empirical[1].

The technique to be discussed presently is a hybrid approach, using a fundamental parameters expression for pure element intensity, fit by multiple regression to several reliable data points. The method is described in detail elsewhere[3]. The advantage of this approach lies in the reduction of the uncertainty associated with a not yet fully developed theoretical approach, and in providing a better basis for interpolation between data points than the totally empirical method.

The technique includes the following sequence:

1) Several pure element intensities are measured using a given set of analytical conditions, and the intensity equation is fit to these points. Figure 1 illustrates the fit for K lines, in this case, showing good success. An L line curve would also be established.

FIGURE 1
FIT TO EXPERIMENTAL DATA POINTS (x)
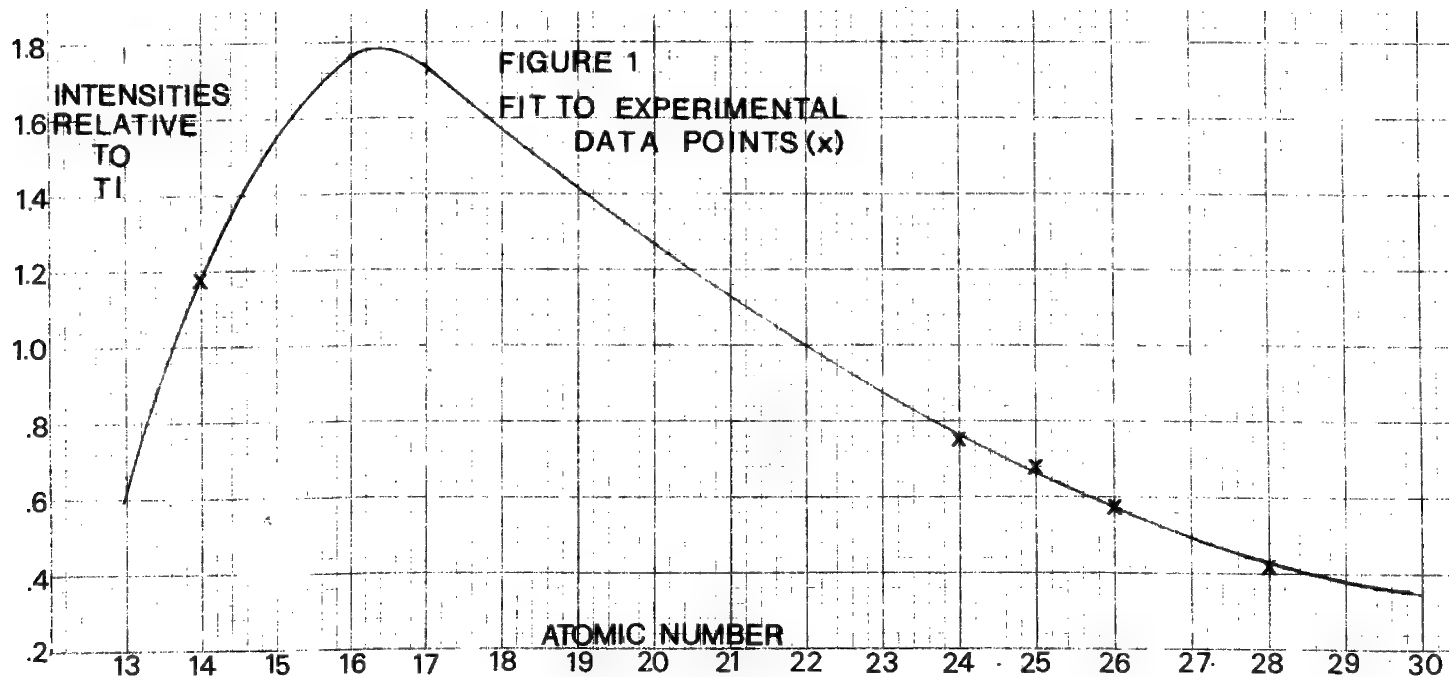
2)   A single standard is measured at the time of analysis, providing a scaling factor for the calibration curve and allowing the calculation of absolute intensities. Alternatively, if intensity data were recorded per unit current in establishing the curve, an incident current measurement could be taken to provide the scaling factor.

3)   Gaussian peaks are generated with the intensity determined in (1) and (2) at the appropriate energy for the $K\alpha$ (or $L\alpha$) line. The width of any peak is determined from an empirical calibration of the given EDS system, using two separated measured peaks. The FWHM at any energy is then predicted from a linear relationship, with slope as derived from the calibration. This calibration should be checked periodically.

4)   The remaining peaks of a given series can then be generated using table values for relative intensities. For example, a $K\alpha$ and $K\beta$ spectrum would be generated where K lines are used for analysis.

Figures 2 and 3 illustrate the match between generated and measured peaks in both intensity and width for Si and Fe.

5)   The generated pure element spectra are then used in least squares fitting to an unknown spectrum in order to calculate k-ratios and provide spectrum deconvolution. The fitting is done iteratively with ZAF correction and background calculation using the program LIFT, described elsewhere[4]. Weight factions are output.
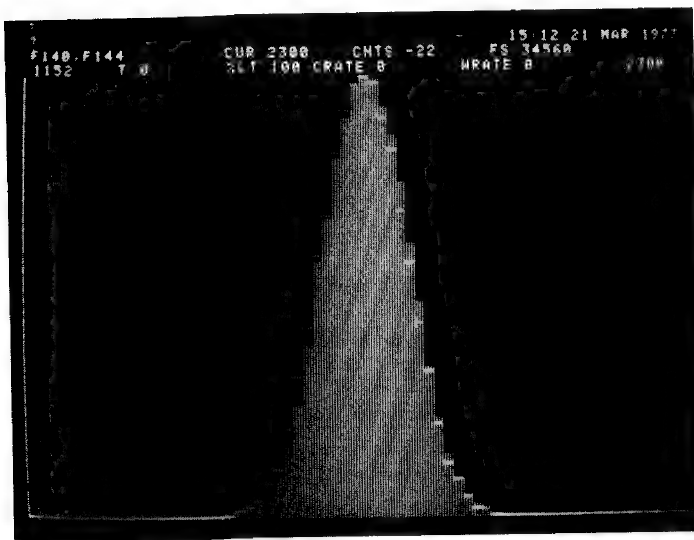
Figure 2: Si: Generated (dots) and Measured (bars)
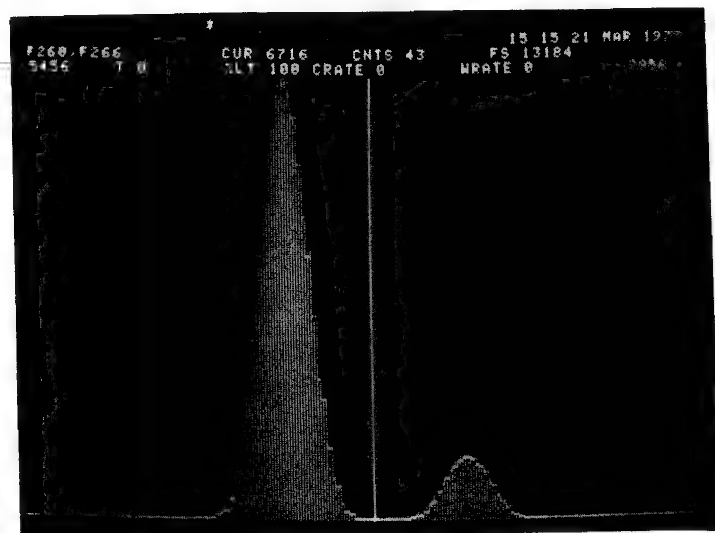
Figure 3. Fe: Generated (dots) Measured (bars)

The technique is semiquantitative since the calibration curve will not be expected to fit perfectly to measured data points, and since the generated Gaussian peaks will not provide as good a fit to real peaks as measured spectra. It would therefore be recommended to store as many measured spectra as possible, and rely on the generated spectra only where appropriate standards are not available. Once a library of standards is constructed (using any combination of measured and generated spectra) rapid semiquantitative analysis can be performed easily on a wide range of samples.

Table 1 shows results obtained on a stainless steel, comparing results from conventionally measured spectra and generated spectra. Figures 4 and 5 compare the fit in the Cr-Mn overlap region for the measured and generated spectra. The error in Mn using the generated spectra can be partially explained by the poorer fit of the Gaussians to the real peaks from the unknown.

The error in Si encountered in the analysis using generated spectra is from a different source. The generated spectra, of course, are ideal--no background, contaminant peaks or statistics. After closer examination of the measured standard spectra, it was noticed that a small Si peak was consistently present. The least squares fitting of the measured spectra provides a first order correction for the constant Si peak, and appropriately assigns only the remaining intensity of the Si peak to the unknown. The generated spectra miss this contribution to the Si intensity from the system.

TABLE 1

RESULTS OF STAINLESS STEEL ANALYSIS

Element	Calculated Concentration Using Measured Peaks	Calculated Concentration Using Generated Peaks
Si	.99	1.5
Cr	18.5	18.1
Mn	1.0	1.5
Fe	69.6	69.8
Ni	8.6	8.5
Reduced Chi-Squared of Fit	.6969	1.3087
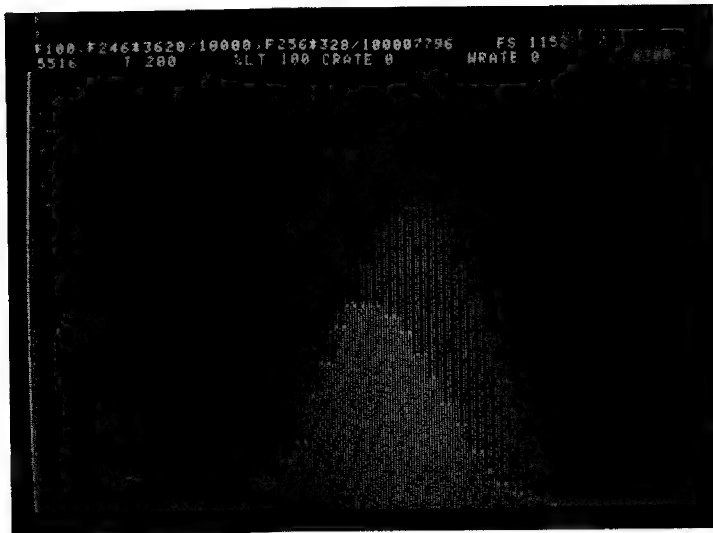
Figure 4.   Fit at Cr-Mn Overlap
            for Generated Spectra
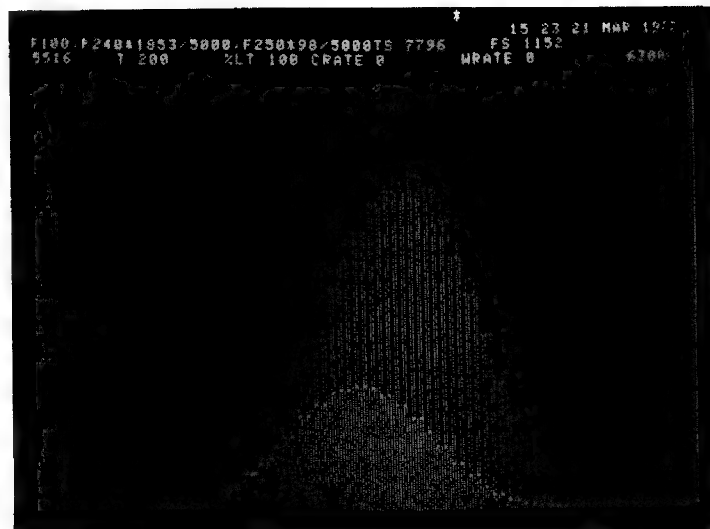
Figure 5.   Fit at Cr-Mn Overlap
            for Measured Spectra

REFERENCES

1. N. C. Barbi, et al., MAS, 1976, 8.

2. J. C. Russ, MAS, 1974, 22.

3. N. C. Barbi, et al., SEM/77, Vol. 1, 307.

4. C. Maggiore and M. Foster, MAS, 1975, 24.

A DEDICATED, LOW COST DATA PROCESSOR FOR SEMI-QUANTITATIVE X-RAY MICROANALYSIS

D. A. Gedcke, E. Elad, and P. E. Henry

ORTEC, Incorporated*
Oak Ridge, TN 37830

The capabilities of energy dispersive x-ray spectrometers on scanning electron microscopes have tended to develop in two different directions. The simpler systems are optimized for qualitative analysis, while full quantitative capability has been provided by more complex computer based systems. Although the latter systems can offer a powerful and flexible approach to quantitative analysis their cost is relatively high.

Many of the practical analytical problems which can be solved by using a scanning electron microscope do not require the ultimate precision in quantitative x-ray spectrometry. Often a semi-quantitative analysis is more appropriate. For this purpose a dedicated, low cost data processor has been developed. As shown in Figure 1, the 755 Data Processor is added to a standard energy dispersive spectrometer and facilitates semi-quantitative calculations by deriving spectral data directly from the multichannel analyser memory. It can provide a hard copy record of the computations for up to nine peaks in each spectrum.
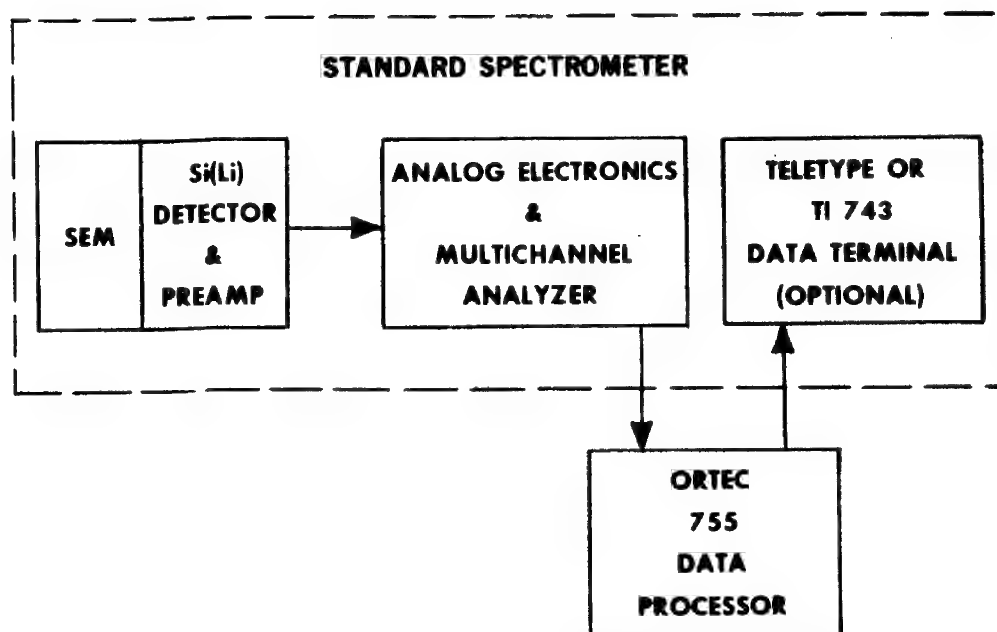
Figure 1. The 755 Data Processor is added to the standard energy dispersive spectrometer system incorporating an ORTEC 6230 Multichannel Analyser.

The microprocessor based unit offers three basic modes of computation:

CPS MODE: Automatic calculation of the net peak intensity (counts per second) above background.

RATIO MODE: The ratio of the net peak intensity for each peak to the net peak intensity of a reference peak in the spectrum.

CONCENTRATION MODE: Concentration calculations for each element based on linear working curves.

The output listing for the CPS mode can be used as input data for a ZAF program on a time-shared computer terminal or a large off-line computer when full quantitative analysis is required. In this case the 755 Data Processor provides rapid recording of net peak intensities while eliminating the possibility of human error inherent in data logging.

The RATIO mode is useful for analysis of biological thin sections where the ratio method compensates for variations in specimen thickness. More generally, the ratio mode can be used to track relative variations in composition on bulk samples.

The CONCENTRATION mode provides quantitative analysis where a set of well characterized standards having compositions similar to the unknown is available. Once the spectrum has been acquired on the unknown the concentrations for nine elements are calculated and listed in approximately 70 seconds.

The performance tests of the 755 Data Processor are best summarized by the results obtained in the concentration mode with a set of ASTM 300 series stainless steel standards. Five standards were employed, with concentrations lying within the ranges listed in Table 1. Three standards were used to establish the working curves, and the remaining two were treated as unknowns. The accelerating voltage was 15 kV, the specimen tilt was 45°, and a preset livetime of 100 seconds was used. The accuracy of analysis for each element in Table 1 was assessed by employing the measured concentrations for all five specimens in the following equation.

TABLE 1. STAINLESS STEEL ANALYSIS

Element	Concentration Range (Weight Fraction)	Percent Relative Standard Deviation in Calculated Concentration
Si	0.0033 - 0.0055	18
Cr	0.1724 - 0.2446	2.5
Fe	0.5317 - 0.7122	1.1
Ni	0.0816 - 0.2014	4.3

Percent Relative Standard Deviation

$$= \frac{100}{\text{Mean Concentration}} \left[\frac{\sum (\text{known concentration} - \text{measured concentration})^2}{\text{number of samples} -1} \right]^{1/2}$$

From Table 1 it can be concluded that the accuracy is within ±5% relative error for major concentration elements.

In conclusion it can be stated that the 755 Data Processor offers an economical solution for fast semi-quantitative analysis.

The authors would like to acknowledge the efforts of J. S. Bishop, who designed the Data Processor with the assistance of R. R. Mayhew.

Automatic Fitting of Calculated Background in Energy Dispersive X-Ray Spectra

by John C. Russ
EDAX Laboratories

In his original publication[1] illustrating the possibility of applying Kulenkaumpff's equation for the generation of continuum[2] to energy dispersive spectra, Reed used two fixed reference points at 2.96 keV and 9.87 keV for fitting. In his application to minerals, these energies were free of peaks (they correspond to the Argon and Germanium K - alpha positions). The relative shape of the background was calculated as

$$B(E) = ((E_0 - E)/E) \, F(\chi) \, \exp(-\Sigma(\mu_i \rho_i t_i))$$

where the first term is the generation term accoring to Kulenkaumpff (E_0 is the incident electron energy), the second term is the absorption of the x-rays in the sample (Read used Philibert's[3] expression for $f(\chi)$, identical to that applied to characteristic x-rays in ZAF corrections), and the third term is the absorption due to the silicon detector's entrance window and dead layer (each with absorption coefficient μ, density ρ, and thickness t). The fixed reference points were then used to adjust the calculated relative shape. This method of background removal was shown by Reed[4] to be useful for quantitative mineral analysis with an energy dispersive system.

An extension of this method by Fiori[5] used a more complex function[6] for the generated background

$$((E_0 - E)/E = b \, (E_0 - E)^2/E)$$

where b is an empirical constant, with Heinrich's[7] expression for $f(\chi)$. Two user selected fitting points were still required, which it was suggested should be the same for standards and background. Good agreement between measured and calculated backgrounds was shown for a variety of pure elements and a complete mineral.

Since the background levels in energy dispersive spectra are frequently low, with resulting poor statistical precision, it seems desirable to use as many fitting points as possible. A least squares procedure can be used to fit the calculated shape to these points to obtain the best values for the proportionality constants. Furthermore, in some cases of automated analysis it can be useful to automatically determine the suitable background reference points. A simple yet effective criterion is to accept points (each point the average of several adjacent channels) that are not higher than the average of their neighbors by a statistically significant amount (for instance two standard deviations). We also found it desirable to reject points significantly lower (again we used two standard deviations) than both neighbors, since these points could be the valley between two unresolved peaks.

This procedure was tested with good success on a variety of pure elements as well as complex metals and minerals. The following figures illustrate typical results. A basic language program to carry out the calculation and fitting, is available from the author.

1. N. G. Ware, S. J. B. Reed, Jnl. Phys. E Vol. 6, 1973, p. 286

2. Kulenkaumpff, Ann. Phys. Lpz. Vol. 69, 1922, p. 548

3. J. Philibert, X-Ray Optics & Microanalysis, 1963, Academic Press, p. 379

4. S. J. B. Reed, N. G. Ware, X-Ray Spectr. Vol. 2, 1973, p. 69

5. C. E. Fiori, etal, Anal. Chem. Vol. 48, 1976, p. 172

6. E. Lifshin, Proc. MAS, 9th meeting, 1974, paper 53

7. K. F. J. Heinrich, H. Yakowitz, Anal. Chem. Vol. 47, 1975, p. 2408

FIGURE 1 a-d: Spectrum and calculated background - Pure elements
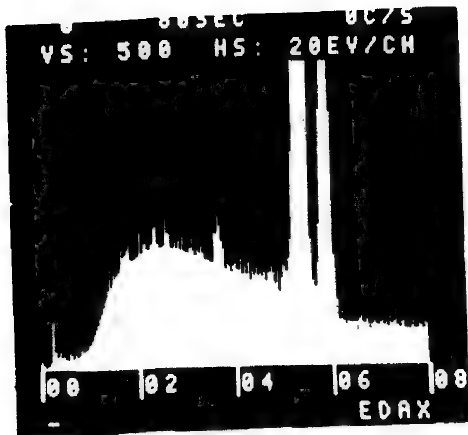
Fig. 1a
Chromium (K lines)
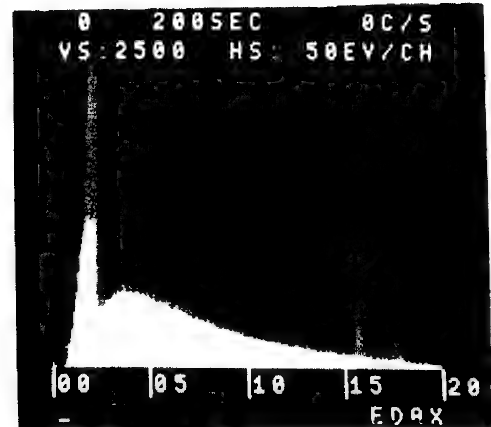
Fig 1b
Zirconium (K and L lines)
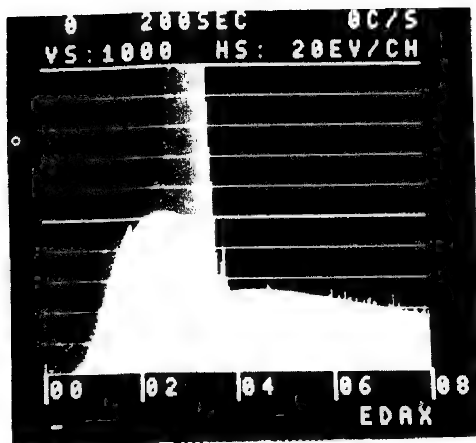
Fig. 1c
Silver (L lines)
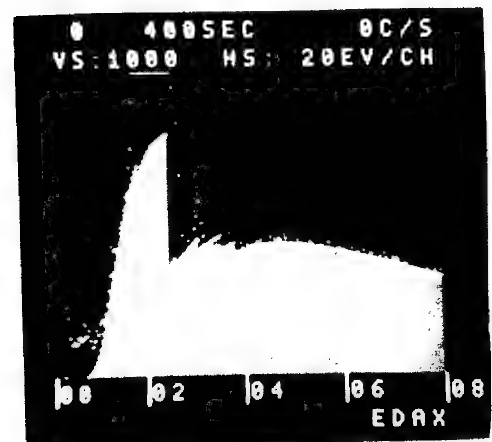
Fig. 1d
Lead (M lines)

FIGURE 2: Spectrum and calculated background
Bronze 86% Cu, 8% Sn, 5% Zn, 1% Fe
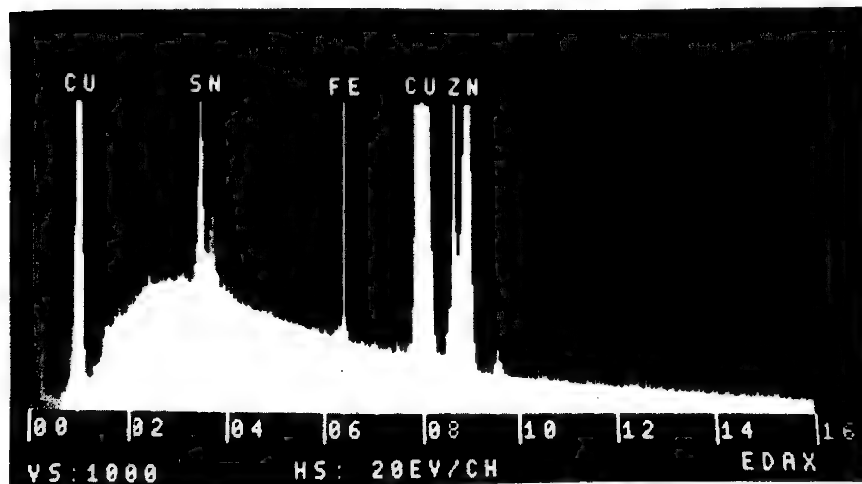
FIGURE 3:
Permalloy
80.1% Ni
14.8% Fe
4.3% Mo
0.49% Mn
0.25% Si
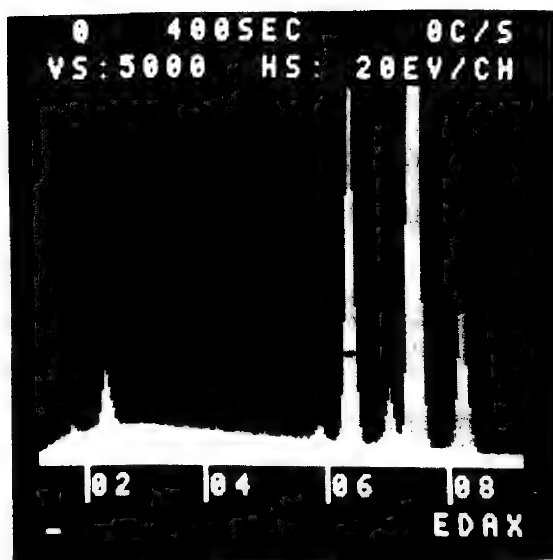
Spectrum and Background
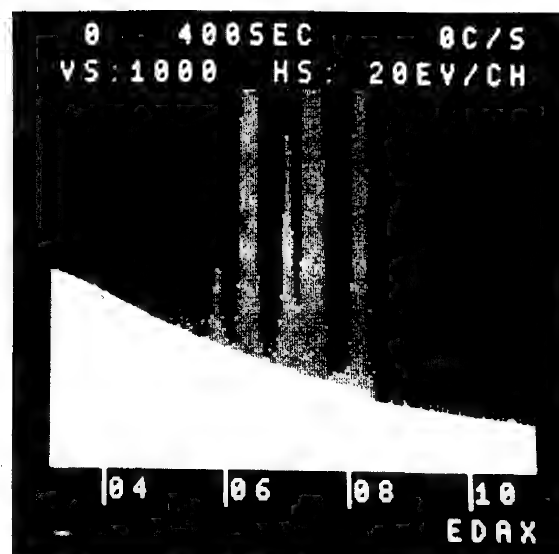
Absorption edges under peaks

RESOLUTION ENHANCEMENT of X-RAY SPECTRA

Peter J. Statham

Electrical Engineering and Computer Sciences Dept.,

University of California, Berkeley, Ca. 94720 .

ooOOOOoo

The histogram recorded with an EDS system is a distorted version of the original x-ray spectrum. The solid-state detector introduces a broadening effect which varies across the energy range and incomplete charge collection and imperfections in electronic performance add further energy-dependent distortion to characteristic peaks. However, electronic noise is superimposed on all signal pulses from the detector and thus produces a uniform broadening throughout the spectrum. We can therefore consider the set of data points, y_i , representing the spectrum in discrete channels $i=0,1,2...(N-1)$, as being related to an underlying 'sharper' spectrum, s_i , by the equation

$$y_i = (g * s)_i + n_i \qquad (1)$$

where g_i is a Gaussian function, n_i represents statistical counting 'noise' and '$*$' denotes the convolution operation. Equation 1 is typical of a number of measurement situations including stepped line and wavelength scans with a crystal spectrometer. Although the most accurate estimate of s_i is obtained when we know the form of the underlying function exactly (e.g. as in peak profile fitting) it is sometimes useful to be able to 'deconvolve' y_i thus obtaining a sharper spectrum. Such a process can be called 'resolution enhancement' .

Mathematical Preliminary

The finite discrete Fourier transform for a set of data points x_i is defined by

$$X_k = \sum_{i=0}^{N-1} x_i W^{ik} \qquad \text{for } k=0,1,2...(N-1) \qquad (2)$$

with the corresponding inverse as

$$x_i = \sum_{i=0}^{N-1} X_k W^{ik} \qquad \text{for } i=0,1,2...(N-1) \qquad (3)$$

where $W = \exp(- 2\pi j/N)$. The transform can be computed very quickly using the Fast Fourier Transform algorithm (1) and is very useful for the following properties which can be deduced from the definitions. It is a linear operation in that the transform of (a_i+b_i) is (A_k+B_k). It obeys a convolution theorem where the transform of $(a*b)_i^c$ is $A_k.B_k$. More explicitly,

$$(a*b)_i^c = \sum_{q=0}^{i} a_{i-q} b_q + \sum_{q=i+1}^{N-1} a_{N+i-q} b_q \qquad (4)$$

which is a 'cyclic' convolution in that when we run out of data points a_{i-q} to complete the usual convolution sum

$$(a*b)_i = \sum_{q=0}^{N-1} a_{i-q} b_q$$

we just cycle round and use points from the other end of the range. In the present case, if s_i smoothly approaches the same value at either extreme of the range $i=0$ to $(N-1)$ then $(g*s)_i$ is the same as $(g*s)_i^c$; thus the Fourier transform equivalent of equation 1 is

$$Y_k = G_k S_k + N_k \tag{5}$$

Since y_i is a real spectrum, $Y_k = \overline{Y}_{N-k}$, where '$^-$' denotes complex conjugate. Conceptually, one can treat Y_{N-k} as being equivalent to Y_{-k} so that $|k| = N/2$ represents the maximum frequency present. Finally , there is the useful relationship

$$\sum_{i=0}^{N-1} x_i^2 = \frac{1}{N} \sum_{k=0}^{N-1} |X_k|^2 \tag{6}$$

which is a form of Parsevals theorem.

Noise

If we consider a large ensemble of spectra, s_i will always be the same but n_i will be different in every case. The noise, n_i , is statistically distributed according to a Poisson distribution and for most practical purposes can be regarded as having zero mean, variance y_i and being uncorrelated from channel to channel. With some manipulation it follows from equation 2 that the mean value or 'expectation' $E(N_k)$ of N_k over the ensemble will be zero and that

$$E(|N_k|^2) = \sum_i (\text{variance of } n_i) = \sum_{i=0}^{N-1} y_i = N_o$$

Optimal Linear Filter

If noise were not present ($N_k=0$), equation 5 could be solved very easily giving $S_k = Y_k/G_k$. Anyone who has ever tried this soon recognises the problem introduced by the noise.

If $g_i = (2\pi\sigma^2)^{-1/2}\exp(-i^2/2\sigma^2)$ then $G_k = \exp(-k^2 2\pi^2\sigma^2/N^2)$, so dividing by G_k for large values of k results in multiplying the noise term by huge numbers; when Y_k/G_k is inverse-transformed the result is totally overwhelmed by the enhanced noise. One way to avoid this problem is to simply stop dividing by G_k when $|k|$ exceeds a certain value. However, this produces objectionable oscillations in the result and it is better to use some sort of smooth roll-off which avoids the pronounced Gibb's phenomenon which occurs with a sharp cut-off. Various approaches have been suggested including use of the 'Hamming window' (2), a Gaussian roll-off above a certain frequency(3,4) and using the Savitzgy-Golay smoothing procedure for the data(5). These solutions utilise some ad-hoc assumptions about the data and some educated guesswork is required in establishing the best parameters for the smoothing. Hunt(6) tried to avoid this by imposing a smoothness constraint on the final result to add some mathematical formalism to the problem but,of course, the choice of smoothness constraint represents the ad-hoc component in this approach.

So, we might ask the question "what is the best that can be achieved using a linear filtering method?". A useful measure is the total square error:

$$e^2 = \sum_{i=0}^{N-1} (s_i - (h*y)_i)^2 \tag{7}$$

where h_i represents a linear filter which is applied to the original spectrum, y_i . Since the noise is unpredictable, the best filter would be one that gives the minimum average ε^2 over a large (hypothetical) ensemble of data sets y_i , that is, one that minimises E(ε^2) . By making use of equation 6 and the statistical properties of the noise, the relationship

$$E(\varepsilon^2) = \frac{1}{N} \sum_{k=0}^{N-1} (|S_k|^2 |1-H_k G_k|^2 + |H_k|^2 N_o) \qquad (8)$$

is obtained where N_o ,as shown above, is the area of the spectrum. This is very useful since it shows explicitly the behaviour with a given filter. If $H_k = 1/G_k$, the first term in the sum is always zero but the second,noise, term becomes progressively larger as k increases. If H_k becomes zero above a certain frequency, the noise contribution ceases but signal-related errors in the first term add to the final error. The filter which minimises $E(\varepsilon^2)$ is

$$H_k = \frac{1}{G_k} \cdot \frac{|G_k S_k|^2}{(|G_k S_k|^2 + N_o)} \qquad (9)$$

which is basically just $1/G_k$ modified by a second term which provides the necessary smoothing; thus the optimal filter is defined for the measure suggested by equation 7.

Results

Unfortunately, we need $|S_k|^2$ to determine the optimum filter, yet s_i is what we are trying to find. Nevertheless, by simulating spectra on a computer together with Poisson-distributed random noise, the performance of various filters can be judged against that of the optimal filter defined by equation 9. An example is shown in fig.1 where the optimal linear filter has been used to enhance a synthetic spectrum of two Gaussian peaks superimposed on a low background. The restoration is quite close to the original but attempts to reduce the peak width further result in objectionable oscillations in the wings of the peaks. A number of features of linear resolution enhancement have been examined and although at the time of writing this abstract,tests are not yet complete, the following conclusions have been drawn:

(1) Even given complete prior knowledge of $|S_k|^2$,the 'power spectrum' of the underlying data, the effective resolution(or peak width) cannot be improved beyond about 2/3 of the original fwhm resolution without producing an unacceptable level of spurious oscillations. Similar limitations have already been noted by a number of authors (e.g.5,7,8) using different enhancement techniques; the present study merely confirms that this is a real limitation to linear methods which cannot be overcome by any feasible increase in the number of recorded counts(which would reduce the relative magnitude of n_i).

(2) The parameters k_c and σ of a Gaussian roll-off filter which is 1 for $|k| < k_c$ and $\exp(-(k-k_c)^2/2\sigma^2)$ otherwise(3) can be adjusted to give a good approximation to the optimal filter so that $E(\varepsilon^2)$, even with a highly-structured spectrum, is only marginally greater than the minimum. The problem is of course how to find the best k_c and σ for an arbitrary experimental spectrum and this will be discussed in the presentation.

(3) If the peak-to-background ratio is low so that $(y_i)^{1/2}$ for the background is greater than about 1/5 peak height, any useful enhancement is virtually impossible to achieve and it is better to just smooth the data using a filter close to optimal (i.e. with $G_k=1$ for all k in equation 9).

(4) The most objectionable feature of enhanced spectra is the superimposed ripples which result from low-pass filtering of the noise and truncation of high frequencies in the signal. Since the ripples can go negative, it is apparent that the linear filtering approach does not exploit all the properties possessed by the 'submerged' data s_i, which must be positive to represent a theoretically feasible x-ray spectrum. It is important to appreciate the characteristics of the spurious components to avoid false interpretation of peaks and other detail in the enhanced spectrum.

Other Techniques

Iterative deconvolution procedures which involve only linear operations are equivalent to linear filtering and although different criteria can be used to control the enhancement(5), the same limitations are still present. Non-linear procedures can achieve better results because it is possible to incorporate constraints which force the final estimate to be always positive. Unfortunately, the methods so far developed(e.g.9) still involve questionable assumptions and the computational cost is very high.

REFERENCES

1. W.T.COCHRAN,J.W.COOLEY,D.L.FAVIN,H.D.HELMS,R.A.KAENEL,W.W.LANG,G.C.MALING, D.E.NELSON,C.M.RADER & P.D.WELCH, IEEE Trans.Audio and Electroacoustics, AU-15, 45-56, 1967.
2. D.W.KIRMSE & A.W.WESTERBERG, Anal.Chem. 43(8),1035-1039,1971.
3. T.INOUYE,T.HARPER & N.C.RASMUSSEN,Nucl.Instr.& Meth. 67,125-132,1969.
4. J.W.COLBY, personal communication concerning paper in Proc.6th International Conference on X-Ray Optics & Microanalysis, Ed.G.Shinoda, K.Kohra and T.Ichinokawa,Univ.Tokyo Press,1972 pp247-251.
5. J.E.STEWART, Applied Spectroscopy, 29(2),171-174, 1975.
6. B.R.HUNT, Math.Biosciences, 8 ,161-179, 1970.
7. R.M.DOLBY, Ph.D.Thesis, University of Cambridge,England,1961.
8. P.J.STATHAM, Proc.9th Ann.Conf. M.A.S.,Ottawa,1974,paper 21.
9. B.ROY FRIEDEN, J.Opt.Soc.America, 62(4), 511-518,1972.

oooOOOOOOOOOOooooooo
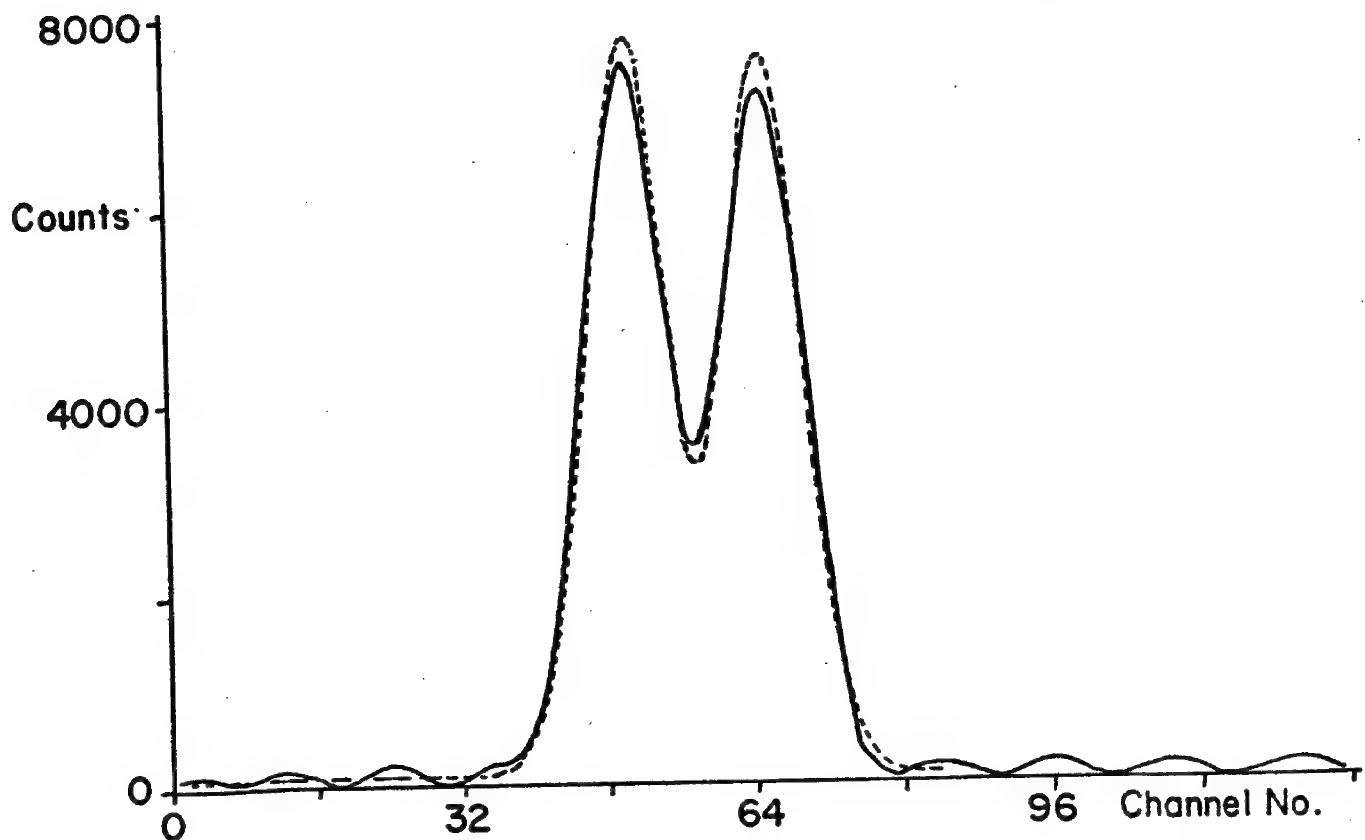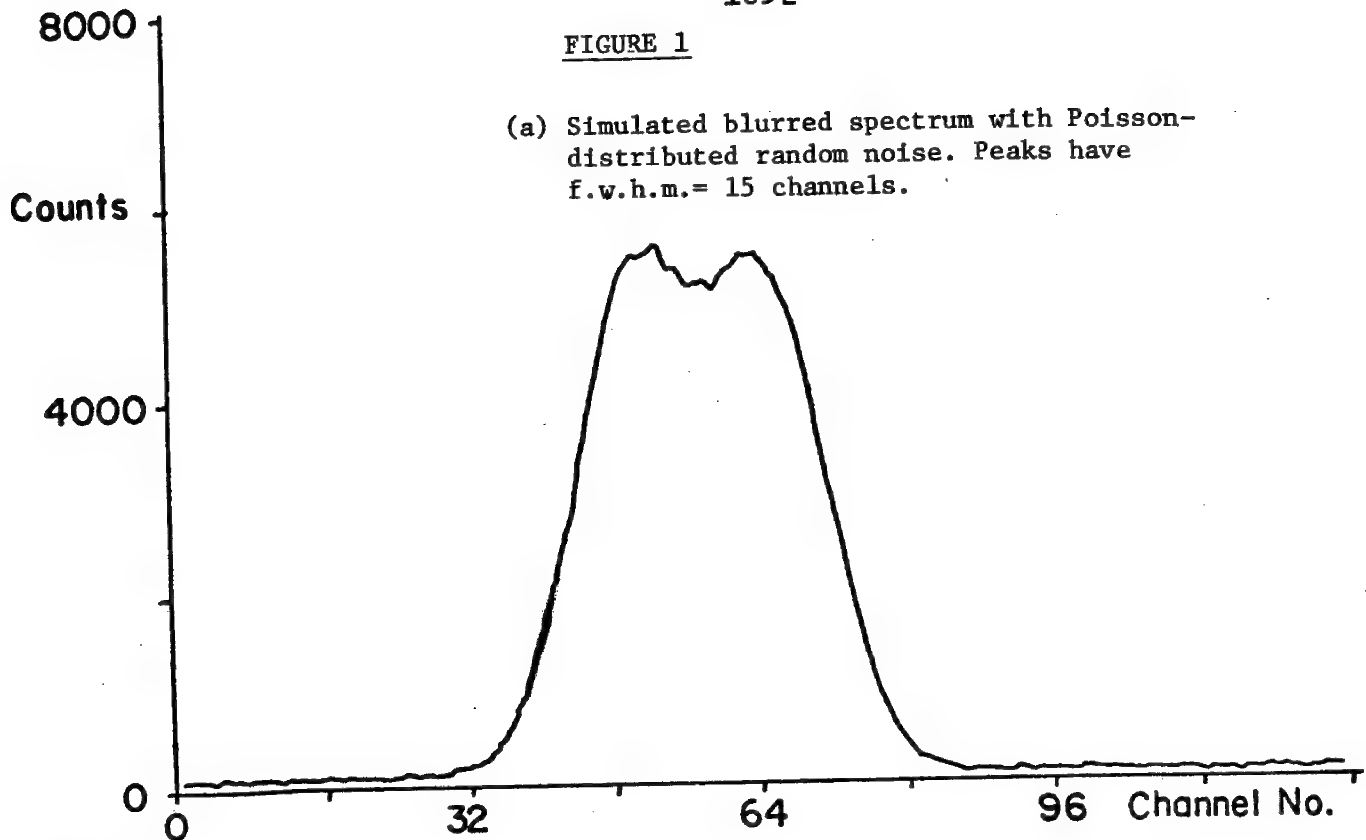
FIGURE 1

(a) Simulated blurred spectrum with Poisson-
distributed random noise. Peaks have
f.w.h.m.= 15 channels.

(b) Solid line shows result of resolution enhancement with optimal linear
filter defined by equation 9. Broken line shows original spectrum :
two peaks, fwhm=10 channels, heights respectively 7650 and 7500 counts
centred at channels 50 and 65, superimposed on a uniform background of
100 counts. In this example, g_i is a Gaussian function with fwhm=11.2
channels.

NEW MEASUREMENTS OF THE VOLTAGE DEPENDENCE OF ABSOLUTE
X-RAY YIELDS USING ENERGY DISPERSIVE SPECTROMETRY

E. Lifshin, M. F. Ciccarelli and R. B. Bolon
General Electric Corporate Research and Development

This paper presents new values of absolute electron excited x-ray production efficiencies obtained at normal electron beam incidence for a variety of elements and operating voltages. These findings, given in terms of generated photons per incident electron per steradian, are important for predicting x-ray outputs from various electron optical systems including: vacuum and x-ray emission tubes, scanning and transmission electron microscopes and electron microprobe analyzers. Such predictions are useful for optimizing desired radiation, determining efficiencies of wavelength dispersive spectrometers, and calculating standard x-ray intensities in conjunction with quantitative microprobe analysis.

The observed x-ray spectrum obtained with electron excitation is a modified version of the spectrum generated within a specimen. To convert from the former to the later, all modifying factors must be taken into account. These include both sample and spectrometer absorption effects, as well as corrections for background removal, spectrometer efficiency and detection system line broadening. Although earlier work utilized crystal spectrometers[1], the results of this study were obtained by energy dispersive spectrometry in the manner previously described by one of the authors[2]. The absolute yield for a line or series was calculated from:

$$N/_{4\pi} = n/[\Omega f(\chi) \cdot i \cdot C]$$

where: n is the observed count rate following background correction for the chosen characteristic line or series, Ω the solid angle, in steradians, subtended by the selected active portion of the detector, $f(\chi)$ the total applied absorption correction after corrections have been made for the beryllium window, gold contact, and silicon dead layer absorption, i the probe current as measured in a faraday cage, and C the number of electrons per coulomb.

Spectra were obtained with a JEOL JXA-50A scanning electron microprobe using both a fixed position Princeton Gamma-Tech detector (40° take-off angle) and a retractable Nuclear Semiconductor detector (35° take-off angle). They were then collected, stored and processed with a Tracor Northern NS-880 MCA system.

Experimentally it was found that the solid angle subtended by the selected active portion of the detector was the critical and limiting measurement. Uncertainty in the detector position behind the Be window necessitated the introduction of a smaller carefully machined Ta aperture as illustrated in Figure 1. Distance from the aperture to the probe point of impact was physically measured for both detectors. Furthermore, in the case of the retractable detector, it was demonstrated that the sample aperture distance could accurately be determined by utilizing the inverse square law dependance of the emitted x-rays. Intensities N_1 and N_2, measured at detector positions, d_1 and d_2, with measured separation Δd, ($\Delta d = d_2 -' d_1$) can be substituted into

$$d_1 = \Delta d/[(N_1/_{N_2})^{\frac{1}{2}} - 1]$$

to give the aperture distance d_1.

In all cases, beam currents were measured in a faraday cage using a calibrated electrometer and the corresponding voltages by the short wavelength cut-off method[3].

Figure 2 illustrates measured absolute yields from a number of elements plotted as a function of the over-voltage ratio. The self absorption correction, $f(\chi)$, used for both background and characteristic peaks, was the polynominal form proposed by Heinrich[4]. Absorption corrections were also made for a 0.3mil Be window, 200Å Au contact and a 0.2μm Si dead layer. The data presented includes the sum of both the $K_{\alpha1,2}$ and $K\beta$ emission lines. It can readily be seen from the plot, that the absolute yields for each element measured can be described by the relationship:

$$N/_{4\pi} = a(U - 1)^b$$

where: U is the over voltage ratio, and a and b are constants for a given element. Values for a and b, obtained by a least squares fit of the data, are tabulated in Table 1.

Based on our experience, it appears that if suitable care is exercised in measuring the detector solid angle, beam current and beam voltage it should be possible to reproducibly determine generated x-ray intensities, independent of the choice of energy dispersive detector. The resulting data could then be described as a function of the overvoltage ratio using only two constants. Given a table of such constants, any standard x-ray intensity could be computed for any take-off angle, beam voltage and current. In practice, however, it is suggested that at least one standard be measured in order to check calibration of the system. This measurement would be used to determine an effective beam current from which all other standards could be computed. Such a procedure would minimize systematic errors.

REFERENCES

1. Green, M. and Cosslett, V. E., J. Phys. D, 1, P245 (1968)

2. Lifshin, E., Proceedings of the Ninth Annual Conference of the Microbeam Analysis Society, Ottawa, Paper 53 (1974)

3. Beaman, D. R., private communication, 1974

4 Heinrich, K. F. J., Yakowitz, H. and Vieth, D. L., Proceedings of the Seventh National Conference on Electron Probe Analysis, San Francisco, Paper No. 3, (1972)

TABLE 1

Coefficients for Fit to Absolute Yield Data

for $K\alpha_{1,2}$ + $K\beta$ Emission Lines

Element	b	a
Mg	1.42	$.114 \times 10^{-4}$
Si	1.35	$.316 \times 10^{-4}$
Ti	1.51	$.631 \times 10^{-4}$
Cr	1.52	$.741 \times 10^{-4}$
Ni	1.47	$.933 \times 10^{-4}$
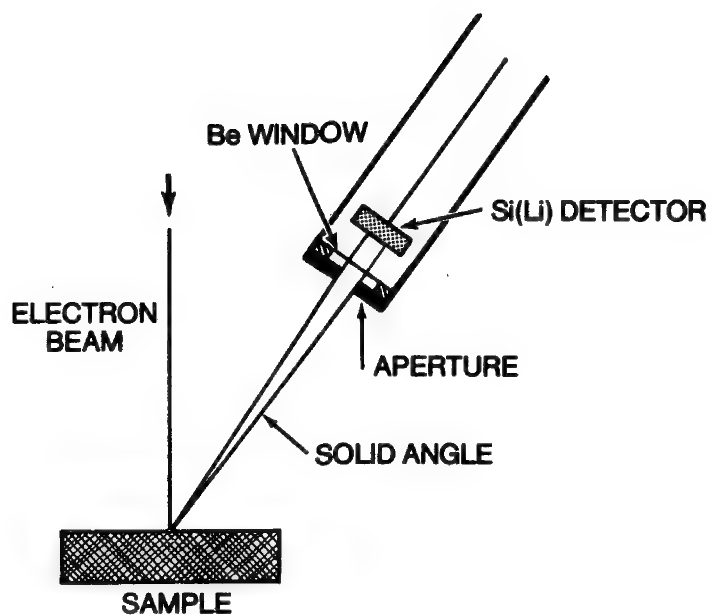
FIGURE 1
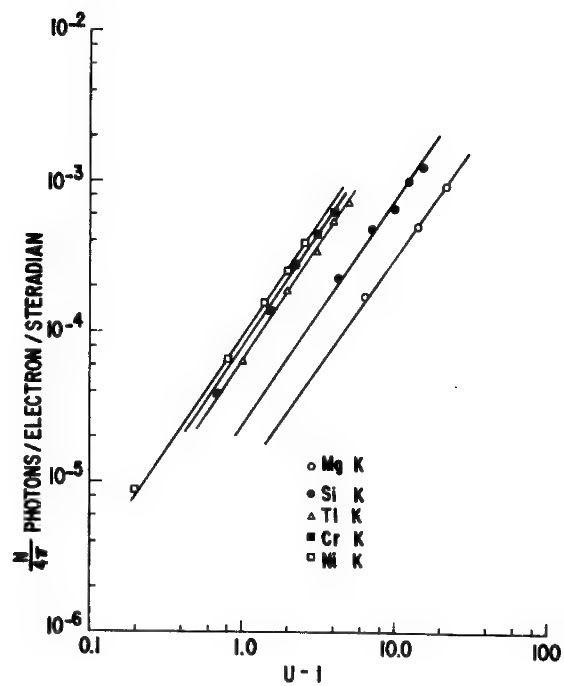
FIGURE 2

Measuring Detector Entrance Windows

by John C. Russ
EDAX Laboratories

Quantitative calculations involving energy-dispersive x-ray spectra require knowledge of several important instrument parameters. In addition to such well-accepted ones as electron voltage, specimen surface orientation, and spectrometer resolution, the thickness of the entrance window is very important. It is needed to compute the spectrometer efficiency as a function of energy, both in calculations of relative pure element intensity in the case where standards of other elements are used, and in the calculation of background in the spectrum arising from continuum x-rays. In the latter case it is particularly important since the low energy background (where detector efficiency varies most rapidly) is the most difficult part to fit accurately, because of its high curvature and the presence of prominent absorption edges.

As a simple and reasonably effective method for measuring window thickness we have for several years used the ratio of L to K lines from copper. Knowing the analyzing conditions (kV and specimen orientation) gives the relative emitted intensities, which can then be used in a straightforward absorption calculation with Beer's law to get the "thickness" of the window. The difficulty arises from the fact that the window consists of not only the beryllium foil (which is itself not of uniform thickness across its area) but also inactive, or dead, silicon on the front face of the detector, and a thin evaporated gold contact. Clearly, measurements at two energies are inadequate to solve for this many variables.

To obtain the individual thicknesses we have found it practical to use the spectrum from a graphite stub. The spectrum shows several features which give information about the composite entrance window: absorption edges for the silicon, and less prominently the gold; a silicon peak arising from fluorescence of the dead layer; and a general fall off in measured intensity at low energies (in the 1 - 1.6 keV range). By simple least squares fitting of these multiple data points we can separately calculate the individual layers, using assumed values of absorption coefficients and densities.

The results allow the recalculation of the complete spectrum, which as shown on the following page agrees quite satisfactorily with the measured spectrum. It is an open question as to whether or not the values obtained are truly accurate. The irregular thicknesses of all three components, and doubtful fundamental parameters, suggest that they are not. However, as long as the same values for thicknesses and fundamental parameters are used in calculations of x-ray absorption, the results will be self-consistent.
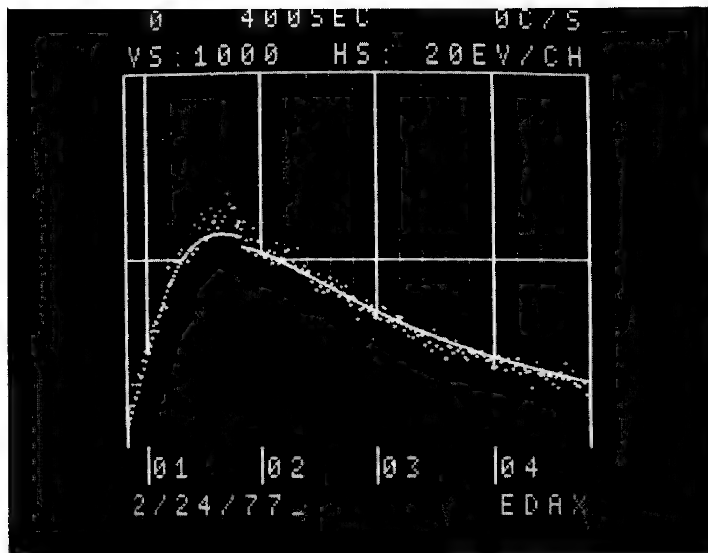
Experience suggests that Be window thicknesses which physical con-
tacting measurements indicate to be in the 7 - 8 μm (by manufactur-
ers specifications 0.3+ mil) range measure from 7 to 10 μm by the
absorption method. These values increase if the x-ray path is not
perpendicular to the window. Silcon dead layers can vary from 500
to 3500A, with 2000A being quite common. Gold contact layers are
normally so thin (<100A) that they cannot be measured with much
accuracy, and may for practical purposes be ignored in calculating
spectrometer efficiencies.

The author will provide a BASIC language listing of the program used
to make the calculation, on request.

SEM of High Sulfur Coal

by

Raymond T. Greer

Department of Engineering Science and Mechanics,
Engineering Research Institute,
and Energy and Mineral Resources Research Institute,
Iowa State University
Ames, Iowa 50011

The microstructure of coal is determined and characterized by combined scanning electron microscope - energy dispersive analysis techniques. Microstructural information on a micrometer size scale is correlated with microchemical information developed by energy dispersive X-ray microanalyses to establish the presence and distribution of pyrite, the primary sulfur bearing inorganic phase in coal. Other complementary analytical techniques such as X-ray diffraction and conventional reflectance and petrographic microscope studies are employed as well. This study evaluates particle size, shape and distribution factors which bear on decisions to try to remove additional sulfide particles to reduce the sulfur content. Subsamples are obtained from complete channel samples or sources such as raw material prepared as appropriate to the major methods of coal conversion.

Data from specimens from six strip mines and two shaft mines in Iowa provide the primary information to be reported. Conventional chemical analyses for these coals show an approximate range of 3 to 7 weight percent for total sulfur and 2 to 4.5 weight percent for pyritic sulfur depending on the particular mine. A single crystal form(individual crystals) of pyrite predominates below 1 μm particle diameters; framboids (agglomerates of single crystals) are important form of pyrite over a size range of a few micrometers to 30 μm diameter; and larger pyrite masses (polycrystalline pyrite, massive intergrowths of pyrite crystals) form the third major category of pyrite observed. The proportion of pyrite in various size ranges is determined and indicates that the major occurrence of the pyrite can be as particles or groupings less than a few hundred micrometers in diameter.

Several practical implications of the research findings can be summarized as follows:

1) useful insight has been gained in understanding the difficulty of sulfur removal using conventional techniques on certain high sulfur coals,
2) microstructural - chemical information suggests an important basis of coal cleaning variations to be expected from mine to mine,
3) uncertainties are to be expected for standard sulfur chemical determinations (a fraction of the pyrite may never get into solution and this can contribute to inaccuracy in total sulfur, pyritic sulfur and organic sulfur values), and
4) coal is generally crushed to -200 mesh at most utilities, but is then burned directly without attempts to clean it at this stage and for this size (-76 μm diameter particles) . . . due to the presence of large amounts of pyrite at this stage, innovative cleaning techniques may offer an important potential to upgrade the coal through additional sulfur removal.

An Energy Dispersive Spectrometer for Elements from 6 to 92

A. Sandborg
R. Lichtinger

Based on more than four years experience with so-called "windowless" energy dispersive detectors, and two generations of prototypes, we believe that the EDAX carbon-oxygen-nitrogen "ECON" detectors have now reached the state of development useful for routine application to general analytical work. They provide the scanning electron microscopist with analytical capability for ultra-light elements down to carbon, while suffering no important limitations for heavier elements. The design has proved to be reliable, easily used, and long-lived.

In a series of technical papers (1-4) the evolution of the design and applications have been described. The present detecting unit design can be interfaced to many SEM's. It requires a port with a 38 mm. diameter (minimum). The microscope vacuum quality is not a critical area of concern, as the detector is well protected by a cryo-trap. When samples that introduce large amounts of contamination are analyzed, a thin organic window can be selected (from outside the vacuum chamber) to further protect the detector, with only a slight loss in light element sensitivity. This window is also used when strongly cathodoluminescing samples are analyzed, to reflect light photons.

The external selector can also be used to close and seal the standard beryllium window, which may be left in place for routine analysis of elements with x-ray energies above 1 keV. The window must also be closed when air is admitted to the sample chamber, as for example in changing samples. To prevent accidents, the window selector is equipped with a microswitch for connection and interlocking with the microscope vacuum control system.

Because of the need to protect the detector from backscattered electrons, a magnetic electron trap is positioned in front of it. The field of the magnet is contained by a front plate so that it cannot affect the electron beam or secondary electron collection in the SEM. The electron trap and cold trap in front of the detector determine the minimum distance from the sample to the detector, but they also form an excellent collimator to eliminate stray x-rays so that no further external collimator is required. In many cases the solid angle is as great or greater than that of conventional energy dispersive detector designs used on SEM's as recently as four years ago. In addition, for most bulk samples the count rates may be increased as needed by increasing the electron beam current.

The open-window ECON detector has been shown to give practical detection of carbon, nitrogen and oxygen. Detection limits of less than 0.5% carbon in iron can be readily achieved. Interference with the peaks of the light elements by L and M peaks of heavier elements has turned out to be less of a problem than was originally feared might be the case. In addition to qualitative and comparative applications, our published reports have thown that it is possible to make good scanning x-ray images. Semiquantitative and quantitative results can be obtained provided that appropriate methods are used. For coating thickness measurements, calibration curves should be used. For bulk analyses, it is best to use standards both to determine the relative pure element intensities and the peak shapes.

ECON detecting units are now available for many SEM's, and are compatible with existing EDAX multi-channel analyzers. They provide additional analytical capability and versatility for the microscopist.

References

1. N. C. Barbi, A. O. Sandborg, J. C. Russ, C. Soderquist, IITRI/SEM/74, p. 151-158

2. N. C. Barbi, J. C. Russ, IITRI/SEM/75, p. 85-91

3. J. C. Russ, G. C. Baerwaldt, W. R. McMillan, X-Ray Spectrometry, 5, 1976 p. 212-222

4. J. C. Russ, IITRI/SEM/76
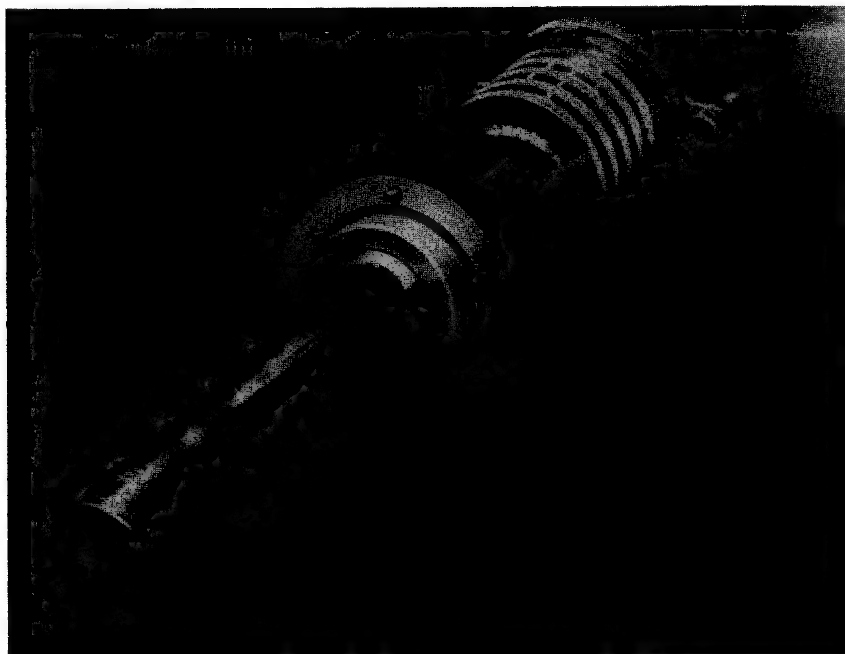
QUANTITATIVE ANALYTICAL ELECTRON MICROSCOPY

G.W. LORIMER

Joint University and UMIST
Department of Metallurgy
University of Manchester
Manchester M1 7HS
England.

Introduction

The forté of the technique of Analytical Electron Microscopy is the capability of correlating high resolution morphological information and crystallographic data with chemical composition. The chemical analysis can be performed by a variety of methods which include X-ray spectrometry and electron energy loss or Auger electron spectrometry. At the present time X-ray spectrometry has the distinct advantage over the other techniques in that quantitative analyses can be carried out for all elements $Z \geqslant 11$ by simple modifications of the well understood and widely accepted microprobe analysis procedures.

Quantitative Analysis

The characteristic X-ray intensity from a given element in a typical specimen which is suitable for examination in the transmission electron microscope is a function of specimen thickness as well as chemical composition. Therefore a technique in which the absolute X-ray intensity from the specimen is compared with that from a standard of known composition - as is done during the microprobe analysis of bulk specimens - has severe limitations.

To a first approximation X-ray absorption and fluorescence effects can be neglected and the <u>ratio</u> of two characteristic X-ray intensities, I_A/I_B, is simply related to the corresponding weight fraction ratios, C_A/C_B, by the expression

$$C_A/C_B = k_{AB} \ I_A/I_B \tag{1}$$

k_{AB} is a constant at a given accelerating voltage and is independent of variations in the specimen thickness. If I_A and I_B are measured simultaneously k_{AB} is also independent of the beam current; if the technique is to be extended to a number of elements the energy dispersive X-ray detector has an obvious advantage over the crystal spectrometer.

Experimental values of k_{AB} for K and K_α X-ray intensities have been obtained by Cliff and Lorimer[1] from thin mineral and alloy standards, by Morgan et al[2] from evaporated salts and by numerous authors for salts in an organic matrix (see for example Hall[3]). Similar data for L lines has been published by Goldstein et al[4] and Sprys and Short[5].

Calculation of a calibration curve for the ratio of K_α radiation to various elements, X, relative to Si ($k = (C_x/C_{Si}) / (I_{Si}/I_x)$) has been carried out by Goldstein et al[4] using the expression

$$k = \frac{A_x (Q_K \ \omega_K \ a)_{Si} \exp - \mu/\rho_{Be}^{Si} \ \rho y)}{A_{Si}(Q_K \ \omega_K \ a)_x \ \exp - \mu/\rho_{Be}^{x} \ \rho y)} \tag{2}$$

where **A** is the atomic weight, Q_K the K shell ionization cross section ω_K the fluorescence yield, a the $K_\alpha/K_\alpha + K_\beta$ ratio and absorption data relevant to the Be window of the solid state detector. Figure 1 shows the comparison between the calculated k values of Goldstein et al[4] and the experimental values of Cliff and Lorimer[1]. Q_{BP}, Q_{GC} and Q_{MM} have been calculated using
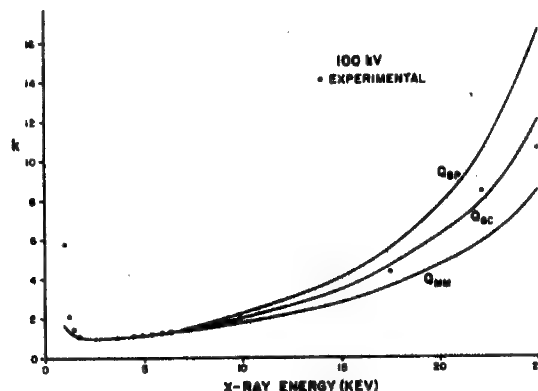
Figure 1. Comparison of calculated and measured k values at 100 kV for K and K_α lines (from Goldstein et al[4]).

equation 2 and k shell ionization cross-section formulas proposed by Powell[6], Green and Cosslett[7] and Mott and Massey[8], respectively. The correlation between the calculated and measured k values is excellent using the Green and Cosslett[7] expression for k shell ionization cross-sections for Z ⩾ Si. The deviation between the two values for low Z was thought to be due to the presence of a polycarbonate film between the X-ray source and the detector[4], but experiments carried out without the film in place have not produced a closer agreement between the two curves.

X-ray Absorption

    When the sample thickness is increased beyond the limit where the thin film criterion is valid account must be taken of X-ray absorption in the specimen. As a ratio of characteristic X-ray intensities is monitored it is the <u>difference</u> in X-ray absorption coefficients which must be considered: if two elements have similar values of μ/ρ the ratio of their characteristic X-ray intensities will not be changed by absorption in the specimen. The effect of absorption in the sample on the observed X-ray intensity ratio has been discussed in detail by Goldstein et al[4]. Figure 2, which is taken from their paper, shows the variation in the observed value of k_{AB} relative to that for an infinitely thin foil k_{AB}(T.F.) as a function of mass thickness/2 for various values of

$$\Delta_{XB-A} = (\mu/\rho_{SPEC}^B - \mu/\rho_{SPEC}^A) \cdot \csc\alpha \qquad (3)$$

where α is the take-off angle.

    In order to account for X-ray absorption it is necessary to know the thickness of the specimen. This can be determined by one of several techniques which include: tilting the foil after the analysis and measuring the separation of the contamination spots produced on the top <u>and</u> bottom of the foil during

analysis[9], using a band of white radiation as a monitor of specimen thickness, Hall[3] or by convergent beam diffraction (Kelly et al[10], Rao[11]).
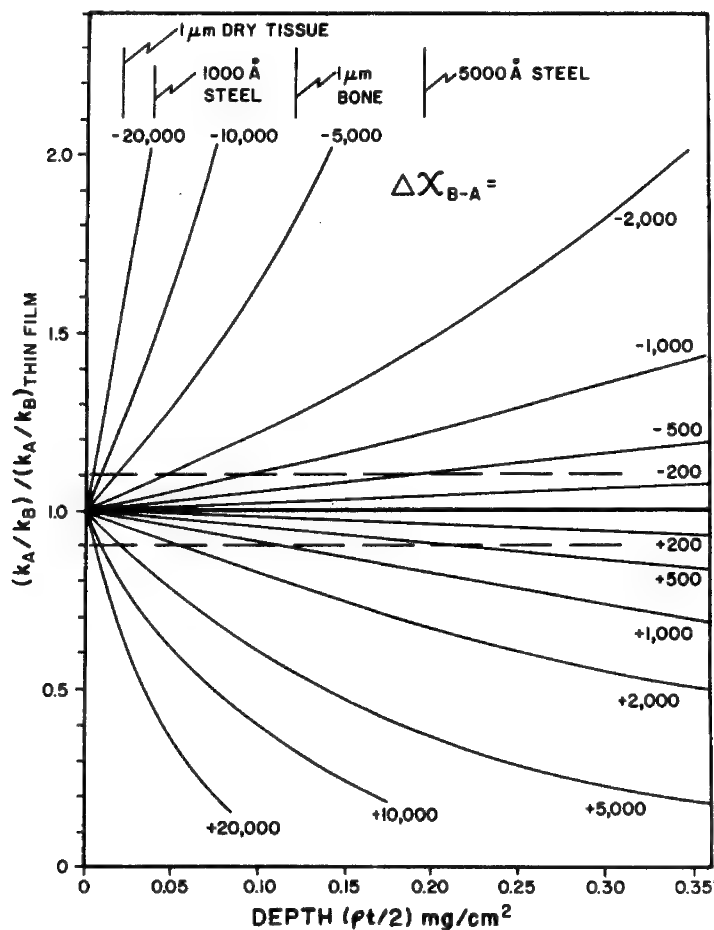
Figure 2.   Variation of k_{AB}/k_{AB}(T.F.) as a function of thickness for various values of ΔX_{B-A} (from Goldstein et al[4]).
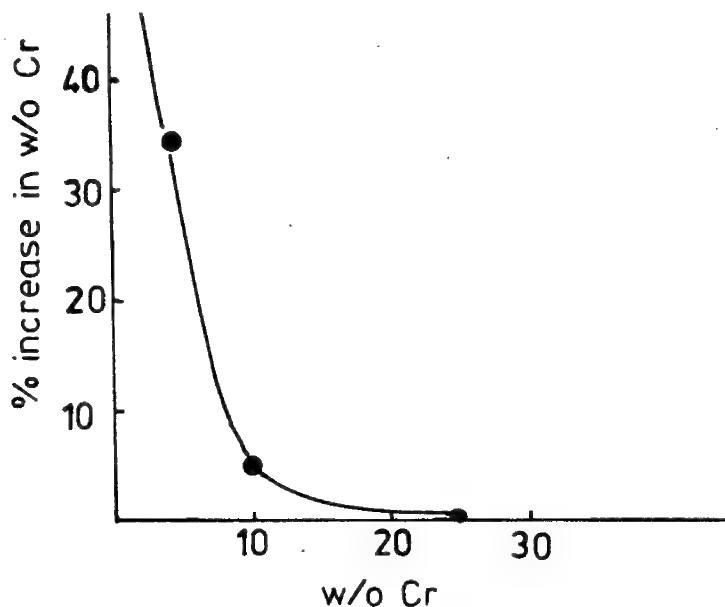
Figure 3.   Effect of fluorescence on the apparent Cr concentration in thin foils (2000-5000 Å) of Fe-Cr alloys.

X-ray Fluorescence

    Figure 3 illustrates the effect of X-ray fluorescence in increasing the apparent chromium concentration in thin foils of three Fe-Cr alloys. The apparent Cr concentration of the alloys is not a sensitive function of specimen thickness and, save for the effects of absorption in thick regions of the specimen and oxide films at the very edge (see below), give reproducible values. The results indicate that where significant fluorescence effects are predicted for the bulk sample   a fluorescence correction must be made to the thin film data.

Surface Films

    Surface films which have a different composition from the bulk sample may be produced during the preparation of thin foils. This is a common occurrence during the electropolishing of metallic samples where aggressive oxidizing conditions may exist. Although the film may only be a few tens or hundreds of Angstroms thick, this may be significant proportion of the total sample in the thin regions of the specimen and the analysis obtained will reflect this. Figure 4 shows the variation in I_{Cu}/I_{Al} for an Al-4w/o Cu alloy
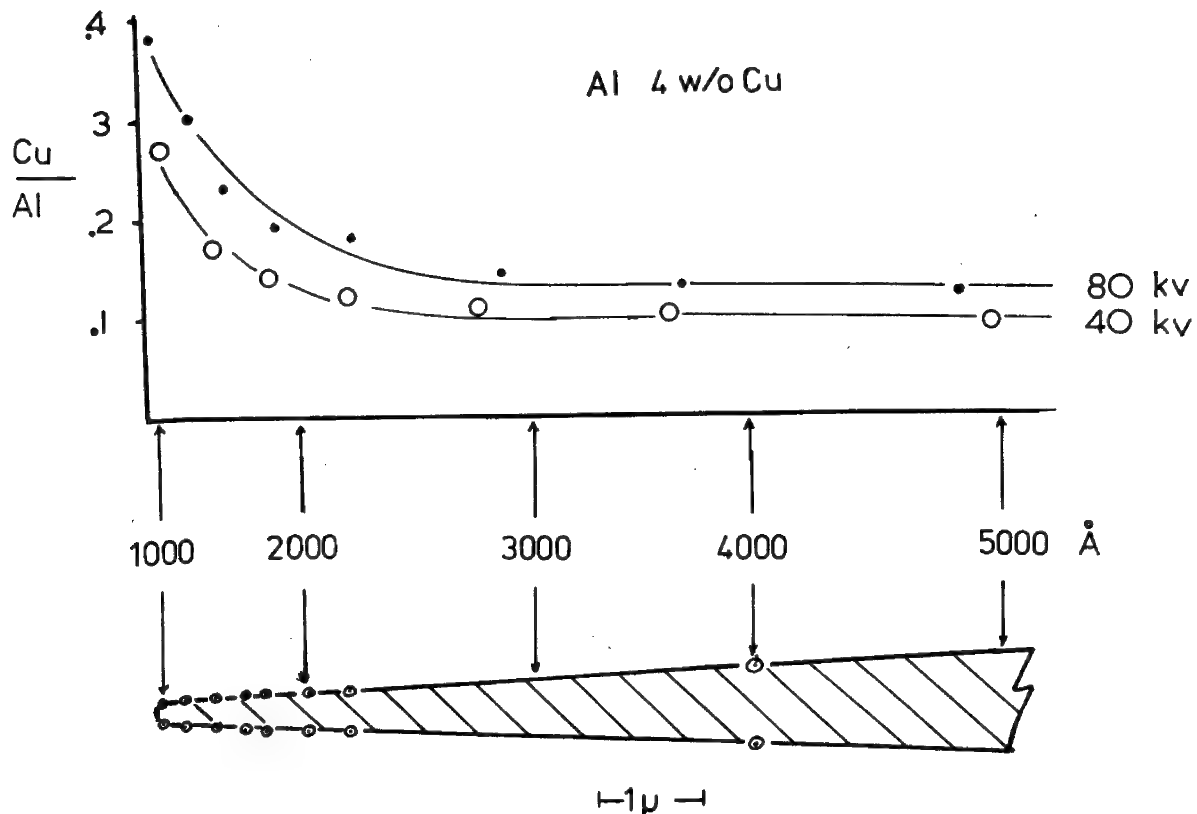
Figure 4.   Al-4 w/o Cu electropolished thin foil showing variation in Cu/Al ratio as a function of specimen thickness (Morris[12]).

as a function of specimen thickness. The apparent increase in the copper
concentration at the edge of the foil is due to the formation of a copper-
rich oxide film. Similar results have been observed in the author's laboratory
when examining other aluminium alloys and numerous steels. With steel samples
it is often possible to eliminate the effect by argon ion etching the sample
for a few minutes at 2-3 kV after electropolishing. In aluminium alloys ion
etching often does not eliminate the effect, although Morris[12] has reported
that ion etching in UHV is successful in removing the Cu-rich surface layer
in Al-Cu.

Spatial Resolution

The spatial resolution for chemical analysis in a thin foil is a function
of Z, specimen thickness and the accelerating voltage. While a detailed
calculation is best accomplished using Monte-Carlo procedures, Goldstein et al[4]
have considered beam broadening arising from a single elastic scattering event.
Figures 5a and b are produced from the data given in Reference 4 and clearly
show the importance of the use of a high accelerating voltage and very thin
specimens if a spatial resolution of a few hundred Angstroms is to be obtained.
These results indicate that it is not possible to obtain a spatial resolution
of a few tens of Angstroms with conventional (electropolished and ion thinned)
thin specimens, even if the analysis probe had, effectively, zero diameter.
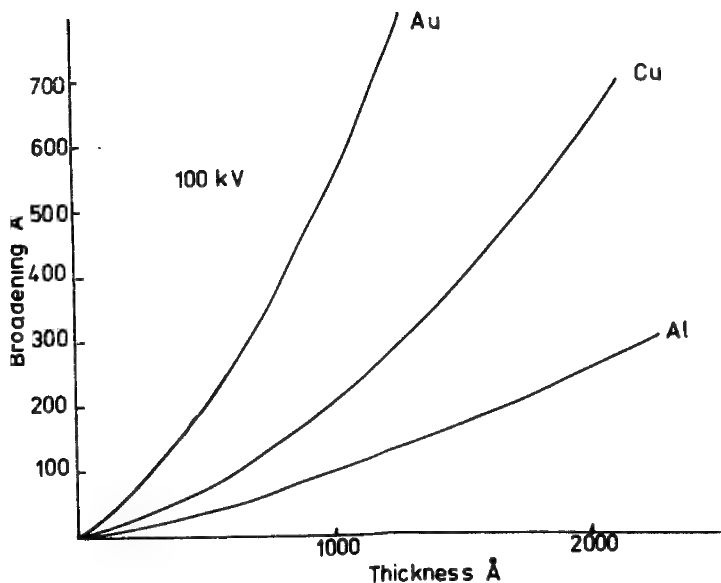
Figure 5a. Variation in beam
broadening as a function of Z
and thickness at 100 kV.
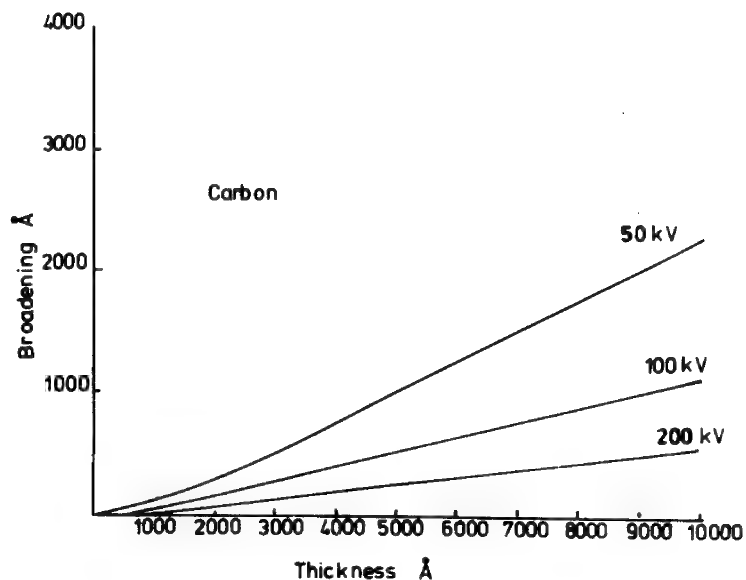
Figure 5b. Variation in beam
broadening as a function of
thickness and accelerating voltage.

Acknowledgements

References

1. G. Cliff and G.W. Lorimer, J. Microscopy, 103, 1975, 203-207.

2. A.J. Morgan, T.W. Davies and D.A. Erasmus, J. Microscopy, 104, 1975, 271-280.

3. T.A. Hall, In Physical Techniques in Biological Research, 2nd Edition, Vol. 1A, Editor G. Oster Academic Press, New York and London, 1971, 157-275.

4. J.I. Goldstein, J.L. Costley, G.W. Lorimer and S.J.B. Reed, submitted to SEM/1977, Editor Om Johari.

5. J.W. Sprys and M.A. Short, Proc. 11th Annula Conference, Microbeam Analysis Society, Miami, Paper 9A, 1976.

6. C.J. Powell, In Workshop on Monte Carlo Electron - Trajectory Calculations, 1977, to be published.

7. M. Green and V.E. Cosslett, Proc. Phys. Soc. 78, 1961, 1206-1214.

8. N.F. Mott and H.S.W. Massey, The Theory of Atomic Collisions, Oxford University Press, London, 1949, 243-244.

9. G.W. Lorimer, G. Cliff and J.N. Clark, in Developments in Electron Microscopy and Analysis, EMAG 75, Editor J.A. Venables, Academic Press, London, 1976, 153-156.

10. P.M. Kelly, A. Jostons, R.G. Blake and J.G. Napier, Phys. Stat. Sol. 31, 1975, 771-780.

11. P. RaO, Proc. 34th Annual EMSA Meeting, 1976, 546-7.

12. P.C. Morris, Private Communication.

MICRO ANALYTIC METHODS IN STEM: DIFFRACTION, EDS AND DARK FIELD IMAGING

R. H. Geiss

IBM Research Laboratory
San Jose, California 95193

A new era in the microcharacterization of materials has evolved following the introduction of scanning attachments for transmission electron microscopes. It is now possible to obtain selected area diffraction patterns from 25 Å areas, elemental analysis from areas less than 200 Å and high resolution dark field and stereo imaging of extremely small crystallites. The purpose of this paper is to discuss and illustrate the use of these techniques in the study of thin films.

Micro-diffraction

Diffraction patterns from very small areas may be obtained using either beam-rocking [1] or convergent beam techniques. With the beam-rocking method the sample is positioned near the center of a strong condenser-objective lens and the microscope is used in the imaging mode at very high magnification. The incident beam is pivoted about the specimen forming a sequence of static dark field images in the image plane of the objective lens.

These images are imposed on the STEM detector and yield intensity maxima whenever Braggs law is satisfied. The associated display on the CRT thus corresponds to a diffraction pattern from the area of the image intercepted by the detector. With this technique diffraction patterns from areas 25 Å in diameter have been obtained. As there is little restriction on the size of the incident beam, a large beam may be used with minimum contamination of the specimen resulting.

The fixed probe or convergent beam method is more widely used principally because of relaxed specimen location requirements. Here a small probe is positioned over the area of interest on the specimen, often in association with STEM imaging. A diffraction pattern from this region is formed in the back focal plane of the objective lens and viewed directly on the viewing screen. Severe contamination of the sample often results even for short beam exposures (10-30 seconds) to the same area. Diffraction patterns obtained by both methods are similar with nominal resolution of 10^{-3} radians.

Using a slightly larger probe, more accurate diffraction data in the form of zone axis patterns (ZAPS) may be obtained from slightly larger diffracting volumes.

The detail in these patterns contains much more crystallographic information than the standard convergent beam patterns. For example, ZAPS have been used to identify complex crystal structures, study lattice parameter changes on the order of 1 part in 10^4 and infer chemical fluctuations on a very fine scale [2].

Micro-elemental Analysis

Recent Monte Carlo calculations and experimental evidence [3] have demonstrated EDS X-ray elemental analysis from areas less than 200 Å diameter. The counting rate was too low to allow high precision quantitative analysis, but the presence or absence of an element was easily detected. With the high brightness guns available it should be possible to achieve even better resolution, possibly less than 100 Å. However, Monte Carlo calculations show that the angular scattering of the incident electrons provides a lower limit to the lateral resolution which depends on many factors including the incident probe size, operating voltage, material, thickness and take-off angle.

Many experimental parameters must be controlled to minimize extraneous "background" spectra [4]. This includes taking precautions which minimize beam tailing [5] effects and using optimum electron optical conditions. These are especially important when investigating very small areas or low concentrations of elements [6].

Dark Field Imaging

High resolution transmission dark field images of selected very small areas may be obtained using the beam-rocking microdiffraction technique by stopping the pivoting incident beam at the diffraction condition of interest. Using this technique we have obtained excellent dark field micrographs from selected areas, usually individual grains, less than 30 Å in diameter. Conversely, under convergent beam diffraction the detector is positioned over any diffracting beam and a scanning image is formed. Theoretically, the two images should be the same, but in practice scanning images have a much poorer S/N than transmission images and, in fact, may not even convey the same diffraction contrast information [7]. Orienting the region of interest to different crystallographic orientations allows one to do defect analysis over small areas, with a practical size limit determined by the tedium of using the goniometer.

Combining the technique of 2 1/2D dark field stereo imaging [8] together with beam rocking high resolution dark field imaging enables one to obtain stereo images showing the 3-dimensional distribution of very small crystallites

20-30 Å in diameter in evaporated films with only those grains oriented within a selected crystallographic zone inside the film observed [9].

References

[1]   R. H. Geiss, SEM/IITRI/I 1976, p. 337-343 (1976).

[2]   B. F. Buxton, J. A. Eades, J. W. Steeds and G. M. Rackham, Phil. Trans. Roy. Soc. 281, p. 171-194 (1976).

[3]   D. F. Kyser and R. H. Geiss, these proceedings.

[4]   J. I. Goldstein and D. B. Williams, SEM/IITRI/I 1977, p. 651-662 (1977).

[5]   R. B. Bolon and M. D. McConnell, SEM/IITRI/I 1976, p. 163-170 (1976).

[6]   D. C. Joy and D. M. Maher, SEM/IITRI/I 1977, p. 325-334 (1977).

[7]   H. L. Fraser, M. H. Loretto and I. P. Jones, SEM/IITRI/I 1976, p. 329-336 (1976).

[8]   W. L. Bell, J. Appl. Phys. 47, p. 1676-1682 (1976).

[9]   R. H. Geiss, to be published.

SPATIAL RESOLUTION OF X-RAY MICROANALYSIS IN STEM

D. F. Kyser and R. H. Geiss

IBM Research Laboratory
San Jose, California 95193

The incorporation of energy-dispersive X-ray spectrometers into STEM instrumentation now allows chemical microanalysis of extremely small volumes in thin foils. With finite thickness foils, angular scattering and energy loss of the incident electrons within the foil will determine the minimum volume in which X-rays are produced. In this work, Monte Carlo calculations of electron scattering, X-ray production, and direct experimental measurements of spatial resolution in X-ray microanalysis are reported.

The Monte Carlo simulation of electron trajectories and X-ray production is similar to that utilized previously by Kyser and Murata [1] for chemical analysis of thin films on substrates, except that the substrate is removed in the present calculations. The electron trajectory simulation is terminated when each electron exits the foil. Consequently, a larger number of electron trajectories can be economically simulated, in contrast to the thick target case. The Monte Carlo model utilizes a "single-scattering" approach wherein the primary electrons are elastically scattered along their trajectory by the atomic nuclei of the target, and lose energy continuously (i.e., linearly with path length) between successive elastic scattering points due to inelastic scattering by the atomic electrons. The inelastic scattering is assumed to be small angle in comparison to the elastic scattering. The production of X-rays along the trajectory is determined by the energy-dependent cross section for ionization of the particular X-ray level of interest. With high beam voltages (e.g., 100 kV) and very thin foils (e.g., 1000 Å) the exact voltage-dependence of the cross-section is not critical for calculations of spatial resolution since the mean energy loss for electrons traversing the foil is relatively small, typically less than 1 volt/Å [2]. Hence, X-ray production in thin foils can be considered to occur almost monoenergetically.

Scattering of the incident electrons away from their direction of incidence is the major factor which determines the spatial resolution of STEM X-ray

microanalysis in foils. An extreme example of the magnitude of this effect is shown in Fig. 1 for 100 kV electrons incident on a 1000 Å Au foil. With 90° electron beam incidence, there will be cylindrical symmetry about the axis of incidence. The spatial distribution of X-ray production in the foil is calculated in the Monte Carlo technique with X-ray production categorized in a 2-dimensional cell histogram. The results shown in Fig. 1 may be thought of as X-ray production curves $\Phi(r)$ at specific values of depth z. The cell size was 25 Å square in Fig. 1, and 100,000 electron trajectories were simulated for each case. For the point source incident beam simulated, there is a large decrease in $\Phi(r = 0)$ as z increases, illustrating the strong effect of angular scattering away from the direction of incidence. Curves such as those shown in Fig. 1 can also be used to calculate $\Phi(z)$, the depth distribution X-ray production. Examples of this will be illustrated, and comments made about its implications in the self-absorption correction for quantitative analysis.

The lateral distribution of total X-ray production in a foil is obtained by summing the depth distribution of $\phi(r)$ at fixed radii and plotting the results in a normalized form $\phi(r)/\phi(\text{total})$ versus radius, r. $\Phi(r)$ is the sum of $\Phi(r)$ from r = 0 to r = r, over the foil thickness t and $\Phi(\text{total})$ is the total available X-ray production throughout the foil ($0 \leq r \leq \infty$). Parameters such as beam voltage E_0, foil thickness t, foil material Z, and beam "size" may then be compared. Finite beam "size" is simulated in the Monte Carlo method by specifying the standard deviation σ of an incident beam, assumed to be Gaussian. A Gaussian random number generator algorithm is used to specify the incident point of each successive electron simulated. Results are shown in Fig. 2 for the specific case of CuKα in a 1000 Å Cu foil. Note that even for $\sigma = 0$, which is the limiting case of incident beam size, there is still a practical limit of about 150 Å "resolution" (i.e., cylinder diameter) within which 90% of the total CuKα production occurs. The "resolution" has been arbitrarily chosen as the radius at the 90% value for $\Phi(r)/\Phi(\text{total})$.

As the electron beam diameter increases, the resolution of microanalysis decreases approaching the diameter $d(\text{FWHM}) = 2.36\,\sigma$ of the incident Gaussian beam, which is equivalent to neglecting the angular scattering of electrons within the foil.

The effect of angular scattering on resolution must be calculated for each specific case of interest (i.e., E_0, t, σ, etc.). Good agreement has been

observed between these Monte Carlo calculations of spatial "resolution" (using the 90% definition) and the calculations of Goldstein et al [3] who used a simple analytical model to approximate beam spreading in thin foils. However, the Monte Carlo method is more general because it is not restricted to ultra-thin foils, point source beams, or even normal beam incidence. Oblique beam incidence which is common [4], may be accommodated, but then another variable (tilt angle) is added to the already lengthy list of experimental variables.

Experimental measurements of the resolution of EDS analysis were made using the Philips 301 STEM electron microscope. Many precautions were taken to minimize the "background" contribution to the EDS spectrum. A thin foil of Si_3N_4 fluxed with Y_2O_3 was used for the experiments [5]. A yittrium rich $Si_3Y_2O_3N_4$ phase crystallizes at the triple points of Si_3N_4 grains. Measurements of Si/Y vs. distance with a small probe translated from the Si_3N_4 matrix to yittrium phase were made for various size probes. For example, with a probe of 150 Å diameter at 100 keV, a resolution of better than 180 Å was obtained for yittrium detection. Such data is consistent with the Monte Carlo calculations such as shown in Fig. 2.

A practical limitation on probe size is set by the available beam current. For extremely small probes, less than 500 Å with a conventional W gun, the X-ray counting rate is too low for quantitative analysis. But one is easily able to detect the presence or absence of an element and can determine semi-quantitative analysis for regions as small as 150 Å in diameter in thin specimens. For many experiments such data is quite satisfactory.

References

[1] D. F. Kyser and K. Murata, IBM J. Res. Develop. 18, 352 (1974).

[2] O. C. Wells, Scanning Electron Microscopy (McGraw-Hill, 1974), p. 38.

[3] J. Goldstein, J. Costley, G. Lorimer, and S. Reed, SEM/1977 (IIT Res. Inst., 1977), p. 315.

[4] R. H. Geiss and T. C. Huang, X-Ray Spect. 4, 196 (1975).

[5] The authors kindly thank Dr. David Clark, University of California, Berkeley, for the specimen.
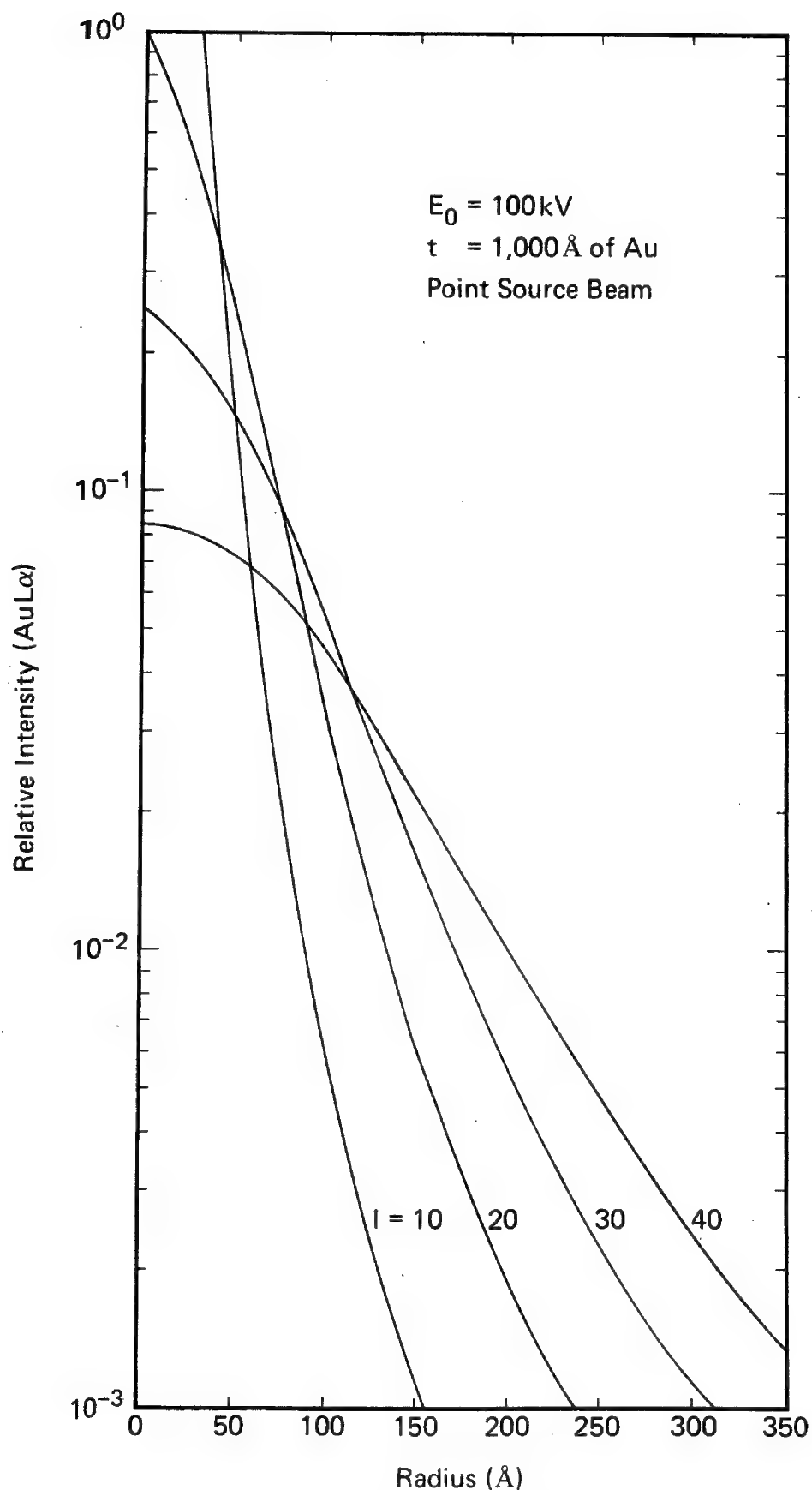
Figure 1. Monte Carlo calculations of the radial distribution of AuLα production versus depth for Au foil.
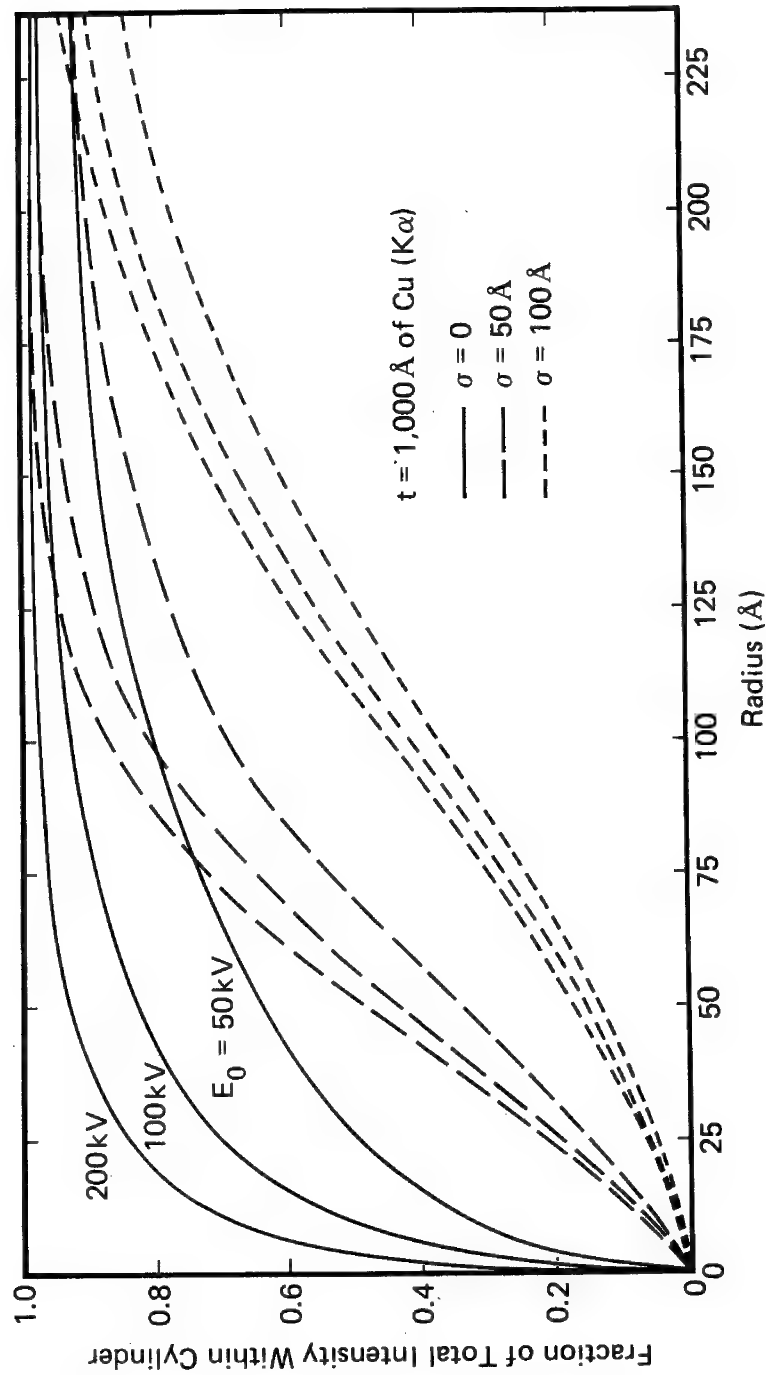
Figure 2. Monte Carlo calculations of the fractional CuKα production contained within a cylinder of radius R for Cu foil.

Ultimate Spatial Resolution of the X-ray Microanalysis of Thin Foils Using an Energy-dispersive Spectrometer

R. König, Battelle-Institut e.V. Frankfurt/M

The spatial resolution of x-ray microanalysis of thin foils is essentially determined by the diameter of the electron beam, if we neglect scattering effects leading to a broadening of the electron beam. With this presumption we can calculate the best attainable resolution considering only the peak/background ratio and the statistical fluctuation of the characteristic x-ray signal detected with an energy-dispersive spectrometer.

In the calculations we start with peak/background considerations taking into account not only the bremsstrahlungs-background generated in the specimen, but also bremsstrahlung, which stems from parts of the electron microscope or the specimen support grid. This radiation may also be detected, when an energy-dispersive spectrometer is used. The derived formula gives furthermore an impression about the influence of the used electron gun (tungsten, field emission etc.) and a beam or specimen drift which may be present. Finally we arrive at an expression for the minimum achievable beam diameter ϕ_{min} if we want to detect a given concentration c_A of the element A in the specimen. The formula has the following structure:

$$\phi_{min} = k_1 \; F_1^{3/8} \; c_A^{-3/4} \; t^{-3/8} \; (C_s/cm)^{1/4} \; (E_c/keV)^{9/8} \left(\frac{U \; (U-1)}{\ln^2 U} \right)^{3/8} \quad [cm]$$

with k_1 = constant value

F_1 = a function of a variety of parameters as the chosen channel width of the detector system, the type of the used electron gun, mass thickness of the specimen etc.

c_A = concentration of the element A

t = counting time

C_s = spherical aberration constant of the final condensor

E_c = critical excitation energy of the element A (K, L_{III}..)
U = overvoltage ratio

The voltage dependence of the above formula will be discussed. It is closely related to the influence of that amount of the bremsstrahlungs-background, which stems from parts of the electron microscope and the specimen support grid.
The peak/background ratio determines the detectibility of a concentration c_A, but it says nothing about the possibility to distinguish between two points with different concentrations of the element A. In this case we have to consider the difference between the two characteristic x-ray signals and their statistical fluctuations. This means, that we need a certain minimum amount of characteristic x-rays of the element A, to resolve a given concentration difference Δc_A, which leads directly to an expression for the minimum achievable beam diameter:

$$\phi_{min} = k_2 \ F_2^{3/8} \ (c_A/\Delta c_A^2)^{3/8} \ t^{-3/8} \ (C_s/cm)^{1/4} \ (E_c/keV)^{3/8}$$
$$\cdot (\ln U)^{-3/8} \quad [cm]$$

with:

k_2 = constant value
F_2 = a function determined by the mass thickness, atomic weight etc. of the specimen and the product of the spatial angle and the detection probability of the detector system

The two relations for the minimum achievable beam diameter give a measure for the best attainable spatial resolution in a given analytical problem. The ultimate spatial resolution is determined by the more unfavourable ϕ_{min} value calculated from the two expressions. Furthermore we can use the derived formulae to optimize our instrument and its settings in terms of spatial resolution. In a calculated example we will see that this may be of special interest in the analysis of elements with low atomic numbers.

CONTAMINATION AND ABSORPTION EFFECTS IN X-RAY
MICROCHEMICAL ANALYSIS OF THIN METAL FILMS

N. J. Zaluzec and H. L. Fraser
Department of Metallurgy and Mining Engineering
and
Materials Research Laboratory
University of Illinois at Urbana-Champaign
Urbana, Illinois 61801 U.S.A.

Over the last ten years several analytical techniques have been developed for quantitative x-ray microchemical analysis of specimens in a transmission electron microscope. In general, all of these methods rely on the validity of the Philibert "thin film" approximation, the basic assumptions being that for a sufficiently thin sample, the effects of energy losses in the incident electron beam, x-ray fluorescence (both by characteristic and continuum radiation), and x-ray absorption within the specimen can be ignored. Generally this "thin film" criterion has been applied to the case of electron transparent specimens; unfortunately such applications are not always valid. A systematic study involving a number of instrument parameters has been undertaken in order to evaluate the feasibility of quantitative x-ray analysis in a combined CTEM/STEM system equipped with a solid state Si(Li) x-ray detector. The results of this study show that instrumental effects seriously impair the ability to perform accurate quantitative analysis as well as degrade the ultimate sensitivity for detection of low concentrations of elements.

From this study, it seems that quantitative analysis in similar instruments is going to be extremely difficult. The limitations appear to be chiefly instrumental in nature. Unfortunately few investigations have treated the problem with sufficient detail

in the past in order to identify and correct for these effects. The two most serious complications arise from specimen contamination and continuum fluorescence effects; both of which, because of their nature, cannot be incorporated into the analytical models and hence must be eliminated by instrumental modifications. The effects of fluorescence are straightforward. In this case, hard x-ray generated within the microscope aperture system excite characteristic x-rays from the whole sample which then augment the electron induced x-ray spectrum. The effects of contamination are more complicated; clearly, the accumulation of significant yet unknown amounts of material on the specimen's surface leads to additional absorption terms which must be accounted for if quantitative results are desired. In addition, both of these effects cause drastic changes in the peak-to-background ratio measured from electron transparent foils and hence seriously affect minimum detectable mass measurements. Finally, it is shown that x-ray absorption effects within the sample itself can become important even when the sample is "electron transparent".

A Study of Spurious X-ray Production
in a Philips EM 300 TEM/STEM

D. B. Williams and J. I. Goldstein

Department of Metallurgy & Materials Science

Lehigh University, Bethlehem, Pa.

Recently it has become apparent that there is a serious obstacle to obtaining quantitative microanalysis data from thin foil specimens in combined TEM/STEM instruments equipped with energy dispersive X-ray detection facilities.[1] The problem is best illustrated by the so-called 'hole count.' That is, placing the electron probe down a hole in the specimen still results in a positive X-ray count, characteristic of a large region of the surrounding specimen. The problem has been documented by several investigators[2,3] and various solutions proposed for different microscopes. However, it is clear that the effect is instrument dependent and therefore any solution must be similarly selective. This paper reports a study and correction of the problem in a Philips EM300 TEM/STEM equipped with a rear entry N.S.I. 30 sq. mm energy dispersive X-ray detector, and a Tracor Northern multichannel analyzer.

The principal cause of the hole count is still a matter of some controversy, but it seems that major contributions must arise from X-ray continuum generated in the electron microscope condenser system, and from stray electrons not eliminated by the condenser apertures. With this in mind, a study of the electron optical layout of the EM300 condenser system has been made, with a view to locating possible sources of X-ray generation, and the subsequent possibility of such X-rays 'seeing' regions of the specimen outside that selected for microanalysis by the electron probe. Figure 1 is a diagram of the condenser system of the EM300. The diagram is to scale in the vertical direction but horizontal dimensions are exaggerated. The fixed and variable apertures are shown, and it is assumed that the electron probe is on the optic axis, thus defining the point desired for microanalysis. The points at which 100 kV electrons, e, can excite characteristic and continuum X-rays are listed 1-4. It is clear that a considerable amount of the X-rays can 'see' regions of the specimen. Since the C_2 aperture is used to control the final probe size, it is responsible for stopping the major flux of 100 kV electrons from travelling down the column.

Whilst the conventional 100 μm thick Pt aperture is sufficient to stop 100 kV electrons, it will only stop $\sim$ 48% of the Pt K_α characteristic X-rays produced at beam voltages > 78.4 kV. Furthermore, using the mass absorption constants C and n given by Heinrich[4] for

$$\mu/\rho = C \lambda^n$$

(where μ/ρ is the mass absorption coefficient and λ is the X-ray wavelength) and by extrapolating to shorter wavelengths, $\sim$ 25% of the 50 kV continuum and $\sim$ 30% of the 100 kV continuum X-rays will pass through the Pt aperture, at e_3 and e_4 in Fig. 1. Even if continuum radiation is produced at the C_1 fixed (e_1) or C_1 variable (e_2) $\sim$ 6.4% of the 50 kV and $\sim$ 8.7% of the 100 kV continuum will pass through both the C_1 and C_2 apertures. These latter two sources are not considered important, in view of the small angular fraction of the total continuum that can reach the specimen. Thus the C_2 variable aperture is considered the major source of spurious X-rays, and the placing of a Pb insert in the column directly below the aperture holder should prevent a substantial portion of both characteristic and continuum X-rays generated there, from reaching the specimen. Such an insert is shown in Fig. 1. It is calculated that a 1 mm thick Pb insert is sufficient, but a somewhat thicker piece is needed in order to be a self-supporting push-fit, in the TEM column. Electron optical considerations (mainly restriction of the conventional TEM image at low magnification and high C_2 defocus conditions) limit the internal diameter to a minimum of 1 mm.

It should be noted that this insert will not result in complete elimination of the problem, merely a reduction to acceptable levels. (In particular it is worth pointing out that the analysis described above indicates that such X-rays should be present in all TEM/STEM's operating at 100 kV using conventional 100 μm thick Pt apertures.) In addition the insert will also prevent any stray electrons passing around the C_2 aperture holder from reaching the specimen.

The conclusions drawn from Fig. 1 were tested by examining the characteristic spectra and hole counts in specimens of pure Al, Cu and Ag, both before and after insertion of the Pb. All spectra were obtained in 60 secs. counting time at fixed spot sizes and tilt angles using a low background Be-insert specimen holder, and all counts were integrated over a fixed channel range.

An idea of the effectiveness of the insert is given in Table 1. This lists the value of the ratio of the total hole count to the continuum background count obtained when the beam was placed on the specimen. Since the latter will vary with specimen thickness, the counts were normalized to the value obtained when the specimen characteristic peak contains 10^4 counts. Thus it may be considered that when the ratio is < 1 the spurious hole count will not have a significant effect on the accuracy of the spectral data obtained from the specimen, and thus meaningful microanalytical data may be obtained.

Clearly, in the specimens examined prior to insertion of the Pb, quantitative microanalysis would only be possible at 40 kV or less. This is consistent with the fact that the continuum generated above the specimen at 40 kV would be low compared to that generated at 100 kV, and therefore the amount coming down the column would not be significant.

However insertion of the Pb results in a large (~ 10X) decrease in the measured ratio, and in almost all cases reduces the hole count sufficiently to permit quantitative microanalysis. The exception is that of Cu at 100/80 kV. The reason for this is uncertain, but the Cu characteristic peak is the hardest radiation that was considered in this investigation.

With the Pb insert in the microscope, the peak to background ratio (P/B) was measured as a function of kV for specimens of Al, Cu, Ag and Au. The results are shown in Fig. 2. (In Al and Cu, K_α lines were measured, and in Ag and Au, L_α lines were measured.) From the figure it is clear that Al and Cu show the expected theoretical increase in P/B with kV, until 100 kV. This indicates that there is still a continuum effect, which is most prevalent at high kV, in agreement with the conclusions drawn from Fig. 1. However, both Ag and Au show no variation of P/B with kV which may be explained by the increase in specimen generated continuum at high atomic numbers.

Finally in common with other workers,[5] it was found that specimen contamination can invalidate the X-ray data obtained, as shown in Fig. 3. In a heavily contaminated Al foil P/B was observed to rise significantly with specimen thickness (indicated by increasing count rates). This demonstrates the severe effect of a contamination layer on very thin regions of the specimen, where absorption of characteristic Al X-rays

will be reflected in low values of P/B. Similar experiments on an initially clean Al foil resulted in only a slight rise of $\sim$ 10% over count rates from 3 x $10^3 \rightarrow$ 3 x 10^4/min.

Acknowledgements

References

1. Williams, D. B. and Goldstein, J. I., 1977 Scanning Electron Microscopy, Ed. O. Johari, IITRI, Chicago, Illinois I, 651.

2. Shuman, H., Somlyo, A. V. and Somlyo, A. P., 1976 Ultramicroscopy, 1, 317.

3. Zaluzec, N. J. and Fraser, H. L., 1976 Proc. 34th EMSA Meeting, Ed. G. W. Bailey, Claitors Publishing Division, 420.

4. Heinrich, K. F. J., 1966, 'X-ray Absorption Uncertainty,' The Electron Microprobe, Eds. McKinley, T. D., Heinrich, K. F. J. and Wittry, D. B., J. Wiley, 296-377.

5. Fraser, H., 1977, reported at AIME spring meeting, Atlanta, Georgia.

TABLE 1

Ratio of the total hole count to the specimen generated continuum background as a function of kV.

Aluminum	100 kV	80 kV	60 kV	40kkV	20 kV
Original Column	10.0	5.0	5.0	1.7	0.6
Pb insert below C_2	0.2	0.5	0.08	0.04	0.04
Copper	100 kV	80 kV	60 kV	40 kV	20 kV
Original Column	*	7.1	3.0	0.5	0.03
Pb insert below C_2	1.9	1.1	0.45	0.1	0.01
Silver	100 kV	80 kV	60 kV	40 kV	20 kV
Original Column	*	1.7	1.0	0.3	0.02
Pb insert below C_2	0.1	0.09	0.01	0.015	0.01

*Data not available
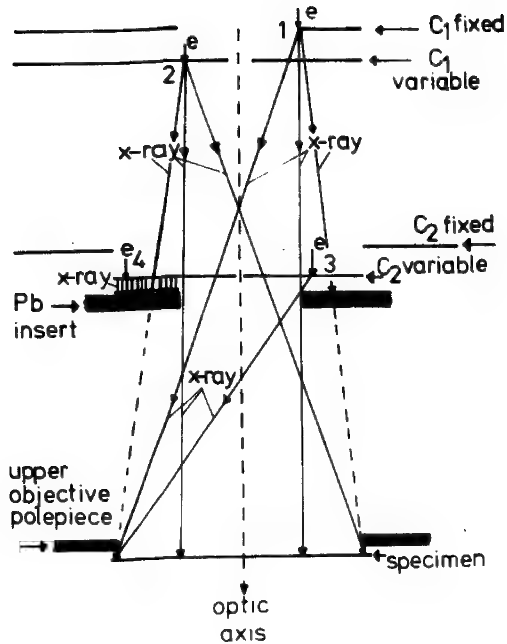
Fig. 1: The condenser system of the EM300 illustrating sources of spurious continuum and characteristic X-rays $e_1 \to e_4$. The placing of a Pb insert below the C_2 variable aperture is shown to prevent a considerable proportion of X-rays generated there from reaching the specimen.

Fig. 2: The variation of P/B with kV for pure elements of a wide range of atomic number.
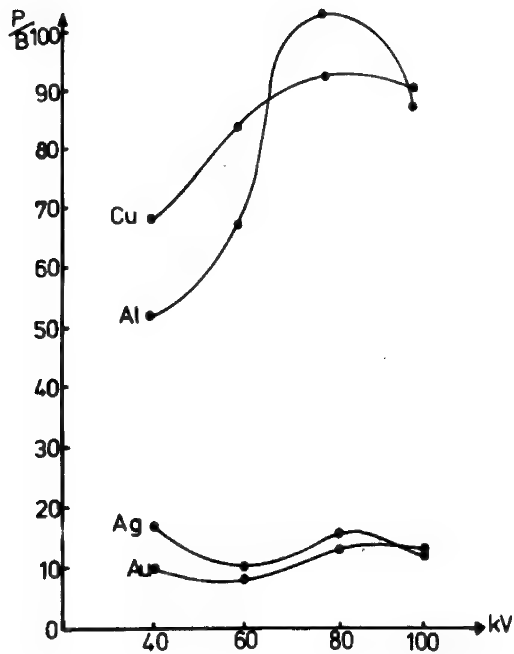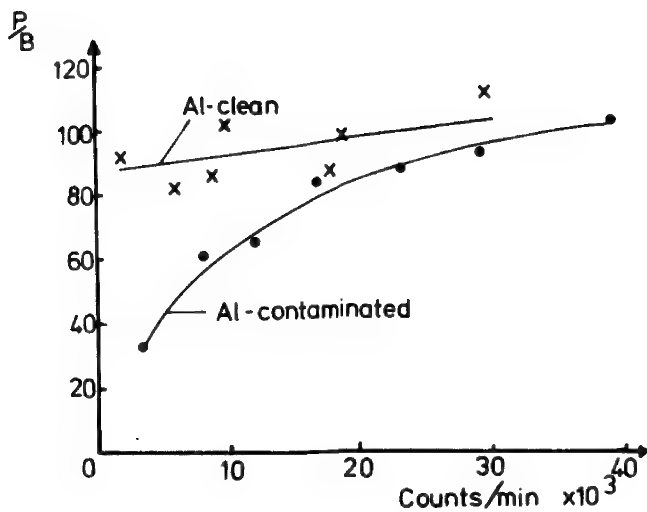
Fig. 3: The effect of contamination on the P/B ratio in pure Al as a function of specimen thickness.

INFLUENCE OF X-RAY INDUCED FLUORESCENCE ON ENERGY DISPERSIVE X-RAY ANALYSIS OF THIN FOILS*

E. A. Kenik and J. Bentley

Radiation Effects and Microstructural Analysis Group, Metals and Ceramics Division, Oak Ridge National Laboratory, Oak Ridge, Tennessee 37830

Cliff and Lorimer (1) have proposed a simple approach to thin foil x-ray analysis based on the ratio of x-ray peak intensities. However, there are several experimental pitfalls which must be recognized in obtaining the desired x-ray intensities. Undesirable x-ray induced fluorescence of the specimen can result from various mechanisms and leads to x-ray intensities not characteristic of electron excitation and further results in incorrect intensity ratios.

In measuring the x-ray intensity ratio for NiAl as a function of foil thickness, Zaluzec and Fraser (2) found the ratio was not constant for thicknesses where absorption could be neglected. They demonstrated that this effect originated from x-ray induced fluorescence by blocking the beam with lead foil. The primary x-rays arise in the illumination system and result in varying intensity ratios and a finite x-ray spectrum even when the specimen is not intercepting the electron beam, an 'in-hole' spectrum. We have developed a second technique for detecting x-ray induced fluorescence based on the magnitude of the 'in-hole' spectrum with different filament emission currents and condenser apertures. Table 1 shows that the 'in-hole' count rate is essentially independent of probe current when changes are produced by different apertures at constant filament emission. On the other hand, the 'in-hole' count rate is strongly dependent on filament emission current for constant probe current. Such dependences are inconsistent with the 'in-hole' spectrum arising from electron "tails" and indicate x-ray induced fluorescence of the specimen. A technique has been developed to analyze these x-rays by scattering them off a mylar film while the electrons pass through a hole in the film. The 'in-hole' spectrum so obtained contains x-ray signals from the specimen holder and scattered lead and molybdenum x-rays from the illumination system.

Figures 1a and 1b illustrate one effect of x-ray induced fluoresence on x-ray analysis using Ni-20 at. % Mo. Figure 1a presents integrated peak intensities as a function of foil thickness (~0.5 μm is the TEM visibility limit) and Fig. 1b presents the ratios of these intensities. Although the ratios for thickness <0.5 μm should be constant (for t >0.5 μm absorption of Mo L x-rays becomes significant), the uncorrected ratios (upper curve of each pair) increase markedly as the foil thickness decreases. This behavior arises from the finite 'in-hole' counts which are larger for higher energy x-rays and is consistent with x-ray induced fluoresence. However, this effect can be corrected for by simply subtracting the 'in-hole' counts from the integrated intensities and recalculating the ratios (lower curves in Fig. 1b).

A second x-ray induced fluorescence effect is associated with x-rays generated in the specimen holder either by backscattered electrons trapped in the objective lens field or by x-rays from the illumination system. X-rays from the holder cause x-ray induced fluorescence of the specimens resulting in incorrect intensity ratios for analysis. For the Ni—20 at. % Mo alloy, the Mo-Ni K_α ratio was determined to be 0.155 in a bronze holder and 0.183 in a beryllium holder. The excess nickel counts for the bronze holder arise from x-ray induced fluorescence of the nickel by the copper K_β x-rays. The use of low z specimen holders thus has two advantages: the removal of extraneous "system peaks" and the minimization of the above effect.

If the experimenter is aware of these experimental pitfalls and avoids their effects, more accurate quantitative analysis of thin foils can be performed using the ratio technique developed by Lorimer et al. (1).

1. G. Cliff and G. W. Lorimer, *J. Microsc.* 103, 203 (1975).
2. N. J. Zaluzec and H. L. Fraser, *34th Ann. Proc. of EMSA* (1976), 420.

Table 1. "In Hole" Count Rates From a Ni_4Mo Specimen as a Function of Probe Current and Condenser Aperture

Condenser Aperture Diameter (μm)	Probe Current (A)	Filament Emission Current (μA)	Count Rate (S^{-1})	
			NiK_α	MoK_α
400	2.5×10^{-9}	72	63.5	35.5
200	6.3×10^{-10}	72	61.0	34.7
100	1.4×10^{-10}	72	54.9	32.1
20	7.5×10^{-11}	72	54.6	31.3
200	1.5×10^{-10}	13	11.7	5.6
400	1.5×10^{-10}	5	3.4	1.6
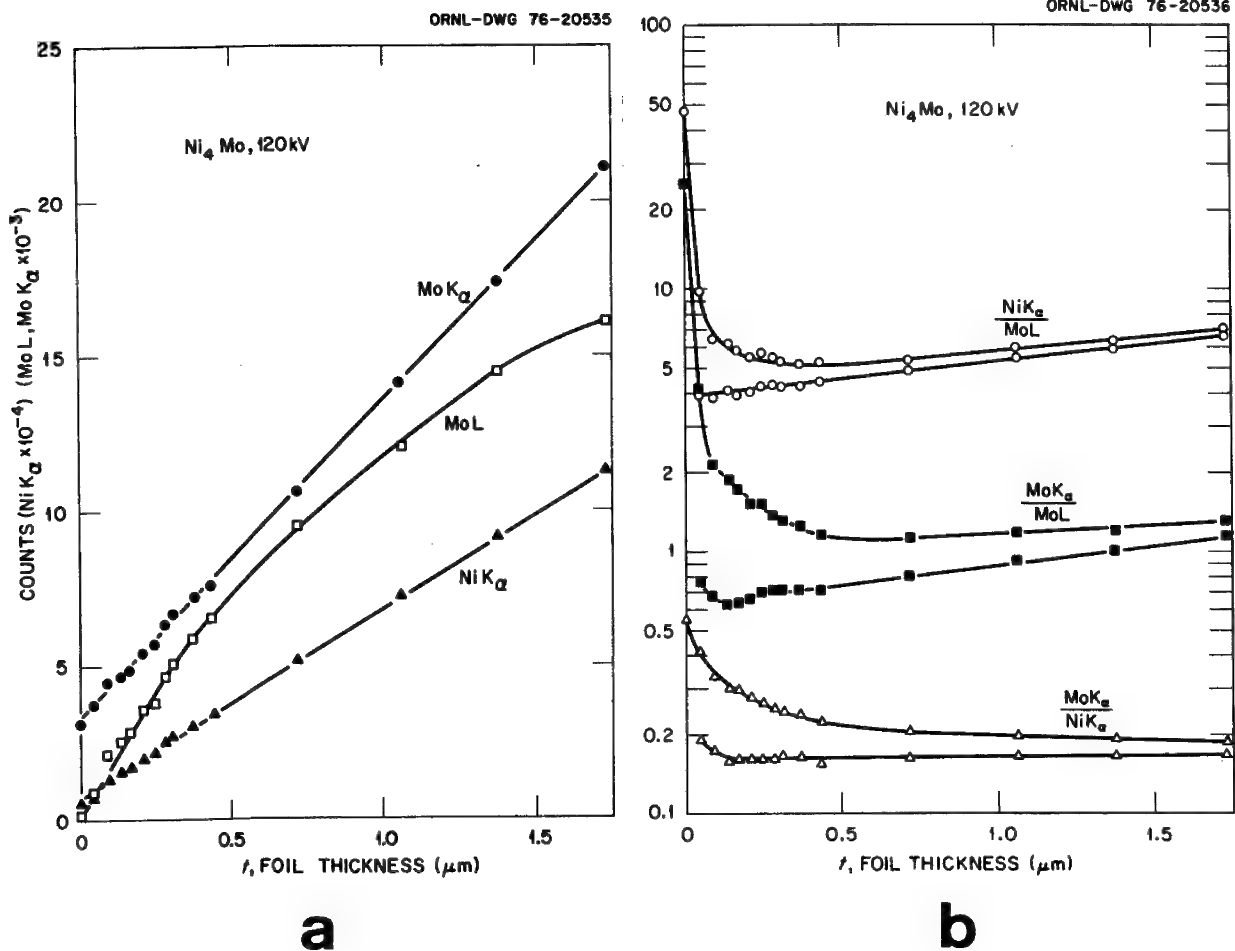
FIG. 1. Effect of x-ray fluorescence in a Ni—29 wt % Mo (Ni_4Mo) alloy. (a) Integrated counts versus foil thickness, t. (b) Ratios of integrated intensities. For each ratio the upper curve shows uncorrected data, and the lower curve shows data corrected by subtraction of x-ray induced fluorescence.

GRAPHITE SUPPORT GRIDS FOR X-RAY ANALYSIS
IN THE ELECTRON MICROSCOPE

R.H. Packwood - E.E. Laufer - W.N. Roberts
Physical Metallurgy Research Laboratories - CANMET-EMR
568 Booth Street, Ottawa, Canada

X-ray emission spectroscopy in the transmission electron microscope (TEM) has been practised for some years in commercial instruments like EMMA (1) or in conventional TEM's to which semiconductor EDS or other X-ray spectrometers have been attached, e.g. (2-6). The combination of TEM and semiconductor EDS systems has proved to be very effective. However, one problem with an EDS is that it lacks well-defined directionality. Consequently, not only the sample but anything within the wide field of view of the detector is a potential source of spurious X-rays generated by scattered electrons. Early experiments show the excitation of the support grid, sample holder and chamber. These unwanted X-rays not only load down the electronic processing system but also mask portions of the X-ray energy spectrum. All three sources can, in principle, be eliminated, either by suitable collimation, by painting with colloidal graphite or by replacement of the offending items by those made from 'soft-X-ray' materials: C, Be, BN.

A sample cup made from graphite has been reported (7) and a Be holder is available from Philips. On our Philips EM300, the manufacturer's double-tilt holder has been modified by replacing the original sample cup with one made of Dural and subsequently dagged. The microscope is equipped with an ORTEC detector installed at sample height and at right angles to the electron beam. Our collimator is shown in Fig. 1. It is dagged inside and out. We have our own two-blade Pt anticontamination trap, which also has been dagged. So far as we can tell, the only remaining source of extraneous X-rays is the Cu grid used to

mount the sample. In principle, this could be eliminated by the use of commercially available grids of nylon or Be. However, the nylon grids presently available are thick and also have poor stability in the electron beam. The Be grids are very expensive.

We recently found that Poco Graphite Inc. produce sheet and other configurations of a pure, fine-grain, high-strength graphite, that is both tough and flexible. This material is normally used for low-wear electrodes in EDM. In particular, we were taken by their 0.005-in. sheet material. From this were manufactured the support grids shown in Fig. 2. Here we have an array of 0.013-in. diameter holes countersunk n one side only. The countersink is required to permit observatiom at the tilt angle of 40° used to present the sample to the EDS. The plain side is used to pick up carbon extraction replicas or similar thin-section material. For the case in point we have extraction replicas taken from a HSLA pipeline steel. Typical inclusions are NbC and cementite, although we also noted arsenic and rare-earth compounds. Figures 3 and 4 show Nb EDS spectra taken from a replica caught on the conventional Cu grid and that resulting from a similar replica caught on the new graphite grid. The residual Cu peak arises from the Cu content of the Dural sample cup: an Al-Mg alloy would have been a better choice. The grids are re-usable either by floating off the old sample or by flame cleaning. Sample grids of 3 mm diameter may be obtained from the authors.

Acknowledgements

References

1) P. Duncumb, Proc. 3rd Conference on "X-Ray Optics and X-ray Microanalysis", (1962) pp 431.

2) R.T. Murray, Jour. Phys. (E), 6, (1973) 19.

3) A. Armigliato, P. Bergamini, L. Morettini, Proc. MAS 9, (1974) paper 15.

4) L. Berenbaum, A.S. Cammarano, Proc. MAS 9, (1974) paper 54.

5) D. Chescoe, B.E.P. Beeston, Proc. MAS 11, (1977) paper 16.

6) J.J. Hren, P.S. Ong, P.F. Johnson, E.J. Jenkins, Proc. MAS 11, (1977) paper 13.

7) N.J. Zaluzec, H.L. Frazer, Jour. Phys. (E), 9, (1976) p 1051.
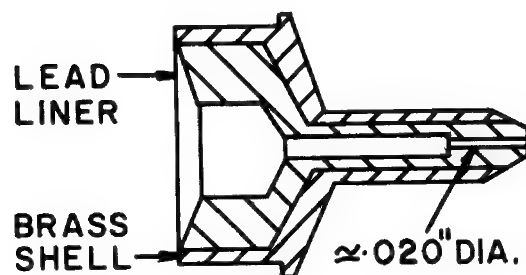
FIG·1
SCHEMATIC OF
COLLIMATOR (≈2X)
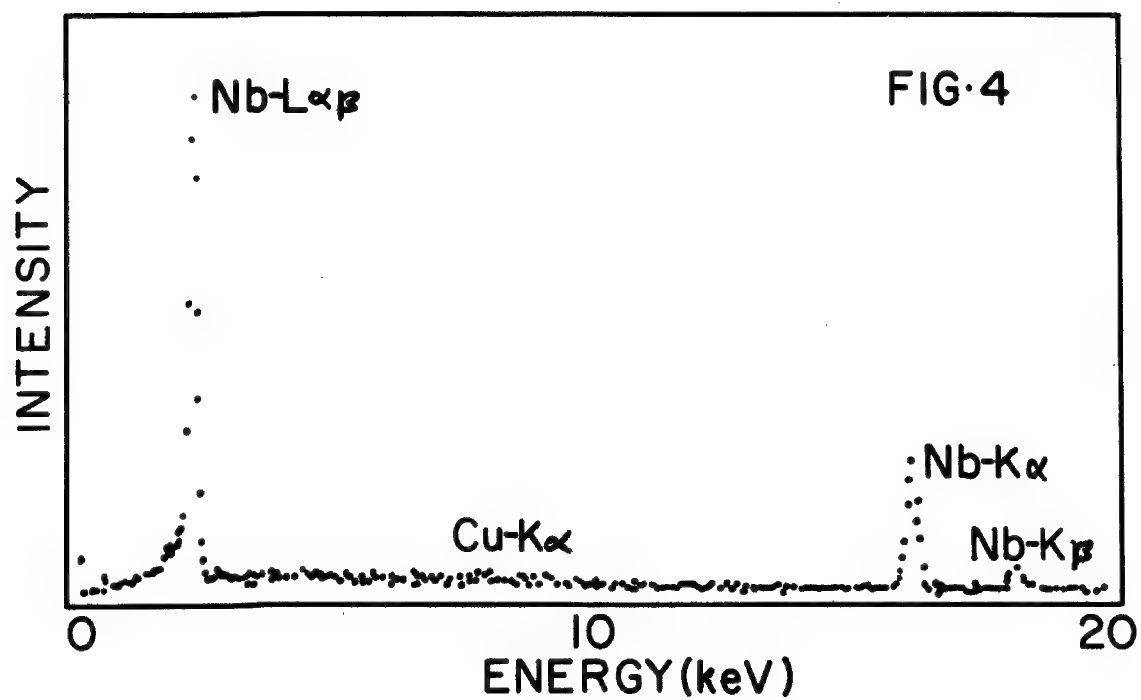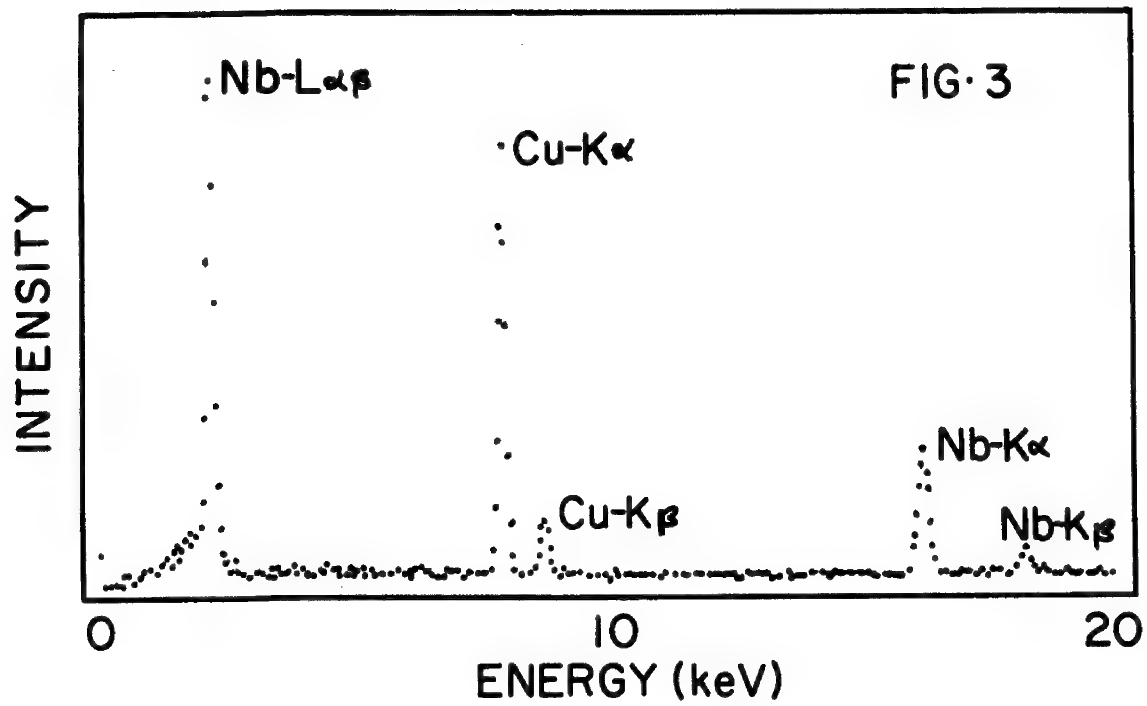
LEAD LINER

BRASS SHELL

≈·020" DIA.

FIG·2
GRAPHITE GRID
(≈11 X)

FIG·3

FIG·4

APPLICATION OF THE MONTE CARLO SIMULATION TO QUANTITATIVE ELECTRON MICROPROBE ANALYSIS OF REFRACTORY THIN FILMS

Serge Cvikevich and Carl Pihl

IBM Systems Products Division
East Fishkill, New York

This paper has two main objectives: first, to give the results of Monte Carlo analysis for films of tantalum-tungsten and titanium-tungsten on silicon substrates; and second, to discuss details of the data analysis procedure including a means to limit its potentially large computing costs.

For reasons previously described by D. F. Kyser and K. Murata[1,2] quantitative electron probe analysis of thin films can best be performed at some excitation potentials which will significantly exceed that required to maintain the scattered electrons within the thickness of the analyzed film. This, however, precludes the application of the conventional ZAF approach and requires the use of a costly Monte Carlo simulation in which a back calculation from composition to expected k ratios is performed.

The relative merits of low KV ZAF and high KV Monte Carlo approaches to quantitative electron microprobe analysis of thin films have been discussed in references (1) and (2). The present work makes use of the software developed by Kyser and Murata. Their Monte Carlo program is used for simulation of electron scattering, the associated energy losses and ionization distribution vs. depth to calculate an intensity ratio k for a given x-ray fluorescence generated in a thin film and a known thick standard target by a focused electron beam. (Fig. 1). Elastic scattering of electrons by atomic nuclei is described by the Rutherford equation, and the Bethe equation is used to account for energy losses between the scattering events. The variable step length of the electron between two scattering events is referred to as the mean free path Λ . For those electrons which cross the boundary between the film and substrate, the ionization rate for elements in the film is set equal to zero unless the electron is eventually backscattered into the film. If a backscattered electron escapes the film surface its energy and direction are saved in the computer (Fig.2a and b). The absorption of x-rays generated in the thin film and thick standard is calculated in the usual way and secondary fluorescence effects are neglected.

The actual data procedure is performed in several stages of iteration and interpolation. Initially, the theoretical calibration curves of k ratio versus composition, with ρt as a parameter, are generated by simulation. In practice, the k ratios for a given composition combination are computed for a number of ρt values in a single computer run. At present, the k ratio generation is done in batch processing mode using an IBM System-370 model 165 computer. Input

variables must include the elements in both film and substrate, absorption coefficients, initial energy, critical excitation energy of elements in the film and number of electron trajectories to be used. Output results include k ratio, composition and film thickness (ρt).

Previous work [1,2] indicates the need for at least 1,200 electron trajectories in order to give a statistically satisfactory computation of k ratio. Cost of simulation is directly related to number of electron trajectories.

A strategy developed in this study is to do the initial stage using only 100 electron trajectories for each composition while making a survey of the entire binary system. Thus k ratios are computed at 5% intervals over the complete range of composition. A typical computer run for one composition and 6 thickness values requires one minute of CPU time. Output results from this survey are stored in a data base for further references.

Following stages of analysis are done in real-time inter-active terminal mode requiring experimentally measured k ratios for input. Graphic display is an output feature.

Figure 3 shows a terminal display of theoretical k ratio versus ρt for the 0.8 tantalum 0.2 tungsten system. The wide range of ρt approaches an effective infinitely thick film. Film thickness in this study is in a range in which the k ratios are related to t by a linear fit as shown in Figure 4. Using the linear fit equation, values of ρt are computed based upon the experimental k ratios for Ta-W. A $\Delta \rho t$ is computed for the particular composition combination. A scan of the previously stored data base results in a plot of $\Delta \rho t$ versus composition as shown in Figure 5. The point at which $\Delta \rho t$ equals zero is the unique solution of composition and film thickness to satisfy the measured k ratios. Figure 6 shows a limited portion of the $\Delta \rho t$ versus tungsten composition curve.

The above procedure gives a rapid and economical initial estimate of film composition. The data base remains available for future work and is valuable where little is known about a given sample. Any refinement is made using a limited range of composition centered around the initial estimate combined with a larger number of trajectories.

In our work we have used the Monte Carlo simulation approach for quantitative electron microprobe analysis of Ta-W and Ti-W films with a nominal thickness of 1000A. Due to the high average atomic number of these films we were able to crosscheck our Monte Carlo results obtained at relatively high electron acceleration potentials with low KV measurements using a conventional ZAF calculation (Colby's Magic IV).[3,4] Table 1 is an example of some of the results obtained.

1. D. F. Kyser and K. Murata, Proceedings Eighth National Conference on Electron Probe Analysis, New Orleans, Louisiana, August 13-17, 1973; paper no. 28.

2. D. F. Kyser and K. Murata, IBM Journal of Research and Development. 18, No. 4., pp 352-363 (1974).

3. J. W. Colby, Advances in X-ray Analysis, Plenum Press (1968), V. 11, pp 287-305.

4. J. W. Colby, Proceedings Sixth National Conference on Electron Probe Analysis, Pittsburgh, Pennsylvania, July 27-30, 1971; paper no. 17.

TABLE 1

Sample No.	Elements	30 KV, MC. (wt. %)	ρt (mg/cm^2)	Low KV,ZAF (wt. %)	Low KV used
1	Ti W O	7.8 92.2	0.177	8.1 92.4 --	8
2	Ta W O	25.4 74.6	0.133	23.1 75.7 1.2	6
3	Ta W O	93.8 6.2	0.130	93.8 6.6 0.2	6

Fig. 1. Geometrical configuration of thin film on substrate, incident electron beam, and X-radiation observed. The pear-shaped surface represents the maximum range of primary electrons, and the shaded region is the volume from which X-radiation is measured.

Fig. 2b Geometry of the initial steps of electron scattering and energy loss in a thin film on a thick substrate.

Fig. 2a Geometry of the initial steps of electron scattering and energy loss in a thick target with a surface at the x-y plane.

0.8 Ta

0.2 W

K R.2 A T .15 I O .1

.05

0

.05 .1 .15 .2

RHO-THICKNESS(MG/CM2)

Fig. 4

0.8 Ta

0.2 W

K 1. R A .8 T I O .6

.4

.2

0

1 2 3 4

RHO-THICKNESS(MG/CM2)

Fig. 3

D .08 E L T .06 A

R .04 H O .02

/ -.7823 C M2 -.02

-.04

.025 .05 .075 .1 .125 .15

COMPOSITION (WEIGHT FRACTION)

Fig. 6

D .15 E L T .125 A

R H .1 O

M .075 G / C .05 M2 .025

-.4843

-.025

Ta

W

.2 .4 .6 .8 1.

COMPOSITION (WEIGHT FRACTION)
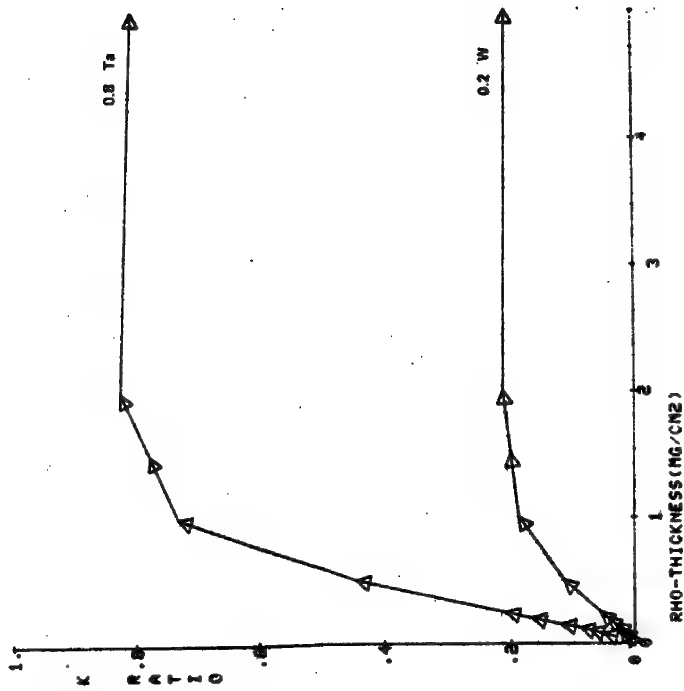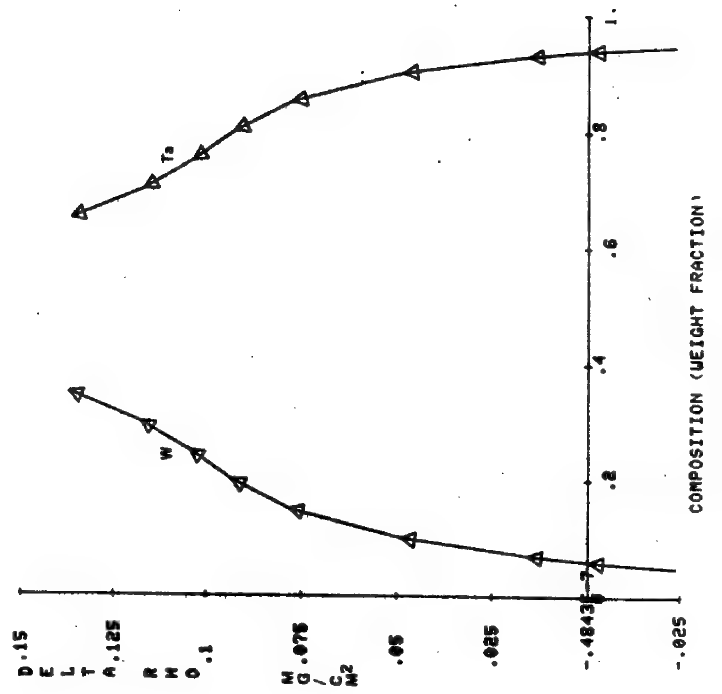
Fig. 5
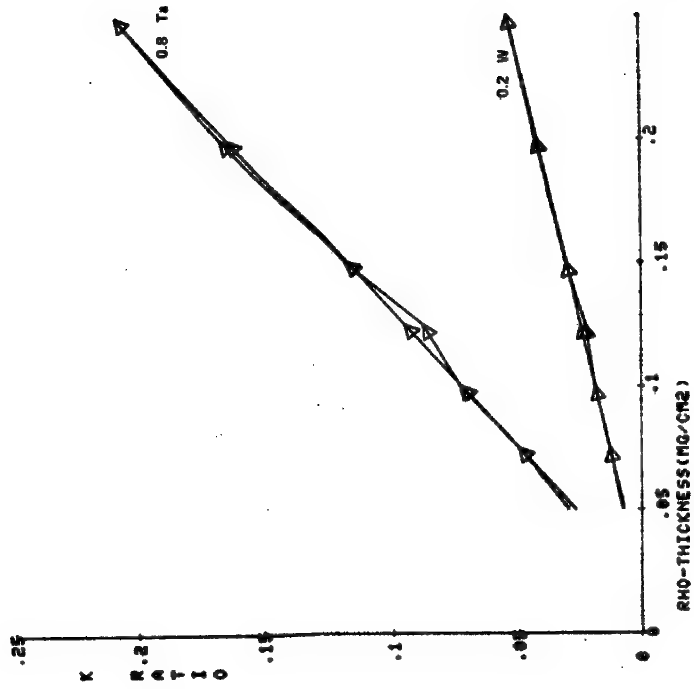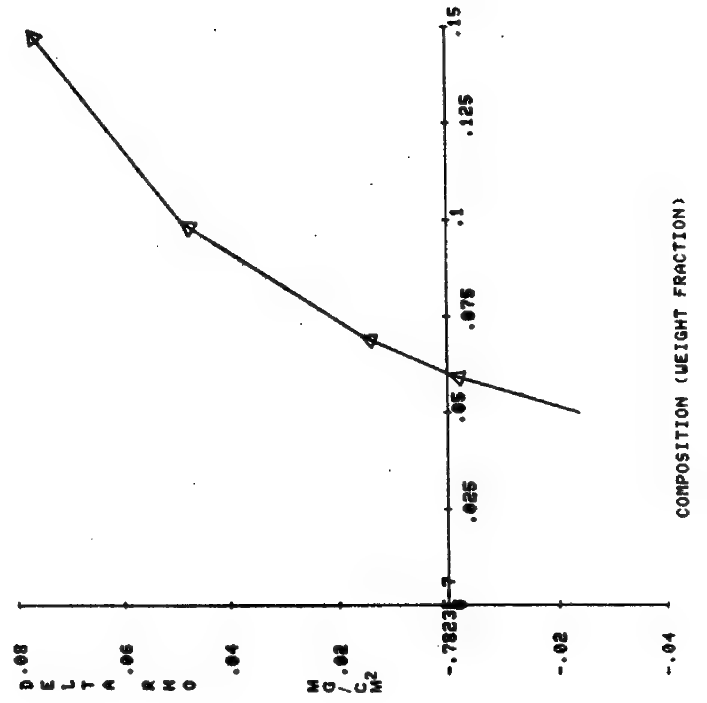
X-RAY MICROANALYSIS IN THE STEM

BY

P. BOVEY, I. WARDELL AND P.M. WILLIAMS

VG MICROSCOPES LTD

East Grinstead, Sussex, England.

The utilisation of a high brightness field emission source in an electron optical system is normally associated with the production of an ultra-fine probe for scanning transmission electron microscopy applications (STEM). A system has been developed to produce a probe of a few Angstroms dimension from a cold field emitter with two lens demagnification, which is capable of resolving 2 Angstroms in the lattice imaging mode. Of perhaps greater interest, however are the benefits which derive from the use of such a system in a microanalytical mode. The high current densities available at the sample (10^{-8} Amp into 50$\overset{\circ}{A}$ diameter probe at 100keV, for example) are ideal for fluorescent X-ray excitation at detectable levels from particles as small as 100$\overset{\circ}{A}$ or less. Furthermore, the ultra high vacuum technology required for effective cold field emission operation results in a contamination free clean, vacuum environment for analysis purposes. The instrument in question is therefore equipped with a solid state energy dispersive detector with computer read out system, and is capable of providing X-ray maps of solid samples with resolutions better than 100$\overset{\circ}{A}$ in 30 seconds or less. Results will be presented for phase separated alloys, alloy extraction replicas, and for catalytically active metal particles at the sub - 100$\overset{\circ}{A}$ level. Analyses may, of course, be accompanied by image read out in any of the other functions of the microscope (bright and dark field STEM, energy loss spectroscopy and micro-diffraction).

MICROCHEMICAL ANALYSIS IN SENSITIZED AUSTENITIC STAINLESS STEEL

Prakash Rao and Eric Lifshin

General Electric Company
Corporate Research and Development
P. O. Box 8
Schenectady, New York 12301

Considerable attention has been focused recently on understanding the detailed mechanism of intergranular stress corrosion cracking (IGSCC) observed in weld sensitized austenitic stainless steels used as structural material components in light water nuclear reactors. Although the general elements of IGSCC of isothermally or furnace sensitized stainless steels of the 18% Cr, 8% Ni type have been known for many years, this prior knowledge has proven to be inadequate to describe quantitatively the cracking phenomenon in weld heat affected zones. For example, although the depletion of chromium to below a critical value of about 12 wt.% in the vicinity of sensitized carbide-matrix interfaces was first proposed by Bain and coworkers(1) in 1933 as being the cause of susceptibility to IGSCC, no direct method for the actual measurement of this depletion was available until recently. Since Bain's original proposal for chromium depletion as the reason for increased susceptibility, there have been refinements to the theory(2, 3) based primarily on thermodynamic and/or diffusion considerations. Other explanations for susceptibility of sensitized stainless steels have been based on solute segregation to grain boundaries(4) and on a noble carbide theory(5). Which of these theories provide a complete explanation for the observed IGSCC phenomenon continues to be an open question.

A major limitation in determining which of the above theories for IGSCC susceptibility bears maximum credibility, has been the inavailability of analytical instrumentation to provide direct measurement of elemental concentrations on the scale of a few hundreds of Angstroms. Diffusion calculations show, for example, that chromium depletion should entend to 1000-2000Å into the matrix from the chromium rich carbide($M_{23}C_6$) - matrix interface, perpendicular to the grain boundary. The conventional electron microprobe with its spatial resolution of the order of one micron is clearly inadequate for microchemical analysis on a scale demanded here. Major improvements in analytical instrumentation, such as the scanning imaging capability on microprobe analysers and interfacing with energy dispersive x-ray detectors, occurred during the sixties and early seventies. These developments lead to commercial scanning electron microscope-microprobe analysers in the early seventies, capable of imaging submicron structure.

In spite of these advances, no corresponding improvements in x-ray spatial resolution occurred. Several factors contributed significantly to this situation. First, electron beam penetration and scattering within the bulk sample often makes it impossible to contain the region of x-ray excitation within the metallurgical phase of interest. The use of thin sections of the type used in conventional TEM, therefore, becomes appealing because with thick samples the initial beam diameter increases with depth into the sample and also larger areas of the surface are excited by backscattered electrons resulting from increased scattering with depth.

A second group of important factors is associated with the unique performance of each instrument. These factors cannot generally be eliminated by the use of thin foil samples but require modifications to the instrumentation itself. Examples of instrumental factors include electron beam tailing caused by electrons scattered in the column, excitation of the specimen holder and surrounding chamber by backscattered electrons, fluorescence of the sample as a result of the use of thin foil apertures and the direct introduction of electrons into the x-ray detection system. Many of these difficulties can be overcome by the use of appropriate collimation, electron traps and specially selected aperture systems. These modifications are usually not provided by the manufacturer and each user is often left to his own resources. In spite of some of these limitations, high resolution x-ray microanalysis using thin foils continues to be a potentially exciting area of research in the future.

A typical system for this purpose consists of an analytical transmission electron microscope equipped with a double tilt goniometer specimen stage and attachments for both secondary electron and transmitted electron (STEM) imaging. The scanning transmission electron microscopy or STEM capability is essential to the system because of the ability to place a finely focused electron probe on any point of metallurgical interest in the transmitted image. In addition, a compatible solid state x-ray detector and a minicomputer-based multichannel analyzer is required to detect, display and store x-ray spectra. In our laboratory, we use a JEOL JSEM 200 transmission/scanning-transmission electron microscope operated at 200KV and equipped with a eucentric goniometer tilting stage and attachments for secondary electron and STEM imaging. Our x-ray microanalysis system consists of a Nuclear Semiconductor Autotrace retractable solid state x-ray detector with an energy resolution of 150eV FWHM coupled with a Tracor Northern NS-880 multi-channel analyzer and a PDP 11/05 minicomputer.

Our analytical electron microscope system was incapable of providing thin foil x-ray microanalysis with spatial resolution of a few hundred Ångstroms without several modifications both in operating conditions and instrumentation. First, optimum STEM operating conditions were developed by (a) using an entirely new second condenser and objective lens setting to provide images with resolution better than that predicted by the instrument manufacturer; (b) using a 20 micron second condenser aperture, a spot size of 50 Å was obtained as measured by an indirect method; (c) knife edge experiments at a crack in an electropolished stainless steel foil which showed that the 50 Å beam excites x-rays from the sample even out to 200 Å from the crack edge, demonstrating that x-ray spatial resolution is limited to about 400 Å in the proximity of the edge, with the probability of a much larger value in thicker regions of the specimen; (d) operating at the highest possible STEM magnification, namely 500,000X; (e) minimizing sample and specimen stage drift to about 1 Å/second by choosing reasonably thick regions of the order of 1000-2000Å; (f) carefully choosing grain boundaries and carbide-matrix interfaces that are parallel to the electron beam to maximize spatial resolution in the immediate vicinity of these interfaces; (g) choosing the interface in a manner that even the limited specimen drift would be parallel to the interface direction, thereby, minimizing x-ray spatial resolution in a direction perpendicular to the interfaces; (h) selecting counting times to minimize the effect of specimen drift. Secondly, spurious sources of x-rays in the specimen chamber itself have been minimized by (a) determining the correct specimen tilt angle to maximize the x-ray signal from the specimen; (b) redesigning the double tilt specimen holder with a graphite insert in the tilting cup; (c)

replacing one of the tilting cups with a Faraday cage in order to monitor beam current on the specimen during an experiment; (d) determining the optimum detector and collimator position with respect to the specimen, to minimize a spurious copper x-ray peak in the spectrum, (e) preventing the superposition of contamination spots on the specimen.

Incorporating the various modifications listed above on our analytical electron microscope system, we have been able to successfully detect and follow chromium depletion at grain boundaries and at carbide-matrix interfaces, which are of key interest in sensitization studies. Austenitic stainless steels containing 18-21% chromium and 8-12% nickel have been examined under several heat treatment conditions. The two to be considered here include the solution annealed case, and the result of a sensitization treatment that makes the austenitic steel very susceptible to IGSCC.

X-ray spectra were systematically collected and stored on a floppy disc system, for later data processing. Integrated x-ray intensities for the chromium, iron and nickel K_α peaks were determined after background subtraction. The remaining characteristic line intensities were converted to composition with the aid of the Cliff and Lorimer method(6), using the expression

$$\frac{I_x}{I_{Fe}} = K_x \frac{C_x}{C_{Fe}}$$

where x refers to either chromium or nickel, I_x/I_{Fe} is the intensity of element x relative to iron at the point of interest and C_x/C_{Fe} is the ratio of the composition of element X, in weight fraction, to the iron composition at the same point. Values of K_x were obtained from measurements with a defocused beam using independently determined composition values for the matrix.

Figure 1 represents a typical systematic elemental concentration determination as a function of distance perpendicular to a "clean" grain boundary between two carbide particles. STEM and SEM images of the same area are shown in the figure after a systematic determination. Zigzagging of the contamination spots, and hence the probe position, is necessitated by the need to obtain spectra at intervals smaller than the contamination spot size, in a direction perpendicular to the boundary while at the same time avoiding spot overlap. Excessive overlap has been observed to generate spurious x-ray peaks.

Figures 2 and 3 show a systematic determination of chromium, iron and nickel concentrations as a function of distance perpendicular to grain boundaries. The heat treatment conditions are shown in the figures. Note the drop in grain boundary chromium concentration from about 21% (solution annealed condition, Figure 2) to 5% (Figure 3) after the austenitic stainless steel had been heavily sensitized.

Figure 4 shows chromium, iron and nickel concentration profiles at carbide-matrix interfaces in two adjacent grains, in the heavily sensitized steel. Actual interface compositions cannot be determined experimentally as a result of beam size effects and uncertainty in the actual interface orientation. However, based on the assumption that the concentration profiles under equilibrium conditions can be approximated by and error function fit, it is possible to determine the carbide-matrix interface composition of 8%, as shown.

Only two examples of heat treatment, namely solution annealing with no attendent sensitization, and solution annealing plus sensitization treatments are discussed here. Very clearly, the depletion of chromium at grain boundaries and at carbide-matrix interfaces has been demonstrated by direct experimental measurement. No attempt is made in this paper to correlate the experimental results with the actual metallurgical variables. It is sufficient to state that there is a direct correlation between the susceptibility to IGSCC of these sensitized stainless steels as demonstrated by response to the modified Strauss test and constant extension rate testing, and depletion of chromium at grain boundaries and carbide-matrix interfaces below the critical 12% required for repassivation.

REFERENCES

1. E. C. Bain, R. H. Aborn, and J. J. B. Rutherford, Trans. Amer. Soc. Steel Treating, 21, 481 (1933)

2. C. Stawstrom and M. Hillert, J. Iron Steel Inst., 207, 77 (1969)

3. C. S. Tedmon, D. A. Vermilyea, and J. H. Rosolowski, J. Electrochem. Soc., 118, 192 (1971)

4. J. S. Armijo, Corrosion, 24, 24 (1968)

5. R. Stickler and A. Vinkier, Trans. ASM, 54, 362 (1961)

6. G. Cliff and G. W. Lorimer, Journal of Microscopy, 103, 203 (1975)

FIGURE CAPTIONS

Figure 1 STEM and SEM images of a systematic elemental concentration determination as a function of distance perpendicular to a "clean" grain boundary between two carbide particles.

Figure 2 Chromium, iron and nickel concentration profiles as a function of distance perpendicular to the grain boundary. Solution annealed condition - 1121°C for 10 minutes followed by water quenching.

Figure 3 Chromium, iron and nickel concentration profiles as a function of distance perpendicular to the grain boundary. Heavily sensitized condition - solution annealed, as above, followed by 677°C heat treatment for 24 hours and water quenched.

Figure 4 Chromium, iron and nickel concentration profiles as a function of distance perpendicular to a carbide-matrix interface. Heavily sensitized condition, as in Figure 3.

SEM

STEM

1 μm

FIGURE 1

118F
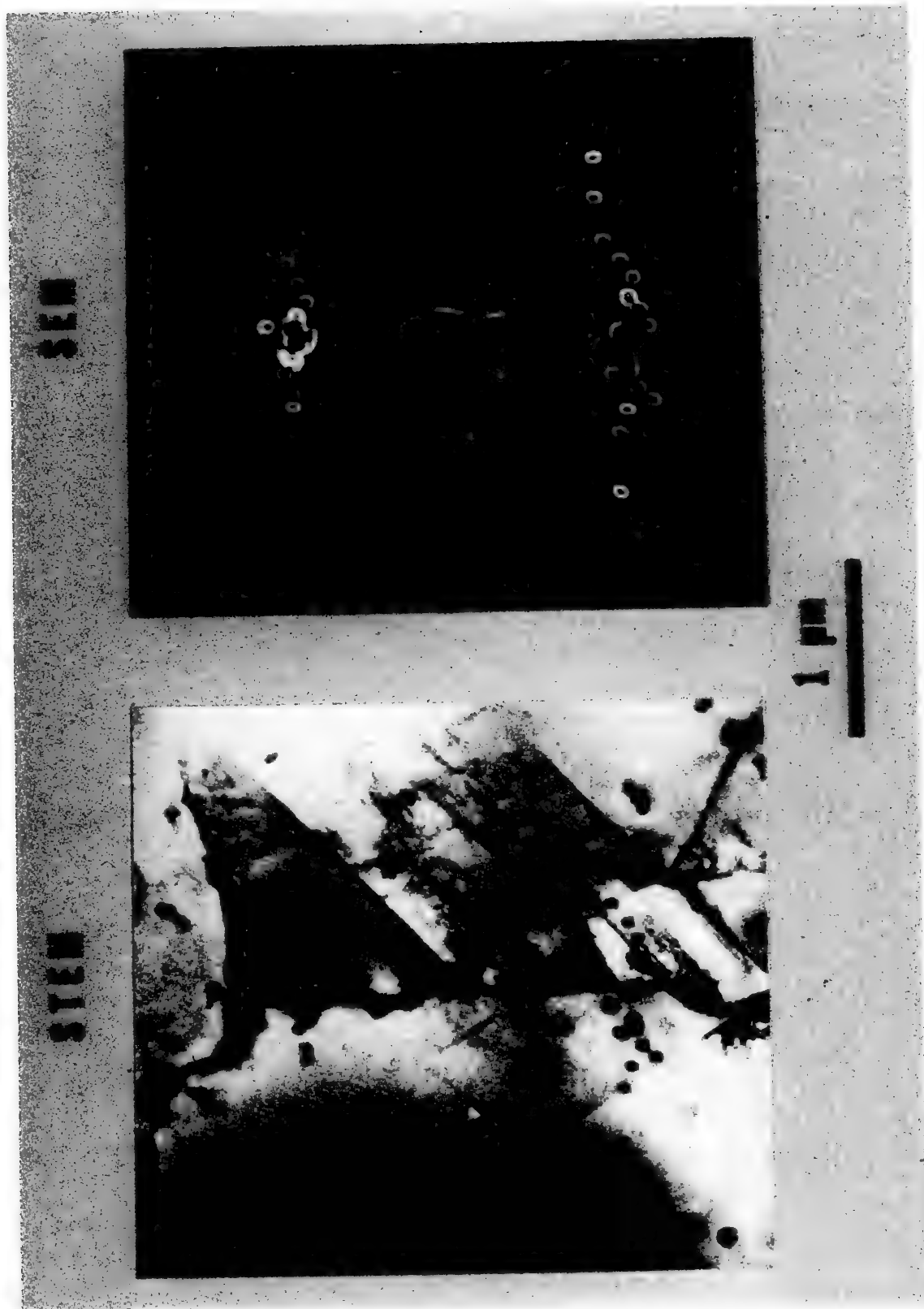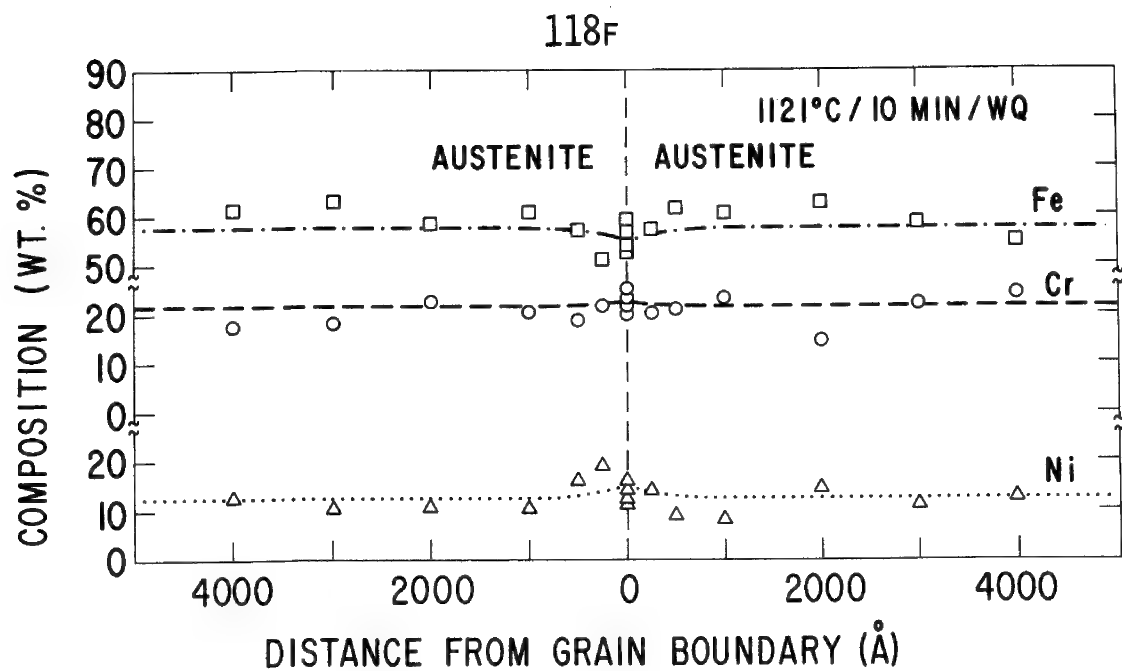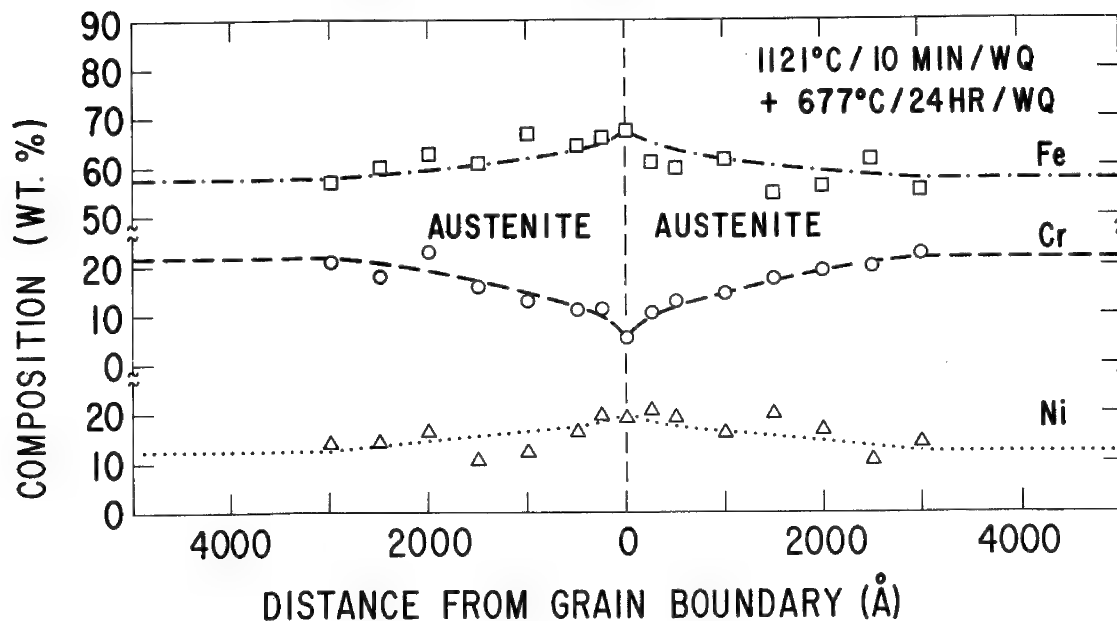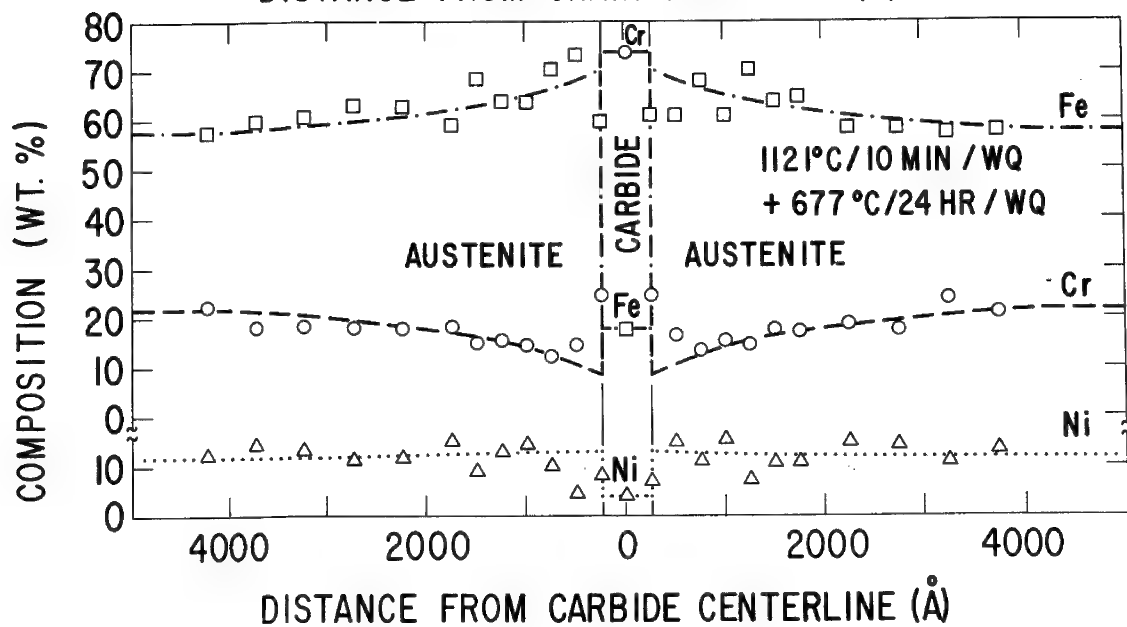
FIGURE 2

FIGURE 3

FIGURE 4

Microcharacterization of semiconductors by cathodoluminescence (CL) and electron beam induced current (EBIC) techniques

The applicability of CL and EBIC to semiconductor characterization problems and the attainable spatial resolutions of both techniques are discussed theoretically. By use of a suitable set-up in combination with a commercial scanning electron microscope (SEM) both methods can be applied simultaneously. Furthermore it can be shown that the theoretically predicted values can be achieved by a sufficient experimental arrangement, and it can be stated that a real micron scaled characterization can be performed by CL and EBIC. For different application problems, the determination of various solid state parameters by CL and EBIC can be shown to coincide with theory.

In detail following statements can be made for CL investigations:

The CL yield is primarily influenced by the ratio t/t_r of radiative to total recombination probability. Thus all solid state properties affecting this ratio can be determined by CL, as will be shown for doping variations, dislocations, temperature, and space charge layers. The spectral distribution of CL is determined by the transitions involved with the luminescent process, whereas by additional determination of the CL decay times -both integral and spectral- the associated recombination times can be evaluated. The spatial resolution attainable with CL is generally determined by the electron energy dissipation function after taking into account diffusion of the produced excess carriers and selfabsorption of CL photons. With a model based on Monte-Carlo calculations, it is shown that spatial resolutions of less than 200nm are attainable, which agrees with the experimentally achieved value for integral CL.

Such experimental results are only possible by development of a highly improved CL set-up. Using a high precision ellipsoidal mirror for photon collection and adapting a vacuum monochromator to the SEM chamber a high detectable signal yield can be achieved, even for spectral CL investigations. Detection itself can be done by photomultipliers or, for real-time spectral analysis, by means of an imaging tube and an optical multichannel analyzer. By additional electrostatic primary electron beam blanking a lock-in amplifier can be used to monitor the photomultiplier signal with extreme sensitivity (-90dB for signal/noise-rejection ratio, -70dB for zero suppression of a steady state CL signal). Time-resolved determination of CL can be attained by blanking of the beam by means of a nanosecond pulse generator and by detecting the CL light pulse with a fast photomultiplier. Amplification can be done either by single photon counting or by use of a boxcar integrator. With these arrangements, spatial resolutions of 200nm are achieved for integral CL measurements of GaAs; for spectral investigations a simultaneous spatial resolution of 500nm with 0.8nm spectral resolution is realized. The time decay of CL can be determined with 1/um spatial and 1.2ns time resolution.

With those general resolution values the following solid state parameters can be investigated: the temperature of the specimen qualitatively by integral CL and quantitatively by spectral CL (by both shift of peak energies and full widths at half maximum) with an accuracy of 3K; the variation of doping concentration in the surroundings of a dislocation and the hereby involved change of the forbidden band gap by spectral CL; a quantitative spectral analysis of the material with 500nm spatial resolution; a determination of the aluminum concentration in the different layers of light emitting and laser diodes of the GaAlAs-type; the decrease of CL decay time in the same epitaxial layers in the temperature range 77K-450K. With integral CL a quantitative analysis is generally not

available, on the other hand it allows a most precise evaluation of the location of microscopic structures of interest.

For EBIC experiments the following details can be given:

The EBIC is a current which only can be induced at the location of a space charge region or an electrical barrier. It can experimentally consist of three different terms, the real beam induced current by excess carriers crossing the electrical barrier, a photocurrent induced by self-absorbed CL photons, and any applied bias current. If one can neglect photo and bias current, the dependence of EBIC on the distance to the barrier is purely exponential with the diffusion length of the minority carriers, assuming a sufficient separation of electron beam and barrier. For a fixed distance EBIC decreases with the increase of recombination probability of excess carriers. Basing on the same theoretical model on energy dissipation as for CL,one can show that for the case of two parallel electrical barriers a spatial resolution of EBIC is possible with less than 1 um,i.e. a separate localization of such two barriers can be done without falsifying of the results.

The experimental set-up for EBIC has to be designed first to allow a simultaneous determination for CL and secondly to permit the use of lock-in amplification. Thereby any bias current can be eliminated by means of a different chopping frequency compared to the bias frequency. Furthermore the electronic circuitry must enable the measurements to be performed with a maximum barrier height change by the primary electron beam of the order of 1 uV. This is to avoid a change of the original state of the device or material by the experiment itself. Therefore many measurements have to be carried out with primary electron beam currents of 10^{-11}A.

In this manner and simultaneously to CL investigations the following examples on the examination of optoelectronic semiconductors are given: two parallel barriers being perpendicular to the surface can be separated with 500nm spatial resolution; in case of GaAlAs laser diodes barriers are detectable being parallel to larger barriers of even opposite polarity; a diffusion length determination can be done even for thin epitaxial layers, a primary electron beam of at least 30keV provided in order to eliminate the influence of surface recombination. By the aid of additional Schottky contacts it is possible both to detect the location of dislocations and to show a change in doping concentration associated with the dislocation.

L.J.Balk and E.Kubalek

Lehrstuhl für Werstoffe der Elektrotechnik
Fachbereich Elektrotechnik
Gesamthochschule Duisburg
Kommandantenstraße 60
D 4100 Duisburg
Fed.Rep.Germany

Single Crystal Characterization by SEM

H.J. Leamy, L.C. Kimerling, and S.D. Ferris

Semiconductor crystals and devices made from them have long been examined by SEM techniques. The familiar "charge collection" or "electron beam induced conductivity" mode [1] of imaging has been widely applied to the examination of p-n junctions and planar IC's. The physical basis of the technique is simple. Carriers generated by an electron beam in the vicinity of a "collecting" field diffuse to the depleted region where they drift in the electric field and thus induce a current in an external circuit. This current, when employed as the SEM video signal, reveals spatial variations in the efficiency with which the carriers are collected. Charge collection micrographs thus contain information regarding the _electrical_ properties of the material under examination.

This technique may be applied to unprocessed semiconductor material if the collection field is supplied by an electron transparent Schottky barrier electrode as shown in Fig. 1. This experimental arrangement offers several advantages. First, no alteration of the state of material during sample preparation occurs because the barrier metallization is deposited at room temperature. Second, the carriers are injected directly into the depletion region of the barrier. Thus, the lateral spread of the beam and consequently the spatial resolution may be increased by decreasing the accelerating voltage of the microscope. Finally, the simple experimental geometry shown in Fig. 1 admits straightforward interpretation and, under certain conditions, quantitative

Fig.1.: Schematic illustration of Schottky barrier charge collection microscopy. Z_D is the depth to which the material is depleted of mobile carriers and R is the electron range.

calculation of the micrograph contrast. These advantages have been realized experimentally by a growing number of workers [2], who have used the technique to study dislocations, stacking faults, precipitates, and dopant striae in several semiconductor materials.

An example of contrast produced by carrier recombination at defects situated below Z_D, the depletion region depth, is shown in Fig. 2. Here, stacking faults and their bounding partial dislocations are visible, as is precipitate decoration of the faults. The resolution of the method is proportional to
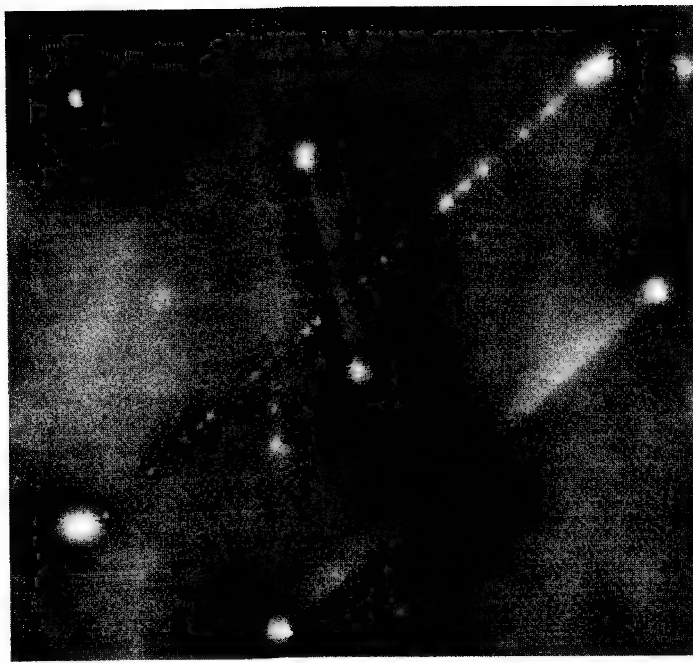
Fig.2.: A charge collection micrograph (20kV) of defects in n type $(5 \times 10^{11}/cm^3)$ silicon.
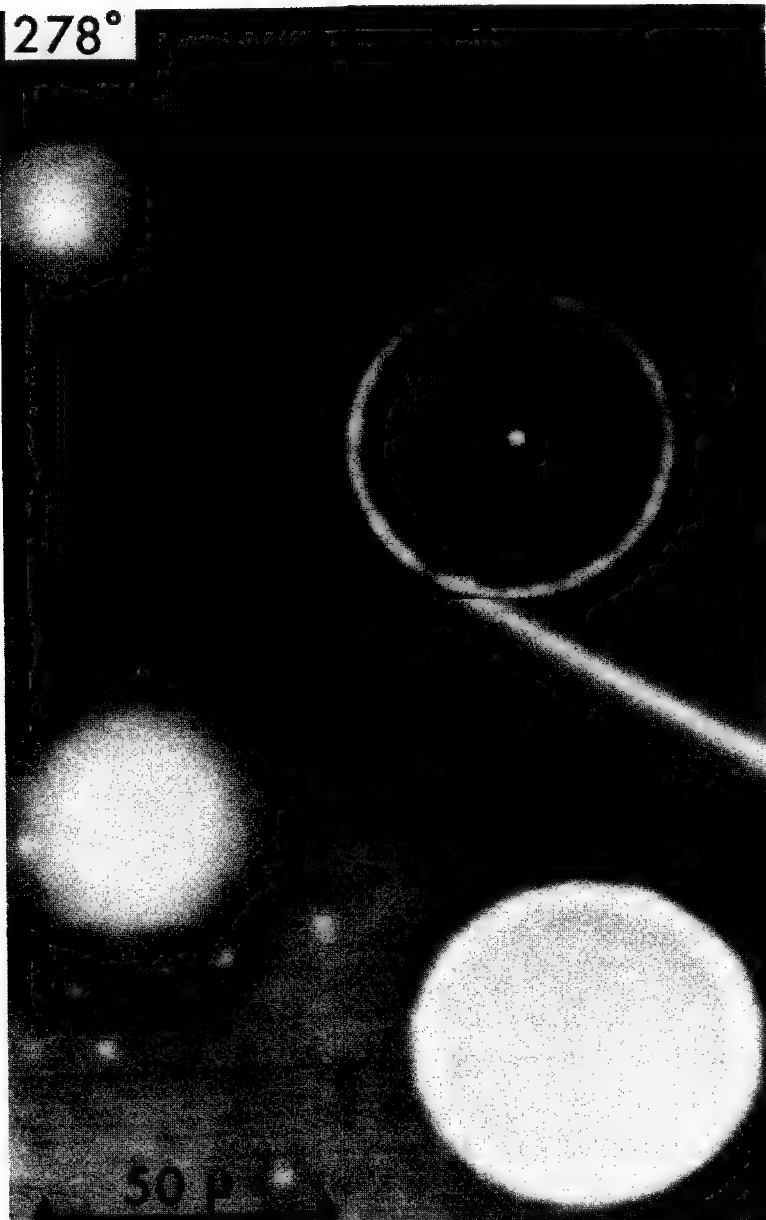
R, the electron range, and at low accelerating voltage is comparable or superior to that obtained by standard characterization methods such as etching or x ray topography. Resoltuion of 0.5 μm detail may be achieved and correspondence with other techniques is excellent, provided that the defects are electrically active, i.e. that they act as recombination centers. The sensitivity of the method thus depend upon the nature of the defect as well as upon the instrumental (SEM) variables. Figure 3, for example, shows that the recombination rate of injected carriers at a stacking fault in silicon is greater at 82°K than at room temperature [3]. This temperature variation arises via the temperature dependence of the fermi level in the sample, which determines the recombination activity at the defect. In fact, the energy level of the defect within the energy gap may be determined by measurement of the temperature dependence of the charge collection contrast. Finally, variations of the doping level within the material are also revealed by the technique [2,4]. Because Z_D is inversely proportional to the square root of the dopant concentration, Z_D and hence the charge collection efficiency vary with doping level. Charge collection current measurements of this effect correlate well with spreading resistance measurements and the technique is applicable at very low doping levels.

Fig. 3.: The temperature variation of charge collection contrast at a stacking (arrowed) in n type Si.

References

1) J.J. Lander, M. Schreiber, T.M. Buck and J.R. Mathews, Appl. Phys. Lett. 3, 206 (1963).

2) H.J. Leamy, L.C. Kimerling, and S.D. Ferris in "Scanning Electron Microscopy/1976 (Part IV)" (IIT Research Institute Chicago Illinois 1976) p. 529.
This reference contains a bibliography of publications up to 1976.

3) L.C. Kimerling, H.J. Leamy, and J.R. Patel, Appl. Phys. Lett. 30, 217 (1977).

4) A.J.R. de Kock, S.D. Ferris, L.C. Kimerling, and H.J. Leamy, J. Appl.Phys. 48, 301 (1977).

SAMPLING SEM FOR SEMICONDUCTOR DEVICE STUDIES

A. Gopinath, K.G. Gopinathan
University College of North Wales
School of Electronic Engineering Science
Bangor
Gwynedd
U.K.

Voltage probing of semiconductor devices provides information which is not available at the terminals and during device development such probing results are of great value to the device engineer. Mechanical point-contact probes are sometimes used but these often cause irreversible device damage, have a poor spatial resolution < 5μm, and the probe strays may in fast devices preclude normal device operation. The electron beam probe of a SEM may be used to perform such measurements, with the advantages of being non-contacting and rapidly and accurately positioned, possessing good spatial resolution, causing minimal device damage (which in any case may be annealed out) and negligible device perturbation, especially if probing is on metallisation areas.

Voltage measurement in the SEM is by means of linearisation of voltage contrast and these schemes have a bandwidth of several hundred Hertz. Measurement of rapidly changing voltages and voltage distributions outside this bandwidth and which are periodic may be examined by sampling techniques, which has until now meant stroboscopic operation.[1,2] This mode is generally set up to operate over a narrow frequency band, which is dictated by the synchronisation loop (to ensure beam pulses maintain a constant phase position), and examination of devices working outside this range often requires new hardware.

The alternative scheme is to interface the SEM with sampling oscilloscope type circuitry. In this system the electron beam, held on spot on the device point at which measurement is to be made, is turned on for the sampling period at the particular time-delay or phase position set by the circuitry. The voltage measurement is during and averaged over the beam-on period by voltage contrast linearisation. By electronically stepping the time delay of the beam pulses after the voltage measurement is completed at each time-delay position, the voltage waveform over the whole period may be resolved. Finally, with the time-delay position of the beam pulses held constant, the beam may be scanned over the specimen to operate the instrument in the stroboscopic mode. The present paper describes a Sampling-SEM based on the above ideas that has been built at Bangor and currently operational. Application of this instrument in the specific device context of switching of very fast bipolar transistors illustrates its capabilities. In slightly modified form it may also be used for the study of some semiconductor materials properties such as minority lifetime measurements and radiative recombination rates under low and high injection levels, but these applications will not be discussed here.

Figure 1 shows a schematic diagram of the system as designed at Bangor. The voltage measurement is performed using a new four-grid retarding-potential analyser[3] which now allows normal focussing of the beam on the specimen. The sampling circuitry comprises of a delayed-trigger generator which drives a beam pulser and a control unit for multiple sampling. The delayed-trigger generator causes a trigger pulse to be generated at precisely the correct delay position and this is also controlled by the multiple-sampler unit which allows multiple samples per delay position to

be obtained. This trigger pulse is fed to the beam pulser which provides
a single beam pulse 100pS wide at the appropriate delay position. The
delayed-trigger generator is a modified form of the Hewlett-Packard 1811A
sampling time-base unit with a maximum sampling frequency of 1 MHz. A
count-down unit is available so that waveforms of repetition frequencies
to 10GHz may be examined with this system.

The beam pulsing unit comprises of a screened meander line placed
between the first and second lenses of the SEM. This is normally biased
so that the beam is off, and the beam pulse is generated when the beam
traverses the chopping aperture on the rising edge of an excitation pulse,
to yield beam pulses of 100pS width. The flyback during the falling
edge of this excitation pulse is blanked by additional blanking plates,
placed orthogonal to and below the meander line. The blanking plate
excitation is also triggered by the delay-generator trigger-pulse after a
specific delay. The positioning of this chopping unit in the column
ensures that chopping degradation is held to a minimum.[4]

The voltage resolution of the system V_{min} is given by the equation:

$$V_{min} = \frac{1}{K} \sqrt{\frac{f_m}{I_b \Delta_w f_r}} \qquad - (1)$$

where f_m is the voltage measurement band width, typically 100Hz

I_b is the beam current in amps

Δ_w is the beam pulse width in seconds

f_r is the repetition frequency of the waveform or the maximum
sampling frequency of 1 MHz, whichever is the lower figure.

The constant of proportionality K is dependent on the specimen and beam
KV and is a figure of merit of the system. This is about 10^7 in the Bangor
system for a copper stub at 12.5 KV beam. Voltage measurements are only
possible upto 10^{-11}A average beam current ($I_b \Delta_w f_r$) and the upper current
limit of say 10^{-7}A is determined by the source.

The system specifications at the present time are :

Time resolution   100pS

Voltage resolution   100mV

Sampling frequency f_r 1 MHz (maximum)

Beam pulse width, Δ_w = 100pS

Beam current during pulse   100nA

In this abstract we show some typical results obtained with this
system on bipolar switching transistors. Figure 2 shows a very fast
switching transistor (WR13A Plessey Co.) input pulse on the base and
output on the collector, the delay being limited by the jitter specification
of the driving pulse generator and hence not resolved. Figure 3 shows a
slower transistor 2N708 switching and illustrates the delay measurement of
0.4 nS between the input pulse at the base and the collector output.

The presentation at the conference will emphasise the new voltage
measurement system, the beam pulsing system and voltage probing results
on devices.

References
1. G.S. Plows, W.C.Nixon: J.Phys.E., 1968, 1 pp 595-600
2. P.J.Fentem, A. Gopinath: IEEE Trans.Electron Devices, 1976, ED-23
                                 pp 1157-63.

3. A.Gopinath, W.J.Tee: J. Phys.E., 1977, to appear.
4. A.Gopinath, M.S.Hill: J. Phys.E., 1977, to appear
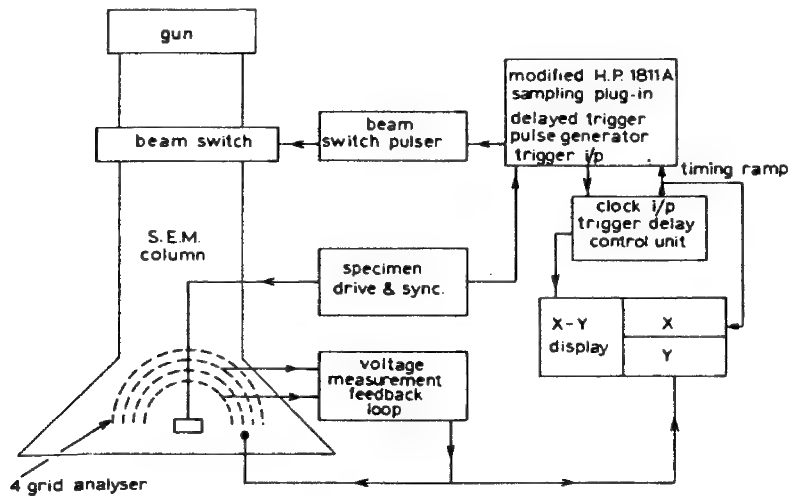
Fig. 1 Schematic diagram of sampling S.E.M.
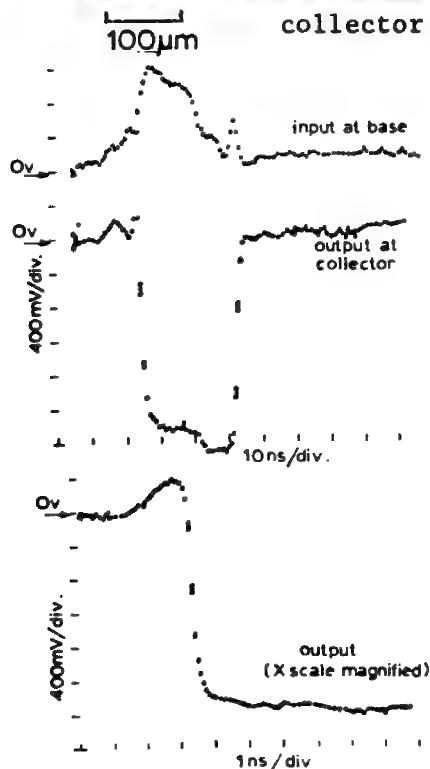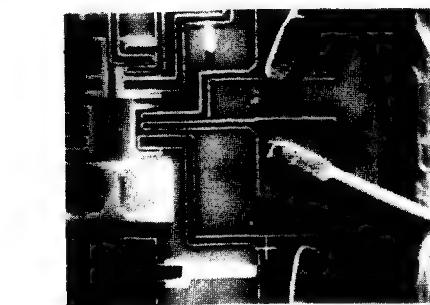
Fig. 2: Switching of WR13A transistor
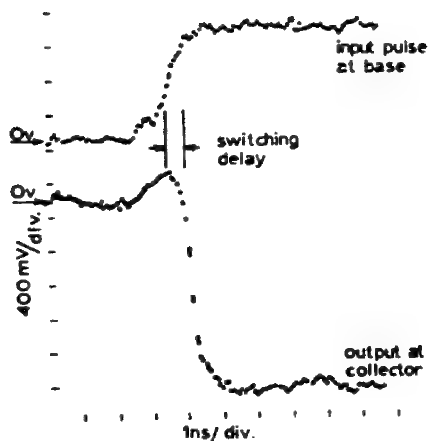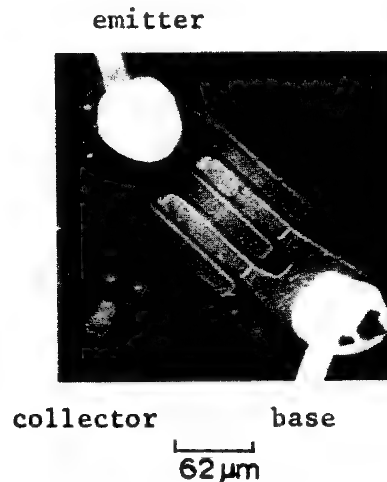
Fig 3: Switching delay in 2N 708 transistor

ELECTRON MICROPROBE ANALYSIS OF CHEMICAL COMPOUNDS

BY X-RAY AND CATHODOLUMINESCENCE SPECTROSCOPY

Eckhard Wolfgang

Siemens Research Laboratories, Munich, Germany

Owing to the progressive miniaturization of electrical and electronic devices in almost all branches of electrical engineering the effects of contamination on device performance is assuming growing importance. An exact knowledge of the chemical composition of the contaminant is essential in order to determine its origin so that appropriate remedial measures can be undertaken.

Contaminants are seldom homogeneous configurations but usually porous layers, particles or whiskers consisting mostly of oxides, nitrides or organic compounds. Conventional quantitative electron microprobe analysis, Auger analysis and SIMS analysis are however not very practical for determing chemical compounds. There is therefore a need for supplementary methods which respond sensitively to chemical compounds while at the same time being independent of the geometry of the contaminant that is to be analysed. Three examples will be cited to show that such requirements can be met by X-ray and/or cathodoluminescence (CL) spectroscopy.

X-ray spectroscopy for the microanalysis of chemical compounds has already been treated by a number of authors [1-5]. Use is made of the difference between the X-ray spectra of atoms and molecules. Among other things additional bands are liable to appear. This happens in the case of carbides, oxides and nitrides of the elements aluminium and silicon widely used in industry. The $K\beta'$ bands appear in the spectrum of aluminium and silicon and their energy level indicates the presence of carbon, oxygen or nitrogen. The analysis of thin films [6,7] and the determination of the degree of oxidation of SiO_x layers [8] are in this way possible.

CL spectroscopy is used mainly for characterizing materials such as GaAs and other luminescent substances [9-11] . However minerals [12], glass materials [13] and organic substances [14] also become luminescent under exposure to an electron beam.

Figure 1a is a schematic representation of a GaAs sample with a deposited Si_3N_4 film. It may be seen from the SEM micrograph (Figure 1b) that bunches of needles have formed, the composition of which needs to be determined. The energy-dispersive spectrum only shows the presence of gallium. Since the whiskers are very thin ($\sim$1μm) and the substrate contains nitrogen the quantitative determination of light elements is dufficult to accomplish. The CL spectrum shows however an emission line in the ultra violet region at 365 nm (Figure 1c) which corresponds exactly to the emission line of gallium nitride.

Figure 2a is a schematic representation of a silicon sample with a Si₃N₄ deposited on its back. During a silicon epitaxy process applied to the front of a sample silicon crystallites and clusters of needles of unknown composition formed on the nitride (Figure 2b). All that the energydispersive spectroscopy can determine from the needles is the presence of silicon. In the Kβ spectrum of the silicon two Kβ'bands, viz. of nitride and oxide (Figure 2c), are observed.

CL analysis provides both higher local resolution and sensitivity. It may be seen from the spectra in Figure 2d that the Si₃N₄ layer has undergone a change during the deposition of silicon, i.e. the CL emission peak has shifted from 635 nm to 535 nm. Comparison with the corresponding Kβ spectrum shows the CL-peak shift to be related to the appearance of the Kβ' bands for silicon-oxide. Both CL lines are observed in the middle of the needles where the "Si₃N₄ line" (635 nm) shows up with greater intensity. In the center of the bunch of needles it is mainly the shortwave CL line which is observed.

Figure 3a shows the cross section of a pair of relay contacts. In a basic experiment the pair of contacts was switched in an atmosphere containing silicon until a distinctly larger contact resistance was observed. A contaminant containing the elements silver, silicon, carbon and oxygen formed at the contact point (Figure 3b). Si is present as SiO_2 (Kβ spectrum in Figure 3c) in the middle of the contact, indicating that the silicon vapor was transformed in the electric arc of the contact into SiO_2 and carbon, while the insulating SiO_2 increased the contact resistance. Somewhat beyond the contaminant containing SiO_2 there is also an indication of the presence of silicon; the contaminant is luminescent (see spectral CL-micrograph in Figure 3d). The contaminant must therefore be an intermediate product between silicon and SiO_2, as can be demonstrated by CL spectroscopy.

The three examples illustrate the possibility of obtaining data for determining the type and origin of chemical compounds from their x-ray and CL spectra. Although it is naturally not possible to identify the chemical composition of all contaminants by this method, it is nevertheless very practical to have a tool on hand with which energy-dispersive x-ray analysis can be supplemented by X-ray and CL spectroscopy.

[1] Baun, W.L.: Electron Probe Microanalysis, ed. by A.J. Tousimis and L. Marton, Academic Press (1969) 155
[2] White E.W., and R. Roy: Solid State Commun. 2 (1964) 151
[3] Esmail E.I., C.J. Nicholls and D.S. Urch: Analyst 98 (1973) 725
[4] Grasserbauer, M.: Microchimica Acta Suppl. 6 (1975) 145
[5] Wiech G.: Microchimica Acta Suppl. 6 (1975) 293
[6] Baun W.L., T.J. Wild, and J.S. Solomon: J. Electrochem. Soc. 123 (1976) 72
[7] Wolfgang E.: Siemens Forsch.-u. Entwickl.-Ber. 3 (1974) 260
[8] Oppolzer,H.,and E. Wolfgang: Microchimica Acta Suppl. 6 (1975) 311
[9] Wittry D.B., and D.F. Kyser: J. Appl. Phys. 35 (1964) 2439

[10] Muir M.D., and P.R. Grant: Quantitative Scanning Electron Microscopy, ed. by D.B. Holt, M.D. Muir, P.R. Grant and I.M. Boswarva, Academic Press (1974) 287

[11] Balk L.J.: Thesis, RWTH Technical University Aachen, Germany (1976)

[12] Hanusiak W.M., and E.W. White: SEM/75 Proc. of the 8th Ann. SEM Symposium, ITTRI, Chicago (1975) 125

[13] Atkinson D.I.H., and P.W. Mc. Millan: J. Mat. Science 9 (1974) 692

[14] De Mets M.: Microscopia Acta 76 (1975) 405
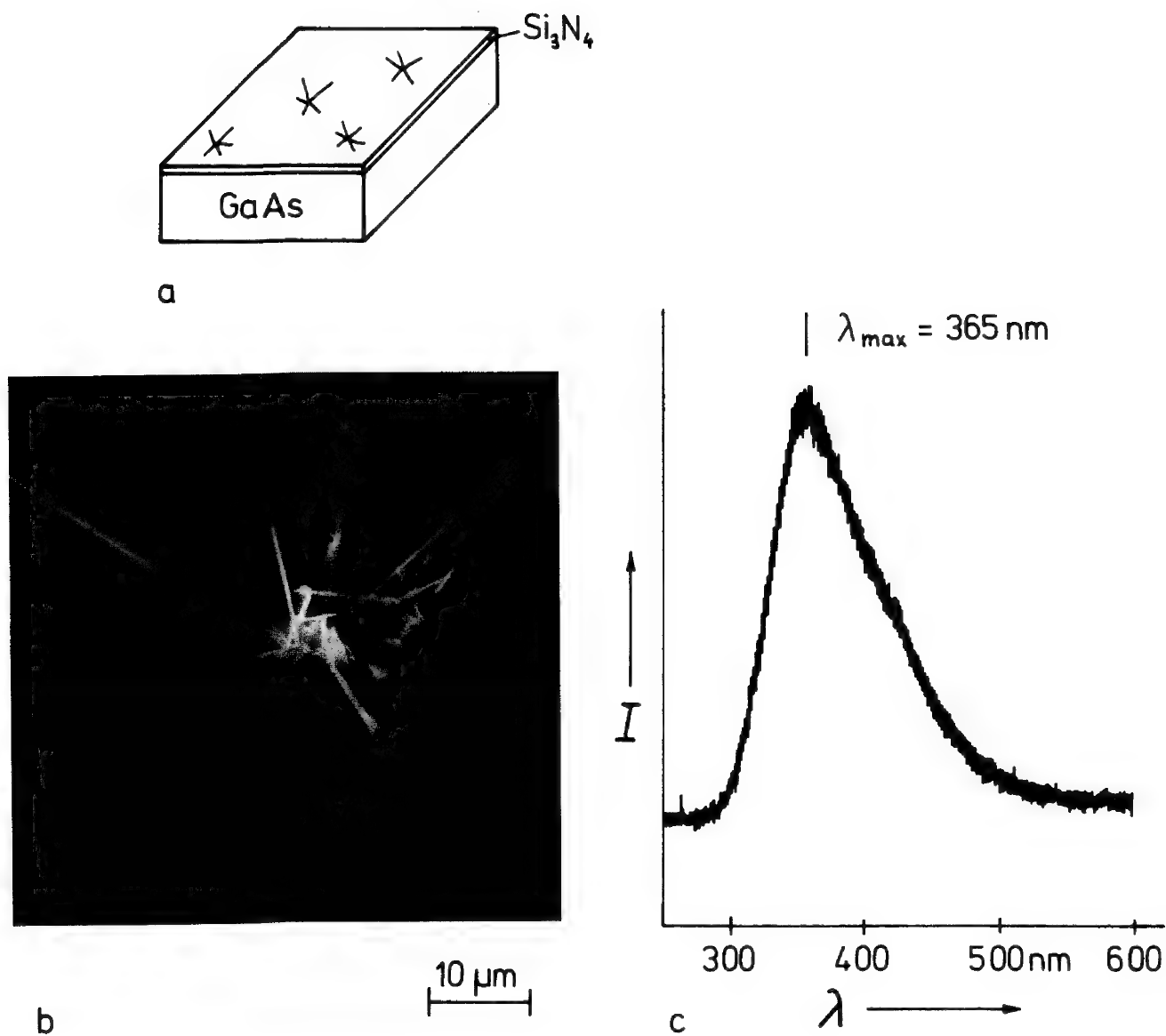
Figure 1 Bunches of needles formed on a Si$_3$N$_4$ layer

    a) schematic representation of the sample
    b) SEM micrograph
    c) CL spectra of the needles. The maximum wavelength
       corresponds to GaN.
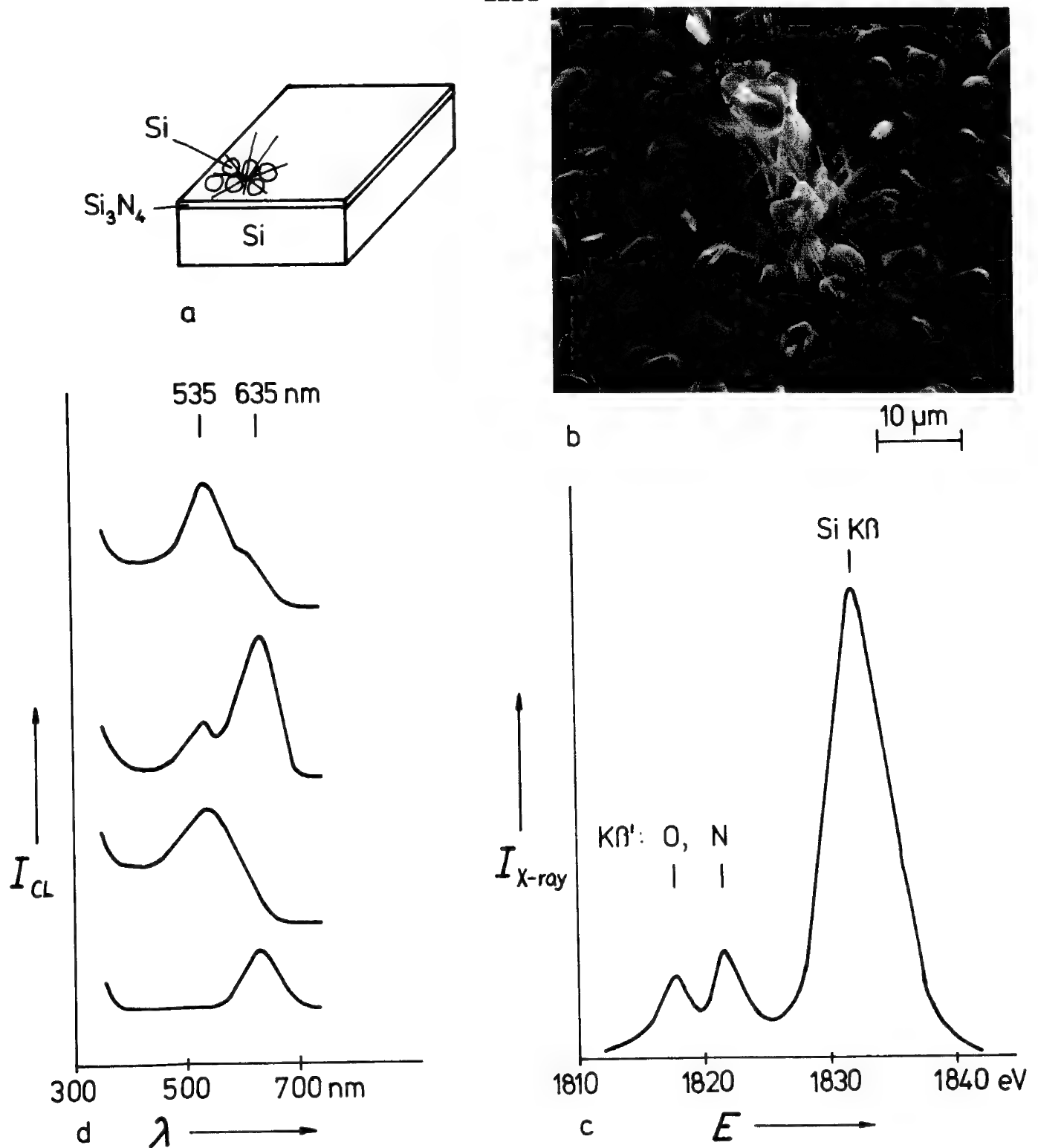
Figure 2   Needles on a Si$_3$N$_4$ layer
  a) schematic representation of the sample
  b) SEM micrograph
  c) Si-Kβ X-Ray spectra of the needles
  d) CL spectra of the needles. From top to bottom: single
     needle, center of the bunch of needles, Si$_3$N$_4$ after
     silicon deposition, Si$_3$N$_4$ before silicon deposition.
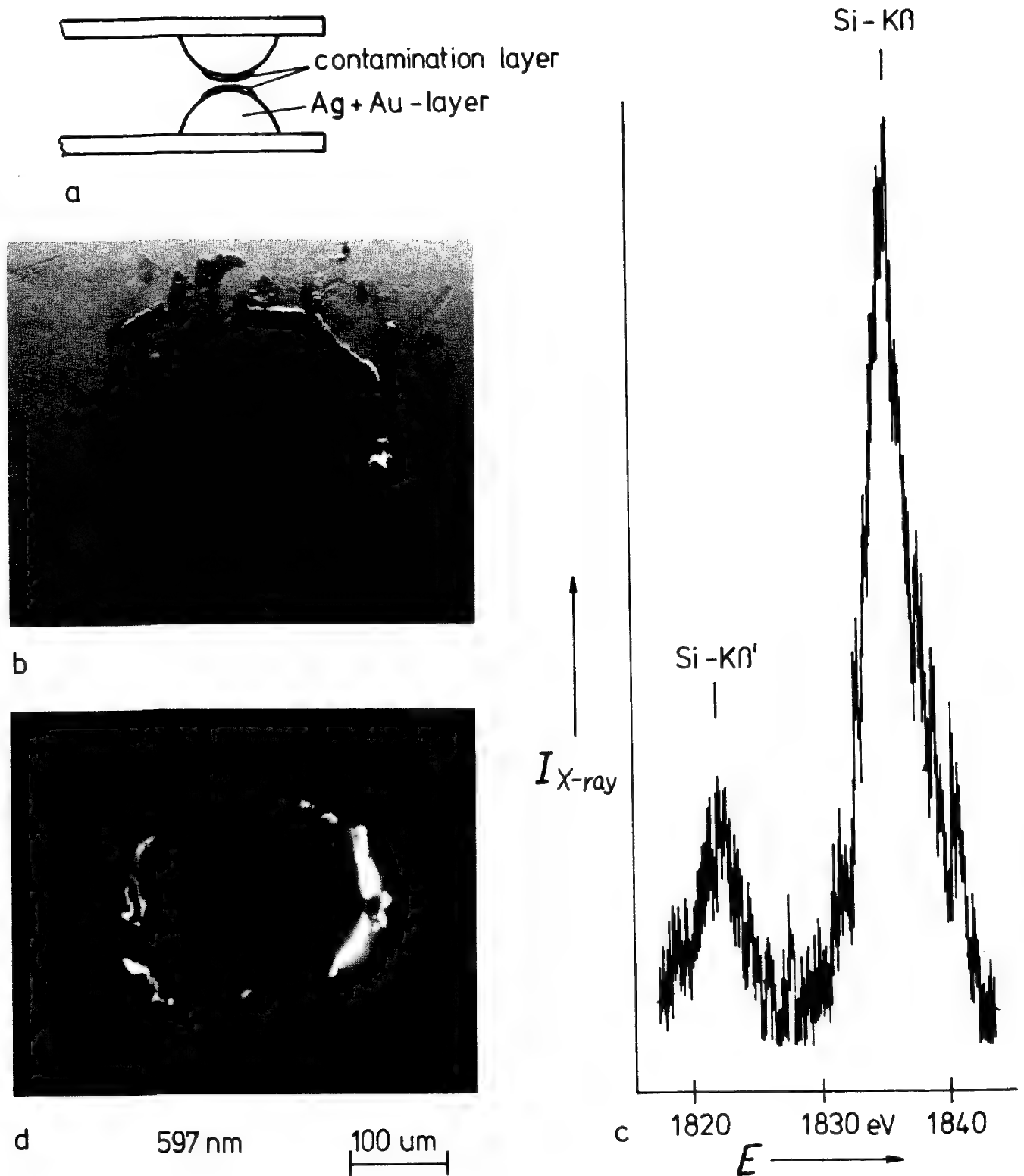
Figure 3   Contaminant layer on relay contacts

a) schematic cross section of a pair of relay contacts
b) SEM micrograph
c) Si Kβ X-ray spectra which indicates the presence of SiO$_2$
d) spectral CL micrograph (λ = 597 nm).

DIFFICULTIES OF INTERPRETING CATHODOLUMINESCENCE SPECTRA

M. J. Mitchell and J. N. Ramsey
IBM - East Fishkill Facility
Hopewell Junction, New York 12533

The electron microprobe or SEM provides the only readily
available method of obtaining electron excitation lumines-
cence spectra from localized sample areas. The equipment
required to establish a cathodoluminescence (CL) channel
on an electron microprobe is simple, reasonably inexpensive,
and does not interfere with normal x-ray analysis.[1,2,3]
However, cathodoluminescence studies have never become a
popular analytical technique to augment the routine use of
a microprobe. One of the main reasons for this is the prob-
lem encountered with interpretation of the CL spectra. Such
cases as direct band gap emission, which are well understood,
give little information to the microprobe user if the spectra
are taken at room temperature. Emission data from impurity
atom activation have been the most widely used and in some
systems, particularly those where the emitting transitions
can be used in lasers, the mechanisms are known and available
in easily obtained, usable form.[4] Increased efforts in photo
and electroluminescence have resulted in several review articles
and data tabulations which are helpful.[5,6,7] Emissions from
within the band gap are of potential interest if the spectra
can be interpreted. While a great deal of classical descrip-
tion terminology exists in the field of luminescence, much of it
only confuses attempts to use solid state theory to explain CL
phenomena.

Electronic bond structure and structural defects have been
classically studied by emission and absorption of light.
Complementary analytical techniques such as electron micro-
scopy, x-ray analysis, chemical or electrical measurements
are usually required to substantiate proposed interpretation
of the data.

In general three types of spectra are routinely encountered in
CL analysis:

1. Emission associated with the band gap.

2. Emission from states within the band gap but excluding
   emission due to impurity ion activation.

3. Emission due to impurity ion activation.

CdS
15 kV
1.5×10^{-7}A

3×10^4 CPS

1×10^6 CPS

EMISSION WAVELENGTH (10^2nm)
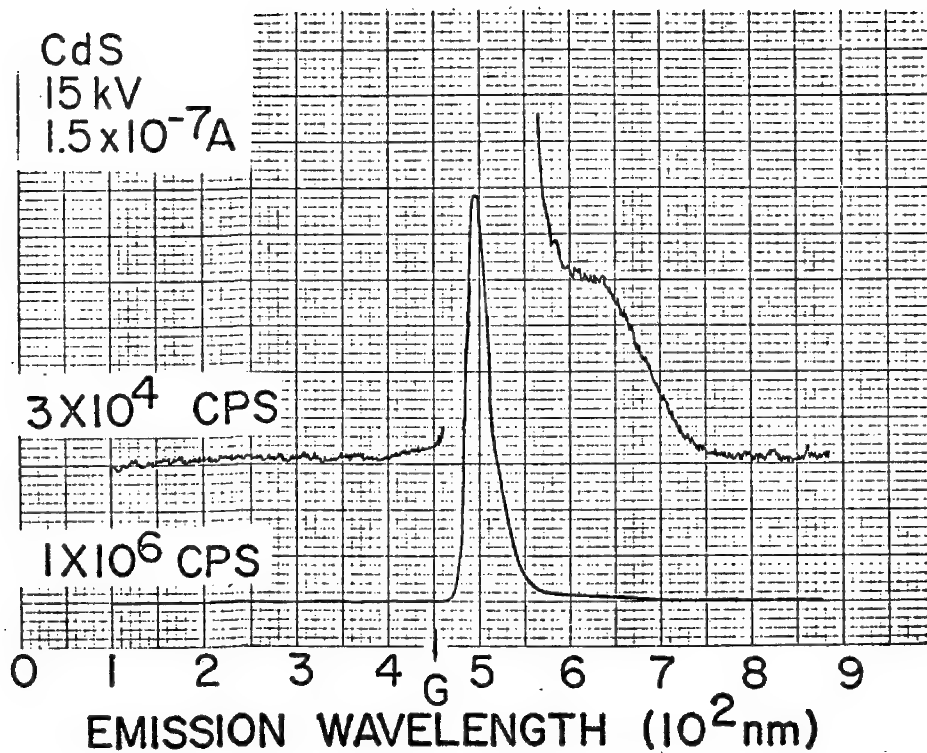
FIG. 1
CADMIUM
SULFIDE

1. The CL spectra of CdS (Fig. 1), is given as an example of a material with an emission associated with a direct band gap transition with the band gap in the visible region (Pt. G, 2.8ev[8] ~4500A). There is no fine structure in the emission peak at ~5000A which is associated with the band gap. The observation that emission occurs at lower energies (longer wavelengths) than absorption is known as Stokes' law of luminescence. The shoulder on the emission peak at 6400A is probably due to damage by electron bombardment. When spectra are taken at LN_2 temperatures or below, fine structure in the emission peak, indicative of specific transitions not resolved at room temperature, may be observed. Unfortunately, obtaining band gap energies for many wide band gap materials can be difficult, and differences often exist between those measured optically and those measured electrically. Optical band gap may be larger than band gaps measured electronically.[8]

2. The CL spectra of MgO, (Fig. 2) is given as an example
of a material with indirect band gap emissions. It has
four peaks in our wavelength range: one in the UV, two in
the visible and a broad one in the very near IR. The band
gap at 8 ev[8] (~1600A) accounts for the emission at ~1800A.
The remainder of the peaks are caused by emissions from
radiative transitions between states within the gap or from
states within the gap to states within the bands themselves.
This can take place in one, two or more steps. An absorp-
tion peak at 4.5-5.0 ev[9] (~2500-2700A) most likely accounts
for the emission peak at ~4400A, leaving the ~5000A peak
unaccounted for in the literature. Fortunately, MgO is
the NaCl crystal structure and compounds of this crystal
type show similarities in emission spectra, allowing the
assumption to be made that this emission is related to a
cluster defect[9] or more probably to an exciton transition[10].
An example will be given in which a known organic contamina-
tion shifts this peak and broadens it toward longer wave-
lengths. The ~8000A broad peak is still under investigation.

In many cases insufficient optical and electrical data
are available on the materials under investigation by CL.
Thus data from materials with analogous crystal structure
may be used. Other than in simple structures, such as NaCl,
the extent is not known to which extrapolations may be made.
This points to the necessity for collections of CL spectra
from a wide variety of materials on which electrical proper-
ties and crystallographic information, such as precise lattice
parameters and structural defect data, are known.

FIG. 2
MAGNESIUM OXIDE

MAGNESIUM OXIDE
6 KV
1.5×10^{-7} A
3×10^4 CPS

EMISSION WAVELENGTH (10^2 nm)

WILLEMITE
$Zn_2SiO_4(Mn^{2+})$
15 KV
$1.0 \times 10^{-7} A$

1×10^3 CPS

1×10^6 CPS
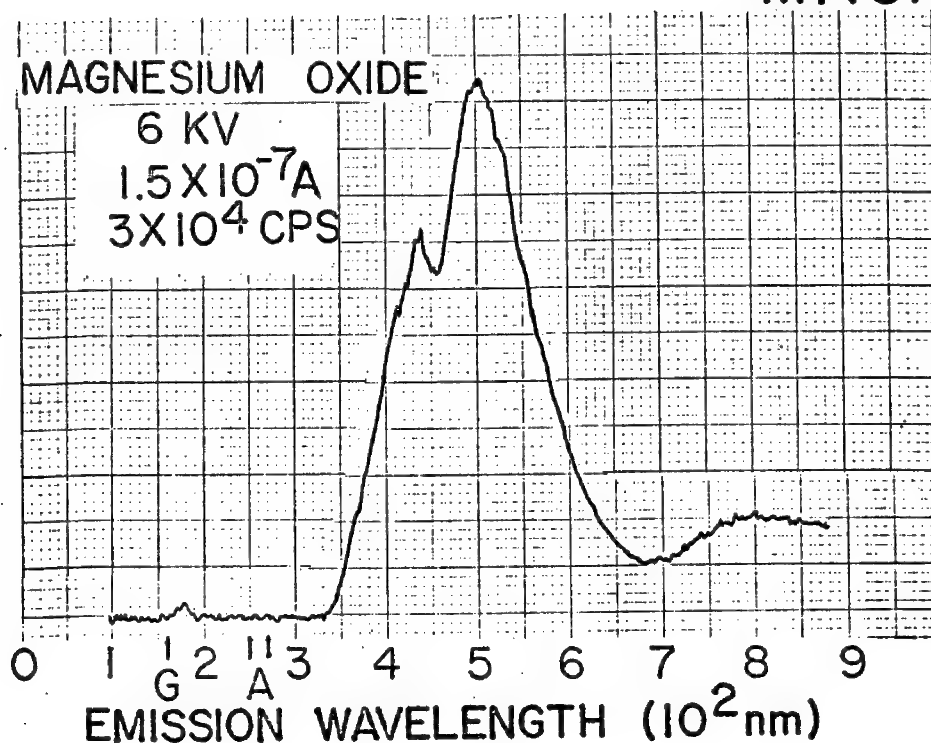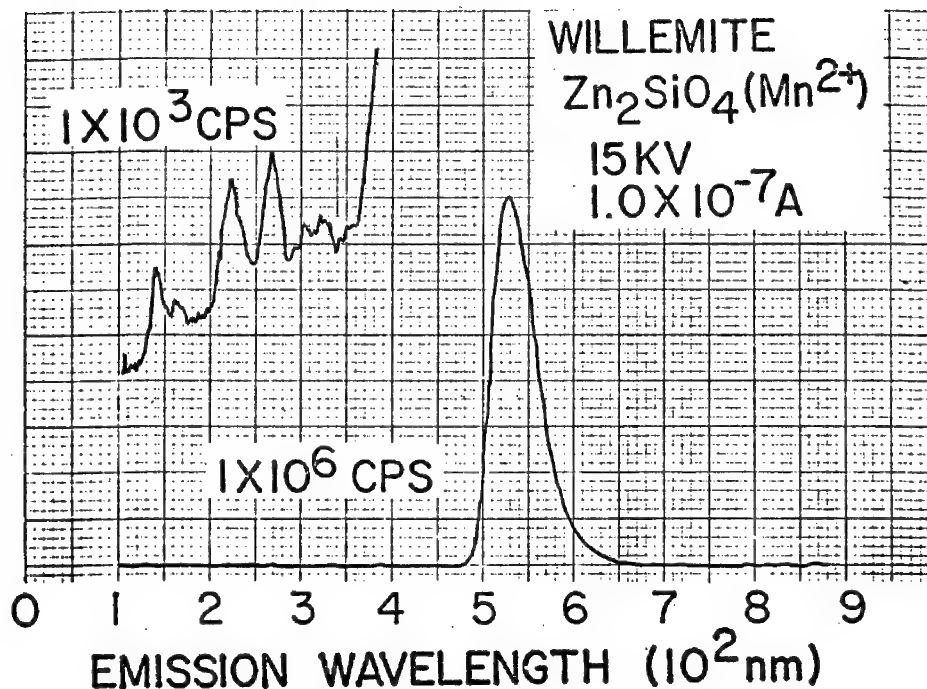
EMISSION WAVELENGTH (10^2 nm)
FIG. 3
WILLEMITE

3. Figure 3 is a typical example of impurity ion activation. The Mn^{+2} electronic states which lie within the band gap of Zn_2SiO_4 allow emission of an intense green line which overshadows all other features of the spectra in the visible and near visible regions. The activated emission features of the spectra have been studied in great detail because of their economic importance, but, in general, no investigations have been made on the intrinsic features of the spectra. A comparison of activated and nonactivated CL spectra of Zn_2SiO_4 and other materials will be given.

Recently more quasi-particle data has become available, especially for simple crystal systems: at least eight are now known in alkali halides[11], e.g. interstitial atoms and ions, vacancies, etc. Further examples will be given on the similarities and differences of CL within a given crystal system.

All in all, data interpretation is still in its infancy. However, enough can be learned now, from a great many systems, to make installation of equipment and data collection worthwhile. Availability of compilations of spectra such as those available for UV or IR absorption will allow easier identification and interpretation of CL data gathered in microprobes and from other methods of electron excitation. Additional CL studies correlated with crystallographic and electrical studies are needed.

REFERENCES

1. Greer, R. T. and E. W. White, "Microprobe Attachment for Quantitative Studies of Cathodoluminescence," Trans. 2nd National Conference of EPMA, 1967, Boston.

2. Kniseley, R. N., F. C. Laabs, and V. A. Fassel "Analysis of Materials by Cathodoluminescence Spectra Excited in an Electron Microprobe," Analytical Chemistry, January 1969, pp. 50-53.

3. Ramsey, J. N. & M. J. Mitchell, "Cathodoluminescence Studies of Various Aluminas at Low kV", Late News Paper, 11th Ann. Conf. Microbeam Analysis Society, Miami Beach, Fla., Aug., 1976.

4. Pressley, R. J., Ed., "Handbook of Lasers", Chemical Rubber Co., 1971.

5. Dean, P.J. "Junction Electroluminescence" in Applied Solid State Science, Vol. 1 (1969) R. Wolff, Editor, Academic Press, N.Y.

6. Goldberg, P., Editor, "Luminescence of Inorganic Solids (1966), Academic Press, N.Y.

7. Lushchik, C., "Edge Luminescence of Excitons in Ionic Crystals" J. of Luminescence, V 11 (Dec., 1975/Feb. 1976) p.285-289 (This journal is the best entree into the current literature.)

8. Kingery, W. D., "Introduction to Ceramics" 2nd Ed., Wiley, N.Y., 1975.

9. Chen, Y., J. L. Kolopus and W. A. Sibley, "Defect Luminescence in Irradiated MgO", J. of Luminescence, V1,2, (1970), p. 633-640.

10. Townsend, P.D., A. Mahjoobi, A. J. Michael and M. Saidoh, "Exciton Luminescence from NaCl (by CL)", J. Phys. Chem: Solid State Phys. V9, 1976, p. 4203-4211.

11. Lushchik, C., "Survey of Luminescence in Alkali Halide Crystals (The Period 1966-1969)", J. of Luminescence V1. 2 (1970), p. 594-609.

MEASUREMENT OF DIFFUSION LENGTHS OF EXCESS CARRIERS IN SEMICONDUCTORS BY THE VOLTAGE DEPENDENCE OF ELECTRON BEAM INDUCED CURRENTS AT SCHOTTKY BARRIERS

C. J. Wu and D. B. Wittry

Departments of Materials Science
and Electrical Engineering
University of Southern California
Los Angeles, California   90007

Measurements of diffusion lengths of excess carriers by electron beam induced currents at a p-n junction[1] or a Schottky barrier[2] have previously used a focussed electron beam located at varying distances from the junction which was normal to the surface bombarded. In these cases, the results are modified by surface recombination effects for small electron beam voltages and by the excess carrier generation distribution for high electron beam voltages. In the present work, we have used a Schottky barrier parallel to the surface bombarded by the electron beam and have varied the electron beam voltage, thus making the results insensitive to surface recombination effects and more suitable for the measurement of small diffusion lengths.

Our theory for the electron beam induced current is based on a modified Gaussian approximation[3] to the depth distribution of the energy dissipation function namely:

$$\phi(u) = A \exp\left[-\left(\frac{u - u_o}{\Delta u}\right)^2\right] - B \exp\left(-\frac{bu}{u_o}\right)$$

where $u = \rho Z/R$, R is the electron maximum range in g/cm^2,   (1)

$$u_o = 0.125, \ \Delta u = 0.350, \ b = 4, \ \text{and} \ A/B = 0.4$$

As shown in Figure 1, the specimen is considered to consist of three regions. In the metal layer it is assumed that the energy is dissipated without producing any excess carriers. The thickness of this layer (e.g. gold) is expressed in terms of an equivalent thickness of the semiconductor (e.g. GaAs). In the space charge depletion region, it is assumed that all the carriers generated are collected, i.e. there are no trapping or recombination processes that would modify the carrier collection efficiency. For the bulk of the semiconductor it is assumed that the carriers diffuse to the boundary of the bulk semiconductor and the transition layer and are then collected with 100% efficiency.

The theoretical collected current is obtained by integrating the carrier generation function over the transition region to obtain a drift current and by solving the diffusion equation for the assumed generation function and appropriate boundary conditions (zero excess carrier concentration at the boundary of the bulk semiconductor and the transition region) to obtain a diffusion current. The collected EBIC signal is the sum of these two currents. In this calculation, the carrier generation function is assumed to be proportional to the energy dissipation function (Eq. 1) and the results are related to the incident beam power $I_o V_o$ by setting the integral of the energy dissipation function equal to the total excess carrier generation rate G_o times the average energy required to produce a hole electron pair ε. Including a correction due to energy loss by backscattered electrons, we have

$$G_0 = \frac{V_o I_o}{\varepsilon q} \left(1 - \eta \frac{\bar{V}}{V_o} \right) \text{ carriers/sec} \tag{2}$$

where q is the electron charge η is the fraction of the incident electrons backscattered[4] and $\bar{V}$ is the average energy of the backscattered electrons in electron volts[4] and ε is given in electron volts.

In order to predict the voltage dependence of the collected current, we have assumed that the energy dissipation function remains of constant shape but scales in proportion to the maximum range of the electrons R. For GaAs we have used the following range energy equation:

$$R = 2.56 \times 10^{-3} \ (V_o/30)^{1.7} \ \text{g/cm}^2 \tag{3}$$

this was previously used by Wittry and Kyser[5] in studying diffusion lengths by the voltage dependence of cathodoluminescence in GaAs.

Theoretical curves obtained for various diffusion lengths and three different thicknesses of gold layer are shown in Figure 2. The results are plotted as a function of the efficiency of excess carrier collection given by I_{EBIC}/qG_o. The results obtained show that diffusion lengths from 1-10 microns can be determined with electron beam voltages of 0 - 50 K eV. From the theory, it is expected that even smaller diffusion lengths could be evaluated i.e. down to 0.1 μ. Experimental results and their agreement with theoretical calculations are shown in Figure 3 for three cases, namely, a Te doped GaAs specimen ($N_d \simeq 2.4 \times 10^{15}$ cm^{-3}) grown by vapor phase epitaxy on GaAs (100 orientation) with a relatively thick gold layer on the surface ($\simeq$ 310A), and a Czochralski-grown specimen of GaAs (111 orientation, doped with Te ($N_d \simeq 4 \times 10^{16}$cm^{-3}) with a thin gold contact ($\approx$ 80 A) and a thick gold contact ($\approx$ 310 A).

In comparing the experimental and theoretical results, we have used a value for ε of 4.9 eV. This value seems to provide good agreement between theory and experiment but should be considered as tentative because it is dependent on the accuracy of the calibration of the high voltage supply. (our high voltage supply must be recalibrated before a best value for ε in GaAs can be determined).

Further experimental results, details concerning the preparation of the Schottky barriers, and an analysis of the accuracy of this method will be given.

Acknowledgements

Thanks are due to J. C. Potosky of USC for technical assistance and to R. J. Stirn and Y. C. M. Yeh of the Jet Propulsion Laboratory for the GaAs and for the use of facilities to fabricate and electrically characterize the Schottky barrier diodes.

References

1. D. B. Wittry and D. F. Kyser, J. Appl. Phys. 36, 1387 (1965).

2. L. Jastrzebski, J. Lagowski, and H. C. Gatos, Appl. Phys. Letters 27, 537 (1975).

3. D. F. Kyser, Proc. of the 6th International Conference on X-ray Optics and Microanalysis, Osaka, 147 (1971).

4. H. E. Bishops results (Ph.D. Dissertation, Cambridge, 1966) were used for these values in comparing theory and experiment.

5. D. B. Wittry and D. F. Kyser, J. Appl. Phys. 38, 375 (1967).

Fig. I
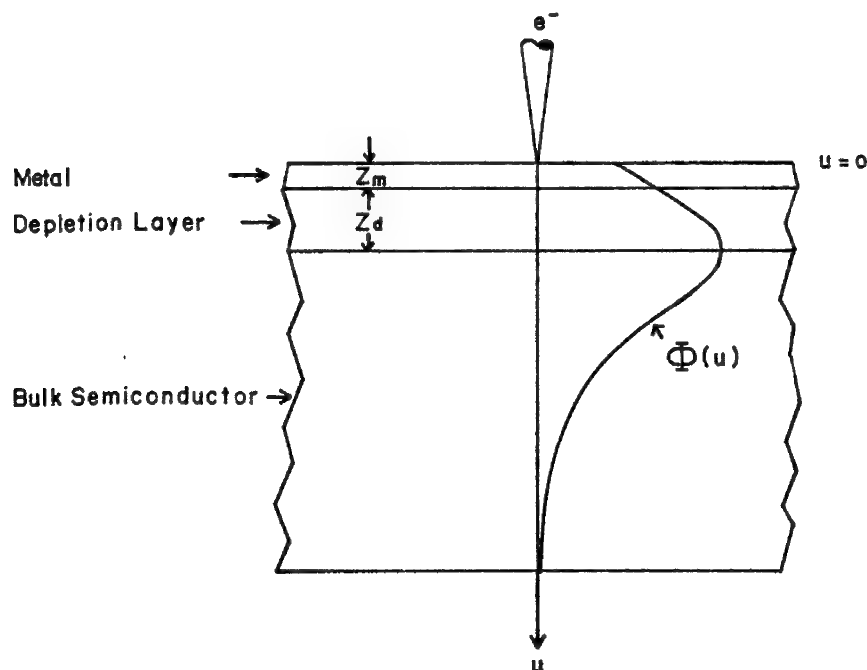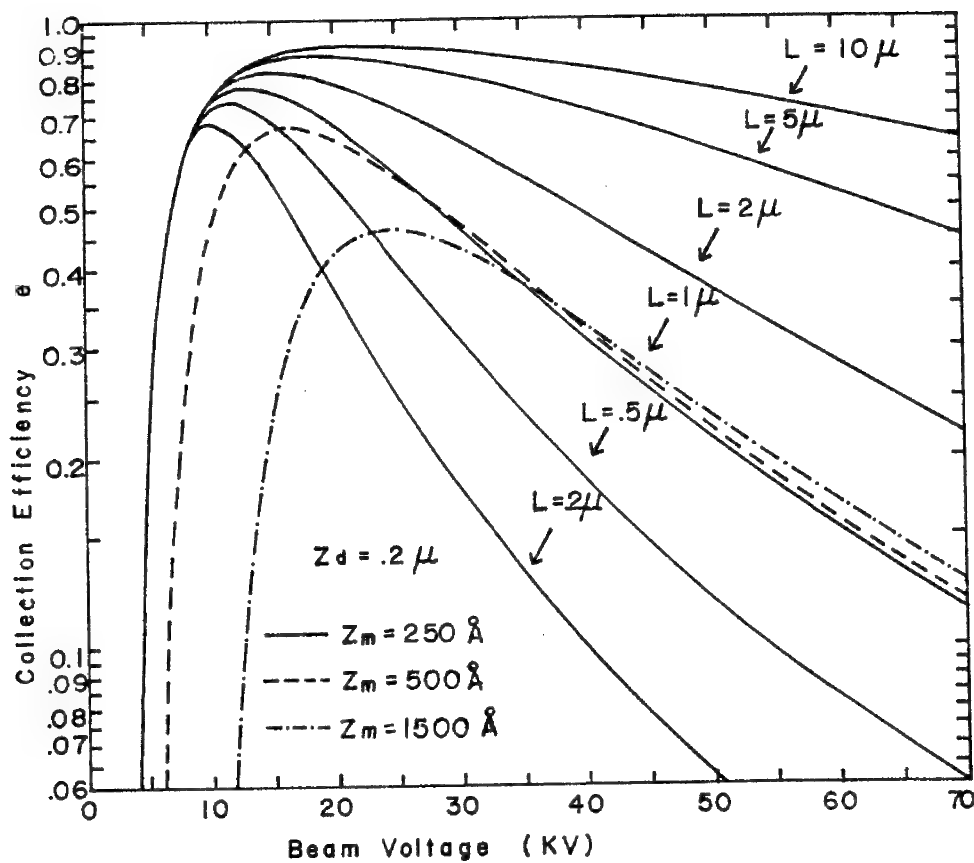
Fig. 2
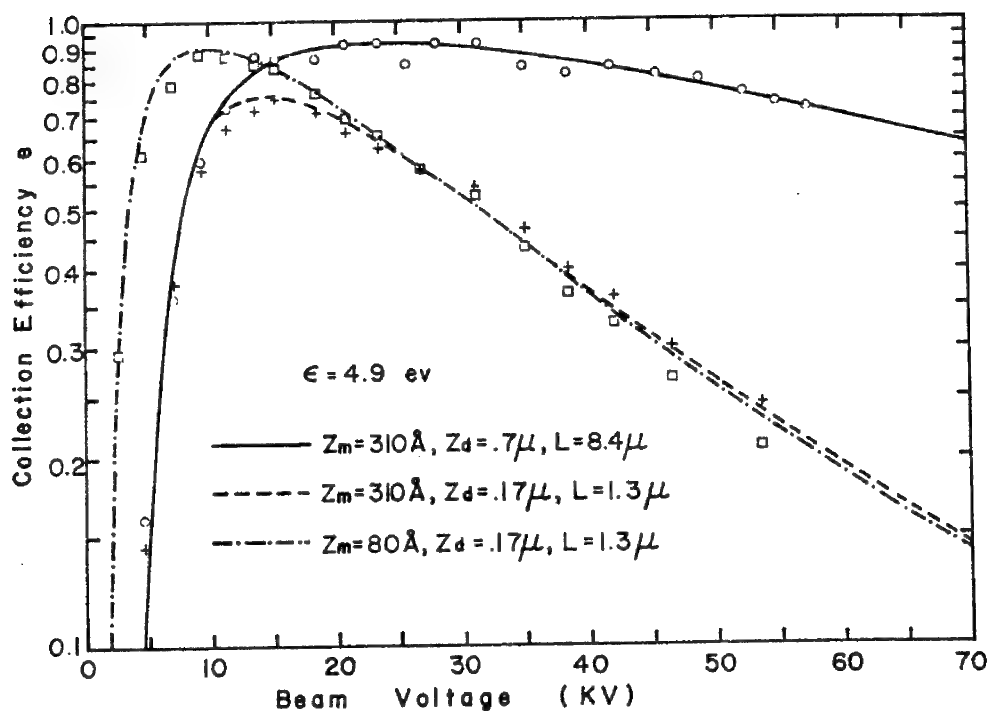
Fig. 3

SECONDARY ELECTRON ENERGY SPECTRA UNDER
BOMBARDMENT OF ELECTRONS AND IONS ON Si

T. Ichinokawa, T. Kawamura and T. Takagi

Department of Applied Physics, Waseda University, Nishi-Ohkubo 4,
Shinjuku-ku, Tokyo 160, Japan

In the energy spectrum of secondary electrons released from
metal targets by electron bombardment, fine structures are often
observed. Chung and Everhart have pointed out that secondary
electrons from metals such as aluminum mainly arise from the
decay of surface and volume plasmons via interband transitions.
On the other hand, Krüger et al. have observed many fine structures
in the energy spectrum of secondary electron emission under the
ion bombardment. These structures are attributed to the decay of
highly excited auto-ionizing states of the bombarding ions.

In the present paper, the energy distribution curve of secondary
electrons and its derivative under the bombardment of electrons
and ions are reported for silicon crystals. The energy distribution
and its derivative are measured by a cylindrical mirror analyser
in a vacuum of 10^{-9} Torr. Surface states are examined by Auger
electron spectroscopy, electron energy loss spectroscopy and
reflection electron diffraction at 10 keV. The 7X7 structure is
observed for Si(111) crystals in an initial state of the clean
surface. The changes of the secondary and Auger electron spectra
are distinctly observed by exposing the specimen in the oxygen
vapor of 10^{-5} to 10^{-7} Torr depending on the exposure time. The
electron diffraction pattern is also changed by the surface oxidation.
Those characteristic features measured by the electron bombardment
are compared to those obtained by the Ar^{+} ion bombardment. The
difference of the secondary and Auger electron spectra between
bombardments of electron and ion are discussed taking account of
the interactions of electron and ion with the crystal surface.

X-Ray Imaging and Analysis of Defect Structure
Induced by Sputtered Metal Film Deposits

H. SUGA and S. WEISSMANN, College of
Engineering, Rutgers University, Piscataway, N.J. 08854

The avoidance of large internal stresses in thin films and substrates is of considerable importance in the use and applications of thin films in microelectronic technologies. Smooth and notched silicon crystals were sputtered with tungsten and tantalum at 200°C introducing deposit layers of 1000-10,000 A. The microplastic sites induced by sputtering were disclosed by X-ray transmission topography and the plastic and elastic strain distributions in the substrate were revealed by X-ray Pendullösung Fringe topography. The curvature of the substrate, generated by the film deposit, was determined by specimen scan using automatic Bragg angle control (ABAC). Fig. 1 shows the dependence of substrate curvature on film deposit. Based on these results, the dependence of maximum stress in the substrate on the amount of film deposit was determined.

DEPENDENCE OF SUBSTRATE CURVATURE
ON FILM DEPOSIT
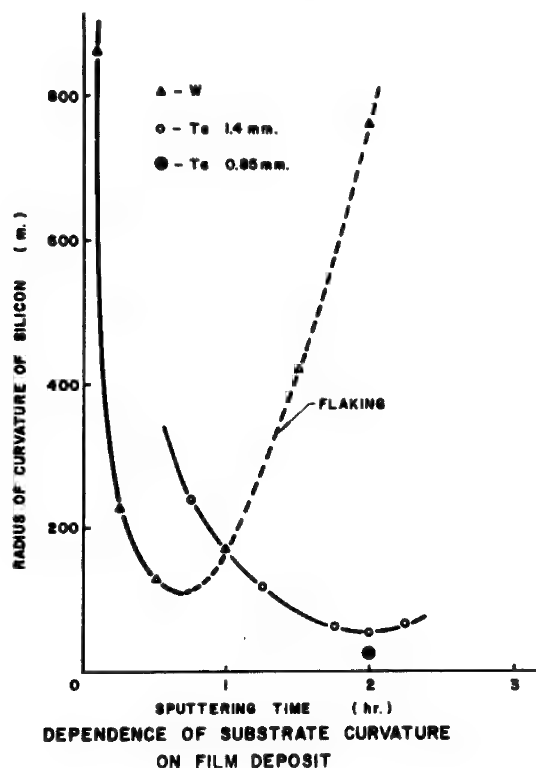
Fig. 1

It has been shown previously (1) that when residual elastic strains are constrained by microplastic sites, the plastic and elastic strains can be removed by annealing, whereby dislocations will emanate from the microplastic sites so as to relieve the constrained residual, elastic strains. This principle of strain relief by annealing was used and applied to characterize the microplastic sites induced by sputtering. By taking X-ray topographs after annealing, with the deposited layers at the entrance surface, and observing the scattering channels of the

dislocations ejected from the microplastic sites, as they traverse the Borrmann fan, the microplastic sites were located at or near the interface of substrate and film deposit. The stress dependence of Ta-sputtered silicon substrate on annealing was obtained by ABAC studies and the results are shown in Fig. 2.

STRESS DEPENDENCE ON ANNEALING
TEMPERATURE
IN Ta-SPUTTERED SI SUBSTRATE
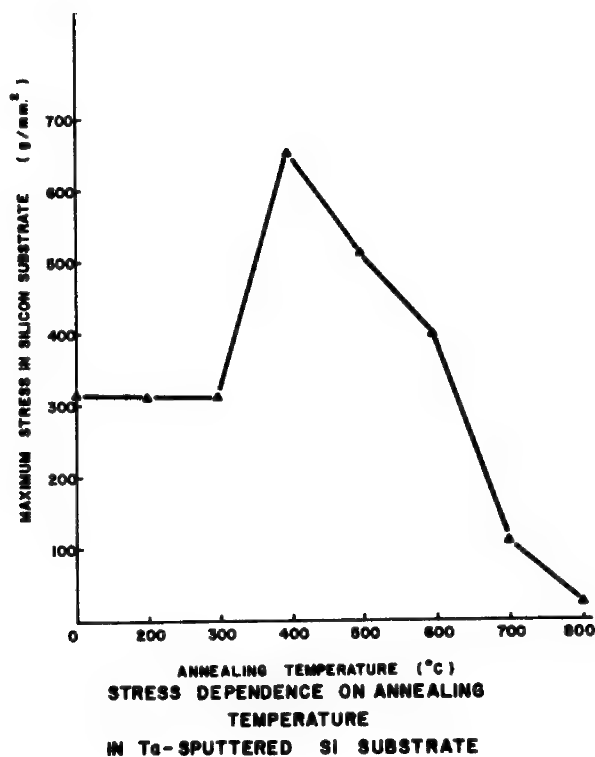
Fig. 2

Ref. I. Y. Tsunekawa and S. Weissmann, Met. Trans. 5, 1585-1593 (1974) Research sponsored by the Metallurgy and Materials Section of NSF.

A "TRANSFER OPTICS" FOR MICROANALYSIS

BY SECONDARY ION EMISSION

G. SLODZIAN and A. FIGUERAS
UNIVERSITE PARIS-SUD
Laboratoire de Physique des Solides

The detection limits of elements in low concentration have not yet been carried out to the point allowed by their practical ionization yield and the capabilities of particle counting techniques, because at low mass resolution it is not possible to differentiate simple ions from cluster ions having the same mass number. One reason among others, is that any increase of mass resolution is paid by a loss of sensitivity.

Here we describe a "transfer optics" which allows our direct imaging system to produce an ion image with the same sensitivity at high and low mass resolution. However, this can only be achieved by reducing the imaging field. The transfer optics offers other possibilities which make the system able to fit specific analytic requirements with great versatility.

It is well known that sputtered ions exhibit both angular and energy dispersions thus any collecting system will necessarily introduce a discrimination among them. Let us summarize the action of the collecting system being used : ion emitted by an object point A of the sample surface are leaving the collecting system as if they were emerging from an image point A'; moreover A' and its neibouring points look as if they were illuminated by a pupil C' (cross-over) the dimensions of which depend on both ejection angles and energies. If a "virtual diaphragm" were placed at C', it would produce angular and energetic discrimination which would limit both the aberrations about A' and the collection efficiency.

The transfer optics acts so as to focus the image of C' on the entrance slit (or diaphragm) of the mass spectrometer and the image of A' on the aperture diaphragm of the same instrument. By adjusting the focus, one can magnify or demagnify the cross-over image being projected on the entrance diaphragm while the focus of the demagnification or magnified image of A' is maintained on the aperture diaphragm. One should note that the entrance and aperture diaphragm dimensions determine the mass resolving power of the spectrometer.

Let us have a demagnified cross-over image and keep diaphragm dimensions leading to low mass resolution (typically 300). Then everything works as if we had enlarged the virtual diaphragm placed at C' and reduced the virtual diaphragm placed at A'. Thus the discrimination produced by the first diaphragm are now less severe, the collection efficiency is consequently improved but the spatial resolution of the ion image of the surface is deteriorated. Moreover, the second diaphragm leads to a reduced viewing field. When mass interference are not to be feared, such working conditions provide the highest sensitivity for a "point analysis" performed with a static ion probe (a probe is here necessary only if one whishes to maintain some spatial resolution).

Let us now demagnify the cross-over image and simultaneously reduce the dimensions of the entrance diaphragm by the same ratio. Then, everything works as if we had kept unchanged the diaphragm at the C' position. Thus, spatial resolution and collection efficiency are also kept unchanged. In addition, if we reduce the aperture diaphragm so as to weaken the spectrometer second order aberrations in the same ratio as the demagnification ratio, the mass resolving power is improved as the inverse of that ratio. However, the viewing field will suffer a new reduction. Finally, we get an ion image for which spatial resolution and collection efficiency are maintained at nearly the same level that previously it had at low mass resolution.

As an example, let us take an element M the atomic concentration of which is about 10 p.p.m.; at such a low concentration a high mass resolving power is often required in order to discriminate M^+ ions from polyatomic cluster ions. Let us assume that the ionization pratical yield is several times 10^{-3}, then it is necessary to sputter away a layer of about 10^3 angströms thickness, in order to record a hundred ions per square micron of the sample surface. The transfer optics allows to keep such a sensitivity with a mass resolving power of the order of 3 500, over a viewing field of about ten microns and with a spatial resolution better than one micron.

It is worthwhile to mention that the energy band pass of the spectrometer as well as its chromatic aberrations were taken into account. Moreover, we experienced unipotential electrostatic lenses working in an accelerating mode and we could demonstrate that both chromatic and spherical aberrations are lower than in the usual retarding mode. Besides, we could take full advantage of the transfer optics possibilities by recording ion image with a channel plate amplifier.

Applications on metallurgical, biological and geological samples will be shown.

-oOo-

SECONDARY ION MASS SPECTROMETRY

A REVIEW OF RECENT ADVANCES

Charles A. Evans, Jr.

Materials Research Laboratory

and

Department of Chemistry

University of Illinois

Urbana, Ill. 61801

The secondary ion mass spectrometry technique has reached a level of maturity such that advances are being made almost as rapidly as questions are being asked! On the fundemental level, the knowledge in ion-surface interactions are being examined for insight into the ion production. Instrumentation for SIMS is undergoing several evolutionary changes and the technique is being widely used to characterize a wide varity of materials. This abstract will outline these advances in each of these areas.

Fundemental

Although the topic has received much attention, little is known about the actual atomic processes involved in secondary ion production. The macroscopic processes influencing ion yields have been widely studied. These include copious O_2 backfilling experiments and some studies on Cs^+ ion bombardment. Only 9 of these workers have addressed the individual processes which cause excitation of electronic levels, deexcitation, screening and electron exchange between the departing atom and the surface. Of the processes influencing the ionization process, oxygen enhancement has received the most attention. Although no comprehensive theories of sputtered ion formation yet exist, it has seemed entirely reasonable that the presence at the ion-bombarded surface of an electron-accepting species would tend to enhance electron abstraction from sputtered neutral species, or inhibit neutralization of sputtered positive ions departing the surface. The detailed mechanism of oxygen enhancement of positive ion emission has been rationalized differently in several models as follows:

i) Oxygen raises the surface work function, suppressing thermal emission of electrons and positive ion neutralization.

ii) Oxygen increases the ionic nature of the bonding in the solid, leading ultimately to ionic lattices from which ions tend to be ejected with little alteration to their charge states. This is the so-called "bond-breaking" model.

iii) Oxygen depletes the conduction band of electrons, ultimately, in the oxide-insulator limit, leaving no electrons available for resonance or Auger neutralization of ions departing the surface after formation in the sputtering collision.

By inverting any of the explanations for oxygen enhancement of positive
ion emission it may be predicted that negative ion emission should be en-
hanced by electropositive substances. Cesium enhancement of negative ion
emission has also been observed by Andersen, Storms, and, recently, in our
own laboratory. Because the effects described above are explicable by all
of the various models of sputtered ion formation, the detailed processes
governing ion formation and neutralization are not greatly illuminated by
their study. Recently, studies have been made on the effect of oxygen upon
negative sputtered ion yields. Logically, any of mechanisms (i) - (iii)
above would predict the suppression of negative ion emission by oxygen.
In an early quantitative study of the oxygen enhancement effect, Morabito
and Lewis observed enhancement of Si^- by oxygen. None of the simple
mechanisms outlined above can rationalize this effect. In order to determine
whether or not the effect with silicon is an isolated phenomenon, we have
investigated the effect of oxygen upon negative ion yields from a number
of materials. All elements investigated show that negative ion yields
are enhanced by oxygen. Enhancement of both positive and negative ion
emission by oxygen bombardment is found for $Si^{\pm}$ from Si, $Cu^{\pm}$ from Cu,
$As^{\pm}$ from GaAsP, $P^{\pm}$ from GaAsP, $Ga^{\pm}$ from GaAsP, and $Au^{\pm}$ from Au. This
observation and study makes it apparant that the simple explanations
above cannot be sustained by involving special case arguments for neg-
ative ion enhancement by oxygen. This work led to the postulation of a
model which invokes chemical and electronic surface heterogeneity, on
an atomic scale, to rationalize enhancement of both positive and negative
ion yields from the same macroscopic bombarded surface.

Instrumentation

There have been several trends in SIMS instrumentation. With the introduction of the concept by Hernandez et al, high mass resolution instruments have been developed by several manufacturers. This capability is automatically incorporated in the AEI IM-20 attachment for the MS-7 mass spectrometer. Cameca has offered an electrostatic analyzer attachment for the original line of instruments and the new design will incorporate high mass resolution in the spectroscopy and imaging modes. Vacuum Generators has designed and constructed a microprobe which promises mass resolutions to 20,000 (10% valley definition). A variety of labs have performed high mass resolution studies using homemade ion sources attached to an existing mass spectrometer. Certainly not every study requires high resolution but when a confident qualitative and quantitative analysis is desired, nothing matches the satisfaction of assuring yourself of the peak's spectral purity.

Another trend is the increase in computerization of SIMS instruments to more readily handle the high data rates produced in multielement depth profiling. These systems generally provide instrument control for peak switching as well as data accumulation and reduction.

The above trend to more sophisticated and expensive instruments is being matched by the increased availability of quadrupole based instruments. Since the initial work on static-SIMS (UHV combined with low primary ion densities for surface studies) a variety of laboratories and manufacturers have turned to the low cost, versatile quadrupole mass filter. Several manufacturers offer quads with a variety of energy filters as attachments to UHV systems. The general mode is to add this accessory to an Auger

electron spectrometry or ion scattering spectrometry system. These "add-on" SIMS systems are best suited to surface studies and for qualitative analyses of surface trace impurities. The additional benefit of hydrogen detection adds to their attractiveness. They generally find limited utility as a high resolution, high sensitivity depth profiler due to the primary ion sources in most Auger and ISS systems. Improvements of the ion sources to provide a capability for oxygen ion bombardment, reduce the problems associated with oxygen backfill in a static vacuum system and the small beam diameter to rastered area ratio will be required for these add-on systems to realize the full capability of the SIMS technique.

Two laboratories have overcome the technical limitations of the above situation by combining the quadrupole with a primary ion source and optics optimized for secondary ion mass spectrometry. Not only do these instruments provide excellent depth profiling but the a-DIDA of Wittmaach provides 2-10 μm diameter primary ion beams. The other system, constructed by Magee at RCA, incorporates stigmatic extraction optics and a spherical electrostatic analyzer which seems to provide an extraction and transmission efficiency approaching those of magnetic sector instruments.

Of potentially great interest to the SIMS user is the recent introduction of viable Cs^+ primary ion sources for ion probes. Although early studies demonstrated the improved sensitivity for the electronegative elements using Cs^+ bombardment, Storms was the first to test a high performance Cs^+ source and demonstrated the improvement in bulk sensitivities obtainable in this mode. Subsequently, the Illinois group has shown that Cs^+ ion bombardment and negative ion spectroscopy can provide $10^{15} - 10^{17}$ atom cm^{-3} detection limits in a sample limited, depth profiling mode for

H,C,O,P,S, and As. They have estimated similar limits for Se and Te.

Applications

Application of secondary ion mass spectrometry have spanned the capabilities of the technique. The areas studied include metallurgy, semiconductor technology, organic compounds and biological materials. Of particular interest are the trends of application research as directed and influenced by instrumentation developments and the demands of modern science and technology. Ultra high vacuum systems and the quadrupoles have engendered much activity in surface studies and static SIMS. Recent work in this area has shown that the low ion doses and accompanying low damage permit the production of quasi-molecular ions characteristic of many common low-volatility organic compounds.

The potential applications of Cs^+ ion bombardment/negative ion spectroscopy/ultra high vacuum is particularly interesting to this author. The new areas of applications include the interstitials (H,C and O) in metallurgy and important impurities (H,C and O) and common dopants (P,S,As,Se and Te) in Si and GaAs technology.

CRITICAL PROBLEMS IN QUANTITATIVE SECONDARY ION MASS SPECTROSCOPY

D. B. Wittry
Departments of Materials Science
and Electrical Engineering
University of Southern California
Los Angeles, California   90007

The development of methods for quantitative analysis using secondary ion mass spectroscopy (SIMS) has been a long and slow process because of the complex nature of sputtering phenomena, the possibility of several mechanisms for the formation of ions during sputtering, and the dependence of observed results on a number of instrumental factors that have not been fully understood. While the detected ion intensities obtained with SIMS basically depend on the product of sputtering rate, the efficiency of ionization of the sputtered particles and the efficiency of detecting the ions produced, each of these factors depend on a large number of parameters. For example:

1. Sputtering rates depend on

    a) the nature of the bombarding ions
    b) the partial pressure of reactive gas and the primary ion
        current density
    c) surface preparation methods
    d) crystallographic effects

2. Ionization efficiency of the secondary ions depends on

    a) the nature of the bombarding ions
    b) the partial pressure of reactive gas and the primary ion
        current density
    c) the composition of the ion-implanted layer

3. The efficiency of detection of ions depends on

    a) the properties of the secondary ion extraction geometry
    b) the energy band-pass of the mass spectrometer
    c) the energy distribution of the sputtered ions
    d) the properties of the secondary ion detector
    e) surface charging effects and effects due to redeposition
        of particles having a charge opposite to the secondary ions.

Many of the parameters that influence the ion intensities detected are interdependent; this has resulted in some controversy concerning differences in results obtained with different instruments or under different analytical conditions. This is particularly true with respect to work done before all of the foregoing factors were fully appreciated. However, significant contributions have been made by many investigators in recent years regarding the importance of these factors, and there is now a general consensus[1] that quantitative

results are best obtained by using intensity ratios (to eliminate the dependence on sputtering rate) and by saturating the surface with a reactive gas either by using primary ions of a reactive gas or by blowing a reactive gas on the surface (to reduce the dependence of ionization efficiency on the vacuum conditions and the current density of the primary beam). In some cases, with saturation of the surface by a reactive gas (e.g. oxygen) crystallographic effects are reduced, but in most cases, there is an important ancillary benefit, namely, the enhancement of ionization efficiency for positive ions. Moreover, there is some indication that oxidation of the surface yields more uniform sputtering of the surface for metallic specimens.

When the analytical conditions are well controlled, there is a general feeling among workers in this field that quantitative results can be obtained with a relative accuracy of less that ± 30% in most cases.[1] This illustrates the well-known fact that SIMS is not a useful quantitative technique for the measurement of elements present in high concentrations. However, since the principle advantage of SIMS is its capabilities for detection of elements present in trace amounts (e.g. at the ppm level or less), the ability to measure concentrations to a relative accuracy of ± 30% represents a significant advance in quantitative analysis because the raw data may yield relative intensities that differ from the relative concentrations by several orders of magnitude and because there are few other analytical methods that can provide comparable values for the minimum mass detectable.[2]

Further improvements in quantitative analysis using SIMS will require more consideration of factors 3a-3e mentioned in the foregoing. These factors will be particularly important in methods of quantitative SIMS based on various models that have been proposed to predict the ionization efficiencies.

These factors will be discussed in greater detail with reference to published work and two approaches will be suggested to minimize the problems associated with these factors.

References

1. U.S.-Japan Seminar on "Quantitative Techniques in Secondary Ion Mass Spectrometry", Honolulu, Hawaii, October 12-17, 1975.

2. D. B. Wittry, Proc. Advanced Techniques in Failure Analysis Symposium - 1976, IEEE Cat. No. 76 CH 1092-6 REG 6.

Use of a Cesium Primary Ion Source on an Ion Microprobe Mass Spectrometer

R. K. Lewis, California Institute of Technology*

P. Williams and C. A. Evans, Jr., MRL, University of Illinois

P. R. Hanley, General Ionex Corp.

A commercially available thermal ionization cesium source has been modified and adapted for use as a primary ion source on the AEI IM20 ion microprobe mass spectrometer at the University of Illinois. This cesium source, shown schematically in Fig. 1, can be readily interchanged with the standard duoplasmatron ion source.

A porous tungsten frit is used as the emitter. The frit and frit heater are held concentric with the ion optical axis by a molybdenum plate which serves as the beam-forming electrode. Approximately 400 watts of power are used to heat the frit to 1100°C. The evaporation rate of the cesium is controlled by a heater attached to the stainless steel cesium reservoir. Freon circulating in the source housing maintains the housing at a safe operating temperature.

The reservoir is loaded with cesium under an inert atmosphere. The area of the frit (~ 12 mm^2) is large enough to allow the inert gas to be pumped through the frit in a few minutes. The source has proven to be remarkably resistant to degradation through exposure to atmosphere.

Above a critical temperature ($\sim 1100^\circ$) the ion yield was nearly 100% and insensitive to temperature changes of the frit. Beam densities ranged from 10 to 20 ma/cm^2 for beam diameters 8 to 20 µms. The beam stability was better than 1% after a one-hour warmup. Cesium contamination of the ion column was negligible after several hundred hours of operation.

The sputtering rates were two to five times greater than that obtained with O_2^+ ions of the same energy. Compared to oxygen, the cesium bombardment produces fewer sputtering artifacts and less ion-induced subatomic mixing which improves the depth resolution obtainable with depth profiling.

The secondary negative ion count rates were obtained for matrix levels of As and P in GaAs, P and Si in Si; for trace levels of H, C, O, P and As in Si, and S in GaAs. Two to three orders of magnitude improvement in detection sensitivities were found for these elements. The detection limits obtained are summarized in Table I. The largest improvements were obtained for those elements which have mass interferences from polymerics containing matrix elements and oxygen which are absent in the mass spectra produced by cesium bombardment.

Depth profiles were obtained for five ion implanted species (H, C, O, S and F). These profiles are very useful in determining ion yields and detection sensitivities when the analysis must be performed under sample limited conditions.

---

* Previously with the Materials Research Laboratory at the University of Illinois.

Table I

Detection limits for Cs^+ ion bombardment
$(atoms/cm^3)$

Species (Matrix)	Signal Limit[a]	Background[b]	Background[c] Limit
As (Si)	6×10^{16}	3×10^{15}	
O (Si)	1×10^{16}	4×10^{19}	1×10^{17}
C (Si)	2×10^{17}	4×10^{18}	1×10^{17}
H (Si)	8×10^{17}	4×10^{19}	1×10^{18}
S (GaAs)	2×10^{17}	2×10^{17}	
F (Si)	2×10^{16}	6×10^{16}	

[a]Concentration giving 100 counts (above background) when
(30×30) $\mu m^2 \times 100$ Å of sample is sputtered.

[b]Concentration which would give a count rate equivalent to the
background signal B.

[c]Concentration which would give a count rate equivalent to $2\sqrt{B}$.
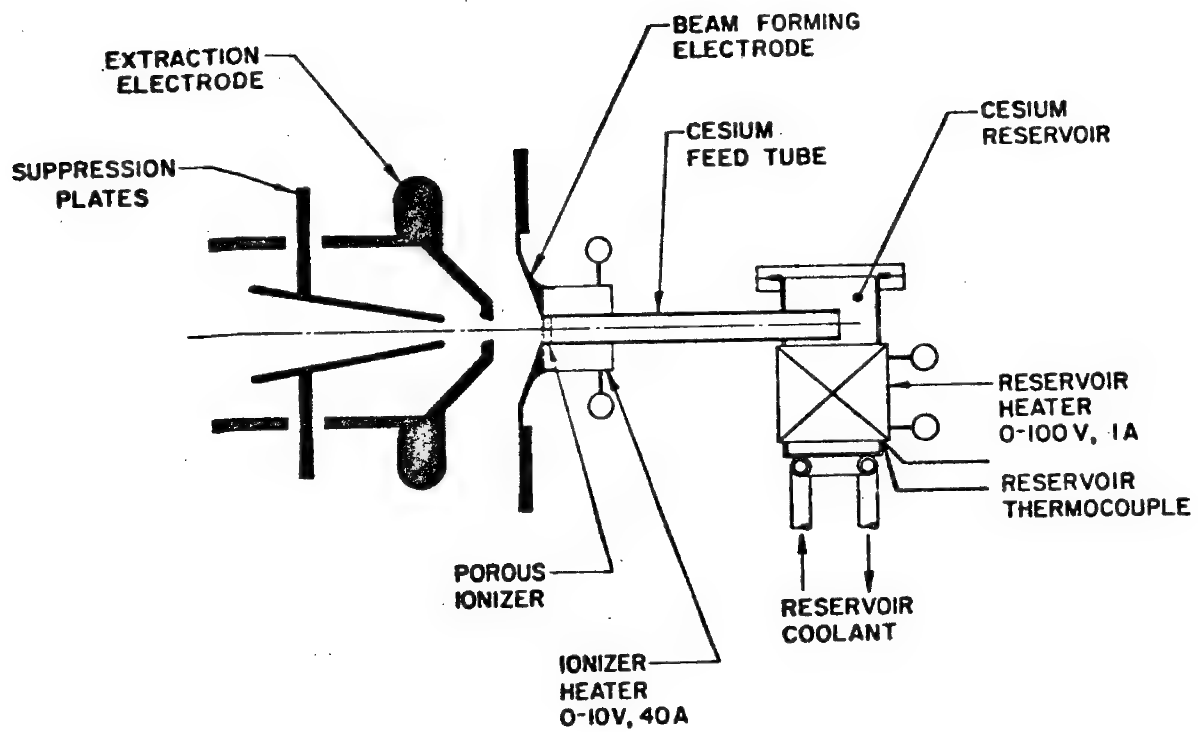
SCHEMATIC—CESIUM ION GUN

Figure 1

DIDA - A MULTIPURPOSE SCANNING ION MICROPROBE

K. Wittmaack
Gesellschaft fuer Strahlen- und Umweltforschung mbH
Physikalisch-Technische Abteilung
D-8o42 Neuherberg, Germany

In this contribution the characteristics of the DIDA scanning ion micro- probe /1/ are presented together with some examples of very recent applica- tions. The system is essentially a differentially pumped UHV secondary ion mass spectrometer with quadrupole mass filter (fig. 1). It is designed such that most of the problems faced in routine analysis of various types of speci- men structures can be solved without modifications in spectrometer configura- tion.

Both noble gas ions and oxygen ions can be produced by the ion source. The primary ion energy is continuously variable from below 1 keV to 15 keV. The (stabilized) beam current can be varied from below 1 nA up to 5 μA. SIMS ana- lysis of the sample composition at the very surface may be carried out at low beam currents either with a defocused static beam or with a raster scanned focused beam. Raster scanning ion images of the lateral distribution of ele- ments at the instantaneous sample surface can be obtained with a resolution of about 2 μm. Raster scanning depth profiling is usually performed in con- junction with an electronic aperture which allows adequate suppression of edge effects /2,3/. Charge build-up on insulating specimens is prevented by simultaneous bombardment with a low energy electron beam.
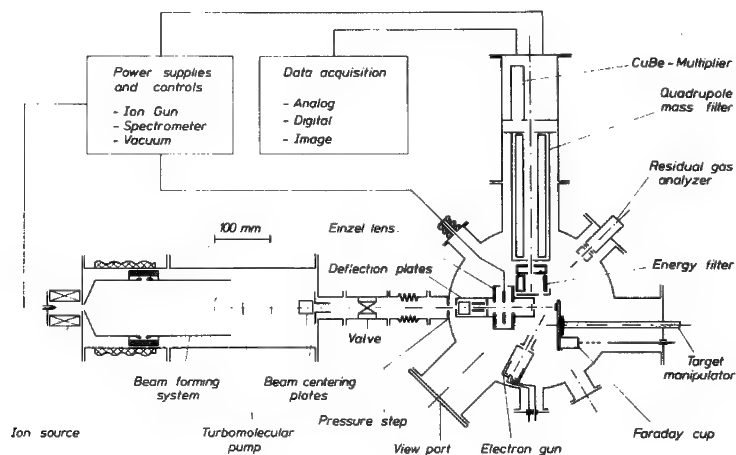
Fig. 1. DIDA scanning ion microprobe (schematic).

The capabilities of the instrument are illustrated by the following exam- ples of recent investigations. Fig. 2 shows a scanning ion image of a grid pattern in a nickel foil. Such a structure can be used both for optimum set- ting of the final lens and for determining the lateral resolution. From the image in fig. 2 a lateral resolution of about 2 μm can be duduced.

An example for a comparative study of the lateral distrubution of differ- ent elements in the same sample is presented in fig. 3. Precipitation of calcium and depletion of manganese at a grain boundary is clearly evident in this case.
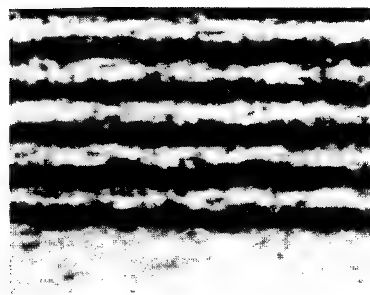
Fig. 2. Scanning ion image of a grid pattern in a thin nickel foil. The width of each slit and grid, respectively, is 4.5 µm. Primary ions: 12 keV O_2^+.

$^{58}Ni^+$ 　　 $\mathbf{I}$ 1o µm

$^{4o}Ca^+$ 　　 $\mathbf{I}$ 25 µm 　　 $^{55}Mn^+$

Fig. 3. Comparison of the lateral distribution of calcium and manganese around a grain boundary in a tungsten oxide mineral. Primary ions: 12 keV O_2^+. Primary ion charge compensation with 5oo eV electrons.

Fig. 4. Scanning ion image of the distribution of potassium in a semi-thin section of the back bone of a mouse. Primary ions: 12 keV O_2^+. Primary ion charge compensation with 5oo eV electtons.

$^{39}K^+$ 　　 $\mathbf{I}$ 2o µm

Fig. 4 shows the lateral distribution potassium in a semi-thin section of the back bone of a mouse. This is a first example of ion microprobe investigations in biological research. Further successful studies on biological specimens may open a new field of ion microprobe applications.
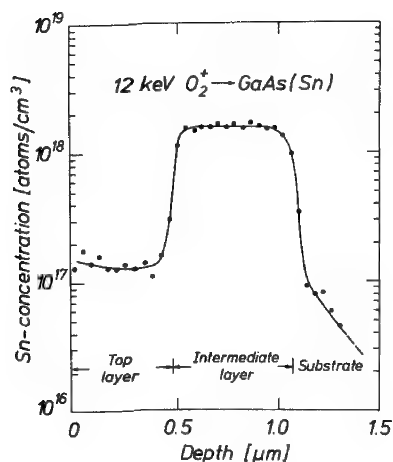
Fig. 5. Depth profile of a double
layer of Sn-doped GaAs on undoped
GaAs.
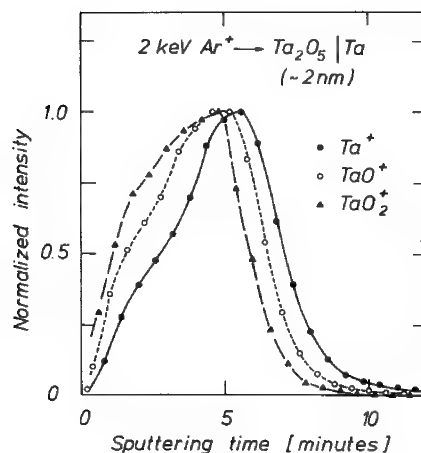
Fig. 6. Depth profile of a room
temperature oxide on a polycrystal-
line Ta foil.

Examples of depth profiling studies are shown in figs. 5 and 6. High speed
depth profiling of tin in gallium arsenide is demonstrated in fig. 5. The
sputtering rate in that particular run was about 2 μm/h, so that the analysis
was completed after 4o minutes. The homogeneity of tin doping of the respec-
tive gallium arsenide sandwich layers is clearly evident. The results of fig.5
indicate that depth profiling of Sn in GaAs can be performed down to concen-
trations of a few $1o^{16}$ atoms/cm^3.

Fig. 6 shows depth profiles of different ions emitted from a room tempera-
ture tantalum oxide on a tantalum foil. It is obvious that each of the ions
recorded quasi-simultaneously in one run reflects the oxygen concentration in
a different way. To achieve an adequate depth resolution in this analysis the
primary ion energy had to be reduced to 2 keV. Note that the depth resolution
thus obtained is better than 1 nm at the trailing edges of the profiles. This
is by far the best depth resolution ever reported.

Further examples of recent applications are presented together with a dis-
cussion of basic limitations of depth resolution in sputter profiling.

References
/1/ K. Wittmaack, Rev. Sci. Instrum. 47 (1976) 157.
/2/ K. Wittmaack, Appl. Phys. Lett. 29 (1976) 552.
/3/ K. Wittmaack, Appl. Phys. 12 (1977) 149.

A COMPUTER-BASED RECORDING SYSTEM

FOR HIGH MASS-RESOLUTION ION-PROBE ANALYSIS

J.V.P.Long, D.M.Astill, J.N.Coles*, & S.J.B.Reed

N.E.R.C. Ion Probe Unit, Madingley Rise, Cambridge CB3 0EZ, England.

Introduction

In ion-probe analysis the mass spectrum typically contains many molecular peaks produced by ionised clusters of atoms, and there is a high probability of interference between these and the monatomic peaks which are generally of interest for analysis, particularly when many elements are present.   With high mass-resolution, however, it is often possible to resolve isobaric molecular and atomic peaks by virtue of their mass defect: for example ^{52}Cr and $(^{26}Mg)_2$ can be separated with a resolution of 2,000 (defined as mass/peak width at 10% peak height), enabling Cr to be detected in the presence of Mg (Reed et al., 1976).

The AEI IM-20 ion probe as installed in this laboratory is based on the double-focusing MS702 spark-source mass spectrometer, which is capable of resolution in excess of 10,000 (Banner & Stimpson, 1974).   An ion counting system, using a slit in place of the photo-plate and an open-ended electron multiplier as the detector, is available on this instrument.   In the ion probe mode the secondary-ion accelerating voltage is fixed, usually at 10 kV, and different masses are selected by varying the magnet current, which, on the original instrument, is controlled manually by means of a potentiometer and a range switch.   Provision is also made for sweeping the magnet and recording the spectrum on a chart recorder.   However, there are no facilities for switching precisely between a number of peaks as is often required in ion-probe analysis, or for recording separate sections of the spectrum at high mass resolution. The computer-based system described here was developed in response to these needs.

Magnet control system

To avoid hysteresis effects it is essential to monitor and control magnetic field rather than the magnet current.   Further, if the system is to be able to step through peaks at high mass resolution in order to record the peak profile in the case of overlapping doublets etc., a short-term stability of a few ppm is required. Long-term drift can, if necessary, be corrected by adjusting the mass scale in the computer between successive sweeps.

---

*Now at: Research School of Earth Sciences, Australian National University, Canberra, Australia.

In the MS702 the magnet gap is only 3 mm wide and the pole-faces are inside the vacuum chamber. This precludes the use of a rotating-coil magnetometer, as employed for example by Wasserburg et al. (1969) for high-precision peak switching. Also, although a Hall element may be inserted elsewhere in the magnetic circuit (Degreve et al., 1974) residual hysteresis is then greater than when the field is monitored in the gap. In the present system two Hall elements consisting of epitaxial n-GaAs (which has the relatively low Hall-voltage temperature coefficient of -0.025% K^{-1}), mounted on a UHV-compatible substrate, and supplied by Dr E.Cohen (Dept. of Electrical Engineering, University of Manchester Inst. of Science & Technology), are used. These measure 10 mm x 10 mm x 1 mm thick and are mounted on a copper plate in the magnet gap, close to the ion path (fig.1), together with a thermocouple to provide a temperature reading for correcting the Hall voltage. The Hall elements are driven by separate highly-stabilised current sources, and their combined output voltages are amplified to provide a 0-10 V signal, which is presented visually as a 6-digit display by means of a precision voltage-controlled oscillator and crystal clock.

The control loop is completed by comparing the amplified voltage with that derived from a digital-to-analogue converter (DAC) and applying the amplified error signal to the existing MS702 power supply (fig.2). The DAC is controlled by a Data General Nova 2 computer, and the control program enables the required mass to be selected by means of a polynomial relating mass to Hall voltage.

Performance

The stability of the digital field reading under open-loop conditions over a few-minute period is better than ± 3 ppm of full scale. Residual hysteresis is such that the apparent position of a peak may differ by 1 part in 2,000 when approached from maximum and minimum field. In practical operation the field is always approached from below, in which case, under closed-loop computer control, the resetting error is better than ± 4 ppm of full scale. Long-term drift is determined almost entirely by temperature changes in the Hall elements: all other critical components are temperature-stabilised to ± 1 K.

References

Banner,A.E. & Stimpson,B.P.
    Vacuum 24 511 (1974).
Degreve,F., Figaret,R., Le Goux,J.J. & Calavrais,L.
    Int. J. Mass Spec. & Ion Phys. 14 183 (1974).
Reed,S.J.B., Long,J.V.P., Coles,J.N. & Astill,D.M.
    Int. J. Mass Spec. & Ion Phys. 22 333 (1976).
Wasserburg,G., Papanastassiou,D.A., Nenow,E.V. & Bauman,C.A.
    Rev. Sci. Instr. 40 288 (1969).
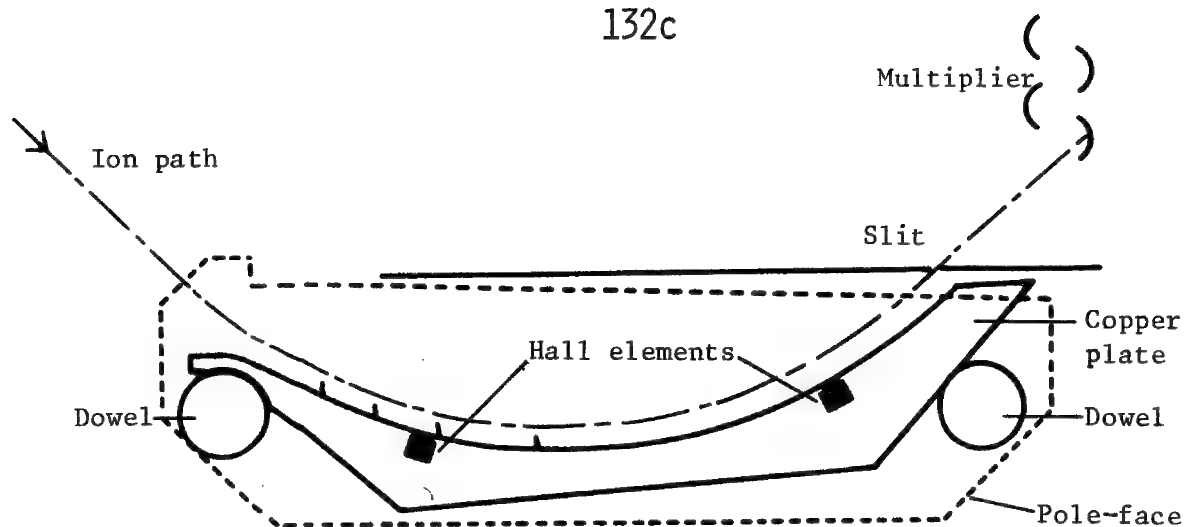
Figure 1. Layout of plate carrying Hall elements for field monitoring.
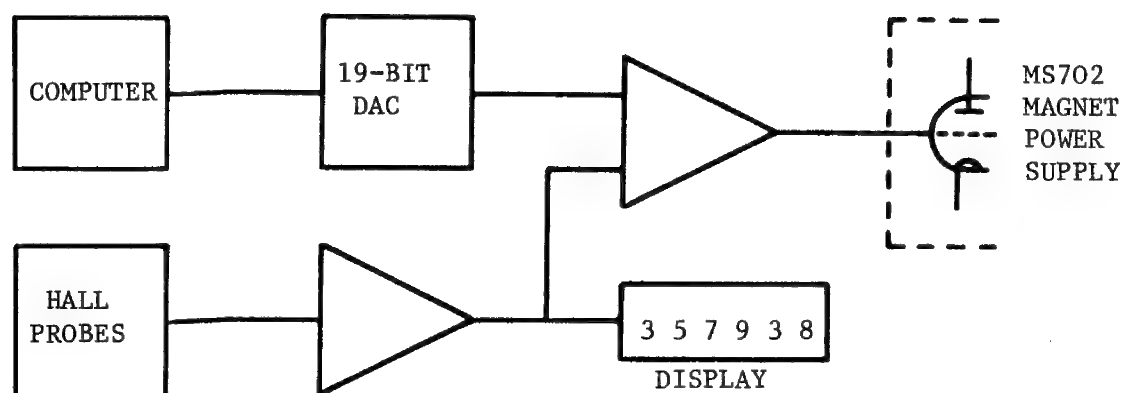
Figure 2. Simplified block schematic diagram of magnet control system.

Figure 3.

Computer-controlled step-scan through
doublet at mass 44 in spectrum from
$CaMgSi_2O_6$ specimen.

One step = 1.6 m.m.u.
Counting time = 1 sec. per step.
Mass resolution = 4,000.

^{44}Ca $^{28}Si^{16}O$
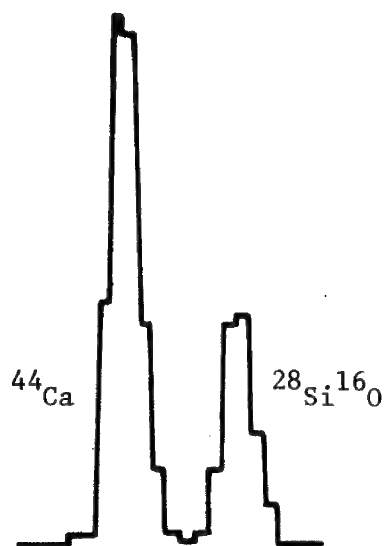
ABSTRACT

A NEW SECONDARY ION EMISSION MICROANALYZER

JM. ROUBEROL - M. LEPAREUR - B. AUTIER - JM GOURGOUT

Société CAMECA
103 Boulevard Saint-Denis
F 92400 Courbevoie

-oOo-

As the IMS 300 our previous instrument, the new CAMECA IMS-3F secondary ion analyzer is based on the concept of a mass selecting ion microscope; it has been designed with the aim of improving especially : mass resolution, sensitivity, image brightness, analysis localisation, isotope ratio measurement, vacuum quality, and simplicity of use.

PRIMARY ION OPTICS

The primary ion beam is generated by a duoplasmatron source. Its accelerating voltage is adjustable up to 20 kV. Positive or negative ion beam can be produced and focused to diameters from about 1 micron to .5 millimeter by a three electrostatic lenses column, the axis of which making a 60° angle with the specimen surface. A raster device may be used to obtain flat bottom crater for in-depth analysis.

EXTRACTION SYSTEM

Secondary ions are extracted perpendicularly to the specimen surface by an accelerating voltage of 5 kV and focused by a set of electrostatic lenses playing the role of a transfer optics that allows, by control of the magnification, to collect the maximum number of ions for the chosen area at a given mass resolution. This system consists of an immersion lens followed by three unipotential lenses, only one being activated at.a time in order to give three preset fields of view : 30, 150 and 450 microns. As a result of the transfer optics use, the sensitivity increases as the field decreases and, for example, high resolution mass analysis can be performed for very small areas.

MASS SPECTROMETER

The mass filtering section has been designed in view :

. To form a compact double focusing mass spectrometer of about 8,000 maximum mass resolution;

. To add global lens action to beam filtering function;

. To be achromatic for the final image;

. To filter in energy the secondary ion beam independently of its angular aperture and for both modes : spectrometry and microscopy.

The answer was an arrangement composed mainly of an electrostatic spherical analyzer (ESA), an intermediate unipotential lens and a magnetic prism. It works as follows :

The entrance diaphragm is located in the object principal plane to the ESA, the energy slit and the intermediate lens being in its image principal plane.

The transfer optics is adjusted in such a way to focus the crossover on the entrance slit and to project a magnified specimen image in the achromatic object plane of the ESA.

The intermediate lens is energized to carry the specimen virtual achromatic image given by the ESA to the achromatic object plane of the magnetic prism. Then the final specimen surface image is achromatic. A stigmator is added to correct the residual astigmatism.

In addition, the position of the magnetic prism in respect to the energy slit and its inclined boundaries are such that one obtains a final stigmatic cross-over at the mass selecting slit.

Finally, the distance between the two prisms and their respective radii are chosen to achieve also an energy focusing at this slit, thus making the whole secondary ion optics totally achromatic.

In practice, the energy slit and the intermediate lens cannot be both in the same plane and the later is slightly shifted towards the magnetic prism.

Geometrical characteristics of the spectrometer are consequently modified to keep the above optical properties.

PROJECTION OPTICS, IMAGE CONVERTER AND ION COUNTING SYSTEM

The mass spectrometer is followed by a two lenses projector permitting to focus at variable magnification either the final cross-over or the virtual secondary ion filtered image on a channel plate and fluorescent screen assembly acting as an ion to electron image converter.

In the first case, it is possible by using a narrow entrance slit and by opening widely the output slit to display the final line and its vicinity, so making very convenient direct observation of multiplet at high resolution.

The channel plate converts positive as well as negative ion beams and improve the image brightness by several order of magnitude compared with the converter used in our previous ion analyzer. As a result, the final image can be photographed by a conventional camera through a viewing port.

An electrostatic deflector is provided to switch the beam from the image converter to an electron multiplier for mass spectra recording and quantitative measurements.

VACUUM SYSTEM

In designing the instrument, great care has been taken to the vacuum quality. Stainless steel has been througoutly used and the entire instrument is bakable.

The primary ion column is evacuated by an oil diffusion pump, the specimen chamber by a turbomolecular pump and the rest of the instrument by two ion pumps.

ELECTRONICS

The electronics of the new ion microanalyzer are such as to control most of the operating parameters, to acquire data and to edit results through a dedicated minicomputer.

-o0o-

OPTICS OF
THE IMS-3F
ION
MICROANALYZER

INTERMEDIATE
LENS

MAGNETIC
PRISM

E. S. A.

B_1'

$M(V+\Delta V)$

Ω

A_2

A_1'

$M(V)$ O_2

B_2'

A_2'

B_1 A_1

O_1' S_2

B_2

PRIMARY
ION
SOURCE

O_1

O_2'

S_1

STIGMATOR

3 LENSES
PRIMARY
COLUMN

S_3

TRANSFER
OPTICS

a' b'

PROJECTOR

DEFLECTOR

IMMERSION
LENS

b a

ELECTRON
MULTIPLIER

CHANNEL
PLATE

SPECIMEN

FLUORESCENT
SCREEN
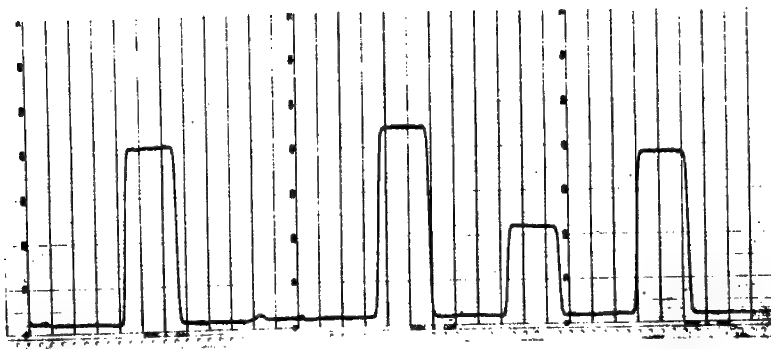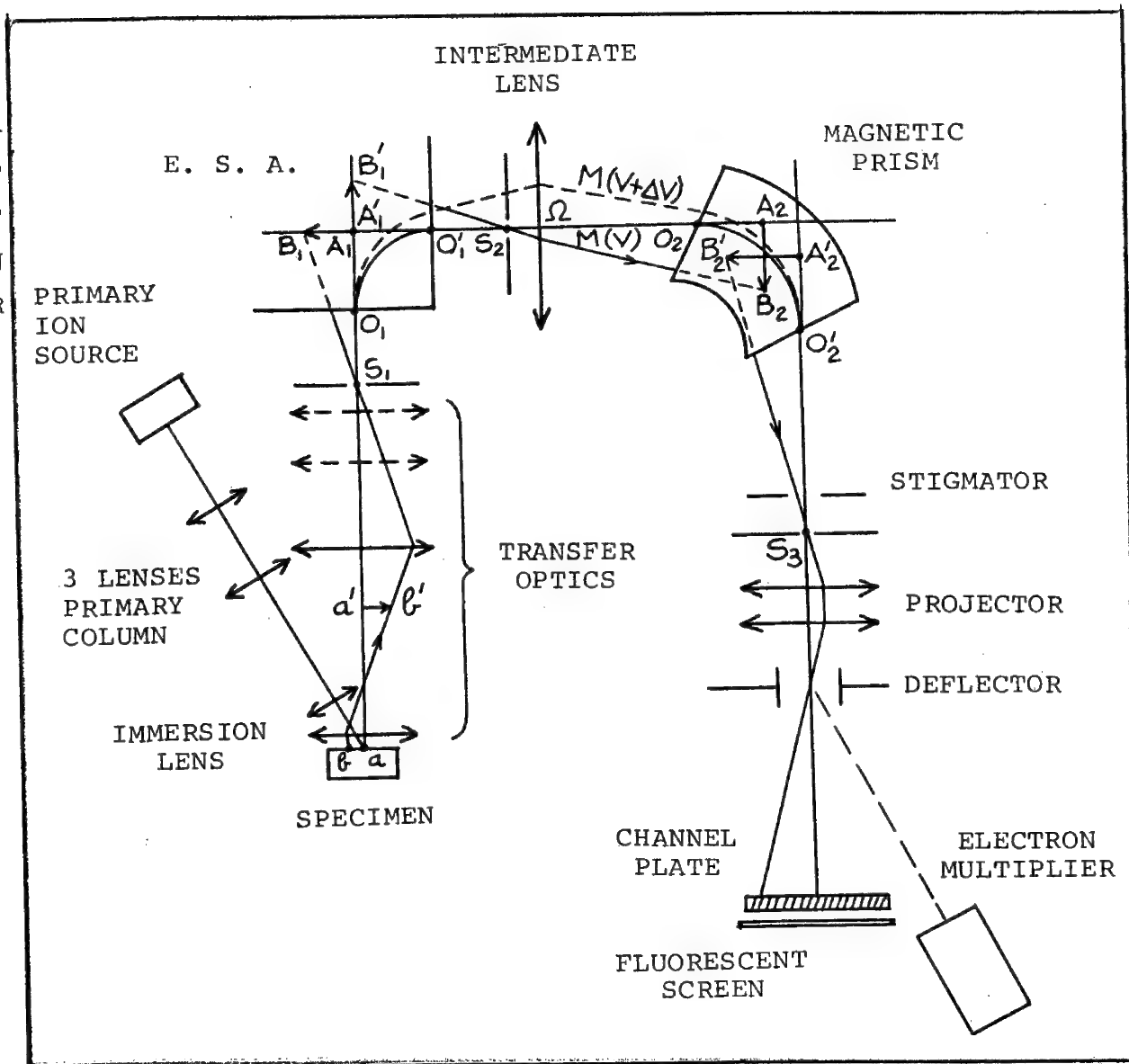
TUNGSTEN SPECTRUM SHOWING FLAT TOP PEAKS
(mass resolution = 450)
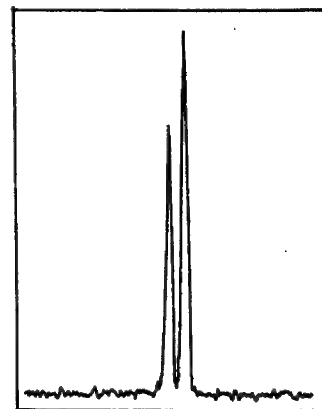
$^{63}Cu^+ - ^{47}Ti^{16}O^+$ doublet
($M/\Delta M = 3\ 700$)

RAPID DATA ACQUISITION USING AN AUTOMATED SIMS QUADRUPOLE MASS ANALYZER FOR SOLIDS: APPLICATION TO HIGH RESOLUTION DEPTH PROFILING

R. L. Conrad, T. A. Whatley, and R. D. Fralick

Applied Research Laboratories
9545 Wentworth Street
Sunland, California 91040

INTRODUCTION

The ARL Quadrupole Mass Analyzer for Solids (QMAS) is capable of precise, rapid secondary ion mass spectrometric (SIMS) analytical data acquisition. The instrument consists of three major components: The primary ion column, the secondary ion column, and the data readout and control system. The primary ion column generates and focuses a primary ion beam onto the sample being analyzed. The secondary ion column collects, mass separates, and detects the sputtered ions generated from the sample. The readout and control electronics operate the unit, process the output signals from the instrument and present them in several different forms to the operator.

The high scan rate of the quadrupole mass filter and the inherent high sensitivity of SIMS (routinely 10^6-10^8 counts per second on major elements) permits statistically significant data to be accumulated at a high rate.

The software system used on the QMAS is BLISS (ARL's Basic Language Integrated Software System). As the system language is BASIC, the operator has complete flexibility both in handling the analytical task and formatting the output results. Two examples of rapid data acquisition and output presentation will be discussed.

ACCUMULATION OF MASS SPECTRA

Qualitative bulk characterization of a sample can be done with the QMAS by incrementally driving the quadrupole over the desired mass range and accumulating digital count data for the secondary ion intensity at each point. The time required to acquire a 1000 point mass spectrum over any mass range depends upon the counting time per point. Figure 1 shows a mass spectrum of aluminum acquired in this manner with a counting time of 0.1 second per point. Total data acquisition time required is 2 minutes. The system can be operated with .001 second counting time requiring only 2 seconds to complete the mass spectrum.

After acquisition the data is filed on a floppy disk as a permanent record, where it is accessible for listing, plotting (Figure 1) or other data reduction as the operator requires. Examples of further data reduction possible with the stored spectrum data are linear spectra plotting, histogram plotting of peak counts or quantitization.

DEPTH PROFILING

The capability to very rapidly acquire mass spectral data finds a logical extension in the study of extremely thin films and of surfaces. With sputtering ion instruments, the sample is eroded during analysis, allowing the characterization of samples to be done in depth. As the rate of sample removal is often 1 to 10 Angstroms per second or greater, it is difficult to do multielement depth profiling through films that are only several monolayers thick. One approach is to slow down the sputter rate by using a lower current density primary beam. This has two drawbacks: The loss of secondary ion yield and the problem of absorption of residual gas onto the sample from the vacuum system.

Another approach is to retain the high sputter rate with its high sensitivity and acquire data very rapidly. With the automation system of the QMAS it is possible to acquire eighteen 100 point mass spectra in as little as two seconds and store the data on disk. This capability permits surfaces and thin films to be studied in detail. The acquired data is stored on floppy disk permitting each spectrum to be plotted or displayed on an oscilloscope. The data may then be viewed as depth profile information and plotted or displayed at the operator's discretion.

Figures 2 and 3 show the depth resolution possible by rapid data acquisition. Figure 2 shows profiles for $^{55}Mn^+$, $^{24}Mg^+$ and $^{27}Al^+$ through a manganese layer on a magnesium film on top of an aluminum substrate. The total depth sputtered is 45 Angstroms as determined by interferometric measurement on deeper craters. Figure 3 was obtained from the same sample by cycling through more rapidly. For both Figures 2 and 3, 200 data points were measured and plotted for each element.

SUMMARY

The high data acquisition rate of the QMAS allows the rapid characterization of a sample using a SIMS instrument. High resolution depth profile data and mass spectra can be obtained from thin films only a few Angstroms thick on the surface of a sample.

134c
ALUMINUM METAL

Figure 1 Digital mass spectrum of stock aluminum. Acquisition time: 2 minutes. Note log scale for intensity.
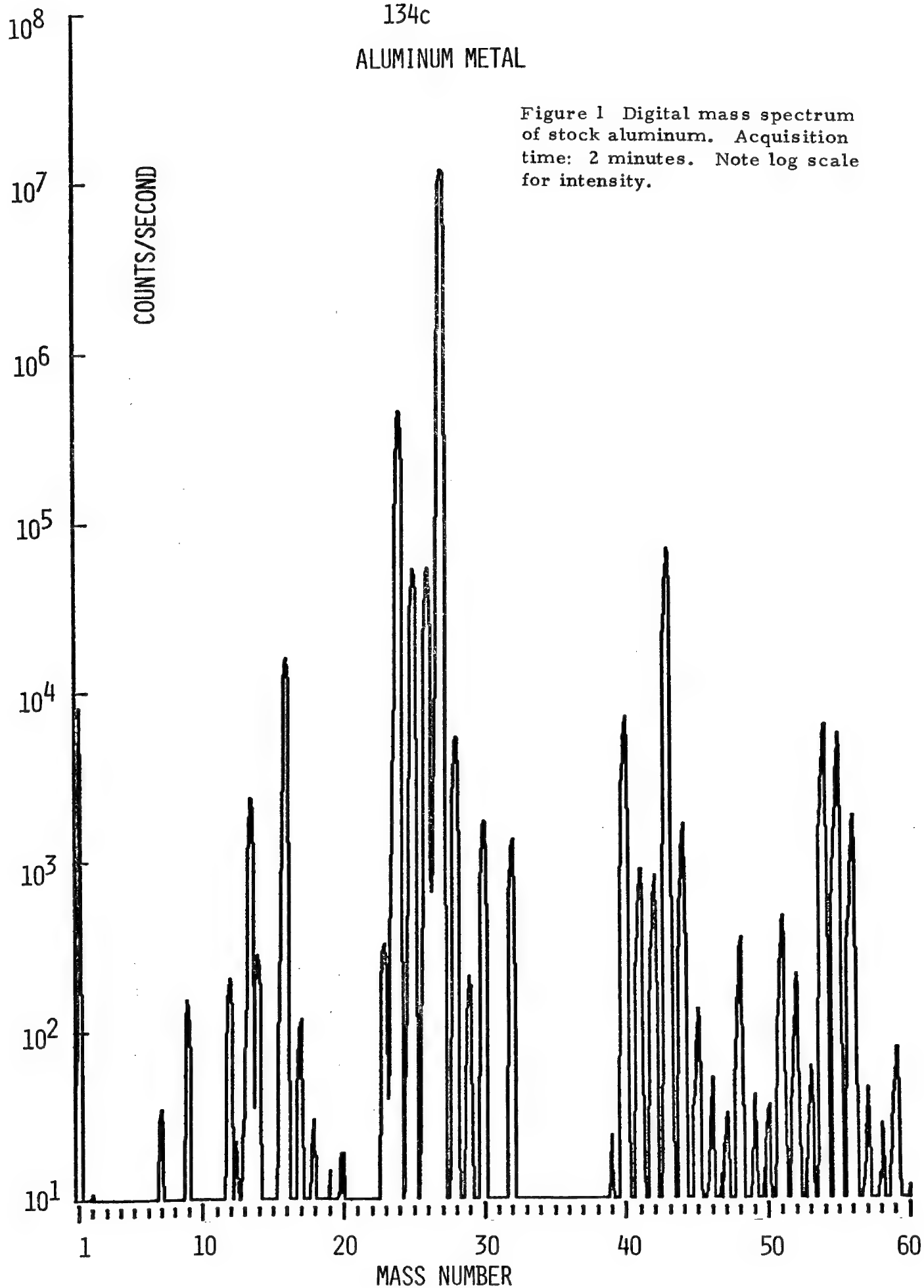
THIN FILMS ON ALUMINUM
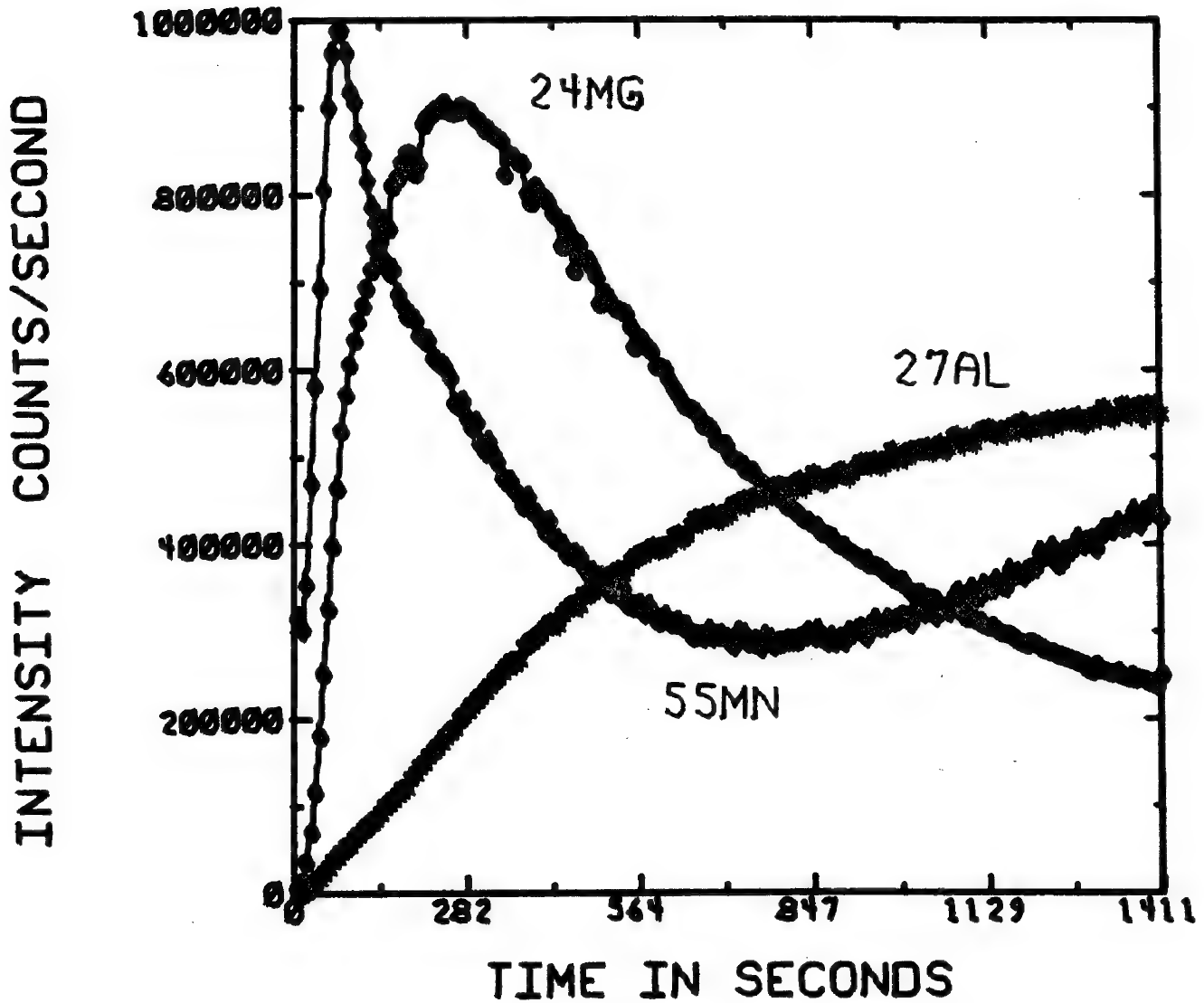
Figure 2   Depth profile through manganese and magnesium
films on aluminum stock.   Total depth of profile
is 45 angstroms.   There are 200 data points per
curve.

THIN FILMS ON ALUMINUM
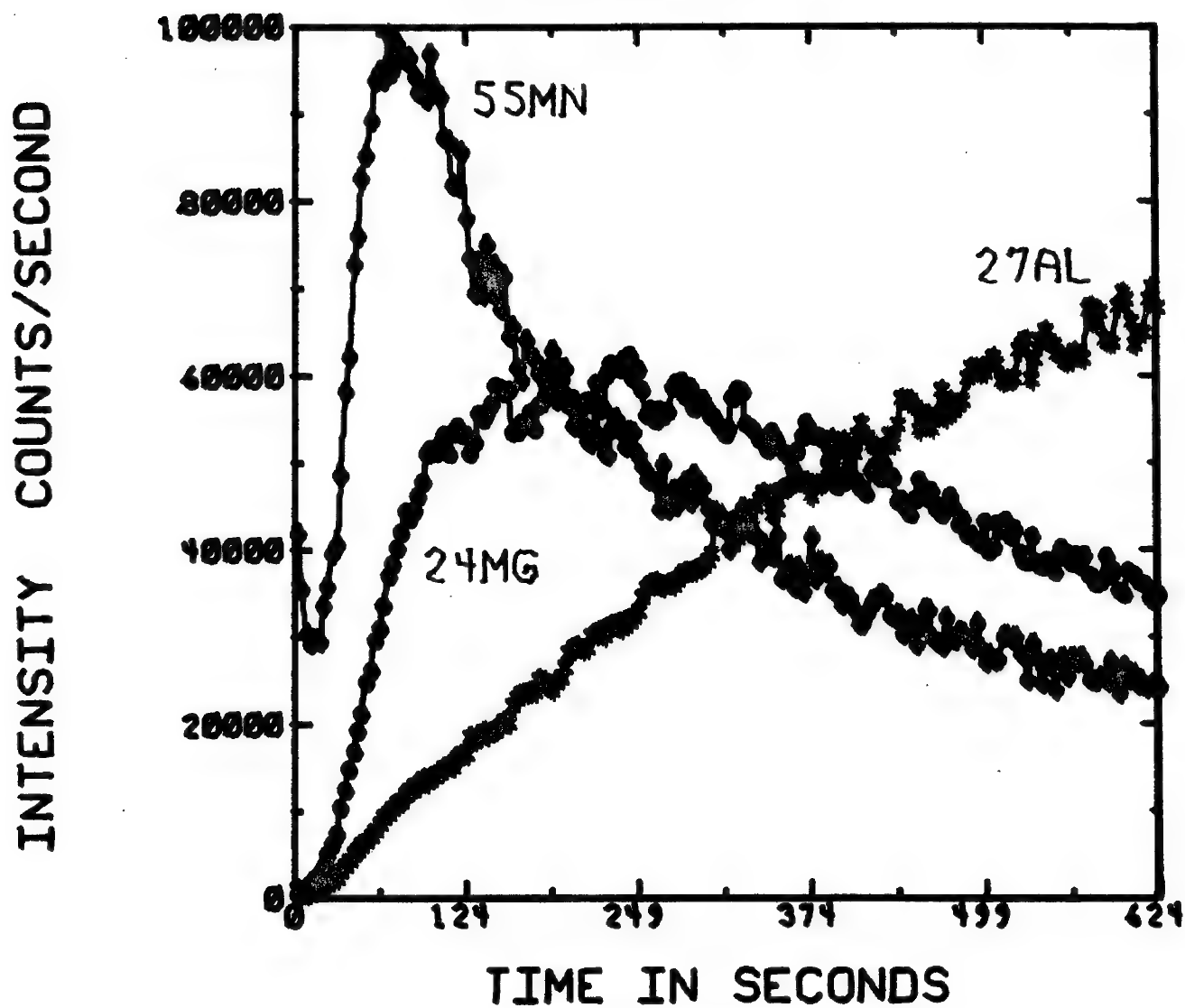
Figure 3   Very high resolution depth profile of the same
aluminum sample as in figure 2.   Total depth
shown here about 20 angstroms.   There are 200
data points per curve.

IMPROVED SIMS DEPTH PROFILES
BY CONTROL OF SAMPLE SURFACE POTENTIAL

T. A. Whatley, R. L. Conrad, and R. D. Fralick

Applied Research Laboratories
9545 Wentworth Street
Sunland, California 91040

Depth profiling using secondary ion mass spectrometry (SIMS) can
be adversely affected by changes in electrical conductivity of the
analyzed region as the sputtering proceeds. The sample surface
is an active ion optic element; its potential affects the trajectory
of ions entering the mass spectrometer. Normally this potential
can be adjusted by applying an external bias to the sample which
is often overcoated with a conductive film to allow this. The bias
voltage can compensate for changes in either net current or elec-
trical conductivity between different samples. Experimentally, the
problem is most severe when the specimen changes conductivity during
a run such as is the case with multilayer specimens having insulating
films. No single biasing adjustment can maintain constant surface
potential in such cases.

A computer controlled system has been developed for the QMAS (Quad-
rupole Mass Analyzer for Solids) which continuously adjusts sample
bias potential to maintain constant surface potential at the analyzed
area for multiconductive thin films and other samples with strong
concentration gradients. Prior to beginning a run the operator
selects, via the initial computer dialog, one or more specific masses
to be used for control of sample biasing. Minor peaks are not used
due to the difficulty of peak seeking at low count rates. Instead,
the bias setting of the immediately previous major peak is used.
Frequently, only one peak is controlled. Peak seeking is accom-
plished under computer control by sweeping the bias voltage to find
the point of maximum transmission each time the mass stepping program
reaches a control mass. The process of finding a maximum requires
about three seconds.

Typical samples for which automated sample biasing has been found to be important are boron implants into silicon oxide layers on silicon. Profiles for such a sample are shown in Figures 1-3. The oxide layer was 5000Å thick and was implanted at 50kV with boron at a fluence of 1×10^{15} atoms/cm^2. The depth of the implant maximum is calculated to be 1600Å with a peak concentration of 8×10^{19} atoms/cc. Figures 1 and 2 show profiles obtained without sample bias adjustment. For the profile of Figure 1 conditions suitable for a conductor were manually set; for the run of Figure 2 the bias was set as for an insulator. The profile in Figure 3 was obtained on the same sample with all conditions identical except that automated bias adjustment was made for every cycle of measurement each time adjusting mass 30 (silicon) for maximum intensity. Values of observed sample bias, which varied from 58 to 93 volts, are indicated at specific depths. The primary beam was $^{16}O^-$ at 10kV. This produces a negatively charged state in the impact area; increasing the positive bias allows maintenance throughout the profile of the correct potential to impart a mean energy of 50eV to the sputtered ions. This maintains high transmission of all species throughout the profile except for a momentary perturbation at the abrupt Si/SiO$_2$ interface. This behavior should be compared to the constant bias conditions of Figure 1 where ion intensity in the insulating phase is abnormally low, or of Figure 2 where there is a steady drift in intensity in the insulator layer and an abrupt loss of signal at the interface with silicon; failure to compensate for changing ion energy has produced serious distortions in the profiles with fixed bias.

B IMPLANT CONDUCTOR BIAS
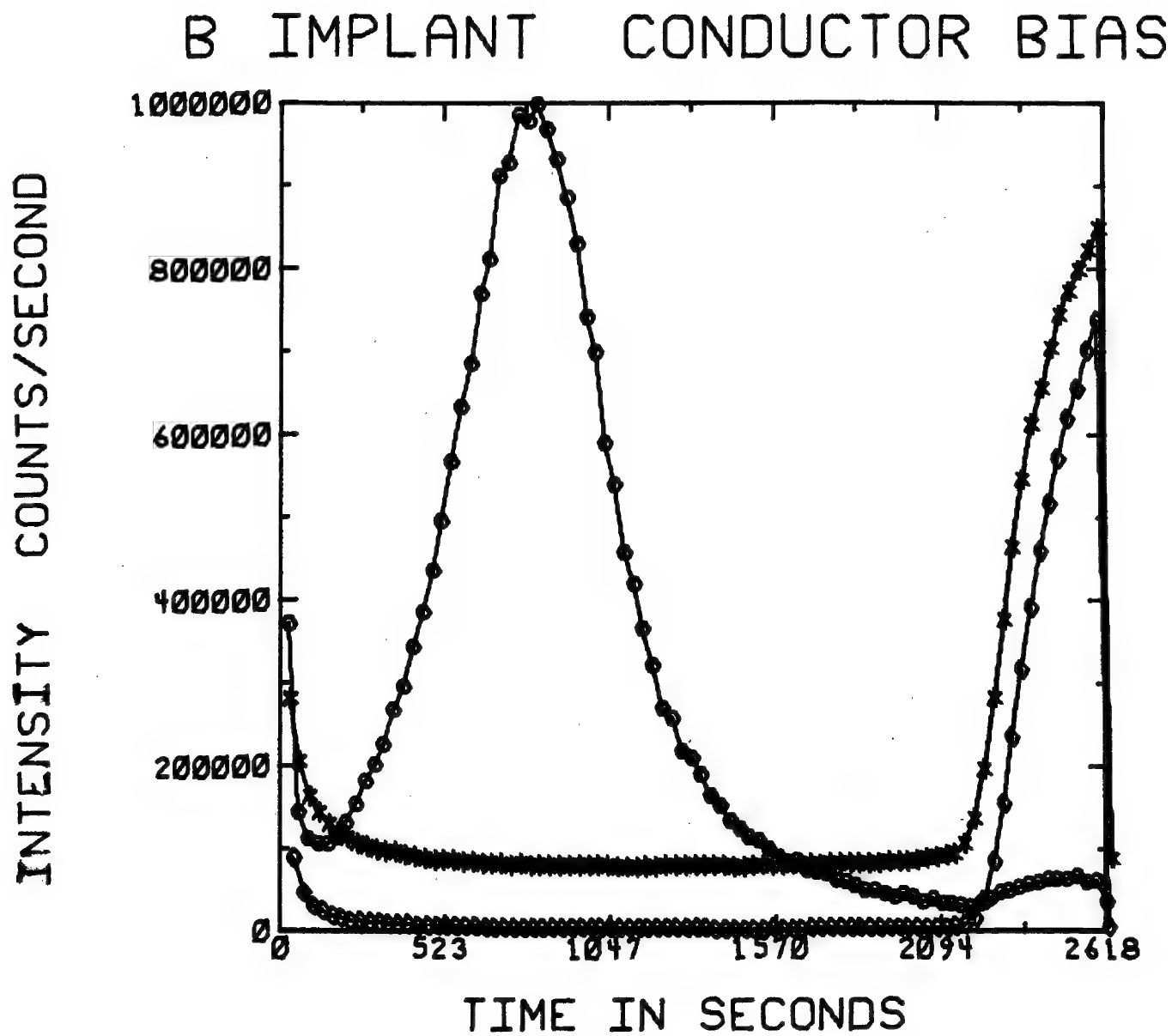
o = 11 X 117
* = 30 X 3
◊ = 44 X 1
FILE NAME 17.1B

Fig. 1. - Boron implant into 5000Å silicon oxide on silicon. Profiled at constant 58 volt sample bias.

B IMPLANT — INSULATOR BIAS
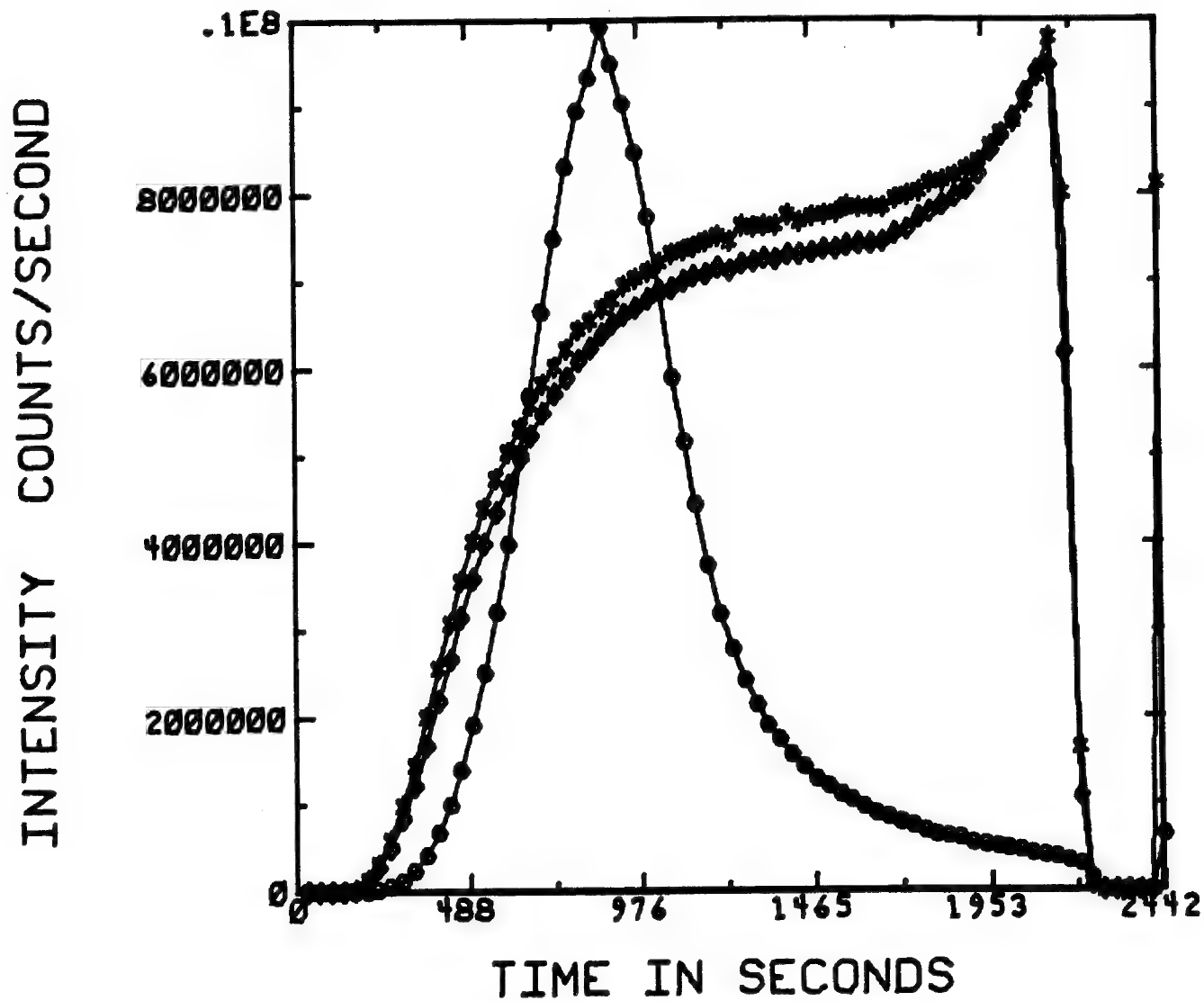

```
o = 11 X 71
* = 30 X 17
◇ = 44 X 4
FILE NAME 17.1E
```

Fig. 2. - Boron implant profiled with constant 93 volt sample bias.

5Ø KV B IN 5ØØØA SIO2/SI
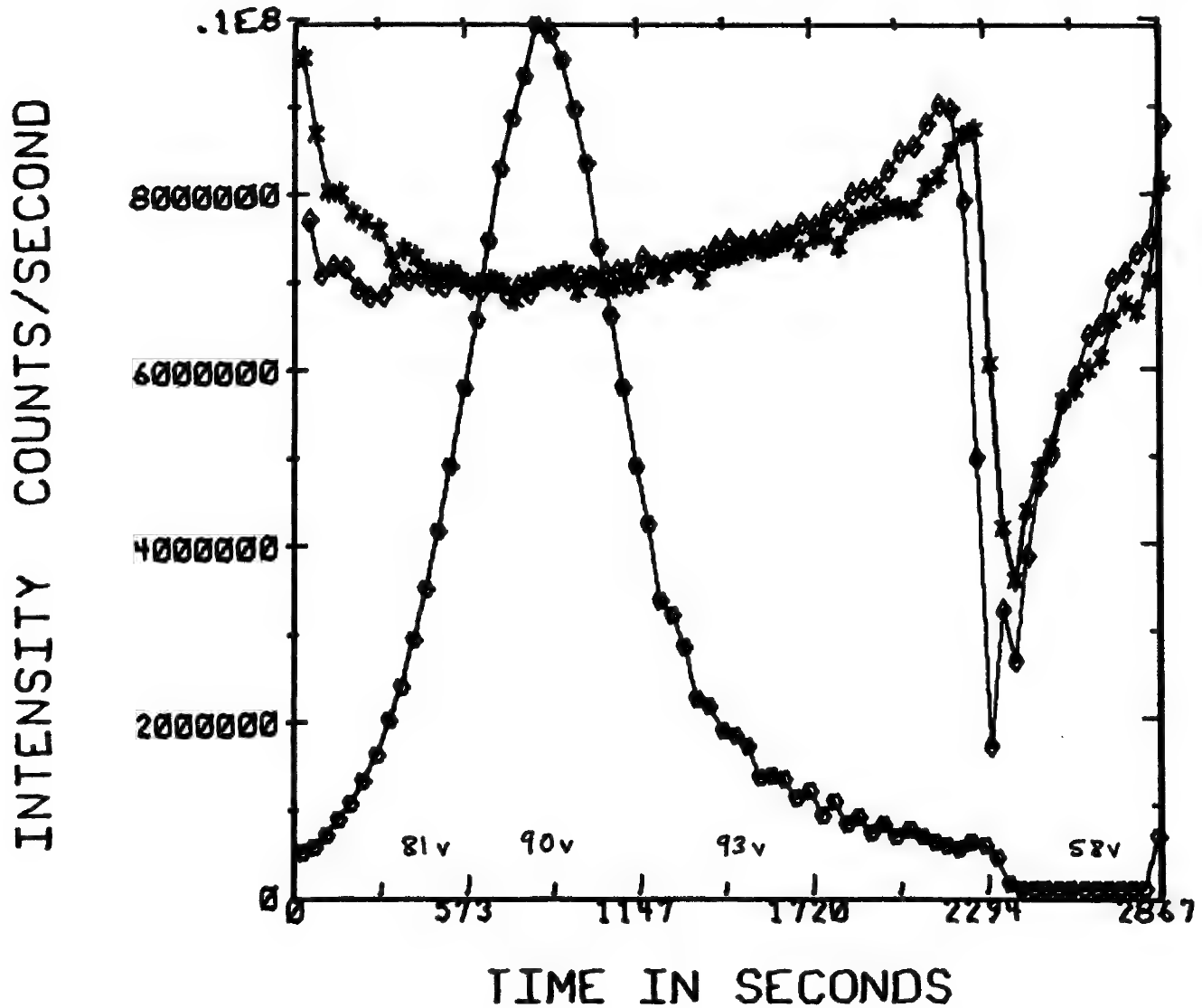
o = 11 X 1Ø6
* = 3Ø X 24
◊ = 44 X 6
FILE NAME 17.1D

Fig. 3. - Boron implant profiled with automatic sample biasing
adjustment on every measurement of the silicon peak.

IRRADIATION EFFECTS IN S.I.M.S. ANALYSIS,
THEIR CONSEQUENSES ON DEPTH RESOLUTION

Y. LIMOGE, R. SEGUIN, J.L. SERAN
COMMISSARIAT A L'ENERGIE ATOMIQUE
CENTRE D'ETUDES NUCLEAIRES DE SACLAY
FRANCE

ABSTRACT

During a secondary ion mass spectrometry analysis, a beam of keV accelerated ions is impinged on the sample surface. In typical depth analysis conditions, the primary ion beam density creates displacements per atom and per second at a stronger rate than the one obtained in classical radiation experiments. Then, these effects can alter the analysis and particulary depth resolution which depends on ion bombardment induced atomic migrations and microtopographical changes.

As experimental test of depth resolution, we have considered the spead of concentration in depth profiling of thin layers (from 220 to 1000 $\overset{o}{A}$) substrate interfaces (initial surface roughness does not exceed some about ten $\overset{o}{A}$). So, the following systems have been studied :

Substrate \ Layer	Si^{30}	$Si^{30}O_2$	Ni^{61}	Cu
Si	(1)	(1)	(5)	(6)
SiO_2		(2)		
Ni			(3)	
Al				(4)

In these experiments the influence of film thickness, primary ion species (Ar^+, O_2^+, O^-) and energies, sputtering rate and oxygen partiel pressure was investigated. Measured depth resolution varies from some about ten to a few hundred $\overset{o}{A}$. Considering silicon substrate (case (1)), primary ion energy is

an important parameter, but not for the systems (2), (3) and (4). In the case of nickel substrate an alteration of depth resolution induced by an oxygen partial pressure, is recorded.

The induced damages (defect clustering and surface microtopographical changes) have been directly observed by T.E.M. on Ni and Si Ni bombarded thin foils (in depth profiling typical conditions).

The discussion of our results [1] emphasizes the following radiation effects :

a) Direct momentum effects and cascad mixing (Si^{30} isotope in silicon substrate). A rough modeling of this effect shows that primary energy as the main effect.

b) Radiation enhanced diffusion effects (possible for the other systems). An analytical study shows that such diffusion effects can arise if $D_{irr}/\dot{x}R_p \gg 1$, where D_{irr} is the radiation enhanced diffusion coefficient, $\dot{x}$ the sputtering rate and R_p the projected range of primary ions. So, depth resolution is R_p dependant if the defects are not mobile and L dependant in the reverse case (L : diffusion length for trapping defects at sinks such as radiation induced dislocation loops).

c) Damage induced surface microroughness (in systems (3) and (4)), by a mecanism described by Hermane [2]. This small microroughness is different from the one wich consists of cones, spikes.... and which can be related to the initial surface polishing [3].

Finaly, the observations made by electron microscopy are well explained by a calculation of the nucleation time and of the defect cluster concentrations; this calculation completes the possible interpretation (b) taking account the effects of radiation enhanced diffusion.

BIBLIOGRAPHY

[1]   Y. LIMOGE, R. SEGUIN; J.L. SERAN - 19è Colloque de Métallurgie
        I.N.S.T.N. Saclay, 22-25 Juin 1976 - à paraître

[2]   N. HERMANE - Rad. Effects 19 (1973) 161-169

[3]   J.L. SERAN - Rapport CEA-R-4717 (1976)

EMPIRICAL STANDARDS FOR QUANTITATIVE ANALYSIS OF BIO-LOGICAL TISSUES BY SECONDARY ION MASS SPECTROMETRY

Margaret B. Bellhorn and David M. File

Albert Einstein College of Medicine, Bronx, N.Y. and Naval Weapons Support Center, Crane, Ind.

Secondary Ion Mass Spectrometry (SIMS) potentially offers many advantages for identification and localization of ions in biological specimens because of its high sensitivity and depth resolution. In order to use SIMS for experiments designed to elucidate physiological mechanisms, one needs to be able to quantitatively measure concentration differences within and between samples.

As a first approach to this goal, we have begun to formulate empirical standards for use in SIMS analysis of biological material embedded in epoxy resins. We have used cast thin films of the protein, gelatin, as a model for soft tissue specimens. The SIMS spectrum for gelatin is similar to that found in tissue (Bellhorn, M.B. and Lewis, R.K., Exp. Eye Res. $\underline{22}$: 505, 1976). Water soluble salts of lithium, rubidium, strontium and copper were used to dope gelatin films with known concentrations of selected ions, which appear to be homogenous in x, y, and z. A plot of the measured added ion intensity versus added ion concentration (weight parts per million) in the gelatin is a smooth monotonic function. Lithium, for example, is readily measured from 1 to 1000 wt ppm, whereas rubidium and strontium are measurable down to 10 wt ppm, and copper to 50 wt ppm, in part because of mass interference which results in a high background. The intrinsic calcium content of the gelatin may be used as an internal standard and a ratio formed by dividing the added ion cts/sec/namp/μ^2 by the reference calcium cts/sec/namp/μ^2. Reproducibility of uncorrected calcium intensity in a series (n=16) of similar samples containing different added ions had a precision of 20%.

In epoxy embedded samples, the epoxy resin permeates the dehydrated tissue to fill the non-tissue space. This provides a solid, homogenous matrix with the tissue as the only other substance present. In order to be able to estimate the relative tissue/Epon volume we have dissolved lipid-soluble standards in Epon 812 as a marker for the epoxy resin. A lipid-soluble vanadium compound is useful as a marker, as it does not appear in tissue, can be readily incorporated into Epon 812, and gives a secondary ion intensity which is a smooth monotonic function from 50 to 1000 wt ppm. Gelatin samples of known composition can be embedded in Epon resins and treated identically to tissue samples, thus serving both as standards and models of biological specimens for SIMS analysis.

The operating conditions of the Cameca IMS 300 used for this study were a positive oxygen primary ion beam with a 5.5 kV accelerating potential and 20×10^{-9} amp beam current. Positive secondary ions were collected from a 70 μ diameter circular area. The rate of sputtering under these conditions was approximately 10 A/sec. These results enable one to calculate that 10^{-19} moles/sec lithium is sufficient for an analysis of biological tissue. These studies also indicate that quantitative analysis of biological specimens by SIMS is well within the limits of physiologically meaningful experiments.

QUANTITATIVE ION MICROPROBE MASS ANALYSIS

USING NEGATIVE SECONDARY IONS

by

J.D. Brown
Faculty of Engineering Science &
The Centre for Interdisciplinary Studies in Chemical Physics
The University of Western Ontario
London, Ontario

and

James M. Short
Xerox Corporation
Xerox Square W114
Rochester, New York 14644

Andersen and Hinthorne (1) proposed a method for quantitative ion probe analysis based on a local thermodynamic equilibrium model. Their computer program, CARISMA, based on this model, while correcting at least approximately for the presence of negative secondary ions, could only be used in its original form for measured positive ion spectra. For those specimens which have significant yields only of negative secondary ions, significant modifications have had to be made to their approach. The purpose of this paper is to describe changes which have been made to this program and to give some results of analysis of standard specimens using negative secondary ion spectra.

In the CARISMA program, negative secondary ion abundances, if calculated, were used only to correct total ion yields with no provision for calculations based totally on negative secondary ion spectra. The following changes have extended the application of CARISMA to negative secondary ion spectra:

(a) Insertion of data and equations on O^- and O_2^- to permit the calculation of the neutral O concentration, n_O from the O^-/O_2^- ratio. This is particularly significant, since negative ion spectra are rich in oxide peaks. The equilibrium equations used to calculate n_O are:

   (i) Dissociation of neutral oxygen molecules

   $$O_2^\circ \underset{\rightarrow}{\leftarrow} 2O^\circ$$

   (ii) Formation of O^-

   $$O^\circ + e \underset{\rightarrow}{\leftarrow} O^-$$

(iii) Formation of O_2^-

$$O_2^o + e \rightleftharpoons O_2^-$$

Based on these three reactions, after substituting for constants

$$n_o = \frac{n_{O_2^-}}{n_{O^-}} \cdot 4.250 \times 10^{21} \ T^{3/2} \ \frac{B_{O^o} B_{O^-}}{B_{O_2^-}} \ e^{-4.748 \times 10^4/T}$$

where B's are partition functions
and T is temperature.

The partition function for O^- and the electronic part of O_2^- is from Bolton (2), while the rotation and vibration contributions for O_2^- are calculated from molecular constants (3).

(b) Inclusion of additional data on neutral oxides and negatively charged oxides. These data are primarily from the JANAF tables, but also include data from other sources.

(c) Provision for partition function data for negative ions. For many negative ions, the only stable electronic state is the ground state. However, a few ions such as C^-, O^- and F^- do have stable excited states.

(d) Insertion, as an option, of a more complete table of partition function coefficients for neutral and singly and doubly charged positive ions due to Bolton (2).

The program has been used for comparison of analyses on standard specimens in which the primary ion beam is O_{16}^- and negative secondary ion spectra are measured. Analyses using CARISMA based on negative secondary spectra are in reasonable agreement with known compositions.

References

(1) Andersen, C.A. and Hinthorne, J. Anal. Chem., **45**, 1421 (1973).

(2) Bolton, T., Dunlap Astrophysical Observatory, private communication.

(3) Stull, D.R. and Prophet, H. JANAF Thermochemical Tables. NSRDS - NBS 37, 1971.

MATRIX SPECIES RATIO METHOD FOR QUANTITATIVE ION PROBE ANALYSIS

John D. Ganjei, Daniel P. Leta, James R. Roth, and George H. Morrison

Department of Chemistry
Cornell University
Ithaca, N. Y. 14853

Quantitative ion probe microanalysis has been limited by the difficulty of relating secondary ion signals to elemental concentrations. Ionization yields have been found to vary greatly with element, matrix, instrumental design and sampling conditions. As a result, normal analytical methods applied to ion probe analysis have been only semiquantitative. The present study describes modifications to the empirical approach that substantially improve precision and accuracy. External standards are used but the effects of chemical environmental differences and experimental conditions are calibrated by matrix species ratios (M_2^+/M^+, M_2O^+/M_2^+, MO^+/M_2^+, etc.) Matrix-sensitive correction factors were first proposed by McHugh (1) and other variations (2,3) have proven successful in specific ion probe applications. The novelty of our method involves the use of an oxygen leak to vary the ambient oxygen pressure upon the sample during ion bombardment. The resultant changes in ion yields have been found to correlate directly to the ratio of matrix species' signals. A profile of elemental sensitivity factors versus the matrix species ratio is constructed by monitoring the secondary ion signals of the elements of interest and several matrix species while varying the ambient oxygen pressure. The sensitivity factors are calibrated with an external standard sample of known elemental concentrations. Using this profile to select the appropriate elemental sensitivity factor has greatly improved the results in the analysis of unknown samples of similar matrix types. Figure 1 shows the elemental sensitivity factor calibration curve for Cr in NBS 662 steel. In this case Fe_2^+/Fe^+ was chosen as the matrix species ratio and the analyte signals were ratioed to Fe^+. High O_2 pressure roughly corresponded to low Fe_2^+/Fe^+ ratios. The results of analyzing other NBS steels using the 662 curve are shown in Table 1. For comparison, uncorrected results are also shown in Table 2 at both low and high O_2 pressures. It is evident that two similar matrices do not necessarily have the same elemental sensitivity factor at the same ambient oxygen pressure. However, a direct correlation does exist between the matrix species ratio and the elemental sensitivity factors.

The concentrations obtained from uncorrected data in Table 2 were determined with constant instrumental conditions. In analyses where constant conditions are not maintained the analytical results will be much worse. One important example is primary beam density at high ambient O_2 pressure. With different beam densities one finds different ionization yields at the same O_2 pressure unless the surface is completely saturated with oxygen during the primary ion bombardment. However, this would not affect the results from Table 1 since the matrix species ratio compensates for different sampling environments.

Data will also be presented for the determination of C, Si, Al, Ti, V, Mn, Nb and Zr in the NBS low alloy steel series. In some cases signals from several sampling areas were averaged in order to minimize sampling error.

The proposed approach has several advantages over existing methods of quantitative ion probe analysis. The empirical basis of the method should make it applicable to all ion probe instrumentation even though instrumental design and sampling conditions may be considerably different. Precision and accuracy have been considerably improved while the requirements for matrix match and experimental condition reproducibility have been relaxed. Further work on other matrices is being performed so that the general utility of the approach can be evaluated. Of special concern are matrices whose major elements have been found to be relatively unaffected by ambient oxygen pressure.

Literature Cited

1. J.A. McHugh, "Secondary Ion Mass Spectrometry," in Methods of Surface Analysis, S.P. Wolsky and A.W. Czanderna, Eds., Elsevier Publ. Co. (1976).
2. H. Tamura, T. Ishitani, and I. Kanamota, "Correction for Ionization Yield," U.S.-Japan Joint Seminar on SIMS, Honolulu, Hawaii (1975).
3. S.J. Larsson, A. Lodding, H. Odelius, and L.G. Petersson, "Calibration Methods for Ion Probe Application to Fluorine in Biological Hard Tissue," U.S.-Japan Joint Seminar on SIMS, Honolulu, Hawaii (1975).

Table 1. Results Using Matrix Species Ratio Method

Sample[a] No.	% Cr Conc.	$^{52}Cr^+/^{54}Fe^+$	$^{112}Fe_2^+/^{54}Fe^+$	S_f[b]	Calc. Conc.	% Error
661	0.69	0.867	0.387	133	0.644	- 6.7
663	1.31	1.40	0.27	107	1.31	0
664	.06	.0683	0.305	115	0.059	1.7
462	.74	0.852	0.365	130	0.66	-10.8
					average error =	4.8

[a] NBS low alloy steel series. [b] Appropriate sensitivity factor derived from Figure 1.

Table 2. Uncorrected Results

Sample No.	$^{52}Cr^+/^{54}Fe^+$	S_f calibrated from 662	Calc. Conc.	% Error
at 8×10^{-7} torr:				
662	0.432	144		
661	0.867	144	0.60	13.0
663	1.40	144	0.97	26.0
664	0.0683	144	0.047	21.7
462	0.852	144	0.059	20.3
			Average error =	20.3
at 4×10^{-8} torr:				
662	0.862	287		
661	1.67	287	0.58	15.9
663	2.66	287	0.93	29.0
664	0.264	287	0.092	53.3
462	1.91	287	0.67	9.5
			Average error =	26.9

Fig. 1 Cr ^1S_f Profile from NBS 662
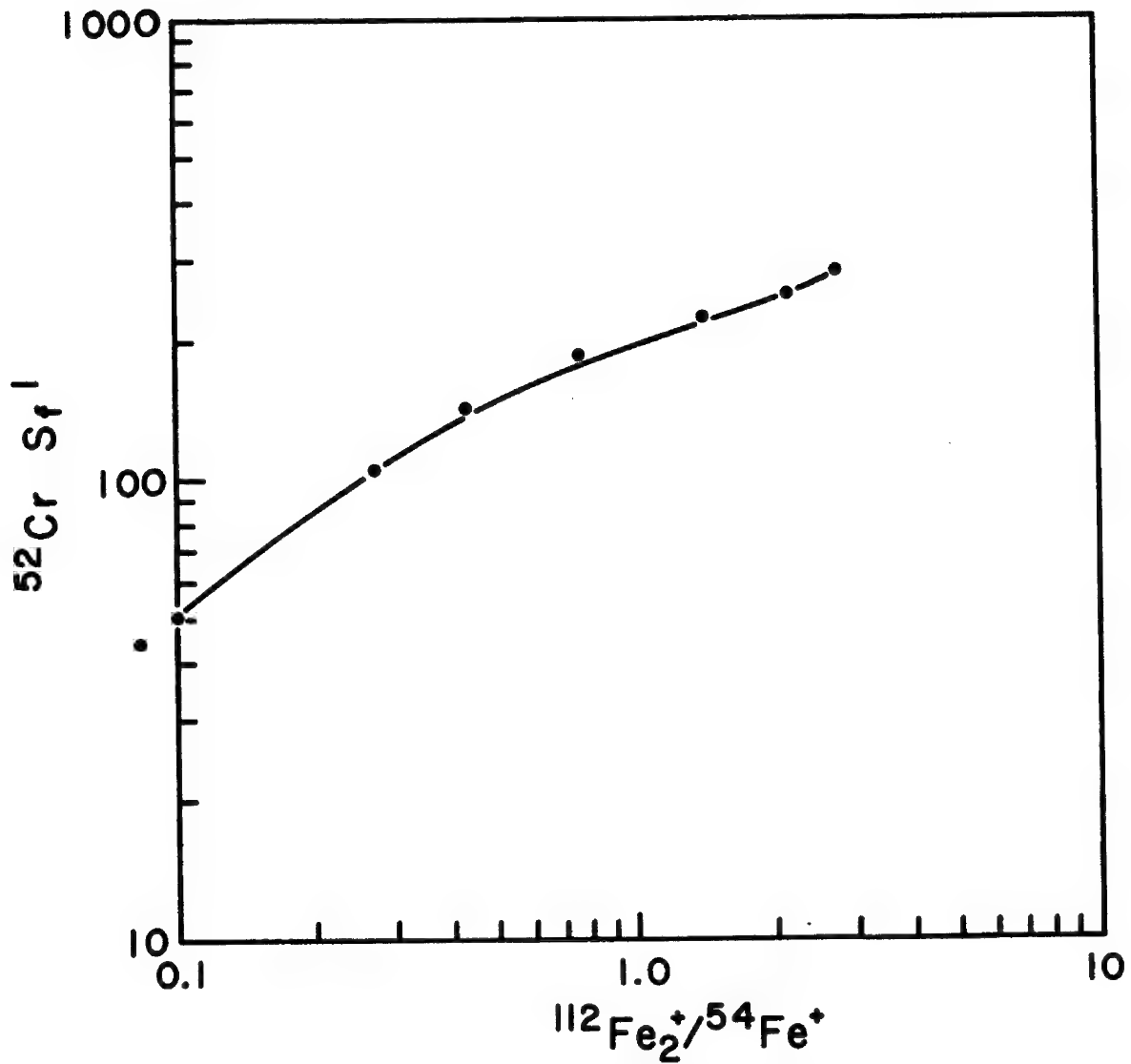
$$^1Cr\ S_f\ =\ \frac{^{52}Cr_{sig}}{^{52}Cr_{conc}}\ \cdot\ \frac{Fe_{conc}\ (arbitrarily\ 100\%)}{^{54}Fe_{sig}}$$

Quantitative Analysis of Glasses by Secondary Ion Mass Spectrometry

Dale E. Newbury
Analytical Chemistry Division
National Bureau of Standards
Washington, D. C. 20234

Abstract

Quantitative analysis by secondary ion mass spectrometry is complicated by the strong matrix effects on the emission of secondary ions. Two general approaches have been employed for quantitative SIMS: the use of relative elemental sensitivity factors [1] and the modeling of the secondary ion emission process by various physical descriptions [2].

To test the accuracy of the quantitative analysis which could be achieved by the various approaches, a series of multi-element glasses have been analyzed [3]. These glasses offer the following advantages: (1) the compositions have been contrived to avoid most significant mass interference problems; (2) the glasses contain five or more metallic or non-metallic ions in addition to oxygen; (3) the oxygen is present at a level of 60 atomic percent and additional oxygen is added by implantation of the primary beam ions; this saturation with oxygen should reduce the sensitivity to surface adsorption of species from the background gas [4]; (4) the glasses are amorphous and single phase, and thus free of crystallographic channeling effects; and (5) silicon is common to virtually all of the glasses studied.

The local thermal equilibrium (LTE) model has been chosen as a representative of the physical models for secondary ion emission [4,5]. Of the numerous models of secondary ion emission, the LTE model is the most completely developed for application to the analysis of a multi-component sample. The LTE approach models the region in which the secondary ions are generated as a dense plasma in thermal equilibrium. The Saha-Eggert ionization equation is used to predict the ratio of ions to neutrals for each element in terms of a temperature, T, and an electron density n_e. Known values for certain elements in a sample, the so-called internal standards, are used to determine the values of T and n_e, and these parameters are used to solve for the other elements in the sample. In addition, an oxide correction can be carried out to allow for those elements which produce significant molecular oxide ions. For the present work, various combinations of internal standards and oxide corrections were applied. The quality of the resulting analyses was measured by calculating an error factor, F:

$$F = C(\text{true})/C(\text{calculated})$$

where C is the concentration. The results reported at the 1976 MAS meeting [6] are summarized in the error histogram of figure 1. Approximately 50% of the analyses fall within a factor of two ($0.5 < F < 2$) of the known values and about 80% within a factor of five ($\overline{0.2} < F < \overline{5}$). For certain elements, such as tantalum, zinc, phosphorus, lead and bismuth, the error factors are always large, as high as 40. Other physical models of ion emission are currently being tested, including the single parameter LTE model of Werner and Morgan [7] and the sputtering model of Prival [8].

Relative elemental sensitivity factors, $S_{x/M}$,

$$S_{x/M} = (i_x/C_x f_x)/(i_M/C_M f_M)$$

where i is the ion intensity, C the atomic concentration, f the isotopic fraction, and x and M refer to any two elements, were determined for all elements in the glasses relative to silicon. The distribution of these sensitivity factors is shown in figure 2, where $S_{x/Si}$ values for 25 elements in various matrices are plotted. Nearly all of the sensitivity factors fall within a factor of five of unity. Thus, the enormous variation seen for the pure elements [5] is greatly reduced when the elements are dispersed in a common matrix, in this case, oxygen.

A first approach to a sensitivity factor analysis can be made with the assumptions that (1) the concentration of silicon is known, and (2) all the values of $S_{x/Si}$ are unity. The error factor histogram which results from this procedure is shown in figure 3. Approximately 35% of the analyses lie within a factor of two, and 80% within a factor of five. Note that even with the crude assumption that $S_{x/Si}=1$, the analysis is virtually as good as the LTE analysis.

Next, average values for $S_{x/Si}$, determined from all of the glasses, were used in the analysis, replacing assumption (2) in the previous paragraph. The error factor histogram in figure 4(a) results. Now, 83% of the analyses fall within a factor of two and 99% within a factor of five. In the range $0.5 < F < 2$, the error factors are replotted, figure 4(b). More than 50% of the analyses fall within 1.2 of the correct value.

The sensitivity factors show some systematic variations, raising the possibility of searching for physical models to predict them. In figure 5, the values of $S_{x/Si}$ for most of the elements in the range $20 < Z < 32$ are plotted. A regular variation is noted, with a large deviation observed for zinc. Sensitivity factors calculated from the pure element ion emission values reported by Andersen [4] are also plotted. The sensitivity factors observed from the glass matrix show a reduced range and a more regular behavior than the values from the pure elements, which probably results from the controlling influence of the massive fraction of oxygen in the glasses. Further work is being carried out to determine the S values relative to a chemically similar element, germanium, and to determine if the systematic behavior is repeated elsewhere in the periodic table.

NBS Glasses
LTE Analysis
O/O_2 , Si/SiO
and no oxide

$F = C(true)/C(LTE)$

311 determinations
$0.5 \leq F \leq 2$ 53%
$0.2 \leq F \leq 5$ 84%

$(1/F) > 5$
6 determinations

$F > 5$
43 determinations

1/F   5   4   3   2   1   2   3   4   5   F

Overestimate   Underestimate
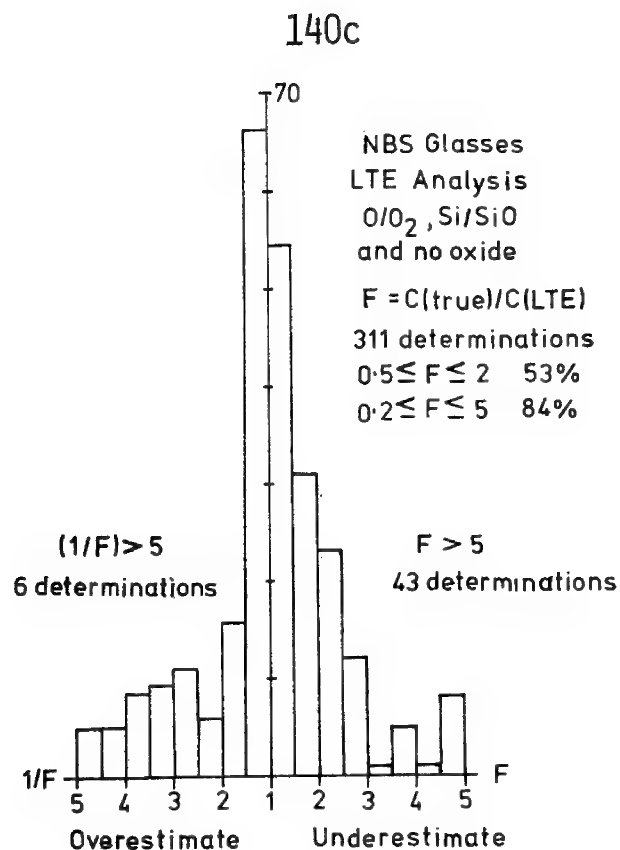
1.   Error factor histogram for analysis with the LTE model.

NBS Glasses
Relative Sensitivity Factors

number 20

$$\beta = \frac{i_x/c_x f_x}{i_{Si}/c_{Si} f_{Si}}$$

$0.5 \leq \beta \leq 2$ 35%
$0.2 \leq \beta \leq 5$ 82%

$\beta < 0.2$
13 cases

$\beta > 5$
7 cases

8   7   6   5   4   3   2   1   2   3   4   5   6   7   8

$1/\beta$ β
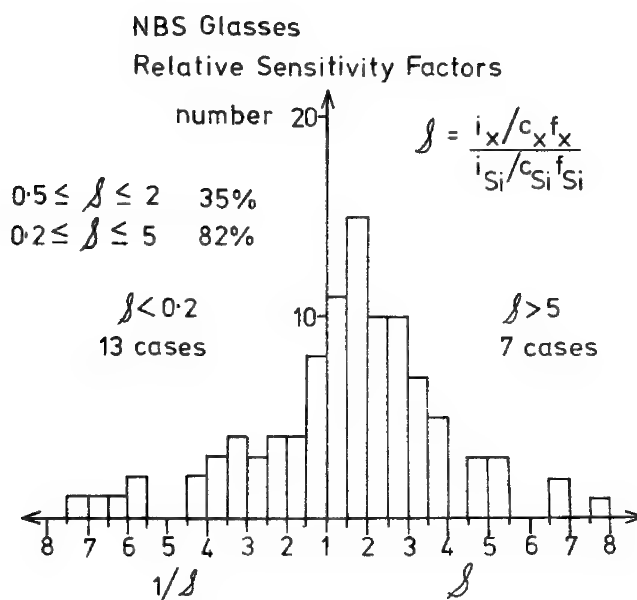
2.   Sensitivity factors relative to silicon for 24 elements in 25 different glasses.

NBS Glasses
Analysis with $S_{A/Si} = 1$

$$F = \frac{C(true)}{C(calc)}$$

$0.5 \leq F \leq 2$ 35%
$0.2 \leq F \leq 5$ 82%

$(1/F) > 5$
7 cases

$F > 5$
13 cases

1/F   F

5 4 3 2 1 2 3 4 5

Overestimate   Underestimate
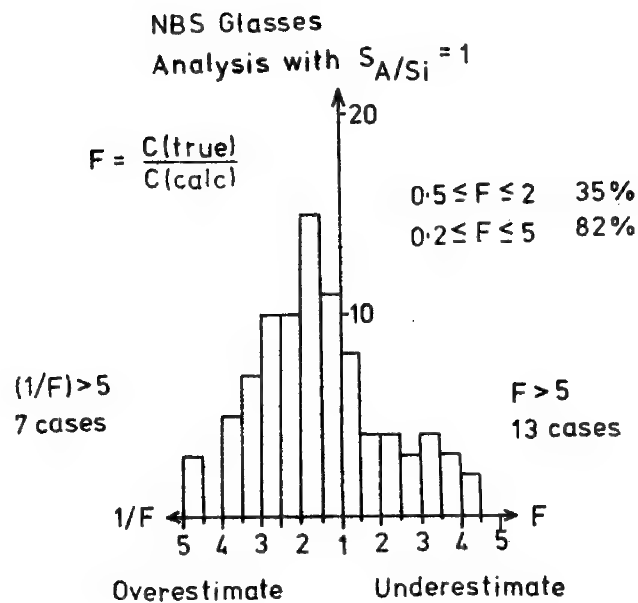
3.   Error factor histogram for analysis with $S_{x/Si} = 1$ for all elements.

(a)

SIMS Analysis
of Glasses with
Averaged Relative
Sensitivity Factors

$0.5 \leq F \leq 2$ 83%
$0.2 \leq F \leq 5$ 99%

$(1/F) > 5$: 1 case

$F > 5$: 0 cases

1/F   F
5 4 3 2 1 2 3 4 5
Overestimate   Underestimate

(b)

SIMS Analysis of
Glasses with
Averaged Relative
Sensitivity
Factors

$0.83 \leq F \leq 1.2$: 53%

1/F   F
2·0 1·8 1·6 1·4 1·2 1 1·2 1·4 1·6 1·8 2·0
Overestimate   Underestimate
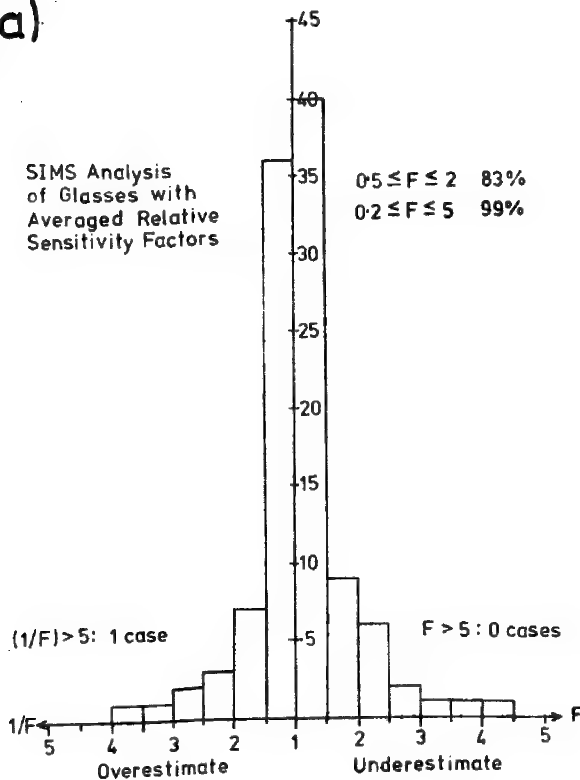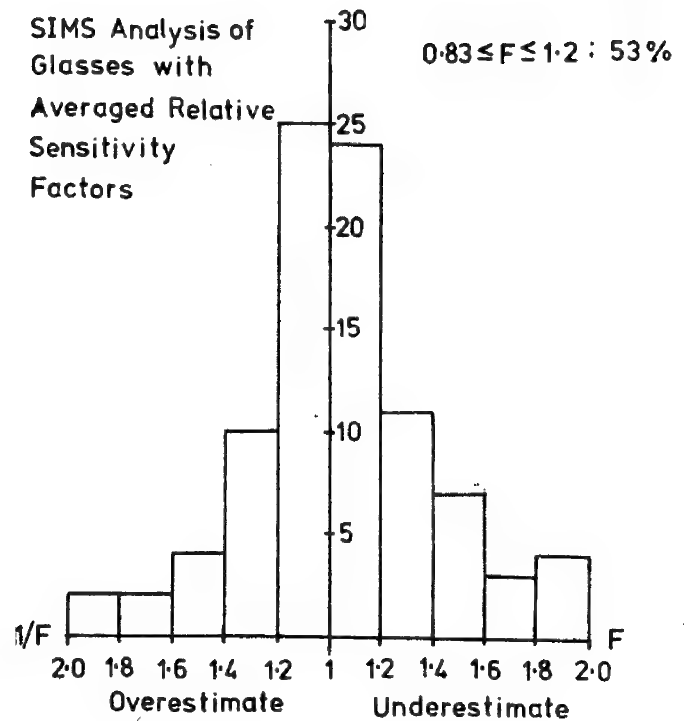
4.   (a) Error factor histogram for analysis with average error factors; (b) data of (a) replotted in range $0.5 \leq F \leq 2$.

It should be noted that the sensitivity factors include all instrumental effects and, therefore, the values reported in figure 5 must not be transfered to a different instrument. Two particular instrumental effects which can influence the sensitivity factors are (1) the detector response as a function of the mass of the ion being detected and (2) the transmission of the spectrometer as a function of the ion species. Secondary ions show considerable variations in energy distribution, and the transmission of a spectrometer can vary widely because of this effect. The instrument response is the subject of an on-going international study [10].

References

[1] McHugh, J. A. in Secondary Ion Mass Spectrometry, Heinrich, K. F. J. and Newbury, D. E., eds., National Bureau of Standards Special Publication 427, Washington, D. C., 129 (1975).

[2] Schroeer, J. M. in Secondary Ion Mass Spectrometry, ibid., 121 (1975).

[3] Marinenko, R. B., Heinrich, K. F. J., Fiori, C. E., Darr, M. M., Blackburn, D. H., Newbury, D. E., and Small, J. A. in Abstract Book, 3rd Annual Meeting of the Federation of Analytical Chemistry and Spectroscopy Societies, Nov. 15-19, 1976, Philadelphia, Pa., paper 247 (1976).

[4] Andersen, C. A. in Microprobe Analysis, Andersen, C. A., ed., Wiley & Sons, New York, p. 531 (1973).

[5] Andersen, C. A. and Hinthorne, J. R., Anal. Chem. 45, 531 (1973).

[6] Newbury, D. E., Myklebust, R. L., and Heinrich, K. F. J. in Proceedings of the 11th Annual Conference, Microbeam Analysis Society, Miami Beach, Florida, paper 42 (1976).

[7] Werner H. and Morgan. A. E., private communication.

[8] Prival, H. in Abstract Book, 3rd Annual Meeting of the Federation of Analytical Chemistry and Spectroscopy Societies, Nov. 15-19, 1976, Philadelphia, Pa., paper 358 (1976).

[9] Satkiewicz, F., private communication.

[10] U.S.-Japan Joint Seminar on Quantitative Techniques in Secondary Ion Mass Spectrometry, Honolulu, Oct. 13-17,1975.
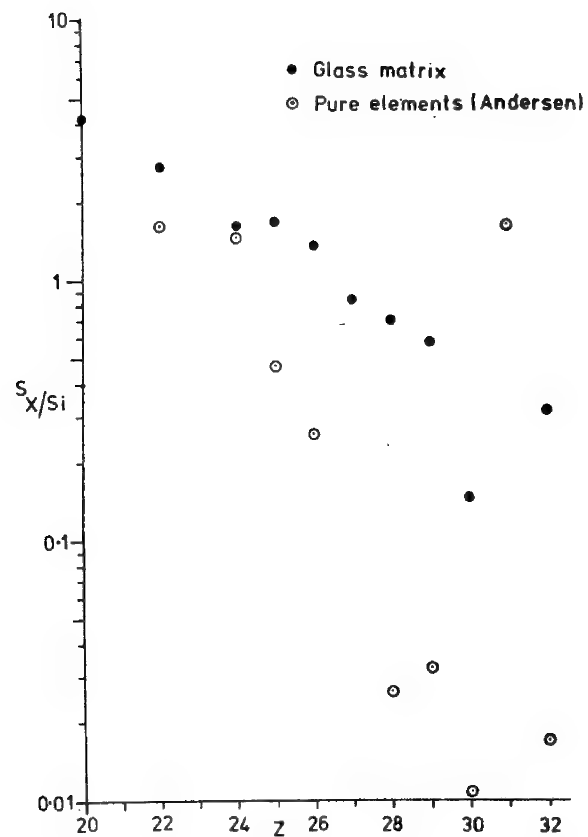
5.   Sensitivity factors relative to silicon measured from glasses and calculated from pure element data of Andersen [4].

CONTRIBUTION TO THE STUDY OF ION EMISSION IN THE Ni-Cu Ni-Fe, Al-Cu, Al-Fe ALLOYS : INFLUENCE OF THE CHEMICAL AFFINITY OF COMPONENTS FOR OXYGEN

Y. LIMOGE, F. MAURICE, J.L. SERAN
COMMISSARIAT A L'ENERGIE ATOMIQUE
CENTRE D'ETUDES NUCLEAIRES DE SACLAY
FRANCE

Ion emission in the chemical process (presence on the surface of a reactive species such as oxygen) is commonly used to improve the detection sensibility and reduce the chemical and lattice effects due to the sample. However, if the chemical affinity for oxygen is not the same for the different elements of the sample, the ratio of the ionization probabilities varies versus these concentrations; then, it is necessary to determine the variation of the ionic constant with the concentration of the element which has the more affinity for oxygen. Therefore, four types of binary alloys have been studied. These alloys have been chosen from Cu, Ni, Fe, Al, the chemical activity of which is sufficiently differenciated :

Ni-Cu	(0,11	→	3,5 at % Ni)
Ni-Fe	(2	→	100 at % Fe)
Al-Cu	(0,5	→	100 at % Al)
Al-Fe	(1	→	58 at % Al)

Each sample has been analyzed using Ar^+ primary ion beam (E = 6 keV) and a variable partial pressure of oxygen in the sample chamber.

Two essential characteristics can be deduced from the results :

a) the ionic constant value remains about equal to unity in the whole range of concentration, such as in the Ni-Fe system where :

$$k_{Fe,Ni} = \frac{i(Fe^+)}{i(Ni^+)} \times \frac{c_{Ni}}{c_{Fe}} \simeq 1,4$$

b) in other systems, on the contrary, the ionic constant value has a large variation range. For example, in the Cu-Al system, $k_{Al,Cu}$, varies from $1,3 \; 10^2$ for the 0,5 at % Al alloy to 3,3 for the 99,5 at % Al alloy.

The discussion of the results makes clear that these two types of behaviour of the ionic constant can be related to some characteristics of the oxides of the alloy components, such as the formation enthalpy and the secondary ion emission yield.

IMMA Surface Analysis of Alloy Steel Using N_2^+ Primary Ion

Toshio SHIRAIWA, Nobukatsu FUJINO,
Jun'ichiro MURAYAMA and Noriaki USUKI

Central Research Laboratories,
Sumitomo Metal Industries, Ltd.,
Nishinagasu-Hondori, Amagasaki,
JAPAN

1. Introduction

In CARISMA quantitation[1] of alloyed elements in steel, results are different according to choice of a couple of internal standards in order to decide the T and Ne^-.

However, experimental calibration curves are usually linear for fairly wide range[2]. The gradients of the calibration curves are applied to Saha-Eggert equation and it is found that there is not always appropriate couple of standards for alloyed steel.

In the present experiments, depth profiles of surface sputtered by O_2^+ ion are investigated using N_2^+ ion primary. The depth-profiles are quite different between pure elements and alloyed elements in steel and the depth-profiles are affected by accelerating potential and current density[3].

Techniques for N_2^+ primary ion are applied to surface analysis of steel and results are also discussed.

2. Experiments

Data were obtained with the ARL IMMA using an electronic aperture and a digital multi-scaler. Operating conditions are as follows: accelerating voltage +6~+20KV; sample potential +2.0KV; primary ions O_2^+ and N_2^+, sample chamber pressure 7~8×10⁻⁷ torr. Compositions of samples are shown in Table 1.

3. Results

3.1 Quantitation of Iron base alloys

Figure 1 is calibration curves of binary and tertiary alloys, where the abscissa is atomic concentration ratio C_{Me}/C_{Fe}, and the ordinate is secondary ion intensity ratio I^+_{Me}/I^+_{Fe}, and there find no much interelement effect due to the third element. These calibration curves are nearly linear. Considering Saha-Eggert's equation, the fact that the calibration curves are linear means that there should be same T and Ne^- for the binary and tertiary alloys. The CARISMA quantitations were applied to the gradients k of Fe-Ni, Fe-Mn, Fe-Cr and Fe-Si systems, and the region of T and Ne^-, which give error within $^+_-20\%$, are shown in Fig. 2. From Fig. 3, the Te and Ne obtained from an binary system is not always appropriate for the third element.

3.2 Depth profile of 10% Cr steel for O_2^+ primary ion

Figure 3 shows depth profiles of 10% Cr steel (FXS 339). Surface contamination is observed up to 50 Å as shown in Ca^+ depth profile. In Fe^+ and Cr^+ profiles, there are unstable region less than about 250 Å depth and the stable region follows. Quantitative analyses are carried on the stable region and it is thought to be a sort of equiribrium state for surface oxidation by O_2 atmosphere, and O_2^+ primary ion implantation, and sputtering[4].

3.3 Depth profiles of surface sputtered by O_2^+ ion using N_2^+ primary ion

After getting the stable state using O_2^+ primary ion, primary ion was immediately changed to N_2^+ in order to know the depth profiles of oxygen, iron and alloyed elements.

In Fig. 4, depth profiles for pure iron and pure chromium are shown. Intensities of Fe^+ and Cr^+ are proportional to O^+ ion intensity, repectively. These O^+ depth profiles suggest the surface chemical oxidation and implantation by O_2^+ ion.

In Fig. 5, depth profiles of iron base binary alloys, Fe-Ni and Fe-Cr, are shown and also dependences of accelerating potential upon the profile are compared for Fe-Si and Fe-Cr alloys. For the high accelerating potential of O_2^+ (18KV), the O^+ intensities decrease according to depth but the depth profiles of alloyed elements are quite different each other.

In Fe-Ni (Fig. 5-1), the profiles of Fe^+ and Ni^+ are similar and nearly same to Fe^+ profile of pure iron.

In Fe-Cr (Fig. 5-2), however, intensity of Cr^+ ion increases at 100~200 Å depth. In Fe-Si (Fig. 5-4), intensity of Si^+ ion has no peak at surface and only show the peak at 100~300 Å depth. In results obtained by lower accelerating potential of O_2^+ (4KV), intensities of Cr^+ and Si^+ ions show sharp peaks as shown in Figs. 5-3 and Fig. 5-5, respectively. The depth of these peaks are about 150 Å. For higher and lower accelerating potential, the depth of the peak of the alloyed element ion is thought to be corresponding to implanting of primary ion.

4. Conclusion

In order to know problems in IMMA quantitation of alloyed steel, analyses by O_2^+ primary ion and depth profile analyses using N_2^+ ion after O_2^+ ion sputtering were done, and following results were obtained.

(1) Gradient of the calibration method are varied by primary ion current density and accelerating potential.

(2) For pure iron and chromium, depth profile of oxygen is proportional to intensities of Fe^+ or Cr^+ ion. It is suggested that oxide is formed by implantation of O_2^+ primary ion.

(3) In alloyed steels, depth profiles of alloyed elements, whose affinity to oxygen are larger than that of iron, show very complicated behavior which suggests selective oxidization or selective vapourization, although experimental and theoretical explanations are remained in future and it is necessary to establish the quantitative analysis by IMMA.

References

1) C. A. Andersen et al., Anal. Chem., <u>45</u>, 1421 (1973)
2) K. Tsunoyama et al., Anal. Chem., <u>48</u>, 832 (1976)
3) T. Shiraiwa et al., U.S.-Japan Joint Seminar on
   "Quantitative Technique in Secondary Ion Mass Spectrometry",
   at Hawaii Univ., 1975
4) McHugh, NBS SP-427, ed. by K.F.J. Heinrich et al., N.B.S.,
   Washington, 1975

Table 1 Chemical composition of alloyed steel (wt.%)

FXS* No.	C	Mn	P	S	Co	Si	Ni	Cr
305	0.005	0.007	0.003	0.005	0.008	2.67		
327	0.011	0.32	0.003	0.006	0.013	0.09	6.00	
338	0.016	0.001	0.003	0.006	0.011	0.31		5.99
339	0.023	0.001	0.003	0.007	0.010	0.31		10.07

* Iron and Steel Institute of Japan Standard
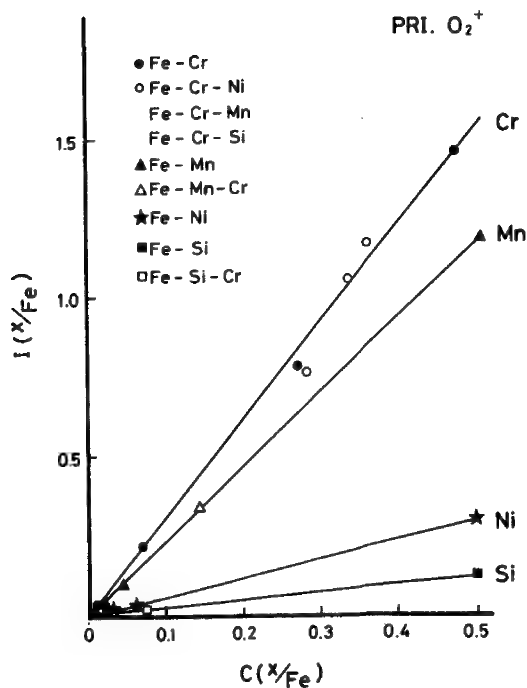
Fig. 1 Calibration curve of Si,
Cr, Mn and Ni in alloy steel
using O₂⁺ primary ion
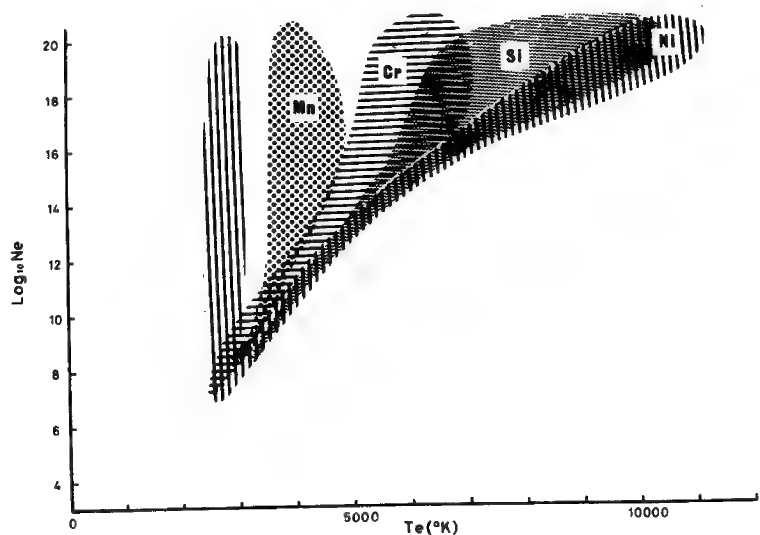
Fig. 2 Map of T and Ne⁻ of Si-Fe,
Cr-Fe, Mn-Fe and Ni-Fe binary
alloy from experimental k (±20%)

142E

^{52}Cr

^{16}O

500KC/sec. 0→

2KC/sec. 0→

|200Å|

Fig. 4-2

^{56}Fe

^{16}O

500KC/sec. 0→

2KC/sec. 0→

|200Å|

Fig. 4-1

Fig. 4 Depth profiles of pure iron and chromium obtained by N_2^+ primary ion after O_2^+ sputtering

Sputtering condition : O_2^+, 18KV, 0.14 mA/cm^2

Depth profile : N_2, 18KV 0.15 mA/cm^2

^{56}Fe

^{52}Cr

^{40}Ca

Fig. 3 Depth profile of Fe-Cr alloy (FXS 339)

Primary ion : O_2^+, 18KV
A : Surface contamination
B : Unstable region
C : Stable region

142F
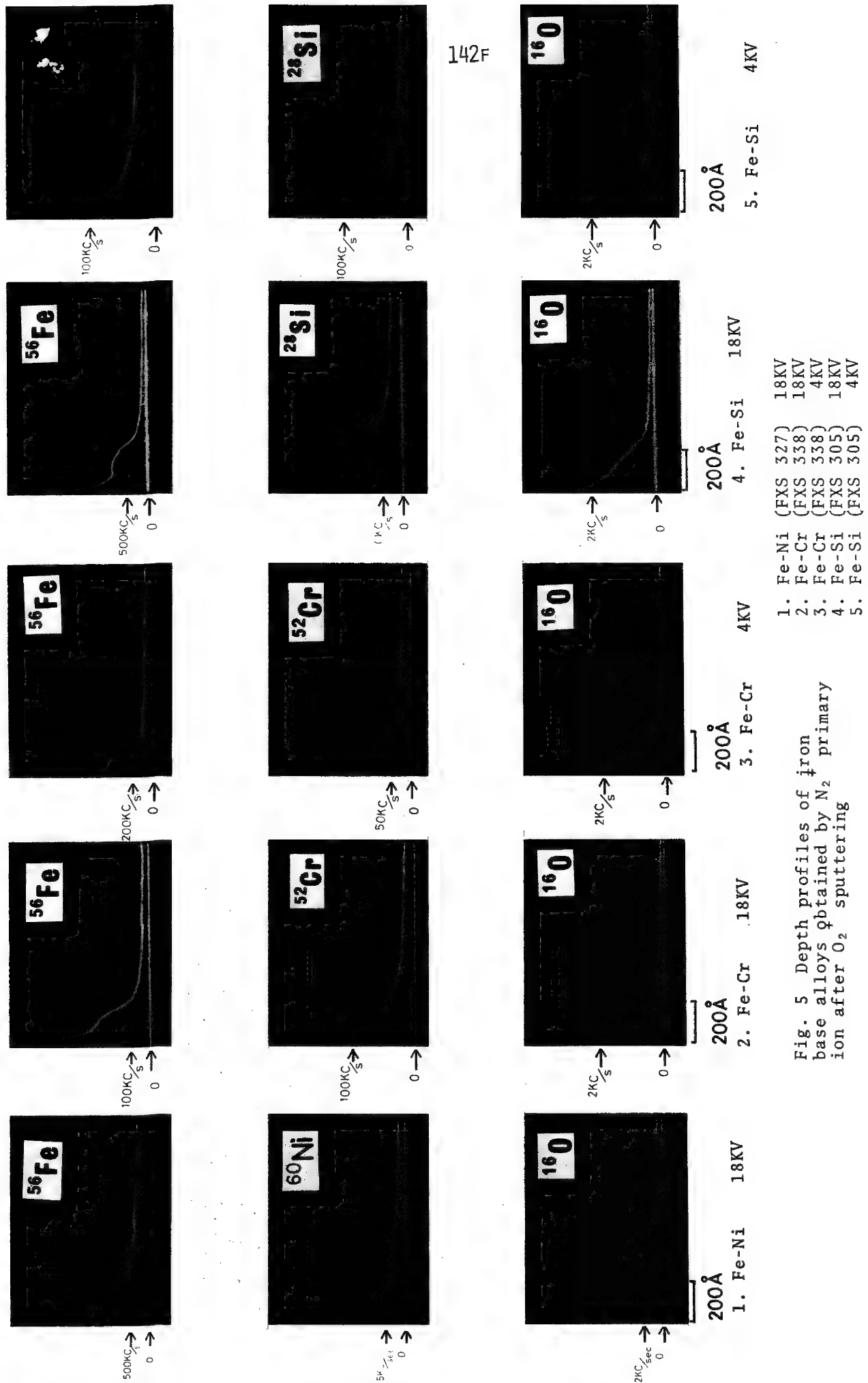
Fig. 5 Depth profiles of iron base alloys obtained by N_2^+ primary ion after O_2 sputtering

1. Fe-Ni   (FXS 327)   18KV
2. Fe-Cr   (FXS 338)   18KV
3. Fe-Cr   (FXS 338)   4KV
4. Fe-Si   (FXS 305)   18KV
5. Fe-Si   (FXS 305)   4KV

1. Fe-Ni   18KV
2. Fe-Cr   18KV
3. Fe-Cr   4KV
4. Fe-Si   18KV
5. Fe-Si   4KV

SECONDARY ION MICROANALYSIS OF SOME PHOSPHATE AND CARBONATE OF CALCIUM BIOMINERALISATIONS.

Dr. R. LEFEVRE - Laboratoire de Biophysique, Faculté de Médecine 94010 - CRETEIL, FRANCE et Institut de Géologie, Université Paris XI, 91405 - ORSAY, FRANCE.

The secondary ion microanalyser (SMI 300 CAMECA) has been used to study calcium biomineralisations because of his very good lateral resolution better than I µm and his high sensibility to small concentrations (1). Calcium biomineralisations, carbonates and phosphates, are present in plants and animals, actual and fossil, normal and pathologic : their study is at the boundary of physiology - biology and mineralogy - geology, because they are cristallised hard tissues produced by secretion in living tissues and because they remain after death in geological formations with mineralogical transformations and migrations of chimical elements during diagenetic process.

1. - <u>Phosphate of calcium biomineralisations: human teeth and bones.</u>
Their mineral substance is <u>hydroxyapatite</u> $Ca_{10}(PO_4)_6(OH)_2$ with substitution of Ca^{2+} by Na^+, K^+ and Mg^{2+} ; PO_4^{3-} by CO_3^{2-} ; OH^- by F^-, Cl^- and others. In <u>normal peritubular dentin</u> (2) and in slerosed tubules a high content in Ca, P and Mg is noted when compared to intertubular dentin (fig. 1) and electron microdiffraction shows the presence of <u>whitlockite</u> $Ca_3(PO_4)_2$ with 1 % in weight of Mg in the same areas. In the external third of enamal of teeth with <u>endemic dental fluorosis</u> (3) periprismatic arcade-formed defects with a lower mineralisation are present suggesting a broadening of the " sheath regions " (fig. 2) ; in more advanced lesions, the prism cores are missing and only the interrod substance remains (fig. 3). In <u>incipient carious lesions</u> in enamel similar defects are observed (fig. 4).

2. - <u>Carbonate of calcium biomineralisations.</u>

The three species of cristallised CO_3 Ca are : <u>calcite,</u> rhomboedral, <u>aragonite</u> and <u>vaterite,</u> orthorombic. The first is known for substitution of Ca^{2+} by Mg^{2+} and low content in Sr (0 to 1000-1500 ppm), the second for higher content in Sr (8000 to 10000 ppm). The stable form is pure calcite and metastable aragonite, magnesian calcite and vaterite are rare in geological biomineralisations.

a) - <u>Diagenetic evolution of triassic red Algae Solenopora (4) (Fig. 5 to 8).</u>
Original cellular membran of magnesian calcite is exceptionally well preserved and the inner part of the cell is filled with diagenetic alternacies of magnesian calcite and sodic aragonite.

b) - <u>Structure and diagenetic evolution of the rostrum of Belemnitidae (5) (Fig. 9 to 12)</u>.

Magnesian calcite and sodic aragonite are present in alternate streaks and suggest that the structure of pure calcitic Belemnitidae used for paleotemperatures measurements is not entirely of biological origin.

c) - <u>Structure of actual calcareous Foraminifera shells (6) (Fig. 13 to 16)</u>.

In a species, <u>Ammonia beccarii (Linné)</u>, inner lamella has higher content in Na and Sr than outer one : the machanism of secretion by biological membran is not homogeneous and influence of environmental conditions and variations in sea-water on the mineralogical nature of shell is not evident.

<u>REFERENCES</u> :

1. - R. LEFEVRE. <u>J. de Microscopie</u>, 22, 2-3, 1975, 335-348.

2. - R. LEFEVRE, R.M. FRANK and J.C. VOEGEL. <u>Calcif. Tis. Res.</u>, 19, 1976, 251-261.

3. - R. LEFEVRE and R.M. FRANK. <u>J. Biol. Buccale</u>, 4, 1976, 29-41.

4. - J.P. CUIF and R. LEFEVRE. <u>C.R.Ac.Sc.</u>, Paris, 278, 1974, D, 2263-2266.

5. - J.P. CUIF, Ч DAUPHIN and R. LEFEVRE. <u>C.R.Ac.Sc.</u>, Paris, 284, 1977, D, in press.

6. - R. LEFEVRE and M.T. VENEC-PEYRE. <u>C.R.Ac.Sc.</u>, Paris, 284, 1977, D, in press.
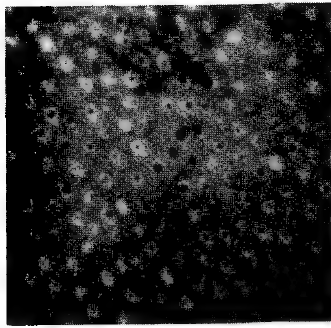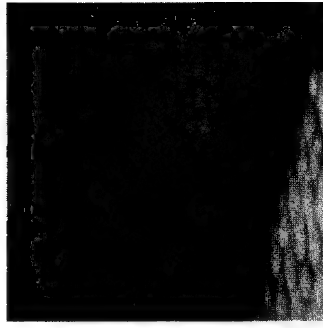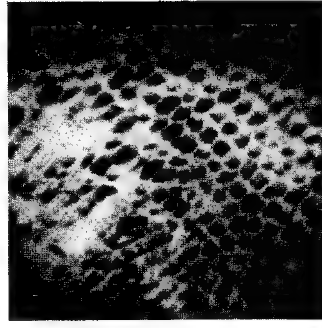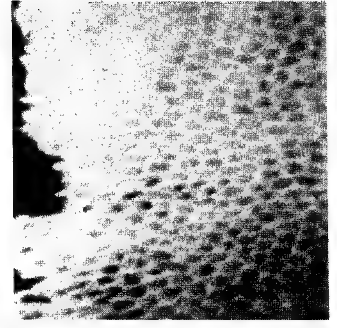
1 Mg 2 Ca 3 Ca 4 Ca
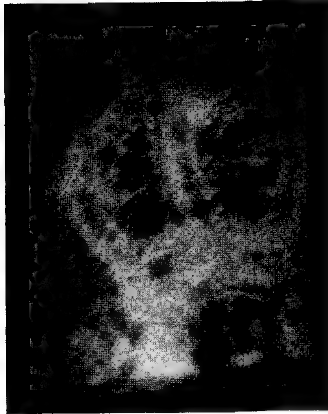
5 Ca 6 Mg 7 Sr 8 Na
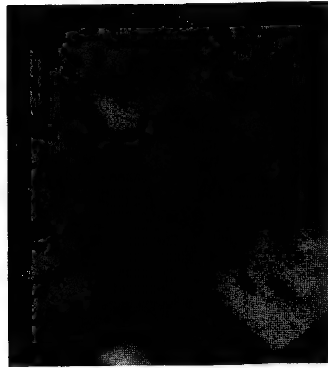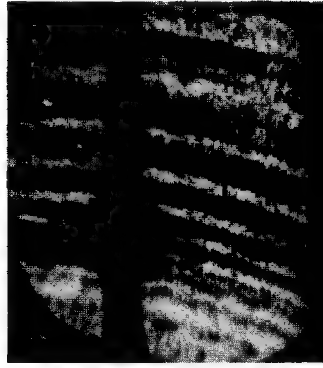
9 Ca 10 Mg 11 Sr 12 Na

13 Na 14 Sr 15 Na 16 Mg

APPLICATIONS DE LA MICROANALYSE EN SCIENCE DES MATERIAUX

J. PHILIBERT

Université de Paris Sud, ORSAY
et Laboratoire de Physique des
Matériaux, C.N.R.S.
92190 - MEUDON BELLEVUE

La place occupée par la Microanalyse en Sciences des Matériaux est devenue de plus en plus importante au cours des ans, par suite de la conjugaison de deux facteurs : d'une part le développement de méthodes analytiques nouvelles et d'appareils nouveaux commercialement disponibles, d'autre part les besoins d'une caractérisation poussée des matériaux.

Le concept de caractérisation s'est développé progressivement : il est apparu de plus en plus évident qu'un matériau ne peut être "caractérisé" seulement par son analyse chimique globale et sa taille de grains. La caractérisation exige la description qualitative et quantitative d'un certain nombre de propriétés, notamment à l'échelle microscopique. En fait elle doit se situer à plusieurs niveaux d'échelle, la limite étant la structure atomique elle-même. Dans ces conditions, confiner la microanalyse au rang d'un service serait absurde. Si c'est généralement le cas en pratique pour les méthodes d'analyse chimique globale - analyse chimique par voie humide, spectroscopie d'émission ou d'absorption atomique, fluorescence X,...., la microanalyse doit absolument s'insérer dans une approche synthétique du matériau. Ceci exige une coordination poussée de l'ensemble des méthodes d'examen et d'analyse, coordination parfois aidée par l'existence d'appareils polyvalents, "versatiles", tels que les divers STEM ; parfois au contraire cette coordination exige de passer par l'utilisation d'une panoplie d'appareils dont un même laboratoire ne peut pas toujours disposer (certaines méthodes nécessitant un accélérateur de particules, type Van de Graaf, par exemple).

A cet égard, il est significatif que le premier microanalyseur à sonde électronique, construit au début des années 50, était équipé d'un microscope optique. Tout aussi significatif le fait qu'on ait plus tard songé à lui adjoindre un microscope électronique pour l'observation en transmission, ou à construire un véritable appareil combiné, microscope électronique plus

analyseur à sonde électronique, qu'il s'appelle EMMA ou STEM. On a vu de
même, de manière significative, la convergence du microscope à balayage conven-
tionnel (SEM) et du microanalyseur à émission X, complété plus récemment de
spectromètre d'électrons Auger. La caractérisation exige en effet que toute
analyse soit effectuée en relation avec la microstructure. Cette idée simple
et familière aux métallurgistes n'a pas toujours été réalisée pleinement dans
d'autres domaines de la science des matériaux. Il est cependant capital de
savoir par exemple si les quelques ppm de l'élément Z dosé se trouvent réparties
en solution solide, ou rassemblés en petits amas, en précipités ou sous forme
d'inclusions. Cette exigence explique en grande partie la course à une échelle
d'analyse toujours plus fine : en 20 ans on est passé du micron à la centaine
d'amgstrõms, et parfois mieux encore.

Cet aspect complémentaire de la microstructure et de l'analyse se traduit
par l'existence de cartes ou de graphes tridimensionnels, obtenus soit par
des méthodes d'éclairement global, soit par balayage : que le signal soit
l'émission X, l'émission lumineuse, les électrons rétrodiffusés, les électrons
secondaires, les électrons transmis élastiques ou inélastiques (notamment fil-
trés en énergie), les électrons Auger,.... Remarquons encore que le besoin
d' "Augergraphies" s'est vite fait sentir, la caractérisation globale de la
composition superficielle étant insuffisante, notamment dans le cas des ségré-
gations intergranulaires observées sur des surfaces de rupture ou de l'analyse
des dispositifs à base de semi-conducteurs. Microanalyse et Microscopie élec-
tronique sous toutes ses formes (CTEM, STEM, SEM) sont manifestement insépara-
bles.

Un besoin analogue s'est manifesté en émission ionique secondaire ; le
spectrogramme de masse des couches superficielles ne suffit pas, la répartition
spatiale de chaque élément doit être connue : on obtient ici une résolution
du micron seulement, qu'il s'agisse d'appareils en optique globale ou en
balayage, mais l'analyse est réellement superficielle (quelques monocouches).
De ce dernier point de vue, elle peut être complétée utilement par la spectro-
métrie Auger. Des appareils combinés (SIMS + Auger) sont d'ailleurs commercia-
lisés.

La caractérisation microscopique d'un matériau comporte en principe la description des aspects suivants :

- microstructure (grains, phases, interfaces, dislocations...)
- structure cristalline (maille, paramètre, ordre...)
- composition chimique (éléments majeurs et mineurs de tout numéro atomique y compris l'hydrogène , traces, analyse isotopique...)
- type de liaison chimique (type de composé, degré de valence...)
- structure électronique (libre parcours et temps de vie des porteurs dans les semi-conducteurs...)

Parmi ces objectifs, seule apparemment la détermination de la liaison chimique à l'échelle microscopique n'a pas connu le même développement que les autres. Les méthodes classiques ou nouvelles, telles que la spectrométrie de photo électrons (XPS et UPS, ou ESCA), les spectrométries X d'émission (potentiel de seuil, isochromate, déplacements de pic,...) se prêtent en effet mal à une détermination très localisée, par suite d'un rapport signal/bruit insuffisant, ou d'une difficulté à localiser l'excitation (ESCA). En outre si elle est réalisable en surface, elle est plus difficile à mettre en oeuvre en profondeur, l'érosion par pulvérisation risquant de détruire ou modifier les liaisons.

Cette caractérisation peut répondre à l'une ou à l'autre de deux exigences bien distinctes en principe, mais qui peuvent se recouvrir largement, jusqu'à la limite d'une caractérisation atome par atome - comme le tentent la microscopie électronique à très haute résolution (localisation et identification d'atomes déterminés, soit dispersés, soit ordonnés) ou la spectrométrie de temps de vol mise en jeu dans "l'atome probe". A part ces cas limites, nous distinguerons :

- une caractérisation superficielle, c'est à dire limitée à une ou quelques couches atomiques, sans exigence spéciale sur sa localisation spatiale. Il s'agit soit d'une étude directe des phénomènes superficiels (adsorption, reconstruction, ségrégation...), soit de l'établissement de "profils" de concentration, avec une résolution en profondeur très élevée. Dans ce deuxième cas, l'analyse s'effectue au fur et à mesure que la surface est érodée, par bombardement dans un plasma ou sous un faisceau d'ions (pulvérisation cathodique).

Dans le premier cas, on peut rechercher une analyse à la fois superficielle et très localisée : des "Augergraphies" ont été obtenues récemment avec une résolution d'environ 300 Å. Des difficultés se présentent dans le cas de surfaces rugueuses (fractographie).

- une caractérisation localisée latéralement et en profondeur. Cette double exigence n'est pas toujours possible sur un échantillon massif, d'où le recours à des répliques extractives (précipités) ou à des lames minces : le microanalyste se doit d'être un microscopiste et réciproquement. L'expérience des dernières années montre que cela n'est pas toujours facile : les données de base de la microanalyse ont été ignorées par des utilisateurs de microscopes équipés de spectromètres à rayons X. Sur un même "point", la caractérisation pourra utiliser la diffraction d'aire sélectionnée, l'examen en champ clair et champ sombre, l'analyse chimique par émission X ou Auger, ou par pertes d'énergie profondes des électrons : actuellement une telle caractérisation devient possible sur un "point" de 100 Å.

Pour illustrer ces considérations générales, on choisira trois exemples de problèmes auxquels est confronté le chercheur en science des matériaux :

- l'analyse et l'identification de fins précipités,
- l'analyse de ségrégations locales,
- l'établissement de profils de concentration (diffusion, implantation, ségrégation, revêtements, dispositifs semi-conducteurs,...)

On essaiera d'évaluer les performances actuelles dans chacun de ces trois domaines - notamment résolution et sensibilité - et de situer les difficultés et les limites - particulièrement le caractère destructif de l'analyse, évident dans le cas des méthodes fondés sur la pulvérisation, mais toujours possible sous l'action d'un faisceau d'électrons assez intense. On montrera la nécessité de recourir à titre complémentaire à plusieurs méthodes, une condition indispensable pour une analyse aussi complète que possible et pour éliminer certains artefacts, bref pour une caractérisation utile et sûre à l'échelle microstructurale.

MAGNETIC DOMAIN OBSERVATION IN Fe-3% Si STEEL

W. G. Morris and P. Rao
General Electric Company
Corporate Research and Development Center
Schenectady, New York

J. W. Shilling
Allegheny-Ludlum Research Center
Brackenridge, Pennsylvania

The observation of magnetic domain structure in ferromagnetic materials, and the correlation of domain structure with magnetic properties, has made large advances in recent years. D. J. Fathers et al (1) developed a theory of Type II magnetic contrast which included the dependence of contrast on accelerating voltage and inclination of the sample to the electron beam. Shimizu et al (2) and Yamamoto et al (3) have developed improved techniques using a 200KV scanning electron microscope, illustrating the benefit obtained in improved contrast by the higher beam energy. Irie and Fukuda (4) have applied the technique to observing domains in Fe-3% Si transformer sheet. In the present work, we will describe the features of a special sample stage, some modifications to the display electronics of a 200KV JEOL SEM, and the magnetic domain structure observed on a variety of samples of Fe-3% Si transformer steel.

The JSEM-200 scanning transmission electron microscope has a large chamber between the second condenser and the objective lens, with direct access to it via two 100 mm dia. ports. A side entry stage was constructed incorporating orthogonal specimen translations as well as variable inclination to the incident beam. Also included were a magnetic yoke for magnetizing and demagnetizing the sample and a load frame for applying tensile stress.

The backscattered electron signal is obtained from a silicon surface barrier detector, followed by amplification and level compensation, then feeding it into the standard display electronics.

The specimen size is typically 105 x 30 x 0.3 mm. A central area 30 x 30 mm is available for observation; the remainder is obscured by the magnetic yoke. The range of magnification is 8x to 1000x, with a resolution of approximately 2μm. In grain oriented (110) [001] Fe-3%Si, domains have been observed in a large variety of samples, from polished and annealed to mill rolled, stress coated, transformer sheet. The domain width and supplementary domain fine structure have been studied as a function of grain orientation. Figure 1 illustrates the domain structure seen in three adjacent grains, where the sample has a forsterite (2MgO·SiO$_2$) coating approximately 5μm thick. The effect of ceramic coatings has been studied by observing the domain structure on a given sample before and after coating, finding that the coating can influence not only the domain spacing, but also the supplementary fine structure.

REFERENCES

1. D. J. Fathers, J. P. Jakubovics, D. C. Joy, D. E. Newbury, H. Yakowitz, Phy. Stat. Sol (a) 20, 535-544(1973); 22, 609-619(1974).
2. R. Shimizu, T. Ikuta, M. Kimoshita, T. Masuyama, H. Nishizawa, T. Yamamoto, Jpn. J. Appl. Phys. 15 967-981(1976).
3. T. Yamamoto, H. Nishizawa, K. Tsuno, Phil. Mag. 34 311-325 (1976).
4. T. Irie and B. Fukuda, AIP Conf. Proc. No. 29, 574-575(1976).

Figure 1. The domain structure varies with grain orientation, as shown in this forsterite coated Fe-3% Si sample.

MICROSEGREGATION IN Al-Zn-Mg ALLOYS

A. Wirsing and G. Judd
Materials Engineering Department
Rensselaer Polytechnic Institute
Troy, New York 12181

INTRODUCTION

The study of solute segregation accompanying heterogeneous precipitation is of interest from fundamental and engineering viewpoints. The Al-Zn-Mg alloy system has served as a model for precipitation hardening in a ternary alloy, and also forms the basis for the 7000 series of commercial Al alloys. In order to measure the solute profiles which develop within precipitate free zones, high spatial resolution as well as microanalytical sensitivity is required. Recent applications of the combined electron microscope-X-ray microanalyser (EMMA)[1] and also electron energy analysis in the transmission electron microscope (EMEA)[2] emphasize the advantages of these techniques in terms of spatial resolution, which are approximately 2000Å for EMMA and 100Å for EMEA. The corresponding spatial resolution of electron probe microanalysis is > 1 μm.

The paper describes the use of the electron microprobe to measure solute redistribution on a fine scale using a statistical technique. The microprobe results are combined with microstructural observations to extend the understanding of the precipitation process. The size of the microprobe spot, in terms of spatial resolution of regions of varying composition is effectively bounded by the region where the primary production of characteristic X-rays falls off to zero. Within this spot, for the case of a pure unalloyed sample, X-ray generation will vary in relation to the local beam current and over voltage, according to the relation:

$$I(x,y,z) \propto i(x,y,z) \left[E(x,y,z) - E_c \right]^n$$

The origin of the coordinates x,y,z, is the point of impingement of the beam with the sample surface. The electron density, i, and electron energy, E, will vary within the spot as the electrons are absorbed and scattered through interactions with the sample. Variations in the x-y plane are often considered Gaussian. The variation with depth may be taken as a linear decrease along x,y = 0. The generated X-ray intensity results from the interaction of these electrons of varying energy with the atoms present at (x,y,z). Thus the intensity generated due to the presence of a composition profile within the beam dimension will differ from that generated by a microvolume containing the same average composition homogeneously distributed within it. For the case of a one-dimensional composition profile in a binary system, a mathematical deconvolution technique can be used to determine the profile.[3] In the ternary Al-Zn-Mg system, the concentration profiles associated with intragranular heterogeneous precipitation will be three dimensional. One dimensional profiles for zinc and magnesium may be expected only at high angle grain boundaries which show copious precipitation.

EXPERIMENTAL

A Materials Analysis Corp. 400S electron probe microanalyser was used to measure the intensity of Mg and Zn characteristic X-rays at 100 points located randomly on the sample. The alloys used were Al-6.8 w% Zn-2.35 wt% Mg, and Al-6.8 wt% Zn-2.3 wt% Mg-0.1 wt% Ti, prepared by making a titanium addition to the former alloy. An alloy of composition Al-9.0 wt% Zn-2.5 wt% Mg produced by powder metallurgy was also studied. This alloy had a grain site of 1.5 μm. Data was in the form of K-ratios corrected for drift, background and dead time. Employing analysis of variance (ANOVA)[4], the variance in intensity about the mean value due to composition profiles was separated from the variance imposed by the sensitivity of analysis. The percent coefficient of variation (% CV) of the ensemble of 100 points was used as a parameter which was related to the microsegregation present at various stages of the precipitation reaction. This parameter reflects the density of sites for heterogeneous precipitation as well as the severity of microsegregation associated with those sites.

RESULTS

The K ratios obtained from the P/M alloy are shown in Fig. 1, sorted in order of increasing K for Mg and Zn. These distributions represent a % CV of 10.1 for Mg and 0.8 for Zn. Fig. 2 shows the % CV for the ternary alloy oil quenched from 510°C to room temperature and aged at 180°C. Fig. 3 shows the % CV for the ternary and Ti addition alloy quenched from 510°C directly to oil at 180°C.

DISCUSSION

The high probability of sampling grain boundary regions in the P/M alloy results in the measurement of considerable variation in K ratio. The abscissa of the figure is essentially the grain size of the P/M material, 1.5 μm.

Samples of differing grain size may be compared by introducing a correction based on the probability of sampling grain boundary regions. In the case of the Ti addition alloy, with a grain size of 230 μm, grain boundaries are sampled in 2.5 times as many points as in the case of the ternary alloy of grain size 600 μm. The results shown are corrected for this effect. In the ternary and Ti addition alloys, increased values of the microsegregation parameter are observed for the slower direct quench to the aging temperature. The higher density of matrix precipitates in the samples quenched to room temperature inhibits the long range redistribution of solute which is seen in the samples directly quenched to the aging temperature. Ti retards the development of microsegregation in these alloys.

REFERENCES

1) G. W. Lorimer, M. J. Nasir, R. B. Nicholson, K. Nuttall, D. E. Ward and J. R. Webb, in Electron Microscopy and Structure of Materials, G. Thomas, Ed., University of California Press, Berkeley and Los Angeles, California, 1972, p. 222.
2) P. Doig, J. W. Edington and M. H. Jacobs, Phil. Mag., 31(2), 1975, 285.
3) E. J. Rapperport, in Electron Probe Microanalysis, A. J. Tousimis and L. Marton, Eds., Advances in Electronics and Electron Physics supplement 6; Academic Press, New York, 1969, p. 117.
4) Irwin Miller and John E. Rround, Probability and Statistics for Engineers, Prentice-Hall, Inc., Englewood Cliffs, New Jersey, 1965.

FIGURE 1

146D

Vickers Hardness 5kg

Magnesium % CV

Zinc % CV

minutes at aging temp

Solution Temp; 510°C
Quench;   oil at room temp.
Aging Temp;   180°C

FIGURE 2

146E
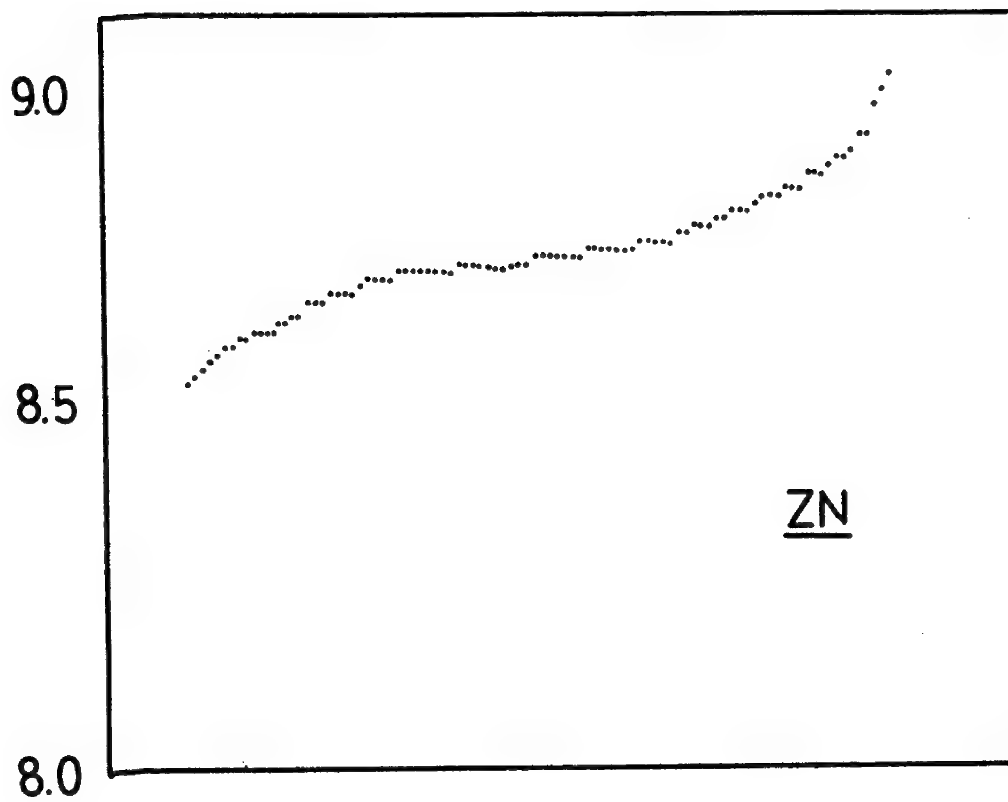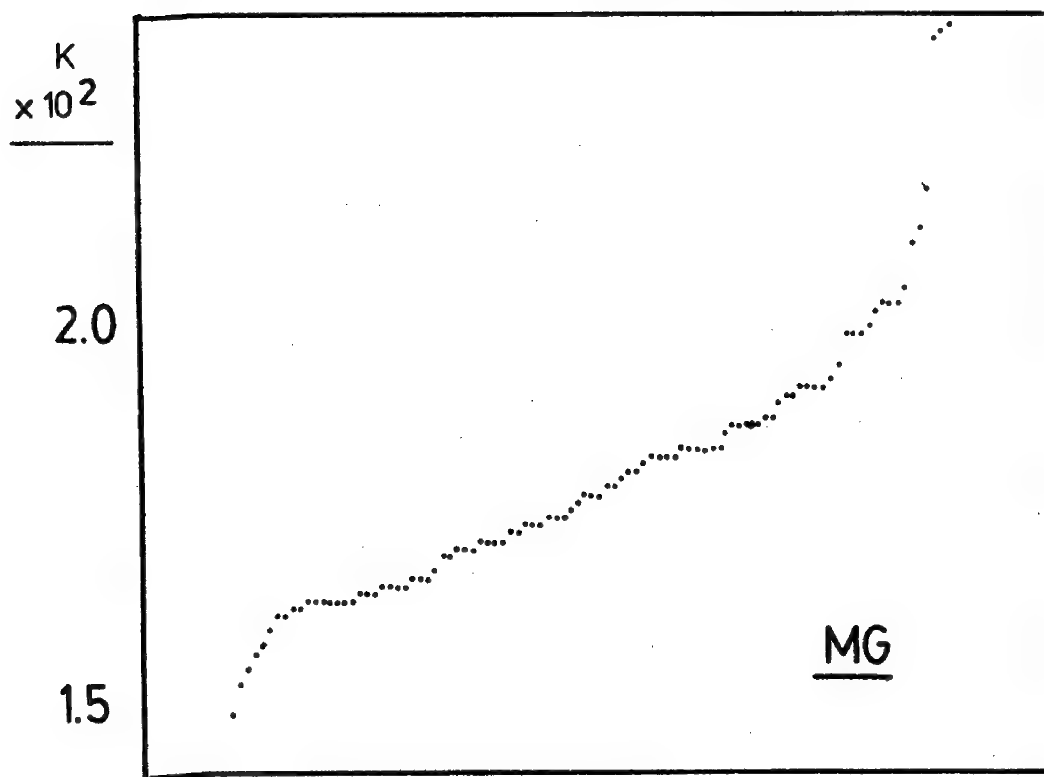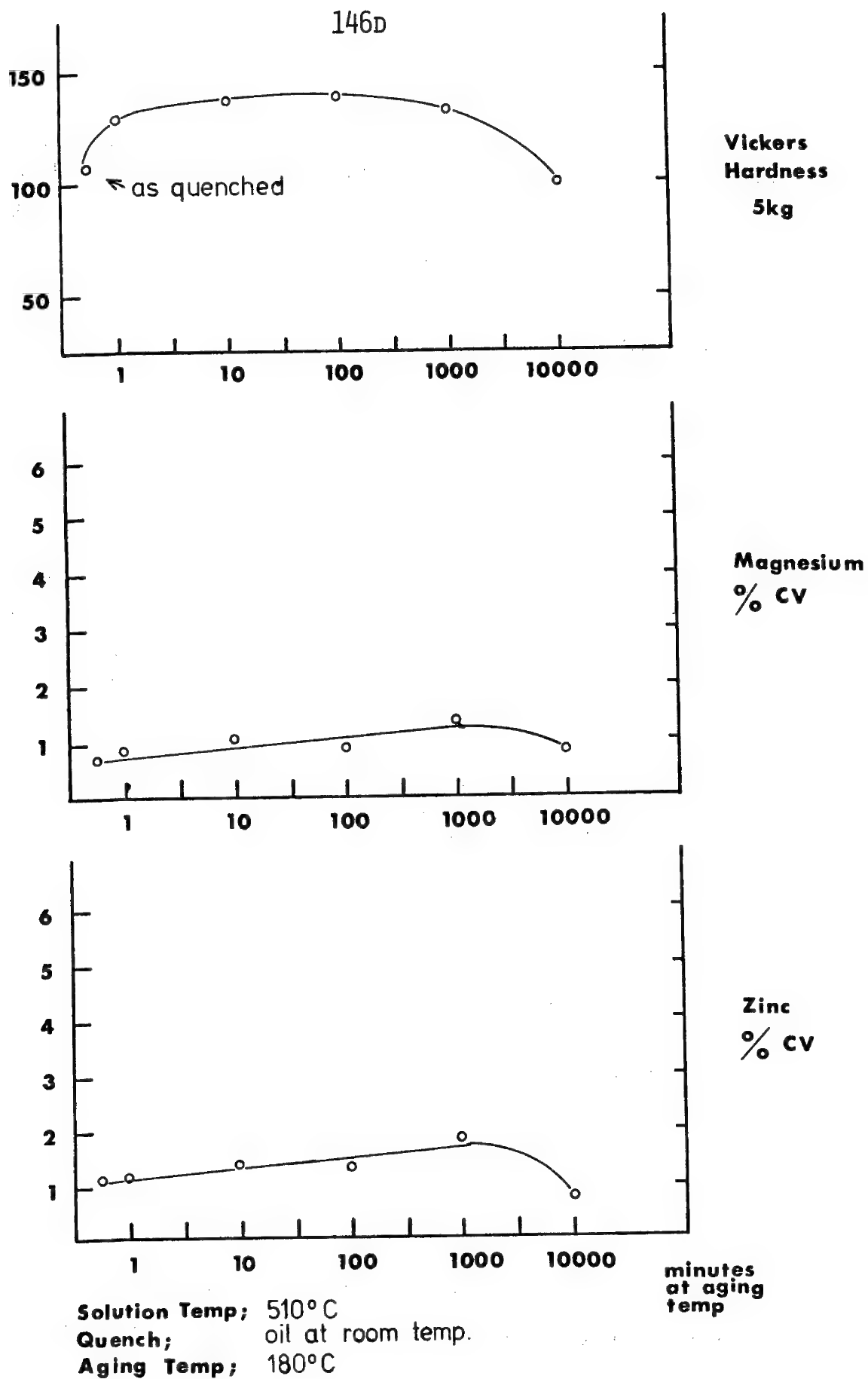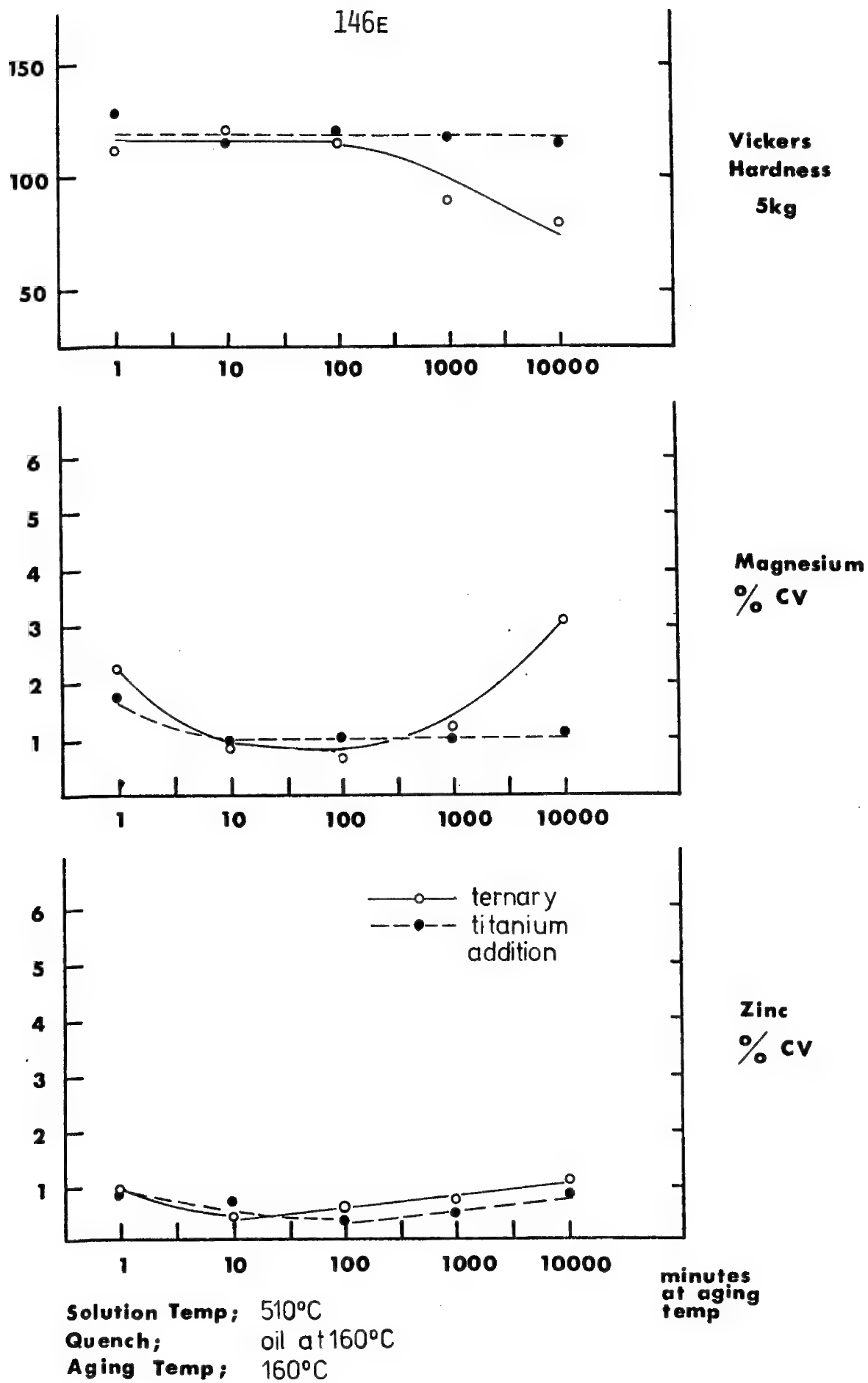
FIGURE 3

DIFFUSION PROCESSES AND WELDABILITY OF HOT PRESSED RENE '41 SUPERALLOYS

S. Tosto - M. Sattin

Fiat

ABSTRACT

The diffusion process of the elements Ni, Cr, Co and Mo in the sandwich-like system RENE '41 - Ni - RENE '41 has been studied by mean of scanning electron microscopy.

The process occurred under yacuum, at temperatures ranging from 1000 to 1130°C with times of treatment form 3 to 5 hours. Some samples were subjected to a load of 2,5 Kg/mm^2 A theoretical model of the diffusion process has been applied to the system in order to extrapolate the experimental data to other conditions of treatment; the calculations allow a prevision of the times and temperatures necessary to obtain a prefixed degree of homogenaization of the system.

The results can be summarized as follows:

a) When the Ni layer on the face to be welded of the super-alloy is deposited by a chemical process, the small amount of phosphorus, still present after the reducing reaction of hypophosphates, reacts with Cr, Ti and Mo.
In this case, a perfect homogeneization of the system is clearly impossible.

b) When the thermal treatments have been performed at temperatures greater then 1000°C, and Al compound (probably Al_2O_3) is present in the welding zone. Also the presence of this compound prevents the homogeneization of the system and lowers the mechanical properties of the junction.

To allow an ease evaluation of the situation in the welding zone and to calculate the degree of homogenization, the intensity of X-rays emitted in the central zone of the junction was compared with that of the superalloy.

The ratio so obtained for each element has been assumed as a measure of the homogeneization degree. The approximation involved can be considered legitimate because the compositions of the compared zones are not very different.

A perfect homogeneization occours when the ratio is equal to 1. Moreover, the experimental profiles allow a quantitative prevision of the diffusion degree at different times and temperatures of treatment. The theoretical model used to describe the diffusion process according to the geometrical arrangement of the system is tha of a thin layer of metal (Ni) inserted between two endless roads of another substance (the superalloy); the solution of the Fick's equation is, in this case, expressed by a combination of error functions. We have assumed that the diffusion coefficient of the various element is constant at a given temperature. The method used to find D from the experimental profiles was the following.

We have selected two samples subjected to different thermal treatments (1000° and 1130°C) and found for each element the proper D coefficient accounting for the experimental profile of $C_i,(X,t)$ at the given temperatures.

For sake of semplicity, we have chosen a D value fitting the equation just with the central point of the experimental curves, but a better result could be obtained by taking the best D fitting the entire experimental profile.

By our procedure, however, the experimental curves and those calculated by the solution of Fick's equation deviate less than 10%; the maximum deviation occours at the inflexion point. The D values so obtainded where used to calculate D_0 and Q expressing the temperature dependence of D.

The calculated D_0, Q and D for Cr, Co, Mo and Ni were compared with those of the same elements when diffusing in pure Ni.

It can be noted that Do and Q are quite different but this is not surprising because our values refer to a diffusion process occourring in the superalloy instead of pure Ni.

The resulting values of D are however of the same order of magnitude but their variation in function of temperature is, of course different.

We then processed a computer program to calculate $C_i(X, t)$ in function of X for given times and temperatures of treatment: as an example we chose the Ni, prefixing in the welding deviations of its concentration of 10% and 5% with respect to superalloy.

Times of 48 h and 151 h were calculated a 1000°C for the two homogenization degrees, while times of 16 h and 53 h respectively at 1130°C.

By rising the temperature to 1200°C times of 12 h and 40 h respectively were calculated.

These results should be correlated with the mechanical properties of the weld; in effect this is a natural corollary of the work because is necessary to know which homogeneization degree lowers the mechanical strength of the welding by a prefixed amount. The allowed decrease of mechanical properties can be in turn evaluted by knowing the required performances of the weld.
In this way, it is possible to program various thermal treatments for given applications of the superalloy.

Electron Probe Testing for Homogeneity of Standards

K. F. J. Heinrich, R. B. Marinenko, and F. C. Ruegg
Analytical Chemistry Division
National Bureau of Standards
Washington, D. C. 20234

Abstract

Standard Reference Materials (SRM's) certified for composition by the National Bureau of Standards have occasionally been used to test the accuracy of microprobe techniques. Such use is justified only if these materials have been previously tested for homogeneity on a micrometer scale, as were the materials cited in Table 1. Two research materials which were also tested for homogeneity on a micrometer scale, are also listed in this table.

Table 1

No.	Type	Form	Elements (Nominal wt %)
SRM 478	Cartridge Brass	Cube & Cylinder	Cu7-3; Zn-27
SRM 479	Fe-Cr-Ni Alloy	Wafer	Fe-71; Cr-18; Ni-11
SRM 480	Tungsten-20% Molybdenum	Wafer	W-78; Mo-22
SRM 481	Gold-Silver	Six Wires	Au-100; 80; 60; 40; 20; 0 Ag-0; 20; 40; 60; 80; 100
SRM 482	Gold-Copper	Six Wires	Au-100; 80; 60; 40; 20; 0 Cu-0; 20; 40; 60; 80; 100
SRM 483	Iron-3% Silicon	Platelet	Fe-97; Si-3
RM 30	Glasses for Microanalysis	Slices	10 Compositions of Various Oxides
RM 31	Glass Fibers for Microanalysis	Fibers	10 Compositions of Various Oxides

In order to simplify and accelerate the testing of materials which are already characterized macroscopically, we have developed a simple, routine technique for studying homogeneity in the micrometer (μm) range with the electron probe. This technique is based on statistical calculations and graphic representations similar to industrial control charts showing the deviations beyond the expected (Poisson) counting statistics.

For the purpose of graphical representation, we abandoned the conventional linear analog ratemeter for recording because of the difficulties in assigning Poissonian boundaries to rate-meter excursions. Instead, a periodic integrator [1] based entirely on digital operations (i.e., a microcomputer) has been developed. This new type of ratemeter will output simultaneously to a teletype (digitally) and a fast strip chart recorder (analog signal) the total number of counts acquired by the scalers in a preselected time period. The signal for each count period remains unchanged on the recorder until the next time period is completed. With a stepping motor on the sample stage, the ratemeter can automatically advance the sample under the electron beam between counting periods in steps of from 1-10 μm. The ratemeter can also be used to select the number of times (one to four) a single spot is sampled before advancing to the next.

To improve the graphic display from the recorder, the signal can be digitally multiplied by any appropriate factor and a bias can be applied to subtract any desired count rate from the signal. This enhances the variations of the graphic signal to any desired level.

An example of the graphic display is shown in figure 1. The sample is SRM 663, one of several NBS stainless steels presently being studied for homogeneity. The elements observed here, molybdenum, chromium and manganese are present in concentrations of 0.03, 1.31 and 1.51 weight percent, respectively. The homogeneity study was performed with a 1 μm electron beam with steps of 1 μm across the sample matrix (visible inclusions were avoided). Counts were accumulated once on each step for ten-second counting periods. The shaded area through the center of the trace represents a range of ±3σ around the average value, assuming Poisson counting statistics (σ = standard deviation = $\sqrt{\text{average number of counts}}$).

Deviations outside this region represent sample inhomogeneities or instrumental variations at the 99.7 percent confidence level. Note that the molybdenum signal falls mostly within this shaded area, while chromium and manganese show larger deviations which coincide for these two elements.

To the left of the figure is a trace recorded from repeatedly counting for ten-second intervals on a stationary 20x20 μm^2 area. An area this size should approximate an average value and such repetition should lie within Poisson counting statistics which it does here. This test verifies that variations outside the ±3σ range in the right trace are in truth due to the sample variability and not to instrumental factors.

A computer program is being developed to numerically evaluate the sample homogeneity, as simply as possible, in terms of spacial distribution. This test will be used to predict the number of random micro measurements required from an inhomogeneous sample to validate its use as a standard and to obtain an accuracy equal or better than a preselected level.

Reference

[1] Heinrich, K. F. J., "Instrumental Developments for Electron Microprobe Readout," in _Advances in X-ray Analysis_ 7, p. 382 (1963).

Figure 1. Ratemeter traces of manganese, chromium and molybdenum simultaneously recorded from SRM 663 stainless steel. In the traces on the right, the sample was advanced 1 μm under the 1 μm electron beam after each ten-second counting period. To the left, the sample was not moved during repeated ten-second counting periods with a 20 μm beam. The shaded regions represent the average number of counts per 10 seconds for the entire trace ±3σ.

HEDL-SA-1242A

MICROPROBE ANALYSIS OF PuO_2-UO_2 NUCLEAR FUEL*

W. I. Clark, D. E. Rasmussen, R. L. Carlson, D. M. Highley

HANFORD ENGINEERING DEVELOPMENT LABORATORY
Richland, Washington
operated by
WESTINGHOUSE HANFORD COMPANY
a subsidiary of Westinghouse Electric Corporation

The nuclear fuel for the Fast Flux Test Reactor (FFTF) located at Richland, Washington is nominally 25 Wt% PuO_2 and 75 Wt% UO_2. Various techniques for producing a homogeneous fuel were studied in the early stages of fuel development. PuO_2-UO_2 mixtures were blended, formed into pellets and irradiated to determine the effect of preparation on fuel performance in Experimental Breeder Reactor II. From these irradiation tests, it was apparent that adequate pre-irradiation characterization of the fuel materials was necessary if post-irradiation examinations were to provide maximum useful information. To meet this objective and to establish a basis for comparing FFTF vendor-produced fuel with irradiation test fuel, a characterization program was developed to determine the pre-irradiation porosity, grain structure and microcomposition characteristics of the fuel. Computer programs were developed to provide improved evaluation of the PuO_2 and UO_2 compositional homogeneity of the nuclear fuel. These software programs utilize elemental composition data generated by the electron microprobe.

Originally computer programs MITRAN and MERIT were developed independently to characterize different aspects of fuel inhomogeneity. Program MITRAN (1) (Microprobe Translation Analysis) was written to locate and quantify PuO_2-rich regions and UO_2-rich regions along a linear traverse. The output from MITRAN includes: number of component rich regions, mean region size, mean region composition, percent of total sample in the regions, region size/composition histograms, and a graph of composition vs. position along the linear trace.

Computer program MERIT was developed to evaluate the homogeneity of the nuclear fuel by calculating an average "Figure of Merit" (2) for a given fuel lot. The local figure of merit at any point in a fuel pellet is defined as the calculated relative rate of energy deposition in UO_2 at that point divided by the deposition rate which would exist in a homogeneous fuel of average composition. The figure of merit represents the limiting thermal response of mixed oxide fuel under transient conditions. A perfectly homogeneous fuel has a figure of merit of 1.0. As the degree of homogeneity decreases the figure of merit becomes less than 1.0. Relatively homogeneous mixed oxide fuel lots have figure of merits ≥ 0.96. Computer program MERIT output includes the average figure of merit and standard deviation along with a histogram of the local figure of merits.

The $M\alpha$ characteristic x-rays from uranium, the $M\beta$ characteristic x-rays from plutonium, and the characteristic x-ray from a third element (usually iron) are measured at 2 micron intervals along a 3000 to 5000 micron linear traverse.

Computer program WESCON is used to convert x-ray intensity data to PuO_2, UO_2 and Fe concentration for use as input to MITRAN and MERIT. WESCON has provisions for correcting drift in the data based on the specimen current and also for normalizing the data. The data is not corrected for absorption or fluorescence.

Although MITRAN and MERIT were developed for different fuel development programs, both are currently used to compare the effect of various process changes in the fabrication of the mixed oxide fuels and to certify the quality of the fuel supplied by vendors. Some of the fabrication parameters which change the microcomposition are the particle size of the original feed material, ball milling conditions, blending time, sintering time, and sintering temperature.

References

(1) Clark, W. I., et al
     "MITRAN - A Computer Program to Calculate Microcomposition Data from Microprobe Step Scans", HEDL-TME-73-35 UC-79b Westinghouse Hanford Co., Richland, WA., February 1973.

(2) Stranik, D. A. and Powers, H. G.
     "Evaluation of PuO_2 Homogeneity in PuO_2-UO_2 Fast Reactor Fuel by Scanning Electron Microprobe", WHAN-FR-20, WADCO Corporation, Richland, Washington, October 1970.

PORTION OF MITRAN COMPOSITION TRACE

FIGURE OF MERIT HISTOGRAM

OUTPUT FROM MITRAN AND MERIT COMPUTER PROGRAMS
VARIATIONS DUE TO SINTERING CONDITIONS

HEDL 7703-105.1
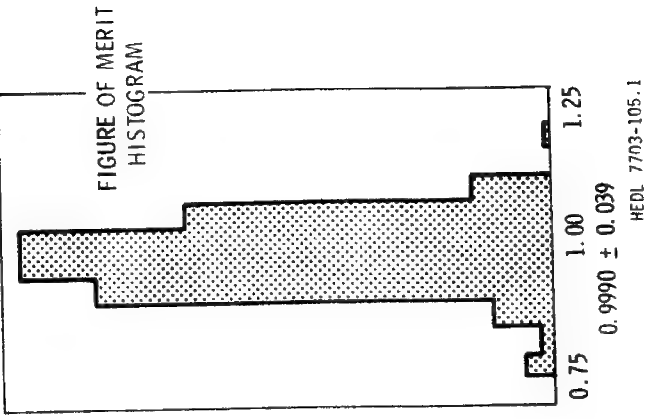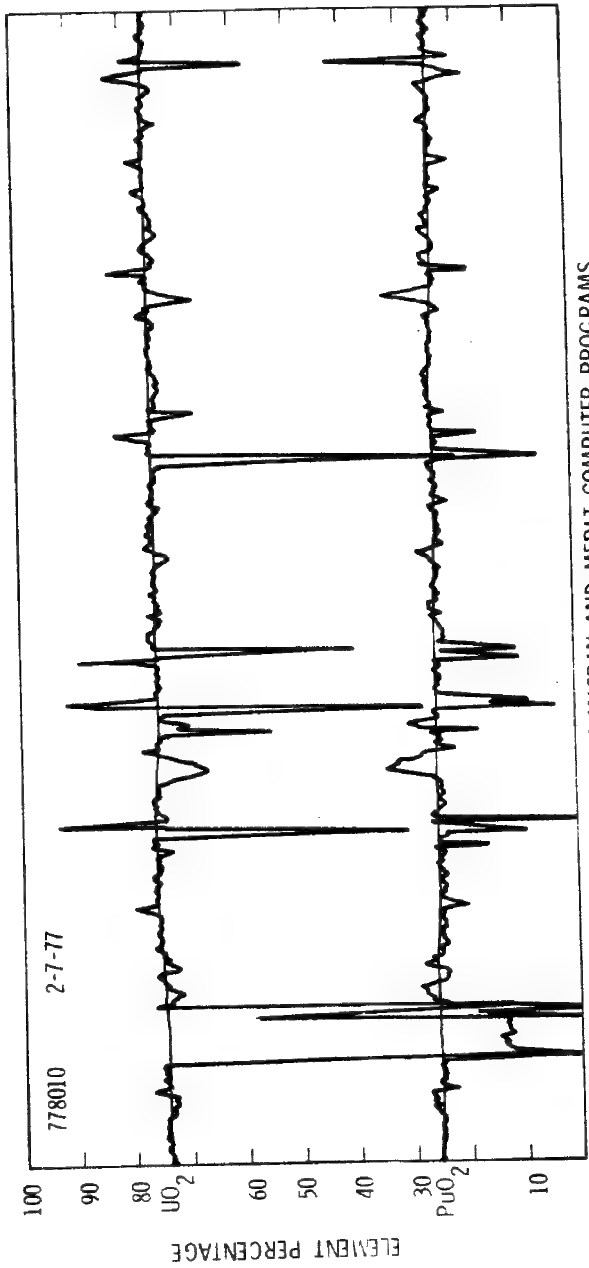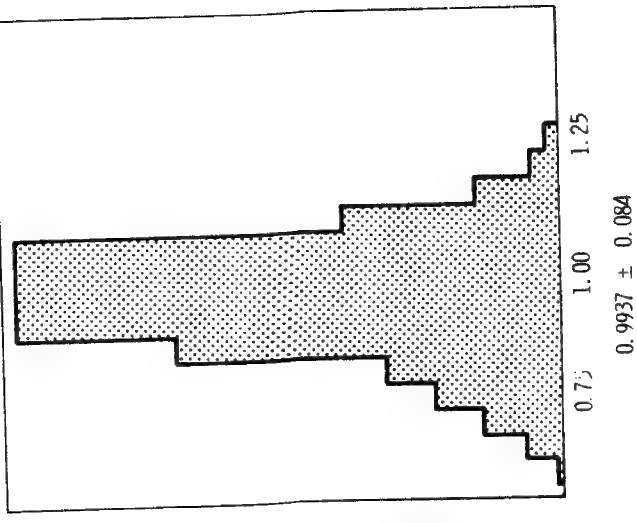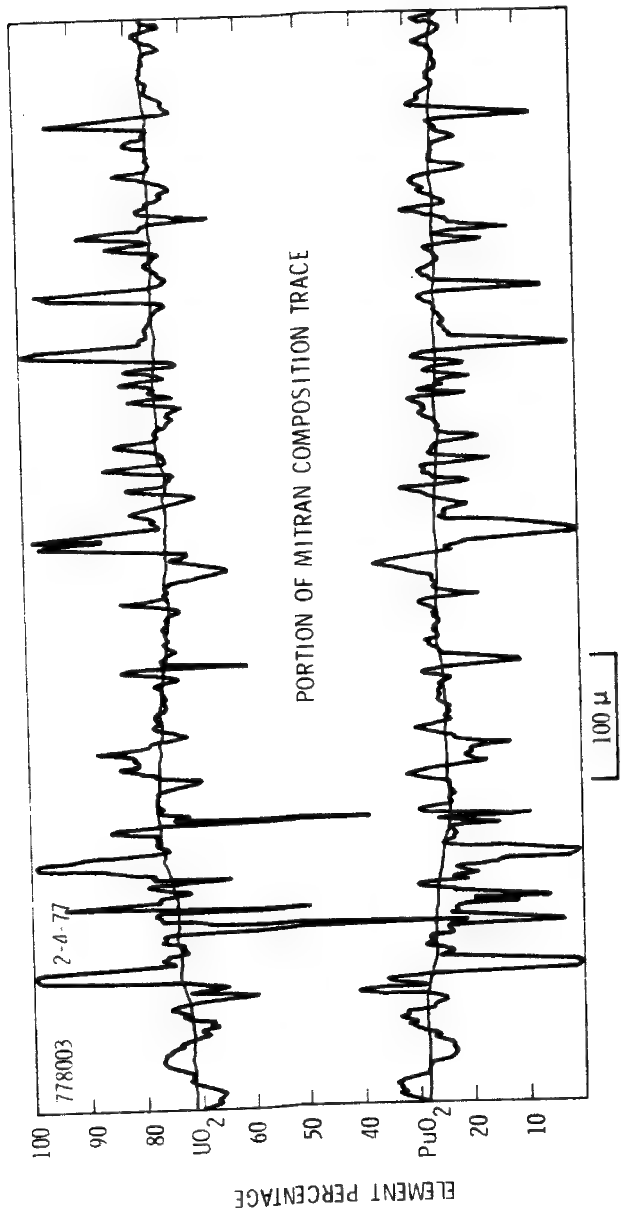
ELECTRON PROBE MICROANALYSIS IN INHOMOGENEOUS

THIN FILMS

by

J.D. Brown
Faculty of Engineering Science &
The Centre for Interdisciplinary Studies in Chemical Physics
The University of Western Ontario
London, Ontario

and

James M. Short and Roger W. LaForce
Xerox Corporation
Xerox Square W114
Rochester, New York   14644

The measured relative X-ray intensities (k-ratios) from a film whose composition varies with depth will vary as a function of incident electron energy. If the normal equations of quantitative analysis are used to convert k-ratios to "average" composition then large errors can result. The errors arise because all conventional methods of quantitative electron probe analysis assume a constant composition in the excited volume, which would be far from the case in a non-uniform film. The purpose of this paper is to describe a method for the analysis of inhomogeneous thin films.

If the depth distribution of X-ray production ($\phi(\rho z)$ curve) is known and the form of the concentration gradient in the film can be assumed, then k-ratios can be calculated. K-ratios computed as a function of electron energy can be compared with measured k-ratios. The closest agreement between calculated and measured ratios indicates the most probable concentration gradient in the thin film.

Calculation of k-ratios requires $\phi(\rho z)$ curves and an assumed concentration profile. The $\phi(\rho z)$ curves were calculated from an equation developed by Parobek (1) by fitting to an extensive series of measured $\phi(\rho z)$ curves (2) at electron energies from 6 to 15 keV. This equation is as follows:

$$\phi(R) = D.k.n \ (kR)^{n-1} \exp(-(kR)^n)$$

where $R = \rho z_0 + \rho z$, k, n and z_0 are constants for any curve and each of these parameters depends on the electron energy, the excitation potential and the average atomic number of the specimen.

D is a constant for any curve and represents the total area under the $\phi(\rho z)$ curve as can be seen by a simple integration.

By multiplying the $\phi(\rho z)$ value for a particular depth by the concentration at that depth, then correcting for absorption in the overlying layer, the emitted intensity from that depth is obtained. Summation over all depths yields the total intensity. Although the $\phi(\rho z)$ curve for X-rays generated in the specimen could not be corrected for any distortions introduced by the concentration gradient, the correction for X-ray absorption along the emission path was corrected for the gradient. Thus, the technique is limited to films whose average atomic number does not vary greatly with depth; hence films containing elements adjacent in the Periodic Table or those containing a small concentration of a second element.

The technique has proven particularly suitable in the determination of arsenic gradients in selenium films. The relative intensity of AsLα is measured at electron energies of from 6 to 17.5 keV in the MAC microprobe. Calculations of intensity ratios based on two assumed concentration distributions are given in Table 1. Such ratios have been compared with measured ratios on characterized films to establish the sensitivity of the calculated ratios to concentration distribution and average total concentration. The technique provides a good measure of maximum surface concentration and the concentration gradient within 0.5 μm of the surface.

TABLE 1

CALCULATED K-RATIOS FOR 1 WT % As in Se

Electron Energy keV	Distribution		
	Uniform 1 wt.%	Exponential decrease*	Linear decrease+
6	0.00992	0.0359	0.0191
8	0.00987	0.0297	0.0186
10	0.00982	0.0247	0.0180
12	0.00976	0.0209	0.0173
15	0.00969	0.0170	0.0166
17.5	0.00964	0.0149	0.0160

*Concentration in wt. percent = $5.03e^{-10,000 \rho z}$ with ρz in μg/cm^2

+Surface conc. 2.0 wt.%, conc. at 500 μg/cm^2 = 0.0 wt.%.

References

(1) L. Parobek. "Determination of Absorption and Atomic Number Corrections in Electron Probe Microanalysis for Energies Below 15 keV", Ph.D. Thesis, University of Western Ontario, 1975.

(2) J.D. Brown and L. Parobek, X-Ray Spectrometry, 5, 36 (1976).

X-RAY MICROANALYSIS OF BORON-RICH LAYERS GROWN DURING B-PREDEPOSITION IN SILICON

A. Armigliato, G. G. Bentini, A. Desalvo[+], R. Rinaldi[++],
R. Rosa and G. Ruffini
Laboratorio LAMEL-C.N.R., Via Castagnoli, 1-40126 Bologna (Italy)
[++]Istituto di Mineralogia dell'Universita, Via S. Eufemia, 19
41100 Modena (Italy).

It is well known (1-3) that during boron predeposition in silicon performed in the operating conditions typical of the planar technology, a heavily B-doped layer (BRL: boron-rich layer) generates between the boron silicate glass and the substrate; the kinetics of predeposition is controlled by such a layer and therefore the knowledge of its composition and structure is important for a thorough understanding of the doping process.

From the structural data reported in the literature (2,3) it turns out that the BRL consists of a mixture of SiB_4, SiB_6 and B_6O (elsewhere referred to as B_7O (4)) phases. X-ray diffraction spectra carried out in our laboratory (5) pointed out that the compound SiB_6 is surely present, although SiB_4 and B_6O cannot be excluded.

In order to gather information about their composition, BRL layers have been analysed by Rutherford backscattering technique of He ions (6) and by X-ray microanalysis. The application of the latter technique to the analysis of a Si-B-O ternary system is of particular interest, since it should allow testing of both the analytical capability of an X-ray microanalyser in thin films containing light elements, and the validity of the required correction procedures.

Experimental techniques

BRL layers of three different thicknesses (300, 400 and 700Å) were obtained as a result of B-predeposition experiments carried out at 1000°C with different compositions of the BBr_3 and O_2 gas fluxes (7). The boron silicate glass was etched away with HF, whereas the BRL's were removed from the silicon substrate by etching with a $HF/HNO_3 = 1/15$ solution and subsequently floated in water. The small pieces of film were collected on microscope grids and then put into the specimen holder.

Two types of X-ray microanalysers have been employed: a fully automated ARL-SEMQ microprobe and a Siemens Elmiskop 101 transmission electron microscope, equipped with a crystal spectrometer. Results of microanalytical work performed with such a TEM set-up have been previously reported at the Ottawa Conference (8). The take-off angles were 52.5° and 15° in the ARL microprobe and in the TEM, respectively; both instruments were operated at 20 KV. The $BK\alpha$, $OK\alpha$ and $SiK\alpha$ X-ray lines were analysed in the ARL microprobe with a PbSD, a RAP and a ADP crystal, respectively, whereas in the TEM with a PbSD ($BK\alpha$ and $OK\alpha$) and a PET crystal ($SiK\alpha$). The electron

[+]Also at Instituto Chimico, Facolta di Ingegneria, Universita di Bologna (Italy).

currents impinging on the specimen were 150 nA in the ARL microprobe and in the μA range in the TEM, due to its lower detection efficiency; this latter condition did not allow us to analyze, with the TEM, specimens of thickness as low as 300Å.

Results:

The BKα, OKα and SiKα X-ray intensities were measured and compared with the corresponding ones obtained from block standards of pure boron, SiO_2, Al_2O_3 and high resistivity silicon. The K-ratios were calculated and are reported in Table I; the oxygen K-ratio ($K_O = I_{OK\alpha}$(sample)/($I_{OK\alpha}$(pure O)) was obtained by computing K_O (SiO_2)(or K_O (Al_2O_3)) in the ZAF expression for SiO_2 (or Al_2O_3). The OKα line was a well resolved peak in the ARL microprobe, whereas with the semifocusing spectrometer of the TEM it occurs at 27.5^O (2θ) and therefore it is not completely resolved from the primary radiation. For this reason in this latter case the area of the OKα peak, instead of the usual P-B value, has been considered.

The K-ratios have been converted into concentrations by using the Philibert-Tixier (9) formula, which for a ternary Si-B-O system can be written in the following way:

$$C_B = \frac{K_B F_B}{K_B F_B + K_O F_O + K_{Si} F_{Si}} \quad ; \qquad C_O = \frac{K_O F_O}{K_B F_B + K_O F_O + K_{Si} F_{Si}} \quad ;$$

$$C_{Si} = \frac{K_{Si} F_{Si}}{K_B F_B + K_O F_O + K_{Si} F_{Si}} \qquad \text{where:} \qquad F = \frac{R f(\chi)_{std}}{Q S' f(\chi)_{film}}$$

In the expression for F, the terms R, S' and $f(\chi)_{std}$ are the corrections for backscattering, stopping power and absorption in the standards, respectively, whereas Q and $f(\chi)_{film}$ are the ionisation cross section and the absorption corrections in the film, respectively. The term $f(\chi)_{film}$ was found to be not negligible, for the BKα and the OKα X-rays, even in the case of the 300Å BRL; therefore it was calculated according to the formula by Philibert-Tixier:

$$f(\chi)_{film} = 1 - \frac{A}{2!} + \frac{A^2}{3!} - \frac{A^3}{4!} + \ldots$$

where $A = \chi \Delta \rho z$.

The absorption correction for boron is the most critical one, because there is a wide spread among the mass attenuation coefficients reported in literature. In Table II are displayed the values of $f(\chi)_{std}$ and $f(\chi)_{film}$ (for a 400Å BRL) calculated by assuming the Heinrich's (10), Henke's (11) and Veigele's (12) mass attenuation coefficients. To calculate the $f(\chi)_{film}$ we used the concentrations deduced from the backscattering experiments.

If the Heinrich's mass attenuation coefficients for boron are used, there is a considerable disagreement between the X-ray microanalysis results and the backscattering analyses. A similar discrepancy has already been reported by other authors (13), who found that the data from Henke led to more correct analytical results on a few boron-beryllium compounds. In our case, the use of both the Henke's and the Veigele's data leads to a closer agreement between the X-ray and the backscattering results with respect to the Heinrich's ones. In Table III are reported the compositions derived by the two techniques for the different specimen thickness. A comparison of the analyses does not allow to conclude which of the two set of mass attenuation coefficients is better.

As to the concentration of the oxygen in the BRL's, there is a discrepancy between the values obtained with the microprobe and the TEM; this is perhaps to be attributed to the different type of standards employed (Al_2O_3 or SiO_2, respectively) and/or to the different thickness of carbon evaporated onto them to make the standards conductive. Work is in progress to reduce this disagreement.

An alternative analytical method is represented by the analysis of the BRL's without removal from the silicon substrate, as in the backscattering experiments. To perform such analysis, the Monte Carlo technique has been utilized. A computer simulation programme based on the single scattering approach has been developed in our laboratory; the model allows, in the most general case, to analyze in a single run a multielement film on a multielement substrate. X-ray absorption and fluorescence corrections have been included. The analytical data on the BRL's discussed above will be compared with the calculations based on the Monte Carlo technique by using different X-ray ionization cross sections.

References

1. G. M. Oleszek and W. M. Whittemore, "Semiconductor Silicon," Electrochemical Society Symposium, 1969, p. 490.
2. M. S. R. Heynes, Electrochem. Technol. 5, 1967, p. 25.
3. E. Arai, H. Nakamura and Y. Terunuma, J. Electrochem. Soc., 120, 1973, p. 980.
4. R. A. Pasternak, Acta Cryst., 12, 1959, p. 612.
5. A. Armigliato, D. Nobili, P. Ostoja, M. Servidori and S. Solmi, Proc. 3rd Int. Symposium on Silicon Materials and Technology, The Electrochemical Society Inc. (Princeton, N.J.), 1977.
6. A. Armigliato, G. G. Bentini, G. Ruffini, G. G. Bentini, G. Ruffini, G. Della Mea and A. Drigo, to be presented at the 3rd Int. Symposium on Ion Beams in Solids, (Washington, June 27-July 1, 1977).
7. P. Negrini, A. Ravaglia and S. Solmi, C.N.R. Internal Report (Nov. 1976).
8. A. Armigliato, P. Bergamini and L. Morettini, Proc. 9th Annual Conference MAS (Ottawa 1974), paper No. 15.
9. R. Tixier and J. Philibert, Proc. 5th Int. Conf. on X-ray Optics and Microanalysis (Tübingen 1968), p. 180.
10. K. F. J. Heinrich, in The Electron Microprobe, T. D. McKinley, K. F. J. Heinrich, D. B. Wittry, Eds., John Wiley & Sons, New York 1966, p. 296.
11. B. L. Henke, R. L. Elgin, R. E. Lent and R. B. Ledingham, Norelco Reporter, 14, 1967, p. 112.
12. Wm. J. Veigele, Atomic Data, 5, 1973, p. 51.
13. D. D. McCoy, W. F. Morris and R. G. Gutmacher, Proc. 10th Annual Conference MAS (Las Vegas 1975), paper No. 29.

Table I - K-ratios ($\times 10^4$).

	300 Å		400 Å		700 Å	
	ARL	TEM	ARL	TEM	ARL	TEM
K_B	75	--	85	43	186	60
K_O	9.5	--	9.5	2.8	15.8	1.7
K_{Si}	20	--	25	6.8	50	14

Table II - Values of $f(\chi)$ for boron

Author	$f(\chi)_{std}$		$f(\chi)_{film}$ (400 Å)	
	15°	52.5°	15°	52.5°
Heinrich	0.180	0.460	0.446	0.737
Henke	0.091	0.305	0.633	0.849
Veigele	0.073	0.265	0.627	0.846

Table III. - Analysis of the boron-rich layers

Film	C(at%)	X-ray microanalysis				nuclear back-scattering
		ARL		TEM		
		Henke	Veigele	Henke	Veigele	
300 Å	B	76.5	70.6	--	--	71.5
	O	10.1	11.4	--	--	11.3
	Si	14.1	17.4	--	--	17.2
400 Å	B	76.3	71.8	77.1	73.5	74.8
	O	8.7	9.9	7.1	8.0	7.1
	Si	15.0	18.3	15.8	18.4	18.1
700 Å	B	80.7	76.1	78.4	73.0	77.0
	O	6.5	7.8	2.8	3.8	4.3
	Si	12.9	16.1	18.9	23.2	18.7

THE DETERMINATION OF THE OPTIMUM CONDITIONS FOR QUANTITATIVE XRAY MICROANALYSIS OF CARBON IN AUSTENITIC STAINLESS STEELS

by

F. COPPOLA[*], F. MAURICE[**], J. RUSTE[***]

[*]   Nuclear Energy National Committee CASCCIA-ROMA (ITALY)

[**]   French Atomic Energy Commission - Nuclear Research Center
        SACLAY (FRANCE)

[***]   Materials Research Center of the "Ecole des Mines" of Paris
        EVRY (FRANCE)

The quantitative Xray microanalysis of carbon in austenitic stainless steels is a difficult problem. The main reasons are that :

- The measured Xray intensity of the carbon K line is weak. Indeed the Xray emission is not very important because of low fluorescence yields ($w_k^c < 10^{-2}$), heavy absorption coefficients and very poor efficiency of multilayer analyzers (lead stearate dodecanoate);

- There is a lack of data on the correction factors, and specially for the absorption coefficient values;

- There are some artefacts due to the experimental method (overlapping of lines, chemical bonding shifts, surface contamination, etc...). For example, the lead stearate analyzing crystal has not sufficient resolution to resolve the overlapping of the carbon K line with some different L spectra multiple order of the austenitic stainless steel components (Table I).

Xray	emission wavelenght	diffraction order	$n\lambda(\overset{\circ}{A})$
CK	44.54	1	44.54
Cr Lα	21.64	2	43.28
Fe Lα	17.59	2 3	35.18 52.77
Ni Lα	14.56	3	43.68

Table I - Some examples of overlapping of lines for carbon analysis in austenitic steel.

The relative difference observed between Carbon K and Cr2Lα or Ni3Lα is less than the analyzing crystal resolution for carbon K line. For that, an electronic discrimination must be done very carefully.

The best adjustements of the counting electronics (choice of the voltage applied to the counter, the amplying gain and the levels of the pulse height analyzer) have been carried on different types of microanalyzers.

The quantitative analysis has been done with a ZAF method, adapted to the case of very light elements (1). The numerical values of absorption coefficients for the carbon K line in the main austenitic steel components (Cr, Fe, Ni, Mo) have been obtained by a fit of absorption correction from experimental analysis of standards of known concentrations (Table II).

Absorber	μ/ρ for CK (g/cm2)
Cr	10150
Fe	12500
Ni	15200
Mo	15500

Table II - Mass absorption coefficients of C K.

From these data, theoretical correction curves have been established, varying the experimental conditions (accelerating voltage, emergence angle) and for several steels (Table III).

Correcting factors		
Operating voltage	Take off angle		
	18°	35°	40°
5 kV	1.395	1.110	1.069
10 kV	2.777	2.270	2.176
15 kV	3.483	3.133	3.051

Table III - Correcting factors for microprobe
analysis of carbon $(0 \rightarrow 6^{w}/o)$ in an
austenitic stainless steel
$(Cr\ 12^{w}/o - Ni\ 10^{w}/o - Mo\ 2^{w}/o)$

The results we have obtained are compared with the experimental known data, with a satisfactory agreement (2) (3) (4).

REFERENCES

(1)   J. RUSTE

Some examples of quantitative analysis of very light elements
(this conference).

(2)   J.P. BREYER, V. LEROY, L. HABRAKEN

Analyse par microsonde électronique du carbone dans les aciers
J. de Microscopie, 20, 2,96 (1974).

(3)   G.L. FISHER, G.D. FARNINGHAM

Quantitative Carbon Analysis of Nickel Steels with the electron
Probe Microanalyzer, ASM Materials Engineering Congress,
Cleveland, Ohio, (1972).

(4)   M. CHAMPIGNY, L. MENY, J. RUSTE

Study of the carburization of an austenitic stainless steels
(the local concentration of C being less than $2^{w}/o$) through
optical and scanning electron microscopy, microhardness, and
quantitative Xray microanalysis of carbon (this conference).

STUDY OF THE CARBURIZATION OF AN AUSTENITIC STAINLESS STEEL

(THE LOCAL CONCENTRATION OF C BEING LESS THAN 2 ^{W}/o)

THROUGH OPTICAL AND SCANNING ELECTRON MICROSCOPY,

MICROHARDNESS, AND QUANTITATIVE XRAY MICROANALYSIS OF CARBON

by Michel CHAMPIGNY[*]

Lucienne MENY[*]

Jacky RUSTE[**]

[*] Technology Department - Applied Metallurgical Research Service
Atomic Energy Commission - Nuclear Research Center of SACLAY - FRANCE -

[**] Materials Research Center of the "Ecole des Mines" of Paris - EVRY - FRANCE

In the sodium cooled fast neutron reactors, carbon can be transferred through sodium from parts of the structure to other parts. The purpose of this paper is to examine the carburization of an austenitic stainless steel (type 316 L), at temperatures from 450 °C up to 650 °C, and the influence of heat treatments at higher temperatures on the distribution of the carbon (solid solution in γ or $M_{23}C_6$ carbides).

The metallographic observations have been done through optical and scanning electron microscopy.

The carburization depth has been confirmed with microhardness measurements.

The quantitative XRay Microanalysis of carbon has been done versus the depth of carburization. The carbon content of the alloys used as standards has been determined by chemical analysis. The best experimental conditions of the XRay Microanalysis have been determined in [1] ; the numerical values of the absorption coefficients for the carbon K line in the considered elements (Cr, Fe, Ni) and alloys have been calculated after [2]. Theoretical correction curves have then been established.

It has then been shown that, for concentrations of $C \leq 2$ ^{w}/o, it does not exist a simple relationship between microhardness measurements and carbon concentration. The mechanical properties of the carburized stainless steel component depend not only on the total carbon concentration (usually given by chemical analysis), but also on :

- the carburization depth of the component
- the local carbon concentration
- the form under which the carbon is present : solid solution in the austenite, and/or $M_{23}C_6$ carbides, their size and their location (within the grains or in the grain boundaries).

The results obtained are compared with the published data [3, 4].

BIBLIOGRAPHY
----

[1]   F. COPPOLA, F. MAURICE and J. RUSTE

Determination of the optimum conditions for quantitative XRay Microana-
lysis in austenitic stainless steels (this conference).

[2]   J. RUSTE

Some examples of quantitative analysis of very light elements
(this conference).

[3]   A. THORLEY and C. TYZACK (UKAEA Risley)

The carburization of stainless steels in sodium containing carbon
impurities and its effect on mechanical properties.

Paper n° 11 - Session 4 : Effects of environment on material properties
in nuclear systems - International Conference on Corrosion organized
by the Bristish Nuclear Energy Society - July 1971

[4]   J.L. KRANKOTA (G.E.C.)

The effect of carburization in sodium on the mechanical properties of
Austenitic Stainless Steels

Transactions of the ASME. Journal of Engineering Materials and Techno-
logy - January 1976 - p. 9-16

Academy of Mining and Metallurgy, Cracow

The Study of Chemical Effect on the Fe K$\alpha_{1,2}$ Emission Lines with an Electron Microprobe for Some Iron Compounds Applied in Metallurgy

by

St. Jasieńska, D. Tomkowicz, J. Janowski

The object of the present study was to demonstrate the possibility of the supplement of the quantitative microanalysis by the study of the chemical effect on X-ray emission lines to obtain a full diagnostic characteristics for mineral components of the ore sinter and pellets. It has been of particular interest to use the chemical shift of Fe K$\alpha_{1,2}$ emission lines for determination of the valence of iron ions from the microvolume under study.

The measurements of the chemical shifts of Fe K$\alpha_{1,2}$ of the investigated compounds were made with an electron microprobe CAMECA type MS-46. To secure high accurancy in determining the relative positions of the lines, all ferrooxides at a time could be studied under the same vacuum and irradiation conditions. Line profiles were scaned at a rate of 0.0003 Å/s. Peak count rates measured at the point of maximum intensity amounts to about 30 000 pulses.

In order to minimize statistical errors in determining the exact position and shape of Fe K$\alpha_{1,2}$ line, the minimum of four measurements was carried out for each sample. The relative shifts of K$\alpha_{1,2}$ peak position for the samples discussed, calculated with respect to the metallic Fe K$\alpha_{1,2}$ are defined as

$$\Delta E(K\alpha_{1,2}) = E(K\alpha_{1,2})_{\text{metallic}} - E(K\alpha_{1,2})_{\text{sample}}$$

The spectrum line position was refined using the computer CDC Cyber by approximation the experimental curve by means of

a least squares fit of the spectrum parameters p^S to the line shape Gauss function $I_{Gs}^{L}(x_i, p_k^{L})$ or superposition of L-Gauss functions

$$I_{th}(x_i, p_j^{s}) = \sum_{L} I_{Gs}^{L}(x_i, p_k^{L}) + T(x_i)$$

where $T(x_i)$ - background
minimalizing an expression

$$\chi^2 = \sum_{i} \frac{[I_{exp}(x_i) - I_{th}(x_i, p_j^{s})]^2}{I_{exp}(x_i)}$$

The refinement spectrum parameters were as follows: the maximum intensity, the position of the line maximum and the half width at half line maximum /FWHM/.

The chemical shift of $K_{\alpha 1,2}$ lines obtained respecting to the metallic iron for the ferrooxide FeO of a nown stoichiometry was - 0.611 eV and for systetic Fe_2O_3 possessing a big grain /100x250μm/ was -0.309 eV. An above mentioned data were taken root as a diagnostic values for the valence determination of an investigated ore sinter and pellets phases.

References
V.V. Nemoshkalenko, Röntgenovskaya emissionnaya spektroskopiya metallov i splavov. Naukova Dumka, Kiev 1972.
W. Nefedow, Bull.Acad.Sci. URSS,Phys. Ser. 28 , 724 /1964/

ACCURATE QUANTITATIVE ANALYSIS OF
OXY-NITRIDES USING SIALON AS A STANDARD

A.J. Mardinly and W.C. Bigelow

University of Michigan
Ann Arbor, Michigan

As is the case for the analysis for oxygen, quantitative analysis
for nitrogen involves so many difficulties that it is generally determined
by difference, particularly in minerals and ceramic materials. Because of
the need for an independent determination of nitrogen as part of an inves-
tigation of a new class of silicon-aluminum-oxygen-nitrogen ceramics, the
"sialons" (1), and in studies of niobium-nitrogen-oxygen compounds, pro-
cedures have been developed which appear to yield reliable results on a
relatively routine basis, and which should be applicable to other similar
materials. Some of these procedures are dependent on the characteristics
of our ARL EMX-SM microprobe, but nonetheless indicate the factors which
should be considered and controlled for other instruments.

The basis for the problems inherent in nitrogen analysis is the low
intensity and peak-to-background ratio which results from the low ioniza-
tion, the low photon yield, and high matrix absorption of the nitrogen line.
The low intensity can be compensated for by using high electron beam
currents. For our work beam currents of 0.15 to 0.20 μA were generally
used. When sample current imaging was needed, the current was reduced to
improve resolution. The best peak-to-background ratio for nitrogen was

obtained with 7 kV electron accelerating potential; however, 10 kV was usually used in practice because it gave better imaging and better analytical results for Si and Al. In using the beam monitor current to correct for drift in the first lens current, it was found that the relationship between the monitor aperture current and sample current became nonlinear at high sample current values due to an unusual distribution of the beam current among the apertures of the monitoring system when it is focused to give high sample currents. This effect is illustrated in Fig. 1. Increasing the size of the aperture in the first lens and increasing the gun emission current with the gun bias will extend the range of linearity.

Since the sialons are insulators, a conductive coating was required. Although carbon is frequently used for this purpose in light element analyses, it has an absorption edge for nitrogen. Aluminum is much better for nitrogen analysis because of its higher electrical conductivity and lower mass absorption coefficient for the nitrogen line. A 100 Å thick layer of Al gives the same conductivity as a 500 Å thick layer of carbon, without the attenuation of intensity. Beryllium would be better than Al but was not used because of potential toxicity problems. The deposition of carbon on the specimen during analysis due to decomposition of organic vapors by the electron beam was prevented by use of the ARL microprobe's anticontamination system (2).

The analysis was performed with a lead stearate pseudocrystal, using a standard flow proportional detector with P-10 gas at atmospheric pressure. Counting rates in the range from 500 to 1000 cps were generally obtained, giving good statistics with reasonable counting times. It was found necessary to make careful adjustments in the spectrometer alignment controls to obtain the maximum counting rates and the narrowest, most symmetrical peak shape. Unidentified, higher order peaks of shorter wavelengths were found very close to the nitrogen peaks. It was usually necessary to use pulse height measurements to distinguish these from the nitrogen peak, and pulse height discrimination to eliminate their interference and contribution to the background.

Since the nitrogen peak occurs near the low wavelength limit of the ARL spectrometer's range where background is relatively high and curves steeply with wavelength, a simple procedure was developed for determining backgrounds, which compensates for this steep curvature. After carefully determining the position of the nitrogen peak maximum, background values were measured at positions just off the peak tails on both the high and low wavelength sides of the peak. Linear interpolation between these values was used to obtain a first approximation to the background at the peak position. This value was corrected for nonlinearity of the background using measurements made at the same spectrometer settings on a material having a density close to that of the specimen in question, but which was known to contain no nitrogen. Al_2O_3 was used for this purpose with the sialon, and niobium metal with the niobium nitride-oxides. Here the ratio of the measured background at the peak position to the value obtained by linear
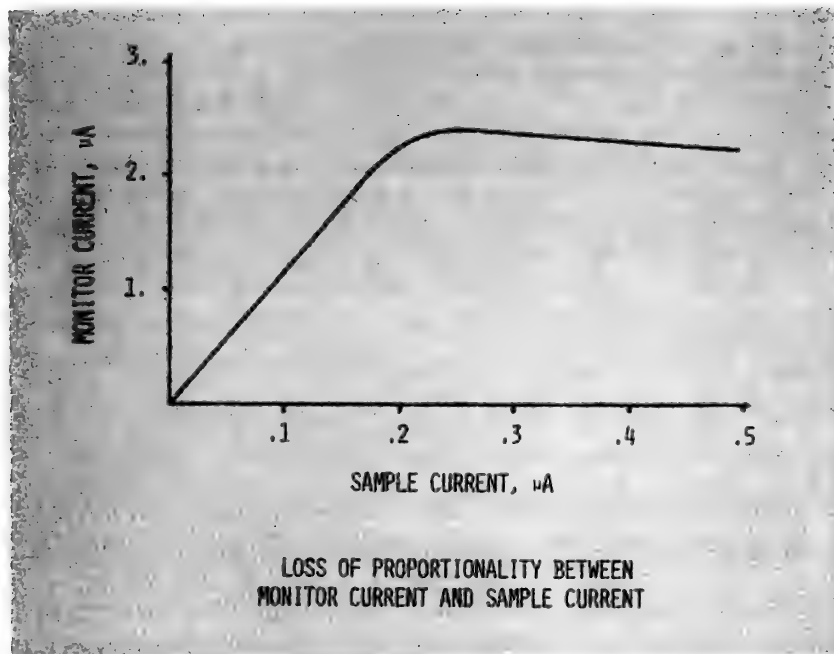
Figure 1
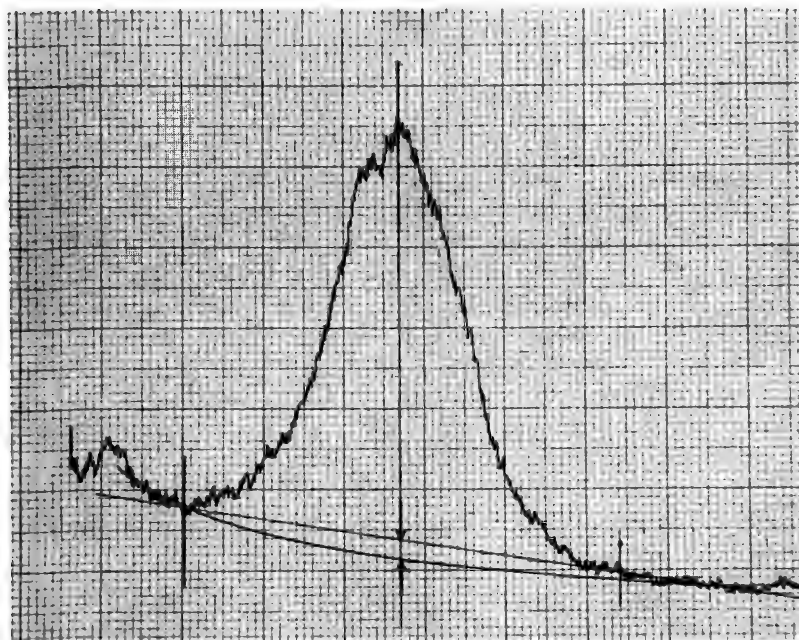
Figure 2

interpolation was determined, and this ratio was used to correct the value of the approximate background obtained by linear interpolation on the nitrogen compounds described above as illustrated in Fig. 2.

The standards used for these nitrogen analyses are three sialons which were carefully prepared and analyzed (3). The reported composition of these are given in Table I. These materials are particularly advantageous for this purpose since they are fully dense, have good homogeneity, and are stable to temperatures above 1700°C. As a check on the internal consistency and reliability of the method, the composition of these materials was determined using pure Al_2O_3 and SiO_2 as standards for aluminum, silicon and oxygen, and each material in turn as the standard for nitrogen. The EMPADR VII program of Rucklidge and Gasparrini (4) was used for data processing because it has been found to give very satisfactory results in analysis of minerals and other ceramic materials. The latest values of the mass absorption coefficients published by Henke and Ebisu (5), and the mean excitation coefficients published by Reed (6), were used to adapt this program for use with these light elements. The results of these analyses are given in Table I. The internal consistency and agreement with chemical analysis is highly acceptable.

TABLE I

Reported Composition (wt pct)		Measured Std. No. 1	Composition (wt pct) Std. No. 2	Std. No. 3
Std. Si	52.5	52.8	53.4	51.2
No. 1 Al	7.3	7.0	7.1	6.8
O	4.2	4.4	4.4	4.3
N	36.0	(35.8)*	35.1	37.7
Std. Si	38.0	39.0	39.5	38.0
No. 2 Al	20.8	20.8	21.0	20.3
O	12.4	10.0	10.0	9.8
N	28.9	30.2	(29.4)*	32.0
Std. Si	19.8	20.9	21.0	20.4
No. 3 Al	38.0	40.2	40.5	39.2
O	22.5	17.8	17.8	17.7
N	19.7	21.2	20.6	(22.7)*

* Self determination

The method is now being used in the analysis of other sialons and also in the analysis of niobium oxynitrides which are formed during solidification of iron-niobium alloys saturated with nitrogen. The results from one series of analyses on 10μ particles formed in one iron-niobium alloy are shown in Table II. X-ray powder diffraction patterns of these particles had suggested that they might be either Nb_4N_3 or NbO_2; however, a clear distinction could not be made because of the similarities in the patterns for these two compounds. Here each of the sialons of Table I was used as a standard for oxygen and nitrogen, and pure Nb metal was used as the niobium standard. From these data the stoichiometry of the particles was estimated to be very close to $Nb_5(N_{0.9}O_{0.1})_4$ or $Nb_{25}N_{18}O_2$. This is close to being a solid solution of $6(Nb_4N_3)\cdot(NbO_2)$, which is consistent with certain thermodynamic predictions, based on the experimental conditions involved.

TABLE II

		Weight %	Atomic %
Std.	Nb	89.6	57.7
No. 1	N	9.3	39.0
	O	1.2	4.3
Std.	Nb	89.7	57.3
No. 2	N	8.9	37.5
	O	1.4	5.2
Std.	Nb	88.9	55.1
No. 3	N	9.9	40.6
	O	1.2	4.4

It is believed that these results demonstrate the feasibility of obtaining acceptable results in the analysis of nitrogen in minerals and ceramic materials using an electron microprobe with standard features and methods which are relatively straightforward and uncomplicated. We are particularly indebted to Dr. L.J. Gauckler for supplying the analyzed sialon standards used here.

References

1. K.H. Jack, "Sialons and Related Nitrogen Ceramics," Journal of Materials Science 11, 1976, pp 1135-1158.
2. Hermann Neuhaus, "Reduction of Contamination Effects in Electron Microprobe Analysis," EMPA Proceedings, 1968, p. 19.
3. L.J. Gauckler, Private Communication.
4. J. Rucklidge and E.L. Gasparrini, "Electron Microprobe Analytical Data Reduction," Dept. of Geology, University of Toronto, 1969.
5. B.L. Henke and E.S. Ebisu, "Low Energy X-ray and Electron Absorption Within Solids" in "Advances in X-ray Analysis," Vol. 17, p. 150, 1974, Plenum Press.
6. S.J.B. Reed, Electron Microprobe Analysis, Cambridge University Press 1975, p. 206.

THE ROLE OF ELECTRON MICROPROBE ANALYSES IN WORKMEN'S COMPENSATION AND PERSONAL INJURY LITIGATION

John T. Armstrong,[*] E. F. Holdsworth,[*+] and P. R. Buseck[*]
*Departments of Chemistry and Geology, Arizona State University,
Tempe, Arizona 85281; +SEM/TEC Laboratories, Tempe, Arizona 85281

The use of electron microprobe analysis of occupational health samples has been accepted by the Arizona State Industrial Commission in a number of workmen's compensation cases. We have used microprobe analysis of individual particles to conclusively establish the presence of potentially toxic species in the workplace. Examination of such samples by electron beam instruments provides important information regarding the distribution of toxic species in aerosol samples--e.g., whether the species are contained in a minor amount in a large portion of the particles or in a major amount in a fraction of the particles; whether they are contained predominately in the respirable size fraction; and whether they are concentrated on particle surfaces. Such information can be used to extend and improve occupational health and safety standards.

Applications encountered in our laboratory involving workmen's compensation and personal injury litigation include: (a) determination of silicosis hazards in various mining and sand and gravel operations, (b) determination of potentially toxic agents in welding fumes and secondary iron foundry emissions, (c) identification of the source of various flying objects which caused injury, and (d) determination of reason for failure of various mechanical components. In certain cases, modal analyses were employed to determine the relative amounts of a potentially toxic species in particle or bulk specimens.

Two workmen's compensation cases with which we have been involved show some of the advantages that the electron microprobe has as a tool in occupational sample analysis. The first case involved determination of free silica--mainly quartz-- in rock and particle samples from a serpentine asbestos mine. The host rock of the ore in this mine is limestone containing abundant serpentine asbestos. Electron microprobe analyses showed that free silica, presumably quartz, occurs in minor to trace amounts in the various samples analyzed. Typical concentrations of quartz in these samples was estimated at between 1 and 100 ppm by volume. In a few samples the observed quartz concentration was as high as 1 to 3%.

Quartz was not found to occur in any large assemblages. Grains as large as 20 to 30 μm in diameter were rarely found. The most common occurrence was in elongated grains 2 μm or less in diameter, at the contacts between grains of calcite and serpentine. A less common but still appreciable occurrence was in 2 μm or less elongated grains in the middle portions of large grains of calcite or serpentine.

The determination of the amount of quartz in these samples would have been difficult by any other technique. The small grain sizes present problems for thin section examination using optical microscopy and the concentrations are too low for reliable X-ray diffraction measurement. Dissolving the calcite in acid to concentrate the silicate minerals would result in decomposing the serpentine and producing free silica. With the electron microprobe, however, the quartz could be readily detected. Energy dispersive spectra and X-ray maps were accepted as conclusive evidence of the presence of quartz by an Arizona State Industrial Commission hearing officer. The microprobe evidence provided an essential legal link in this case and judgment was awarded to the plaintiff.

In the second case, a workman was injured by a small piece of metal entering his eye. The point of contention was whether the metal shard came from the head of a hammer which the worker was using or if it had come from some object unassociated with the workplace.

The metal shard ($\sim$ 2 mm diameter) could not be dissolved, ground up, or otherwise altered due to its possible future legal evidence value. Therefore non-destructive analysis was the only allowable approach to characterize this sample.

Electron microprobe analyses of the hammer face and the metal shard showed them to be of identical composition within the limits of experimental error. Further, SEM examination showed matched fracture surfaces on the shard and on a small indentation in the hammer face. The combination of electron microprobe analysis and SEM imagery was considered conclusive evidence of the shard coming from the hammer face in the opinion of legal representatives of the involved parties.

Electron microprobe analysis has a series of distinct advantages in litigation applications: the analysis can be performed in situ and non-destructively; use of a wavelength dispersive spectrometer eliminates the possibility of interference or misidentification of elements; the secondary electron images, X-ray maps, and energy dispersive spectra make impressive and easily explainable presentative material; the nature of samples encountered in such applications are often extremely small and ideal for analysis with this technique.

Effects of Elastic Lattice Bending on X-Ray Transmission Patterns of Silicon Crystals

Z. H. KALMAN,* H. SUGA and S. WEISSMANN
College of Engineering, RUTGERS UNIVERSITY, Piscataway, New Jersey 08854

X-Ray divergent beam photographs in transmission were obtained from dislocation-free, smooth and notched silicon crystals subjected to elastic bending. Anomalous transmission (AT) patterns were obtained from unstrained crystals such as that shown in Fig. 1. On bending, the in-
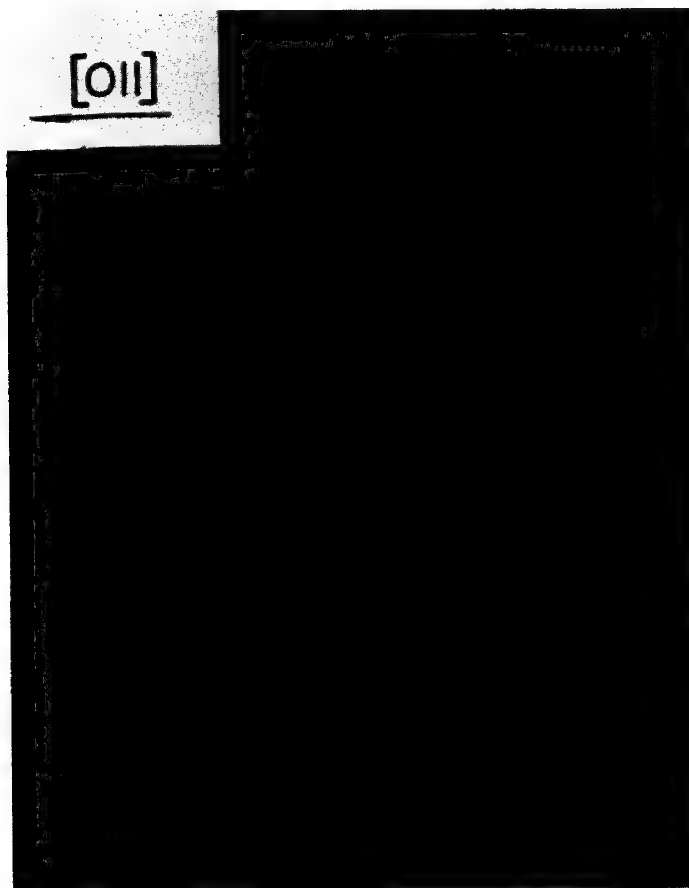
Fig. 1. Anomalous transmission, divergent beam pattern of unstrained silicon crystal. Cu radiation, crystal thickness ~1 mm ($\mu.t$ ~14). Positive print.

tensity of the line pattern decreased, and those reflections pertaining to (hkl) planes subjected to the bending moment shortened drastically, as shown previously (1). Concurrently with the gradual disappearance of the AT pattern on increased bending, down to a radius of curvature of a few meters, there appeared a new pattern of reflections. This pattern exhibited the general characteristics of a kinematic pseudo Kossel pattern with reflection and deficiency lines such as that shown in Fig. 2. With increased bending, the intensity of the latter pattern increased, and this increase was approximately proportional to the intensity decrease of the AT pattern. On release of the bending moment, the
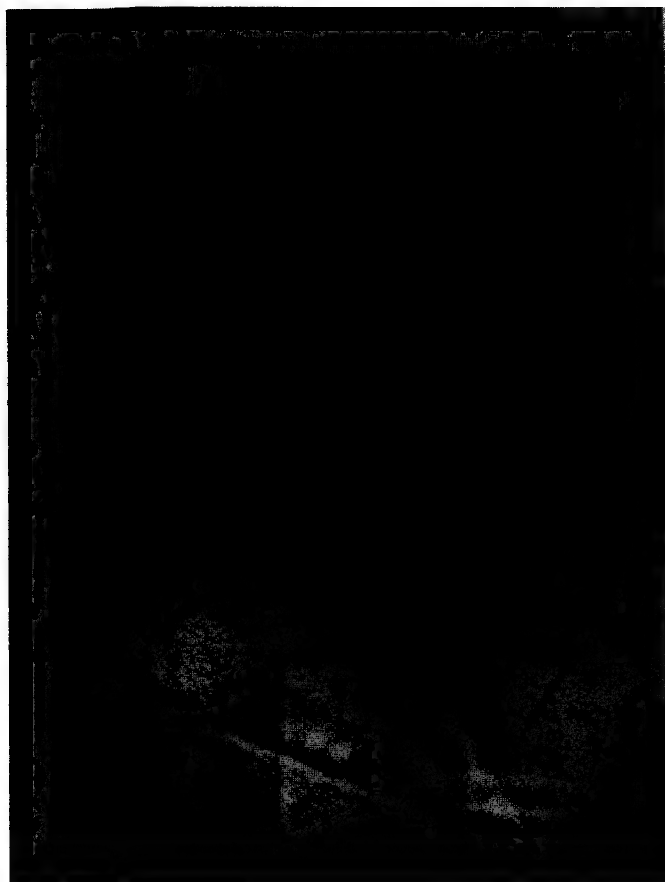
Fig. 2. Transmission pattern of Si crystal bent to a radius of curvature ~3 m. Bending axis parallel to [110]. Coexistence of predominantly kinematic pattern with remnants of AT indicated by arrows. Positive print.

kinematic pattern disappeared completely and the original AT pattern was fully restored, thus confirming the elastic nature of the bending process.

Since the appearance of the kinematic pattern gives evidence of an increased strain gradient, the divergent beam method was used to explore the strain distribution in front of the notch when the silicon crystals were elastically bent. These studies were coordinated with X-ray topographic investigations of bent silicon crystals, in particular with the distortions of the pendellösung fringe pattern near the notch.

Reference

1. S. Weissmann and Z. H. Kalman, Phil. Mag., 15, 539-547 (1967).

ELECTRON BEAM MICROFABRICATION SYSTEMS

Alec N. Broers

IBM T. J. Watson Research Center
Yorktown Heights, New York 10598

Integrated circuit components are built into single crystal semiconductor wafers by a series of processes which use patterned resist layers. Images are normally formed in the resist layers by exposure to ultraviolet (UV) light through a contact mask. The minimum features that can be formed with this method are about 2.5μ in size. Devices with smaller dimensions however, are faster, and potentially cheaper because more of them can be built into a single wafer. Considerable effort has therefore been expended on improving the resolution and reliability of the image forming process. Electron beam, x-ray and UV methods are all being explored and each method offers unique advantages. This paper briefly describes the two basic electron beam methods; scanning and image projection. A fuller description of novel lithography processes, and a more complete set of references has been given by the author elsewhere. (Proc. Electron & Ion Beam Conf., Wash., D. C. (1976)).

Scanning Electron Beam Systems

In these systems the pattern is written with a small electron beam which is generally controlled (deflected and turned on and off) by a computer. It is the only method used so far to successfully make fully operating silicon devices with a capability that exceeds conventional contact printing in terms of linewidth and overlay tolerance. Masks made by scanning electron beam are also needed for replication methods such as x-ray lithography.

Figs. 1-4 show the basic operating modes of four scanning E/B systems recently described. In all cases the electron beam cannot be scanned over the whole sample so electronic scanning has to be combined with mechanical movement to cover the sample and a method has to be provided to accurately maintain the position of the beam with respect to the wafer. In figs. 1 and 2 a direct beam to sample reference measurement is made before each complete section (chip) of the pattern is exposed. The measurement is made by using scanning electron microscope methods to locate four marks at the corner of each field, and is used to check for beam position, scan rotation and orthogonality, and to calibrate scan amplitude. In figs. 3 and 4 laser interferometry is relied upon to maintain positional reference after an initial, or occasional, direct beam to sample measurement. Combinations of the two basic methods are possible and for mask making laser interferometry may be advantageous in all systems.

In cases where the chip is written by pure electronic scanning, two basic methods have been employed; raster (fig. 1) and vector (fig. 2). With raster scanning the beam scans the entire pattern area and is turned on where required. In vector writing the beam is directed only to points where exposure is required. Vector scanning is more efficient because no time is wasted scanning areas not requiring exposure, however, it places more stringent requirements upon the deflection system in terms of dynamic accuracy and in particular eddy current errors. Raster scanning makes it easier to apply corrections for deflection aberrations and pattern distortion. Vector scanning allows more efficient data compaction.

In fig. 3 the beam is electronically scanned only in one direction and continuous mechanical movement is used for the other direction. Chips are written strip by strip, the same strip on every chip being written before proceeding to the next strip. In fig. 4 the electron beam is scanned in
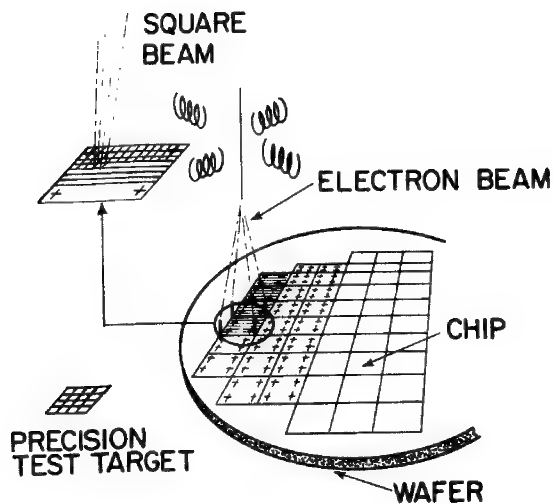
Fig. 1 Operating mode for EL1; a
high throughput electron beam system
designed for manufacturing. System
features include:
a) 2-dimensional full chip scan.
   (stepped raster-square beam)
b) Stepped table.
c) Distortion correction.
d) Every chip align.
See papers by H. Yourke and E. Weber;
J. Mauer, H. Pfeiffer and W. Stickel;
L. Loughran, M. Michail, P. Ryan, and
H. Engelke; D. Davis, R. Moore, M.
Williams and O. Woodard. Proc. Int.
Electron Devices Meeting, Wash., D.C.
(1976)

Fig.2 Operating mode for Vector-
scan type electron beam system.
System features include:
a) 2-dimensional full-chip scan.
b) Distortion free deflection.
c) Stepped table.
d) Alignment at every chip.
High performance systems of this
type have been described by T.H.P.
Chang, A. D. Wilson, A. J. Speth
and C. H. Ting. Proc. 7th Inter.
Electron Ion & Laser Beam Conf.
(1976), G. L. Varnell, D. F.
Spicer et al. Proc. 6th Inter.
Electron Ion & Laser Beam Conf.
(1974) and others.

Fig.3 Operating mode for EBES; an
electron beam system designed ini-
tially for mask making. System
features include:
a) 1-dimensional line scan-(raster).
b) Continuously moving table.
c) Full wafer align.
d) Laser interferometer feeds table
   position back to e-beam.
D. R. Herriot, R. J. Collier,
D. S. Alles and J. W. Stafford, IEEE
Electron Devices ED-22, p385(1975)
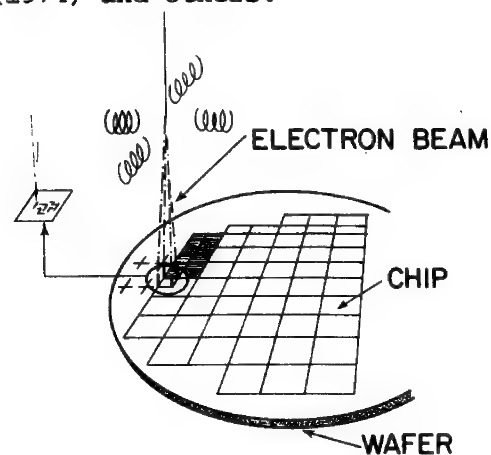
Fig.4 Operating mode for Masqueur
Electronique described by O. Cahen,
R. Sigille, J. Trotel, Proc. 5th Int.
Electron Ion & Laser Beam Conf.(1972)
System features include:
a) 2-dimensional partial chip scan
   (vector).
b) stepped table.
c) full wafer align.
d) Laser interferometers reference
   electron beam to table.

two dimensions over small areas which are then 'stitched' together to make chips. In both these systems the performance of the electron beam deflection system does not have to be as good as it is for figs. 1 & 2, but errors due to beam drift or wafer distortion are not corrected as frequently.

Throughput of scanning electron beam systems was originally limited by electron optical performance; that is by the beam current resist sensitivity criterion. However, this situation has largely been alleviated by the discovery of resists with improved sensitivity, and also by electron optical advances in the following three areas: 1) Improved electron gun design and new cathode materials, in particular LaB_6 , have increased brightness from about 10^5 A/cm -ster. (20KV) to 10^6 A/cm -ster. Field emission cathodes may yield a further increase. 2) Computer aided design of the final lens/deflection system unit has led to an increase in field size of about five times and a two-fold increase in beam aperture. 3) Shaped beam systems (fig.5) have been developed which increase the number of pattern elements exposed by the beam at each beam position. Such systems increase beam current for a given edge sharpness by more than an order of magnitude over typical round beam systems (fig.6). Overall throughput for today's scanning electron beam systems is complex and in addition to depending on the beam current/resist sensitivity criterion, also depends on the speed of the digital control system and the mechanical stage.

Electron Beam Projection Systems

These systems potential have lower cost per exposure than scanning systems for the following reasons. (A) Pattern information is stored in a mask and does not have to be fed serially to the beam for each exposure. This reduces equipment cost. (B) The field that can be covered in a single exposure is larger and the exposure time per unit area is shorter.

Fig. 7 shows the reduction type of projection system. Köhler illumination of a 10X mask is provided by an LaB_6 cathode electron gun and a magnetic condenser lens system. A symmetric magnetic doublet, in which six of the eleven third order aberrations are corrected, projects the mask image onto the sample. Field size is larger than for scanning systems mainly because the beam half angle can be much smaller. The small beam angle is tolerable because millions of points are exposed simultaneously and the current density in the image can be lower for a given exposure rate. The mask is a freely suspended metal foil and its fabrication for general pattern shapes is a problem delaying application of this method to device production. Several ways for overcoming the 'stencil' problem have been proposed. Replacement of the foil with a photocathode has also been demonstrated.

A 1:1 electron projection system is shown in fig.8 which employs a photocathode masked with a thin metal pattern. Photoelectrons are accelerated onto the wafer's surface and a uniform magnetic field focuses them with unity magnification. Sample and wafer can, in principle, be as large as desired and 5cm diameter samples have been successfully exposed. In the system shown in fig.6 image position is detected by collecting characteristic x-rays from marks on the sample. Magnetic deflection is then used to position the pattern with respect to the wafer. Because the sample forms part of the imaging system its flatness is very important in determining pattern distortion and for silicon wafers an electrostatic chuck may be essential for satisfactory performance. Back-scattered electrons also give rise to a background exposure which reduces contrast.

Proximity effects, which arise because electrons are scattered in the resist layer and back-scattered from the sample, are more difficult to compensate with full pattern projection systems than with scanning systems. This may be a significant restriction for dimensions below 0.5μ.
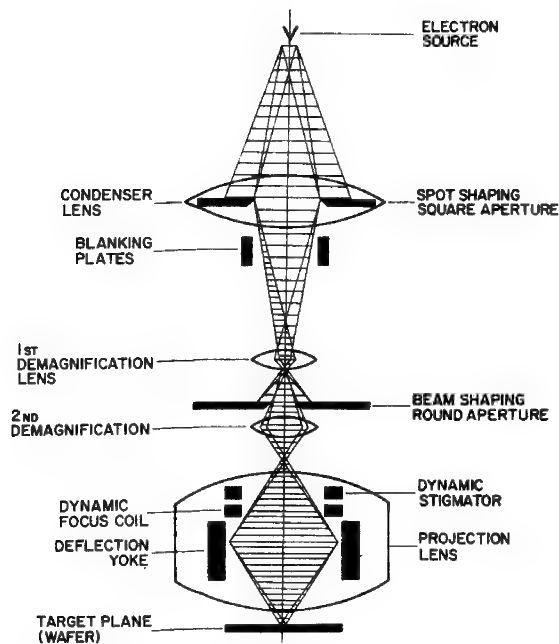
Fig. 5 Square Beam Imaging concept
used in EL1 (fig.1). H. C. Pfeiffer
J. Vac.Sci.Tech.12, p.1170(1975) &
H. C. Pfeiffer & K. H. Loeffler, 7th
Inter. Electron Microscopy Conf.,
Grenoble p. 63 (1970)
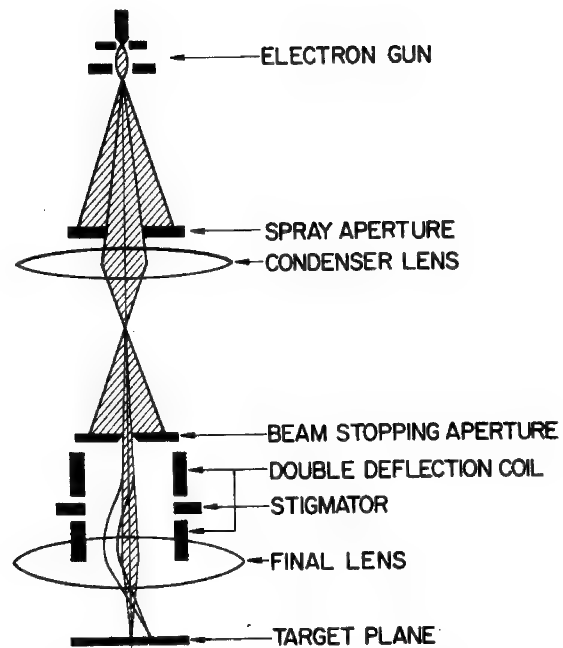
Fig.6 Two lens round beam optical
system similar to type used in
most scanning E/B fabrication
systems. It is similar to that of
conventional surface S.E.M.'s ex-
cept that the final lens and deflec-
tion yoke are optimized for larger
scan fields & lower distortion (see
for example E. Munro, Optik 39, p.
450 (1974)). A third lens is often
included to allow beam current to
be altered without changing focus.
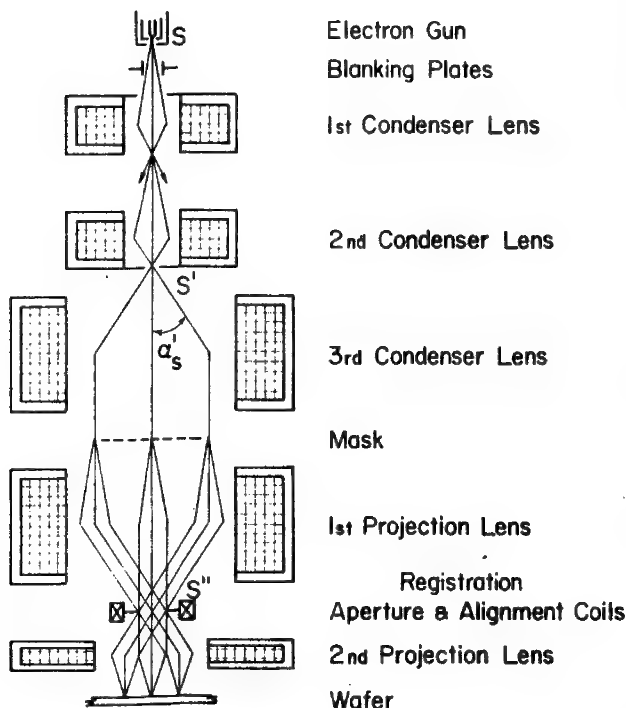
Fig.7 10:1 Electron beam projection
system described by M.B.Heritage.
J.Vac.Sci.Technol., 12, p.1135(1975)
System is operated as large field
S.E.M. for set-up and focusing.
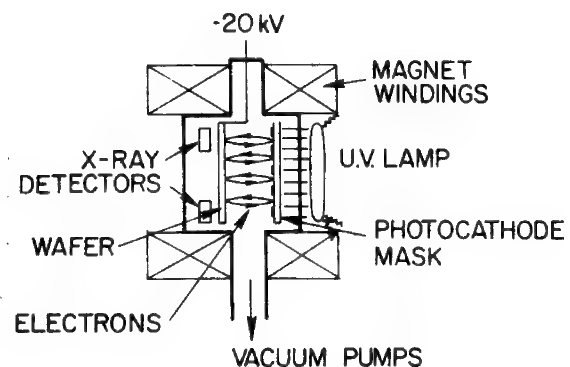
Fig. 8 1:1 photocathode electron
beam projection system of type
described by J. P. Scott, IEEE
Trans. on Electron Devices ED-22
p. 409 (1975). This type of
system was first described by
T.W.O'Keefe, J.Vine and R.M.
Handy, Solid State Electron,
12, p.841 (1969).

MICROFABRICATION FOR INTEGRATED ELECTRONICS

E.D. Wolf

Hughes Research Laboratories, Malibu, CA 90265

The two previous papers in this Presidential Symposium dealt with the two new lithographies, electron beam and x-ray. An attempt will be made in this paper to sum up the total capability for making small structures and the resultant impact on integrated microelectronics.

The evolution of lithography applicable to microelectronics is sketched approximately in Fig. 1 and shows that photon lithography has progressed well beyond the 5 μm linewidth limit obtained with conventional contact photolithography, the principal lithography of present microelectronics. These improvements have come about with the use of projection (1,2) and conformal mask photolithography (3), deep UV radiation (4) and x-rays (3,5) to reduce diffraction and scattering. Projection photolithography suffers from depth of focus limitations and standing wave problems (6) and will probably limit with a minimum linewidth of 0.5 to 1 μm. X-ray lithography may be useful for replication at submicrometer linewidths, but will probably require step-and-repeat exposure because of dimensional instabilities in the x-ray mask and high temperature processed wafers. Outstanding problems of multi-level registration, low defect density thin film masks, and expensive high flux sources (synchrotron) limit the present usefulness of x-ray lithography for submicrometer lithography.

Scanning electron beam lithography is the most promising and currently effective method for both photomask fabrication (at 1 to 5 μm linewidths) (7) and direct wafer writing (≤ 3 μm linewidths) (8) and offers the flexibility of software pattern change, precise linewidth control and improved resolution and alignment. Recently, A.N. Broers, et al. (9) fabricated 80 Å wide metal lines using electron beam contamination/polymerization to form an ion sputter mask that protected the resultant lines from sputter removal. Thus the evolution of high resolution lithography is approaching molecular dimensions and offers the future possibility of selective molecular alterations of inorganic molecules. The fundamental limit to linewidth is the range of the secondary ionization process produced by the incident radiation, i.e., $\ell_m \sim d_b + 2R_\delta$, where d_b is the diameter of the incident radiation and R_δ is the lateral range of the secondary ionization.

But for the near future can useful devices make use of these rapidly diminishing dimensions, or will the physics of some types of devices limit the degree to which high resolution lithography can be applied. Theoretical models and calculations (10,11) for metal-oxide-semiconductor (MOS) devices suggest that minimum gate lengths of 500 to 2500 Å are perhaps possible and still maintain the conventional device physics of these systems. Even if the limit is 5000 Å (0.5 μm) this represents an areal density increase of 100x over conventional 5 μm linewidths. So we can expect a second and even greater revolution in the 1980's than we are currently experiencing in silicon microelectronics caused by significant improvements in functional density, lower power and yields. Table 1 provides a more complete list of reasons why the new lithographies will become increasingly important.

The new lithographies are necessary but far from sufficient for improving integrated electronics. Equally challenging are the new demands placed on materials research and the pattern transfer technologies of etching and depositing materials using the resist patterns as in-contact stencil masks. A representative sampling of various processing steps are shown in Fig. 2 and illustrate just a small fraction of the wealth of processing options open to the device processing engineer who must optimize a particular set of the

procedures for each specific device he wishes to fabricate. The new demands placed on materials (e.g., the surface-area-to-volume ratio is increasing rapidly) as well as on linewidth control and alignment of multiple mask levels are dramatic as illustrated in Fig. 3, which compares a conventional 5 μm MOS gate metallization with a projected ultimate limit 0.25 μm MOS gate metallization. The choices of linewidth uncertainty and alignment accuracy are somewhat arbitrary but values were assumed to ensure high quality pattern exposure. In some cases the surface-area-to-volume ratio can be as high as 90:1 for polysilicon CCD electrodes when fabricating small cell memories.

There are further concerns in integrated electronics that are beyond the scope of this brief abstract, but sufficiently important to mention for completeness. The new submicrometer linewidth device/circuit designs now demand new approaches that test fundamental limits of device physics and require more attention to the interconnection problems of timing, power dissipation and real estate.

Representative devices/circuits are shown in Figs. 4-7 with explanatory figure captions. These and other state-of-the-art devices/circuits from various laboratories will be discussed to illustrate several device/circuit technologies that these new lithographies are impacting.

1. H.J. Schuetze and K.E. Hennings, Solid State Technol., 9, 31 (1966).
2. D.A. Markle, Solid State Technol., 17, 50 (1974).
3. H.I. Smith, Proc. IEEE 62, 1361 (1974).
4. B.J. Lin, J. Vac. Sci. Technol., 12, 1317 (Nov/Dec 1975).
5. E. Spiller, D.E. Eastman, R. Feder, W.D. Grobman, and W. Gudat, J. Appl. Phys., 47, 5450 (1976).
6. S. Middelhoek, IBM J. Res. Devel., 14, 117 (1970).
7. D.S. Alles, F.R. Ashley, A.M. Johnson, and R.L. Townsend, J. Vac. Sci. Technol., 12, 1252 (Nov/Dec 1975).
8. H.S. Yourke and E.V. Weber, Technical Digest, p. 431, International Electron Devices Meeting, Washington, D.C., Dec. 1976.
9. A.N. Broers, W.W. Molzen, J.J. Cuomo, and N.D. Wittels, Appl. Phys. Lett., 29, 596 (1976).
10. B. Hoeneisen and C.A. Mead, Solid State Electron., 15, 891 (1972).
11. R.M. Swanson, Technical Report No. 4963-1, Contract No. DAAB07-72-C-0229, National Institute of Health Grant No. 5 P01 GM17940-05, December 1974.
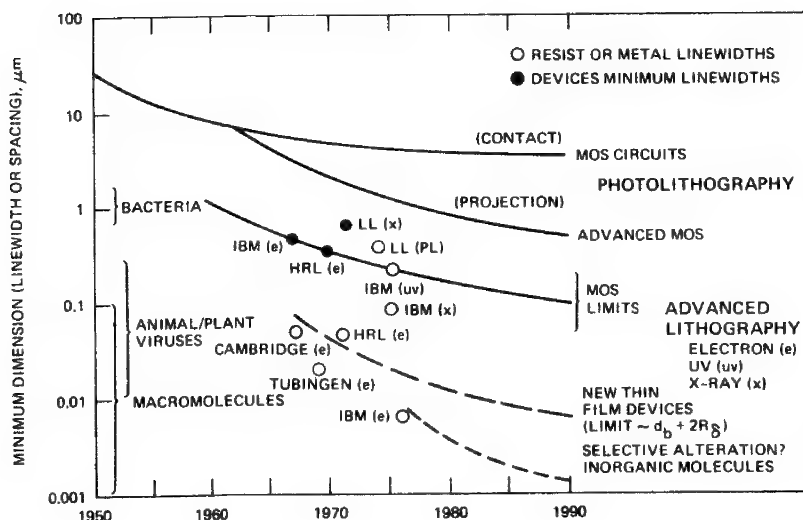
FIG. 1. Approximate evolution of lithography applicable to microelectronics. Solid lines and above represent actual or very probable technologies and below the lower solid line are speculations indicative of the need for much more research. A few representative data points are shown with abbreviated laboratory origin.

TABLE 1. Advantages of Submicrometer Lithography and in Particular Electron Beam Lithography

- LOWER POWER
- HIGHER FREQUENCY   } PERFORMANCE
- HIGHER PACKING DENSITY
  - DEVICE
  - INTERCONNECT
- FASTER TURNAROUND WITH EB PATTERN GENERATOR
- HIGHER YIELD   } ECONOMICS
  - AUTOALIGN
  - LINEWIDTH CONTROL
- HIGHER RELIABILITY

FIG. 2. Four representative process paths for microstructure fabrication. Similar steps can be used with negative resists to produce other microstructure elements.

CONVENTIONAL MOS (PL)   ULTIMATE MOS (EBL)

L = 5 μm   L = 0.25 μm

a		b
$130.0\ \mu m^2$	SURFACE AREA, A_s	$0.63\ \mu m^2$
$50.0\ \mu m^3$	VOLUME, V	$0.031\ \mu m^3$
$0.5\ \mu m$	ΔL TOLERANCE (10 %)	$0.025\ \mu m$
$0.5\ \mu m$	ALIGNMENT (± 0.1 L)	$0.025\ \mu m$
$\left(\dfrac{A_s}{V}\right)_b \Big/ \left(\dfrac{A_s}{V}\right)_a$	~8-FOLD INCREASE IN SURFACE AREA/VOLUME	
$\dfrac{\Delta L_b}{\Delta L_a}$	~20-FOLD INCREASE IN PROCESSING CONTROL	
$\dfrac{ALIGN_b}{ALIGN_a}$	~20-FOLD INCREASE IN ALIGNMENT ACCURACY	

FIG. 3. Comparison of conventional 5 μm gate length MOS processing with the new submicrometer processing near the predicted limit of MOS devices. Increased control of materials and interfacial properties as well as device geometry are required at submicrometer linewidth.

1.7 μm

FIG. 4. Aluminum electrodes on lithium niobate — part of a 4.1 GHz surface acoustic wave transducer.
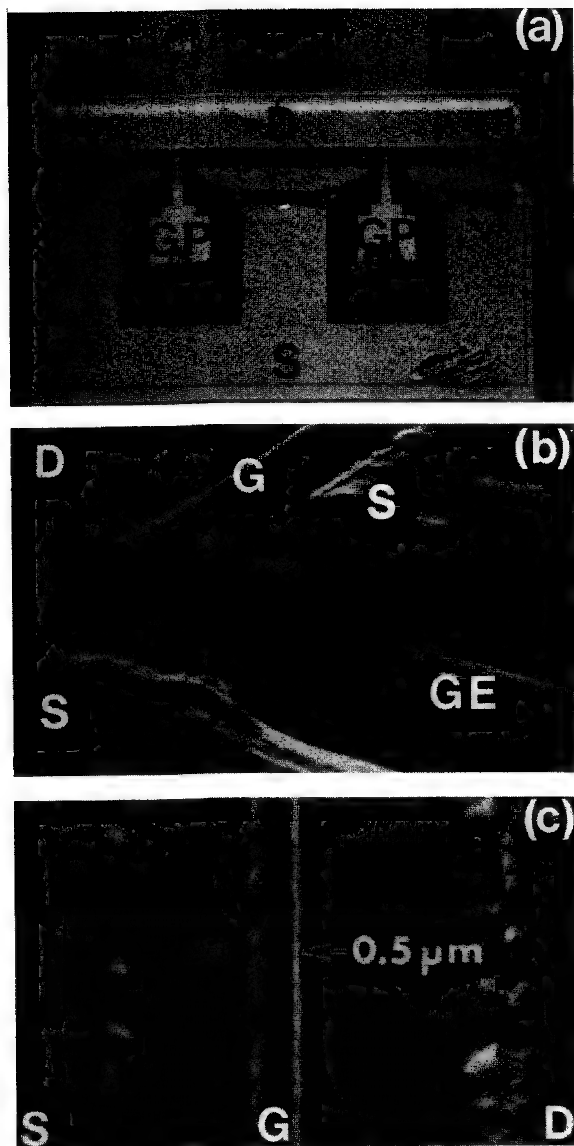
FIG. 5. (a) Optical photomicrograph of electron beam fabricated GaAs Schottky barrier field effect transistor (SBFET). (b) Scanning electron micrograph of channel area showing the source (S), the drain (D), gate (G) and gate extension (GE). (c) Scanning electron micrograph of the channel showing the 0.5 μm gate (G), source (S) and drain (D).
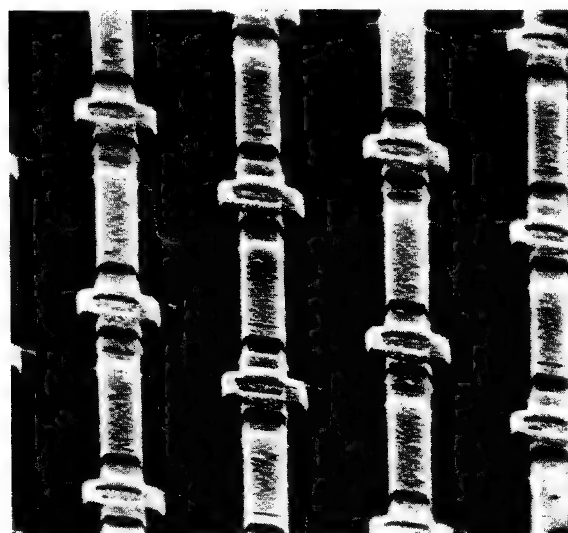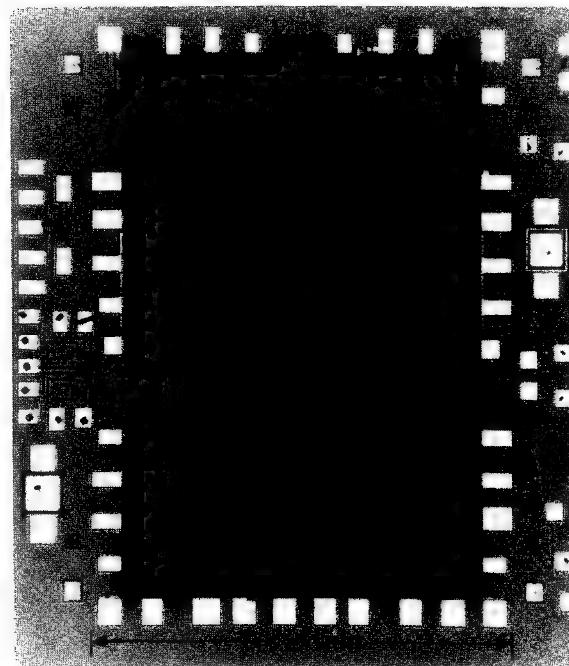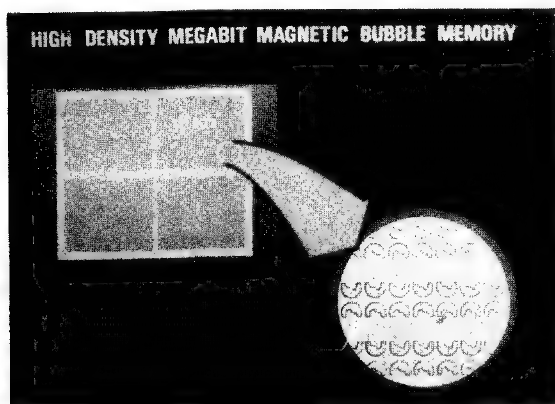
FIG. 6. Photomicrograph of 8192-bit memory chip fabricated using electron beam lithography and advanced silicon FET technology (top). Scanning electron micrograph of the memory array area showing aluminum metallization that is 1.85 μm in width (bottom). (Photo courtesy of P. Chang, IBM Watson Research Center.)

FIG. 7. Electron beam fabricated chrome photomask and replicated 1 megabit magnetic bubble memory. (Photo courtesy of G. Varnell, Texas Instruments.)

X-RAY REPLICATION OF SUBMICROMETER LINEWIDTH PATTERNS*

Henry I. Smith and D.C. Flanders

Lincoln Laboratory, Massachusetts Institute of Technology, Lexington, Massachusetts   02173

Scanning electron beam lithography has been used for a number of years to write submicrometer linewidth patterns in radiation sensitive films (resist films) on substrates. On semi-infinite substrates, electron backscattering severely limits the exposure latitude and control of cross-sectional profile for patterns having fundamental spatial frequencies below about 4000 Å[1]. Recently, STEM's have been used to write patterns with linewidths below 100 Å. To avoid the detrimental effects of electron backscattering however, the substrates had to be carbon foils about 100 Å thick [2,3]. X-ray lithography using the very soft radiation in the range 10 - 50 Å avoids the problem of backscattering and thus permits one to replicate on semi-infinite substrates patterns with linewidths of the order of 1000 Å and less, and in addition provides means for controlling cross-sectional profiles. X-radiation in the range 4-10 Å on the other hand is appropriate for replicating patterns in the linewidth range above about 3000 Å, and thus is most appropriate for microelectronic applications [4 - 6]. It is important to emphasize that x-ray lithography is only capable of replicating mask patterns. The x-ray mask must be generated by some other means such as electron beam lithography, holographic lithography, photolithography or a combination of these.

Figure 1 illustrates the type of high aspect ratio, high resolution relief structure that can be realized in a PMMA film using x-ray lithography at the Cu_L wavelength of 13.3 Å. The C_K radiation at 44.7 Å can provide even higher resolution (~ 50 Å) and thus should enable one to replicate the extreme resolution patterns realizable in a STEM [2,3]. In this talk, the technology of soft x-ray lithography will be described including mask making methods, source design and construction, tradeoffs between wavelength and resolution, and methods for modelling the exposure-development process.

---

(1). R.J. Hawryluk, H.I. Smith, A. Soares, A.M. Hawryluk, J. Appl. Phys. vol. 46, pp 2528-2537, June 1975.

(2). A.N. Broers, W.W. Molzen, J.J. Cuomo, N.D. Wittels, Appl. Phys. Lett. vol. 29, pp 596-598, Nov. 1976.

(3). H.P. Zingsheim, pp 357-364, Proceedings Scanning Electron Microscopy, 1977, ed. Om Johari, Chicago Press Corp.

(4). D. Maydan, G.A. Coquin, J.R. Maldonado, S. Somekh, D.Y. Lou and G.N. Taylor, IEEE Trans. Electron. Devices, ED-22 429, July 1975.

(5). S.E. Bernacki and H.I. Smith, IEEE Trans. Electron. Devices, ED-22 (1975) 421.

(6). See Proceedings, 14th Symposium on Electron Ion and Photon Beam Technology, Palo Alto, California May 1977.

Fig. 1. Scanning electron micrograph of the cross section of a 1600 Å linewidth grating pattern exposed in a PMMA film on a SiO_2 substrate using Cu_L x-radiation at 13.3 A.
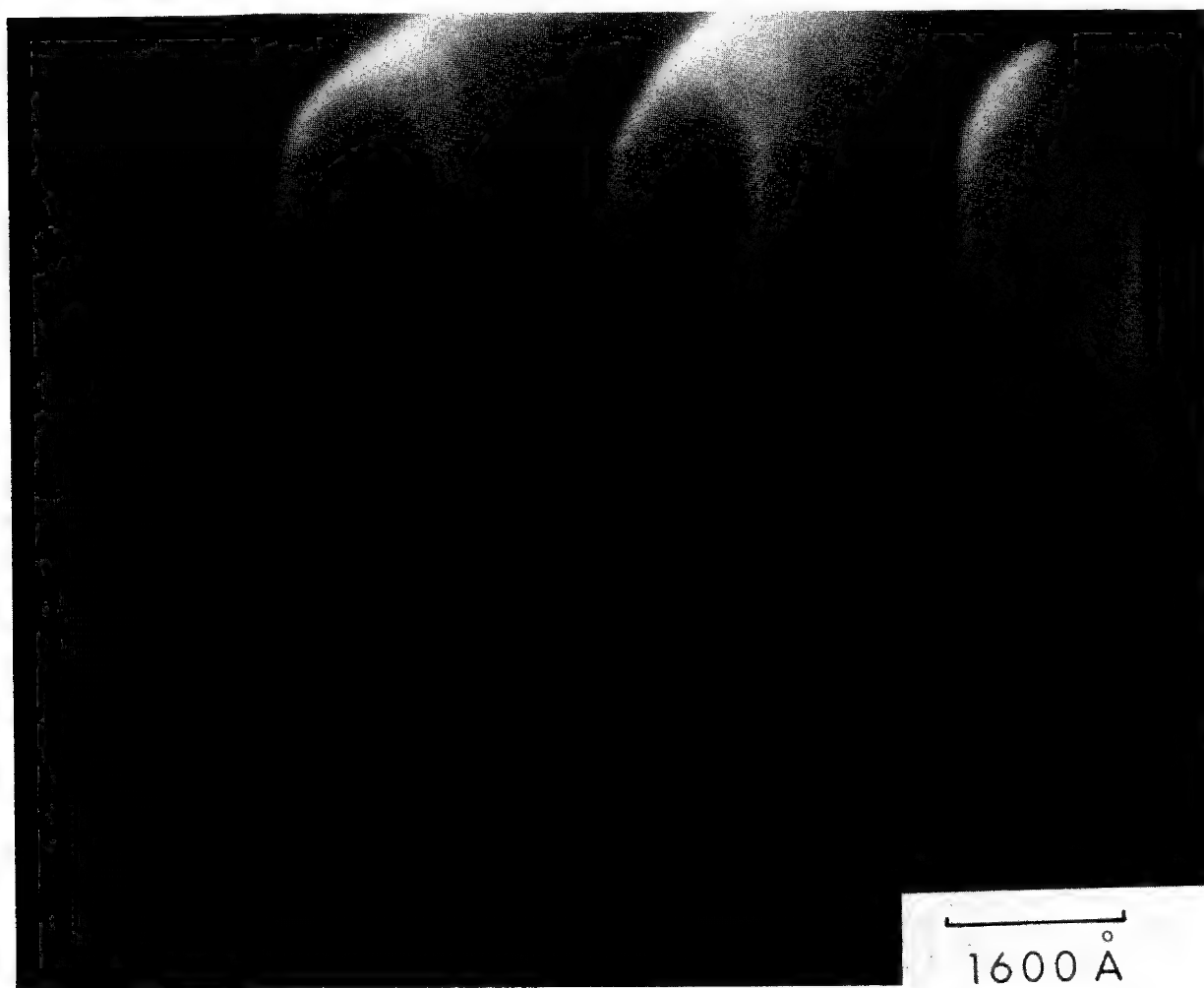
1600 Å

ELECTRON PROBE ANALYSIS OF ULTRA SMALL VOLUMES IN PHYSIOLOGY

C. Lechene, R. R. Warner and T. H. Strunk

Biotechnology Resource in Electron Probe Microanalysis
Harvard Medical School
Boston, Massachusetts

Electron probe microanalysis can be used to analyze in the same sample more elements in much smaller volumes than any other ultramicroanalytical method (1). Consequently, electron probe microanalysis is becoming a major tool in biology.

Liquid Droplet Analysis:

Picoliter volumes are withdrawn with capillary glass micropipettes from biological systems during in vivo experiments. These samples in addition to standard solutions are prepared by a special freeze drying procedure. Their composition is determined by electron probe microanalysis by comparing the intensities of the characteristic X-ray lines from the sample to those of the standards. This method has found wide applications in renal physiology (2,3 4) and in reproductive biology (5,6,7,8,9). The site and the mechanism of ionic movement through the renal epithelium can be studied. For example, an inhibition of phosphate reabsorption by parathormone in the distal nephron has been found (2). A lack of significant back flux of phosphate through the proximal tubule epithelium has been documented (4). Simultaneous measurement of seven elements (Na, K, Ca, Mg, Cl, P, S) in proximal nephron tubular fluid has revealed that compared to a control condition, in presence of the impermeant anion $SO_4^=$, the K concentration decreases below that of plasma and divalent cation concentrations are dissociated: [Ca] increases while [Mg] decreases below their plasma concentration. For reproductive biology the composition of the follicular fluid has been found to be identical to that of plasma (5,8). The microenvironment of the early embryo in the oviduct and at the time of uterine implantation has been shown to vary with the site and the time and to be characterized overall by a strikingly high potassium concentration (9). The accumulation of fluid in the blastocyst has been shown to depend on active inward movement of sodium (6,7). In auditory physiology, the composition of the endolymph and perilymph has been determined by the group of T. Weiss and L. Frishkopf at M.I.T. showing a very high [K] and very low [Na] in the endolymph of several species.

Measurement of carbon allows the quantitation of one organic compound in a mixed salt solution. Using an ODPB crystal with a Cameca MS 46 electron probe (11 KV accelerating voltage, 80μ beam diameter, and 200μ beam current) raffinose concentration and its variation has been determined and correlated with the movement of Na and other ions through the proximal nephron epithelium (10).

Protein interferes with an easy manipulation of these extremely small volumes of liquid. A technique for separation of the protein by

ultrafiltration centrifugation of submicroliter volumes has been developed using dialysis membrane in a microhematocrit tube.

To avoid concentration by loss of water from samples of subnanoliter sizes, extreme precautions are necessary. The samples are maintained under paraffin oil. The paraffin oil is saturated with water by vigorous shaking and is centrifuged immediately before use. Control experiments have shown that even under freshly saturated oil the samples concentrate more than 30% in one hour when kept at room temperature. Concentration does not occur when the temperature is kept below -70°C for a period of time exceeding several weeks.

After being prepared on a beryllium support, the samples can be kept in a dry atmosphere. Of practical importance, preliminary tests have shown that they can be sent (air freight) between distant laboratories without significant changes in their composition.

We are comparing results obtained by using only one standard solution of mixed salts of known composition with those obtained by the usual procedures using the linear calibration obtained with five standard solutions. The results are identical if not better in precision by using the single standard calibration technique. This could result in an important shortening of the time needed to prepare the samples.

Isolated Cell Analysis:

Populations of individual human red blood cells, each with a volume of approximately 100 femtoliters, are sprayed on vitreous carbon discs. Elemental distribution and correlations between Fe, S and P, and between Na, K and Cl, are established by analyzing large populations of cells one by one [quantitation of monovalent ions in individual cells is possible by using cells loaded with known ionic concentrations] (11). While waiting for the equipment to analyze the cells kept in a frozen hydrated state, assays have been made by spraying the cells on vitreous carbon supports maintained close to liquid nitrogen temperature and subsequently freeze dried. Very preliminary results show a surprisingly enhanced Na characteristic intensity while there are few changes in the intensity lines of the other elements as compared to the preparation at room temperature.

Tissue Analysis:

Preparation by freeze drying was used for the analysis of the elemental content in rat pituitary gland. The intermediate lobe was found to be very rich in calcium and the posterior lobe high in sulfur (12). However, for the analysis of diffusible elements, particularly in tissue with large

extracellular spaces which do not contain a protein matrix, freeze drying cannot provide reliable results (13,14). Moreover, freeze drying cannot provide reliable quantitative analyses per wet weight; indeed, it is very unlikely that the different tubular compartments have an identical water content; therefore, even the use of standards prepared and analyzed under the same conditions cannot eliminate this uncertainty.

A method which will likely avoid translocation of diffusible elements and which will allow one to measure concentrations per wet weight is the preparation and analysis of the sample kept frozen hydrated (14,15). In the method we are developing, kidney samples are frozen in isopentane precooled in liquid nitrogen. Then they are placed in a bath of liquid nitrogen for the entire preparation until introduction into the cold stage of the electron probe. The samples, hard like rocks, are trimmed with a jewelry saw, mounted in a polished holder and maintained in place with a mixture of glycerol in saline. The surface to be probed is exposed by sawing with a jewelry saw or a wire loop saw. In preliminary experiments, frozen hydrated kidneys were analyzed with a Camebax electron probe using a cold stage attachment (14,16). Sample temperature was maintained at approximately −160°C during the analysis. Longitudinal scans from the cortex to the papilla (30KV, focused beam, 20nA) showed a marked increase in sodium and chloride concentration occurring at the boundary between outer and inner medulla and leveling off in the papilla of antidiuretic rat kidneys. In water diuretic rat kidneys, sodium and chlorine concentrations did not increase at the inner medullary boundary, could be elevated in the middle of the papilla and decreased towards the tip of the papilla.

In rabbits which have been injected with iodinated contrast material (B.J. Hillman, N.K. Hollenberg and D.K. Kido, Harvard), the iodine was found very concentrated in the papilla. More importantly, a homogeneous iodine signal was found in the frozen luminal content of tubular sections. Potassium mapping the tubular cells surrounded the iodine mapping the lumina. Such a result is the first step in the analysis of the adjacent cellular and extracellular contents.

In conclusion, if the ultimate use of electron probe microanalysis in biology is the routine analysis of attoliter volumes in cells, its scope is far from being limited to the analysis of intracellular organelles. Solutions of physiological problems concerning organs, tissue or cell functions , or concerning hormone or drug actions, often need the knowledge of the elemental composition of cells and of their microenvironment. Towards this aim, by quantitating the entire elemental content in volumes on the order of picoliters or femtoliters, electron probe microanalysis does far better than any other ultramicroanalytical method. By the development of routine preparative methods its use is broadening and electron probe micoranalysis is becoming a major tool in physiological studies.

REFERENCES

1. Lechene, C. and R.R. Warner. Ultramicroanalysis. X-ray spectrometry by electron probe excitation. Annual Review of Biophysics and Bioengineering. 6: 57-85, 1977.

2. Knox. F. G. and C. Lechene. Distal site of action of parathyroid hormone phosphate reabsorption in the thyroparathyroidectomized dog. Am. J. Physiol. 229: 1556-1560, 1975.

3. Knox. F. G., J. A. Haas and C. Lechene. Effect of parathyroid hormone on phosphate reabsorption in the presence of acetazolamide. Kid. Int. 10: 216-220, 1976.

4. Greger, R. F., F. C. Lang, F. G. Knox and C. Lechene. Absence of significant secretory flux of phosphate in the proximal convoluted tubule. Am. J. Physiol. 232(3): F235-F238.

5. Roblero, L, J. Biggers and C. Lechene. Electron probe microanalysis of the elemental microenvironment of oviductal cleavage stages of the mouse. J. Reprod. and Fertil. 46: 431-434, 1976.

6. Borland, R. M., J. Biggers and C. Lechene. Kinetic aspects of rabbit blastocoele fluid accumulation - an application of electron probe microanalysis. Devel. Biol. 50: 201-211, 1976.

7. Borland, R.M., J.D. Biggers and C. Lechene. Studies on the composition of mouse blastocoele fluid using electron probe microanalysis. Develop. Biol. 55: 1-8, 1977..

8. Chong, A. P., M. L. Taymor and C. Lechene. Electron probe microanalysis of the chemical elemental content of human follicular fluid. Am J. Obstet and Gynec. (In press)

9. Borland, R. M., S. Hazra, J. D. Biggers and C. Lechene. The elemental composition of the environments of the gametes and preimplantation embryo during the establishment of pregnancy. Biol. Reprod. 16: 147-157, 1977.

10. Warner, R. R. and C. Lechene. Electron probe analysis of limiting transepithelial inorganic ion concentration differences across the rat proximal tubule. Proc. 11th Annual Conference. Microbeam Analysis Society, Miami, Florida, August 1976. 59A-59E.

11. Lechene, C., C. Bronner and R. G. Kirk. Electron probe microanalysis of chemical elemental content of single human red cells. J. Physiol. 90: 117-126, 1977.

REFERENCES, Cont.

12. Merriam, G. R., F. Naftolin and C. Lechene. An electron probe study of elemental distribution in the rat pituitary. Proc. 10th Annual Conference, Microbeam Analysis Society, Las Vegas. 42A-42F, 1975.

13. Dörge, A., R. Rick, K. Gehring, J. Mason and K. Thurau. Preparation and applicability of freeze-dried sections in the microprobe analysis of biological soft tissue. J. Microscopie Biol. Cell. 22: 205-214, 1975.

14. Lechene, C., T. Strunk, R. R. Warner and C. Conty. Perspectives in electron probe microanalysis of biological samples kept frozen. Proc. 10th Annual Conference, Microbeam Analysis Society, Las Vegas, 49A-49E, 1975.

15. Moreton, R. B., P. Echlin, B. L. Gupta, T. A. Hall and T. Weis-Fogh. Preparation of frozen hydrated tissue sections for X-ray micro-anlaysis in the scanning electron microscope. Nature 247: 113-115, 1974.

16. Lechene, C. and J.V. Bonventre. Electron probe study of the urinary concentrating mechanism elemental cortico-papillary gradient in forzen hydrated rat kidney. Proc. 11th Annual Conference, Microbeam Analysis Society, Miami, Florida, August 1976. 61A-61G.

SOME ASPECTS OF THE MICROANALYSIS OF FROZEN-HYDRATED TISSUE SECTIONS

B.L. Gupta, T.A. Hall & R.B. Moreton, Biological Microprobe Laboratory,
Department of Zoology, Cambridge University, Cambridge, CB2 3EJ, U.K.

In this presentation we shall summarise the procedure we have
developed for the microanalysis of frozen-hydrated tissue sections, and
describe some of the problems and some of the results to date.

For the study of electrolyte concentrations it is necessary to work
with rapidly frozen tissues. Data from other laboratories, as well as our
own, indicate that one can learn much about intracellular electrolyte
distributions from frozen-dried or freeze-substituted specimens (Appleton,
1974; Dörge et al. 1975; Forrest & Marshall, 1976; Koepsell et al, 1974;
Shuman et al, 1977), but frozen-hydrated preparations seem essential for a
meaningful X-ray microanalysis of small extracellular spaces, for example
luminal or serosal spaces or lateral extracellular spaces or canaliculi
associated with secretory epithelial cells.

Our usual procedure is to quench-freeze a small piece of tissue, cut
sections in a cryostat or cryokit at a temperature between -80 and -130°C,
transport the sections in the frozen-hydrated state (below -150°C) to the
cold stage (-170°C) of our JEOL JXA - 50A scanning
microanalyser, select fields from the scanning transmission image, and
analyse for 80 sec per field with probe voltage of 50 kV and current in the
range 2-10 nA. With a section 1-μm thick and current in the neighbourhood
of 10 nA, the spatial resolution of the X-ray analysis is about 200 nm.

In most of our studies the tissue is suspended prior to quench-freezing
in a physiological medium of known composition in order to establish its
functional state, and this medium remains as a peripheral layer in the
sections. An organic substance of high molecular weight, such as Dextran,
is added to the medium to reduce ice-crystal damage on freezing, to improve
sectioning, and to aid in quantitative analysis.

Quantitative analysis can be based on the equation

$$C_a \ (sp) = \frac{(N_a/W)_{sp}}{(N_a/W)_{st}} \ C_a(st)$$

where C_a is the mass fraction of element $\underline{a}$ (which may be expressed as mM of
element $\underline{a}$ per kg of total mass), N_a is the number of characteristic quanta
of element $\underline{a}$ registered during a run, $\underline{W}$ is the number of quanta recorded
simultaneously in a band of the X-ray continuum (from the specimen itself,
after correction for other sources of continuum radiation), and $\underline{sp}$ and $\underline{st}$
refer respectively to an analysed field in the specimen and to the peripheral
standard. One assumption underlying the equation is that specimen and
standard have the same mean atomic number (and hence the same efficiency
of generation of continuum radiation per unit mass). This assumption will
be accurate for fully hydrated material if the organic additive makes the
dry-weight fraction of the peripheral standard similar to that of the
specimen, and the assumption may then remain valid even under partial
dehydration if peripheral standard and specimen dehydrate to a similar
degree.

In the measurement of mass fractions (mM of element per kg of specimen),
an uncertainty arises due to the loss of organic mass which may be induced

by the electron beam during analysis. Whereas one may determine the magnitude of this effect for pure preparations of particular organic molecules (sugars, proteins, etc.) it is difficult to predict the loss which may occur in the irradiation of a micro-area of genuine tissue, which is a special and un-modelable complex of such molecules. However, for frozen-hydrated specimens the degree of uncertainty associated with mass loss is much less than for frozen-dried specimens because most of the mass in the frozen-hydrated tissue consists of water rather than organic material.

Signal-to-background ratios in frozen-hydrated sections are of the order of five times poorer than in frozen-dried sections. This poses difficulties for energy-dispersive X-ray spectrometry, especially in analysing for sodium in physiological concentrations. Our sodium measurements are done with a diffracting spectrometer (RAP crystal) even though we must consequently use currents of 2-10 nA and specimen thicknesses of approximately 1 μm to get adequate X-ray intensity.

Of the many difficulties associated with the analysis of frozen-hydrated sections, three will be noted here: stability of specimens under the electron beam, confirmation of the maintenance of hydration, and the formation of adequate images.

Stability of specimens: Our sections are mounted on Al-coated nylon films, against which they have been gently pressed to secure a good contact. When the sections are in uniform contact, they can remain hydrated under beam currents up to 10 nA, but deep-frozen sections are not always flat and they do not tend to adhere well to the supporting film. Specimens in poor contact are unstable under the beam. We have not yet found a way of ensuring uniform intimate contact routinely.

Confirmation of hydration: Sections may easily dehydrate inadvertently prior to or during analysis. After analysis we generally dehydrate specimens by removing them from the cold stage and allowing them to warm up in the vacuum of the microanalyser. They are then returned to the cold stage and examined again. This deliberate dehydration should produce drastic predictable changes in X-ray signal-to-background ratios and in image contrast; if these effects are not observed, the sections were not near full hydration prior to warmup. This procedure enables one to assess the degree of hydration which prevailed prior to warmup, and we find that specimens during analysis have often been _partially_ dehydrated. (An alternative criterion of hydration, the observation of a diffraction pattern from ice, may not indicate so readily the _degree_ of hydration.)

Image formation: With our instrumentation, image contrast in 1-μm fully hydrated sections is virtually _nil_, but a dehydration of a few percent of the water content is enough to yield adequate images. Since the contrast presumably arises from non-uniform dehydration, this procedure is not strictly compatible with the assumption of uniform dehydration under-lying the use of the equation above for quantitative analysis, but the associated errors are small.

The foregoing considerations are illustrated by recent studies on insect Malpighian tubules (Gupta, 1976; Gupta et al, 1976), salivary glands (Gupta et al, 1977a) and rectal papillae (Gupta et al, 1977b). These studies also demonstrate that the electrolyte distributions are not obliterated during specimen preparation, and that the quantitative measurements are in reasonable agreement with data obtained by other methods.

But it is important to keep in mind the distinctions between mM of element per kg of tissue (as measured by the microprobe analysis of frozen-hydrated tissues), mM of element per kg of dry tissue (as measured after freeze-drying), mM of free element per liter of cytosol, and elemental activity expressed in units of mM per liter.

For a much more detailed discussion of the analysis of frozen-hydrated sections we would refer to a recent article (Gupta et al, 1977c).

References

Appleton, T.C. (1974). J. Microscopy 100, 49-74.

Dörge, A., Rick, R., Gehring, K., Mason, J. & Thurau, K. (1975). J. de Microscopie et de Biologie Cellulaire 22, 205-214.

Forrest, Q.G. & Marshall, A.T. (1976). Proc. 6th European Congress on Electron Microscopy (Jerusalem), Vol II (editor Y. Ben-Shaul). pps. 218-220. Tal International Publishing Company, Israel.

Gupta, B.L. (1976). In "Perspectives in Experimental Biology" (Vol. I, editor P. Spencer Davies). pps. 25-42. Pergamon Press, Oxford.

Gupta, B.L., Hall, T.A., Maddrell, S.H.P. & Moreton, R.B. (1976). Nature (London) 264, 284-287.

Gupta, B.L., Hall, T.A., Berridge, M.H. & Moreton, R.B. (1977a, in press, abstract only). Proc. 27th International Congress of Physiological Sciences, Paris.

Gupta, B.L., Hall, T.A., Wall, B.J. & Moreton, R.B. (1977b, in press, abstract only). Proc. 27th International Congress of Physiological Sciences, Paris.

Gupta, B.L., Hall, T.A. & Moreton, R.B. (1977c, in press). In "Transport of Ions and Water in Animals" (editors B.L. Gupta, R.B. Moreton, J.L. Oschman & B.J. Wall). Academic Press, London.

Koepsell, H., Nicholson, W.A.P., Kriz, W. & Höhling, H.J. (1974). Pflügers Arch. 350, 167-184.

Shuman, H., Somlyo, A.V. & Somlyo, A.P. (1977). Proc. 10th Annual SEM Symposium (editor O. Johari). IIT Research Institute, Chicago.

ELECTRONPROBE MICROANALYSIS OF FROZEN HYDRATED BULK SPECIMENS:

BASIC EXPERIMENTS

W. Fuchs

2nd Department of Physiology, SFB 38, project C2, Univ. of the
Saarland, 6650 Homburg/Saar, W.-Germany

To maintain the original distribution pattern of diffusible
elements in biological samples, electronprobe microanalysis is
carried out with frozen hydrated bulk specimens and frozen hydrated
sections, analysed at temperatures below 130 K.

Aiming toward quantitative analysis, the specimen should neither
increase nor decrease in mass during preparation and analysis. In-
strumentation has been developed in several laboratories for a
contamination free handling of frozen hydrated bulk specimens. In
this technique the area to be analysed is set free by freeze cleaving
in high vacuum at 100 K. The specimen is then transfered onto the
pre-cooled stage of the SEM by use of a cooled transportable airlock.
By keeping the specimen below 140 K, desorption is kept negligibly
small.

If examined in the SEM, these specimens appear featureless,
details of intracellular structures being invisible. Sufficient
surface structure is only obtained if controlled etching of a few
100 Å is allowed. This depth is considered to be small as related
to the depth of X-ray excitation in bulk specimens. This assumption,
however, is not necessarily justified.

Ice has a very low intrinsic conductivity and surface and space charging appears when uncoated specimens are irradiated with non-penetrating electrons. Model calculations predict a movement of the space charging front to the surface, reducing the depth of analysis to 0.1 μm within one second (5 keV, and 10^{-10} A). Although coating with a grounded conductor abolishes the surface potential, the build-up of an internal space charge field is still possible. The internal charging of the specimen with its supposed flattening of the X-ray source volume is of central importance not only in view of the preparation technique (etching) and the stability under the beam (heating, drift of ions), but also with respect to quantitation of the X-ray spectra obtained. If the electron distribution in energy and depth is changed, a straight-forward application of the conventional ZAF correction may lead to errors.

To study the charging process in detail, we have collected simultaneous specimen currents from top and bottom of an ice layer preparation. Ice layers of 1 to 50 μm thickness were evaporated on a 1000 Å thick aluminum electrode and covered with a 800 Å thick carbon layer. These sandwiches were irradiated in the SEM through the front electrode, using beam voltages in the range between 2 and 30 kV, beam current between 10^{-10} and 10^{-9} A and irradiated areas between spot size and 100 μm x 100 μm. By use of a separate Faraday cup located behind the sandwich, the transmission of electrons passing through the rear electrode was also recorded. The time dependence of front and rear current and, additionally, the secondary electron emission was studied for non-penetrating and fully penetrating beams. Open circuit conditions (front electrode "floating") and short circuit conditions (front electrode grounded) were used.

Both the transient and steady state currents recorded can be interpreted in terms of a) an internal space charge front which moves to the surface and b) the build-up of radiation induced conductivity.

1) Uncoated specimens (or in the open circuit mode): The capacitive current recorded from the rear electrode, after switching the beam on, vanishes with time, if the initial electron range is smaller than half of the foil thickness. Under these conditions the secondary electron emission increases with the same time constant. Both effects together reflect the expanding space charge and its movement closer to the specimen surface. Some of the injected charge remains in the specimen (bright area in the SEM picture), but can be removed if the charged area is scanned with penetrating electrons.

For deeper penetrating beams, the rear current jumps directly to a constant value when the beam if turned on. The level recorded is dependent on the distance to the rear electrode. This behaviour can be explained by the build-up of an induced conductivity.

2) Front electrode grounded: The current drawn from this electrode increases to a steady level at steady state space charge distribution. It decreases slowly after turning the beam off. From this current the mean depth of the space charge distribution can be computed.

Information on the depth of the interaction volume may also be obtained directly from the effect of freeze-drying on peak background ratios of ED-spectra. Droplets of frozen electrolyte solutions were freeze dried stepwise and analysed with a Si(Li) detector having a Be-window of 3.8 μm thickness. With increasing etching time, the initially intense oxygen peak decreases to almost zero, whereas the peak/background ratio for the elements Na through Ca increases.

Information on the depth of analysis (as obtained above), together with information about the amount of ice within the specimen (oxygen K_α signal) may allow quantitative analysis of frozen hydrated specimens even in cases where controlled freeze etching was performed.

"Electron Probe Analysis of Muscle"

A. P. Somlyo, Avril V. Somlyo and H. Shuman
Pennsylvania Muscle Institute of the University of Pennsylvania, 51 North
39th Street, Philadelphia, Pennsylvania 19104

This review will summarize our results with quantitative energy dispersive electron probe analysis of freeze-dried cryo sections of smooth and striated muscle. The major purpose of these studies was to determine whether the physiological distribution of diffusible ions is preserved in cryo sections obtained after rapid freezing in super-cooled Freon 22 and to determine the intracellular distribution of Cl and of the Ca storage sites in muscle. The instrumentation and methods have been described in detail elsewhere (1, 2).

The results to be presented show that: 1) in smooth muscle the cytoplasmic [Cl] significantly exceeds that predicted by a Gibbs-Donnan distribution and the mitochondria partially exclude Cl; 2) the SR is a major Ca storage site in smooth muscle; 3) the composition of the SR of striated muscle is not similar to that of the extracellular fluid. We also confirmed the presence of sequestered Ca in the SR of the terminal cisternae of striated muscle.

1. Shuman, H., Somlyo, A. V. and Somlyo, A. P.: Quantitative electron probe microanalysis of biological thin sections: methods and validity. Ultramicroscopy. 1:317-339, 1976.

2. Shuman, H., Somlyo, A. V. and Somlyo, A. P.: Theoretical and practical limits of Ed x-ray analysis of biological thin sections. Scan. Elect. Micros., IIT Res. Inst. 1:663-672, 1977.

THE EFFECTS OF CYTOCHALASIN B ON CALCIUM TRANSPORT BY

THE CHORIOALLANTOIC MEMBRANE OF THE CHICK EMBRYO

James R. Coleman and A. Raymond Terepka
Department of Radiation Biology and Biophysics
University of Rochester School of Medicine and Dentistry
Rochester, New York 14642

Electron Probe X-ray microanalysis has proven particularly useful in the study of transcellular calcium transport by epithelia because the electron probe can be used to resolve the activities of individual cells during the process. This is important because calcium transporting epithelia usually contain more than one cell type, and usually, not all cells act in unison. If as is necessary in whole tissue studies, the total amount of calcium transported by an epithelium is assumed to be transported equally by all the cells present, one concludes that each cell handles a smaller amount of calcium than is truly the case if only some of the cells participate at any one time.

We have employed electron probe analysis to investigate calcium transport by the chorioallantoic membrane of the embryonic chick as well as small intestine of both rat and chick. These studies have identified which cells of these tissues take up calcium during the transport process. These cells had the characteristic ruffled borders of cells which are engaged in endocytosis and led us to propose a model (1), based on an earlier suggestion by Wasserman and Kallfelz (2), for calcium transport that might involve an endocytosis-like mechanism.

Cytochalasin B is an agent which is known to interfere with endocytosis, although it has been shown to affect other membrane associated processes as well (1-4). We reasoned that if the calcium transport mechanism did involve an endocytosis-like mechanism, then it should be inhibited by Cytochalasin B.

Chorioallantoic membranes were removed from chicks which had been incubated seventeen to nineteen days. Membranes were exposed to 1 mM calcium in a Krebs-Ringers solution, pH 7.4 for 90 minutes in a Dubnoff shaker (5). Bulk calcium uptake was measured by including ^{45}Ca in the incubation medium. Membranes were exposed to Cytochalasin B at concentrations of 5 and 10 µg/ml for 1 hour. Cytochalasin B was dissolved in dimethyl sulfoxide (DMSO) before being added to the incubation medium, so that control experiments were performed to assess the effect of DMSO on calcium uptake. Each membrane was cut into four portions: two were exposed to calcium in the presence of cytochalasin B, or to DMSO (the solvent for

cytochalasin B); and the other pieces were exposed to calcium alone. Calcium uptake was measured by determining the ^{45}Ca content of the tissues, and expressed as nmoles Ca/cm^2 of membrane.

For electron probe analysis and transmission electron microscopy, membranes were fixed with glutaratdehyde which contained oxalate to precipitate calcium, followed by post-fixation in OsO$_4$, dehydration in ethanol and embedding in Spurrs epoxy for sectioning (6).

Results of these experiments are shown in Table I. The effect of cytochalasin B is to decrease calcium uptake by the chorioallantoic membrane but not to the level of inhibition produced by DNP. This may be due to the fact that DMSO significantly increases the amount of calcium taken up by the membrane.

Electron probe analysis shows that calcium localizations previously reported to be associated with active calcium transport in this membrane are found only rarely in tissues treated with cytochalasin B. The effect of DMSO appeared to be a general increase in the permeability of cell membranes to calcium since there was no significant increase in the number of calcium localizations associated with active transport.

TABLE I

Calcium Uptake as Percent of Paired Control

	%	S.E.	N
DNP (2×10^{-4}M)	33.6	±2.8	8
CB 2 µg/ml	51.2	±8.0	6
5 µg/ml	56.2	±11.2	5
10 µg/ml	48.1	±8.0	16
DMSO 10^{-3}M	104.0	±12.8	5
4×10^{-3}M	117.6	±12.1	6

REFERENCES

1. Coleman, J.R. and Terepka, A.R. J. Histochem. Cytochem. 20:401 (1972).

2. Wasserman, R.H. and Kallfelz, F.A. In: Biological Calcification: Cellular and Molecular Aspects. (H. Schraer, ed.) Appleton-Century-Crofts, New York (1970) p. 313.

3. Lin, S. and Spudick, J.A. J. Biol. Chem. 249, 5778 (1974).

4. Taverna, R.D. and Langdon, R.G. Biochim. Biophys. Acta 323:207 (1973).

5. Kletzein, R.F., Perdue, J.F. and Springer, A. J. Biol. Chem. 247:2964 (1972).

6. Loten, E.G. and Jeaurenaud, B. Biochem. J. 140:185 (1974).

7. Armbrecht, H.J., Terepka, A.R. and Gunter, T.E. Biochim. Biophys. Acta 426:547-556 (1976).

ACKNOWLEDGEMENTS

DETERMINATION OF CELLULAR ELECTROLYTE CONCENTRATIONS IN FREEZE-DRIED BIOLOGICAL SOFT TISSUES USING ELECTRON MICROPROBE ANALYSIS

Adolf Dörge, Roger Rick, Klaus Gehring, Richard Bauer and Klaus Thurau.

Physiologisches Institut der Universität München, 8 München 2, Pettenkoferstraße 12, W.- Germany.

The further investigation of cell function presupposes the exact knowledge of intracellular electrolyte concentrations. Especially in cases in which the tissue is composed of different cell types, the microprobe analysis is of great value in determining the cellular electrolyte concentrations. In order to obtain some further insights in transmembranal and transcellular electrolyte transport processes, microprobe analysis has been performed on freeze-dried cryosections of various organs (frog and toad skin, toad urinary bladder, rat kidney and nerve fiber).

Shock-freezing of the tissues was performed in cooled propane ($- 186^{\circ}$ C). The tissue was cut in a cryotome into about 1 μm thick sections, which were then sandwiched between two collodion films and freeze-dried. Both cutting and freeze-drying was performed at $- 80^{\circ}$ C. The sections were analyzed in a scanning electron microscope using an energy dispersive X-ray detector. The acceleration voltage was 15 kV and the probe current selected was 0.5 nA. During analysis small areas of the sections (1 μm^2) were scanned for 200 sec. The resulting spectrum was transferred to a computer for separating characteristic from uncharacteristic radiations. Quantification on the basis of wet weight concentrations was achieved by comparing the X-ray intensities obtained from the cells with that of an internal standard. The standard was introduced by covering the tissue immediately prior to shock-freezing with an albumin standard solution, containing extracellular electrolyte concentrations.

Fig. 1 demonstrates the principle of this method using a freeze-

dried frog skin section. The spectra were obtained in the albumin layer (A) and in an epithelial cell (B). The spectrum obtained in the albumin layer is characterized by typical extracellular electrolyte distribution pattern with high Na and Cl and low K signals, whereas the cellular spectrum shows an intracellular composition with high P and K and low Na and Cl peaks. Since the concentrations of the standard are known, the direct comparison of the elemental peaks provides the cellular wet weight concentrations of the respective electrolytes.

Compared to previous chemical or radiochemical analysis, generally lower cellular Na and higher cellular K values are obtained. In frog skin epithelium, for example, 4 to 5 times lower Na concentration values have been found using electron microprobe analysis. Gross differences between nuclear and cytoplasmic Na and K concentrations as reported for chemical analysis of cell fragments have never been observed for the various cell types investigated.
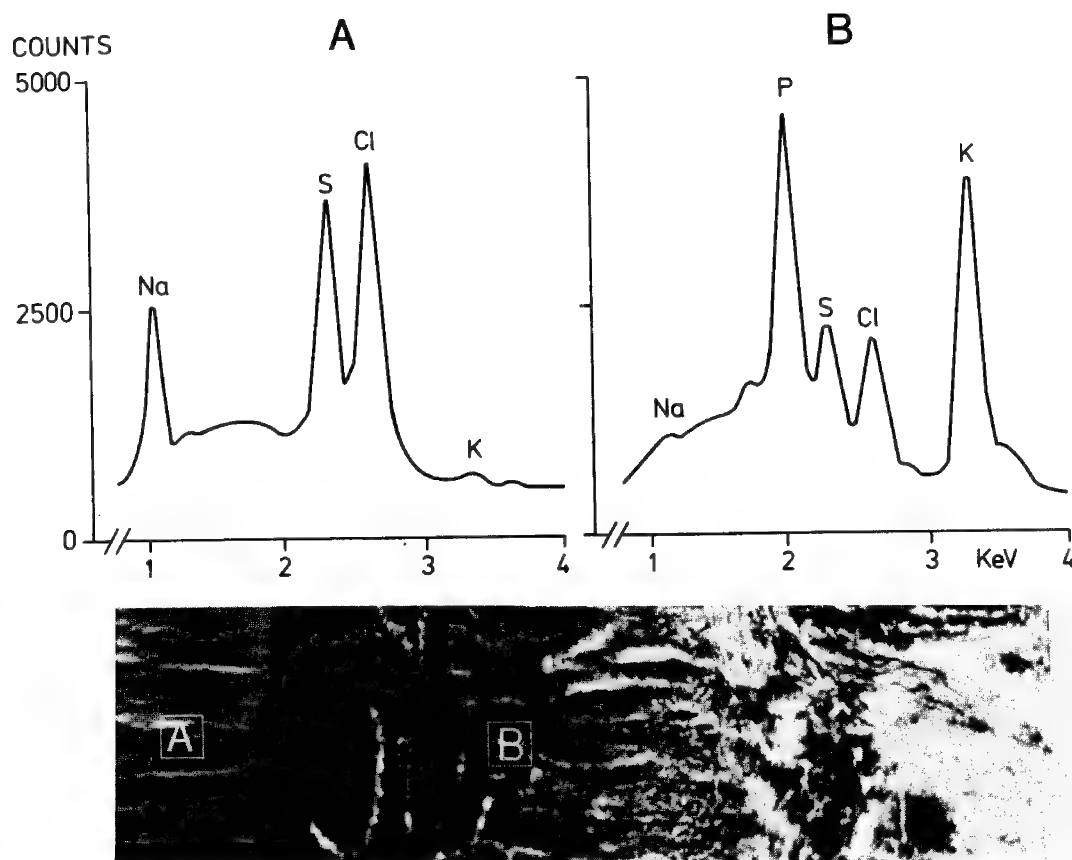
Fig. 1: Scanning transmission image of a freeze-dried frog skin section and energydispersive X-ray spectra obtained in the albumin layer (A) and in an epithelial cell (B).

MICROANALYSIS IN BIOLOGY : A REVIEW OF SOME SPECIFIC PROBLEMS.

P. Galle and J.P. Berry
Département de Biophysique de la Faculté de Médecine de Créteil,
6, rue du Général Sarrail, 94000 - CRETEIL, FRANCE.

For a long time, X ray microanalysis remained the only method for chemical analysis of microscopic or submicroscopic volumes. Now, at least 5 new methods are proposed and commercial instruments are already available. However, X ray microanalysis is still the most currently used and it will be more detailed here.

X RAY MICROANALYSIS.

The purposes of biologists in microanalysis generally differ from those pursued in other fields of research. Consequently, an adapted special instrumental configuration is often required.

A very good visualization of the sample is the first necessity, the study of relations between structure and function of the cell being the main purpose of the biologist. In X ray microanalysis a choice is offered between 4 different methods of visualization : 1) conventional transmission electron microscopy (CTEM) is always the best one when thin sections can be obtained (fig.1). 2) for usual thick sections, the light microscope (L.M.) gives the most useful informations particularly after staining of the sections. 3) although of higher resolution, the Scanning electron microscope (S.E.M.) gives poor useful informations compared to L.M. since the inner structures of the section cannot be detected. Only a few applications can take advantage of this method (frozen tissue specimens). 4) the Scanning transmission electron microscope (S.T.E.M.) working with a low intensity electron beam does not fullfill ideal conditions for X rays microanalysis of elements at a low concentration. Finally, C.T.E.M. and L.M. appear to be the two methods which are the most frequently required.

Quantitative analysis is generally the main préoccupation in X ray microanalysis ; however, in biology, quantitative measurements of chemical concentrations in the volume to be analyzed is often of less importance or even has no signification ; otherwise quantitative analysis may be impossible to realize, due to the very low concentration of the elements to be analyzed (intracellular Na,extracellular Ca...)which are often at the limit of detectability in X ray analysis. We can understand then why, until now, most of results obtained in biology by X ray microanalysis concern only qualitative studies.

Artefact is another important difficulty in biology. Atmospheric Dusts (Si, Al, Fe, Ca, Ti ...) remain under the electron probe when the sample is a section of soft tissue while they are ejected from

the probe in the case of a metallic polished surface. This very common artefact may be only avoided by visualization of the sample at a high resolution with a C.T.E.M. (ultra thin sections). Many other varieties of artefacts (4) have been already discussed in details (preparation of the sample, Ion diffusion, extraneous X rays, peak overloping in energy dispersive analysis etc...).

ION MASS MICROANALYSIS.

New possibilities in biological research are offered by this method : the analysis of the lightest elements, the analysis of trace elements and the study of isotopic ratios. Besides, the distributions of elements can be obtained directly without the help of any scanning and the resolution in the image is much better on bulk samples since the volume of ion diffusion in the sample is very small (<100 Å in depth) ; this advantage is particularly useful for the study of hard tissues such as bones or teeth (fig.2).
However, some difficulties appear in biology : 1) visualizing the sample at the ultrastructural level is not possible ; 2) the interpretation of mass spectra is sometimes difficult, due to the great variety of polyatomic ions emitted from an organic matrix : CH, CH_2, C_2H_2, C_2H_3, C_2H_4 ... ; these polyatomic ions may be confused with monoatomic ions (ex : ^{27}Al and $^{27}C_2 H_3$ or ^{56}Fe and ^{56}CaO).This difficulty may be avoided by high resolution spectra available on most commercial instruments but then images of element distribution can no more be obtained. This is until now the main preoccupation in biological applications of this method (2, 3, 8, 11).

CATHODOLUMINESCENCE.

A new possibility is offered by this method : the study of some molecules of biological interest ; these molecules may be luminescent by themselves under the probe, or marked with a specific luminescent molecule (fluoresceine, thioflavine) : " immunocathodoluminescence " (Fig. 3).
There are two main difficulties in biology : 1) the low intensity of cathodoluminescence emitted by molecules (much lower than that emitted by crystals) and 2) the destruction of organic molecules under the electron probe. These phenomena make analysis difficult ; it is therefore necessary to work at very low temperature, and with a low intensity electron beam what reduces the intensity in the cathodoluminescent signal. Improvements in the methods of collection of the cathodoluminescent signal are in course and recent results (5, 6) seems to be promising.

ELECTRON ENERGY LOSSES.

Theorically, the study of extremely small volumes, approaching the limit of resolution of electron microscopy is possible with

this method. In pratice, intense energy losses in the spectra are not characteristic of the elements involved (plasmon losses) ; characteristic energy losses are of very low intensity and generaly covered by the background with the exception of the lightest elements ; at the present time non characteristic energy losses in an organic matrix are not very well known. More informations on the value of these energy losses are required for an analytical use of that method.

REFERENCES.

1 - Castaing R., et Slodzian G., 1962 . Microanalyse par émission ionique secondaire. J. Microscopie, 1, 395-410.

2 - Galle P., 1970 . Sur une nouvelle méthode d'analyse cellulaire utilisant le phénomène d'émission ionique secondaire. Ann. Phys. Biol. Med., 4, 84-94.

3 - Galle P., 1973 . Cellular microanalysis : a comparison betwen electron microprobe and secondary ion emission microanalysis. In " Microprobe analysis as applied to cells and tissues ", 1 vol., pp.89-105, Ac. Press. Ed.

4 - Galle P., 1975 . Les artefacts en microanalyse par sonde électronique. J. Microscopie, 22, 315-332.

5 - Giles P.L., 1975. Cathodoluminescence. J. Microscopie, 22, 357-369.

6 - Haggis G.H., Bond E.F., and Fulcher R.G., 1976. Improved resolution in cathodoluminescent microscopy of biological material. J. Microscopie, 108, 177-184.

7 - Hall T.A., 1971 . The microprobe assay of chemical elements in : "Physical Techniques in Biological Research" 2 nd Edition, Vol. 1 A, Oster G. Ed., Acad. Press., pp.157-275.

8 - Lefevre R., 1975 . La microanalyse par émission ionique secondaire et son application aux tissus calcifiés humains. J. Microscopie, 22, 335-348.

9 - Kauffmann R., Hillenkamp F., Nitsche R., Schürmann M. and Unsold E., 1975 . Biomedical applications of Laser Microprobe Analysis. J. Microscopie, 22, 389-398.

10 - Slodzian G., 1963 : Etude d'une méthode d'analyse locale chimique et isotopique utilisant l'émission ionique secondaire. Thèse Paris, Masson Ed. Paris.

11 - Truchet M., 1975 . Application histologique de la microanalyse par émission ionique secondaire. J. Microscopie, 22, 465-474.
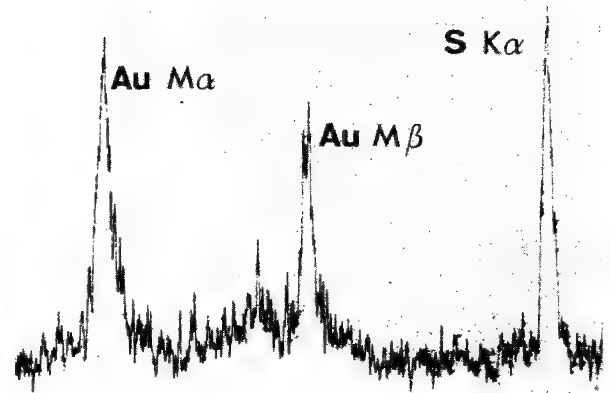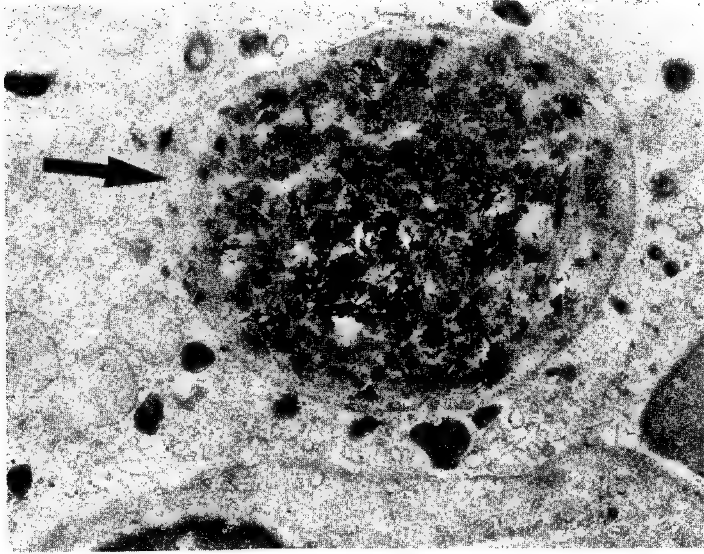
Figure 1. X ray analysis on an ultrathin section : Bone marrow biopsy in a patient after gold salts injections : demonstration of gold concentration in the lysosome of a monocyte (arrow). magn. = 120.000

Figure 2. Ion mass analysis : distribution of Fluorine at the surface of a bone section. mag.=300. Such a distribution is impossible to obtain by X ray microanalysis.

Figure 3. Immunocathodoluminescence : distribution of a macromolecule, Immunoglobuline G (IgG), on a smear of human lymphocytes. Anti IgG antigens molecules marked with fluoresceine have been specifically fixed on the IgG molecules located at the surface of the cells. magn.= 1.200.

CHROMIUM CONCENTRATION BY PROXIMAL RENAL TUBULAR CELLS.
AN ULTRASTRUCTURAL, MICROANALYTICAL AND CYTOCHEMICAL STUDY.

Jean-Pierre Berry, Ph.D.[1], Jacques Hourdry, Ph.D[2], Pierre Galle, M.D.[1]
and Georges Lagrue, M.D[3]

1. Laboratoire de biophysique, Faculté de Médecine de Créteil,
   6, rue du Général Sarrail 94000 - CRETEIL, FRANCE.
2. Laboratoire de Biologie-Vertébrés, Centre d'Orsay, Université
   de Paris Sud 91405 - ORSAY, FRANCE.
3. I.N.S.E.R.M. U 139, Groupe de Recherches sur les Néphropathies
   Hôpital Henri Mondor - 94000 - CRETEIL, FRANCE.

Chromium is implicated as a constituent of urban and
industrial pollution products. According to certain authors, this
element is principally excreted by the kidney. Among the various
chromium salts, potassium bichromate has a specification on nephrons.

We undertook the present study to determine which renal
cells concentrate chromium following weekly sub-cutaneous injec-
tions of potassium bichromate (injections of 0.17 mg chromium/
100g for 8 months).

We performed an electron microscopic morphological study,
a histochemical study to determine the nature of the organelles
involved by visualizing acid phosphatase activity, an X-ray micro-
analysis (CAMECA MS 46) study to demonstrate mineral elements on
ultra-thin sections.

The lesions observed were only at the level of proximal
tubules. Three stages in evolution of the lesions can be distin-
guished :

a) The cytoplasm has a normal appearance and small va-
cuoles contain several granules. These vacuoles present acid
phosphatse activity and are analagous to phagolysosomes. Micro-
analysis demonstrates chromium in the granules, about 50 A in
diameter.

b) The chromium, in the form of fine granules, is concentrated in dense patches within large vacuoles. Microanalysis demonstrates a lead precipitate reflecting enzymatic activity as well as the presence of chrome, each in different intra-vacuolar regions. These vacuoles are analagous to autolytic vacuoles.

c) The vacuoles are completely filled with chromium (residual vacuoles). Necrosis eliminates the entire cytoplasm.

We have thus demonstrated :

- A defensive and cellular protection mechanism involving the storage of the toxic element within lysosomes, and

- A chromium-specific process, compared to other elements already studied, consisting of concentration and elimination by the nephron.
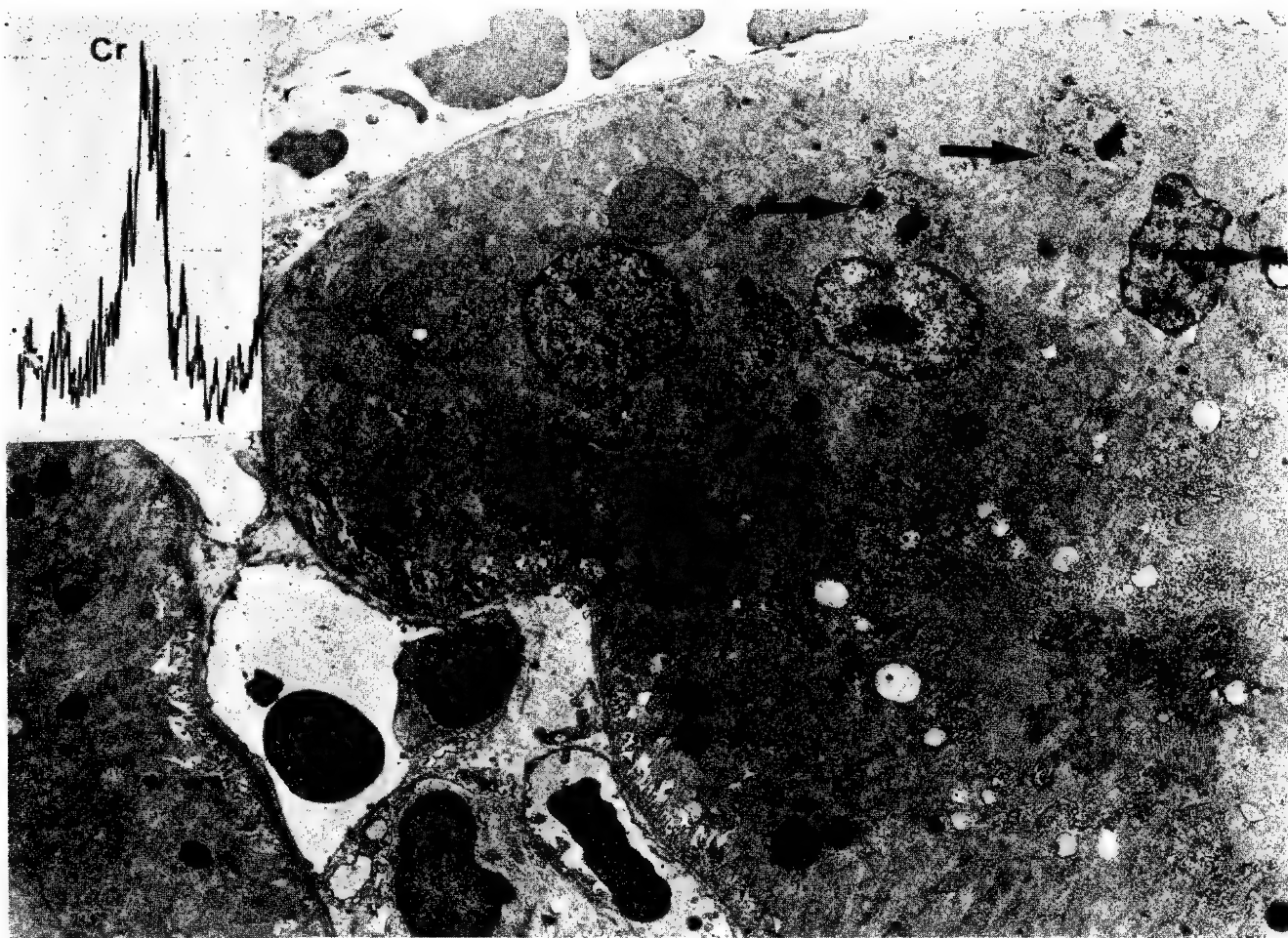
Figure 1.

Treatment with potassium bichromate for two months.

General view showing several secondary vacuoles (arrows).

X 6.000

Chromium spectrum obtained from a dense patch.

At high magnification, dense chromium granules appear in the opaque patch (arrow). X 165.000.
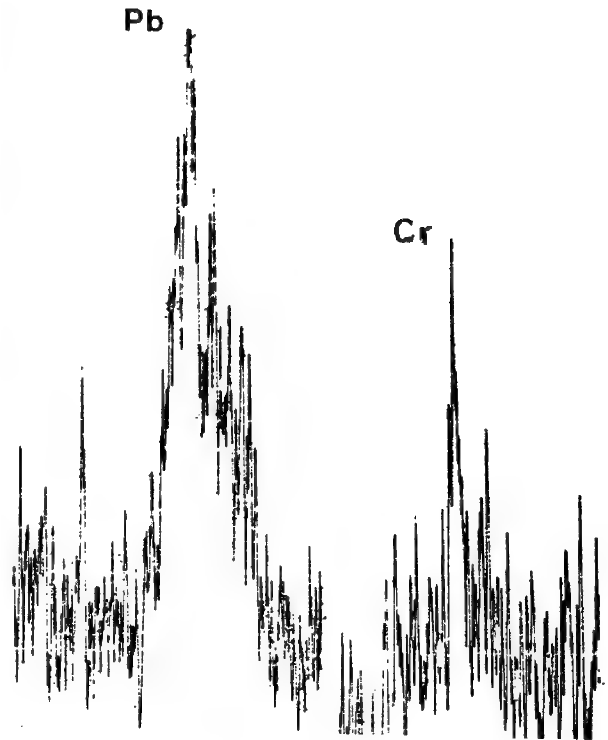
Figure 2.

Treatment with potassium bichromate for two months. Acid phos-
phatase activity.

In the two secondary vacuoles (1 and 2), acid phosphatase
activity is demonstrated by a lead phosphate precipitate.
X 21.000.

Apposed secondary vacuoles, each containing and opaque patch
(1 and 2). The reaction product is more abundant at the peri-
phery of the vacuoles. X 32.000

The microprobe demonstrates the presence of chromium in each
opaque patch and lead in the rest of the vacuole.

ANALYTICAL ELECTRON MICROSCOPY OF CALCIUM SITES
IN A GIANT SMOOTH MUSCLE CELL : PRELIMINARY RESULTS

G. NICAISE and M.L. HERNANDEZ-NICAISE

Laboratoire d'Histologie et Biologie Tissulaire
Université Claude-Bernard. 69621 VILLEURBANNE. France

Most important contributions to the cellular physiology of excitable cells have been made studying giant cells from various invertebrates. The only giant smooth muscle cell so far described is the mesogleal muscle fiber of *Beroe* (Ctenophora). Frequently this cell has a diameter of 40 μm and a length of up to 1 cm (fig. 1). A systematic study of this giant smooth muscle cell is proceeding in our laboratory, including a search for intracellular calcium reservoirs. The first series of experiments involved the use of strontium as a tracer, resulting in the labeling of both the endoplasmic reticulum and the mitochondria (Hernandez-Nicaise, 1976). In the present paper we report our attempts to carry on this work using X-ray microanalysis
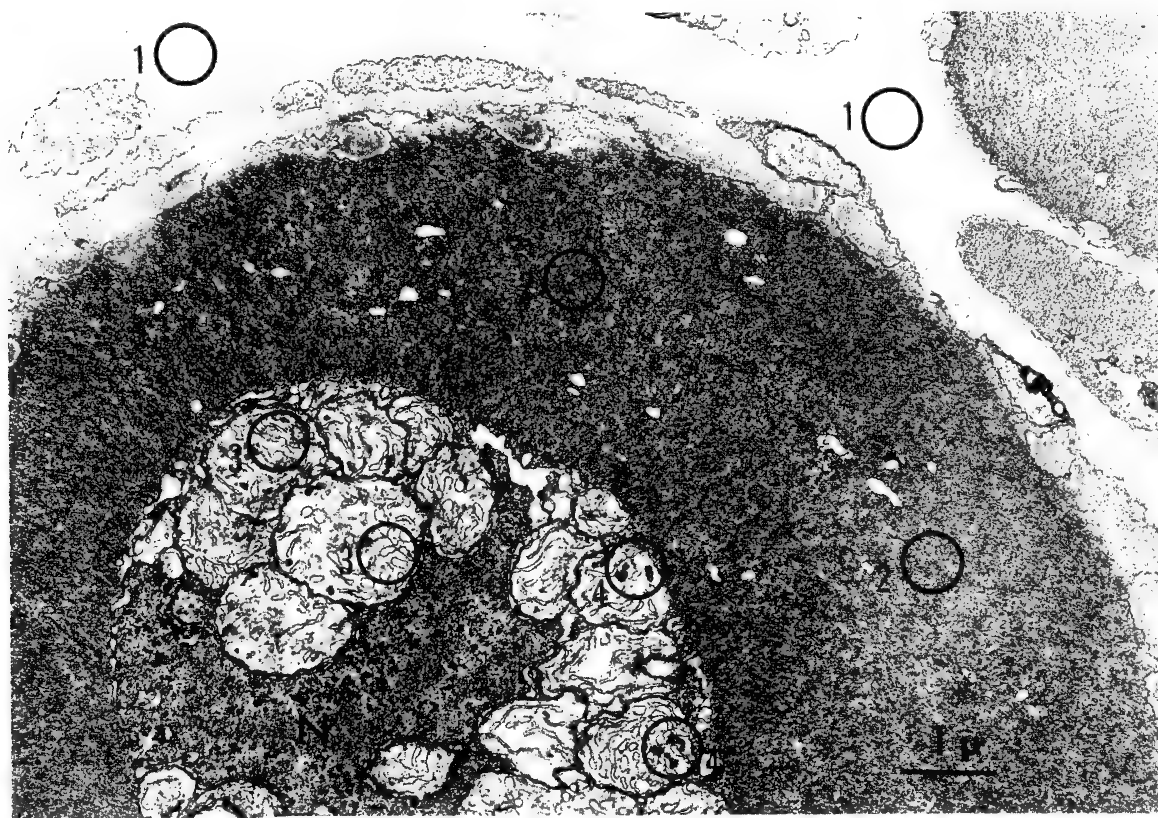
Fig. 1. Transverse section of a giant smooth muscle cell of *Beroe*. N = nucleus. 0 : typical areas analyzed, 1 = mesoglea, 2 = myofilaments, 3 = part of mitochondrion devoid of inclusions, 4 = part of mitochondrion containing granules.

Whole animals were dipped into cold glutaraldehyde as controls, then dissected and osmium-treated before embedding in Epon. Other specimens were similarly treated after incubation of body wall pieces in artificial sea-water where calcium replaced magnesium (CaC12 70 mM) or strontium replaced calcium and magnesium (SrC12 70 mM). For other blocks 20% of the sodium was replaced by potassium in the artificial sea-water (KC1 100 mM). Sections approximately 150 nm thick were collected on carbon coated-formvar film on 75 mesh copper grids. Staining with heavy metals was omitted except for the treatment with osmium tetroxide, which in this case was necessary to visualize the cell components. The microprobe used was a CAMEBAX system equipped with two wavelength X-ray dispersive spectrometers and

We used an acceleration voltage of 50 kV and a probe current of 100 nA. Repetitive 40 seconds counts were made over 1) mesoglea (extracellular connective tissue), 2) myofilaments, 3) mitochondria devoid of inclusions and 4) mitochondria containing matrix granules.

In strontium-incubated tissue, significant evidence of strontium localization was only seen in mitochondria (or parts of mitochondria) containing several granules. In our analysis conditions (PET crystal, Lα line) the wavelength dispersive spectrometer does not provide enough sensitivity to determine for example if the reticulum contains strontium or only osmium.

The sensitivity was far better for calcium (PET crystal, Kα line). On a control specimen, the granule-containing mitochondria gave counts up to 1244 (with a background of 78) in 40 sec.. Ten counts were made for each of the four organelles or areas listed above ; their means ($\pm$ s.d.) are respectively : 1) 26 ± 6, 2) 98 ± 24, 3) 58 ± 16, 4) 494 ± 197. The greater range of results for granule-containing mitochondria appears to be due to the extreme density of calcium in the granules : the count for a given analyzed area seems related to the number and size of these inclusions. Using homogeneity analysis, the results for 1), 2) and 3) are significantly different from each other and particularly the calcium density of myofilaments is greater than that in granule-free mitochondria ($P < 0.001$).

We performed similar measurements on a block which has been incubated in calcium-rich/potassium-rich artificial sea-water. The results are : 1) 18 ± 6, 2) 74 ± 14, 3) 71 ± 15, and there is no significant difference between mitochondria and myofilaments. Considering that the section analyzed was probably thinner than the control, these results cannot be directly compared with the former but it is stressed that within a given section, this change in calcium distribution is probably due to the incubation treatment.

The physiological significance of this calcium distribution is debatable since most of the analyzed calcium could have been displaced during the fixation procedure (see for example Yarom *et al.*, 1974). However, the differences found in different experimental conditions demonstrate changes in the capacity of the fixed tissue to store calcium, which can be related to the state of the calcium-binding proteins at the time of fixation.
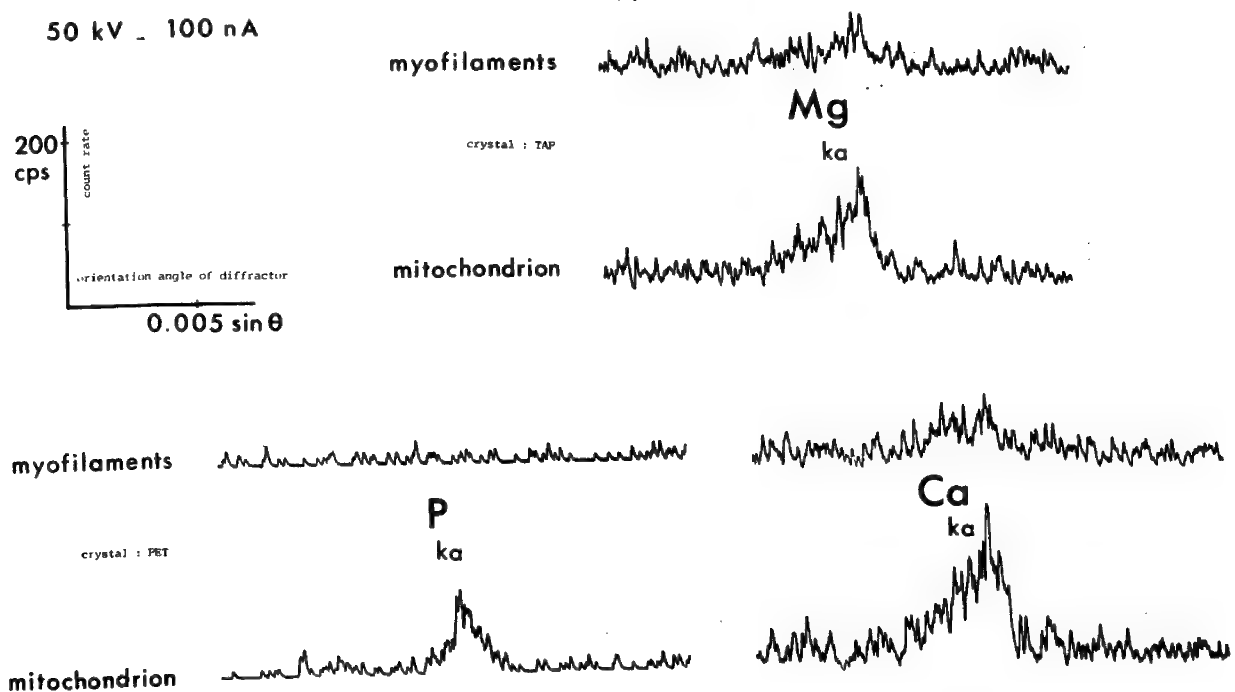
Fig. 2. Wavelength spectra for Kα lines of Mg, P and Ca on a mitochondrial area containing 6 granules and on myofilaments nearby.

Certainly the mitochondria *in situ* are able to store large amounts of calcium in their matrix granules. Further experiments are needed to show how and when these organelles release their stored calcium. In these experiments, more micro-analysis will be needed as osmium largely contributes to the electron opacity of the intramitochondrial granules.

A qualitative investigation of the magnesium and phosphorus content of these granules was performed on control tissue for comparison with the homologous inclusions known in mammalian mitochondria (Pasquali-Ronchetti *et al.*, 1969). Wavelength spectra were recorded for magnesium, phosphorus and calcium from a mitochondrial area containing six granules and from the myofilaments nearby (fig. 2). Two conclusions can be drawn : i, the chosen model resembles mammalian tissue, ii, attention (and spectrometers) should be focused on magnesium in the future studies of intramitochondrial matrix granules and their possible role in muscle physiology, if one considers the frequent interaction between calcium and magnesium in cell metabolism.

REFERENCES

HERNANDEZ-NICAISE M.L. (1976). Sites d'accumulation du strontium dans une fibre musculaire lisse géante. *J. Micr. Biol. Cell.*, 27, 14a.

PASQUALI-RONCHETTI I., GREENAWALT J.W. and CARAFOLI E. (1969). On the Nature of the Dense Matrix Granules of Normal Mitochondria. *J. Cell Biol*, 40, 565-568.

YAROM R., PETERS P.D. and HALL T.A. (1974). Effect of Glutaraldehyde and Urea Embedding on Intracellular Ionic Elements. X-ray Microanalysis of Skeletal Muscle and Myocardium. *J. Ultrastruct. Res.*, 49, 405-418.

MATURATION OF MEMBRANE TRANSPORT FUNCTION IN DOG RED BLOOD CELLS:

AN ELECTRON PROBE STUDY

R. Gary Kirk[1], Ping Lee[2] and D.C. Tosteson[1]

[1]Department of Pharamcological and Physiological Sciences,
The University of Chicago, Chicago, Illinois   60637 and
[2]Department of Physiology and Biophysics, West Virginia
University, Morgantown, West Virginia   26506.

In this study we analyse the K, Na and Fe in mature red blood cells and bone marrow cells of dog to understand the sequence of events in the maturation of membrane transport function and hemoglobin production during erythropoiesis. We have chosen to study this problem in dog because, in contrast to humans which have high potassium (HK) red cells, and to sheep and cattle which have either high or low potassium (LK) red cells, the dog has only LK red cells. The erythroblastic stem cells in the bone marrows presumably are of HK type. Therefore transformation of these HK stem cells to LK red cells must occur at some point during differentiation and maturation of the erythroblasts in the bone marrow.

In genetically LK sheep, Blunt and Evans (1963) have found that young red cells entering the circulation during rapid hematopoiesis after massive hemorrhage contain more potassium than the cells which are normally released into the circulation. Lee, Woo and Tosteson (1966) subsequently found that modification of membrane cation transport properties precedes the loss of high potassium content in these young cells. This finding is consistent with the demonstration by Tosteson and Hoffman that cation composition in HK and LK sheep red cells is determined by the pump and leak parameters of the membrane and that a change in these parameters will result in an alteration of the cation composition (1960). For this reason we have taken the changes in K and Na content and ratio of K/Na in the cells as indications of the changes in membrane transport properties. In this study we consider the iron (Fe) content to be synonymous with the hemo-globin content and any increase in iron as indicative of an increase in hemoglobin. This treatment is acceptable because Fe uptake into the marrow cells is normally very rapid and after entering the cell the Fe is incorporated into the hemoglobin. The incorporation is nearly complete and occurs within a few minutes (Noyes, Hosain and Finch, 1964; Ganzonic, 1969). By studying the relationship between K/Na ratio and the Fe concentration we can deduce the time-course of the matura-tion of the membrane transport function in relation to hemoglobin synthesis.

Red blood cells of dogs were obtained by drawing blood into heparinized tubes. The blood was washed 4x with ice-cold $MgCl_2$ (0.12 M) by repeated centri-fugation (350 g, 5 min.) and resuspension of the cells in the $MgCl_2$ solution to remove all the white cells and the sodium and potassium ions in the plasma. To obtain the bone marrow, the center sections of femurs were used in order to reduce the level of blood contaminating the marrow cell preparations. The marrow cells were collected by flushing the marrow cavity with cold NaCl (0.155 M) containing heparin (1 unit/ml). These cells were then washed free of Na by centrifugation and resuspension in $MgCl_2$ (0.12 M). For electron probe analysis the cells were sprayed onto pyrolytic graphite discs as described previously by

Lechene, Bronner and Kirk (1977). Samples were then analysed for K, Na and Fe with (1) an ETEC Autoscan microscope equipped with two automated wavelength spectrometers and light optics, (2) a raster which scanned an area (8μ x 8μ) containing a single cell, (3) a 15 KV accelerating voltage and (4) a beam current of 100 nA.

Figure 1A shows the relationship between X-ray intensity due to Na and that due to Fe in single mature red cells. A linear relationship between the two quantities indicates that the water content of mature red cells is directly proportional to the hemoglobin content because Na is the major cation in dog red cells and therefore can be used as an indicator for water content. In order to obtain an estimate of the range of variation in hemoglobin concentration in mature red cells, values for Fe/(K + Na) were computed. It is seen that these values have a variation of about 2.5 fold (Figure 1B) in contrast to the almost 6-fold variation in the Fe content (Figure 1A). We interpret these results to mean that there is a wide range of variation in hemoglobin content and that the variation in volume of these cells is considerably more than the variation in hemoglobin concentrations. All the red cells show a very low K/Na ratio irrespective of their hemoglobin concentration indicating that upon entering circulation the red cells are already of low potassium type. About 30% of the circulating red cells contain higher Fe levels than bone marrows cells suggesting the occurrence of hemoglobin synthesis in the circulating blood. This result is consistent with the facts that more than 50% of the hemoglobin synthesis occurs during the reticulocyte stage (i.e. after extrusion of the nuclei from the normablasts) and that as high as 14% of the total red cell hemoglobin is synthesized after the reticulocytes have entered the circulation in the red cells of mice and men (Papayannopoulou and Finch, 1975). Bone marrow cells contain higher levels of K and Na than circulating red cells. Most of these cells having high hemoglobin concentration (indicated by the Fe/(K + Na) ratio) are cells with low K/Na ratios (Figure 1D). In addition, an appreciable number of cells with low hemoglobin concentration have low K/Na ratios. These results indicate that membrane transformation from HK to LK type must occur fairly early during the differentiation of the erythroblastic stem cells. It occurs before hemoglobin synthesis is appreciable and probably even before the normablasts lose their nuclei to become reticulocytes. In this regard it may be noteworthy that in dogs the stress reticulocytes produced after hemorrhage do not have the same high K content as in sheep stress reticulocytes. From these results it is reasonable to conclude that the maturation of membrane transport function in dog erythroblastic cells is completed earlier than that of LK sheep cells.

References

1. Blunt, M.H. and J.V. Evans. 1963. Changes in the concentration of potassium in the erythrocytes and in hemoglobin type in Merino sheep under a severe anaemic stress. Nature 200:1215.

2. Ganzoni, A.M. 1969. Iron uptake and heme synthesis in rat reticulocytes. Helv. Med. Acta 34:416.

3. Kirk, R.G., M.A. Crenshaw and D.C. Tosteson. 1974. Potassium content of single human red cells measured with an electron probe. J. Cell. Physiol. 84:29.

4. Lechene, C.P., C. Bronner and R.G. Kirk. 1977. Electron probe microanalysis of chemical elemental content of single human red cells. J. Cell. Physiol. 90:117.

5. Lee, P., A. Woo and D.C. Tosteson. 1966. Cytodifferentiation and membrane transport properties in LK sheep red cells. J. Gen. Physiol. 50:379.

6. Noyes, W.D., F. Hosain and C.A. Finch. 1964. Incorporation of radioiron into marrow heme. J. Lab. Clin. Med. 64:574.

7. Papayannopoulou, Thalia and C.A. Finch. 1975. Radioiron measurements of red cell maturation. Blood Cells 1:535.

8. Tosteson, D.C. and J.F. Hoffman. 1960. Regulation of cell volume by active cation transport in high and low potassium sheep red cells. J. Gen. Physiol. 44:169.

Acknowledgements
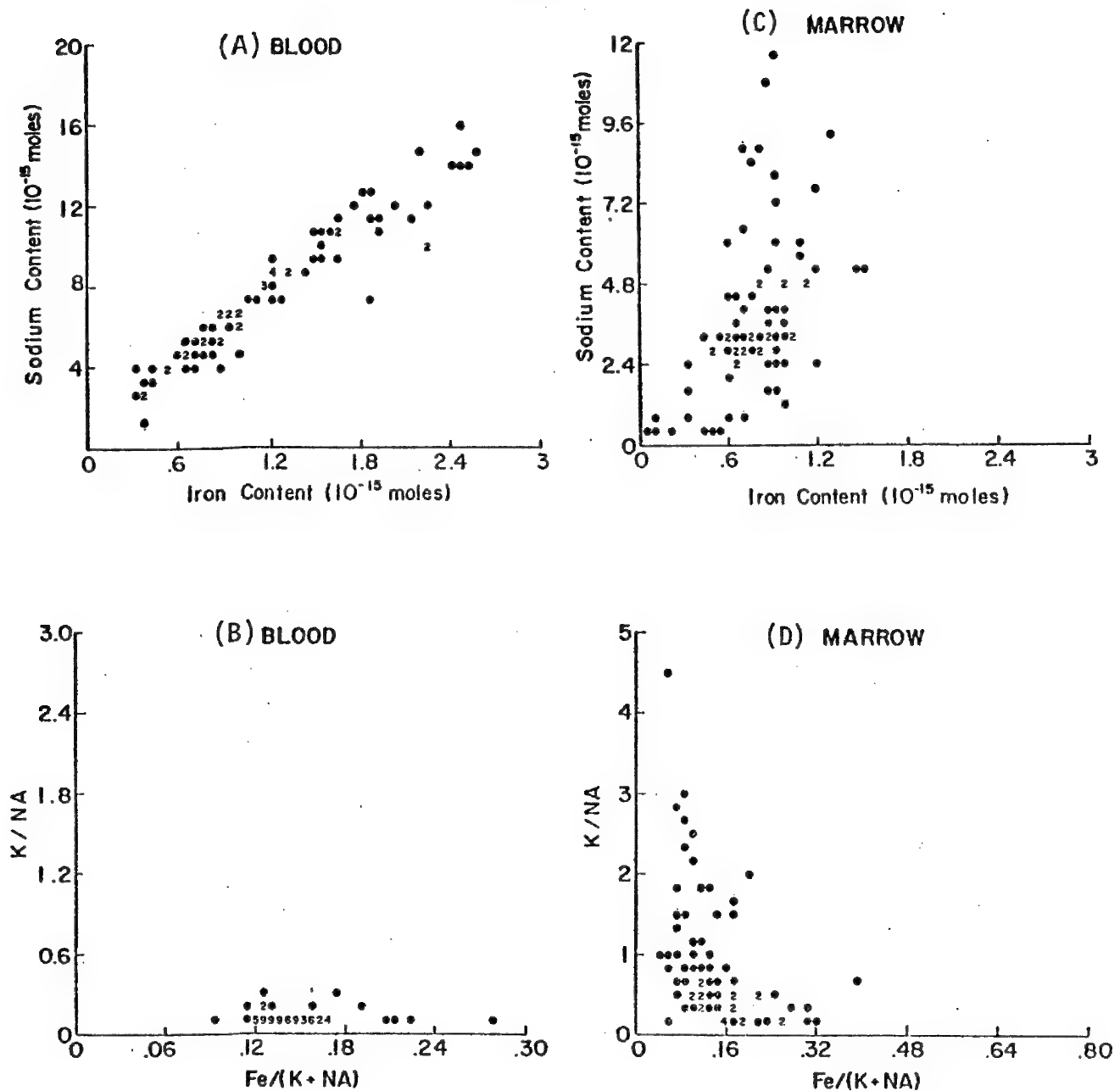
Figure 1. Comparison of Fe and Na contents (A, C upper graphs) and relationships of K/Na and Fe/(K + Na) content ratios (B, D lower graphs) in dog red blood cells and bone marrow cells. Circles locate results obtained from single cells and the numbers give the number of cells located at a given point. The ratios are ratios of total contents which have been calculated from calibration curves previously described by Kirk, Crenshaw and Tosteson (1974).

X-RAY MICROANALYSIS OF ACTIVE TRANSEPITHELIAL
Na TRANSPORT IN AMPHIBIAN SKINS:
EVIDENCE FOR A SYNCITIAL Na TRANSPORT COMPARTMENT

Roger Rick, Adolf Dörge, Klaus Gehring, Richard Bauer,
Anthony D.C. Macknight, Alexander Leaf and Klaus Thurau.

Physiologisches Institut der Universität München, 8 München 2,
Pettenkoferstraße 12, W.- Germany.

In epithelia such as frog skin or toad urinary bladder, which are
composed of several different cell types and layers, the question
arises wether all cells or only one distinct cell type shares in
the active transport of Na. In an attempt to answer this question
the electrolyte concentrations in individual epithelial cells un-
der various functional states of transepithelial Na transport were
determined by X-ray microanalysis. The measurements were performed
on 1 um thick freeze-dried cryosections in a scanning electron
microscope to which an energy dispersive X-ray detector had been
adapted. Quantification of electrolytes was achieved by comparing
the X-ray intensities obtained in the cells with those of an in-
ternal albumin standard. The experiments were performed on iso-
lated pieces of frog abdominal skin and toad urinary bladder,
which were incubated in Ussing-type chambers under short-circuited
conditions.
Fig. 1 shows the cellular Na concentrations (in mmole/kg wet wt)
of the various epithelial layers of the frog skin under control
condition, both sides of the skin bathed with NaCl Ringer's so-
lution, and after addition of 10^{-4} M ouabain to the inner bathing
solution. In the control the average Na concentration of all cell
layers, except the dead outer cornified layer, was 9 mmole/kg
wet wt. After inhibition of the active Na transport step by oua-
bain, the Na concentration increased to 109 mmole/kg wet wt. This
effect was almost completely abolished by simultaneously blocking
the Na influx from the outside bathing solution by using either
Na-free solutions or by adding amiloride (10^{-4} M). The increase
in cellular Na could be reversed when after ouabain, Na was

removed from the outer bathing solution. This effect was not observed when, by adding amiloride, the Na efflux to the outer medium was prevented.

As shown in Fig. 2 the changes of the cellular Na concentrations were accompanied by almost identical but reciprocal changes of the cellular K values. After ouabain the K concentration decreased from 115 to 14 mmole/kg wet wt. No changes occured when together with the inhibition of the active transport step the influx of Na was blocked by removing Na or adding amiloride. The decrease of cellular K could be even reversed when, after ouabain the outside bathing solution was replaced with a Na-free solution. With Na-free solutions containing amiloride this effect could not be observed.

From this data it has to be concluded that all layers of the frog skin epithelium exchange their Na predominately with the outside bathing solution. This view is supported by the finding that almost no change in cellular Na occured after replacing the inside bathing solution by Na-free isotonic solutions, while replacing the outside bathing solution by distilled water resulted in a decrease of Na to almost zero in all epithelial layers. Since in frog skin epithelium only the outermost living cell layer, the stratum granulosum, is directly exposed to the outer bathing medium the observed Na exchange of the deeper epithelial layers with the outside bathing solution can only occur via intercellular junctions to the superficial layer. Thus, with regard to active transepithelial Na transport the epithelium of frog skin can be regarded as a functional syncitium. A possible exception may represent the rare mitochondria-rich cells and the cells of the epithelial glands, which showed a different behavior under some experimental conditions.

Similar results have been obtained for the toad urinary bladder epithelium. Although the basal cells of this epithelium have no direct access to the mucosal bathing solution, they exchanged their Na mainly with this side, thus indicating that also in this epithelial structure intercellular communications exist between the different epithelial layers.
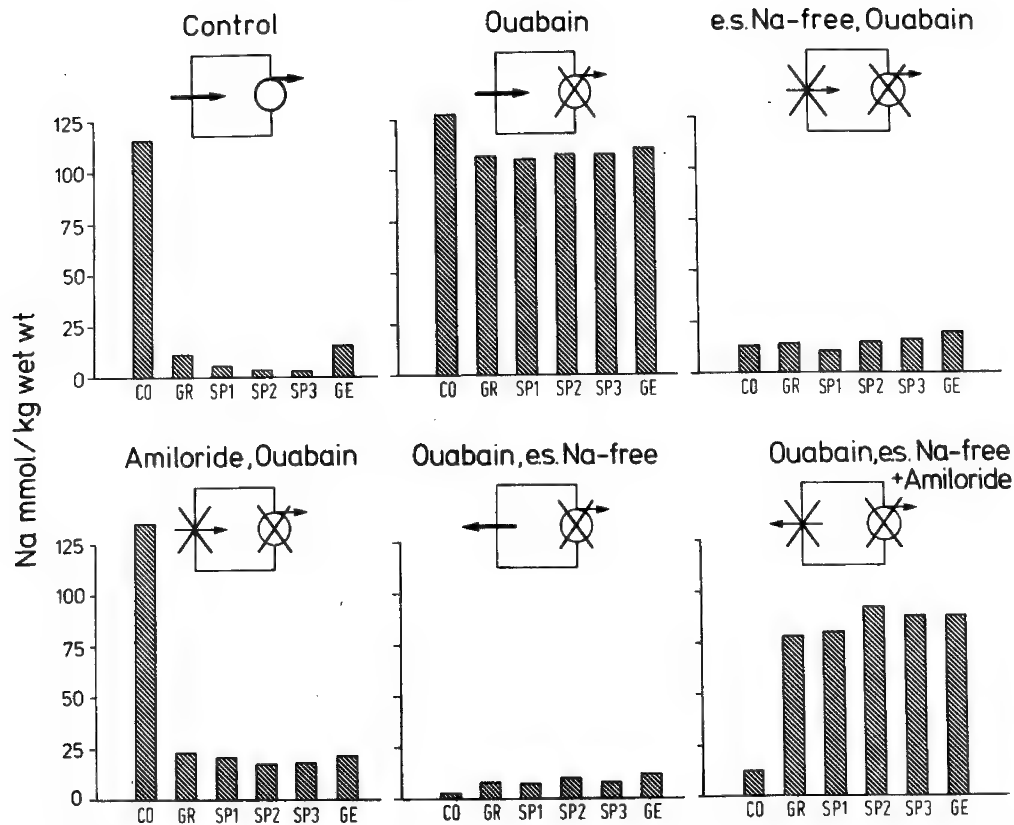
Fig. 1: Cellular Na concentrations of the various epithelial layers of frog skin under different experimental conditions; cornified (CO), granular (GR), spinal (SP) and germinal (GE) cell layer.
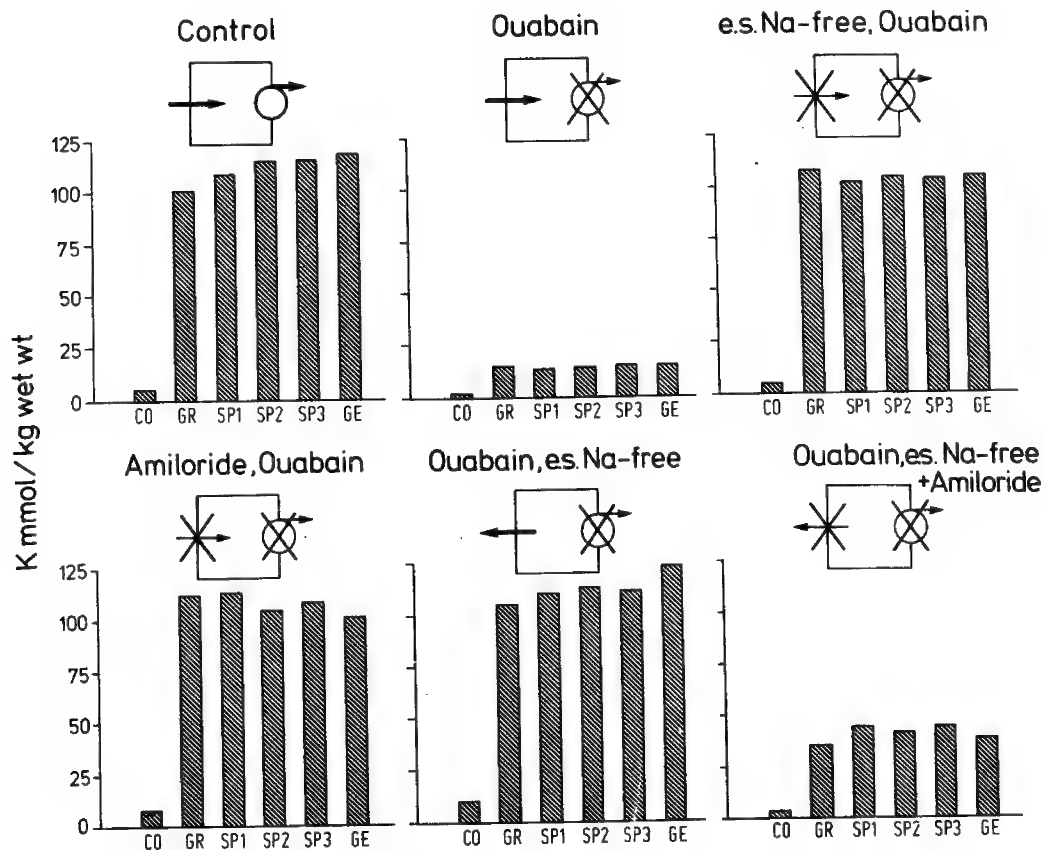
Fig. 2: Cellular K concentrations of the various epithelial layers of frog skin under different experimental conditions.

SPECIMEN DAMAGE CONSIDERATIONS IN CHOOSING THE PROBE FOR THE MICROANALYSIS OF THIN BIOLOGICAL MATERIALS

Janos Kirz

W. W. Hansen Laboratories of Physics
Stanford University, Stanford, CA 94305, and

Department of Physics
State University of New York, Stony Brook, N.Y., 11794*

David Sayre

IBM T.J. Watson Research Center
Yorktown Heights, N.Y., 10598

James Dilger

Department of Physics
State University of New York, Stony Brook, N.Y., 11794

For the study of the major constituents of thin biological specimens the analysis of the emitted characteristic x-rays is - at least in principle - a low background procedure. The limitations are well known:[1]

a) With the electron probe the specimen must be in vacuum. Dehydration and heavy coating with a conducting layer may lead to substantial distortions. Proton probes[2] and x-ray probes[3] have been used to overcome this problem.

b) Detection and analysis of the ultrasoft x-rays from C, N, and O is a difficult instrumental problem. One way around it is to ignore the x-rays, and analyze the energy loss suffered by the transmitted electron probe instead[4].

c) The yield of characteristic x-rays is low for the light elements due to the low fluorescence rate. More intense probes, and patience would solve this problem, except that,

d) Radiation damage limits the exposure to an amount $< 10^9$ rads $< (10^4$ joules/gram absorbed energy). For higher exposures substantial mass loss and changes in composition are observed[5], unless the specimen is kept at cryogenic temperatures, or is protected by a thick metal coating.

As this last effect appears to be the ultimate limitation of the technique, we calculate the minimum detectable mass, MDM as a function of the radiation dose, and the nature of the incident probe. We find that [6]

$$MDM > 7 \times 10^{-30} \frac{1}{D} \left[\frac{A}{\sigma\omega} \ \frac{1}{\rho} \frac{dE}{dX} \right] \qquad (1)$$

where D is the radiation dose in rads; A is the atomic weight, σ the cross section for K shell vacancy formation, and ω the fluorescence yield for the element under investigation. $\frac{1}{\rho}\frac{dE}{dX}$ is the stopping power of the specimen for the given probe. We find that for fast charged probes (electron energies above 10 keV, proton energies above 5 MeV) incident on typical biological material the bracketed term in (1) is 10^{24} MeV/gram for all light elements (6 < Z < 20) to within a factor of 3. The limit on MDM at 10^9 rads becomes 7×10^{-15} grams.

For x-ray microprobes the MDM depends both on Z and on the energy of the x-ray probe, the most favorable energy being just above the absorption edge. This choice leads to a MDM at 10^9 rads which varies between 10^{-16} grams for Z=6 and 7×10^{-18} grams for Z=20. X-ray microprobes appear therefore to have the best potential sensitivity for Z > 10.

For lighter elements transmitted electron energy loss analysis is the most favorable from the damage point of view. For 10^9 rads we find MDM > 10^{-17} grams for Z=6, but for Z=20 MDM rises to 10^{-15} grams.

---

* permanent address.

1. T. A. Hall in Physical Aspects of Biological Research, G. Oster, Ed. Vol I, 1971. Academic Press, New York.

2. P. Horowitz et al. Science 194, 1162 (1976).

3. P. Horowitz and J. A. Howell, Science 178, 608 (1972). W. A. P. Nicholson in Microprobe Analysis as Applied to Cells and Tissues, T. Hall, P. Echlin, and R. Kaufman Eds. Acad. Press. 1974.

4. M. Isaacson and D. Johnson, Ultramicroscopy 1, 33 (1975). C. Colliex et al. Ultramicroscopy 1, 301 (1976).

5. M. S. Isaacson in Principles and Techniques of Electron Microscopy, M. A. Hayat Ed. Vol 7, 1976; Van Nostrand Reinhold Publ. New York.

6. J. Kirz, D. Sayre and J. Dilger, Ann. N.Y. Acad. Sci. in press.

ELECTRON PROBE ANALYSIS OF FLUORINE UPTAKE IN MINERALIZED TISSUES

John W. Edie

Dows Research Institute
College of Dentistry
University of Iowa
Iowa City, Iowa 52242

The incorporation of Fluorine in human enamel has long been thought to be an important caries preventative. This has prompted the attempt to enhance F levels in teeth through external means, such as fluoridated drinking water and tooth pastes. A more recent concern is the possible adverse effects F may have on normal body functions. For instance, increased susceptibility to cancer may be suggested from data comparing death rates in fluoridated water regions with those in non-fluoridated regions. It is believed that F input to the body will exceed F output and that a major reservoir for this excess is mineralized tissue. For these reasons, the analysis of F in mineralized tissue, bone as well as teeth, is important in caries research and in attempts to understand possible health hazard implications.

A common method of F analysis uses the F electrode, which requires acid dissolution and a need for relatively gross specimens. The accuracy of the technique is good, but variations of F level, as perhaps associated with morphological features, are not possible to discern using this method. Electron probe microanalysis offers the potential to determine F levels to a few hundred parts per million with at least moderate accuracies and with spatial resolutions approaching a micrometer.

A common method of specimen preparation for mineralized tissue is in the form of embedded, sectioned and polished blocks. However, mineralized tissues with substantial proportions of organic matrix or plastic present have been observed to influence characteristic x-ray count rates (1). The changing light element composition of the specimen, as a result of electron irradiation (electron dose $\gtrsim 10^{-9}$ C/um^2), produces a dynamic counting condition which adversely affects absolute quantitation and interpretation. The effect can be controlled using a deproteination technique (2) and an embedding medium with rapid polymerization, low penetration characteristics. Care must also be taken to prevent an accumulation of ground material on the surface of the polished specimen.

For greater x-ray spatial resolution, it is usually advantageous to examine long wavelength x-ray emissions from an infinitely thick, low density specimen using low accelerating voltages (3). However, F levels in mineralized tissues will frequently be quite reduced ($<$ 500 ppm) and it is important to maximize the F counting conditions to improve the detection limits. Figure 1 shows the F count rate sensitivity on a fluoro-apatite (FAP) crystal standard for a range of accelerating voltages. The data was acquired on an ARL EMX-SM microprobe using an RAP crystal and a proportional detector with a stretched polypropylene window. The sensitivity (P), peak to background ration (P/B) and P^2/B ratio are displayed on a scale normallized to the maximum value. The minimum limit of detection exists for maximum P^2/B, which is observed to occur around 12 kV. This voltage is routinely used for analyses of mineralized tissues in our laboratory, but at the expense of optimal x-ray spatial resolution.

There are complications in F analysis that are caused by electron irradiation. Figure 2 displays the F count rate on a FAP standard for selected accelerating voltages as a function of electron dose. The count rates are normallized to initial count rates. The FAP standard exhibits stable count rates for the heavier constituents, Ca and P, over wide ranges of electron irradiation for these same accelerating voltages. The strange behavior for F count rates on FAP, as noted in Figure 2, must reflect a changing environment for F in the crystal due to energy transfer or thermal effects. Note that for an accelerating voltage of 12 kV, the count rate increase will be only a few percent for electron doses less than 10^{-8} C/um^2. Similarly, the count rate is observed to increase almost 50% for more prolonged exposures. This effect limits either the detectability limit for F or the x-ray spatial resolution, for the usual method of increasing electron dose to improve x-ray statistics will reduce the measurement reliability unless electron beam diameter is increased.

A wide variety of mineralized tissues have been examined under the conditions of 12 kV accelerating voltage and $\gtrsim 10^{-8}$ c/um^2 electron dose. A typical example would be that of a pelvic bone biopsy along the Iliac crest obtained from a patient with kidney disease.* The patient was known to have

* The specimen was provided by Dr. D. Taves, Pharmacology, Univ. of Rochester, N.Y. and Dr. F. Parkins, College of Dentistry, Univ. of Iowa, Iowa City, Iowa.

elevated F levels due to an inability of the kidney to excrete F in the urine. Figure 3 shows a survey SEM of the specimen prepared for microprobe analysis. The regions analyzed for F uptake were from the exterior edge of the cortical plate (CP) to the bone interior and across the filamentous trabecular bone. Figure 4 is a BSE image of a region of the cortical plate. The analysis proceeded in 10 μm steps from the outer edge on the right and proceeded to the left across the entire bone (see irradiation mark). The uncorrected F weight percents were estimated using the FAP crystal as standard and are displayed in Figure 5. Most mature mineralized tissue is sufficiently similar to FAP (especially if the organic matrix is removed and there is no plastic present) that the magnitude of the ZAF correction will be substantially less than other contributing systematic errors. The uncorrected F Wt.%'s should therefore be good approximations to actual concentrations if irradiation effects are minimized.

It is obvious that extensive variations in F content exist in the step scan. Repeated runs yielded average values of 2600 ppm F (N=98, S.D.=800 ppm) for the cortical plate region and 6110 ppm F (N=24, S.D.=120 ppm) for the interior filamentous bone region. An adjoining specimen had been analyzed using a F electrode and was found to possess a F concentration of 2586 ppm. This value compares favorably with an average microprobe value over the entire bone specimen, especially when microprobe results are corrected for the omission of the organic matrix. Of greater importance, however, is the immense variation in F content within the specimen. Step scans over regions similar to those shown in Figure 4 indicated F levels on exterior edges up to 15,000 ppm, while interior values could be less than 500 ppm--a relative F content variation approaching 50 times.

The above illustration is but one of many analyses of bone, enamel and dentine in our laboratory. A summary of the observations made as a result of these analyses would be:

1. Outer surface regions of mineralized tissue which has been exposed to fluids with F content will incorporate the F within the tissue. The level of F uptake on the exterior surface is directly related to the F concentration in the fluid.

2. An exponential diminishment of F into the tissue takes place from the exposed surface. This apparent diffusion of F into the tissue is dependent upon the state of mineralization of the tissue. In

highly mineralized tissue, such as enamel, the F content will diminish to uniform interior values in 10-30 μm, while the distance may exceed 100 μm for bone and dentine.

3. Either measurement precision or x-ray spatial resolution is sacrificed in the microprobe analysis of F in mineralized tissues. The dynamic x-ray counting effects resulting from electron exposure would be more likely to give somewhat elevated results for F. However, there is apparent good agreement with average values obtained from gross specimens using other means of analysis.

REFERENCES

1. Edie, J. and P. Glick. Dynamic effects on quantitation in the electron probe analysis of mineralized tissues, Proc. Eleventh Nat. Conf., Microbeam Anal. Soc., Miami (1976), 65A-65F.

2. Termine, J., E. Eanes, D. Greenfield and M. Mylen. Hydrazine-deproteinated bone mineral, Calc. Tiss. Res. 12, 1973, 73-89.

3. Andersen. C. An introduction to the electron probe microanalyzer and its application to biochemistry, Methods of Biochem. Anal., Vol. 15, D. Glick, Ed., Interscience, N.Y., 1967, 147-270.
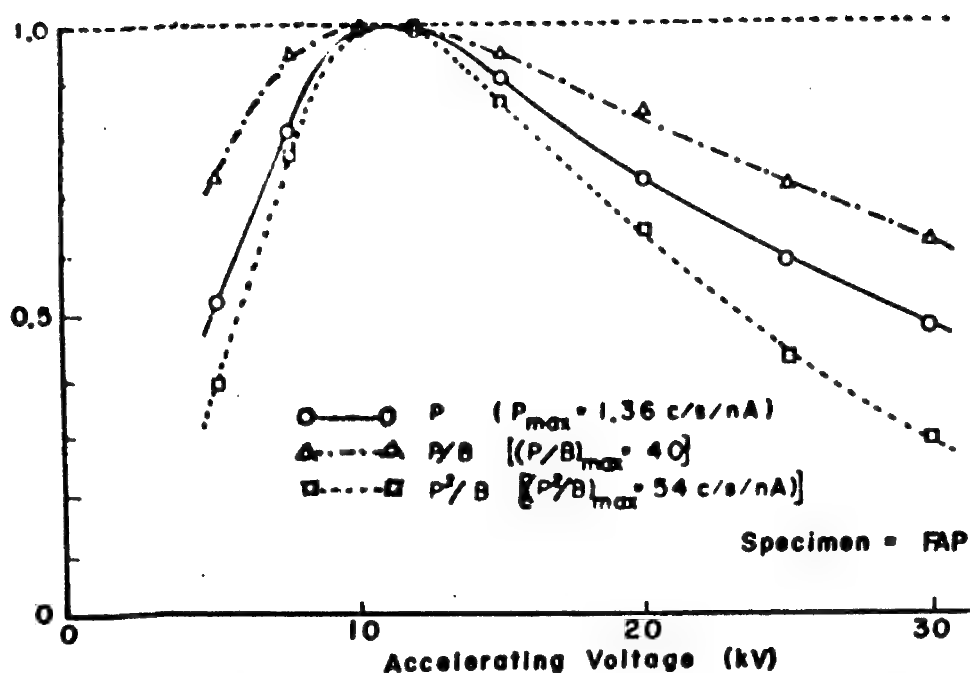
Figure 1. F sensitivity, peak to background ratio and P^2/B for a range of accelerating voltages is displayed. Values normallized to maximum values are shown. The specimen was a fluoro-apatite (FAP) crystal.
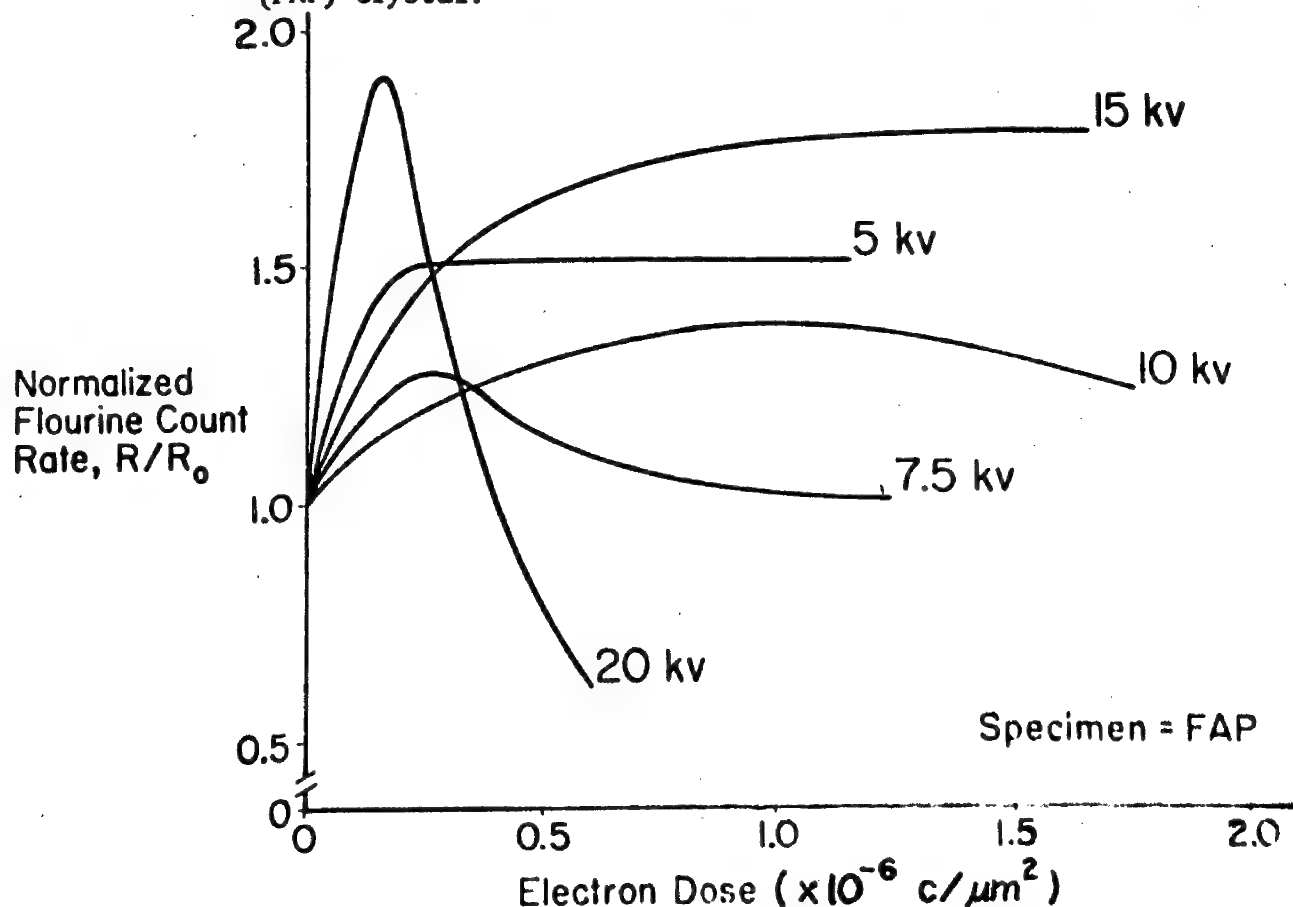
Figure 2. F count rate is plotted as a function of electron dose for selected acceleration voltages. The count rates normallized to initial values on a FAP crystal are shown.
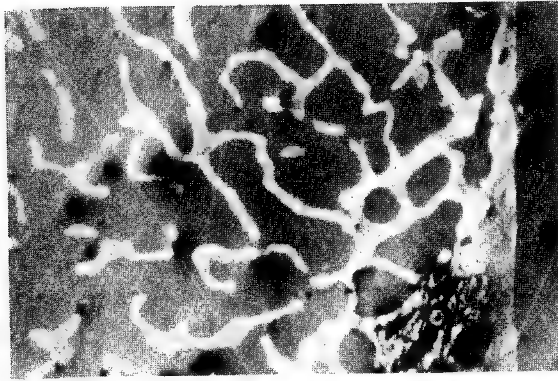
Figure 3. A survey SEM image of a pelvic bone biopsy prepared for microprobe examination is shown. Analysis regions were the cortical plate region and the interior filamentous bone. Magnification about 30x.

Figure 4. A BSE image of an isolated region of the cortical plate for the specimen displayed in Figure 3. A step scan, using 10 um increments, proceeded from the right-hand exterior surface through the interior of the bone (see irradiation mark). Magnification about 225x.
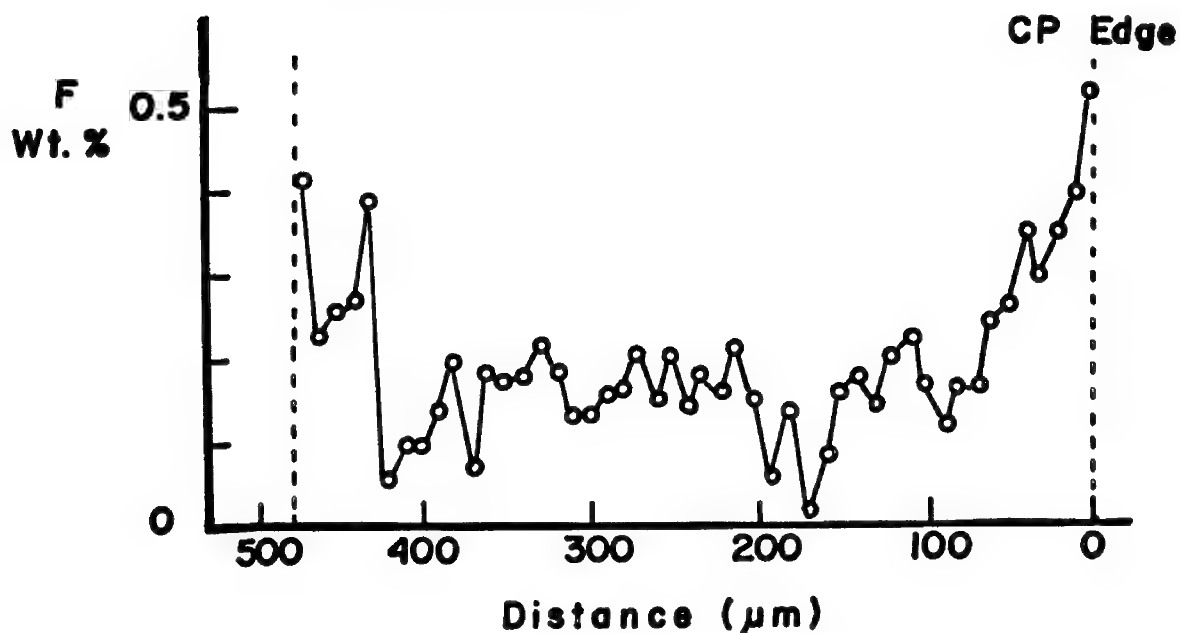
Figure 5. The uncorrected F weight concentrations for points along the step scan of Figure 4 are shown. The standard was a FAP crystal and the operating parameters included 12 kV accelerating voltage and less than 10^{-8} C/um^2 electron dose for each analysis point.

X-Ray Microanalysis of

Calcium Phosphate Solids Prepared Anhydrously

as Calibration Standards for Mineralized Tissues

William J. Landis
Department of Orthopaedic Surgery
Harvard Medical School
Children's Hospital Medical Center
Boston, Massachusetts 02115

The fine structure and organization of bone and other mineralized tissues have been characterized principally by electron optical and analytical studies utilizing aqueous methods of sample preparation, including conventional procedures with osmium, glutaraldehyde, and other chemical fixatives diluted in water. Although much information has been obtained from such investigations, the precise composition of the calcium phosphate mineral deposits in hard tissues remains uncertain, partly because these routine techniques have failed to reduce or eliminate the significant changes induced in the mineral by aqueous solvents. It has been demonstrated, for example, that aqueous methods of tissue fixation and preparation lead directly to translocation of diffusible ions (9), dissolution and reprecipitation of mineral salts (1,2,6,10,11), and mineral phase transformations (6,10). Consequently, when such aqueous procedures are used, it is difficult to interpret clearly morphological features observed or microanalyzed and, in particular, to determine accurately the composition and nature of the calcium phosphate deposits in hard tissue and their relationship to certain intracellular and extracellular tissue components.

In order to obtain by x-ray microanalysis more exact estimations of calcium and phosphorus in the inorganic deposits of bone and other mineralized tissues, a number of anhydrous techniques have been developed in this laboratory utilizing organic solvents (8) and ultracryomicrotomy (7) as alternative methods to conventional aqueous specimen preparation procedures. Previous analytical studies and x-ray diffraction (5,6), both of calcium phosphate solids precipitated in vitro and of bone mineral, have shown that

there is little or no detectable change in the mineral when it is exposed to certain organic solvents or to freeze drying, and quantitative measurements (5) and electron microscopy (8) have indicated that less than 2% of the total mineral mass is lost when only organic solvents are used for specimen preparation. This study presents the results of experiments utilizing x-ray probe micro-analysis to monitor changes in a number of synthetic calcium phosphate solids, prepared for examination by anhydrous means. The data obtained indicates that, compared to dry, untreated powder preparations, the calcium phosphate solid samples processed anhydrously show no significant changes in their calcium-to-phosphorus intensity ratios while the same samples exposed to aqueous solvents generate detectable differences.

Calcium phosphate solids prepared _in vitro_ included a calcium metaphosphate $[Ca(PO_3)_2$, experimentally determined molar Ca/P ratio = 0.50], monetite $[CaHPO_4$, molar Ca/P = 1.00], brushite $[CaHPO_4 \cdot 2H_2O$, Ca/P = 1.03], octacalcium phosphate $[OCP, Ca_8H_2(PO_4)_6 \cdot 5H_2O$, Ca/P = 1.34], an amorphous calcium phosphate solid prepared at neutral pH [ACP, Ca/P = 1.42], a poorly crystalline calcium phosphate containing some poorly crystalline hydroxyapatite [PC HA, overall Ca/P = 1.45], tricalcium phosphate $[Ca_3(PO_4)_2$, Ca/P = 1.50], and a well crystallized hydroxy-apatite $[Ca_5OH(PO_4)_3$, Ca/P = 1.62]. X-ray and electron diffraction patterns were obtained from the dry powders and compared with published values to confirm the appropriate solid structures. Electron microscopy was used to examine the morphology of the samples and to indicate whether more than one phase was present in a given preparation. The calcium and phosphorus composition of each individual solid was determined by wet chemical analysis (3,4) from which the above molar ratios were calculated. The particular solids selected were chosen so as to provide a wide range of calcium-to-phosphorus ratios and to include some of those samples which could possibly be present in the solid phase mineral deposits of bone and other hard tissues which were later to be examined.

The various synthetic calcium phosphate solids were prepared for x-ray probe microanalysis by a variety of techniques designed to follow the procedures used for the preparation of bone tissue (7,8). These included: (1) Individual dry powders used as controls by sprinkling them onto carbon-reinforced, parlodion-coated 75 mesh copper grids; (2) Samples of the same dry powders processed anhydrously in organic solvents (8) as follows: the dry solids were placed in Beem capsules filled with 100% ethylene glycol at room temperature and then into a vacuum desiccator on a shaker for 24 hours at 4°C. The capsules were centrifuged to sediment the powders and the glycol was replaced with

Cellosolve, the monomethyl ether of ethylene glycol. The Cellosolve was changed twice at 12 hour intervals, after which it was replaced with a mixture of propylene oxide-epon (1:1). After one week, the propylene oxide-epon mixture was replaced by epon. Embedded calcium phosphate solids were then thin-sectioned at ∿800Å on 100% ethylene glycol with diamond knives and collected on copper grids; (3) A technique used to simulate anhydrous ultra-cryomicrotomy (7), in which the dry samples were first frozen in Beem capsules to -196°C and then transferred to -70°C for six hours. They were collected by gently touching them to cold copper grids; (4) Calcium phosphate solids prepared using standard aqueous procedures (8), with fixation in either 2.5% glutaraldehyde or 2.5% glutaraldehyde-paraformaldehyde, dehydration in graded ethanols, and embedding in epon.

Following the preparation of all samples, a thin carbon film was evaporated onto the grids to stabilize the specimens in the electron beam. X-ray and electron diffraction patterns obtained from the treated solids showed no detectable changes in the minerals compared to the dry powder controls, with the exception of ACP. This sample on x-ray diffraction analysis demonstrated a phase transformation to poorly crystalline hydroxyapatite following aqueous fixation in both glutaraldehyde and glutaraldehyde-paraformaldehyde and its subsequent processing in the conventional manner.

X-ray probe microanalysis was performed using the same sections from which electron diffraction patterns had been obtained. This data, summarized in Table 1, was obtained with a JEOL JSM-35 scanning electron microscope equipped with a KEVEX x-ray detector and a Tracor Northern (NS-880) analytical system. Excitation energies of 39 keV and counting times of 100 seconds were used to examine between 5 and 10 individual mineral deposits on each grid. For estimations of calcium-to-phosphorus intensity ratios in specimens, the characteristic K_α emissions for each element were used. The number of counts under the elemental peak of interest (E) was integrated over an appropriate counting interval and from that figure was subtracted the value of background counts ($\bar{B}$). $\bar{B}$ was determined from the mean of the integrated counts from two small intervals, one on either side of the interval for the elemental peak E, using windows of five channels each with 20eV/channel. The quantity (E-$\bar{B}$) was obtained for both calcium and phosphorus generated from the mineral deposits (on peak) and the intensity ratio of the two elements was calculated as follows,

correcting for any counts generated away from the deposits (off peak):

$$I_{Ca/P} = \frac{[(E-\overline{B})_{\text{on peak}} - (E-\overline{B})_{\text{off peak}}]_{Ca}}{[(E-\overline{B})_{\text{on peak}} - (E-\overline{B})_{\text{off peak}}]_{P}}$$

Errors in the energy dispersive analysis of Table 1 are expressed as 2x standard deviation of the mean. The data show that anhydrous treatments utilizing organic solvents or ultracryomicrotomy do not significantly change the calcium-to-phorphorus ratios compared to dry powders. Aqueous treatments, on the other hand, clearly alter the ratios and produce greater standard deviation of mean values.

When the Ca/P intensity ratio is plotted as a function of Ca/P molar ratio for the selected calcium phosphate solids, a calibration curve is obtained for determining the Ca/P molar ratio of unknown specimens examined by x-ray microanalysis (Figure 1). Since the anhydrous methods employing organic solvents or ultracryomicrotomy do not significantly alter the physical and chemical characteristics of those synthetic calcium phosphate solids investigated by x-ray and electron diffraction and probe microanalysis, the techniques can be extended to examine calcium phosphate deposits in biological mineralized tissues, including bone, teeth, and calcified cartilage. This laboratory is proceeding in that direction.

References

1. Boothroyd, B., J. Cell Biol. 20, 165 (1964).

2. Boothroyd, B., in Steve-Bocciarelli, D. (Ed.), Electron Microscopy, Vol. II, p. 429. Tipografia Poliglotta Vaticana, Rome, 1968.

3. Clark, E.P., and Collip, J.B., J. Biol. Chem. 63, 461 (1925).

4. Dryer, R.L., Tammes, A.R., and Routh, J.I., J. Biol. Chem. 225, 177 (1957).

5. Glimcher, M.J., in Greep, R.O., and Astwood, E.B. (Eds.), Handbook of Physiology: Endocrinology, Vol. VII, p. 25. American Physiological Society, Washington, D.C., 1976.

6. Glimcher, M.J., and Krane, S.M., in Gould, B.S., and Ramachandran, G.N. (Eds.), A Treatise on Collagen, Vol. IIB, p. 68. Academic Press, New York, 1968.

7. Landis, W.J., Hauschka, B.T., Rogerson, C.A., and Glimcher, M.J., J. Ultrastruct. Res. In press.

8. Landis, W.J., Paine, M.C., and Glimcher, M.J., J. Ultrastruct. Res. In press.

9. Morgan, A.J., Davies, T.W., and Erasmus, D.A., Micron 6, 11 (1975).

10. Termine, J., in Slavkin, H.C. (Ed.), The Comparative Molecular Biology of Extracellular Matrices, p. 443. Academic Press, New York, 1972.

11. Thorogood, P.V., and Craig Gray, J., Calc. Tiss. Res. 19, 17 (1975).

Legends

Table 1. Quantitative x-ray microprobe Ca/P analysis of mineral standards prepared by anhydrous and aqueous means. Errors represent twice the standard deviation of mean intensity ratios. Molar ratios were experimentally determined by wet chemical analysis.

Figure 1. Ca/P intensity ratio as a function of Ca/P molar ratio for selected calcium phosphate solids. Data represents analysis from frozen-thawed solids in Table 1.

Table 1

QUANTITATIVE X-RAY MICROPROBE Ca/P ANALYSIS OF MINERAL STANDARDS

Treatment	Ca/P Intensity Ratio $(5 \le n \le 10)$							
	$Ca(PO_3)_2$	Monetite	Brushite	OCP	ACP	PC HA	$Ca_3(PO_4)_2$	HA
Dry Powder	0.60±.02	1.32±.09	1.36±.11	1.74±.10	1.88±.08	1.85±.16	2.02±.30	2.17±.27
Ethylene Glycol	0.59±.04	1.32±.11	1.35±.12	1.73±.25	1.90±.11	1.92±.14	1.88±.18	2.17±.32
Freeze-Thaw	0.60±.03	1.31±.10	1.35±.13	1.73±.14	1.90±.10	1.87±.14	1.92±.20	2.17±.25
Aqueous Glutaraldehyde	0.54±.04	1.22±.08	1.15±.05	1.59±.17	1.80±.35	1.80±.30	1.70±.10	1.70±.21
Aqueous Glutaraldehyde-Paraformaldehyde	1.52±.04	1.27±.11	1.17±.04	1.71±.26	1.74±.23	2.06±.48	1.71±.14	1.96±.13
Molar Ratio (Ca/P)	0.50	1.00	1.03	1.34	1.42	1.45	1.50	1.62

Figure 1
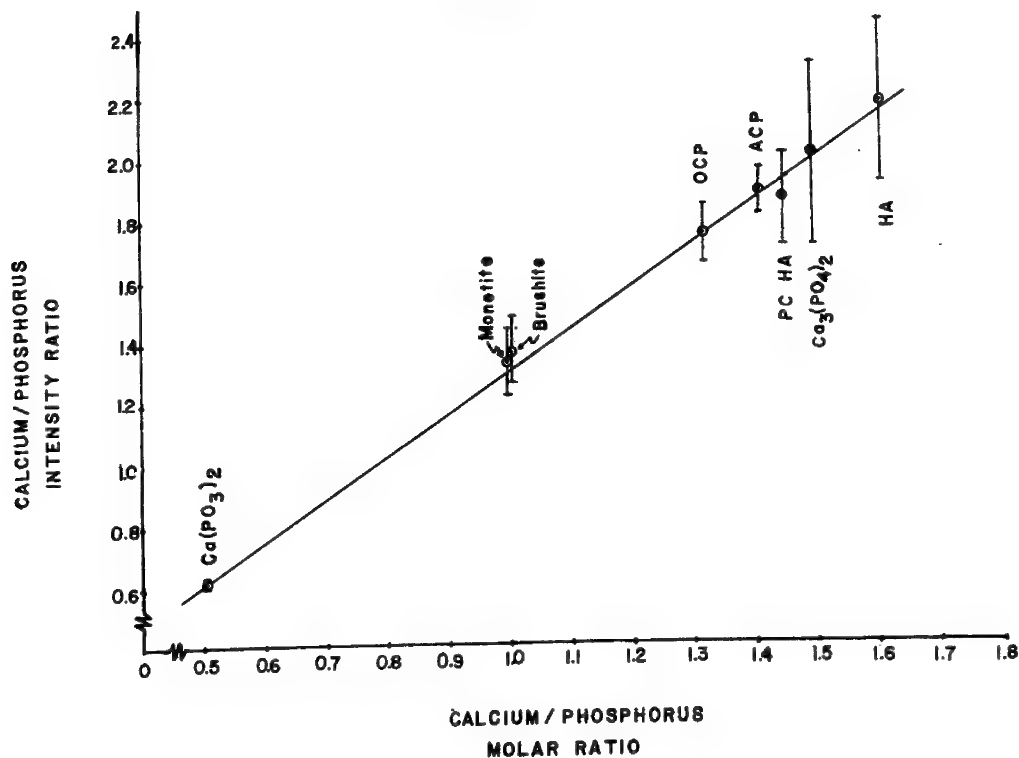
Figure 1

USE OF ELECTRON-BEAM LITHOGRAPHY IN THE FABRICATION OF MULTICHANNEL DEPTH PROBES FOR STUDIES OF NEURAL ACTIVITY*

P. Pochay, L. F. Allard, L. T. Rutledge and K. D. Wise
The University of Michigan, Ann Arbor, Michigan

Introduction

Solutions to a variety of problems related to the organization and function of the nervous system require electrophysiological data recorded at two or more spatial locations. In some cases the nature of the data required permits recordings to be made point by point with a single microelectrode. However, in other cases, the data must be recorded from the different locations simultaneously, necessitating the use of an array of recording electrodes. Historically, the required microelectrode arrays have been fashioned by cementing individual microelectrodes together,[1] by pulling bundles of glass capillary tubing into multiple micropipettes,[1,2] and more recently by using photoengraving techniques.[3-5] A new approach, reported here, uses electron-beam engraving to produce multiple recording sites on the surface of a metalized glass micropipette. There are several attractive features associated with this approach. The glass micropipettes are easily produced with commercial equipment. Electron-beam engraving permits micron-order accuracy in the definition and positioning of the recording sites. Virtually identical areas may be exposed at all recording sites resulting in fairly close matching of the recording impedance levels. The glass micropipette supporting structure can be produced with a very gradual taper which minimizes tissue damage, and the multiple recording sites reduce the number of

---

P. Pochay is with the Biophysics Program; L. T. Rutledge is with the Department of Physiology; L. F. Allard is with the Department of Materials and Metallurgical Engineering; K. D. Wise is with the Department of Electrical and Computer Engineering.

insertions which must be made. The devices described here are designed as depth probes for recording slow-wave activity in the brain.

Fabrication

The following procedure has been used to produce multiple independent recording sites on the surface of a single glass micropipette.

Micropipettes are drawn with a commercial puller from 1 mm O.D. glass capillary tubing. Puller controls are set to produce a gradual taper from about 10 μm diameter near the tip to about 20 μm diameter 2 mm from the tip. The entire tapered portion is about 1 cm in length. The tapered portion of each pipette is coated by vacuum evaporation with 200 $\overset{o}{A}$ of chromium followed by 2000 $\overset{o}{A}$ of gold. Pipettes are coated in batches of 10 or 12 and rotated during evaporation to insure a uniform coating.

The positive electron beam resist, polymethylmethacrylate (PMMA), is applied by lowering each pipette, tip first, into a solution of 5 gms of PMMA in 8 ml of chloroform and then withdrawing it slowly. This produces a coating varying in thickness from about 0.25 μm near the pipette tip, where the most critical engraving is required, to about 2 μm near the upper end of the taper. Coated pipettes are baked at $180^{o}C$ for 15 minutes.

Exposure of the electron-beam resist has utilized an ARL Model EMX-SM Electron Microprobe Analyzer. The beam was controlled by a pattern generator which was constructed to interface with the existing sweep circuits to produce a 64-scan raster. A pair of electrostatic deflection plates, added to the microprobe analyzer near the electron gun, is used to electronically blank the beam as required. A 1 KHz clock and binary counter, synchronized with the sweep drive, are used to scan a 1702A read-only memory (EROM) which contains a representation of the desired pattern in the form of 8 longitudinal lines. A second 1702A EROM controlled by the step generator, selects 1 of the 8 possible lines for any given sweep. The circuit is wired so that a 1 (high level) data bit from the EROM causes 90 volts to be applied to one deflection plate, effectively blanking the beam.

The PMMA-coated pipettes are lightly cemented into longitudinal grooves in short pieces of 3/16 inch hex rod. The rod holders are placed in horizontal 60° grooves cut radially in the top of a cylindrical carrier which fits into the microprobe analyzer and permits accurate indexing of rotation about the micropipette axis. Pipettes are positioned with tips extending toward the center of the carrier, which can hold nine pipettes at one time along with a small polished piece of willemite.

As the first step in the electron beam exposure procedure, the loaded carrier is placed into the microprobe analyzer and the willemite sample is located under the electron beam. The pattern generator is set to produce the front surface tip pattern (Fig. 1). Sample current is set at 0.9 nA and the beam is carefully focused. The sweep rate is about 1 μm/ms. The resulting fluorescent pattern on the willemite is roughly aligned with markings on an eyepiece reticule by small adjustments to the mechanical position controls of the optical microscope. Precise positioning and alignment are then accomplished by use of the electronic controls on the sweep-circuit time-base generators with adjustment of the magnification factor to bring the locations of the recording sites into registry with selected marks on the reticule. The beam is then blanked and a micropipette is aligned with the pattern location by means of the mechanical stage controls. The pipettes are viewed as silhouettes in transmitted light, the tips being used as reference points. The pipette is exposed once to the complete electron beam pattern. Then each of the other pipettes is exposed in a similar fashion. Upon completion of the batch, the carrier is removed from the microprobe analyzer and the pipettes are rotated 180°. The 1702A EROM producing the front surface pattern (Fig. 1) is replaced with one giving the pattern for the back surface. The alignment and exposure procedure is repeated to complete the definition of the tip electrode patterns.

At this point, the pipettes are removed from the microprobe, and developed in Methylisobutyl Ketone:n-propanol:(1:3) for 30 s, followed by heating to 120°C for 10 min. The metalization is then removed from exposed areas with commercial etchants and the results are inspected optically at 400X. Probes without serious defects are recoated with PMMA, baked at 180 C for 15 minutes and returned to

the microprobe analyzer. The metallization is now engraved to define a separate lead extending from each recording site up the shank to the external lead connections. The pattern generator is set to produce 10 parallel lines in the center of the field, covering an area 250 µm long by 5 µm wide. Each pipette in turn is positioned so that the exposed area will be parallel to the pipette axis and centered on the pipette surface. The first exposure is made so that the end of the exposed region just overlaps the end of the region where the metallization was removed in the previous step. After this exposure, the pipette is moved 250 µm along its axis, exposed again, and so on to the end of the metallization. When all pipettes have been exposed in this way, the carrier is removed, each pipette is rotated 120^{0} around its axis (for a three-channel pipette), and the series of line exposures is repeated. This series is followed by one more 120^{0} rotation about the pipette axis and a third line exposure series. Each pipette is then developed and etched to remove the metallization from the exposed lines. The PMMA is removed in chloroform and each of the 3 separate leads thus formed is connected at the upper end of the shaft to a length of 25 µm-diameter gold wire, using a small droplet of silver conducting paint to make electrical contact. The silver contacts are coated with a thin layer of epoxylite, which also is used to insulate the gold wire. The epoxylite is cured at $350^{0}C$ for 30 minutes, and the pipettes are recoated with PMMA as outlined above. They are then returned to the microprobe where the pattern generator is set to expose only the recording sites. Development in MIK:n-propanol:(1:3) for 30 s completes the processing.

Results

Figure 3 shows scanning electron micrographs of the recording sites on a bipolar device constructed by the above procedure. Figure 3a shows a continuous gold ring around the micropipette shank which consitutes the recording site nearest the micropipette tip. Figure 3b shows the second recording site, consisting of a gold ring with a gap to permit passage of the lead from the first recording site. The interelectrode separation along the shank is 100 µm. Figure 2 shows a set of recordings made with this device in cat neocortex. The response was elicited by direct electrical stimulation of the neocortex with a pair of platinum surface electrodes located 5 mm

from the recording site and has the expected features. Channel 1 was recording near the surface of the cortex and Channel 2 was 100 μm deeper. The records were obtained by averaging the response for 50 presentations of the stimulus with a Technical Measurements Corporation computer of average transients, Model 400A. The difference trace was obtained by averaging the output of a differential amplifier having Channel 1 and Channel 2 as inputs. The ability to extract and amplify such difference signals is a major asset in many types of experiments on the nervous system.

The amplitudes and band widths of the recorded signals indicate that the electrical properties of the recording sites are within the range expected. The recording impedance levels are less than 10 MΩ at 1 KHz and both the interelectrode coupling capacitance and the shunt capacitance to ground from the electrode cannot exceed a few picofarads. The recording properties of these electrodes are now being carefully studied.

References

1. K. Frank and M. C. Becker, "Micrcelectrodes for Recording and Stimulation," in *Physical Techniques in Biological Research*, vol. 5, W. L. Nastuk, Ed., New York:Academic Press, 1964, ch. 2.

2. S. Rush, E. Lepeschkin, and H. O. Brooks, "Electrical and Thermal Properties of Double-Barreled Ultra Microelectrodes," *IEEE Trans.* on *Bio-Medical Engineering*, vol. BME-15, pp. 80-93, April 1968.

3. K. D. Wise, J. B. Angell, and A. Starr, "An Integrated-Circuit Approach to Extracellular Microelectrodes," *IEEE Trans.* on *Bio-Medical Engineering*, vol. BME-17, pp. 238-247, July 1970.

4. K. D. Wise and J. B. Angell, "A Low-Capacitance Multielectrode Probe for Use in Extracellular Neurophysiology," *IEEE Trans.* on *Bio-Medical Engineering*, vol. BME-22, pp. 212-219, May 1975.

5. J. Skrzypek and E. Keller, "Manufacture of Metal Microelectrodes with the Scanning Electron Microscope," *IEEE Trans.* *Bio-Medical Engineering*, vol. BME-22, pp. 435-438, September 1975.

EXPOSED Au RECORDING SITE

PMMA INSULATION

GLASS PIPETTE WALL

BACK SIDE

FRONT SIDE
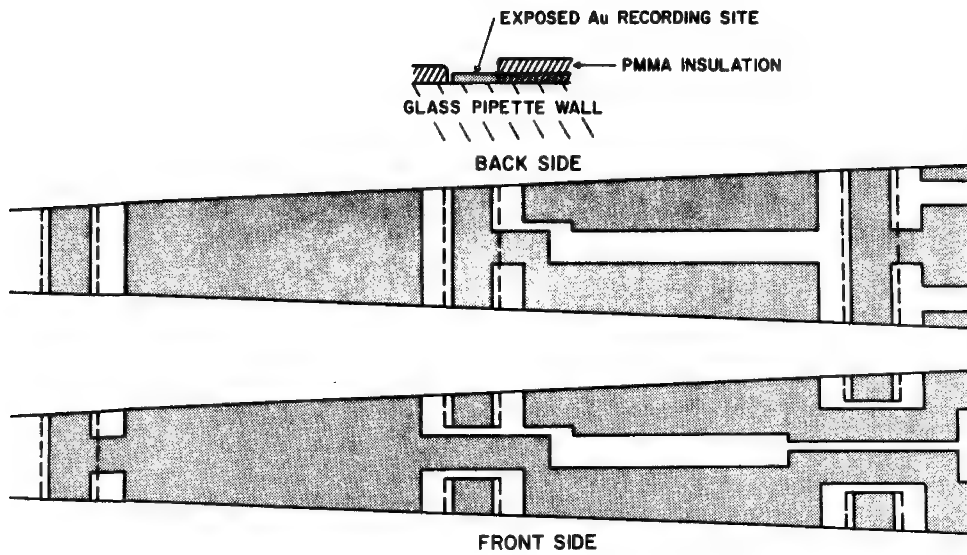
FIG. 1   DIAGRAM OF THE EXPOSURE PATTERN USED TO PRODUCE A

THREE-CHANNEL MICROELECTRODE.

500 mV/DIVISION

CHANNEL NO. I

500 mV/DIVISION

CHANNEL NO. 2

500 mV/DIVISION

DIFFERENCE

TIME, 50 ms
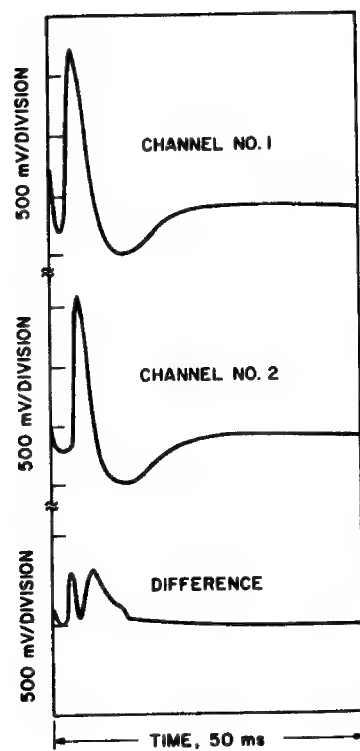
FIG. 2   SLOW-WAVE RECORDINGS

FROM CAT NEOCORTEX MADE

WITH A MULTICHANNEL

DEPTH PROBE.

175G
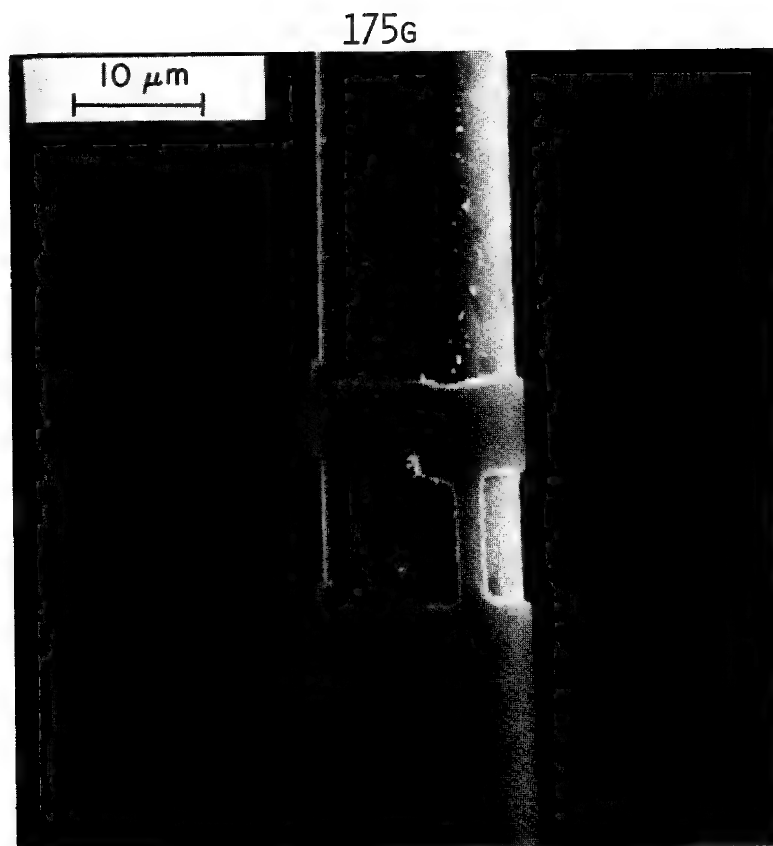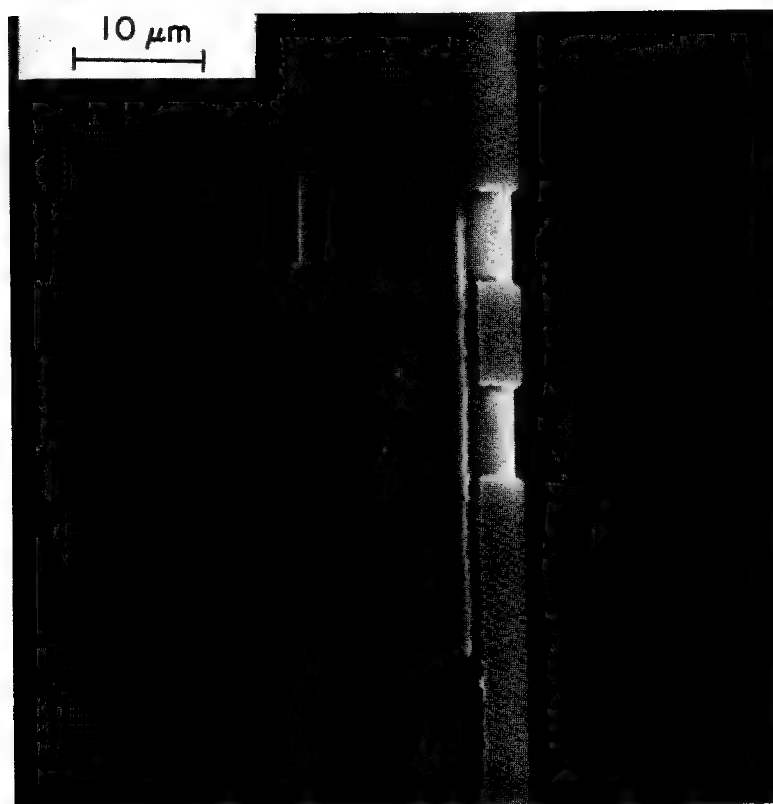
FIG. 3   SCANNING ELECTRON MICROGRAPHS OF A MULTICHANNEL DEPTH PROBE
FABRICATED USING ELECTRON-BEAM LITHOGRAPHY.   (a) FIRST RECORDING
SITE, LOCATED NEAR THE PIPETTE TIP; (b) SECOND RECORDING SITE,
LOCATED 100 μm BEHIND THE FIRST SITE (FURTHER UP THE SHANK) AND

A SCANNING ELECTRON MICROSCOPY STUDY OF THE ATTACHMENT OF A THROMBORESISTIVE
SURFACE COATING TO A MEMBRANE BLOOD OXYGENATOR

H. S. Borovetz, R. K. Matta, K. J. Goitein, T.-K. Hung, M. H. Weissman, and
R. L. Hardesty

Departments of Surgery and Civil Engineering, University of Pittsburgh,
Pittsburgh, Pennsylvania 15261

The need for systemic heparin anticoagulation during extended cardiopulmonary
bypass (CPB) remains a serious impediment to clinical CPB support of circu-
latory and respiratory failures, especially in the newborn. Recent devel-
opment of thromboresistive substrates which can be used to treat extracor-
poreal surfaces in contact with blood offers the potential for elimination of
systemic blood heparinization. The present paper describes a scanning elect-
ron microscopy study of the attachment of one such substrate, tridodecyl-
methylammonium chloride (TDMAC), to a novel micro-membrane oxygenator.

Figure 1 shows a cross-sectional image of the alternating pattern of micro-
channel conduits for blood flow through the oxygenator. The micro-channels
were fabricated on thin metal sheets with an approximate semi-circular shape
(150 + 25 microns in radius). The gas exchange to the blood flow in the
channels was accomplished through a micro-porous membrane which was placed
across the diametric plane of the channels (1). Treatment of the micro-
channels and membrane surfaces with a 7% TDMAC coating solution followed a
modified single step process developed at Battelle Memorial Institute. The
effect of submersion time of the plates and membranes in the TDMAC solution
on the integrity of the coating layer can be seen in Figure 2. A single dip
coat for three hours leads to a uniform coating of the channel surface (Fig.
2a); the interstitiun and microscopic protrusions of an uncoated channel are
depicted in Fig. 2b. When the submersion time is reduced to 30 seconds, ir-
regular areas devoid of substrate are found in the coating layer (refer to
Figure 3). Attachment of TDMAC to the micro-porous membranes was assessed
using x-ray spectrometry. The membranes were first sputter-coated with ap-
proximately 300 angstroms of gold and a small area (one to four cubic microns)
was then isolated for x-ray analysis. Figure 4a shows the energy spectrum for
a typical piece of uncoated micro-porous membrane. From left to right the
three major energy peaks correspond to silicone, gold, and chlorine respect-
ively. The membrane material is fabricated from PVC acrylonital cast on a
polyester cloth and made hydropobic with silicone fluid. The energy peaks for
silicone and chlorine are therefore to be expected. A shift in the relative
density of counts occurs for silicone and chlorine following three hours of
treatment of the membrane material with 7% TDMAC. The peak shown in Figure 4b
indicates the attachment of the tridodecylmethylammonium chloride macro-
molecule to the membrane surface.

In conclusion it has been shown that scanning electron microscopy and x-ray
spectrometry provide important information for the assessment of the surface
integrity of thin layers of coating. The authors are currently evaluating
TDMAC along with other potential anti-thrombogenic substrates, such as pyro-
lytic carbon, albumin, and tallow metallographic polish, for their thrombo-
resistance and surface adhesion after exposure to blood perfusion.

1. T.-K. Hung, H. S. Borovetz, R. L. Hardesty, and M. H. Weissman, in Proc.
    International Conference on Bioengineering, Pretoria, South Africa (1977).

Fig. 1. Cross-sectional view of the alternating pattern of etched channels.
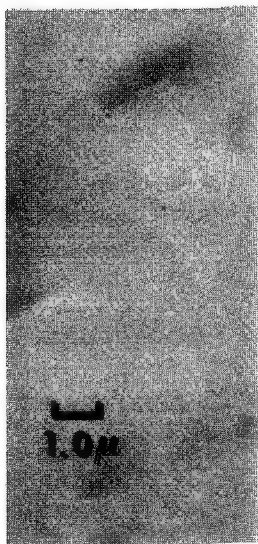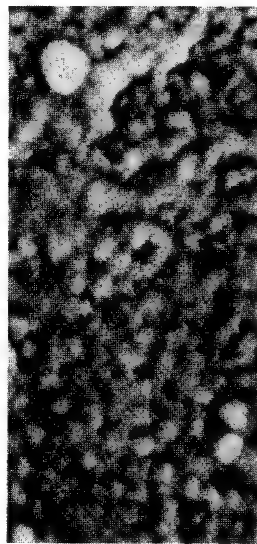
(a)   (b)

Fig. 2. (a) Photomicrograph of an
etched channel following three hours
of treatment with 7% TDMAC solution.
         (b) Surface interstitium and
microscopic protrusions for a typical
uncoated etched micro-channel.
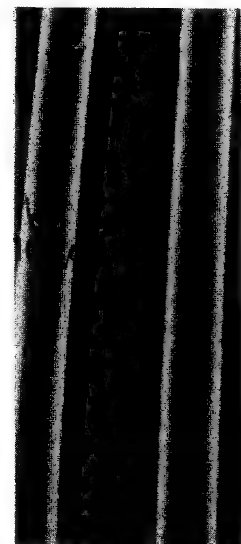
(a)   (b)

Fig. 3. Effect of submersion time
on the coating uniformity of the
TDMAC treatment. (a) thirty seconds
dip coat; (b) three hours submersion
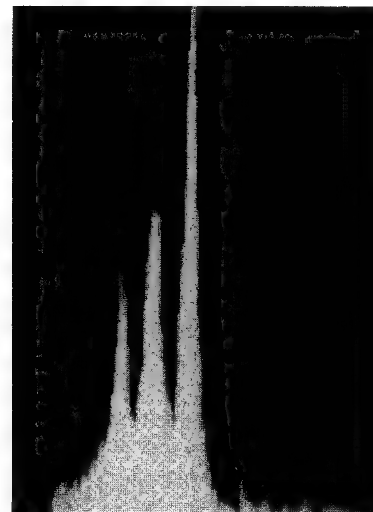
(a)   (b)

Fig. 4. (a) Spectrum of an uncoated piece of membrane. (b) Shift in the rel-

ELECTRON MICROANALYSIS OF ORGANIC SULFUR IN COAL

R. Raymond, Jr., T. G. Gregory, R. Gooley
Los Alamos Scientific Laboratory
Geological Research Group G-6
Los Alamos, NM   87545

The quantity of coal that will be used to meet future U.S. energy requirements is staggering. Many of the problems of coal utilization, including air and water pollution, are linked to sulfur, the most important minor element occurring in coal.

The paucity of published reports concerning the use of the electron probe microanalyzer (EPM) in previous coal studies shows that the instrument has been neglected in this field. Yet the unique capabilities of the EPM can provide information inaccessable through other methods of analysis. The advantages of detailed microanalysis of coal are obvious considering its heterogeneous fine-grained nature. Furthermore, energy dispersive (EDS) or wavelength dispersive (WDS) techniques can be applied to ensure that the x-ray signal from an element of interest is not due to the presence of that element in some unexpected compound.

Greer (1) has shown that determinations of the organic sulfur content in coal by conventional methods are inaccurate because of the inability to separate micrometer-size particles of FeS_2 from the coal matrix. We are studying the occurrence and distribution of organic sulfur in coal by EPM. The use of EDS and WDS techniques ensure that the sulfur is not due to the presence of sulfide or sulfate minerals. In addition, the absence of chemical shift of the WDS signal shows that the sulfur is not present as sulfate.

We have developed a standard suitable for quantitative EPM analysis of organic sulfur in coal. The standard consists of spherical carbon beads originally prepared at LASL for use in nuclear fuel cells. The beads are 75-200 μm in diameter and contain 4.1 ± 0.1 wt% sulfur, determined by thermal neutron capture-prompt gamma ray spectroscopy.

The sulfur is present in the beads due to the use of sulfuric acid in the preparation process. The standard is available for distribution on request by writing to the authors.

Chemical shift measurements (WDS) were made on the beads, elemental sulfur, organic sulfur in coal, pyrite and barium sulfate. The sulfur peak for the beads is skewed slightly toward sulfate, but not enough to cause analytical error during organic sulfur analysis in coal. We estimate that reduction from sulfate to sulfur in the beads is more than 95% complete. Reduction occurred during processing when the beads were heated at 500°C for two weeks in a hydrogen atmosphere.

Sulfur x-ray intensity measurements were made on 200 beads for determination of intra- and inter-bead homogeneity. Using the statistical methods described by Goldstein (2) it was determined that the inter-bead standard deviation in sulfur content for 25 beads is less than 2.5% relative at the 95% confidence level and less than 3.1% at the 99% confidence level. For 200 beads, the standard deviation is less than 0.7% relative at the 95% confidence level and less than 0.9% at the 99% confidence level. In all cases, the intra-bead variation is less than the inter-bead variation.

We are determining the organic sulfur content of various macerals in high-sulfur coals from the Illinois Basin and low-sulfur coals from the Raton (northern New Mexico and southern Colorado) and Appalachian Basins. Organic sulfur in macerals from these regions appears to vary consistently: sporinite > vitrinite $\geq$ resinite > fusinite. Figure 1 is a secondary electron image of a portion of a polished sample of low-sulfur coal from the Appalachian Basin. The organic sulfur contents of the macerals shown appear to be typical for the entire sample (Table 1).

The EPM results also indicate that the organic sulfur content is greater in high-sulfur coal than in low-sulfur coal, but the difference is not proportional to the difference in total sulfur content (Table 1). The amount of pyrite present then appears to be the primary cause for sulfur variation. Abundant fine-grained pyrite is observable microscopically in the high sulfur sample.

Stach et al. (3) have shown that certain maceral groups such as exinites have high relative amounts of CH_2 groups compared to vitrinites or micrinites, suggesting an advantage of using coals rich in exinites for coal gasification; we suggest that exinites rich in sporinites may be disadvantageous due to high organic sulfur contents. Furthermore, our preliminary results indicate that with efficient pyrite extraction from high-sulfur coals the remaining sulfur content will be no greater than that in low-sulfur coals.

REFERENCES

1. Goldstein, J. I., 1976, "Statistics of X-ray Analysis," (abs.) Proc. Eleventh Ann. Conf. MAS, p. T1A-T1H.

2. Greer, R. T., 1976, "Nature and Distribution of Pyrite in Iowa Coal," Proc. Thirty-Fourth Ann. EMSA Mtg., p. 620-621.

3. Stach, E., M.-Th. Mackowsky, M. Teichmuller, G. H. Taylor, D. Chandra, and R. Teichmuller, 1975, Stach's Textbook of COAL PETROLOGY, Gerbruder Borntraeger, Berlin, 428 p.
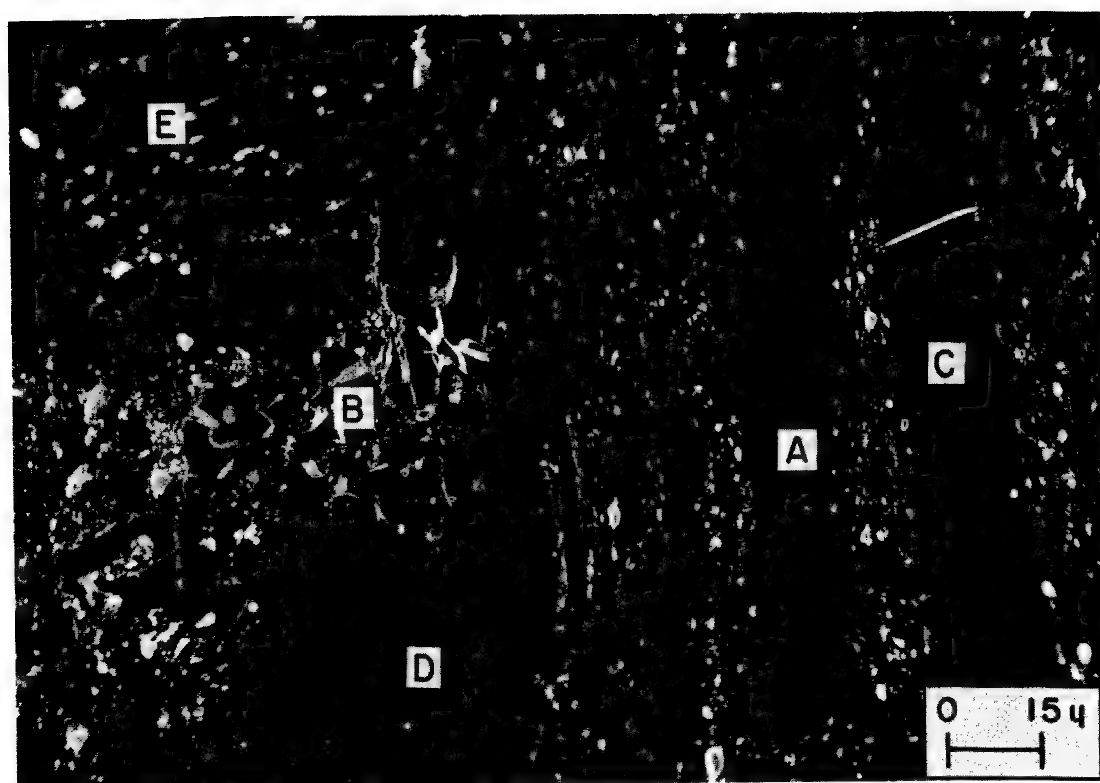
Figure 1.   Secondary electron image of a polished sample of low sulfur coal from the Appalachian Basin (x800).
A = Sporinite; B = Fusinite; C, D, & E = Vitrinite.

TABLE I

PERCENT ORGANIC SULFUR IN ILLINOIS, APPALACHIAN
AND RATON BASIN COAL MACERALS

Macerals	Illinois Basin High Sulfur	Appalachian Basin Low Sulfur	Raton Basin Low Sulfur
Sporinite	2.0	1.3	0.92
Vitrinite	1.5	0.85	0.55
Resinite	1.2	0.60	0.54
Fusinite	0.48	0.29	0.42

TECHNIQUE FOR THE "BEFORE AND AFTER" STUDY OF CLAY MINERALS USING THE SCANNING ELECTRON MICROSCOPE AND ENERGY DISPERSIVE X-RAY ANALYSIS.

R. L. Thomas, C. W. Crowe, and B. E. Simpson
Dowell Division of The Dow Chemical Company
Tulsa, Oklahoma

Introduction

The subject of clay minerals and their effect upon oil-bearing rock has long been of considerable interest to the petroleum industry. In recent years, several papers have appeared in the industry literature discussing clay chemistry in general[1-5] and Scanning Electron Microscope (SEM) studies in particular[6,9]. The question most often addressed in these studies is this: "How is a particular clay mineral affected by a particular fluid under a given set of conditions?" To arrive at an effective and workable answer, there must be a way to observe the same clay platelet both before and after exposure to a fluid under study. The purpose of this paper is to present the details of just such a method.

Apparatus and Equipment Modifications

All SEM work was done with a Cambridge Model S-600 microscope equipped with a Kevex EDX detector interfaced with a Tracor-Northern NS-880 analyzer. In order to utilize maximum take-off angle from a relatively flat surface normal to the electron beam, the sample stage of the S-600 was modified to obtain longer working distances than is normally possible with this equipment. Maximum obtainable working distance with the standard Cambridge stages is about 22 mm.[7] This was extended to 44.5 mm with the modifications. In addition the special

stage was constructed to hold four specimens at once and
still maintain full X, Y, and Z movements available in the
S-600. Rigid mounting of the specimen stubs by means of set
screws allowed easily reproducible positioning and relocation
of the areas of interest.

Experimental

In order to simulate actual oil well conditions as closely
as possible, all clay minerals were observed in place in sand-
stone from the Berea formation. This is a common rock used
in laboratory studies and is representative of oil-bearing
formations containing clay minerals. Samples were prepared
for SEM examination by depositing an approximately 300 A thick
coating of aluminum in a vacuum evaporator. To prevent oxida-
tion as much as possible, the samples were kept under vacuum
until immediately before transfer to the SEM stage. Aluminum
was chosen as the coating material due to its ease of removal
in either acid of alkalai.[8] After SEM-EDX examination and
photomicrograph recording, the aluminum coating was removed
with 28% hydrochloric acid and the core sample was allowed to
dry. The core sample was now exposed to the fluid under study,
allowed to dry, coated with aluminum and placed in the SEM.
The exact spot of the previous examination was located and
the same series of micrographs and EDX spectra obtained.

Results and Discussion

Initial results showed that the rather harsh treatment of
removing the aluminum coating with 28% hydrochloric acid had
some effect on the chemistry of the clays. Traces of chlorine,
iron, calcium, and some other elements showed up in the "after"
EDX analyses of the control specimens. This indicated that
the acid must be penetrating the rock, dissolving some of the

minerals, and redepositing them as salts on the surface upon drying. This problem was solved by first saturating the aluminum coated sandstone specimens with water before applying the acid. The water was forced into the available pore spaces of the rock thus preventing penetration by the acid. Using this method, the EDX spectra of the "after" control samples were identical to those of the "before".

After the method was perfected and the problems with the blank overcome, several oil well treating fluids were examined using the procedure described above. Detailed results of this work are described elsewhere[9] but the basic conclusion is as follows: The "before and after" technique is an effective means of examining clay minerals in core samples and has been shown to support conclusions drawn from other means of testing core response to oil well fluids.

References

[1] Gray, D. H. and Rex, R. W., Proc. 14th Conf. on Clays and Clay Minerals, Pergamon Press, London (1966), Volume 32, p. 18.

[2] Veley, C. D., J. Pet. Tech. (1969), Volume 21, p. 1111.

[3] Reed, M. G., J. Pet. Tech. (1972), Volume 24, p. 860.

[4] Grim, R. E., Jour. Geology (1942), Volume 50, p. 225.

[5] Haskin, C. A., Society of Petroleum Engineers of AIME Preprint No. 5692, Proc. of Symposium on Formation Damage (1976), p. 35.

[6] Holub, B. W., Maly, G. P., Noel, R. P., and Weinbrandt, R. M., Society of Petroleum Engineers of AIME Preprint No. 4787, Proc. of Symposium on Formation Damage (1974), p. 187.

[7] Steroscan S-600 Scanning Electron Microscope Operators Manual, Cambridge Instrument Co., Issue 1, No date given, Appendix 1.

[8] Wells, O. C., "Scanning Electron Microscopy", McGraw-Hill, New York, 1974, p. 335.

[9] Thomas, R. L., Crowe, C. W., and Simpson, B. E., Society of Petroleum Engineers of AIME Preprint No. 6007, Presented at the 51st Annual Fall Technical Conference and Exhibition of SPE-AIME, New Orleans, Louisiana, October 3-6, 1976.

The Use of Phase Transformations and Exsolution in Calcic Plagioclase Feldspar as Indicators of Geologic History

T. L. Grove[*]

Hoffmann Laboratory

Harvard University

Cambridge, Massachusetts   02138

Method of Study

The transmission electron microscope (TEM) and the electron microprobe have been used to characterize calcic plagioclase feldspars (An_{65}-An_{85}) from a wide variety of geologic environments. Samples from volcanic, shallow plutonic, deep-seated plutonic and regional metamorphic environments have been studied. The thermal histories recorded by plagioclase in these samples nearly span the range of cooling histories experienced by terrestrial rocks. The heat equation was used to qualitatively estimate thermal history in terms of a time integrated cooling rate. The geometry of the intrusive and boundary conditions appropriate to the geologic setting of the sample were used as input to Lovering's [1] solution. In order to correlate observations of microstructure with bulk composition, plagioclase crystals were analyzed with the electron microprobe, thinned by ion bombardment and then studied with the TEM. TEM observations of antiphase boundaries (APBs) and exsolution were used to infer the transformation-exsolution sequence over the An_{65} to An_{85} compositional range.

Phase Transformations and Exsolution

Calcic plagioclase (An_{75}-An_{85}) undergoes the transformation sequence from high to low temperature [2,3].

$$C\bar{1}, \ c = 7\overset{\circ}{A} \rightarrow I\bar{1}, \ c = 14\overset{\circ}{A} \rightarrow P\bar{1}, \ c = 14\overset{\circ}{A}$$
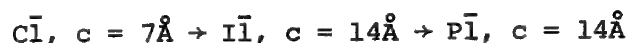
The $C\bar{1} \rightarrow I\bar{1}$ transformation involves ordering of Al and Si on tetrahedrally coordinated equipoints, and $I\bar{1} \rightarrow P\bar{1}$ is a low-temperature displacive transformation. The two types of antiphase domains related to the transformations can be distinguished in the TEM. An_{65} to An_{75} plagioclase undergoes the transition $C\bar{1}$ to intermediate plagioclase. Intermediate plagioclase

---

[*]Now at: Department of Earth and Space Sciences, State University of New York, Stony Brook, N. Y. 11794.

is inferred to have a one-dimensional periodic antiphase structure (similar to CuAuII and other binary alloys) in which the periodic antiphase domains have $I\bar{1}$ symmetry and are related by the translation lost in the $C\bar{1} \to I\bar{1}$ transition. Additionally, exsolution of an $I\bar{1}$ and intermediate plagioclase phase occurs. Optically visible (500X) two-phase intergrowths of this exsolution are known as Huttenlocher intergrowths [4,5].

Effects of Cooling History on Microstructure

The integrated cooling rate (°C/year) and bulk composition are plotted on the diagram below. The bulk compositions studied are shown by dark horizontal lines for each sample. On the right is the temperature at which cooling began. To the right of the vertical dashed line at An_{75} the transformation sequence is: $C\bar{1}$ to $I\bar{1}$, to the left it is $C\bar{1}$ to intermediate plagioclase. The lighter curved lines show the compositional range over which submicroscopic and optically discernible two-phase intergrowths of $I\bar{1}$ and intermediate plagioclase are observed. The most striking effect of cooling history is the compositional extent of two-phase intergrowths. Upon slower cooling exsolution occurs in increasingly calcic bulk compositions and the coexisting phases are An_{66} and An_{85-90}. In the most rapidly cooled samples there is no evidence of exsolution. The morphology of $C\bar{1} \to I\bar{1}$ APBs in An_{75} to An_{85} changes as a function of both thermal history and bulk composition. The morphology and concentration of defect structures in intermediate plagioclase also change in response to cooling history. Nearly all plagioclases contain evidence in diffraction patterns and images for short-range ordered domains with $P\bar{1}$ symmetry. The presence of the $P\bar{1}$-like domains is indicated by the dotted pattern on the figure. These TEM observations indicate that the thermal history of a rock can be deduced by studying the submicroscopic textures in a single, zoned plagioclase crystal.

References

1. Lovering, T. S. (1935) Bull. Geol. Soc. Amer. 46, 69-93.

2. Müller, W. F. et al. (1973) Contr. Mineral Petrol. 40, 63-74.

3. McLaren, A. C. and Marshall, D. B. (1974) Contr. Mineral Petrol. 44, 237-250.

4. Huttenlocher, H. (1942) Schweiz Mineral Petrol. Mitt. 35, 326-366.

5. Nissen, H. U. (1968) Schweiz Mineral Petrogr. Mitt. 48, 53-56.

Acknowledgment
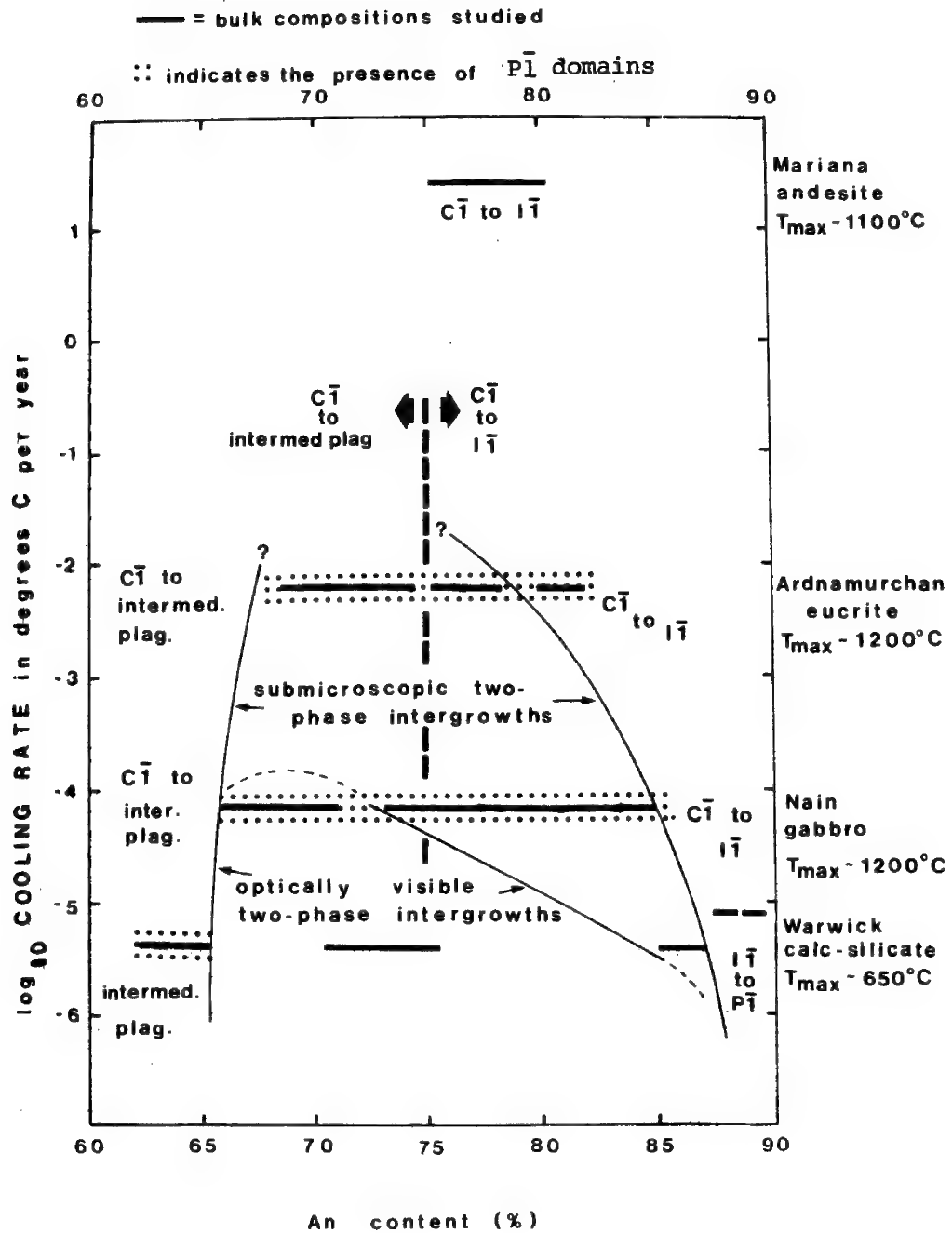
ION MICROPROBE ANALYSIS OF PLAGIOCLASE FELDSPARS $(Ca_xNa_{1-x}Al_{1+x}Si_{3-x}O_8)$ FOR MAJOR AND MINOR ELEMENTS.

Ian M. Steele[*]

Ian D. Hutcheon[†]

Todd N. Solberg[*]

Robert N. Clayton[*†] and

Joseph V. Smith[*]

[*]Department of the Geophysical Sciences
[†]Enrico Fermi Institute
University of Chicago, Chicago, Illinois 60637

A suite of well characterized, natural plagioclase feldspars across the binary series $NaAlSi_3O_8-CaAl_2Si_2O_8$ has been examined using an AEI-IM20 ion microprobe. Emphasis was placed on spectral interpretation at high mass resolution, especially with respect to interferences and a preliminary attempt was made to obtain quantitative results for minor and trace elements. Other ion microprobe studies of mineral samples (e.g. ref. [1,2]) relate to data obtained at low mass resolution. Reed et al. (ref. [3]) showed that minor concentrations (10-3000ppmw) of Cr in $CaMgSi_2O_6$ (i.e. constant matrix) gave a linear concentration vs. count rate under high resolution conditions.

Forty-two samples were mounted in a single one-inch epoxy disk, polished, and carbon coated. Several grains of each sample were then analyzed using an electron microprobe for Al,Si,Ca,Na,K,Fe,Mg,Sr,Ba,Ti, and P with detection limits near 50ppmw. All ion probe data were obtained using a mass analysed ^{16-}O beam with a current density of ~1 mA/cm^2; sample chamber pressure was maintained at less than 5 x 10^{-8} torr and the sample region was cooled to liquid N_2 temperature. Points previously analysed with the electron-probe were relocated for ion-probe analysis. Secondary ion intensities were measured with an electron multiplier and ion counting. We have previously reported (ref. [4]) effects of tuning our extraction system on the relative intensities of the transmitted SI (secondary ion) intensities; briefly, we quantified the effects of energy selection in the extraction optics and showed how a change in extraction potentials affects the energy bandpass causing a change in the relative intensities of transmitted species. To minimize this effect the extraction conditions were not varied after maximization on one particular sample.

Spectral Features

Existing bulk analyses of feldspars (e.g. ref. [6]) were used as a guide to selection of elements likely to occur as substituents, and we systematically examined the secondary spectra for these elements to determine detection limits and conditions necessary to give an interference-free signal. Table 1 presents a summary of detected elements. Special comments follow: Li and B were easily detected in all samples; Be has an rather intense Al^{+3} interference and has not yet been studied. Mg isotopic data are of interest because of observed anomalies in bulk samples from certain meteorites; however, ^{25}Mg has an unresolvable interference of $(NaAl)^{++}$ which may limit accuracy. Its presence is inferred from the presence of $(NaSi)^{++}$ and the generally higher SI yield of Al^{+} over Si^{+}. K has a high SI yield but in contrast to other elements like Ba,Li and Sr shows a steadily decreasing signal with time for a stationary spot for all samples; presumably K migration is occurring. Low resolution scans in the region $^{m}/e=135-178$ (rare-earth region) showed peaks at every mass but detailed examination of intensities was inconsistent with these being totally due to rare earth elements, even though these occur at the 0.1-10ppm level; these peaks probably result from complex molecules containing up to 5 atoms. In addition the regions 149-154 and 166-170 are dominated by BaO and BaO_2 components for Ba levels in natural samples. We conclude that claims for quantitative determination of REE on any ion-probe should be taken with caution unless a detailed spectral interpretation is presented. By instrumental adjustments (ref. [4]) we can reduce the interferences in the REE region relative to Ba and presumably relative to REE; possibly this technique could be carried to a point where the REE could be recognized and determined without large errors. Peak stripping has been applied to Sr isotopes in Ca-rich feldspars to obtain $^{87}Sr/^{86}Sr$ (ref. [5]) values which are of geochemical interest for age determination. We have identified interferences in this region using high resolution and obtained approximate intensities for each peak (Table 2). In addition to the CaSiO and CaAlO interferences recognized in ref. [5], we observe Si_2O_2, $SiAlO_2$, and Al_2O_2. The Al_2O_2 interference is significant at m/e = 86 because its nearly monoisotopic nature precludes peak stripping to obtain accurate $^{87}Sr/^{86}Sr$ values.

Quantitative analysis

A:) Major elements (Ca,Na,Al,Si). The major element concentrations in these

samples are well known and Fig. 1 shows plots of ion probe raw count rates vs. composition. For each element the points scatter about a visually drawn curve. There is a tendency for linearity from $CaAl_2Si_2O_8$ to $\sim Na_{.7}Ca_{.3}Al_{1.3}Si_{2.7}O_8$ and a second trend for all elements for more Na-rich compositions. The considerable deviation from the line precludes accurate composition determination using these calibration curves. However, by plotting raw count rates as $Al^+/(Al^++Si^+)$ vs. composition a line is obtained enabling composition determination by reference to standards. We are presently trying to understand reasons for the variation of raw count rate from the lines on Fig. 1. Crystal orientation, at least for this mineral group, does not seem to affect count rate, at least to the extent shown on Fig. 1 ($\pm 20\%$).

B:) Minor elements. Although Li,B,Mg,K,Fe,Sr and Ba are detected in all 42 samples, only Mg,K and Fe occur commonly in sufficient concentration to provide electron-probe reference data; K, however presents a problem because of the previously mentioned count rate loss with time. In Fig. 2a we show low-resolution (no significant interferences) raw count-rates for ^{24}Mg vs. electron-probe data as circles. Because raw count rate data for Si and Al do not lie on a line while the count rate ratio $Al^+/(Al^++Si^+)$ does, at least some of the scatter shown on Fig. 1 may be due to differing overall yields of SI. We thus adjusted the ^{24}Mg count rates by the deviation of the ^{40}Ca count rate from the line drawn on Fig. 1b, (i.e. $Mg_{adjusted} = Mg_{raw} \times (Ca_{raw}/Ca_{line})$) where raw refers to raw counts, line refers to counts defined by line on Fig. 1. This adjusted count rate should compensate for a variation in total SI yield. These adjusted data are shown as crosses on Fig. 2. The sample with six determinations is clearly improved by this normalization and provides a measure of precision over a 3 hour time period ($\sim \pm 5\%$). Several points at high Mg levels fall outside this range but considering the large electron probe error (~ 50ppmw) at these generally low concentrations we conclude that errors are within $\sim \pm 10\%$ of the amount present. We do not, however, see any recognizable matrix effect at least for Mg although samples are biased toward Ca-rich compositions.

Iron occurs generally at higher concentration levels than Mg and electron probe data should be better; however, ion probe data must be obtained at high resolution which probably makes the data more susceptible to fluctuations. Fig. 2b shows electron probe vs. ion probe raw count rates for Fe but here the data show a greater spread and a range of $\sim \pm 25\%$ from an average line - about twice as great as for Mg. Adjusted data based on Si (Ca data were not obtained) had little effect on reducing the spread. This experiment was repeated on a separate day, and

it is interesting to note that the same spread of data was observed and each
sample maintained the same relative position in the spread. We conclude
that the spread is not due to random errors but is a function of the samples or
of the sample mount. (A similar feature was noted for repeated Mg data).
No correlation with composition was observed for the data on Fig. 2b.

Conclusion: Plagioclase feldspar compositions can be obtained to better than $\pm 5\%$
accuracy using a calibration curve. The minor elements Mg and Fe appear to
be accurate to within 10 and 25% of the amount present, respectively; other minor
elements detected include B,Li,Ti,P,V,Mn,Sr and Ba and with suitable calibration
standards are expected to show similar accuracy. The procedure requires high mass
resolution and known standards but does not rely on theoretical-mathematical
correction procedure such as described in ref. [1].

References

[1] Andersen, C. A. and J. R. Hinthorne (1973) Thermodynamic approach to the
quantitative interpretation of sputtered ion mass spectra. Anal. Chem. 45,
p.1421-1438.

[2] Meyer, C., D. H. Anderson and J. G. Bradley (1974) Ion microprobe mass analysis
of plagioclase from "non-mare" lunar samples. Proc. Fifth Lunar Sci. Conf. 1.
p.685-706.

[3] Reed, S. J. B., J. V. P. Long, J. N. Coles and D. M. Astill (1976) Ion microprobe
trace element analysis with high mass resolution. Int. J. Mass. Spect. Ion Phys.,
22, p. 333-338.

[4] Steele, I. M., I. D. Hutcheon, T. N. Solberg, J. V. Smith and R. N. Clayton (1977)
Effect of energy selection on quantitative analysis in secondary ion microanalysis.
Int. J. Mass Spect. Ion Phys., 23.

[5] Hinthorne, J. R., and R. L. Conrad (1975) The application of peak stripping to
problems in ion probe microanalysis. Proc. Microbeam Analysis Society 10th Conf.
paper #74.

[6] Smith, J. V. (1974) Feldspar Minerals. Vols. 2: Chemical and textural properties.
Springer.

Table 1. Detected elements, detection limit, resolution and special comments for elements in plagioclase.

analytical mass	resolution*	detection limit**	comments
^{7}Li	low	10ppb	^{28}Si^{+4} should be small based on absence of ^{27}Al^{+4}, low intensity of ^{28}Si^{+3}, and ^{7}Li/^{6}Li ratio.
^{11}B	low	10ppm(?)	Interference-free; ^{10}B has ^{30}Si^{+3} interference which can be subtracted using ^{28}Si^{+3} intensity; detection limit estimated from sparse analyses.
^{24}Mg	low	100ppb	NaH^{+} interference can be reduced to trivial levels using LN$_2$ in source; ^{48}Ca^{+2} interference is trivial.
^{31}P	high	30ppm	Na$_2$O^{+} interference is significant; because P~ correlates with Na, interference is important for all compositions.
^{39}K	high	100ppb	NaO^{+} interference can be resolved; high K yield and generally high K concentration (~.3 wt.%) might allow low resolution.
^{47}Ti	high	20ppm	^{48}Ti has unresolvable Ca interference; interference at ^{m}/e=47 may be Na$_2$H^{+}; peak stripping at ^{m}/e=48 may be possible at low RP.
^{51}V	high	?(~10ppm)	NaSi^{+} interference
^{55}Mn	high	?(~10ppm)	Na$_2$O and AlSi interference
^{56}Fe	high	1ppm	intense CaO^{+} interference
^{88}Sr	high	100ppb	complex spectra; see later.
^{138}Ba	low	100ppb	comparison of 5 isotopes indicates that interferences are less than 5% at observed concentrations.

*Resolution - low ~100; high ~3500. (M/ΔM).
**Based on signal of ~3 cts/sec; value listed is ~10 times that calculated and should be rather conservative.

Table 2. Interferences in ^{m}/e range 88-80, Lake Co., Oregon plagioclase (~Ca$_{.65}$Na$_{.35}$Al$_{1.65}$Si$_{2.35}$O$_8$). Data in cts/sec; Rb-not detected.

88 - Sr+Ca$_2$	5700	86 - Sr+Ca$_2$	700	83 - Ca$_2$	14
CaSiO^2	100	CaSiO+CaAlO	150	CaAlO+NaCaO	11,000
Si$_2$O$_2$+SiAlO$_2$	500	Al$_2$O$_2$	170	80 Ca$_2$	500
87 - Sr+Ca2	500	85 CaSiO+CaAlO	250		
CaSiO+CaAlO	230	84 - Sr+Ca$_2$	800		
SiAlO$_2$	70	CaSiO	3000		
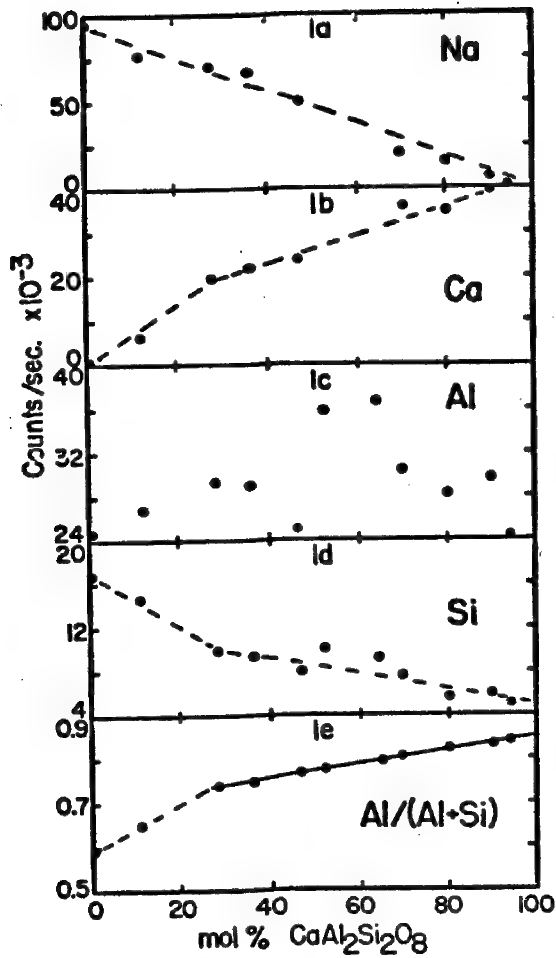
Fig. 1a-d. Count-rate vs. composition for major elements in feldspar. Note that these do not lie on the visually drawn lines. These lines also show an apparent slope change at the Na-rich end. Fig. 1e shows the count rate ratio Al/(Al+Si) which is near-linear and enables composition determination.
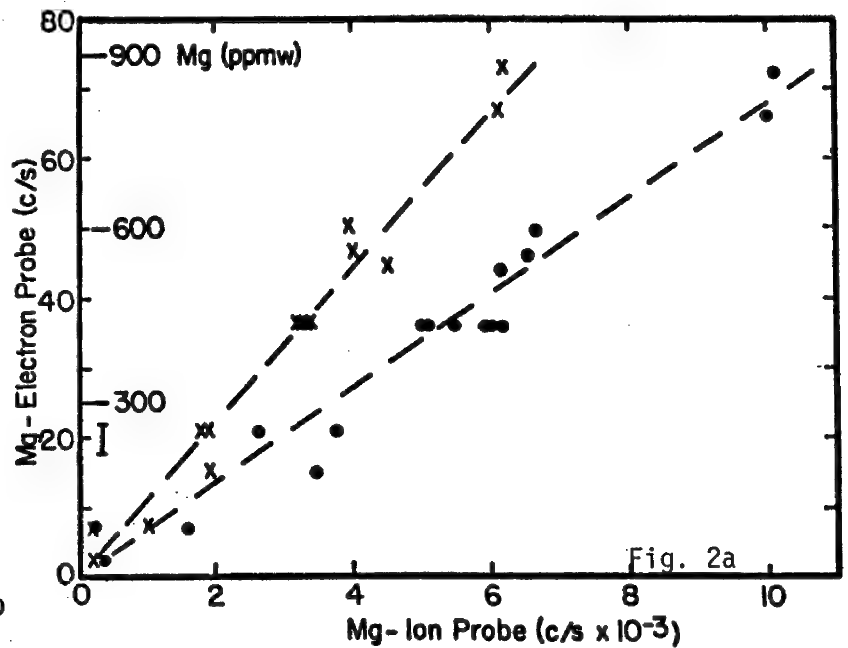
Fig. 2a. Raw counts (circles) from ion probe vs. known concentration. Crosses are adjusted Mg counts as described in text. Error in electron probe data is indicated by vertical bar near origin.
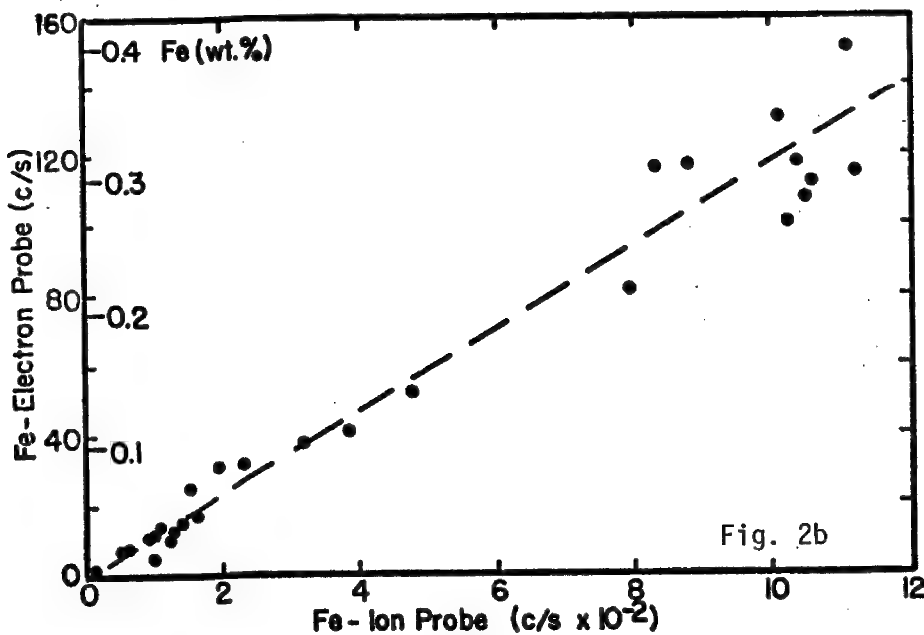
Fig. 2b. Raw Fe counts from ion probe vs. known composition from electron probe.

THE USE OF ENERGY DISPERSIVE ANALYSIS FOR THE STUDY OF PHASE AGGREGATES

A. A. Chodos, A. L. Albee and J. E. Quick

Division of Geological and Planetary Sciences
California Institute of Technology
Pasadena, California 91125

Introduction

Petrologic, metallurgic and ceramic studies of heterogeneous aggregates of phases commonly require a knowledge of the abundance of each phase, the average composition of each phase, and the total bulk composition. We have discussed previously two approaches for obtaining the bulk composition using a computer-controlled electron microprobe with wavelength dispersive analysis (WDA): the "defocussed beam" (DBA) and the "point-count" (PCA) methods (Gancarz and Albee, 1973; Albee et al, 1977). The use of energy dispersive analysis (EDA) greatly increases the usefulness of these approaches.

An aggregate of phases can be described by a series of mass balance equations:

$$C_{11}X_1 + C_{12}X_2 + \cdots \; C_{1n}X_n = S_1$$

$$C_{21}X_1 + C_{22}X_2 + \cdots \; C_{2n}X_n = S_2$$

$$\vdots$$

$$C_{m1}X_1 + C_{m2}X_2 + \cdots \; C_{mn}X_n = S_m$$

Where C_{ij} is the weight fraction of element i in phase j, X_j is the weight fraction of phase j in the aggregate, and S_i is the weight fraction of element i in the total aggregate. DBA determines directly the S_i's, i.e., the bulk composition, by averaging the analyses of a number of large areas. PCA measures the C_{ij}'s and X_j's, which are themselves exceedingly useful information, and calculates the S_i's from them. Identification of the phase at a statistically significant number of grid points on a surface provides a measure of the volume percent of each phase (Chayes, 1956). Volume percentages are transformed to weight percentages (X_j's) using the density of each phase. If the phases are homogeneous, a single analysis of each phase provides the C_{ij}'s, but if they are inhomogeneous an average composition must be obtained for the C_{ij}'s.

It is important to note that for any given set of phases (i.e., a particular C_{ij} matrix) the bulk composition can be represented just as rigorously by the X_j's as by the S_i's. A bulk composition expressed in elements or oxide concentrations can be transformed to a bulk composition expressed in phase concentrations using the inverse of the C_{ij} matrix, i.e., $\overline{X}_j = \overline{S}_i \cdot \overline{C_{ij}^{-1}}$. Hence an EDA spectrum can be expressed alternatively in terms of equal numbers of elements, oxides, actual phases present, or selected end member components.

EDA offers significant advances over WDA for both DBA and PCA. EDA gathers the entire spectrum in a single measurement at much lower currents (0.005 vs 0.05μA) and contamination from impregnation material and loss of volatiles from some phases can be reduced greatly. Focus is much less critical to analytical accuracy, and DBA can be carried out on mm diameter areas, rather than being limited to 50-100μm areas. In addition, less attention is required to maintain focus during traverses for PCA.

Procedures were developed on a MAC-5-SA3 electron microprobe interfaced to a PDP-8L computer for control and on-line WDA-processing. The EDA utilizes an ORTEC 161 eV Si(Li) detector interfaced to a Tracor Northern NS-880 multichannel analyser with 24K of memory and a DSD-210 dual floppy disk. Stage control programs are written in FOCAL for the PDP-8L, and EDA programs are written in FLEXTRAN for the NS-880; the two systems are linked via the interrupt "flag" on the scaler-timer.

Point-Count Analysis (PCA) Program

Basically, the program identifies the phase present at grid points (X_j's) on a polished thin section and accumulates an average spectrum for each phase (C_{ij}'s). The grid point locations are controlled by specifying five stage coordinates, forming a pentagon that bounds the grid, and a grid interval in microns. The EDA program uses preset windows for 10 elements: Mg, Al, Si, P, S, K, Ca, Ti, Cr, Fe are used for PCA of lunar samples. A spectrum is gathered at each grid point for five seconds in one half of the memory of the NS-880 and, simultaneously, calculations are carried out on the spectrum for the preceeding point in the other half of the memory. Background corrections utilize a spectrum with a fixed shape, whose magnitude is fixed by counts in a preselected background window. K-values relative to oxides are calculated for each point and stored sequentially on the disk along with the identification of the phase. This information is summarized every 100 points with a final summary printed out at the end of the run.

The most critical factor in automated PCA is correct and rapid identification of the phase producing the spectrum at each grid point. Not only do the individual phases have a range in composition, but each "point" is ~ 1 μm and its spectrum can represent a mixture of several phases. Identification programs based only on a series of branching statements were successful only when written specifically for a given sample and were not of general use. The present program uses an exact transformation of the K-value spectrum from 10 elements to 10 phases as discussed above. A file of K-values for reference phases is created, utilizing actual compositions of phases in the sample and/or end members of phases with variable composition. The analyst specifies up to three C_{ij} matrices for three specific sets of phases. These matrices are pre-inverted using a FLEXTRAN routine so that exact transformation into as many as three different phase spaces can be made rapidly at each analysed grid point. A match for a single phase is indicated by a high positive value for a component and a mixture is indicated by high positive values for several components. A large negative value for a component indicate that the composition of the point is outside that C_{ij} space.

Our present practice is: 1) Voids are identified by a low K-value sum and counted as a measure of sample porosity. 2) If the sum of negative components is more negative than -20% that C_{ij} matrix is rejected and the next matrix tested. If all three C_{ij} matrices are rejected the spectrum is stored as an unknown. 3) If, after subtracting the total negative values successively from the smallest positive values, any phase has a value greater than +80% it is a positive identification. Otherwise the point is designated as a mixture of all phases with normalized concentrations > 10%. Only true fits, not mixtures, are accumulated in the average spectrum for each phase. Total PCA time is decreased substantially by testing the C_{ij} matrices in proper order and decreased somewhat by reducing the matrice size so that trace phases are labeled as unknowns. These can be identified rapidly and assigned in an editing program.

During PCA of typical lunar basalts 2-3 x 10^3 grid points are analysed on an area of about 5 cm^2 with a running time of 5-8 hours and with 97-99% of the points

identified. The reference spectra, the C_{ij} matrices, the K-values for each point, and the identification for each point, are stored on a floppy disk for possible reprocessing by companion programs. An editing program interactively processes the points that were assigned as unknowns or mixtures. It allows assignment or reassignment of these points, and adjusts the phase abundances and averaged phase compositions accordingly. Another program allows oscilloscope display on the NS-880 of K-value data for any phase. This includes element A vs element B, element A vs frequency, three-element triangular plots, etc.

The averaged K-values for the phases can be used to calculate an average composition and then a bulk chemical analysis. However, we have found it preferable to calculate a bulk composition using a WDA analysis for each phase that closely fits the average K-values determined by the point count. This generally provides better values for minor elements and lighter elements in the calculated bulk composition.

Defocussed Beam Analysis (DBA) Program

Obtaining the bulk composition on a large polished section of a typical phase aggregate by DBA is subject to a number of errors and the point-count method is generally preferable (Gancarz and Albee, 1973; Albee et al., 1977). However, in some studies it is important to obtain an approximate bulk composition of a phase aggregate, especially when dealing with small fragments. For this reason DBA has been used extensively in the study of small fragments from the lunar soil. EDA offers a distinct advantage over WDA in that all elements can be analysed simultaneously on a larger spot in a much shorter time.

The various correction procedures for a conventional homogeneous target assume that the recorded spectrum reflects the chemical composition of both the electron path and the x-ray path for all quanta recorded in the spectrum. DBA uses a larger area than conventional microanalysis but the depth of electron penetration remains the same as for a small spot (2-3 μm for 15 kV in silicates). If the grain size is very small (<< 2 μm) the average path may approximate that for a homogeneous sample and standard correction procedures are applicable. If the grain size is large (>> 2 μm) both the electron path and the x-ray path for a given quantum may be largely or entirely within a particular mineral phase. A correction factor for the hetereogeneous target can be calculated for each radiation, weighting the homogeneous correction factors specific to the composition of each phase (C_{ij}'s) and by the abundance of each phase (X_j) e.g.

$$\beta_{Si}^{m} = \frac{C_{Si}^{\phi} \cdot X^{\phi} \cdot \beta_{Si}^{\phi} + \ldots + C_{Si}^{n} \cdot X^{n} \cdot \beta_{Si}^{n}}{\sum\limits_{o}^{n} C_{Si}^{\phi} \cdot X^{\phi}}$$

where β_{Si}^{m} is the hetereogeneous correction based on the phase abundance, β_{Si}^{ϕ} is the homogeneous correction factor for Si radiation in phase ϕ, C_{Si}^{ϕ} is the concentration of Si in phase ϕ, and X^{ϕ} is the abundance of phase ϕ. If the phases are homogeneous this correction need not be applied to each individual spot, but can be applied to the accumulated spectrum from many large spots.

We use a variant of the point-count program on fragments too small or too fine-grained for good PCA; this program accumulates an EDA spectrum from overlapping beam areas covering the entire available surface. Analyses of the individual phases are used to construct a C_{ij} matrix representing the average composition of the phases.

Approximate X_j's are calculated from the K-value spectrum using the C_{ij} inverse matrix. The C_{ij}'s are used to calculate a homogeneous correction factor for each radiation in each phase, the C_{ij}'s and X_i's are then used to calculate a hetereogeneous correction factor for each radiation in each phase, this correction factor and the K-values provide a first approximation of the chemical composition, which is used in a reiteration.

Discussion

The use of EDA for PCA and DBA illustrate the usefulness of energy dispersive analysis with a computer-based multichannel analyser in a petrographic laboratory. The procedures described can be extended to size and shape analysis of particular aggregates. EDA under computer control provides routine quantitative measurement of properties for which petrographers have had typically only crude visual estimates.

Acknowledgements

References

Albee, A. L., Quick, J. E., and Chodos, A. A. (1977) Source and magnitude of errors in "broad-beam analysis" (DBA) with the electron probe: Lunar Science VIII, Lunar Science Institute, Houston, Texas, p. 7-9.

Chayes, F. (1956) Petrographic model analysis, John Wiley & Sons, Inc., New York.

Gancarz, A. J. and Albee, A. L. (1973) Microprobe analysis of the bulk composition of phase aggregates. Proc. 8th Nat. Conf. Probe Analysis.

Rock Compositions by Defocussed Beam Analysis

J.F. Bower, J.A. Wood, S.M. Richardson,
H.Y. McSween, Jr., G. Ryder

Bulk chemical analyses are frequently desirable for small fragments of rock which are observed only in thin sections, a common occurrence particularly in the study of meteorite and lunar samples. For this purpose we have adopted a defocussed beam analysis (DBA) procedure using a 100μm-diameter beam (beyond this diameter the focusing conditions of the spectrometer are seriously violated). This allows a much larger area to be analyzed than is possible with a focussed beam, and by averaging a number of individual defocussed beam analyses, a representative composition of the fragment can be obtained. A special data reduction procedure is required.

Within any one broad beam analysis point, several mineral types, each with its own characteristic chemistry, are likely to be sampled. The ZAF corrections for homogeneous target materials are inadequate for the DBA procedure, because each mineral phase requires its own ZAF corrections, appropriate to its particular chemical composition. Therefore, the program calculates a provisional norm from the oxide composition. A norm calculated from the weight per cent of the oxides of the elements analyzed gives the compositions and abundances of a thermodynamically stable set of standard minerals formed from these components. The siting of elements in different normative minerals is determined, and ZAF corrections appropriate to these minerals are made in subsequent iterations. For example, if Al_2O_3 is sited in anorthite, $CaAl_2Si_2O_8$, then during the next iteration, corrections for MgO absorption on Al_2O_3 are not necessary. The mechanics of this DBA data reduction are outlined in the flow chart.

The accuracy of the method depends chiefly on how representative an area of this sample is selected, which, in turn, is dependent upon mineral grain size, modal proportion of each mineral present, and the number of 100μm-points analyzed. For rocks with grain sizes of 1 - ~100μm the statistical uncertainty (σ) in the concentration of each oxide can be calculated by the formula:

$$\sigma = \frac{\sqrt{N}}{N} \times 100 = \frac{d}{\sqrt{Am}} \times 100,$$

where σ = uncertainty,
   N = number of mineral grains analyzed which contain that element,
   d = mean diameter of the mineral,
   A = total area sampled by the defocussed beam points,
   m = modal proportion of the mineral in the rock.

These sampling errors are presented in Table 1. In coarse-grained rocks in which the beam is likely to sample only one mineral phase at a time, the size of the beam is immaterial, and the sampling uncertainty reduces to:

$$\sigma = \frac{\sqrt{N}}{N} \times 100 = \frac{1}{\sqrt{mn}} \times 100,$$

where n is the number of defocussed beam analyses averaged (cf. Table I). Statistics of sampling produce greater analytical uncertainties than does the data reduction procedure.

Table II shows a comparison of the bulk compositions obtained by our DBA method with those obtained by x-ray fluorescence. This was an empirical test to determine the accuracy of the DBA technique with this special data reduction. The data are for a fine-grained mid-ocean ridge basalt and a porphyritic andesite from Northern Chile, thin sections of which were provided by W.I. Ridley, Lamont-Doherty Geological Observatory.

FLOW CHART FOR
DATA REDUCTION

Raw counts

Preliminary data reduction (ZAF) assuming homogeneous target

Program calculates norm for the analysis and compositions of normative minerals

i.e., 30% pyroxene, 68% plagioclase, 2% phosphate minerals

Reiterate

Program calculates siting of each element in various minerals

i.e., 15% of Ca in pyroxene, 80% in plagioclase, 5% in phosphate minerals

Second data reduction (ZAF) assuming each element is sited in one or more target minerals as calculated above

Composition compared with that obtained for last iteration, if magnitude of change relative to some suitable Δ:

$>\Delta$ $<\Delta$

Print composition, norm, go to next analysis

TABLE I

Sampling Error (1σ) Based On 100μm Diameter Beam,

30 Spot Analyses

Grain Diameter (d)	Modal Proportion (m)		
	1%	10%	30%
1μm	2%	0.7%	0.4%
10μm	21	7	4
100μm	206	65	38
coarse-grained rocks	183	58	33

TABLE II

COMPARISON OF BULK CHEMICAL ANALYSIS (WT % OXIDES)

BY DIFFERENT TECHNIQUES

	DSDP BASALT 9-82-7-1R9 (Estimated grain size, 5-100 mμ)		ANDESITE 368 FROM NORTHERN CHILE (Estimated grain size, 5-200 mμ)	
	DBA Data Reduction (Average of 30 Points)	Unpublished XRF Analysis By J.M. Rhodes, NASA	DBA Data Reduction (Average of 30 Points	Unpublished XRF Analysis By J. Roobol, Leeds Univ.
Na_2O	2.75	2.81	3.72	3.85
MgO	6.03	6.27	3.46	4.20
Al_2O_3	14.09	13.41	16.36	16.40
SiO_2	50.91	49.2	58.72	57.90
P_2O_5	0.10	0.17	0.19	0.27
K_2O	0.46	0.43	2.46	2.42
CaO	10.81	10.65	6.93	6.32
TiO_2	1.76	1.91	1.04	1.04
Cr_2O_3	0.01		0.0	
MnO	0.17	0.19	0.07	0.10
FeO	11.34	12.29 + 0.94%H_2O	5.99	6.63
TOTAL	98.43	98.27 (includes Fe_2O_3)	98.94	99.13 (includes Fe_2O_3)

Minor and Trace Element Analysis in the Automated Mode:
Selection of Optimum Sampling Conditions

S. Brande and A. E. Bence

Department of Earth and Space Sciences
State University of New York
Stony Brook, New York   11794

Trace and minor elements in some mineral systems (olivines, pyroxenes, Fe-Ti oxides, feldspars, etc.) are important indicators of their host rock petrogenesis. Their concentrations and their intraphase distributions can provide constraints on temperatures of crystallization from a melt, cooling histories, subsolidus equilibration temperatures, diffusion rates, etc. In the routine microprobe analysis of minerals, few laboratories are concerned with the quantitative analysis of elements in concentrations less than about 1000 ppm since considerable additional effort is required to obtain statistically meaningful data. As a consequence, much potentially valuable information is lost.

We have developed analytical procedures which enable us to routinely collect data for minor and trace elements in the automated mode and to ascertain the detectability limits and confidence levels as the data are being collected. We are able to vary the sampling conditions (counting time, number of replications, beam current) during data collection to optimize the results including minimization of total analysis time. The procedure involves a brief search through a variety of sampling conditions until a statistically significant peak signal $\{(P + B) - B\}$ is detected for an element in specific mineral systems. Conditions so determined are then used in subsequent analyses. Experience has shown that relatively few analyses need be taken to establish the optimum sampling condition for that element for the confidence level desired. We use an automated program with the ability to find the sampling condition optimized for each element of interest because different elements inherently have different detectability limits in the same sample. No one sampling routine, with given counting time and numbers of replications, will provide statistics adequate for detection of all trace and minor elements of interest.

The "minimum sampling condition" is defined as that sampling condition (specified by a given counting time and number of replications) for which the least total analysis time is required to detect a significant peak signal at a predetermined confidence level. The "minimum sampling condition" for an element may be found during automated probe operation by varying the sampling time (t) and number of replications (n). Other conditions, e.g., beam current, may be varied as well, since we use beam current integration to determine counting time. The operator establishes the minimum and maximum values of these variables at the beginning of a run. In the example given below which is used to illustrate the technique, we have chosen minimum and maximum values for time and number of replications as (2.5, 20 sec.) and (2, 8 replications), respectively. The search for the "minimum sampling condition" is computer controlled. A simplified flow chart is shown diagrammatically in Figure 1. For each element of interest, the program can direct the search through a matrix of variable sampling conditions as shown in Figure 2. For each specified sampling condition (t,n), the sample is analyzed for the given element's peak + background and background signal. The detection criterion, described below, is then evaluated. If the element is not detected, then new sampling conditions are tried until a peak signal is detected, or the boundary sampling conditions are reached, in which case the element is considered for practical purposes to be absent. A matrix of possible sampling conditions is given in Figure 2.

The sequential search for "minimum sampling conditions" for an element requires the detection of a statistically significant x-ray signal from that element. The criterion used to detect a given x-ray peak is the statistical significance of the difference between the peak + background and background mean counts, and is assessed by application of the Student's t-test for the difference between two means. For each sampling condition, counts are collected at peak, and upper and lower background wavelengths. The upper and lower backgrounds are used to construct the background signal at the peak wavelength. Then, for all replications at that sampling condition, the lower confidence limit of the mean of the total counts, and the upper confidence limit of the mean of the background counts, are calculated.

If the former is greater than the latter, then a statistically significant signal due to the presence of that element has been detected over background (at that alpha level and degrees of freedom).

As an example using this procedure, we have analyzed the Clear Lake plagioclase standard for which selected trace elements have been determined by isotope dilution, spark source mass spectrometry, and ion microprobe techniques. Results for Fe, Mg, and K are presented in Table 1. The sequence of sampling conditions leading to the "minimum sampling condition" of Fe is shown in Figure 2, and illustrated in Figure 3 (data in Table 1). Note that the Fe peak is highly resolved at maximum time and minimum replications. We suspect that less analysis time is required for adequate peak resolution. So we try the minimum time, but do not get peak resolution. We find the "minimum sampling condition" at the intermediate time. Analogous procedures showing the change in peak resolution with changes in time were used to find the "minimum sampling condition" for Mg (Figure 2, Table 1).

Our program of initial study of the trace and minor elements provides us with the minimum amount of machine time necessary for their detailed analysis in the given sample for specified confidence levels. Therefore, the larger the study, the more time will be saved by the determination of the "minimum sampling condition" for each element, and the smaller the relative cost of this initial determination.

Reference

Rohlf, F. James and Robert R. Sokal (1969) *Statistical Tables*. W. H. Freeman and Co.

Lake County
Plagioclase Standard

	Time (sec)	n	$\bar{Y}_{(P+B)}$	$s_{\bar{Y}(P+B)}$	$\bar{Y}_{(B)}$	$s_{\bar{Y}(B)}$	$\bar{Y}_{(P+B)}-ts_{\bar{Y}}$[1]	$\bar{Y}_{(B)}+ts_{\bar{Y}}$[1]	Concentration[2] (ppm)
Fe	2.5	2	71	9	33	5	< 0	100	2954(1127)
Mg	2.5	2	72	5	57	1	9	74	302(90)
K	2.5	2	61	12	11	2	< 0	36	1245(332)
Fe	2.5	4	81	6	35	4	63	47	3731(435)
Mg	2.5	4	87	6	56	6	69	74	543(109)
K	2.5	4	51	5	12	1	35	16	996(83)
Fe	2.5	8	80	7	35	2	63	40	3653(257)
Mg	2.5	8	93	6	58	2	79	63	603(36)
K	2.5	8	51	7	14	3	34	21	913(83)
Fe	5.1	2	146	6	57	1	70	66	3576(233)
Mg	5.1	2	185	25	120	4	< 0	170	603(271)
K	5.1	2	105	9	33	5	< 0	90	913(83)
Fe	20.3	2	612	10	252	2	485	282	3653(117)
Mg	20.3	2	758	7	453	10	662	586	663(0)
K	20.3	2	454	10	133	7	327	215	996(0)

[1] t-value taken from Rohlf and Sokal, 1969, Table Q, with α = 0.05 (95% confidence interval), degrees of freedom = n - 1.

[2] Means and their standard errors.

Figure 1. Summary flowchart of computer program for automated probe operation for finding "minimum sampling conditions" of trace and minor elements.
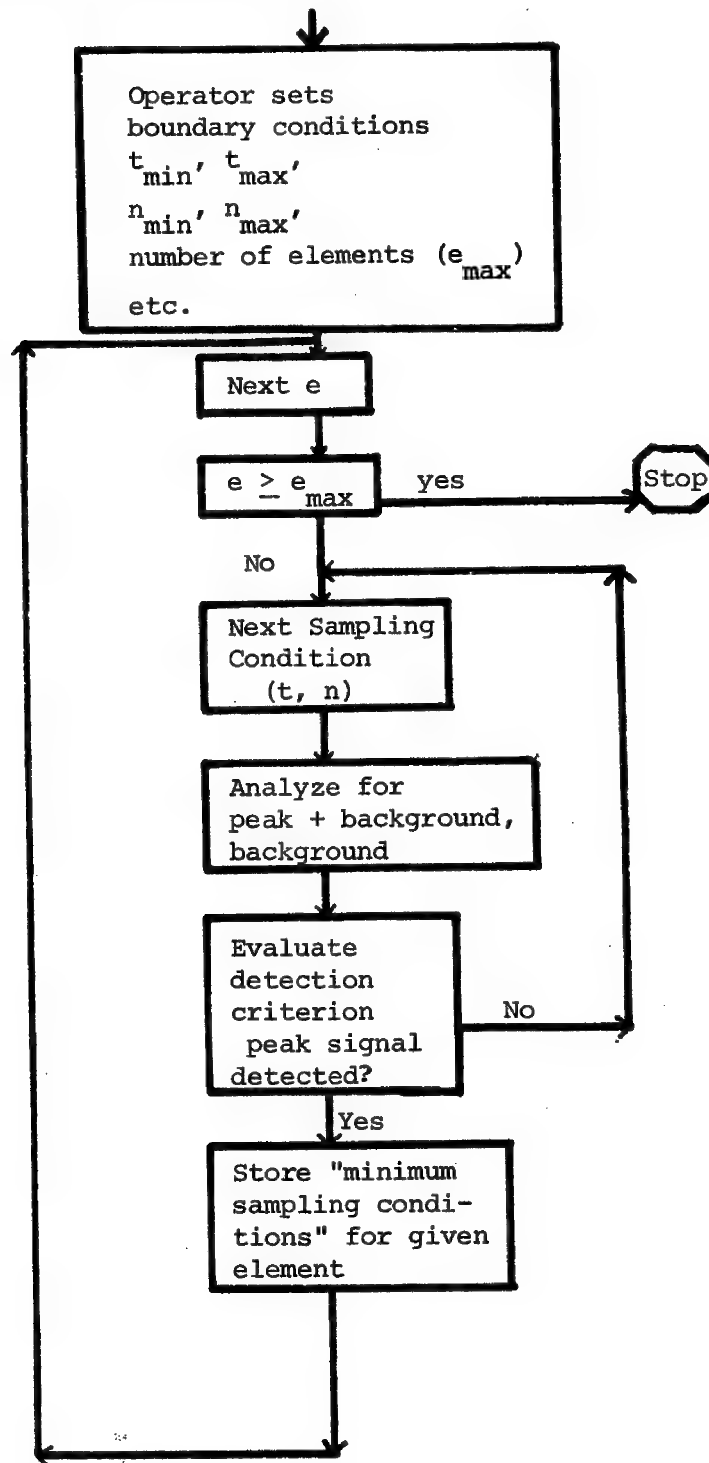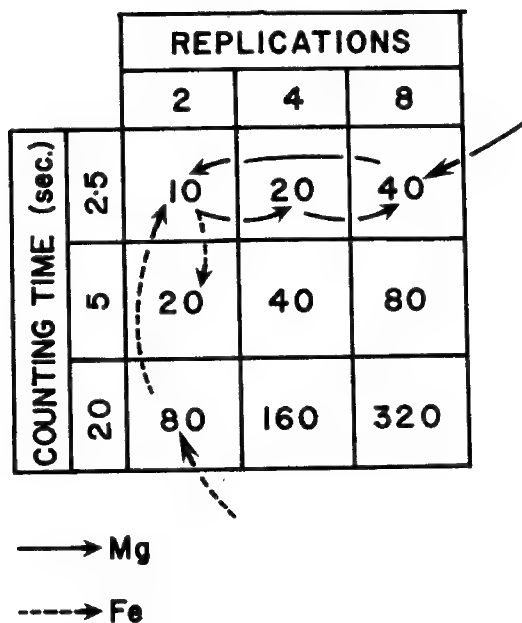
Figure 2. Matrix of possible sampling conditions (t,n), their total analysis times, and pathway to optimal sampling condition, for Fe and Mg. Total analysis time = counting time x replications x 2. (The factor of 2 indicates the number of replications of table 1/4 to upper, and 1/4 to lower, backgrounds.)
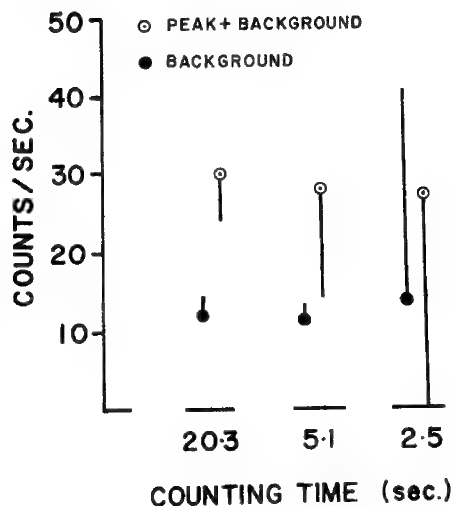
Figure 3. Variation in peak resolution from background of Fe with counting time (data from Table 1). Circled dots indicate location of mean; extended vertical bar equal in length to 1/2 the 95% confidence interval of the mean (two-tailed test). Peak + background and background bars displaced on abscissa, only for purposes of clarity.

QUANTITATIVE ANALYSIS OF TRACE ELEMENT CONCENTRATIONS OF NI AND CR IN BASALTIC GLASSES

C.H. Nielsen
Graduate School of Oceanography
University of Rhode Island
Kingston, R.I. 02881

The determination of the trace element composition of very small volumes of basaltic glasses, mounted as petrographic thin sections, is made possible only through the careful application of the electron probe microanalyzer. However, when analyzing trace elements (in glasses) there exist two restrictions associated with the electron probe technique; namely (1) the loss of volatile elements during analysis under the beam and (2) minimum detectability limits which approach the concentration of the trace elements of interest. In most microprobe studies loss of volatiles is not a problem and detectability limits are improved through optimization of the electron beam parameters. Detectability limits are improved through optimization of the electron beam parameters. Detectability limits of 10 to 20 ppm are routinely achieved by employing a beam voltage of ~20 kv, absorbed currents of ~0.3 µA and long counting times (100 sec). Unfortunately these conditions are unacceptable when analyzing basaltic glass for elements such as Na, S, Cl and F due to their high degree of volatization. Therefore the aim of this study was to determine the optimum working conditions under which reasonable detectability limits could be achieved without appreciable volatile loss and then to characterize the precision and sensitivity of the technique under these conditions.

It was determined that the problem of volatization during analysis could be minimized by operating with a beam voltage of 15 kV and an absorbed current of 0.01 µA. Under these conditions a loss of less than 5% was observed for Na, S, F and Cl in a glass matrix for counting times of up to 800 seconds.

It was of primary interest to analyze the basaltic glass sections for Ni and Cr, however, the same spots would later be analyzed for the volatiles. Hence the reduced beam conditions would have to be used for all trace elements. In order to characterize the precision and sensitivity of the measurement of trace amounts

of Ni and Cr a study was made on GSJ standard reference rock JB-1.[1]   A fused
rock powder bead of JB-1 containing 135 ppm Ni and 409 ppm Cr was analyzed under
the above conditions with a JEOL model JXA-50A microprobe.   It can be seen in
figure 1 that a typical wavelength scan of JB-1 for Ni revealed a peak with
intensity of ~14 cps and a corresponding peak to background ratio of ~1.20.   A
similar scan for Cr yielded a peak rate of ~11 cps and a peak to background ratio
of ~1.80 as shown in figure 2.   In order to convert the peak intensities to
concentrations the system was calibrated for Ni using a nickel-olivine standard
and for Cr using a chromite standard both on LiF analyzing crystals.   It was found
that application of the Bence-Albee or ZAF MAGIC IV correction schemes resulted
in a maximum change of less than 10% for both Ni and Cr.   Therefore the intensity
ratios were corrected for beam drift but not for matrix effects.   A total of 50
separate measurements were made of Ni and Cr using the trace element automation
provided by Krisel control consisting of eight replications of 100 second duration
per measurement.   The results of the study have been compiled in histogram form and
are illustrated in figure 3 for Ni and figure 4 for Cr.   The horizontal axes
represent the percent of relative error while the vertical axes represent the
frequency of each analysis error.   The results of a statistical analysis on each
histogram are listed in table 1.

	Nickel	Chromium
JB-1 Trace Amount	135 ppm	409 ppm
Total No. of Analyses	50	50
Arithmetic Mean	-0.7	-1.3
RMS Error	8.35	5.28
1 Standard Deviation	8.21	5.09
% of Errors within ±1%	18	22
% of Errors within ±2%	31	52
% of Errors within ±3%	42	70
68% of Errors within ±%	7.0	3.0
No. of Positive Errors	20	24
No. of Negative Errors	30	26

Table 1.

As seen in table 1 the precision of the analyses for both Ni and Cr is much
better than might be expected.   Preliminary studies on trace amounts of S, Cl, and
F suggest precisions comparable to those reported above.

A theoretical estimate of the sensitivity of the microprobe technique at trace levels can be made using Ziebold's[2] relationship which states that

$$C_{DL} \geq 3.29 \, a \Big/ \sqrt{nt \, P \cdot P/B} \ .$$

Here the sensitivity or detectability limit, C_{DL}, is proportional to the conversion parameters, a, the number of replications, n, counting time, t, peak rate, P, and peak to background ratio, P/B. In the case of Ni the theoretical C_{DL} is 55 ppm. This is in good agreement with the experimental results as determined by Theisen's[3] expression

$$C_{DL} = \frac{C_s}{\overline{N}_s - \overline{N}_B} \cdot \frac{\sigma t \sqrt{2}}{\sqrt{n}} \ .$$

Here C_s is the concentration of the standard, $\overline{N}_s$ is the mean count rate from the standard, $\overline{N}_B$ is the mean background taken from the unknown, n is the number of replications, t is the student's factor and σ is the standard deviation of the n measurements of the peak to background ratio taken from the unknown. It was found that Theisen's expression yielded an average C_{DL} of 48 ppm for Ni and 39 ppm for Cr.

References

1. A. Ando, H. Kurasawa, Te. Ohmori and E. Takeda, Geochemical Journal 8 (1974) 175.

2. T.O. Ziebold, Analytical Chemistry 39 (1967) 859.

3. R. Theisen, "Quantitative Electron Microprobe Analysis" Springer-Verlag, N.Y., 1965.
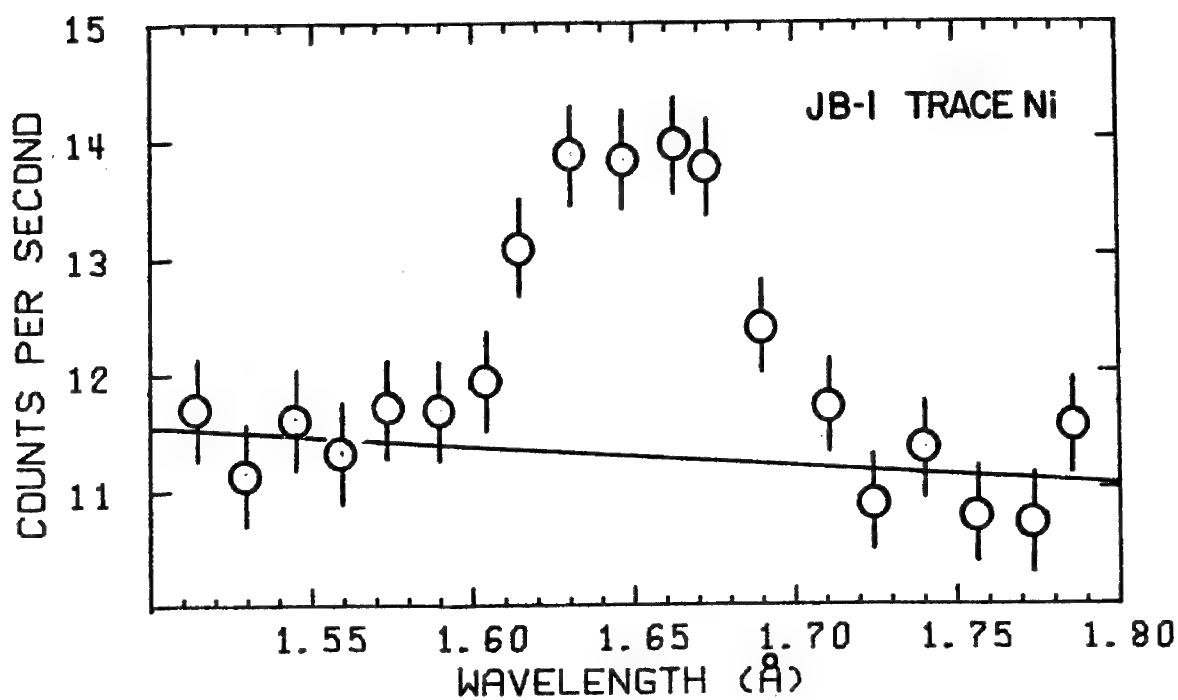
Figure 1
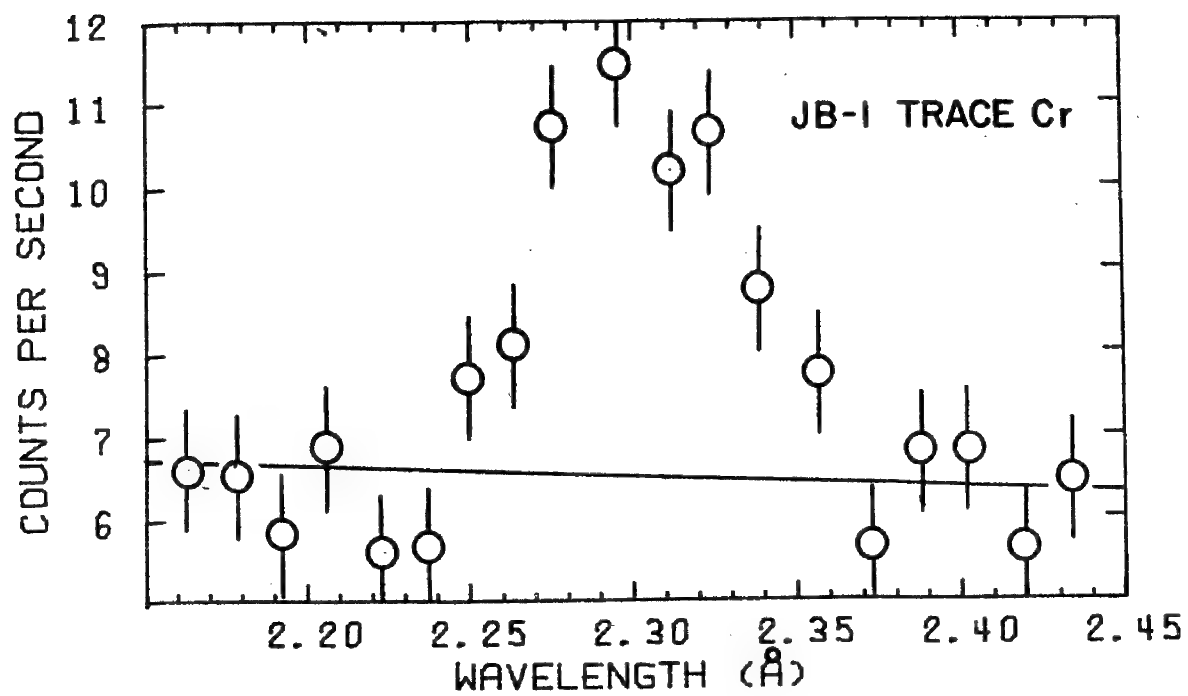
Figure 2
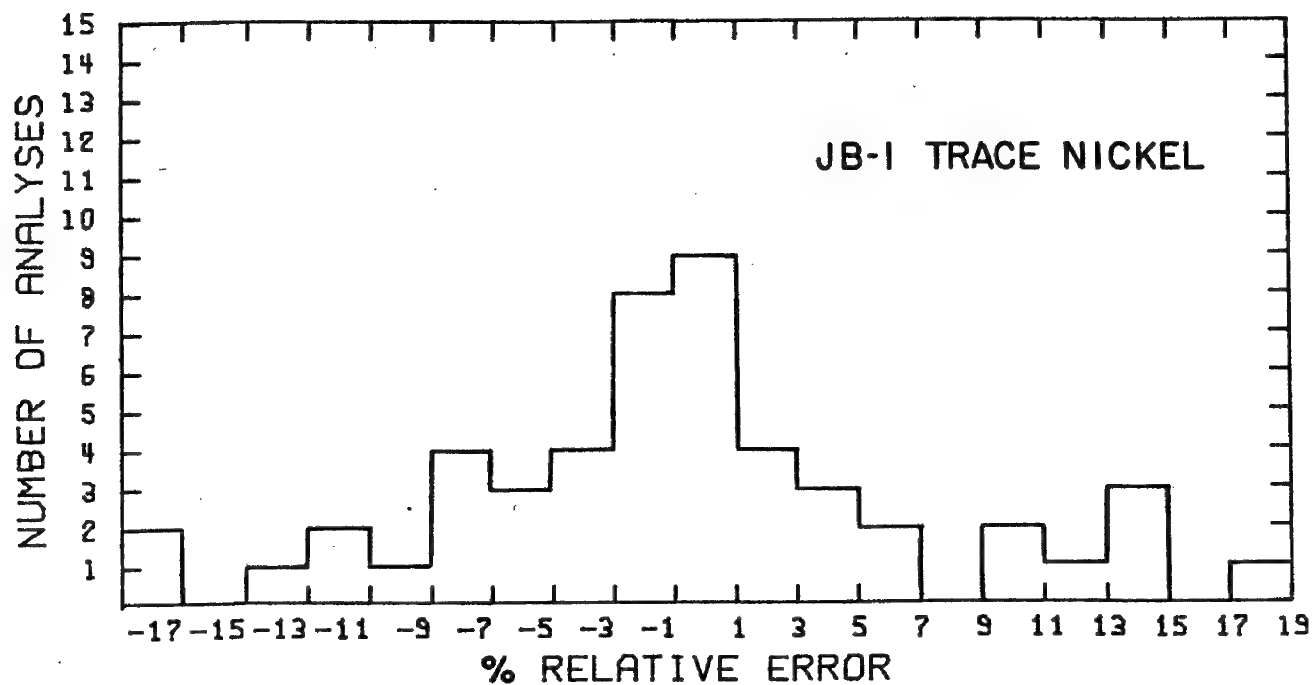
Figure 3
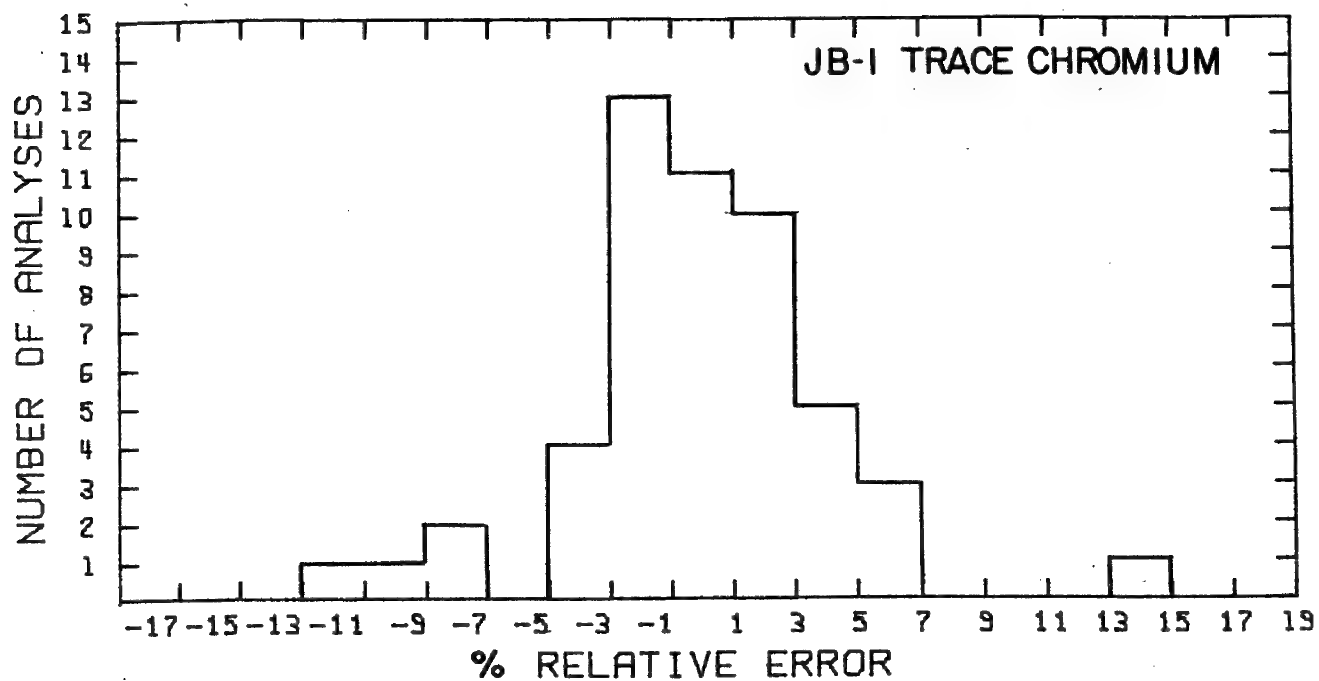
Figure 4

Abstract

A rapid-analysis program for use in
microprobe studies of plagioclase and olivine

H.D. Huntington, S.A. Morse, W.A. Ranson

Introduction

Mineral species that form simple isomorphous series involving the substitution of two of three elements lend themselves to rapid analysis by the electron microprobe. A rapid-analysis computer program has been developed for the solid solution series encountered in the minerals plagioclase and olivine. This method requires the measurement of only three elements, and the subsequent calculation of the remaining elements on the basis of stoichiometry. Use of this technique on three-spectrometer instruments allows the spectrometers to remain stationary, thus reducing analysis time to a single fifteen second counting period.

Plagioclase feldspar solid solution series

For the plagioclase solid solution series from albite ($Na\ Al\ Si_3O_8$) to anorthite ($Ca\ Al_2\ Si_2\ O_8$) the oxides CaO, Na_2O, and K_2O are measured. Potassium is included because it commonly substitutes for Na, especially in soda-rich members of the plagioclase series. The remaining oxides, SiO_2 and Al_2O_3 are calculated:

$$\text{Weight \% } Al_2O_3 = [2\ (\text{mole \% Ca}) + \text{mole \% K} + \text{mole \% Na}] \times \frac{\text{molecular weight } Al_2O_3}{2}$$

$$\text{Weight \% } SiO_2 + [2\ (\text{mole \% Ca}) + 3\ (\text{mole \% Na} + \text{mole \% K})] \times \text{molecular weight } SiO_2$$

Both the measured and calculated weight percents are corrected using the Bence-Albee iterative technique, rather than by utilizing a working curve. The measured data is thus used in the calculation of the unmeasured oxides, but the mole percent anorthite and the mole percent orthoclase are calculated from the measured quantities only. The output after each analysis consists of the mole percent anorthite, the mole percent orthoclase, the concentration of potassium (in parts per million), and the sum of the weight percents of the oxides, both measured and calculated. After the desired number of analyses of a sample have been completed, the results may be averaged and the standard deviation computed for each of the parameters listed above. In addition the maximum and minimum mole percents of anorthite and the number of samples averaged are given.

Olivine solid solution series

For the olivine solid solution series from forsterite ($Mg_2Si\ O_4$) to fayalite ($Fe_2\ Si\ O_4$) the oxides MgO, FeO, and MnO are measured. Manganese is included because it is the chief dilutant of Mg and Fe in the olivine series. The only other oxide, SiO_2, is calculated:

$$\text{Weight \% } SiO_2 = [(\text{mole \% Mg} + \text{mole \% Mn} + \text{mole \% Fe})/2] \times \text{molecular weight of } SiO_2$$

For olivines the output following each analysis consists of the mole percent tephroite, and the sum of the weight percents of the measured and calculated oxides. As in the case of the plagioclase series the SiO_2 in olivines is calculated and summed with the measured oxides in order that the results can be corrected using the Bence-Albee iterative technique. Sample averages and standard deviations are analogous to those described for the plagioclase series.

Procedure and application

Separated mineral samples are contained in multiple-sample grain mounts, and the standard procedure is to analyze ten grains from each sample. The program output consists of averages of these results as described in the previous sections. Computer commands within the program allow the operator to delete analyses of mineral grains having unacceptable sums or which obviously are not members of the isomorphous series being considered.

An example of current usage of this rapid-analysis computer program at the University of Massachusetts involves an analysis of the change in olivine composition in the Kiglapait layered intrusion, Labrador. Within the stratigraphic succession of the intrusion olivine compositions range from Fo_{72} (Lower Zone troctolites) to Fo_4 (Upper Zone ferrosyenites), and an effort is now being made to document in detail the change in olivine composition in the intervening stratigraphy. Another example of application concerns anorthosites in the Nain complex of central Labrador. A field area west of the Kiglapait intrusion has been mapped and sampled in detail, and multiple analyses of plagioclases have been performed by the rapid technique. These data are valuable because they aid in defining the compositional range of the anorthosite. Furthermore, the distribution of plagioclase compositions within the field area will show any systematic change in composition across the area and perhaps define individual intrusive bodies within the anorthosite massif.

THE USE OF AN AUTOMATED MICROPROBE
IN GEOSCIENCES APPLICATIONS

G. REMOND[1] - R. GIRAUD[1] - C. CONTY[2] - M. TONG[2]

(1) BRGM - Service Géologique National
BP 6009-45018 ORLEANS-CEDEX - France

(2) CAMECA - 103 Boulevard Saint-Denis
92400 COURBEVOIE - France

-o0o-

1/ Aims

We propose to draw attention to the possibilities created in all the fields of the earth sciences by the introduction of automated electron microprobes. Before describing the means and methods to be put into action, it is fitting to specify reasons, regarding the number of analyses, as well as the precision, which justify the different steps to be taken for data acquisition and data reduction.

Through automation, the electron microprobe has become a device comparable in its analytical rhythm to other means such as, for example, the optical emission spectrometry (quantometry) with direct readings.

In the field of petrology, the search for an important analytical rhythm is warranted by the need for a statistical treatment of exact chemical data. It is thus possible to obtain information on the chemistry of a rock or of one of its constituents, starting from a very great number of measurements carried out on different minerals set out in several samples. Similar research can be made on glass obtained by the melting of the materials with or without the addition of a flux. Afterwards one can realize different thermodynamical parameters which may give information on the evolution of the natural systems. However, the statistical data reduction must not let one neglect the precision of the measurements.

Indeed, in the field of experimental mineralogy it is especially the precision of the analysis which is the determining factor. In fact, the study of the variations of stochiometric readings of certain minerals can be a thermal or barometric indicator. These same data are indispensable for directing and modify the experimental conditions to be realised for tests of synthesis of materials. The precision of the analyses

should be better than one percent for a system containing numerous elements of very different atomic number and concentration. It will then be possible to establish, from the analytical results, the chemical formulae of materials whose compositions are very closely related. The use of the automated microprobe analyzer offers at the same time possibilities for the modal analysis of the rocks. This aids us in choosing the steps to take in the evaluation of ore deposits.

To find answers to these problems, we fitted the associated CNRS-BRGM laboratory with an automated CAMECA-MBX electron microprobe. The quantitative analysis on a routine basis of very differing materials, takes the leading place in the fulfilment of our project for achieving our aims.

2/ <u>Needs in analytical methods</u>

On the whole, the problems of the earth sciences show the need for two orders of importance of precision. The two following cases can be distinguished :

. Analyses bearing only on a limited number of elements where an order of importance of the concentrations is sufficient to take away the incertainty of the nature of the minerals which could not be recognized optically.

. Analyses needing a precise chemical balance sheet.

The possibility of being able to satisfy these two objectives with the same analytical means was one of the parameters taken into consideration when deciding on the equipment to keep among the choices existing at the moment, as much in the field of processing units as in the methods of detection and analysis of X-rays.

The different approches of automation were discussed time and again |1| to |7|. The present cost of computers of average power allows us to contemplate the feasibility of an automated microprobe. It is this solution which we have adopted. In practice, to be fully effective and to satisfy our two objectives, rapidity and accuracy, it is desirable that the technology used should permit the two following conditions :

a/ The measurements of the intensities of the wavelengths characteristic of all elements to be analysed are carried out on the same electron beam location. <u>This procedure is particularly recommended in the case of the analysis of finely-zoned samples</u>.

b/ The reduction of the experimental data corresponding to a given position of the electron beam on the surface of the sample, are carried out before starting to collect specific information about another part of the preparation. <u>This procedure offers a step-by-step verification of the results, which allows us to direct the research and to select, at each moment, the areas in the sample which are to be analysed</u>.

3/ Choice of methods

The advantages of the simultaneous analysis of the elements were discussed |8| in the case of the study of natural materials. Simultaneous analysis can be performed using the following techniques :

- multiple fixed monochromators
- automated scanning monochromators
- E D S

or a combination of all three.

For the questions of organization of our laboratory, and taking into account the variety of the tasks, we were led to create two distinct laboratories, one specializing in electron microscopy with the possibility of qualitative analysis by energy dispersive spectrometer, the other in quantitative analysis.

This is why we equipped our MBX instrument with four automated spectrometers of the WDS type. This specialization of the MBX presumes that all the samples are prepared in polished sections and set out perpendicularly to the direction of the electron beam. As a result of this, the functioning in SEM of the instrument is only used in the locating of the zones to be analysed. This is accomplished directly, without any changes in the conditions of excitation required for microanalysis with the WDS spectrometer. In this configuration, the instrument is equipped with a non-tilting sample specimen stage which allows us to get rid of errors due to the position of the sample in regards to the direction of the incident beam. The equipment is completed by an optical system used to observe the specimen in reflected light, as well as in transmitted polarised light, allowing an easy and quick recognition of the areas to be analysed. The entire instrument, in fact, offers such stability that the calibration of the system for a series of repetitive analysis needs only be done once a day.

4/ Applications

The carrying out of the analyses calls for a collection of programs for control of the instrument, data acquisition and data reduction. Some of them are linked and used as analytical programs. The language which has been used until recently is CLASS (CANBERRA Laboratory Automation Software System) which is an interpreter language.

We propose to illustrate the use of the automated equipment in the case of a quick exploratory study of a compound, then a quantitative analysis on a routine basis of silicates and natural sulphides.

4.1. - Exploratory study

With our equipment, the four monochromators are scanned simultaneously, each of them in 1 000 channels. The width of a channel is then about 5 eV for the Lif crystal and 1 eV for the TAP crystal. The information is analysed by the computer and the peaks which have an intensity of 1.5 times above background are detected. The scanning of the entire spectra of the elements from F to U takes about 4 to 5 minutes. The time needed to calculate and to print the positions of the emission lines and their net counts is on the order of 30 seconds for each WDS.

Examples of analysis of natural samples are given on Fig. 1. The time taken to obtain data is seven minutes. These delays are very acceptable in comparison to the time taken for obtaining the data for the measuring of the intensities with an EDS system. We benefit also from the high values of the signal to noise ratio of the WDS spectrometers and despite the limited number of channels, a sligthly better peak separation.

Indeed, the examples show that the characteristic radiations of elements in weak concentrations have been resolved and this allows us to estimate the limit of detection by this exploratory method to concentrations of approximately 0.5 %. On top of this, it is possible to control automatically the PHA as the exploration of the range of wavelengths for the crystal proceeds, which allows us to eliminate all multiple orders of fundamental lines.

4.2. - Quantitative analysis

A flow chart of a quantitative analysis is illustrated in Fig. 2. It calls for a sum of programs of control and analyses |15|. At the level of the acquisition of experimental data, the speed and the precision of the measurments are closely linked to the efficiency of the programs in searching for analytical rays and the locating of the analyser crystals in the course of repetitive analyses. The crystal explores by successive scannings , step by step a very narrow field around the theoritical position of the emission of the radiation analysed. The centre of gravity of a small portion of the peak near its maximum is calculated. We then verify that the reproducibility of the crystal's position is within 5 steps, which corresponds to an error of $5_{10}-5$ on the value of $\sin\theta$. Shifts due to chemical binding are generally larger and one has to be aware of this effect when using the standardization procedure. Because we use oxyde standards for the analysis of silicates, the shifts are not significant.

This procedure allows us to limit the time of an analysis without any loss of accuracy. In practice, in the case of a

silicate for which 10 or 12 elements are to be analysed, the time for three successive sequences is on the order of three minutes.

A ZAF program is available to reduce the experimental data. The results delivered by this program are practically identical to those of the program MAGIC IV |16|. In forward mode the average length of a calculation is presently with the inter- preter language a few tens of minutes. To overcome this dif- ficulty, we have adopted several stages in the development of the software of data processing. Being interested primarily in the analysis of silicates, we used the matrix correction method with predetermined "influence" coefficients. We then looked for a way of generalizing this method of calculation for all natural materials, to be able to cope without delay with almost all our problems. The final objective is to in- clude, in the near future, in our software package, control programs, acquisition programs and a ZAF data reduction pro- gram written in the fast compiler FORTRAN language.

The method of matrix correction tends to become as general as much in X-ray fluorescence as in microanalysis |17||18||19| |20||21|. It is especially well suited to the case of repeti- tive, routine analysis of the same mineral.

Indeed, a certain number of characteristic parameters of the sample studied are common at each individual measurement and can be stored. Therefore, rather than introducing repeatedly the same parameters, we replaced the ZAF correction at each analysis by a matrix method using αAB coefficient of "influ- ence" calculated beforehand by this same ZAF method.

The determination of the coefficient AB is obtained from a polynominal representation of $\frac{CA}{KA}$ versus CA in different binary compounds AB. In general, an estimation of $\frac{CA}{KA}$ versus CA is satisfactory in the case of the study of silicates. We have also been able to check that approximation remains valid in the case of the analysis of sulphides where the effects of atomic number and fluorescence are high |22|.

The programs "CORREX and ALPHA" written by HENOC and TONG |23| allow the direct determination of the relation :

$$\beta x = \frac{CA}{KA}$$

relative to the pure element for each value of the concentra- tion CA in a binary compound AB. These values are needed in the calculation of the coefficients of influence in a first order approximation following the relation

$$\alpha AB = \frac{\beta x - x}{1 - x}$$

where x is a particular value of CA in the compound AB being

considered. We have shown |22| that the variations between the corrected values of the same experimental data, carried out with the help of the coefficient αAB corresponding to $x = 0,25$ and by the ZAF model, remain on the order of one percent in the case of the major elements of silicates and sulphides.

For the analysis of the minor or trace elements, the variations between the two methods of calculation is somewhere between 3 and 5 %. The results of Fig. 3 show that with the methods which have been briefly described, the automated sequential analysis lets us satisfy our two aims speed and precision. These methods work as well for sulphides for which in the same family the ratio between two elements frequently changes, as well as they do for silicates.

5/ Conclusions

The wavelength dispersive analysis using an automatized sequential method lends itself as much to the needs of exploratory research as to the obtainment of an accurate chemical balance sheet of all the natural materials. Thanks to the software at our disposal, we can combine the resolution and the high signal to noise ratio characteristic of the WDS with the speed of qualitative analysis formerly obtainable only with EDS.

These advantages are consistent with the exigencies required in speed and accuracy of the quantitative analysis on a routine basis. The preparation and standardization of the instrument having being carried out, a complete chemical balance sheet of the area analysed is obtained in less than 4 minutes. At the present time, program in FORTRAN are at our disposal and we are beginning to use them for both the control of the instrument and for the data reduction.

In exploratory analysis, for example, it is possible to increase the number of channels explored to 2 400 instead of 1 000 at the present time, thanks to the speed of calculation of the data thus obtained. From the point of view of the quantitative processing of the experimental data, it is possible to increase the speed of execution of the ZAF program. This allows us to complete the possibilities of the matrix calculation with predetermined "influence" coefficients. This latter method is in fact limited, since the calculated values of these coefficients are only usable for clearly defined conditions of excitation. Moreover, it is insufficient in the case of the quantitative analysis of the minor or trace elements in the minerals due to the first order approximation error made in the calculation of the "influence" coefficients.

|1| CHAMBERS W.F. - 8th Nat. Conf. E.R.A.S.A, August 13-17, 1973
New-Orleans, La, n° 41

|2| CHODOS A.A., ALBEE AL, GANCARZ A.J., LAIRD J - 8th Nat. Conf.
E.P.A.S.A., August 13-17, 1973 - New-Orleans, La, n° 45

|3| ESTILL W.B., BENTHUSEN D.E., 8th Nat. Conf. E.P.A.S.A.,
August 13-17, 1973, New-Orleans, La n° 43.

|4| HOLZWARTH W., QUIGGE E., PREWITT C.T., 8th Nat. Conf.
E.P.A.S.A., New-Orleans, La, n° 42

|5| KYSER D.F., AYERS G.L., HORNE D.E., 8th Nat. Conf. E.P.A.S.A.
August 13-17, 1973, New-Orleans, La, n° 44

|6| HATFIELD W.T., 11th Ann. Conf. M.A.S., August 9-13, 1976
Miami Beach, Florida, n° 67

|7| KANG W.T., 11th Ann. Conf. M.A.S., August 9-13, 1976,
Miami Beach, Florida, n° 3

|8| JAROSEWICH E., OBERMEYER C., NELEN J. - 9th Ann. Conf. M.A.S.
July 22-26, 1974, Ottawa, Canada, n° 20

|10| DESBOROUGH G.A., HEIDEL R.H., Jour. Research U.S. - Geol
Survey, 1974, 2, n° 4, 441-446

|11| SERVANT J.M., MENY L., CHAMPIGNY M.,
X-ray Spectrometry, 1975, 4, 99-107

|12| GASPARRINI E., Minerals Sci. Engng, 1976, 8, n° 1, 3-22

|13| BEAMAN D.R., SOLOSKY L.F., 9th Ann. Conf. M.A.S.
July 22-26, 1974, Ottawa, Canada n° 26

|14| REMOND G., J. Microsc. Spectrosc. Electrn., 1976, 1 497-504

|15| GIRAUD R., REMOND G., Bull. BRGM, to be published

|16| COLBY J.W., 6th Nat. Conf. E.P.A.S.A., July 27-30, 1971,
Pittsburg. Pen. n° 7

|17| ZIEBOLD T.D., OGILVIE R.E., The electron Microprobe,1966,
J. WILEY Ed., 378-389

|18| BENCE A.E., ALBEE A.L., J. Geol, 1968,76, 382-403

|19| ALBEE A.L., RAY L., Anal. Chem., 1970, 42, n° 12, 1408-1414

|20| CLAISSE F., 9th Ann. Conf. M.A.S., July 22-26, 1974
Ottawa, Canada

|21| REMOND G., JOHANZ, GIRAUD R., JOSEPH E., Bull. Soc. fr.
Mineral. Cristallogr., 1974, 97, 211-216.

|22| REMOND G., GIRAUD R., TONG M., Bull BRGM to be published

|23| HENOC J., TONG M.,
Private communication, to be presented at the 8th Int.
Conf. on X-ray optics and microanalysis, August 18-24, 1977,
Boston, Mass.

FIG. 1 - EXAMPLE OF QUALITATIVE ANALYSIS

A/ - INITIALISATION OF 4 WDS USING AN ANDRADITE MINERAL $(SiO_4)_3 Ca_3 Fe_2)$

- Positions are in $\sin\theta \times 10^5$
- TAP controls peak on Si; PET crystal on Ca; LiF crystal on Fe
- Reference positions obtained by averaging 3 peak search routines

B/ QUALITATIVE ANALYSIS OF AN ORTHOSE MINERAL $(Si_3 AlO_8) K$

Note :
Low concentration of Na $(Na_2O=0.3 \%)$ on spectrometer N1 and 2 and of Fe $(Fe_2O_3 = 0.8 \%)$ on spectrometer n° 3 are detected

---

```
SPECTRO. > ANDRADITE

    # OLD POS. & FREQ. :

DATE :  5    T : 13 HR 29 MN

X = 13368  Y = 26510  Z =  4171


T =  1.0 SEC

NO.SP  POSITION      INTENSITE(C/S)
   1     27735         2501.000
   2     27735         1345.000
   3     48082          459.0000
   4     38383          741.0000
```
) (initial
) theoritical
(positions

```
WAIT FOR INIT.) !!

X = 13368  Y = 26510  Z =  4171


T =  1.0 SEC

NO.SP  POSITION      INTENSITE(C/S)
   1     27747         2520.000
   2     27688         2547.000
   3     48076         .480.0000
   4     38475         1997.000


X = 13368  Y = 26510  Z =  4171


T =  1.0 SEC

NO.SP  POSITION      INTENSITE(C/S)
   1     27747         2456.000
   2     27686         2487.000
   3     48084          444.0000
   4     38474         2160.000


X = 13368  Y = 26510  Z =  4171


T =  1.0 SEC

NO.SP  POSITION      INTENSITE(C/S)
   1     27743         2509.000
   2     27685         2451.000
   3     48080          476.0000
   4     38475         2070.000
```
) ( ) (peak
) ( ) (search
) ( ) (routine

```
INIT.SPECTRO. FOR SIKA(TAP/SP1) SIKA(TAP/SP2) FEKA(LIF/SP3) CAKA(PET/SP4

    # NEW POS. & FREQ. FOR ANDRADITE :

X = 13368  Y = 26510  Z =  4171


T =  1.0 SEC

NO.SP  POSITION      INTENSITE(C/S)
   1     27735         2509.000
   2     27735         2544.000
   3     48082          439.0000
   4     38383         2132.000
```
) (reference
) positions
(

```
DATE :  5    T : 13 HR 37 MN
```

```
QUAL.1

REF. OF EXP. IS ? ORTHOSE

ONLY 1 SPECTRO. ? NO

DATE :  5    T : 13 HR 43 MN
  1ST SPECTRO . : TAP
  2ST SPECTRO . : TAP
  3ST SPECTRO . : LIF
  4ST SPECTRO . : PET

DATE :  5    T : 13 HR 50 MN

__ SPECTRO. NO  1 __

___LAMBDA/(A)___PEAK_____BG__P-BG/(C)___

    7.141      27853       1012     26841
    8.313       8614        339      8275
   14.23        1847         78      1769
    7.449       1301        140      1161
    6.771       1302        149      1153
   16.63         507         23       484
    8.004        527        140       387
   11.21         340         85       255
   11.88         199         62       137


DATE :  5    T : 13 HR 51 MN

__ SPECTRO. NO  2 __

___LAMBDA/(A)___PEAK_____BG__P-BG/(C)___

    7.141      24125        807     23318
    8.313       7947        320      7627
   14.23        1516         64      1452
    7.449       1237        111      1126
    6.771       1162        138      1024
   16.63         466         23       443
    8.004        462        122       340
   11.21         321         61       260


DATE :  5    T : 13 HR 52 MN

__ SPECTRO. NO  3 __

___LAMBDA/(A)___PEAK_____BG__P-BG/(C)___

    1.940        114         57        57


DATE :  5    T : 13 HR 52 MN

__ SPECTRO. NO  4 __

___LAMBDA/(A)___PEAK_____BG__P-BG/(C)___

    3.733       4590        104      4486
    3.439        637        121       516
    2.327        288        151       137
    2.432        284        132       152
    2.621        233        124       109


DATE :  5    T : 13 HR 53 MN
```

FIG. 2 - FLOW CHART OF AN AUTOMATED QUANTITATIVE ANALYSIS

CDMBX

Set of routines for the control of the instrument

APPGEO

Geological quantitative analysis program

FIG. 3
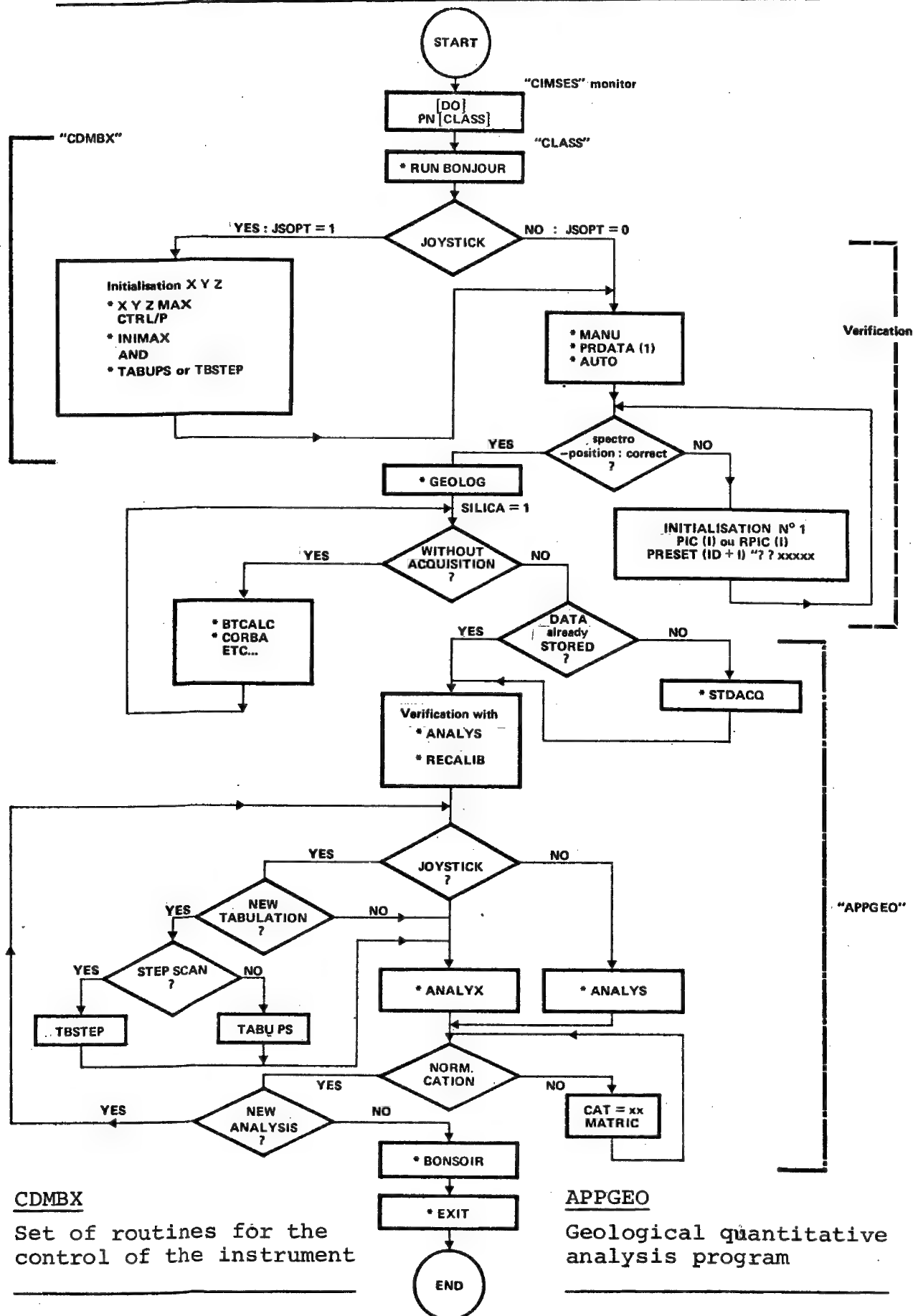
DATE : 3   T : 9 HR 21 MN ①

ELEMENT	PEAK	BG	CONC
NA2O	561.1	10.80	.0833
SIO2	5764.	36.60	.6101
FEO	3.600	5.400	-.0008
TIO2	14.00	15.60	.0000
AL2O3	1787.	16.80	.1765
MGO	5.400	8.400	-.0004
MNO	4.200	2.400	.0009
K2O	23.80	7.800	.0022
CR2O3	3.000	2.400	.0003
CAO	25.60	13.80	.0015

DATE : 3   T : 9 HR 23 MN

NORMALISATION : CAT = ? 8

ELEM. COMPL. = ? N

OXIDE	WEIGHT % UNCORR.	CORRECTED	CATIONS PER 8 OXYGENS
NA2O	.0833	.1118	.9372
SIO2	.6101	.6968	3.012
FEO	0.000	0.000	0.000
TIO2	.0000	.0000	.0001
AL2O3	.1765	.1942	.9898
MGO	0.000	0.000	0.000
MNO	.0009	.0010	.0039
K2O	.0022	.0025	.0142
CR2O3	.0003	.0003	.0013
CAO	.0015	.0017	.0078
O	0.000	0.000	0.000
TOTAL	.8752	1.008	4.967 ITER. : 2

DATE : 3   T : 9 HR 25 MN

DATE : 3   T : 9 HR 36 MN ②

ELEMENT	PEAK	BG	CONC
NA2O	247.9	10.20	.0360
SIO2	3906.	31.80	.4127
FEO	687.2	5.400	.3223
TIO2	46.60	28.20	.0025
AL2O3	205.1	14.40	.0190
MGO	21.00	13.20	.0010
MNO	32.40	0.000	.0166
K2O	139.4	6.000	.0190
CR2O3	3.200	3.600	-.0002
CAO	152.6	13.80	.0184

DATE : 3   T : 9 HR 38 MN

NORMALISATION : CAT = ? 23

ELEM. COMPL. = ? 0

NBRE MOLES H2O = ? 1

OXIDE	WEIGHT % UNCORR.	CORRECTED	CATIONS PER 23 OXYGENS
NA2O	.0360	.0707	2.232
SIO2	.4127	.4759	7.751
FEO	.3223	.3510	4.781
TIO2	.0025	.0026	.0323
AL2O3	.0190	.0243	.4683
MGO	.0010	.0015	.0382
MNO	.0166	.0181	.2499
K2O	.0190	.0203	.4225
CR2O3	0.000	0.000	0.000
CAO	.0184	.0189	.3311
O	0.000	.0183	0.000
TOTAL	.8477	1.002	16.30 ITER. : 2

DATE : 3   T : 9 HR 40 MN

DATE : 1   T : 13 HR 39 MN ③

ELEMENT	PEAK	BG	CONC
S	881.7	12.00	.2155
AS	43.80	10.20	.0066
FE	13.20	21.00	-.0028
SB	847.3	30.60	.2345
PB	450.0	14.40	.5214
CU	26.00	30.60	-.0022

DATE : 1   T : 13 HR 40 MN

ELEM. COMPL. = ? N

OXIDE	WEIGHT % UNCORR.	CORRECTED
S	.2155	.1875
AS	.0066	.0086
FE	0.000	0.000
SB	.2345	.2512
PB	.5214	.5581
CU	0.000	0.000
O	0.000	0.000
TOTAL	.9781	1.005 ITER. :

DATE : 1   T : 13 HR 41 MN

DATE : 1   T : 15 HR 25 MN ④

ELEMENT	PEAK	BG	CONC
S	1048.	7.200	.2581
AS	56.20	10.80	.0089
FE	10.20	15.60	-.0019
SB	1656.	27.00	.4678
PB	3.400	6.000	-.0031
CU	547.2	24.00	.2539

DATE : 1   T : 15 HR 26 MN

ELEM. COMPL. = ? N

OXIDE	WEIGHT % UNCORR.	CORRECTED
S	.2581	.2552
AS	.0089	.0164
FE	0.000	0.000
SB	.4678	.4804
PB	0.000	0.000
CU	.2539	.2536
O	0.000	0.000
TOTAL	.9889	1.005 ITER. : 1

DATE : 1   T : 15 HR 27 MN

(1)   ANALYSIS OF AN ANHYDROUS SILICATE
(2)   ANALYSIS OF AN HYDROUS SILICATE
       To proceed with data reduction the number of modes of H2O must be entered
(3) (4) ANALYSIS OF NATURAL SULPHIDES (3 : Boulangerite – 4 : Chalcostibine)

Multi-user Microprobe Operating System

Dr. Guy Yagunoff

Geology Department, University of Massachusetts, Amherst, MA 01002

The purchaser and user of modern microanalysis systems is faced with a wide variety of choices in machine configuration, automation and data reduction capabilities. The choice of a general purpose analytical instrument or an instrument optimized to perform a specific task is crucial to the determin ation of the appropriate system. While the University and generalized research laboratories will in general desire the most versatile system, industrial users, often, should look for lower cost, more efficient systems for specific tasks. Factors in considering the proper instrument are speed, complexity of analysis, the type of correction routine or routines best suited to the analysis, the available funds, and in-house personnel.

The general electron microprobe system consists of a source of high energy electrons, a number of wavelength dispersive spectrometers, possibly a solid state energy dispersive system, and a controlling computer facility. Several useful options are facilities for auto focusing and location of samples, micro computer control assemblies, bulk data and program storage facilities, and other computer peripherals.

The quality of each of the above components is a factor in product choice and I will attempt to order the importance of each choice. The quality of the software or computer programs which operate the instrument, while often neglected, are as vital to proper operation as proper hardware selection. This neglect has caused several excellent instruments to be slow or limited in versatility. The choice of a software system is determined in the capability and desire of the end user to modify the running programs. In a university environment the programs should be easily modified so that each task can be custom designed by the investigator. The industrial user on the other hand may be wiser to choose a turn key system which is essentially a black box cared for by the manufacturer.

This presentation will concentrate on methods for configuring an academic oriented multi-user system and cover in detail the choice of computer programs. Criteria for the computer, computer operating systems, languages, both compiled and interpreter types, and correction routines will be covered. The ease of modification and philosophy behind many available systems will be discussed and commented upon. The interaction between software and hardware will be outlined in the context of a general purpose analytical instrument.

An outline of the advantages, disadvantages, and interactions of each hardware and software choice will be presented. A comment upon the needs for improvements by the manufacturers and some thoughts on the future of micro-beam analysis facilities will also be offered.

TRENDS IN ELECTRON ENERGY LOSS SPECTROSCOPY

C. COLLIEX and P. TREBBIA

Laboratoire de Physique des Solides, Université Paris-Sud,
91405, ORSAY, France.

The physical foundations for the use of electron energy loss spectroscopy towards analytical purposes, seem now rather well established and have been extensively discussed through recent publications (1),(2). In this brief review we intend only to mention most recent developments in this field, which became available to our knowledge. We derive also some lines of discussion to define more clearly the limits of this analytical technique in materials science problems.

The spectral information carried in both low ($0<\Delta E<100eV$) and high ($>100eV$) energy regions of the loss spectrum, is capable to provide quantitative results. Spectrometers have therefore been designed to work with all kinds of electron microscopes and to cover large energy ranges for the detection of inelastically scattered electrons (for instance the L-edge of molybdenum at 2500eV has been measured by van Zuylen (3) with primary electrons of 80 kV). It is rather easy to fix a post-specimen magnetic optics on a STEM, but Crewe has recently underlined that great care should be devoted to optimize the collecting power and the energy resolution of the whole system (5).

Despite their relatively low intensity the signals associated to the excitation of core levels are quite suitable for a promising use in microanalysis because they are truly characteristic and can be interpreted with relatively few mathemathical treatments (see references (1) and (4) for a more complete discussion). Moreover experimental data, such as the determination of total scattering cross sections similar to those displayed in fig.1, are now available. It is therefore possible to extend the theoretical predictions that Isaacson and Johnson (6) had established for biological problems, to more realistic estimations of detection limits in typical metallurgical specimens.

Such a situation is illustrated in fig.2 for the measurement of the Al-K and Cu-L$_{23}$ signals in thin foils of Al$_x$Cu$_{1-x}$ alloys. The counting rate is calculated with the formula:

$$R_{tot}(\Delta E) = J_o \cdot \eta_\alpha(\Delta E) \cdot \left[N_{Al} \cdot \left(\frac{d\sigma}{dE}\right)_{Al} + N_{Cu} \cdot \left(\frac{d\sigma}{dE}\right)_{Cu} \right]$$

where J_o is the primary flux of electrons, $\eta_\alpha(\Delta E)$ is the angular collection efficiency, $N_{Al} = xN$ and $N_{Cu} = (1-x)N$ are the numbers of atoms of Al and Cu in the selected volume which is analysed, $(d\sigma/dE)_{Al}$ and $(d\sigma/dE)_{Cu}$ designate the partial cross sections for Al and Cu.

The criterion for the detection of a concentration x in a volume of N atoms is that the signal S (hachured area in fig.1) integrated over an energy window $\delta = 500$ eV obeys the unequality $S / \sqrt{S + B} > 3$, where the background B includes the matrix contribution and the non characteristic contribution of the element itself. From these results which correspond to specific experimental conditions ($J_o = 30$ A/cm^2, $\alpha_{coll} = 10^{-2}$ rad, counting time of 500 s for 500 eV), only general laws of variation must be retained. It is easier to detect Cu in Al matrix than Al in Cu matrix. The minimum concentration is limited by the intense background counting rate for which the detector response is no longer linear. The minimum detectable mass of a pure element is limited by the intensity of the signal itself and can therefore be improved with higher brightness illumination and counting rates.

The use of coincidence techniques has been suggested (7) to improve the sensitivity of the method for the detection of low atomic concentrations. It involves the simultaneous detection of core-loss electrons and of the secondary emission for the same hole. For the analysis of thin foils it would rather concern X-ray than Auger electrons. However it must be emphasized that, if the background contribution in energy loss spectroscopy is nearly reduced to zero, the total signal is even worst than the X-ray signal by itself. No great advantage can therefore be expected and simple X-ray microanalysis of thin foils seems more suitable for areas of 1000 x 1000 Å² and more, in spite of its weaker detection efficiency.

All these considerations actually apply to amorphous or very crystalline samples. In a monocrystal the diffraction conditions can modulate greatly the intensity of a characteristic core signal and care must be taken when using the energy loss spectrum to give compositional informations about crystalline materials. Experiments under development with the STEM instrument in Cambridge show that the silicon L-peak and the zero loss peak vary in quite a different way with position across a stacking fault image (8). The distribution of the electron wave fields within the crystal must then be considered.

Thanks are due to all those who have kindly substantiated this paper through fruitful discussions or communications.

(1) C.Colliex, V.E.Cosslett, R.D.Leapman and P.Trebbia (1976), Ultramicroscopy, 1, 301.
(2) D.B.Williams and J.W.Edington (1976), J. Microscopy 108, 113.
(3) P. van Zuylen (1976), Proc.Eur. Conf. Electron Microscopy, Jerusalem,434.
(4) R.D.Leapman (1976), Ph. D. dissertation, Cambridge university.
(5) A.V.Crewe (1977), Optik 47, 299.
(6) M.Isaacson and D.Johnson (1975), Ultramicroscopy 1, 33.
(7) D.B.Wittry (1976), Ultramicroscopy 1, 297.
(8) A.J.Craven and D.Spalding (1977), private communication.
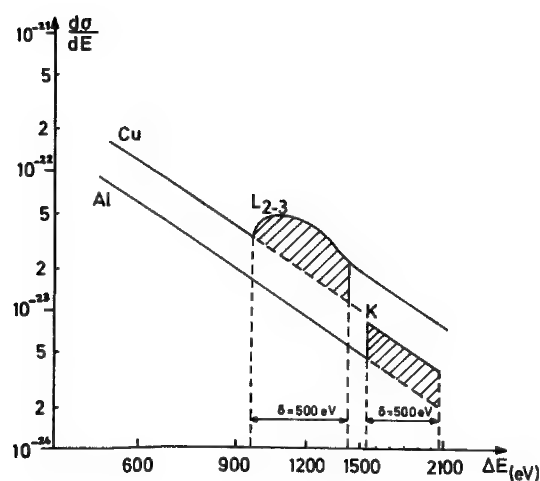
Figure 1
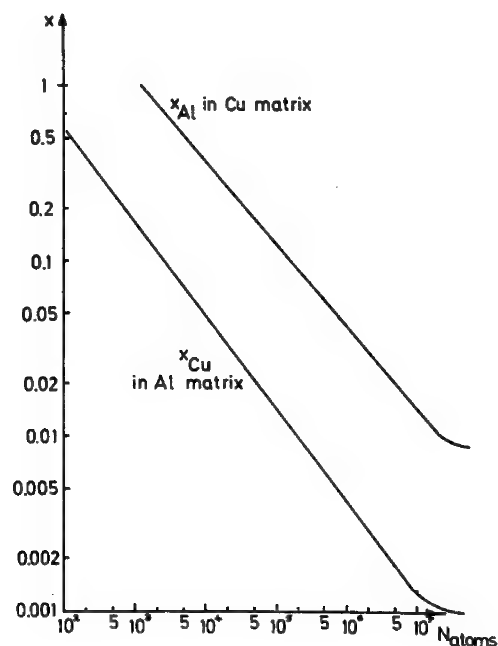
Figure 2

ON THE DESIGN OF MAGNETIC SPECTROMETERS FOR ELECTRON ENERGY
LOSS SPECTROSCOPY

J. R. Fields

Department of Biophysics, The Johns Hopkins University
Baltimore, Maryland 21218

In designing an energy loss spectrometer, one can avoid the need
for a highly regulated high voltage supply by decelerating the
electrons prior to the energy analysis.[1,2] However, with present
technology it is equally feasible to regulate the high voltage to
a few parts per million and to use a magnetic spectrometer to
analyze the fast electrons.[3] With that approach one requires a
magnetic analyzer which will perform optimally in a given appli-
cation. Specific cases have been treated, notably that of con-
stant angular magnification[4], and theoretical calculations suffi-
cient for most design problems have been performed.[5-9] Even so,
it is not always clear how to formulate design criteria which
can be used to determine values of the various parameters which
describe a magnetic spectrometer. Moreover, the ideal focusing
case has not been treated for any but constant angular magnifica-
tion instruments. Reference 10, of which this paper is an ab-
stract, is therefore intended to acquaint one with the flexibility
available in spectrometer design and to illustrate the use of
transfer coefficients in formulating mathematical statements of
design criteria. In addition, a general method for constructing
ideal field boundary contours and assessing aberrations of a pro-
posed design is presented for uniform field magnets.

The first order properties of a magnet depend on the inclinations
α_1 and α_2 of the field boundaries to the optic axis, the sector
angle θ, the field gradient n, and the orbit radius r. By vary-
ing these parameters, one can hope to achieve focal lengths and/
or magnifications in the median (energy dispersing) and perpendi-
cular planes which are well matched to the rest of the optical
system. If desired, the spectrometer can be designed for opera-
tion with auxiliary quadrupole and/or round lenses. One impor-
tant consideration is to insure that the magnification at the
energy dispersing plane of the beam - defining aperture or slit
is commensurate with the desired energy resolution. Also, the
range of the momentum transfer component (or scattering angle)
in the median plane over which the energy loss signal is averaged
will depend on the angular acceptance of the system. Within
limits, though, the optics of the median and perpendicular planes
may be chosen independently. Thus one could entertain the design
of an instrument in which electrons diffracted in the perpendicu-
lar plane are imaged at a two dimensional detector along with
electrons dispersed according to energy loss in the median plane.
For our own purposes of improving contrast and providing for
energy loss data on selected picture elements, though, we were
content to build a spectrometer which forms a stigmatic image of
the sample plane at the detector.

Once a tentative set of first order parameters has been chosen,
appropriate field boundary curvatures can be determined. As
Hintenberger[6] showed, the condition for second order focus only
fixes the value of a certain linear combination of the boundary
curvatures. Hence, an additional constraint is required. For
example, one may also demand that the angular magnification be

constant as discussed by Kerwin and Geoffrion[4]. If, however, the dispersion plane of the spectrometer is to be magnified as in our design, the requirement that the line of dispersion be normal to the optic axis proves to be more useful. So-called ideal focusing may be achieved if the boundary contour is not restricted to be circular, although an additional constraint must again be imposed.

Transfer coefficients[7,9], which represent the Taylor series expansion of the function which maps a point in phase space from one reference plane to another, may be used to determine values of first and second order parameters from the specified design criteria. However, another approach which we have exploited in the analysis of uniform field magnets is to derive expressions for first order derivatives which are valid for an arbitrary ray. Thus, one can set up first order differential equations which may be integrated numerically to find the trajectory (at the magnet exit) of any chosen entering ray. Alternatively, field boundary contours may be constructed which perfectly image all rays of a fixed energy emanating from an object in the median plane. Using these tools, the designer should be well equipped not only to arrive at an optimal design, but also to determine its adequacy in comparison with the comparable ideal design.

References:

1. G. H. Curtis and J. Silcox: Rev. Sci. Instrum. $\underline{42}$, 630 (1971).
2. P. C. Gibbons, J. J. Ritsko, S. E. Schnatterly: Rev. Sci. Instrum. $\underline{45}$, 1546 (1975).
3. A. V. Crewe, M. Isaacson, D. Johnson: Rev. Sci. Instrum. $\underline{42}$, 411 (1971).
4. L. Kerwin and C. Geoffrion: Rev. Sci. Instrum. $\underline{20}$, 381 (1949).
5. R. Herzog: Zeit. f. Physik $\underline{89}$, 786 (1934).
6. H. Hintenberger: Zeit. Naturforsch. $\underline{3a}$, 125 (1948).
7. K. L. Brown, R. Belbeoch, P. Bounin: Rev. Sci. Instrum. $\underline{35}$, 481 (1964).
8. P. Bounin: Rev. Sci. Instrum. $\underline{38}$, 1305 (1967).
9. H. A. Enge, Deflecting Magnets, in Focusing of Charged Particles, Vol. 2, Albert Septier, ed. (Academic Press, New York, 1967).
10. J. R. Fields, Magnetic Spectrometers: Approximate and Ideal Designs. To be published in Ultramicroscopy. See also, J. R. Fields, Proc. 34th EMSA Conf., 538 (1976).

"Computer Control of a Hitachi HU 11A - Wien Spectrometer Electron Spectroscopy-Microscopy System."[+]

P. E. Batson* and J. Silcox
School of Applied and Engineering Physics
Cornell University, Ithaca, New York 14853

In this paper, we describe a computer controlled electron microscope-electron spectrometer system controlled on-line with a mini-computer and our experiences with this system over the past five years. The primary purpose of the system is the exploitation and understanding of inelastic electron scattering particularly in transmission. It is now apparent that, particularly for low Z elements, inelastic scattering is a very promising microanalytical tool[1]. In addition, it is a unique probe of electronic structure[2]. However, full realization of these capabilities rests on a number of technological elements not the least of which is an ability to handle complex instrumentation and large quantities of data rapidly. Effective use of computer techniques is clearly a factor in this and we identify here a number of features that we have found valuable.

BASIC SYSTEM

The basic system is a Wien electron spectrometer mounted underneath a Hitachi HU 11A transmission electron microscope[3]. The microscope provides normal features in beam handling and specimen characteristics. We have added scan coils in two perpendicular directions between the intermediate and projector lenses so that either the image or the diffraction pattern can be conveniently located or scanned in a desirable direction. Electrons then pass through a 150μ wide slit located underneath the camera, are decelerated to a few hundred eV in energy and are passed through perpendicular electric and magnetic fields of appropriate sign and magnitude to produce equal and opposite forces on an electron that has lost no energy. Electrons that have lost energy are deflected in a direction perpendicular to the slit so that an energy loss spectrum is produced. The result is a two-dimensional intensity distribution as a function of energy (perpendicular to the slit) or position along the slit (either position in an image or angle in a diffraction pattern). If qualitative data are needed rapidly, a photographic plate is used. For precise data, a scintillator, light pipe, photomultiplier system for electron counting is used. A field lens matching trajectories between the microscope and spectrometer is also used.

CONTROL SYSTEM

The units of the system controlled digitally are the X and Y scan coils in the electron microscope, the three spectrometer parameters including the offset voltage, U_c, and the electric, E, and magnetic, B, fields of the analyser, a variable voltage V(t) added to the U_c and a programmable counter. The spectrometer parameters, U_c, E and B are set to determine focus and dispersion whereas V(t) is used to alter the energy of electrons passing through the system undeviated. A manual controller was constructed to permit operator setting of system parameters during normal exploratory studies whereas for precision work the system was interfaced with a PDP 11/20 mini-computer in a central facility serving a number of research groups. Some features of the control system are as follows.

The digital system is organized around 15-bit commands delivered to the devices, representing 3-bit addresses plus 12-bits of data. The X-Y scan coils are straightforward and use two of the available eight 3-bit words. The programmable counter uses two 3-bit addresses, one to set up the time interval of the count (variable between 1-128ms) and to initiate the count and one to accompany the completed count back to the computer. The counter, not the computer, controls the timing leaving the computer free to do other more complicated tasks and freeing the counter from errors due to logic or programming delays due to external control. Finally, the control circuits for the spectrometer use two addresses. One command sets the spectrometer parameters, U_c, E and B using visual alignment for most purposes. The other command sets the value of $V(t)$ and thus controls the energy of electrons passing through the system in an undeviated path.

COMMENTS

A system of this type is valuable in particular for precision intensity measurements recorded over long periods of time. We have been able to reproduce data from the same sample with no discernible difference over periods of time of order $1\frac{1}{2}$years. However, accomplishment of this depends upon a number of procedures in which computer control plays a key role. Thus, the incident beam intensity depends on angular half width. In order to reset the half width to sufficient precision we have had to set the second condenser lens current using an angular scan of the incident beam. The energy half width is very difficult to reset and we have had to resort to Fourier transform techniques. Thus the energy spectrum of the incident beam is deconvoluted from the full energy spectrum and a Gaussian of standard width reconvoluted with the data to provide the end spectrum. Under these conditions, the spetra are reproducible.

For a number of our experiments[4] long term counts to achieve good statistics have been necessary. In such cases, beam alignment drift has caused problems and a program incorporating a feedback loop to the scan coils correcting for beam drift was found necessary.

*Present address: Department of Physics, University of Cambridge, Cambridge, England.

1. M. Isaacsen and D. Johnson, Ultramicroscopy, 1, 33 (1975).
2. For a review see e.g. J. Silcox, Scanning Electron Microscopy/1977, Vol. 1, 393, edited: O. Johari, 1977.
3. G. H. Curtis and J. Silcox, Rev. Sci. Inst., 42, 630 (1971).
4. P. E. Batson, C. H. Chen and J. Silcox, Phys. Rev. Letters, 37, 937 (1976).

DATA ACQUISITION AND HANDLING UNIT FOR A QUANTITATIVE USE OF ELECTRON
ENERGY LOSS SPECTROSCOPY

P. TREBBIA, P. BALLONGUE and C. COLLIEX

Laboratoire de Physique des Solides, Université Paris-Sud, 91 405
ORSAY - France.

An effective use of electron energy loss spectroscopy for chemical charac-
terization of selected areas in the electron microscope can only be
achieved with the development of quantitative measurements capabilities.

The experimental assembly, which is sketched in Fig.1, has therefore been
carried out. It comprises four main elements.
1) The analytical transmission electron microscope is a conventional
microscope fitted with a Castaing and Henry dispersive unit (magnetic
prism and electrostatic mirror). Recent modifications include the improve-
ment of the vacuum in the specimen chamber (below 10^{-6} torr) and the
adaptation of a new electrostatic mirror.
2) The detection system, similar to the one described by Hermann et al (1),
is located in a separate chamber below the fluorescent screen which
visualizes the energy loss spectrum. Variable apertures select the
electrons, which have lost an energy ΔE within an energy window smaller
than 1 eV, in front of a surface barrier solid state detector RTC BPY
52 100 S.Q. The saw tooth signal delivered by a charge sensitive pream-
plifier (decay time of 5.10^{-5} S) is amplified, shaped into a gaussian
profile through an active filter and counted by a single channel analyser.
The logic output signal is then dispatched towards a log-lin ratemeter
and the subsequent interface. A good vacuum on the detector surface is
maintained with the help of a liquid nitrogen anticontamination device and
several screens have been inserted to shelter the detector from all spu-
rious radiations. Darkness current is below 0.1 c/s and linear counting
rates are measured to 10^4 c/s.
3) Great care has been devoted to generally improve the stability of the
high voltage power supplies. Moreover this system has been designed so
that the energy loss spectrum is scanned in front of the detector. This is
achieved by the variation (between 0 and 1000 V) of the output of an
auxilliary programmable Fluke calibrator, which modifies the primary elec-
tron energy before the specimen. The 16 bits information for a remote con-
trol of this very accurate (3.10^{-5} of output level) voltage supply is
transferred through an infrared optical line.
4) The Tracor Northern TN 11 computer with peripherals governs the data
acquisition procedure (energy range of interest - number of channels-
number of cycles ..) . Moreover it can dynamically modify the dwell time
per channel i.e. the scanning speed in fonction of the counting rate for
a given ΔE window (< 1 eV). The TN 11 also handles the data and displays
them either through a teletypewriter, a TV screen or a high performance
X-Y plotter.

As the characteristic chemical information is scattered over the whole
spectrum extending to a few thousands of volts, various programs of calcu-
lations have been elaborated. Apart the operations of data acquisition
and reading, they include now two principal modes of analysis. A first
one concerns the energy range between 0 and 200 eV and extracts, from the
crude spectrum, the energy loss function and optical constants after a few
deconvolution procedures and a Kramers-Kronig transformation. It has been
adapted from Wehenkel's program (2) to our experimental situation (3). As
an auxiliary result, it provides an estimate of the thickness of the

analysed area. A second one is devoted to the determination of the chemical concentration from X-ray losses signals, and follows the rules which have been explained in Colliex et al (4). It includes a least-squares fitting with reference spectra which is actually similar to an X-ray analysis routine program, applied to different shapes of signal.

1. K.H. Hermann, D. Krahl, A. Kübler, K.H. Müller, V. Rindfleisch (1971) in "Electron Microscopy in material science", 236 (Ed. U. Valdre-Academic Press).
2. C. Wehenkel (1975). J. Physique 36, 199
3. C. Colliex, M. Gasgnier and P. Trebbia (1976) J. Physique 37, 397.
4. C. Colliex, V.E. Cosslett, R.D. Leapman and P. Trebbia (1976), Ultramicroscopy 1, 301.
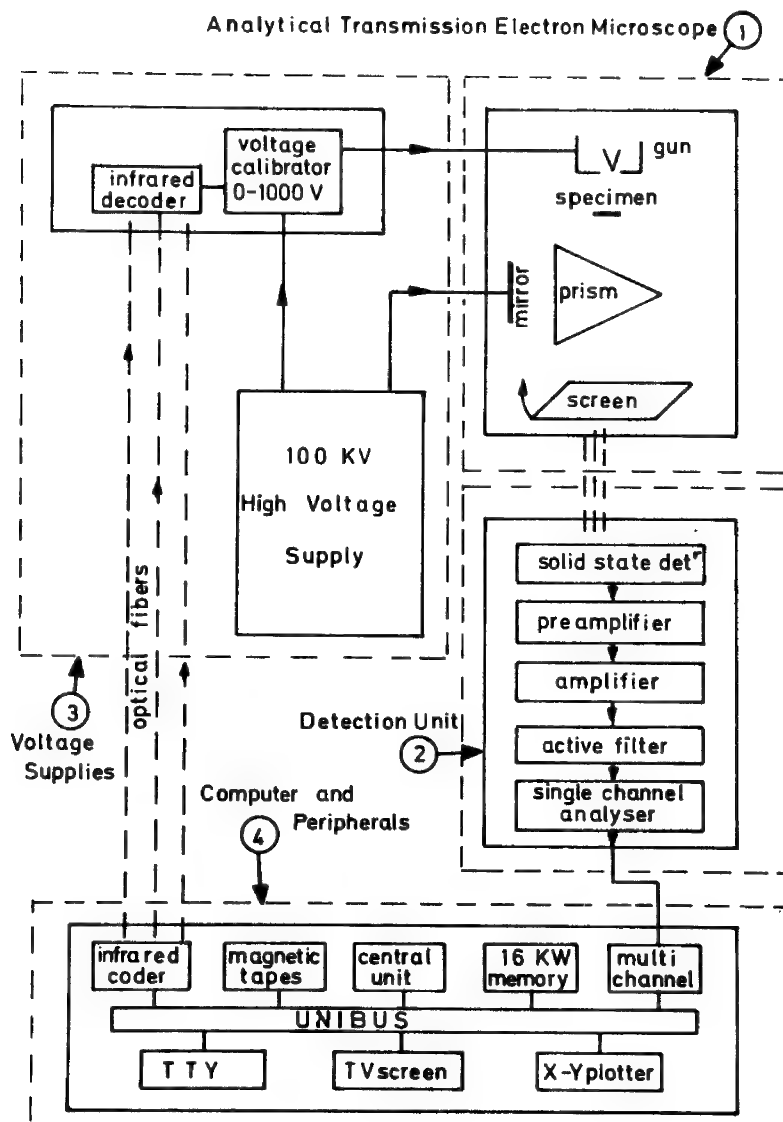
Fig 1

DATA ANALYSIS IN ELECTRON ENERGY LOSS SPECTROSCOPY

J.C.H. Spence

Department of Physics, Arizona State University, Tempe, Arizona 85281

The sensitivity of the shape of K shell excitation differential energy loss peaks to the atomic environment suggests that this technique may be useful in determining the chemical state, amount, type and distribution of small quantities of light elements embedded in a host matrix (1,2). In order to extract useful information about, say, the bonding of atoms from K-shell spectra it is important to ensure that satellite peaks arising from multiple scattering are not allowed to mask genuine features which reflect the final density of states for a particular transition. In addition, for the rapid identification of several species, the vast multitude of closely spaced K, L, M and N losses possible from a specimen of unknown composition containing many elements together with their associated plasmon satellites makes it imperative that a systematic method of background subtraction be used which eliminates both multiple scattering and the effects of instrumental broadening. An asymmetric spectrometer energy loss impulse response may also lead to the appearance of spurious peaks in a spectrum.

A method of data analysis which takes all these effects into account has been described (3). Two loss spectra $z(E)$ and $g_0(E)$ must be recorded, the first obtained from the specimen and the second, with the specimen removed, giving the instrumental impulse response. Strictly, these spectra should cover the same energy range, made sufficiently large to include all features in the spectra (including the zero loss peak) and to ensure that both spectra fall to zero at either end of the range. Then a fourier coefficient $R(k)$ of the fully deconvoluted single scattering energy loss distribution $r(E)$ can be obtained from

$$R(k) = M(k)\ln\{A_0 \frac{Z(k)}{G_0(k)}\} \tag{1}$$

where $Z(k)$ and $G_0(k)$ are the complex fourier coefficients of $z(E)$ and $g_0(E)$ respectively, $\ln(x)$ is the complex natural logarithm of x, and A_0 is an unimportant constant approximately equal to the ratio of the peak heights of the recorded impulse response to the zero-loss peak in the experimental plural loss spectrum. The use of an incorrect value of A_0 results in a spurious narrow origin peak in the single loss spectrum which is of no consequence for the analysis of high energy loss peaks. The effect of small changes in the instrumental impulse response operating on $z(E)$ from that collected as $g_0(E)$ have also been shown to have a similar effect. The division of fourier coefficients in equation (1) can easily be performed by computer and the single loss spectrum $r(E)$ synthesized by fourier summation. This spectrum is convoluted with $m(E)$ (with fourier coefficients $M(k)$), a narrow symmetrical peaked function needed to control noise on $r(E)$. A gaussian of specified width may be used or the original impulse response. The noise on the retrieved spectrum $r(E)$ will be found to increase as $m(E)$ is made narrower than $g_0(E)$ in an attempt to improve the energy resolution of the retrieved spectrum beyond that of the electron spectrometer. The form of this trade-off between resolution increase and declining signal to noise ratio has been investigated (4) and found to depend sensitively on the form of $g_0(E)$.

The recorded single loss spectrum $r(E)$ does not contain the large background contribution from multiple single electron and phonon excitation processes seen on experimental data and so may be used for the determination of reaction cross sections σ_{ij} or quantities of material from a comparison of peak areas. For Poisson scattering from a specimen covered with a total thickness t' of contaminant, the single loss spectrum retrieved using (1) is

$$r(E) = r'(E) * m(E)$$

where

$$r(E) = \sum_j \sum_i \sigma_{ij} N_{ij} f_{ij}(E) + t' \sum_j \frac{1}{\lambda_j} f_j(E) + \delta(E) \qquad \{2\}$$

where $f_{ij}(E)$ is the normalized single loss distribution for process i in species j with concentration N_{ij} (projected areal density) and λ_j and $f_j(E)$ are the path lengths and single loss distributions for processes occurring in the contaminant. The important processes are plasmon excitation, valence single electron excitations, phonon losses and inner shell bound electron losses. In addition, by manipulating the width of $m(E)$, equation $\{1\}$ allows a particular narrow feature to be sought in the fine structure of the retrieved spectrum which may be beyond the energy resolution of the spectrometer.

Equation $\{1\}$ applies to spectra which include all scattering angles -- in practice a large aperture should be used. To reduce the time needed to collect data, unequally spaced energy increments may also be used. The signal to noise ratio for a particular process in the single loss spectrum has been shown to be a maximum if this spectrum is retrieved from a plural loss spectrum collected from a specimen whose thickness is equal to the path length for the process of interest.

Several alternative procedures have been suggested for background subtraction which do not require the collection of data over such a large range. All amount to the introduction of *a priori* information and may be tested against the results of equation $\{1\}$, which assumes only Poisson statistics for the scattering. An economical approximation has been described (5) which is useful where the single electron and plasmon excitation multiple loss spectrum can be measured separately at low energies and then used as the function $g_0(E)$ in equation $\{1\}$. In a similar way it can be shown (4) that all surface and thickness independent processes (such as oxide losses and surface plasmon excitations) can be removed from the retrieved single loss spectrum by using as $g_0(E)$ the experimental spectrum collected from a very thin specimen, while $z(E)$ remains the spectrum collected from a thicker specimen. Examples of the application of this equation to experimental spectra can be found in (6).

References
1. Egerton, R. F., et al.: Proc. EMAG 75, p. 129 (A.P. 1976).
2. Isaacson, M. and D. Johnson: Ultramicroscopy 1, 33 (1975).
3. Johnson, D. W. and J.C.H. Spence: J. Phys. D. 7, 62 (1974).
4. Johnson, D. W., Ph.D. Thesis, University of Melbourne (1974).
5. Egerton, R. F. and M. J. Whelan: Phil. Mag. 30, 739 (1974).
6. Spence, J.C.H. and A.E.C. Spargo: Eighth Int. Cong. E.M., p. 391 (Aust. Acad. Sci., Canberra) (1974).

THE USES OF ELECTRON ENERGY LOSS SPECTROMETRY IN BIOLOGY

D. E. Johnson

Center for Bioengineering, RF-52, University of Washington
Seattle, Washington 98195

The uses of electron energy loss spectrometry in biological microscopy range from the simple filtering of energy loss electrons to remove their degrading effect in conventional transmission microscopes, to the detailed use of the information carried by energy loss electrons in determining molecular and elemental composition on a microscopic level. The electron energy loss spectrum, to the extent that it is characteristic of the specimen, reflects the atomic and molecular energy levels of the specimen. In considering the uses of electron energy loss spectrometry in biology it is convenient to separate the energy loss events into two groups, those characteristic of the molecules present and those characteristic of the elements present.

1)   <u>Characteristic of molecular composition</u>
a)   The energy loss spectrum of organic materials in the region below $\sim$10ev energy loss reflects the same molecular transitions as ultraviolet and vacuum ultraviolet absorption spectra in this energy region and is equally characteristic of the molecules present.
b)   In the region from $\sim$10ev to 50ev are energy loss events resulting from additional single electron excitations and ionizations modified by collective effects in the solid. They generally fall into a broad peak at about 20ev and are much less characteristic of the molecules present although they are useful in the calculation of optical constants from energy loss spectra.
c)   The energy loss spectrum at the leading edge of core electron excitations can reflect the chemical bonding states of the atoms in organic compounds. [e.g., transitions from the slightly different ($\sim$0.5ev) Carbon K energy levels of the different carbon atoms in an aromatic hydrocarbon.]

The extent to which 1a and 1c above can be useful in determining molecular composition or chemical bonding states on a microscopic level is of course determined by the cross section for the given group of energy loss events (σ_c) and the initial number (N_0) of molecules within the volume irradiated by the electron beam. There is a more fundamental limitation, however, in that in biological material the maximum number of characteristic events is limited by radiation damage of the molecules. If the number of undamaged molecules at a radiation dose D decreases exponentially $[N = N_0 EXP(-D/D_c)]$, then the number of characteristic energy loss events (= C) obtained for a dose D, is given by:
$C = (\sigma_c/\sigma_D) \cdot N_0 [1 - EXP(-D/D_c)]$ with σ_D = damage cross section = $1/D_c$
and the maximum number of events obtainable: $C_{max} = (\sigma_c/\sigma_D) \cdot N_0$

For example, in observing characteristic energy loss spectra of nucleic acid bases: σ_c(0-10ev) $\simeq$ 2X10^{-2}Å^2/molecule and σ_D for base damage in a DNA molecule $\simeq$ 10^{-1}Å^2/molecule, (at 25Kev, Ref. 1), so that C_{max} = 0.2 N_0. This means that to observe 1000 events, $\sim$5000 base molecules would have to be included in the beam area. The cross section for transitions characteristic of chemical bonding states in these molecules may be smaller than the above σ_c by $\sim$10^2 with a corresponding increase in the number of required molecules within the beam. Because of this radiation damage limitation the above technique will probably have only limited application.

2) Characteristic of Elemental Composition

The energy loss spectrum of organic materials in the region from a few hundred to several thousand ev shows characteristic peaks due to ionization of inner shell electrons of the atoms present. The use of electron energy loss spectrometry for elemental microanalysis, because of its high geometrical collection efficiency and lack of dependence on the fluorescence factor, can result in a substantial increase in sensitivity compared to x-ray microanalysis (2). This is particularly true for low atomic number biological materials (Z = 3 to 20). Radiation damage is a limitation to this technique only to the extent that atoms, following ionization, move within or actually leave the specimen. This can be important in certain materials but is generally reduced by specimen cooling and is no more a problem than for x-ray microanalysis.

Elemental microanalysis appears to be the most promising application of electron energy loss spectrometry in biological research. This application will be the most successful in an instrument specifically designed for energy loss microanalysis and probably used in conjunction with an energy dispersive x-ray spectrometer system. Figure 1 shows schematically the system being developed at the University of Washington for this type of combined microanalysis system. The salient features are: 1) A projector lens to compress scattering angles and thus increase collection efficiency of the energy loss spectrometer. 2) A projector lens to magnify the dispersion plane for easier parallel detection. 3) A parallel collection device--initially a photodiode array operated in the electron detection mode. 4) Processing and display with the same computer-multichannel analyzer system as used for the x-ray detection. For the study of chemical bonding states using energy loss spectrometry, a field emission source with its small energy spread ($\sim$0.2ev) will be necessary and is planned as a future development.

1. M. Isaacson, D.E. Johnson and A.V. Crewe: Rad. Res. 55:205(1973).

2. M. Isaacson and D.E. Johnson: Ultramicroscopy 1,33(1975).
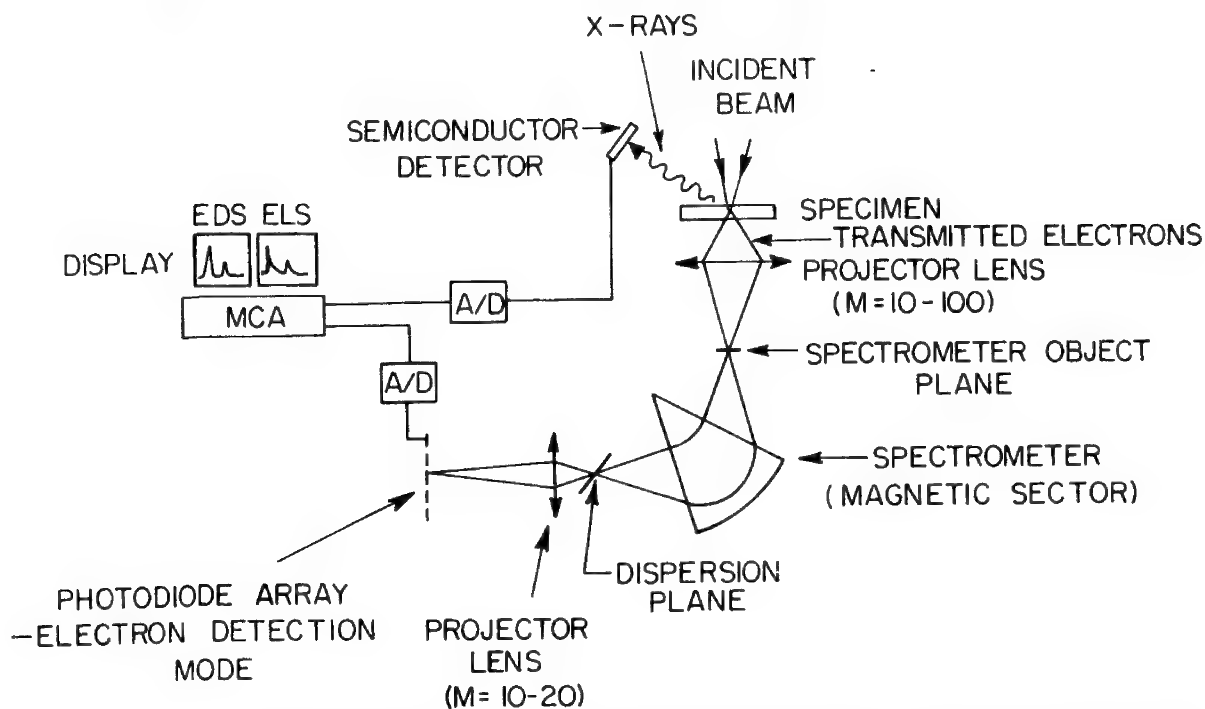
Fig. 1. A schematic diagram of the combined energy dispersive x-ray and electron energy loss microanalysis system being developed at the University of Washington.

CONSIDERATIONS ON THE USE OF ELECTRON AND PHOTON BEAMS FOR DETERMINING
MICRO-CHEMICAL ENVIRONMENT*

M. Isaacson[†] and M. Utlaut

Department of Physics and the Enrico Fermi Institute, The University of
Chicago, Chicago, Illinois 60637

Over the last half decade there has been growing interest in the use of
synchrotron radiation as a tunable x-ray source for performing chemical and
electronic spectroscopy of matter (e.g., 1). Concurrent with this (although
a lot less visable in the popular literature) has been the increasing trend
towards utilization of electron energy loss spectroscopy (ELS) within an
electron microscope environment (e.g., 2). From the point of view of mater-
ials analysis, it is worthwhile to compare electron and photon beams insofar
as their detective sensitivity is concerned. This is of interest since, for
many applications, one must decide whether ELS within an electron microscope
or setting up an experiment at a synchrotron radiation facility will give one
the desired information. This paper represents a preliminary study aimed at
making such a comparison. (The reader is alerted to keep in mind that extra-
polation of such a comparison beyond the limited scope of what we intend can
be dangerous!)

The quantities which can be useful in comparing ELS and synchrotron radiation
are: 1) the relative cross sections of the processes involved (in our case,
the photo-absorption cross section, σ_γ, and the differential inelastic elect-
ron scattering cross section, $d\sigma/dE$; and 2) the number of particles per unit
area per unit time per unit energy bandwidth which can be made to impinge
upon the specimen.

One can show that in the absence of background, the minimum number of atoms
of a given type which can be detected is inversely proportional to the prod-
uct of the particle flux of the incident beam times the cross section for
detecting a particular process. We can define a sensitivity factor for part-
icle probes to be $S_e = J_e \, d\sigma/dE$ for electron beams and $S_\gamma = J_\gamma \sigma/\Delta E$ where J_e
is the electron flux at the specimen and J_γ is the photon flux per ΔE energy
bandwidth (the rotating electrons in storage rings emit a continuum of photon
energies which must then pass through a monochromator which accepts a given
energy band). Thus, a useful figure of merit comparing electron beams and
synchrotron radiation beams is $R = S_e/S_\gamma$.

In the case of inner shell ionization and excitation, the ratio of different-
ial inelastic electron scattering cross section to the photo absorption cross
section is given (non-relativistically) by $(d\sigma/dE)/\sigma_\gamma \approx [\ln(4\times10^5/E)]/170E$
for 100 KeV electrons. Thus, the photo absorption cross section is orders of
magnitude larger than the electron energy loss cross section in the region of
interest for analysis, say E from 100-5000 eV. At first glance, it would
appear that ELS in an electron microscope is less sensitive.

However, it is the product of the flux times the cross section J_γ which is
important. We can get the flux from considerations of the brightness of the
respective sources. For synchrotron sources, we have shown the brightness
per eV bandwidth for two storage ring sources (3,4). Electron beams are
orders of magnitude brighter since one can obtain brightnesses per eV band-
width much greater than 6×10^{27} electrons/sec/cm^2/sterad/eV for cold field
emission sources.

Using the values of brightness for DORIS and assuming the photon beam to be directed towards a 2 cm x 2 cm aperture 40 meters from the source (3), we can calculate our figure of merit for different electron probe current densities. As an example, assume a value of J_e = 10A/cm^2 which is a typical value that can be obtained in a conventional electron microscope (i.e., about 3nA in a 2000 Å diameter probe). For the sodium K line (E_K = 1072 eV), using 100 KeV electrons, the figure of merit R = 71 if we assume a 10 mrad spectrometer collecting aperture (referred to the specimen). If we could focus this 2 cm x 2 cm photon beam to 2 mm x 2 mm with no loss of intensity, then we would still only get R = .71 (5).

We find that over most values of energy loss (E) corresponding to K shell ionization (of the low to medium Z elements), electron beam systems have a higher detective sensitivity than synchrotron radiation beams. Even taking into account the different thickness samples used to get optimum signal to background for the two techniques, electron beams are still competitive with synchrotron sources with the added advantage of being able to measure energy losses for different momentum transfers. Moreover, in an electron microscope environment one gets direct spatial information at the microscopic level as well.

1. M.L. Perlman, E.M. Rowe and R.E. Watson, Physics Today, July (1974) p.30.
2. M.S. Isaacson and J. Silcox, Ultramicroscopy, 2 (1977) in press.
3. C. Kunz, in Proc. IV International Congress on VUV Radiation Physics, Hamburg, (eds. E. Koch, R. Haensel and C. Kunz), Pergamon-Vieweg (Braunschweig, 1974).
4. S. Doniac, I. Lindau, W.E. Spicer and H. Winick, J. Vac. Sci. Tech., 12, 1123 (1975).
5. M.S. Isaacson and M. Utlaut, (to be published).
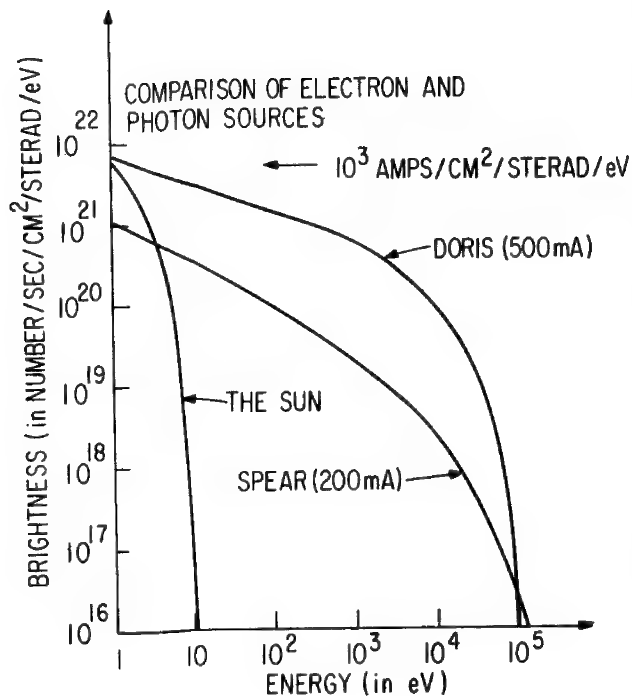
Figure 1. Brightness of photon sources. The brightness of the synchrotron sources are based on a source size of 1 x 10 mm^2 and are for emission into an angle perpendicular to the plane of the orbit of about 1-10 mrad. The curve for DORIS is for the storage ring at Hamburg assuming 500 mA circulating current of 3.5 GeV electrons (3). The curve for SPEAR is for the storage ring at Stanford assuming a circulating current of 200 mA at 4.5 GeV (4). The brightness is defined as number of particles/unit area/sec in an eV bandwidth. We show the brightness of the sun and for an electron source whose brightness is two orders of magnitude less than the maximum brightness obtainable using a conventional hot filament.

SUBCELLULAR LOCALIZATION OF FLUORINATED SEROTONIN IN HUMAN PLATELETS BY ELECTRON ENERGY-LOSS SPECTROSCOPY

J.L. Costa,[1] D.C. Joy,[2] D.M. Maher,[2] K.L. Kirk[3] and S.W. Hui[4]

[1]Clinical Neuropharmacology Branch, NIMH, Bethesda, Md. 20014; [2]Bell Laboratories, Murray Hill, NJ 07974; [3]Laboratory of Chemistry, NIAMDD, Bethesda, Md. 20014; and [4]Dept. of Biophysics, Roswell Park Memorial Institute Buffalo, NY 14263.

Fluorinated organic molecules have considerable potential as tracers in biological systems, since a number of fluorinated analogs demonstrate biological activity similar to that of the parent molecule[1]. To date, however, the subcellular localization of fluorine has been hampered by the relatively low sensitivity of conventional X-ray microanalysis systems to fluorine. Electron energy-loss spectroscopy, in contrast, is a very efficient method for detecting light elements. We have capitalized on the high sensitivity of this technique to fluorine to identify and localize fluorinated serotonin at a subcellular level in human platelets.

Intact human platelets were incubated with 10^{-5} M concentrations of either serotonin (5HT) or 4,6 difluoroserotonin (DF5HT)[2] for 30 minutes at 37°C. Following the incubation period, air-dried whole mounts[3] were prepared on 200 mesh copper grids coated with collodion and carbon. Individual platelets were examined at 80 kv in the STEM mode (10 nm spot size), utilizing a Jeol 100B microscope equipped with a field emission gun, a scanning attachment, an electron spectrometer, and a Kevex analysis recording system. Cells were imaged (slow-scan mode) by using only electrons which had lost 680 electron volts (fluorine K-line loss). In this mode, cells were seen to contain numerous electron-lucent areas 100-200 nm in diameter, presumably representing areas containing high concentrations of fluorine (Figure 1). To verify the presence of fluorine, we obtained energy-loss spectra from several regions within the platelet illuminated with a 10 nm stationary spot. Energy-loss spectra obtained from regions appearing electron-lucent in the 680 ev loss STEM mode contained prominent, well-defined absorption edges at the 680 ev loss region, characteristic of the K-line loss of fluorine (Figure 2). Some spectra obtained with a stationary spot from adjacent areas on the platelet cytoplasmic apron contained small absorption edges in the 680 ev loss region; spectra obtained from the supporting collodion film demonstrated no absorption edges in this region (Figures 3 and 4). Furthermore, platelets incubated with 5HT contained no electron-lucent areas when imaged in the STEM mode using only 680 ev-loss electrons. When probed at various points with a 10 nm stationary spot 5HT-incubated platelets also produced spectra with no 680 ev absorption edges.

These results demonstrate the potential of electron energy-loss spectroscopy for the detection and distributional mapping of light elements. Thus, our documentation of the sequestration of fluorine (presumably associated with DF5HT) in discrete intracellular compartments of human platelets exemplifies the use of the technique to evaluate the disposition of a fluorinated organic molecule in a biological specimen. The method is quite sensitive to small amounts of material (theoretical detection limit, 10^{-21} grams), provides signal-to-noise ratios superior to those obtainable with X-ray microanalysis, and can produce element-specific maps with good resolution (< 10 nm) and image quality. In addition, a quantitative as well as a qualitative evaluation of light-elemental composition can be obtained.

REFERENCES

1. P. Goldman, Science 164:1123 (1969).
2. DF5HT was synthesized according to the procedure described by K. L. Kirk, J. Heterocyclic Chem. 13:1253 (1976).
3. Y. Tanaka, J. L. Costa, K. D. Pettigrew, Y. Yoda and R. J. Cushing, 33rd Ann. Proc. EMSA, Las Vegas, Nevada, 1975, pp. 322-323.
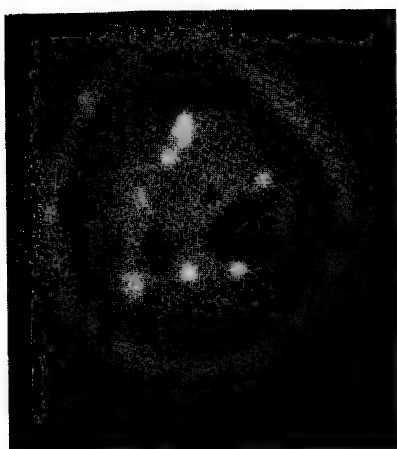
Fig. 1 Air-dried platelet incubated with DF5HT, imaged with fluorine K-loss electrons only. Several electron-lucent areas are apparent.

Fig. 2 Energy-loss spectrum recorded from a DF5HT-treated platelet when a lucent area seen in the 680 ev-loss mode was probed with a stationary 10nm spot. A prominent absorption edge for fluorine is present at 680 ev.

Fig. 4 Energy-loss spectrum recorded when the cytoplasmic apron (organelle-free region) of a DF5HT-treated platelet was probed (10nm stationary spot). A small fluorine edge is present.
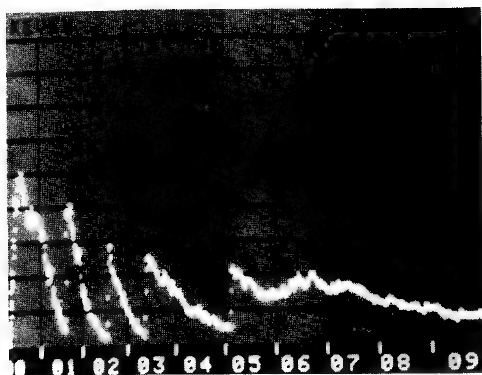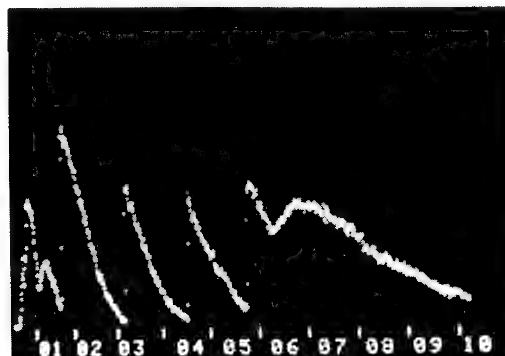
Fig. 3 Energy-loss spectrum recorded when the grid film from the specimen examined above was probed (10 nm stationary spot). No fluorine edge is present.
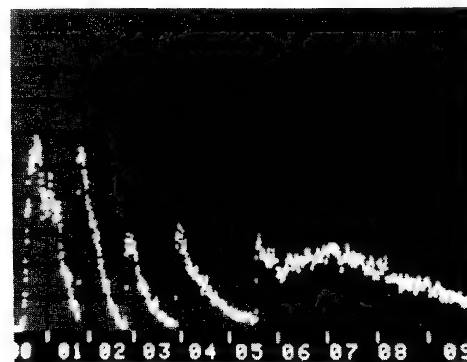
"The Use of Electron Energy Loss Spectrometry for the Study of Materials."

J. Silcox
School of Applied and Engineering Physics
Cornell University, Ithaca, New York 14853

Electron energy loss spectrometry provides unique and valuable information in the study of materials. In particular, angular dependence of the scattering can be used to provide the dispersion relation of the particular excitation i.e. $\Delta E = \hbar\omega(q)$ where ΔE is the energy loss and q is the wave vector of the excitation. These studies are valuable in giving directly the dynamical properties of the electronic system. They also are valuable in microanalytical studies which are concerned with angle integrated spectra. Variations in angular scattering between the matrix and a particle in the specimen can cause severe problems in energy loss microanalysis and an understanding of losses becomes important. We discuss here experiments on single particle valence electron scattering in aluminum that illustrate the nature of the available information at low energy loss and outline our experience with correction procedures for dealing with multiple scattering which is a substantial problem in obtaining precise data.

Aluminum is a relatively simple system for the valence electrons which exhibits both inter-band and intra-band scattering. In straight forward terms intra-band scattering involves valence electron transitions that pass between a state below the Fermi-level to above it with a momentum change $\Delta p = \hbar q$ that stays within a Brillouin zone of the reciprocal lattice whereas an inter-band transfer for this system will involve a q transfer that crosses a Brillouin zone boundary. Thus in general, many more electrons will participate in intra-band scattering at small momentum transfer than in inter-band scattering and the intra-band scattering is thus a dominant factor in losses, particularly if the collective plasmon losses are included. Detection of inter-band losses at small momentum transfer on the other hand involves transitions that occur close to a Brillouin zone boundary. A detectable peak can be identified if there is a high joint density-of-states. These features are small in general but can be identified through distinctive crystallographic features.

In aluminum, the Fermi surface crosses the [200] Brillouin zone boundary in a circle of radius approximately G/4 where G is the magnitude of the [200] reciprocal lattice vector. In the neighborhood of this circle a high joint density of states exists for states just below and above the Fermi surface and an inter-band peak ∽ 1.5eV at small q is detected. This loss was identified first in optical reflectivity[1]. The high joint density of states persists for occupied and unoccupied states separated by an offset vector q parallel to the Brillouin zone boundary. Thus, an electron scattering experiment looking for scattering vectors parallel to the Brillouin zone might pick up such a peak whereas a scattering experiment in a direction different from the boundary would not. Such an experiment for aluminum performed by Petri[2] and Otto revealed a linear increase in the inter-band transition. In our instrument, we have been able to follow the transition out to scattering vectors corresponding to G/2 and find that the linear increase levels off at approximately 9eV. This suggests exploration of the band structure by these means although a theory accounting in detail for intensity variations is not yet available.

More detailed measurements have been carried out on intra-band scattering. A particular recent feature[3] of interest has been the region of scattering corresponding to $q \sim 1.7\text{Å}^{-1}$ i.e. approximately half way to the reciprocal lattice vector. Multiple scattering is a problem in this regime and in particular, quasi-elastic scattering coupled to electronic scattering is a severe problem. The reason is that the appropriate methods[4] for treating multiple scattering involve Fourier deconvolution techniques and to avoid substantial truncation errors, the intensity at the limits of the data block need to be small. If one plans to go to perhaps 3Å^{-1}, then experimentally the intensity in this region is dominated (to 90% or more) by the quasi-elastic-electronic term which extends to extremely wide angles. It is necessary first to develop a method of subtraction of this term. We have used an image spectrum i.e. an angle integrated spectrum to develop such a subtraction. Following this, multiple Fourier deconvolution is carried out providing a single scattering spectrum, showing the single particle intra-band scattering and the damping of the plasmon mode in this regime of ω-q space.

1. H. Ehrenreich, H. R. Phillip and B. Segall, Phys. Rev., 132, 1918 (1963).
   N. W. Ashcroft and K. Sturm, Phys. Rev., B3, 1898 (1971).
2. E. Petri and A. Otto, Phys. Rev. Letters, 34, 1283 (1975).
3. P. E. Batson, C. H. Chen and J. Silcox, Phys. Rev. Letters, 37, 937 (1976).
4. G. K. Wertheim, J. El. Spect., 6, 239 (1975).
   D. Misell, A. F. Jones, J. Phys. A, 2, 540 (1969).
   T. Grove, Ultramicroscopy, 1, 15 (1975).
   D. W. Johnson, J. C. M. Spence, Proc. 8th Int. Cong. El. Microscopy, II, II, 386 Canberra (1974).

QUANTITATIVE METALLURGICAL APPLICATIONS

OF PLASMON ENERGY LOSS MICROANALYSIS

by

D. B. Williams

Department of Metallurgy & Materials Science, Lehigh University,

Bethlehem, Pennsylvania 18015

In certain Al and Mg base alloys, the electron band structure may be considered to approximate to that of a free-electron metal, in which the conduction band electrons are free to move, and constitute a so-called free-electron gas. When such materials are studied in the transmission electron microscope, the principal energy loss sustained by the 100 kV imaging electrons is that of plasmon excitation (quantized oscillations of the electron gas). By placing an electron spectrometer beneath the viewing screen of the microscope, with a limiting entrance slit, the energy loss spectrum from a line in the bright field image may be obtained. As shown in Fig. 1, the spectrum is simple, consisting of a zero loss line and plasmon loss lines corresponding to one or more plasmon excitations: it has been shown that the spectral peak position may be related directly to composition with an accuracy of < 1 wt%[1] and a spatial resolution of < 10 nm.[2] The empirical change of peak position with composition for several Al-base alloys is shown in Fig. 2. From this data, changes in peak separation across the spectrum may be interpreted in terms of composition changes along a line in the image. The technique has been applied to the study of a number of phase transformations, and to the determination of low temperature diffusion data.

By placing the spectrometer entrance slit underneath a grain boundary, the solute composition profiles accompanying grain boundary precipitation were investigated in several alloys. A typical result is shown in Fig. 3. Solute depletion has occurred either side of a grain boundary in Al-12 àt% Li containing equilibrium δ (AlLi) precipitates. No other technique is capable of detecting Li quantitatively on this scale. This may assume importance with the development of fatigue resistant aluminum alloys containing Li.[3] Similar profiles down to 100 nm in width have been observed in several alloys.[4] In particular in Al-Zn-Mg alloys[5] Mg supersaturations have been detected within precipitate free zones (P.F.Z.) thus demonstrating that the P.F.Z. does not arise solely as a result of solute depletion, but that vacancy concentrations must play an active role. This is consistent with the theory of P.F.Z. formation developed by Lorimer and Nicholson[6] amongst others.

The discontinuous reaction is another type of grain boundary precipitation resulting in the formation of lamellar phases behind a moving grain boundary. There are contradictory theories concerning the principal mode of solute redistribution in such reactions.[7] Both interface and bulk diffusion control of particular reactions have been observed. By placing the spectrometer entrance slit across the advancing interface it has been demonstrated conclusively in Al-Li[8] and Mg-Al[9] alloys that, over a wide temperature range, there is no detectable volume diffusion within 5 nm of the advancing interface. As shown in Fig. 4, solute redistribution must occur at the interface, thus demonstrating interface diffusion control of

the reaction in an unambiguous manner. Detection of non-equilibrium solute concentrations in the lamellae (see Fig. 5) gives direct support for Cahn's theory[10] of cellular precipitation.

Splat-quenching, or rapid quenching from the melt is capable of producing both amorphous and crystalline alloys with exotic properties. The precipitation processes from such materials are complex, but plasmon energy loss measurements[11] have already demonstrated conclusively that even in the crystalline state, no bulk solute diffusion occurs in spite of the presence of apparently conventional grain boundary precipitates, as shown in Fig. 6. Thus it is clear that all solute redistribution must occur in the liquid phase during the few microseconds prior to complete solidification.

The high spatial resolution of the technique may be utilized to detect bulk composition profiles developed at low temperatures ($\sim 100^\circ$C in Al alloys). From such profiles, bulk volume diffusion coefficients may be obtained.[4] Results from Al-Mg are shown in Fig. 7. There is a decrease of six orders of magnitude in the measurable value of D compared with conventional techniques. Two points may be noted from this data: 1) extrapolation from high to low temperature data can be justified in this (and other) systems; 2) there is a real possibility of accurate determination of phase diagrams at low temperatures. This has hitherto been impossible in view of the inordinately lengthy heat treatment times required to obtain diffusion profiles measurable by conventional microanalytical techniques.

In conclusion, although the technique is limited to certain alloys, it offers, within these well defined limits, the most accurate quantitative high resolution microanalysis data available to date, and must be considered a significant contributor to the field of electron energy loss microanalysis.

Acknowledgements

References

1. Hibbert G. and Edington J. W. 1972 J. Phys. D. (Appl. Phys.) 5, 1780.

2. Cundy S. L., Metherell A. J. F., Whelan M. J., Unwin P. N. T. and Nicholson R. B. 1968 Proc. Roy. Soc. A307, 267.

3. Sanders T. H. and Mauney D. A. 1977 Proc. 106th AIME Annual Meeting, Atlanta, Ga.

4. Doig P. and Edington J. W. 1973 Phil. Mag. 28, 961.

5. Doig P., Edington J. W. and Hibbert G. 1973 Phil. Mag. 28, 971.

6. Lorimer, G. W. and Nicholson R. B. 1969 The Mechanism of Phase Transformations in Crystalline Solids (Institute of Metals, London) 33, 36.

7. Hillert M. 1972 Met. Trans. 3, 2729.

8. Williams D. B. and Edington J. W. 1976 Acta Met. 24, 323.

9. Porter D. A. and Edington J. W. 1977 Proc. Roy. Soc. submitted for publication.

10. Cahn J. W. 1959 Acta Met. 7, 18.

11. Williams D. B. and Edington J. W. 1976 Phil. Mag. 34, 235.

12. Bishop M. and Fletcher K. E. 1972 Int. Met. Rev. 17, 203.

197c

Fig. 1: An energy loss spectrum from a thin Al-foil showing the zero (no loss) line and several quantized loss lines. The actual value of the energy loss at point A is determined by measing the spectral peak separations along A-A'.
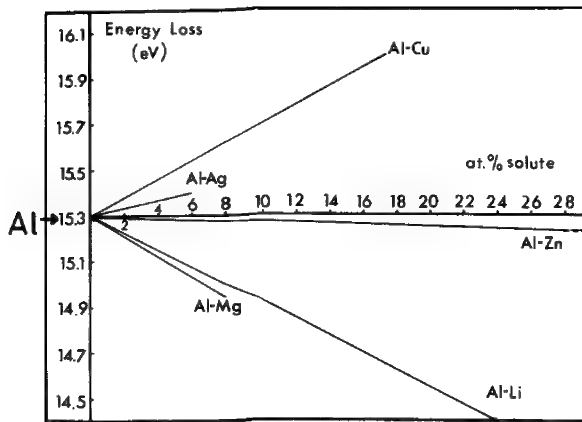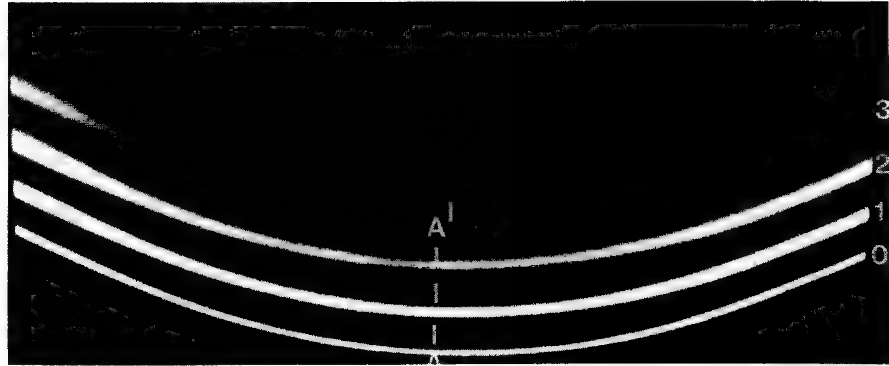
Fig. 2: The empirical variation of the plasmon energy loss of pure Al with additions of various solutes.
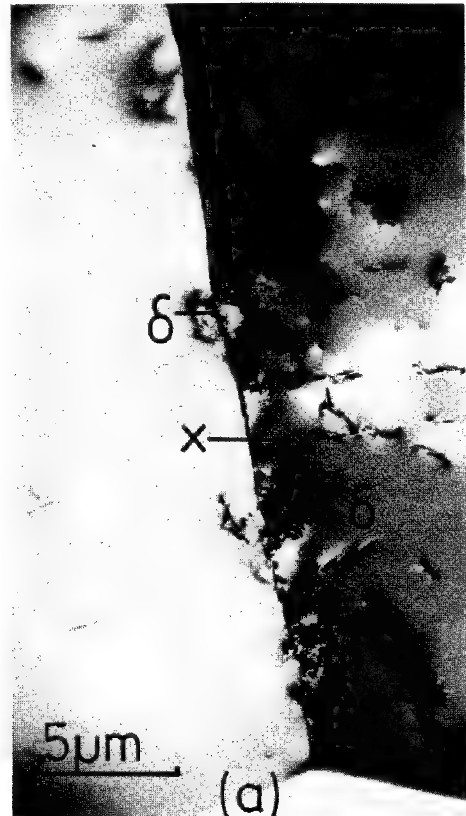
Fig. 3a: Grain boundary δ precipitation in an Al-12 at% Li alloy.

Fig. 3b: Composition profile along X-X in Fig. 3a showing matrix Li depletion accompanying the grain boundary precipitation.
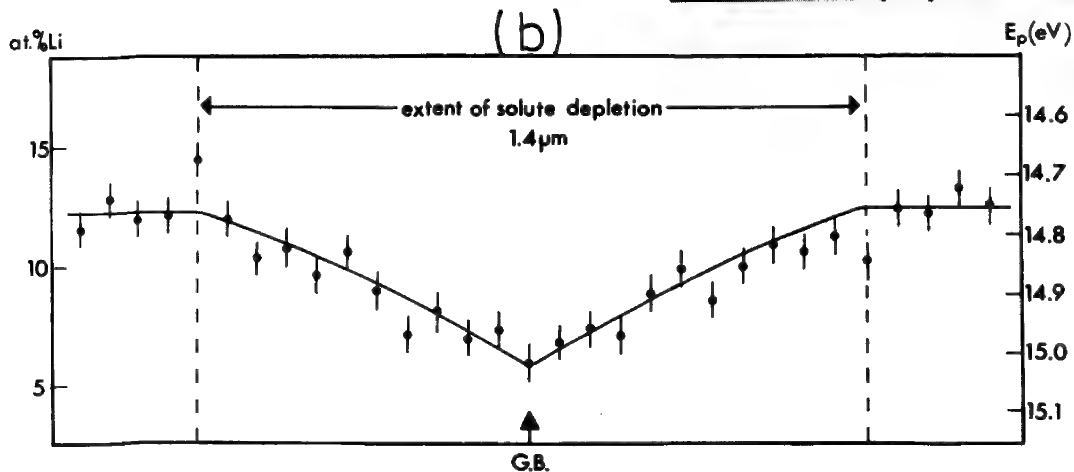
Fig. 4a: The grain boundary discontin-
uous reaction in Al-12 at% Li.

Fig. 4b: The discontinuous change in
Li concentration along X-X in Fig. 4a.

(a)

(b)

(a)
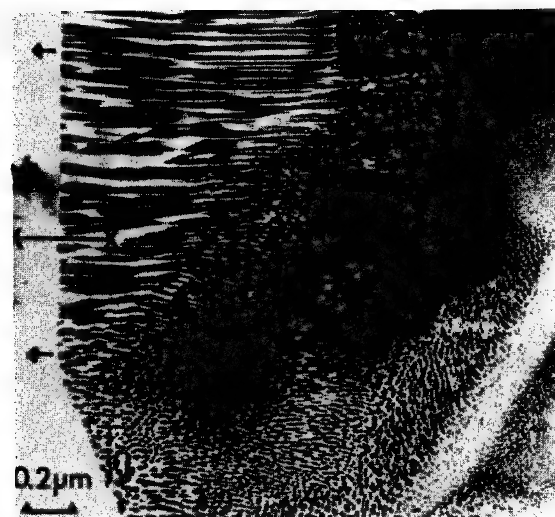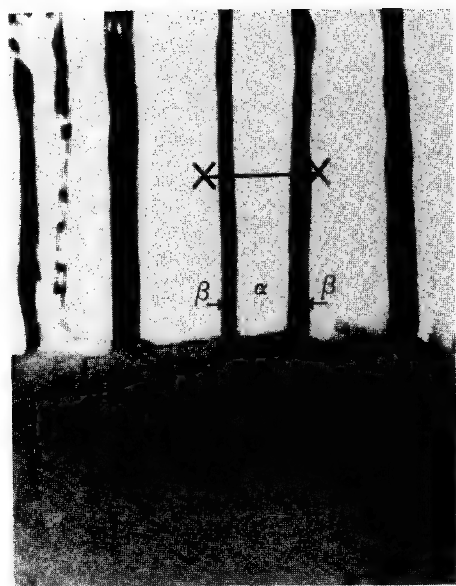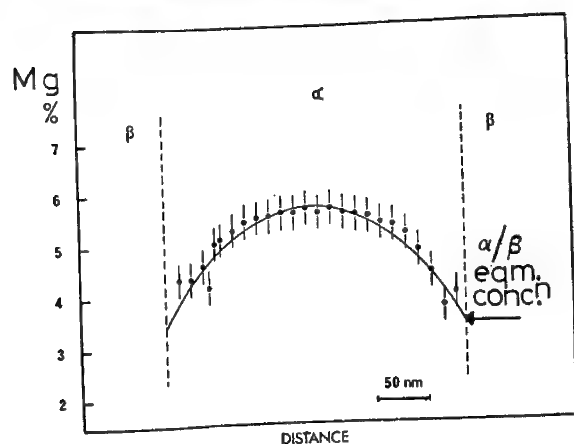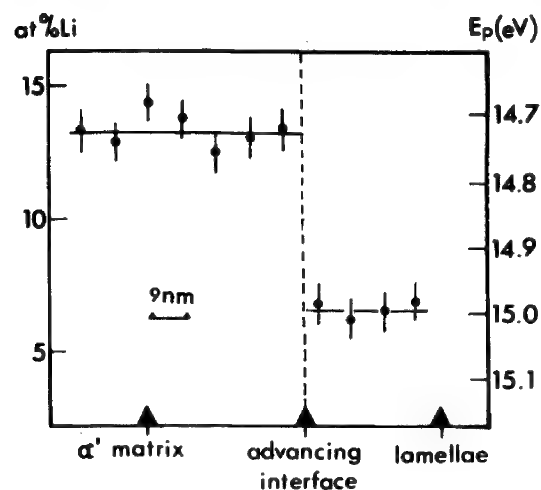
(b)

Fig. 5a: The discontinuous reaction
in Mg-9 wt% Al showing alternate
lamellae of α, (Mg solid solution)
and β ($Mg_{17}Al_{12}$).

Fig. 5b: The Mg distribution in the
α lamella, along X-X in Fig. 5a. The
α/β equilibrium concentration is shown,
thus demonstrating that the bulk of
the lamella has a non-equilibrium
composition.

Fig. 6a: Grain boundary θ precipitation in splat-quenched Al-17.3 at% Cu.

Fig. 6b: Data demonstrating the absence of bulk solute diffusion around θ precipitates, along X-X in Fig. 6a.
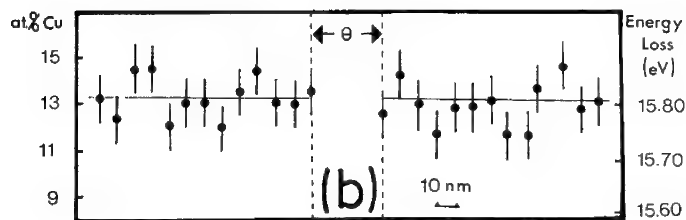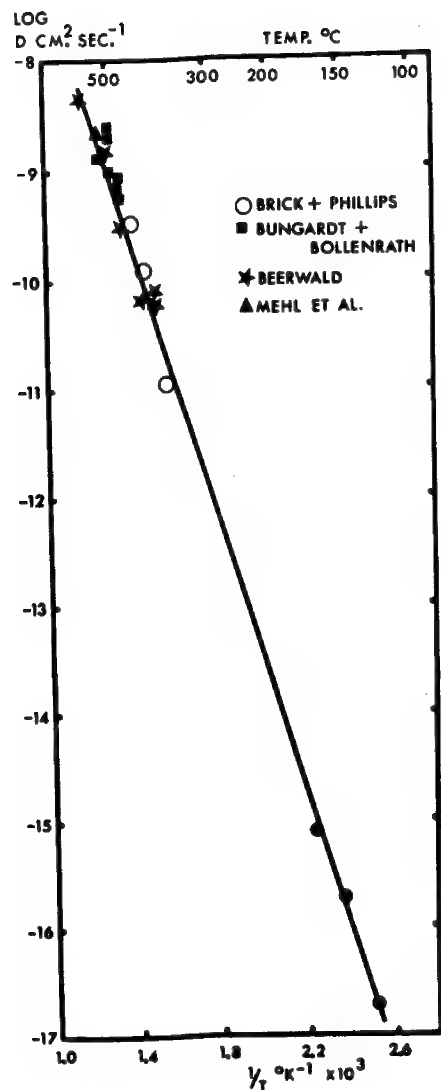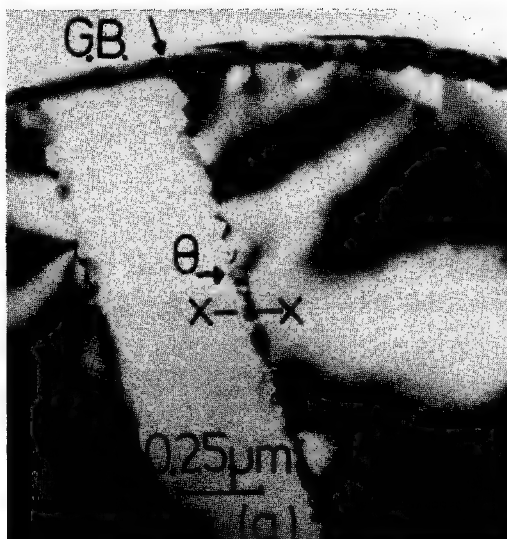
Fig. 7: Arrhenius plot showing the measured diffusivity of Mg in Al-7 wt% Mg using grain boundary profiles (solid circles),[4] compared with previous data using conventional techniques. (Data from ref. (12).)

THE EFFECT OF ENERGY LOSS ON LATTICE FRINGE IMAGES OF DYSPROSIUM OXIDE

A. J. Craven and C. Colliex

Cavendish Laboratory, Madingley Road, Cambridge CB3 OHE, England

Energy filtered 7.5 $\overset{o}{A}$ lattice fringes from type C crystalline dysprosium oxide, (Dy_2O_3), have been recorded with a V.G. Microscopes HB5 STEM. A spectrum from the specimen is shown in fig. 1. The principal features are a collective 'plasmon' excitation (P) at 15.7 eV and a 5P core-loss (C) at 37.2 eV (1). Fig. 2a, b, c, d are lattice fringe images recorded in 100 seconds with an objective (i.e. probe) semi-angle of 8 mrad and a collector semi-angle of 1 mrad. Fig. 2a is unfiltered and fig. 2b, c, d are filtered with an 8 eV energy window centred on 0 eV, 16 eV and 37 eV respectively. The lattice fringes persist in the images formed with loss electrons, but their visibility is much reduced because of lower contrast and higher noise. The contrast was measured from line traces and for one set of results was 0.17 ± 0.02 for the unfiltered image, 0.27 ± 0.02 for the zero loss image, 0.21 ± 0.02 for the plasmon image and 0.27 ± 0.03 for the core loss (contrast $= 2(I_{max} - I_{min})/(I_{max} + I_{min})$). Thus the contrast is some 40% lower in the unfiltered image than in the zero loss image and approximately the same as in the 37 eV image.

A complete treatment of inelastic imaging is complicated. However, a simple approach based on the angular distribution of inelastic scattering produces contrast changes of this magnitude. Low energy inelastic scattering preserves diffraction contrast (2) and so, to a first approximation, the inelastic scattering only increases the collector aperture. Thus the fringe contrast is reduced. Rather than integrate over the effective collector aperture provided by the inelastic scattering, an estimate of the contrast can be obtained by calculating the maximum value, β_0, of the collector angle which does not reduce the fringe contrast significantly. Scattering through greater angles will average to zero contrast, so that the total contrast is a fraction, f, of the ideal contrast, where f is the fraction of electrons scattered through angles less than β_0. f can be obtained by integration of $1/(\phi^2 + \phi_E^2)$, the inelastic scattering distribution, giving $\ln(\beta_0/\phi_E)/\ln(\phi_M/\phi_E)$ where ϕ_E is $\Delta E/2E$ and ϕ_M is taken as the classical recoil angle of a free electron, i.e. $\sqrt{(2\phi_E)}$.

β_0 can be estimated from the fringe shift caused by a tilt β_0. A shift of a quarter of a period can be tolerated, so that β_0 is $0.25\,\theta$ where θ is twice the Bragg angle ($\theta \approx 5.6$ mrad). This neglects spherical aberration and a better estimate can be obtained by restricting the change in path difference between the zero order and diffracted beams to $\lambda/4$. The path difference between a ray inclined at θ to the axis and the axial ray is $- (C_s\theta^4/4 + \Delta Z\theta^2/2)$. This difference changes most slowly when ΔZ is $- C_s\theta^2$ and at this defocus $\beta_0 \sim 2$ mrad. With this value of β_0, f is 60% for $\Delta E = 16$ eV and 50% for $\Delta E = 37$ eV, compared with the experimental values of 78% and 62%. Considering the approximations, the agreement is quite good.

1. C. Colliex, M. Gasgnier and P. Trebbia, J. de Physique, 37, 397 (1976).
2. A. Howie, Proc. Roy. Soc., A271, 268 (1963).

FIG. 1. Energy spectrum from Dy_2O_3

a) Unfiltered

b) Zero loss
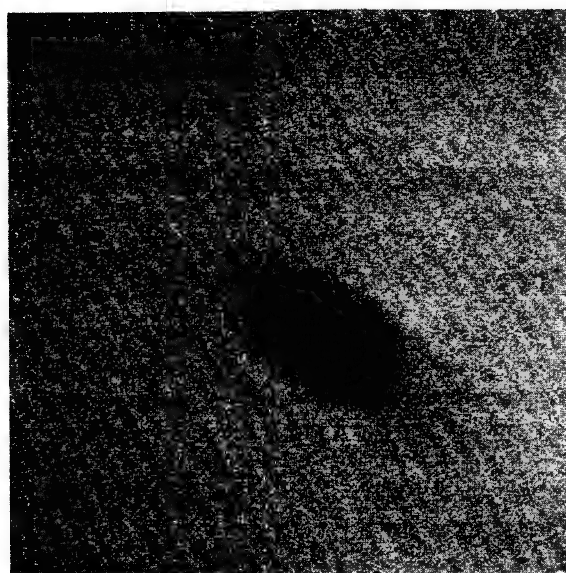
c) Plasmon loss (16 eV)
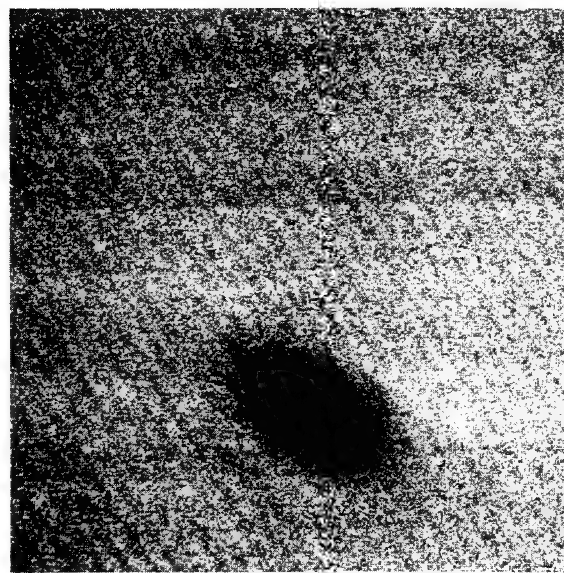
d) 5p core-loss (37 eV)

FIG. 2. 7.5 Å lattice fringes from Dy_2O_3. Filtered images have a window of 8 eV.

Practical Materials Microanalysis by Electron Spectrometry

by

David C. Joy and Dennis M. Maher
Bell Laboratories
Murray Hill, New Jersey 07974

INTRODUCTION

Electron energy-loss spectroscopy (EELS) is the study of the inelastic scattering events which an electron undergoes during its passage through a suitably thin material. When an analysis of the elemental constituents of the material is required the most important inelastic events are the ionizations of inner shells of the atom since these cause discontinuities ("edges") in the EEL spectrum at energies which are characteristic of a particular element. A simple electron spectrometer combined with a transmission electron microscope makes it possible to use these edges for selective identification of elements having atomic numbers Z equal to and greater than 3 (i.e. lithium and above). Therefore EELS can be regarded as an adjunct to the more conventional energy-dispersive X-ray spectroscopy (EDXS), which is restricted to elements with $Z \geq 11$ (i.e. magnesium and above). This paper outlines the design parameters of an EEL spectrometer optimized for elemental microanalysis, the coupling of the spectrometer to an electron microscope and a basic approach to data collection and analysis.

THE SPECTROMETER

Type   The spectrometer is a symmetric (90°), magnetic sector analyzer which is interfaced below the camera chamber of a 100 kV transmission electron microscope. The dispersion is 4 μm/eV and therefore with a "slit" width (i.e. detector aperature) of 80 μm the resolution (FWHM) is typically 20 eV. A scintillator/photomultiplier electron detector and either analog or digital signal processing are used.

Energy Range   Since a major application of EELS in materials science will be the detection of light elements it is, in this regard, necessary that the energy dispersion extends only as far as the K edge of magnesium (1300 eV). In practice a total dispersion of 2 keV is obtained easily at 80 or 100 kV, and this allows K edge studies up to Si, as well as the detection of L, M or N edges from all other elements (Z > 2) in the periodic table. Just as in the case of EDXS, the full energy spectrum need only be observed when the constituents of the sample are completely unknown. Because an EEL spectrum at present is serially scanned, rather than recorded in parallel, it is desirable to cover the smallest energy range possible so as to maximize the signal/noise ratio for a given scan interval.

Energy Resolution   Typically electron spectrometers
have had a resolution of 1 eV or less (i.e. FWHM).   While
such a performance is useful, particularly in the study of
plasmon peaks and fine-structure phenomena, this resolution
is not necessary for the detection of edges.   Figure 1
shows the energies of edges in the spectral range up to 700 eV.
Even in this region, which is potentially the most densely
populated part of a spectrum, a resolution of 20 eV (indicated
by the width of the triangles) is adequate to separate all
edges.   Since at these and higher energy losses, the edges
are naturally tens of electron volts wide, a spectrometer
resolution of 20 eV is acceptable in order to separate
and delineate all edges.   This resolution makes lesser
demands on the stability of the microscope and spectrometer
power supplies.   Moreover a good signal/noise ratio is
readily obtained since the noise found in spectra recorded
at higher resolution is eliminated.   Figure 2 shows the low
energy portion of an EEL spectrum from a silicon crystal
recorded with 20 eV resolution.   Because of this resolution,
the zero loss and plasmon peaks are not well resolved but the
L edges are clearly observed above background.   Figure 3 shows
the corresponding K edge of silicon, again recorded with
20 eV resolution.

Angular Acceptance   The last significant parameter for
EEL microanalysis is the angular acceptance of the spectrometer.
The characteristic scattering angle $\theta_E = E_K/2E_0$ (where E_K is
the edge energy and E_0 the incident beam energy) is of the
order of 10^{-2} rad and so the acceptance angle will need to be
of this value.   For the highest sensitivity the ratio,
peak/(background)$^{1/2}$, must be maximized as in the EDXS case.
Recent measurements[1] confirm earlier studies[2] and show
that, for each characteristic energy loss, there is an
optimum collection aperture.   At 80 kV this varies from about
5×10^{-4} rad for Li_K, to about 10^{-2} rads for Si_K.   This
variation implies that in cases where several elements are
thought to be present, it may be desirable to record spectra
at different acceptance angles to ensure optimum detectability.

THE SPECTROMETER AND THE MICROSCOPE

As shown by Egerton and Lyman[3] the coupling of the
spectrometer to the microscope is critical if efficient and
convenient operation is to be achieved.   In transmission
electron microscopes, including those with scanning attachments,
the necessary conditions can be met by using the diffraction
pattern in the backfocal plane of the objective lens as the
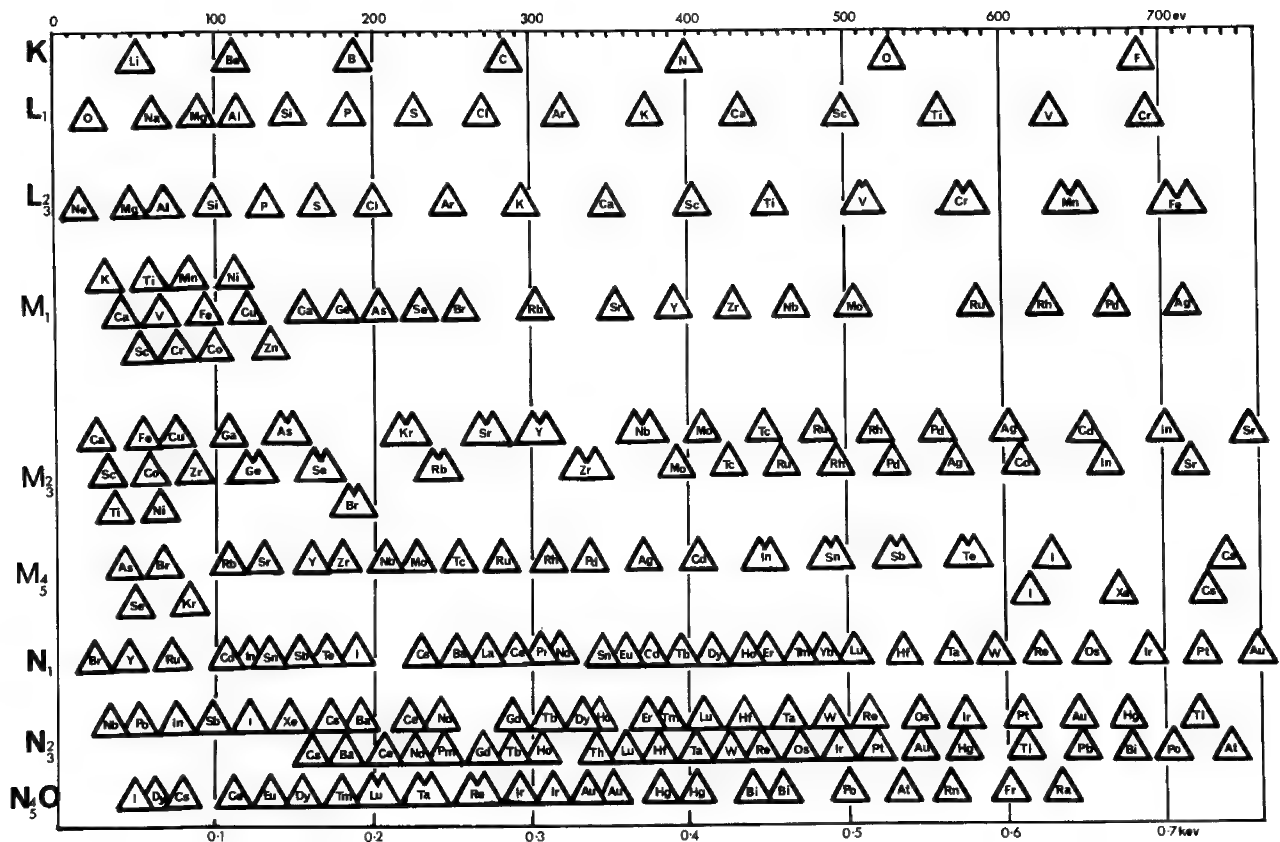
Figure 1. Position of ionization edges in energy
loss range 0-700 eV.
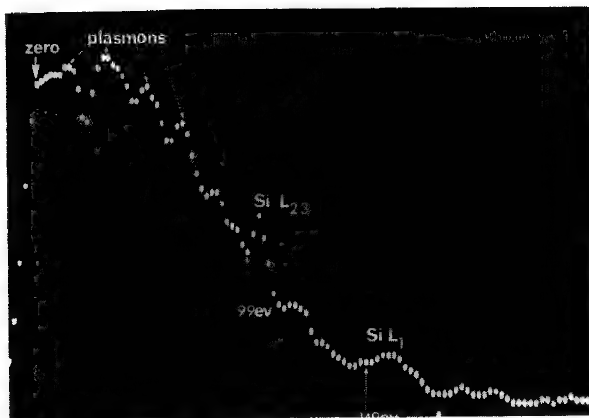
Figure 2. EEL spectrum of Si
recorded at 80 kV with 20 eV
resolution. Each channel
represents a 2 eV increment
in energy loss. Time per
channel 30 msec.
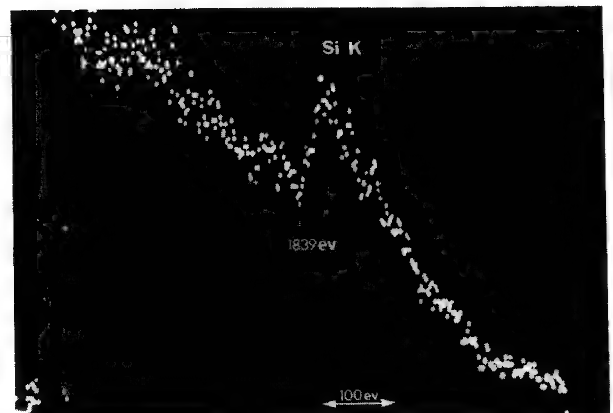
Figure 3. EEL spectrum of Si
showing the K edge. Conditions
as for Figure 2.

object plane of the spectrometer. This permits the same
optics to be used for both conventional and scanning-
transmission operation, since the position of the backfocal
plane is approximately constant. In either mode the angular
acceptance angle is then set by the objective aperture.
Because the diffraction camera length in the backfocal plane
is small, relatively large scattering angles and specimen
areas can be analyzed without loss of resolution. In STEM
the area examined is determined by the probe diameter or the
area scanned, while in CTEM the area to be analyzed can be
selected on the image by means of the intermediate aperture,
as is done in selected-area diffraction.

DATA RECORDING AND PROCESSING

The recording and processing of EEL spectra can be simpli-
fied by using the counting circuitry, multichannel analyzer (MCA)
and display facilities usually found in EDXS systems. The
electrons can be pulse counted and stored in the MCA using the
multi-scaling mode. The wide dynamic range of an EEL spectrum
(typically 10^4 to 1 between zero loss and 2000 eV) is
accommodated easily by the MCA while still allowing log
compression or scale expansion for the observation of individual
edges. Furthermore the smoothing and integration routines
provided for X-ray spectra are equally applicable to EELS.
The spectra shown in this paper were recorded using a KEVEX 5100
X-ray MCA. By setting the energy range scanned to 2048 eV,
each channel in the MCA represents a 2 eV increment and thus
the alphanumeric calibration of the MCA display is retained.
Typically the entire 2 keV spectrum is recorded in 30 seconds.
Preliminary attempts at quantitative work have also shown that
linear background subtraction and peak integration routines
designed for X-ray spectra are of some value.

Even in relatively simple materials a multiplicity of
edges may be found in the EEL spectrum. Using a table such
as in Figure 1, edges are identified from their energy and
shape, starting from the highest energy loss. Once a K edge
has been identified the corresponding L, M, N edges can then
be noted and removed from further consideration. For this
purpose the ability of EDXS-MCA systems to mark and display
regions of interest is invaluable. If EELS is used together
with an EDXS, both types of spectra can be recorded. In this
way the X-ray data can be used to identify some of the
EEL edges.

In STEM operation an image can be formed through the spectrometer from electrons which have lost a specified amount of energy. Because the entire recording period is now spent examining one energy loss region, the effective signal/noise ratio is high and good elemental maps can be obtained even though, in a spectrum, the corresponding edge may not be prominent. Figure 4 shows an example of a carbide platelet in a Ti-V alloy imaged in the carbon K loss (280-300 eV). The carbon present in a contamination spot (c) can also be seen to be "in contrast". The corresponding EEL spectrum is shown in Fig. 5.

CONCLUSION

A spectrometer of limited resolution but properly interfaced to transmission electron microscope and EDXS recording system can be used routinely to perform microanalysis with submicron spatial resolution. Although the principles of quantitation are not yet fully developed, the ability to identify and localize such elements as carbon and oxygen is already proving to be of great practical value in materials science.

REFERENCES

1) Joy, D. C., and Maher, D. M., to be published.

2) Egerton, R. F., Rossouw, C. J., and Whelan, M. J. in "Advances in Microscopy and Microanalysis" (ed. J. A. Venables), Inst. of Physics, London (1975), pp. 124-31.

3) Egerton, R. F., and Lyman, C. E., in "Advances in Microscopy and Microanalysis" (ed. J. A. Venables), Inst. of Physics, London (1975), pp. 132-5.
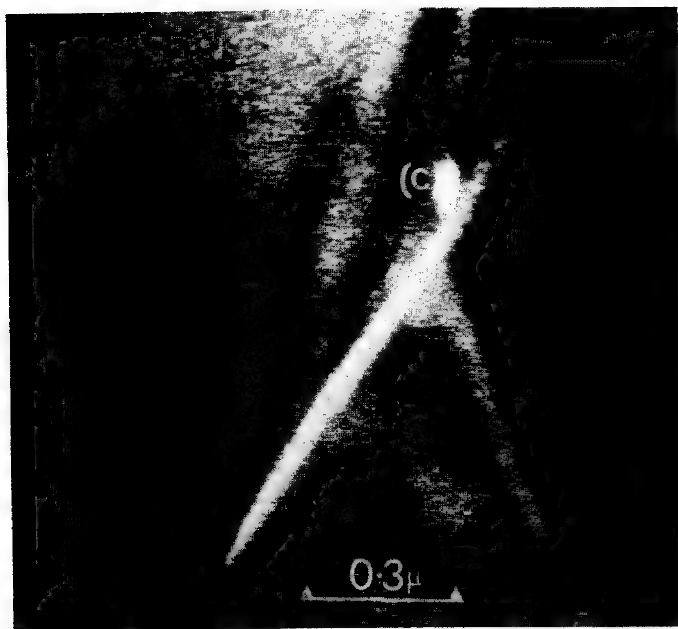
Figure 4. Carbide platelet in
Ti-V alloy imaged with carbon
K-loss electrons using STEM.
The spot (c) is a contamination
mark from the beam and also
contains carbon. The image
was recorded at 80 kV in
25 seconds using a 20 eV
      energy window.
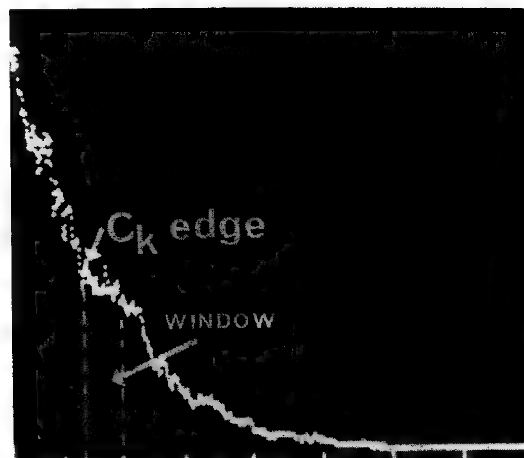
Figure 5. EEL spectrum
from carbide platelet
(Fig. 4) showing C_k edge
and 20 eV window.
Spectrum was recorded
in spot mode (dia $\sim$ 100 Å).

The Application of Electron Energy Loss Spectroscopy
in Glass - Ceramic Microstructural Analysis

R. M. Anderson and A. Kumar

IBM System Products Division, East Fishkill
Hopewell Junction, New York 12533

The identification of unknown phases in crystallized glasses or
ceramics has been difficult because the phases are generally
composed of many elements; they crystallize into low-symmetry
lattices; they contain numerous impurities, which may alter
crystal structure or allow the observation of metastable phases;
and they are not well represented in standard compilations of
crystal data. Compounding the problem is the fact that energy-
dispersive x-ray analysis (EDX) for elemental content can not be
employed for elements with Z<11. This eliminates any possibility
of qualitative analysis of the important Li, Be, and B glasses as
well as determination of O, C and N content.   Electron Energy
Loss Spectrometry (ELS) has been shown to be a powerful method
for the analysis of light elements (1). The ELS method is far
more efficient at detecting light elements than x-ray detection,
because the yield of energy loss electrons to inner shell excita-
tion and ionizations is unity and because the electrons, which
have lost energy encountering the sample, are scattered through
very small angles, with the result that collection efficiencies
are high. Therefore a modern, STEM/SEM-equipped transmission
electron microscope fitted with both an energy loss analyzer and
an energy dispersive x-ray detector is particularly well suited
for the analysis of glasses and ceramics.

   In an attempt to exploit the apparent potential of such a
total analytical electron microscope for research on glass and
ceramics, we prepared a mixture of commercial grade MgO, SiO_2,
Al_2O_3, and Li_2O powders which were melted into a glass at 1650°C.
Optical emission spectroscopy of the glass revealed B, Ca, Mn, K,
Ti, As, Na, Pb, and Zn impurities. DTA analysis showed crystal-
lization exotherms at 650, 795 and 950°C; specimens were prepared
after heat treatment of the glass at those temperatures. The
instrument used was a JEOLCO 100C equipped with a field emission
gun, STEM and SEM capability, and a JEOLCO electron velocity
analyzer (2,3).   The instrument is also fitted with a Canberra
EDX system that uses a Kevex x-ray detector.

   As formed, the glass matrix contained small crystalline
needles, which dissolved in favor of spherical precipitates at
650°C. At 795°C we observed a mixture of crystalline phases that
reduced to a system of plates at 950°C. The list of phases
identified at the intermediate steps is long; here we will only
report one example from the 950°C results. Figure 1 shows a
dark-field micrograph and a selected area electron diffraction
pattern (SAD) of a plate fragment on the carbon support film.
The plates are large and nearly all lying flat on the carbon
film; this leads to SAD patterns containing very few usable
d-spacings. Figure 2 shows an EDX spectrum from the plate. It
shows strong Al and Si plus weak K and Ca peaks (the Ti signal
probably arises from the Ti grid, and the Cu peak comes from the
specimen holder). Figure 3 shows the ELS spectra with a plasmon
peak at 25 eV, a Ca M(I) edge at 42 eV, a Mn M(II-III) edge at 49
eV, a Li L(I) edge at 56 eV, an Al L(II-III) edge at 72 eV, and a
Si L(II-III) edge at 99 eV. Figure 4 depicts an enlarged,

expanded view of the oxygen K edge at 532 eV further along on the Fig 3 spectra. The fine structure on the oxygen K edge provides information on the chemical binding states of the various elements with oxygen in a fashion complementary to the ESCA method. In the ELS case, however, since there is no requirement that the excited electron be emitted from the sample, the transition energies one measures are absolute and not sensitive to the work function of the sample.

With a reduced elemental list consisting of Al, Si, Li, O, Ca, and Mn, it was a relatively simple matter to match the plate's diffraction data with β-Spodumene, $Li_{0.6}Al_{0.6}Si_{2.4}O_6$. The Ca and Mn are presumably in solid solution in the β-Spodumene. It is clear that ELS and EDX combined in a modern analytical instrument is a potent tool for microstructural analysis in glass or ceramic systems.

1. Isaacson, M. & Johnson, D., Ultramicroscopy, 1 (1975) p 33.
2. Harada, Y., et. al., Proc. EMSA, (1976) p 528.
3. Harada, Y., et. al., JEOL News, 14e, (1976) p 2.

Fig 1. Dark-field of plates.

Fig 2. SAD of Fig 1 large plate
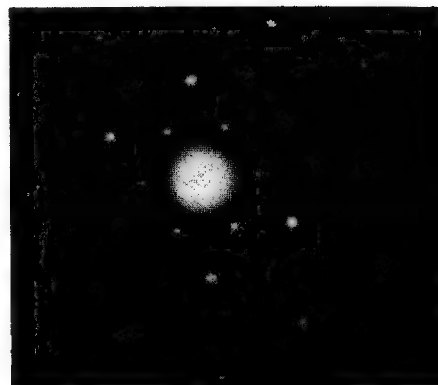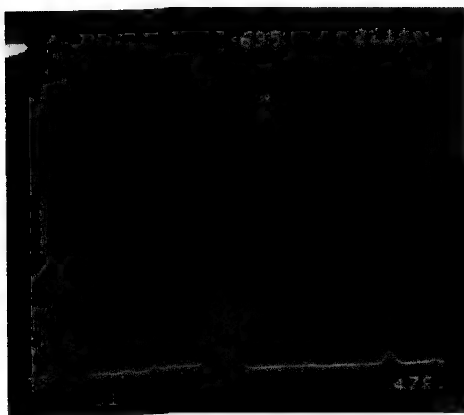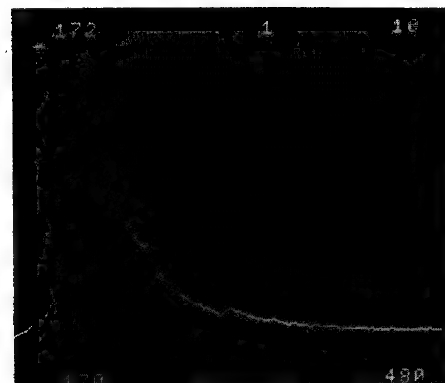
Fig 3. EDX spectra from plate.

Fig 4. ELS spectra

Fig 5. ELS spectra around oxygen 532 eV edge.
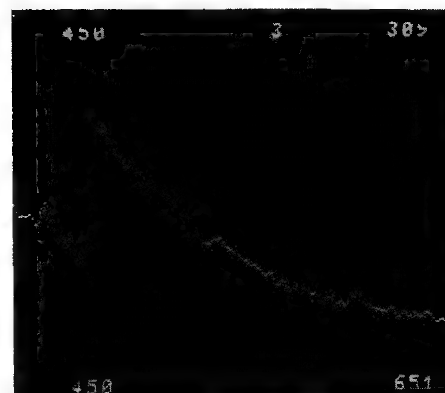
CROSS-SECTIONS FOR K-SHELL EXCITATION BY FAST ELECTRONS

R. F. Egerton and D. C. Joy

University of Alberta, Edmonton, Canada and
Bell Laboratories, Murray Hill, N. J.

The cross-section for excitation of an electron from the innermost shell of a given atom can be determined directly by measuring the proportion of fast incident electrons which have suffered an appropriate energy loss, or (if the X-ray or Auger yields are known) from the number of X-ray quanta or Auger electrons emitted as a result of de-excitation.

In the direct method, this cross-section is obtained as a function of α, the maximum scattering angle allowed into the detector, and for a thin specimen it is given by:

$$\sigma_K(\alpha) = \frac{1}{nt} \cdot \frac{I_K(\alpha)}{I_t(\alpha)} \tag{1}$$

where n is the number of atoms per unit volume of specimen, t is the specimen thickness, $I_K(\alpha)$ represents the number of K-loss electrons reaching the detector and I_t represents the total number of fast electrons entering the detector,[1] for the same value of α. Equation (1) can also be used[12] for microanalysis of low-atomic-number elements in order to measure n or nt if $\sigma_K(\alpha)$ is known. Partly because of this potential use in microanalysis, measurements of $\sigma_K(\alpha)$ have been made by a number of workers[1-5] by means of electron spectroscopy. Results for the elements carbon, nitrogen and aluminum are shown in figure (1).

$\sigma_K(\alpha)$ can also be calculated from Bethe theory. Using relativistic kinematics,[6]

$$\sigma_K(\alpha) \simeq \frac{2\pi e^4}{M_o v^2 \overline{E}} \; f_K \; \ln \left[1 + \left(\frac{2\alpha E_o}{\overline{E}} \right)^2 \right] \tag{2}$$

where e, M_o, v_o and E_o are the charge, rest mass, velocity and kinetic energy of the fast electrons, $\overline{E}$ is the mean energy loss[1] due to K-shell excitation and f_K is the oscillator strength, given[7] by $f_K \sim 2.1 - 0.037z$, for atomic numbers z < 20. The Bethe predications, represented by the solid curves in figure (1), are seen to fit the experimental data quite well.

The angular dependence represented by equation 2 should continue up to an angle α of the order of $(\overline{E}/E_o)^{1/2}$, above which the intensity rises due to the existence of a Bethe ridge.[1,6] However, the oscillator strength f_K must eventually saturate with α. Making the crude assumption that f_K remains constant then drops abruptly to zero at $\alpha = (\overline{E}/E_o)^{1/2}$, equation (2) gives the total K-shell cross-section, for scattering through all angles, as:

$$\sigma_K(\pi) = \frac{2\pi e^4}{M_o v_o^2 \overline{E}} \; f_K \; \ln \left(\frac{4E_o}{\overline{E}} \right) \tag{3}$$

This saturation value, which is identical to Bethe's original formulation[8] except that f_K here replaces his $(2b_K)$, is shown in figure 1 (horizontal broken lines). More recent calculations give formulae similar to equation (3) but with differing constants in front of and within the logarithmic term.[11]

$\sigma_K(\pi)$ can also be obtained from X-ray or Auger measurements, assuming that the emission is isotropic. Values[9-11] for C, N and Al, extrapolated[11] to E_O = 80 keV are represented on figure 1. Two comments can be made from a comparison of the data: (a) The Auger and X-ray values, if accurate, suggest that $\sigma_K(\alpha)$ saturates at $\alpha < (\overline{E}/E_O)^{1/2}$. (b) The energy loss data show no evidence of this saturation, values at 0.1 rad being larger than the Auger or X-ray values for $\alpha = \pi$.

References

1. R. F. Egerton, Phil. Mag. 31, 199 (1975).
2. M. Isaacson, J. Chem. Phys. 56, 1813 (1972).
3. Y. Kihn, Thèse 3e cycle, Toulouse (1975).
4. R. D. Leapman and V. E. Cosslett, Phil. Mag. 33, 1 (1976).
5. C. J. Rossouw, private communication.
6. M. Inokuti, Rev. Mod. Phys. 43, 297 (1971).
7. J. Durup and R. L. Platzman, Disc. Faraday Soc. 31, 156 (1961).
8. H. Bethe, Ann. Phys. 5, 325 (1930).
9. G. Glupe and W. Mehlorn, Phys. Letters 25A, 274 (1967); Journal de Physique 32, C4-40 (1971).
10. W. Hink and A. Ziegler, Z. Phys. 226, 222 (1969).
11. C. J. Powell, Rev. Mod. Phys. 48, 33 (1976).
12. R. F. Egerton, C. J. Rossouw and M. J. Whelan, Proc. 34th EMSA Conference, 516 (1976).
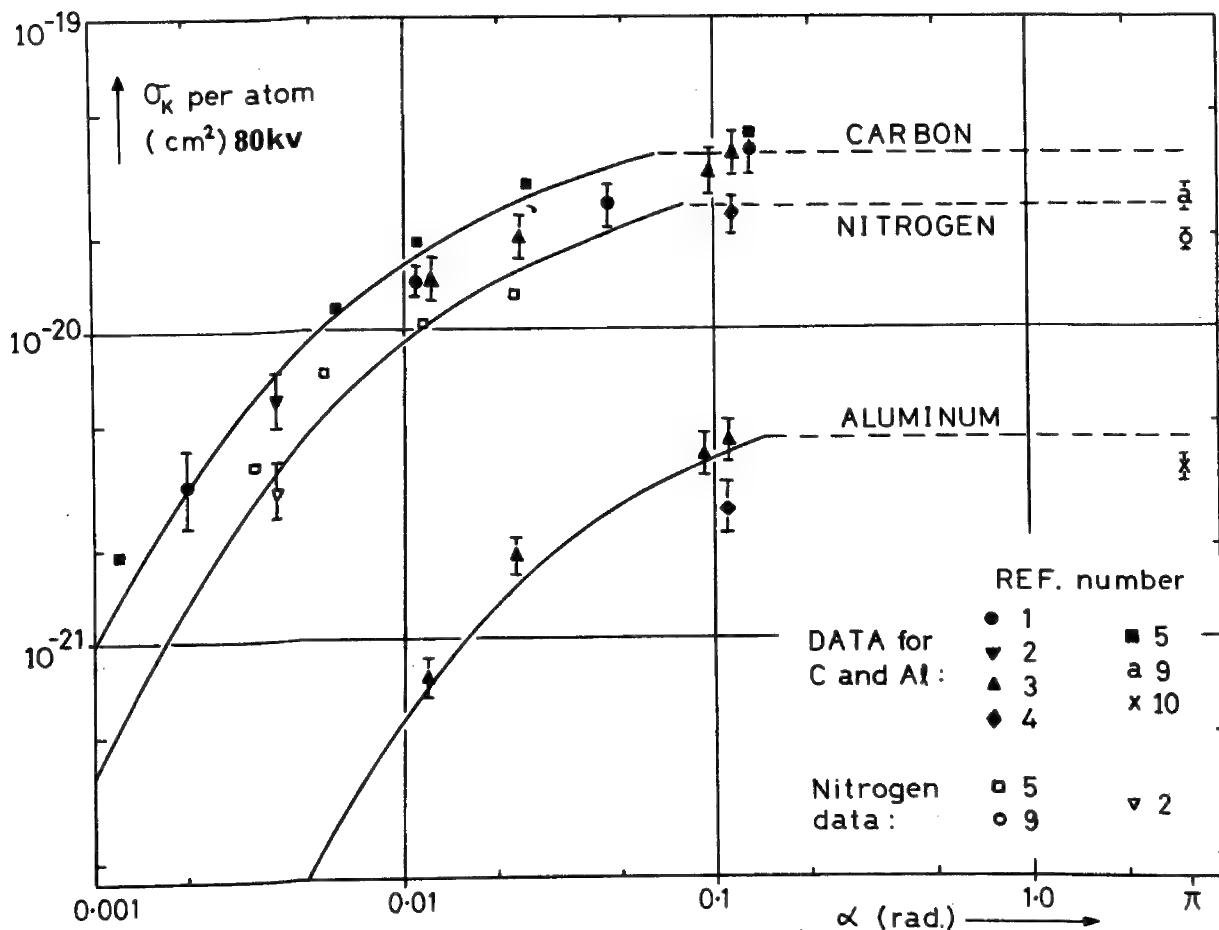
Fig. 1. Comparison of values of $\sigma_K(\alpha)$ from electron spectroscopy measurements with calculated values from relativistic Bethe theory. The horizontal line shows the saturation cross section $\sigma_K(\pi)$. Calculated ionization cross sections for X-ray production are shown for comparison.

AN EFFICIENT LENSING ELEMENT FOR X-RAYS*

N. M. Ceglio**

Lawrence Livermore Laboratory
University of California
Livermore, California 94550

and

Henry I. Smith

Lincoln Laboratory
Massachusetts Institute of Technology
Lexington, Massachusetts 02173

Introduction

Research in a variety of fields (x-ray - lithography, - microscopy, -lasers; thermonuclear fusion diagnostics;...) could significantly benefit from a capability for efficient beam manipulation (collimation, focusing, beam expansion and reduction) of x-rays in the way that optical light can be routinely manipulated. Achievement of such an x-ray beam manipulation capability awaits the development of low f/number x-ray lensing devices which would be efficient and simple to implement in the laboratory. We have designed an efficient x-ray lens with an effective speed of order f/40 for ~ 1Å-100Å x-rays. Fabrication of this lensing element appears feasible using existing microfabrication technology.

Physical mechanisms which have been used for x-ray beam manipulation in the past are grazing incidence reflection (GIR) from accurately figured and polished surfaces or diffraction using perfect crystals or microscopically precise transmission gratings and zone plates. GIR devices are broadband, have large f/number, require precision alignment and for these reasons are generally inappropriate for multi-element beam manipulation systems. Diffraction devices are narrowband, but are inefficient either because of the distribution of incident energy into multiple diffraction orders (gratings and zone plates), or the narrow angular acceptance of Bragg crystals. These limitations again make such devices generally inappropriate for use in multi-element beam manipulation systems. Refractive x-ray focusing devices have generally not been available because of the relatively large value of the absorption parameter, η, at x-ray wavelengths. ($\eta \equiv k/\delta \simeq .1 - 1$ at x-ray wavelengths whereas $\eta \ll 1$ at optical wavelengths. k, δ are defined in terms of the refractive index, n, of the lensing material: $n \equiv 1 - \delta + ik$).

Design Concept

We propose to couple diffraction and refraction in a single element to achieve efficient x-ray concentration into a single order focal spot. In

this device, diffraction is used to produce efficient ray bending (without absorption) while refraction is used only to provide appropriate phase adjustment among the various diffraction orders to insure a single order output. The mechanism for ray bending (diffraction) is decoupled - somewhat - from the absorption mechanism. Refraction is used only to achieve small shifts in phase so that the associated attenuation need not be prohibitive.

The proposed x-ray lens might accurately be described as a Blazed Fresnel Phase Plate (BFPP).[1] A BFPP is a Fresnel zone structure with a spatially distributed phase shift <u>within</u> each Fresnel zone. The spatial distribution of the phase shifts is chosen to concentrate all unabsorbed energy into a single focal spot. The comparative focusing capabilities of a Fresnel Zone Plate, Fresnel Phase Plate, and a Blazed Fresnel Phase Plate are presented in Table I.

| Device | FRACTIONAL DISTRIBUTION | | | |
	1st Order Real Focus	Absorbed	Undiffracted	All Other FOCI
FZP	.1	.5	.25	.15
FPP	$(\frac{2-\gamma}{\pi})^2$	$.5(1 - (1 - \gamma)^2)$	$(\frac{\gamma}{2})^2$	$\sim 1.5 \ (\frac{2-\gamma}{\pi})^2$
BFPP	$(1 - \gamma)^2$	$1 - (1 - \gamma)^2$	0	0

TABLE I: Comparative Energy Distribution for a FZP, FPP, and BFPP. ($\gamma \equiv 1 - \exp(-\pi n)$ is the fractional amplitude attenuation occuring in a phase shifting zone of the FPP.)

Design Calculations

For a converging (BFPP) lens each adjacent Fresnel zone pair must satisfy the condition:

$$t(r) \cdot \delta(r) = \frac{\lambda (r^2 - r_m^2)}{2 r_1^2} \tag{1}$$

$m = 0, 2, 4, \ldots$
$r_m \leq r \leq r_m + 2$

whereas for a diverging (BFPP) lens each adjacent Fresnel zone pair must satisfy

$$t(r) \cdot \delta(r) = \lambda \{1 - \frac{(r^2 - r_m^2)}{2r_1^2}\} \tag{2}$$

$m = 0, 2, 4, \ldots$
$r_m \leq r \leq r_m + 2$

where
  r is the radial coordinate
  t is the material thickness
  r_m is the outer radius of the mth Fresnel zone
  r_1 is the radius of the central zone
  δ is defined by: $n = 1 - \delta + ik$

So then, appropriate blazing can be achieved either by modulating material thickness at constant refractive index or by modulating the refractive index (presumably by doping) at constant material thickness.

   Preliminary calculations of x-ray lens efficiency and "effective speed" are presented in Table II for a few different materials[2] at various x-ray wavelengths. In Table II, Δr, is the width of the outermost zone of the Fresnel zone structure. $\Delta r \sim 500 \text{Å}$ appears within the reach of existing microfabrication technology; $\Delta r \sim 100 \text{Å}$ would require modest extensions of that technology. The parameter, F, is chosen as a measure of lens efficiency. It is the fraction of energy emitted by an isotropic point source which can be collimated into a parallel beam by the lens. It takes into account x-ray absorption by the lens material and its finite numerical aperture. (For comparative purposes it should be noted that an f/10 lens at optical wavelengths, i.e., negligible absorption, has $F \sim 6.2 \times 10^{-4}$).

MATERIAL	λ	Δr	F	Effective f/#
Silicon	24Å	500Å	4×10^{-5}	f/40
	24Å	100Å	9×10^{-4}	f/9
	44Å	500Å	2×10^{-5}	f/56
	44Å	100Å	6×10^{-4}	f/10
Aluminum	25Å	500Å	4×10^{-5}	f/40
	25Å	100Å	1×10^{-3}	f/8

Table II; Calculated values for x-ray lens efficiency, F, and 'speed', f/#, for a few different wavelengths and materials.

   Additional efficiency calculations for a wider range of wavelengths and materials shall be presented along with the CTF and MTF for the BFPP. Spin-off concepts such as a blazed transmission phase grating for efficient coherent beam splitting of x-rays will be discussed. Matters of fabrication feasibility and tolerances shall also be addressed.

---

1) It is important to note that a (BFPP) is not a Fresnel lens in the conventional sense. The conventional Fresnel lens is a prismatic focusing system. It

is made up of a series of concentric, circularly symmetric prisms - generally of equal annular width. The conventional Fresnel lens brings rays to focus using refraction. Diffraction effects caused by the small size of the annular, prismatic grooves lead to image blurring. Whereas for the BFPP image resolution improves as the minimum zone width for the structure decreases.

2) No attempt has been made to optimize lens efficiency by material choice in Table II.

Electron- and ion microprobe analysis of clayified roots in thin sections of soil.

A.P. von Rosenstiel[1], J.D. Brown[2], D.J. Gras[1], E.B.A. Bisdom[3], S.Henstra[4] and A. Jongerius[3].

1) Metal Research Institute TNO, Apeldoorn, Netherlands
2) University of Western Ontario/London/Canada/at present at Metal Research Inst.
3) The University of Western Ontario, London, Canada (on sabbatical leave at the Metal Research Inst.TNO)
4) Metal Research Institute TNO, Apeldoorn, Netherlands

Clayified alder roots were found in a Humaquept (Soil Survey Staff, 1975) near Bathmen, Netherlands. The roots consist under the light microscope of humified remnants of the original tissue and yellow to brown rather homogeneous fine grained material. In the latter oriented clayey substance could be discerned at several places (Bisdom and Jongerius, 1977).

The concept of clayified root was introduced in soil micromorphology by Parfenova et al. (1964). The phenomenon was rare and probably caused by a more complex process than a simple infilling of the root with material moved from other parts in the soil profile. They envisaged reactions between colloidal solutions - introduced into the root tissue without disturbing its anatomical structure - and decomposition products of the decayed root itself, leading to the formation of secondary clay minerals inside the root.
Analysis of clayified root sections by SEM, electron-, and ion microprobe analysis showed Si and Al as main components and a large number of trace elements. By IMMA analysis a clear distinction was possible between amorphous root sections and embedding plastic material.

The following conclusions can be drawn from these combined IMMA, SEM-EDXRA and light microscopic data obtained from thin sections of plastic impregnated and hardened soil material.

Light microscopic observations showed in situ formation of clayey material at some sites in the alder root. So far no X-ray diffraction studies could be made of the material in the root. Analyses with IMMA indicated a rather homo-geneous distribution of elements throughout the clayified root, independent of measurements done in areas with newly formed clayey material or sites with rather high percentages of decayed root tissue. This possibly indicates that organic compounds, apart from the few pieces of visible organic matter, are also present in areas with newly formed clay. This agrees with the hypothesis of Parfenova et al.(1964) which suggests that organic matter may play a role during the formation of secondary clay minerals. It remains an open question, however, whether this is an active role leading to the formation of biogenic

clay (Parfenova et al.1964), or a passive one whereby the organic components only represent one of the factors in an environment favourable for the formation of secondary clay minerals.

Bisdom, E.B.A. and Jongerius, A.(1977). SEM-EDXRA and/or IMMA analysis of cutans, an indurated horizon and clayified roots in this sections of some Dutch soils. Proceedings Fifth Int.Working-Meeting on Soil Micromorphology. Granada,Spain (in press).

Parfenova,E.I., Mochalova,E.F. and Titova,N.A.(1964). Micromorphology and chemism of humus-clay new-formation in forest soils. In: Jongerius, A. (Editor). Soil Micromorphology. Elsevier, Amsterdam, 201-212.

Soil Survey Staff (1975). Soil Taxonomy. Agricultural Handbook No.436, U.S.A., 754 pp.

Quantitative carbon analysis in steels with the ion microprobe

A.P. von Rosenstiel[1], J.D. Brown[2], D.J. Gras[1]

1) Metaalinstituut TNO, Apeldoorn/Netherlands
2) University of Western Ontario/London/Canada
   at present at Metaalinstituut TNO, Apeldoorn/Netherlands

Quantitative carbon analysis in steels using on ion microprobe was investigated to determine the dependence of sensitivity, accuracy and precision on instrumental parameters, such as the primary ion beam species and current density, the polarity of secondary ions, and the structure of the steels. A series of low carbon steel standards with similar martensitic structures were used as calibration standards. Intensities from $^{12}C^+$, $^{16}O^+$, $^{32}O_2^+$, $^{56}Fe^+$, $^{52}Cr^+$, $^{55}Mn^+$, and $^{58}Ni^+$, were measured in the positive secondary spectrum and $^{12}C^-$, $^{16}O^-$, $^{32}O_2^-$, $^{14}N^-$ and $^{72}FeO^-$ in the negative secondary spectrum. Primary ion species used were $^{40}AR^+$, $^{28}N_2^+$, $^{32}O_2^+$ and $^{16}O^-$. To evaluate the effect of chemical state, an Fe_3C standard and two carbon standards each containing 1,1 weight percent carbon, but one having the carbon present in solid solution and the other as pecipitated carbids were also used.

The secondary ion intensity data was either directly plotted to obtain calibration curves or converted to composition using LTE model calculations. The limitations, sensitivity and accuracy of carbon analyses of steels for the various modes of operation and calculation of ion microprobe have been determined.

AUTHORS, AFFILIATIONS, AND PAPER NUMBERS

J. L. Abraham   University of California at San Diego, School of Medicine, Department of Pathology, La Jolla, CA 92093   11

P. J. Adelmann   Clarkson College of Technology, Department of Physics, Potsdam, NY 13676   80

A. L. Albee   California Institute of Technology, Division of Geological and Planetary Sciences, Pasadena, CA 91125   181

L. F. Allard   The University of Michigan, Department of Materials and Metallurgical Engineering, Ann Arbor, MI 48109   23 / 175

M. Ancey   Institut de Recherches de la Sidérurgie Francaise, 185, rue Président Roosevelt - 78100 Saint-Germain-en-Laye, France   26

R. M. Anderson   IBM Corporation, Department 875, Building 300-400, Hopewell Junction, NY 12533   15 / 200

M. Andreani   Laboratoire des Faisceaux Electroniques, Institut de Physique, Ecole Centrale des Arts et Manufactures, Grande Voie des Vignes, 92290 Chatenay-Malabry, France   29 / 30

N. S. Andrushenko   Leningrad University, Leningrad, USSR   --

A. Armigliato   Laboratorio LAMEL-C.N.R., Via Castagnoli, 1-40126 Bologna, Italy   151

J. T. Armstrong   Arizona State University, Departments of Chemistry and Geology, Tempe, Arizona 85281   41 / 42 / 156

D. M. Astill   N.E.R.C. Ion Probe Unit, University of Cambridge, Madingley Rise, Cambridge CB3 OEZ, England   132

D. T. Attwood   University of California, Lawrence Livermore Laboratory, Livermore, CA 94550   56

B. Autier   Société CAMECA, 103 Boulevard Saint-Denis, F 92400 Courbevoie, France   133

P. Azou   Laboratoire des Faisceaux Electroniques, Institut de Physique, Ecole Centrale des Arts et Manufactures, Grande Voie des Vignes, 92290 Chatenay-Malabry, France   29 / 30

F. Bacon   General Electric, Corporate Research and Development, Schenectady, NY 12345   72

L. J. Balk   Lehrstuhl für Werkstoffe der Elektrotechnik, Fachbereich Elektrotechnik, Gesamthochschule Duisburg, Kommandantenstrasse 60, D 4100 Duisburg, Fed. Rep. Germany   119

P. Ballongue   Laboratoire de Physique des Solides, Université Paris-Sud, 91 405 Orsay, France   191

N. C. Barbi	Princeton Gamma-Tech, Inc., P. O. Box 641, Princeton, NJ 08540	100
F. Bastenaire	Institut de Recherches de la Sidérurgie Francaise, 185, rue Président Roosevelt, 78100 Saint-Germain-en-Laye, France	26
P. E. Batson	School of Applied and Engineering Physics, Cornell University, Ithaca, NY 14853	190
R. Bauer	Physiologisches Institut der Universität München, 8 München 2, Pettenkoferstrasse 12, W.-Germany	166 171
N. Baumgarten	AMR Corporation, 160 Middlesex Turnpike, Bedford, Massachusetts 01730	33
D. R. Beaman	The Dow Chemical Company, 574 Building, Midland, MI 48640	74
M. B. Bellhorn	Albert Einstein College of Medicine, 111 East 210th Street, Bronx, NY 10467	137
A. E. Bence	State University of New York, Department of Earth and Space Sciences, Stony Brook, NY 11794	38 183
K. R. Benoit	AMR Corporation, 160 Middlesex Turnpike, Bedford, Massachusetts 01730	16
G. G. Bentini	Laboratorio LAMEL-C.N.R., Via Castagnoli, 1-40126, Bologna, Italy	151
J. Bentley	Radiation Effects and Microstructural Analysis Group, Metals and Ceramics Division, Oak Ridge National Laboratory, Oak Ridge, Tennessee 37830	114
J. P. Berry	Départment de Biophysique de la Faculté de Médecine de Créteil, 6, rue du Général Sarrail, 9400 - Creteil, France	167 168
E. K. Biegert	Rice University, P. O. Box 1892, Houston, Texas 77001	93
W. C. Bigelow	The University of Michigan, Department of Materials and Metallurgical Engineering, Ann Arbor, MI 48109	23 155
G. Blaise	Université de Paris-Sud, Orsay, France	2
J. Böcker	Institut für Metallphysik, Universität Göttingen, Hospitalstr. 12, D-3400 Göttingen, Germany	32
R. B. Bolon	General Electric, Corporate Research and Development, Schenectady, NY 12345	104
J. L. Bomback	Ford Motor Company, Research Staff, P. O. Box 2053, Dearborn, MI 48121	68
H. S. Borovetz	University of Pittsburgh, Departments of Surgery and Civil Engineering, Pittsburgh, PA 15261	176
I. B. Borovskii	Institute of Solid State, Physics, Academy of Science, 142432 Chernogolovka, Moscow Reg., USSR	--

L. E. Davis	Physical Electronics Industries, Inc., 6509 Flying Cloud Drive, Eden Prairie, MN 55343	71
R. H. Day	University of California, Los Alamos Scientific Laboratory, P. O. Box 1663, Los Alamos, NM 87545	58
W. R. DeBoskey	IBM Corporation, P. O. Box 12195, Research Triangle Park, NC 27709	49
P. B. DeNee	Department of Anatomy, West Virginia University, Morgantown, West Virginia 26505	10
A. Desalvo	Laboratorio LAMEL-C.N.R., Via Castagnoli, 1-40126 Bologna, Italy	151
J. Dilger	State University of New York, Department of Physics, Stony Brook, NY 11794	172
W. Donnelly	Microspec Corporation, 265-G Sobrante Way, Sunnyvale, CA 94086	33
A. Dörge	Physiologisches Institut der Universität München, 8 München 2, Pettenkoferstrasse 12, W.-Germany	166 171
T. J. Driscoll	College Park Metallurgy Research Center, U.S. Department of the Interior, Bureau of Mines, College Park, Maryland 20740	67
P. Duncumb	Tube Investments Research Laboratories, Hinxton Hall, Saffron Walden, Essex, England	4
N. A. Dyson	University of Birmingham, Departments of Physics and Experimental Pathology, P. O. Box 363, Birmingham B15 2TT, England	92
J. W. Edie	University of Iowa, Dows Research Institute, College of Dentistry, Iowa City, Iowa 52242	173
R. F. Egerton	University of Alberta, Edmonton, Canada	201
E. Elad	ORTEC, Inc., 100 Midland Road, Oak Ridge, Tennessee 37830	101
T. L. Elsberry	University of California, Los Alamos Scientific Laboratory, P. O. Box 1663, Los Alamos, NM 87545	58
C. A. Evans, Jr.	University of Illinois, Materials Research Laboratory, Urbana, Illinois 61801	128 130
E. J. Fasiska	Materials Consultants & Laboratories, Inc., 1567 Old Abers Creek Road, Monroeville, PA 15146	76
L. C. Feldman	Bell Laboratories, 600 Mountain Avenue, Murray Hill, NJ 07974	89
S. D. Ferris	Bell Laboratories, 600 Mountain Avenue, Murray Hill, NJ 07974	120

H. Lichte	Institut für Angewandte Physik, Universität Tübingen, Tübingen, Germany	20
R. Lichtinger	EDAX International, Inc., P. O. Box 135, Prairie View, IL 60069	107
E. Lifshin	General Electric Company, Corporate Research and Development, P. O. Box 8, Schenectady, NY 12301	104 118
Y. Limoge	Commissariat a L'Energie Atomique, CEN-Saclay, Boite Postale No. 2, 91190 Gif-Sur-Yvette, France	136 141
A. S. Lodhi	Van de Graaff Laboratory, Tehran Nuclear Research Center, Atomic Energy Organization of Iran, P. O. Box 3327, Tehran, Iran	87 94
J. V. P. Long	N.E.R.C. Ion Probe Unit, University of Cambridge, Madingley Rise, Cambridge CB3 OEZ, England	132
G. W. Lorimer	Joint University and UMIST, Department of Metallurgy, University of Manchester, Manchester M1 7HS, England	108
G. V. Lukianoff	IBM System Products Division, East Fishkill Facility, Hopewell Junction, NY 12533	9
A. Lurio	IBM Thomas J. Watson Research Center, P. O. Box 218, Yorktown Heights, NY 10598	90
N. C. MacDonald	Physical Electronics Industries, Inc., 6509 Flying Cloud Drive, Eden Prairie, Minnesota 55343	64
A. D. C. Macknight	Physiologisches Institut der Universitat Munchen, 8 Munchen 2, Pettenkoferstrasse 12, W.-Germany	171
D. M. Maher	Bell Laboratories, 600 Mountain Avenue, Murray Hill, NJ 07974	195 199
A. J. Mardinly	The University of Michigan, Materials and Metallurgical Engineering, Ann Arbor, MI 48109	155
R. B. Marinenko	Analytical Chemistry Division, National Bureau of Standards, Washington, D. C. 20234	148
F. W. Martin	Department of Physics and Astronomy, University of Maryland, College Park, Maryland 20742	85
H. Maruyama	Rigaku Corporation, 12-9-3, Matsubara, Akishima, Tokyo, Japan	54
E. S. Mashkova	Institute of Nuclear Physics, Moscow State University, 117234 Moscow, USSR	79
G. D. Mateescu	Case Western Reserve University, Department of Chemistry, Cleveland, Ohio 44106	63

| K. Murata | University of Osaka Prefecture, College of Engineering, Department of Electronics, Mozu, Umemachi, Sakai, Osaka, Japan | 14 |

| J. Murayama | Sumitomo Metal Industries, Ltd., Central Research Laboratories, Nishinagasu-Hondori, Amagasaki, Japan | 142 |

| R. L. Myklebust | Analytical Chemistry Division, National Bureau of Standards, Washington, D. C. 20234 | 27 96 |

| K. Nagami | University of Osaka Prefecture, College of Engineering, Department of Electronics, Mozu, Umemachi, Sakai, Osaka, Japan | 14 |

| D. A. Nauman | Western Electric, Department 553, P. O. Box 1104, Indianapolis, Indiana 46206 | 77 |

| P. B. Needham, Jr. | College Park Metallurgy Research Center, Bureau of Mines, U. S. Department of the Interior, College Park, MA 20740 | 67 91 |

| D. E. Newbury | National Bureau of Standards, Analytical Chemistry Division, Washington, D. C. 20234 | 27 140 |

| G. Nicaise | Laboratoire D'Histologie et Biologie Tissulaire, Université Claude Bernard, 69621 Villeurbanne, France | 169 |

| C. H. Nielsen | University of Rhode Island, Graduate School of Oceanography, Kingston, RI 02881 | 184 |

| B. Niemann | Universitäts-Sternwarte, Göttingen, Germany | 60 |

| R. E. Ogilvie | Massachusetts Institute of Technology, Department of Materials Science and Engineering, Cambridge, Massachusetts 02139 | 7 28 37 62 |

| K. Ogiso | Rigaku Corporation, 3-9-12, Matsubara, Akishima, Tokyo, Japan | 55 |

| H. Okuzumi | Commissariat a L'Energie Atomique, CEN-Saclay, Boite Postale No. 2, 91190 Gif-Sur-Yvette, France | 13 |

| R. H. Packwood | Physical Metallurgy Research Laboratories, CANMET-EMR, 568 Booth Street, Ottawa, Ontario, Canada | 115 |

| T. A. Pandolfi | Varian Associates, 611 Hansen Way, Palo Alto, CA 94303 | 69 |

| A. D. Pavlova | Institute of Nuclear Physics, Moscow State University, 117234 Moscow, USSR | 79 |

| H. Payrovan | Van de Graaff Laboratory, Tehran Nuclear Research Center, Atomic Energy Organization of Iran, P. O. Box 3327, Tehran, Iran. | 94 |

| F. Pellerin | Commissariat a L'Energie Atomique, CEN-Saclay, Boite Postale No. 2, 91190 Gif-Sur-Yvette, France | 13 |

G. Slodzian	Universite Paris-Sud, Laboratoire de Physique des Solides, Orsay, France	127
H. I. Smith	Lincoln Laboratory, Massachusetts Institute of Technology, Lexington, Massachusetts 02173	160
J. V. Smith	The University of Chicago, Department of the Geophysical Sciences, 5734 S. Ellis Avenue, Chicago, IL 60637	180
K. C. A. Smith	Cambridge University, Engineering Department, Trumpington Street, Cambridge CB2 1PZ, England	6
T. N. Solberg	The University of Chicago, Department of the Geophysical Sciences, 5734 S. Ellis Avenue, Chicago, IL 60637	180
A. P. Somlyo	University of Pennsylvania, Pennsylvania Muscle Institute, 51 North 39th Street, Philadelphia, Pennsylvania 19104	164
A. V. Somlyo	University of Pennsylvania, Pennsylvania Muscle Institute, 51 North 39th Street, Philadelphia, PA 19104	164
G. R. Sparrow	3M Analytical Systems, 3M Center, St. Paul MN 55101	78 81
J. C. H. Spence	Arizona State University, Department of Physics, Tempe, Arizona 85281	192
G. Springer	Falconbridge Nickel Mines Limited, Metallurgical Laboratories, P. O. Box 900, Thornhill, Ontario, Canada	43
P. Statham	University of California, Department of Electrical and Computer Sciences, Berkeley, CA 94720	95 103
I. M. Steele	The University of Chicago, Department of the Geophysical Sciences, 5734 S. Ellis Avenue, Chicago, IL 60637	180
W. Storch	Physikalisches Institut, Universität Würzburg, Würzburg, Germany	88
T. H. Strunk	Harvard Medical School, Biotechnology Resource in Electron Probe Microanalysis, 45 Shattuck Street, Boston, Massachusetts 02115	161
H. Suga	Rutgers University, College of Engineering, P. O. Box 909, Piscataway, NJ 08854	126 157
T. Takagi	Waseda University, Department of Applied Physics, Nishi-Ohkubo 4, Shinjuku-ku, Tokyo 160, Japan	125
M. Tavakoly	Nuclear Medicine Section, Tehran Nuclear Research Center, Atomic Energy Organization of Iran, P. O. Box 3327, Tehran, Iran	94
N. J. Taylor	Varian Associates, 611 Hansen Way, Palo Alto, CA 94303	69

AMR CORPORATION

160 Middlesex Turnpike
Bedford, Massachusetts 01730

Contact: K. A. Lindberg, (616) 275-1400

Product Line: Manufacturer and distributor of scanning electron microscopes and a
  complete line of accessories.

APPLIED RESEARCH LABORATORIES

9545 Wentworth Street
P. O. Box 129
Sunland, California 91040

Contact: Bryce I. Hanna, (213) 352-6011

Product Line: Electron microprobes, ion microprobes, optical emission spectrometers,
  x-ray fluorescence instrumentation.

Sales Offices:
  239 Newburyport Turnpike, Topsfield, MA 01983, (617) 887-8995
  20200 W. Outer Drive, Dearborn, MI 48124, (313) 565-6633
  842 Hamilton Mall, Allentown, PA 18101, (215) 434-7441

BABCOCK & WILCOX COMPANY

Alliance Research Center
P. O. Box 835
Alliance, Ohio 44601

Contact: Alex S. Miller, (216) 821-9110 Ext. 360

CAMECA INSTRUMENTS, INC.

37 Brownhouse Road
Stamford, Connecticut 06902

Contact: Robert J. Hessler, (203) 348-5252

Product Line: Electron probe analyzers, scanning electron microscopes, combination
  SEM/EPA instruments and ion mass analyzers. The IMS-800, a new SIMS instrument,
  has the features of improved performance at a lower price. The new IMS is the
  only direct imaging instrument available. The CAMECA MBX is a flexible combination
  SEM/EMP with an extensive array of accessories.

EDAX INTERNATIONAL, INC.

P. O. Box 135
Prairie View, Illinois 60069

Contact: Frank Mannino, (312) 634-0600

Product Line: Energy dispersive x-ray microanalysis systems (qualitative and
  quantitative) for SEM, TEM, STEM, electron microprobes, supported by SEM
  applications laboratory, training schools, and service.

Sales Offices:
  P. O. Box 194, Pelham, NY 10803, (914) 576-3117
  205 Holly Lane, Orinda, CA 94563, (415) 254-8685
  P. O. Box 2253, Boulder, CO 80306, (303) 443-3610

ETEC CORPORATION

3392 Investment Boulevard
Hayward, CA 94545

Contact: Mrs. P. J. Breton, (415) 783-9210

Product Line: High performance electron microprobes and scanning electron
  microscopes. Modular design allows alternative configurations to be offered with
  a wide range of retrofittable accessories. Instruments are available for manual
  operation, with automated control through dedicated minicomputers, with shielding
  for imaging and analysis of radioactive materials, and for laboratory and
  manufacturing electron beam lithography. Microbeam products include: Autoscan,
  Omniscan, Autoprobe, LEBES, Vistascan, Viewpoint, Biosem, and ADRES.

Sales Offices:
  Midland Park, NJ, (201) 444-4446
  Des Plaines, IL, (312) 297-0114
  Alexandria, VA, (703) 549-1660
  Atlanta, GA, (404(962-0402
  Houston, TX, (713) 488-3562

INTERNATIONAL SCIENTIFIC INSTRUMENTS, INC.

1400 Stierlin Road
Mountain View, California 94043

Contact: Wim Derksen, (415) 965-8600

Product Line:
  ISI has just announced two new scanning electron microscopes: the model SUPER IIIA
  and the model ISI-60. Both low cost instruments offer a wide range of standard
  accessories and operation modes. In addition to these instruments, a complete
  line of scanning electron microscopes suited for any application and any budget.

Sales Offices:
  795 North Mountain Road, Newington, CT 06111, (203) 246-5639
  799 Roosevelt Road, Glen Ellyn, IL 60137, (312) 858-1244
  1840-18 Jerry Way, Norcross, GA 30093, (404) 233-7218
  6655 Hillcroft, Suite 100, Houston, TX 77081, (713) 777-0321
  CAL-SEM Associates, 1926 Pacific Coast Hwy, Redondo Beach, CA 90277, (213)375-5422

JEOL U.S.A. INC.

477 Riverside Avenue
Medford, Massachusetts 02155

Contact: Thomas G. Huber, (617) 391-7240

Product Line: Manufacturer of scanning electron microscopes, transmission electron
  microscopes, scanning electron microprobes, and electron energy loss spectrometers.

Sales Offices:
  Chicago, IL, (312) 825-7164
  Ridge Instruments, Tucker, GA
  828 Mahler Road, Burlingame, CA 94010, (415) 697-9220
  Sequelec Ltd., 5925 Monkland Avenue, Montreal, Quebec, Canada

KEVEX CORPORATION

898 Mahler Road
Burlingame, California 94010

Contact: Richard J. Cushing, (415) 697-6901

Product Line: X-ray energy spectrometers, qualitative and quantitative analysis
  systems. Analytical spectrometers for x-ray, electron energy loss, and associated
  analyses. Si(Li) detectors, special interfaces to scanning electron microprobes,
  transmission electron microscopes and electron microprobes.

Sales Offices:
  P. O. Box 637, Williamstown, Mass. 01267
  9410 Island Road, North Ridgeville, OH 44039
  Toktela, Inc., Box 41, Upperville, VA 22176
  P. O. Box 44, Grapeville, TX 76051

WALTER C. McCRONE ASSOCIATES, INC.

2820 South Michigan Avenue
Chicago, Illinois 60616

Contact: Robert Z. Muggli or Ian M. Stewart, (312) 842-7100

Product Line: Analytical services in disciplines such as: pharmaceuticals,
  forensic sciences, contamination control, metallography, air and water pollution,
  painting and document authentication, and corrosion. Analytical tools available:
  electron and ion microprobes, TEM, SEM, EMMA, ESCA, XRD, XRF, GC-MS, IR-UV and
  optical microscopy.

Sales Office:
  5620 Greenbriar, Houston, TX, (713) 528-7421

MICROSPEC CORPORATION

265-G Sobrante Way
Sunnyvale, California 94086

Contact: Richard C. Wolf or William D. Donnelly, (408) 733-3540

Product Line: WDX-210 wavelength dispersive x-ray spectrometer systems. X-ray microanalysis systems for use as accessories on scanning electron microscopes and other electron beam instruments. Capable of quantitative x-ray analysis of all elements down to beryllium, atomic number 4. Unique design permits attachment to most SEM electron columns without interference to other detectors or operational modes.

3M COMPANY

3M Center
Analytical Systems, Building 209-B
St. Paul, Minnesota 55101

Contact: Thomas W. Kenny, (612) 733-0606

Product Line: Ion scattering spectrometers (ISS) with or without secondary ion mass spectrometer (SIMS) capabilities. A variety of detection and excitation accessories are available.

UNITED SCIENTIFIC CORPORATION
ANALYTICAL INSTRUMENT DIVISION

1400 D Stierlin Road
P. O. Box 1389
Mountain View, California 94042

Contact: William D. Stewart or Patricia Freter, (415) 969-4646

Product Line: Automated x-ray analysis systems, including x-ray tube and isotopes, Si(Li) x-ray detector, and computer-based x-ray analyzer; Si(Li) x-ray detection systems for use on scanning electron microscopes, transmission electron microscopes and electron microprobes; Si(Li) x-ray detectors for basic research; and portable x-ray spectrometers.

Sales Offices:
Scientific Systems Sales Corp., 6901 Jericho Turnpike, Syosset, NY, (516)921-3737
Contemporary Science, Inc., 500 E. Northwest Hwy, Mt. Prospect, IL, (312)255-3793
Scanatlanta Scientific Instruments, 1645 Tully Circle, N.E. Atlanta, GA (404) 321-5454
The Buhrke Company, 2180 Sand Hill Road, Suite 160, Menlo Park, CA, (415)854-5689

ORTEC, INCORPORATED

100 Midland Road
Oak Ridge, Tennessee 37830

Contact: Paul E. Henry, (615) 482-4411 Ext 501

Product Line: Energy dispersive systems for scanning electron microscopes,
  electron microprobes, and transmission electron microscopes. Electronics for
  wavelength dispersive spectrometers.

Sales Offices:
  101 Colonial Drive, Irwin, PA 15624
  P. O. Box 66462, Los Anglels, CA 90066
  P. O. Box 631, Cary, NC 27511
  24222 Via Luisa, Mission Viejo, CA 92675
  4511 Merrie Lane, Bellaire, TX 77401

THE PERKIN-ELMER CORPORATION

411 Clyde Avenue
Mountain View, California 94043

Contact: Ned Shikashio, (415) 961-0461

Product Line: Transmission and scanning electron microscopes and a complete line
  of accessories.

Sales Offices:
  15 Firstfield Road, Gaithersburg, MD, (301) 840-1650
  328 Eisenhower Lane, Lombard, IL (312) 495-9440
  1110 Los Alamitos Boulevard, Los Alamitos, CA (213) 596-2512
  Montreal, Canada, (514) 735-1121

PHILIPS ELECTRONIC INSTRUMENTS INC.

85 McKee Drive
Mahwah, New Jersey 07430

Contact: J. D. Rodgers, (201) 529-3800

Product Line: Transmission electron microscopes, scanning electron microscopes,
  x-ray spectrometer systems, and x-ray diffraction systems.

Sales Offices:
  Main Line Professional Building, Suite A 1104, Rt. 130, Cinnaminson, NJ,
    (609) 829-4454
  7525 Long Avenue, Skokie, IL 60076, (312) 676-1714
  11141 Georgia Avenue, Suite 210, Silver Spring, MD, (301) 933-3002
  3000 Scott Boulevard, Suite 113, Santa Clara, CA 95050, (408) 247-5333
  3760 Cahvenga Boulevard W., Suite 101, North Hollywood, CA 91604, (213) 980-2884

PHYSICAL ELECTRONICS INDUSTRIES, INC.

6509 Flying Cloud Drive
Eden Prairie, Minnesota 55343

Contact: Reginald W. Spiller, (612) 941-5540 Ext. 67

Product Line: ESCA/Auger electron spectrometers, scanning auger microprobes, thin film analyzers, secondary ion mass spectrometers, specialized combination systems, and a broad range of components including electron energy analyzers, sputter-etching systems, specimen manipulators, x-ray generators, UV sources, and sample introduction stages. Physical Electronics also operates an analytical service laboratory for custom surface analysis.

Sales Offices:
960 S. Springfield Avenue, Springfield, NJ 07081, (201) 376-3650
1550 Northwest Hwy., Park Ridge, IL 60068, (312) 297-7730
324 N. Central Expy., Richardson, TX 75080, (214) 231-8861
1922 The Alameda, San Jose, CA 95126, (408) 247-7767
570 Kelley Boulevard, North Attleboro, MA 02760, (617) 695-7504
Empire Towers, Glen Burnie, MD 21061, (301) 761-3053

PRINCETON GAMMA-TECH, INC.

Box 641
Princeton, New Jersey 08540

Contact: Thomas J. Dempsey, (609) 924-7310

Product Line: X-ray energy dispersive and x-ray fluorescence microanalysis systems. An application laboratory and extensive program library.

Sales Offices:
Box 641, Princeton, NJ 08540, (609) 924-7310
701 Morewood Pkwy., Rocky River, OH 44116, (216) 331-0120
21718 Rotherham, Spring, TX 77373, (713) 353-0078
Box 4319, Thousand Oaks, CA 91359, (805) 497-2427

QBI INTERNATIONAL

2034 Golden Gate Avenue
San Francisco, California 94115

Contact: Quentin A. Brown, (415) 929-1622

Product Line: New products and replacement equipment for the SEM and electron microprobe lab including: video components and systems; crystals and detectors; data acquisition systems; and computer systems including automation.

Sales Office:
Box 6A, Russell Road, Bloomington, IN, (812) 336-6244

CHARLES M. TAYLOR CO.

P. O. Box 7087
Stanford, California 94305

Contact: Dr. Charles M. Taylor, (415) 497-3479

Product Line: Different types of multi-element standards for microbeam analysis by
SEM, microprobe, and ion probe using energy, wavelength, and mass spectrometers.
The standards available exceed 135 different metals, alloys, or compounds. Bence-
Albee standards are available. Also supply sample holders for ARL-EMX and
ARL-EMX-SM stages and many types of sample holders and polishing jigs for sample
preparation.

TRACOR NORTHERN

2551 West Beltline Highway
Middleton, Wisconsin 53562

Contact: David C. Wherry, (608) 831-6511

Product Line: Wide range of data processing instrumentation for x-ray analysis.
Products include data acquisition, reduction and automation instruments for
electron microprobe, SEM, TEM, and x-ray fluorescence analysis. Specialize in
computer controlled multichannel analyzers for x-ray energy and wavelength
dispersive spectroscopy, but also produce analysis systems for nuclear, NMR, ESR,
Mossbauer, neutron activation, fast fourier transform and diode array optical
spectroscopies.

Sales Offices:
Scientific Systems Sales Corp., 6901 Jericho Tpk., Syosset, NY 11791, (516) 921-3737
Contemporary Science, Inc., P. O. Box 205, Mt. Prospect, IL 60056, (312) 255-3793
Pulcir, Inc., P. O. Box 357, Oak Ridge, TN 37830, (615) 483-6358
Buhrke Company, 2180 Sand Hill Road, Suite 160, Menlo Park, CA 94025, (415)854-5689
Tracor Europa, Schiphol Airport Amsterdam, Bldg. 106, P. O. Box 7553, Amsterdam,
   The Netherlands, (020) 41-1865

VARIAN ASSOCIATES

Vacuum Division
611 Hansen Way, MS G017
Palo Alto, California 94303

Contact: Douglas R. Hillier, (415) 493-4000 Ext. 2815

Product Line: Analytical surface analysis equipment including Auger spectrometers,
low energy electron diffraction system, UHV vacuum systems and components. A new
automated Auger microprobe features spatial resolution capability of 0.2 microns,
permanent storage of direct energy data, digital processing of Auger data and
clean pumping UHV equipment.

Sales Offices:
25 Route 22, Springfield, NJ 07081, (201) 376-6610
Ste 306, 25000 Euclid Avenue, Euclid, OH 44117, (216) 261-2115
4940 El Camino Real, Los Altos, CA 94022, (415) 968-4936